On the use of computational fluid dynamics for predicting natural displacement ventilation flows through a large enclosure.

Stephen Anthony Howell MEng. (Hons)

This thesis is submitted to the University of Newcastle upon Tyne in partial fulfillment of the requirements for the degree of Doctor of Philosophy

December, 2003

To my dad, who always encouraged me

Abstract

One of the major barriers to the adoption of passive engineering strategies in buildings, such as the provision for ventilation by natural means, is the limitation of the predictive techniques currently available for their design. At present there are three generic predictive methods for buoyancy-driven natural ventilation flows: simple analytical modelling, experimental water-based scale-model testing and computational fluid dynamics (CFD). In addition, there is a shortage of experimental data from real buildings for the validation of such predictive methods.

This work was concerned with current and emerging methods for predicting buoyancy-driven natural displacement ventilation flows within buildings. There were two main objectives for this research; to conduct a thorough experimental study on the natural ventilation flow through a full-scale enclosure representative of a real building with air as the fluid medium in order to provide benchmark data for model validation and to use this benchmark data to identify the preferred method for predicting detailed airflow patterns and thermal stratification for natural displacement ventilation flows within buildings.

A single benchmark case that has received much attention in the past 15 years was identified for the experimental program: the natural displacement ventilation flow through an enclosure with low-level and high-level openings, driven by a point source of buoyancy at floor level. A simple mathematical model was proposed to describe this flow, which was validated experimentally using the small-scale water-based salt-bath technique (Linden et. al., 1990). More recently, another small-scale water-based technique has been developed and used to verify the mathematical models (Chen et. al., 2001). The simple models have also been validated numerically using the CFD approach (Cook, 1998).

Despite the widespread interest in this class of ventilation flow, there had not yet been any experimental validation work reported to the authors knowledge using a full-scale air-based enclosure. To address this, a full-scale air-enclosure was constructed as part of this work and the natural displacement ventilation flow through the space investigated for a number of heat sources and for a range of opening configurations. In particular, the temperature stratification established within the enclosure and the displacement flow rates through the space were monitored and are

presented. The rate of heat transfer through the walls of the enclosure and the surface temperatures of the walls were not recorded.

In terms of its geometrical size, the full-scale experimental enclosure was representative of an occupied space within a real building. Due to budgetary constraints, however, it was constructed from chipboard sheet material rather than more traditional building materials, so that the thermal properties of the walls were not necessarily representative of a real building. Nonetheless, the experimental data presented does form a valuable set of benchmark data for a naturally-driven ventilation flow with air as the fluid medium that does not suffer from geometrical scaling problems.

It was found that the simple analytical models that have been proposed to date and the water-based scale-modelling do not compare favourably with the data from the experimental study. It is thought that this is because the analytical models and the water-based scale-models effectively assume that the only significant transport mechanism within the space is convection, so that the mechanisms of diffusion and thermal radiation are neglected.

Realistic predictions for this type of ventilation flow can be achieved using the CFD technique, which is not affected by scaling restrictions and can be easily extended to model additional physical processes including turbulent transport and thermal radiative transfer. This approach does, however, require further development before it can be used routinely, particularly with respect to the prediction of rates of heat transfer at solid walls. Reasonable agreement with the experimental benchmark data from the full-scale enclosure was observed only when the thermal radiation model was incorporated within the CFD-model. Improved agreement was observed when the radiation absorption characteristics of air due to the content of water vapour in the atmosphere were properly represented. The choice of which turbulence closure should be employed was found to be of secondary importance. It would, therefore, appear that thermal radiative transfer is an important transport mechanism within enclosures with air as the fluid medium.

It is concluded that the CFD-technique has the potential to accurately predict the detailed airflow patterns and thermal stratification for buoyancy-driven natural ventilation flows within buildings where simpler analytical models or water-based experimental methods have limitations. A FV-radiation model should be incorporated into the CFD-model, and the absorption coefficient κ should be in the range $0.10m^{-1} < \kappa < 0.15m^{-1}$. If possible, the rate of heat transfer at the walls of an enclosure should be prescribed in advance, as further work is required before this information can be realistically determined as part of a CFD-simulation.

Acknowledgements

I would like to express my gratitude to a number of organisations and individuals for their help and assistance during the course of my research.

Firstly, I would like to thank Cundall Johnston and Partners LLP and the Engineering and Physical Sciences Research Council (EPSRC) for providing the funding that enabled this research to be undertaken. I would also like to thank the University of Newcastle upon Tyne for providing the facilities necessary to complete this research.

I would like to thank my supervisor Dr. Ian Potts who has been a friendly source of encouragement, support and guidance for almost a decade.

For his invaluable help during the design and construction of the experimental facility my thanks go to Michael Foster. Thanks are also due to Don Ross, Derek Simm and Richard Warhurst for their support during my time in Newcastle upon Tyne.

I am grateful for the assistance from Dr. Malcolm Cook of De Montfort University, Leicester, during the final stages of writing this thesis. I would also like to express my appreciation to Dr. Keith Littlebury and Dr. Elizabeth Garry of Mobius Dynamics for their understanding during the completion of this work.

For his encouragement and guidance during my formative years as a young engineer, I am indebted to David Gandy of Cundall Johnston and Partners LLP. Without his support this research would not have been possible.

For their support throughout my undergraduate and postgraduate studies, my sincere thanks go to Mrs Jacqueline Jenkins and her husband, George Jenkins.

I would also like to thank Iain Charlton, Mark Halpin and Dr. Jo Scott for their many inspirational contributions, encouragement and friendship.

Finally, I would like to thank Ms. Liza Lincoln for her love and affection, and her novel methods to ensure the completion of this thesis.

List of contents

List of figures

List of tables

Nomenclature

A [m^2]	Area
A^* [m^2]	Effective area of the openings to the enclosure
a [m^2]	Area of the individual openings to the enclosure
a_P [kg s^{-1}]	Coefficients in the discretized equations
a_{nb} [kg s^{-1}]	Coefficients in the discretized equations
B [m^4 s^{-3}]	Buoyancy flux
b [m]	Plume radius
C [m K]	Wien's constant
C [ ]	Empirical coefficient for Cambridge mathematical model
c [ ]	Pressure loss coefficient
c [ ]	Coefficient for the best-fit curves for the measured temperature profiles
C_μ [ ]	Empirical turbulence modelling constant
$C_{1\varepsilon}$ [ ]	Empirical constant in the ε-equation
$C_{2\varepsilon}$ [ ]	Empirical constant in the ε-equation
$C_{3\varepsilon}$ [ ]	Empirical constant in the ε-equation
c_d [ ]	Discharge coefficient
c_p [J kg^{-1} K^{-1}]	Specific heat capacity at constant pressure
c_v [J kg^{-1} K^{-1}]	Specific heat capacity at constant volume
D_ϕ [m^2 s^{-1}]	Coefficient of diffusion for flow parameter ϕ
E [J]	Energy
E [ ]	Wall roughness parameter for standard wall function
e [J kg^{-1}]	Specific internal energy
e [m]	Unit vector
e_i [m]	i-th component of the unit vector **e**
f [s^{-1}]	Frequency

G_k [m^{-2} s^{-3}]	Rate of production of the kinetic energy of turbulence per unit mass k
g [m s^{-2}]	Acceleration vector due to gravity
g_i [m s^{-2}]	i-th component of the acceleration vector **g** due to gravity
g' [m s^{-2}]	Reduced gravitational acceleration
H [m]	Height of enclosure
H [m]	Representative length scale
h [J kg^{-1}]	Specific enthalpy
h [W m^{-2} K^{-1} s^{-1}]	Heat transfer coefficient at a solid surface
h [J s]	Planck's constant
h [m]	Height of interface
I [W m^{-2} $srad^{-1}$]	Radiative intensity
I [A]	Electrical current
J_f [kg s^{-1}]	Mass flow rate across a cell face
k [J K^{-1} m^{-1} s^{-1}]	Thermal conductivity
k [m^{-2} s^{-2}]	Kinetic energy of turbulence per unit mass
L [m]	Effective path length
l [m]	Turbulence length scale
l_m [m]	Turbulence mixing length
m [ ]	Coefficient for the best-fit curves for the measured temperature profiles
$\dot{m}$ [kg s^{-1}]	Mass flow rate
N [mol m^{-3}]	Molar density of salt in solution
n [ ]	Unit normal vector
n_i [ ]	i-th component of the unit normal vector **n**
p [Pa]	Pressure
$\tilde{p}$ [Pa]	Piezometric pressure
Pe [ ]	Peclet number
Pr [ ]	Prandtl number
q [W m^{-2} s^{-1}]	Rate of heat flux
R [J kg^{-1} K^{-1}]	Gas constant for a perfect gas

R [Ω]	Electrical resistance
r [m]	Position vector
r_i [m]	i -th component of the position vector **r**
Ra [ ]	Rayleigh number
Re [ ]	Reynolds number
s [ ]	Direction vector
s [ ]	Unit vector
s_ϕ [*varies*]	Source term for flow parameter ϕ
T [K]	Temperature
t [ ]	Unit tangential vector
t [s]	Time
U [m s^{-1}]	Representative velocity scale
u [m s^{-1}]	Velocity vector
u_i [m s^{-1}]	i -th component of the velocity vector **u**
u_m [m s^{-1}]	Turbulence mixing velocity magnitude
u^* [ ]	Dimensionless velocity for standard wall function
V [m^3]	Volume
V [m^3 s^{-1}]	Volume flux
V [V]	Electrical potential or voltage
v [m s^{-1}]	2nd (vertical) component of the velocity vector **u**
v [m s^{-1}]	Component of velocity perpendicular to interference fringes at the LDA meaurement location
x [m]	Position vector
x_i [m]	i-th component of the position vector **x**
y [m]	2nd (vertical) component of the position vector **x**
y_P [m]	Separation of wall-adjacent cell-centre to wall surface
y^* [ ]	Dimensionless distance from wall surface for standard wall function

α [ ]	Directional absorptivity
α [ ]	Plume entrainment coefficient
α_ϕ [ ]	Under-relaxation factor for flow parameter ϕ
β [K^{-1}]	Coefficient of volumetric expansion
Γ_ϕ [kg m^{-1} s^{-1}]	Coefficient of diffusivity for flow parameter ϕ
Δ_ϕ [*varies*]	Source term for deferred correction of higher-order differencing scheme for flow parameter ϕ
δ_{ij} [ ]	Kronecker delta
ε [m^{-2} s^{-3}]	Rate of dissipation of the kinetic energy of turbulence per unit mass k
ε [ ]	Emissivity of a greybody
$\varepsilon(L)$ [ ]	Emittance along a path of gas of length L
ε_{ijk} [ ]	Alternating tensor
θ [rad]	General angle
κ [m^{-1}]	Absorption coefficient
κ_P [m^{-1}]	Planck mean absorption coefficient
λ [m]	Wavelength
μ [kg $m^{-1}s^{-1}$]	Molecular viscosity
μ_T [kg $m^{-1}s^{-1}$]	Turbulent viscosity
Ξ_ϕ [*varies*]	Source term for secondary diffusion on unstructured, non-orthogonal mesh for flow parameter ϕ
ξ [ ]	Non-dimensional height of interface
ρ [kg m^{-3}]	Density
ρ [ ]	Directional reflectivity
σ [W m^{-2} K^{-4}]	Stefan-Boltzmann's constant
σ_s [m^{-1}]	Scattering coefficient
σ_ϕ [ ]	Schmidt number for flow parameter ϕ
τ [ ]	Directional transmittivity
τ_{Wall} [Pa]	Shear stress at a wall surface

Φ [J m^{-3} s^{-1}]	Rate of dissipation of energy due to viscous effects
$\Phi(\mathbf{s}_i, \mathbf{s})$ [ ]	Scattering phase function
ϕ [*varies*]	General flow parameter
ψ [*varies*]	General flow parameter
ω [s^{-1}]	Vorticity vector
ω_i [s^{-1}]	i-th component of the vorticity vector ω
ω [srad]	General solid angle

1.0 Introduction

1.1 Background

Almost half of the total energy consumption in the UK is used in buildings, and this is dominated by electricity use for heating, ventilation, air-conditioning and lighting systems (CIBSE, 1998). Clearly, if more environmentally friendly strategies could be employed for the design of the building services, such as the provision for ventilation by natural means, then this energy consumption, together with the related emissions of carbon dioxide that account for three-quarters of all greenhouse gas emissions, could be significantly reduced.

One of the major barriers to the adoption of such passive engineering schemes, however, is the limitation of the predictive techniques currently available for their design. At present there are three generic predictive methods for buoyancy-driven natural ventilation flows: simple analytical modelling, experimental water-based scale-model testing and computational fluid dynamics (CFD). There are, however, limitations with each technique. Together with a shortage of experimental data from real buildings for the validation of such predictive methods, it is perhaps not surprising that a building developer would not wish to embrace an energy efficient design if it cannot be shown to work before the construction stage.

One case that has received much attention over the past 15 years is the natural displacement ventilation flow through an enclosure with low-level and high-level openings driven by a point source of buoyancy at floor level. A simple analytical model, henceforth dubbed the Cambridge mathematical model, was proposed to describe this flow by Linden et. al. (1990). Numerous extensions to this model of increasing complexity have been and continue to be reported, many of which were included in the recent review by Linden (1999). The Cambridge model has been validated experimentally using the salt-bath technique (Linden et. al., 1990), a small-scale water-based method in which saline solution is used to generate density differences and drive the displacement flow. More recently, another small-scale water-based technique that uses electrolytically generated fine hydrogen bubbles to generate density differences and drive the flow has been developed and used to verify

the Cambridge mathematical model (Chen et. al., 2001). In addition, the Cambridge model has also been validated numerically using the CFD approach (Cook, 1998).

Despite the widespread interest in this class of ventilation flow, all of the previous experimental validation work to the authors knowledge had used small-scale water-based methods rather than considering the flow through a full-scale enclosure with air as the fluid medium. Another natural convection flow that has received significantly more attention in the past is the flow within a differentially heated thermal cavity. It is known from the experimental work for this arrangement, however, that the observed stratification within the cavity is dependent upon whether the fluid medium is water or air, even for apparently dynamically similar arrangements, and it has been suggested that this difference may be due to the absence of thermal radiation effects in the water-based experiments (Olson et. al., 1990). It is, therefore, unclear whether the water-based salt-bath technique and fine-bubble technique used to verify the Cambridge model are representative of the flow in a real building, where the fluid medium is air.

1.2 Aims of this research

This work was concerned with current and emerging methods for predicting buoyancy-driven natural displacement ventilation flows within buildings. There were two main objectives for this research –

- to conduct a thorough experimental study on the natural ventilation flow through a full-scale enclosure representative of a real building with air as the fluid medium in order to provide benchmark data for model validation, and
- to use this benchmark data to identify the preferred method for predicting detailed airflow patterns and thermal stratification for natural displacement ventilation flows within buildings.

1.3 Outline of this thesis

Following this introduction, the governing concepts that describe the physical processes that occur in real buildings are introduced in §2.0, and an introduction to the science of CFD relevant to the natural displacement ventilation flow under consideration, together with a summary of the use of CFD within building design is provided in §3.0. The Cambridge mathematical model and the related experimental salt-bath and fine-bubble techniques are considered in §4.0, together with a summary of other important experimental results.

The full-scale test enclosure constructed as part of this work and the experimental principles and apparatus employed to measure the flow are described in full in §5.0, with the experimental results provided and discussed in §6.0. The results of the CFD study are presented and discussed in §7.0, and the conclusions from the present work are summarized in §8.0, together with some suggestions for further work. For reference purposes, the experimental data from the full-scale air enclosure and all of the predictions from the CFD study are provided as addenda to this thesis.

2.0 Governing concepts for air flows in buildings

2.1 Introduction

This chapter provides an introduction to the governing concepts for air-flows observed in buildings, upon which all of the remaining analysis can be based. In §2.2, the Lagrangian and Eulerian frameworks are introduced, the former being appropriate if each individual particle within a flow of interest is monitored, and the latter allowing specific flow variables to be monitored at a fixed point in space. The governing equations for the flow of a non-isothermal Newtonian fluid are then introduced in Eulerian formulation in §2.3, together with some additional relations that allow the governing equations to be simplified.

Introductions into the phenomena of turbulence and of thermal radiation are presented in §0 and §2.5 respectively, as they are both major transfer mechanisms for flows encountered within real buildings. A summary of the plume theory due to Morton et. al. (1956), which is used later in this work, is also provided in §2.6.

Finally, the coupling between the thermal stratification within and external to an enclosure and the ventilation flow rate through the enclosure is demonstrated in §2.7.

2.2 Lagrangian and Eulerian frameworks

The governing equations of fluid motion for any fluid are derived from three fundamental conservation laws of physics, namely the conservation of mass, linear momentum and energy. Each conservation law applies to a given quantity or parcel of matter, which is easily identifiable. Considering the physics of individual fluid particles is called Lagrangian formulation, and it is usual to use this approach when studying rigid-body dynamics. Using this approach, it is appropriate to express time derivatives of any property ϕ using the substantial derivative $d\phi / dt$, which is the time derivative observed moving with the fluid parcel.

When studying the flow of a fluid, which is assumed to be a continuum, this method to predict the motion of millions of infinitesimal fluid parcels becomes extremely cumbersome. Instead it is more convenient to use Eulerian formulation

where the flow field is described at each point in space as a function of position and time. With Eulerian formulation, it is appropriate to use the local time derivative $\partial\phi/\partial t$, which is the observed rate of change of the fluid property at any particular fixed position in space.

The substantial and local time derivatives are related by

$$\frac{d\phi}{dt} = \frac{\partial\phi}{\partial t} + u_i \frac{\partial\phi}{\partial x_i}, \tag{2.2.1}$$

where $u_i\,\partial\phi/\partial x_i$ is the *convective* rate of change of ϕ and is due to the transport of the fluid parcel to a new position

2.3 Governing equations for non-isothermal Newtonian fluid flow

2.3.1 Conservation laws

The governing equations for fluid flow stem from the fundamental conservation laws of physics. Using index notation in Cartesian co-ordinates the governing equations in Eulerian formulation are (Batchelor, 1967)

- Continuity equation (Conservation of mass):

$$\frac{\partial\rho}{\partial t} + \frac{\partial(\rho u_i)}{\partial x_i} = 0. \tag{2.3.1}$$

- Navier-Stokes equation (Conservation of linear momentum):

$$\frac{\partial(\rho u_i)}{\partial t}\mathbf{e}_i + \frac{\partial(\rho u_j u_i)}{\partial x_j}\mathbf{e}_i = \frac{\partial}{\partial x_j}\left(\mu\left(\frac{\partial u_i}{\partial x_j} + \frac{\partial u_j}{\partial x_i}\right)\right)\mathbf{e}_i + \rho g_i \mathbf{e}_i - \frac{\partial p}{\partial x_i}\mathbf{e}_i. \tag{2.3.2}$$

- Energy equation (Conservation of internal energy):

$$\frac{\partial(\rho\theta)}{\partial t} + \frac{\partial(\rho u_i \theta)}{\partial x_i} = \frac{\partial}{\partial x_i}\left(k\frac{\partial T}{\partial x_i}\right) - p\frac{\partial u_i}{\partial x_i} + \Phi. \tag{2.3.3}$$

The governing equations presented are quite general, since only two assumptions have thus far been introduced: the constitutive laws for a Newtonian, viscous fluid, and a Fourier fluid for the conduction of heat respectively.

2.3.2 Additional relations

In their current form the governing conservation laws cannot be solved because there remain more unknown variable quantities than governing equations. It is

therefore necessary to introduce additional thermodynamic relations in order to close the system of equations.

If it is assumed that the fluid behaves as a perfect gas in thermodynamic equilibrium, then the perfect gas law can be used to prescribe the pressure p in terms of the other thermodynamic properties of the fluid, density ρ and temperature T

$$p = \rho R T \,, \tag{2.3.4}$$

where R is the gas constant for the fluid under consideration.

In addition, the specific heat capacity at constant volume c_v for a perfect gas, which is usually considered to be a constant, relates the specific internal energy of the gas e at a point to its temperature T at that point

$$e = c_v T \,. \tag{2.3.5}$$

Alternatively, the specific heat capacity at constant pressure c_p for a perfect gas relates the specific enthalpy of the gas h at a point to its temperature T

$$h = c_p T \,, \tag{2.3.6}$$

where the specific enthalpy is defined as

$$h = e + \frac{p}{\rho} \,. \tag{2.3.7}$$

2.3.3 Simplified governing equations for buoyancy driven flows

A number of assumptions that are valid for the buoyancy driven flows encountered in buildings can significantly simplify the governing equations.

2.3.3.1 The continuity equation

If any changes in the density of the fluid are assumed to be small, then the velocity field is solenoidal

$$\frac{\partial u_i}{\partial x_i} = 0 \,. \tag{2.3.8}$$

2.3.3.2 Navier-Stokes equation

For an effectively incompressible fluid where changes in the fluid density $\Delta\rho$ are small in comparison to the actual density ρ_0, it is often beneficial to work in terms of the piezometric pressure field $\tilde{p}$, since this parameter remains constant for a body of fluid with a uniform density. The piezometric pressure is defined as

$$\tilde{p} = p - \rho_0 g_i x_i , \tag{2.3.9}$$

where p is the static pressure and $\rho_0 g_i x_i$ is the hydrostatic head measured from some chosen datum. Differentiation with respect to x_i yields

$$\frac{\partial \tilde{p}}{\partial x_i} = \frac{\partial p}{\partial x_i} - \rho_0 g_i . \tag{2.3.10}$$

Substitution of this into (2.3.2), with the assumption of a solenoidal velocity field leads to

$$\frac{\partial(\rho_0 u_i)}{\partial t}\mathbf{e}_i + \frac{\partial(\rho_0 u_i u_j)}{\partial x_j}\mathbf{e}_i = \frac{\partial}{\partial x_j}\left(\mu \frac{\partial u_i}{\partial x_j}\right)\mathbf{e}_i + (\rho - \rho_0) g_i \mathbf{e}_i - \frac{\partial \tilde{p}}{\partial x_i}\mathbf{e}_i . \tag{2.3.11}$$

2.3.3.3 The energy equation

Introducing the specific enthalpy $h = c_p T$ into the energy equation (2.3.3), for an incompressible fluid with density ρ_0 leads to

$$\frac{\partial(\rho_0 c_p T)}{\partial t} + \frac{\partial(\rho_0 u_i c_p T)}{\partial x_i} = \frac{\partial}{\partial x_i}\left(k \frac{\partial T}{\partial x_i}\right) + \frac{\partial p}{\partial t} + u_i \frac{\partial p}{\partial x_i} + \Phi . \tag{2.3.12}$$

For an incompressible flow, however, any variations in pressure will be negligible in comparison to the absolute value of the ambient pressure, so that it is reasonable to assume that any contribution from the substantial derivative of pressure (the second and third terms on the R.H.S) is insignificant. Neglecting also the dissipation term Φ leads to the equation for the conservation of energy for an incompressible flow

$$\frac{\partial(\rho_0 T)}{\partial t} + \frac{\partial(\rho_0 u_i T)}{\partial x_i} = \frac{\partial}{\partial x_i}\left(\frac{k}{c_p}\frac{\partial T}{\partial x_i}\right). \tag{2.3.13}$$

2.3.4 Vorticity equation

The vorticity ω is a vector quantity that describes the degree of rotation throughout the fluid domain, and is defined as the curl of the velocity field

$$\omega_i = \varepsilon_{ijk} \frac{\partial}{\partial x_j} u_k . \tag{2.3.14}$$

The vorticity equation can be derived from the Navier-Stokes equation

$$\frac{\partial(\rho_0 \omega_i)}{\partial t}\mathbf{e}_i \frac{\partial(\rho_0 u_j \omega_i)}{\partial x_j}\mathbf{e}_i = \frac{\partial}{\partial x_j}\left(\mu \frac{\partial \omega_i}{\partial x_j}\right)\mathbf{e}_i + \frac{\partial(\rho_0 \omega_j u_i)}{\partial x_j}\mathbf{e}_i . \tag{2.3.15}$$

2.4 Turbulence

2.4.1 Introduction

For the case of a laminar fluid flow, any random perturbations which arise in the flow due to naturally occurring imperfections are damped out due to the viscous forces within the fluid, and the flow remains in the stable, laminar state. In contrast, however, if the inertial forces associated with the perturbations are significant enough to overcome the viscous damping effects, then the flow is unstable and the flow will be in the turbulent state. Indeed, most flows of practical interest, both naturally occurring flows and those arising under engineered conditions, including ventilation airflows within buildings, fall in to the latter category of turbulence.

Turbulent flows exhibit many distinguishing characteristics (Tennekes and Lumley, 1972). They are observed to be randomly unsteady and irregular, so that the deterministic prediction of the instantaneous value of a fluid parameter such as fluid velocity at a point becomes impossible. The random fluctuations always occur in all three spatial dimensions, even when the mean flow varies only in one or two dimensions.

A particle subjected to the random fluctuations will on average increase its separation from a nominal starting position. This can be determined from a simple geometrical argument, and is known as the 'random walk hypothesis'. As a result, turbulent flows exhibit enhanced rates of diffusivity, in terms of mass, momentum and heat transfer.

The turbulent fluctuations are observed to exist over a wide range of length and time scales. The longest length scale is usually comparable to some characteristic length within the physical fluid domain. The spectrum of turbulent wavelengths then extends continuously to a minimum length scale.

Turbulent flows are highly rotational and are characterised by high levels of fluctuating vorticity. Indeed, the explanation for the continuous spectrum of length scales can be deduced from the transport equation for vorticity (2.3.15)

$$\frac{\partial(\rho_0\omega_i)}{\partial t}\mathbf{e}_i\frac{\partial(\rho_0 u_j\omega_i)}{\partial x_j}\mathbf{e}_i=\frac{\partial}{\partial x_j}\left(\mu\frac{\partial\omega_i}{\partial x_j}\right)\mathbf{e}_i+\frac{\partial(\rho_0\omega_j u_i)}{\partial x_j}\mathbf{e}_i.$$

The terms on the L.H.S. are the familiar transient and convection terms that describe the rate of change of vorticity and the effect of the mean flow upon the vorticity field. The first term on the R.H.S. represents the viscous diffusion of vorticity down a vorticity gradient.

Consider next the second term on the R.H.S. If the *i*-direction and the *j*-direction are not aligned, the *i*-component of the vorticity ω_i receives a contribution from ω_j due to the effect of the velocity gradient $\partial u_i/\partial x_j$. This has the effect of twisting the vortex with vorticity originally in the *j*-direction, so that it becomes aligned with the *i*-direction. This is called 'vortex twisting' and is illustrated in Figure 2.1.a.

If the *i*-direction and the *j*-direction are aligned and $\partial u_i/\partial x_i$ is positive, the vortex is elongating in the direction of the vorticity and the *i*-component of the vorticity ω_i will increase. Furthermore, from continuity the cross-section of the vortex must decrease. This is 'vortex stretching' and is illustrated in Figure 2.1.b.

If the *i*-direction and the *j*-direction are aligned and $\partial u_i/\partial x_i$ is negative, the vortex is squashed and the *i*-component of the vorticity ω_i will decrease. From continuity the cross-section of the vortex will therefore increase. This is 'vortex compression'.

In the case of laminar flows, where the flow is stable, the mechanisms of vortex stretching and vortex compression are equally likely to occur. If the flow is turbulent, however, then two points close together on a vortex line will tend to move apart due to the random walk hypothesis, so that vortex stretching becomes more dominant than vortex compression. As a consequence of this, the cross-section and corresponding length scale of the vorticity for a turbulent flow will tend to continuously decrease to smaller and smaller length scales, hence the complete spectrum of turbulence wavelengths.

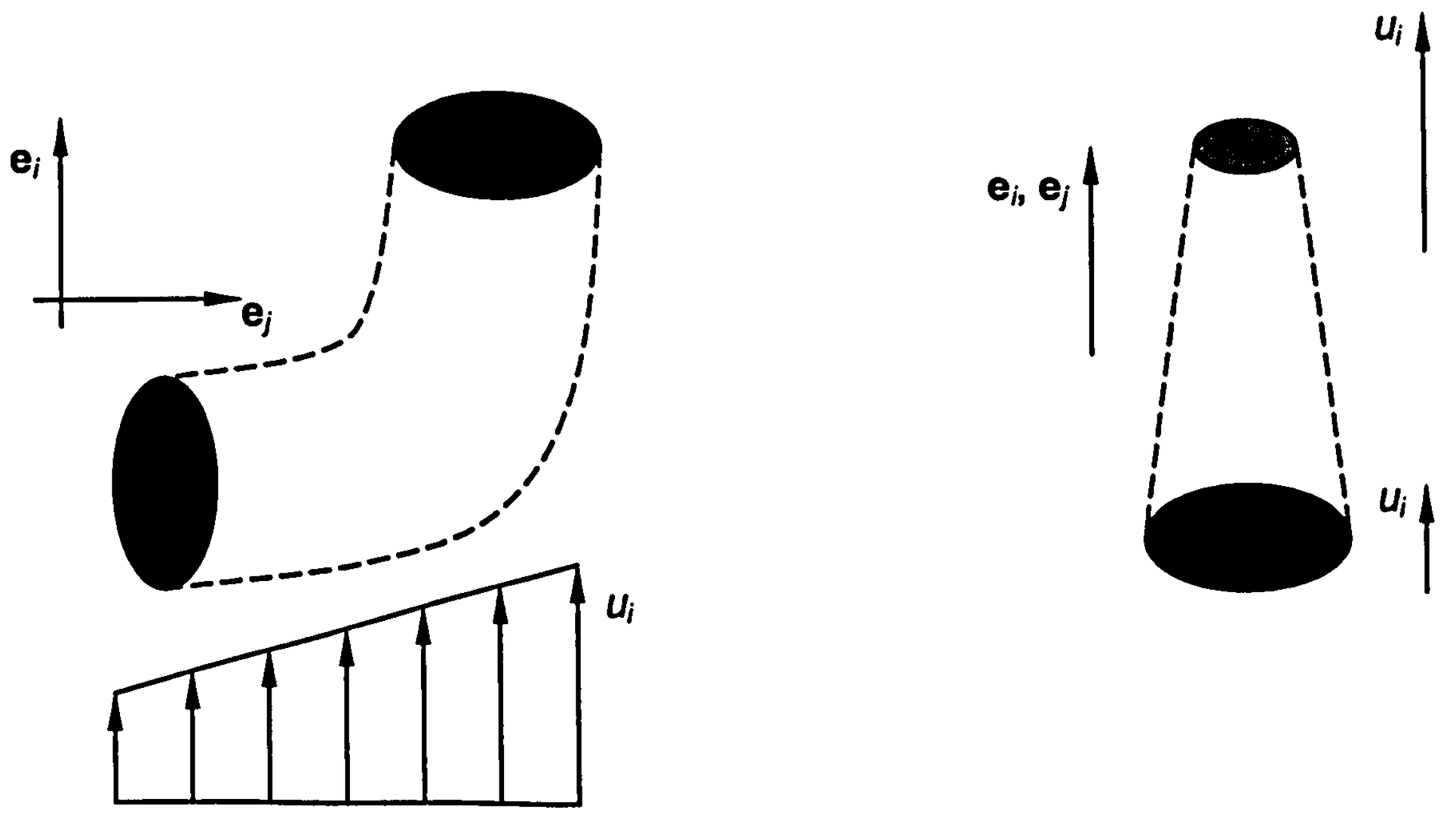

Figure 2.1 - a) Vortex twisting b) vortex stretching.

At the largest length scales of turbulence the flow is essentially inviscid. As the length scale is decreased, however, the effects of viscous diffusion become

increasingly significant. The viscous actions tend to diffuse vorticity, counteracting the amplifying and scale-reducing effects of vortex stretching, thus enforcing a lower limit upon the smallest scale of turbulence.

In addition, as the viscous effects become more important, the kinetic energy associated with the turbulent structures is increasingly converted and dissipated into thermal energy. Turbulent flows are therefore always dissipative. They require a continuous supply of energy from the primary flow, to compensate for the viscous losses at the small scale. This energy is extracted from the primary flow and supplied to the largest-scale turbulent structures, and is then cascaded down through the entire turbulence spectrum of length scales due to vortex stretching. The rate at which energy is supplied to the turbulent motion is entirely dependent upon its interaction with the primary flow at the large scale, and only this amount of energy can be cascaded down to the smallest scales and dissipated. Although viscous effects are the cause of dissipation, they cannot control the rate of dissipation. Rather, the length scale of the smallest eddy structure in a turbulent flow must adjust in order to dissipate all of the energy supplied from the larger scales.

The instantaneous flow quantities in any turbulent flow are described by the same governing equations as laminar flows, namely the continuity equation (2.3.8), the Navier-Stokes equation (2.3.11) and the energy equation (2.3.13). The instantaneous random characteristics of a turbulent flow, however, are rarely of interest to the engineer. What are usually of relevance are the mean values of the flow parameters, such as the mean velocity and mean pressure. To this end, Reynolds (1895) adopted a statistical approach to develop a system of equations that govern the mean flow quantities, rather than the actual, instantaneous quantities. His approach was to decompose each instantaneous fluid quantity into an average and fluctuating component, as described in the sections that follow. Furthermore, since there are no new assumptions introduced into the new 'Reynolds-averaged' equations of motion, they remain exact. They are, however, no longer closed.

2.4.2 Reynolds-averaging

Reynolds' approach was to express the instantaneous value of any flow parameter ϕ at a particular point $\mathbf{x}$ and time t in a turbulent flow as the sum of the mean value $\bar{\phi}$ and the fluctuation from the mean value ϕ'

$$\phi(\mathbf{x},t)=\bar{\phi}(\mathbf{x},t)+\phi'(\mathbf{x},t). \qquad (2.4.1)$$

For a general turbulent flow, where the boundary conditions may change with time, the practice of 'ensemble averaging' should be adopted (Wilcox, 1998). This is the value that would be obtained by averaging the individual values at that location in space and time from N identical experiments

$$\bar{\phi}(\mathbf{x},t)=\lim_{N\to\infty}\frac{1}{N}\sum_{1}^{N}\phi(\mathbf{x},t). \tag{2.4.2}$$

For the special case of stationary turbulence, where on average the turbulence at a location does not vary with time, the ensemble average is identical to the time average at that point

$$\bar{\phi}(\mathbf{x})=\lim_{\Delta t\to\infty}\frac{1}{\Delta t}\int_{t}^{t+\Delta t}\phi(\mathbf{x}). \tag{2.4.3}$$

Furthermore, by definition, the ensemble average of the fluctuation from the mean value is zero

$$\bar{\phi'}(\mathbf{x},t)=\lim_{N\to\infty}\frac{1}{N}\sum_{1}^{N}\phi'(\mathbf{x},t)=0. \tag{2.4.4}$$

As a consequence of the definitions introduced above, it is valid to say that for the general flow parameters ϕ and ψ

$$\overline{\phi(\mathbf{x}_\phi,t_\phi)+\psi(\mathbf{x}_\psi,t_\psi)}=\bar{\phi}(\mathbf{x}_\phi,t_\phi)+\bar{\psi}(\mathbf{x}_\psi,t_\psi), \tag{2.4.5}$$

and

$$\overline{\phi(\mathbf{x}_\phi,t_\phi)\cdot\psi(\mathbf{x}_\psi,t_\psi)}=\bar{\phi}(\mathbf{x}_\phi,t_\phi)\cdot\bar{\psi}(\mathbf{x}_\psi,t_\psi), \tag{2.4.6}$$

where $\mathbf{x}_\phi$ and t_ϕ are the position and time respectively at which the ensemble average is evaluated for the parameter ϕ, and $\mathbf{x}_\psi$ and t_ψ are the position and time at which the average is evaluated for the parameter ψ.

Furthermore, the fluctuating component of a fluid parameter ϕ is statistically independent of the mean component of any other fluid parameter ψ, such that

$$\overline{\phi'(\mathbf{x}_\phi,t_\phi)\cdot\psi(\mathbf{x}_\psi,t_\psi)}=0, \tag{2.4.7}$$

for any turbulent flow. In contrast, however, the fluctuating component of ϕ is not, in general, statistically independent of the fluctuating component of ψ, so that

$$\overline{\phi'(\mathbf{x}_\phi,t_\phi)\cdot\psi'(\mathbf{x}_\psi,t_\psi)}\neq 0, \tag{2.4.8}$$

although the statistical correlation does decrease as the spatial separation $\mathbf{x}_\phi - \mathbf{x}_\psi$ or the temporal separation $t_\phi - t_\psi$ is increased.

2.4.3 The Reynolds-averaged continuity equation

Substituting the Reynolds decomposition for the instantaneous velocity (2.4.1) into the continuity equation (2.3.8), and then taking the ensemble average leads to the Reynolds-averaged continuity equation

$$\frac{\partial \overline{u}_i}{\partial x_i} = 0 . \tag{2.4.9}$$

It is observed that this result is identical in form to the general continuity equation used to describe the instantaneous velocity field in a fluid flow.

2.4.4 The Reynolds-averaged Navier-Stokes equation

Introducing the relation (2.4.1) into the instantaneous Navier-Stokes equation (2.3.11), and then taking the average of each term leads to

$$\rho_0 \frac{\partial \overline{u}_i}{\partial t}\mathbf{e}_i + \rho_0 \frac{\partial (\overline{u}_i \overline{u}_j)}{\partial x_j}\mathbf{e}_i = \frac{\partial}{\partial x_j}\left(\mu \frac{\partial \overline{u}_i}{\partial x_j} - \rho_0 \overline{u_i' u_j'} \right)\mathbf{e}_i + (\overline{\rho} - \rho_0) g_i \mathbf{e}_i - \frac{\partial \overline{p}}{\partial x_i}\mathbf{e}_i . \tag{2.4.10}$$

This result is the Reynolds-averaged Navier-Stokes equation. It is identical in form to the Navier-Stokes equation for the instantaneous flow parameters, with the exception of the Reynolds stress $-\rho_0 \overline{u_i' u_j'}$. This term exists as a consequence of the non-linear term in the Navier-Stokes equation, because the velocity fluctuations u_i' and u_j' are to some extent correlated (2.4.8). The term is an extra variable for which there is no governing equation, hence the turbulence closure problem.

2.4.5 The Reynolds-averaged energy equation

For any turbulent buoyancy driven flow, the effects of velocity and temperature fluctuations due to the turbulence must be accounted for. A similar Reynolds-averaging approach is adopted for the energy equation, where the temperature field T is represented as the sum of the mean temperature $\overline{T}$ and the fluctuation from the mean T'. This leads to

$$\frac{\partial(\rho_0\overline{T})}{\partial t}+\frac{\partial(\rho_0\overline{u}_i\overline{T})}{\partial x_i}=\frac{\partial}{\partial x_i}\left(\frac{k}{c_p}\frac{\partial\overline{T}}{\partial x_i}-\rho_0\overline{u_i'T'}\right). \tag{2.4.11}$$

This equation is similar to the equation for instantaneous temperature field (2.3.13), with the addition of the term comprising the Reynolds heat flux $-\rho_0\overline{u_i'T'}$, which represents the enhanced transport of energy due to turbulent fluctuations. As with the Reynolds stresses that appear in the Reynolds-averaged Navier-Stokes equation, this term is an extra variable for which there is no extra equation.

2.4.6 The Reynolds stress equation

In fact, it is possible to derive an equation to describe the Reynolds stress tensor directly from the Navier-Stokes equation, but this will contain further new variables for which there are no equations.

The Reynolds stress equation is obtained by multiplying the entire Navier-Stokes equation by the instantaneous turbulent fluctuation $u_j'\mathbf{e}_j$ and then taking the average of each term. This leads to the result

$$\frac{\partial(\rho_0\overline{u_i'u_j'})}{\partial t}+\overline{u}_k\frac{\partial(\rho_0\overline{u_i'u_j'})}{\partial x_k}=-\frac{\partial(\rho_0\overline{u_i'u_j'u_k'})}{\partial x_k}$$

$$-\left(\rho_0\overline{u_j'u_k'\frac{\partial\overline{u}_i}{\partial x_k}}+\rho_0\overline{u_i'u_k'\frac{\partial\overline{u}_j}{\partial x_k}}\right)-\left(\overline{\rho'u_j'}g_i+\overline{\rho'u_i'}g_j\right) \tag{2.4.12}$$

$$-\left(\overline{u_j'\frac{\partial p'}{\partial x_i}}+\overline{u_i'\frac{\partial p'}{\partial x_j}}\right)+\mu\left(\frac{\partial^2(\overline{u_i'u_j'})}{\partial x_k^2}-2\overline{\frac{\partial u_i'}{\partial x_k}\frac{\partial u_j'}{\partial x_k}}\right).$$

This expression is a transport equation for the Reynolds stress $-\rho_0\overline{u_iu_j}$. This result, however, contains a new unknown triple product $\overline{u_iu_ju_k}$, so that the system of equations remains unclosed. Indeed, each time a transport equation is derived for a 'moment' of the turbulent fluctuations, a new unknown variable is introduced. This is the essence of the turbulent closure problem.

2.5 Thermal radiation

All matter at a finite absolute temperature emits energy by means of electromagnetic radiation as the individual atoms and molecules that constitute the matter attempt to lower their own internal energies. The emission spans a continuous

spectrum of wavelengths that depend upon the temperature of the emitting material. At temperatures below 1000°C the emission is associated almost entirely with infrared wavelengths, so that it manifests itself as a transfer of thermal energy.

In contrast to the other modes of thermal energy transfer, conduction and convection, radiative transfer does not require the presence of an intermediate medium to transport the energy, but is in fact impeded by the presence of a medium. The degree to which the radiative transfer is attenuated depends upon the properties of the intermediate medium. Many solids are essentially opaque to thermal radiation, so that any incident radiation can only penetrate a small distance into the surface of the material. These substances are described as adiathermanous and thermal radiation is considered to be a surface phenomenon. For materials that are transparent to thermal radiation, attenuation is less significant. Such media are described as diathermanous and thermal radiation is considered to be a volumetric phenomenon.

2.5.1 Radiative intensity

Whilst radiation is emitted by matter in all possible directions, the directional distribution of the radiation may not be uniform in all directions. To properly account for the directional dependence of the radiation field, it is necessary to introduce the concept of radiative intensity *I*.

The spectral radiative intensity I_λ at some position **r** is defined as the rate at which radiative energy *E* within the unit wavelength interval $d\lambda$ and in the direction of the unit vector **s** passes through the unit area *dA* per unit solid angle $d\omega$. As illustrated in Figure 2.2, the geometry is such that the unit solid angle $d\omega$ is centred on the unit vector **s**, which is itself normal to the unit area *dA*. Furthermore, the unit wavelength interval $d\lambda$ is centred on the wavelength λ. The spectral radiative intensity I_λ is, therefore, a function of position vector **r**, direction vector **s** and wavelength λ

$$I_\lambda(\mathbf{r},\mathbf{s},\lambda) = \frac{dE}{dt \cdot d\lambda \cdot dA \cdot d\omega}. \tag{2.5.1}$$

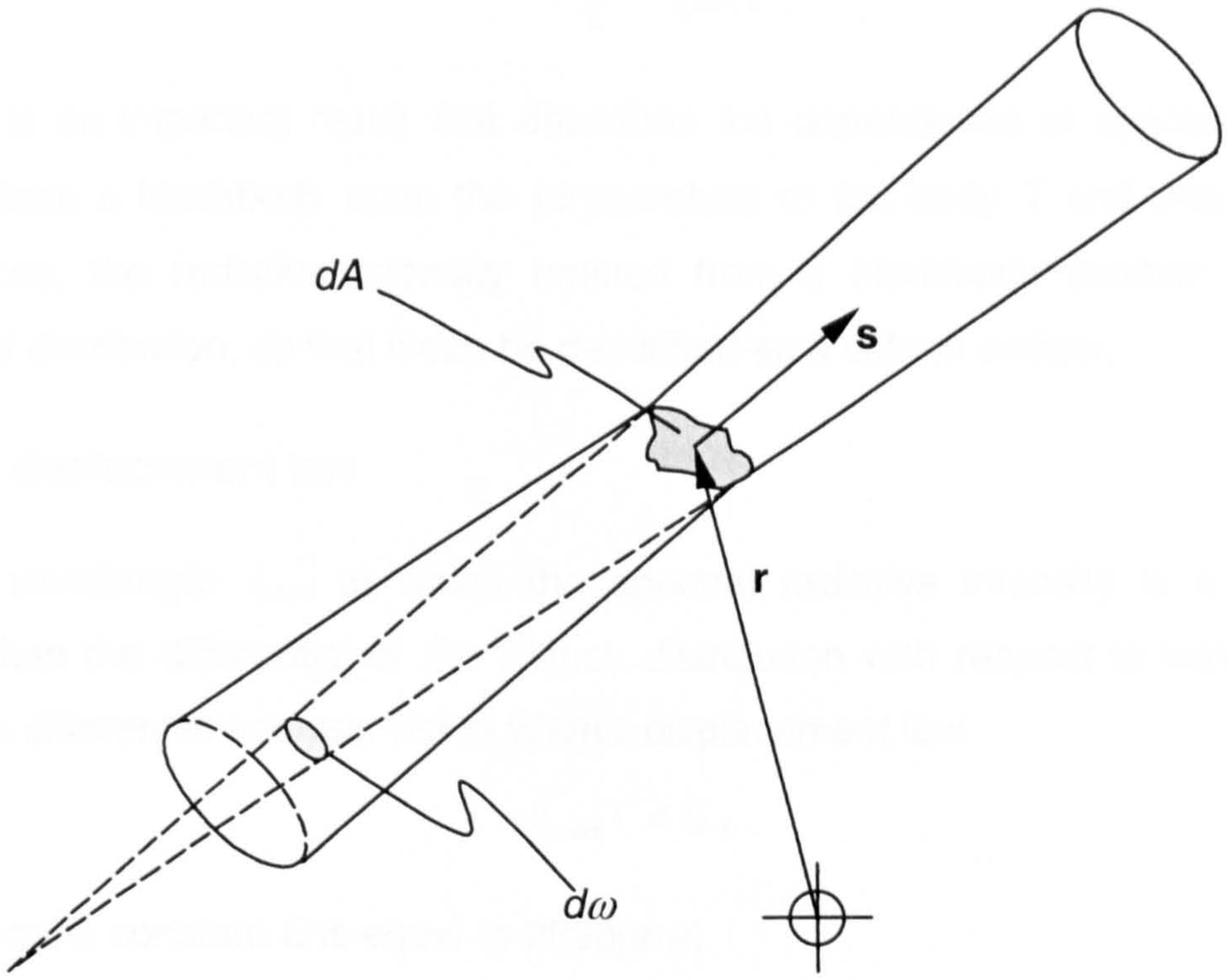

Figure 2.2 - Geometry for definition of spectral radiative intensity I_λ

The total radiative intensity I is simply the sum of the spectral radiative intensities over all possible wavelengths and is only dependent upon position vector **r** and direction vector **s**

$$I(\mathbf{r},\mathbf{s}) = \int_0^\infty I_\lambda(\mathbf{r},\mathbf{s},\lambda)d\lambda = \frac{dE}{dt \cdot dA \cdot d\omega}. \tag{2.5.2}$$

2.5.2 Blackbody radiation

A blackbody is an ideal body of matter that absorbs and retains all radiation that is incident upon it. Furthermore, as a consequence of Kirchhoff's law it follows that a blackbody in thermodynamic equilibrium must also emit an equal amount of energy in order for that equilibrium to be maintained.

2.5.2.1 The Planck distribution

The spectral distribution of blackbody emission can be determined from a consideration of quantum mechanics, and was first proposed by Planck (Modest, 1993)

$$I_{\lambda b}(\lambda,T)=\frac{2hc_0^2}{\lambda^5\left[\exp\left(\frac{hc_0}{\lambda kT}\right)-1\right]}. \tag{2.5.3}$$

This is an important result that describes the dependence of spectral radiative intensity from a blackbody upon the temperature of the body T and wavelength λ. Furthermore, the radiative intensity emitted from a blackbody exhibits a uniform directional distribution, so that it can be described as a diffuse emitter.

2.5.2.2 Wien's displacement law

The wavelength λ_{max} at which the spectral radiative intensity is a maximum occurs when the differential of the Planck distribution with respect to wavelength is zero. This differential analysis yields Wien's displacement law

$$\lambda_{max}T = C, \tag{2.5.4}$$

where the constant C is equal to 2898μmK.

2.5.2.3 The Stefan-Boltzmann law

The total radiative intensity I_b from a blackbody can be determined by integrating the Planck distribution over all possible wavelengths. The result is the Stefan-Boltzmann law

$$I_b(T)=\int_0^\infty I_\lambda(\lambda,T)=\frac{\sigma}{\pi}T^4, \tag{2.5.5}$$

where the Stefan-Boltzmann constant σ is equal to 5.671×10^{-8} W/(m^{2}K^4). From this relation it is apparent that the total radiative intensity from a blackbody is dependent only upon the absolute temperature of the body.

2.5.3 Non-blackbody radiation

The idealized concept of the blackbody provides a benchmark against which it is possible to compare the radiative performance of other materials. In general, for a real body of matter, not all of the incident radiation will be absorbed and retained. Some will be reflected away at the surface, whilst some will be transmitted through the body, as illustrated in Figure 2.3. From a radiation balance for the real body

$$\alpha_\lambda+\rho_\lambda+\tau_\lambda=1, \tag{2.5.6}$$

where the spectral directional absorptivity α_λ is that fraction of incident spectral radiative intensity that is absorbed by the body, the spectral directional reflectivity ρ_λ is the proportion of incident spectral radiative intensity that is reflected and the spectral directional transmissivity τ_λ is the proportion of incident spectral radiative intensity that is transmitted through the body. It is observed that all three properties depend upon the direction and wavelength of the incident radiation.

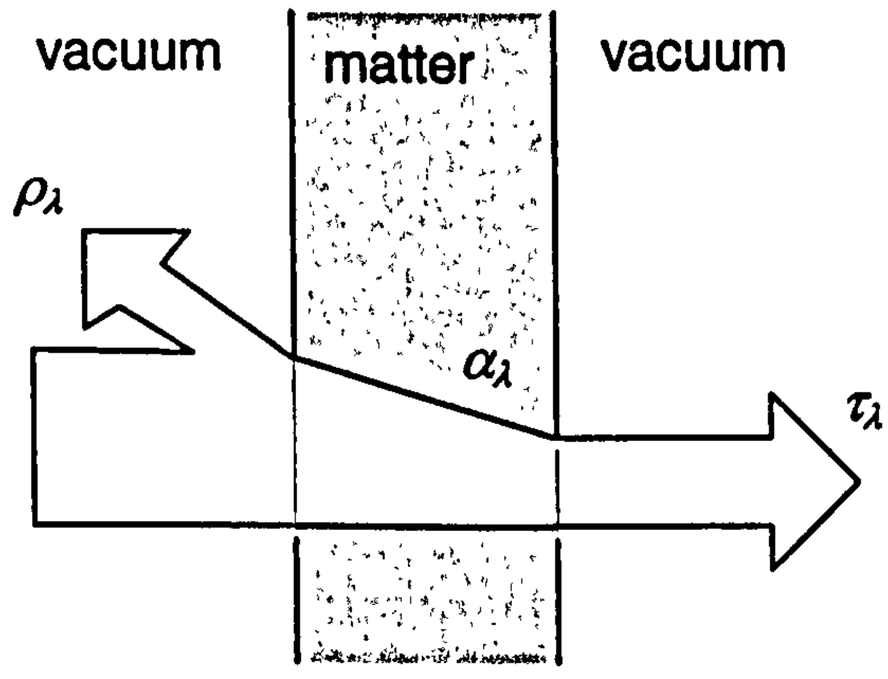

$$\alpha_\lambda(\mathbf{s},\lambda) = \frac{I_{\lambda,\text{absorbed}}(\mathbf{s},\lambda)}{I_\lambda(\mathbf{s},\lambda)} \leq 1$$

$$\rho_\lambda(\mathbf{s},\lambda) = \frac{I_{\lambda,\text{reflected}}(\mathbf{s},\lambda)}{I_\lambda(\mathbf{s},\lambda)} \leq 1$$

$$\tau_\lambda(\mathbf{s},\lambda) = \frac{I_{\lambda,\text{transmitted}}(\mathbf{s},\lambda)}{I_\lambda(\mathbf{s},\lambda)} \leq 1$$

Figure 2.3 - Absorption, reflection and transmission of thermal radiation

Only the radiative intensity that is absorbed will contribute to an increase in the internal energy of the body. In order to maintain radiative equilibrium, the real body must also emit energy. As a consequence of Kirchoffs law, however, if the reflectivity or the transmittivity are non-zero, then this will be lesser amount of thermal energy than would be predicted by the Stefan-Boltzmann law for a blackbody. The emissivity ε of a body is then defined as the ratio of the radiation emitted from a body compared to that emitted by a blackbody at the same temperature,

$$\varepsilon_\lambda = \frac{I_\lambda}{I_{b\lambda}}. \tag{2.5.7}$$

2.5.4 Radiative transfer for participating media

In contrast to a vacuum, an intermediate medium such as a gas or the gaseous vapour of a compound can participate in the radiative transfer of energy by three mechanisms. Firstly, the gaseous molecules within the medium can absorb radiative

energy, in the process raising the internal energy of the molecule. Secondly, since the gaseous molecules are at a finite temperature, emission of radiative energy will occur. Finally, the gaseous molecules may scatter incident radiative intensity, so that it is redirected. In addition, because the gaseous molecules are distributed throughout the medium, then participation with radiative transfer must be considered to be a volumetric phenomenon, which occurs throughout the medium.

2.5.4.1 Attenuation by absorption

As radiative energy travels through a participating medium, it may be absorbed by the gaseous molecules within the medium. If energy is absorbed, it is converted locally into internal energy and manifests itself as an increase in local temperature.

Consider the spectral radiative intensity I_λ that passes through a small volume element dV in the direction **s**. It is observed that the attenuation of radiative intensity is directly proportional to the magnitude of the local intensity, as well as the distance travelled, so that

$$\left(dI_\lambda\right)_{abs} = -\kappa_\lambda \cdot I_\lambda ds\,. \tag{2.5.8}$$

The absorption coefficient $-\kappa_\lambda$ has dimensions of reciprocal length, and the negative sign is introduced to shown that radiative intensity is reduced due to absorption. The absorption coefficient is a material property of the medium, and may depend upon the local temperature, pressure and composition of the medium, and upon the wavelength of the incident radiation.

2.5.4.2 Augmentation by emission

Consider a small element of the medium dV. In accordance with the Stefan-Boltzmann law, the amount of thermal energy emitted from the element is entirely dependent upon the local temperature T and the emissivity ε for the element, which will in turn depend upon the quantity of gaseous molecules within the element. Henceforth, if the element were to be removed from its position within the medium and subsequently placed within a black enclosure filled with a non-participating medium, the amount of energy emitted from the element would remain unaffected by its new situation. If the new system were to be maintained at the same temperature as the element, the radiative intensity would be equal in all directions, and equal in magnitude to the blackbody intensity predicted by the Planck distribution.

Furthermore, in order for the element to remain in thermodynamic equilibrium, the amount of energy spontaneously emitted by the element must be equal to that

absorbed by the element. As a consequence there must be no change in spectral radiative intensity in the direction **s**

$$(dI_\lambda)_{abs} + (dI_\lambda)_{em} = 0, \tag{2.5.9}$$

$$\Rightarrow \quad (dI_\lambda)_{em} = \kappa_\lambda \cdot I_{\lambda b} ds, \tag{2.5.10}$$

where $(dI_\lambda)_{em}$ is the change in spectral radiative intensity due to spontaneous emission, $I_{\lambda b}$ is the blackbody spectral intensity predicted by the Planck distribution, and the constant of proportionality for emission is equal to that for absorption κ_λ.

2.5.4.3 Redirection by scattering

Consider once again the small elemental volume *dV*. Incident radiation may be redirected by scattering as it passes through the element. In contrast to the mechanisms of absorption and emission, scattering does not affect the local energy balance of the element.

Incident intensity in the direction **s** will be attenuated to some degree by out-scattering away from that direction. It is observed that out-scattering is similar to absorption in that the degree of attenuation of radiative intensity is directly proportional to the magnitude of the local intensity, and the distance travelled

$$(dI_\lambda)_{sca} = -\sigma_{s\lambda} \cdot I_\lambda ds. \tag{2.5.11}$$

The scattering coefficient -$\sigma_{s\lambda}$ also has dimensions of reciprocal length and is a material property of the medium. Its value may depend upon the local temperature, pressure and composition of the medium, the size of the scattering particles, and upon the wavelength of the incident radiation.

In-scattering of thermal radiation from all other directions will augment the radiative intensity in the direction **s**. In order to describe the directional distribution of scattered radiation it is necessary to introduce the scattering phase function Φ_λ, which defines the probability that incident radiation from one direction $\mathbf{s}_i$ will be scattered into the direction **s**, and is equal to unity if the scattering is isotropic. The change in radiative intensity due to in-scattering from all incoming directions $\mathbf{s}_i$ is then given by

$$(dI_\lambda)_{sca} = \frac{\sigma_{s\lambda}}{4\pi}\int^{4\pi}\Phi_\lambda(\mathbf{s}_i,\mathbf{s})\cdot I_\lambda(\mathbf{s})\cdot ds d\omega\,. \qquad (2.5.12)$$

2.5.4.4 The governing equation for radiative transfer in participating media

Combining the relations established for the mechanisms of absorption, emission and scattering of thermal radiative energy leads to the governing equation for radiative transfer in a participating medium

$$dI_\lambda = (dI_\lambda)_{abs} + (dI_\lambda)_{em} + (dI_\lambda)_{sca}, \qquad (2.5.13)$$

$$dI_\lambda = -\kappa_\lambda I_\lambda ds + \kappa_\lambda I_{\lambda b} ds - \sigma_{s\lambda} I_\lambda ds + \frac{\sigma_{s\lambda}}{4\pi}\int^{4\pi}\Phi_\lambda(\mathbf{s}_i,\mathbf{s})\cdot I_\lambda(\mathbf{s})\cdot ds d\omega, \qquad (2.5.14)$$

$$\frac{dI_\lambda}{ds} = -(\kappa_\lambda + \sigma_{s\lambda})I_\lambda + \kappa_\lambda I_{\lambda b} + \frac{\sigma_{s\lambda}}{4\pi}\int^{4\pi}\Phi_\lambda(\mathbf{s}_i,\mathbf{s})\cdot I_\lambda(\mathbf{s})\cdot d\omega\,. \qquad (2.5.15)$$

This is the radiative transfer equation (RTE), and describes the spatial gradient of spectral radiative intensity in the direction **s**.

If the intermediate medium can be considered to be grey, so that the absorption coefficient κ_λ and the scattering coefficient $\sigma_{s\lambda}$ may be considered to be constant over all wavelengths, and if the scattering phase function may also be considered to be constant over all wavelengths, then it is possible to integrate the RTE over all wavelengths to obtain an equation governing the total intensity

$$\frac{dI}{ds} = \int_0^\infty \frac{dI_\lambda}{ds}\,d\lambda\,, \qquad (2.5.16)$$

$$\Rightarrow \qquad \frac{dI}{ds} = -(\kappa + \sigma_s)I + \kappa I_b + \frac{\sigma_s}{4\pi}\int^{4\pi}\Phi(\mathbf{s}_i,\mathbf{s})\cdot I(\mathbf{s})\cdot d\omega\,, \qquad (2.5.17)$$

or, substituting for the blackbody radiative intensity from the Stefan-Boltzmann law (2.5.5) yields

$$\frac{dI}{ds} = -(\kappa + \sigma_s)I + \kappa\frac{\sigma T^4}{\pi} + \frac{\sigma_s}{4\pi}\int^{4\pi}\Phi(\mathbf{s}_i,\mathbf{s})\cdot I(\mathbf{s})\cdot d\omega\,, \qquad (2.5.18)$$

where T is the local fluid temperature.

2.5.5 Overall energy conservation

The radiative participation of an intermediate gas leads to an additional source or sink of energy s_{rad} that must be included in the equation for the conservation of energy (2.3.13), which yields

$$\frac{\partial(\rho_0 T)}{\partial t}+\frac{\partial(\rho_0 u_i T)}{\partial x_i}=\frac{\partial}{\partial x_i}\left(\frac{k}{c_p}\frac{\partial T}{\partial x_i}\right)+s_{rad}\,, \tag{2.5.19}$$

where

$$s_{rad}=\int_0^\infty\left(\kappa_\lambda\left(\int_{4\pi} I_\lambda\, d\omega-4\pi I_{b\lambda}\right)\right)d\lambda\,. \tag{2.5.20}$$

The source term s_{rad} comprises a positive contribution due to the absorption of radiative energy from all directions and a negative contribution due to emission. For each term, the spectral contributions are integrated over all frequencies, so that s_{rad} represents the difference between the total absorption and total emission at any position in the flow.

2.5.6 Absorption and scattering coefficients for air at room temperature

2.5.6.1 Underlying physics for radiative absorption of air at room temperature

Radiative absorption occurs when an incident photon is captured by a gas molecule within the medium, thereby forcing the transition of the molecule from its initial energy state to a new higher energy state. Radiative emission is the reverse process, resulting in the release of a photon and a transition from the initial energy state to a lower energy state.

In general, the total energy of a molecule E is given by

$$E=E_{rot}+E_{vib}+E_{elec}\,, \tag{2.5.21}$$

where the energy of rotation E_{rot} is the kinetic energy associated with the rotation of the molecule as a rigid body, the energy of vibration E_{vib} is the kinetic energy connected with the individual nuclei vibrating about their equilibrium positions, and the electronic energy E_{elec} is the potential energy of the molecular electron arrangement. Each component of the molecular energy E_{rot}, E_{vib} and E_{elec} are quantized, so that they are bound to certain discrete values specified by an integral quantum number (Modest, 1993). Any transition between energy states is referred to as a bound-bound transition, and also can adopt only certain discrete values. Furthermore, the energy of a photon is described by Einstein's photoelectric equation

$$\Delta E = E_2 - E_1 = hf\,, \tag{2.5.22}$$

where h is Planck's constant and f is the frequency of the radiation. As a consequence, an intermediate gas can only absorb incident radiation of certain discrete frequencies. Consequently, the absorption spectrum for the gas will comprise a collection of discrete spectral lines, although each line will exhibit a finite line width due to Heisenberg's uncertainty principle. In addition, there are other mechanisms, such as Doppler broadening and collision broadening (Siegel and Howell, 2001), which cause the distribution about each spectral line to widen.

The exact nature of the allowable energy transitions are determined by the molecular structure of the intermediate gas. Of particular importance is the dipole moment associated with a gas molecule. If a molecule does not possess a permanent dipole moment, then there cannot be any changes in the kinetic energy of rotation for the molecule. This is true of any monatomic or diatomic gas where the electron cloud is distributed symmetrically, such as nitrogen N_2 or oxygen O_2. Although more complex symmetrical molecules such as carbon dioxide CO_2 or methane CH_4 do not possess a permanent dipole moment, it is possible for them to acquire such a moment due to the modes of vibration feasible within the molecule.

Any changes in the kinetic energy of vibration result in a change in the dipole moment of the molecule. For any monatomic or diatomic gas such as nitrogen or oxygen, the dipole moment must remain zero due to the symmetry of the molecule, so that transitions due to vibrational energy cannot occur. The number of independent modes of vibration v_i for a polyatomic are given by

$$v_i = 3N - 6 \text{ for a non-linear molecule,} \tag{2.5.23}$$

and

$$v_i = 3N - 5 \text{ for a linear molecule,} \tag{2.5.24}$$

where N is the number of atoms within the molecule. As such water vapour H_2O has three modes of vibration and carbon dioxide has four modes, although for the latter only one mode is radiatively active in the infra-red portion of the electromagnetic spectrum.

At typical room temperature, the energy transitions which are of importance in the infra-red portion of the electromagnetic spectrum are those entirely due to a change in both the rotational and vibrational energies. As a result, monatomic and diatomic gases such as nitrogen and oxygen, which are of course the most abundant gases in our atmosphere, do not significantly participate in thermal radiative transfer. At room temperature, therefore, absorption is entirely due to the radiative participation of other

more complex components of the atmosphere, such as carbon dioxide and water vapour. Of these, it is the participation of water vapour that is the most significant.

2.5.6.2 Scattering

The nature of scattering of radiative intensity along a path is dependent upon the relative size of the particles within the intermediate gas with respect to the wavelength of the incident radiation. If the two quantities are comparable, then the degree of scattering may be determined by employing simple geometric optics. Radiative scattering in the presence of foreign particles, such as a dust cloud or fog, is described by the detailed theory developed by Mie (1908).

In the absence of any foreign particles, the scattering of radiative intensity along a path is entirely due to interaction with the gas molecules within the medium. This scenario was first analysed by Rayleigh (1881), and it is observed that the intensity of the scattered radiation varies inversely with the fourth power of the wavelength of the incident radiation. Rayleigh scattering is an important mechanism for atmospheric phenomena, and can explain the blue colour of the sky. For engineering applications, however, including ventilation airflows within buildings, Rayleigh scattering is insignificant due to the short path lengths involved (Sparrow and Cess, 1978).

2.6 Plume theory

The strength of the source of buoyancy is such that within a short distance of the source, all variations in density are small compared to the actual density of the fluid. As a consequence, it is legitimate to invoke the Boussinesq approximation, which states that the flow is essentially incompressible (except for the buoyancy term in the Navier-Stokes equation), even though it is the differences in density that motivate the flow.

The behaviour of a vertical buoyant plume from a point source of buoyancy in an unstratified stationary ambient fluid is described by the well-established plume theory of Morton et. al. (1956). By considering conservation of mass, vertical momentum and density deficiency, the latter being a consequence of the conservation of energy, and with the assumption that the magnitude of the entrained horizontal velocity is proportional to the magnitude of the vertical velocity along the axis of the plume at that height, where the constant of proportionality is the entrainment coefficient α, they deduced the following relations

$$b = \frac{6\alpha}{5} y, \tag{2.6.1}$$

$$v = \frac{5}{6\alpha}\left(\frac{9}{10}\alpha\frac{B}{\pi}\right)^{1/3} y^{-1/3}, \tag{2.6.2}$$

and

$$g' = \frac{\Delta\rho}{\rho} g = \frac{5}{6\alpha}\frac{B}{\pi}\left(\frac{9}{10}\alpha\frac{B}{\pi}\right)^{-1/3} y^{-5/3}, \tag{2.6.3}$$

where b is the radius of the plume at a height y above the plume source, v is the vertical velocity along the axis of the plume at height y and g' is the reduced gravity at height y. The buoyancy flux B, which is a measure of the strength of the plume, remains constant at all heights for a plume in an unstratified ambient fluid. For a thermal plume, it is equal to

$$B = E\frac{R \cdot g}{p \cdot c_p}, \tag{2.6.4}$$

where E is the rate of energy release at the heat source, R and c_p are the gas constant and the specific heat of the fluid medium, p is the ambient pressure and g is the magnitude of the acceleration vector due to gravity.

The magnitude of the entrainment coefficient α is dependent upon the shape of the profile adopted to represent the velocity and buoyancy flux in the plume. It is observed that the distributions are well represented by a Gaussian profile. A top-hat profile is often used, however, since this allows a more simple mathematical analysis, although the entrainment coefficient for each profile are related

$$\alpha_{\text{top-hat}} = \alpha_{\text{Gaussian}} \times \sqrt{2}\,. \tag{2.6.5}$$

The entrainment coefficient for the Gaussian profile has been determined experimentally by Rouse et. al. (1952)

$$\alpha_{\text{Gaussian}} = 0.083, \tag{2.6.6}$$

which leads to

$$\alpha_{\text{top-hat}} = 0.117. \tag{2.6.7}$$

2.7 Stratification-flow rate coupling for the ventilation of an enclosure

When designing any real building, it is important to predict with reasonable accuracy the temperature stratification within the occupied regions of the building, as this will affect the quality of the environment in the space. For naturally ventilated

buildings, however, an accurate prediction of the temperature field throughout the flow domain is of critical importance, as this will influence the magnitude of the stack effect that is responsible for driving the flow.

For an incompressible, low-velocity flow such as those observed in buildings, the vertical gradient of piezometric pressure is given by

$$\frac{d\tilde{p}}{dy} = -(\rho - \rho_0)g\,, \tag{2.7.1}$$

which is a statement of the vertical component Navier-Stokes equation (2.3.11) for a stagnant flow. As a consequence of this, if there are variations in the fluid density, the piezometric pressure field will be non-zero, hence the stack effect. For small density changes that are entirely due to variations in the temperature field, this leads to

$$\frac{d\tilde{p}}{dy} = \frac{R\rho_0^2}{p}(T - T_0)g\,, \tag{2.7.2}$$

where R is the gas constant for the fluid, p is the absolute ambient pressure, and T_0 is the temperature of the fluid corresponding to the density ρ_0.

Consider an enclosure that is connected to the ambient reservoir by two openings, one at high-level and one at low-level. If the temperature field within the space is dissimilar to that outside, then the corresponding vertical piezometric pressure distributions must also be different. As a consequence of this, there will generally be a difference in pressure across, and an associated flow through, each respective opening.

Integrating (2.7.2) with respect to y leads to

$$\tilde{p}(h) = \frac{R\rho_0^2}{p} g \int_{y=0}^{y=h} (T(y) - T_0)dy\,, \tag{2.7.3}$$

The difference in piezometric pressure due to the internal stratification within the enclosure $\Delta\tilde{p}_{int}$ at the openings will be

$$\Delta\tilde{p}_{int} = \frac{R\rho_0^2}{p} g \int_{y=b}^{y=t} (T_{int}(y) - T_0)dy\,, \tag{2.7.4}$$

and that due to the stratification surrounding the enclosure $\Delta\tilde{p}_{ext}$ at the openings will be

$$\Delta\tilde{p}_{ext} = \frac{R\rho_0^2}{p} g \int_{y=b}^{y=t} (T_{ext}(y) - T_0) dy \,, \tag{2.7.5}$$

where t and b are the elevations of the top and bottom openings respectively. In general $\Delta\tilde{p}_{int}$ and $\Delta\tilde{p}_{ext}$ will be different. To compensate for this, there will be pressure differentials across each opening subject to the constraint

$$\Delta\tilde{p}_{inlet} + \Delta\tilde{p}_{outlet} = \Delta\tilde{p}_{int} - \Delta\tilde{p}_{ext} \,, \tag{2.7.6}$$

where $\Delta\tilde{p}_{inlet}$ and $\Delta\tilde{p}_{outlet}$ are the differences in pressure across the lower and upper openings respectively, for the case where $\Delta\tilde{p}_{int} > \Delta\tilde{p}_{ext}$, due to heating within the space.

2.7.1 Velocities at openings

The local flow velocity v at each opening is related to the pressure drop at that opening by the momentum theorem (Batchelor, 1967)

$$v_{outlet} = \sqrt{\frac{2\Delta p_{outlet}}{\rho_0}} \,, \tag{2.7.7}$$

and

$$v_{inlet} = \sqrt{\frac{2c\Delta p_{inlet}}{\rho_0}} \,, \tag{2.7.8}$$

where c is a coefficient introduced to account for the pressure loss at the lower sharp-edged opening. The mass flow rate $\dot{m}$ at each opening is then given by

$$\dot{m}_{outlet} = \rho_0 c_d a_t v_{outlet} = c_d a_t \sqrt{2\rho_0 \Delta p_{outlet}} \,, \tag{2.7.9}$$

and

$$\dot{m}_{inlet} = \rho_0 a_b v_{inlet} = a_b \sqrt{2\rho_0 c \Delta p_{inlet}} \,, \tag{2.7.10}$$

where c_d is the discharge coefficient introduced to account for the vena contracta downstream of the sharp-edged upper opening.

With the additional constraint that the mass flow rate through the lower opening must be equal to the mass flow rate through the upper opening, the flow rate through the enclosure is given by

$$\dot{m} = A^* \sqrt{\rho_0 \left(\Delta\tilde{p}_{int} - \Delta\tilde{p}_{ext}\right)} \,, \tag{2.7.11}$$

where A^* is an effective area of the openings, defined by (Linden, 1999)

$$A^* = \frac{c_d a_t a_b}{\left(\frac{1}{2}\left(\frac{c_d^2}{c} a_t^2 + a_b^2\right)\right)^{\frac{1}{2}}}. \qquad (2.7.12)$$

It is therefore immediately apparent that the rate of ventilation through the space is entirely constrained by the difference in the shape and magnitude of the temperature stratification internally within, and external to, the enclosure.

2.8 Summary

This chapter has introduced the governing concepts for air-flows observed in buildings, upon which all of the remaining analysis can be based. The Lagrangian and Eulerian frameworks have been introduced, the former being appropriate if each individual particle within the flow is to be monitored, and the latter allowing flow variables to be monitored at a fixed point in space. The governing equations for the flow of a non-isothermal Newtonian fluid were then introduced in Eulerian formulation, together with some additional relations that allow the governing equations to be simplified.

Introductions into the phenomena of turbulence and of thermal radiation have been provided, as they are both major transfer mechanisms for flows encountered within real buildings.

The plume theory of Morton et. al. (1956) was also provided, as this is used extensively in §4.0. Finally, the coupling has been demonstrated between the thermal stratification within and external to an enclosure, with an opening at high-level and at low-level, and the ventilation flow rate through the enclosure.

3.0 Computational fluid dynamics

3.1 Introduction

Although the equations that govern fluid flow are rigorous, they are non-linear are notoriously difficult to solve. Indeed to this day, the analytical solutions for only a few flows exhibiting simple geometry have been derived. With the development of digital computers, however, emerged the field of computational fluid dynamics (CFD), where the governing equations are solved numerically. This is achieved by dividing up the particular geometry of interest into a number of discrete non-overlapping control volumes or cells, the collection of cells comprising the region or domain of interest being termed a computational mesh. It is assumed that the value of each flow parameter throughout each cell can be represented by a single value stored at a node located at the centre of the cell. The governing equations for the fluid flow are then integrated over each cell in turn, yielding a system of algebraic discretized equations that can be solved in an iterative manner using a computer.

As the physical size of the computational cells is reduced, so that the spatial discretization becomes more refined, this numerical approximation becomes a more accurate model of the particular flow of interest. With this refinement, however, the number of cells and therefore algebraic equations that must be solved are increased. As a consequence, the necessary computer resources required to perform a fluid flow simulation are also increased. Indeed, it is often the available computer resource, such as computer memory and run time, that is the determining factor for the quantity and therefore physical size of the computational cells.

The description that follows is based upon the work of Mathur and Murthy (1997), as this is the unstructured implementation adopted by the commercial CFD-solver code Fluent that was used throughout this work. This approach is particularly flexible and allows the computational cell to be any arbitrary shape. The discretization procedure is described for the steady-state form of the general transport equation only.

3.2 General form of the convection-diffusion transport equation

A comparison of the continuity equation, Navier-Stokes equation and energy equation shows that each conforms to the form of the general transport equation for the fluid parameter ϕ

$$\frac{\partial(\rho_0\phi)}{\partial t}+\frac{\partial(\rho_0 u_i\phi)}{\partial x_i}=\frac{\partial}{\partial x_i}\left(\Gamma\frac{\partial\phi}{\partial x_i}\right)+s_\phi . \qquad (3.2.1)$$

The first term on the LHS is the rate of change term at a particular position in space. The second term on the LHS is referred to as the 'convection' term. It is characterised by the fact that it contains the first derivative of a mass flux, and its role is to ensure that the value of a property ϕ at any point in the flow is convected through the flow domain with the flow.

The first term on the RHS is referred to as the 'diffusion' term. Its role is to ensure that the value of a property ϕ is diffused in equal measure in all directions, where Γ is the coefficient of diffusivity.

Equation	ϕ	Γ	s_ϕ
Continuity	1	0	0
x-Navier-Stokes	u	μ	$-\frac{\partial\tilde{p}}{\partial x}$
y- Navier-Stokes	v	μ	$-(\rho-\rho_0)g-\frac{\partial\tilde{p}}{\partial y}$
z- Navier-Stokes	w	μ	$-\frac{\partial\tilde{p}}{\partial z}$
Energy	T	k/c_p	0
x-Vorticity	ω_x	μ	$\frac{\partial(\rho_0\omega_x u)}{\partial x}+\frac{\partial(\rho_0\omega_y u)}{\partial y}+\frac{\partial(\rho_0\omega_z u)}{\partial z}$
y-Vorticity	ω_y	μ	$\frac{\partial(\rho_0\omega_x v)}{\partial x}+\frac{\partial(\rho_0\omega_y v)}{\partial y}+\frac{\partial(\rho_0\omega_z v)}{\partial z}$
z-Vorticity	ω_z	μ	$\frac{\partial(\rho_0\omega_x w)}{\partial x}+\frac{\partial(\rho_0\omega_y w)}{\partial y}+\frac{\partial(\rho_0\omega_z w)}{\partial z}$

Table 3.1 - Summary of the flow variable ϕ, diffusivity coefficient Γ and the source term s_ϕ for each of the governing flow equations

The remaining term on the RHS s_ϕ is referred to as the volumetric 'source' term and includes, for example, the contribution from the pressure gradient term and the gravitational term in the Navier-Stokes equation.

A summary of the appropriate diffusion coefficient Γ and source term s_ϕ for a selection of flow parameters is provided in Table 3.1.

3.3 Discretization of the convection-diffusion transport equation

The steady-state form of the general convection-diffusion transport equation is

$$\frac{\partial(\rho_0 u_i \phi)}{\partial x_i} = \frac{\partial}{\partial x_i}\left(\Gamma \frac{\partial \phi}{\partial x_i}\right) + s_\phi . \qquad (3.2.1)$$

Integration of this result over an arbitrary control volume dV leads to

$$\int_V \frac{\partial(\rho_0 u_i \phi)}{\partial x_i} \cdot dV = \int_V \frac{\partial}{\partial x_i}\left(\Gamma \frac{\partial \phi}{\partial x_i}\right) \cdot dV + \int_V s_\phi \cdot dV , \qquad (3.3.1)$$

where V is the volume of the control volume. Applying Gauss' divergence theorem to the convection and diffusion terms leads to

$$\int_A n_i \rho_0 u_i \phi \cdot dA = \int_A n_i \Gamma \frac{\partial \phi}{\partial x_i} \cdot dA + \int_V s_\phi \cdot dV , \qquad (3.3.2)$$

where A is the bounding surface of the control volume, and n_i is the outward-facing component of the unit normal to the surface A in the i-direction. This result is valid for any control volume with a continuous bounding surface A.

Consider the control volume illustrated in Figure 3.1. The discretization procedure requires that the value of any flow parameter is constant throughout the entire volume, and can be represented by the value at the node P located at the cell-centre. In addition, the surface of the control volume is discretized, so that it can be represented by a number of discrete non-overlapping planar faces. The value of each flow parameter is also considered to be constant for each face f, and is represented by the value at the centre of the face ϕ_f.

Adopting this discretization approach, the previous result becomes

$$\sum_f J_f \phi_f = \sum_f \Gamma_f A_f \left(n_i \frac{\partial \phi}{\partial x_i}\right)_f + s_{\phi,P} V_P \qquad (3.3.3)$$

where the mass flow rate at a face J_f is determined from

$$J_f = \rho_0 A_f (n_i u_i)_f \,, \qquad (3.3.4)$$

and is positive if the flow is leaving the control volume.

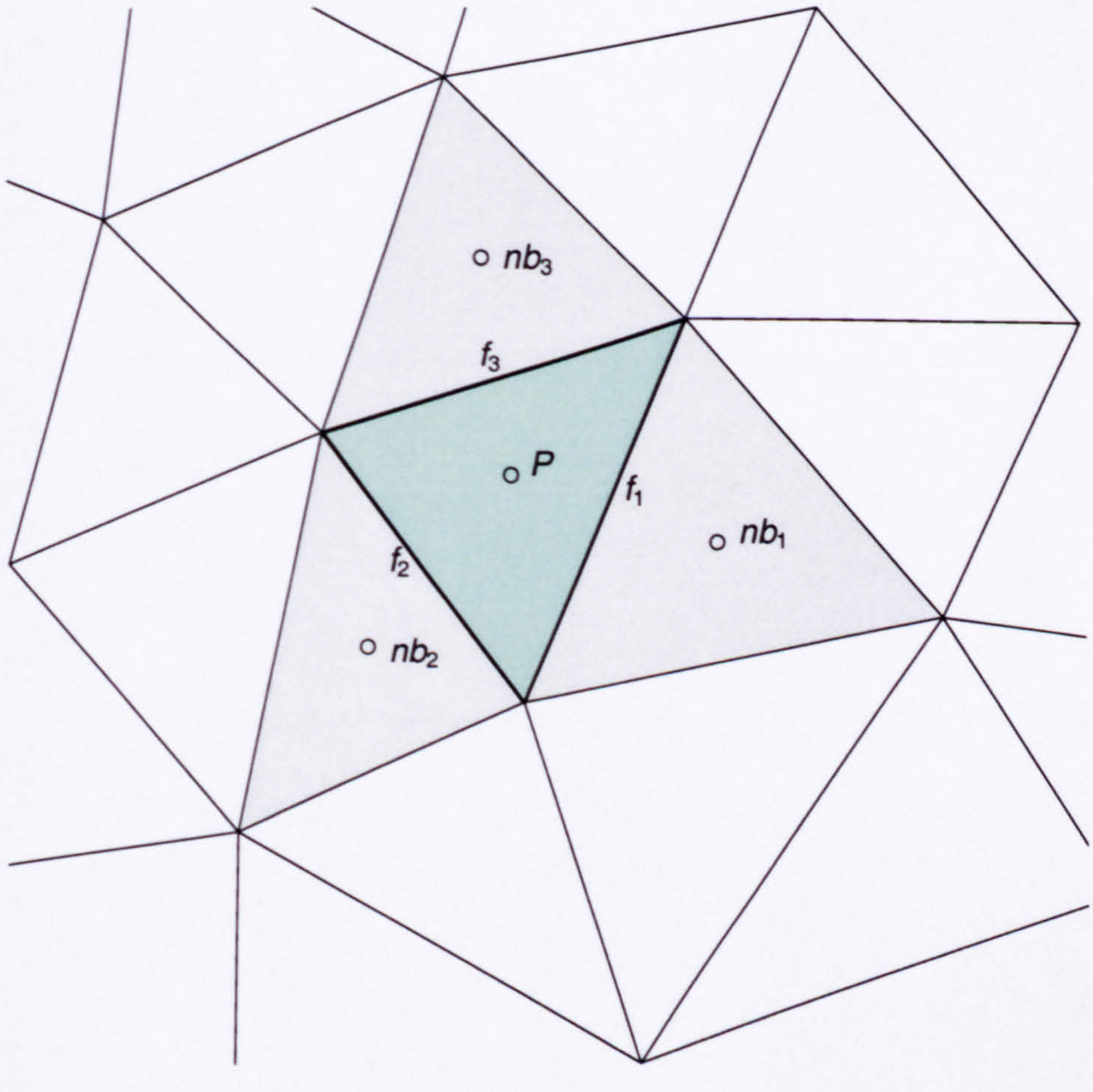

Figure 3.1 - Control volume *P* and cell-faces *f*, together with neighbouring control volumes *nb*

3.3.1 Convection term

The convection term represents the product of the mass flow rate across a particular face J_f and the value of ϕ at that face ϕ_f, summed over all bounding faces to the control volume Σf.

During a computation the value of the mass flow rate at each face is determined from the flow field at the previous iteration. The face value ϕ_f, however, is assumed to be unknown, and must be determined by some form of interpolation from cell-centre values in neighbouring cells. The manner in which this interpolation is performed can have a significant effect upon the stability and convergence properties of the discretized equations during the calculation procedure. It turns out that the only interpolation scheme that is unconditionally stable is the upwind differencing scheme, where the face value of ϕ is assumed to be equal to the value of ϕ at the nearest upwind cell,

$$\phi_f = \phi_{\text{upwind}} . \qquad (3.3.5)$$

This differencing scheme is only first-order accurate and can lead to so-called 'numerical diffusion' (Patankar, 1980). Indeed, this can be especially severe on coarse or unstructured grids.

In order to achieve higher-order accuracy, it is possible to use a more accurate, higher-order differencing scheme explicitly, using old values from the previous iteration, combined with implicit upwind differencing,

$$\phi_f = \phi_f^{\text{upwind}} + (\phi_f^{\text{higher-order}} - \phi_f^{\text{upwind}})^{\text{old}} . \qquad (3.3.6)$$

This deferred correction approach allows a higher-order solution to be obtained whilst the differencing scheme remains unconditionally stable.

Several higher-order differencing schemes have proven to be popular, including second-order central differencing, second-order upwind differencing, and the third-order upwind QUICK scheme (Leonard, 1979).

In practice, the convection term is determined from

$$J_f \phi_f = \phi_P \max(0, J_f) - \phi_{nb} \max(0, -J_f) + \Delta_\phi , \qquad (3.3.7)$$

where the term

$$\Delta_\phi = J_f (\phi_f^{\text{higher-order}} - \phi_f^{\text{upwind}})^{\text{old}} . \qquad (3.3.8)$$

is the explicit contribution from the deferred correction procedure.

3.3.2 Diffusion term

The diffusion term at the face *f* is given by

$$D_f = \Gamma_f A_f \left(n_i \frac{\partial \phi}{\partial x_i} \right)_f . \qquad (3.3.9)$$

In order to evaluate this diffusion term, it is necessary to express the gradient of ϕ at the face in terms of the neighbouring cell-centre values, ϕ_P and ϕ_{nb}. This is achieved using the simple relationship derived from the geometrical argument outlined in Figure 3.2 and Figure 3.3, which relates the three unit vectors **n**, **s** and **t**

$$n_i = \frac{1}{n_j s_j} s_i - \frac{t_k s_k}{n_j s_j} t_i . \qquad (3.3.10)$$

Substituting this into the diffusion term leads to

$$D_f = \Gamma_f A_f \left(\frac{1}{n_j s_j} s_i \frac{\partial \phi}{\partial x_i} \right)_f - \Gamma_f A_f \left(\frac{t_k s_k}{n_j s_j} t_i \frac{\partial \phi}{\partial x_i} \right)_f , \qquad (3.3.11)$$

$$\Rightarrow \qquad D_f = \Gamma_f A_f \left(\frac{1}{n_j s_j} \frac{(\phi_{nb} - \phi_P)}{\delta s} \right) - \Gamma_f A_f \left(\frac{t_k s_k}{n_j s_j} t_i \frac{\partial \phi}{\partial x_i} \right)_f . \qquad (3.3.12)$$

The first term on the right-hand side of (3.3.12) is the primary diffusion term and is equivalent to a second-order central-difference scheme.

The second term is the secondary diffusion term, and is due to the fact that in general, a computational mesh may not be orthogonal. Indeed its contribution, which is treated explicitly in the discretized equations, can become significant for highly skewed meshes. For a three-dimensional mesh composed of polyhedra of arbitrary shape, the evaluation of this term is not straightforward. Mathur and Murthy (1997) express the term as the difference between the total diffusion term and the primary diffusion term, so that

$$D_f = \Gamma_f A_f \left(\frac{1}{n_j s_j} \frac{(\phi_{nb} - \phi_P)}{\delta s} \right) + \Gamma_f A_f \left(n_i \overline{\frac{\partial \phi}{\partial x_i}} - \frac{1}{n_j s_j} s_i \overline{\frac{\partial \phi}{\partial x_i}} \right)_f , \qquad (3.3.13)$$

where the over-bar across the gradient terms represent the average of the derivatives determined at the two adjacent cells, *P* and *nb*.

In practice, the diffusion term is written

$$D_f = \Gamma_f A_f \left(\frac{1}{n_j s_j} \frac{(\phi_{nb} - \phi_P)}{\delta s} \right) + \Xi_\phi , \qquad (3.3.14)$$

where the term Ξ_ϕ is the explicit contribution due to secondary diffusion.

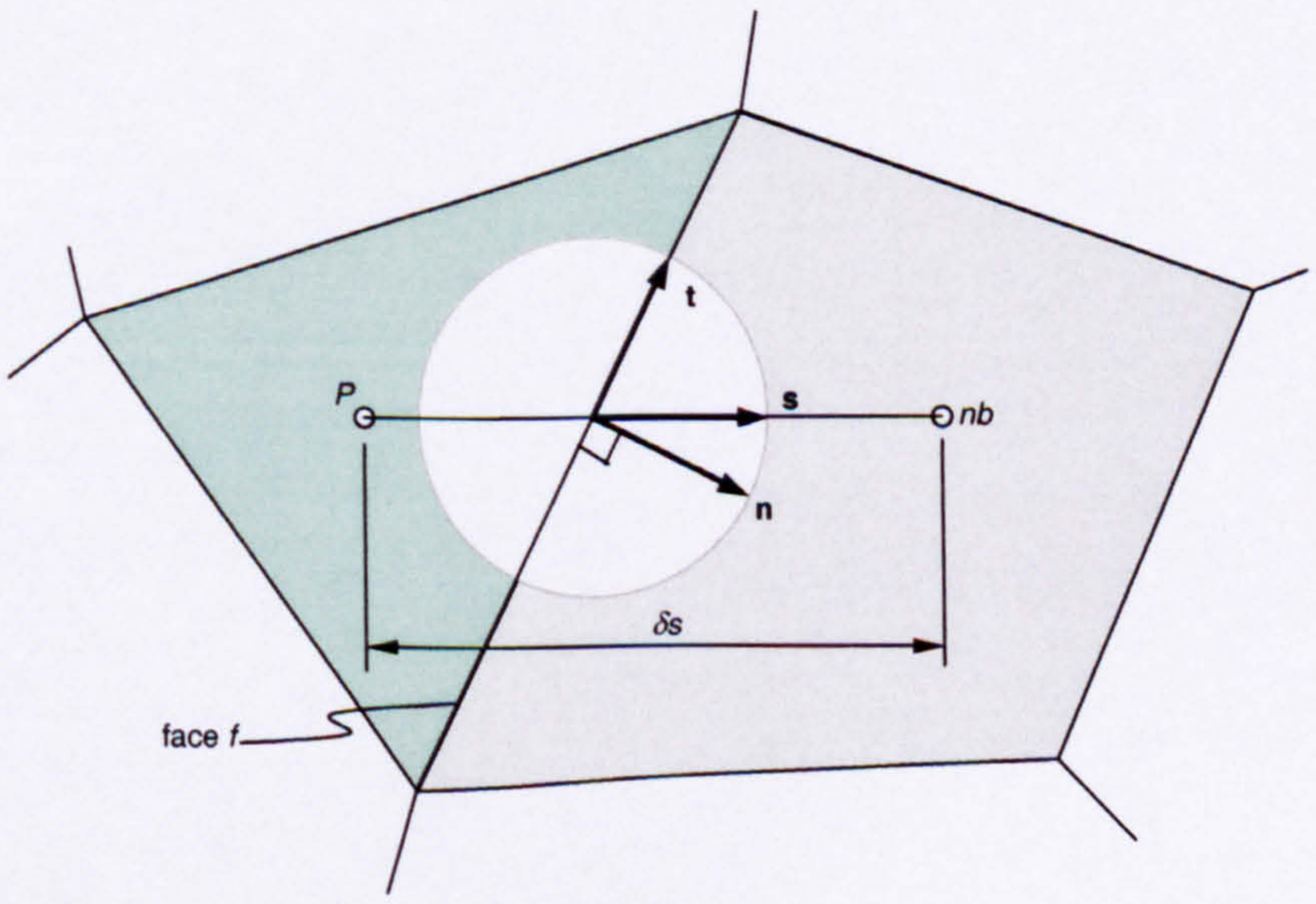

Figure 3.2 - Control volume *P* and cell-face *f*, together with neighbouring control volume *nb*

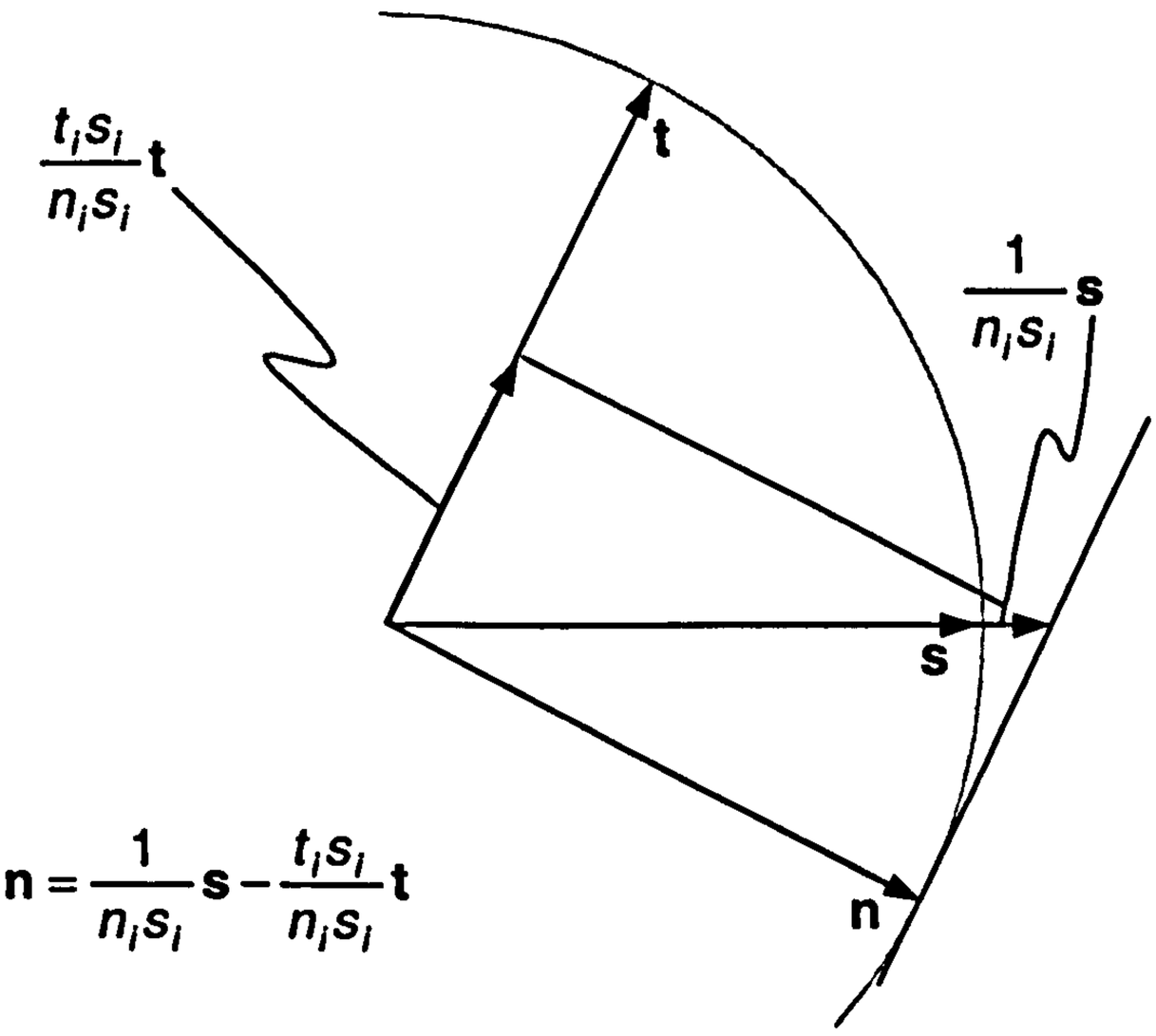

Figure 3.3 - Relationships between the three unit vectors, **n**, **s** and **t**

3.3.3 Gradient computation- reconstruction gradient and gradient

The secondary diffusion term described above requires information regarding the gradient of the variable ϕ at the cell centres of the neighbouring cells *P* and *nb*. Only the value of ϕ is stored at the cell centres, however, so that the gradient of ϕ must be calculated in some fashion. The method preferred by Mathur and Murthy (1997) is to use a linear reconstruction based upon Gauss' divergence theorem.

The discretized form of the divergence theorem states

$$\left(\frac{\partial \phi}{\partial x_i}\right)_P V_P = \sum_f A_f (n_i \phi)_f \,, \qquad (3.3.15)$$

so that the gradient of ϕ is simply

$$\left(\frac{\partial \phi}{\partial x_i}\right)_P = \frac{1}{V_P} \sum_f A_f (n_i \phi)_f \,. \qquad (3.3.16)$$

Mathur and Murthy introduce a factor α to ensure that the reconstruction procedure does not introduce local extrema, so that their reconstructed gradient is given by

$$\left(\frac{\partial \phi}{\partial x_i}\right)_{P,\text{recon}} = \frac{\alpha}{V_P} \sum_f A_f (n_i \phi)_f \,. \qquad (3.3.17)$$

In order to evaluate this gradient term, the value of the variable ϕ must be known at each face bounding the control volume *P*. This is obtained simply as the arithmetic mean of the neighbouring cell centre values ϕ_P and ϕ_{nb}.

The reconstruction gradient is used to reconstruct the value of ϕ at any face of the control volume P using the approximation

$$\phi_{f,P} = \phi_P + r_i \left(\frac{\partial \phi}{\partial x_i} \right)_{P,\text{recon}} . \qquad (3.3.18)$$

where r_i are the respective components of the vector from the node P to the centroid of the face f. Note, however, that the face value $\phi_{f,P}$ computed from the reconstruction gradient at the cell P will not generally be equal to the value $\phi_{f,nb}$ computed from the reconstruction gradient at the cell nb. When employing this method to determine the diffusivity at a face Γ_f, it is imperative that a consistent approach is adopted; otherwise the discretization scheme will no longer be necessarily conservative.

The gradients at the cell centres P and nb used to evaluate the secondary diffusion terms are determined by reapplying Gauss' divergence theorem to the control volume,

$$\left(\frac{\partial \phi}{\partial x_i} \right)_P = \frac{1}{V_P} \sum_f A_f \left(n_i \tilde{\phi} \right)_f , \qquad (3.3.19)$$

where the value of $\tilde{\phi}_f$ at each face is the average of the face values reconstructed from the control volume P and the neighbouring control volume nb

$$\tilde{\phi}_f = \frac{\phi_{f,P} + \phi_{f,nb}}{2} . \qquad (3.3.20)$$

3.3.4 Momentum interpolation for cell face velocities

In accordance with Table 3.1, the source terms for each component of the Navier-Stokes equation contain a contribution from the local gradient of pressure. For any particular cell P, the gradient of pressure must be determined at the centre of the cell, so that the value of pressure is required at each of the cell-bounding faces. Depending upon the method employed to predict the face pressures, however, it is possible that the pressure gradient at the cell centre may be entirely dependent upon the values of pressure stored at neighbouring nodes so that it could be independent of the value of pressure stored at that particular cell. If this is the case, then a checkerboard pressure field would remain undetected by the discretized Navier-Stokes equations (Patankar, 1980).

A popular method to prevent the development of a checkerboard pressure field using a single, non-staggered grid arrangement is to use the 'momentum interpolation' practice due to Rhie and Chow (1983) to evaluate the mass flux at each cell face J_f.

Employing their approach, the individual components of velocity at the face are determined from

$$u_{i,f} = \overline{u_i} - \overline{\left(\frac{V_p}{a_P}\right)}\left(\overline{\frac{\partial p}{\partial x_i}} - \frac{\partial p}{\partial x_i}\right)_f , \qquad (3.3.21)$$

where the over-bar represents the average of the quantity determined at the two adjacent cells, *P* and *nb*.

The mass flow rate is given by

$$J_f = \rho_0 A_f n_i \overline{u_i} - \rho_0 A_f \overline{\left(\frac{V_p}{a_P}\right)}\left(n_i \overline{\frac{\partial p}{\partial x_i}} - n_i \frac{\partial p}{\partial x_i}\right)_f . \qquad (3.3.22)$$

Following a similar procedure to that outlined for the determination of the diffusion terms in §3.3.2, the final term on the right-hand side is given by

$$\rho_0 A_f n_i \frac{\partial p_f}{\partial x_i} = \rho_0 A_f \left(\frac{1}{n_j s_j}\frac{(p_{nb} - p_P)}{\delta s}\right) + \rho_0 A_f \left(n_i \overline{\frac{\partial p}{\partial x_i}} - \frac{1}{n_j s_j} s_i \overline{\frac{\partial p}{\partial x_i}}\right)_f . \qquad (3.3.23)$$

Substituting this into the expression for the mass flow rate leads to

$$J_f = \rho_0 A_f n_i \overline{u_i} - \rho_0 A_f \overline{\left(\frac{V_p}{a_P}\right)}\left(\frac{1}{n_j s_j}\frac{(p_{nb} - p_P)}{\delta s} - \frac{1}{n_j s_j} s_i \overline{\frac{\partial p_f}{\partial x_i}}\right). \qquad (3.3.24)$$

Using this interpolation technique, the cell face velocity depends upon the values of pressure at the nodes either side of the face, *P* and *nb*, so that a 'checkerboard' pressure field would be detected and corrected.

3.3.5 Discretized equations

Recall the discretized general transport equation (3.3.3), which describes the transport of the variable ϕ for a particular control volume *P*

$$\sum_f J_f \phi_f = \sum_f \Gamma_f A_f \left(n_i \frac{\partial \phi}{\partial x_i}\right)_f + s_{\phi,P} V_P . \qquad (3.3.3)$$

Substituting into this equation the convection and diffusion terms established previously, (3.3.7) and (3.3.14) respectively, leads to the following linear equation for the value of ϕ for the control volume *P*, in terms of the value of ϕ at the neighbouring nodes *nb*

$$a_P \phi_P = \sum_f a_{nb} \phi_{nb} + S_{\phi,P}\,, \tag{3.3.25}$$

where

$$a_{nb} = \left[\max(0,-J_f) + \Gamma_f A_f \left(\frac{1}{n_j s_j} \cdot \frac{1}{\delta s} \right) \right]_f, \tag{3.3.26}$$

$$a_P = \sum_f a_{nb}\,, \tag{3.3.27}$$

and

$$S_{\phi,P} = \sum_f \left[-\Delta_\phi + \Xi_\phi - J_f \phi_P \right]_f + s_{\phi,P} V_P\,. \tag{3.3.28}$$

Here the summation is over all of the faces of control volume P, and the subscript nb denotes the neighbouring cell which shares the face f with P.

The source term $S_{\phi,P}$ contains any volumetric sources of ϕ. For example, when the Navier-Stokes equation is discretized using the above procedure, this term contains a volumetric source of velocity due to the pressure gradient term. This term also contains the explicit contributions due to higher-order differencing for the convective term Δ_ϕ and the secondary diffusion term Ξ_ϕ. The source term also contains a contribution from the product $J_f \phi_P$ at each face. From continuity, however, this term is zero and can be ignored.

The source term $S_{\phi,P}$ should also contain flux contributions at boundaries. This is to satisfy the Scarborough condition (1958), which states that for the numerical stability of a set of linear equations to be ensured, the following condition must be true

$$\frac{\sum |a_{nb}|}{|a_P|} \begin{cases} \leq 1 \text{ at all nodes} \\ < 1 \text{ at at least one node} \end{cases}. \tag{3.3.29}$$

For internal nodes, the contributions from all neighbouring nodes are to be determined implicitly, so that $\sum a_{nb} = a_P$.

For nodes adjacent to a boundary, the contributions from the boundary cell are evaluated explicitly and incorporated directly into the source term, so that the transport coefficient at that face a_{boundary} is zero. As a result $\sum a_{nb} < a_P$, and the Scarborough criterion is satisfied.

3.3.6 Linearized Navier-Stokes equation

The Navier-Stokes equation presented in §2.3.3.2 is a non-linear differential equation, and is notoriously difficult to solve by analytical means. When it is cast into the general convection-diffusion form, the velocity terms are necessarily separated

into those that appear in the convection terms of the transport coefficients and that which is substituted for the transported parameter ϕ, for which the equation is solved. The equation has, in effect, been linearized and can be solved in an iterative manner. The convection terms in the transport coefficients are evaluated using an initial guess for the velocity field, the equation is then solved yielding an improved velocity field that is used to evaluate the transport coefficients for the subsequent iteration.

3.3.7 Under-relaxation

Introducing the superscript n to represent the current iteration, the discretized general transport equation at the node P is

$$a_P \phi_P^n = \sum_f a_{nb} \phi_{nb}^n + S_{\phi,P}, \qquad (3.3.30)$$

In practice it is often necessary to under-relax this equation during the solution procedure to maintain numerical stability. The equation is modified, so that only a fraction α of the modification is made to ϕ

$$a_P \phi_P^n = \alpha\left(\sum_f a_{nb} \phi_{nb}^n + S_{\phi,P}\right) + (1-\alpha) a_P \phi_P^{n-1}. \qquad (3.3.31)$$

Redefining the coefficient a_P to include the under-relaxation coefficient α

$$a_P = \alpha \sum_f a_{nb}, \qquad (3.3.32)$$

leads to a modified form of the discretized general transport equation

$$a_P \phi_P^n = \sum_f a_{nb} \phi_{nb}^n + \left[S_{\phi,P} + (1-\alpha) a_P \phi_P^{n-1}\right]. \qquad (3.3.33)$$

3.3.8 Discretization errors and mesh independence

The variation in the local flow parameters for the flow of air in any real building will be smooth and continuous, as described by the governing equations for the flow. When the governing equations are discretized, however, they are no longer smooth. Instead, the flow field is represented entirely by the values calculated at the centre of each discrete volume within the computational mesh, which inevitably introduce truncation errors into the analysis that are manifested as numerical diffusion throughout the flow domain (Patankar, 1980). As a result, therefore, the exact solution to each of the discretized governing equations is generally dependent upon the resolution of the computational mesh.

The truncation errors inherent in the CFD-approach and associated numerical diffusion may be reduced by refining the computational mesh so that the centres of neighbouring cells are nearer, particularly in the regions where the variation of the flow parameters is significant. As the mesh becomes more refined, the improvement in the solution will converge towards the exact solution for the flow, as defined by the governing equations before the discretization process.

Clearly if the mesh is refined, the number of cells within the mesh will increase. As a consequence of this, there will be an increase in the computational resource required to deliver the solution, in terms of computer memory and the length of time necessary to perform the CFD-simulation, and indeed the disk space required to store the solution files.

There must, however, be some point at which the numerical solution is close enough to the exact solution, so that further mesh refinement will not significantly affect the predicted flow solution and is therefore unnecessary. At this point, the solution can be considered to be mesh independent. Following the prediction of a flow on a given computational mesh, the prediction should be repeated, ideally with a refined mesh, in order to confirm that the solution achieved is indeed mesh independent.

3.4 Solving the discretized equations

3.4.1 Pressure-velocity field coupling and the SIMPLE algorithm

The numerical solution of the flow field requires knowledge of the pressure field throughout the flow domain, due to the presence of the pressure gradient source term in the Navier-Stokes equation. For an incompressible ideal gas, however, all variations in the pressure field are due to local accelerations of fluid, and are decoupled from any small variations in local fluid density. As such, it is impossible to determine the pressure field by application of the equation of state, so that a different approach must be employed.

Perhaps the most widely used method for the solution of incompressible flows is the SIMPLE algorithm (Semi-Implicit Method for Pressure-Linked Equations) of Patankar and Spalding (1972). The method is based upon an iterative guess-and-correct procedure to solve the governing equations, where the continuity equation is used as a constraint equation for the velocity field calculated from the Navier-Stokes equation.

The Navier-Stokes equation is first solved using a guessed pressure field p^* to obtain the components of velocity u_i^*

$$a_P u_{i,P}^* = \sum_f a_{nb} u_{i,nb}^* - \left(\frac{\partial p^*}{\partial x_i}\right) V_P + s_{u_i} V_P , \qquad (3.4.1)$$

In general the components of velocity u_i^* will not satisfy the continuity equation

$$\sum_f \rho A_f \left(n_i u_i^*\right)_f = S_m \neq 0 , \qquad (3.4.2)$$

where S_m is a mass source term.

The pressure correction p' is defined as the difference between the correct pressure field and the guessed pressure field

$$p = p^* + p' . \qquad (3.4.3)$$

Similarly, the velocity correction u_i' is defined as the difference between the correct velocity field and the velocity field obtained using the guessed pressure field

$$u_i = u_i^* + u_i' . \qquad (3.4.4)$$

Subtracting (3.4.1) from the discretized Navier-Stokes equation leads to an equation for the velocity correction u_i'

$$a_P u_{i,P}' = \sum_f a_{nb} u_{i,nb}' - \left(\frac{\partial p'}{\partial x_i}\right) V_P . \qquad (3.4.5)$$

At this point, the velocity correction is unknown, so the first term of the RHS of equation (3.4.5) is neglected. This is the main assumption of the SIMPLE algorithm and yields

$$u_{i,P}' = -\frac{V_P}{a_P}\left(\frac{\partial p'}{\partial x_i}\right). \qquad (3.4.6)$$

This approximation does not affect the accuracy of the final converged solution because in that limit velocity corrections at every node will be zero.

Returning to the continuity restraint

$$\sum_f \rho A_f \left(n_i \left(u_i^* + u_i'\right)\right)_f = 0\,, \tag{3.4.7}$$

$$\Rightarrow \qquad \sum_f \rho A_f \left(n_i u_i'\right)_f = -S_m\,. \tag{3.4.8}$$

This result requires knowledge of the product $n_i u_i'$ at each face for the control volume P, the value of which can be determined at cell-centres using (3.4.6).

$$n_i u_{i,P}' = -\frac{V_P}{a_P}\left(n_i \frac{\partial p'}{\partial x_i}\right). \tag{3.4.9}$$

The factor V_P/a_p can be determined as an arithmetic mean of the cell-centre values at the cells neighbouring the face. The remainder of the term must be determined using a procedure similar to that used for the diffusion term in §3.3.2. This leads to

$$\left(n_i u_i'\right)_f = \frac{V_P + V_{nb}}{a_P + a_{nb}}\left(\frac{1}{n_j s_j}\frac{\left(p_{nb}' - p_P'\right)}{\delta s} + \Xi_{p'}\right). \tag{3.4.10}$$

The term corresponding to the secondary diffusion term may be neglected because in the limit of the final converged solution, pressure correction field will be zero throughout the computational domain.

Substituting this result into (3.4.8) leads to the following linear equation for the pressure correction at the control volume P, in terms of the pressure correction at the neighbouring nodes nb

$$b_P p_P' = \sum_f b_{nb} p_{nb}' + S_m\,, \tag{3.4.11}$$

where

$$b_{nb} = \left[\rho A_f \frac{V_P + V_{nb}}{a_P + a_{nb}}\left(\frac{1}{n_j s_j}\cdot\frac{1}{\delta s}\right)\right], \tag{3.4.12}$$

and

$$b_P = \sum_f b_{nb}\,. \tag{3.4.13}$$

Once again, the summation is over all of the faces of control volume P, and the subscript nb denotes the neighbouring cell which shares the face f with P.

The calculated pressure corrections are summed with the guessed pressure field to obtain a new improved estimate of the pressure field

$$p = p^* + \alpha_p p' , \qquad (3.4.14)$$

where α_p is an under-relaxation factor used to stabilize the computational procedure. Using (3.4.6) the velocity corrections are also calculated, and added to the guessed velocity field, to give a velocity field that satisfies continuity.

The procedure is repeated until a velocity field is obtained which satisfies the continuity equation and the Navier-Stokes equation simultaneously.

3.4.2 Numerical convergence

The SIMPLE algorithm and its derivatives that were employed to solve the flows considered in this work are iterative calculation procedures that commence with some guessed flow field, usually a null field, which is gradually improved so that the exact solution to the algebraic system of discretized equations is approached. As with any iterative procedure, the calculated flow field will only ever converge towards the exact solution to the system of discretized equations: the exact solution will never actually be achieved. There must, however, come a point when the calculated field may be considered to have converged upon the exact solution, where the two may be considered to be the same, so that variations in the calculated flow field due to further iterations would be unperceivable and therefore unnecessary.

A popular method for defining the convergence criteria is to consider the imbalance in each of the discretized equations to be solved. For the discretized equation describing the transport of the parameter ϕ at a given computational cell (3.3.25), the magnitude of this imbalance is referred to as the residual R_ϕ for that cell

$$R_\phi = \left| \sum_f a_{nb}\phi_{nb} + S_{\phi,P} - a_P\phi_P \right| . \qquad (3.4.15)$$

Rather than examine the imbalance over the whole field at each iteration, it is more convenient to sum the residual over all of the cells in the computational domain, so that a single quantity can be monitored for each flow variable.

$$\sum R_\phi = \sum_{\text{domain}} \left| \sum_f a_{nb}\phi_{nb} + S_{\phi,P} - a_P\phi_P \right| . \qquad (3.4.16)$$

The sum of the residuals $\sum R_\phi$ is a measure of the absolute imbalance for each of the discretized equations to be solved. A better method to define the convergence criteria is to use the scaled sum of the residuals $\sum r_\phi$

$$\sum r_\phi = \frac{\sum_{\text{domain}} \left| \sum_f a_{nb}\phi_{nb} + S_{\phi,P} - a_P\phi_P \right|}{\sum_{\text{domain}} |a_P\phi_P|}, \qquad (3.4.17)$$

which provides a measure of the relative imbalance for each of the discretized equation.

As the calculation proceeds, the residuals for each of the flow parameters should continue to fall throughout the domain. The rate of convergence will be affected by the under-relaxation factors chosen prior to the start of the calculation. If low under-relaxation factors are adopted then the rate of convergence, particularly in the early stages of the numerical process, is also usually low. Increasing the under-relaxation factors will tend to increase the rate at which the calculated field approaches the exact solution. If, however, they are increased too much, then the iterative procedure may become unstable and may tend to diverge.

3.5 Turbulence modelling

3.5.1 Introduction

Although any turbulent flow is completely described by the same governing equations as laminar flows, it is not yet possible to solve them using the CFD approach for routine engineering problems. The problem is that in order to obtain an accurate prediction of a turbulent flow, it is necessary to resolve all of the scales of the turbulence, with regard to both space and time. The direct numerical simulation (DNS) of a turbulent flow requires a very fine spatial discretization in order to capture the small-scale effects of the turbulence, coupled with a transient solution approach employing a very small time-step to model correctly the unsteady nature of turbulence. Successful DNS simulations using this procedure have been performed for a few simple flow problems, providing useful information about the nature of turbulence that cannot easily be measured. With current computer technology, however, this type of numerical procedure is prohibitive for general engineering applications.

Another approach that is gaining in popularity is large eddy simulation (LES), whereby only the scales of turbulence that are larger than some arbitrary cut-off scale are resolved, and the smaller scales of turbulence are modelled. The justification for this method is that it is mainly the largest, anisotropic eddies that interact with the primary flow, contain most of the kinetic energy of turbulence, and are responsible for

most of the turbulent transport. The smaller eddies, however, are more universal in character, tending to be more homogeneous and isotropic than the larger eddies, and are therefore more suitable for a modelling approach.

The cut-off scale is typically taken to be the local size of the computational mesh. The governing equations are then subjected to a spatial filter that removes the effects of the smaller-scale eddies, and the resulting space-averaged resolvable-scale equations govern only the flow and turbulence structures in the range above the cut-off scale. The smaller-scale eddies are represented by a sub-grid model. The resolvable-scale equations contain extra sub-grid terms that account for the removal of energy from the resolvable scales to the small-scale structures of turbulence. It is the sub-grid modelling techniques that remain the fundamental deficiency with the LES approach, and are the subject of much research at the present.

In order to simulate any given fluid flow problem using the LES approach, it is necessary to solve the resolvable-scale equations as a transient, three-dimensional computation. In addition, it is usually necessary to construct a reasonably fine mesh in order to resolve eddies down to the inertial sub-range, where the assumptions of universal and isotropic behaviour become valid. As such, the LES approach still requires a significant computing resource.

Problems also arise at wall boundaries, where the turbulent eddies become anisotropic at small scale, and so the definition of the cut-off length scale is no longer clear. Further, for flows with buoyancy effects present, the current sub-grid scale models are inadequate, or at least require further research.

According to Ferziger (1996), "Improved models for both the small-scale turbulence and the wall layer are needed if LES is to become a useful engineering tool". This view is also adopted by Xu (1998), who is of the opinion that "LES is still premature for practical room airflow simulation".

To date, most practical simulations of turbulent flows have been restricted to solving for the mean flow quantities, governed by the Reynolds-averaged equations introduced in §0. The Reynolds-averaged equations are, in fact, exact equations, since no new approximations are introduced during their derivation. The equations, however, are no longer closed because of the new variables, the Reynolds stress tensor and the Reynolds heat flux, for which it is not possible to find a closed governing equation.

In order to solve the Reynolds-averaged equations for a particular flow, it is necessary to introduce appropriate models for the new variables.

3.5.2 The Boussinesq hypothesis

The Reynolds stress $-\rho_0\overline{u_i'u_j'}$ represents the diffusion of momentum due to turbulent fluctuations. Many researchers have compared this behaviour with that of the random motion of molecules in a dilute gas which, according to the kinetic theory of gases, give rise to viscous stresses. Boussinesq (1877) suggested that the Reynolds stress could be described in much the same way as a viscous stress, in terms of a velocity gradient and a 'turbulent' or 'eddy' viscosity

$$-\rho_0\overline{u_i'u_j'} = \mu_T\left(\frac{\partial\overline{u}_i}{\partial x_j}+\frac{\partial\overline{u}_j}{\partial x_i}\right)-\frac{1}{3}\rho_0\overline{u_k'u_k'}\delta_{ij}, \qquad (3.5.1)$$

where the second term on the R.H.S. is necessary to obtain the proper trace of the Reynolds stress tensor in the case of an incompressible flow. That is, for the case when $i = j$, (3.5.1) reduces to

$$-\rho_0\overline{u_i'u_i'} = 2\mu_T\frac{\partial\overline{u}_i}{\partial x_i}-\rho_0\overline{u_i'u_i'} = -\rho_0\overline{u_i'u_i'}, \qquad (3.5.2)$$

for an incompressible flow.

This approach has been pursued by many in the field of turbulence modelling. For a solenoidal velocity field it allows the Reynolds-averaged Navier-Stokes equation to be written in an identical form to the instantaneous Navier-Stokes equation

$$\rho_0\frac{\partial\overline{u}_i}{\partial t}\mathbf{e}_i+\rho_0\frac{\partial(\overline{u}_i\overline{u}_j)}{\partial x_j}\mathbf{e}_i = (\overline{\rho}-\rho_0)g_i\mathbf{e}_i-\frac{\partial\overline{\tilde{p}}}{\partial x_i}\mathbf{e}_i+\frac{\partial}{\partial x_j}\left[(\mu+\mu_T)\frac{\partial\overline{u}_i}{\partial x_j}\right]\mathbf{e}_i, \qquad (3.5.3)$$

where $(\mu+\mu_T)$ is the effective viscosity. Following a similar argument, the Reynolds heat flux $-\rho_0\overline{u_i'T'}$ represents the diffusion of heat due to turbulent fluctuations. The enhanced thermal diffusivity can be modelled using a similar 'gradient-diffusion' hypothesis

$$-\rho_0\overline{u_i'T'} = \frac{\mu_T}{\mathrm{Pr}_{Turb}}\frac{\partial\overline{T}}{\partial x_i}, \qquad (3.5.4)$$

where the turbulent Prandtl number Pr_{Turb} is the ratio between the rate of turbulent diffusion of momentum and the rate of turbulent diffusion of energy, and is usually assumed to be constant in eddy-viscosity models. In particular,

$$\mathrm{Pr}_{Turb} = 0.85. \qquad (3.5.5)$$

With this approximation, the Reynolds-averaged energy equation becomes

$$\frac{\partial(\rho_0\overline{T})}{\partial t}+\frac{\partial(\rho_0\overline{u}_i\overline{T})}{\partial x_i}=\frac{\partial}{\partial x_i}\left[\left(\frac{\mu}{\mathrm{Pr}}+\frac{\mu_T}{\mathrm{Pr}_T}\right)\frac{\partial\overline{T}}{\partial x_i}\right]. \qquad (3.5.6)$$

Likewise, the turbulent diffusion of a general flow parameter ϕ may be represented by the gradient-diffusion hypothesis, which is analogous to the Boussinesq hypothesis

$$-\rho_0\overline{u_i'\phi'}=\frac{\mu_T}{\sigma_\phi}\frac{\partial\overline{\phi}}{\partial x_i}, \qquad (3.5.7)$$

where σ_ϕ is a turbulent Schmidt number, determined empirically.

The turbulent viscosity is usually significantly greater than the molecular viscosity in regions away from walls. This explains why turbulent flows are observed to have high rates of mixing, and are dissipative in nature. It still remains, however, to find a suitable method to determine the turbulent viscosity.

3.5.3 Zero-equation models of turbulence

3.5.3.1 Prandtl's mixing-length hypothesis

In 1925, Prandtl proposed the mixing length hypothesis. This development assumes that the fluid is divided into small distinct parcels moving with constant velocity and without interaction over a short length. At the end of this path the lump of fluid becomes mixed with the fluid at the new point, thus transferring its momentum to the fluid at the new position. This is directly analogous to the free and random movements of gas molecules between collisions that is the basis of the kinetic theory of gases, from which the molecular viscosity is given by

$$\mu=\frac{1}{3}\rho\langle c\lambda_c\rangle, \qquad (3.5.8)$$

where $\langle c\lambda_c\rangle$ is the mean of the product of the speed of each individual gas molecule c, and the mean free path of that gas molecule at that speed λ_c. Prandtl supposed that a result analogous to this could be used to determine the turbulent viscosity

$$\mu_T=\frac{1}{3}\rho_0 u_m l_m, \qquad (3.5.9)$$

where the mixing-velocity u_m is the velocity at which a discrete parcel of fluid moves, and the mixing-length l_m is the distance a parcel of fluid moves before it is

mixed at the new position. Prandtl introduced a further assumption for the mixing-velocity (Wilcox, 1998)

$$u_m = 3l_m \frac{\partial \overline{u}_i}{\partial x_j}, \qquad (3.5.10)$$

which, when incorporated into (3.5.9) yields

$$\mu_T = \rho_0 l_m^2 \frac{\partial \overline{u}_i}{\partial x_j}. \qquad (3.5.11)$$

This approach of Prandtl, however, has simply replaced the unknown turbulent viscosity μ_T of Boussinesq by another unknown, the mixing-length l_m, so that the Reynolds averaged equations remain unclosed.

For a number of simple flow cases, it is found that the mixing-length can be determined by a simple algebraic expression involving some characteristic length scale for that flow. Such cases include wall-bounded flows, and free shear flows such as wakes, mixing layers and jets. For those cases, it is found that the mixing-length hypothesis can predict the flow reasonably well. Unfortunately, the algebraic expression is different for each case, so that no general formula for the mixing-length exists. Furthermore, for general flow problems, which may include separation and recirculation, there is usually no obvious characteristic length scale so that it is not possible to use Prandtl's approach.

3.5.4 One-equation models

From the kinetic theory of gases, it is known that the absolute temperature of a fluid T at a point is a measure of the average kinetic energy of the individual gas molecules at that point. The kinetic theory also provides a relationship between the molecular viscosity of a gas, and its absolute temperature

$$\mu \propto \rho \lambda_c \sqrt{T}. \qquad (3.5.12)$$

Continuing the comparison between turbulence and the molecular model of a gas, Prandtl (1945) assumed that the kinetic energy of the turbulent fluctuations is analogous to the absolute temperature of the fluid at a point. Defining the kinetic energy of turbulence per unit mass k as

$$k = \frac{1}{2}\overline{u_i' u_i'}, \qquad (3.5.13)$$

leads to a new definition of the turbulent viscosity

$$\mu_T = C_\mu \cdot \rho l \sqrt{k}\,, \tag{3.5.14}$$

where l is a turbulence length scale and C_μ is an empirical constant. An exact transport equation for the turbulent kinetic energy k is readily obtained from the Reynolds Stress equation (2.4.12), by contracting the indices and dividing each term by 2

$$\frac{\partial(\rho_0 k)}{\partial t} + \frac{\partial(\rho_0 \bar{u}_j k)}{\partial x_j} = \frac{\partial}{\partial x_j}\left(\mu \frac{\partial k}{\partial x_j}\right) + s_k\,, \tag{3.5.15.a}$$

where

$$s_k = -\rho_0 \overline{u_i' u_j'} \frac{\partial \bar{u}_i}{\partial x_j} - \overline{\rho' u_i'} g_i - \frac{1}{2}\frac{\partial}{\partial x_j}\left(\rho_0 \overline{u_i' u_i' u_j'}\right) - \frac{\partial}{\partial x_j}\left(\overline{u_i' p'}\right) - \mu\left(\overline{\frac{\partial u_i'}{\partial x_j}}\right)^2 . \tag{3.5.15.b}$$

This result is in the form of the general convection-diffusion equation. There are, however, several unknown terms which are collected together into the source term. Although they are unknown variables, each term in the source term represents a physical turbulent process (Wilcox, 1998), so that they can be replaced by a suitable model for that process. Using the turbulent process models introduced in Table 3.2, the k-equation becomes

$$\frac{\partial(\rho_0 k)}{\partial t} + \frac{\partial(\rho_0 \bar{u}_j k)}{\partial x_j} = \frac{\partial}{\partial x_j}\left(\left(\mu + \frac{\mu}{\sigma_k}\right)\frac{\partial k}{\partial x_j}\right) + s_k\,, \tag{3.5.16.a}$$

where

$$s_k = \mu_T \left(\frac{\partial \bar{u}_i}{\partial x_j}\right)^2 + \beta g_i \frac{\mu_T}{\mathrm{Pr}_{Turb}} \frac{\partial \bar{T}}{\partial x_i} - \rho_0 \varepsilon\,. \tag{3.5.16.b}$$

With this 'one-equation' approach, the turbulent viscosity is dependent upon where the flow has been, thus taking into account the flow history. For this reason, it is an improvement over the mixing-length hypothesis. The one-equation approach, however, remains unclosed, since there still remains two unknown quantities, the turbulent length scale and the rate of dissipation of the kinetic energy of turbulence per unit mass ε.

Source term	Turbulent process	Model
$-\rho_0 \overline{u_i' u_j'} \frac{\partial \bar{u}_i}{\partial x_j}$	Production term: the rate at which energy is transferred from the primary flow to the large scale turbulent structures	Boussinesq hypothesis: $-\rho_0 \overline{u_i' u_j'} = \mu_T \frac{\partial \bar{u}_i}{\partial x_j}$
$-\overline{\rho' u_i'} g_i$	Buoyancy production term: the rate at which turbulence kinetic energy is created due to buoyancy effects	Gradient-diffusion hypothesis: $-\overline{\rho' u_i'} = \frac{\mu_T}{\mathrm{Pr}_{Turb}} \beta \frac{\partial \bar{T}}{\partial x_i}$
$-\frac{1}{2}\frac{\partial}{\partial x_j}\left(\rho_0 \overline{u_i' u_i' u_j'}\right)$	Turbulent diffusion term: rate at which turbulence kinetic energy is transported due to turbulent fluctuations	Gradient-diffusion hypothesis: $-\rho_0 \overline{u_i' u_i' u_j'} = \frac{\mu_T}{\sigma_k} \frac{\partial k}{\partial x_j}$
$-\frac{\partial}{\partial x_j}\left(\overline{u_i' p'}\right)$	Pressure diffusion term: rate at which turbulence kinetic energy is transported due to correlation of pressure and velocity fluctuations	Neglected: $-\frac{\partial}{\partial x_j}\left(\overline{u_i' p'}\right) = 0$
$-\mu\left(\overline{\frac{\partial u_i'}{\partial x_j}}\right)^2$	Dissipation term: rate at which turbulence kinetic energy is dissipated into thermal energy by viscous effects at the small scale	New definition: $\varepsilon = \frac{\mu}{\rho_0}\left(\overline{\frac{\partial u_i'}{\partial x_j}}\right)^2$

Table 3.2 - Modelling the turbulent processes in the transport equation for turbulence kinetic energy.

3.5.5 Two equation models

In order to complete the turbulence closure, and for it to be of use in general engineering computations, it is necessary to somehow prescribe the turbulent length scale and the rate of dissipation of turbulence kinetic energy for any arbitrary turbulent flow. To date, this has usually been achieved by introducing a new differential transport equation for a second turbulence parameter, thus creating a 'two-equation model of turbulence'. From this second parameter, the turbulence length scale *l* and the rate of dissipation ε are determined from some algebraic dimensional argument, without prior knowledge of the flow. This approach was first suggested by Kolmogorov (1942). He introduced a second differential transport equation for the specific rate of dissipation of turbulent kinetic energy *f*. Because of its extra

complexity, however, this model remained unused until the advent of a sufficiently powerful computing platform.

Many different turbulence parameters have been proposed for the second transport equation, and to date there is no consensus as to which provides the most universal description of turbulence. From the literature, it is apparent that some models perform better for some flows, but that for many simple turbulent flows including wakes and jets the proposals for the second turbulence equation are equivalent (Launder and Spalding, 1974).

Each of the second parameters proposed are simply related by dimensional arguments to the length scale of turbulence and the eddy viscosity, and can be written as the product $k^m l^n$ as outlined the summary of Table 3.3.

Model	Model parameters	Second variable	Length scale	Dissipation rate
Kolmogorov (1942)	k-f	$f \propto k^{1/2} l^{-1}$	$l \propto k^{1/2} f^{-1}$	$\varepsilon \propto k^{1} f^{1}$
Rotta (1951)	k-l	$l \propto k^{0} l^{1}$	$l \propto k^{0} l^{1}$	$\varepsilon \propto k^{3/2} l^{-1}$
Spalding (1969)	k-W	$W \propto k^{1} l^{2}$	$l \propto k^{1/2} W^{-1/2}$	$\varepsilon \propto k^{1} W^{1/2}$
Saffman (1970)	k-ω^2	$\omega^2 \propto k^{1} l^{-2}$	$l \propto k^{1/2} (\omega^2)^{-1/2}$	$\varepsilon \propto k^{1} (\omega^2)^{1/2}$
Jones and Launder (1972)	k-ε	$\varepsilon \propto k^{3/2} l^{-1}$	$l \propto k^{3/2} \varepsilon^{-1}$	$\varepsilon \propto k^{0} \varepsilon^{1}$
Rodi and Spalding (1970)	k-kl	$kl \propto k^{1} l^{1}$	$l \propto k^{-1} (kl)^{1}$	$\varepsilon \propto k^{5/2} (kl)^{-1}$
Wilcox (1988)	k-ω	$\omega \propto k^{1/2} l^{-1}$	$l \propto k^{1/2} \omega^{-1}$	$\varepsilon \propto k^{1} \omega^{1}$
Speziale et. al. (1990)	k-τ	$\tau \propto k^{-1/2} l^{1}$	$l \propto k^{1/2} \tau^{1}$	$\varepsilon \propto k^{1} \tau^{-1}$

Table 3.3 - Summary of some of the proposed two-equation turbulence closures

The standard-$k\varepsilon$ model of turbulence (Jones and Launder, 1972) has enjoyed the most use throughout many fluid applications, and there has been more validation comparisons using this model of turbulence than any other.

3.5.6 The -$k\varepsilon$ model of turbulence

It is possible to derive an exact transport equation for the rate of dissipation of turbulence kinetic energy ε from the Navier-Stokes equation. The result, however, is a complex equation containing many new unknown correlations that must be modelled. As with the exact transport equation for turbulence kinetic energy, it is possible to group together terms that describe physical turbulent processes. The models

introduced to describe them are rather more dubious, however, and it is for this reason that it is the scale-determining equation that is the deficient equation in most turbulence models.

3.5.6.1 The standard-$k\varepsilon$ model of turbulence

The standard-$k\varepsilon$ model (Jones and Launder, 1972) is based upon modelled transport equations for the turbulence kinetic energy k (3.5.16) and its rate of dissipation ε, given by

$$\frac{\partial(\rho_0\varepsilon)}{\partial t}+\frac{\partial(\rho_0\overline{u}_j\varepsilon)}{\partial x_j}=\frac{\partial}{\partial x_j}\left(\left(\mu+\frac{\mu_T}{\sigma_\varepsilon}\right)\frac{\partial\varepsilon}{\partial x_j}\right)+s_\varepsilon, \qquad (3.5.17.a)$$

where
$$s_\varepsilon=C_{1\varepsilon}\frac{\varepsilon}{k}\left[\mu_T\left(\frac{\partial\overline{u}_i}{\partial x_j}\right)^2+C_{3\varepsilon}\beta g_i\frac{\mu_T}{\mathrm{Pr}_{Turb}}\frac{\partial\overline{T}}{\partial x_i}\right]-C_{2\varepsilon}\rho_0\frac{\varepsilon^2}{k}, \qquad (3.5.17.b)$$

and the turbulent ε-Schmidt number σ_ε, and $C_{1\varepsilon}$, $C_{2\varepsilon}$ and $C_{3\varepsilon}$ are empirical constants.

The source term for the ε-equation closely resembles that of the k-equation. It comprises a production term due to the effects of the mean flow, a production term due to the effects of buoyancy, and a destruction term. But for the introduction of an empirical constant and the factor of (ε / k), each term is identical to the equivalent term in the k-source term s_k.

The turbulent viscosity is determined using the simple algebraic relation based upon a dimensional argument

$$\mu_T=C_\mu\rho_0\frac{k^2}{\varepsilon}. \qquad (3.5.18)$$

The values for the empirical constants for the standard model are defined as (Launder and Spalding, 1974)

$$C_\mu=0.09,\ C_{1\varepsilon}=1.44,\ C_{2\varepsilon}=1.92,\ \sigma_k=1.00,\ \text{and}\ \sigma_\varepsilon=1.30. \qquad (3.5.19)$$

These values are obtained by considering the flow for a number of simple flows, such as the decay of isotropic homogeneous turbulence behind a grid, and the flow in the region close to a solid boundary.

The value of the constant $C_{3\varepsilon}$ is not specified in the paper of Launder and Spalding. As such, there remains some dispute about what value it should assume. Some workers (Cook, 1998) have assumed that the buoyancy production term can normally be neglected, so that $C_{3\varepsilon} = 0$. If the term is not neglected, then $C_{3\varepsilon} = 1$. Rodi

(1993) states that various researchers have found that the buoyancy term in the ε-equation is important for vertical buoyant shear layers, but is negligible for horizontal layers. An approximation that satisfies both conditions is proposed by Henkes et. al. (1991)

$$C_{3\varepsilon} = \tanh\left|\frac{v}{u}\right|, \qquad (3.5.20)$$

where v is the component of the flow velocity parallel to the gravitational vector and u is the component of the flow velocity perpendicular to the gravitational vector. This approximation is adopted for the present study.

The standard-$k\varepsilon$ model has proven to be the most widely used two-equation turbulence model. It is a relatively simple model that can, perhaps surprisingly, provide reasonable accuracy for a wide range of turbulent flows. Because of its simplicity it is fairly robust and economic to use. The model is, however, known to have several weaknesses. In particular, the model constants are tuned to provide reasonable agreement for a planar jet, so that when applied to the case of the axisymmetric jet, the model greatly over-predicts the turbulent viscosity and therefore the rate of spread of the jet. This is known as the plane-jet/round-jet anomaly and is a major failing of the standard-$k\varepsilon$ closure (Pope, 1978). Furthermore, for strongly strained flows such as the flow over a surface-mounted cube, the standard-$k\varepsilon$ model again tends to significantly over-predict the turbulent viscosity.

It is widely recognised that the deficiencies in the performance of the standard-$k\varepsilon$ model are mainly due to the modelled dissipation rate equation, and the standard eddy viscosity formulation. In an effort to improve its performance, many researchers have sought to design new formulations for the ε-equation and the eddy viscosity formulation.

3.5.6.2 The *realizable*-$k\varepsilon$ model of turbulence

According to experimental and DNS evidence, the eddy-viscosity coefficient C_μ is not a constant. It is observed that $C_\mu = 0.09$ for the inertial sub-layer of a boundary flow, and $C_\mu = 0.05$ for homogeneous shear flow. In addition, it is observed that for some flows which exhibit large mean rates of strain, the standard eddy viscosity formulation can predict non-realizable negative components of normal Reynolds stress, and can be in violation of the Schwarz constraint for shear components of the Reynolds stress (Wilcox, 1998).

The realizable-$k\varepsilon$ model of turbulence (Shih et. al., 1995) introduces a new eddy viscosity formulation to ensure realizability with regard to these physical constraints

$$C_\mu = \frac{\varepsilon}{A_0 \varepsilon + A_S U^* k}, \qquad (3.5.21)$$

where
$$U^* = \sqrt{S_{ij} S_{ij} + \Omega_{ij} \Omega_{ij}}\ , \qquad (3.5.22)$$

for a stationary frame of reference, and

$$A_0 = 4.04 \text{ and } A_S = \sqrt{6}\cos(\phi), \qquad (3.5.23)$$

where
$$\phi = \frac{\arccos\left(W\sqrt{6}\right)}{3},\ W = \frac{S_{ij} S_{jk} S_{ki}}{\tilde{S}^3} \text{ and } \tilde{S} = \sqrt{S_{ij} S_{ij}}\ . \qquad (3.5.24)$$

In addition to the new formulation for the eddy viscosity, the closure also introduces a new model equation for the rate of dissipation of turbulence kinetic energy. The new ε-equation is developed from a consideration of the enstrophy ω^2, a name given to describe the mean-square vorticity fluctuations at a position in the flow. An equation for the enstrophy can be derived from the vorticity equation (2.3.15) in a similar manner to the derivation of the *k*-equation (3.5.15). By considering an approximate high Reynolds number budget for the enstrophy (Tennekes and Lumley, 1972), and recognising that under such conditions $\rho\varepsilon = \mu\omega^2$, a new model equation for the dissipation rate was proposed

$$\frac{\partial(\rho_0 \varepsilon)}{\partial t} + \frac{\partial(\rho_0 \bar{u}_j \varepsilon)}{\partial x_j} = \left(\mu + \frac{\mu_T}{\sigma_\varepsilon}\right)\frac{\partial^2 \varepsilon}{\partial x_j^2} + s_\varepsilon, \qquad (3.5.25.a)$$

where
$$s_\varepsilon = C_1 S \varepsilon + C_{1\varepsilon} C_{3\varepsilon} \beta g_i \frac{\mu_T}{\mathrm{Pr}_{Turb}} \frac{\partial \bar{T}}{\partial x_i} - C_2 \rho_0 \frac{\varepsilon^2}{k + \sqrt{\nu\varepsilon}}. \qquad (3.5.25.b)$$

The model constants are given by

$$C_1 = \max\left(0.43, \frac{\eta}{\eta + 5}\right),\ C_2 = 1.90,\ \ \sigma_k = 1.00, \text{ and } \sigma_\varepsilon = 1.20, \qquad (3.5.26)$$

where
$$\eta = \frac{Sk}{\varepsilon}, \qquad (3.5.27)$$

and $C_{1\varepsilon}$ and $C_{3\varepsilon}$ are defined as for the standard-$k\varepsilon$ model.

The main difference between the new realizable ε-equation and the standard ε-equation is that the production term is no longer dependent upon the eddy viscosity μ_T. Furthermore, there is no longer the possibility of encountering a singularity in the destruction term since the denominator is always greater than zero.

It was claimed that this turbulence closure resolves the plane-jet/round-jet anomaly suffered by the standard-$k\varepsilon$ model, that is the realizable-$k\varepsilon$ model is able to

predict the spreading rate for axisymmetric jets and planar jets alike (Shih et. al., 1995).

3.5.6.3 The RNG-$k\varepsilon$ model of turbulence

Another recent extension to the standard-$k\varepsilon$ closure is due to Yakhot et. al., (1992). They apply renormalization group (RNG) methods to describe the inertial range of small-scale turbulent eddies in a qualitative manner. The effects of the small-scale turbulence are represented by means of a random forcing function in the Navier-Stokes equation. The small scales of motion are then systematically removed from the governing equations by expressing their effects in terms of larger scale motions, eventually leading to a set of large-scale equations of motion.

The RNG theory yields a differential formula for the effective viscosity that accounts for low Reynolds number effects (Choudhury, 1993)

$$d\left(\frac{\rho^2 k}{\sqrt{\varepsilon\mu}}\right) = 1.72\frac{\hat{\nu}}{\sqrt{\hat{\nu}^3 - 1 + C_\nu}}d\hat{\nu}, \qquad (3.5.28)$$

where

$$\hat{\nu} = \frac{\mu_{eff}}{\mu}, \qquad (3.5.29)$$

and

$$C_\nu \approx 100. \qquad (3.5.30)$$

In the high Reynolds number limit, (3.5.28) leads to

$$\mu_T = C_\mu \rho_0 \frac{k^2}{\varepsilon}, \qquad (3.5.31)$$

where $C_\mu = 0.0845$, which is close to the value $C_\mu = 0.09$ determined empirically for the standard-$k\varepsilon$ closure.

The RNG-$k\varepsilon$ model also includes a new strain-dependent R-term in the ε-equation

$$\frac{\partial(\rho_0\varepsilon)}{\partial t}+\frac{\partial(\rho_0\bar{u}_j\varepsilon)}{\partial x_j}=\left(\mu+\frac{\mu_T}{\sigma_\varepsilon}\right)\frac{\partial^2\varepsilon}{\partial x_j^2}+s_\varepsilon, \qquad (3.5.32.a)$$

where
$$s_\varepsilon=C_{1\varepsilon}\frac{\varepsilon}{k}\left[\mu_T\left(\frac{\partial\bar{u}_i}{\partial x_j}\right)^2+C_{3\varepsilon}\beta g_i\frac{\mu_T}{\mathrm{Pr}_{Turb}}\frac{\partial\bar{T}}{\partial x_i}\right]-C_{2\varepsilon}\rho_0\frac{\varepsilon^2}{k}-R, \qquad (3.5.17.b)$$

$$R=\frac{C_\mu\rho\eta^3(1-(\eta/\eta_0))}{1+\beta\eta^3}\frac{\varepsilon^2}{k}, \qquad (3.5.17.c)$$

and
$$\eta=\frac{Sk}{\varepsilon}. \qquad (3.5.17.d)$$

The model constants are given by

$$C_1=1.42,\ C_{2\varepsilon}=1.68,\ \eta_0=4.38,\ \beta=0.012,\ \sigma_k=1.393,\text{ and } \sigma_\varepsilon=1.393. \qquad (3.5.33)$$

For weakly strained flows, the RNG-$k\varepsilon$ model tends to yield results comparable to those from the standard-$k\varepsilon$ model. For strongly strained flows, such as the flow over a surface-mounted cube, the RNG-$k\varepsilon$ model will tend to predict a lower turbulent viscosity than the standard-$k\varepsilon$ model, which is an improvement when compared to the flow observed experimentally.

3.6 Radiation modelling

3.6.1 Introduction

To predict the radiant heat transfer within a building, it is necessary to solve the radiative transfer equation (2.5.15) which governs radiative exchange for participating media. There are several methods available for the solution of this equation. For the present work, the Fluent implementation of the finite-volume method (Murthy and Mathur, 1998) is used, which was designed to be incorporated within their own unstructured mesh framework (Mathur and Murthy, 1997). This approach is particularly flexible and has a number of advantages. It accounts for absorption, scattering and emission within the medium, and allows the absorption coefficient to depend upon local flow properties such as pressure, temperature and humidity. The model allows for non-isotropic scattering, and can be easily extended to allow for the solution of a non-grey medium, where the absorption coefficient may vary with the wavelength of the incident radiation.

3.6.2 Finite Volume approach

3.6.2.1 Discretization

As with the general transport equation, the radiative transport equation must be discretized in order to obtain a numerical solution of the radiation field. The integro-differential equation is replaced by a system of linear algebraic equations that can be solved in a similar fashion to the other transport equations that describe the fluid flow. The governing equation, however, describes the variation of (spectral) radiative intensity, which, from §2.5.1, is dependent upon position vector **r** and direction vector **s**. As such it must be discretized with respect to position and direction.

For the spatial discretization it is possible to use the same computational grid as that used for the solution of the other transport equations, thus eliminating the need to create and store another mesh in computer memory.

For the directional discretization, the whole angular space 4π must be divided into a number of discrete non-overlapping solid angles ω_i. This is achieved by defining the system of spherical co-ordinates illustrated in Figure 3.4, where the polar angle θ and the azimuthal angle ϕ can describe the direction of any particular direction vector **s**. Each octant of angular space is then discretized into $N_\theta \times N_\phi$ solid angles, as shown in Figure 3.5.

The centroid of each solid angle ω_i is represented by a corresponding unit direction vector $\mathbf{s}_i$, which can be defined by the associated polar and azimuthal angles θ_i and ϕ_i. The extents of each solid angle are given by $\Delta\theta$ and $\Delta\phi$.

For each individual solid angle, the radiative transfer equation is cast into the form of the general transport equation, which can then be solved using the same methods as for other properties. For a three dimensional calculation, a total of $8N_\theta N_\phi$ transport equations must be solved.

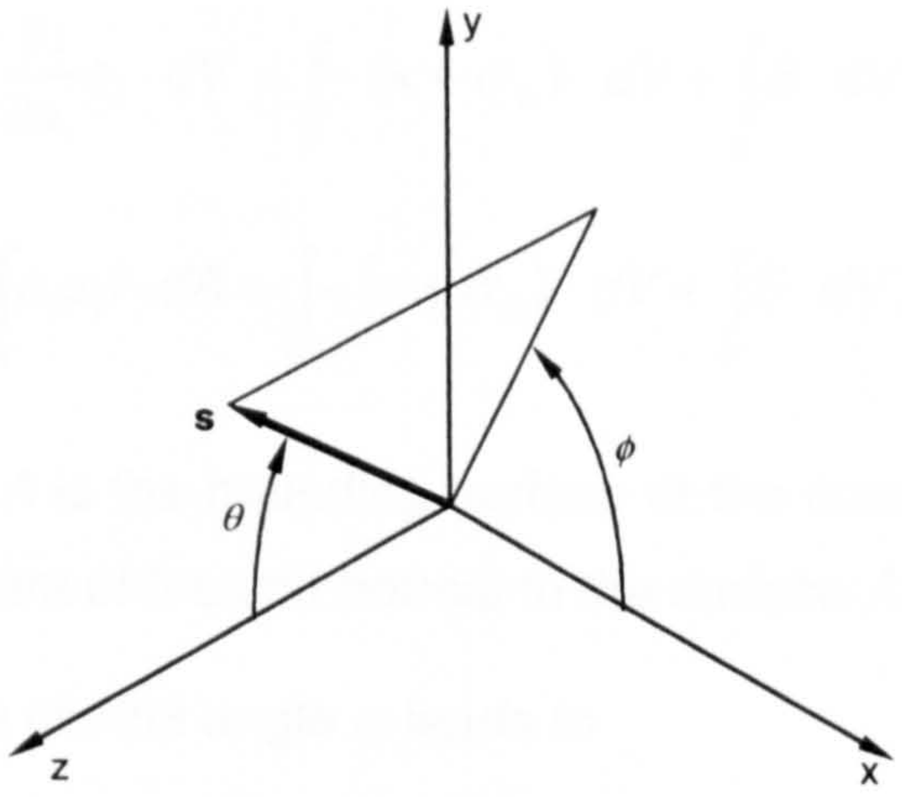

Figure 3.4 - Spherical co-ordinate system for use with angular discretization

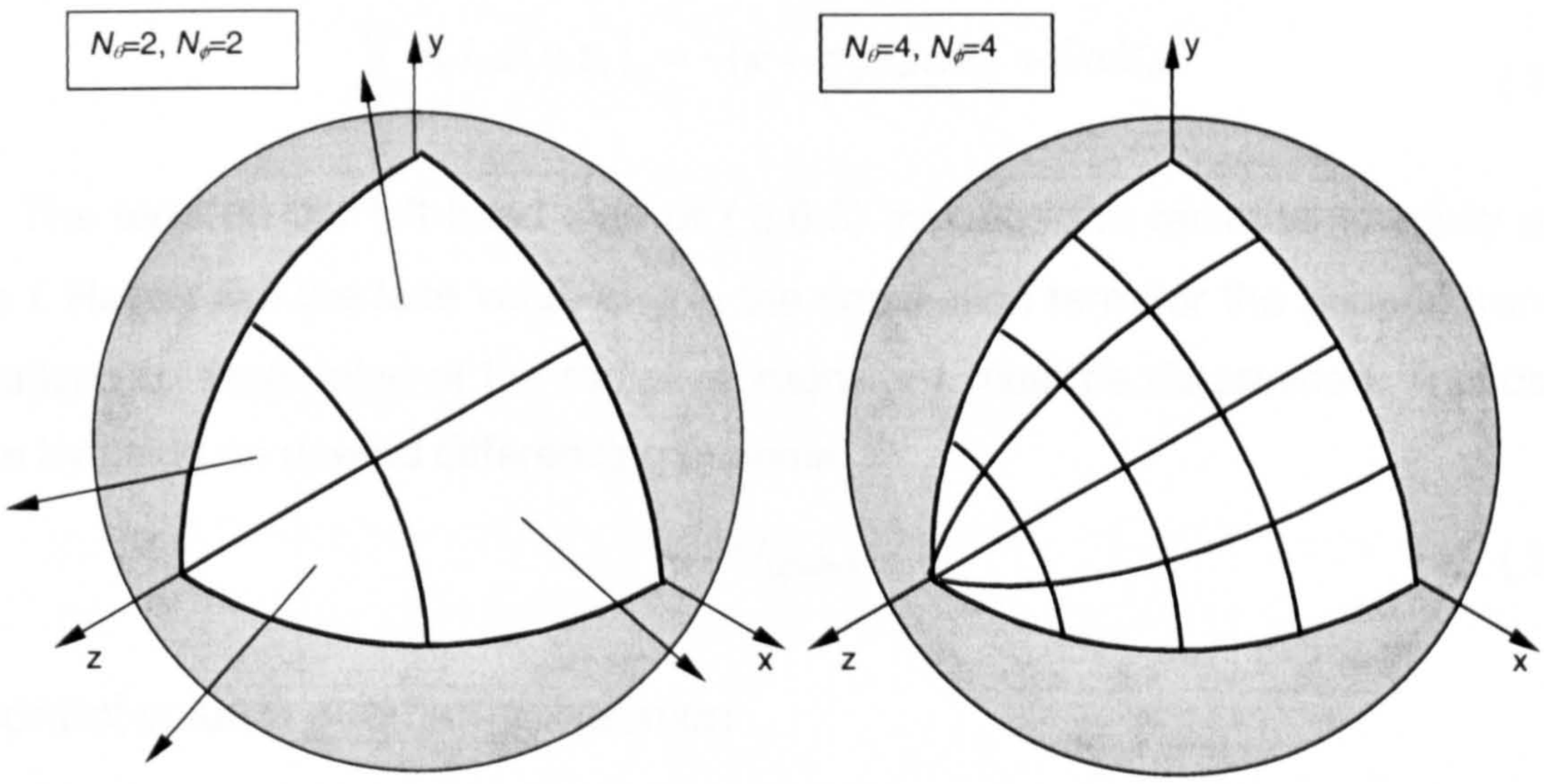

Figure 3.5 - Angular discretization of one octant.

3.6.2.2 Control volume balance

Recall the radiative transfer equation (RTE) for a grey, radiatively participating gas, which describes the spatial gradient of total radiative intensity in the direction **s** (2.5.18)

$$\frac{dI}{dx_i} s_i = -(\kappa + \sigma_s) I + S, \qquad (3.6.1)$$

where s_i are the components of **s**, and the source term S is given by

$$S = \kappa \frac{\sigma T^4}{\pi} + \frac{\sigma_s}{4\pi} \int^{4\pi} \Phi(\mathbf{s}_i, \mathbf{s}) \cdot I \cdot d\omega . \qquad (3.6.2)$$

Applying the same control volume integration as described in §3.2, and then applying Gauss' divergence theorem to the term on the left-hand side leads to

$$\int_V \frac{\partial I}{\partial x_i} s_i \cdot dV = \int_V -(\kappa + \sigma_s) I \cdot dV + \int_V S \cdot dV , \qquad (3.6.3)$$

$$\int_A n_i s_i I \cdot dA = \int_V -(\kappa + \sigma_s) I \cdot dV + \int_V S \cdot dV , \qquad (3.6.4)$$

where once again A is the bounding surface of the control volume, and n_i is the outward-facing component of the unit normal to the surface A in the i-direction.

Integration over the control angle ω leads to

$$\int_A \int_\omega n_i s_i I \cdot d\omega dA = \int_V \int_\omega -(\kappa + \sigma_s) I \cdot d\omega dV + \int_V \int_\omega S \cdot d\omega dV . \qquad (3.6.5)$$

For the discretized control volume P, this becomes

$$\sum_f A_f I_f \omega (n_i s_i)_f = -(\kappa + \sigma_s) I_P \omega V_P + S \omega V_P . \qquad (3.6.6)$$

The term on the left-hand side of (3.6.6) includes the radiative intensity at the face f. Rather like the face value of ϕ in the convection term for the general transport equation, the face value of the radiative intensity I_f must be determined. This can be done by using an upwind differencing scheme

$$I_f = I_{\text{upwind}} . \qquad (3.6.7)$$

3.6.2.3 Control volume overhang/pixelation

In general, the boundaries of the discrete solid angles will not be aligned with the control-volume faces of the spatial grid, particularly if a coarse angular discretization is used for the radiation field. This can lead to the problem of control-volume overhang (Murthy and Mathur, 1998), where a particular control angle may straddle a control-volume face, so that it is partially incoming and partially outgoing to the face. For the present work, a solid angle is considered to be wholly outgoing at a face if

$$(n_i s_i)_f \geq 0 . \qquad (3.6.8)$$

Otherwise it is assumed to be wholly incoming.

3.6.2.4 Extra computational requirements

When modelling three-dimensional turbulent, buoyancy driven flows without thermal radiation effects, it is necessary to solve seven discretized equations at each control volume: one for each component of the Navier-Stokes equation, one for energy transport, one for the pressure correction equation and two for the transport of turbulence quantities (if a two-equation turbulence model is used).

When modelling radiation using the finite-volume method described above, it is necessary to solve a transport equation for each individual direction. Even for a coarse angular discretization where, say $\theta = \phi = 45°$, there are 32 directions and therefore 32 transport equations must be solved for radiative intensity. The extra computational effort required to solve a flow where thermal radiation effects are important is therefore immediately apparent: the time and computer memory required to perform such a calculation is more than four times that required for a similar problem without thermal radiation.

If the angular discretization is refined, so that $\theta = \phi = 22.5°$, there are 128 directions and associated transport equations to solve for radiative intensity.

During the course of a computation, it is not necessary to solve the transport equations for radiative intensity at every iteration for the flow field. Indeed, for this study the radiative transport equations are only solved at every tenth iteration of the flow field. For this reason, with 32 directions, the runtime required for a certain number of iterations is only increased by about 50%.

3.6.3 Modelling the monochromatic absorption coefficient

For conditions commonly encountered within buildings, radiative participation by the intermediate air is almost entirely due to absorption due to the moisture content of the atmosphere.

A comprehensive spectral line-by-line database for the absorption spectra of 36 molecular species has been developed (Rothman et. al., 1996). The database, named HITRAN, includes almost 50000 entries for the individual lines comprising the absorption spectrum of water vapour.

The absorption spectrum for water vapour is illustrated in Figure 3.6. It is clear that the absorption spectrum for water vapour is an irregular function of the frequency of the incident radiation, comprising many thousand individual spectral lines. Adopting the finite-volume approach, however, and solving for the spectral radiative intensities corresponding to the frequency of each spectral line, and to the frequencies of the transparent windows in the absorption spectrum between adjacent lines, remains prohibitive and is likely to remain so for the foreseeable future. Instead, it is necessary to integrate the contributions from individual lines across the absorption spectrum.

From Figure 3.6 it is evident that at room temperature only the absorption lines within two bands are important; those in the rotational band, in the range 0-500cm^{-1} and those in the vibration-rotation band, in the range 1400-1900cm^{-1}.

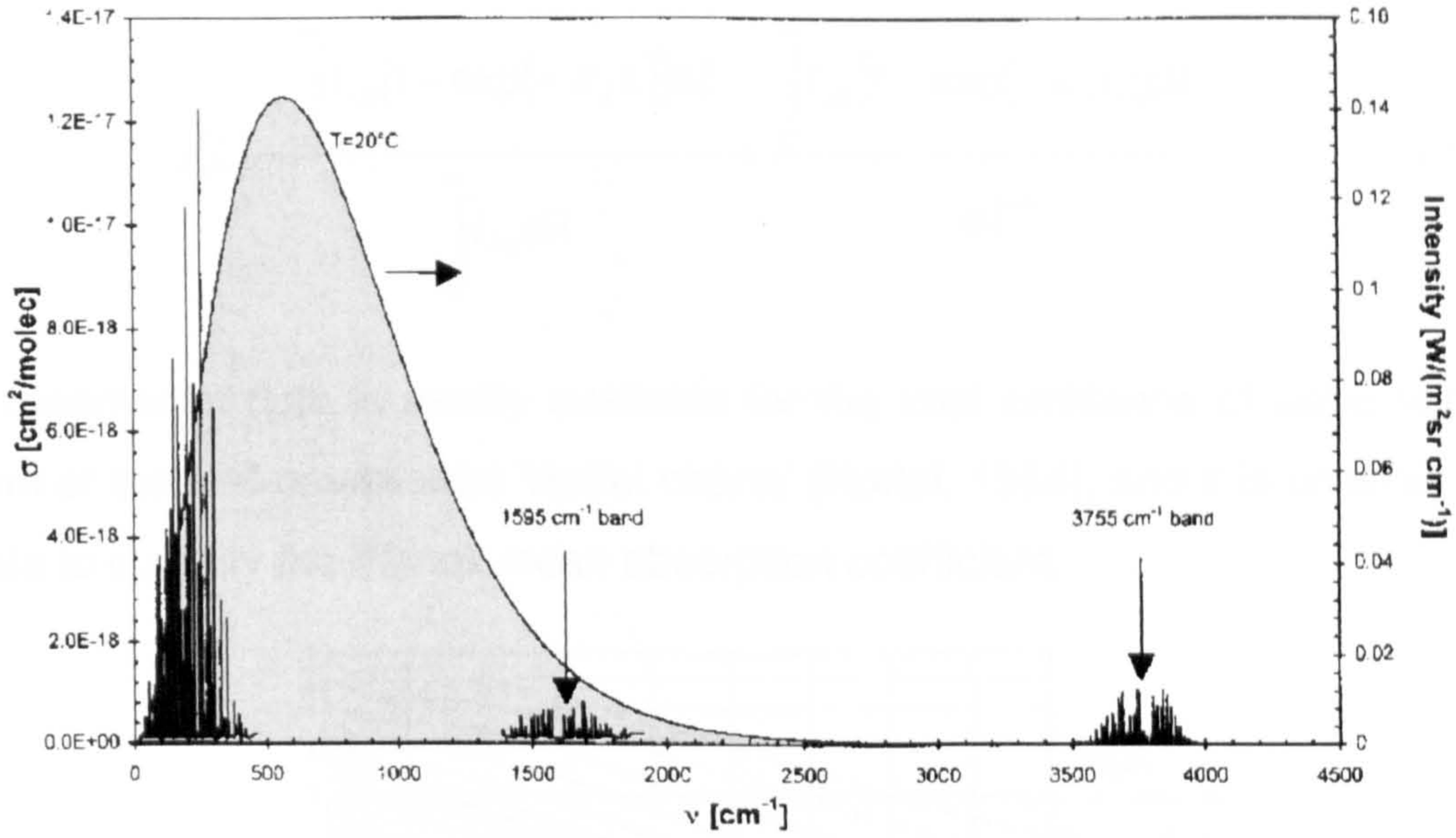

Figure 3.6 - Absorption spectra of water vapour, combined with the spectral intensity of a black body at a temperature of 20°C (from Schenker and Keller, 1995)

A common simplification is to assume that the medium behaves as a grey gas, so that the absorption coefficient is independent of the frequency of the incident radiation and can be represented by some mean value across the entire spectrum of frequencies. For the case of an optically thin medium, the appropriate mean absorption coefficient is the Planck mean absorption coefficient, defined as (Abu-Romia and Tien, 1967)

$$\kappa_P = \frac{\int_0^\infty \kappa_\lambda I_{\lambda b} d\lambda}{\int_0^\infty I_{\lambda b} d\lambda} . \qquad (3.6.9)$$

Usually in the past, researchers have concentrated upon describing the absorptivity of a body of non-scattering medium with a specified thickness rather than the absorption coefficient for the medium itself. Consequently, most of the information available in the literature relates to the absorptance or the emittance along a path in a gas. The total emittance $\varepsilon(L)$ along an effective path length L in a non-scattering gas is defined as (Siegel and Howell, 2001)

$$\varepsilon(L) = \frac{\int_0^\infty I_{\lambda b}[1-\exp(-\kappa_\lambda L)]d\lambda}{\int_0^\infty I_{\lambda b} d\lambda} = \frac{\int_0^\infty I_{\lambda b}[1-\exp(-\kappa_\lambda L)]d\lambda}{\sigma T^4}. \qquad (3.6.10)$$

Experimental data is readily available for the total emittance of water vapour in the form of the well-established 'Hottel charts' (Hottel, 1954), and it is possible to use this data to quantify the Planck mean absorption coefficient.

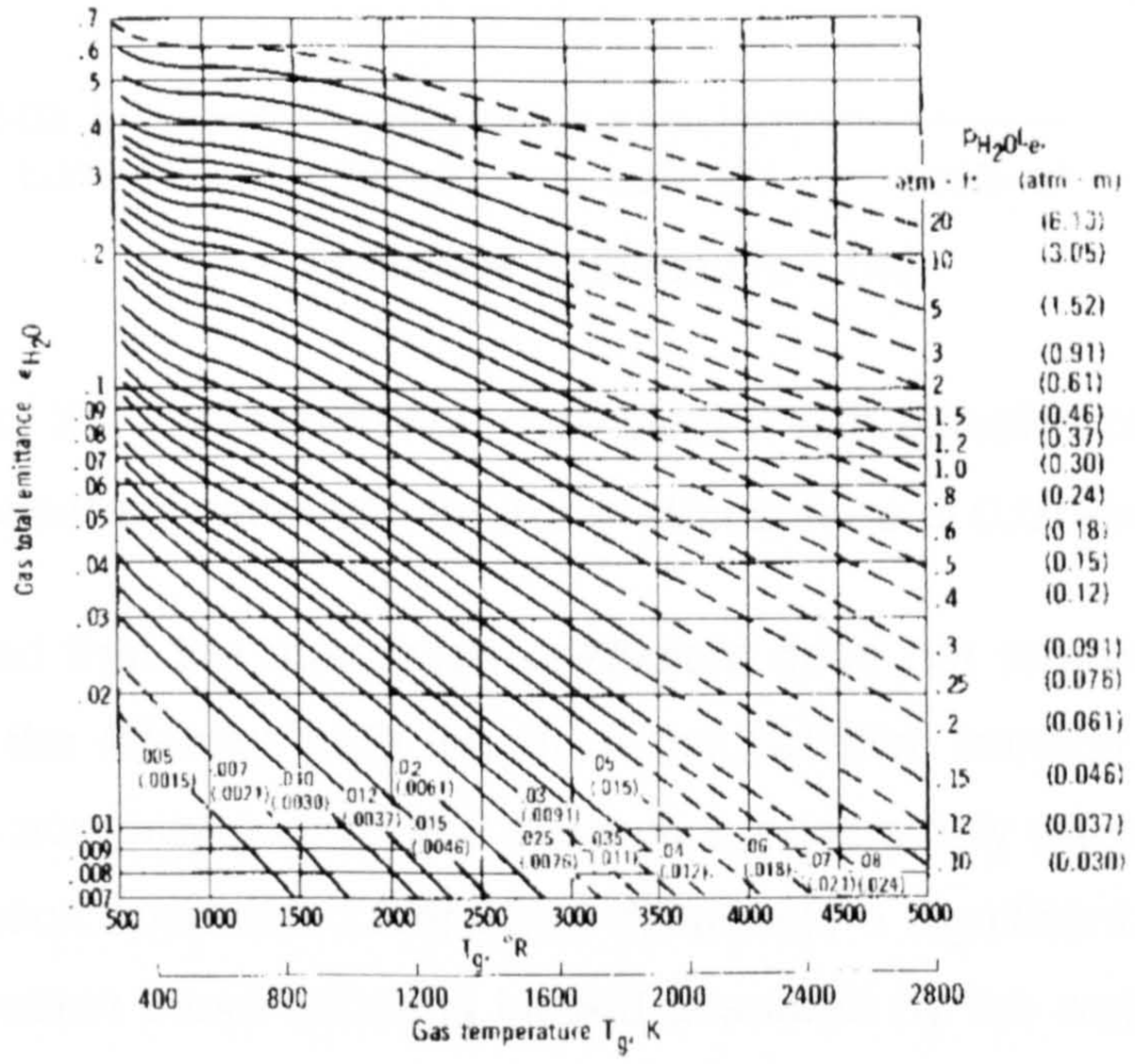

Figure 3.7 - Hottel chart showing the total emittance of water vapour in the limit of zero partial pressure in a mixture having a total pressure of 1.0atm (adapted from Siegel and Howell, 2001)

From Figure 3.7, data regarding the variation of the total gas emittance with the product of the partial pressure of water vapour and the effective path length is extracted for a temperature of 500°R, which corresponds to 4.6°C. Based upon this data, and with the assumption that the partial pressure of water vapour in the atmosphere is approximately equal to 0.01atm, which corresponds to a relative humidity approximately equal to 50%, the variation of the total absorption coefficient κ with effective path length L can be determined from (3.6.9) and (3.6.10), and is presented in Figure 3.8.

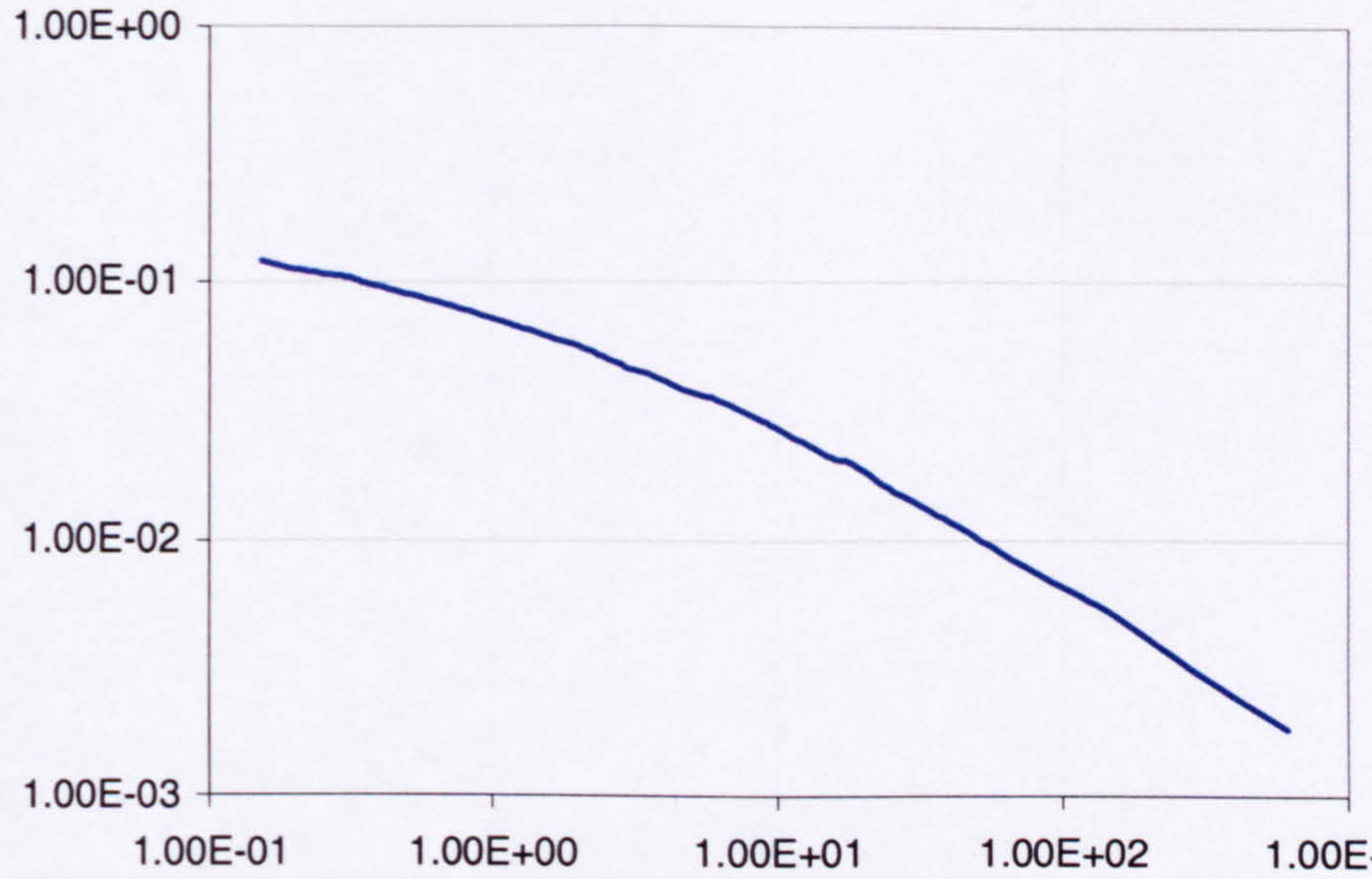

Figure 3.8 - Variation of the total absorption coefficient κ with effective path length L, for a partial pressure of water vapour in the atmosphere of 0.01atm (≈50%RH)

It is observed that the absorption coefficient does not remain constant, but is dependent upon the effective path length of the radiation transfer. This is because water vapour is a non-grey gas, so that absorption occurs only within restricted bands within the absorption spectrum. Over short distances, a significant proportion of the radiative energy within those bands is indeed absorbed by the water vapour. As the distance is increased, however, the spectral radiative intensity at the absorption band wavelength has already been absorbed, whereas the spectral radiative intensity at all other wavelengths can continue unaffected. As a consequence, at large distances the total proportion of energy absorbed becomes independent of the effective path length, so that the total absorption coefficient κ tends to become inversely proportional to the effective path length L.

The Planck mean absorption coefficient κ_P introduced in (3.6.9) is equal to the total absorption coefficient κ in the limit as the effective path length tends towards zero. From Figure 3.8, this is approximately equal to

$$\kappa_P \approx 0.12\text{m}^{-1}. \qquad (3.6.11)$$

Over short distances less than $1/\kappa_P$, it is reasonable to assume that the mixture behaves as a grey gas with a constant total absorption coefficient equal to the Planck mean absorption coefficient κ_P, (Modest, 1993).

3.7 Boundary conditions

Only three generic types of boundary were employed to describe the natural displacement flow considered in this work. They were:

- Solid 'no-slip' wall boundary
- Open pressure boundary
- Symmetry boundary.

3.7.1 Solid 'no-slip' wall boundary condition

For laminar flow calculations, the wall shear stress τ_{Wall} is evaluated using

$$\tau_{Wall} = \mu \frac{\partial u}{\partial n}, \qquad (3.7.1)$$

where $\partial u/\partial n$ is the gradient of velocity normal to the wall. For a stationary wall, this is calculated as

$$\tau_{Wall} = \mu \frac{u_P}{y_P}, \qquad (3.7.2)$$

where u_P is the magnitude of the velocity at the wall adjacent cell and y_P is the separation of the wall-adjacent cell centre from the wall surface. For flows where there may be a significant velocity gradient adjacent to the wall, a suitably refined mesh should be employed at the surface of the wall in order to resolve the flow in this region.

For turbulent flow calculations, the wall shear stress is determined using the standard wall functions of Launder and Spalding (1974). The mean flow velocity at the centre of the wall-adjacent cell is given by

$$u^* = \frac{1}{\kappa} \ln(E y^*), \qquad (3.7.3)$$

where

$$u^* = \frac{\rho_0 u_P \sqrt[4]{C_\mu k_P^2}}{\tau_{Wall}}, \qquad (3.7.4)$$

$$y^* = \frac{\rho_0 y_P \sqrt[4]{C_\mu k_P^2}}{\mu}, \qquad (3.7.5)$$

the wall roughness parameter for a smooth wall $E = 9.8$ and k_P is the magnitude of the turbulence kinetic energy at the centre of the wall adjacent cell. Strictly, this logarithmic law for the wall adjacent velocity is only valid for the fully-developed flow across a flat plate for $100 < y^* < 500$. It is used generally, however, to describe the

behaviour of all flows, including recirculating and developing turbulent flows, adjacent to solid wall surfaces.

With regard to the turbulence parameters, the *k*-equation is solved throughout the entire flow domain, including the wall-adjacent cell, subject to the condition that the gradient of *k* normal to a solid wall is equal to zero

$$\frac{\partial k}{\partial n} = 0 . \qquad (3.7.6)$$

It is assumed that turbulent equilibrium prevails in the region next to the wall, so that the rate of production of turbulence kinetic energy is equal to its rate of destruction. The rate of production $G_{k,P}$ at the wall-adjacent cell is determined from

$$G_{k,P} = \frac{\tau_{Wall}^2}{\kappa \rho_0 y_P \sqrt[4]{C_\mu k_P^2}}, \qquad (3.7.7)$$

and the rate of dissipation ε_P from

$$\varepsilon_P = \frac{\left(\sqrt[4]{C_\mu k_P^2}\right)^3}{\kappa y_P}. \qquad (3.7.8)$$

A number of alternative thermal boundary conditions are possible at a solid wall boundary. The simplest is that of a constant specified heat-flux *q*. For an adiabatic wall, the heat-flux at the wall boundary is explicitly set to zero.

Alternatively, the convection thermal boundary condition may be used, with the heat flux determined from

$$q = h_f \left(T_{Wall} - T_P\right) + q_{rad} = h_{ext} \left(T_{ext} - T_{Wall}\right), \qquad (3.7.9)$$

where h_{ext} is the external heat transfer coefficient, T_{ext} is the external heat-sink temperature, q_{rad} is the radiative heat flux incident upon the surface of the wall and h_f is the fluid-side heat transfer coefficient determined from the thermal law-of-the-wall (Launder and Spalding, 1974).

Another possibility is the radiation thermal boundary condition, where

$$q = h_f \left(T_{Wall} - T_P\right) + q_{rad} = \varepsilon_{ext} \sigma \left(T_\infty^4 - T_{Wall}^4\right), \qquad (3.7.10)$$

where e_{ext} is the emissivity of the external surface of the wall and T_∞ is the temperature of the external radiation sink.

A mixed convection/radiation thermal boundary condition is also possible, where the wall heat flux is given by

$$q = h_f(T_{Wall} - T_P) + q_{rad} = h_{ext}(T_{ext} - T_{Wall}) + \varepsilon_{ext}\sigma\left(T_{\infty}^4 - T_{Wall}^4\right) \qquad (3.7.11)$$

3.7.2 Open pressure boundary condition

At an open pressure boundary, the local piezometric pressure $\tilde{p}$ is specified explicitly at the boundary. Representative values for the turbulence quantities k and ε must also be provided in case the flow is entering the computational domain.

3.7.3 Symmetry boundary condition

At a symmetry boundary, the direction of the flow is necessarily parallel to the boundary, as there cannot be flow through a symmetry plane. Furthermore, the derivative of each of the flow parameters normal to the symmetry plane must be equal to zero

$$\frac{\partial \phi}{\partial n} = 0. \qquad (3.7.12)$$

3.8 Review of CFD used in building design

3.8.1 Introduction

A review of the current status of CFD and its application to predicting air-flows within buildings was published in the early nineties (Jones and Whittle, 1992). Since then, there have been many new developments in the field of CFD and its application within the built environment, and a relevant selection of this work is reviewed here. Most of this work has been concerned with which is the preferred method for predicting the effects of turbulence for forced ventilation and natural convection flows within buildings. More recently, however, a small number of workers have investigated numerically the effect of incorporating thermal radiative transfer upon their CFD-predictions.

3.8.2 Modelling turbulence

3.8.2.1 Forced ventilation

Beausoleil-Morrison and Clarke (1998) reported that the standard-$k\varepsilon$ model correctly predicts the velocity field within an enclosure that is mechanically ventilated. Heat transfer is over-predicted, however, in regions where the flow tends to

relaminarize. This is due to the standard-$k\varepsilon$ model overestimating the eddy viscosity in such regions.

Chen and Jiang (1992) suggested that the standard-$k\varepsilon$ model is the most appropriate turbulence model for computing room air-flows. They arrived at this conclusion even though the only two-equation model of turbulence they considered was the standard-$k\varepsilon$ model. They do concede, however, that the wall function method is not suitable for predicting the heat exchange coefficient near a wall, and suggest that a low-Reynolds number -$k\varepsilon$ model could be used instead.

Chen (1995) later performed a comparison of different -$k\varepsilon$ models for indoor air flow computations, which included forced ventilation and natural ventilation and mixed ventilation. He evaluated the performance of the standard-$k\varepsilon$ model, the low-Reynolds number -$k\varepsilon$ model of Lam and Bremhorst (1981), the two-layer -$k\varepsilon$ model of Rodi (1991), the two-scale -$k\varepsilon$ model Kim and Chen (1989), and the RNG-$k\varepsilon$ model of Yakhot and Orszag (1986). He concluded that some models perform better in some cases and more poorly in others, so that the choice of turbulence model is crucial to the numerical prediction obtained. The RNG-$k\varepsilon$ model was recommended as the best 'universal' turbulence model for indoor air flows.

Nielsen (1998) investigated the use of several different turbulence modelling techniques for the prediction of room air-flows. He suggested that different kinds of flows could be modelled using different turbulence models, but that in his experience the standard-$k\varepsilon$ model was satisfactory for many room air-flows.

3.8.2.2 Natural convection

If the heat transfer capabilities of a particular turbulence model are not accurate, then it is not surprising that the velocity field is not predicted particularly accurately for buoyancy-driven flows.

Xu and Chen (1998) have compared the performance the standard-$k\varepsilon$ model, together with two low-Reynolds number models with the experimental data of Olson et. al. (1990) for the airflow in a room with differentially heated vertical walls. They concluded that the flow-field and the vertical temperature profile predicted by the low-Reynolds number models are in good agreement with experimental data, whereas they are not when the standard-$k\varepsilon$ model is employed. They also confirm that the inclusion of thermal radiation in a numerical simulation can significantly improve the predictions obtained.

Similar observations were reported by Chen et. al. (1990). They compared the performance of the standard-$k\varepsilon$ model and the low-Reynolds number model of

Lam and Bremhorst (1981) for the within two differentially heated cavities: a small-scale water-based square cavity and a large-scale air-based tall cavity. For the water cavity they reported that with the low-*Re* model the predicted velocity field was in good agreement with the measured data, whereas with the standard-$k\varepsilon$ model it was not. For the air cavity it was reported that the predictions for the velocity field with the low-*Re* model were in better agreement with the measured data than for the standard-$k\varepsilon$ model. Furthermore, the rate of heat transfer predicted at the heated wall by the low-*Re* model was in good agreement with the measured data, whereas this was significantly over-predicted by the standard-$k\varepsilon$ model.

In 1992, a workshop on turbulent natural convection in enclosures with differentially heated vertical side-walls was organised, (Henkes and Hoogendoorn, 1993). They introduced a two-dimensional square enclosure as their standard test case, and invited ten international groups to participate in their computational comparison exercise. From this workshop emerged a reference numerical solution for the enclosure. It was found that the rate of heat transfer was generally over-predicted by the standard-$k\varepsilon$ model.

3.8.3 Modelling thermal radiative transfer

As part of their numerical study of the differentially heated Olson room, Xu and Chen (1998) included a radiation model to allow surface-to-surface radiative transfer. They found that the inclusion of the thermal radiation model significantly improved their CFD-predictions obtained.

Numerical investigations into the effect of including a model for the thermal radiative transfer within a full-scale room have been performed by Glicksman and Chen (1998) and by Kondo et. al. (2000). They concluded that thermal radiation, including the interaction of the radiation absorbed by the moisture content of air, has an important influence upon the temperature stratification within a space, and that this influence may become increasingly important for large spaces with a correspondingly large volume of gas within the space.

3.9 Summary

Computational fluid dynamics is a powerful technique for the prediction of air-flows within the built environment. For laminar problems, if numerical discretization errors are minimized, a CFD-prediction can provide an exact solution to the flow under consideration if suitable boundary conditions for the flow are specified. When turbulence is encountered, however, the effects of the turbulence must be modelled

upon the mean flow. There are many turbulence models in the literature, and many have been widely used with much success for high-Reynolds number flows. For the low-Reynolds number, transitional flows encountered in most buildings, however, there is no consensus upon which turbulence model is the most appropriate to use.

In contrast to some other experimental techniques, the CFD approach does not suffer from the problems associated with scaling, so that it can be legitimately applied to low-velocity flows. A further benefit is that a CFD prediction will provide a complete representation of the flow throughout the entire solution domain, whereas any experimental technique will only provide information at a few pre-selected measuring positions. In addition, if a particular physical process such as thermal radiative transfer is suspected of having an effect upon the flow, it is usually possible to incorporate the effects of this process into a CFD-prediction by solving an extra equation for the additional process. This is not always possible for other experimental techniques.

4.0 Cambridge mathematical model for natural displacement ventilation and its validation

4.1 Introduction

Towards the end of the nineteen-eighties, a group of workers at the University of Cambridge, England, were working on a novel new technique for the prediction of buoyancy driven natural displacement ventilation flows in buildings. This was at a time when computers were still relatively expensive and primitive in comparison to those found widespread today, so that computer simulation for the prediction of such flows was not considered a practical option.

Their approach was to simulate the stack effect within a small-scale model of a building by using fresh water and saline solutions to create density differences, which are analogous to those observed in full-scale buildings due to variations in temperature. This technique was used to evaluate the ventilation performance of several new buildings in England, including the Queen's Building at De Montfort University, Leicester, the Cable and Wireless Building, Coventry, the atrium section of the Westminster and Chelsea Hospital, London, and the BRE Energy Efficient Office at Garston, London.

In addition to the experimental 'salt-bath' technique, the group also devised a mathematical model to describe the natural displacement ventilation flow. They found excellent agreement between the predictions of the flow by the mathematical model and the results from the salt-bath experiments for a number of geometrical configurations.

The mathematical model described the natural displacement ventilation flow motivated by a point source of buoyancy positioned at floor-level within an enclosure. This model, dubbed the basic mathematical model, is discussed in §4.2. It initially formed part of the Doctoral thesis of Lane-Serff (1989), although a later paper (Linden et. al., 1990) is generally considered to be the starting point for this field of work. The original work also included a two-dimensional mathematical model and related experimental work, representative of a line source of buoyancy. For the

discussions that follow, however, the discussion will be entirely restricted to the three-dimensional case with a point source of buoyancy.

Many extensions to the original mathematical model have been devised, and a review of this field of work was recently published (Linden, 1999). Since that review, work in this field has continued, and a brief review of this progress is provided in §4.3.

The salt-bath technique and other more recent water-based experimental methods are introduced and discussed in §4.4 and §4.5 respectively, and a numerical investigation of the Cambridge mathematical model is reviewed in §4.6. Previous experimental work by the present author, which is believed to be the only experimental investigation of the natural displacement ventilation under consideration with air as the fluid medium, is described in §4.7.

Whilst most of the previous verification of the Cambridge mathematical model has been performed using the water-based salt-bath and fine-bubble techniques, the fluid medium in a real building will, of course, be air. Whether or not the flow observed during a water-based experiment is representative of that in a real building is an issue that remains unchallenged in the literature thus far. In order to address this, a number of other important experimental results are presented in §4.8.

4.2 Basic mathematical model

The original mathematical model proposed by the Cambridge group describes the natural displacement ventilation flow through an enclosure with high-level and low-level openings, motivated by a single point source of buoyancy on the floor of the enclosure.

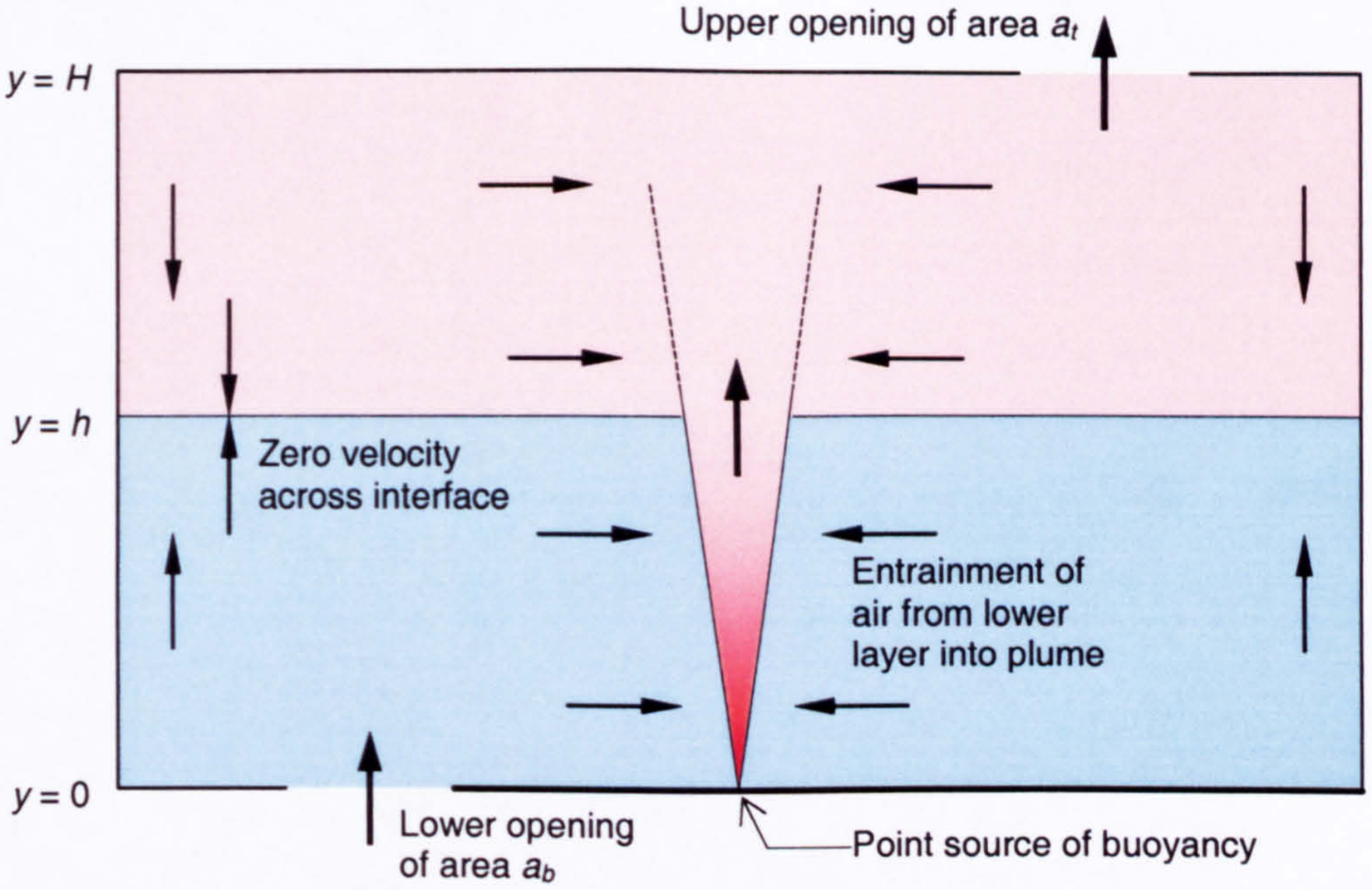

Figure 4.1 - Natural displacement ventilation flow through an enclosure, generated by a single point source of buoyancy at floor level (adapted from Linden et. al., 1990).

Initially the space within the enclosure and the entire surrounding region is maintained at a constant ambient density ρ_0. If a point source of buoyancy is then introduced at floor level within the space, a turbulent, buoyant plume will ascend from the source, entraining fluid from within the enclosure as it rises. Upon reaching the ceiling of the enclosure, the relatively light fluid within the plume will spread along the ceiling, forming a layer of lighter fluid at high level within the enclosure. Some of the fluid will re-circulate at high level, so that in the upper region of the space, the plume will entrain lighter than ambient fluid.

The Cambridge workers assume that convection is the only significant mechanism for transport within the space. As a consequence, it is assumed that no diffusion occurs between the ambient fluid at low level within the space and the lighter than ambient fluid at high level, so that a sharp interface between the two layers of fluid will develop.

Some of the fluid in the buoyant, upper layer will escape from the high-level opening. From continuity, a corresponding volume of ambient fluid is introduced into the enclosure through the low-level opening. Eventually, when the steady state is reached, a simple stratification is established between the two layers of fluid within the enclosure, as illustrated in Figure 4.1. At this point, the mass flow rate through each opening will be equal to the mass flow rate within the buoyant plume as it passes through the interface between the two layers of fluid.

The strength of the source of buoyancy is such that within a short distance of the source, all variations in density are small compared to the actual density of the fluid. As a consequence, it is legitimate to invoke the Boussinesq approximation, which states that the flow is essentially incompressible (except for the buoyancy term in the Navier-Stokes equation), even though it is the differences in density that motivate the flow.

Based upon this representation of the flow, and using the plume theory from §2.6, the Cambridge group showed that the dimensionless depth of the cool ambient layer of fluid $\xi = h / H$ is given by (Lane-Serff, 1989)

$$\frac{A^*}{H^2} = C^{\frac{3}{2}} \left(\frac{\xi^5}{1-\xi} \right)^{\frac{1}{2}}, \qquad (4.2.1)$$

where H is the difference in height of the top and bottom openings, A^* is the effective area of the openings of the enclosure (§2.7), and the constant C is given by

$$C = \frac{6}{5} \alpha \left(\frac{9}{10} \alpha \right)^{\frac{1}{3}} \pi^{\frac{2}{3}}. \qquad (4.2.2)$$

From these relations, it is apparent that the depth of the cool ambient layer of fluid is entirely dependent upon the geometry of the enclosure, and is independent of the strength of the source of buoyancy.

The difference in density $\Delta\rho$ between the buoyant layer of fluid at high-level and the ambient fluid is, however, dependent upon the strength of the buoyancy source. This difference in density is determined from

$$\Delta\rho = \frac{\rho_0 g'}{g}, \qquad (4.2.3)$$

where ρ_0 is the ambient fluid density, g is the acceleration due to gravity, and g' is the reduced gravity within the plume as it crosses the interface (§2.6). The pressure distribution within the enclosure is shown in Figure 4.2, and shows the neutral level, defined as the height at which there is no difference in pressure across the envelope of the enclosure.

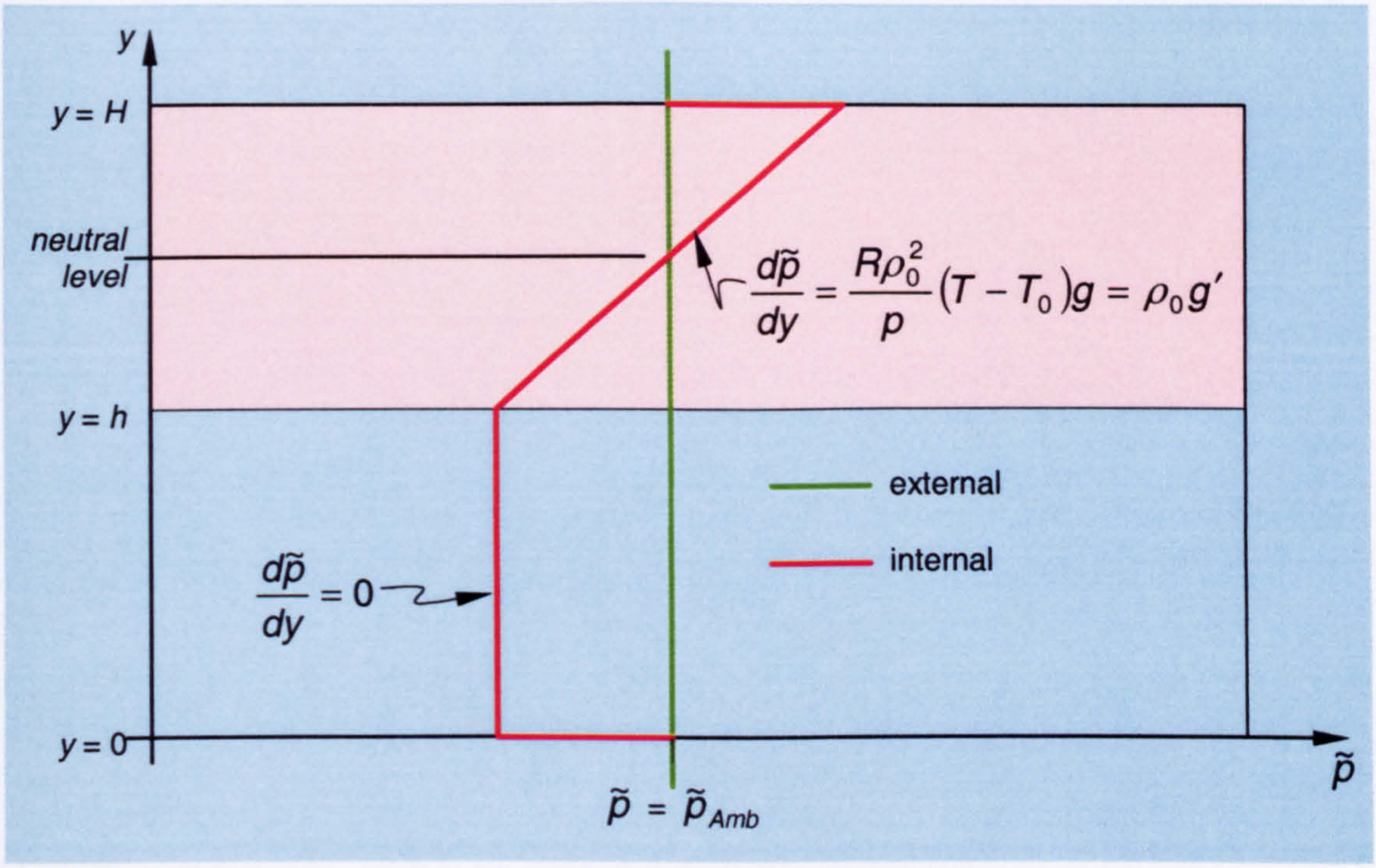

Figure 4.2 - Pressure distribution for the steady-state displacement ventilation flow

4.3 Extensions to the basic mathematical model

Many extensions to the original work have been performed, and a review of this field of work was recently published (Linden, 1999). Since then progress in this field has continued, some of which is briefly reviewed here.

The original paper (Linden et. al, 1990) included a simple extension to the mathematical model to describe the natural displacement flow resulting from several equi-strength sources of buoyancy, distributed such that the resulting buoyant plumes do not interact. This work was later extended to account for two sources of buoyancy of differing strength at floor level (Cooper and Linden, 1996). For this case it was proposed that a stable three-layer stratification would result, where the heights of each interface would depend upon the geometry of the enclosure and upon the ratio of the strengths of the sources of buoyancy. The same authors also developed an approximate model for the displacement flow resulting from multiple sources of buoyancy of differing strength at floor level (Linden and Cooper, 1996). They postulated a layered stratification, with each plume terminating in its own distinct layer. Each of the extended mathematical models was validated using the salt-bath technique.

The original model can also be modified to account for a point source of buoyancy at a height that is different to floor level within the enclosure (Howell, 1998). This allows the model to describe the displacement flow motivated by a point source of buoyancy at a finite height within the space. This modification also enables the

model to describe the flow motivated by a distributed source of buoyancy, such as a sun patch at floor level, since the plume arising from a source of buoyancy distributed over a finite horizontal area can be traced back to a point source of buoyancy with zero initial mass flux and a negative initial momentum flux (Caulfield, 1991). This approach, however, is physically suspect as it requires the fluid to travel in both directions in the region below the source, which for a distributed source of buoyancy at floor level is also outside the bounds of the enclosure.

In addition to the investigation of natural ventilation motivated entirely due to the stack effect, the Cambridge group have also conducted a significant amount of research into the combined effect of buoyancy and wind induced natural ventilation, a summary of which is included in the review by Linden (1999).

An extended model has also been developed for the single buoyancy source case that incorporates the transport of radiative energy between the surfaces of the ceiling and the floor (Li, 2000). It was claimed that the new model would better predict the ventilation flow rate through a real building space when compared to the original Cambridge mathematical model, although no experimental results were provided to back-up this claim. It was shown that as a consequence of the inclusion of radiative heat transfer, the height of the interface is affected by the strength of the heat source.

The original model has also been extended to describe the displacement flow within an enclosure with a third opening at some intermediate height (Chen and Li, 2002). They identified three distinct modes of ventilation, depending upon the heights of the interface and of the neutral level with respect to the height of the middle opening. Importantly, they discovered that the mode of ventilation that occurs is not necessarily uniquely determined by the geometry of the enclosure, but may also depend upon the initial conditions within the space. This paper is the first to report upon the possibility of flow bifurcation with natural displacement flows in enclosures motivated entirely by the stack effect, although this issue has been previously discussed for combined buoyancy/wind driven flows (Li et. al., 2001) and recommends that this is a challenging area for future research. Once again, however, this work is purely theoretical and only a numerical investigation is presented so that there are no experimental results to verify the proposed theory.

Further extensions to the original model have recently appeared in the literature to describe the natural ventilation flow through two connected spaces, representative of a tall atrium and an adjoining storey (Holford and Hunt, 2002). The original model is used to describe the displacement flow within the storey. It is assumed that the buoyant fluid that subsequently leaves the storey collects in the adjoining atrium before escaping to the ambient reservoir. In addition to the flow from the storey, the

atrium space may be directly ventilated by a low-level opening to the exterior. Alternatively, it may have no such low-level opening, rather like a chimney, where the only route for air to enter the atrium is through the storey. It is suggested that direct ventilation of the atrium is detrimental to the ventilation of the storey, and that the best design is a compromise that offers adequate ventilation of both spaces.

4.4 Verification by salt-bath technique

The Cambridge group verified their mathematical models using the 'salt-bath' technique. Their approach was to simulate the natural displacement flow in the laboratory using a small-scale model of an enclosure, with water as the fluid medium, and introduce saline solution to generate density differences, analogous to those generated by temperature variations in a full-scale building.

4.4.1 Experimental set-up

The actual experiments were performed using a small-scale Perspex enclosure measuring 0.3m long × 0.25m high × 0.2m wide (Linden et. al., 1990). This enclosure was submerged into a large tank of fresh water representing a static environment surrounding the building.

Saline solution was introduced into the enclosure via a small downward pointing tube in the ceiling of the enclosure. Saline solution is more dense than fresh water, so that the buoyancy forces act downward and the layer of ambient fluid remains in the upper region of the enclosure. This is the reverse circumstance to that for a heat source in a building, so that each salt-bath experiment is essentially conducted upside-down. For the remainder of discussions in this thesis, and in order to avoid unnecessary confusion, all references are as for real building with a source of buoyancy at floor level.

A series of holes were drilled in the ceiling and floor of the enclosure. The holes, which could be opened or closed during experiments, allowed the workers to investigate the natural displacement flow for a number of different opening configurations.

The large surrounding tank, which measured 0.6m × 0.6m × 13.0m was necessarily large so that as each experiment proceeds, the concentration of salt in the ambient fluid remained negligible.

Typical values for the volume flux V and buoyancy flux B during the experiments were

$$V = 2 \times 10^{-5}\ \mathrm{m^3\ s^{-1}}, \tag{4.4.1}$$

and

$$B = 1 \times 10^{-5}\ \mathrm{m^4\ s^{-3}}, \tag{4.4.2}$$

from which the reduced gravity g' at the source is calculated to be

$$g' = \frac{B}{V} = 0.5\ \mathrm{m\ s^{-2}}. \tag{4.4.3}$$

This corresponds to a density difference $\Delta\rho / \rho = 0.051$, and a molar density of salt in the incoming saline solution $N = 864 \mathrm{mol\ m^{-3}}$.

4.4.2 Dynamic similarity

In order to achieve dynamic similarity, it was necessary to ensure that certain non-dimensional parameters describing the flow within the scale model are representative of those found in a full-scale building. They identified the Reynolds number *Re* and Peclet number *Pe*, which represent the relative importance of convection and diffusion, as the quantities that are important to match between the small-scale and full-scale, where

$$Re = \frac{\rho U H}{\mu}, \tag{4.4.4}$$

and

$$Pe = \frac{\rho U H}{\Gamma_\phi}, \tag{4.4.5}$$

and U and H are representative values of the velocity and length scale for the flow within the enclosure. In particular, they presumed that for flows in buildings both quantities are large, so that the full-scale flow was independent of viscous and diffusive effects.

It will be convenient for later discussions to introduce suitable definitions for U and H here. Let H be the height of the experimental enclosure, and U be the velocity in an unconstrained plume at a distance H from a point source of buoyancy. For the small-scale experiments, therefore, it would suffice to ensure that both quantities are also large. From (2.6.2) and for the typical value of buoyancy flux B given earlier (4.4.2), the velocity U is equal to

$$v = \frac{5}{6\alpha}\left(\frac{9}{10}\alpha\frac{B}{\pi}\right)^{1/3} H^{-1/3} = 7.837 \times 10^{-2}\mathrm{m/s}, \tag{4.4.6}$$

so that the Reynolds number and Peclet number are equal to

$$Re = 1.959 \times 10^4, \tag{4.4.7}$$

and

$$Pe = 1.217 \times 10^7, \tag{4.4.8}$$

where the density of water $\rho = 1000$ kg m^{-3}, the viscosity of water $\mu = 10^{-3}$ m^2 s^{-1}, and the diffusion coefficient for salt in water D_{NaCl} is equal to (Cussler, 1997)

$$D_{NaCl} = \frac{\Gamma_{NaCl}}{\rho} = 1.61 \times 10^{-9} \text{ m}^2 \text{ s}^{-1}. \tag{4.4.9}$$

4.4.3 Limitations of the salt-bath technique

4.4.3.1 Transport of heat by molecular diffusion

One of the fundamental assumptions made by the Cambridge workers was that the Reynolds number and Peclet number for a full-scale building are large, so that the natural displacement flow at the full-scale is independent of viscous and diffusive effects. They based their analysis upon a characteristic velocity scale representative of the velocity within the plume and a characteristic length scale representative of the height of a building. The plume, however, only occupies a small fraction of the volume within an enclosure and as such is not representative of the velocity within the bulk of the space. Indeed, in a full-scale building it is observed that there are many regions of almost stagnant air where the air velocity is almost negligible. In such regions it is not valid to neglect diffusion as a mechanism for transport.

If diffusion effects are not neglected, it is necessary to ensure dynamic similarity with another non-dimensional quantity, the Schmidt number *Sc*. This quantity is defined for a particular flow parameter ϕ as the ratio of the fluid viscosity μ and the diffusivity of the parameter Γ_ϕ

$$Sc_\phi = \frac{\mu}{\Gamma_\phi}. \tag{4.4.10}$$

For the case where the flow parameter under investigation is the fluid temperature, this quantity is called the Prandtl number *Pr*

$$Sc_T = Pr = \frac{c_p \mu}{k}. \tag{4.4.11}$$

The Prandtl number is actually a fluid property, as it is determined entirely from other fluid properties. For air, the Prandtl number is equal to

$$Pr_{air} = 0.71, \qquad (4.4.12)$$

so that the rate of diffusion of heat in air is comparable to the rate of diffusion of momentum. For the diffusion of salt in water, the Schmidt number is equal to

$$Sc_{NaCl} = 621. \qquad (4.4.13)$$

It is immediately apparent that full similarity cannot be achieved between the natural displacement flow in the salt-bath experiments and that in a full-scale building, since the diffusivity of salt in water is almost one thousand times less significant than the diffusivity of heat in air. Indeed, this limitation of the technique was recognised by the original Cambridge workers (Lane-Serff, 1989). For regions of almost stagnant fluid this may be particularly important, and could lead to significant differences between the flow observed in the salt-bath model and that observed in a full-scale room.

4.4.3.2 Transport of heat by turbulent diffusion

Since the fluid properties for air at room temperature are known and are fixed, the Reynolds number for a full-scale enclosure containing air is dependent only upon the height of the enclosure and the velocity in a plume at that height above the source, which from the plume theory presented in §2.6 is in turn dependent upon the strength of the heat source. The relationship between the height of the enclosure and the strength of the heat source with air as the fluid medium required to achieve a Reynolds number of $Re = 1.959 \times 10^4$, which is the same as that for the salt-bath experiment with the typical value for buoyancy flux B presented earlier (see (4.4.7)), is shown in Figure 4.3 below.

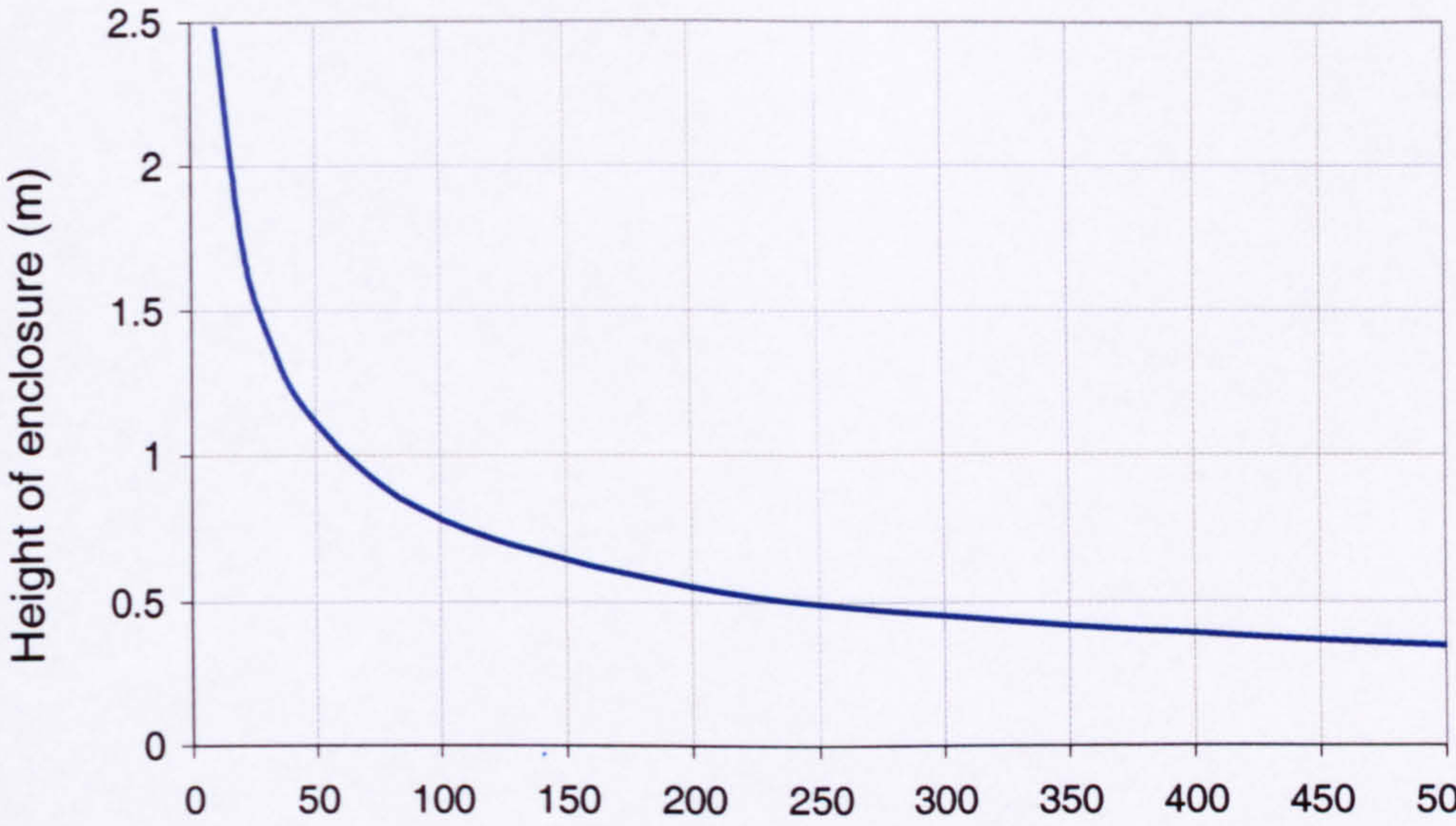

Figure 4.3 - Graph to show variation of enclosure height with strength of heat source, required to achieve a Reynolds number of 1.959×10^4, for $\rho_{AIR} = 1.225$ kg/m^3 and $\mu_{AIR} = 1.71\times10^{-5}$ m^2 s^{-1}

Although it is not known exactly what heat source the Cambridge workers intended to simulate with their salt-bath for the typical value of buoyancy flux given, Figure 4.3 shows how the experiment with $Re = 1.959\times10^4$ may be compared to the flow within a dynamically similar enclosure with air as the fluid medium. It may be representative of

1. a full-scale room of height 2.5m with a point heat source of only 10W;
2. a fully-grown male sitting performing sedentary work with a (sensible) energy release rate of say 80W, within an enclosure of height 0.88m
3. a fully-grown male working at a computer terminal with a combined energy release rate of say 300W, within an enclosure of height 0.45m.

Generally, the Reynolds number for the flow within a real building will be greater than this. Within a full-scale room of height 2.5m there may often be a number of heat sources in excess of 10W. Likewise, for a fully-grown male with an energy release rate of 80W, an enclosure of height 0.88m would be to small to contain the person.

Since the flows encountered within buildings are usually transitional between the laminar and turbulent states, the flow may be particularly sensitive to the precise value of Reynolds number. As a consequence, it is likely that the degree of turbulent diffusion in the salt-bath will be less, to some extent, than that which may be observed in a full-scale room.

In order to increase the Reynolds number for the salt-bath flow to a value that is perhaps more representative of the flow within a real building, it is necessary to either

increase the height of the Perspex enclosure or increase the buoyancy flux within the plume. The buoyancy flux may be increased by increasing the salt concentration within the saline solution introduced at the source of the plume, or by increasing the volume flux at the plume source. In the salt-bath experiments to date, however, this volume flux was necessarily small to ensure that the plume behaved approximately as a pure plume, which by definition must have a zero volume flux at source.

4.4.3.3 Transport of heat by radiation

Thermal radiative transfer is not present in the salt-bath technique, since the flow for an experiment is entirely isothermal. There is growing evidence (§4.8), however, that thermal radiation may be a significant mechanism for transport of heat for the natural convection class of flows found in buildings.

4.4.3.4 Realistic boundary conditions

The fabric of a real building is thermally massive so that it will absorb heat through the day and release heat at night. The salt-bath technique is restricted, however, in terms of the boundary conditions that may be applied at solid surfaces. In particular, it is not possible for salt to diffuse through a solid wall, and so the boundary is necessarily analogous to an adiabatic wall.

4.5 Verification by other water-based experimental techniques

4.5.1 The thermal water-bath technique

Recently, the Cambridge group has extended their experimental investigations to the case of temperature differences in water (Linden, 1999). They have found that there is excellent quantitative agreement between the temperature stratified experiments and the salt stratified experiments.

Introducing temperature differences to motivate the displacement flow through an experimental enclosure offers two distinct improvements over the salt-bath technique. Firstly, the Prandtl number of water (at 15°C) is equal to

$$Pr_{water} = 7.46, \qquad (4.5.1)$$

so that the transport of heat by molecular diffusion is more realistically described than with saline solution. Secondly, this technique allows a wider range of boundary conditions to be applied at solid boundaries.

It is not possible, however, to achieve such a large Reynolds number as for the salt-bath experiments, so that the transport of heat by turbulent diffusion may be even

less than for the salt-bath experiments. In addition, water is radiatively opaque in the infra-red portion of the spectrum, so that thermal radiation effects are once again not accounted for.

4.5.2 The fine-bubble technique.

Recently, a new technique has been developed for the experimental modeling of the displacement ventilation flows under consideration (Chen et. al., 2001). The technique utilizes electrolytically generated fine hydrogen bubbles within a scale model of an enclosure with water as the fluid, in order to simulate the thermally motivated convection flows found in a full-scale building.

The new technique is undoubtedly simple, ease to use and economical. The experimental system comprised five components; a small-scale enclosure, a large surrounding tank, a copper wire cathode, a graphite anode and a constant voltage DC power supply. The small-scale enclosure used measured 0.2 m long × 0.1 m wide × 0.2 m high, and was submerged in a larger tank measuring 0.9 m long × 0.345 m wide × 0.45 m high. The point source of buoyancy was made of 0.5mm diameter copper wire, connected to the negative pole of a DC electricity supply. The anode was a graphite plate measuring 10 mm × 8 mm × 60 mm, located within the larger tank. A saline solution was used as the fluid media for the experiments, with a salt content of 3.0 wt% used to increase the electrical conductivity of the solution. A small amount of surfactant was also added to reduce bubble coalescence in the low-velocity regions such as the buoyant layer below the ceiling within the small-scale enclosure.

4.5.2.1 Slip velocity of the hydrogen bubbles

There exists a slip velocity of approximately 5.0 mm/s between the immiscible fine bubbles and the saline solution, the effects of which must be minimized so as not to significantly affect the flow field.

In the region of the plume, provided that the slip velocity is small compared to the mean local flow in the plume, it was found that the turbulent structure and entrainment of the bubble-plume was similar to that of a thermal-induced or a concentration-induced plume, so that it can be accurately described by the plume theory of §2.6 (Chen and Cardoso, 2000).

In the region away from the plume, however, the slip velocity may not be insignificant with respect to the local velocity, particularly for experiments with large openings and a weak source of buoyancy. Under such circumstances this may have a significant effect upon the flow field.

4.5.2.2 Transport of heat by molecular diffusion

The diffusivity of hydrogen bubbles in water was estimated to be

$$D_{H_2} = \frac{\Gamma_{H_2}}{\rho} = 5.10 \times 10^{-9}\ \mathrm{m^2\ s^{-1}}, \qquad (4.5.2)$$

leading to a Schmidt number equal to

$$Sc_{H2} = 196. \qquad (4.5.3)$$

The diffusivity of the hydrogen bubbles in water is, therefore, much less significant than the diffusivity of heat in air, which may be particularly important for regions of almost stagnant fluid. As for the salt-bath experiments, this could lead to significant differences between the flow observed at the small-scale and that observed in a full-scale room.

4.5.2.3 Transport of heat by turbulent diffusion

A typical value for the buoyancy flux B during the experiments was (Chen et. al., 2001)

$$B = 1.14 \times 10^{-6}\ \mathrm{m^4\ s^{-3}}. \qquad (4.5.4)$$

Together with the height of the small-scale enclosure, the Reynolds number for the flow, based upon the definition given in §4.4.2, was found to be

$$Re = 8.067 \times 10^{3}. \qquad (4.5.5)$$

This is lower than the Reynolds number for the typical salt-bath experiment, so that the degree of turbulent diffusion in the small-scale model will once again be less, to some extent, than that which may be observed in a full-scale room.

4.5.2.4 Transport of heat by radiation

As for the salt-bath technique, thermal radiative transfer is not present in the fine-bubble technique, since the flow for an experiment is entirely isothermal. This could, once again, lead to significant differences between the flows measured at the small-scale and those observed for a full-scale enclosure.

4.5.2.5 Limitation of realistic boundary conditions

It is not possible for hydrogen bubbles to diffuse through a solid wall. As for the salt-bath technique, therefore, the boundary is necessarily analogous to an adiabatic wall.

4.6 Numerical verification by the CFD technique

The computational fluid dynamics approach (CFD, see §3.0) has also been used to simulate and investigate the Cambridge mathematical model for natural displacement ventilation (Cook, 1998). Three benchmark flows were considered: a two-dimensional enclosure with effectively linear openings and buoyancy source, a three-dimensional enclosure with finite openings and a line source of buoyancy, and a three-dimensional enclosure with finite openings and a point source of buoyancy. Each benchmark case considered was representative of a full-scale enclosure with air as the fluid medium. For benchmark three, which is of particular interest, the enclosure measured 5.1 m long × 2.55 m high × 1.0 m wide, and at the centre of the floor was a square heat source of 200W measuring 0.1 m × 0.1 m. The ambient temperature was assumed to be 18°C. Two different turbulence models, the standard-$k\varepsilon$ model and the RNG-$k\varepsilon$ model (§3.5.6), were employed to describe the effects of the turbulent structures within the flow. Thermal radiation effects were neglected.

Criteria for the basis of comparison between the CFD predictions and the earlier work of the Cambridge group were established, both for the displacement flow as a whole, and for the region of the plume in isolation. For the displacement flow analysis, a general comparison of the flow field was made, ensuring that there was indeed a plume rising from the heat source, that there was inflow to the enclosure through the low level openings and outflow through the high level openings, and that an interface did indeed form between a layer of buoyant fluid at high level and ambient fluid at low level. For quantitative comparison, the variation of the height of the interface was examined for a variety of opening configurations and for different strengths of heat source. The variation of reduced gravity across the interface was also investigated. For the plume in isolation, the variation of plume width, volume flow rate and reduced gravity within the plume with distance above the heat source were analysed and compared to the theoretical relationships presented in §2.6.

Excellent qualitative agreement was reported between the CFD predictions and the salt-bath experiments and mathematical model of Linden et. al. (1990), with respect to the general comparison of the flow field. It was found, however, that the turbulence models employed over-predicted the rate of entrainment into the plume. Analysis of the plume in isolation showed that the top-hat entrainment constant for the plume with the standard-$k\varepsilon$ model of turbulence was predicted to be

$$\alpha_T^{\text{standard-}k\varepsilon} = 0.14\,, \qquad (4.6.1)$$

and for the RNG-$k\varepsilon$ turbulence model, it was predicted to be

$$\alpha_T^{\text{RNG-}k\epsilon} = 0.11. \qquad (4.6.2)$$

A comparison between the variation of the height of the interface and the buoyancy change across the interface with the effective area of the openings A^* for the CFD predictions was in good agreement with the predictions of the Cambridge mathematical model with a modified entrainment constant $\alpha_T = 0.14$.

4.7 Air-based experimental studies

It is thought that the only experimental investigations of the natural displacement ventilations under consideration with air as the fluid medium were conducted by the present author at the University of Newcastle upon Tyne, England (Howell, 1998, and Howell and Potts, 1998). Temperature and velocity measurements were presented for an enclosure measuring 1.0 m long × 1.0 m high × 0.6 m wide. The temperature rise within the enclosure was obtained using a *k*-type back-to-back thermocouple arrangement. One junction of the thermocouple remained fixed in the floor of the enclosure, whilst the other was allowed to move along several linear vertical loci. The system provided the difference in temperature between the two junctions, which was recorded at many heights within the space. The vertical component of the centreline velocity at one of the lower openings was also measured using the laser Doppler anemometry system described in §5.7.1.

Having tried many small electrical sources of heat unsuccessfully, the heat source used for the study was a candle, which satisfied the point source criterion and provided sufficient heat output to sustain a displacement flow through the enclosure and establish measurable temperature differences within the space. By monitoring the temperature of the air leaving the upper openings of the enclosure, the heat output of the candle was estimated to be in the range of 10 W to 15 W.

Using air as the fluid medium represented an improvement over the other water-based experimental investigations that had been conducted. There was no longer any discrepancy in the Prandtl number of the fluid, so that it was expected that the transport of heat due to molecular diffusion would be better represented. Thermal radiation was also present as a mechanism for heat transfer.

Based upon the estimation of the heat output of the candle, the Reynolds number for the flow is approximately

$$Re = 1.231 \times 10^4. \qquad (4.7.1)$$

This is higher than that for the fine-bubble technique, but below that for the salt-bath technique. As a consequence, the degree of turbulent diffusion in the air

enclosure will once again be less, to some extent, than that which may be observed in a full-scale room.

The results of this study show that the temperature remained constant in the layer of fluid below a height of about 0.4 m, whilst above this layer, the temperature increased in an approximately linear manner with height. No interface was observed between a layer of ambient air at low level and a layer of buoyant air at high level. This was in disagreement with the salt-bath experiments and Cambridge mathematical model.

4.8 Other important experimental results

Although the geometrical arrangement of the experimental investigations described in this subsection do not conform to that described by the Cambridge mathematical model and cannot therefore be used for direct comparison, they do highlight some important differences between water-based small-scale flows and air-based full-scale flows.

4.8.1 Natural displacement ventilation in a full-scale enclosure

Recently, an experimental study of the natural ventilation of a full-scale enclosure was performed at the University of Loughborough, England (Eftekhari, 2000). The enclosure was a portable cabin measuring 3.3 m long × 2.2 m high × 3.0 m wide, located externally in a sheltered area. Ventilation of the enclosure was achieved by four louvered openings, two at low level and two at high level, with a vertical distance of 1.25 m between the centre of the openings at each level. During the experiments the size of the high-level and low-level openings were varied from 0.07 m^2 to 0.12 m^2. Temperature and velocity data obtained at four locations and six heights within the room were recorded.

During the course of the experiments there were two 2kW heaters, located in adjacent corners, each of which provided a source of buoyancy. In addition, there were three personal computers arranged within the space, each of which would also be a source of buoyancy. Due to the sheltered position of the cabin there was no solar heat gain within the space. Results for the temperature stratification occurring on two typical days in winter are presented.

Whilst the heater arrangement did not correspond exactly to the point source of buoyancy at floor level assumed in the basic Cambridge model, it could be described by some of the extensions to the basic model presented in §4.3. In any case, the results for the temperature stratification would provide some indication of whether a

sharp interface does indeed form between a layer of ambient air at low level and a layer of buoyant air at high level.

Examination of the temperature measurements reveal that no such interface occurred during the experiments performed. For one of the experiments performed, below a height of about 1.0m the vertical temperature gradient remained constant at approximately 10-12°C/m, and above that height the temperature gradient was reduced at about 2-3°C/m. For the other experiment, it was observed that the temperature gradient remained constant at about 2-3°C/m for the entire height of the enclosure.

4.8.2 Natural convection in a full-scale differentially heated cavity.

During the nineteen-eighties an investigation of the natural convection flow within a full-scale experimental enclosure was conducted at the Massachusetts Institute of Technology, Cambridge, United States (Olson, 1986, Ferm, 1984, Olson et. al. 1990). The facility was a large-scale differentially heated cavity, measuring 7.9 m long × 2.5 m high × 3.9 m wide, with a hot wall at one end and a cold wall at the opposing end. The flow within the space was investigated for an empty room, and with the inclusion of a vertical partition extending from the floor to the mid-height of the room.

The hot end wall comprised an array of electric radiant heating panels, mounted behind a 1.6 mm thick sheet of aluminium, to provide an isothermal reflective surface. The cold wall was cooled by an array of copper solar collector panels, through which chilled water from a storage reservoir was pumped. The temperatures of the end walls were maintained constant to within ±1.0°C, and the resulting Rayleigh number *Ra* for the flow was in the range of $2.0\text{-}3.1\times10^{10}$.

Vertical temperature profiles were obtained along the long axis of symmetry of the enclosure using T-type thermocouples mounted on a vertical, moveable post. For flow visualisation purposes wood smoke was injected into the room and its movement was captured using video system. Vertical temperature profiles are presented at various locations within the space, together with sketches of the flow pattern observed, although there are no velocity measurements provided.

In an additional investigation, a 1:5.5 scale-model of the full-scale room was constructed, and the refrigerant gas R114 was used as the fluid medium, (Olson et. al., 1990). R114 is a dense gas, so the length scale of the model can be reduced whilst the Reynolds number and Rayleigh number remain constant. Furthermore, R114 has a Prandtl number of 0.8, which is close to 0.71, the value for air. The experimental data from the full-scale room and the R114 scale-model were

found to be in excellent agreement, even though similarity for the radiative heat transfer between the two experimental facilities was not achieved.

A comparison of the data from the full-scale room and the R114 scale-model to the data from water-based differentially heated cavities with similar Rayleigh number (Nansteel and Grief, 1981, and Anderson et. al., 1985), show that the water models significantly over-predicted the vertical temperature gradient within the enclosure. When internal partitions were included, the shape of the temperature profile was no longer in agreement with that of the full-scale room, so that a qualitative comparison was not possible. The thermal stratification for the water-based experiments exhibit a distinct interface between cool fluid at low level within the space and buoyant fluid at high level, yet no such interface was observed for the flow in the full-scale room or the R114 scale-model. It was suggested that the absence of thermal radiation in the water-based experiments may contribute to the different flow patterns and thermal stratification observed in those studies (Olson et. al. 1990).

4.8.3 Mechanical displacement ventilation

Workers at the Technical University of Eindhoven, The Netherlands, have recently performed an experimental study of a mechanically-driven displacement ventilation flow through a full-scale enclosure (Loomans, 1998). Their experimental room was constructed within a larger climate chamber and measured 9.7 m long × 2.7 m high × 5.16 m wide. Air was supplied to the room mechanically via a floor mounted unit connected to a plenum unit within the floor void, and was removed via a high-level slot. A number of heat sources were arranged within the space, including a thermal mannequin used to simulate the thermal gain from a real person, two computers and some lighting.

Although the volume flow through the enclosure was controlled mechanically, and the arrangement of the sources of heat do not correspond to a point source of heat at low-level, the results from this study still provide useful information on how air behaves generally in a full-scale enclosure. In particular, it is noted that the vertical temperature profile does not exhibit any sharp interface between a layer of ambient air adjacent to the floor and a layer of buoyant air at high level. Instead it is observed that the temperature increases with height for the entire height of the space, and that the rise in temperature is more pronounced at low-level. This corresponds to the thermal stratification detected for the natural displacement ventilation flow observed by Eftekhari §4.8.1.

4.9 Summary

The results obtained from the salt-bath experiments exhibit excellent agreement with the predictions obtained from the Cambridge mathematical model for natural displacement ventilation of an enclosure. Both the salt-bath technique and the mathematical model assume that the transport of momentum and heat is entirely due to convection, so that the transport mechanisms of diffusion and thermal radiation are neglected. This may be why such good agreement exists between the two methods. Whether this is a reasonable and valid assumption can only be confirmed by comparison to measurements obtained from a full-scale enclosure, with air as the fluid medium.

Although the contribution from Li (2000) is in effect no more than a mathematical exercise, it is interesting to note that they also identify the absence of thermal radiation as a limitation of the original model.

Rarely is an occupied space within a building realistically described by a single point source of buoyancy at floor level. Although there have been many contributions to the basic mathematical model in the literature, the mathematics can become rather complex even for relatively simple extensions, so that the new models could not be easily applied routinely for design purposes.

The CFD approach has also been used to simulate and investigate the Cambridge mathematical model for natural displacement ventilation (Cook, 1998). The standard-$k\varepsilon$ and the RNG-$k\varepsilon$ closures were employed to describe the effects of the turbulent structures within the flow, and thermal radiation effects were neglected. Excellent qualitative agreement was reported between the CFD predictions and the salt-bath experiments and mathematical model of Linden et. al. (1990) in that a layer of ambient fluid was predicted to form at low-level within the space, with a layer of buoyant fluid above, separated by a sharp interface. The rate of entrainment into the plume, however, was over-predicted.

With the exception of an earlier contribution by the present author, (Howell and Potts, 1998), it is thought that all of the experimental evidence supporting the Cambridge mathematical model has been provided from water-based experimental techniques: mainly the salt-bath technique and more recently the fine-bubble technique. In a real building, however, the fluid medium will be air. Previous experimental work on differentially heated cavities §4.8.2 has shown that even for geometrically similar cavities, with similar Reynolds number Re and Rayleigh number Ra, the predicted vertical temperature distribution within the cavity can differ significantly depending upon whether the fluid medium is water or air: water-based experiments may exhibit a distinct interface between cool fluid at

low-level within the space and buoyant fluid at high level, yet no such interface was observed for the corresponding, dynamically-similar flow in a large-scale room with air as the fluid medium, (Olson, 1990). Whether or not the water-based salt-bath and fine-bubble techniques are representative of the flow in a real building is, therefore, a key issue, and it is one that remains unchallenged in the literature thus far.

5.0 Experimental facility

5.1 Introduction

Prior to this work, all experimental investigations for the natural displacement ventilation flow through enclosures had been performed using small-scale water-based experimental techniques. The aim of the present experimental work was to provide thorough and reliable data for the natural displacement ventilation flow through a full-scale enclosure with air as the fluid medium, which would be more representative of any similar flow within a real building than had been attempted thus far.

This chapter describes the full-scale enclosure constructed and the experimental procedures employed to measure velocities and temperatures during the experimental work. In particular, §5.2 comprises an outline of the underlying physics for the thermometry techniques used to measure temperatures as part of the experimental work, with §5.3 outlining the physics of anemometry used to measure velocities. The design of the test-enclosure is discussed in §5.4, and the measurement system used and the experimental procedures followed for recording the internal temperatures, the external temperatures and the velocities at the lower opening are described in §5.5, §5.6 and §5.7 respectively.

5.2 Platinum resistance thermometry

It is generally observed that the electrical resistances of metals are temperature-dependent, so that a measurement of electrical resistance can be used as a measurement of temperature. Platinum is a noble metal and therefore has a wide, non-reactive temperature range. It is obtainable in a state of high purity, so that a resistive element manufactured from platinum will contain few impurities and exhibit a stable and predictable temperature-resistance relationship.

5.2.1 Platinum temperature-resistance relationship

Platinum has a simple temperature-resistance relationship, so that it is well suited to resistance thermometry.

$$\frac{R_T}{R_0} = 1 + aT + bT^2 , \qquad (5.2.1)$$

where R_T is the thermometer resistance at temperature T, R_0 is the thermometer resistance at 0°C, T is the temperature in °C, and the empirical constants $a = 3.90803\times10^{-3}$ and $b = -5.775\times10^{-7}$. To a first order approximation,

$$\frac{\Delta R}{\Delta T} = aR_0 , \qquad (5.2.2)$$

where ΔR is the change in the resistance of the sensor for a given change in temperature ΔT. From Figure 5.1, it is clear that the temperature-resistance relationship can be assumed to be linear without introducing significant error.

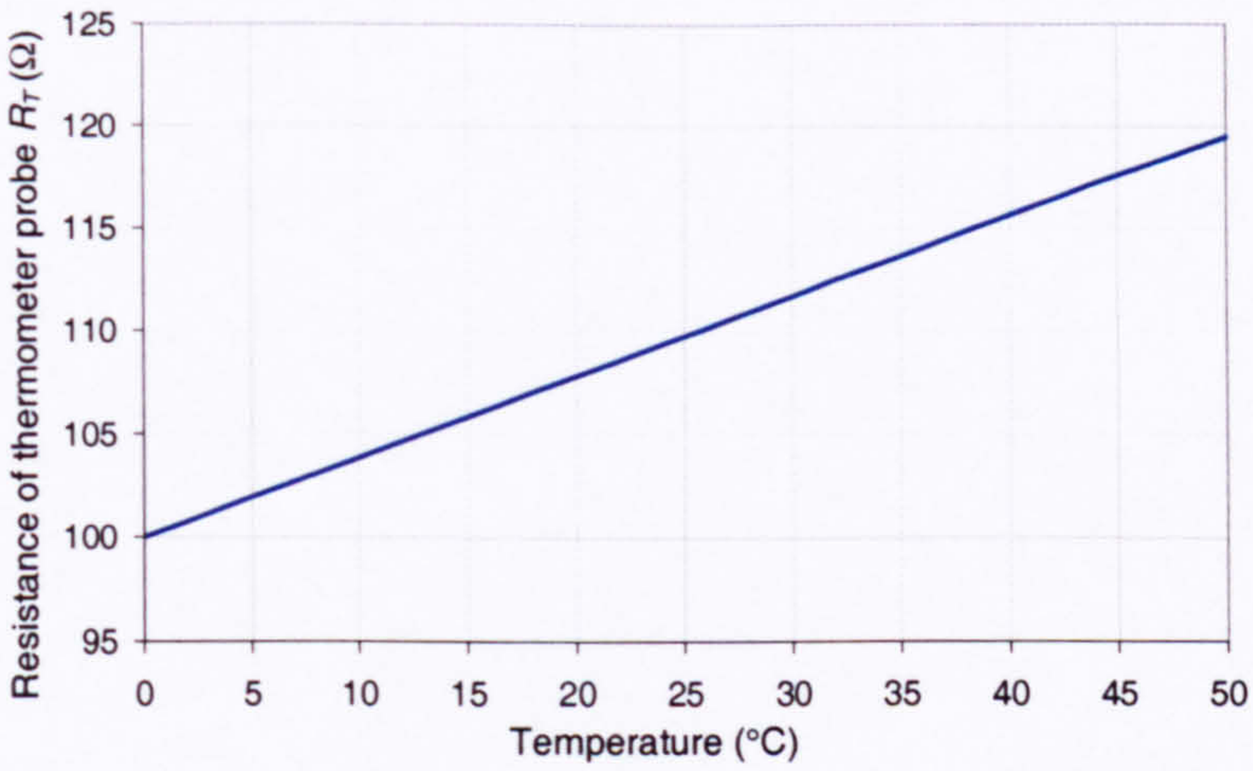

Figure 5.1 - Graph to show platinum temperature-resistance relationship for a standard 100Ω sensor

5.2.2 Sensitivity of the resistance thermometer

When measuring the resistance of a platinum resistance thermometer, it is necessary to pass a current through the resistive element. If the current is known, then a measurement of the voltage drop across the sensor will provide a measure of its resistance and therefore its temperature. The sensitivity of the thermometer is therefore given by

$$\frac{\Delta V}{\Delta T} = aIR_0 , \qquad (5.2.3)$$

where ΔV is the change in voltage across the sensor for a given change in temperature ΔT, and I is current flowing through the sensor. In order to improve the sensitivity of the device, it is therefore necessary to increase either the resistance of the element or the current flowing through it. For an applied current of 1mA through a

standard 100Ω sensor, the sensitivity of the thermometer is 391μV/°C. This is almost a tenfold increase in sensitivity over a k-type thermocouple, where the sensitivity is 41μV/°C.

5.2.3 Self-heating

The current flowing through the sensor will inevitably induce resistive heating in the sensor element, which will in turn raise the temperature of the sensor above that which it is trying to measure. This effect is known as 'self-heating'.

The error introduced due to self-heating effects will be proportional to the amount of heat generated in the sensor, and inversely proportional to the rate at which the excess heat can be transferred from the sensor to the surrounding environment. The effect is therefore minimized if the element is in good thermal contact with the ambient, and if the flow in the vicinity is fast flowing. This cannot be controlled in the case of the full-scale enclosure, however, because the surrounding flow is slow moving air. It is therefore necessary to reduce the heat generated in the sensor, which is in turn proportional to the resistance of the sensor and to the square of the current through the sensor. For this reason, resistance thermometers tend to have a high resistance, so that the applied current can be minimized whilst maintaining a suitable sensitivity for the instrument. In still air, an applied current of 1mA through a standard 100Ω sensor will raise the sensor temperature by about 0.05°C.

5.2.4 Accuracy of platinum resistance thermometry

Platinum resistance thermometers, which are accurate to ±0.2°C at an ambient temperature of 25°C, are the preferred instrument for recording the small differences in temperature. In comparison, the most accurate thermocouple available, according to BS 4937 Part 30:1993, is the T-type thermocouple, which is accurate to ±0.5°C.

5.3 Laser Doppler anemometry - the differential Doppler technique

When two lasers of the same frequency intersect the formation of stationary planar interference fringes is observed in the intersection region, due to the superposition of the two beams. From Figure 5.2 and simple trigonometry, it can be shown that if the laser beams intersect at an angle 2θ, then the spacing between two consecutive fringes s is given by

$$s = \frac{\lambda}{2\sin\theta}, \tag{5.3.1}$$

where λ is wavelength of the laser beams.

The volume of intersection is small and ellipsoidal in shape. If a small particle passes through this intersection region with a component of velocity v perpendicular to the interference fringes, it will scatter light with frequency f given by

$$f = \frac{v}{s} = \frac{2v\sin\theta}{\lambda}. \tag{5.3.2}$$

If it is assumed that particles suspended in a fluid move with the local fluid velocity, then this provides a method of determining that local fluid velocity. This is the essence of the differential Doppler technique.

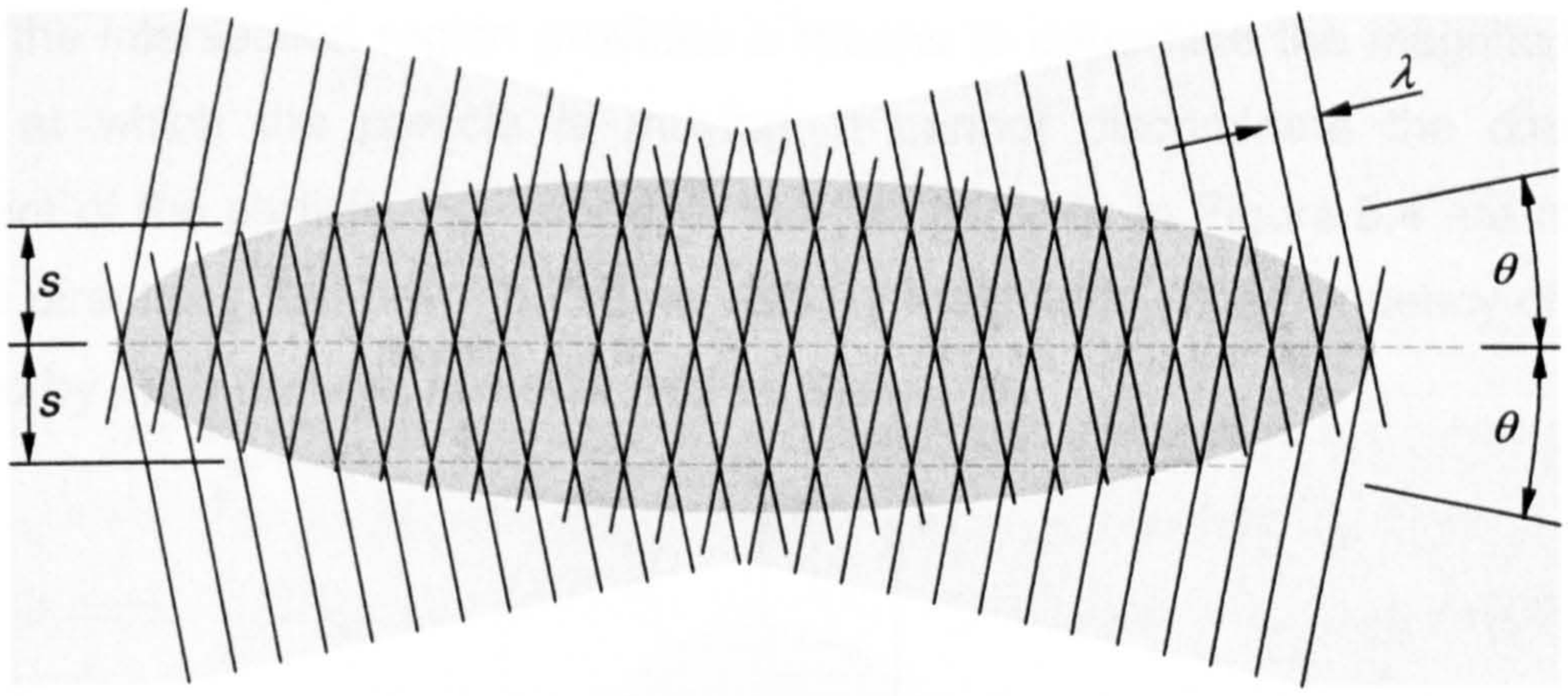

Figure 5.2 - Diagram showing the geometry of the wave fronts of the intersecting beams, and the resulting interference fringes

In practice, each laser beam has a Gaussian radial intensity distribution. The radius of the beam r_0 is then defined is the distance at which the intensity is $1/e^2$ of the maximum along the centreline of the beam. The intersection region or measurement volume is an ellipsoid, as shown in Figure 5.3, with dimensions

$$r_x = \frac{r_0}{\sin\theta}, \quad r_y = \frac{r_0}{\cos\theta}, \quad r_z = r_0. \tag{5.3.3}$$

Furthermore, the Gaussian beams intersect at their waist, which is the position at which the cross-section of the beam is a minimum. At this position, the beam exhibits plane wave fronts, so that the interference fringes formed in the measurement volume are indeed planar.

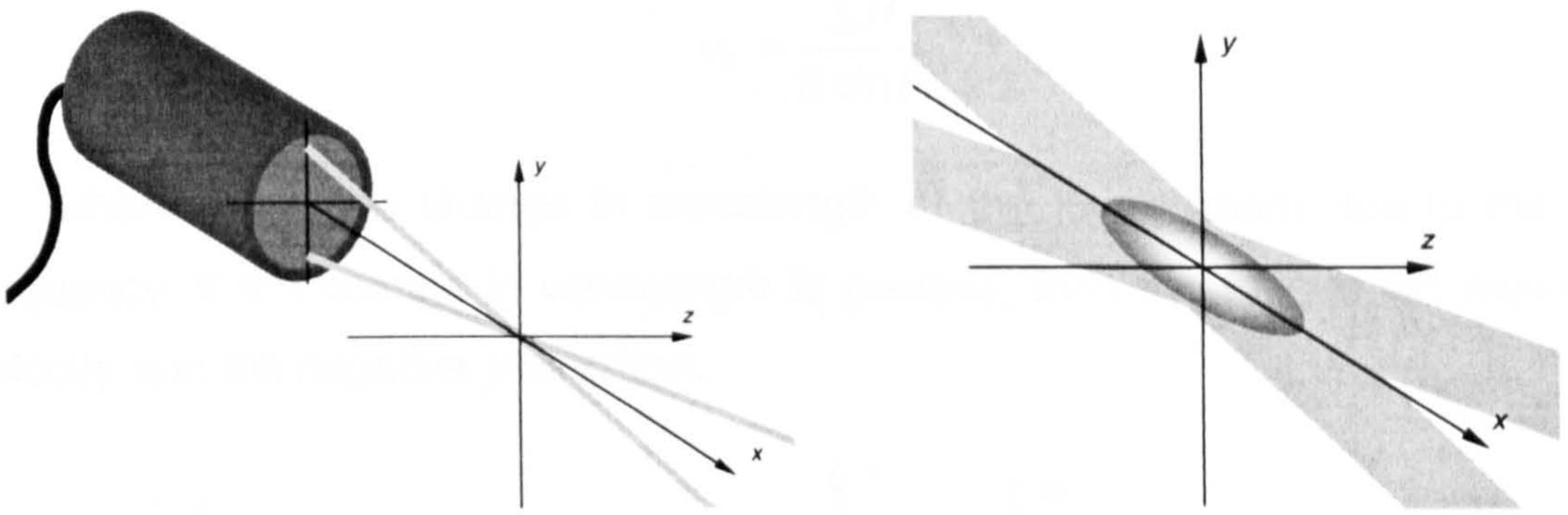

Figure 5.3 - Diagram showing the co-ordinate system for the intersection region

5.3.1 Frequency shifting

Although measuring the frequency *f* of the light scattered by a particle moving through the intersection region provides a means to determine the magnitude of the velocity at which the particle is moving, it cannot discriminate the direction of movement of the particle. For example, the two particles in Figure 5.4 are moving in opposite directions, but have the same velocity magnitude. The frequency of the light scattered by each particle, however, will be the same.

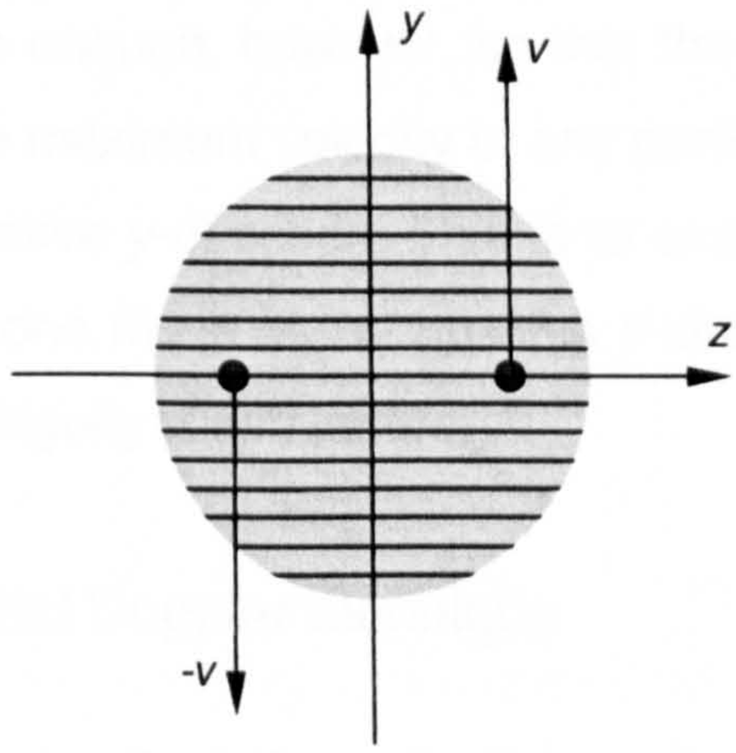

Figure 5.4 - Diagram showing the geometry of the wave fronts of the intersecting beams, and the resulting interference fringes

One technique that is often used to overcome this problem involves shifting the frequency of one of the laser beams. The resulting change in wavelength of that laser has the effect of producing a moving system of planar fringes in the interference zone. From simple trigonometry, it can be shown that if a small frequency shift is applied to one of the laser beams, as illustrated in Figure 5.5, then the fringes will move in the direction shown with a velocity v_f given by

$$v_f = \frac{\Delta\lambda f}{2\sin\theta}, \qquad (5.3.4)$$

where $\Delta\lambda$ is the change in wavelength of the lower beam due to the shift in frequency. If the change in wavelength is positive, then the fringes will move with a velocity v_f in the negative y-direction.

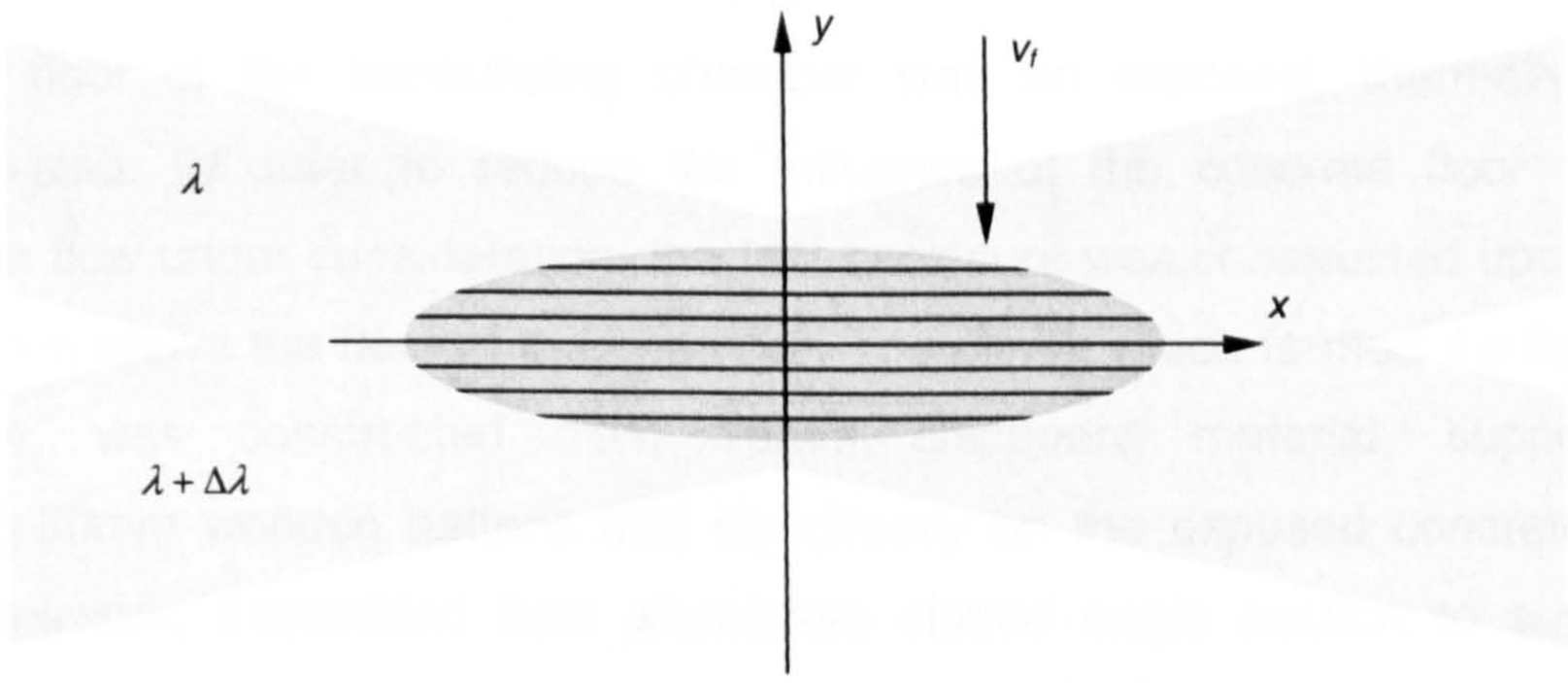

Figure 5.5 - System of moving fringes in the interference zone

The magnitude of the change in wavelength $\Delta\lambda$ must be small in comparison to the actual wavelength λ of the laser beams so that the moving fringes remain in the x-z plane. It must be large enough, however, so that the velocity at which the fringes move v_f is greater than the maximum velocity of any particle which moves through the control volume in the negative y-direction. This is to ensure that all particles passing through the interference zone move in the positive y-direction relative to each fringe, so that any directional ambiguity is eliminated.

5.3.2 Accuracy of the differential Doppler technique

The differential Doppler technique is the preferred method for measuring low-velocity flows. They are non-intrusive, unlike a hot-wire anemometer that may introduce a thermal plume of its own at the measurement location. Furthermore, the LDA technique can measure velocities down to the order of 10^{-2}m/s (Maybrey, 1994).

5.4 Full-scale enclosure

The experimental enclosure was constructed alongside a wind tunnel within a large chamber at the Old Brewery facility, University of Newcastle-upon-Tyne, England. This chamber was selected to house the test-enclosure as it provided two essential features for the experimental work. Firstly, the envelope of the chamber was well sealed, so that any interference due to external wind effects was minimized. Secondly, the physical dimensions of the chamber were large compared with those of

the test-room, and the openings to the enclosure were positioned sufficiently far from the walls of the chamber so that they should not affect the ventilation flow through the test-room. Indeed, the height of the chamber was about two and a half times that of the test-room, and there was sufficient room at the end walls of the test-room so that the flow through the openings was unaffected by the presence of the boundaries of the chamber.

The floor of the surrounding chamber was an exposed, thermally-massive concrete slab. In order to reduce the influence of the concrete floor upon the ventilation flow under consideration, the test-enclosure was constructed upon a plinth raised 0.1m above the floor of the chamber. The plinth, which formed the floor of the enclosure, was constructed from 18mm chipboard material, supported by 100mm × 50mm wooden battens that lay directly on the exposed concrete slab. A rigid framework, assembled from aluminium slotted angle section to support the enclosure walls was constructed upon this plinth. The walls and ceiling for the enclosure were formed from 12mm chipboard panels that were subsequently attached to the inside of the frame such that the internal surfaces within the enclosure were smooth. Any gaps at joints between the panels were sealed, so that the enclosure was airtight, and the internal surfaces of the space were painted matt white to protect the chipboard from smoke particles introduced as seeding for the LDA measurements.

The test-enclosure, which is shown in Figure 5.6 and Figure 5.7, measured 7.32m long × 2.32m wide × 2.44m high so that in terms of geometrical size, it was representative of an occupied space within a real building. A plan of the large chamber, showing the relative locations of the experimental enclosure, the wind tunnel and the boundaries of the chamber is provided in Figure 5.8. Ideally the enclosure would have been constructed from traditional building materials so that the thermal properties of the construction would have been representative of a real building. The resources available for this study, however, did not allow for the construction of such an enclosure, hence the chipboard construction.

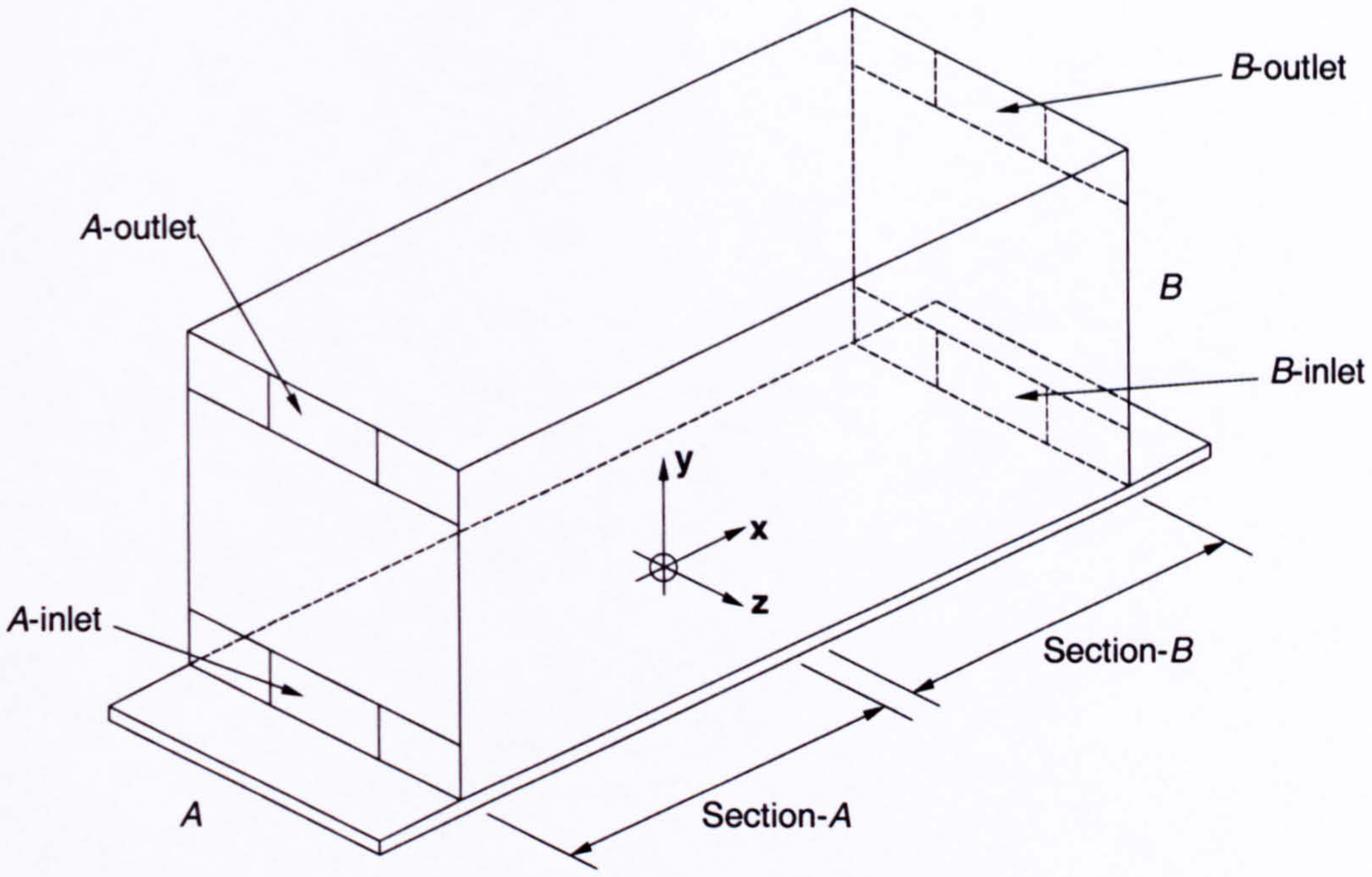

Figure 5.6 - Schematic view of the test-enclosure, showing the adopted coordinate system

Figure 5.7 - The test-enclosure, viewed from the *A*-end

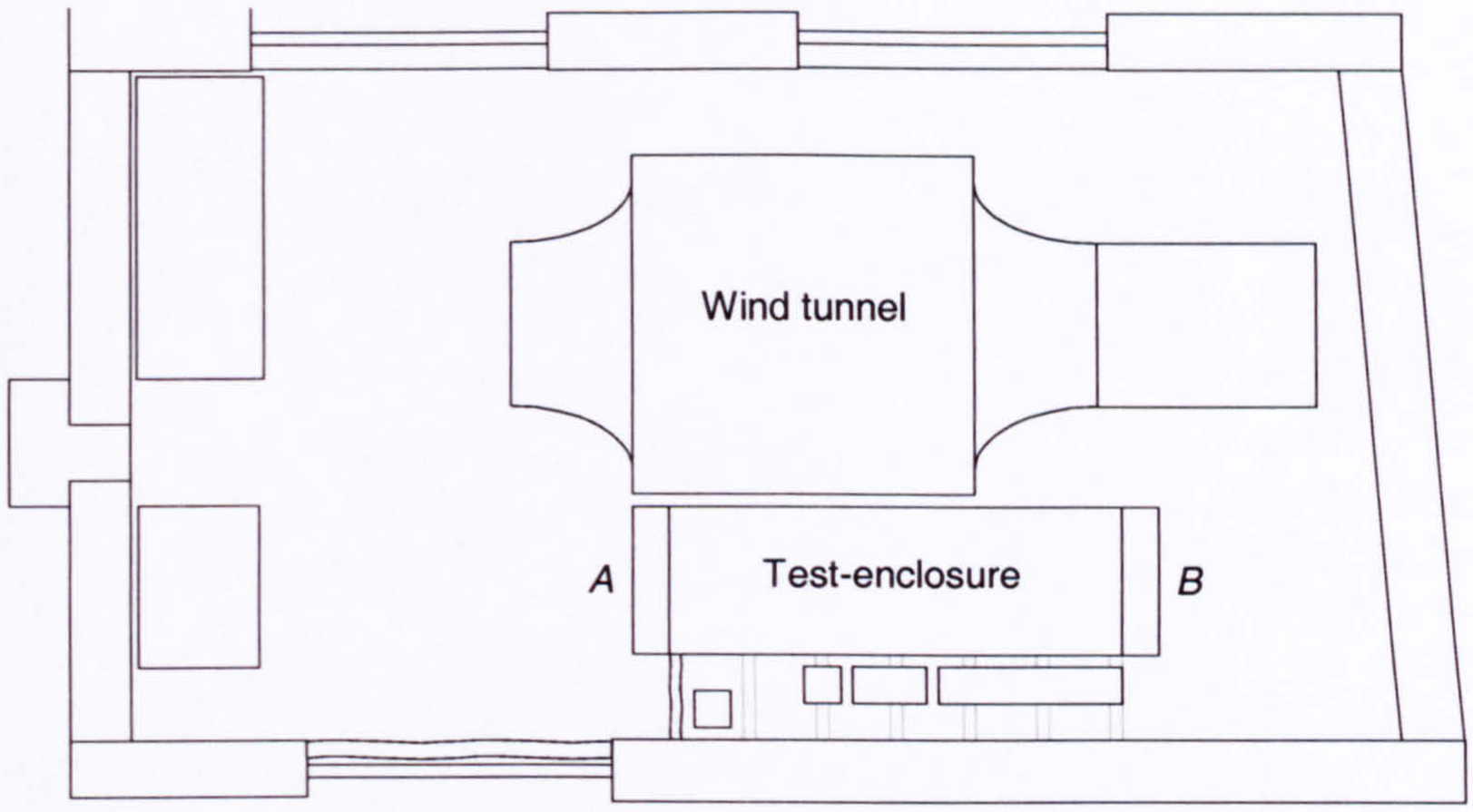

Figure 5.8 - Plan view of large chamber

The end walls shown in Figure 5.9 were manufactured from polycarbonate sheet, so that the inside of the enclosure was visible from outside. It was these walls that incorporated the openings to the enclosure. The size of each opening could be adjusted by sliding a polycarbonate panel to the required position, the panel being secured in place by a channel machined into the structural batten used to keep the polycarbonate sheet rigid. The panels at low-level were L-shaped, so that a small length of duct of known area was formed at each inlet.

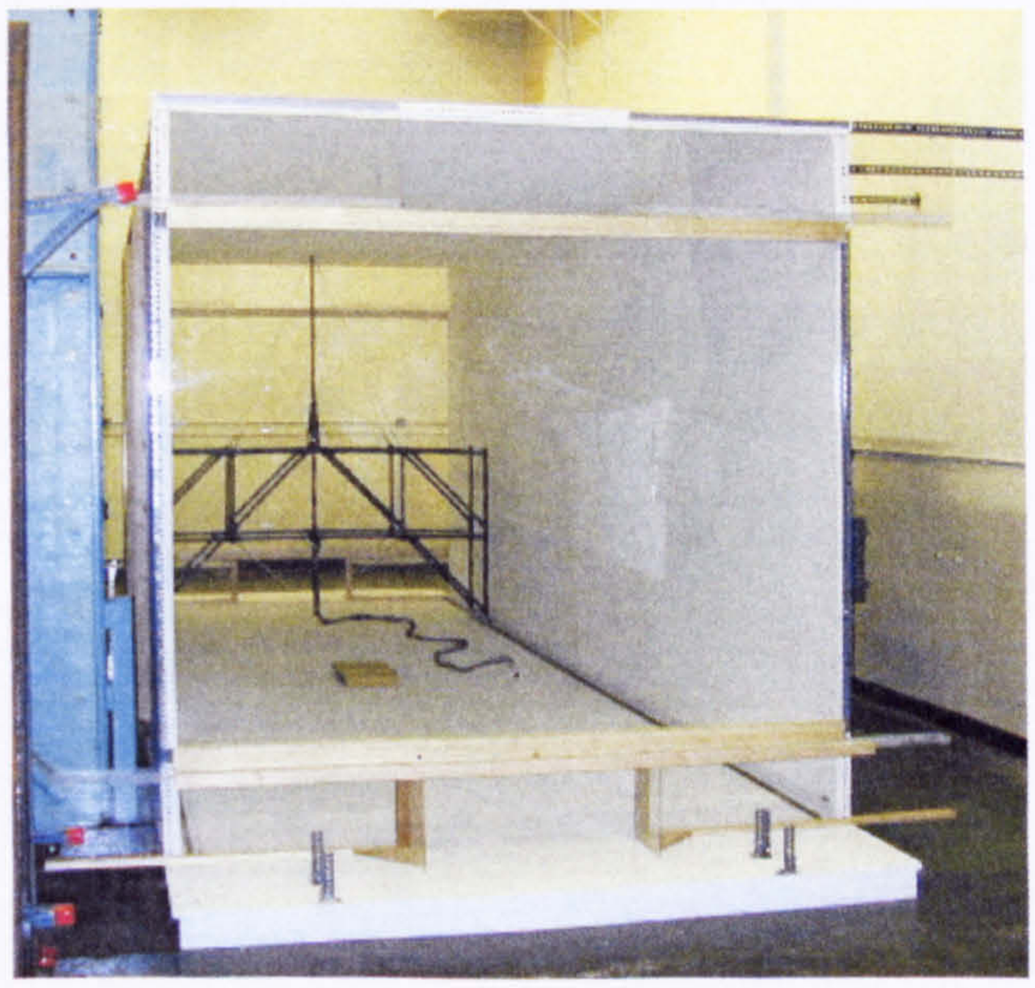

Figure 5.9 - The test-enclosure, viewed from the A-end, showing the polycarbonate end-walls and opening panels

An electric heat source located in the centre of the floor of the room provided the source of buoyancy to motivate the ventilation flow. Two heat sources were employed during the course of the experimental program, as shown in Figure 5.10. Initially a 225W plate heater measuring 0.4×0.2m was used, but this was later replaced with a commercial 1500W 'boiling ring' of diameter 0.18m. The latter had the advantage of

more closely approximating a point source of buoyancy, which is one of the assumptions employed in the Cambridge mathematical model. In addition, the second heater provided a variable heat output, so that the effect of the strength of the heat source upon the flow could be investigated. Finally, the higher heat output of the boiling ring resulted in higher temperatures within the space, so that the relative errors in the temperature measurements were reduced.

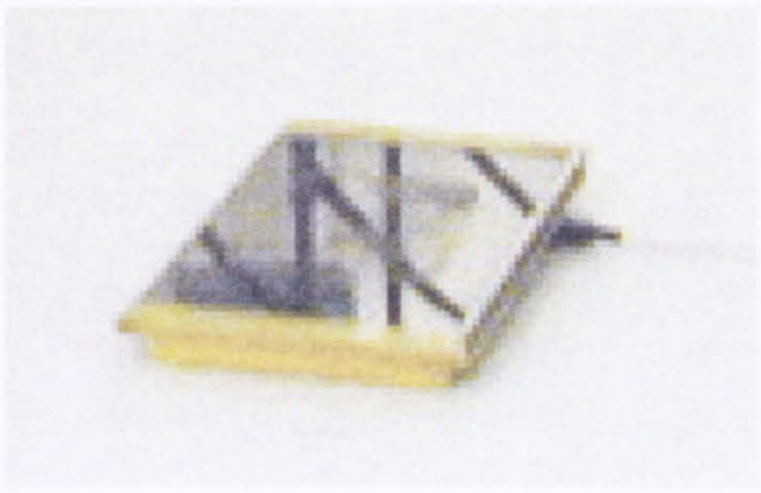

Plate heater

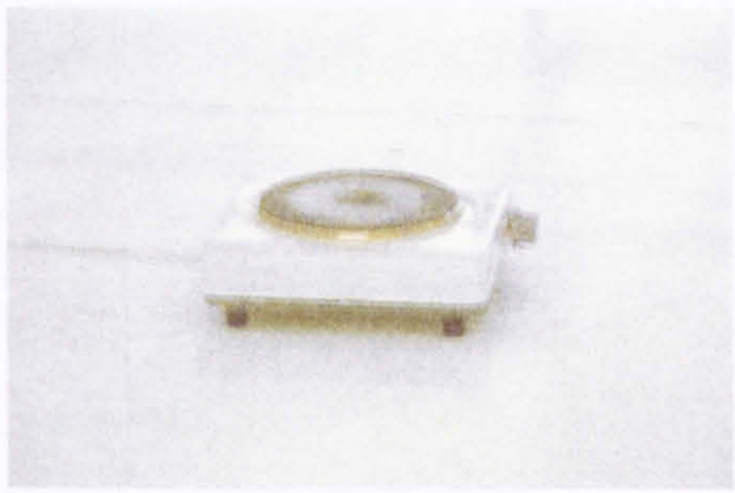

Boiler ring

Figure 5.10 - Plate heater and boiler ring heat sources

5.5 Internal temperature measurements within the enclosure

Shielded platinum resistance thermometers were the preferred instrument for recording the small differences in air temperature within the space during this study. The relative expense of each platinum resistance thermometer limited the quantity of resistance thermometers available for this study to twelve.

For the first series of experiments with the plate heater as the source of buoyancy, a single thermometer was positioned in the low-level opening at the *B*-end of the enclosure to record the temperature of the ambient air entering the space, as shown in Figure 5.11. The remaining eleven thermometers were mounted with uniform spacing on a vertical mast that could be translated along the length of the enclosure, as shown in Figure 5.12. The lowest thermometer upon the mast was mounted at a height $y = 0.10$m and the highest at a height $y = 2.35$m with a spacing equal to 0.225m. In effect, the space within the enclosure was split into eleven approximately equi-height segments and a thermometer positioned at the centre of each segment, as illustrated in Figure 5.13.

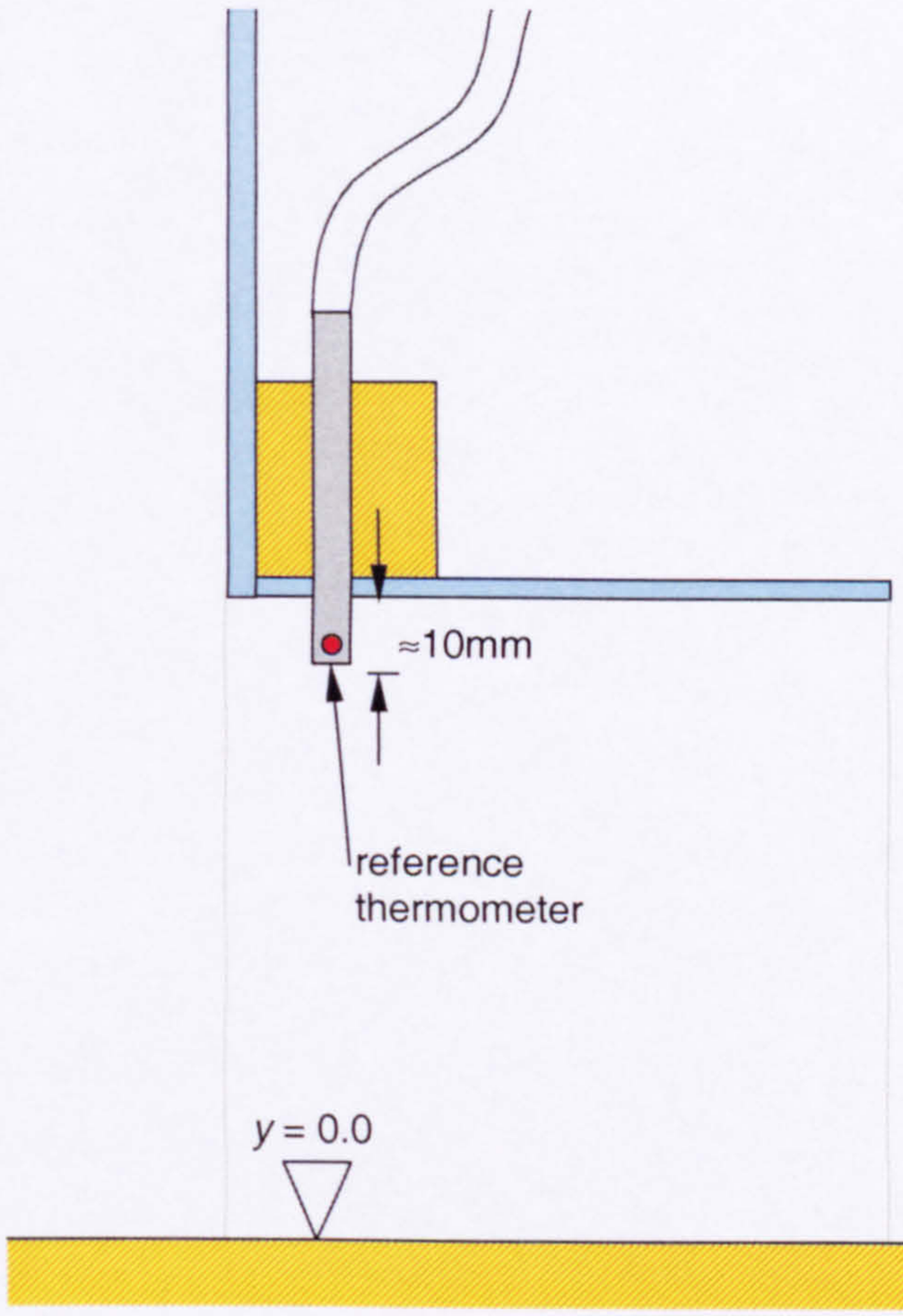

Figure 5.11 - Vertical section through one of the low-level openings, showing the location of the reference thermometer location.

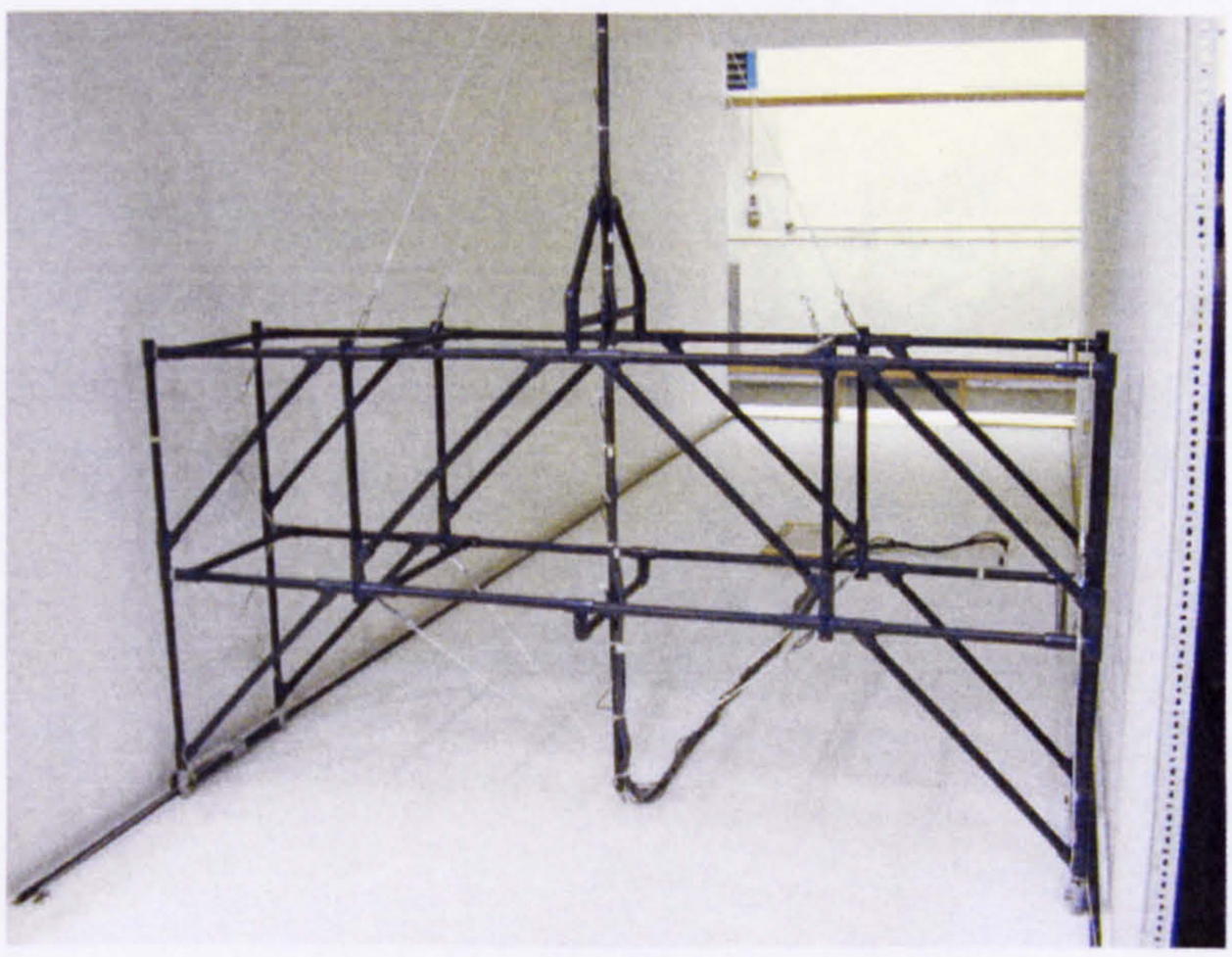

Figure 5.12 - Vertical mast with resistance thermometers attached.

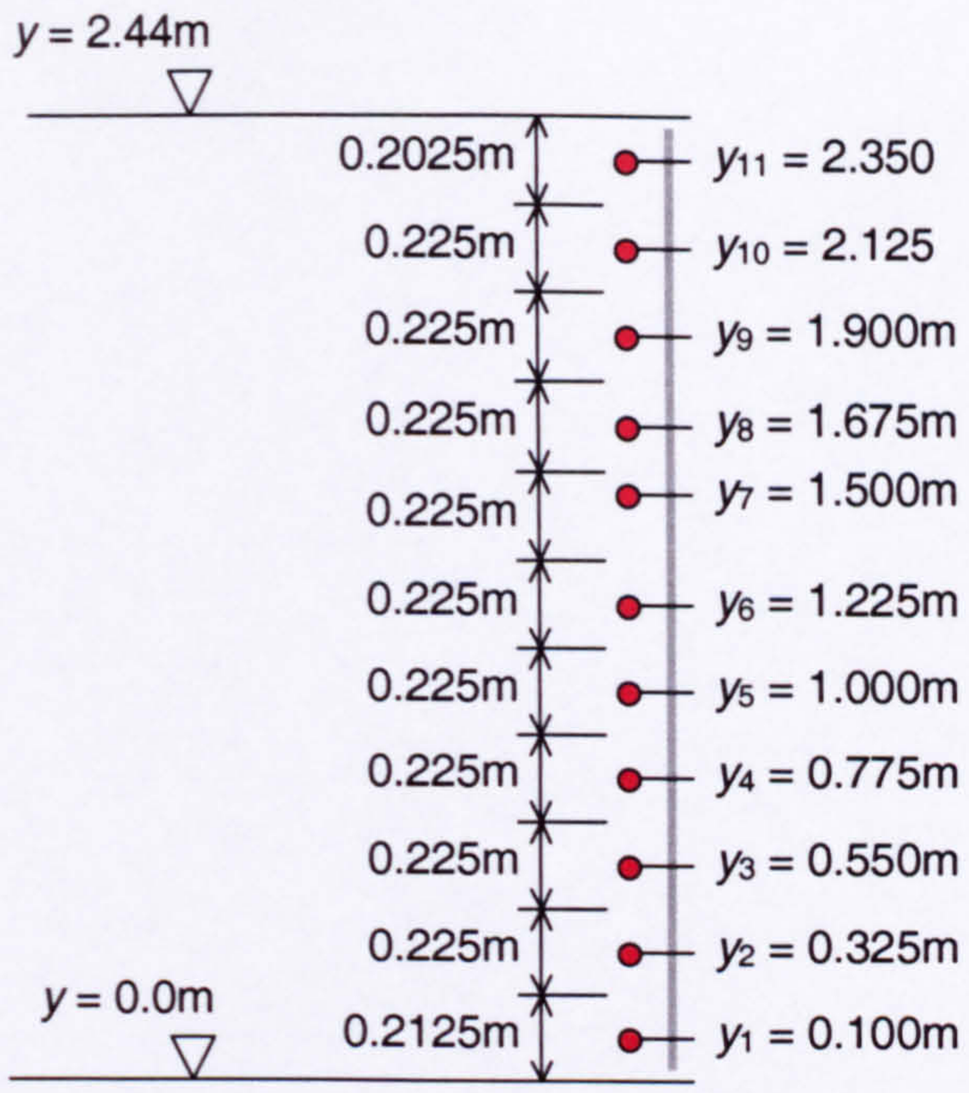

Figure 5.13 - *y*-locations for mast-mounted thermometers during experiments with the plate heater as the heat source.

The experimental recordings from this first series showed that the flow was unsymmetrical, due to the imperfect construction of the surrounding chamber. For all subsequent experimental studies, which employed the boiler ring as the source of buoyancy, a thermometer was located in each of the low-level openings, with the remaining ten thermometers equi-spaced on the vertical mast. The height of the heated surface of the boiler ring above floor level was greater than that of the plate heater. Combined with the greater heat output from the boiler ring, it was necessary to raise the position of the mast to prevent it from melting as it passed over the heated surface. The mast, therefore, was raised 0.05m so that the lowest thermometer was mounted at a height $y = 0.15$m and the highest thermometer at a height $y = 2.40$m, with a uniform spacing equal to 0.25m, as illustrated in Figure 5.14. As a consequence, the highest thermometer was mounted only 0.04m from the surface of the ceiling for all of the experimental work with the boiler ring as the heat source.

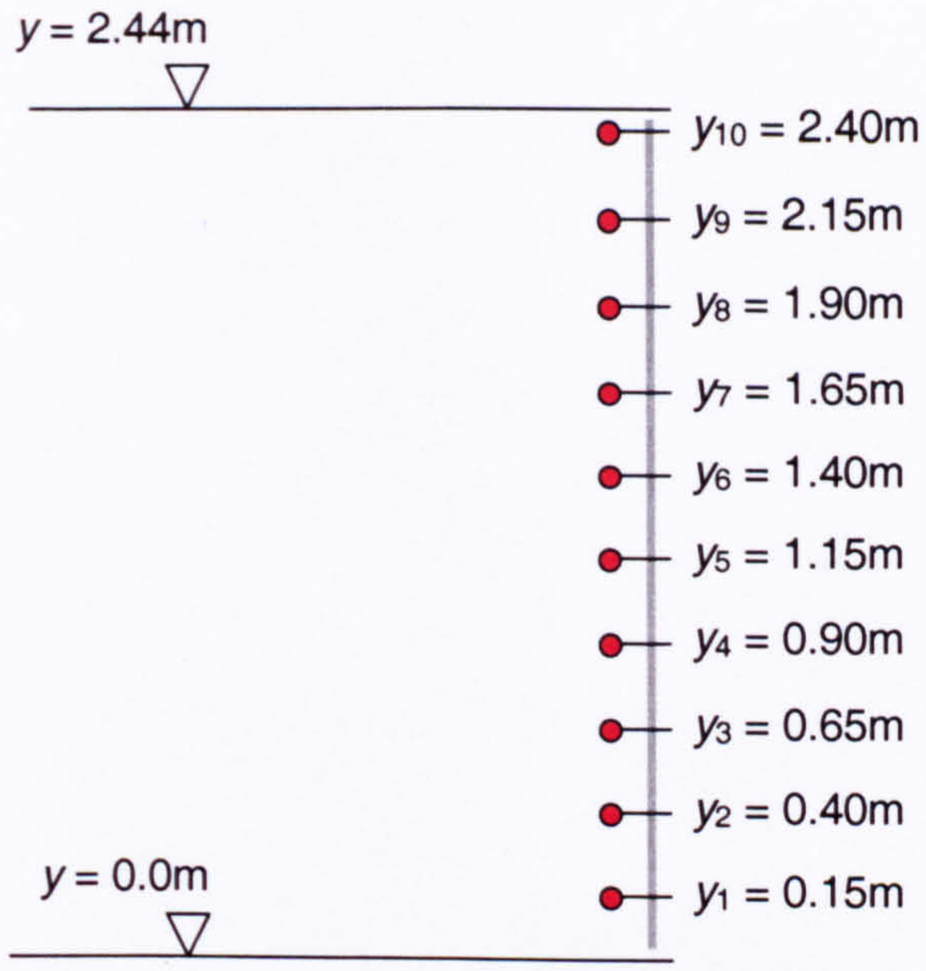

Figure 5.14 - *y*-locations for mast-mounted thermometers during experiments with the boiler ring as the heat source.

The vertical mast was supported by a frame, which itself was supported by rollers engaged on guide rails, so that it could be accurately traversed along the *x*-axis of the test-room. The frame was positioned from outside the enclosure by means of a pulley and rope system, and the guide rails had periodic notches machined into the upper edge for accurate and repeatable location of the frame. The pulley and rope system is shown in Figure 5.15.

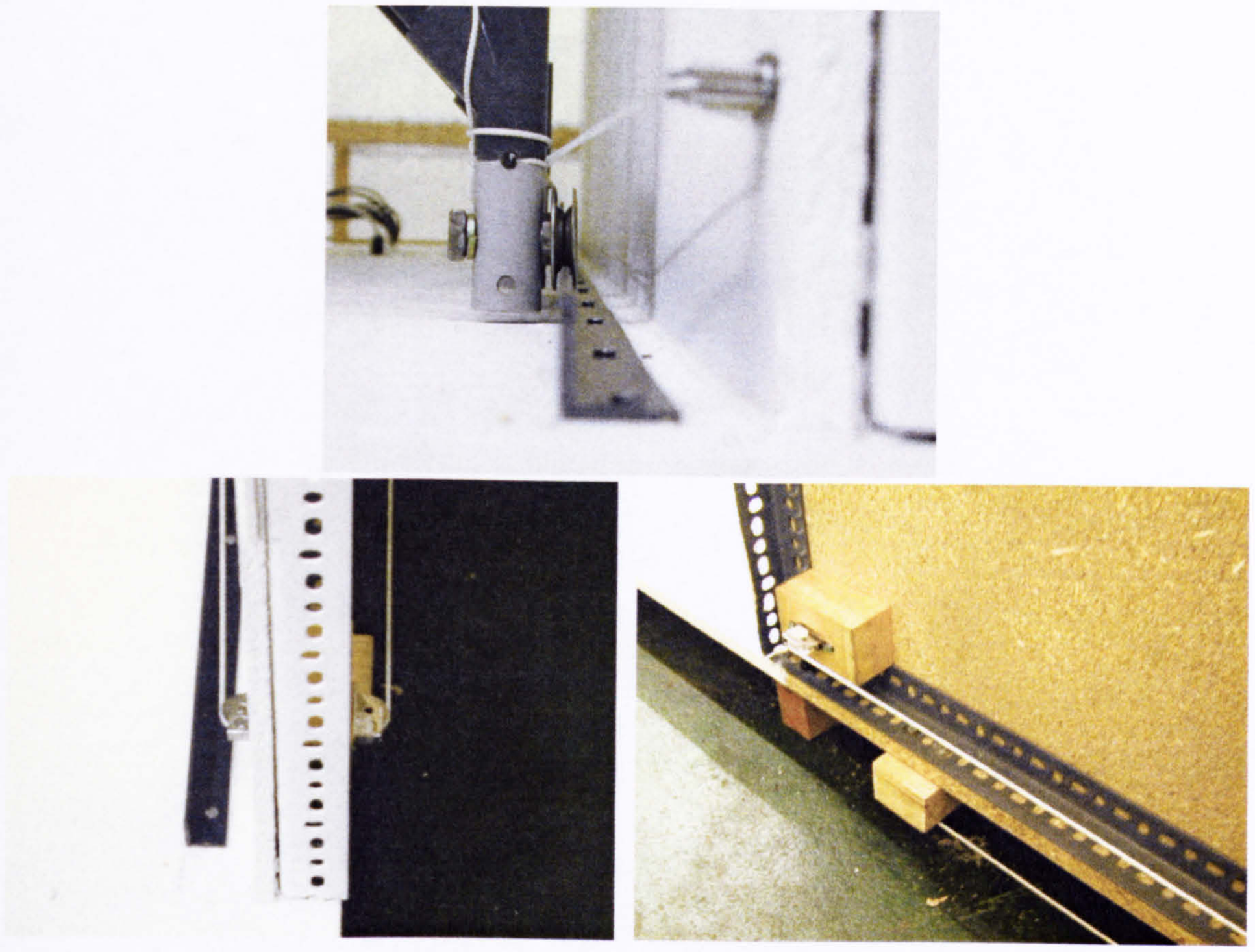

Figure 5.15 - Selected views of the pulley and rope system used to relocate the vertical mast and associated framework.

One constraint upon the design of the vertical mast and associated framework was that it could not be manufactured from a thermally conducting material, as this could influence the temperatures to be measured within the space. They were, therefore, manufactured from a rigid polythene piping system.

Furthermore, the mast and supporting structure was designed to allow the mast to be traversed in a variety of *z*-locations, as illustrated in Figure 5.16. Due to time restrictions, however, only the central mast position ($z = 0.0$m) was utilised.

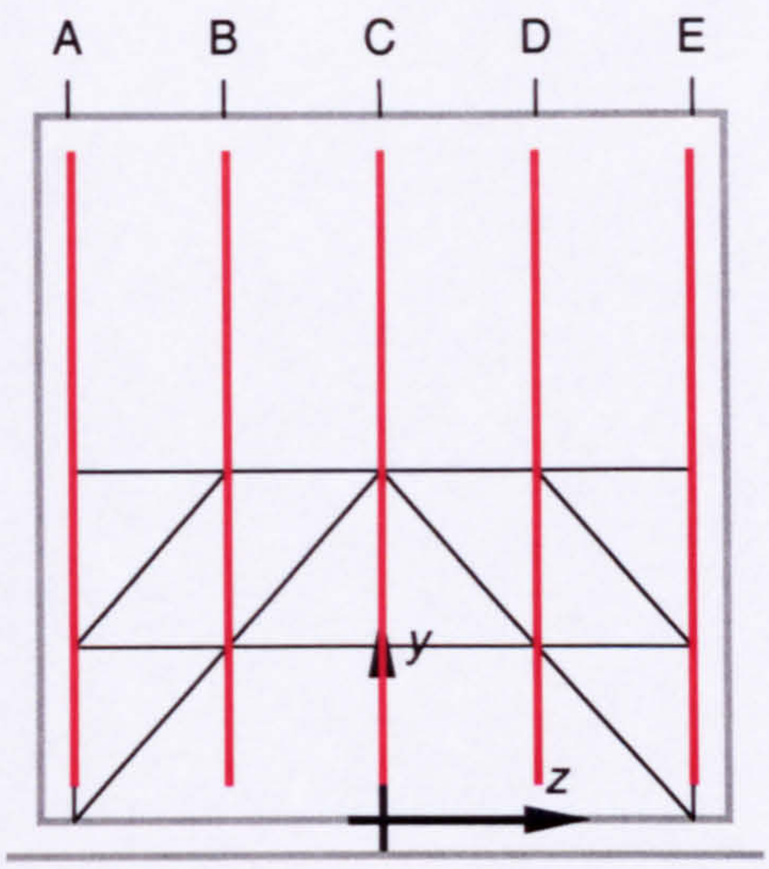

Mast Position C, corresponding to the symmetry plane $z = 0.0$m, was the only position used during this experimental study

Figure 5.16 - Sketch of traverse structure and the five possible mast positions, viewed from the *A*-end of the test-room

5.5.1 Temperature measurement system

Each of the twelve platinum resistance thermometers, with a standard resistance of 100Ω at a temperature of 0.0°C, was incorporated into a fixed-bridge circuit as illustrated in Figure 5.17. Each thermometer was connected in three-wire configuration, with the two leads to the sensor on adjacent arms of the bridge, so that the lead resistance was cancelled out from any measurement. The remaining arms of the bridge R_1, R_2 and R_3 were high-precision resistors, accurate to within ±0.1% of their nominal 100Ω resistance. The supply voltage to each bridge V_s was maintained at approximately 100mV, so that resistive self-heating of the thermometer elements was insignificant.

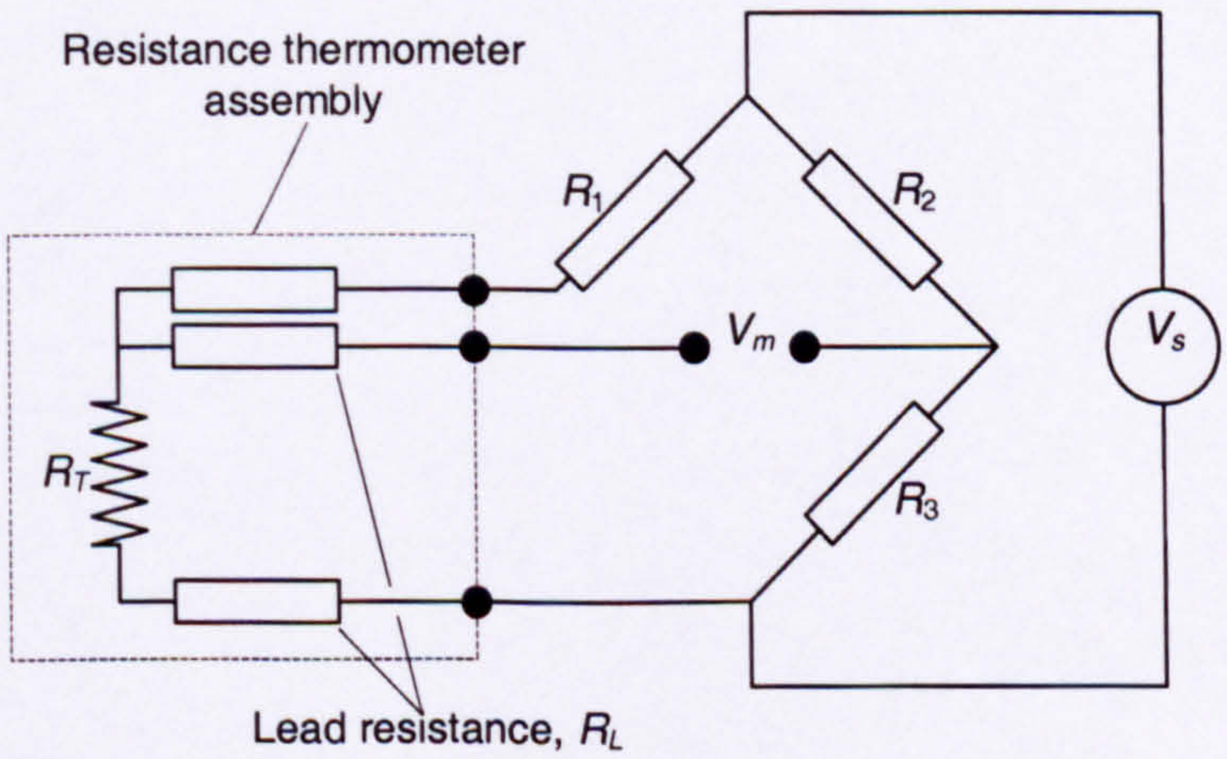

Figure 5.17 - Fixed bridge with the resistance thermometer in three-wire configuration

The imbalance voltage across each bridge V_m varied with the change in resistance of the associated thermometer element, according to the relation

$$V_m = V_s \frac{\Delta R}{2(2R + \Delta R)}. \qquad (5.5.1)$$

Each voltage imbalance therefore provided a measure of the temperature of each corresponding thermometer, as illustrated in Figure 5.18. The imbalance voltage was monitored by a programmable amplifier, with a gain of 1000, and was then converted to a digital signal, which was subsequently transferred to a PC for further analysis. Each byte of data from the digital signal corresponded to a 2.5μV change in the imbalance voltage, which is approximately one-fortieth of a degree Celsius. The data rate was approximately 2000 readings per second, and at each point 2048 readings were taken.

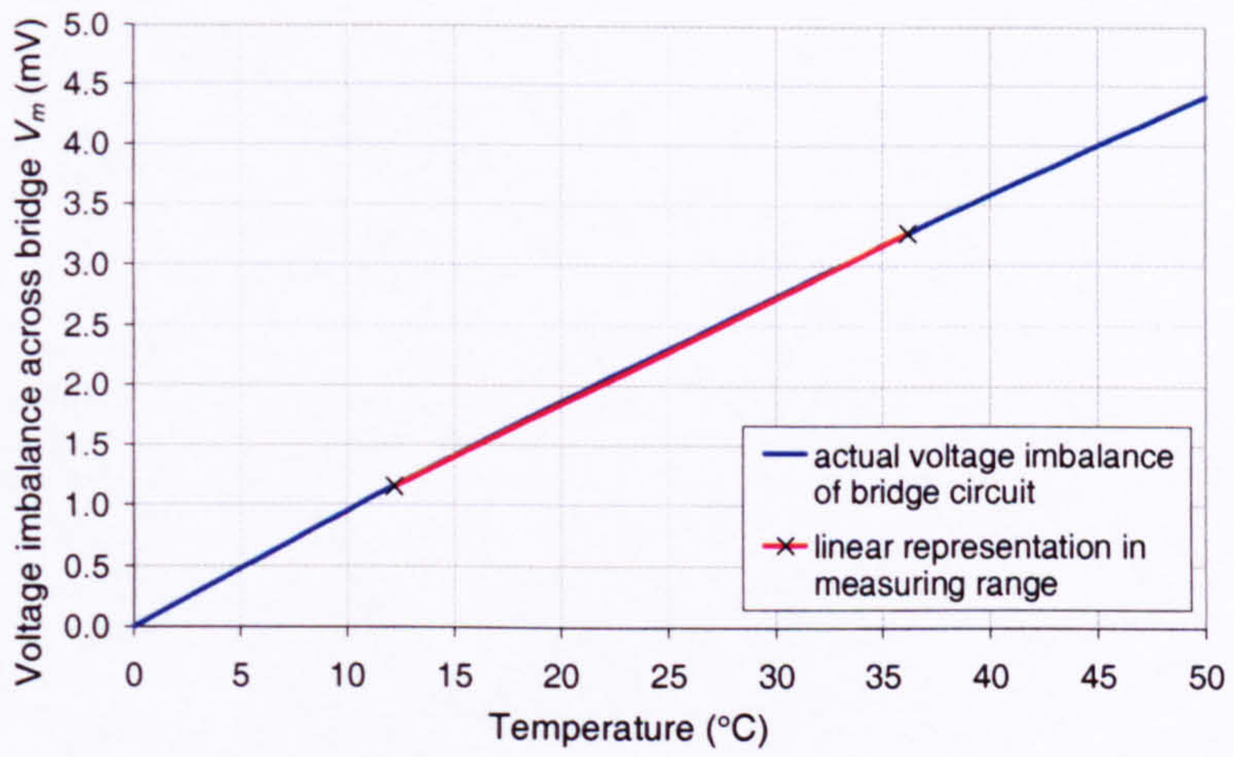

Figure 5.18 - Graph to show the variation of voltage imbalance with temperature for the bridge circuit

The thermometers were calibrated using a water-bath, the temperature of which was monitored with a mercury-in-glass thermometer, accurate to within 0.1°C. Although the platinum temperature-resistance relationship for the thermometer elements was quadratic in nature, for the small changes in temperature that occurred within the enclosure, it was acceptable to assume a linear relationship without introducing significant error. Calibration was performed at two temperatures, one at each end of the range of temperatures expected during the experiments. Assuming a linear variation of temperature with resistance, a third temperature in the middle of the expected range was measured. The variation between individual thermometers at the third temperature was less than one-tenth of a degree Celsius.

5.5.2 Experimental procedure

Each experiment necessarily had to be completed within a single day, usually between 09:30 and 16:00, which allowed a maximum time of six and a half hours per experiment.

Before the start of each experiment, the mast upon which the thermometers were mounted was moved to the position $x = -1.5$m, midway along *A*-section of the test-enclosure. Following the activation of the heat source, usually at approximately 09:45, the transient temperature profile at this position was recorded until steady-state was reached. The mast was then traversed to the *A*-end of the space for the start of the steady-state recordings. A short break was allowed, usually around half an hour, between moving the mast and starting the steady-state recordings to allow any disturbances caused by moving the mast to diminish.

The steady-state phase of each experiment usually commenced at around 13:00. During this phase of the experiment, the mast was traversed along the *x*-axis, from the *A*-end to the *B*-end of the test-room, and the temperature was recorded at every other measuring position (every half metre). The mast was then traversed back to the *A*-end of the room recording the temperature at the measuring positions that had been missed on the first traverse. Finally, the three measuring positions at the centre of the room, in the vicinity of the plume were measured. This experimental sequence is illustrated in Figure 5.19. In order to minimize disturbance of the airflow within the test-room, the mast was traversed slowly and was kept in each measuring position for approximately five minutes to allow the thermometers to reach equilibrium with the local conditions, although a longer period was allowed for the central three locations, in the vicinity of the thermal plume. As a consequence, the duration of each steady-state experiment was of the order of two to three hours.

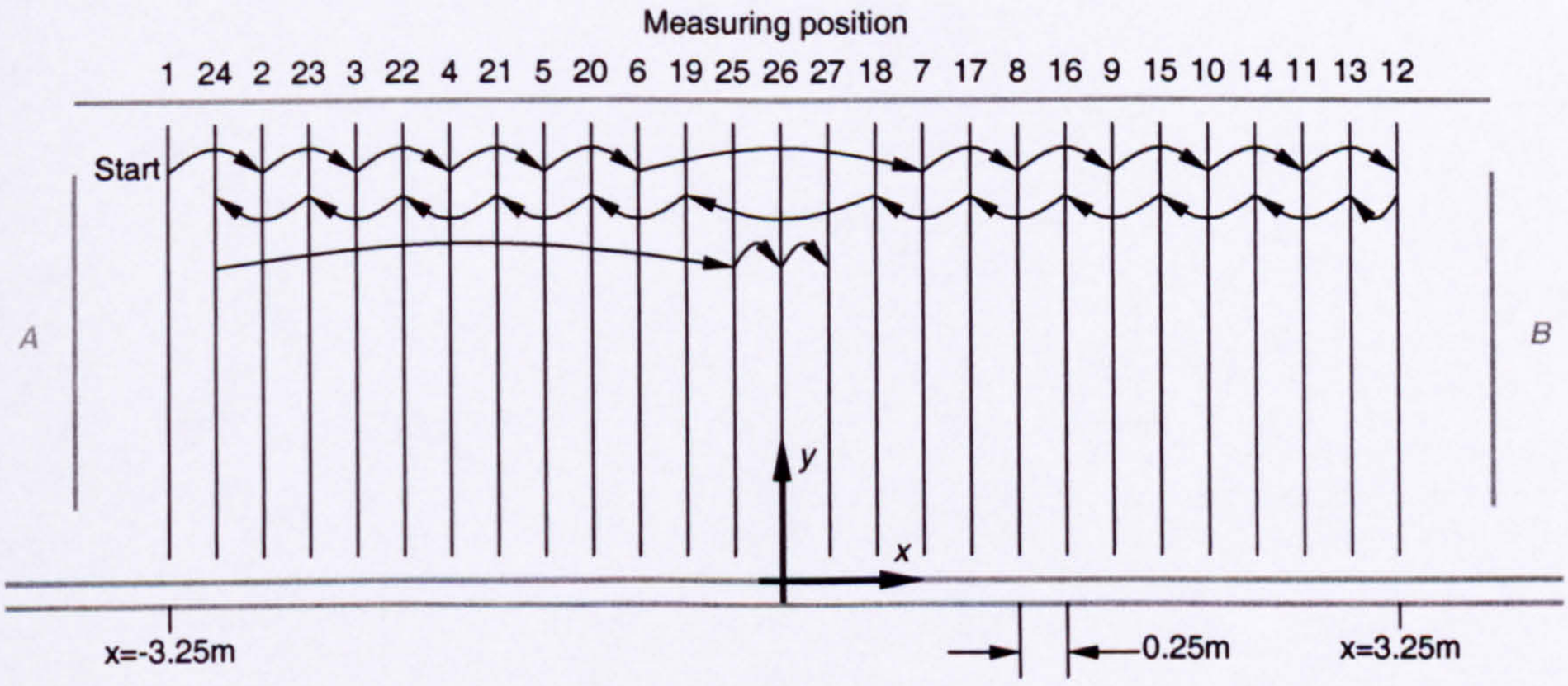

Figure 5.19 - Sketch of test-room showing mast positions for measuring temperature

5.6 External temperature measurements within the surrounding chamber

It was initially assumed that the temperature within the surrounding chamber would be approximately constant, so that any thermal stratification outside of the test-enclosure would be insignificant when compared to the stratification within the

space. During the course of the experiments, however, it emerged that this was not the case, and that the external stratification should also be recorded.

It was not possible to obtain any further platinum resistance thermometers to measure the external stratification due to their relative expense. Furthermore, it was deemed unacceptable to relocate any of the thermometers from the mast within the space, since this would reduce the recordings for the internal temperature profile. The external temperature stratification was therefore recorded using thermocouple technology. Furthermore, only a single k-type thermocouple, accurate to ±0.5°C, was used so that possible experimental error between several, separate thermocouples was eliminated. The thermocouple was rotated between measuring positions at four heights, as illustrated in Figure 5.20, so that a time history of temperature could be determined by interpolation at each of the four measuring locations. Fortunately the temperature at each measuring location was stable and varied smoothly with time, so that the instantaneous external temperature profile could be determined at any instant during an experiment.

At the end of the experimental program, the thermocouple was calibrated with the platinum resistance thermometers using a water-bath, so that the differences in temperature measured outside of the enclosure and inside the space could be accurately determined retrospectively.

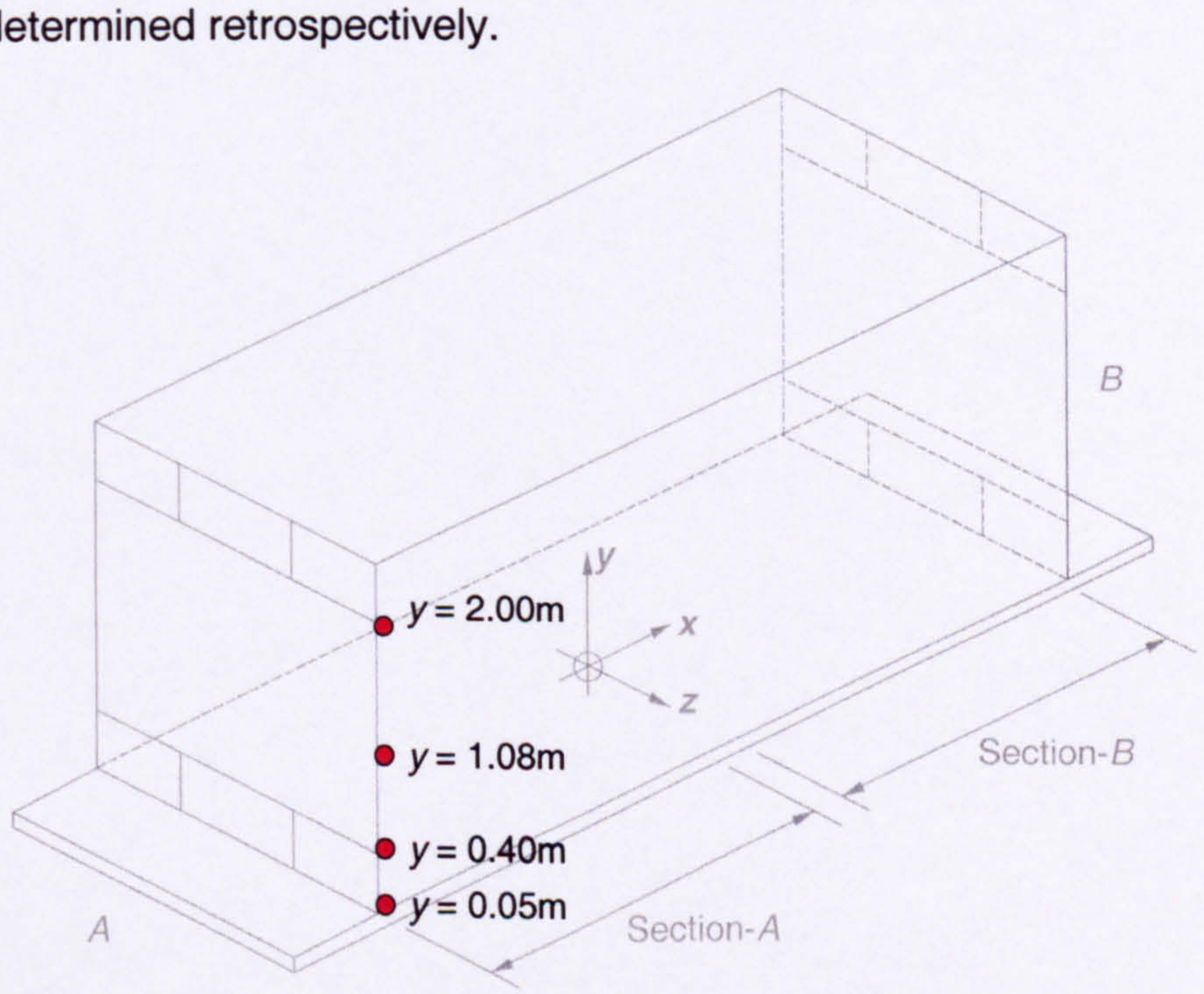

Figure 5.20 - Sketch of test-room showing the measuring positions for the external stratification

5.7 Velocity measurements

Although it was the objective of this study to obtain detailed information regarding the flow within the test-enclosure, it was not practical to measure each component of velocity throughout the internal space. Velocity measurements were therefore confined to the inlet plane at the low-level opening at the *A*-end of the enclosure, and only the component of velocity perpendicular to the inlet plane was recorded. This would allow the volume flow rate through the enclosure to be estimated for each experiment.

The inlet velocity was measured using laser Doppler anemometry. Smoke was used to seed the flow, and was delivered to the vicinity of the inlet by the piping arrangement shown in Figure 5.21. The upward component of velocity of the smoke as it emerged from the supply pipe was small in comparison to the inward component of velocity of the air entering the enclosure, so that the flow field in the region of the inlet was not significantly affected by the smoke supply.

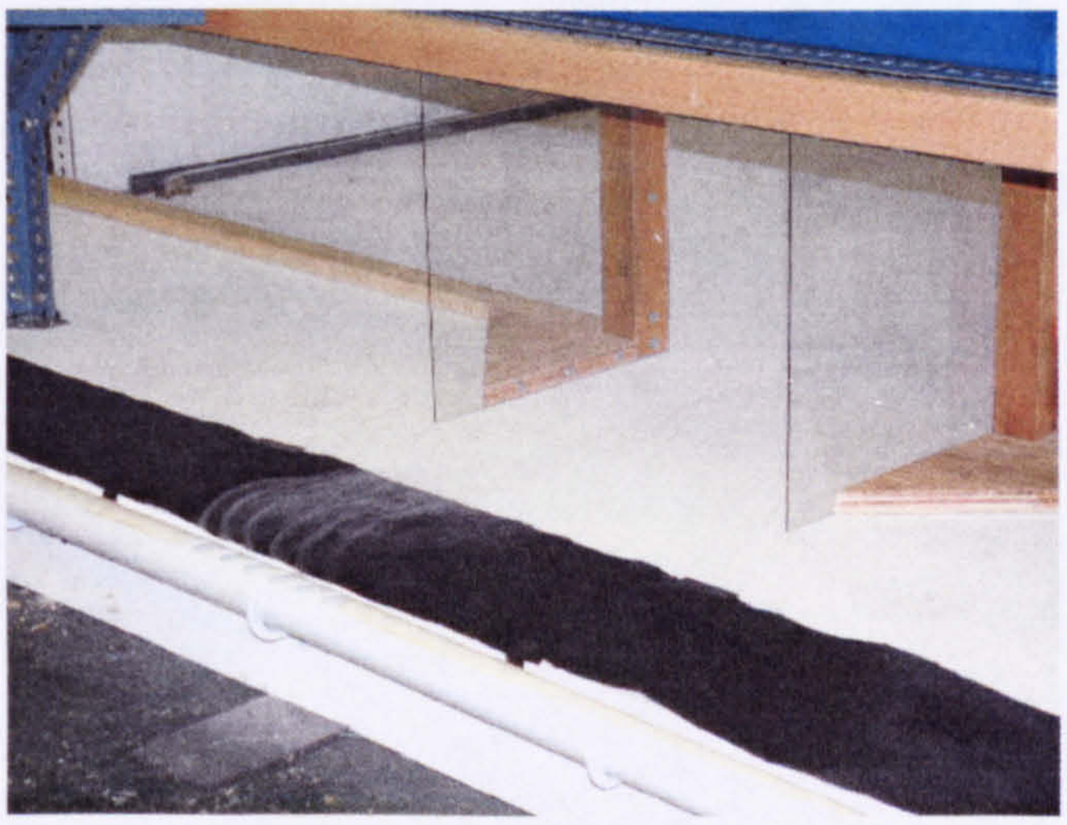

Figure 5.21 - Piping arrangement used to deliver smoke to the vicinity of the inlet

The laser probe used incorporated the two laser beams and the receiving sensor that recorded the frequency of the scattered laser light. The measuring location at the intersection of the two laser beams was 350mm from the probe.

The laser probe was mounted on two traverses, as shown in Figure 5.22, so that the velocity measurement position could be moved accurately to any position in a fixed *y*-*z* plane through the short length of duct at the inlet (the *x*-coordinate for the measuring position was fixed at -3.72m). The spatial accuracy of each traverse was of the order of 1mm, whilst the physical dimension of the measurement volume at the laser intersection is approximately 1.3mm. The laser is shown 'in action' during an experiment in Figure 5.23.

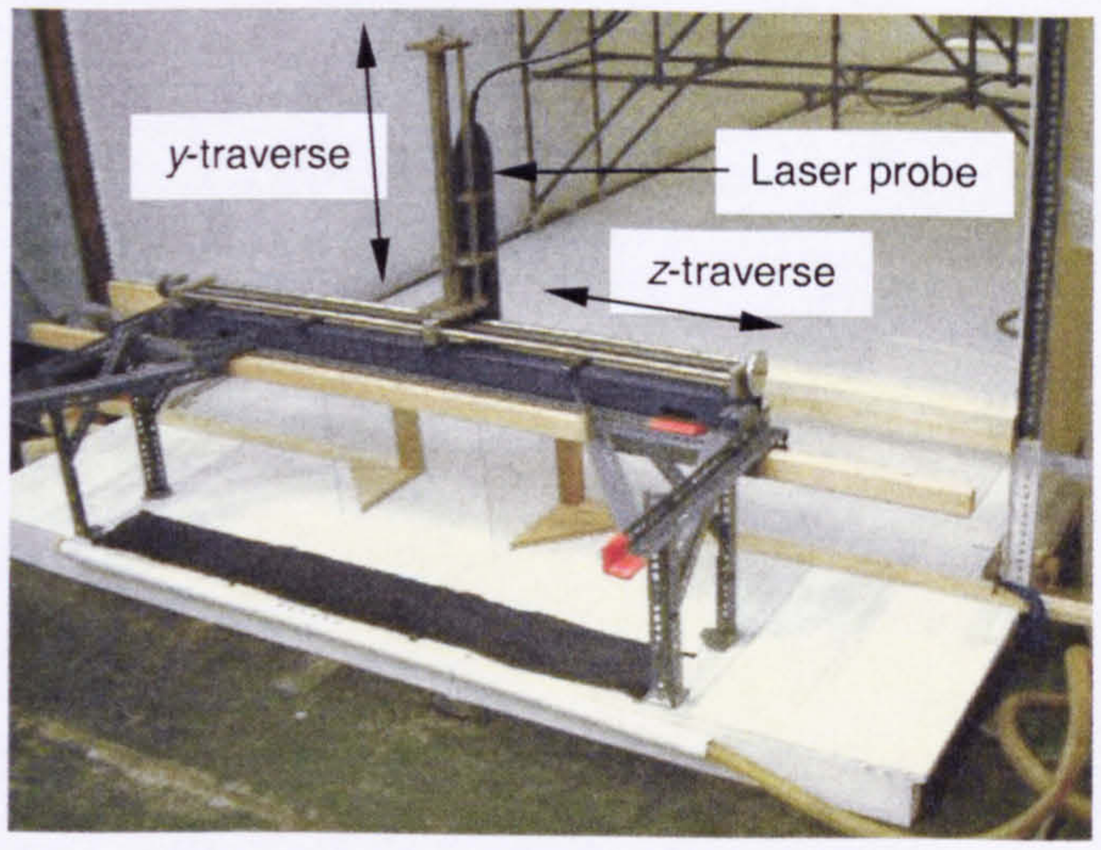

Figure 5.22 - Laser probe and traversing system

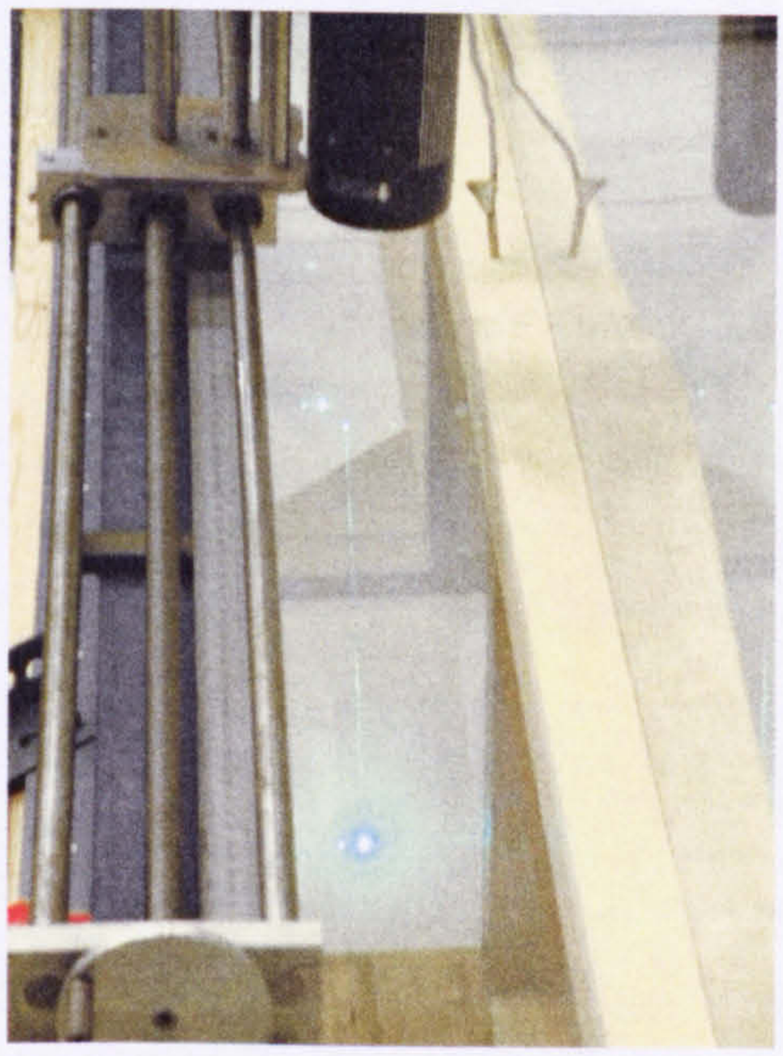

Figure 5.23 - The laser 'in action' during an experiment

5.7.1 Laser Doppler anemometry system

The LDA system used in this study was manufactured by TSI Incorporated and is illustrated in Figure 5.24. A list of the individual components is provided in Table 5.1.

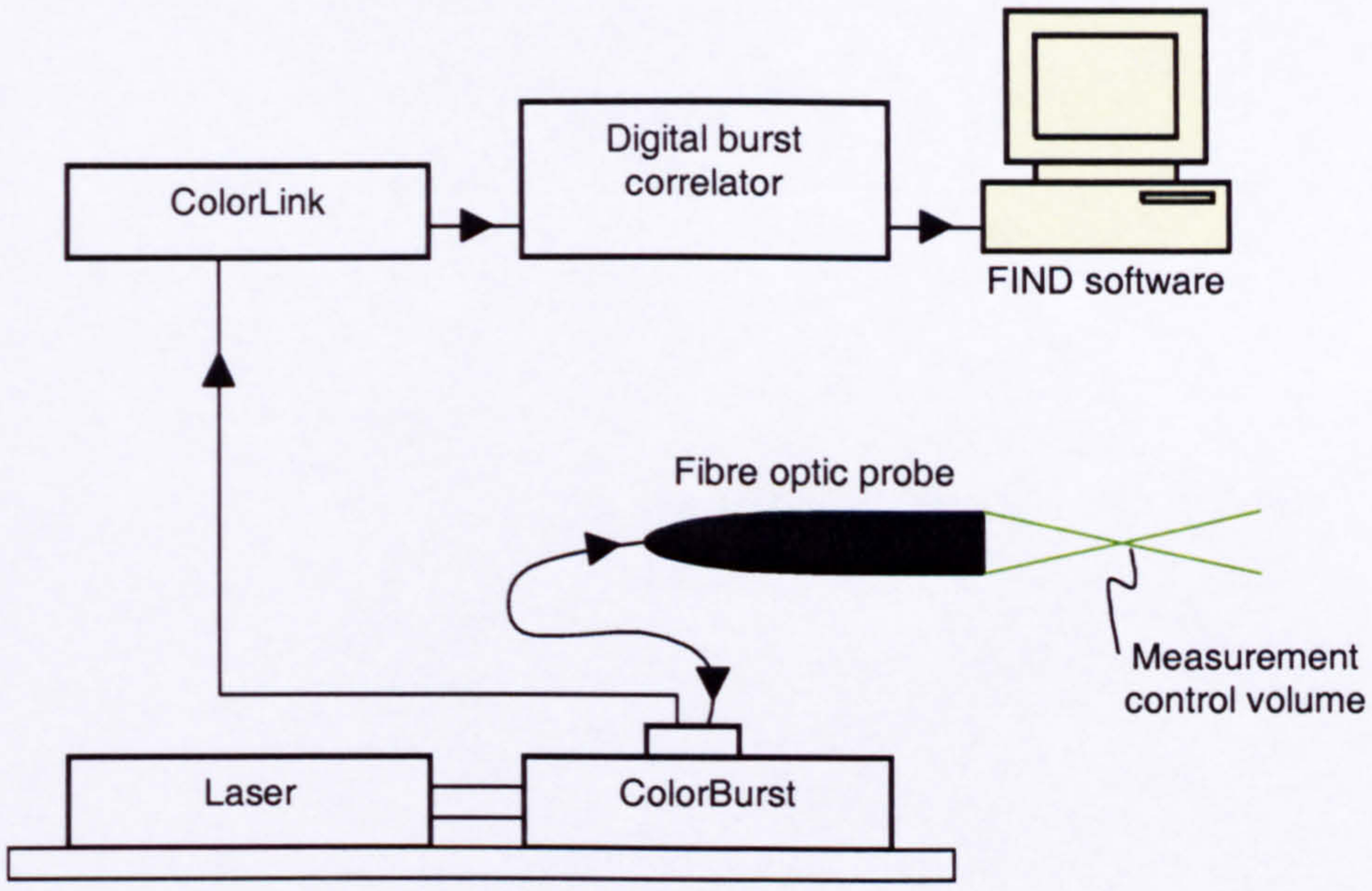

Figure 5.24 - Arrangement of the LDA system

The laser beam from the 2kW argon-ion laser was aimed through the beam collimator into the ColorBurst unit, where it was separated into three pairs of laser beams: two green beams, two blue beams and two violet beams. In addition, the ColorBurst unit incorporated a Bragg cell that was used to shift the frequency of one of the output beams in each pair. The magnitude of the frequency shift was 40MHz.

Item	*Model*
2kW argon-ion laser	Model 85 (Lexel)
Beam collimator	Model 9108
COLORBURST multicolour beam separator	Model 9201
Fibre-optic couplers	Model 9271
Fibre-optic probe, with 350mm focusing lens	Model 9831
COLORLINK multicolour receiver	Model 9230
Digital burst correlator	Model IFA 550

Table 5.1 - Components of the LDA system

The collimator was necessary to control the divergence of the laser beam, and ensure that the laser waist position occurred at the intersection region at the focal point of the transmitting lens, so that the interference fringes in the intersection region were indeed planar.

The ColorBurst was designed so that a pair of beams was used for the measurement of one component of velocity. The system available for this study was a single-component system, so that only the pair of green laser beams was used.

The fibre-optic probe focused the green beams from the ColorBurst at the measurement volume. In addition, the probe incorporated the receiving optics required to collect the light scattered by particles moving through the bright interference fringes within the measurement volume. This design of probe allowed the relocation of the measurement volume with relative ease, without the need for repositioning and realigning the entire LDA system. The scattered light was transmitted to ColorLink unit for subsequent post-processing.

The ColorLink unit separated the scattered light received into the three channels of colour: green, blue and violet. Each channel can be subsequently passed through a photomultiplier tube within the ColorLink unit, which converted the scattered light into an electrical analogue output. As the system used was a single-channel system, only the green channel was available and subsequently analysed. This analogue signal was then analysed by the digital burst correlator and the proprietary FIND software provided by TSI Inc. to obtain the velocity distribution at the measuring volume, and statistical measures such as the mean velocity and its standard deviation.

5.7.2 Experimental procedure

Before the start of each experiment, the laser probe was positioned so that the measuring control volume coincided with the centre of the inlet, as illustrated in Figure 5.25. The inward component of velocity at that position was then regularly recorded throughout the transient phase following the activation of the heat source, usually from 09:45 to 12:30.

During the steady-state phase of each experiment, the measuring volume was systematically moved to each node in a uniformly spaced grid, comprising eight horizontal rows and 10 vertical columns. The height of the opening remained constant for all experiments and therefore so did the vertical grid spacing. As the width of the opening was varied between experiments, however, the horizontal grid spacing was altered to remain one-tenth of the opening width. To identify each measuring location, the rows and columns of the grid are indexed from A to H and from A to J respectively. At the start of each experiment, the measuring location coincided with that at column A, row A, and it was subsequently traversed through the other measuring locations within row A. Upon completion of the top row, the LDA probe was lowered to record at row B and the probe was traversed back towards column A. This movement was repeated until all of the measurement locations had been monitored, as illustrated by the arrow in Figure 5.25.

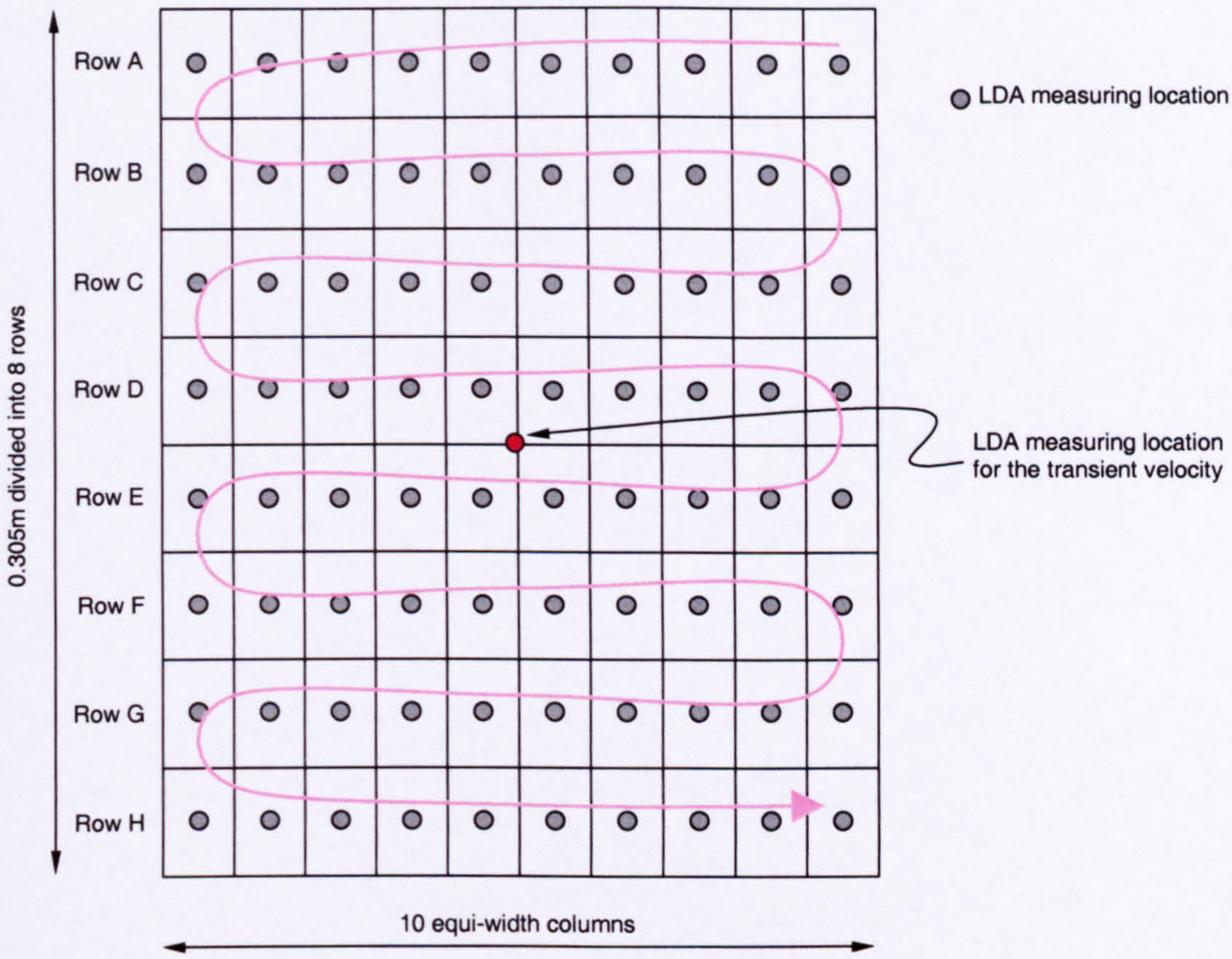

Figure 5.25 - Sketch of grid at opening *A*-inlet for velocity measurements, looking towards the *A*-end of the enclosure from outside (i.e. in the positive *x*-direction)

The duration of a single velocity measurement would be influenced by the density of the smoke particle seeding at the measurement location during the recording interval: a recording would continue for a maximum of one minute unless a predefined total of 8192 smoke particles had been registered, in which case the recording would immediately come to an end. If the seeding was particularly poor, then there may have been fewer than 20 smoke particles registered, in which case the recording was judged to be unreliable. Most recordings consisted of data from at least 100 smoke particles within one minute, and a small proportion included data from 8192 particles over a shorter period. Perhaps 20% of the recordings consisted of data from between 20 and 100 smoke particles within one minute.

It was often the case, particularly towards the top of the opening and close to the vertical walls, that velocity recordings would be judged to be unreliable due to poor seeding. If this was the case, then the measurement would be repeated so that a satisfactory recording could be obtained. In the event that no reasonable recording was forthcoming after three to four attempts, then the velocity at that location would be determined by interpolation from the measured velocities at neighbouring measurement locations.

The duration of the steady-state phase of the experiment was generally about three hours, usually between 13:00 and 16:00. With eighty measurement locations, this corresponded to approximately two minutes per measurement location. If a significant number of recordings were repeated towards the top of the opening, which was usually the case, then there would be insufficient time left to complete the velocity measurement at all of the remaining measurement locations. Instead, the recordings within an entire row (or two rows) close to the centre height of the opening, where the inward component of velocity was generally found to be uniform, may be abandoned and interpolated from the measured data from the rows immediately above and below, thus reducing the total number of measurement locations to seventy (or sixty), in order to ensure that the experiment would be completed by 16:00.

5.8 Summary

Prior to this work, all experimental investigations for the natural displacement ventilation flow through enclosures had been performed using small-scale water-based experimental techniques. The aim of the present experimental work was to provide thorough and reliable data for the natural displacement ventilation flow through a full-scale enclosure with air as the fluid medium, which would be more representative of any similar flow within a real building than had been attempted thus far.

The full-scale enclosure designed for this purpose was presented in this chapter. The enclosure measured 7.32m long × 2.32m wide × 2.44m high so that in terms of geometrical size, it was indeed representative of an occupied space within a real building. Due to budgetary constraints, however, it was constructed from chipboard sheet material rather than more traditional building materials, so that the thermal properties of the walls were not necessarily representative of a real building.

Two floor-level heat sources were used during the course of the experimental program. Initially a 225W plate heater measuring 0.4×0.2m was used, but this was later replaced with a commercial 1500W 'boiling ring' of diameter 0.18m. The latter had the advantage of more closely approximating a point source of buoyancy, which is one of the assumptions employed in the Cambridge mathematical model.

The air temperature within the enclosure was recorded using shielded platinum resistance thermometers, which were mounted on a vertical mast that could be translated along the *xy*-symmetry plane of the enclosure. Twelve thermometers were used in total: for the plate heater experiments eleven were mounted on the mast with one located in the low-level *B*-opening, and for the boiler ring experiments ten were mounted on the mast with one located in each of the low-level openings.

During the later experiments, the external temperature profile surrounding the enclosure was recorded using a single k-type thermocouple.

For the boiler ring experiments detailed measurements of the inward component of velocity at the low-level *A*-opening were recorded using a laser Doppler anemometer, where smoke was used to seed the incoming flow.

6.0 Experimental results from the full-scale enclosure

6.1 Introduction

The experimental recordings of temperature and velocity for all of the natural ventilation studies performed upon the full-scale room described in §5 are presented in this chapter. In total there were 33 studies performed over a period stretching from January 2001 to September 2001. For each new study it would generally take in the region of three to four hours following the activation of the heat source for the natural ventilation flow through the test-room to reach steady-state. The duration of the experiment once at steady-state would usually be two to three hours, so that a single study would take an entire day to complete.

The internal temperature distribution within the enclosure was monitored for three series of experiments, each corresponding to a different heat source: the plate heater with a heat output of 225.0W and the boiler ring with an output of 368.0W and 490.5W. For each heater configuration several experiments were performed, each for a different width of the openings to the enclosure. In addition, experiments were performed with the boiler ring heat output set to 39.6W, 91.1W and 155.8W, with the width of the openings equal to 0.4m.

Although the measurements from the thermometers provided information regarding the temperature distribution within the space, it was the temperature differences that motivated the ventilation flow through the enclosure that is of interest. All of the temperature data must, therefore, be manipulated and compared to some reference temperature, the selection of which is discussed in §6.2.1. The experimental temperature data for all of the experimental studies are then presented as a deviation from the reference temperature in §6.2.2.

For the experiments with the 490.5W boiler ring as the heat source the external stratification was recorded simultaneously with the internal temperature measurements. For most of the experiments, the experimental data for the external temperature profile was reasonably represented by a logarithmic curve-fit. Further analysis of the internal and external thermal environment for this heater configuration allowed the inward component of velocity at the low-level openings to be determined

using the stratification-flow rate theory introduced in §2.7, which was used to estimate of the rate of heat loss through the fabric of the walls of the enclosure. This analysis is presented in §6.2.3 and demonstrates that a significant proportion of thermal energy was lost through the walls of the enclosure, particularly for the smaller opening configurations considered. A general discussion of the experimental temperature measurements for all experimental studies is provided in §6.2.4.

The recordings of the inward component of velocity at the low-level opening are presented and discussed in §6.3. A comparison of the measured velocities with those calculated from the temperature data presented in §6.2.3 is included. Good agreement was observed so that the theoretical stratification-flow rate coupling discussed in §2.7 would, therefore, appear to be valid.

6.2 Temperature measurements

6.2.1 Reference temperature

For the first series of experiments with the plate heater as the source of buoyancy, one of the thermometers was mounted in the top of the low-level opening at the *B*-end of the test enclosure to provide a reference temperature with which to compare all other temperature recordings. For the later studies with the boiler ring as the heat source, a reference temperature was positioned in each of the low-level openings to quantify non-symmetrical effects due to the imperfect construction of the surrounding chamber. The two temperatures recorded at the reference thermometers, however, were generally not equal. It is, therefore, important to consider how to use the two temperatures recorded to determine a single reference temperature from which to compare all of the other temperature recordings within the space.

Several alternatives are possible, such as simply taking the mean of the two values. Alternatively, one could use the temperature recorded at the opening at the *A*-end of the room as the reference temperature for all temperatures measured within section-*A* of the enclosure, and similarly use the temperature recorded at the opening at the *B*-end of the room as the reference temperature for all temperatures measured within section-*B* of the space.

Following an analysis of the various options, the reference temperature was taken as the maximum temperature recorded at either of the two reference thermometers. When the data from all of the experimental studies had been analysed, this option for the reference temperature resulted in the most clearly defined trend for the variation of the internal temperature profile with opening area.

All experimental results in this work are, therefore, defined in terms of the rise in temperature ΔT above the reference temperature T_{ref}

$$\Delta T(x,y) = T(x,y) - T_{ref} = T(x,y) - \max(T_A, T_B). \qquad (6.2.1)$$

6.2.2 Presentation of steady-state temperature measurements

The temperature data from all of the experimental studies is provided in Addendum One. For each study, three items of data are presented. Firstly, a plot of the rise in temperature above the reference temperature with respect to the height above the floor within the space is provided, to immediately illustrate the shape of the temperature profile within the enclosure. A curve of best-fit to the experimental profile, constructed from four linear segments, is also included on the plot, together with the external temperature profile for those studies where this information was recorded. Secondly, an isopleth map of the temperature rise along the symmetry plane running the length of the enclosure (plane $z = 0.0$m) is provided. Finally, a plot of the temperature rise at each of the reference thermometers located in the low-level openings to the enclosure is also given.

Each of the four linear best-fit segments may be represented in the form

$$\Delta T_{\text{best-fit}}(y) = my + c, \qquad (6.2.2)$$

where $\Delta T_{\text{best-fit}}$ is the linear best-fit segment to the rise in temperature above the reference temperature, y is the height above the floor within the space, and m and c are constants. A summary of the constants m and c for the four best-fit segments for each of the experimental studies is provided in Table 1 of Addendum One.

6.2.2.1 Plate heater with an output of 225.0W for various opening configurations

A summary plot of the four-segment curves of best fit for the rise in temperature within the enclosure for all of the experimental studies employing the plate heater with an output of 225.0W as the source of buoyancy is given in Figure 6.1. For this series of experiments, the external temperature stratification was not recorded.

Each 'best-fit' curve for the internal temperature profile comprises two separate portions. In the region between a height of 0.1m and 1.0m each profile exhibited a steep linear increase in temperature, approximately equal to 1.4°C/m. Between a height of 1.0m and 2.35m, the temperature continued to rise, but the rate of increase with respect to height was much reduced, the vertical temperature gradient roughly equal to 0.3°C/m.

It was observed that this generic profile for the internal temperature was the same for all of the experimental studies with this heating arrangement. As the effective area of the openings was increased, the magnitude of the temperature rise within the space was reduced, so that the only effect of changing the area of the openings was to translate the profile along the temperature axis.

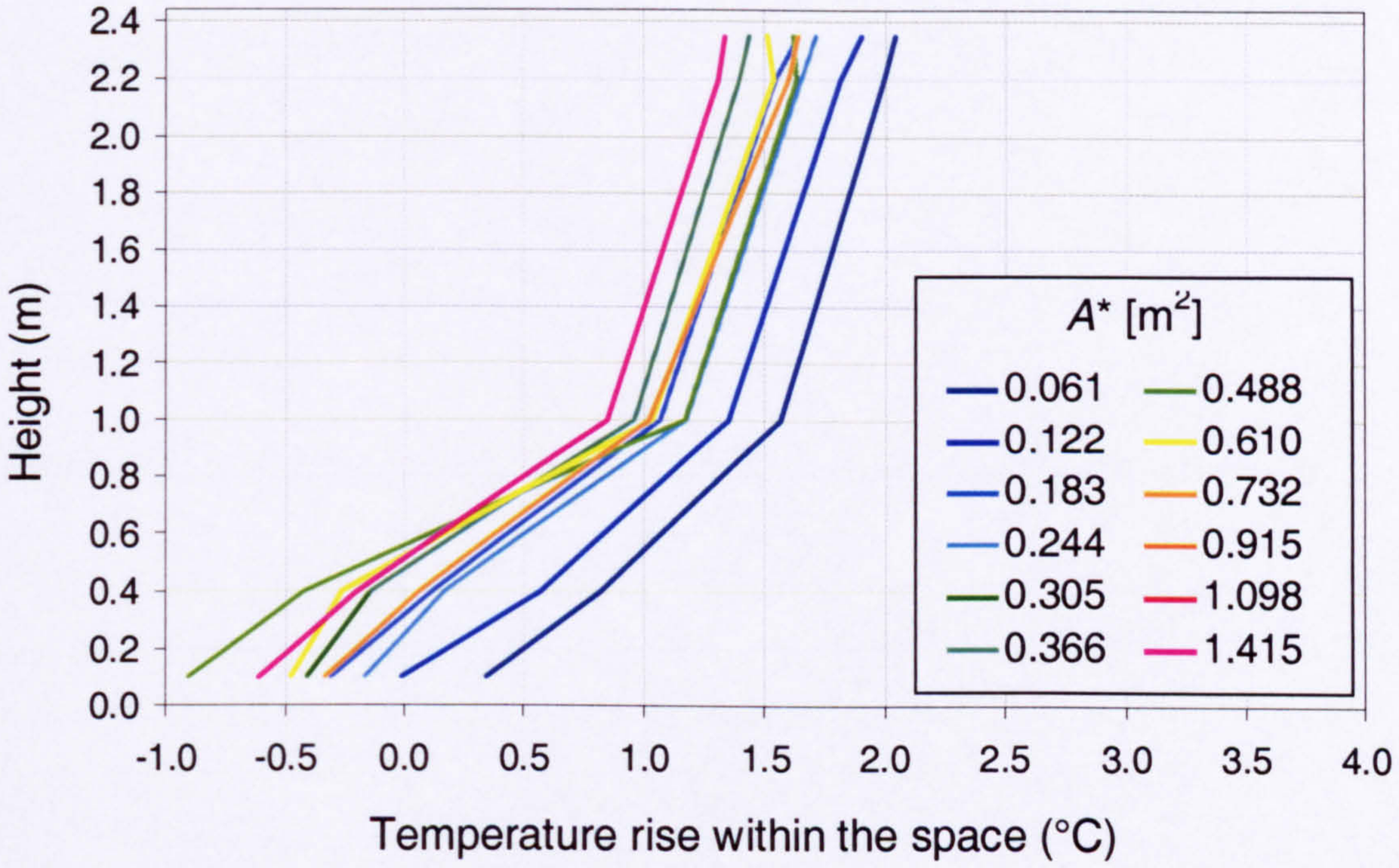

Figure 6.1 - Summary of the four-segment 'best-fit' curves for the internal rise in temperature, with a heat output from the plate heater of 225.0W

For this heater configuration, the isopleth maps of internal temperature rise (Figures 1 to 9, Addendum One) reveal that the stratification within the space was generally not symmetrical. It was observed that the air entering through the low-level opening at the *A*-end of the enclosure was consistently cooler than that entering at the *B*-end. It is also observed that the temperature of the air close to the ceiling at the *A*-end of the enclosure was noticeably cooler than that just below the ceiling at the *B*-end of the enclosure. The lack of symmetry was manifested mainly at the lowest level of the test-room, within 0.3m of the floor, and to a lesser extent at the highest level, within say 0.4m of the ceiling. For the remainder of the space, however, the temperature field was approximately symmetrical (Howell and Potts, 2002).

From the isopleth maps of internal temperature rise, it was observed that particularly towards the *A*-end of the enclosure, the vertical temperature profile tends to checkerboard, so that the profile at alternate monitoring locations are similar. This 'Toblerone-effect' was caused by the global variation of the internal temperature field over the period of an experiment. This was a consequence of having to traverse the thermometer mast along the length of the enclosure and then back again in order to

record the temperature field upon the *xy*-plane of symmetry: towards the *A*-end of the enclosure, approximately two hours may have elapsed between the recording of the temperature profile in one measurement location and the subsequent temperature measurement at the adjacent locations. This global variation in the internal temperature field was probably due to the relatively long warm-up period required for the plate heater, particularly for the larger openings considered, so that the steady-state field may not quite have been established before the start of the temperature measurement phase.

The 'Toblerone-effect' was less significant towards the *B*-end of the enclosure and, if the entire temperature field could be measured simultaneously, it would be eliminated altogether.

6.2.2.2 Boiler ring with an output of 368.0W for various opening configurations

A summary plot of the four-segment curves of best fit for the rise in temperature within the enclosure for all of the experimental studies employing the boiler ring with an output of 368.0W as the source of buoyancy is given in Figure 6.2. For this series of experiments, the external temperature profile was not recorded.

The best-fit curves with this heater configuration were well represented by a single linear segment for the majority of the space, with a rate of increase of internal temperature with respect to height approximately equal to 1.0°C/m. It was observed, however, that the layer of air close to the floor of the enclosure, and in the layer directly below the ceiling, a single linear segment would no longer suffice. In the layer of air between the heights of 0.15m and 0.4m, the temperature gradient with respect to height was visibly greater, approximately equal to 1.5°C/m. In the layer between 2.2m and 2.4m there was no further significant rise in temperature.

Once again, it was observed that the shape of the internal temperature profile was roughly the same for all of the experimental studies with this heater configuration. As the effective area of the openings was increased, the profile of internal temperature rise was simply shifted to a lower position on the temperature axis.

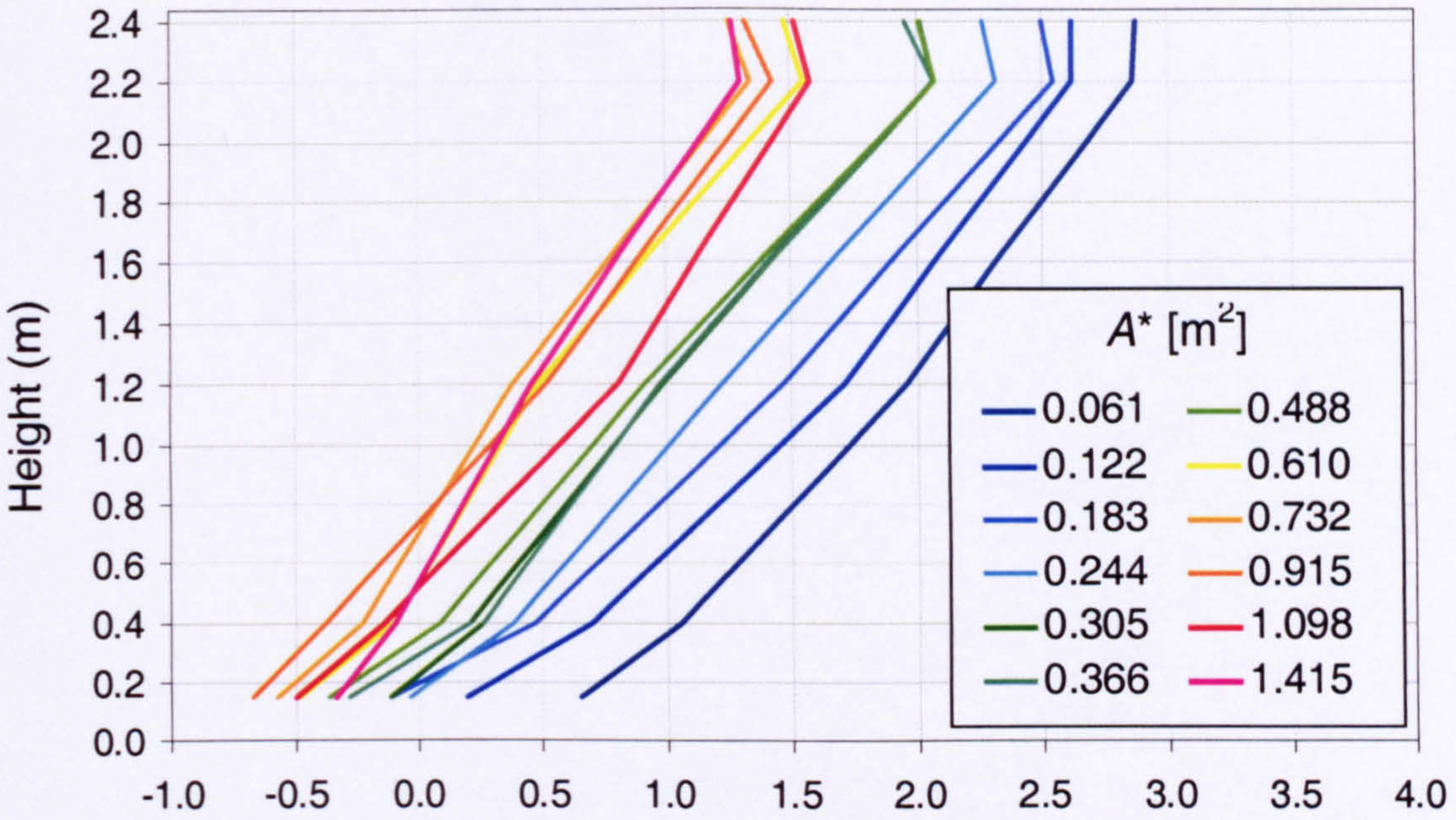

Figure 6.2 - Summary of the four-segment 'best-fit' curves for the internal rise in temperature, with a heat output from the boiler ring of 368.0W

From the isopleth maps of internal temperature rise for this heater configuration (Figures 13 to 24, Addendum One), it was observed that once again the air entering through the low-level opening at the *A*-end of the enclosure was consistently cooler than that entering at the *B*-end, perhaps by as much as 1.0°C. This difference in inlet air temperature was confirmed by the graphs of reference temperature, also in Addendum One. The isopleth maps, however, show that the stratification within the space was more symmetrical than for the experimental studies with the plate heater as the source of buoyancy.

For this heater configuration, the 'Toblerone-effect' was apparent, so that the traverse of the temperature mast may have commenced before the steady-state temperature field within the enclosure was properly established.

6.2.2.3 Boiler ring with an output of 490.5W for various opening configurations

For the experimental studies with the 490.5W boiler ring as the heat source, the thermal stratification outside of the room was also recorded, the 'best-fit' profiles of which are presented in Figure 6.3.

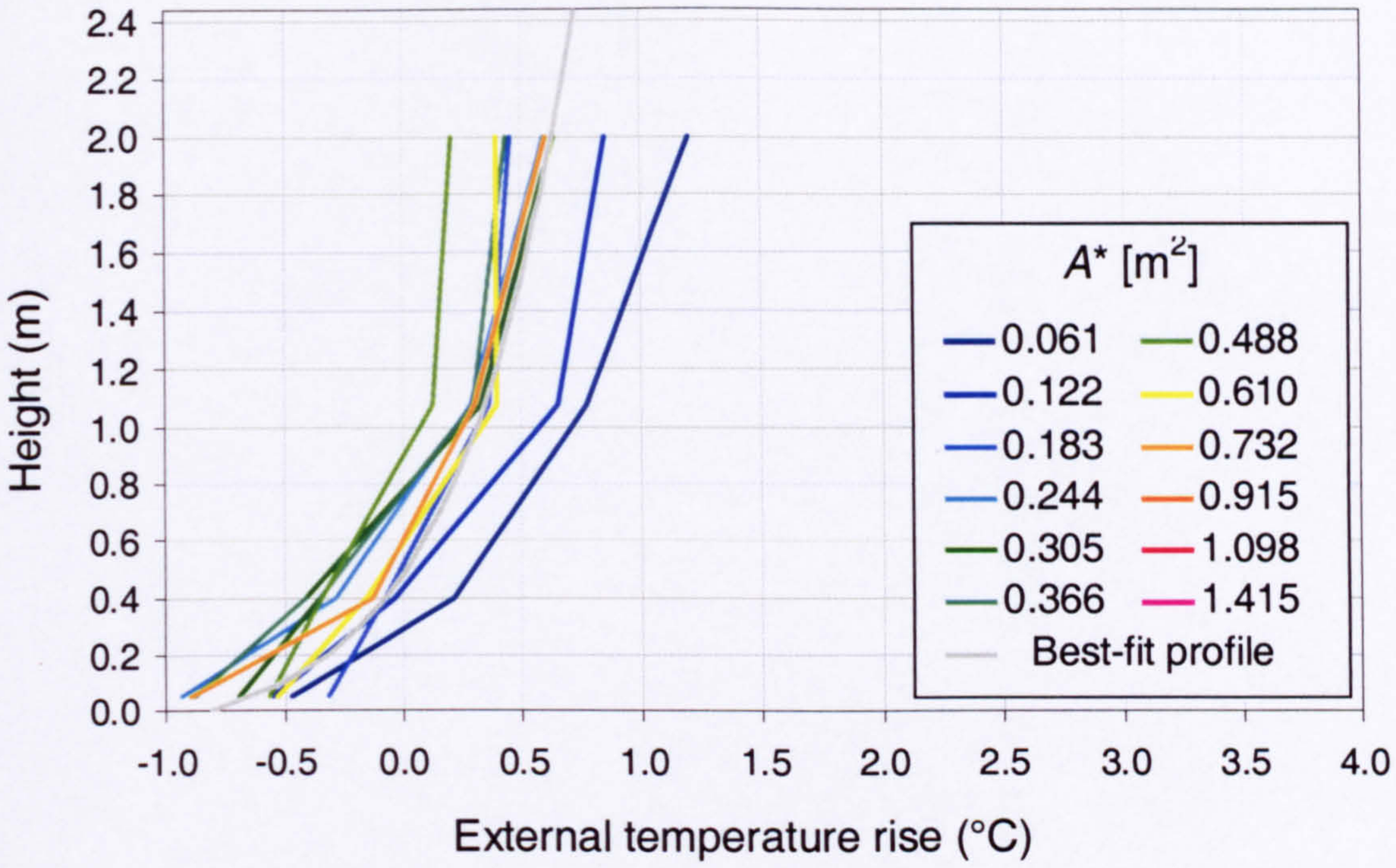

Figure 6.3 - Summary of the 'best-fit' curves for the external rise in temperature, with a heat output from the boiler ring of 490.5W

With the exception of perhaps three experiments ($A^* = 0.061m^2$, $A^* = 0.122m^2$ and $A^* = 0.488m^2$), the external temperature was reasonably represented by a best-fit logarithm law of the form

$$\Delta T_{ext}(y) = \frac{1}{2}\ln\left(\frac{y+0.12}{0.6}\right). \qquad (6.2.3)$$

With regard to the internal temperature measurements for the 490.5W boiler ring, a summary plot of the four-segment curves of best fit for the rise in temperature within the enclosure for all of the experimental studies employing the boiler ring with an output of 490.5W as the source of buoyancy is given in Figure 6.4. The 'best-fit' external temperature profile as described by (6.2.3) is also shown on the plot.

The best-fit curves with this heater configuration must be represented by a minimum of four linear segments, as it was possible to identify four distinct layers of air within the space. In the layer of air between the heights of 0.15m and about 0.4m, the temperature gradient with respect to height was relatively steep, approximately equal to 2.0°C/m. Above this zone and up to a height of approximately 1.0m the rise in temperature was less marked, with a gradient of roughly 0.7°C/m. In the layer of air between the heights of 1.0m and 2.2m the rate of increase of temperature with respect to height was observed to increase to approximately 1.2°C/m. In the region between the heights of 2.2m and 2.4m there was no further rise in temperature: indeed, for many of the experimental studies, the temperature was observed to fall slightly in this region, perhaps by as much as 0.2°C.

Once again, it was observed that the shape of the internal temperature profile was roughly the same for all of the experimental studies with this heater configuration, so that the only effect of increasing the effective area of the openings was to translate the temperature profile to a lower position along the temperature axis.

The isopleth maps of internal temperature rise for this heater configuration (Figures 25 to 33, Addendum One), show that the stratification within the space was approximately symmetrical for the experimental studies with this heater configuration. With the exception of two experiments, the plots of reference temperature show that the temperature of the incoming air at the *A*-end differed no more than 0.4°C from that entering at the *B*-end of the enclosure.

For this heater configuration, the 'Toblerone-effect' was again apparent, so that the traverse of the temperature mast may have commenced before the steady-state temperature field within the enclosure was fully established.

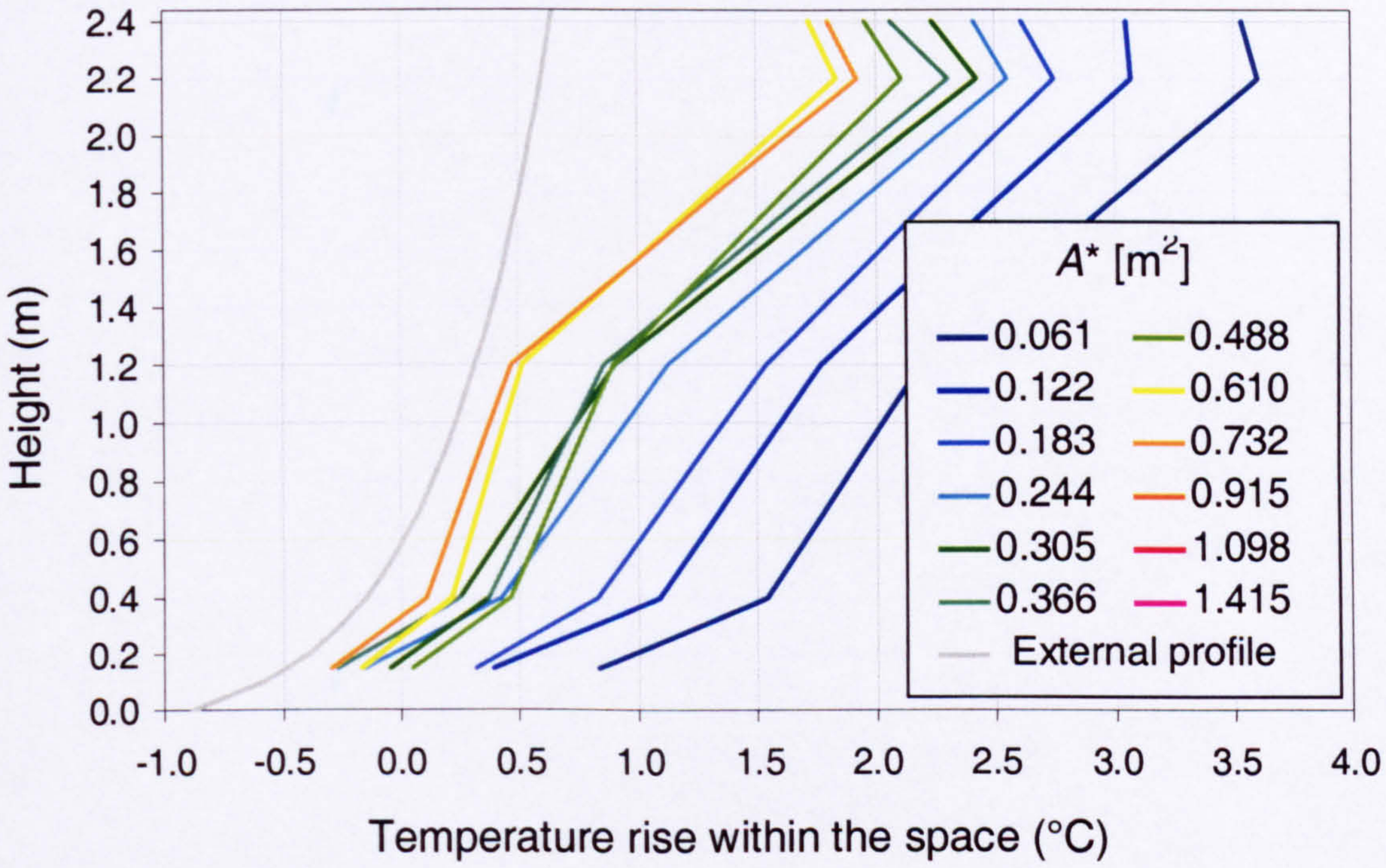

Figure 6.4 - Summary of the four-segment 'best-fit' curves for the internal rise in temperature, with a heat output from the boiler ring of 490.5W

6.2.2.4 Boiler ring with varying output for an opening width of 0.4m

Three additional experimental studies were performed to determine in more detail what effect the strength of the heat source had upon the stratification within the space. The boiler ring heat output was set to 39.6W, 91.1W and 155.8W and the width of the openings was maintained at 0.4m, so that the effective area of the openings A^* was equal to 0.244m^2. A summary plot of the four-segment curves of best fit for the internal temperature profile for the three extra studies, together with the 368.0W and

490.5W profiles measured previously is given in Figure 6.5. The 'best-fit' external temperature profile as described by (6.2.3) is also shown on the plot.

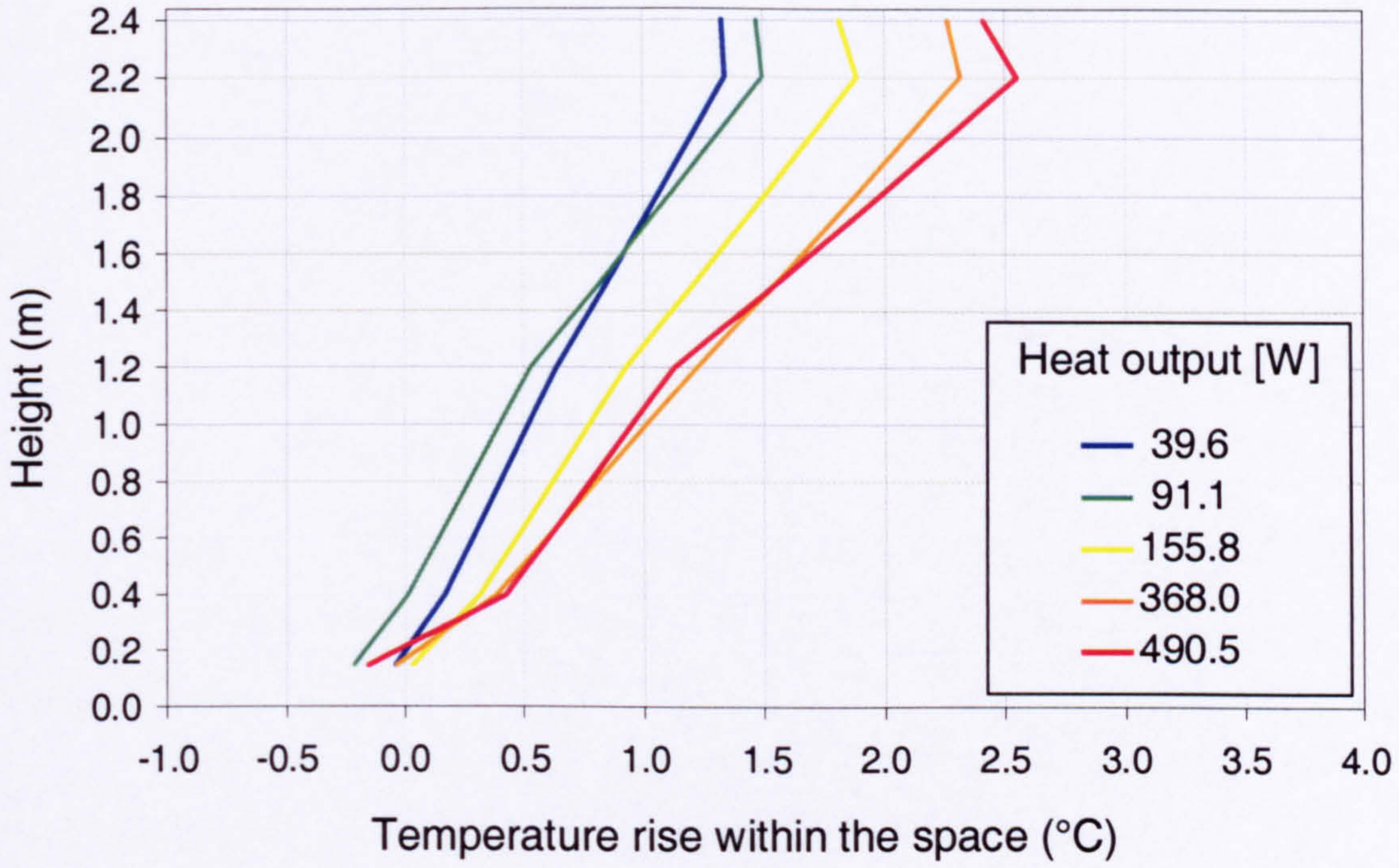

Figure 6.5 - Summary of the four-segment 'best-fit' curves for the internal rise in temperature, for a range of heat outputs from the boiler ring, for $A^* = 0.244m^2$

For this opening configuration, it was observed that below a height of approximately 1.2m, the rate of increase of temperature rise with respect to height within the space was similar for each of the experimental studies and is roughly equal to 0.7°C/m. Above this it was observed that the temperature gradient with respect to height was increased with the strength of the heat source.

Once again, it was observed that the temperature gradient with respect to height was visibly greater in the layer of air between the heights of 0.15m and 0.4m, and that there was no further temperature rise or, indeed, there was a slight temperature fall in the layer between 2.2m and 2.4m.

The isopleth maps of temperature rise within the space for these five studies (Figures 10 to 12, 16 and 28, Addendum One) show that the temperature of the incoming air was roughly the same at each of the low-level openings. This was confirmed by the associated plots of reference temperature. The isopleth maps also show that the internal stratification was roughly symmetrical for each of the five experimental studies.

6.2.3 Further analysis of the steady-state temperature measurements from the experiments with the 490.5W boiler ring as the heat source

For the experimental studies with the boiler ring as the heat source with an output of 490.5W, both the internal and external temperature profiles were measured simultaneously. Together with the theoretical coupling introduced in §2.7 between the stratification within and surrounding the enclosure and the flow rate through the space, the inward component of velocity at the low-level openings to the space can be determined. This can, in turn, be used to estimate the proportion of energy lost through the fabric of the enclosure walls.

The internal and external temperature profiles were approximated by best-fit curves constructed from a series of linear segments, where each segment was described by the two constants m and c, the values of which are provided Table 1 and Table 2 of Addendum 1. Using this information, the internal and external piezometric pressure differentials $\Delta\tilde{p}_{int}$ and $\Delta\tilde{p}_{ext}$ were calculated according to

$$\Delta\tilde{p}_{int} = \frac{R\rho_0^2}{p} g \int_{y=0.0\text{m}}^{y=2.44\text{m}} (T_{int}(y) - T_0)\,dy\,, \qquad (2.7.4)$$

and

$$\Delta\tilde{p}_{ext} = \frac{R\rho_0^2}{p} g \int_{y=0.0\text{m}}^{y=2.44\text{m}} (T_{ext}(y) - T_0)\,dy\,, \qquad (2.7.5)$$

where ρ_0 was the reference density for the fluid, and the temperature profiles were integrated between $y = 0.0$m at the lower limit and $y = 2.44$m at the upper limit. The reference density ρ_0 followed from the reference fluid temperature T_0, which was determined by performing an average over the measured temperatures along the xy-plane of symmetry within the space: it was observed that they were all in the range $20.0°\text{C} < T_0 < 25.0°\text{C}$.

Assuming that the pressure loss coefficient c at the inlet and the discharge coefficient c_d at the outlet were equal to unity, then the difference in pressure $\Delta\tilde{p}_{int} - \Delta\tilde{p}_{ext}$ was equally divided between the pressure differentials at the low-level and high-level openings. Based upon this approach, the pressure differential at the low-level opening $\Delta\tilde{p}_{inlet}$ and the corresponding inward component of velocity at the low-level opening v_{inlet} were determined for each opening configuration and are listed in Table 6.1, with a plot of the inlet *velocity* against the effective area of the openings A^* shown in Figure 6.6.

Effective area of openings A*	T_0	ρ_0	$\Delta\tilde{p}_{int}$	$\Delta\tilde{p}_{ext}$	$\Delta\tilde{p}_{inlet}$	v_{inlet}
0.061m^2	21.1°C	1.200kg/m^3	0.2198Pa	0.0677Pa	0.0761Pa	0.356m/s
0.122m^2	21.1°C	1.200kg/m^3	0.1757Pa	0.0452Pa	0.0652Pa	0.330m/s
0.183m^2	20.0°C	1.204kg/m^3	0.1529Pa	0.0235Pa	0.0647Pa	0.328m/s
0.244m^2	24.2°C	1.187kg/m^3	0.1153Pa	0.0162Pa	0.0495Pa	0.289m/s
0.305m^2	24.8°C	1.185kg/m^3	0.0987Pa	0.0165Pa	0.0411Pa	0.263m/s
0.366m^2	22.8°C	1.193kg/m^3	0.0999Pa	0.0113Pa	0.0443Pa	0.272m/s
0.488m^2	21.0°C	1.200kg/m^3	0.1003Pa	-0.0008Pa	0.0506Pa	0.290m/s
0.610m^2	21.4°C	1.199kg/m^3	0.0713Pa	0.0182Pa	0.0265Pa	0.210m/s
0.732m^2	20.6°C	1.202kg/m^3	0.0689Pa	0.0208Pa	0.0240Pa	0.200m/s

Table 6.1 - Velocity predicted at the low-level opening for each opening width considered with the boiler ring output set to 490.5W

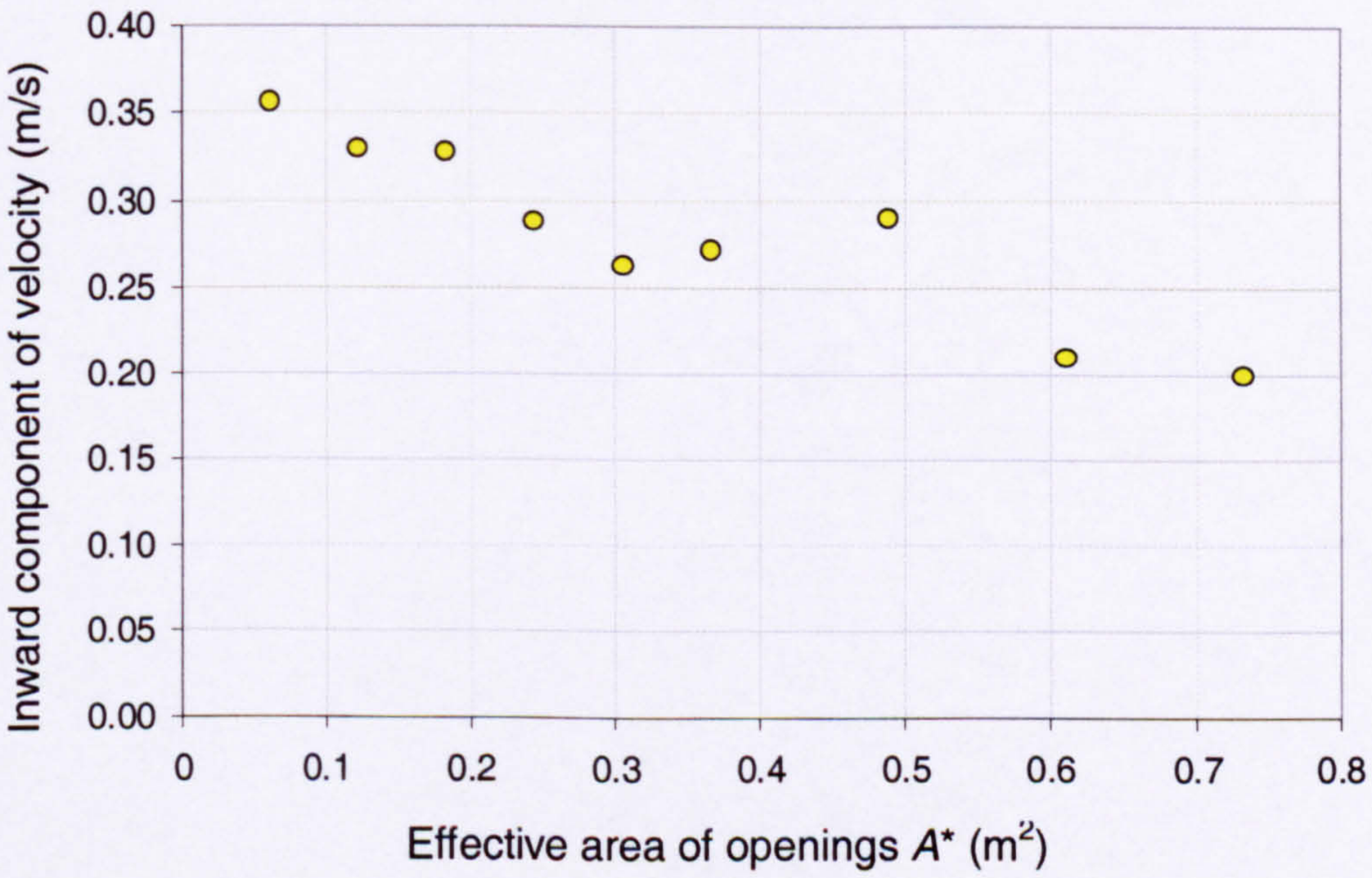

Figure 6.6 - Plot of the calculated inlet velocity at low-level opening against the effective area of the openings to the enclosure A^* for the 490.5W boiler ring

From Figure 6.6, as the area of the openings was increased there was a general downward trend in the inward component of velocity calculated at the lower openings. Perhaps the exception to this trend was the velocity for the effective area of opening $A^* = 0.488\text{m}^2$. For this particular experimental study, however, the rise in

temperature surrounding the enclosure was lower than for the other studies (Figure 6.3), with a correspondingly low external piezometric pressure differential $\Delta\tilde{p}_{ext}$: indeed, from Table 6.1 this study was the only one for which $\Delta\tilde{p}_{ext}$ was negative, thereby augmenting the pressure distribution driving the flow through the enclosure rather than opposing the flow. The higher than expected calculated velocity for this opening configuration was, therefore, due to the reduced external stratification surrounding the enclosure.

Having determined the inward velocity at the low-level openings, the rate at which energy was convected through the space $\Delta\dot{E}$ was determined according to

$$\Delta\dot{E} = \dot{m}c_p\Delta T\,, \qquad (6.2.4)$$

where the mass flow rate $\dot{m}$ was calculated using the inlet velocities listed in Table 6.1, and ΔT was the rise in temperature within the space between the heights of $y = 0.0$m and $y = 2.44$m, which was estimated using the values of m and c describing the best-fit curves for the internal temperature stratification (Table 1, Addendum 1). The rate at which energy was lost through the fabric of the enclosure walls was then determined from a simple energy balance

$$\dot{E}_{walls} = \dot{E}_{heater} - \Delta\dot{E} = 490.5W - \Delta\dot{E}\,, \qquad (6.2.5)$$

and is provided in Table 6.2.

Effective area of openings A*	$\dot{m}$	ΔT	$\Delta\dot{E}$	$\dot{E}_{walls}$
0.061m^2	0.0261kg/s	3.13°C	81.9W	408.6W
0.122m^2	0.0483kg/s	3.08°C	149.2W	341.3W
0.183m^2	0.0722kg/s	2.60°C	189.1W	301.4W
0.244m^2	0.0837kg/s	2.91°C	244.8W	245.7W
0.305m^2	0.0951kg/s	2.81°C	269.1W	221.4W
0.366m^2	0.1190kg/s	2.36°C	281.8W	208.7W
0.488m^2	0.1700kg/s	2.15°C	367.8W	122.7W
0.610m^2	0.1538kg/s	2.12°C	327.7W	162.8W
0.732m^2	0.1760kg/s	2.34°C	413.0W	77.5W

Table 6.2 - Rate of energy loss predicted through the fabric of the enclosure walls for each opening width considered with the boiler ring set to 490.5W

A plot of the variation of the calculated rate of energy loss with the effective area of the openings A^* is given in Figure 6.7. It was observed that for the smaller openings, a high proportion of the 490.5W of thermal energy introduced into the space by the boiler ring escaped from the space by conduction through the fabric of the enclosure walls. As the openings were increased, this proportion was reduced as the loss by convection through the openings became more significant, so that the adiabatic assumption at the walls of the enclosure became an increasingly realistic approximation.

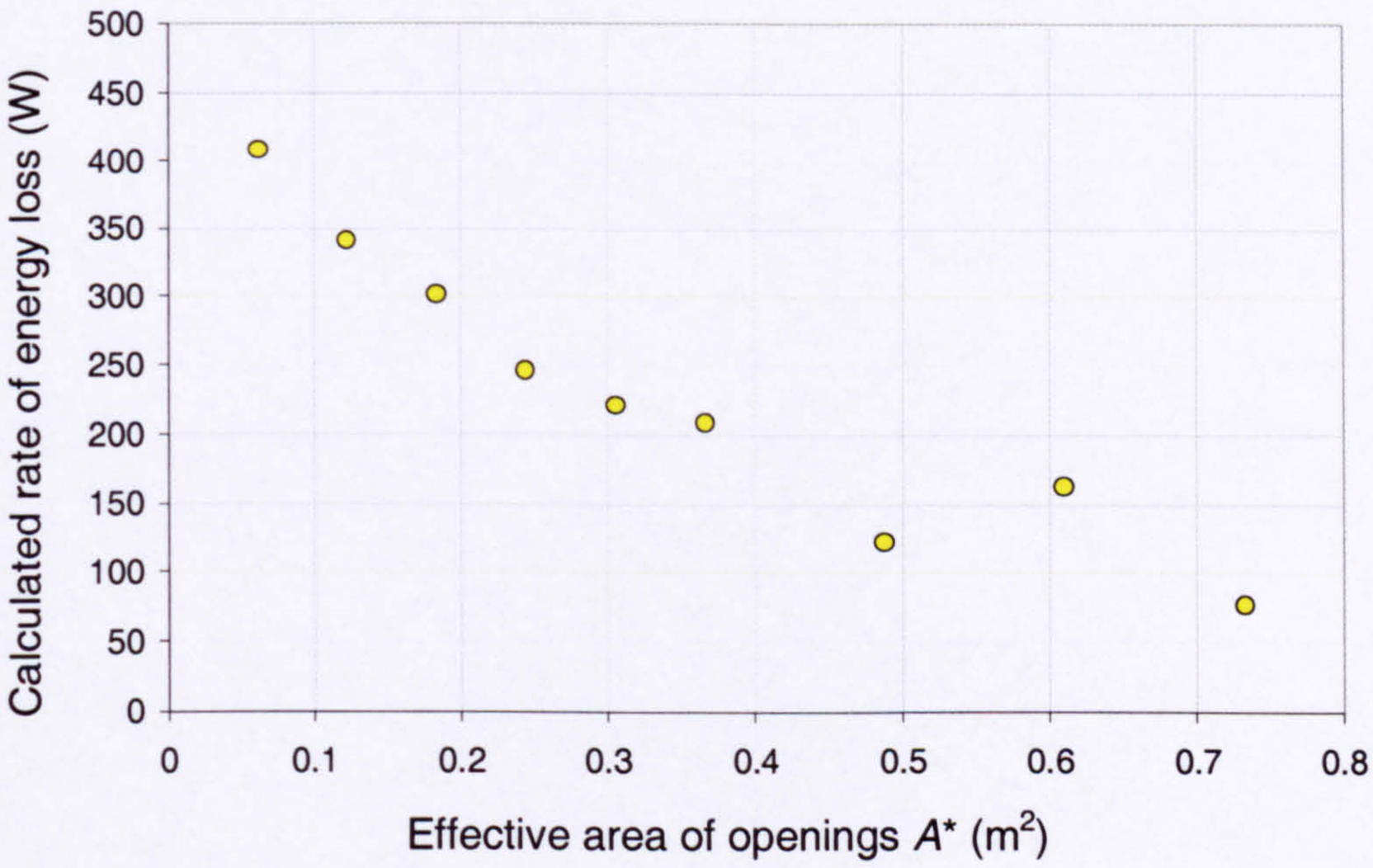

Figure 6.7 - Plot of the calculated rate of energy loss through the fabric of the enclosure walls against the effective area of the openings to the enclosure A^* for the 490.5W boiler ring

6.2.4 Discussion of temperature measurements

6.2.4.1 General form of the internal stratification within the enclosure

For all of the experimental studies, it was observed that no layer of ambient air at low-level within the space was established, nor was there a sharp interface between two layers of fluid at a different temperature. This was in contrast to the stratification observed in the water-based experiments, and that predicted by the Cambridge mathematical model, where there were two layers of fluid predicted: a layer of ambient fluid at low-level within the space a layer of buoyant fluid above, with the two layers separated by a sharp interface.

This may in part be due to differences in the rate of heat transfer at the enclosure walls: for the Cambridge mathematical model and water-based scale-model

experiments the walls are effectively adiabatic, whereas for the full-scale experimental enclosure the rate of heat transfer through the walls was non-zero. For the larger opening configurations with the full-scale enclosure, however, as the amount of energy that was convected through the enclosure was increased, the proportion of thermal energy lost through the walls was reduced, so that the adiabatic approximation at the enclosure walls became increasingly more realistic. Even for the larger openings, however, there was no sharp interface or layer of ambient air at low-level within the space.

Perhaps a more important cause of the observed differences was the presence of additional transport mechanisms within the full-scale room. First of all, the transport of heat by molecular diffusion is not accurately represented by water-based experimental methods. For air, the Prandtl number is equal to

$$Pr_{AIR} = 0.71, \qquad (6.2.6)$$

so that the rate of diffusion of heat in air is comparable to the rate of diffusion of momentum. For the diffusion of salt in water, the Schmidt number is equal to

$$Sc_{NaCl} = 621, \qquad (6.2.7)$$

and for hydrogen bubbles, the Schmidt number is equal to

$$Sc_{H2} = 196. \qquad (6.2.8)$$

The diffusivity of salt in water is, therefore, almost one thousand times less significant than the diffusivity of heat in air, and the diffusivity of hydrogen bubbles is about three-hundred times less significant than the diffusivity of heat in air. Full similarity cannot, therefore, be achieved between the natural displacement flow in the small-scale water-based experiments and that in a full-scale air-enclosure.

In addition, the transport of heat by radiation is absent from the salt-bath and the fine-bubble experiments since they are entirely isothermal. In contrast, the mechanism of thermal radiative transfer was present in the full-scale air enclosure and will be present in a real building.

Finally, the Reynolds number *Re* for the flow within the full-scale enclosure was greater than that for the salt-bath experiment with the typical value of buoyancy flux quoted earlier (4.4.7)

$$Re_{\text{salt-bath}} = 1.959 \times 10^4. \qquad (4.4.7)$$

The calculation of the Reynolds number for the flow with the plate heater is not useful as the relatively large rectangular area of the heated surface was not representative of a point source of buoyancy. Assuming that the boiler ring was

characteristic of a point source, however, with an output of 368.0W the Reynolds number for the flow was equal to

$$Re_{368.0W} = 6.447 \times 10^4, \qquad (6.2.9)$$

and with an output of 490.5W

$$Re_{490.5W} = 7.095 \times 10^4. \qquad (6.2.10)$$

As the flow within the enclosure away from the plume was likely to be transitional between the laminar and turbulent regimes, the higher Reynolds number for the flow within the full-scale enclosure would indicate that the degree of turbulent diffusion would have been greater than for the similar flows in the salt-bath experiments. This is an additional mechanism that may have contributed to the non-existence of sharp changes in temperature within the full-scale room.

6.2.4.2 Non-symmetry of the internal stratification and thermal radiative transfer

For the experiments with the 225.0W plate heater and the 368.0W boiler ring heater configurations in particular, it was apparent that the distribution of temperature within the space was not symmetrical. The lack of symmetry was manifested mainly at the lowest level of the test-room, within 0.3m of the floor, and to a lesser extent at the highest level, within say 0.4m of the ceiling. For the remainder of the space, however, the temperature field was approximately symmetrical (Howell and Potts, 2002). The non-symmetry was due to a difference in the temperature of the fluid entering the space at the low-level openings: the air entering through the opening at the *A*-end of the enclosure was usually cooler than that entering at the *B*-end. Correspondingly, the temperature of the air close to the ceiling at the *A*-end of the enclosure was noticeably cooler than that just below the ceiling at the *B*-end of the enclosure. It is thought that this effect may be due to radiative thermal transfer from the surface of the ceiling to the surface of the floor since the non-symmetry is limited to the layers of air close to the ceiling and the floor.

Furthermore, if the transfer of thermal energy from the surface of the ceiling to the surface of the floor by radiation was significant then a thermal equilibrium would have been established where there would be an associated transfer of thermal energy to the ceiling from the layer of warm buoyant air directly below, and an associated transfer of thermal energy from the surface of the floor to the layer of incoming air above, as illustrated in Figure 6.8. As a consequence, the surface of the floor would have been warmer than the layer of incoming ambient air directly above, and the surface of the ceiling would have been cooler than the layer of warm buoyant air

directly below, so that the maximum temperature T_{max} would have occurred at some height $y_{T\text{-max}}$ below the ceiling.

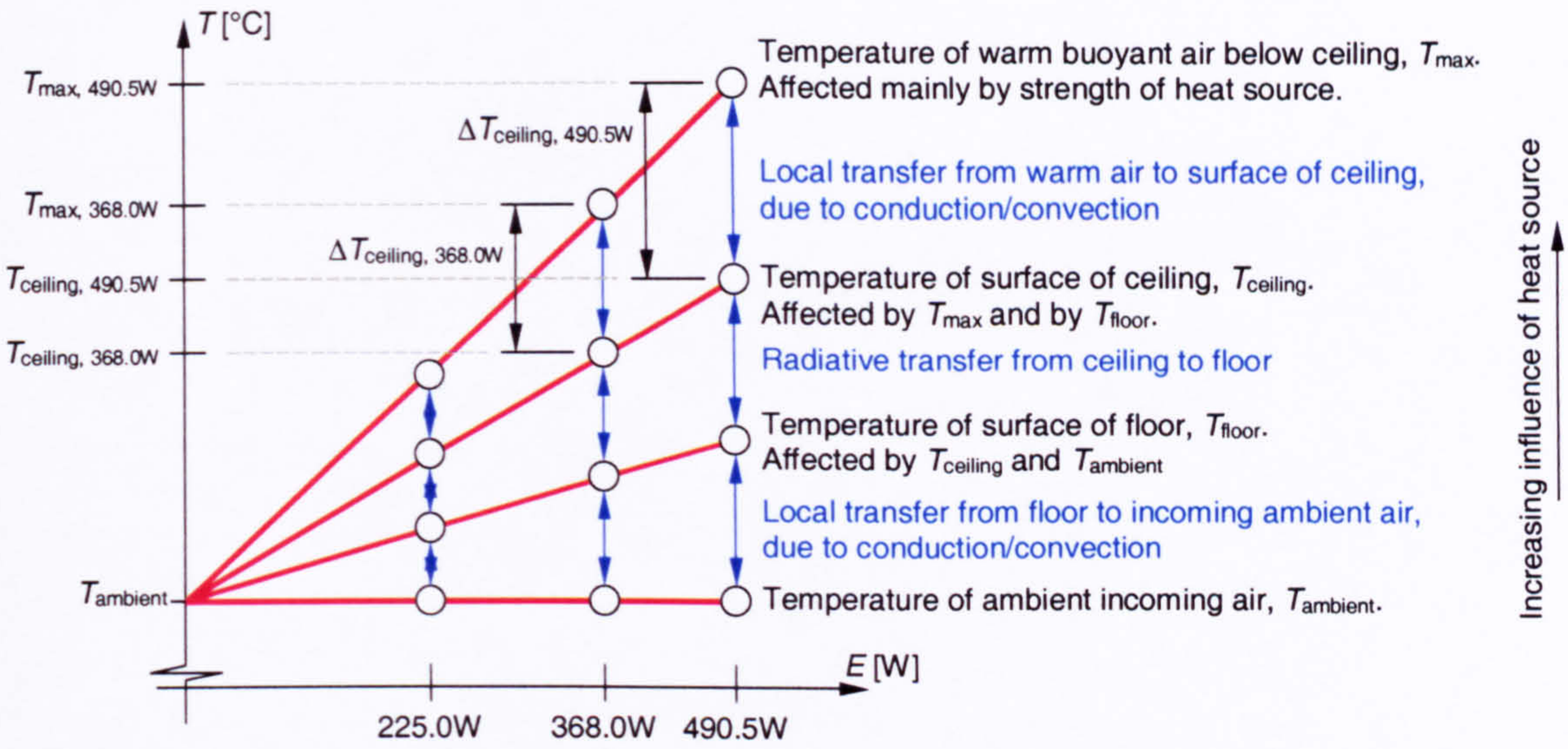

Figure 6.8 - Thermal equilibrium within the space required for significant thermal radiative transfer between the surfaces of the floor and ceiling.

In order of decreasing influence, the strength of the heat source would have had the most significant influence upon the temperature of the warm layer of air below the ceiling, followed by the temperature of the surface of the ceiling, and then the temperature of the floor surface. The magnitude of the temperature difference between the layer of warm air below the ceiling and the surface of the ceiling would, therefore, have increased with the strength of the heat source

$$\Delta T_{ceiling,\ 490.5W} > \Delta T_{ceiling,\ 368.0W} > \Delta T_{ceiling,\ 225.0W}. \qquad (6.2.11)$$

Although the surface temperatures of the ceiling and of the floor were not recorded, it is thought that the thermal equilibrium described with thermal radiative transfer from the ceiling to the floor is consistent with the temperatures recorded at the two highest thermometer locations upon the mast for the experiments with the boiler ring as the heat source, where the highest thermometer was only 40mm below the surface of the ceiling (Figure 6.9). With the boiler ring output set to 368.0W the temperature recorded at the highest thermometer was approximately equal to that measured at the second highest thermometer (Figure 6.2), so that the highest thermometer may have been above $y_{T\text{-max}}$. With the boiler ring output set to 490.5W the temperature recorded at the highest thermometer was generally lower than that measured at the second highest thermometer (Figure 6.4), so that the highest thermometer was above $y_{T\text{-max}}$ and, in accordance with (6.2.11), $\Delta T_{ceiling}$ was greater than for the 368.0W boiler ring.

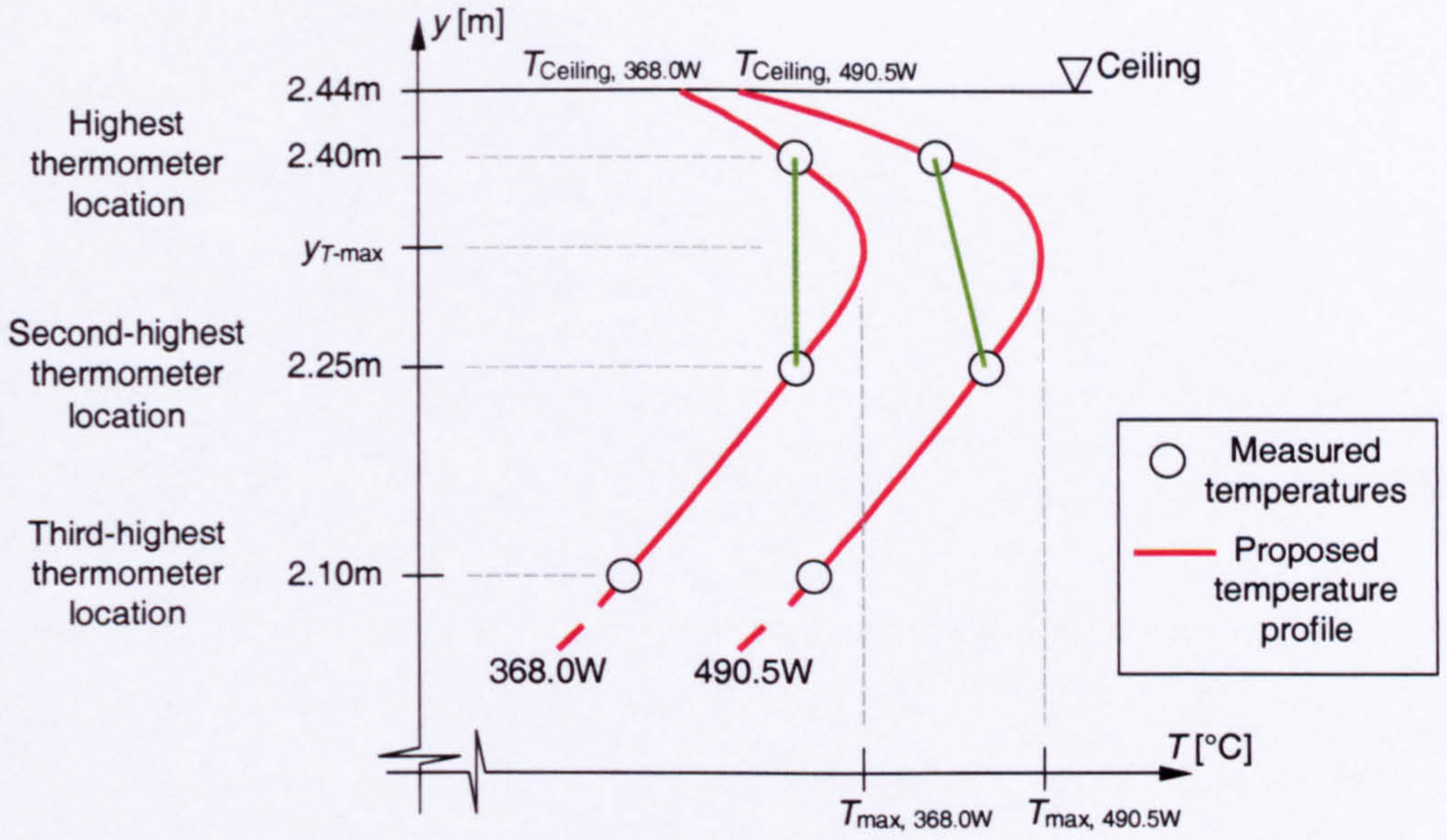

Figure 6.9 - Proposed temperature profile in the region below the ceiling

For the experiments with the plate heater as the heat source the heater output was only 225.0W so that the magnitude of the temperature difference between the layer of warm air below the ceiling and the surface of the ceiling was less significant than for the boiler ring experiments. In addition, the highest thermometer was located 90mm below the surface of the ceiling so that the thin cooled layer of air in contact with the ceiling was not detected.

6.3 Velocity measurements

6.3.1 Presentation of the steady-state velocity measurements

Recordings for the inward component of velocity at measuring locations forming a regular grid at the *A*-end low-level opening of the enclosure were taken for experimental studies with the boiler ring as the source of buoyancy, and are presented in Addendum Two. For each experimental study, the data is presented as two plots: the inward velocity component against *y*-coordinate (vertical position) and *z*-coordinate (horizontal position), to illustrate the velocity profile in elevation and plan view respectively. To supplement the plotted data, an isopleth map of the inward component of velocity at the *A*-end opening is also provided.

Although the temperature data, both internal and external, and the velocity data ideally should have been recorded during the course of the same experimental study, so that the same external environment would prevail for each set of data, this was not always practicably possible. For the studies with the heat output of the boiler ring equal to 368.0W, the temperature and velocity data were recorded separately. For the experiments with a heat output of 490.5W, and the extra studies where the heat

output was varied with the opening width maintained at 0.4m, the temperature and velocity data were indeed recorded during the same study.

It is observed from the experimental plots showing the velocity profile in elevation that, for the middle section of the opening comprising columns C to H, the inward component of velocity was generally fairly uniform over the lower three-quarters of the height of the opening, including the layer immediately adjacent to the floor. Above this region, however, the velocity tended to be lower.

For the smaller openings with an effective area A^* below say $0.4m^2$, it is observed from the plots showing the velocity profile in plan view that the inward component of velocity was roughly symmetrical and was lower at each of the sidewalls of the opening than at the central region, such that the velocity may be approximately described as parabolic. For the larger openings, however, it is observed that the profile of incoming velocity is generally more uniform across most of the inlet, although the inward velocity component tends to fall significantly in the region close to one of the sidewalls of the inlet channel. In addition, the sidewall at which this fall occurs was not always the same, but varied between experimental studies.

A summary plot for the inward component of velocity at the *A*-end low-level opening, averaged over the entire opening, against the effective area of the openings for the boiler ring with a heat output of 368.0W and 490.5W is presented in Figure 6.10. It was observed that as the effective area of the openings to the enclosure was increased, there was a gentle reduction in the inward component of velocity at the *A*-end opening when averaged over the entire area of the opening for both of the heating configurations considered. It was also apparent that when averaged over the entire opening the inward velocity was generally higher for the boiler ring with a heat output of 490.5W than with a heat output of 368.0W.

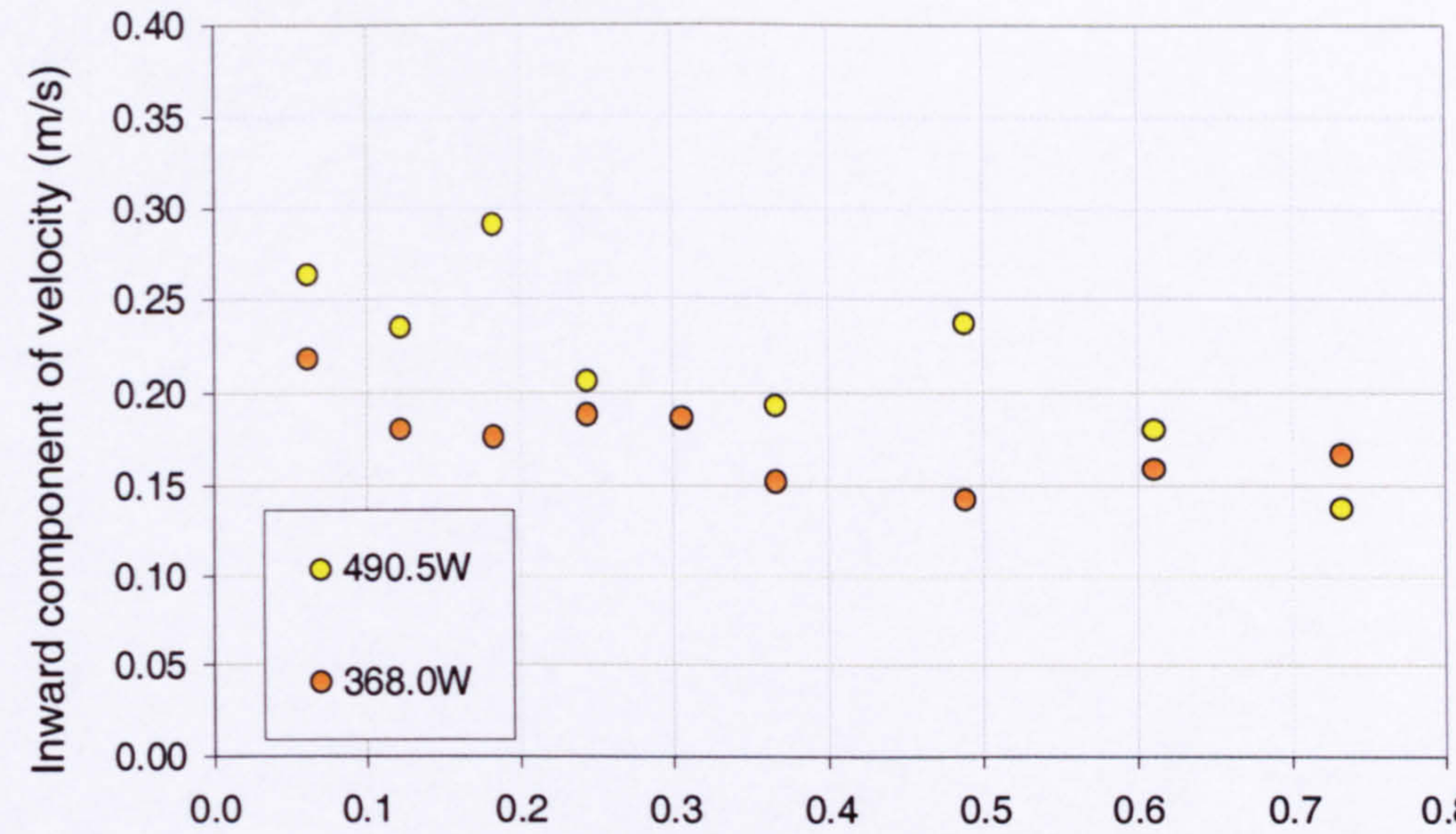

Figure 6.10 - Plot of the inward component of velocity at the *A*-end low-level opening, averaged over the entire opening, against the effective area of the openings to the enclosure *A**

A plot for the inward component of velocity at the *A*-end low-level opening, averaged over just the central portion of the opening (discarding those measuring locations in columns A, B, I and J and rows A, B, G and H), against the effective area of the openings is presented in Figure 6.11. This plot also shows that the inward velocity is generally greater for the higher heat output from the boiler ring, and shows a downward trend in the averaged inward component of velocity with increasing opening area. Generally, the inward velocity when averaged over just the central portion is approximately twenty-five percent greater than when averaged over the entire opening.

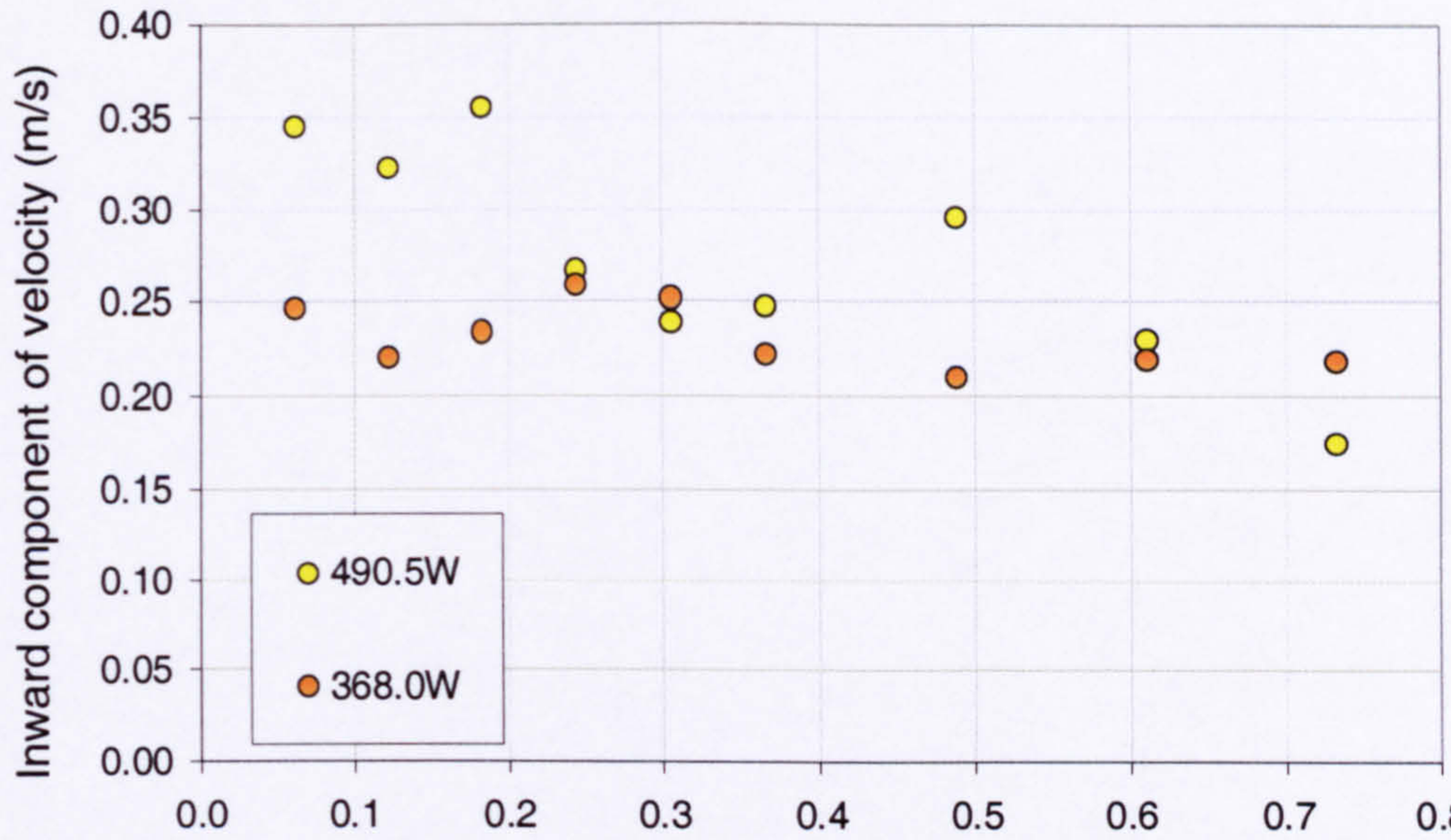

Figure 6.11 - Plot of the inward component of velocity at the *A*-end low-level opening, averaged over just the central portion of the opening, against the effective area of the openings to the enclosure A^*

For some opening configurations, most noticeably $A^* = 0.732m^2$, the velocity measured for the 368.0W heat input was unexpectedly high, so that it was greater than that measured for the corresponding 490.5W experiment. Although the external temperature profile was not recorded for the 368.0W experiments, it is thought that perhaps the external stratification was reduced during that particular experiment with a correspondingly low external piezometric pressure differential $\Delta\tilde{p}_{ext}$, and as a consequence of the theory introduced in §2.7, an increased flow rate through the enclosure was observed.

6.3.2 Discussion of velocity measurements

6.3.2.1 General form of the velocity profile at the low-level opening

Looking in plan, the profiles of the inward component of velocity for the experimental studies with an effective area A^* below $0.4m^2$ were roughly symmetrical, with lower velocities at each sidewall of the opening. The deceleration at each sidewall may have been caused entirely by viscous drag effects due to the presence of each wall. Alternatively, they may be associated with small regions of separation at each sidewall. For the smaller openings, the length of the channel aligned with the inflow in the *x*-direction for the smaller openings was of the same order or greater than the width of the opening, so that the incoming flow at the inlet plane on which the velocity recordings were taken would necessarily have been approximately parallel to

the walls of the inlet channel, and any regions of separation and recirculation of air along the sidewalls of the inlet would have been small and symmetrical. In addition, the horizontal cross-stream component of fluctuating velocity for the smaller openings would have been dampened by the presence of the sidewalls, so that the profile of inward velocity was not observed to be uniform for the smaller openings.

For larger openings, however, the length of the channel in the *x*-direction at the inlet was less than the width of the opening, so that the likelihood of significant separation of flow at the edges of the inlet would have increased, especially for the largest openings. In addition, the flow of air approaching the inlet at the *A*-end of the enclosure would generally not have been perfectly symmetrical, due to the imperfect construction of the surrounding chamber, so that the separation region would have been more pronounced at one side of the inlet channel, as shown in Figure 6.12. This may be why for the experimental studies with the larger openings, the velocity profile in plan was observed to be unsymmetrical, with a low component of inward velocity at only one sidewall. In addition, the horizontal cross-stream component of fluctuating velocity at the centre of the opening would not have been dampened by the presence of the sidewalls, so that the profile of inward velocity was roughly uniform across most of the width of the opening.

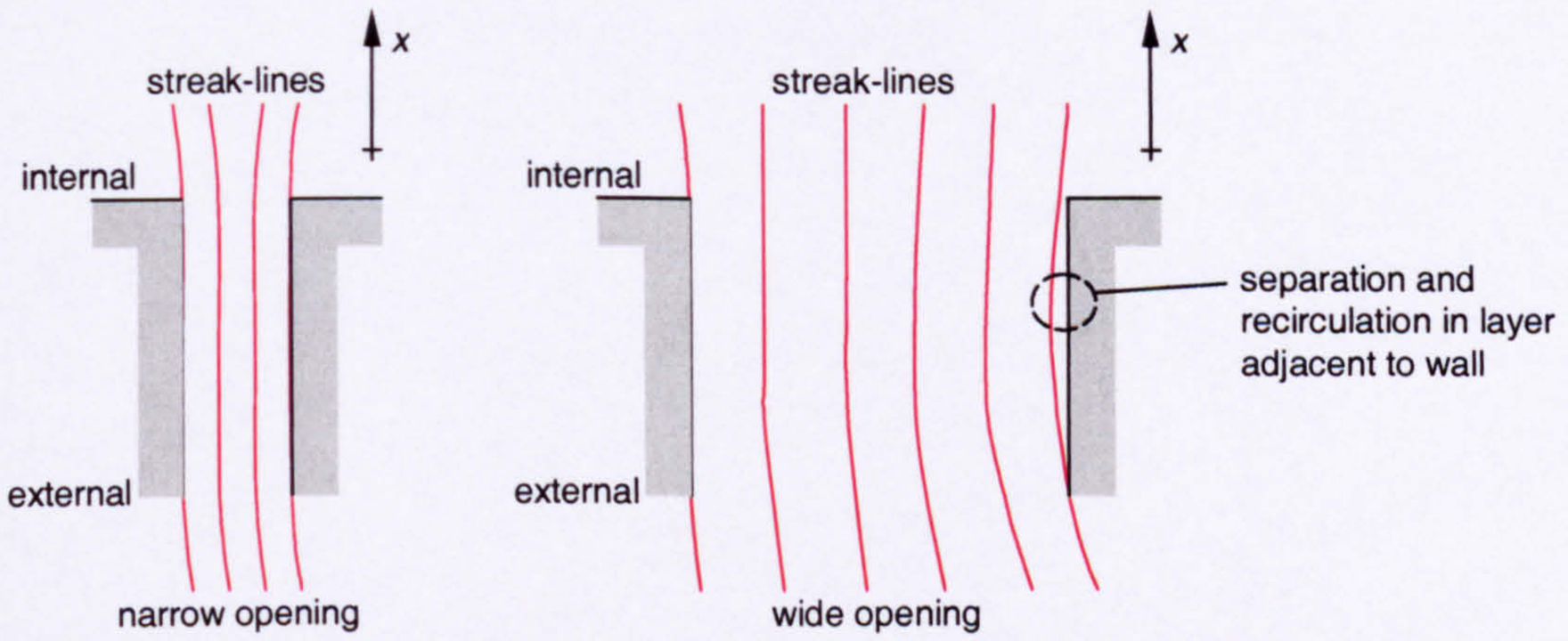

Figure 6.12 - Plan view illustration of streak-lines for a narrow and wide opening

Looking in elevation, the measured profiles show that the inward component of velocity remains approximately constant for most of the height of the opening. It is observed, however, that the magnitude of the inward velocity recorded within the top row of LDA measuring locations (row A) above a height of 0.27m was generally lower than for the rest of the space. It is thought that this is also due to a separation of the flow. The presence of the floor within the external chamber will ensure that the fluid entering the space at the lower part of the opening will flow horizontally. For the fluid entering at the upper part of the opening, however, there is no such constraint and the

flow will not necessarily flow horizontally. As a consequence, there will be a separation of the flow adjacent to the roof of the opening, as illustrated in Figure 6.13.

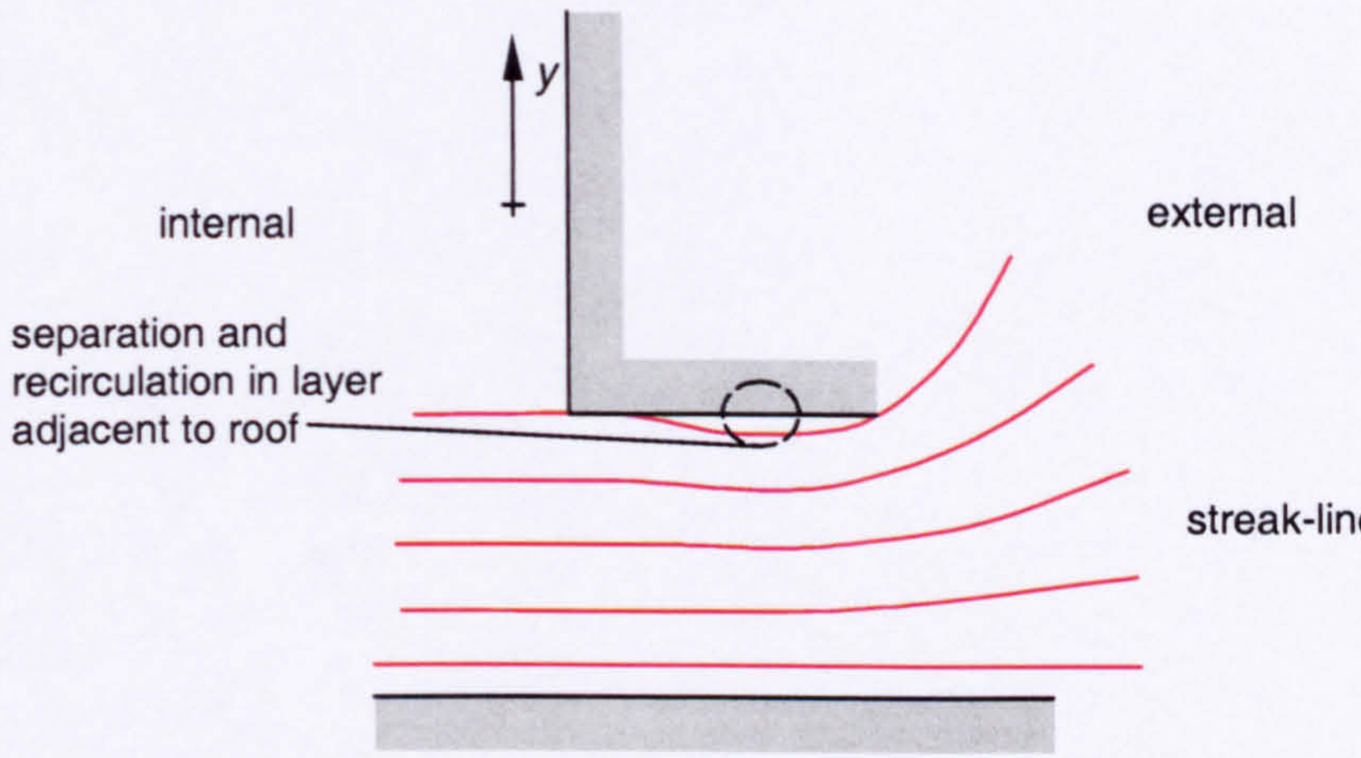

Figure 6.13 - Elevation view illustration of streak-lines through the lower opening

6.3.2.2 Comparison of the measured and calculated velocities for the 490.5W boiler ring

The calculated inward components of velocity listed in Table 6.1 are compared in Figure 6.14 with the measured inlet velocities averaged over the central section of the low-level opening for the experiments with the 490.5W boiler ring as the heat source. It was observed that there was good agreement between the calculated velocities and those that were measured during the experimental studies. The theoretical coupling between the thermal environment within and surrounding the enclosure and the flow rate through the enclosure introduced in §2.7 would, therefore, appear to be valid.

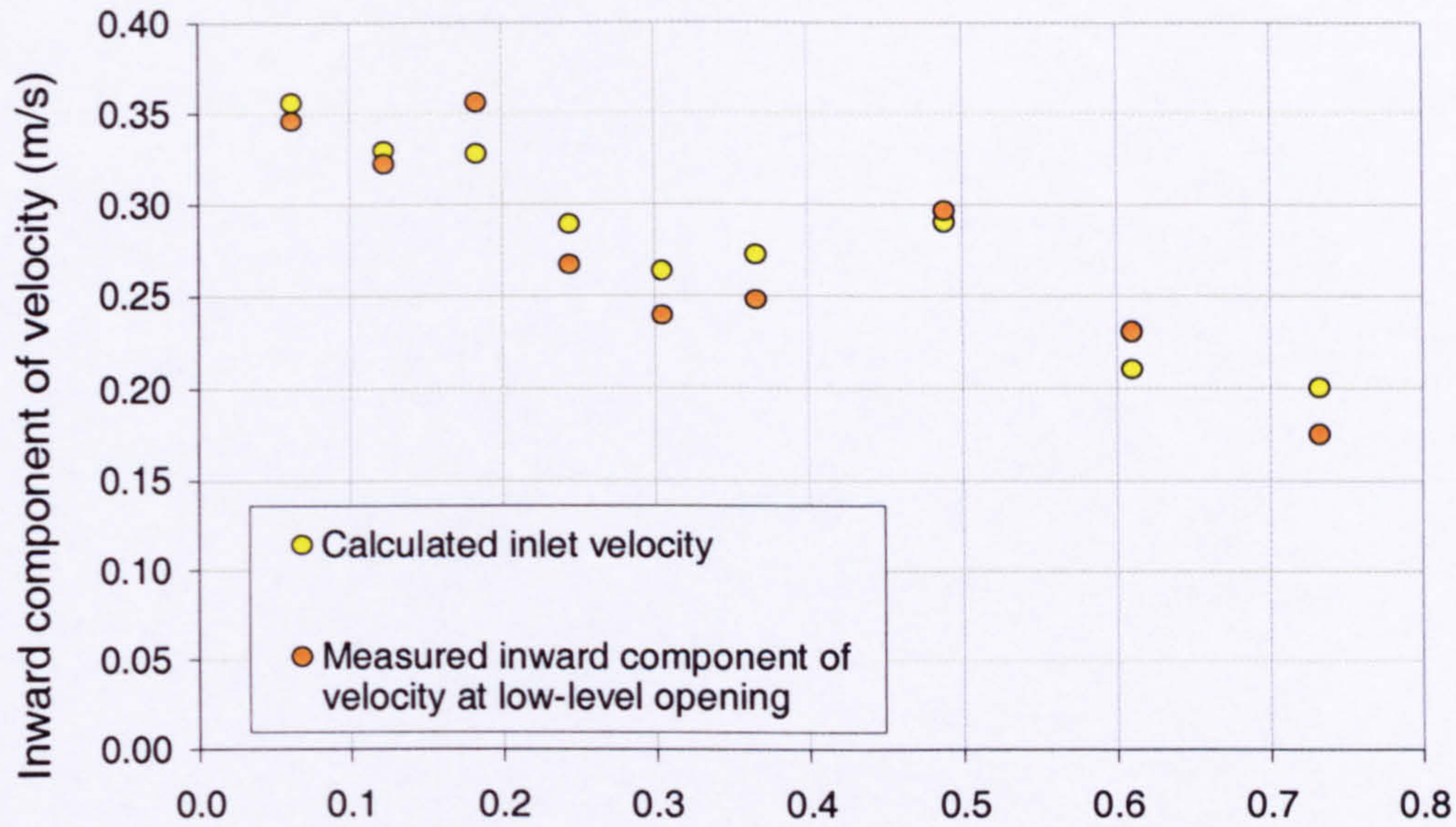

Figure 6.14 - Plot of the calculated inlet velocity and the measured inward component of velocity at the *A*-end low-level opening, averaged over just the central portion of the opening, against the effective area of the openings to the enclosure *A** for the boiler ring output set to 490.5W

6.4 Summary

From an energy balance for the experimental enclosure presented in §6.2.3, it is observed that a significant proportion of the thermal energy introduced into the space by the heat source during the experimental phase escaped from the space by conduction through the fabric of the enclosure walls. This proportion was particularly high for the smaller opening configurations considered. As the openings were increased, this proportion was reduced as the loss by convection through the openings became more significant, so that the adiabatic assumption for the walls of the enclosure becomes an increasingly realistic approximation. Although the full-scale experimental enclosure was geometrically representative of an occupied space within a real building, the chipboard construction of the enclosure walls were not necessarily representative of a real building. Nonetheless, the experimental data presented does form a valuable set of benchmark data for a naturally-driven ventilation flow with air as the fluid medium that does not suffer from geometrical scaling problems.

With regard to the temperature distribution within the experimental enclosure, it was observed that no layer of ambient air at low-level within the space was established, nor was there a sharp interface between two layers of fluid at a different temperature. This is in contrast to the stratification observed in the water-based experiments, and that predicted by the Cambridge mathematical model. This may in part be due to differences in the rate of heat transfer at the enclosure walls: for the

Cambridge mathematical model and water-based scale-model experiments the walls are effectively adiabatic, whereas for the full-scale experimental enclosure the rate of heat transfer through the walls was non-zero. It is thought, however, that a more important cause of the observed differences was the presence of additional transport mechanisms within the full-scale room: the diffusive actions of molecular diffusion and turbulent diffusion of thermal energy were more significant within the full-scale enclosure, and thermal radiative transfer including the absorption of thermal radiation due to the water vapour content of the atmosphere may also tend to smooth the temperature field with air as the fluid medium.

It was observed that for each heater arrangement investigated the internal temperature profile was well represented by a unique generic shape for that heater arrangement, regardless of the opening configuration, (Figure 6.1 for the 225.0W plate heater, Figure 6.2 for the 368.0W boiler ring and Figure 6.4 for the 490.5W boiler ring). As the effective area of the openings was increased, the magnitude of the temperature rise within the space was reduced, so that the only effect of changing the area of the openings was to translate the generic shape along the temperature axis.

For a given opening configuration, it was apparent that as the heat output was increased (with the boiler ring as the source of buoyancy), the vertical temperature gradient remained approximately constant within the lower section of the enclosure. Within the upper section of the space, however, the vertical temperature gradient increased with a corresponding rise in temperature within the enclosure at high-level (Figure 6.5).

For the experiments with the 225.0W plate heater and the 368.0W boiler ring heater configurations, it is apparent that the distribution of temperature within the space was not symmetrical, but that the lack of symmetry was limited mainly to within 0.3m of the floor and to a lesser extent within 0.4m of the ceiling. This non-symmetry adjacent to the floor is essentially due to the fact that air entering the room at inlet *A* is consistently about 0.25°C cooler than air entering at inlet *B*, due to the imperfect construction of the surrounding chamber. It is suggested that the non-symmetry in the layer below the ceiling may be caused by thermal radiative transfer from the surface of the ceiling to the surface of the floor directly below.

Furthermore, for the experiments with the boiler ring output set to 368.0W the temperature recorded at the highest thermometer was approximately equal to that measured at the second highest thermometer (Figure 6.2), and with the output set to 490.5W the temperature recorded at the highest thermometer was generally lower than that measured at the second highest thermometer (Figure 6.4), where the uppermost thermometer location was only 40mm from the surface of the ceiling. It is

thought that this may be due to thermal radiative transfer from the ceiling to the floor, cooling the surface of the ceiling so that the maximum temperature T_{max} within the layer of warm buoyant air at high-level within the space would have occurred at some height $y_{T\text{-}max}$ below the ceiling.

Good agreement is observed between the velocity calculated at the inlet and the measured inward component of velocity, averaged over the central portion of the low-level opening, for a range of opening configurations with the boiler ring output set to 490.5W. The theoretical stratification-flow rate coupling discussed in §2.7 would, therefore, appear to be valid.

7.0 CFD-predictions for the full-scale enclosure

7.1 Introduction

It was found in §6.0 that the Cambridge mathematical model and the small-scale water-based experimental methods do not compare favourably with the data collected during the experimental studies performed within the full-scale enclosure constructed as part of this work, probably due to the effective absence of the mechanisms of diffusion and thermal radiation. The application of the Cambridge mathematical model and the water-based experiments to the modelling of natural displacement ventilation flows within full-scale air enclosures was, therefore, deemed to be limited. In contrast, CFD has already proven to be successful in the prediction of some flow types found in full-scale buildings. The application of the CFD-technique to the modelling of the natural displacement ventilation flow through the full-scale enclosure is, therefore, explored and discussed in this chapter.

The greatest success with the CFD technique has been found when predicting the velocity field for isothermal forced ventilation flows within rooms. When predicting non-isothermal forced ventilation flows, it has often been found that the velocity field can be predicted with reasonable accuracy but that the rates of wall heat transfer are often over-predicted and that the temperature field is generally more difficult to accurately predict. The realistic prediction of a buoyancy-driven natural ventilation flow through a full-scale test enclosure, where the velocity field is greatly influenced by the temperature field, therefore provides a particular challenge to the CFD analyst.

Following the first experimental results in January 2001, the CFD approach was employed to predict the natural displacement ventilation flow through the full-scale test enclosure described in §5.4. Preliminary CFD-simulations were performed for the flow through the enclosure, with the 225.0W plate heater as the source of buoyancy at the centre of the floor within the enclosure. Two widths of opening were considered, 0.3m and 0.8m, corresponding to an effective area of the openings A^* equal to $0.183m^2$ and $0.484m^2$ respectively. For each width of opening, the commercial CFD-preprocessor code Gambit (version 2.0) was used to construct an unstructured computational mesh conforming to the geometry of the heat source and the test enclosure within the larger chamber. The commercial CFD-solver code

Fluent (version 5.4), which is based upon the principles outlined in §3.0, was then used to predict the ventilation flow through the enclosure.

In September 2001 a new computing resource became available which enabled a much wider and more thorough numerical analysis of the flow through the enclosure. Simulations were performed for each of the three heat source configurations considered during the experimental study of the flow through the full-scale enclosure. For each heat source configuration, the flow was predicted for nine widths of opening, ranging from 0.1m to 1.2m and including the two widths of opening previously considered. The CFD-preprocessor code Gambit (version 2.0) was again used to construct each computational mesh, together with the CFD-solver Fluent (version 5.7) for predicting the flow through the enclosure. It is this more thorough study that is presented and discussed within this work.

7.2 CFD set-up

7.2.1 Computational mesh

For each simulation, the experimental test-room was modelled as an enclosure within the larger chamber, obviating the need to apply specific boundary conditions in the region of the openings to the room. In accordance with the experimental set-up, the datum point ($x = y = z = 0.0$) for the simulations was taken to be at the centre of the floor within the enclosure.

Although the test enclosure was not positioned symmetrically at the centre of the larger chamber, all of the other aspects of the geometry of the flow were symmetrical about the two axes of the enclosure. Only one-quarter of the physical domain, therefore, was modelled, with planes of symmetry defined along the *x*-y and *z*-y planes of the test-room, as shown in Figure 7.1.

Each computational mesh comprised approximately 70,000 cells. The edge length for each mesh in the vicinity of the openings and heat source, within the space generally and outside the space were 0.02m, 0.1m and 0.3m respectively. The computational mesh for the test enclosure was unstructured to allow the transition between small cells necessary within the enclosure, and larger cells in the region outside the space that is of less interest. An example computational mesh is illustrated in Figure 7.2.

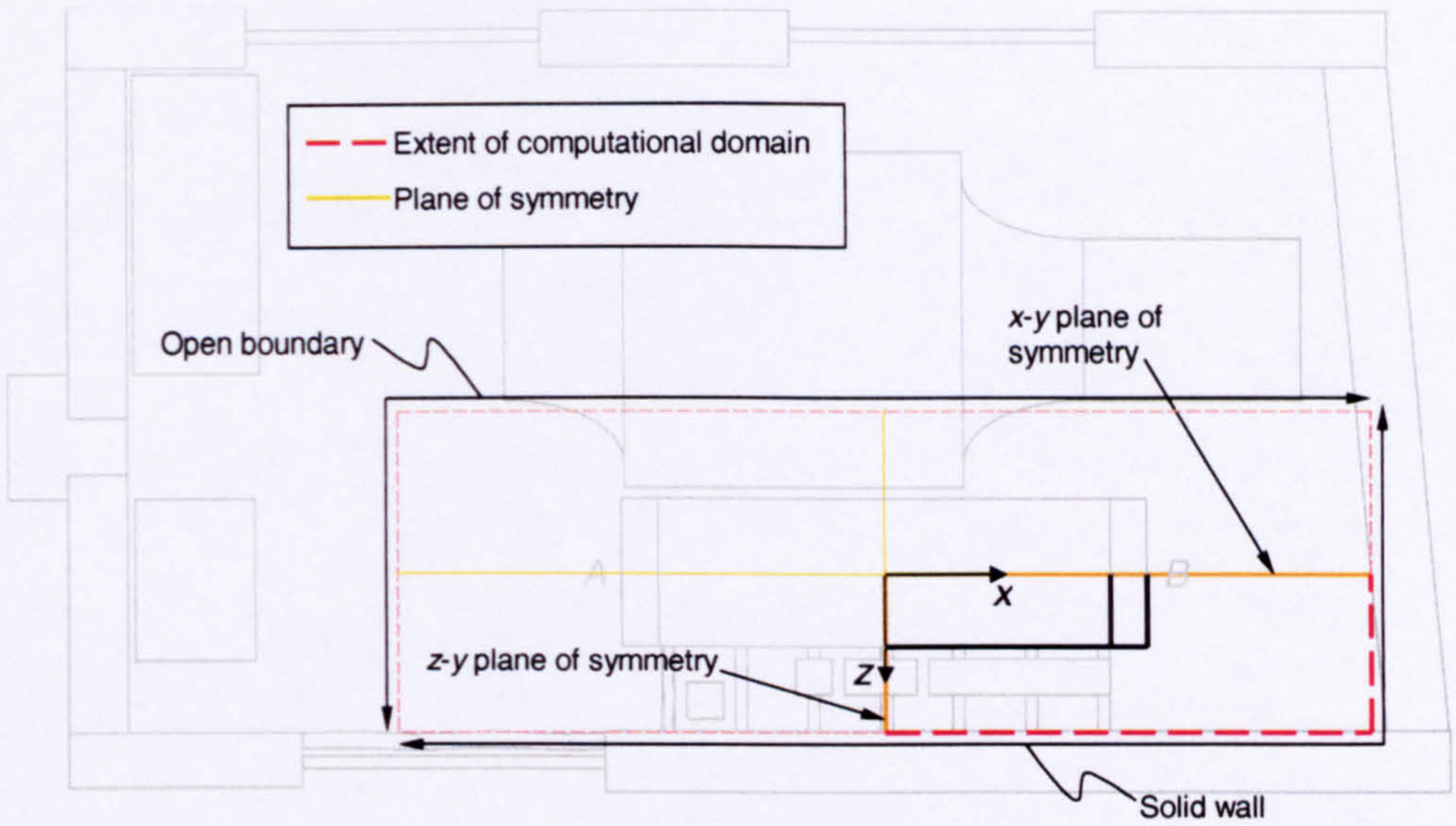

Figure 7.1 - Plan view of large chamber, showing the experimental enclosure and the extent of the computational domain

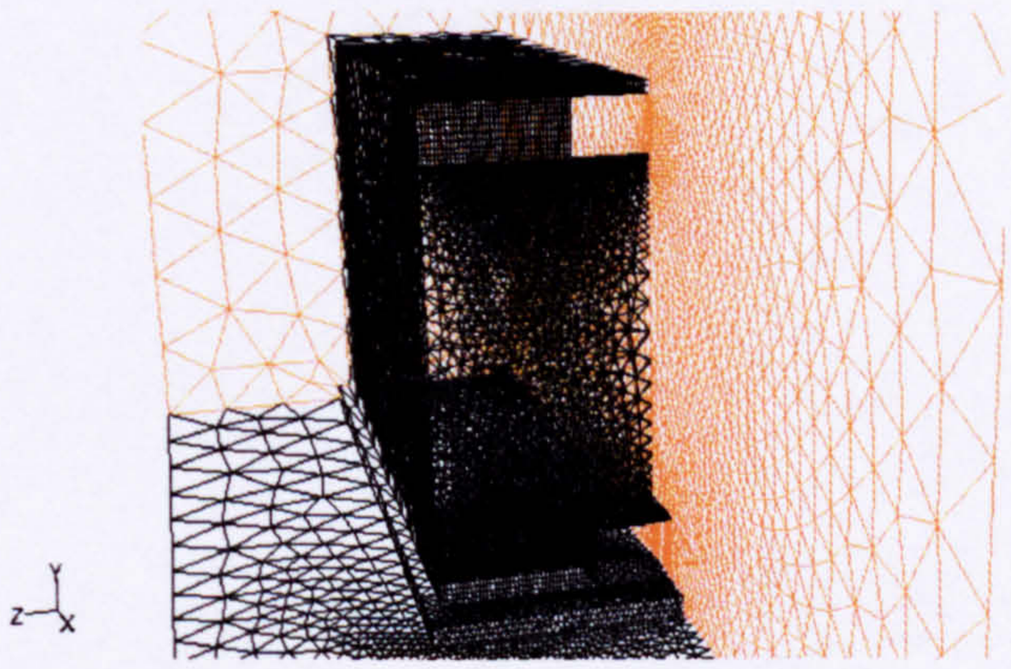

Figure 7.2 - An example of a computational mesh employed for the CFD-analysis

7.2.2 Physical models

7.2.2.1 Modelling the basic fluid flow

The finite-volume discretization of the Navier-Stokes equations was solved using the Fluent code, version 5.7. Since the ventilation flow was non-isothermal, the transport equation for the conservation of energy was also solved. The SIMPLE algorithm of Patankar and Spalding (1972, §3.4.1) was employed to calculate the pressure field. The algebraic multi-grid approach of Hutchinson and Raithby (1986) was used to solve each of the transport equations.

The fluid medium modelled was air, which was described by the incompressible-ideal-gas option within the Fluent code. For this option a constant operating pressure is assumed, so that all variations in the fluid density field are

entirely due to variations in the temperature field. The properties of air that were assumed for this work are presented in Table 7.1.

Molecular weight, M_r	28.96 kg kmol^{-1}
Viscosity, μ	1.71x10^{-5} kg m^{-1} s^{-1}
Thermal conductivity, k	2.0x10^{-2} J K^{-1} m^{-1} s^{-1}
Specific heat, c_p	1005 J kg^{-1} K^{-1}

Table 7.1 - Properties of air assumed for this work

The operating temperature T_{op} and pressure p_{op} were specified as 15°C and 101.32kPa respectively. The acceleration due to gravity **g** was defined as 9.81m/s in the negative *y*-direction.

7.2.2.2 Modelling turbulence

In addition to solving the governing fluid flow equations in laminar form, a number of turbulence modelling options implemented within the Fluent code were used, including the standard-$k\varepsilon$ model, the realizable-$k\varepsilon$ model and the RNG-$k\varepsilon$ (renormalization group) model. Since there is no clear consensus as to which is the preferred manner of modelling turbulence within full-scale enclosures, the laminar flow option and the three -$k\varepsilon$ closures were each used to predict the flow through the full-scale enclosure, in order to investigate the variation in the flow predictions due to the turbulence modelling approach adopted.

7.2.2.3 Modelling thermal radiation effects

Since a number of workers have recently suggested that thermal radiation effects may be important when predicting air flows in buildings, they were investigated as part of this work. Implemented within the Fluent code were a selection of radiation models, including the finite-volume approach introduced in §3.6.2. For each combination of heat source, opening width and turbulence model, five different thermal radiation model configurations were analysed: one simulation was performed without the radiation model enabled, another was performed with the radiation model enabled but with the absorption of thermal radiation within the fluid medium due to the water vapour content of air neglected, and a further three simulations were performed with the radiation model enabled for an absorption coefficient of 0.05m^{-1}, 0.10m^{-1} and 0.15m^{-1} respectively. Such a thorough study would allow the sensitivity of the predictions of the full-scale natural displacement ventilation flow with respect to

thermal radiative transfer and the absorption coefficient of the fluid medium to be investigated.

With regard to the directional discretization adopted, each octant was divided into 2×2 control directions. A total of 32 directions were therefore defined, each with an extra corresponding transport equation to solve for the radiative intensity in that direction.

7.2.3 Boundary conditions

The boundary conditions for the flow can be grouped into four categories: the heated element of the heat source, the remaining solid surfaces of the heater casing, the solid walls of the enclosure, and the external extents of the computational domain.

7.2.3.1 Heat source and remaining surfaces of the heater casing

The heated surface of the heat source was represented as a wall boundary condition with a constant positive heat flux, which was specified to match that of the heat source under consideration. For the 225.0W plate heater, the heated element of which measured 0.4m × 0.2m, the heat flux was specified as 2.81kW/m^2. For the boiler ring, the heated element of which measured 0.18m in diameter, a heat flux of 14.5kW/m^2 and 19.3kW/m^2 was specified for a heat output of 368.0W and 490.5W respectively. The remaining solid surfaces of the heater casing were represented by an adiabatic wall boundary condition.

7.2.3.2 Solid walls of the test enclosure

The solid walls of the test enclosure were also represented by a wall boundary condition. From the review of the existing literature it was known that one of the challenging aspects of modelling non-isothermal ventilation flows within buildings is accurately determining the magnitude of the thermal flux through the fabric of the solid wall boundaries. A number of the options implemented within the Fluent code for modelling the rate of heat transfer at the enclosure boundaries were therefore used, to investigate their effect upon the predicted ventilation flow through the space. Initially each wall was assumed to be adiabatic. As suggested in §6.2.3, this may become a reasonable approximation as the width of the openings is increased, but it is not a good assumption for the smaller opening configurations considered. In addition, with the radiation model enabled, the conduction, radiation and mixed thermal boundary conditions introduced in §3.7 were investigated in turn for a range of radiative absorption coefficient. The particular details specified at each of the wall boundaries are detailed in Table 7.2.

Wall	Parameter	Value
Long vertical wall / ceiling	Material	Chipboard
	Thermal conductivity	14.4J K^{-1} m^{-1} s^{-1}
	External emissivity	1.0
	External flow temperature	15°C
	Internal emissivity	0.8
	Thickness	0.012m
Floor	Material	Chipboard
	Thermal conductivity	14.4J K^{-1} m^{-1} s^{-1}
	External emissivity	1.0
	External flow temperature	15°C
	Internal emissivity	0.8
	Thickness	0.018m
End	Material	Polycarbonate
	Thermal conductivity	5.3J K^{-1} m^{-1} s^{-1}
	External emissivity	1.0
	External flow temperature	15°C
	Internal emissivity	0.8
	Thickness	0.002m

Table 7.2 - Details of the wall boundary conditions employed during the CFD-analysis

7.2.3.3 External extents of computational domain

The remaining surfaces, which defined the extents of the computational domain, were positioned to coincide with the solid walls of the larger chamber at the *B*-end of the test-enclosure, in that quadrant where they were closest to the enclosure. For the experimental facility, this location corresponded to a solid wall boundary for the extent of the domain in the positive *x*- and *z*-direction, but corresponded to an open boundary in the negative *x*- and *z*-direction. There was, therefore, a choice as to which type of boundary condition to apply at the domain extents. It was found that the flow through the enclosure was not significantly affected by the nature of the boundary condition at the domain extents. For the majority of the CFD-simulations performed, a condition of constant static pressure and constant temperature was enforced at the domain extents to represent an open boundary.

For some of the larger widths of opening, an alternative boundary condition was also considered at the domain extents, so that some representation of the external temperature profile measured during the experimental phase of this work could be incorporated into the flow simulations. In particular, the temperature profile defined by

(6.2.3) was enforced at the domain extents, which were necessarily changed to a solid wall boundary condition in order to maintain numerical stability.

7.2.4 Solution strategy

A common strategy was followed during the CFD-prediction phase, which is shown schematically in Figure 7.3. Initially for each area of opening and each heat source configuration, the flow was first solved using first-order upwind differencing for convective terms in the governing equations, as this is the simplest and most robust differencing scheme. It was solved without the use of a turbulence model or the radiation model, with the assumption of adiabatic walls and a uniform temperature enforced at the domain extents. Each of the three turbulence models were then enabled in turn and their effect upon the prediction of the flow investigated. Next, the radiation model was enabled with the absorption of radiation by the fluid medium neglected and the flow again solved. For each of the eight initial cases, the convective differencing scheme was improved to the third-order QUICK differencing scheme (Leonard, 1979) in order to reduce the effects of numerical diffusion that may be significant for a flow solved on an unstructured mesh. The effects of the absorption coefficient for the fluid were then investigated upon the flow for the three values considered. Two other parameters were then considered. Firstly, the alternative methods for predicting the wall heat flux were investigated, and secondly, for the opening widths of 0.8m and 1.2m only (corresponding to an effective area A^* equal to $0.488m^2$ and $0.732m^2$ respectively), the external temperature profile represented by (6.2.3) was enforced at the domain boundaries to investigate the effect of the external thermal stratification upon the flow.

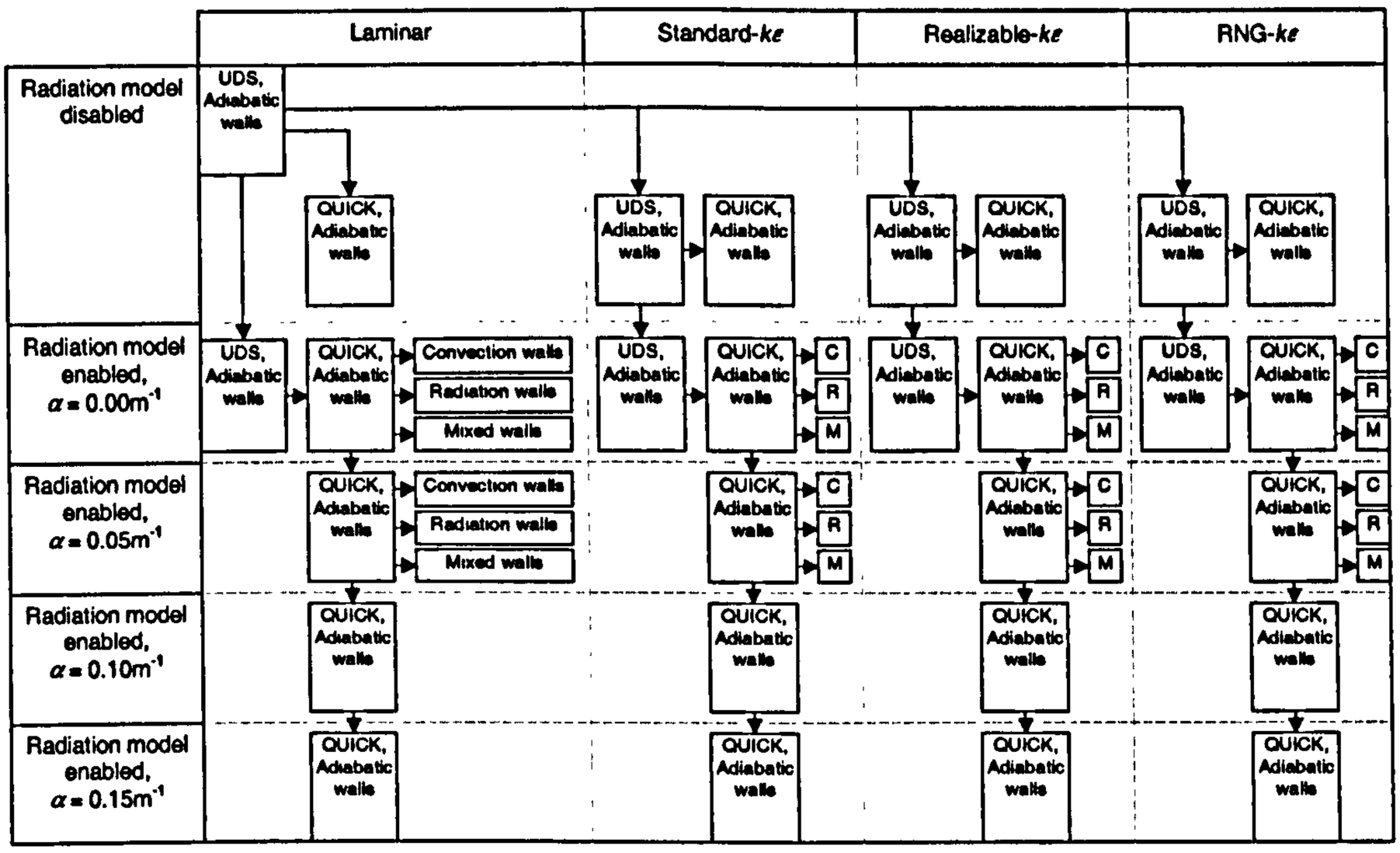

Figure 7.3 - Strategy adopted for each combination of heater and opening configuration during for CFD-prediction phase of this work

7.2.4.1 Convergence criteria

The default convergence criteria recommended by the CFD-solver were used and are listed in Table 7.3

Equation	Convergence criteria
Continuity	Sum of the mass imbalance < 10^{-3}
Momentum	Scaled sum of the residuals < 10^{-3}
Temperature	Scaled sum of the residuals < 10^{-6}
Turbulence kinetic energy	Scaled sum of the residuals < 10^{-3}
Rate of dissipation of turbulence kinetic energy	Scaled sum of the residuals < 10^{-3}
Radiative intensity	Scaled sum of the residuals < 10^{-6}

Table 7.3 - Convergence criteria used during the CFD-analysis

7.2.4.2 Under-relaxation

The under-relaxation factors used during the CFD-study are listed in Table 7.4

Equation	Under-relaxation factor α
Continuity	0.8
Momentum	0.1
Temperature	1.0
Turbulence kinetic energy	0.4
Rate of dissipation of turbulence kinetic energy	0.4
Radiative intensity	1.0

Table 7.4 - Under-relaxation factors used during the CFD-analysis

7.3 CFD-predictions for the temperature field

The vertical profile of the temperature rise above that predicted at the reference thermometer location for each of the CFD-simulations performed, together with the corresponding measured profile from the experimental program are presented graphically in Addendum 3. The profiles represent the internal temperature computed on the *xy*-plane of symmetry in the space away from the thermal plume rising above the heat source, in the range $0.75\text{m} \leq x \leq 3.0\text{m}$.

For a given opening width and heat source, it is observed that the CFD-profiles for the internal temperature may vary significantly, depending upon which combination of physical models were selected to describe the fluid flow. A detailed discussion into the effect of the turbulence model, radiation model and wall heat transfer model for each heat source considered is presented below, with guidance as to which combination of modelling techniques may be considered as the preferred CFD-approach.

7.3.1 Plate heater with an output of 225.0W for various opening configurations

For each of the CFD-simulations with the plate heater as the source of buoyancy, if the walls of the experimental enclosure were modelled as adiabatic it was observed that for the smallest opening configuration considered the temperature rise within the space was greatly over-predicted, regardless of which turbulence or radiation modelling approach was employed. For example, with the width of the opening equal to 0.1m, most of the CFD-results predict that the temperature in the layer of air below

the ceiling within the space would be of the order of 5°C above that at the reference location in the low-level opening, whereas the measured temperature rise was only 2°C (Figure 1, Addendum 3).

As the width of the openings was increased, then the agreement between the predicted temperature rise below the ceiling and that that had been measured during the experimental program was much improved. This is to be expected. It was demonstrated in §6.2.3 that for the smaller openings considered, a high proportion of thermal energy introduced into the space by the heater escaped from the space by conduction through the fabric of the enclosure walls. As the openings were increased, this proportion was reduced as the loss by convection through the high-level openings became more significant. As the openings are increased, therefore, the adiabatic assumption for the walls of the enclosure becomes increasingly realistic.

When the fluid-side heat-transfer coefficient at the internal surface of the enclosure walls was determined using the law of the wall described in §3.7, the rate of heat flux was greatly over-predicted so that the temperature rise calculated within the space was less than that measured within the experimental enclosure for all opening configurations. This is not a great surprise: it was reported in §3.8 that many workers have discovered that the rate of thermal flux is over-predicted using the standard wall function method. Recall that the standard wall function approach is strictly applicable only for fully-developed flow over a flat plate, where the non-dimensional distance of the wall adjacent cell centre y^+ is greater than 11.63, and preferably in the range of 100-500. Examination of the calculated y^+ for the present simulations, however, revealed this to be only a fraction of that value over large areas of the internal surfaces of the enclosure. To increase the y^+ value at a particular wall-adjacent cell it is necessary to increase the distance of the centre of that cell from the wall boundary. In order to increase the y^+ distance to the preferred minimum value of 11.63, the wall adjacent cells for the present simulations would need to be increased to such an extent that they would fill the space within the enclosure, which is clearly not appropriate. The methods considered as part of this work to predict the rate of transfer of thermal energy at solid walls are simply inadequate to accurately predict the heat loss through the fabric of the enclosure. Instead, an alternative method for predicting the wall heat transfer is required.

Although it is imperfect, the adiabatic approximation at the enclosure walls is perhaps a reasonable assumption for the larger opening configurations. If it is adopted, it will, at least, allow a comparison of the influence of the remaining modelling parameters upon the flow, such as the turbulence and radiation modelling approaches employed. Upon that basis, the predicted profiles for the temperature rise

within the space for a width of opening of 0.8m and 1.2m, corresponding to an effective area of opening $A^* = 0.488m^2$ and $A^* = 0.732m^2$ respectively, with the adiabatic approximation in place at the walls of the enclosure are now discussed in detail.

7.3.1.1 Width of opening equal to 0.8m ($A^* = 0.488m^2$)

7.3.1.1.1 Radiation model disabled

The temperature profile predicted with a constant external temperature imposed at the extents of the domain for each turbulence modelling approach considered with the radiation model disabled is provided in Figure 7.4 below, together with the measured temperature profile. Each of the predicted profiles presented were obtained using the first-order upwind differencing scheme, as numerical convergence difficulties were experienced when the QUICK differencing scheme was employed for these four cases.

The predicted profiles within the enclosure are similar for each of the turbulence modelling approaches considered, and comprise three distinct stratified layers of air. The first layer of air is at low-level, where the temperature of the fluid is roughly constant and is equal to the ambient temperature enforced at the extents of the domain. The second layer is within the core of the space and exhibits a steep vertical gradient in the temperature rise within the space. The third layer is at high-level, where the vertical gradient in the temperature rise is still apparent but the magnitude of which is much reduced.

For the laminar, realizable-$k\varepsilon$ and RNG-$k\varepsilon$ profiles, the depth of the low-level ambient layer of air is approximately 1.0m, above which the middle layer of air extends to a height of roughly 1.7m. For the standard-$k\varepsilon$ profile the low-level layer of fluid is not so deep, and extends to a height of say 0.8m, with the layer above extending to a height of about 1.5m.

For each of the four profiles, the vertical temperature gradient within the middle layer of fluid is approximately equal to 2.5°C/m. Within the upper-layer of fluid, the vertical temperature gradient is roughly 1.0°C/m for the laminar, realizable-$k\varepsilon$ and RNG-$k\varepsilon$ profiles, and is about 0.7°C/m for the standard-$k\varepsilon$ profile.

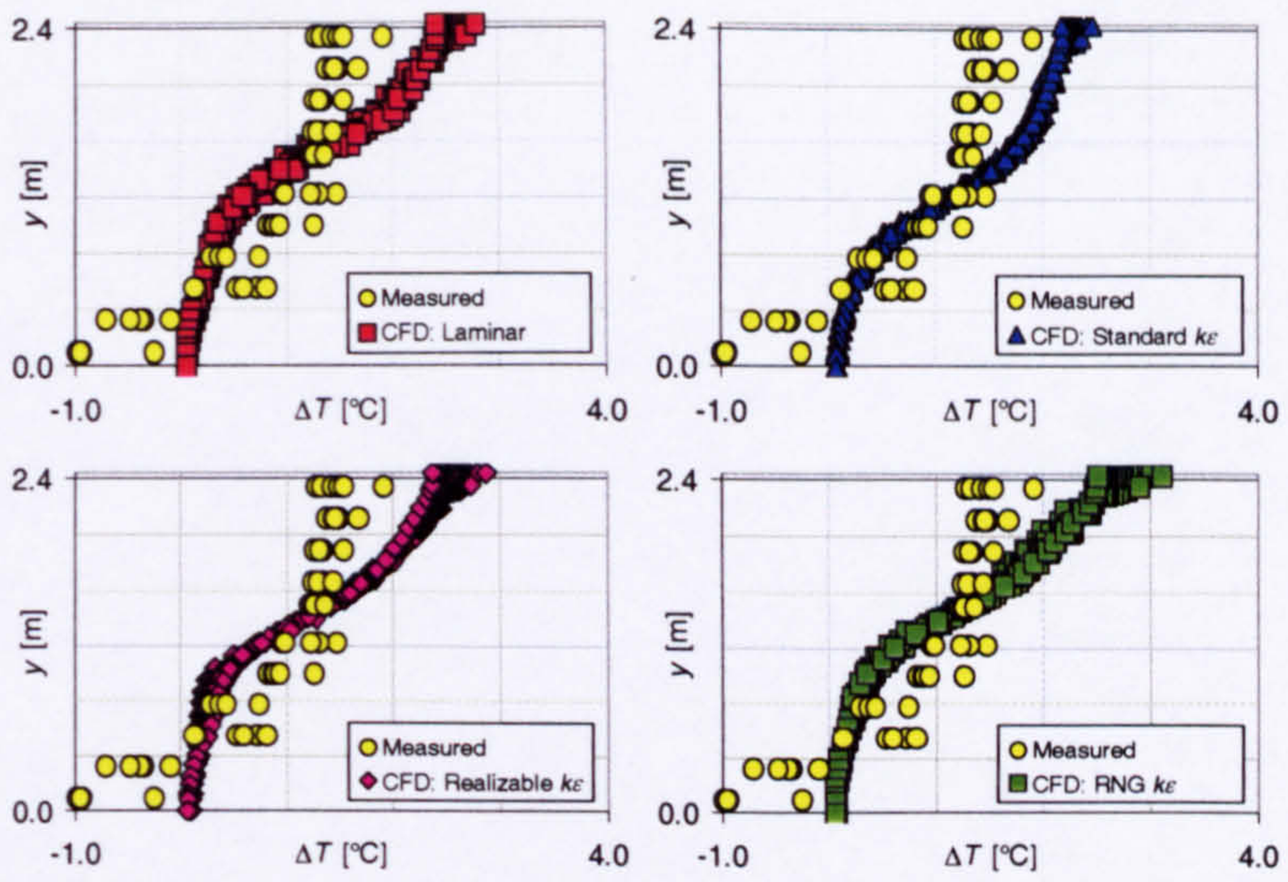

Figure 7.4 - Internal temperature profiles: 225.0W plate heater; $A^* = 0.488m^2$; radiation model disabled; uniform external temperature enforced at the domain extents; first-order upwind differencing employed for convection terms

The temperature profile predicted with the measured external temperature imposed at the extents of the domain for each turbulence modelling approach considered is provided in Figure 7.5 below, together with the measured temperature profile.

With the external temperature stratification in place, it is observed that the difference in the vertical temperature gradient for the middle layer and that for the upper layer is more apparent: there is a more distinct change between the middle layer and the upper layer. It is also observed that the magnitude of the temperature rise predicted within the space above that computed at the reference thermometer location is almost 1.0°C lower than for the corresponding predictions with a uniform temperature enforced at the domain extents.

With the measured external temperature profile in place a noticeable vertical temperature gradient within each low-level opening is predicted. As a consequence, the temperature predicted at the reference thermometer location, as that measured during the experimental work, is not necessarily representative of the average temperature of the fluid entering the space. The magnitude of the temperature rise within the space, however, will fall when compared to that predicted with a uniform external temperature field. Indeed, within the lower part of the space there may even be a drop in the temperature compared to the calculated reference temperature, due to the cooler air entering the space immediately adjacent to the floor.

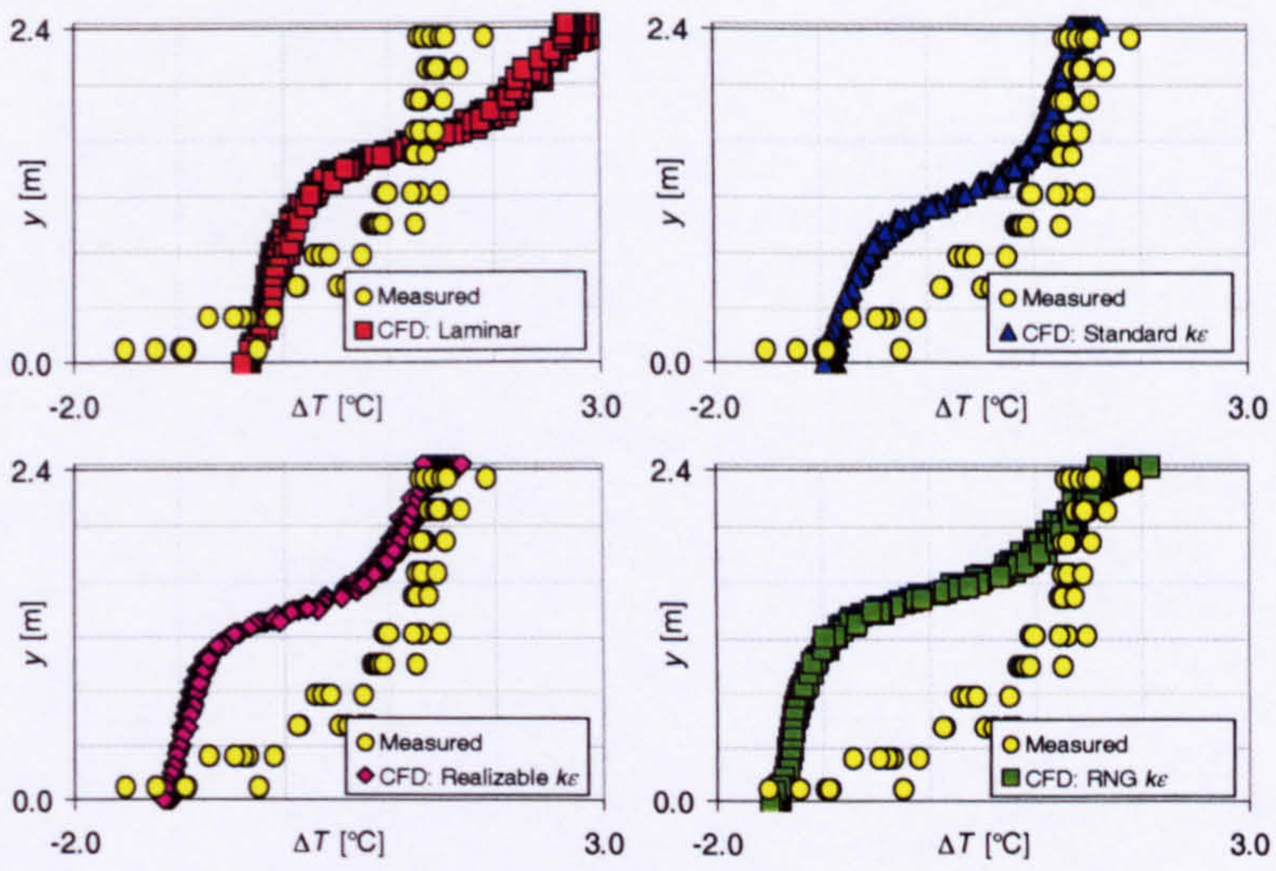

Figure 7.5 - Internal temperature profiles: 225.0W plate heater; $A^* = 0.488m^2$; radiation model disabled; measured external temperature profile enforced at the domain extents; first-order upwind differencing employed for convection terms

Regardless of which external temperature boundary condition was adopted, one might suggest that the predicted profiles are representative of two layers of air: one layer of ambient air at low-level within the space and a layer of buoyant air at high-level, separated by a thin interface region where the vertical temperature gradient is a maximum. This is, of course, the description of the flow assumed by the Cambridge mathematical model for natural displacement ventilation flows presented in §4.0, which was confirmed experimentally by others employing both the salt-bath technique and the gas bubble technique. This is not, however, in good agreement with the measured temperature profile from the experimental program performed as part of this work.

7.3.1.1.2 Radiation model enabled, absorption of radiation throughout the fluid medium neglected ($\kappa = 0.0m^{-1}$)

The temperature profiles predicted with a constant external temperature imposed at the extents of the domain and with the radiation model enabled but neglecting absorption of radiation within the fluid medium for this opening configuration is presented in Figure 7.6 below, together with the measured temperature. The profiles were predicted using the third-order QUICK differencing scheme.

The predicted profiles with the radiation model enabled are much improved. Each profile exhibits a relatively steep vertical temperature gradient, approximately equal to 2.5°C/m in the layer of fluid immediately next to the floor, which becomes less steep within the central core of the space, of the order of 0.6°C/m. This change in the predicted vertical temperature gradient occurs at a height of about 0.5m, which is lower than for the measured profile.

The predicted profiles show a significant increase in the rate of change of the rise in temperature with respect to height in the layer immediately below the ceiling within the space, where the gradient is roughly 2.0°C/m. This is not in agreement with the measured profile where the rise in temperature above that at the reference thermometer location was observed to be approximately constant in this region. Furthermore, it is observed that the magnitude of the rise in temperature above the reference temperature for the computed profiles is over-predicted by about 0.5°C to 1.0°C when compared to the measured profile.

It is noted also that the predicted surface temperature of the floor is significantly higher than the air immediately adjacent to it, due to direct radiative transfer from the relatively warm ceiling. Whether the temperature of the surface of the floor of the enclosure was indeed above that of the incoming air flowing over it remains unknown, since the surface temperature distribution over the floor was not a parameter that was recorded during the experimental phase of this work.

It should be noted that although the high surface temperature of the floor at $y = 0.0$m may appear to be discontinuous from the rest of the profile, this is only because the predicted temperatures throughout the fluid domain are presented only at discrete locations defined by the nodes forming part of the computational mesh. The profile should be interpreted as though it is continuous from the fluid region directly towards the surface of the floor, so that there will be a sharp increase in the temperature of the fluid very close to the wall, within the zone between the floor and the floor-adjacent node.

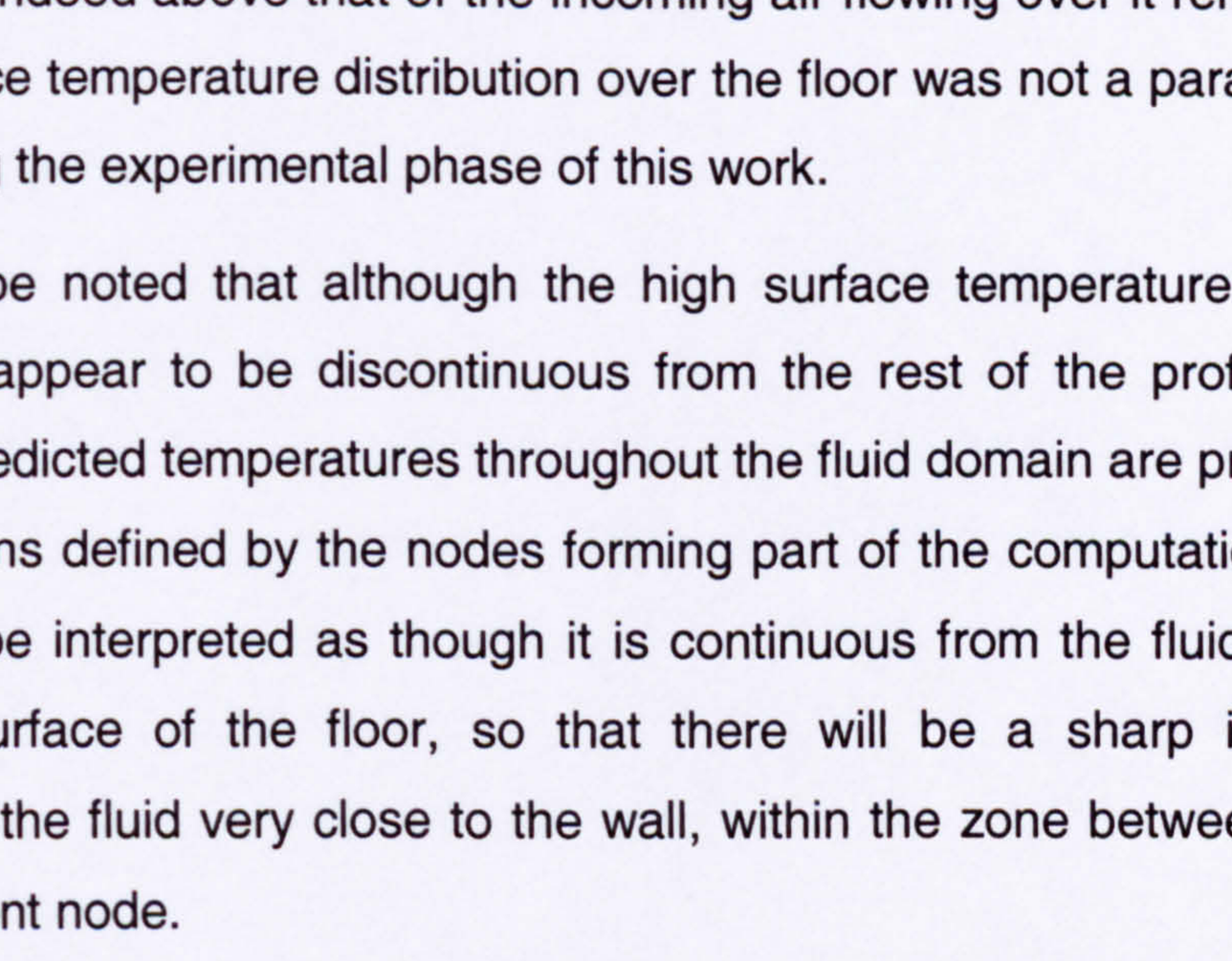

Figure 7.6 - Internal temperature profiles: 225.0W plate heater; $A^* = 0.488\text{m}^2$; radiation model enabled, $\kappa = 0.0\text{m}^{-1}$; uniform external temperature at the domain extents; QUICK differencing employed for convection terms

The temperature profile predicted with the measured external temperature imposed at the extents of the domain for each turbulence modelling approach considered is provided in Figure 7.7 below, together with the measured temperature profile.

The shape of each of the profiles remains unaffected by the incorporation of the measured external stratification at the domain boundaries: each profile still has a region within 0.5m of the floor where the vertical temperature gradient is of the order of 2.5°C/m, which drops to 0.6°C/m within the central core of the space and then increases once more to 2.0°C/m in the region immediately below the ceiling. With the external temperature stratification in place, however, it is observed that the magnitude of the rise in temperature above the reference temperature for the computed profiles is now under-predicted by about 1.0°C when compared to the measured profile.

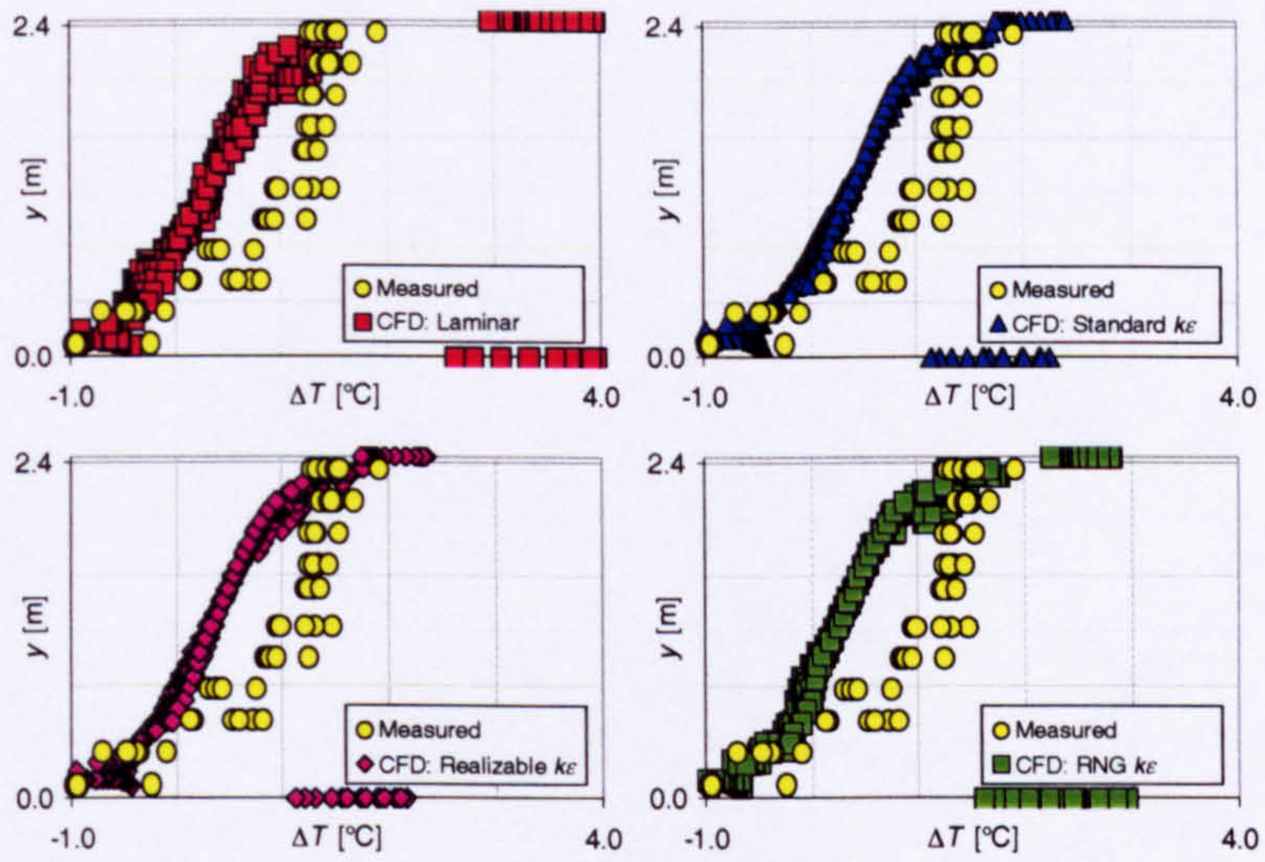

Figure 7.7 - Internal temperature profiles: 225.0W plate heater; $A^* = 0.488m^2$; radiation model enabled, $\kappa = 0.0m^{-1}$; measured external temperature profile enforced at the domain extents; QUICK differencing employed for convection terms

7.3.1.1.3 Radiation model enabled, absorption of radiation throughout the fluid medium included ($\kappa \neq 0.0m^{-1}$)

For this opening configuration, the internal temperature profiles predicted with a constant external temperature imposed at the extents of the domain and with the radiation model enabled for each non-zero absorption coefficient considered ($\kappa = 0.05m^{-1}$, $\kappa = 0.05m^{-1}$ and $\kappa = 0.15m^{-1}$) are presented in Figure 7.8, Figure 7.9 and Figure 7.10 below, together with the measured temperature.

With a non-zero absorption coefficient, each profile remains almost unchanged in terms of the shape of the profile and the magnitude of the temperature rise within the region between the floor and a height of 2.0m, when compared to the corresponding

profile predicted with the absorption coefficient equal to zero. An improvement, however, is observed within the layer of fluid immediately below the ceiling.

Although the profiles with an absorption coefficient $\kappa = 0.05\text{m}^{-1}$ still predict an increase in the vertical temperature gradient in the layer immediately below the ceiling, which is not in agreement with the measured profile, this increase is less significant than for the cases where radiative absorption was neglected throughout the fluid medium. For the absorption coefficient $\kappa = 0.10\text{m}^{-1}$ and $\kappa = 0.15\text{m}^{-1}$, the profiles no longer show a significant increase in the vertical temperature gradient in the layer below the ceiling, which is in agreement with the measured profile.

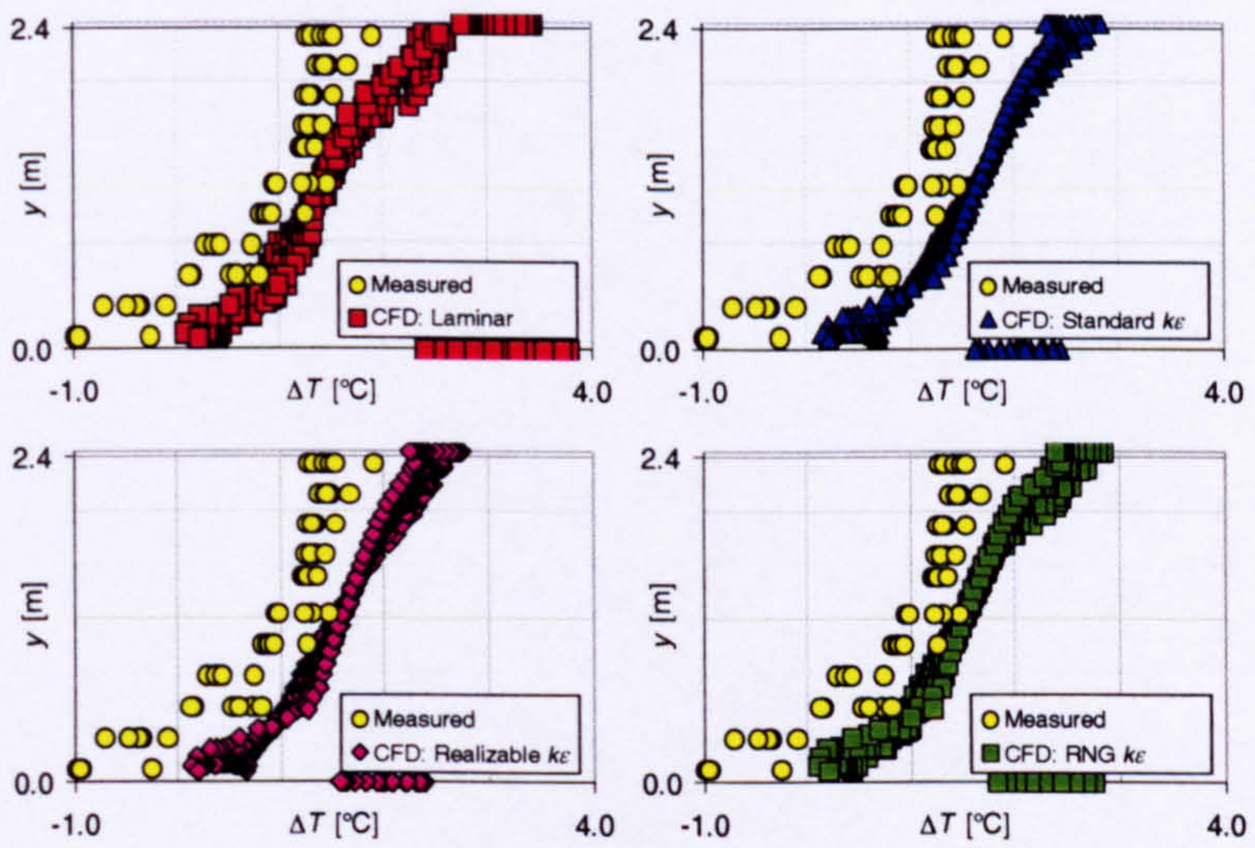

Figure 7.8 - Internal temperature profiles: 225.0W plate heater; $A^* = 0.488\text{m}^2$; radiation model enabled, $\kappa = 0.05\text{m}^{-1}$; uniform external temperature at the domain extents; QUICK differencing employed for convection terms

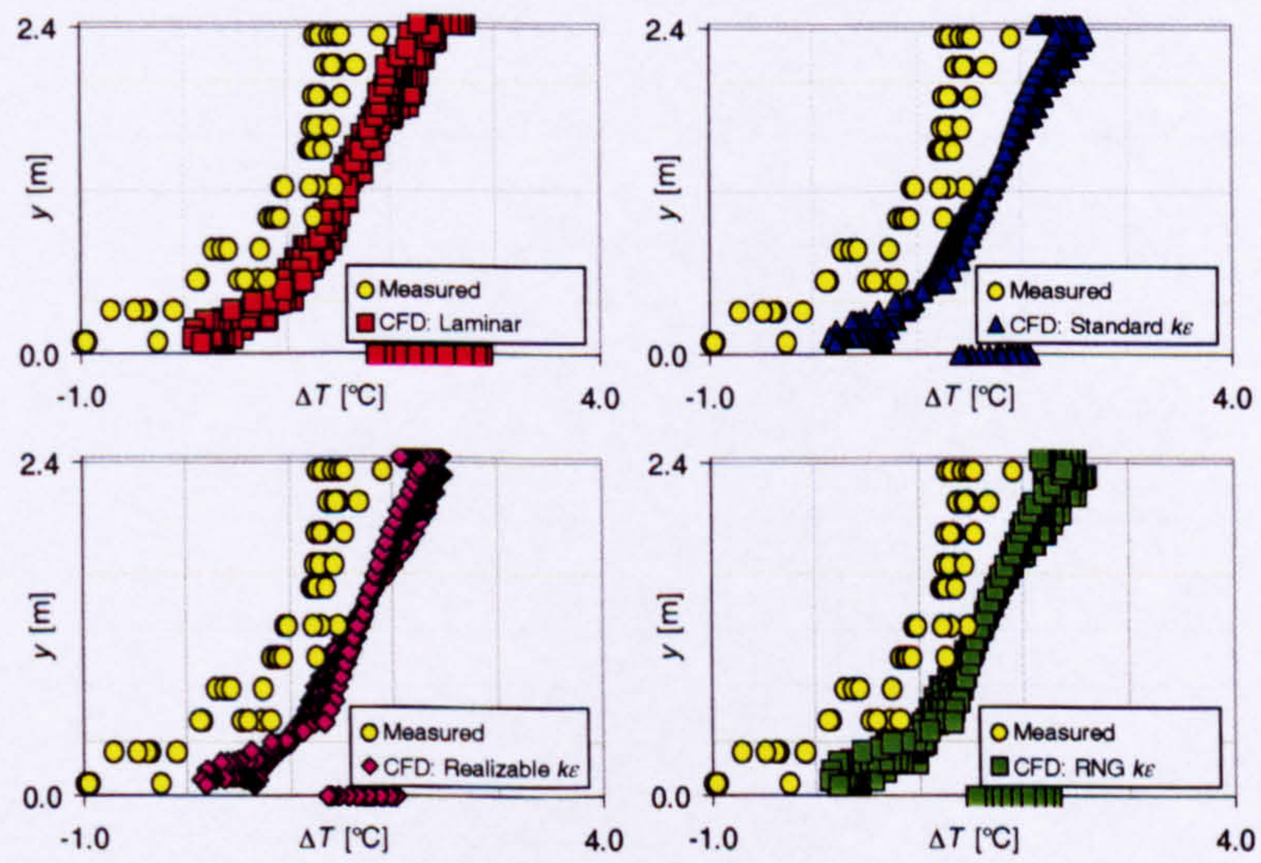

Figure 7.9 - Internal temperature profiles: 225.0W plate heater; $A^* = 0.488\text{m}^2$; radiation model enabled, $\kappa = 0.10\text{m}^{-1}$; uniform external temperature at the domain extents; QUICK differencing employed for convection terms

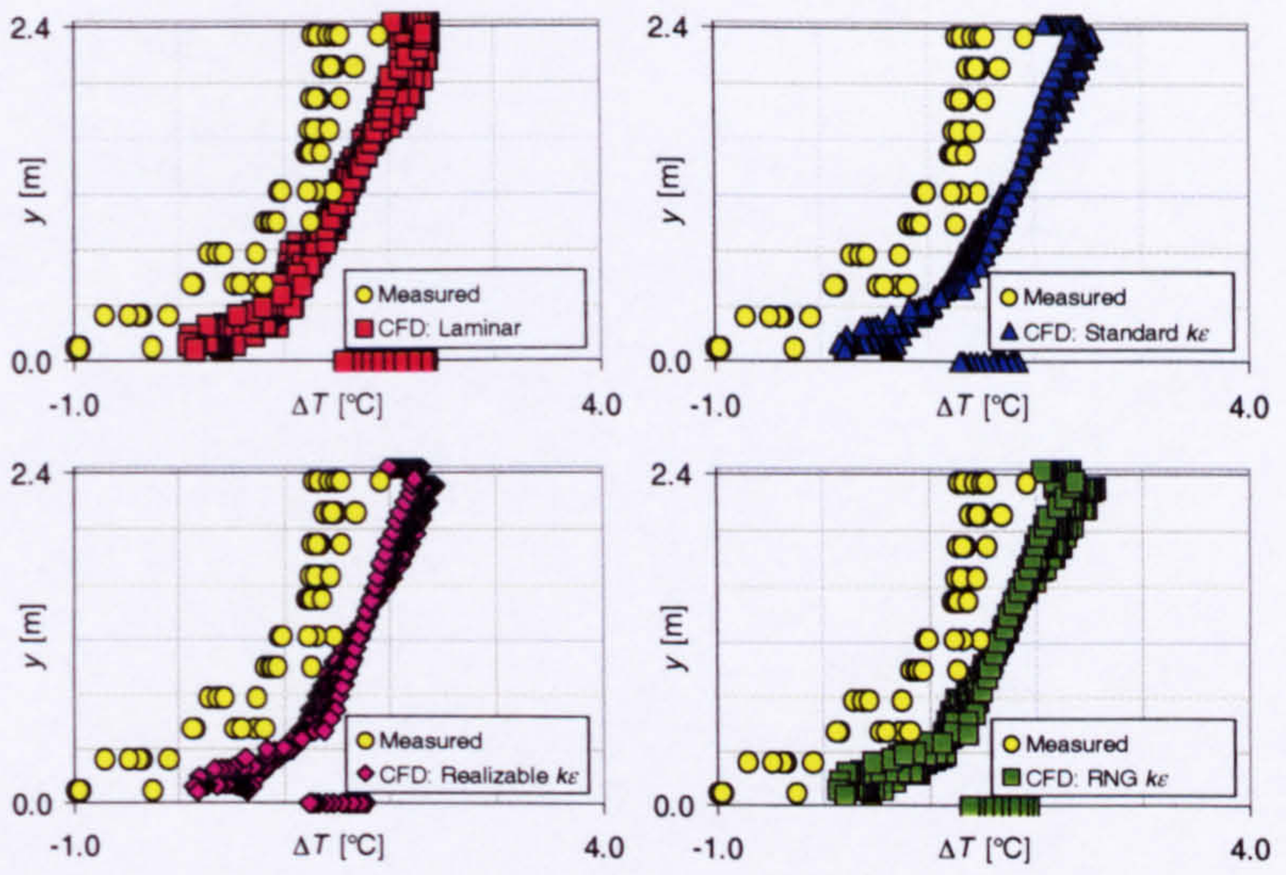

Figure 7.10 - Internal temperature profiles: 225.0W plate heater; $A^* = 0.488m^2$; radiation model enabled, $\kappa = 0.15m^{-1}$; uniform external temperature at the domain extents; QUICK differencing employed for convection terms

The temperature profiles predicted with the measured external temperature imposed at the extents of the domain for each turbulence modelling approach considered are provided in Figure 7.11, Figure 7.12 and Figure 7.13 below, together with the measured temperature profile.

Any changes in the shape of the predicted profiles are insignificant when compared to the corresponding profile with a uniform temperature applied at the domain extents, although changes in the magnitude of the temperature rise above that at the reference thermometer location are observed: with the external temperature stratification in place, agreement between the predicted temperature rise within the space and that measured during the experimental phase is much improved.

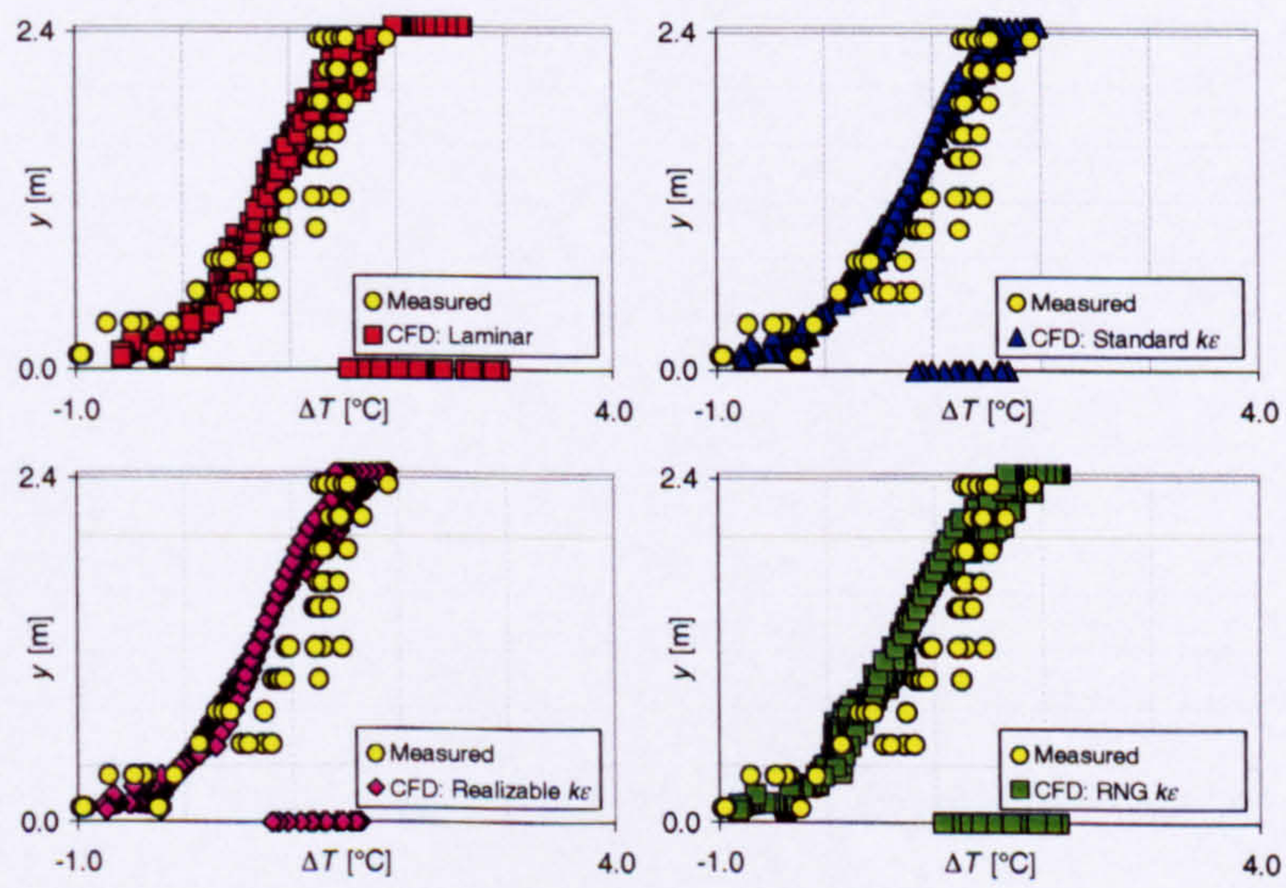

Figure 7.11 - Internal temperature profiles: 225.0W plate heater; $A^* = 0.488m^2$; radiation model enabled, $\kappa = 0.05m^{-1}$; measured external temperature profile enforced at the domain extents; QUICK differencing employed for convection terms

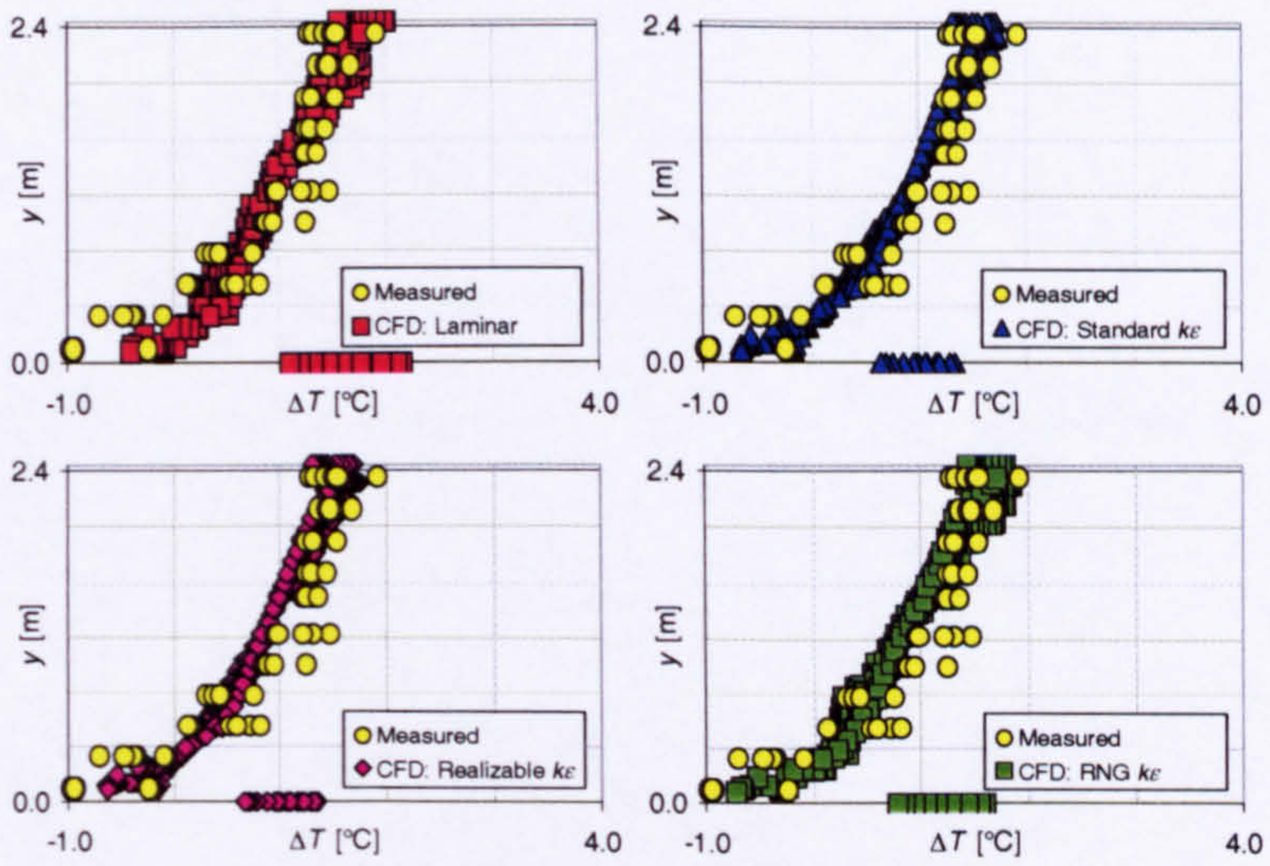

Figure 7.12 - Internal temperature profiles: 225.0W plate heater; $A^* = 0.488m^2$; radiation model enabled, $\kappa = 0.10m^{-1}$; measured external temperature profile enforced at the domain extents; QUICK differencing employed for convection terms

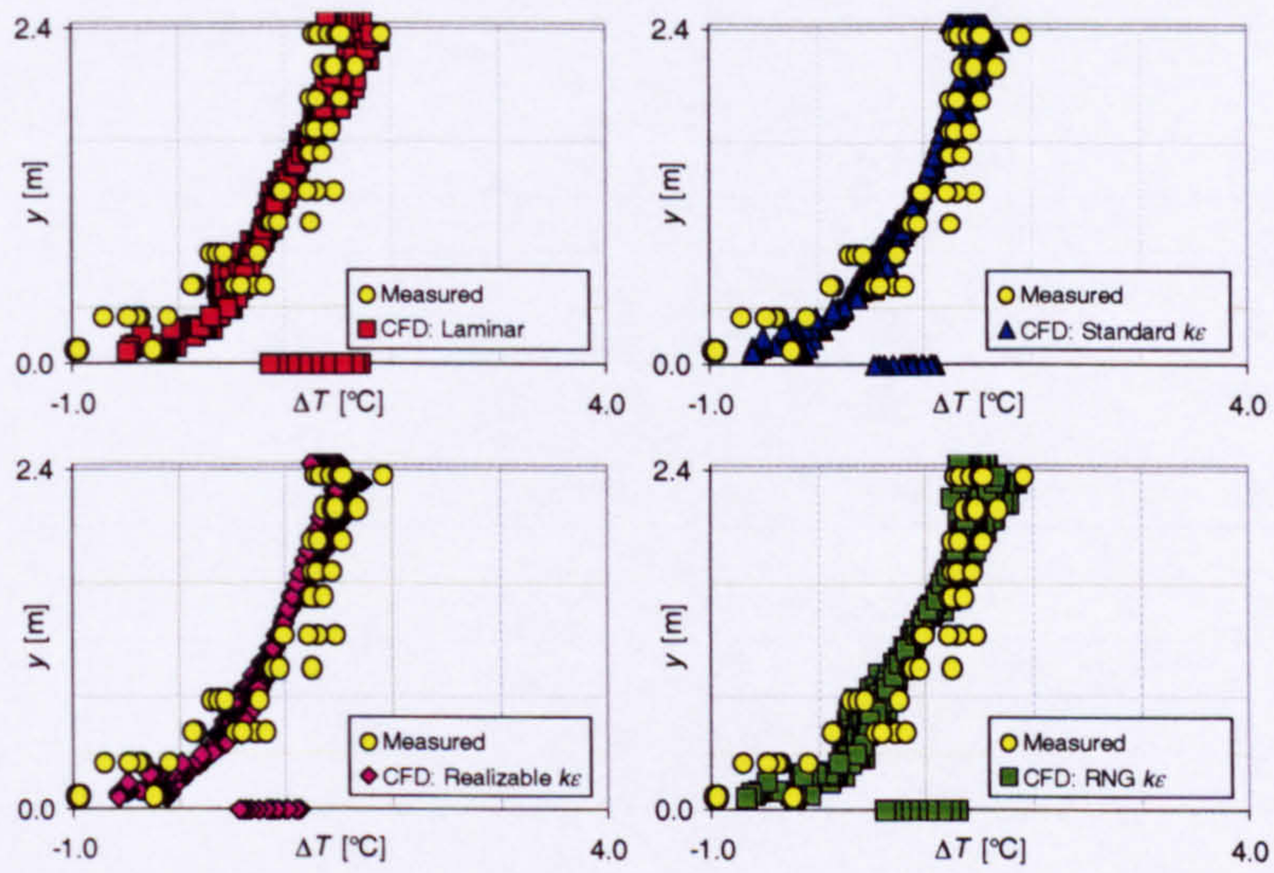

Figure 7.13 - Internal temperature profiles: 225.0W plate heater; $A^* = 0.488m^2$; radiation model enabled, $\kappa = 0.15m^{-1}$; measured external temperature profile enforced at the domain extents; QUICK differencing employed for convection terms

7.3.1.2 Width of opening equal to 1.2m ($A^* = 0.732m^2$)

7.3.1.2.1 Radiation model disabled

The temperature profiles predicted with a constant external temperature imposed at the extents of the domain for this opening configuration with the radiation model disabled are provided in Figure 7.14 below, together with the measured temperature profile. Again, the profiles were obtained using the first-order upwind differencing scheme, as numerical convergence difficulties were experienced when the QUICK differencing scheme was used.

The temperature profiles predicted within the enclosure with the laminar and the RNG-$k\varepsilon$ turbulence modelling approach are similar. They exhibit two layers of air: a layer of ambient air at low-level and extending up to a height of about 1.3m, above which there is a layer of air that extends to the ceiling in which the vertical temperature remains constant, approximately equal to 2.0°C/m.

With the standard-$k\varepsilon$ turbulence model the predicted profile comprised three layers, similar to those observed with this heat source for the opening width equal to 0.8m: a layer of ambient air at low-level, a layer within the core of the space where the vertical temperature gradient is a maximum, and a layer at high-level, where the vertical temperature gradient is reduced. The depth of the layer of ambient air at low-level is about 1.0m, and the middle layer then extends to a height of roughly 1.7m. The temperature gradient within the middle layer is equal to about 2.5°C/m, with that in the layer above equal to roughly 0.8°C/m.

The temperature profile predicted with the realizable-$k\varepsilon$ turbulence closure falls between that computed using the laminar and RNG-$k\varepsilon$ approach on one hand, and that with the standard-$k\varepsilon$ approach on the other. It is possible to classify the realizable-$k\varepsilon$ profile as a three-layer stratification, as for the standard-$k\varepsilon$ profile, but the change in the vertical temperature gradient between the middle layer and the upper layer is much less apparent: 1.6°C/m within the middle layer and approximately 1.0°C/m within the upper layer.

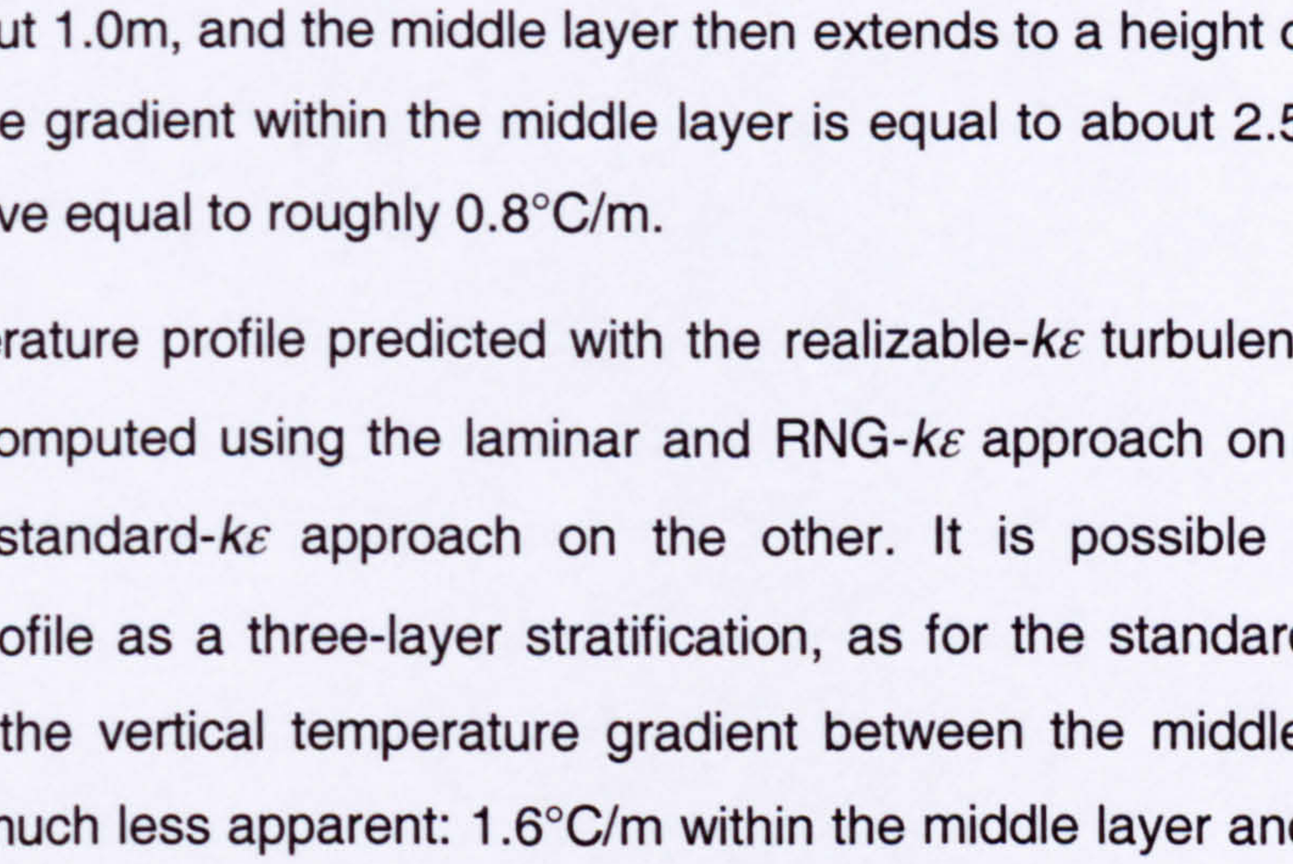

Figure 7.14 - Internal temperature profiles: 225.0W plate heater; $A^* = 0.732m^2$; radiation model disabled; uniform external temperature at domain extents; first-order upwind differencing employed for convection terms

The temperature profile predicted with the measured external temperature imposed at the extents of the domain for each turbulence modelling approach considered is provided in Figure 7.15 below, together with the measured temperature

profile. The application of the external stratification is observed to affect the predicted temperature profiles within the upper part of the space.

In contrast to the two-layer profiles that had been forecast with the laminar and RNG-$k\varepsilon$ turbulence modelling approaches with a uniform ambient temperature field, three-layer profiles are now predicted due to the dissection of the upper layer previously predicted, the height of the division being equal to about 2.0m. Below this height in the central part of the space the vertical temperature gradient is a maximum, equal to approximately 2.8°C/m. Above this height the vertical temperature gradient is roughly equal to 2.0°C/m for the laminar profile and 0.8°C/m for the RNG-$k\varepsilon$ profile. The depth of the ambient layer of fluid at low-level within the space remains unchanged for each profile.

The standard-$k\varepsilon$ and realizable-$k\varepsilon$ profiles remain three-layer, but the difference in the vertical temperature gradient between the two upper layers is more evident. For the standard-$k\varepsilon$ profile, the gradient in the middle layer is nearer 3.0°C/m, and is equal to approximately 0.6°C/m in the upper layer. For the realizable-$k\varepsilon$ profile, the gradient in the middle layer is also roughly 3.0°C/m, but in the upper layer is equal to about 1.0°C/m.

Due to the application of the external stratification, each of the predicted profiles for the internal temperature rise show a non-zero vertical temperature gradient in the region immediately adjacent to the floor of the enclosure. In addition, there is also a small temperature drop observed in this region, although the magnitude of this drop is much less than that for the same heat source with an opening width of 0.8m.

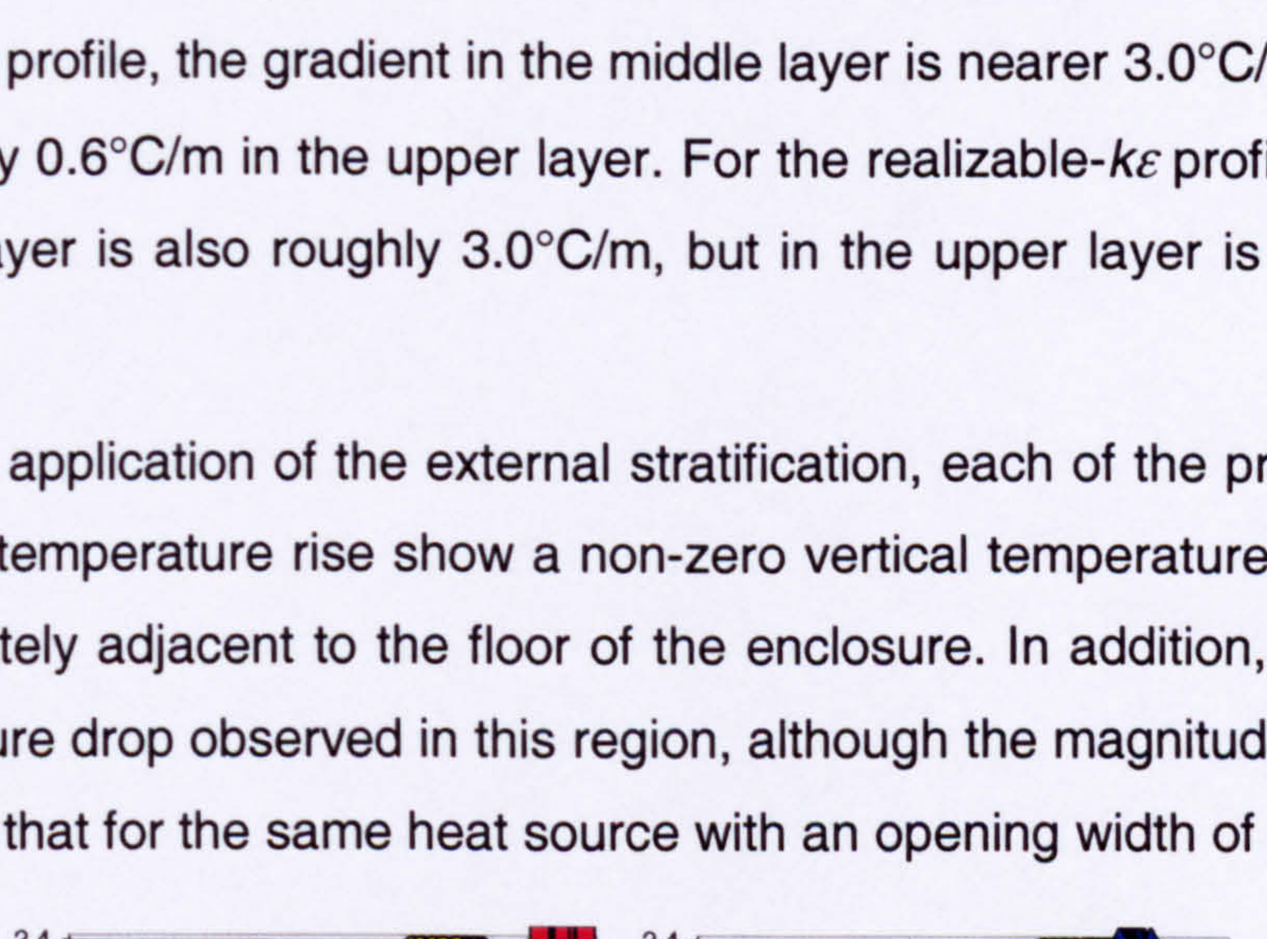

Figure 7.15 - Internal temperature profiles: 225.0W plate heater; $A^* = 0.732m^2$; radiation model disabled; measured external stratification at domain extents; first-order upwind differencing employed for convection terms

7.3.1.2.2 Radiation model enabled, absorption of radiation throughout the fluid medium neglected ($\kappa = 0.0 m^{-1}$)

The temperature profiles computed with the radiation model enabled but neglecting absorption of radiation within the fluid medium for this opening configuration is presented in Figure 7.16 below, together with the measured temperature. The profiles were obtained using QUICK differencing.

The predicted temperature of the surface of the floor for each case is higher than the incoming air flowing over the floor, due to thermal radiative transfer from the relatively warm ceiling. The predicted surface temperature of the floor is of the order of 4.0°C higher than the adjacent fluid for the laminar case, 3.0°C higher for the RNG-$k\varepsilon$ case, and 2.0°C higher for the standard-$k\varepsilon$ and realizable-$k\varepsilon$ cases.

The four computed profiles vary slightly in the layer of fluid within 0.3m of the floor of the enclosure. For the laminar and RNG-$k\varepsilon$ profiles, a small increase in the temperature rise is apparent in the layer close to the floor, so that the heated layer of fluid adjacent to the relatively warm surface of the floor is sufficiently thick to encompass the floor-adjacent nodes. For the standard-$k\varepsilon$ and realizable-$k\varepsilon$ profiles, the temperature rise appears to be roughly constant, as the heated layer of fluid is not sufficiently thick to encompass the floor-adjacent nodes.

Above this layer, the four computed profiles are similar for each of the turbulence modelling approaches considered. In the layer between the heights of 0.3m and 0.6m the vertical temperature gradient is approximately equal to 1.0°C/m and is equal to 0.7°C/m in the core of the space for each turbulence modelling approach. In the layer of fluid immediately below the ceiling each of the predicted profiles show a significant increase in the rate of change of temperature with respect to height, which is not in agreement with the measured profile where the rise in temperature above ambient was observed to be approximately constant in this region.

The magnitude of the temperature rise predicted above that at the reference location for each of the profiles is in good agreement with the measured data within the middle section of the space, although the temperature rise is over-predicted in the layers of fluid immediately above the floor and below the ceiling.

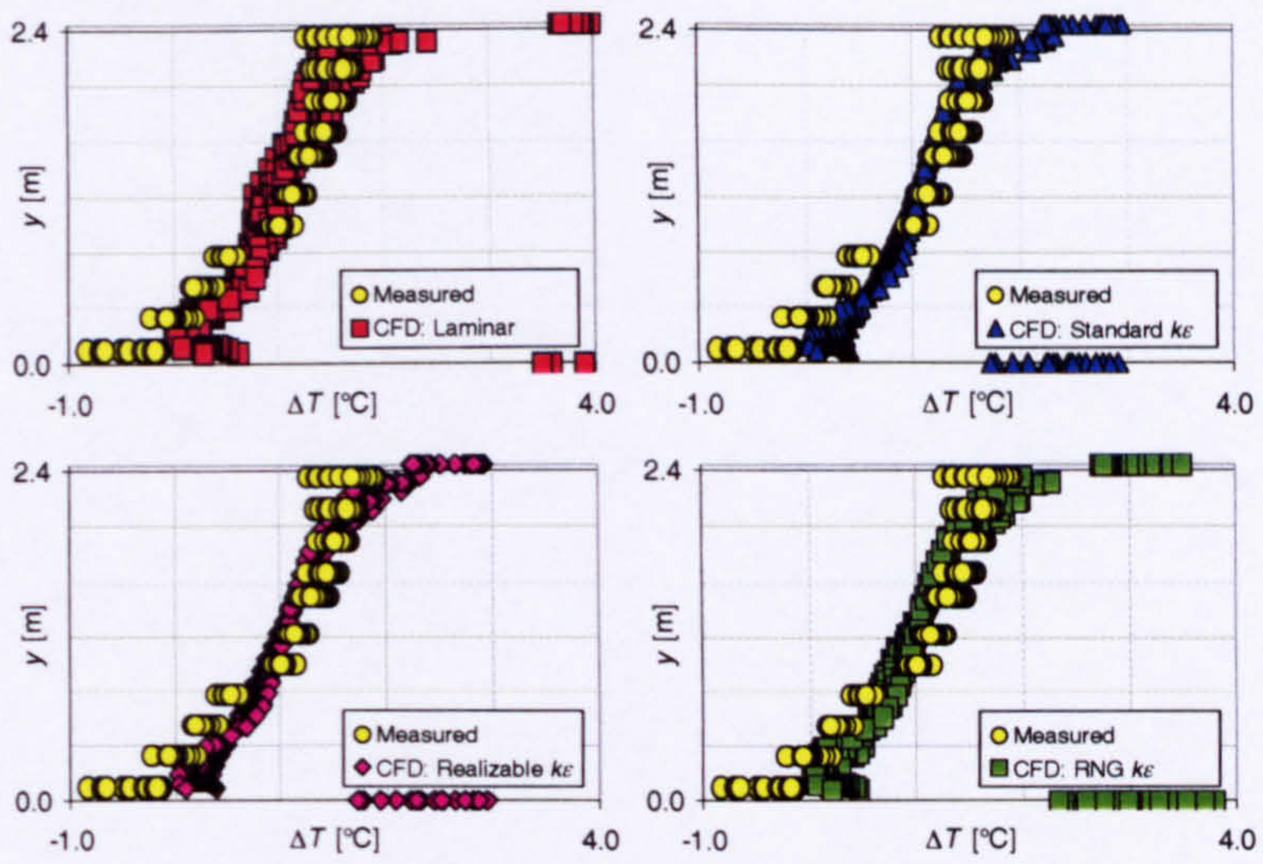

Figure 7.16 - Internal temperature profiles: 225.0W plate heater; $A^* = 0.732m^2$; radiation model enabled, $\kappa = 0.0m^{-1}$; uniform external temperature at domain extents; QUICK differencing employed for convection terms

The temperature profile predicted with the measured external temperature imposed at the extents of the domain for each turbulence modelling approach considered is provided in Figure 7.17 below, together with the measured temperature profile.

With the external stratification in place, the temperature gradient above the floor is approximately equal to 1.0°C/m within the layer of fluid up to a height of 0.6m. Above this height, there is little change in the shape of the predicted profiles. The magnitude of the rise in temperature above the reference temperature for the computed profiles is in good agreement with the measured profile in the layers of fluid just above the floor, but is under-predicted in the core of the space and is over-predicted in the layer just below the ceiling.

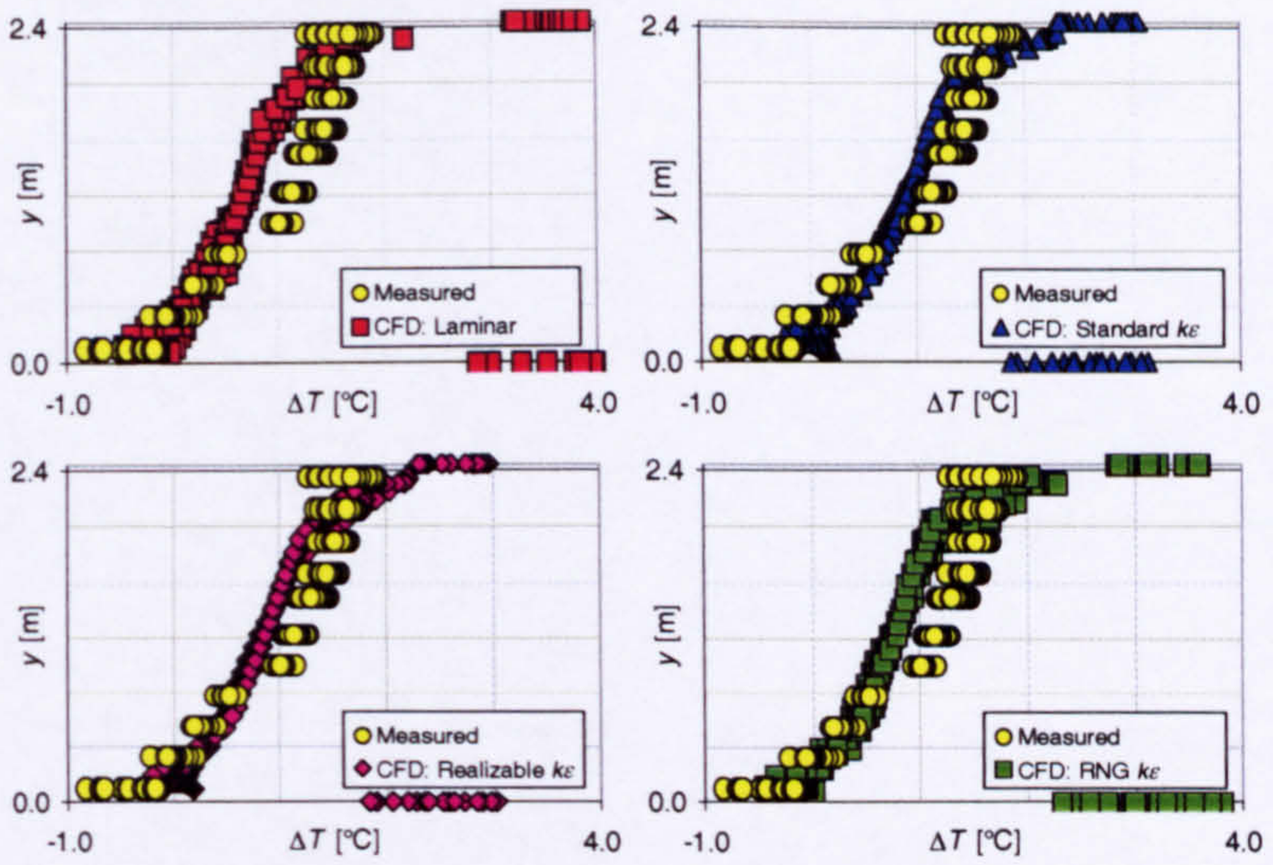

Figure 7.17 - Internal temperature profiles: 225.0W plate heater; $A^* = 0.732m^2$; radiation model enabled, $\kappa = 0.0m^{-1}$; measured external stratification at domain extents; QUICK differencing employed for convection terms

7.3.1.2.3 Radiation model enabled, absorption of radiation throughout the fluid medium included ($\kappa \neq 0.0m^{-1}$)

The internal temperature profiles predicted for this opening configuration with a constant external temperature imposed at the extents of the domain and with the radiation model enabled for each non-zero absorption coefficient considered ($\kappa = 0.05m^{-1}$, $\kappa = 0.10m^{-1}$ and $\kappa = 0.15m^{-1}$) are presented in Figure 7.18, Figure 7.19 and Figure 7.20 below, together with the measured temperature.

Each profile remains almost unchanged in terms of the shape of the profile and the magnitude of the temperature rise within the central region of the space when compared to the corresponding profile predicted with the absorption coefficient equal to zero.

As the absorption coefficient κ is increased from zero, it is observed that the predicted temperatures of the surfaces of the ceiling and of the floor fall significantly. Consider the laminar case for example. With the absorption coefficient $\kappa = 0.0m^{-1}$, the predicted surfaces temperatures of the ceiling and of the floor above the reference temperature is of the order of 4.0°C, whereas with $\kappa = 0.05m^{-1}$ they are about 3.0°C and with $\kappa = 0.10m^{-1}$ they fall to about 2.0°C. The profiles with an absorption coefficient $\kappa = 0.05m^{-1}$ still predict an increase in the vertical temperature gradient in the layer immediately below the ceiling, which is not in agreement with the measured profile, although this increase is less significant than for the cases where radiative absorption was neglected. For the absorption coefficient $\kappa = 0.10m^{-1}$ and $\kappa = 0.15m^{-1}$,

the profiles no longer show a significant increase in the vertical temperature gradient in the layer below the ceiling, which is in agreement with the measured profile.

It is also noted that for a non-zero absorption coefficient, the laminar and RNG-$k\varepsilon$ profiles no longer show an apparent rise in temperature in the thin layer immediately adjacent to the floor. This is a consequence of the fall in the surface temperature of the floor, so that the heated layer of fluid immediately next to the floor is less thick and is no longer sufficiently deep to encompass the floor-adjacent nodes of the computational mesh.

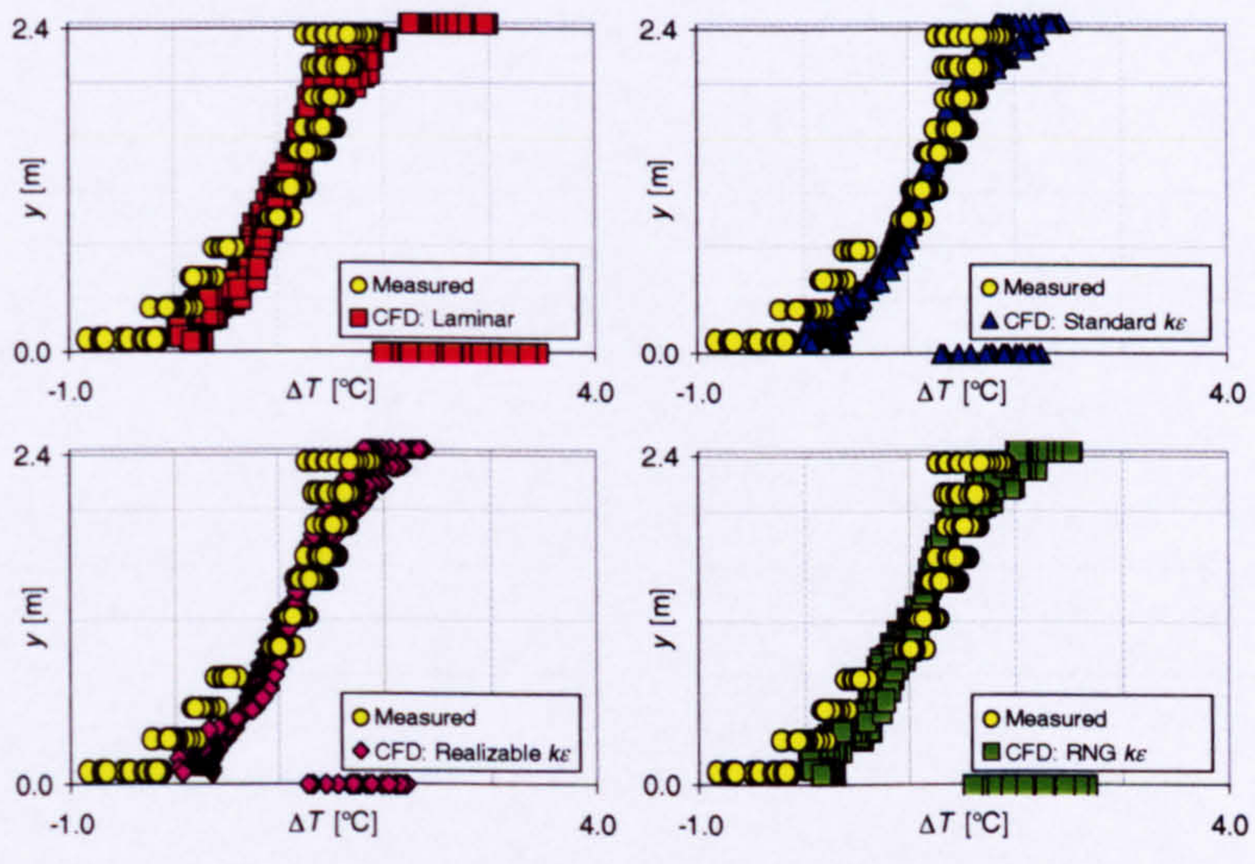

Figure 7.18 - Internal temperature profiles: 225.0W plate heater; $A^* = 0.732m^2$; radiation model enabled, $\kappa = 0.05m^{-1}$; uniform external temperature at the domain extents; QUICK differencing employed for convection terms

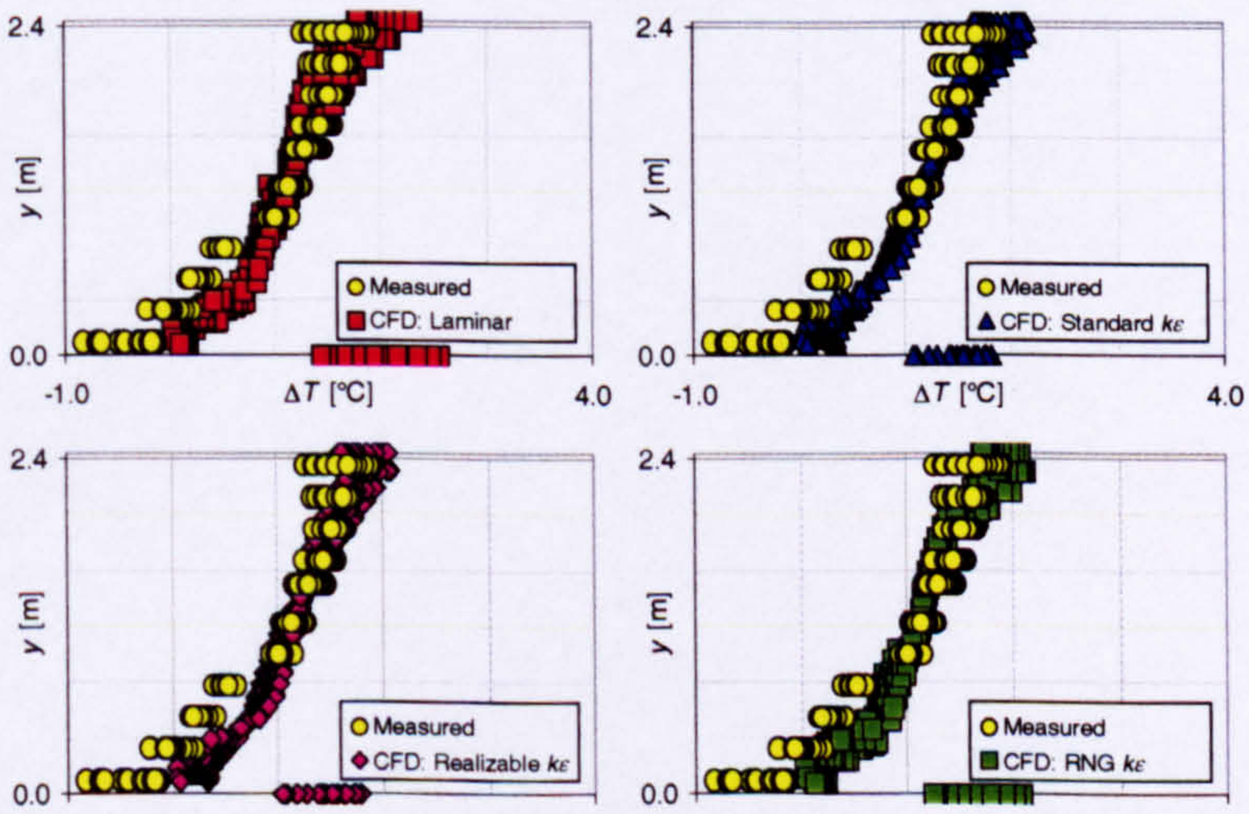

Figure 7.19 - Internal temperature profiles: 225.0W plate heater; $A^* = 0.732m^2$; radiation model enabled, $\kappa = 0.10m^{-1}$; uniform external temperature at the domain extents; QUICK differencing employed for convection terms

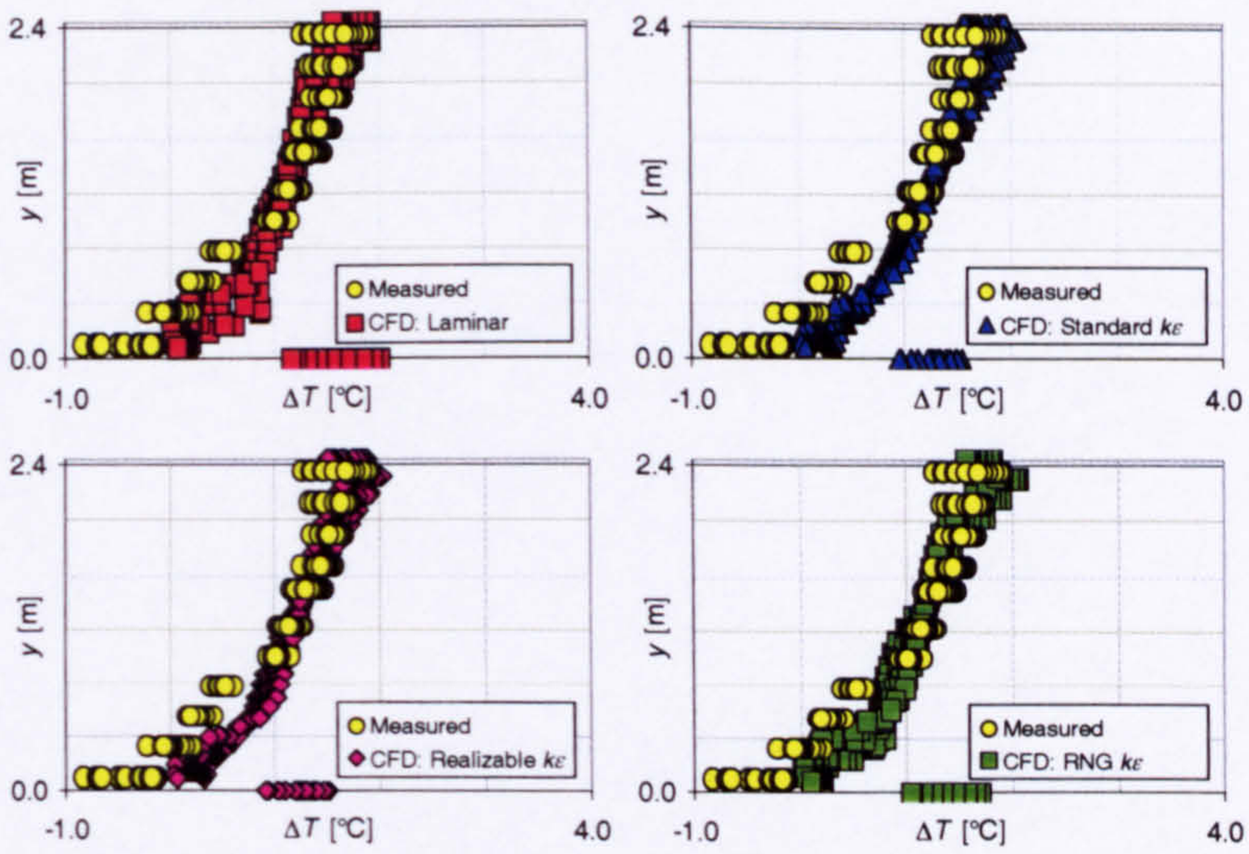

Figure 7.20 - Internal temperature profiles: 225.0W plate heater; $A^* = 0.732m^2$; radiation model enabled, $\kappa = 0.15m^{-1}$; uniform external temperature at the domain extents; QUICK differencing employed for convection terms

The temperature profiles predicted with the measured external temperature imposed at the extents of the domain for each turbulence modelling approach considered are provided in Figure 7.21, Figure 7.22 and Figure 7.23 below, together with the measured temperature profile.

Any changes in the shape of the predicted profiles are not significant when compared to the corresponding profile with a uniform temperature applied at the domain extents. The magnitude of the temperature rise predicted above that at the reference thermometer location, however, is affected. With the external temperature stratification in place, the rise in temperature predicted above that at the reference thermometer location is reasonable in the layer within 0.8m of the floor for each of the turbulence modelling approaches considered. In the upper half of the space, the laminar and RNG-$k\varepsilon$ profiles tend to under-predict the temperature rise by the order of 0.5°C, but the agreement between the standard-$k\varepsilon$ and realizable-$k\varepsilon$ predictions and the measured profile is better than this.

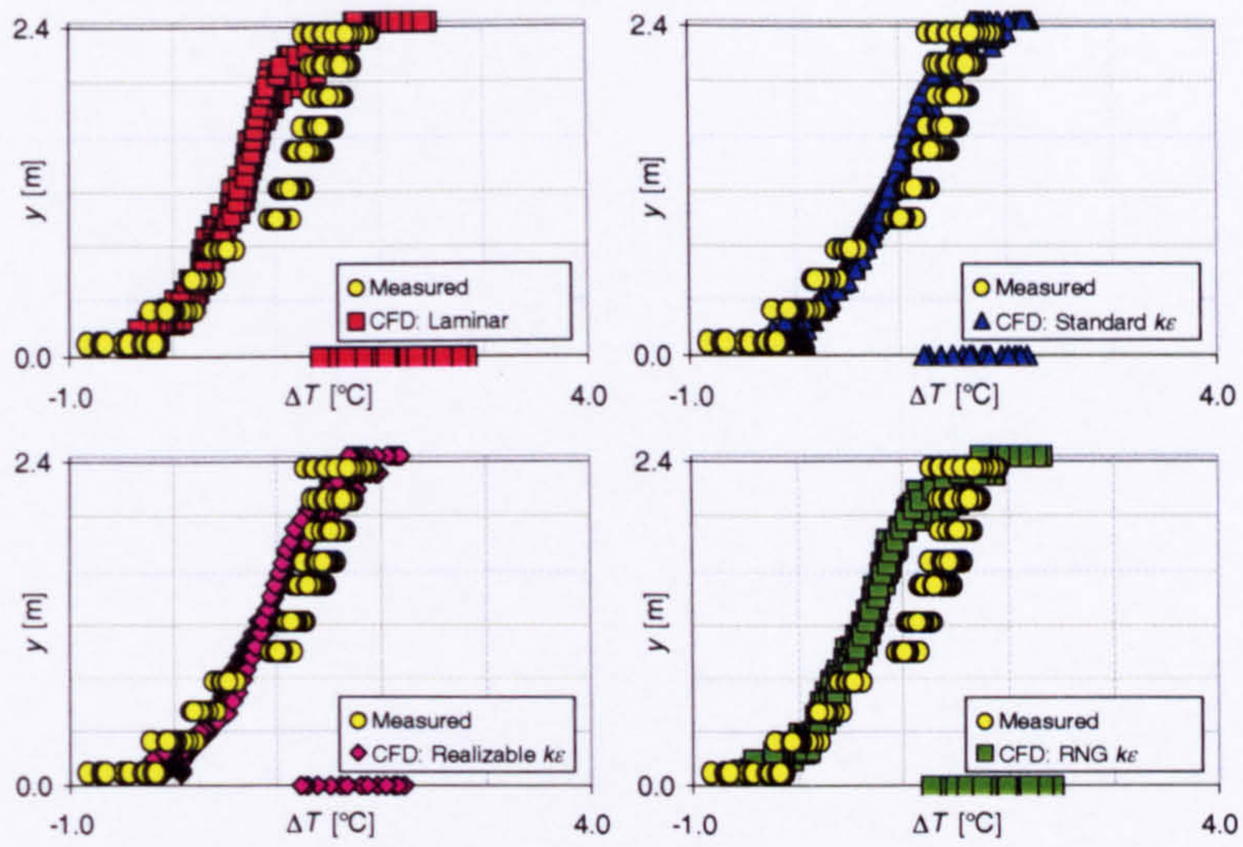

Figure 7.21 - Internal temperature profiles: 225.0W plate heater; $A^* = 0.732m^2$; radiation model enabled, $\kappa = 0.05m^{-1}$; measured external temperature profile enforced at the domain extents; QUICK differencing employed for convection terms

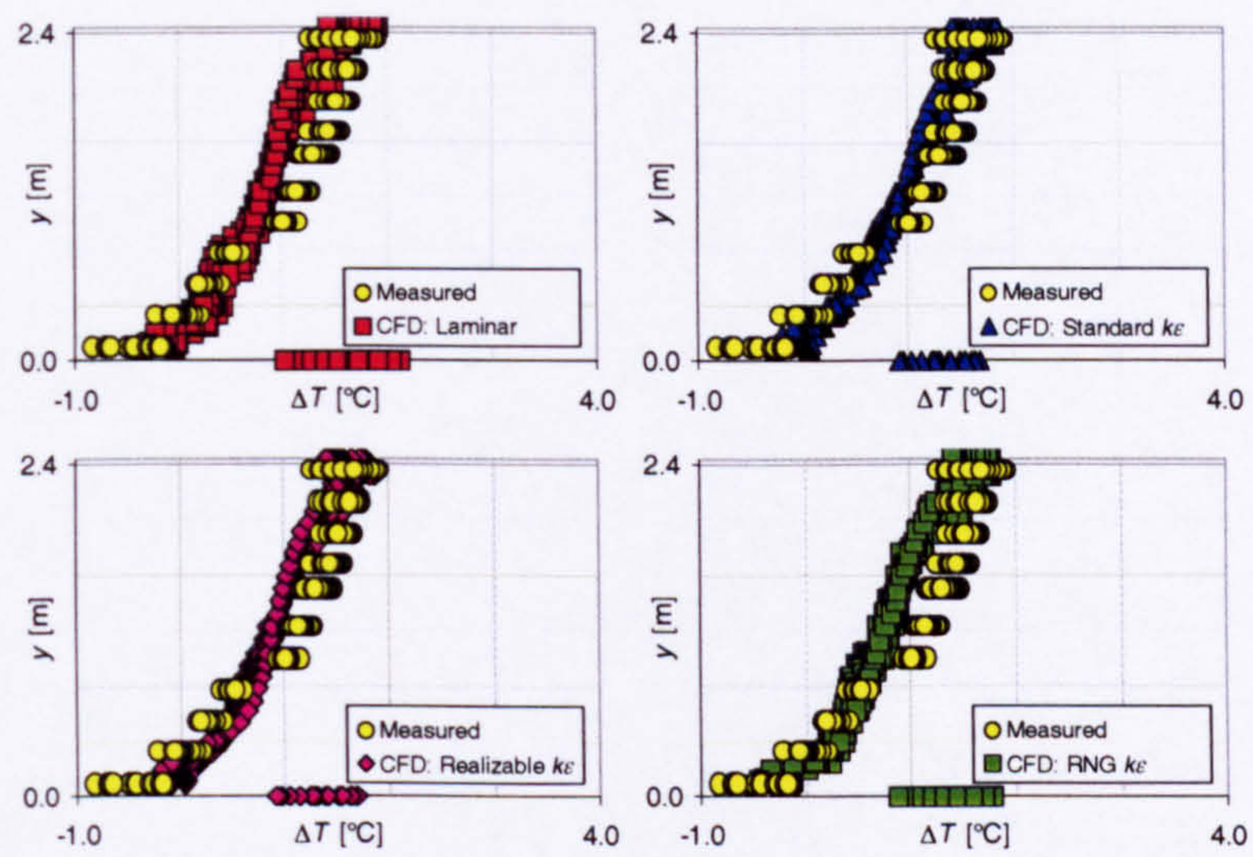

Figure 7.22 - Internal temperature profiles: 225.0W plate heater; $A^* = 0.732m^2$; radiation model enabled, $\kappa = 0.10m^{-1}$; measured external temperature profile enforced at the domain extents; QUICK differencing employed for convection terms

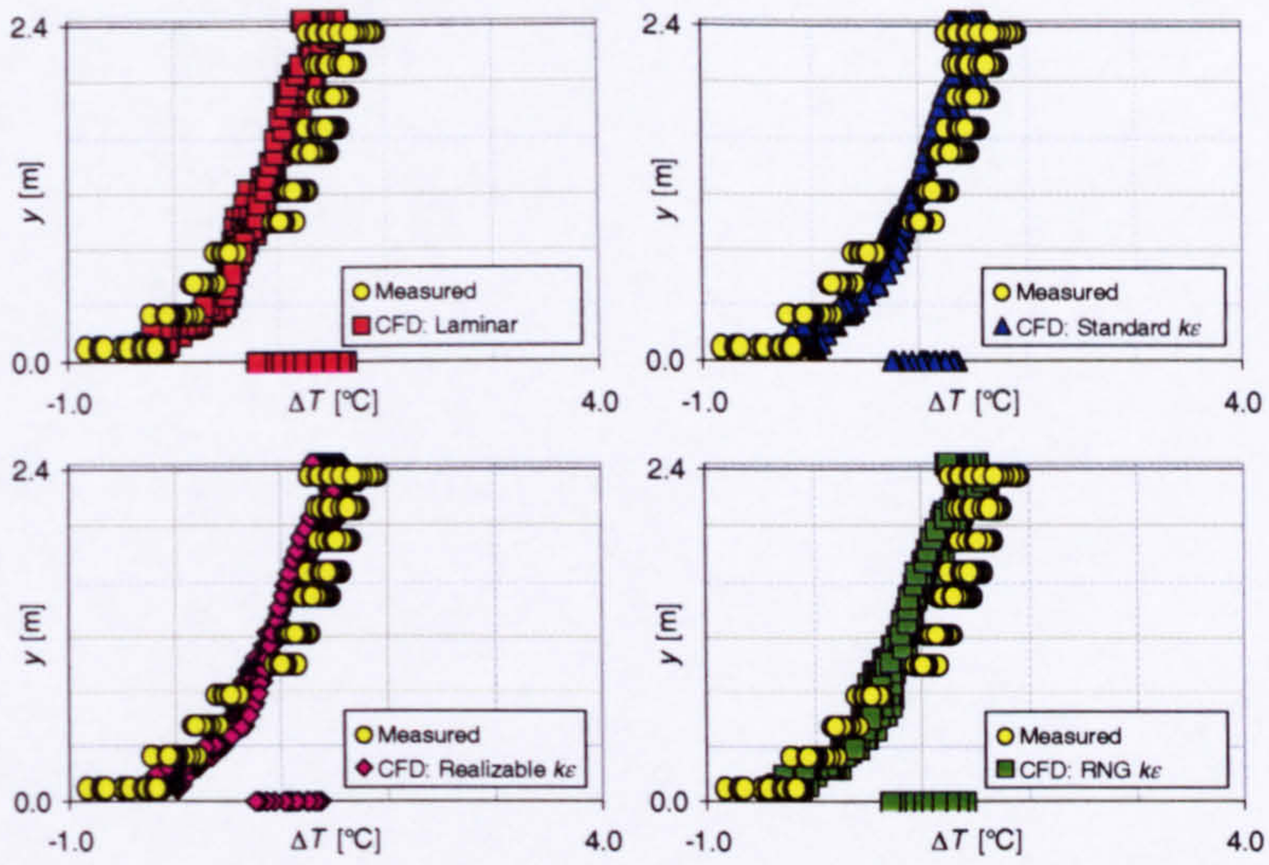

Figure 7.23 - Internal temperature profiles: 225.0W plate heater; $A^* = 0.732m^2$; radiation model enabled, $\kappa = 0.15m^{-1}$; measured external temperature profile enforced at the domain extents; QUICK differencing employed for convection terms

7.3.2 Boiler ring with an output of 368.0W for various opening configurations

As for the CFD-simulations with the plate heater, when the boiler ring was employed as the source of buoyancy with an output of 368.0W and the adiabatic approximation was enforced at the walls of the enclosure, the temperature rise within the space was greatly over-predicted for the smaller opening configurations, regardless of which turbulence or radiation modelling approach was employed. For example, with the width of the opening equal to 0.1m, most of the CFD-results predict that the temperature in the layer of air below the ceiling within the space would be of the order of 8°C above that at the reference location in the low-level opening, whereas the measured temperature rise was only 3°C (Figure 10, Addendum 3).

As the width of the openings was increased, the adiabatic assumption at the enclosure walls became increasingly realistic and the agreement between the predicted temperature rise within the space and that that had been measured during the experimental program was again improved.

When the heat-transfer coefficient at the internal surface of the enclosure walls was determined using the law of the wall, the rate of heat flux was again greatly over-predicted so that the temperature rise calculated within the space was less than that measured within the experimental enclosure for all opening configurations. This provides further evidence that the currently available methods to predict the rate of transfer of thermal energy at solid walls are simply inadequate to accurately predict the heat loss through the fabric of the enclosure, and that an alternative method for predicting the wall heat transfer is required.

The predicted profiles for the temperature rise within the space for a width of opening of 0.8m and 1.2m, corresponding to an effective area of opening $A^* = 0.488m^2$ and $A^* = 0.732m^2$ respectively, are discussed in detail in the sub-sections that follow.

7.3.2.1 Width of opening equal to 0.8m ($A^* = 0.488m^2$)

7.3.2.1.1 Radiation model disabled

The temperature profiles predicted with a uniform external temperature and the adiabatic approximation at the enclosure walls and with the radiation model disabled are provided in Figure 7.24 below, together with the measured temperature profile. Each of the predicted profiles presented were obtained using the first-order upwind differencing scheme, as numerical convergence difficulties were experienced when the QUICK differencing scheme was employed.

It is immediately apparent from this information that the agreement between the predicted temperature profile and the measured temperature profile is poor, regardless of the turbulence modelling approach adopted.

The predicted laminar profile is a two-layer stratification. The lower layer of air extends from the floor up to a height of about 1.5m and is at the same temperature as that predicted at the reference thermometer location. Above this there is a layer of air that extends to the ceiling in which the vertical temperature remains constant, approximately equal to 4.0°C/m.

The predicted standard-$k\varepsilon$ profile comprised three layers: a layer of ambient air at low-level, a layer within the core of the space where the vertical temperature gradient is a maximum, and a layer at high-level, where the vertical temperature gradient is reduced. The depth of the layer of ambient air at low-level is about 0.9m, above which the middle layer extends to a height of roughly 1.7m. The temperature gradient within the middle layer is equal to about 3.2°C/m, with that in the layer above equal to roughly 1.0°C/m.

The predicted realizable-$k\varepsilon$ and RNG-$k\varepsilon$ profiles fall between that forecast using the laminar approach and that computed with the standard-$k\varepsilon$ approach. Each profile is a three-layer stratification, as for the standard-$k\varepsilon$ profile, but the change in the vertical temperature gradient between the middle layer and the upper layer is much less apparent. For the realizable-$k\varepsilon$ profile, the vertical temperature gradient is approximately equal to 4.0°C/m within the middle layer and 1.6°C/m within the upper layer. For the RNG-$k\varepsilon$ profile, the vertical temperature gradient is roughly 5.0°C/m within the middle layer and 4.0°C/m within the upper layer.

There is almost a smooth transition from the standard-$k\varepsilon$ profile, which clearly predicts a three-layer stratification, through the realizable-$k\varepsilon$ profile and then the RNG-$k\varepsilon$ profile, towards the two-layer laminar profile. It is also observed that the depth of the ambient layer of air at low-level within the space will increase along this transition. The depth of this layer is a minimum for the standard-$k\varepsilon$ profile, approximately equal to 0.9m, and increases to 1.2m for the realizable-$k\varepsilon$ profile, 1.4m for the RNG-$k\varepsilon$ profile, and is a maximum of 1.5m for the laminar profile.

The predicted standard-$k\varepsilon$ profile isapproximately representative of two separate layers of air, each of which is well mixed and therefore comprising fluid at a uniform temperature, as described by the Cambridge mathematical model for natural displacement ventilation flows. This is not, however, in good agreement with the measured temperature profile from the experimental program performed as part of this work.

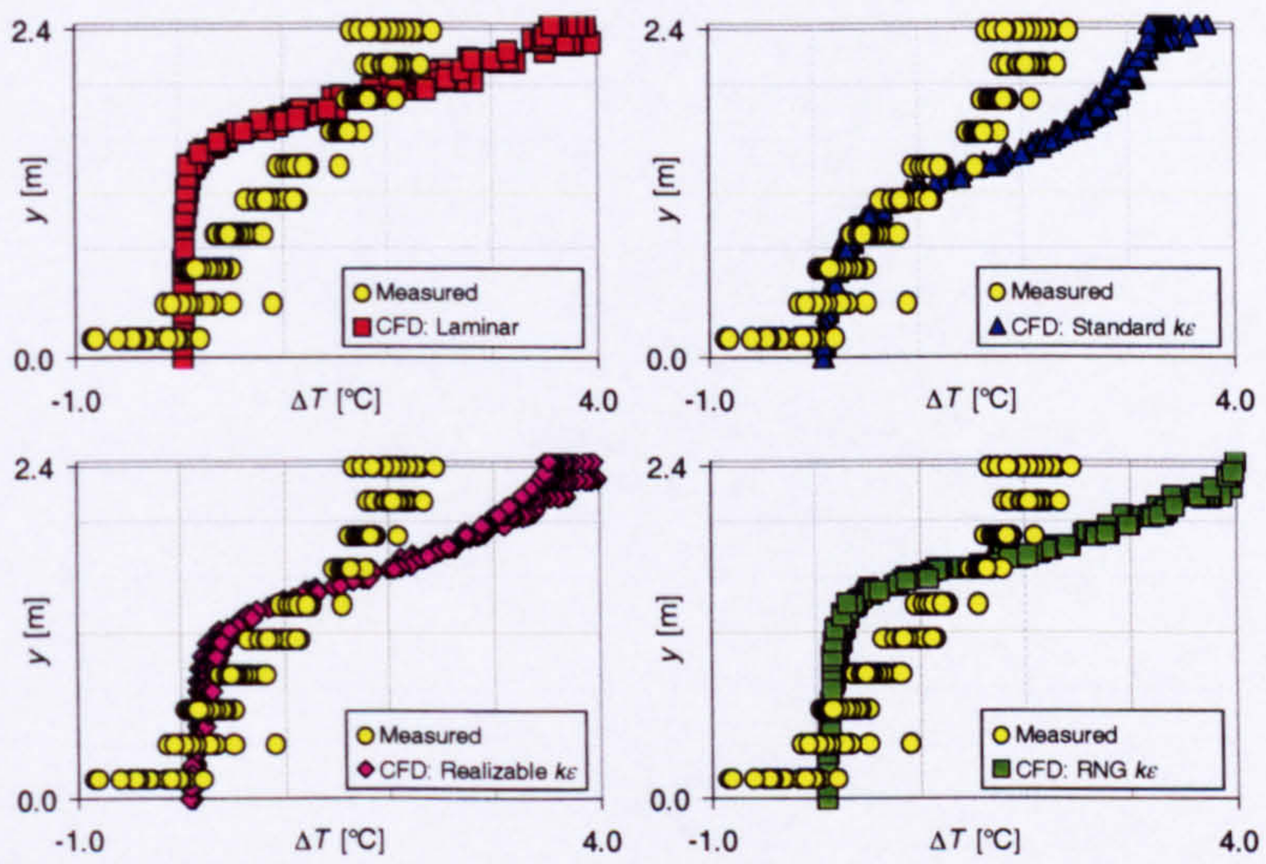

Figure 7.24 - Internal temperature profiles: 368.0W boiler ring; $A^* = 0.488m^2$; radiation model disabled; uniform external temperature enforced at the domain extents; first-order upwind differencing employed for convection terms

The temperature profile predicted with the measured external temperature imposed at the extents of the domain for each turbulence modelling approach considered is provided in Figure 7.25 below, together with the measured temperature profile.

With the external stratification in place it is clear that for the three-layer profiles, the difference in the vertical temperature gradient between the middle layer and the upper layer of fluid is more pronounced. For the standard-$k\varepsilon$ profile, the vertical temperature gradient in the middle layer is now approximately equal to 5.0°C/m, with that in the upper layer equal to about 0.5°C/m. Similarly, for the realizable-$k\varepsilon$ profile, the gradients in the respective layers are 5.0°C/m and 1.6°C/m, and for the RNG-$k\varepsilon$

profile they are 10.0°C/m and 3.0°C/m. The depth of the low-level layer of ambient air for the realizable-$k\varepsilon$ and RNG-$k\varepsilon$ profiles remains unchanged, but is increased marginally to about 1.0m for the standard-$k\varepsilon$ profile.

The depth of the low-level layer of ambient air for the laminar profile remains unchanged at 1.5m. It is observed, however, that the vertical temperature gradient is predicted to be a maximum of about 7.0°C/m immediately above this ambient layer, and that in the layer lower just below the ceiling it is approximately 4.0°C/m. The laminar profile is, therefore, also representative of a three-layer stratification.

In addition, each of the predicted profiles now exhibit a small temperature drop, perhaps of the order of 0.2°C at most, in the ambient layer of fluid in the lower part of the enclosure.

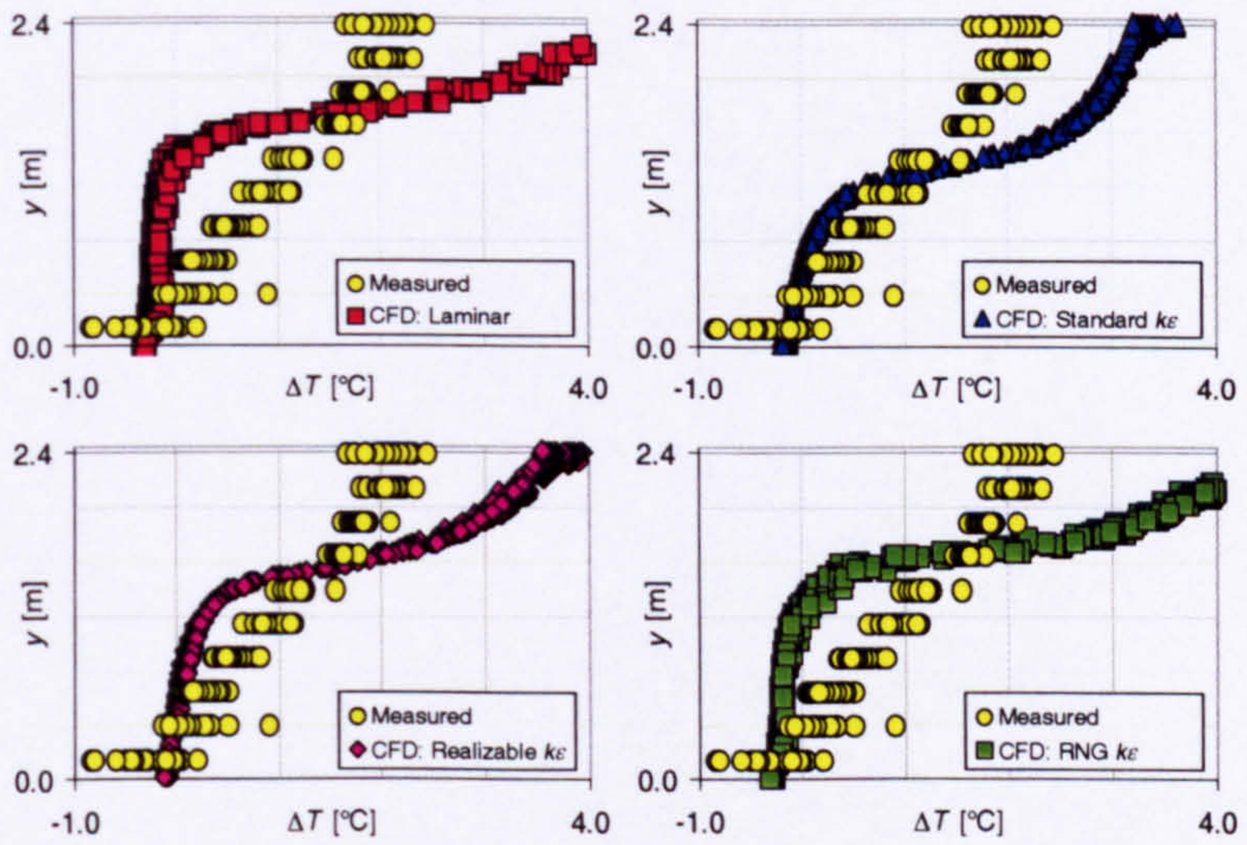

Figure 7.25 - Internal temperature profiles: 368.0W boiler ring; $A^* = 0.488m^2$; radiation model disabled; measured external temperature profile enforced at the domain extents; first-order upwind differencing employed for convection terms

7.3.2.1.2 Radiation model enabled, absorption of radiation throughout the fluid medium neglected ($\kappa = 0.0m^{-1}$)

The temperature profiles predicted employing QUICK differencing for the standard-$k\varepsilon$, realizable-$k\varepsilon$ and RNG-$k\varepsilon$ turbulence modelling approaches with the radiation model enabled but neglecting absorption of radiation within the fluid medium for this opening configuration are presented in Figure 7.26 below, together with the measured temperature profile. Numerical convergence difficulties were experienced for the laminar case, and so a profile is not presented.

With the radiation model enabled, the agreement between the available predicted temperature profiles and the measured temperature profile within the space is improved in that the computed profiles each exhibit approximately the same vertical

temperature gradient as the measured profile for a large section of the core of the space: 1.0°C/m for each of the CFD-profiles compared with approximately 1.2°C/m for the measured profile. The actual rise in temperature, however, is over-predicted by approximately 1.0°C throughout the entire space for each of the predicted profiles.

The computed temperature rise of the surface of the floor due to radiative energy transfer from the warm ceiling is of the order of 3.0°C to 4.0°C above that at the reference thermometer location for the standard-$k\varepsilon$ and realizable-$k\varepsilon$ profiles, but is greater for the RNG-$k\varepsilon$ case, in the range 3.5°C to 5.0°C. Each of the CFD-profiles presented, however, show the temperature rise to be roughly constant in the layer immediately above the floor, so that the floor-adjacent nodes of the computational mesh must be outside of the thin heated layer of fluid that will exist at the surface of the floor.

In the layer immediately below the ceiling all of the CFD-profiles predict that there will be a steep increase in the vertical temperature gradient. This is in contrast to the measured profile where the rise above the reference temperature in this zone remains approximately constant or indeed may fall.

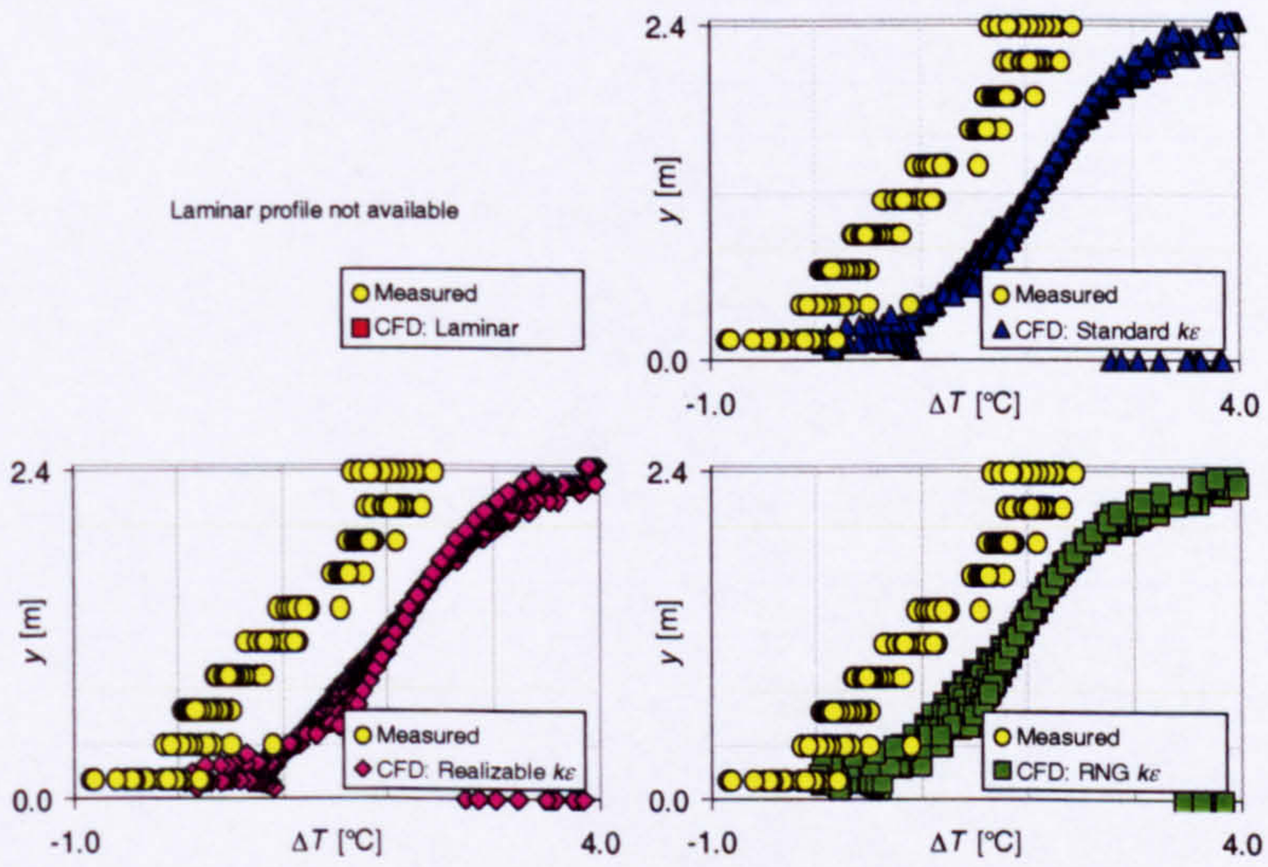

Figure 7.26 - Internal temperature profiles: 368.0W boiler ring; $A^* = 0.488m^2$; radiation model enabled, $\kappa = 0.0m^{-1}$; uniform external temperature at the domain extents; QUICK differencing employed for convection terms

The standard-$k\varepsilon$, realizable-$k\varepsilon$ and RNG-$k\varepsilon$ internal temperature profiles predicted with the measured external temperature imposed at the extents of the domain are provided in Figure 7.27 below, together with the measured temperature profile. Once again, the laminar profile is not presented.

It is observed that the rise in temperature predicted at the surface of the floor for each of the profiles is significantly lower with the measured external stratification in

place throughout the space surrounding the enclosure: the floor surface temperature is at most 1.2°C above that predicted at the reference thermometer location.

It is also clear that the application of the external stratification has improved the magnitude of the temperature rise within the space. The temperature rise predicted by the standard-$k\varepsilon$ profile remains of the order of 1.0°C above the measured profile, but for the realizable-$k\varepsilon$ profile the difference is reduced to about 0.8°C, and for the RNG-$k\varepsilon$ profile it is of the order of 0.5°C.

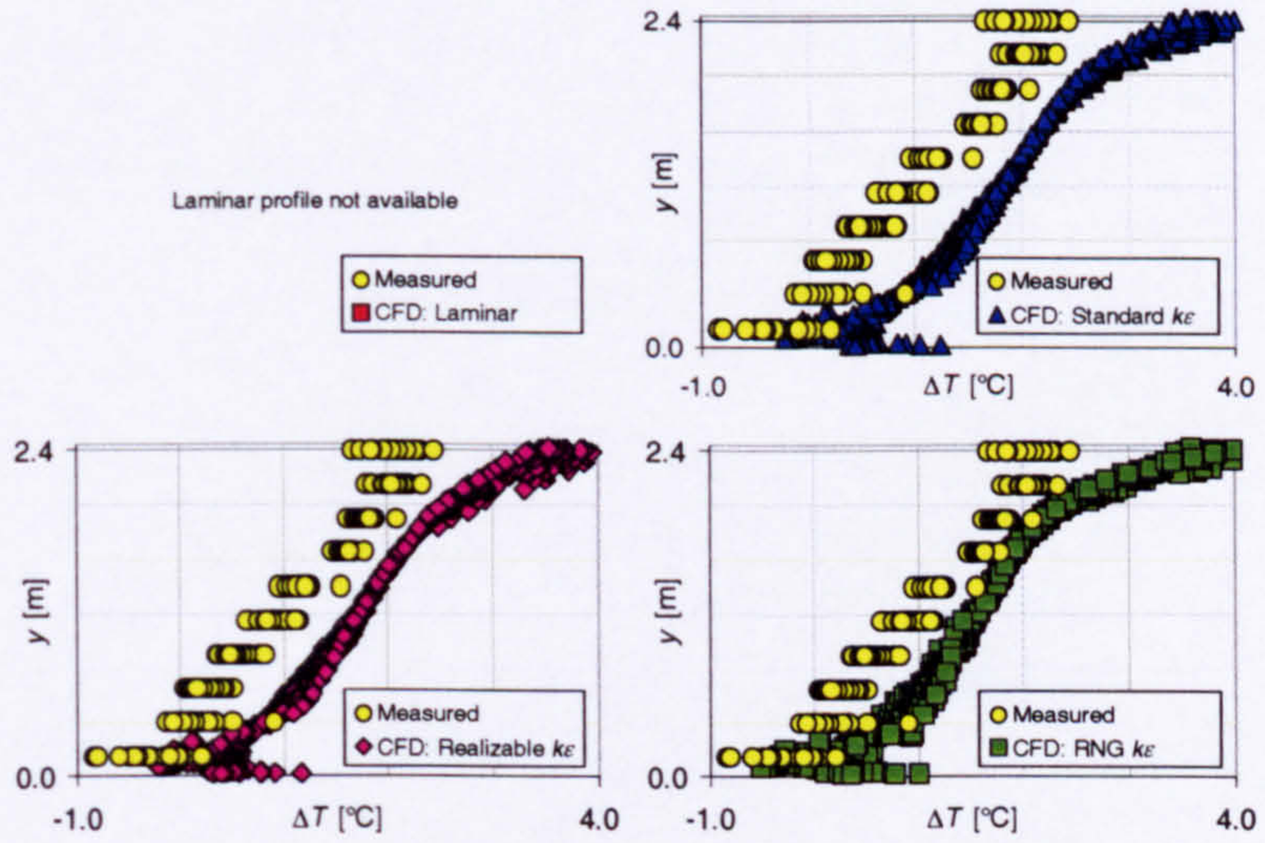

Figure 7.27 - Internal temperature profiles: 368.0W boiler ring; $A^* = 0.488m^2$; radiation model enabled, $\kappa = 0.0m^{-1}$; measured external temperature profile enforced at the domain extents; QUICK differencing employed for convection terms

7.3.2.1.3 Radiation model enabled, absorption of radiation throughout the fluid medium included ($\alpha \neq 0.0m^{-1}$)

For this opening configuration, the internal temperature profiles predicted with a uniform temperature imposed at the extents of the domain and with the radiation model enabled for each non-zero absorption coefficient considered ($\kappa = 0.05m^{-1}$, $\kappa = 0.05m^{-1}$ and $\kappa = 0.15m^{-1}$) are presented in Figure 7.28, Figure 7.29 and Figure 7.30 below, together with the measured profile.

Below a height of 2.0m, the main consequence of the application of a non-zero absorption coefficient is a variation in the predicted temperature rise of the surface of the floor; as the absorption coefficient is increased, the rise in the surface temperature of the floor is reduced. The rest of each profile remains essentially unchanged from the zero absorption coefficient profiles in this zone. The magnitude of the rise in temperature within the bulk of the space is over-predicted by approximately 1.0°C for the laminar and RNG-$k\varepsilon$ profiles, and by roughly 1.2°C for the standard-$k\varepsilon$ and realizable-$k\varepsilon$ profiles.

With a nonzero absorption coefficient, the standard-$k\varepsilon$ and realizable-$k\varepsilon$ profiles no longer predict an increase in the vertical temperature gradient in the layer below the ceiling. Furthermore, as the absorption coefficient is increased, the predicted surface temperature rise of the ceiling is observed to decrease, to the point where for $\kappa = 0.15\text{m}^{-1}$, the computed surface temperature of the ceiling is lower than that of the air in the layer flowing below the ceiling.

With a nonzero absorption coefficient, the laminar and RNG-$k\varepsilon$ profiles continue to predict an increase in the vertical temperature gradient in the layer below the ceiling, although the rise in temperature in this layer, together with the surface temperature of the ceiling, becomes less as the absorption coefficient is increased.

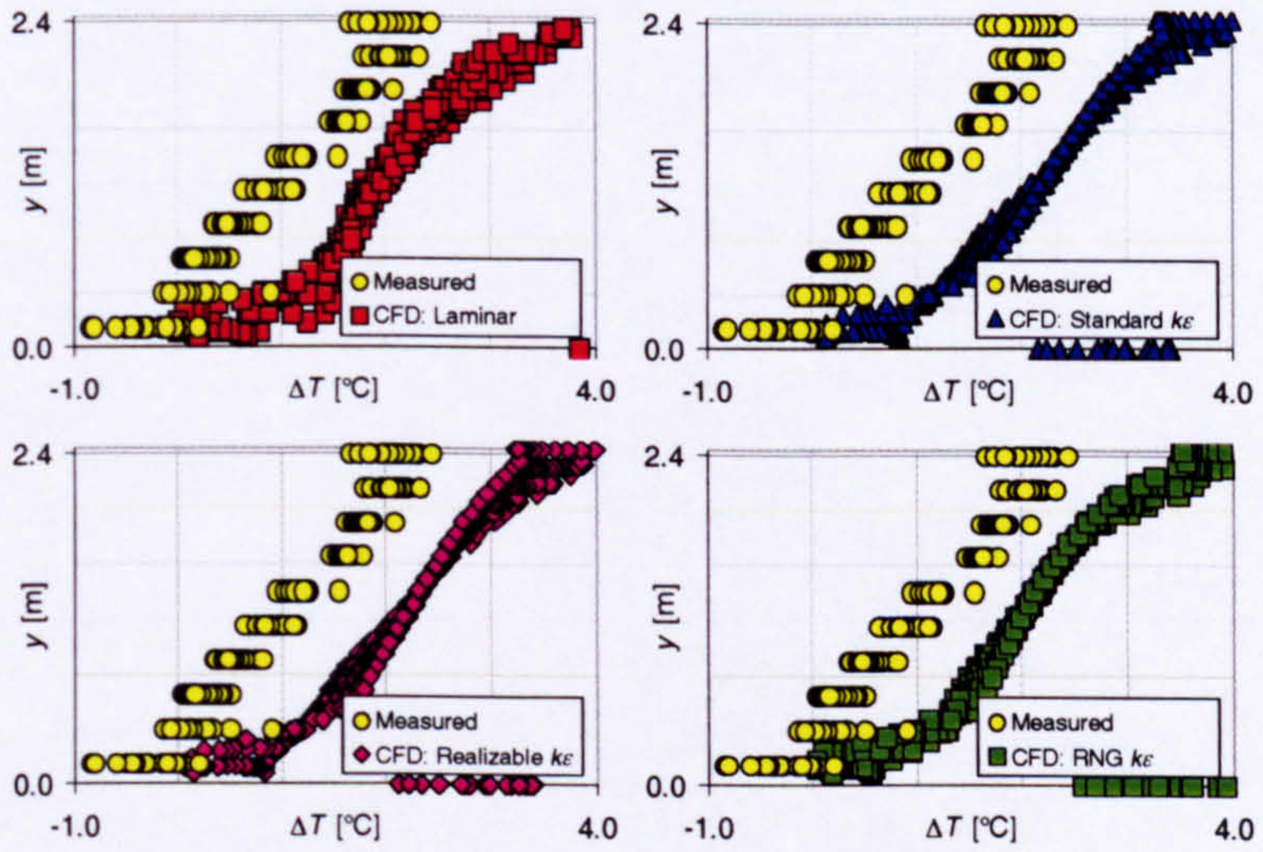

Figure 7.28 - Internal temperature profiles: 368.0W boiler ring; $A^* = 0.488\text{m}^2$; radiation model enabled, $\kappa = 0.05\text{m}^{-1}$; uniform external temperature at the domain extents; QUICK differencing employed for convection terms

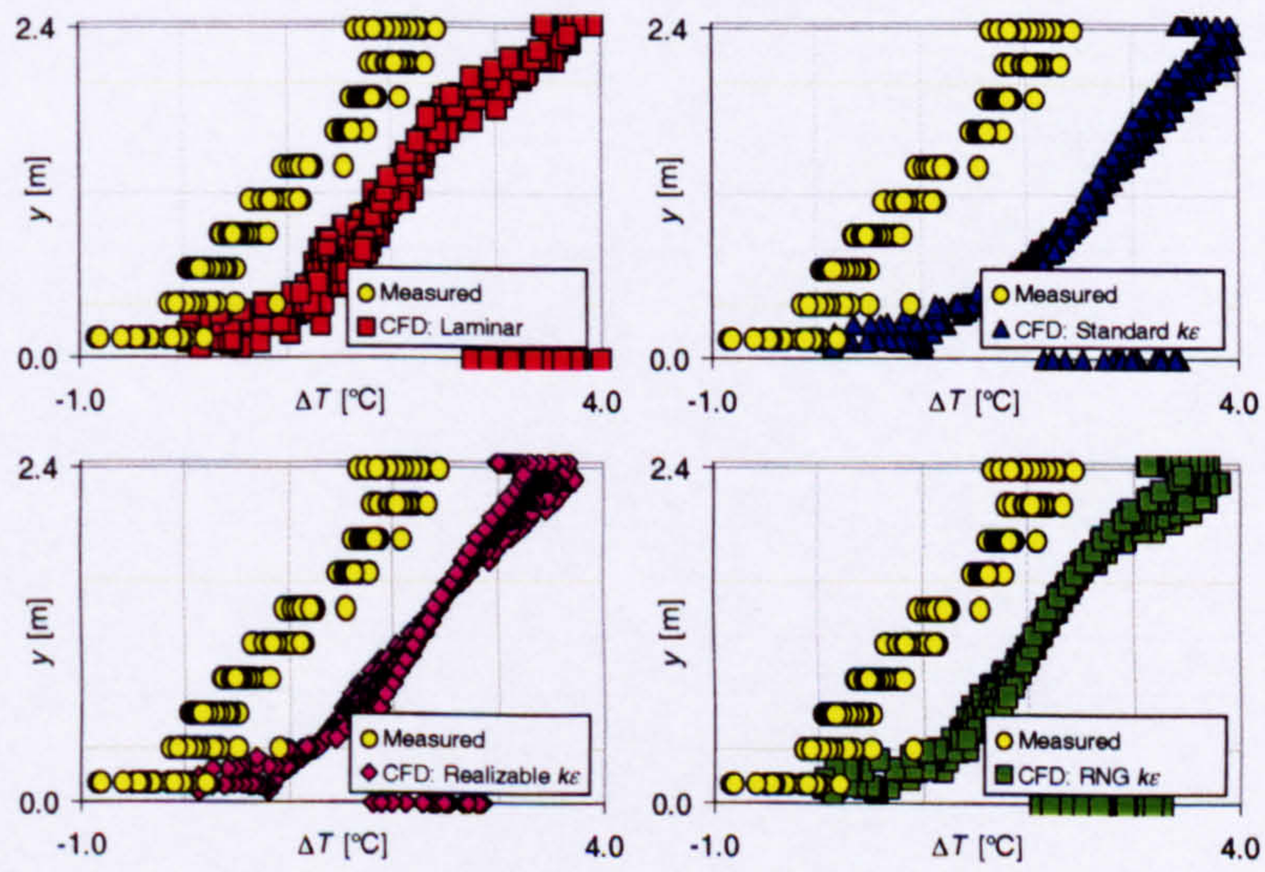

Figure 7.29 - Internal temperature profiles: 368.0W boiler ring; $A^* = 0.488\text{m}^2$; radiation model enabled, $\kappa = 0.10\text{m}^{-1}$; uniform external temperature at the domain extents; QUICK differencing employed for convection terms

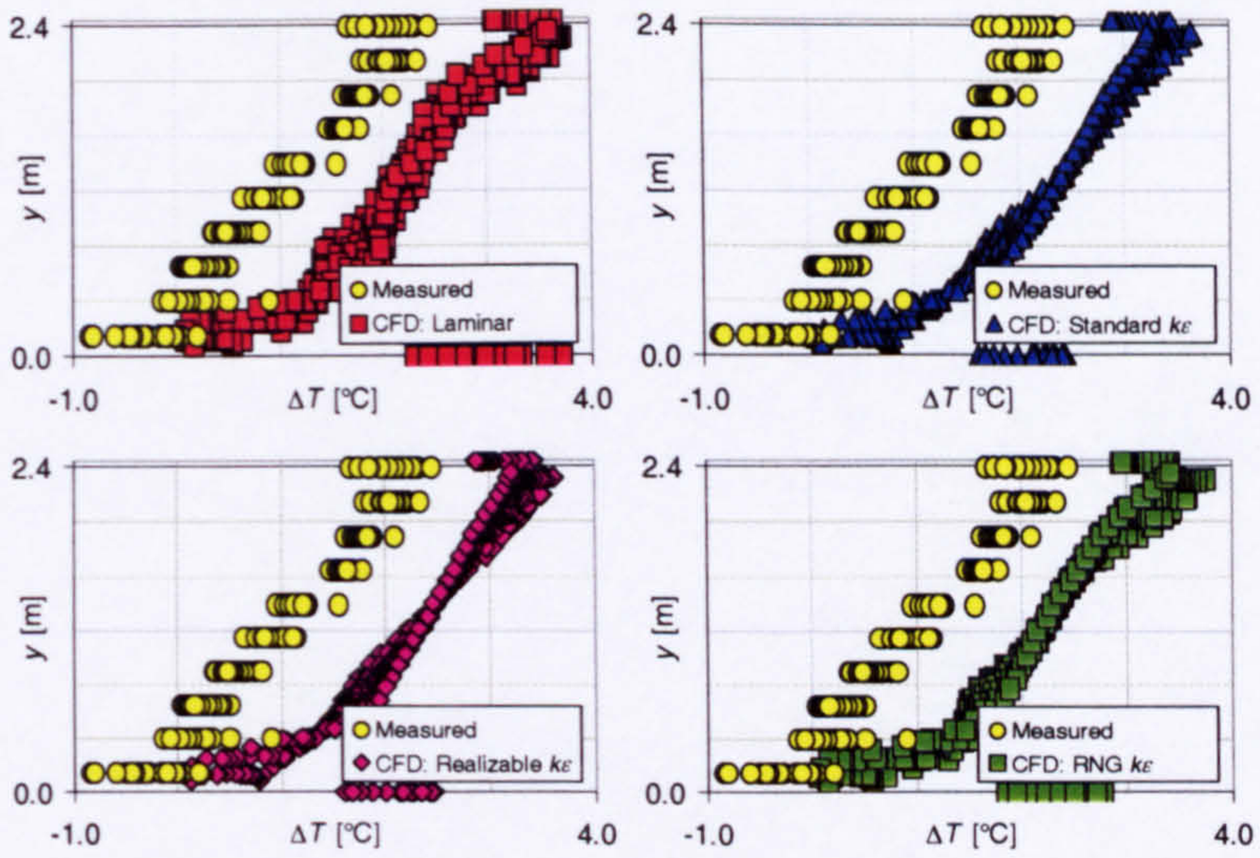

Figure 7.30 - Internal temperature profiles: 368.0W boiler ring; $A^* = 0.488m^2$; radiation model enabled, $\kappa = 0.15m^{-1}$; uniform external temperature at the domain extents; QUICK differencing employed for convection terms

The temperature profiles predicted with the measured external temperature imposed at the extents of the domain for each turbulence modelling approach considered are provided in Figure 7.31, Figure 7.32 and Figure 7.33 below, together with the measured temperature profile.

With the external stratification in place, improved agreement is observed between the measured profile and the CFD-profiles with regard to the magnitude of the temperature rise within the space: for the laminar and RNG-$k\varepsilon$ profiles, the predicted temperature rise within the space is within about 0.6°C of the measured profile for the bulk of the space, and for the standard-$k\varepsilon$ and realizable-$k\varepsilon$ profiles this difference is within 1.0°C.

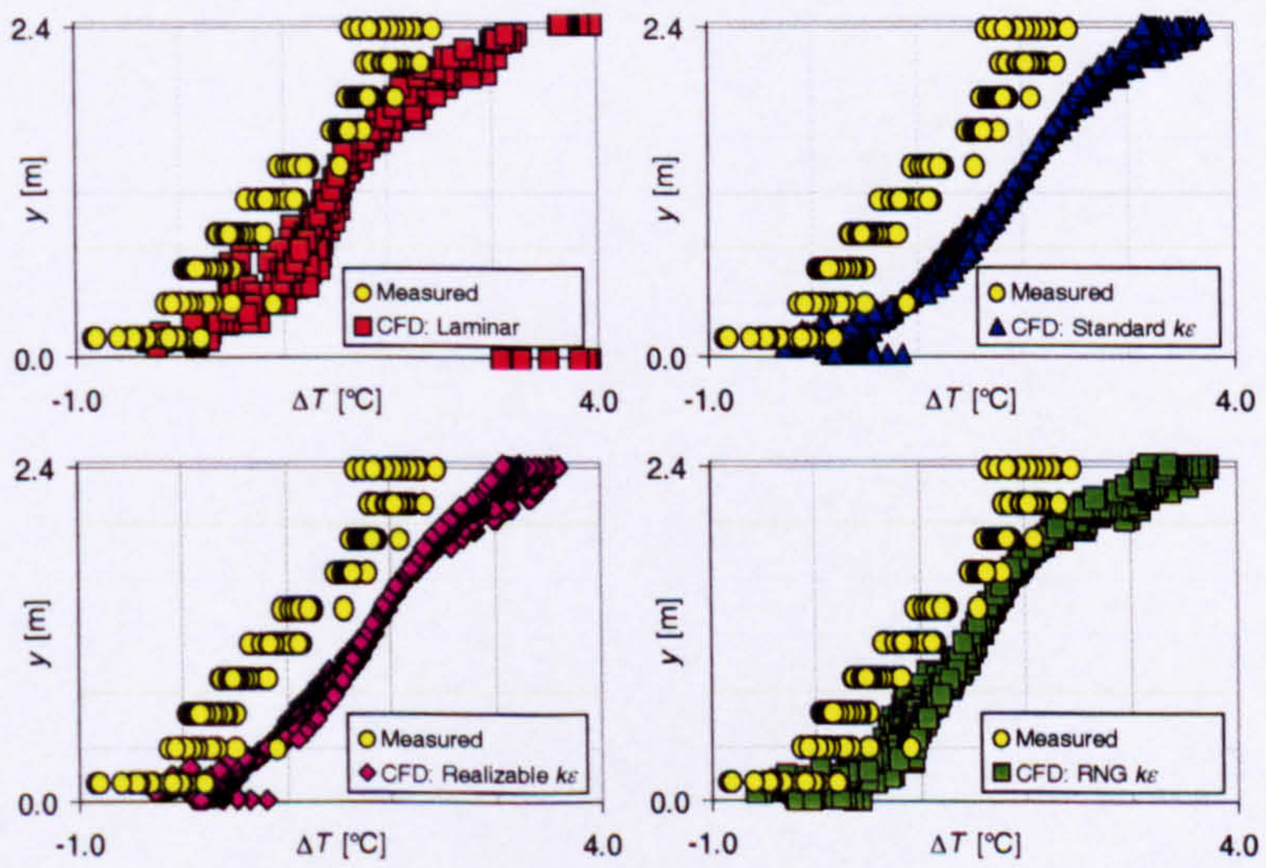

Figure 7.31 - Internal temperature profiles: 368.0W boiler ring; $A^* = 0.488m^2$; radiation model enabled, $\kappa = 0.05m^{-1}$; measured external temperature profile enforced at the domain extents; QUICK differencing employed for convection terms

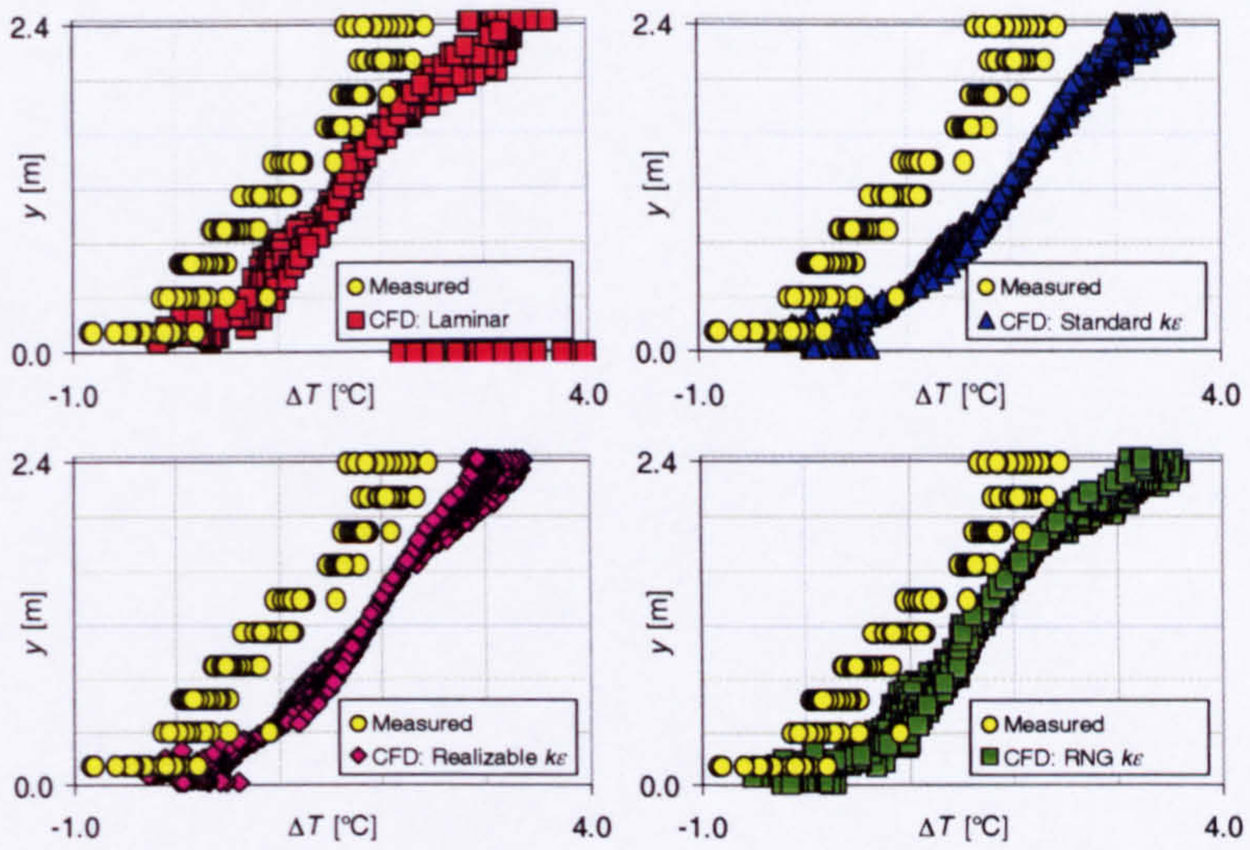

Figure 7.32 - Internal temperature profiles: 368.0W boiler ring; $A^* = 0.488m^2$; radiation model enabled, $\kappa = 0.10m^{-1}$; measured external temperature profile enforced at the domain extents; QUICK differencing employed for convection terms

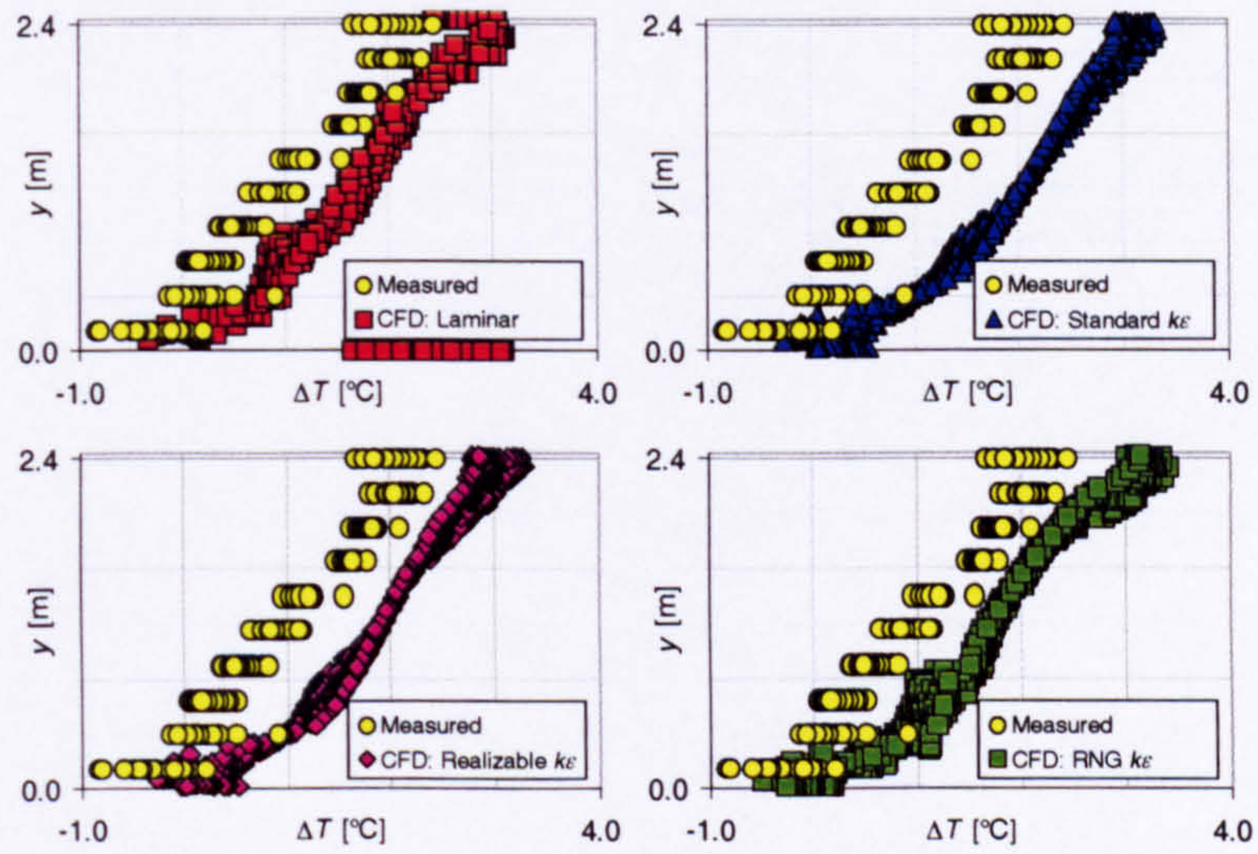

Figure 7.33 - Internal temperature profiles: 368.0W boiler ring; $A^* = 0.488m^2$; radiation model enabled, $\kappa = 0.15m^{-1}$; measured external temperature profile enforced at the domain extents; QUICK differencing employed for convection terms

7.3.2.2 Width of opening equal to 1.2m ($A^* = 0.732m^2$)

7.3.2.2.1 Radiation model disabled

The temperature profiles predicted with a constant external temperature imposed at the extents of the domain for this opening configuration with the radiation model disabled are provided in Figure 7.34 below, together with the measured temperature profile. The profiles were obtained using the first-order upwind differencing scheme.

The laminar and RNG-$k\varepsilon$ profiles predict a layer of ambient air extending from the floor up to a height of about 1.6m, with another layer above that extends to the ceiling

in which the vertical temperature remains constant, approximately equal to 6.0°C/m. Similarly, The realizable-$k\varepsilon$ profile predicts a layer of ambient air extending up to a height of about 1.4m, with a layer of air above that extends to the ceiling in which the vertical temperature is equal to 3.0°C/m.

The standard-$k\varepsilon$ profile comprises a layer of ambient air at low-level, a layer within the core of the space where the vertical temperature gradient is a maximum, and a layer at high-level, where the vertical temperature gradient is reduced. The depth of the layer of ambient air at low-level is about 1.3m, and the middle layer then extends to a height of roughly 1.7m. The temperature gradient within the middle layer is equal to about 4.0°C/m, with that in the layer above equal to roughly 1.5°C/m.

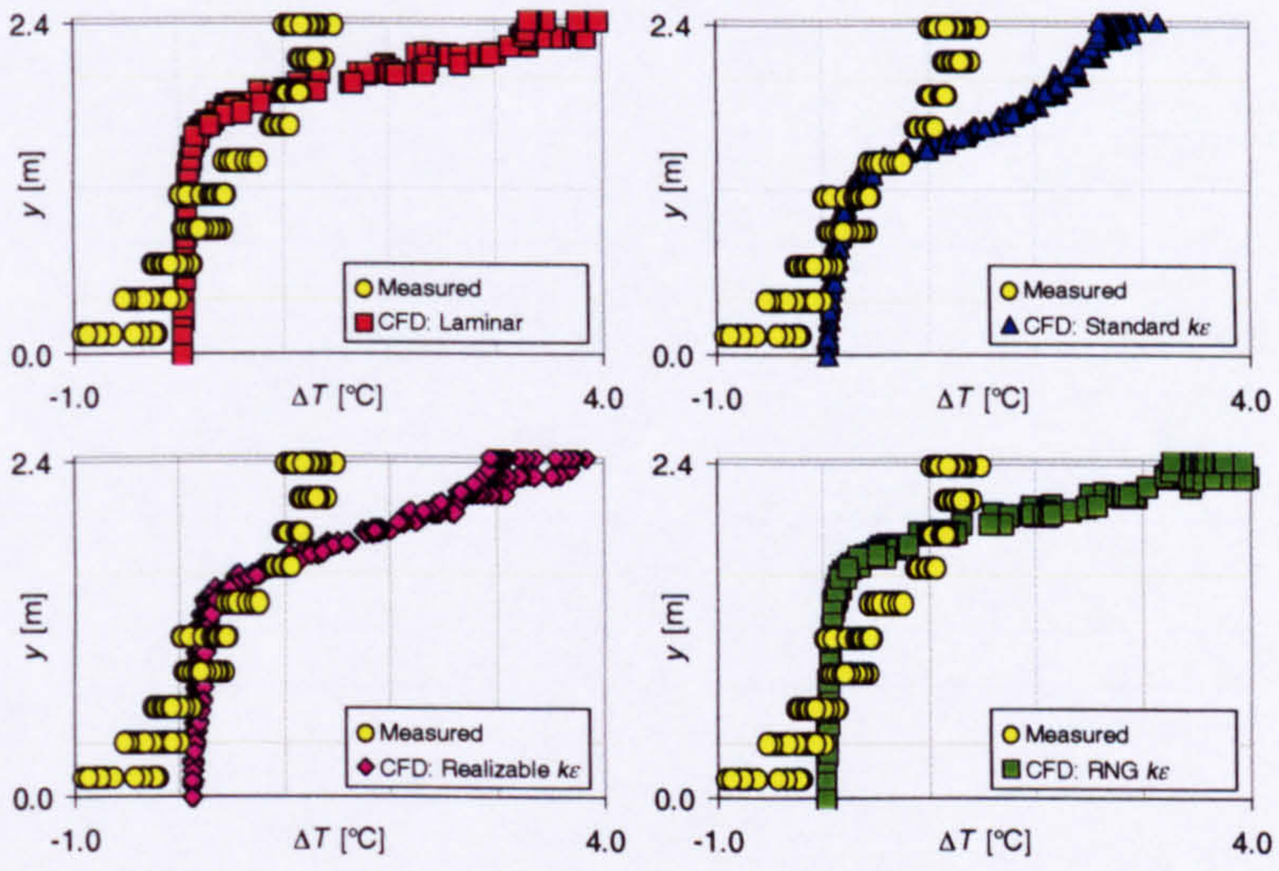

Figure 7.34 - Internal temperature profiles: 368.0W boiler ring; $A^* = 0.732m^2$; radiation model disabled; uniform external temperature at domain extents; first-order upwind differencing employed for convection terms

The temperature profile predicted with the measured external temperature imposed at the extents of the domain for each turbulence modelling approach considered is provided in Figure 7.35 below, together with the measured temperature profile.

The laminar and RNG-$k\varepsilon$ profiles still comprise two layers of air, an ambient layer at low-level, and a layer above in which the vertical temperature is 6.0°C/m. The height of the interface between the two layers is predicted to be slightly lower, however, at about 1.5m. The standard-$k\varepsilon$ profile remains three-layer, but the difference in the vertical temperature gradient between the two upper layers is more prominent: the gradient in the middle layer is about 5.0°C/m, and is equal to approximately 1.0°C/m in the upper layer. Due to the application of the external stratification, the temperature of the ambient layer of fluid at low-level is marginally

below that at the reference thermometer location for the laminar, RNG-$k\varepsilon$ and standard-$k\varepsilon$ profiles.

With the external stratification in place, the depth of the layer of ambient air at low-level predicted using the realizable-$k\varepsilon$ turbulence closure remains unchanged at 1.4m, and the temperature in this layer is the same as that predicted at the reference location. Above this, however, the profile exhibits two distinct layers, the first with a vertical temperature gradient of 5.0°C/m extending to a height of about 1.9m, and another layer above with a temperature gradient of roughly 2.0°C/m.

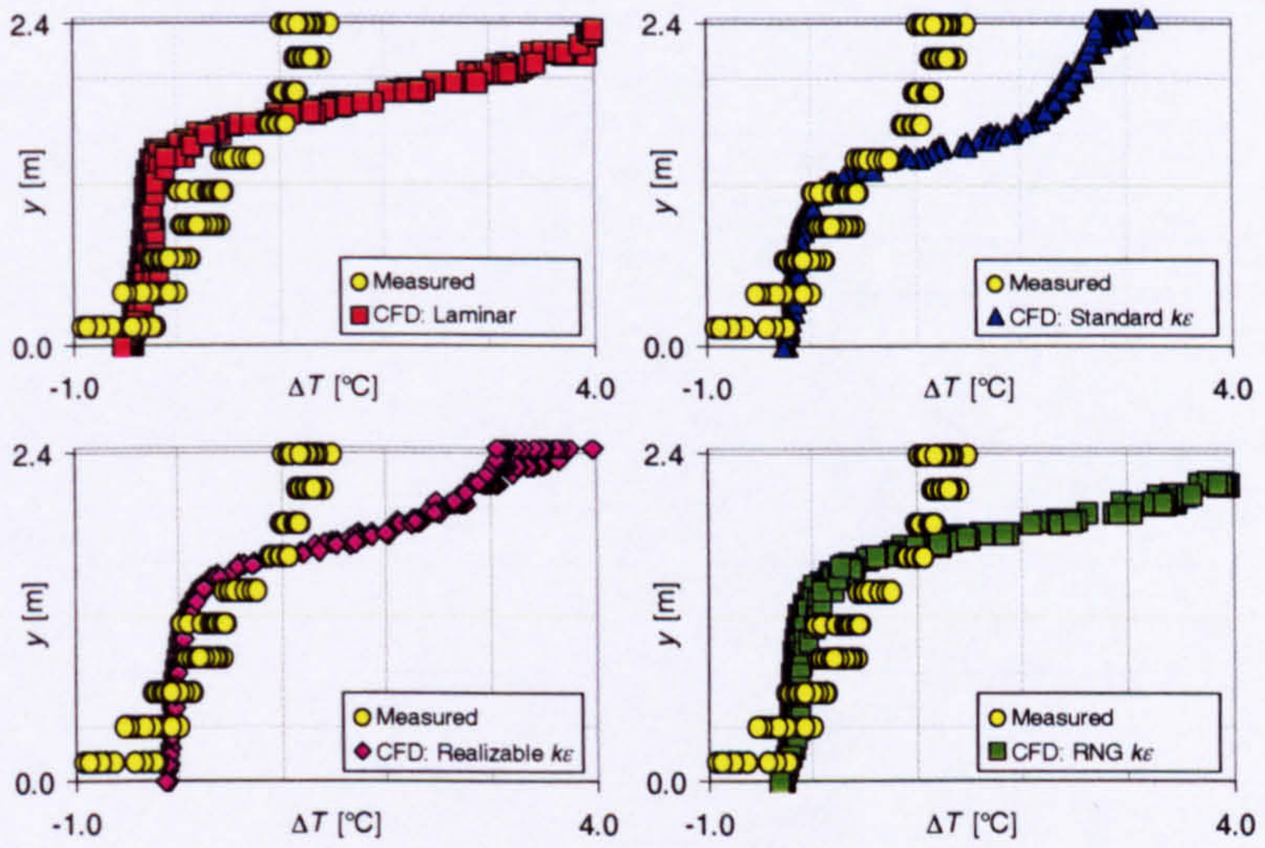

Figure 7.35 - Internal temperature profiles: 368.0W boiler ring; $A^* = 0.732m^2$; radiation model disabled; measured external stratification at domain extents; first-order upwind differencing employed for convection terms

7.3.2.2.2 Radiation model enabled, absorption of radiation throughout the fluid medium neglected ($\kappa = 0.0m^{-1}$)

The standard-$k\varepsilon$, realizable-$k\varepsilon$ and RNG-$k\varepsilon$ profiles computed using QUICK differencing with the radiation model enabled but neglecting absorption of radiation within the fluid medium for this opening configuration are presented in Figure 7.36 below, together with the measured temperature. Numerical convergence difficulties were experienced for the laminar case, and so a profile is not presented.

Once again, the predicted temperature of the surface of the floor is higher than the incoming air flowing over the floor with the radiation model enabled, due to thermal radiative transfer from the relatively warm ceiling. The predicted surface temperature of the floor is of the order of 4.0°C higher than the adjacent fluid for the RNG-$k\varepsilon$ case, and 3.0°C higher for the standard-$k\varepsilon$ and realizable-$k\varepsilon$ cases. For the RNG-$k\varepsilon$ profile, a small increase in the temperature rise in the layer just above the floor is evident in the profile presented, so that the heated layer of fluid that exists

immediately next to the floor is sufficiently thick to encompass the floor-adjacent nodes of the computational mesh. For the standard-$k\varepsilon$ and realizable-$k\varepsilon$ profiles the heated layer of fluid is not sufficiently thick to encompass the floor-adjacent nodes, so that the temperature rise appears to be roughly constant within say 0.3m of the floor.

Each of the profiles presented show a steep vertical temperature gradient equal to about 2.5°C/m at a height of 0.5m. Above this and throughout the bulk of the space, the gradient for each of the computed profiles is approximately equal to 0.8°C/m, which is similar to that for the measured experimental profile. The magnitude of the temperature rise predicted within the space, however, is over-predicted by approximately 1.2°C in this region when compared to the measured profile.

Each of the predicted profiles show a significant increase in the rate of change of temperature with respect to height in the layer of fluid immediately below the ceiling, which is not in agreement with the measured profile where it was observed to be approximately constant.

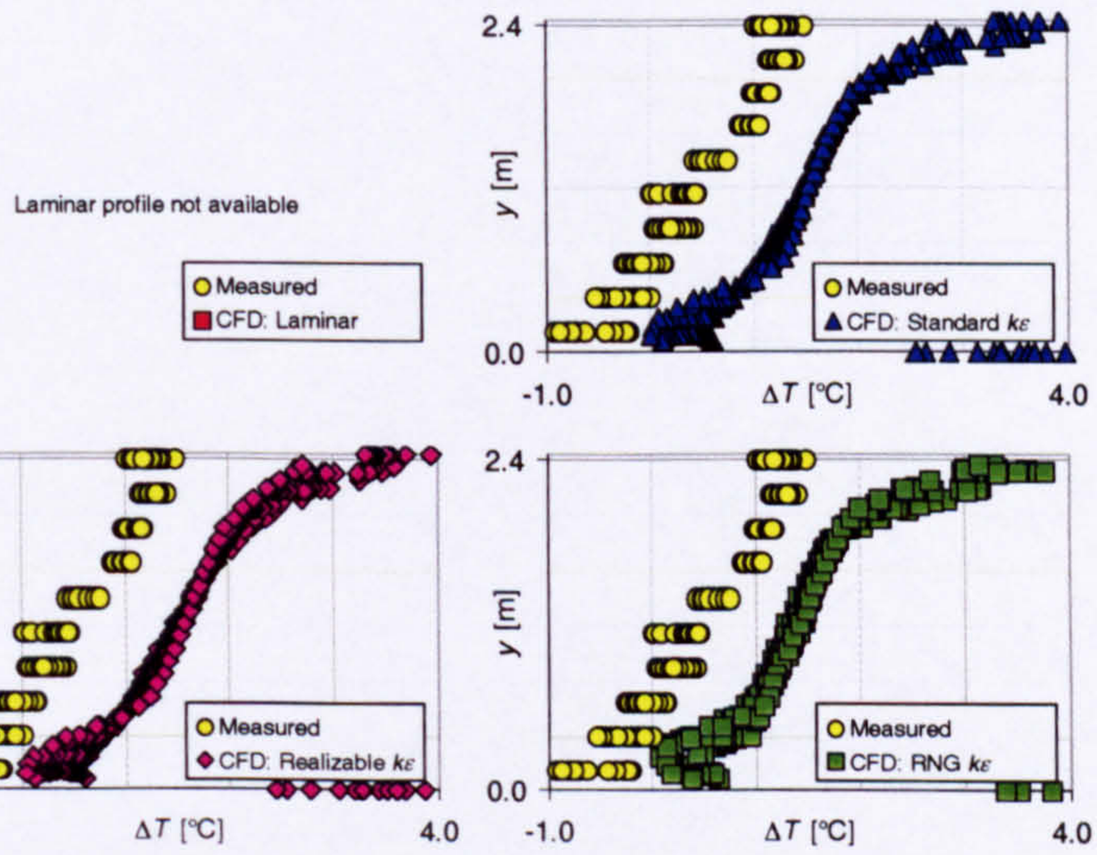

Figure 7.36 - Internal temperature profiles: 368.0W boiler ring; $A^* = 0.732m^2$; radiation model enabled, $\kappa = 0.0m^{-1}$; uniform external temperature at domain extents; QUICK differencing employed for convection terms

The temperature profiles predicted with the measured external temperature imposed at the extents of the domain for the standard-$k\varepsilon$, realizable-$k\varepsilon$ and RNG-$k\varepsilon$ turbulence modelling approaches are provided in Figure 7.37 below, together with the measured temperature profile.

It is observed that the application of the external stratification has had only a minor impact upon the predicted profiles of temperature rise within the space. The magnitude of the internal temperature rise for each CFD-profile is over-predicted by approximately 1.0°C within the central section of the space when compared to the

measured profile, which is a marginal improvement upon the predicted profiles obtained with a uniform temperature applied at the domain extents.

It is also apparent that for the RNG-$k\varepsilon$ profile, the heated layer of fluid immediately next to the floor is no longer deep enough to encompass the floor-adjacent nodes.

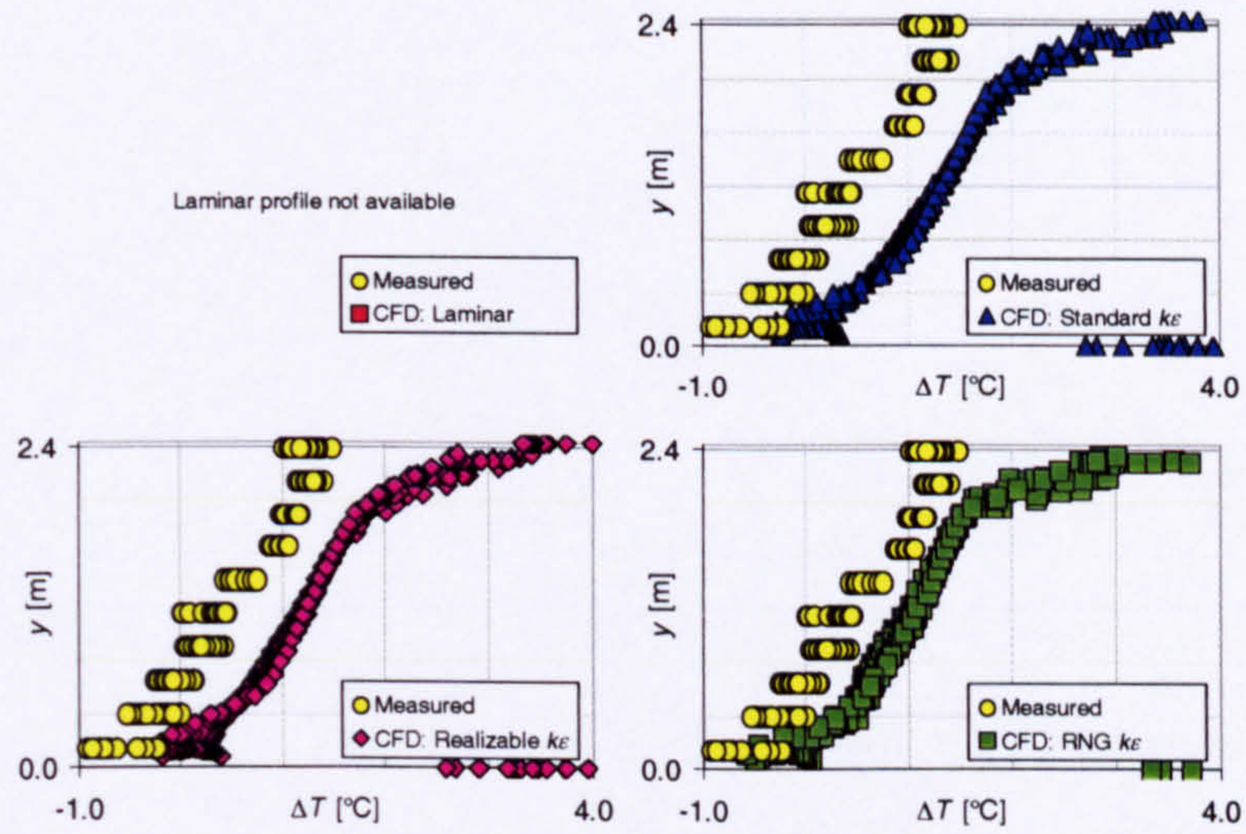

Figure 7.37 - Internal temperature profiles: 368.0W boiler ring; $A^* = 0.732m^2$; radiation model enabled, $\kappa = 0.0m^{-1}$; measured external stratification at domain extents; QUICK differencing employed for convection terms

7.3.2.2.3 Radiation model enabled, absorption of radiation throughout the fluid medium included ($\kappa \neq 0.0m^{-1}$)

The internal temperature profiles predicted for this opening configuration with a constant external temperature imposed at the extents of the domain and with the radiation model enabled for each non-zero absorption coefficient considered ($\kappa = 0.05m^{-1}$, $\kappa = 0.10m^{-1}$ and $\kappa = 0.15m^{-1}$) are presented in Figure 7.38, Figure 7.39 and Figure 7.40 below, together with the measured profile.

As the absorption coefficient κ is increased from zero, it is observed that the surface temperature of the ceiling is reduced. As a consequence, there is a fall in the amount of thermal radiative energy transferred from the surface of the ceiling to the surface of the floor, so that the surface temperature of the floor is also reduced. Consider, for example, the profiles predicted with the standard-$k\varepsilon$ turbulence closure. With the absorption coefficient $\kappa = 0.0m^{-1}$, the computed surface temperature rise of the ceiling is of the order of 4.0°C, and the surface temperature rise of the floor is roughly 3.5°C relative to the temperature at the reference thermometer location. With $\kappa = 0.05m^{-1}$, the predicted temperature rise at the surface of the ceiling is about 3.2°C, and that at the surface of the floor is say 2.8°C. With $\kappa = 0.10m^{-1}$, the predicted

temperature rise at the surface of the ceiling is about 2.8°C, and that at the surface of the floor is say 2.2°C. Finally, with $\kappa = 0.15\text{m}^{-1}$, the predicted temperature rise at the surfaces of the ceiling and the floor are approximately 2.5°C and 1.8°C respectively.

As a consequence of the fall in the predicted surface temperature at the ceiling, it is also observed that the vertical temperature gradient in the layer immediately beneath the ceiling is reduced as the absorption coefficient is increased. For each of the profiles with $\kappa = 0.05\text{m}^{-1}$, and for the laminar and RNG-$k\varepsilon$ profiles with $\kappa = 0.10\text{m}^{-1}$ and $\kappa = 0.15\text{m}^{-1}$, there remains apparent an increase in the vertical temperature gradient in the layer just below the ceiling, but this increase is less significant than for the cases where radiative absorption was neglected throughout the fluid medium. For the absorption coefficient $\kappa = 0.10\text{m}^{-1}$ and $\kappa = 0.15\text{m}^{-1}$, however, the standard-$k\varepsilon$ and realizable-$k\varepsilon$ profiles no longer show an increase in the vertical temperature gradient in the layer below the ceiling, which is in agreement with the measured profile.

Throughout the bulk of the space within the enclosure, each of the CFD-profiles predict the magnitude of the rise in temperature above the reference temperature to be of the order of 1.2°C greater than the measured temperature rise.

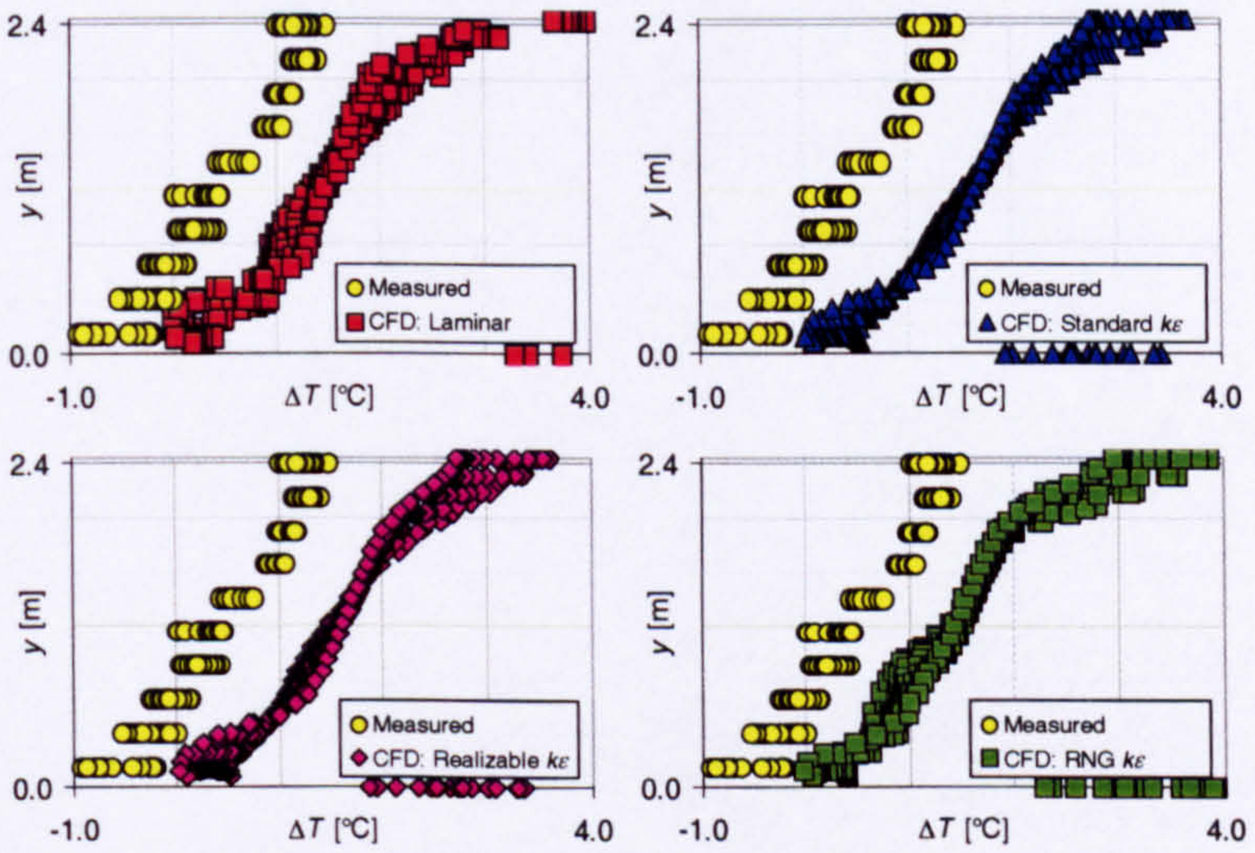

Figure 7.38 - Internal temperature profiles: 368.0W boiler ring; $A^* = 0.732\text{m}^2$; radiation model enabled, $\kappa = 0.05\text{m}^{-1}$; uniform external temperature at the domain extents; QUICK differencing employed for convection terms

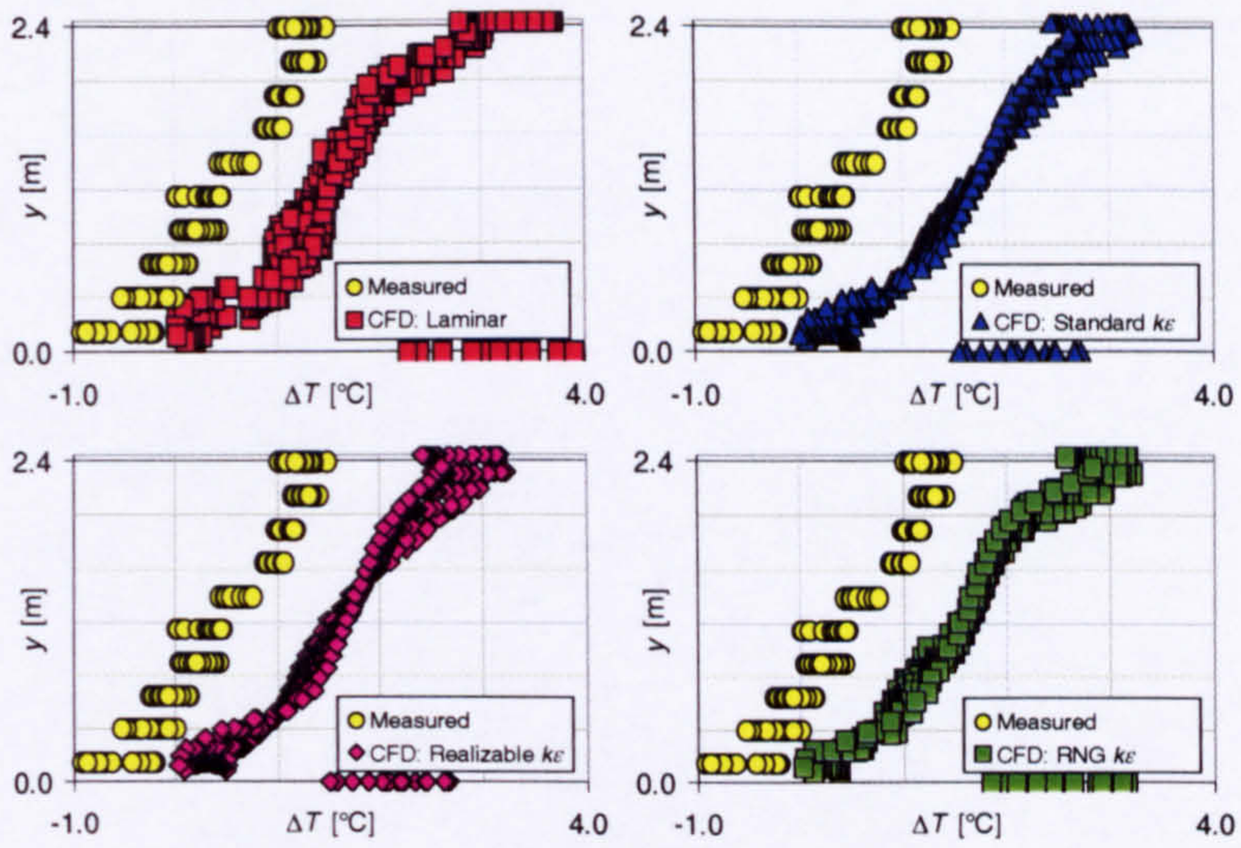

Figure 7.39 - Internal temperature profiles: 368.0W boiler ring; $A^* = 0.732m^2$; radiation model enabled, $\kappa = 0.10m^{-1}$; uniform external temperature at the domain extents; QUICK differencing employed for convection terms

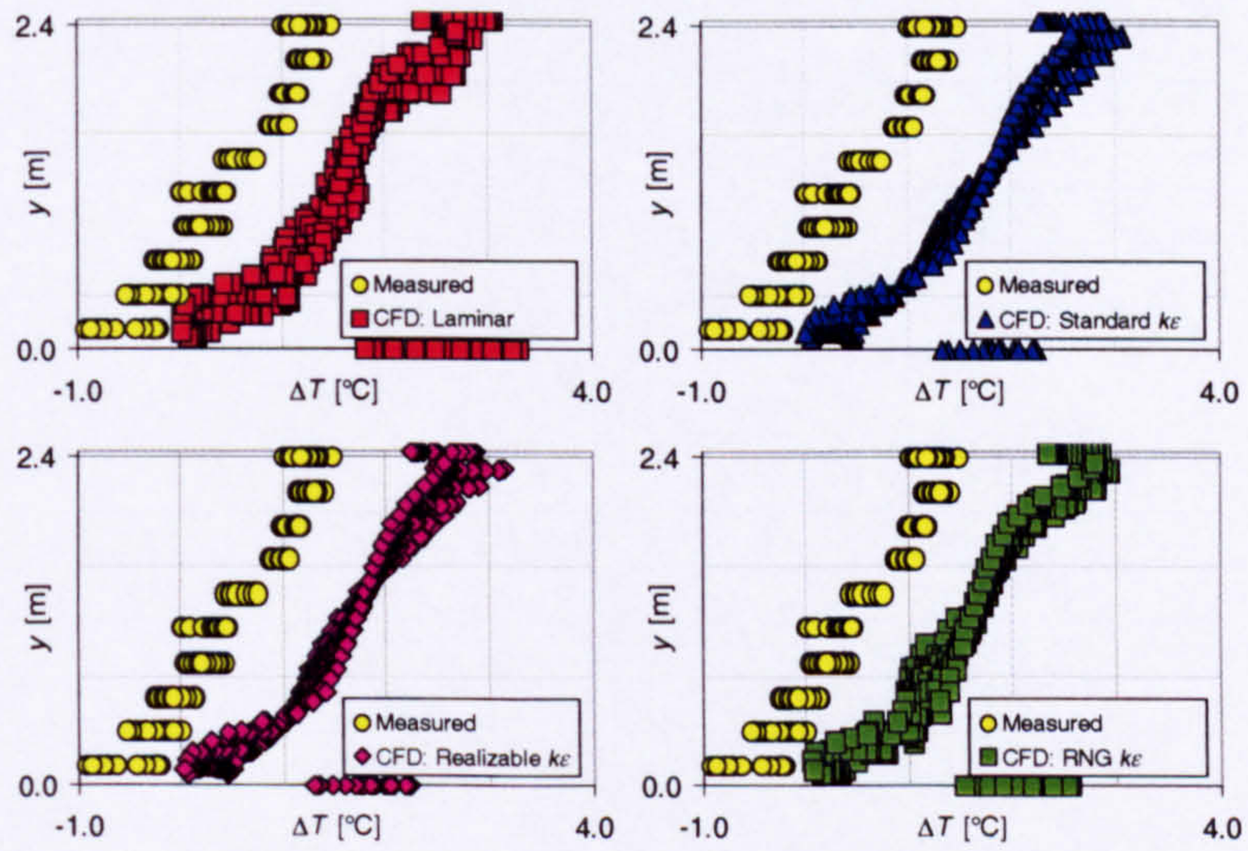

Figure 7.40 - Internal temperature profiles: 368.0W boiler ring; $A^* = 0.732m^2$; radiation model enabled, $\kappa = 0.15m^{-1}$; uniform external temperature at the domain extents; QUICK differencing employed for convection terms

The temperature profiles predicted with the measured external temperature imposed at the extents of the domain for each turbulence modelling approach considered are provided in Figure 7.41, Figure 7.42 and Figure 7.43 below, together with the measured temperature profile.

It is observed that the incorporation of the external stratification generally does not yield significant changes in the shape of the predicted CFD-profiles, a slight reduction in the surface temperature rise at the ceiling and at the floor for each of the profiles perhaps is the only difference. The magnitude of the temperature rise predicted above that at the reference thermometer location, however, does change. For the laminar and RNG-$k\varepsilon$ profiles the temperature rise within the space is

over-predicted by approximately 0.8°C, and for the standard-$k\varepsilon$ and realizable-$k\varepsilon$ profiles it is over-predicted by about 1.0°C.

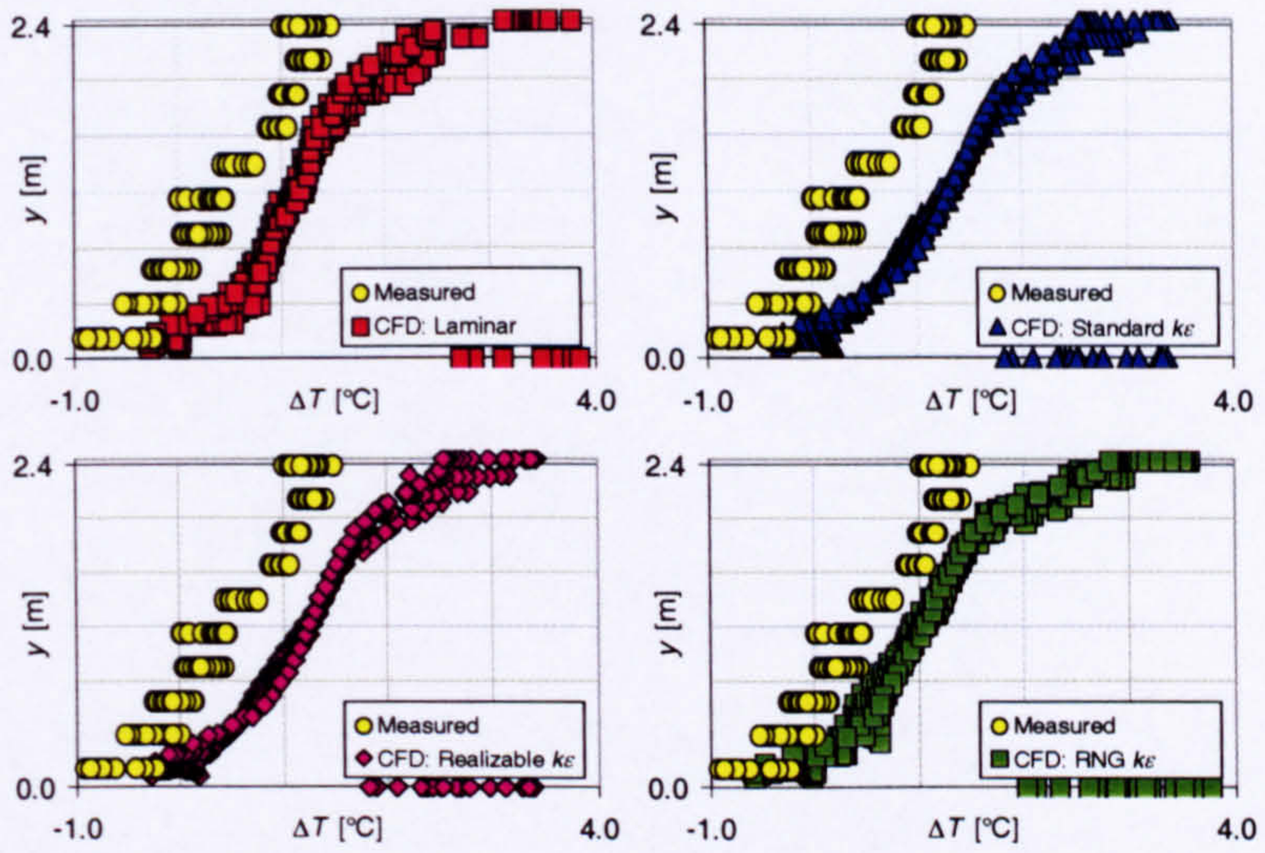

Figure 7.41 - Internal temperature profiles: 368.0W boiler ring; $A^* = 0.732m^2$; radiation model enabled, $\kappa = 0.05m^{-1}$; measured external temperature profile enforced at the domain extents; QUICK differencing employed for convection terms

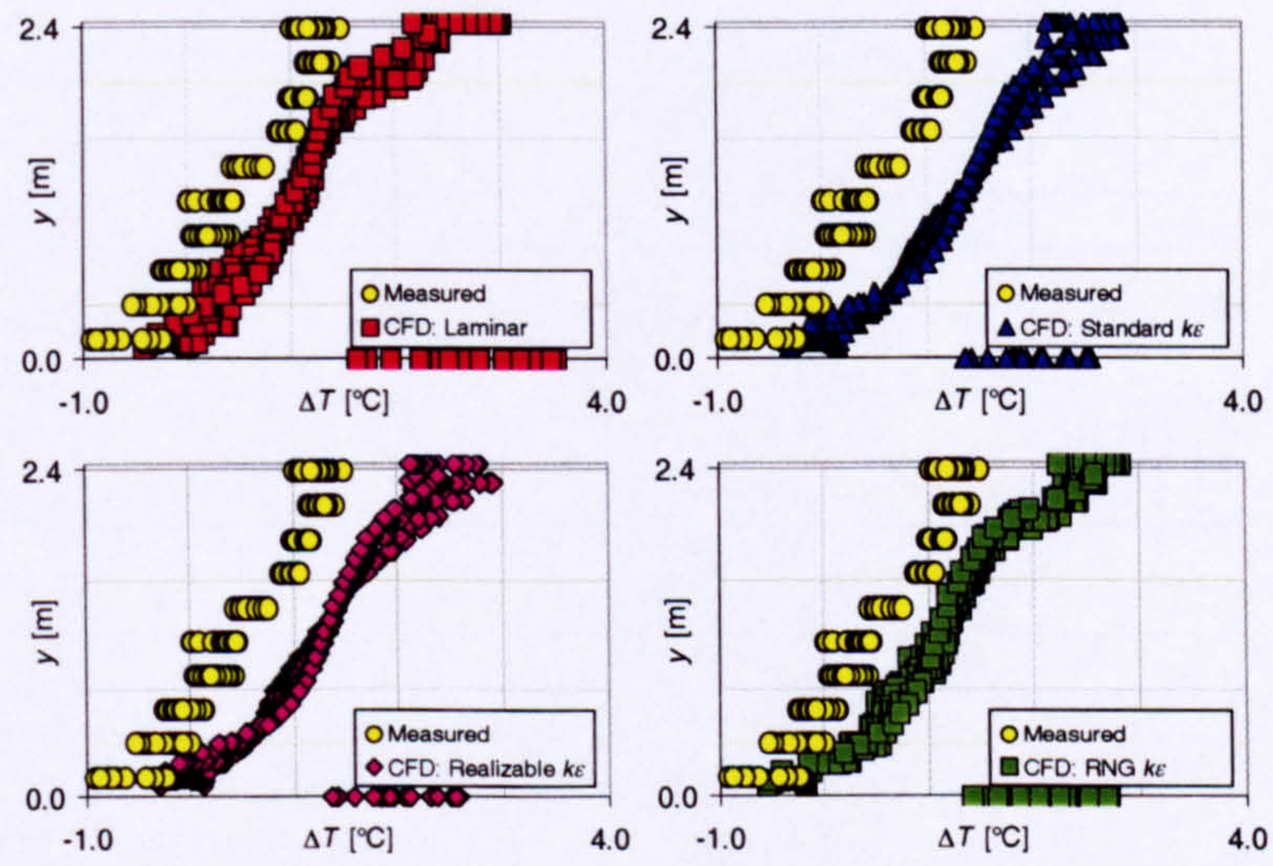

Figure 7.42 - Internal temperature profiles: 368.0W boiler ring; $A^* = 0.732m^2$; radiation model enabled, $\kappa = 0.10m^{-1}$; measured external temperature profile enforced at the domain extents; QUICK differencing employed for convection terms

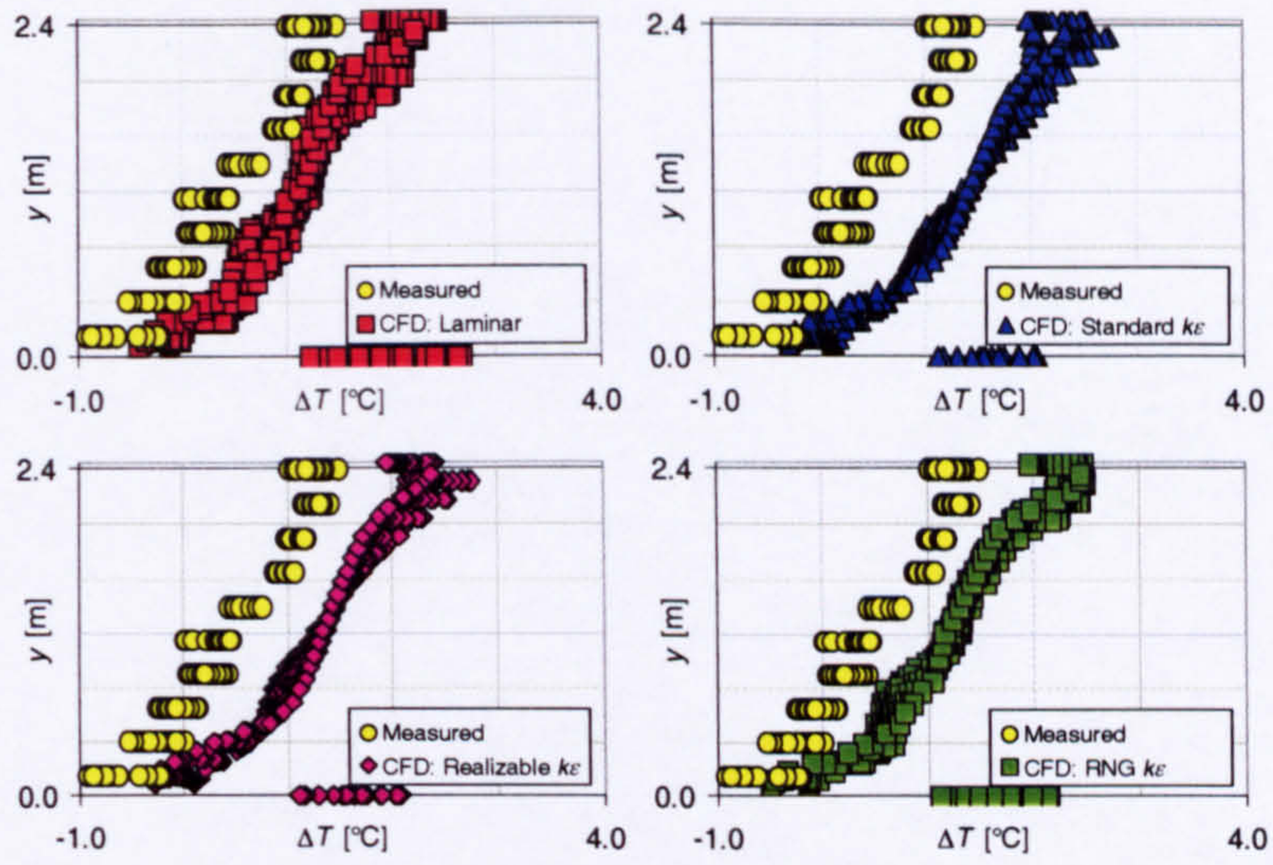

Figure 7.43 - Internal temperature profiles: 368.0W boiler ring; $A^* = 0.732m^2$; radiation model enabled, $\kappa = 0.15m^{-1}$; measured external temperature profile enforced at the domain extents; QUICK differencing employed for convection terms

7.3.3 Boiler ring with an output of 490.5W for various opening configurations

As for the previous two heater configurations, it was found that for the smaller openings the temperature rise within the enclosure was greatly over-predicted when the adiabatic approximation was employed at the walls to the enclosure, regardless of the turbulence modelling approach adopted. Once again, the agreement improved between the predicted temperature and that that had been measured within the space as the width of the openings was increased, as the adiabatic assumption for the walls of the enclosure became increasingly realistic for the larger opening configurations. When the heat-transfer coefficient at the internal surface of the enclosure walls was determined using the law of the wall, the rate of heat flux was once more greatly over-predicted so that the temperature rise calculated within the space was less than that measured during the experimental phase of this work for all opening configurations.

The predicted profiles for the temperature rise within the space for a width of opening of 0.8m and 1.2m, corresponding to an effective area of opening $A^* = 0.488m^2$ and $A^* = 0.732m^2$ respectively, with the adiabatic approximation enforced at the walls of the enclosure are discussed in detail in the sub-sections that follow.

7.3.3.1 Width of opening equal to 0.8m ($A^* = 0.488m^2$)

7.3.3.1.1 Radiation model disabled

The temperature profiles predicted with the adiabatic approximation at the enclosure walls and without the employment of the radiation model are provided in Figure 7.44 below, together with the measured temperature profile. The profiles were obtained using the first-order upwind differencing scheme.

The laminar and RNG-$k\varepsilon$ CFD-profiles comprise two distinct layers. The lower layer of air extends from the floor up to a height of about 1.5m and is at the same temperature as that predicted at the reference thermometer location. Above this there is a layer of air that extends to the ceiling in which the vertical temperature remains constant, approximately equal to 5.0°C/m.

The standard-$k\varepsilon$ and realizable-$k\varepsilon$ CFD-profiles are representative of three layers of air. The lower layer is predicted to be at the same temperature as the reference thermometer, and extends from the floor up to a height of 1.0m for the standard-$k\varepsilon$ profile and 1.2m for the realizable-$k\varepsilon$ profile. Above this, the middle layer extends to a height of 1.6m and 1.8m for the standard-$k\varepsilon$ and realizable-$k\varepsilon$ profiles respectively. The vertical temperature gradient within the middle layer is approximately equal to 4.5°C/m, compared to 1.2°C/m in the upper layer for the standard-$k\varepsilon$ profile. For the realizable-$k\varepsilon$, the vertical temperature gradient is equal to 6.0°C/m in the middle layer and 2.5°C/m in the upper layer.

The predicted standard-$k\varepsilon$ profile in particular may again be representative of two separate layers of well-mixed air, each at a uniform but different temperature, as described by the Cambridge mathematical model for natural displacement ventilation flows. Once again, however, this is not in agreement with the measured temperature profile from the experimental enclosure.

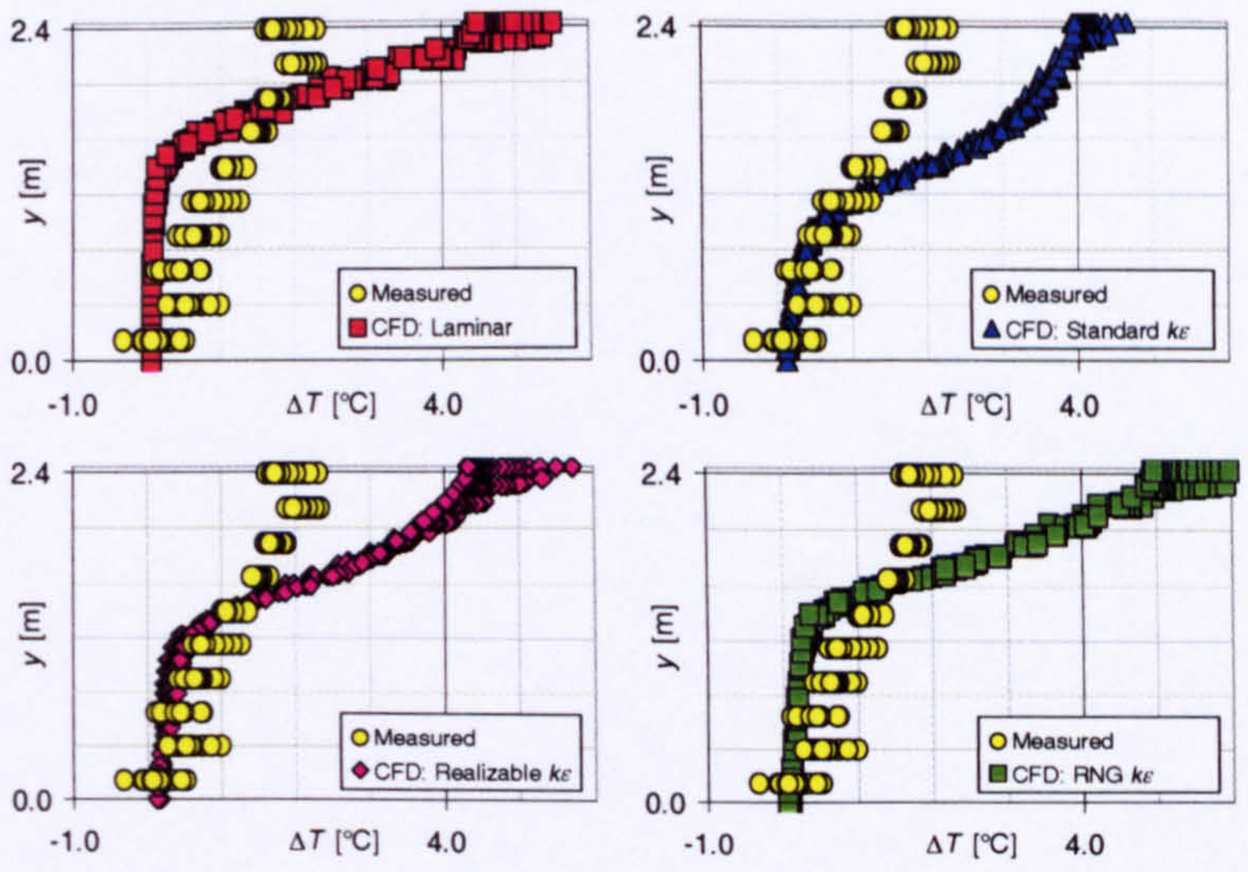

Figure 7.44 - Internal temperature profiles: 490.5W boiler ring; $A^* = 0.488m^2$; radiation model disabled; uniform external temperature enforced at the domain extents; first-order upwind differencing employed for convection terms

The temperature profile predicted with the measured external temperature imposed at the extents of the domain for each turbulence modelling approach considered is provided in Figure 7.45 below, together with the measured temperature profile.

For the laminar and RNG-$k\varepsilon$ profiles, it is observed that the layer predicted above the ambient air with the uniform external temperature in place has now become two distinct layers, so that each has become a three-layer profile. For each case, depth of the ambient layer of air remains unchanged at 1.5m, although the temperature within this layer is predicted to be approximately 0.2°C lower than that at the reference thermometer position. Above this, however, there is now a layer of air stretching to a height of about 1.9m in which the vertical temperature gradient is approximately equal to 10.0°C/m. Extending from the top of this layer to the ceiling is a further layer of fluid with a temperature gradient equal to about 3.0°C/m.

For the standard-$k\varepsilon$ and realizable-$k\varepsilon$ profiles, the divide between the upper two layers is more pronounced with the external stratification in place. The vertical temperature gradient is equal to 7.0°C/m in the middle layer and 1.0°C/m in the upper layer for the standard-$k\varepsilon$ profile, and is equal to about 10.0°C/m and 2.0°C/m in the middle and upper layer respectively for the realizable-$k\varepsilon$ profile. The height of the interface between the middle layer and the upper layer is 1.6m and 1.7m for the standard-$k\varepsilon$ and realizable-$k\varepsilon$ cases respectively.

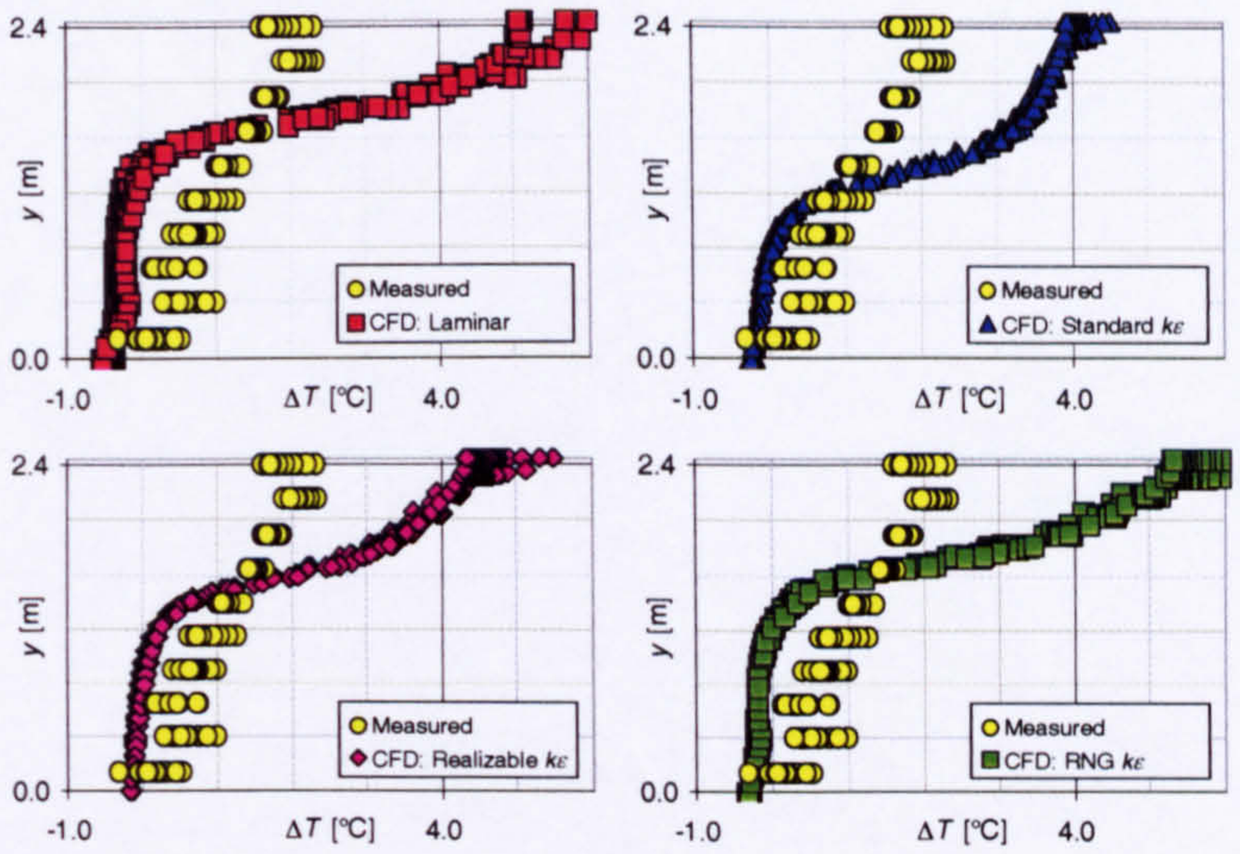

Figure 7.45 - Internal temperature profiles: 490.5W boiler ring; $A^* = 0.488m^2$; radiation model disabled; measured external temperature profile enforced at the domain extents; first-order upwind differencing employed for convection terms

7.3.3.1.2 Radiation model enabled, absorption of radiation throughout the fluid medium neglected ($\kappa = 0.0m^{-1}$)

The predicted profiles for the rise in temperature within the space using QUICK differencing with the radiation model enabled but neglecting absorption of radiation within the fluid medium for this opening configuration are presented in Figure 7.46 below, together with the measured temperature profile. Only the standard-$k\varepsilon$, realizable-$k\varepsilon$ and RNG-$k\varepsilon$ profiles are provided: numerical convergence difficulties were experienced for the laminar case, and so a profile is not presented.

Once again, enabling the radiation model yields a significant improvement in the agreement between the computed profiles and the measured profile. With the radiation model employed, the vertical temperature gradient within much of the central section of the space is equal to 1.0°C/m for each of the computed profiles, as it is for the measured profile. The actual rise in temperature, however, is over-predicted by approximately 1.0°C throughout the entire space for each of the predicted profiles.

A temperature rise of the order of 3.0°C to 4.0°C above that at the reference thermometer location is predicted at the surface of the floor when the standard-$k\varepsilon$ or realizable-$k\varepsilon$ turbulence closure is used, compared with a rise of 4.0°C to 5.0°C with the RNG-$k\varepsilon$ model. Each CFD-profile, however, shows the temperature rise to be roughly constant in the layer within 0.3m of the floor, so that the floor-adjacent nodes of the computational mesh must be outside of the thin heated layer of fluid at the surface of the floor.

Each of the computed profiles predict an increase in the vertical temperature gradient at two distinct elevations: between the heights of 0.3m and 0.6m, each profile shows the gradient to be approximately equal to 3.0°C/m, and in the region within 0.3m of the ceiling it is predicted to be about 4.0°C/m. The measured profile, however, exhibits no such increase in the vertical gradient of temperature at either elevation.

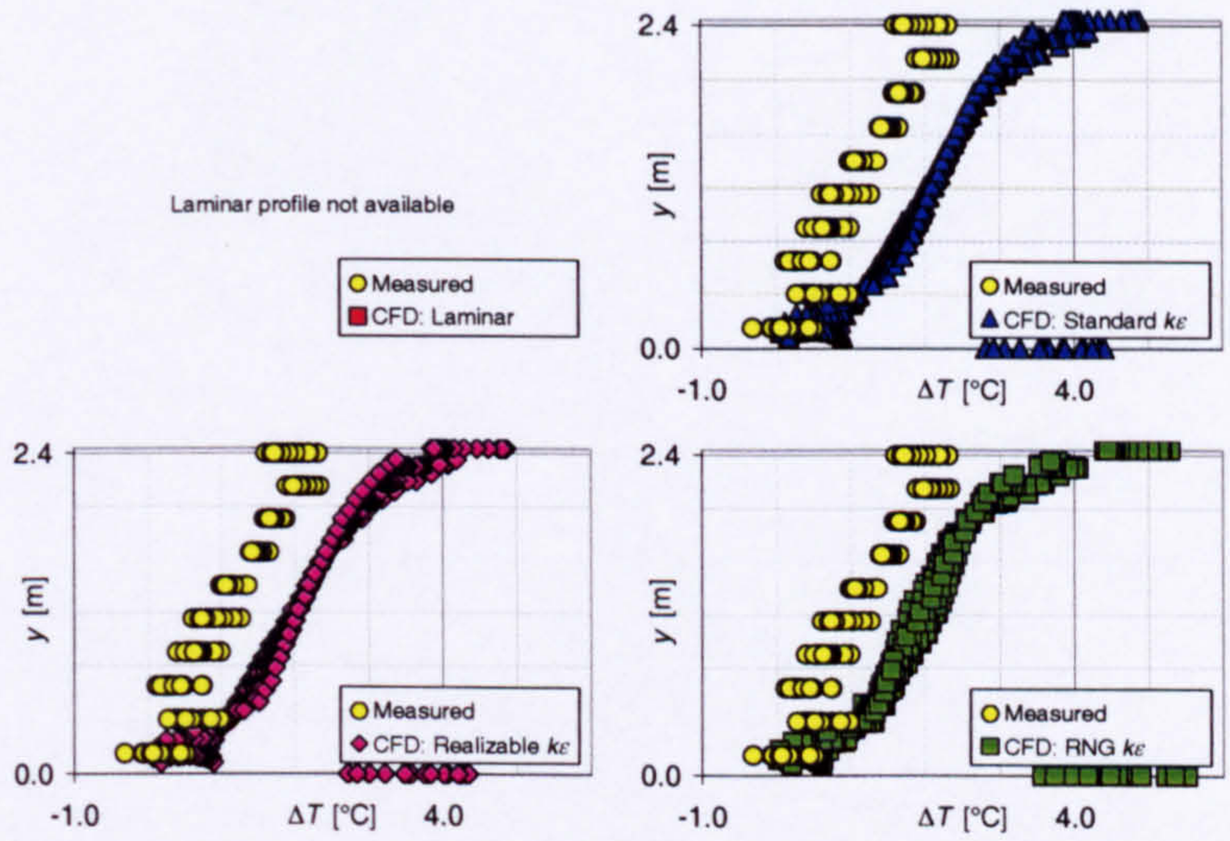

Figure 7.46 - Internal temperature profiles: 490.5W boiler ring; $A^* = 0.488m^2$; radiation model enabled, $\kappa = 0.0m^{-1}$; uniform external temperature at domain extents; QUICK differencing employed for convection terms

The CFD-profiles for the internal temperature rise with the measured external stratification imposed at the extents of the domain are provided in Figure 7.47 below, together with the measured temperature profile. Once again, the laminar profile is not presented.

It is observed that the computed profiles are almost unaffected by the application of the external stratification at the domain extents: the temperature rise predicted at the surface of the floor remains unchanged, but there is a marginal improvement in the magnitude of the computed internal temperature rise, which is over-predicted by approximately 0.8°C throughout the entire space for the standard-$k\varepsilon$ and realizable-$k\varepsilon$ profiles, and by about 0.5°C for the RNG-$k\varepsilon$ profile.

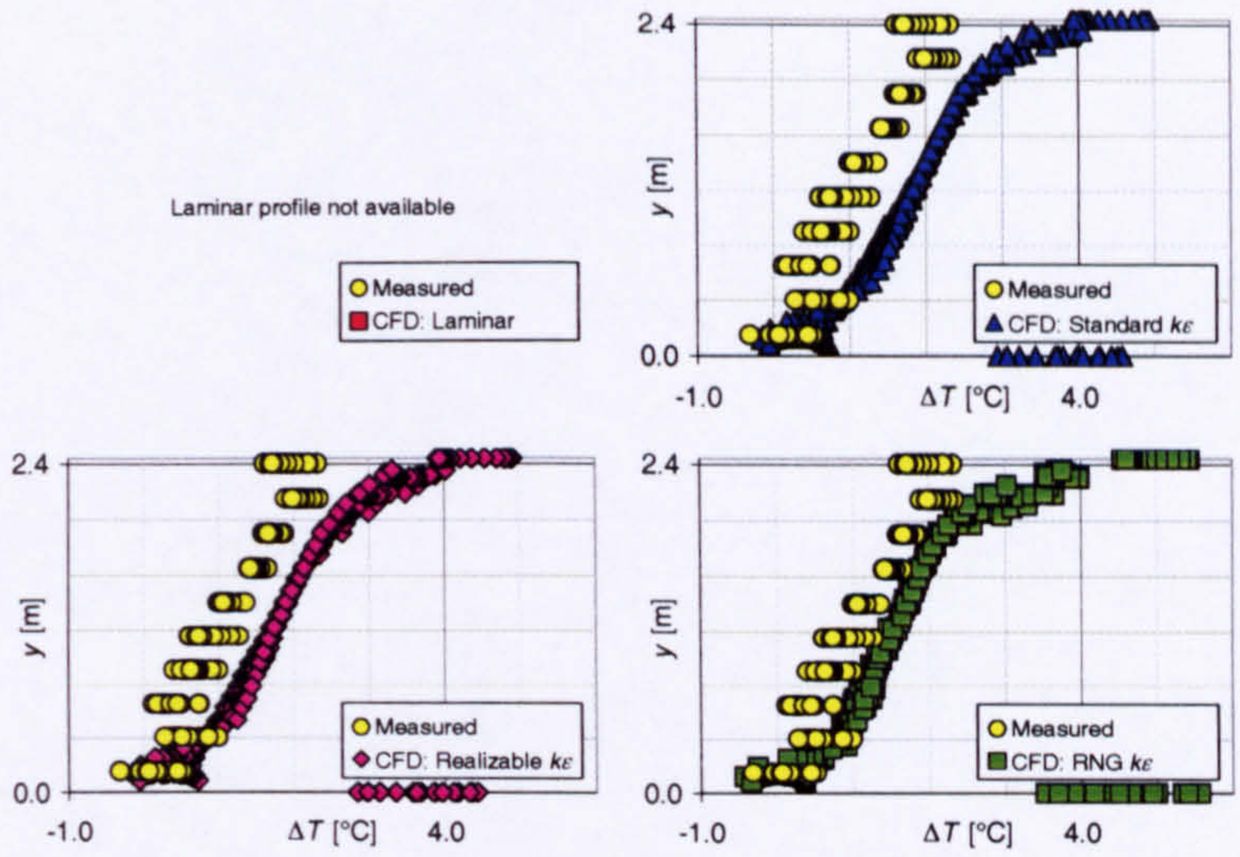

Figure 7.47 - Internal temperature profiles: 490.5W boiler ring; $A^* = 0.488m^2$; radiation model enabled, $\kappa = 0.0m^{-1}$; measured external stratification at domain extents; QUICK differencing employed for convection terms

7.3.3.1.3 Radiation model enabled, absorption of radiation throughout the fluid medium included ($\kappa \neq 0.0m^{-1}$)

The internal temperature profiles predicted for this opening configuration with a constant external temperature imposed at the extents of the domain and with the radiation model enabled for each non-zero absorption coefficient considered are presented in Figure 7.48, Figure 7.49 and Figure 7.50 below, together with the measured profile.

It is observed that the surface temperature of the ceiling is reduced as the radiative absorption coefficient is increased, with a corresponding fall in the surface temperature of the floor. Furthermore, the increase in the vertical temperature gradient in the layer immediately below the ceiling becomes less apparent as the absorption coefficient κ is increased. With $\kappa = 0.05m^{-1}$, in the layer within 0.3m of the ceiling there is a rise in temperature of about 0.5°C for the standard-$k\varepsilon$ and realizable-$k\varepsilon$ profiles and 0.7°C for the RNG-$k\varepsilon$ profile, compared to 1.0°C and 1.5°C respectively for each profile with a zero absorption coefficient. With $\kappa = 0.10m^{-1}$, there is no significant rise in temperature in the layer within 0.3m of the ceiling for the standard-$k\varepsilon$, realizable-$k\varepsilon$ and RNG-$k\varepsilon$ profiles, although there is an increase of 0.5°C predicted in this zone for the laminar profile.

The magnitude of the rise in temperature above that at the reference location is over-predicted by approximately 1.0°C throughout the central section of the space for the laminar and RNG-$k\varepsilon$ profiles, and by about 1.2°C for the standard-$k\varepsilon$ and realizable-$k\varepsilon$ profiles.

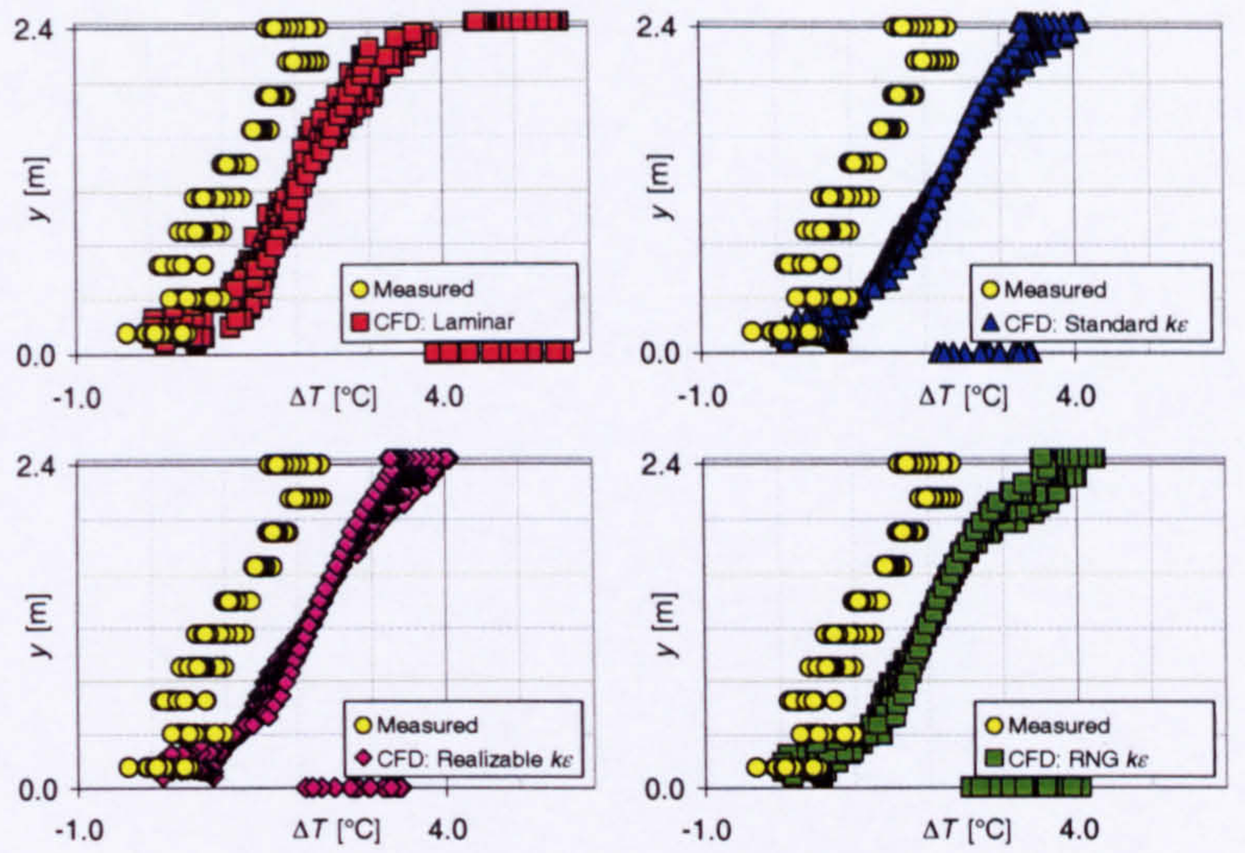

Figure 7.48 - Internal temperature profiles: 490.5W boiler ring; $A^* = 0.488m^2$; radiation model enabled, $\kappa = 0.05m^{-1}$; uniform external temperature at the domain extents; QUICK differencing employed for convection terms

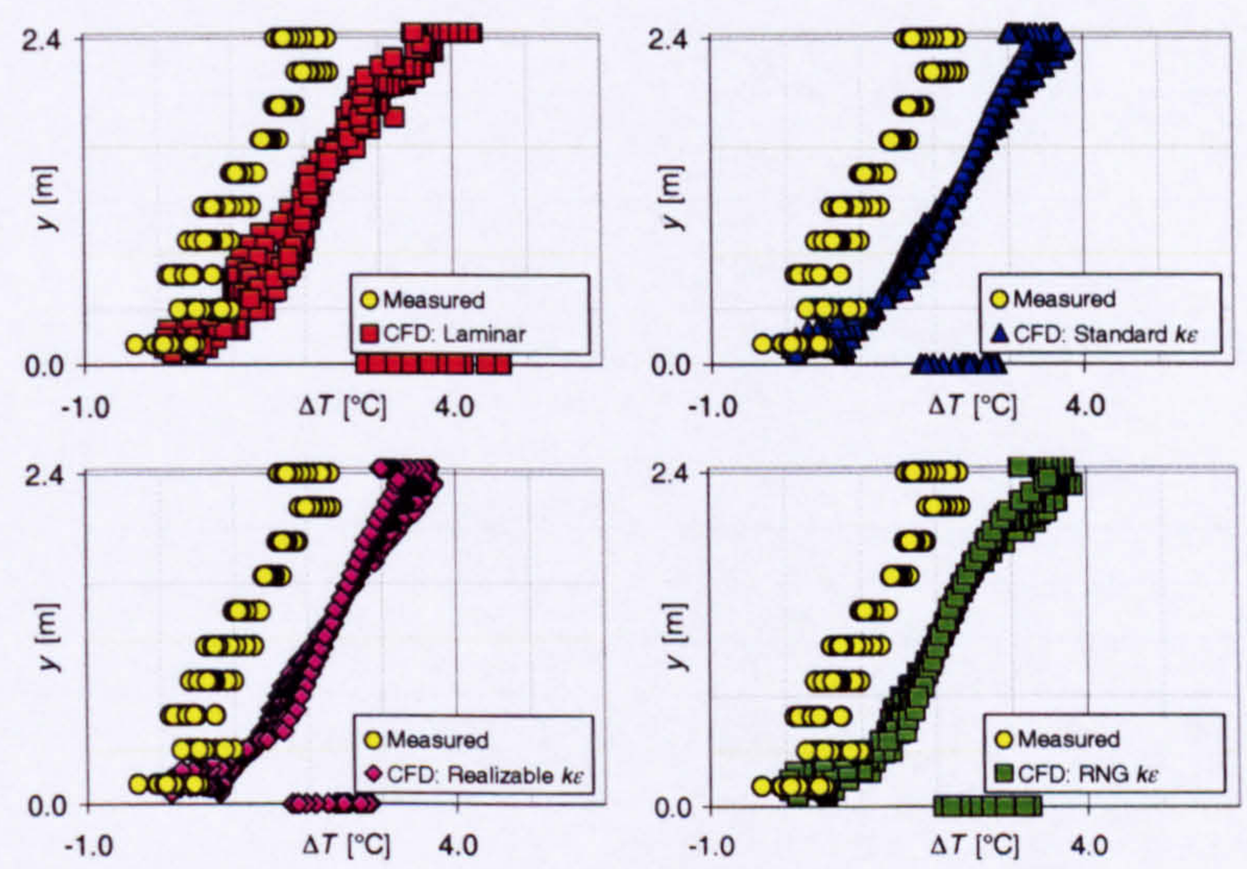

Figure 7.49 - Internal temperature profiles: 490.5W boiler ring; $A^* = 0.488m^2$; radiation model enabled, $\kappa = 0.10m^{-1}$; uniform external temperature at the domain extents; QUICK differencing employed for convection terms

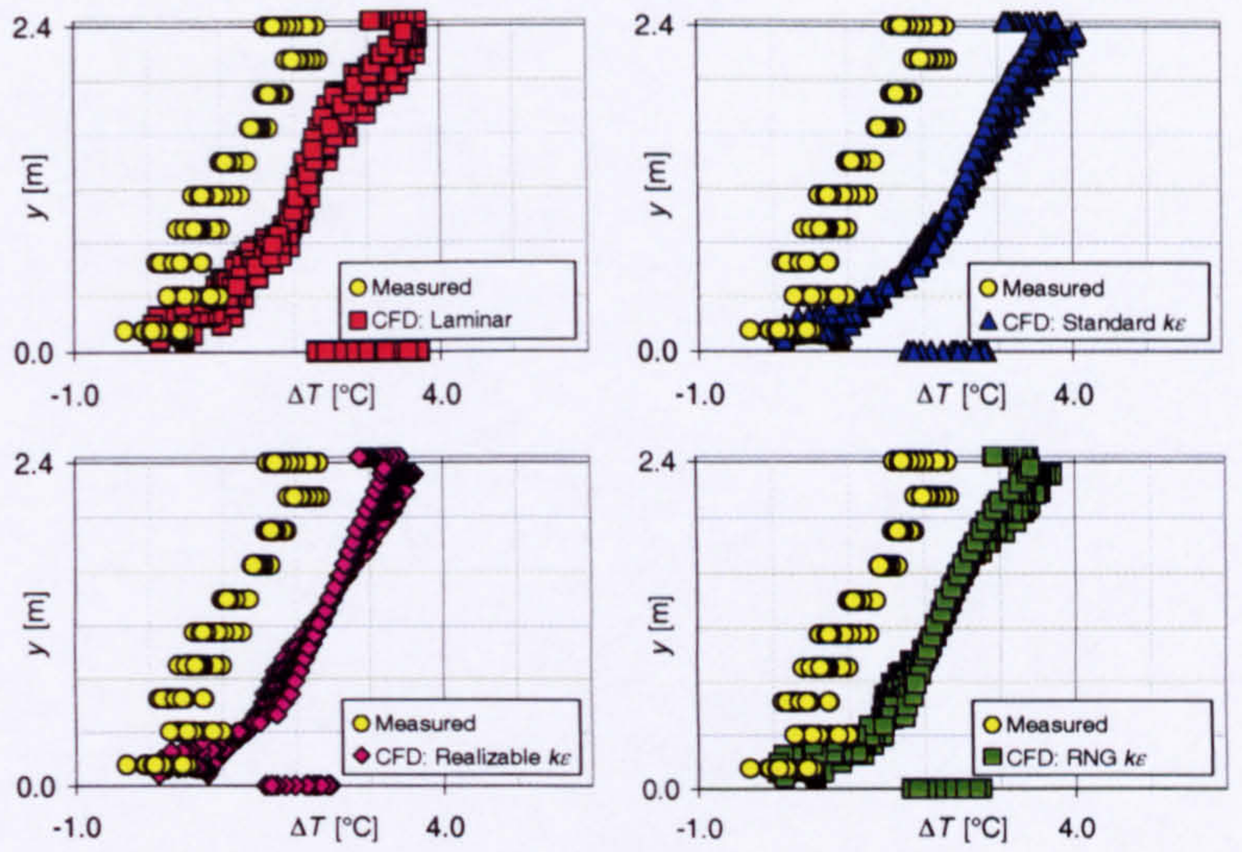

Figure 7.50 - Internal temperature profiles: 490.5W boiler ring; $A^* = 0.488m^2$; radiation model enabled, $\kappa = 0.15m^{-1}$; uniform external temperature at the domain extents; QUICK differencing employed for convection terms

The CFD-profiles with the measured external temperature imposed at the extents of the domain are provided in Figure 7.51, Figure 7.52 and Figure 7.53 below, together with the measured temperature profile.

With the external stratification in place, improved agreement is observed between the measured profile and the CFD-profiles with regard to the magnitude of the temperature rise within the space: for the laminar and RNG-$k\varepsilon$ profiles, the difference between the computed temperature rise within the space and the measured profile is within 0.5°C, whilst for the standard-$k\varepsilon$ and realizable-$k\varepsilon$ profiles this difference is within 1.0°C.

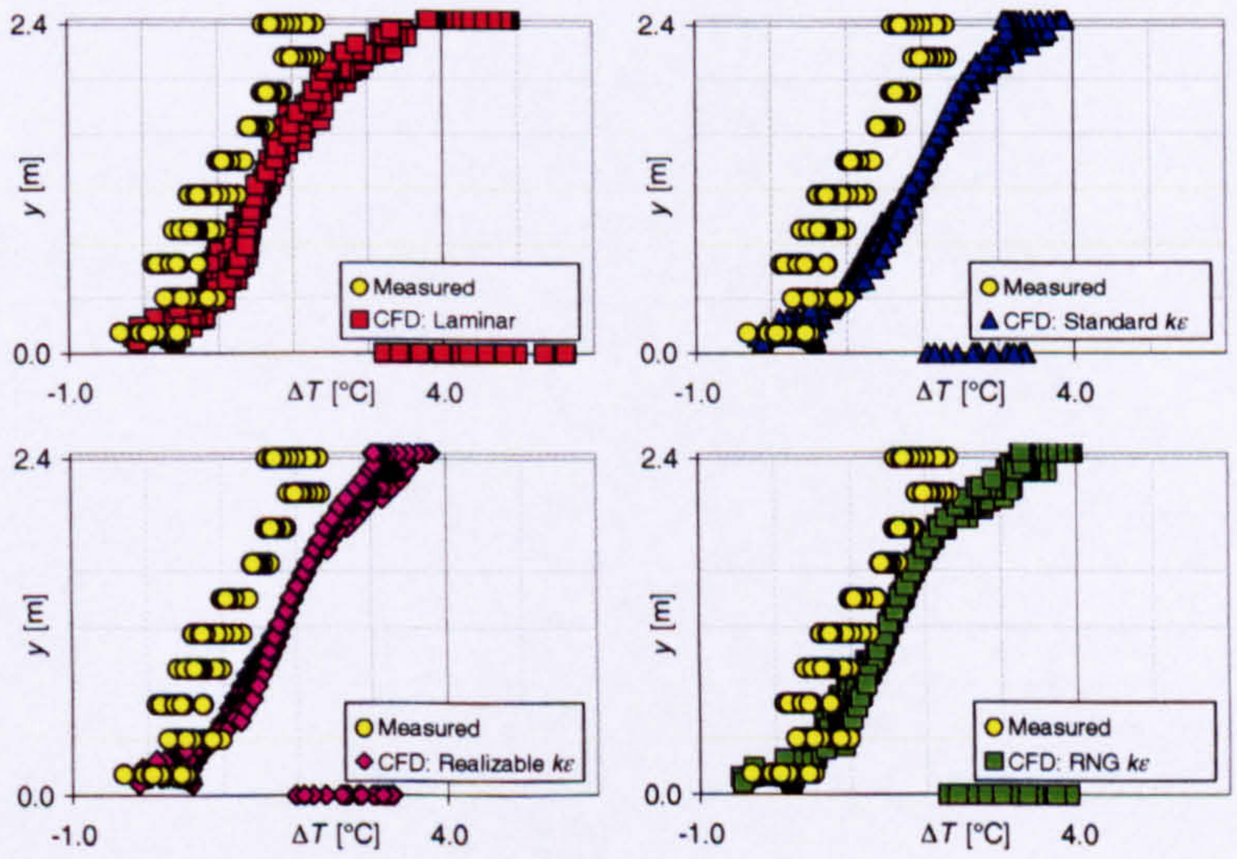

Figure 7.51 - Internal temperature profiles: 490.5W boiler ring; $A^* = 0.488m^2$; radiation model enabled, $\kappa = 0.05m^{-1}$; measured external temperature profile enforced at the domain extents; QUICK differencing employed for convection terms

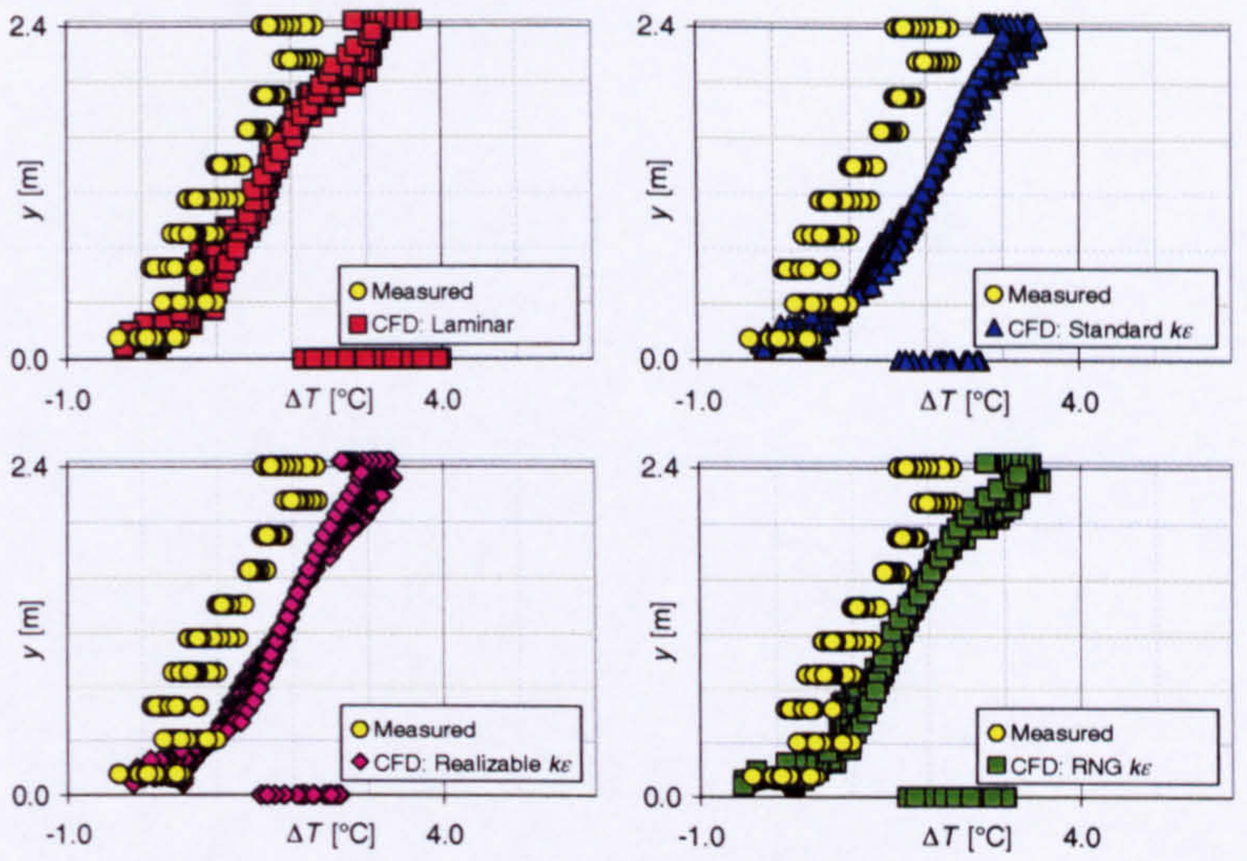

Figure 7.52 - Internal temperature profiles: 490.5W boiler ring; $A^* = 0.488m^2$; radiation model enabled, $\kappa = 0.10m^{-1}$; measured external temperature profile enforced at the domain extents; QUICK differencing employed for convection terms

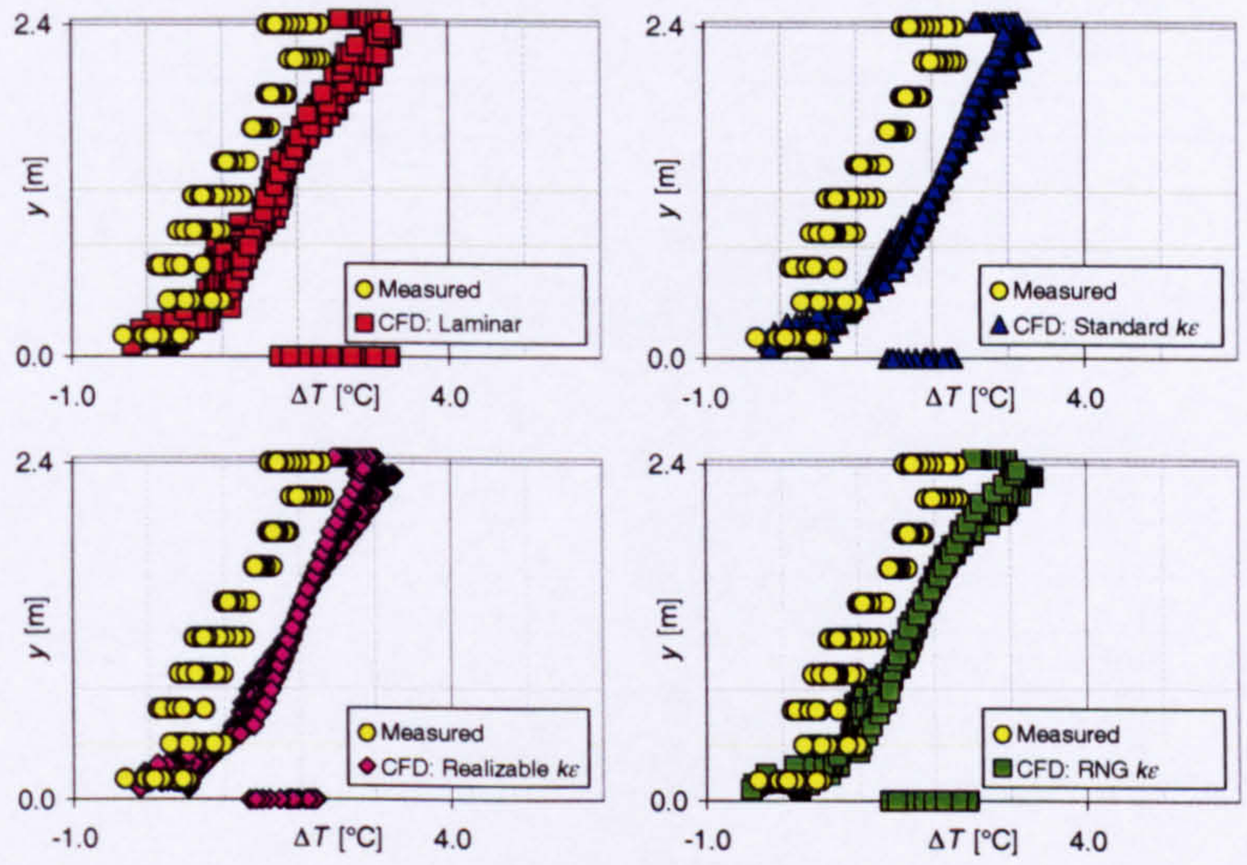

Figure 7.53 - Internal temperature profiles: 490.5W boiler ring; $A^* = 0.488m^2$; radiation model enabled, $\kappa = 0.15m^{-1}$; measured external temperature profile enforced at the domain extents; QUICK differencing employed for convection terms

7.3.4 Width of opening equal to 1.2m ($A^* = 0.732m^2$)

7.3.4.1 Radiation model disabled

The temperature profiles predicted with a constant external temperature imposed at the extents of the domain for this opening configuration with the radiation model disabled are provided in Figure 7.54 below, together with the measured temperature profile. The profiles were obtained using the first-order upwind differencing scheme.

The laminar and RNG-$k\varepsilon$ profiles predict the formation of two layers of air: a layer of ambient air extending from the floor up to a height of about 1.7m, with another layer

above that extends to the ceiling in which the vertical temperature remains constant, approximately equal to 7.0°C/m.

The standard-$k\varepsilon$ and realizable-$k\varepsilon$ profiles comprise a layer of ambient air at low-level, a layer within the core of the space where the vertical temperature gradient is a maximum, and a layer at high-level, where the vertical temperature gradient is reduced. For the standard-$k\varepsilon$ profile, the depth of the layer of ambient air at low-level is about 1.3m, above which the middle layer extends to a height of roughly 1.7m. The temperature gradient within the middle layer is equal to about 4.0°C/m, with that in the layer above equal to roughly 1.5°C/m. For the realizable-$k\varepsilon$ profile, the layer of ambient air at low-level extents to about 1.4m above the floor, and the middle layer extends from that point to a height of roughly 2.1m. The temperature gradient within the middle layer is equal to about 5.0°C/m, with that in the layer above equal to roughly 3.0°C/m.

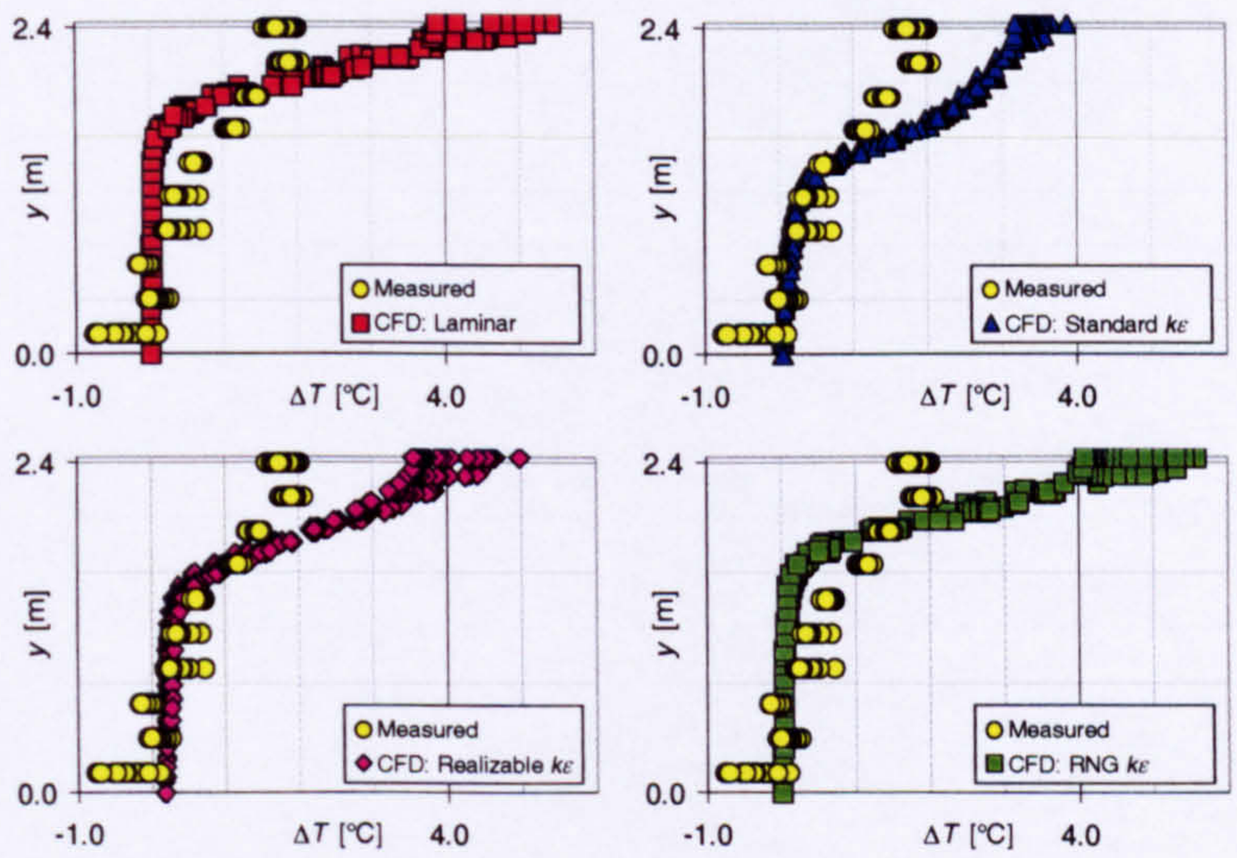

Figure 7.54 - Internal temperature profiles: 490.5W boiler ring; $A^* = 0.732m^2$; radiation model disabled; uniform external temperature enforced at the domain extents; first-order upwind differencing employed for convection terms

The temperature profiles predicted with the measured external temperature imposed at the extents of the domain are provided in Figure 7.55 below, together with the measured temperature profile.

For the laminar and RNG-$k\varepsilon$ profiles, the depth of the ambient layer of fluid within the lower part of the space is equal to 1.5m with the measured external stratification in place, a reduction of about 0.2m. Furthermore, the vertical temperature gradient is no longer constant for the entire zone above the layer of ambient air for either profile. The gradient in the middle layer, which extends to a height of 2.1m, is approximately equal to 8.0°C/m, with that in the upper layer equal to roughly 5.0°C/m.

For the standard-$k\varepsilon$ and realizable-$k\varepsilon$ profiles, the upper two layers are more distinct with the external stratification in place. The height of the interface between the middle layer and the upper layer for the standard-$k\varepsilon$ is roughly 1.6m, whilst for the realizable-$k\varepsilon$ profile it is about 1.9m. The vertical temperature gradient is approximately equal to 6.0°C/m in the middle layer and 1.0°C/m in the upper layer for the standard-$k\varepsilon$ profile, and is equal to about 7.0°C/m and 2.0°C/m in the middle and upper layer respectively for the realizable-$k\varepsilon$ profile.

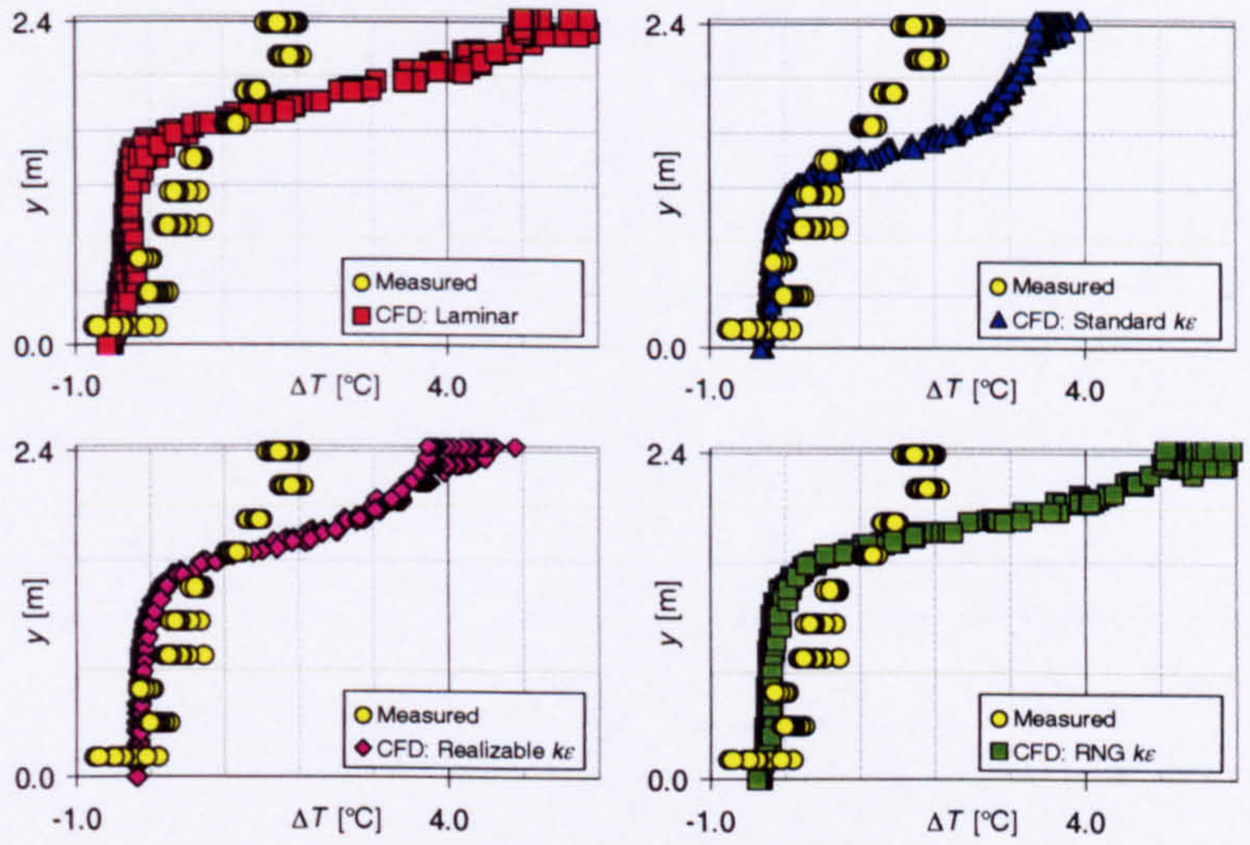

Figure 7.55 - Internal temperature profiles: 490.5W boiler ring; $A^* = 0.732m^2$; radiation model disabled; measured external temperature profile enforced at the domain extents; first-order upwind differencing employed for convection terms

7.3.4.1.1 Radiation model enabled, absorption of radiation throughout the fluid medium neglected ($\kappa = 0.0m^{-1}$)

The CFD-profiles of the internal rise in temperature computed using QUICK differencing with the radiation model enabled but neglecting absorption of radiation within the fluid medium for this opening configuration are presented in Figure 7.56 below, together with the measured profile. Only predictions for the standard-$k\varepsilon$, realizable-$k\varepsilon$ and RNG-$k\varepsilon$ cases are presented: numerical convergence difficulties were experienced for the laminar case, and so a profile is not provided.

With the radiation model enabled, thermal radiative transfer between the faces of the ceiling and the floor result in the surface temperature of the latter that is significantly higher than that of the temperature of the incoming air flowing across it: the predicted rise in temperature above the reference temperature at the surface of the floor is in the range 2.5°C to 4.5°C for the standard-$k\varepsilon$ and realizable-$k\varepsilon$ cases, and is in the range 3.0°C to 5.0°C for the RNG-$k\varepsilon$ case, compared with a temperature rise in the adjacent fluid of say 0.3°C. For each profile, the heated layer of fluid is not

sufficiently thick to cover the floor-adjacent nodes of the computational mesh, so that the temperature rise appears to be roughly constant within 0.3m of the floor. Between the elevations of 0.3m and 0.6m each profile exhibits a relatively steep vertical gradient of temperature rise, equal to about 2.0°C/m. Within the central section of the space, above a height of 0.6m, each profile predicts a vertical gradient of temperature rise roughly equal to 0.7°C/m, compared with 1.2°C/m for the measured profile. In addition, at the mid-height of the enclosure, the magnitude of the temperature rise within the space is over-predicted by approximately 1.0°C for each of the computed profiles.

In the layer of fluid immediately below the ceiling, each of the CFD-profiles show a significant increase in the rate of change of temperature with respect to height: in this layer, the temperature gradient is predicted to be about 3.0°C/m for the standard ke and realizable ke profiles and roughly 4.0°C/m for the RNG-$k\varepsilon$ case.

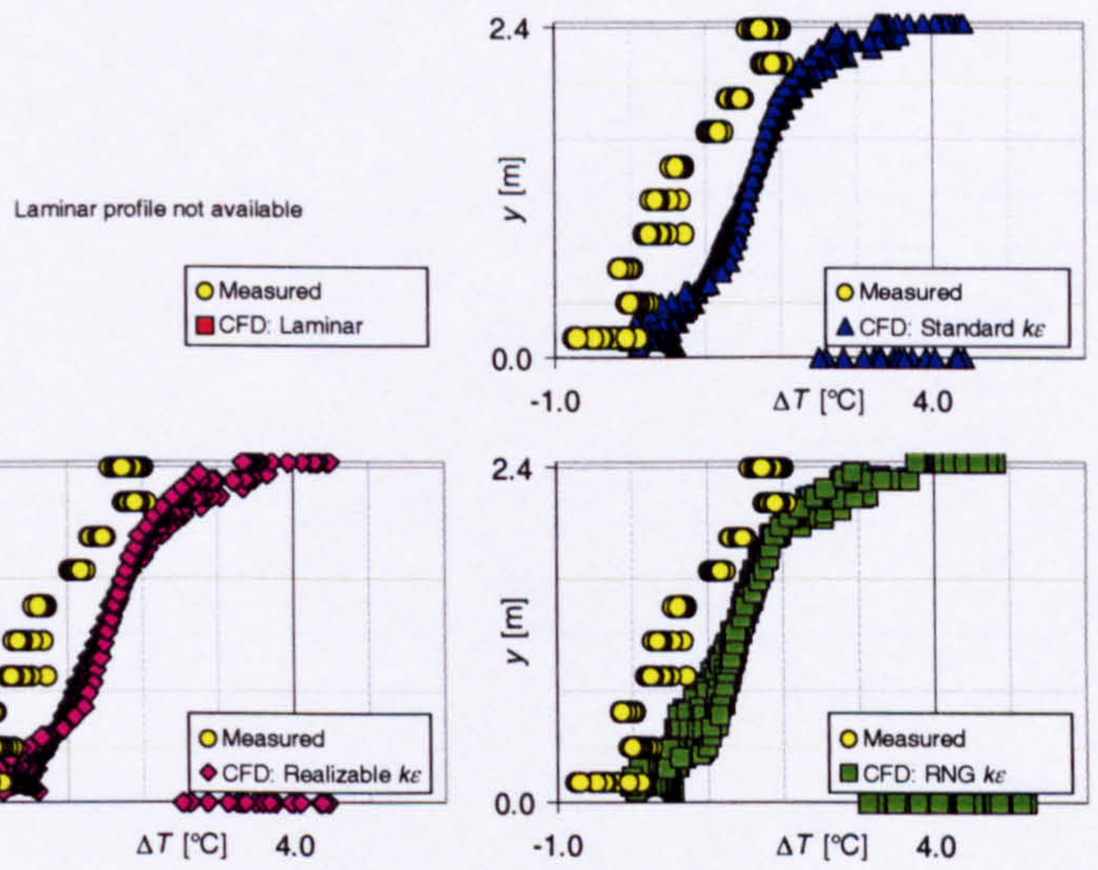

Figure 7.56 - Internal temperature profiles: 490.5W boiler ring; $A^* = 0.732m^2$; radiation model enabled, $\kappa = 0.0m^{-1}$; uniform external temperature at domain extents; QUICK differencing employed for convection terms

The temperature profiles predicted with the measured external temperature imposed at the extents of the domain are provided in Figure 7.57 below, together with the measured temperature profile.

It is observed that the application of the external stratification has not significantly affected the shape of the CFD-profiles, although the agreement between the magnitude of the predicted temperature rise within the space and that measured during the experimental phase of this work is improved. At the mid-height of the enclosure, the magnitude of the temperature rise within the space is over-predicted by around 0.8°C for the standard-$k\varepsilon$ profile, 0.65°C for the realizable-$k\varepsilon$ profile and 0.5°C for the RNG-$k\varepsilon$ profile.

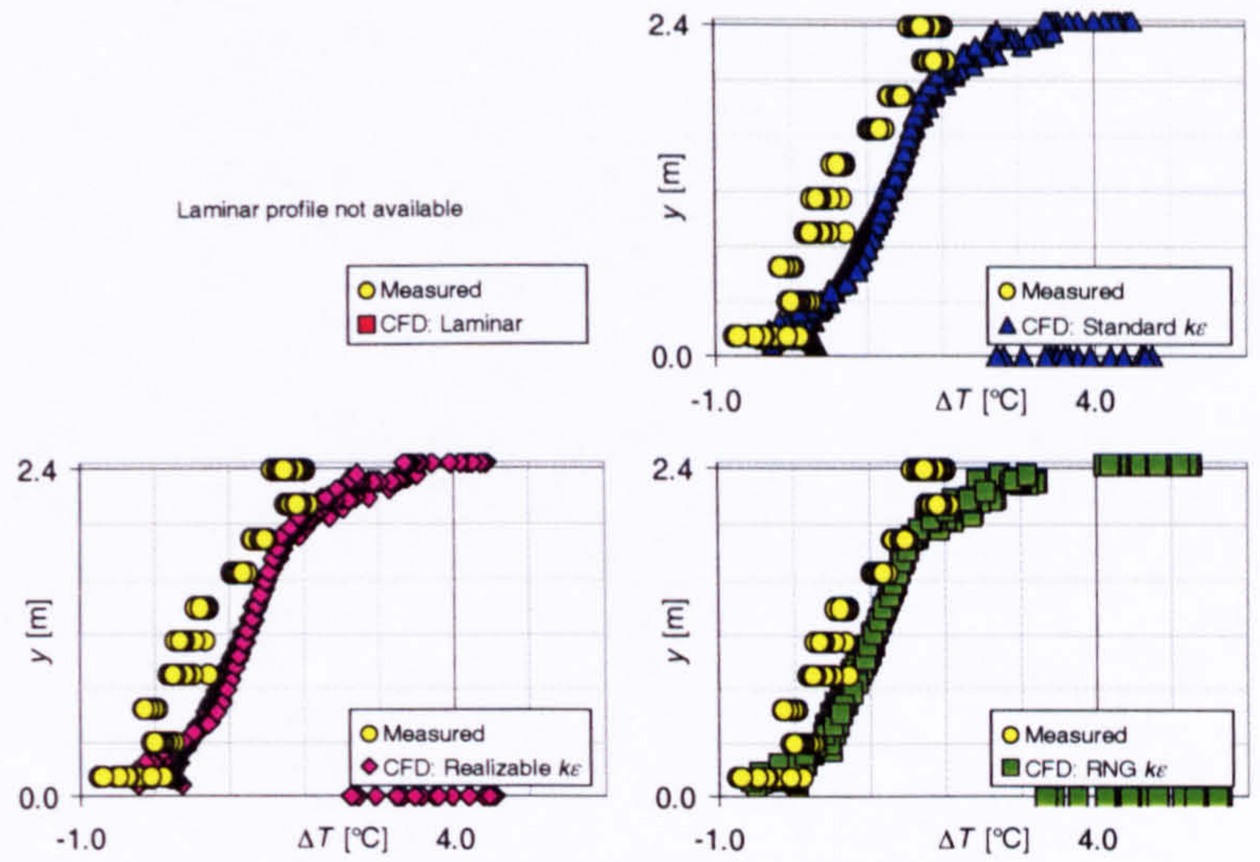

Figure 7.57 - Internal temperature profiles: 490.5W boiler ring; $A^* = 0.732m^2$; radiation model enabled, $\kappa = 0.0m^{-1}$; measured external stratification at domain extents; QUICK differencing employed for convection terms

7.3.4.1.2 Radiation model enabled, absorption of radiation throughout the fluid medium included ($\kappa \neq 0.0m^{-1}$)

The profiles of internal temperature rise predicted for this opening configuration with a constant external temperature imposed at the extents of the domain and with the radiation model enabled for each non-zero absorption coefficient considered are presented in Figure 7.58, Figure 7.59 and Figure 7.60 below, together with the measured profile.

With a non-zero absorption coefficient it is observed that the surface temperature of the ceiling and of the floor is reduced. For the standard-$k\varepsilon$ and realizable-$k\varepsilon$ profiles, for example, the temperature of the surfaces of the ceiling and of the floor are predicted to be of the order of 4.0°C and 3.5°C, 3.2°C and 2.7°C, 2.8°C and 2.0°C, and 2.6°C and 1.8°C for an absorption coefficient equal to $0.00m^{-1}$, $0.05m^{-1}$, $0.10m^{-1}$ and $0.15m^{-1}$ respectively.

It is also observed that as the absorption coefficient is increased from zero, the rise in the vertical temperature gradient in the layer immediately beneath the ceiling is less significant. For each of the profiles with $\kappa = 0.05m^{-1}$, and for the laminar and RNG-$k\varepsilon$ profiles with $\kappa = 0.10m^{-1}$ and $\kappa = 0.15m^{-1}$, the increase in the vertical temperature gradient in the layer just below the ceiling remains, but this increase is less significant than for the cases with the absorption coefficient $\kappa = 0.0m^{-1}$. For the standard-$k\varepsilon$ and realizable-$k\varepsilon$ profiles with $\kappa = 0.10m^{-1}$ and $\kappa = 0.15m^{-1}$, however, there is no longer an increase in the vertical temperature gradient in the layer below the ceiling.

Within the central section of the space, better agreement is observed between each of the computed profiles and the measured profile with a non-zero absorption coefficient. For each of the profiles the vertical temperature gradient predicted in the central zone is approximately equal to 0.85°C/m, which is marginally closer to the measured gradient than that predicted with $\kappa = 0.0\text{m}^{-1}$. The magnitude of the rise in temperature above the reference temperature at the mid-height of the enclosure is about 1.0°C greater than the measured temperature rise at that height, for each of the CFD-profiles with a non-zero absorption coefficient.

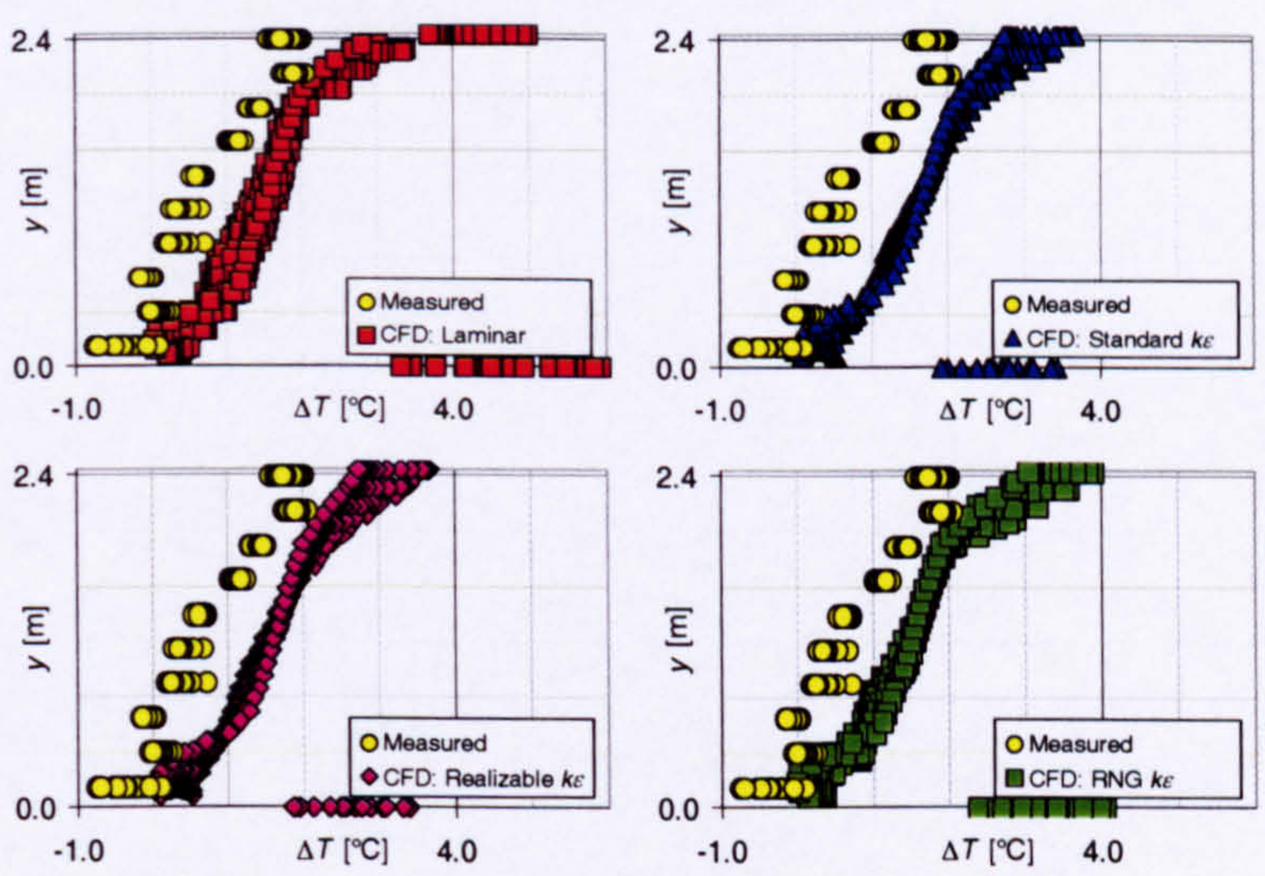

Figure 7.58 - Internal temperature profiles: 490.5W boiler ring; $A^* = 0.732\text{m}^2$; radiation model enabled, $\kappa = 0.05\text{m}^{-1}$; uniform external temperature at the domain extents; QUICK differencing employed for convection terms

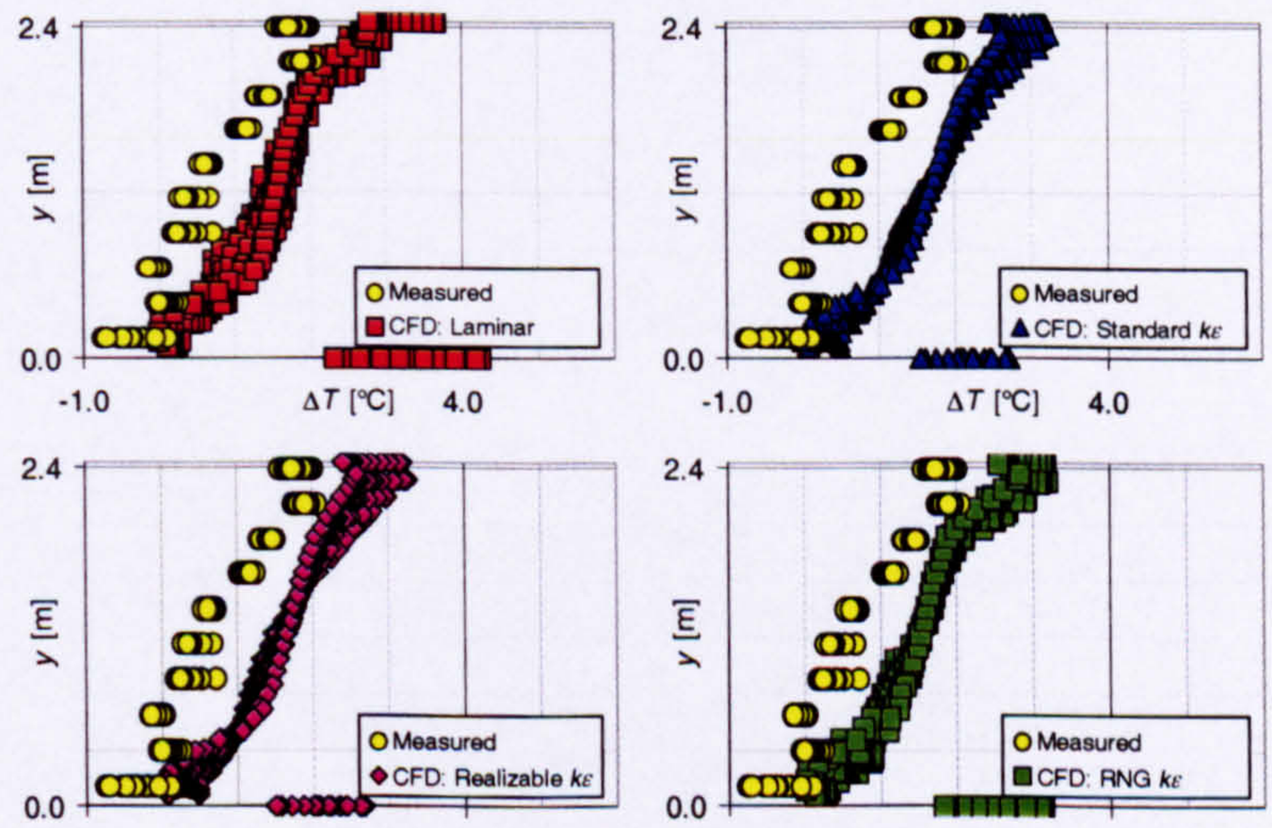

Figure 7.59 - Internal temperature profiles: 490.5W boiler ring; $A^* = 0.732\text{m}^2$; radiation model enabled, $\kappa = 0.10\text{m}^{-1}$; uniform external temperature at the domain extents; QUICK differencing employed for convection terms

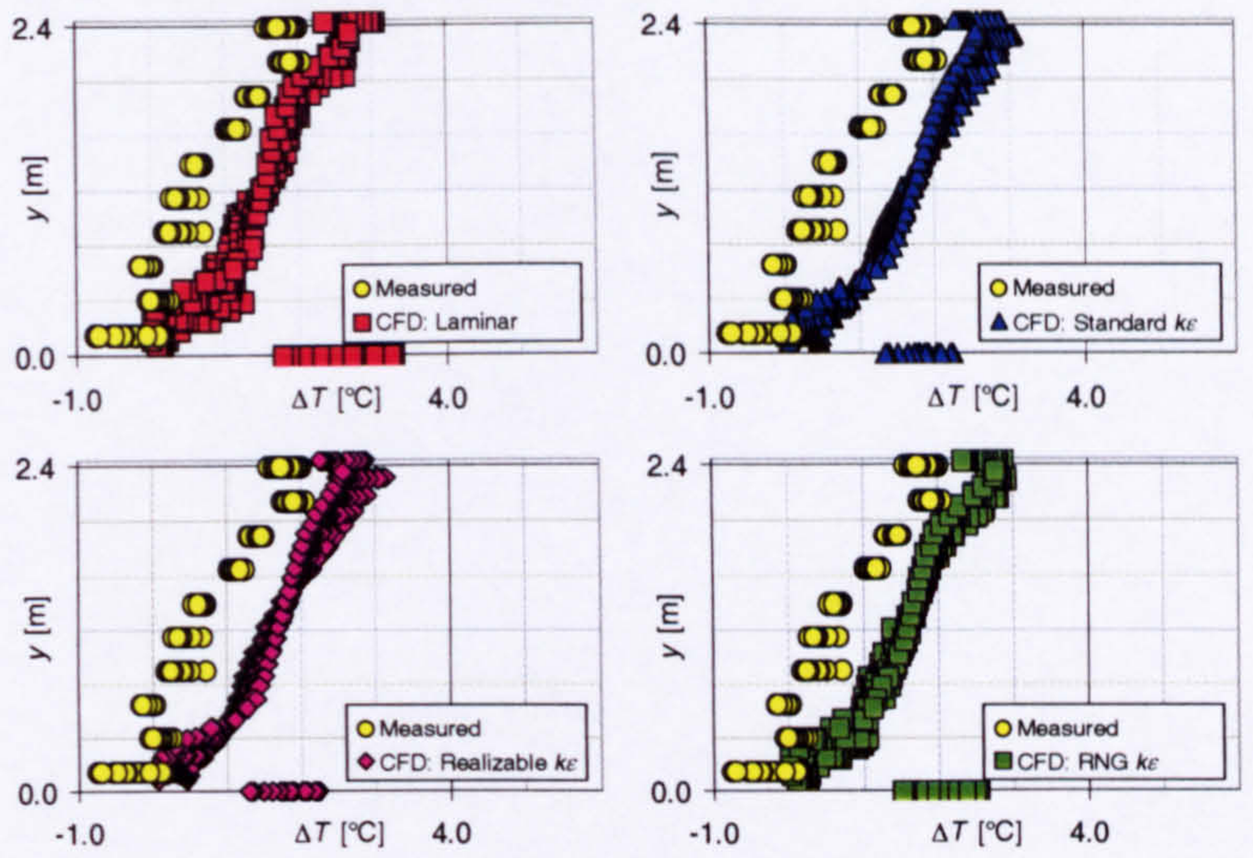

Figure 7.60 - Internal temperature profiles: 490.5W boiler ring; $A^* = 0.732m^2$; radiation model enabled, $\kappa = 0.15m^{-1}$; uniform external temperature at the domain extents; QUICK differencing employed for convection terms

The temperature profiles predicted with the measured external temperature imposed at the extents of the domain are provided in Figure 7.61, Figure 7.62 and Figure 7.63 below, together with the measured temperature profile.

It is observed that with the external stratification in place, there is no significant change in the shape of the predicted CFD-profiles. The magnitude of the temperature rise predicted above that at the reference thermometer location, however, is improved. For the laminar and RNG-$k\varepsilon$ profiles the temperature rise computed at the mid-height of the space is approximately 0.6°C greater than that measured, and for the standard-$k\varepsilon$ and realizable-$k\varepsilon$ profiles it is about 0.8°C greater than that measured at the same height.

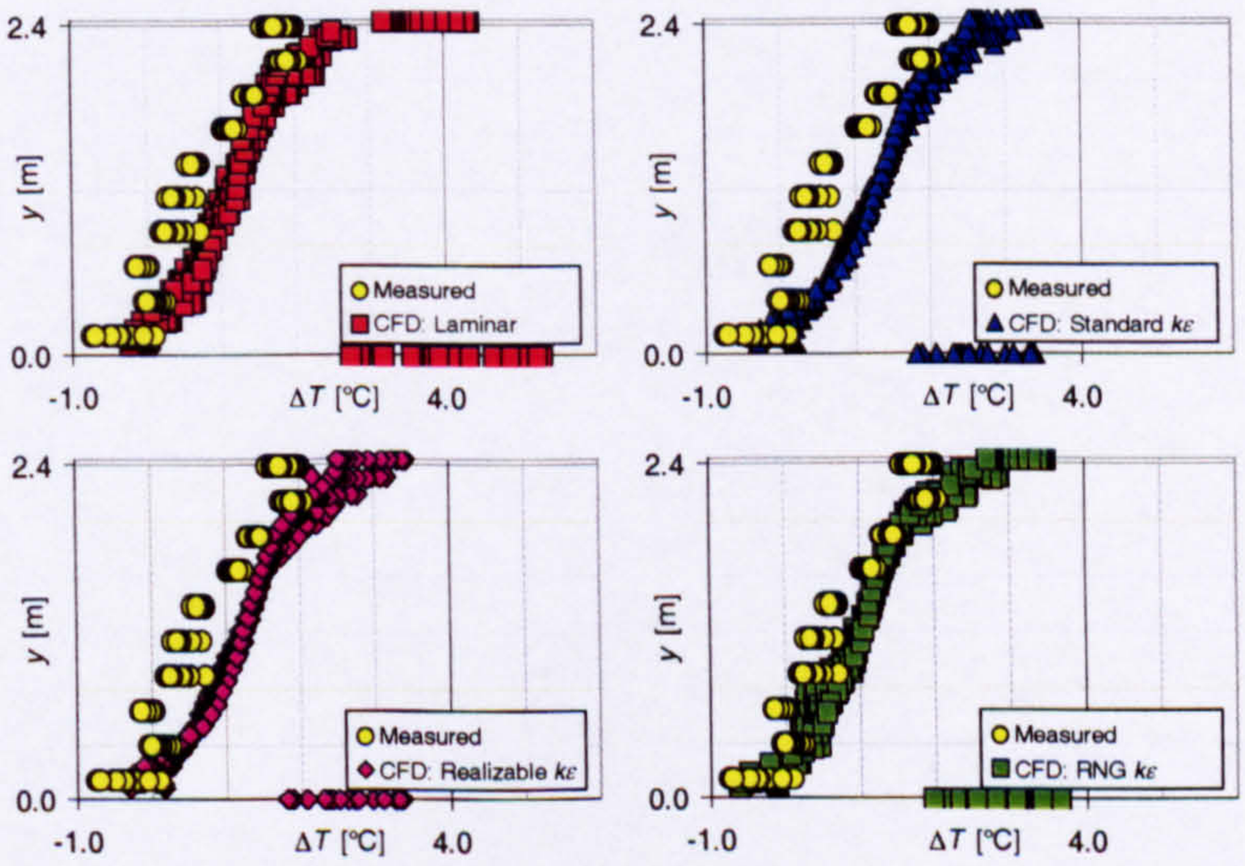

Figure 7.61 - Internal temperature profiles: 490.5W boiler ring; $A^* = 0.732m^2$; radiation model enabled, $\kappa = 0.05m^{-1}$; measured external temperature profile enforced at the domain extents; QUICK differencing employed for convection terms

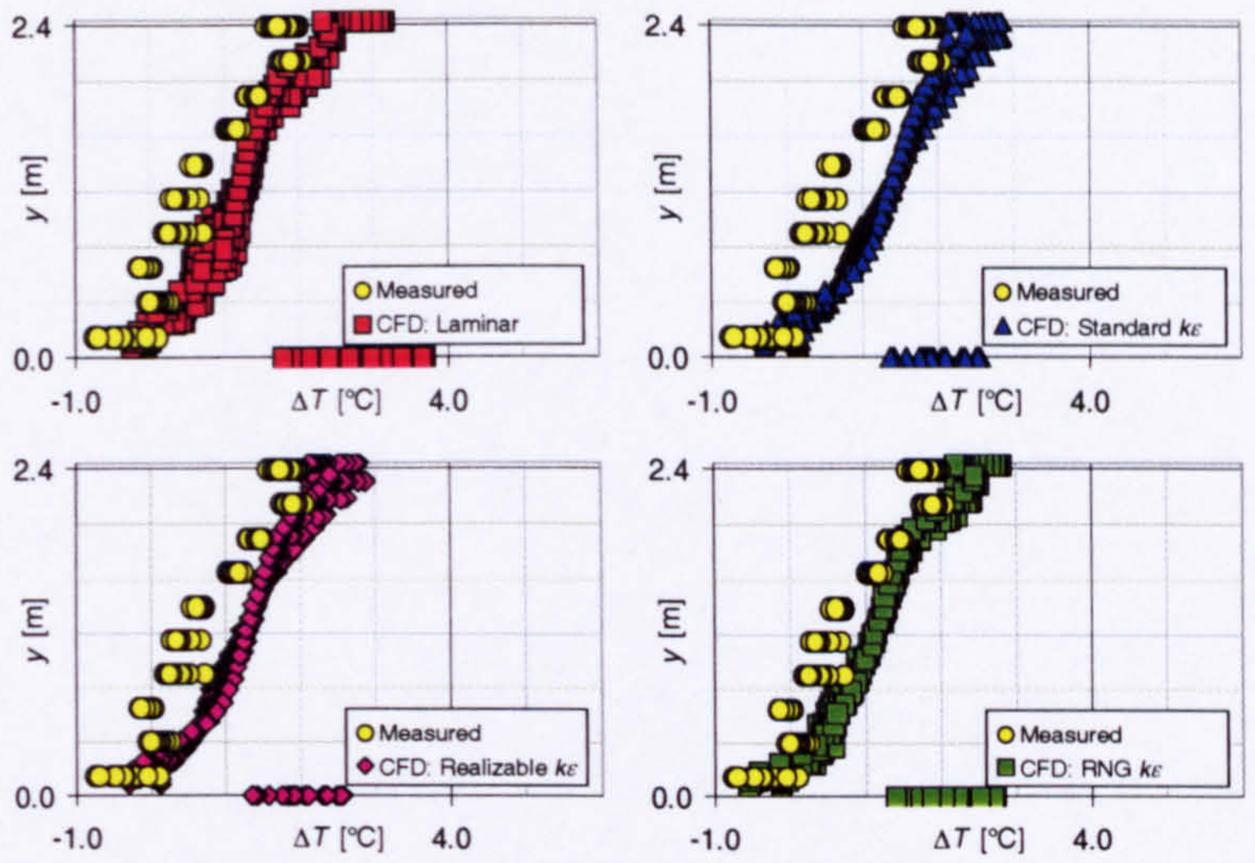

Figure 7.62 - Internal temperature profiles: 490.5W boiler ring; $A^* = 0.732m^2$; radiation model enabled, $\kappa = 0.10m^{-1}$; measured external temperature profile enforced at the domain extents; QUICK differencing employed for convection terms

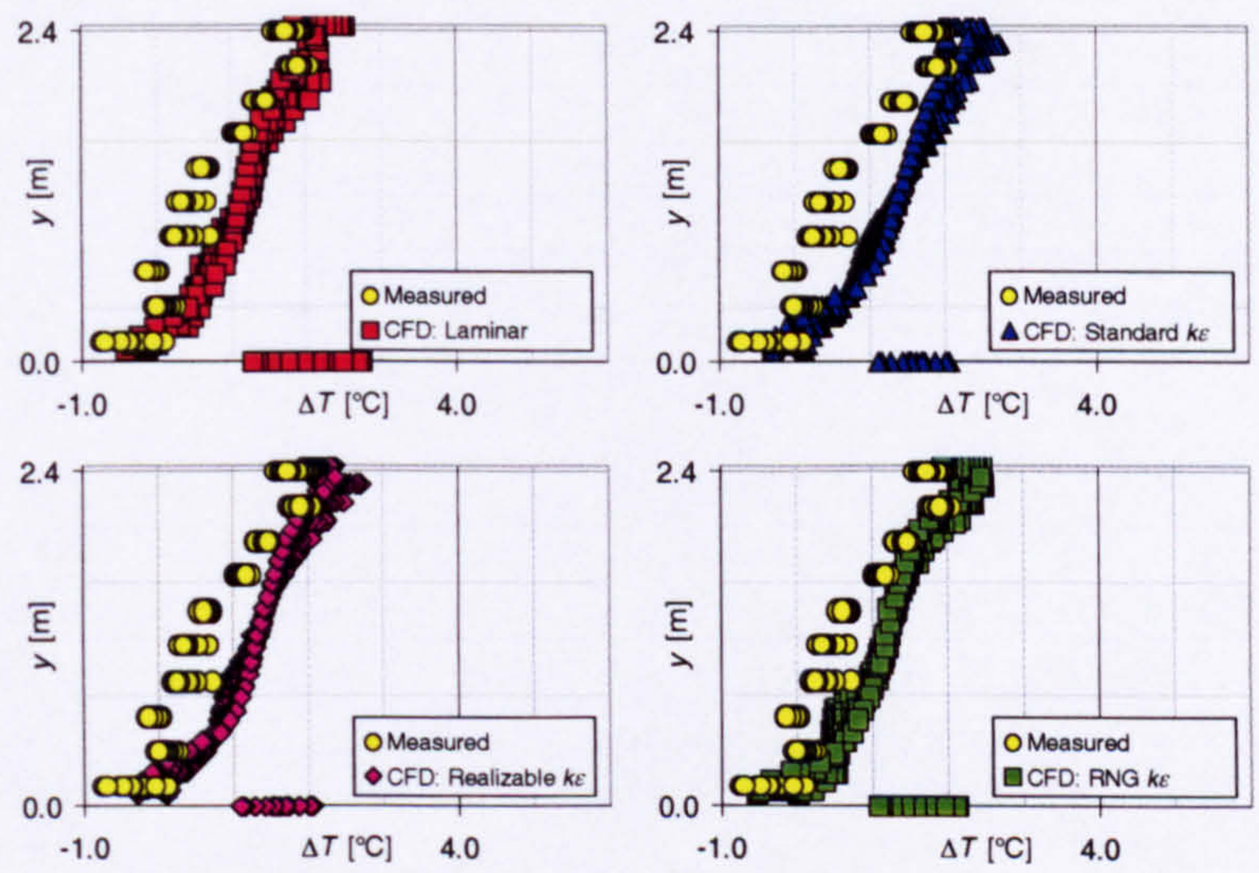

Figure 7.63 - Internal temperature profiles: 490.5W boiler ring; $A^* = 0.732m^2$; radiation model enabled, $\kappa = 0.15m^{-1}$; measured external temperature profile enforced at the domain extents; QUICK differencing employed for convection terms

7.3.5 Apparent trends in the CFD-profiles

For the six combinations of opening width and heat source configuration considered with the adiabatic assumption at the enclosure walls, a number of general trends are apparent regarding the effect upon the flow of particular turbulence closures and radiation model definition, which are now summarised.

7.3.5.1 With the radiation model disabled

If thermal radiative transfer is neglected, each of the CFD-profiles predicts that there will be a layer of air at low-level within the space, within which the temperature is

equal to that at the reference thermometer location. For the two opening configurations considered in detail, the depth of this ambient layer of air is usually sufficient to encompass the entire space up to and beyond the mid-height of the enclosure. During the experimental phase of this work, however, the predicted layer of ambient air at low-level was never observed within the space.

With the radiation model disabled and a uniform temperature enforced at the domain extents, the laminar and RNG-$k\varepsilon$ profiles tend to be representative of two layers of air: the ambient layer within the lower-part of the space, and another layer above with a constant vertical temperature gradient that extends to the ceiling. The standard-$k\varepsilon$ profile is generally representative of three layers of air: the layer of ambient air at low-level, a layer within the core of the space where the vertical temperature gradient is a maximum, and a layer at high-level, where the vertical temperature gradient is significantly reduced. The realizable-$k\varepsilon$ profile is usually intermediary between the laminar and RNG-$k\varepsilon$ profiles on one hand and the standard-$k\varepsilon$ profile on the other: above the layer of ambient air at low-level it tends to predict a layer within the core of the space where the vertical temperature gradient is a maximum, and a layer at high-level, where the vertical temperature gradient is marginally less than that in the middle layer.

The application of the external stratification around the enclosure, as measured during the experimental phase of this work, generally affects the CFD-profiles in two respects. Firstly, the temperature within the layer at low-level tends to be below that at the reference thermometer location, regardless of the turbulence modelling approach. Secondly, the difference between the vertical gradient of temperature in the middle and upper layers for the standard-$k\varepsilon$ and realizable-$k\varepsilon$ profiles is more pronounced, whilst the laminar and RNG-$k\varepsilon$ profiles show distinct middle and upper layers.

With the radiation model disabled, the standard-$k\varepsilon$ profiles tend to be representative of the internal stratification predicted by the Cambridge mathematical model, that is a layer of ambient air at low-level within the space, with a layer of well-mixed, constant temperature buoyant air above, the two layers being separated by a sharp interface. This description of the internal stratification, however, was never observed during the experimental phase of this work.

An isopleth map of the temperature rise above that at the reference thermometer location predicted with the standard-$k\varepsilon$ model for turbulence for the case with the 490.5W boiler ring as the heat source and an effective area of the openings $A^* = 0.488m^2$ is presented in Figure 7.64, with the associated velocity vector map in Figure 7.65.

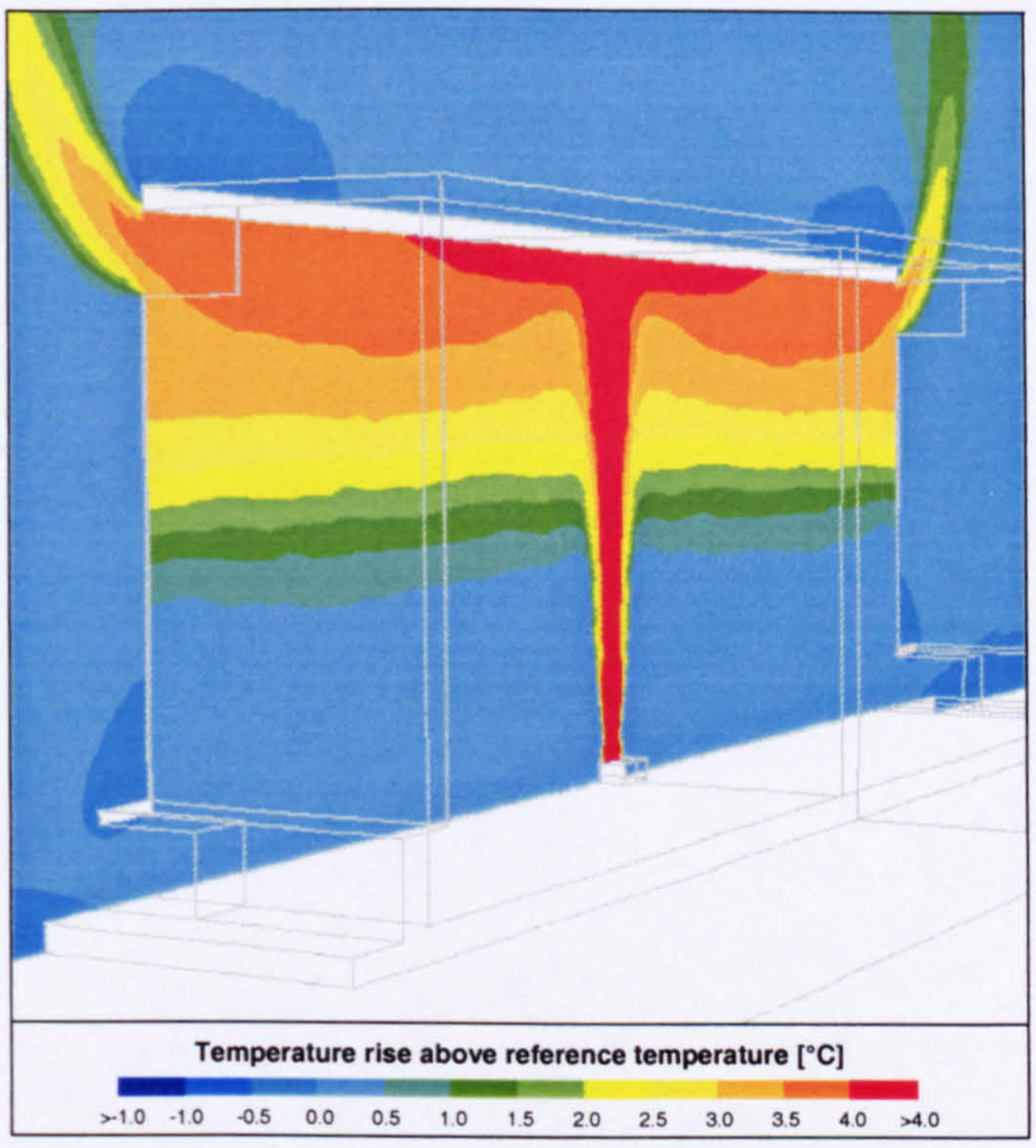

Figure 7.64 - Isopleth map of temperature rise above that at the reference thermometer location on the *x*-*y* plane of symmetry: 490.5W boiler ring; $A^* = 0.488\text{m}^2$; radiation model disabled; uniform external temperature enforced at the domain extents; standard-$k\varepsilon$ turbulence model; first-order upwind differencing employed for convection terms

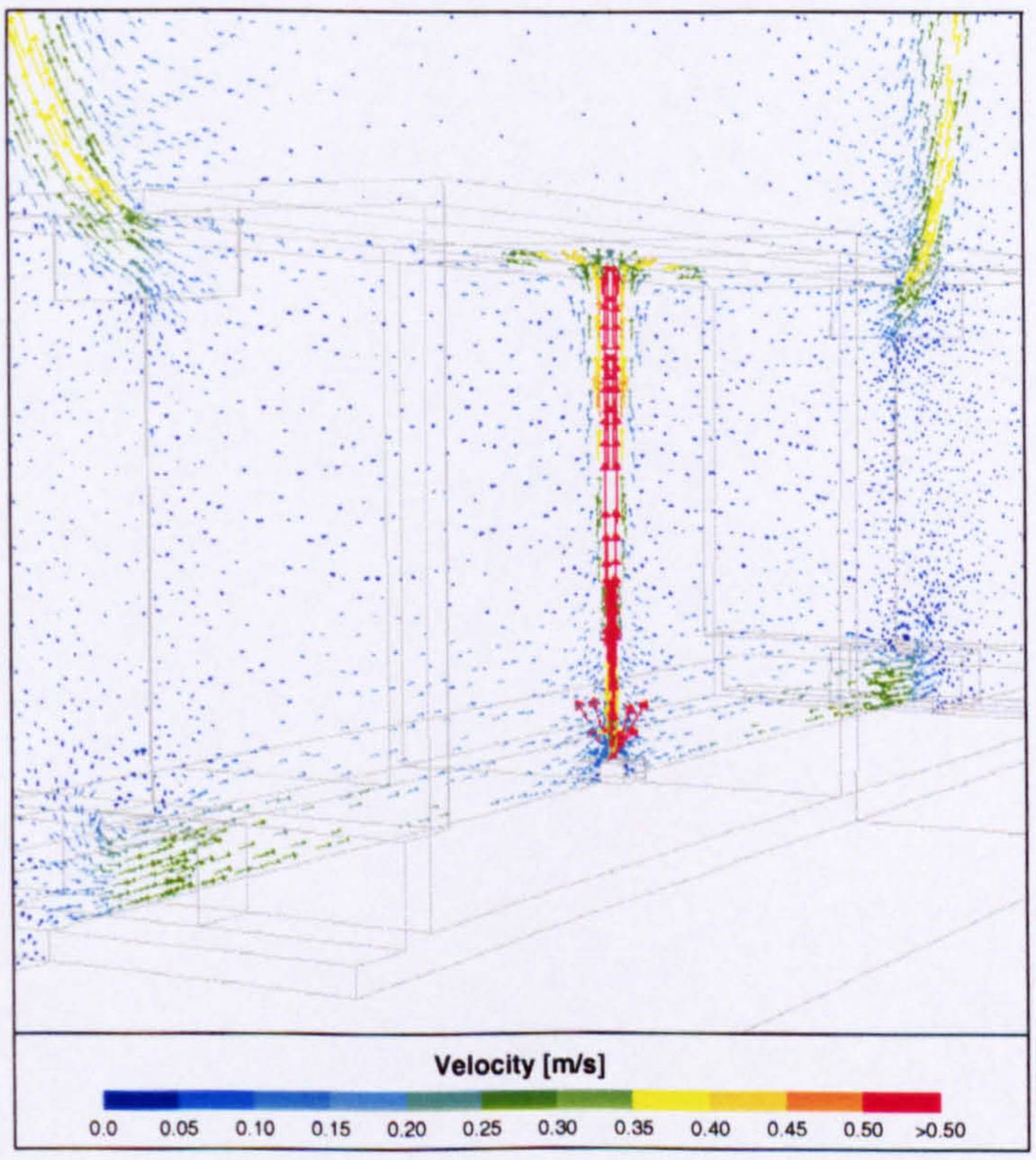

Figure 7.65 - Velocity vector map on the *x*-*y* plane of symmetry: 490.5W boiler ring; $A^* = 0.488\text{m}^2$; radiation model disabled; uniform external temperature enforced at the domain extents; standard-$k\varepsilon$ turbulence model; first-order upwind differencing employed for convection terms

7.3.5.2 With the radiation model enabled but neglecting absorption of radiation throughout the fluid medium ($\kappa = 0.0 m^{-1}$)

With thermal radiative transfer effects included, each of the CFD-profiles exhibit a roughly uniform vertical temperature gradient within much of the central section of the space, the magnitude of which is generally similar to that of the measured profile for each combination of heat source and opening width considered. With this observation alone it is sufficient to conclude that with the radiation model enabled, the agreement between the CFD-predicted temperature field within the space and the measured profile is much improved. It is noted, however, that the magnitude of the rise in temperature within the space above that at the reference thermometer location is generally over-predicted.

With the radiation model enabled, there appears to be significant thermal radiative transfer between the surfaces of the ceiling and the floor: each of the CFD-profiles predicts the surface temperature of the floor to be significantly higher than the temperature of the air flowing over it. Generally, the predicted temperature rise of the surface of the floor is least for the standard-$k\varepsilon$ profile, is slightly greater for the realizable-$k\varepsilon$ profile and then the RNG-$k\varepsilon$ profile, and is greatest for the laminar profile.

Although the high surface temperature at the floor may appear to be discontinuous from the rest of the profile, this is only because the predicted temperatures throughout the fluid domain are presented only at discrete locations defined by the nodes forming part of the computational mesh. Indeed, the profile is continuous from the fluid region directly towards the surface of the floor, so that there will be a sharp increase in the temperature of the fluid very close to the wall. For the standard-$k\varepsilon$ and realizable-$k\varepsilon$ profiles, this layer tends to be particularly thin, so that the floor-adjacent nodes are unaffected by its presence. For the laminar and RNG-$k\varepsilon$ profiles, however, the heated layer is often sufficiently deep to encompass the floor-adjacent nodes, so that a small increase in the fluid temperature above the surface of the floor is observed.

With the radiation model enabled but with the absorption coefficient equal to zero, it is observed that the CFD-profiles predict a further rise in the vertical temperature gradient in the layer beneath the ceiling, regardless of the choice of turbulence modelling approach. This is not in agreement with the measured profile where the rise in temperature above that at the reference thermometer location was observed to be approximately constant in this region.

An isopleth map of temperature rise above the reference temperature and a corresponding velocity vector map are presented in Figure 7.66 and Figure 7.67 for the case with the 490.5W boiler ring as the heat source and an effective area of the openings $A^* = 0.488m^2$, employing the standard-$k\varepsilon$ model for turbulence.

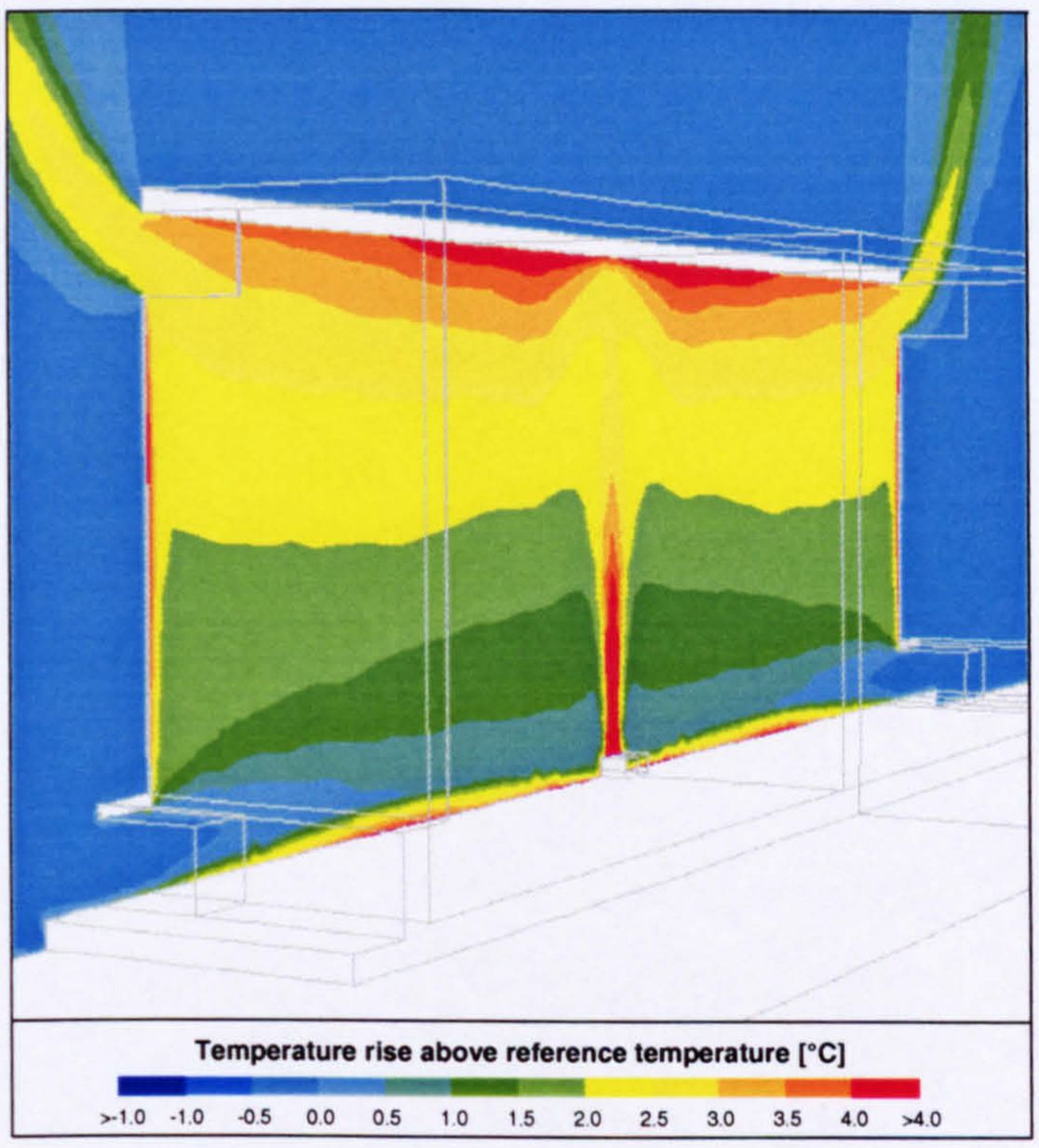

Figure 7.66 - Isopleth map of temperature rise above that at the reference thermometer location on the *x*-*y* plane of symmetry: 490.5W boiler ring; $A^* = 0.488m^2$; radiation model enabled, $\kappa = 0.0m^{-1}$; uniform external temperature enforced at the domain extents; standard-$k\varepsilon$ turbulence model; QUICK differencing employed for convection terms

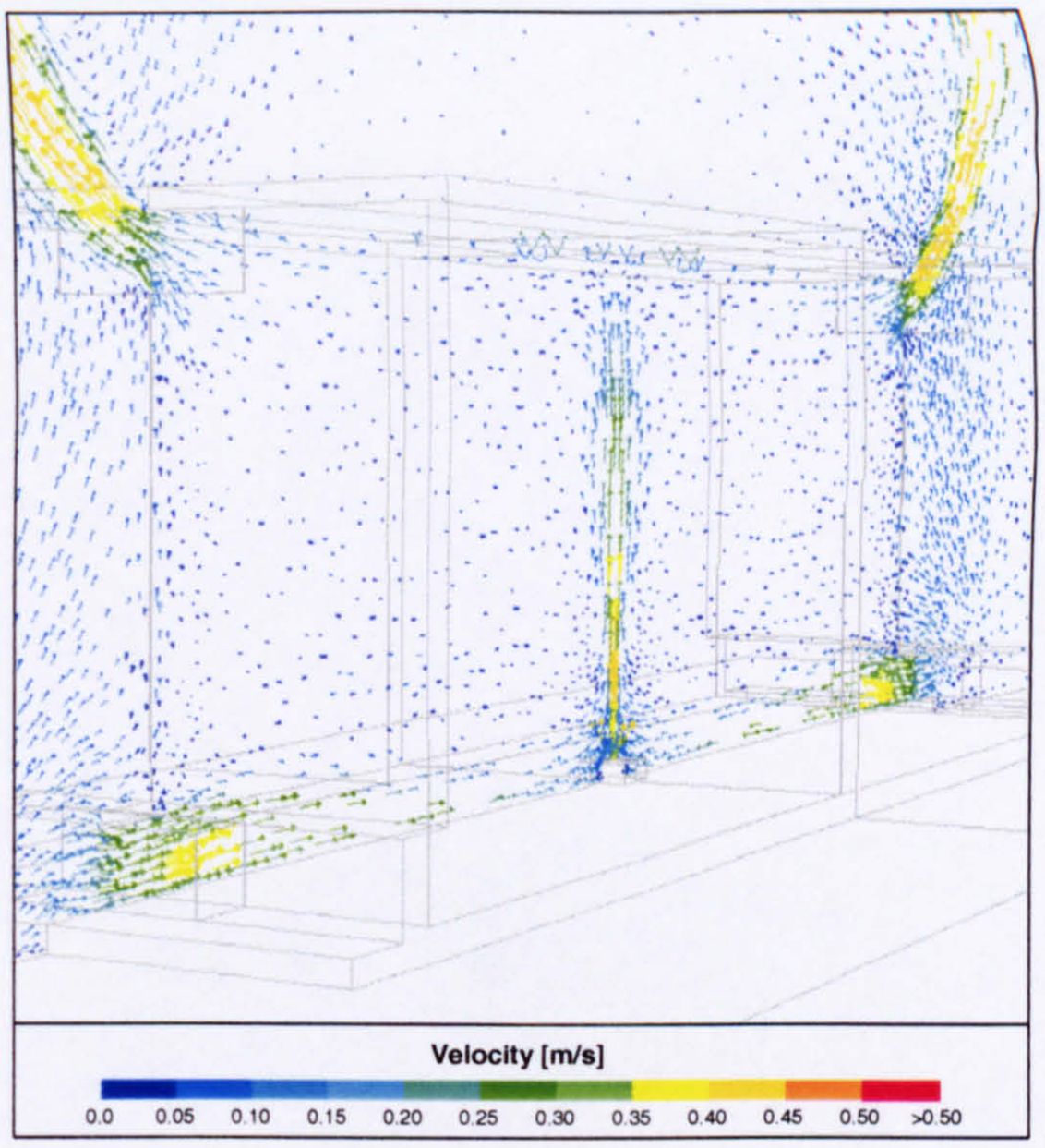

Figure 7.67 - Velocity vector map on the *x-y* plane of symmetry: 490.5W boiler ring; $A^* = 0.488m^2$; radiation model enabled, $\kappa = 0.0m^{-1}$; uniform external temperature enforced at the domain extents; standard-$k\varepsilon$ turbulence model; QUICK differencing employed for convection terms

7.3.5.3 With the radiation model enabled but including absorption of radiation throughout the fluid medium ($\kappa \neq 0.0m^{-1}$)

With a non-zero absorption coefficient representing the absorption of thermal radiative energy by the water vapour component of air, further improvement is generally observed between the CFD-profiles and the measured profile, particularly in the layer immediately below the ceiling. With $\kappa = 0.05m^{-1}$, there remains an increase in the vertical temperature gradient in this layer, but the increase is significantly less that for the corresponding prediction with the zero absorption coefficient. In the layer below the ceiling with $\kappa \geq 0.10m^{-1}$, there is no longer an increase in the vertical temperature gradient for the standard-$k\varepsilon$ and realizable-$k\varepsilon$ profiles, which is in agreement with the corresponding measured profile. For the laminar and RNG-$k\varepsilon$ profiles, however, the increase in the temperature gradient below the ceiling generally persists, particularly for the more powerful heat sources, although this increase is less apparent.

Furthermore, it is normally the case that with the radiation model enabled, the predicted temperature field is less affected by the turbulence modelling approach adopted, particularly when a non-zero absorption coefficient is used. It appears, therefore, that the primary modelling concern for predicting this type of natural

displacement ventilation flow is that the radiation model should be enabled with the absorption coefficient in the range $0.10m^{-1} < \kappa < 0.15m^{-1}$, and that which turbulence closure is used is really of secondary importance.

Isopleth maps of the temperature rise above the reference temperature for the case with the 490.5W boiler ring as the heat source and an effective area of the openings $A^* = 0.488m^2$, employing the standard-$k\varepsilon$ model for turbulence, for each non-zero absorption coefficient considered are presented in Figure 7.68, Figure 7.70 and Figure 7.72. The associated velocity vector maps are presented in Figure 7.69, Figure 7.71 and Figure 7.73.

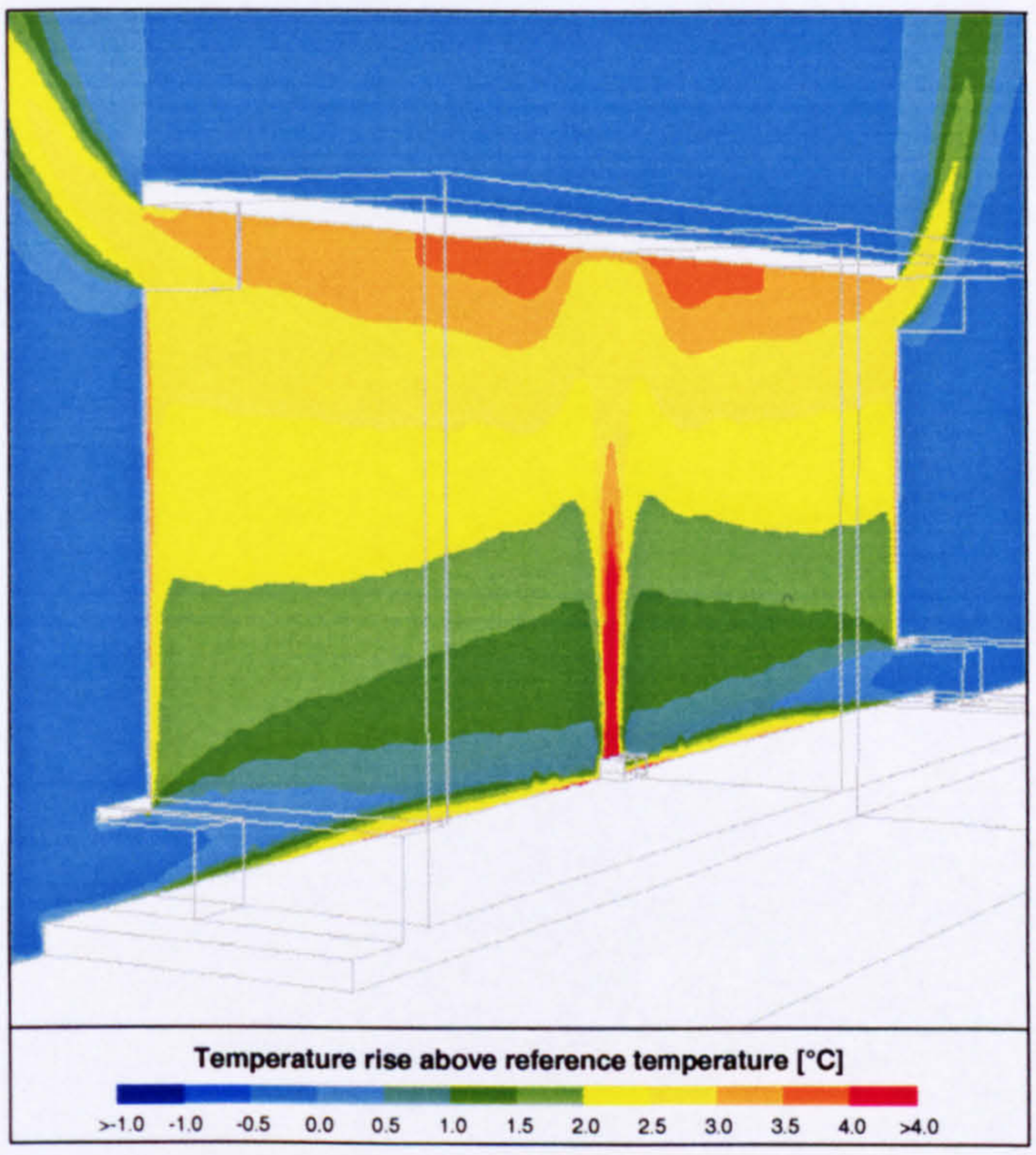

Figure 7.68 - Isopleth map of temperature rise above that at the reference thermometer location on the *x-y* plane of symmetry: 490.5W boiler ring; $A^* = 0.488m^2$; radiation model enabled, $\kappa = 0.05m^{-1}$; uniform external temperature enforced at the domain extents; standard-$k\varepsilon$ turbulence model; QUICK differencing employed for convection terms

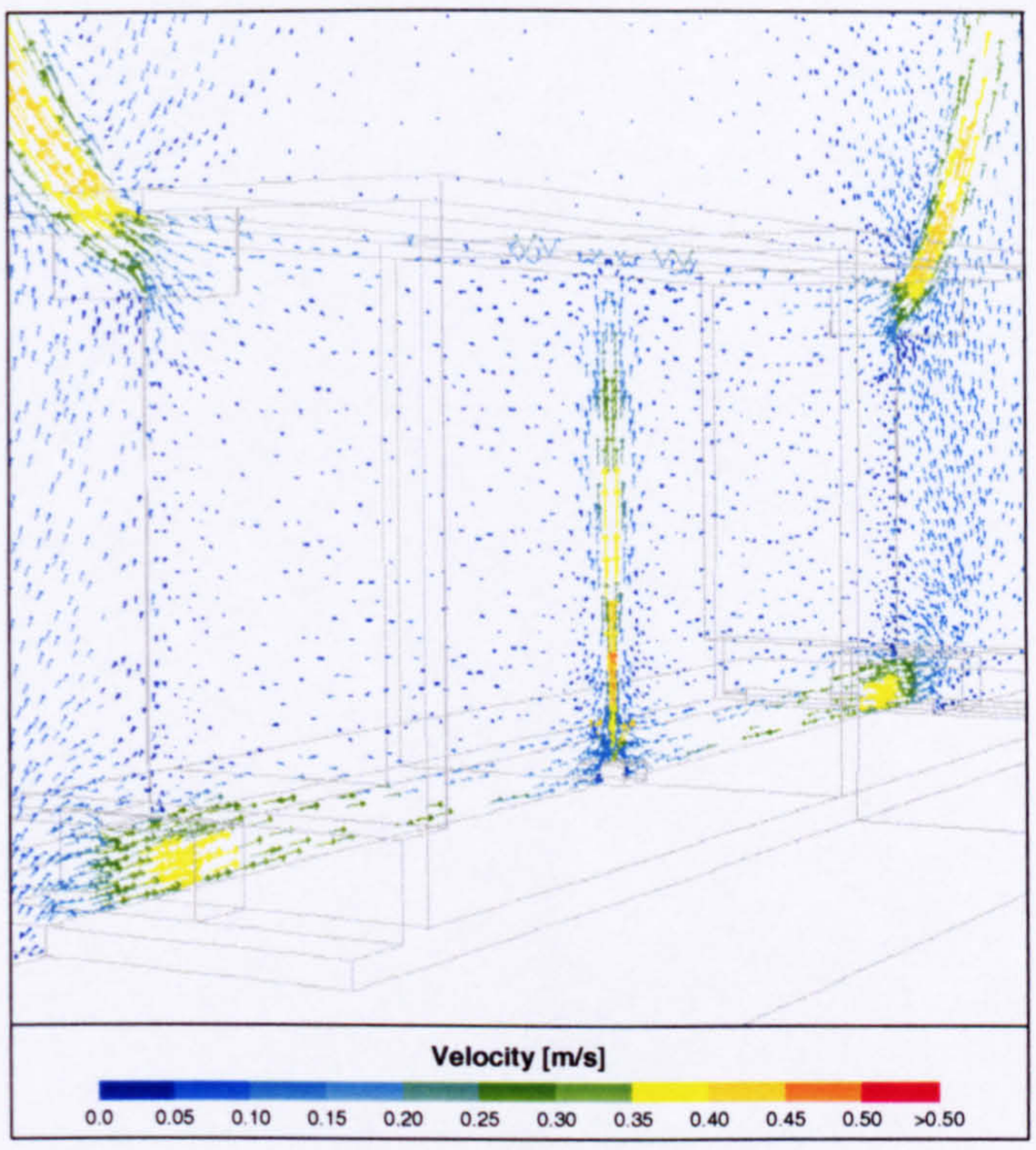

Figure 7.69 - Velocity vector map on the *x-y* plane of symmetry: 490.5W boiler ring; $A^* = 0.488\text{m}^2$; radiation model enabled, $\kappa = 0.05\text{m}^{-1}$; uniform external temperature enforced at the domain extents; standard-$k\varepsilon$ turbulence model; QUICK differencing employed for convection terms

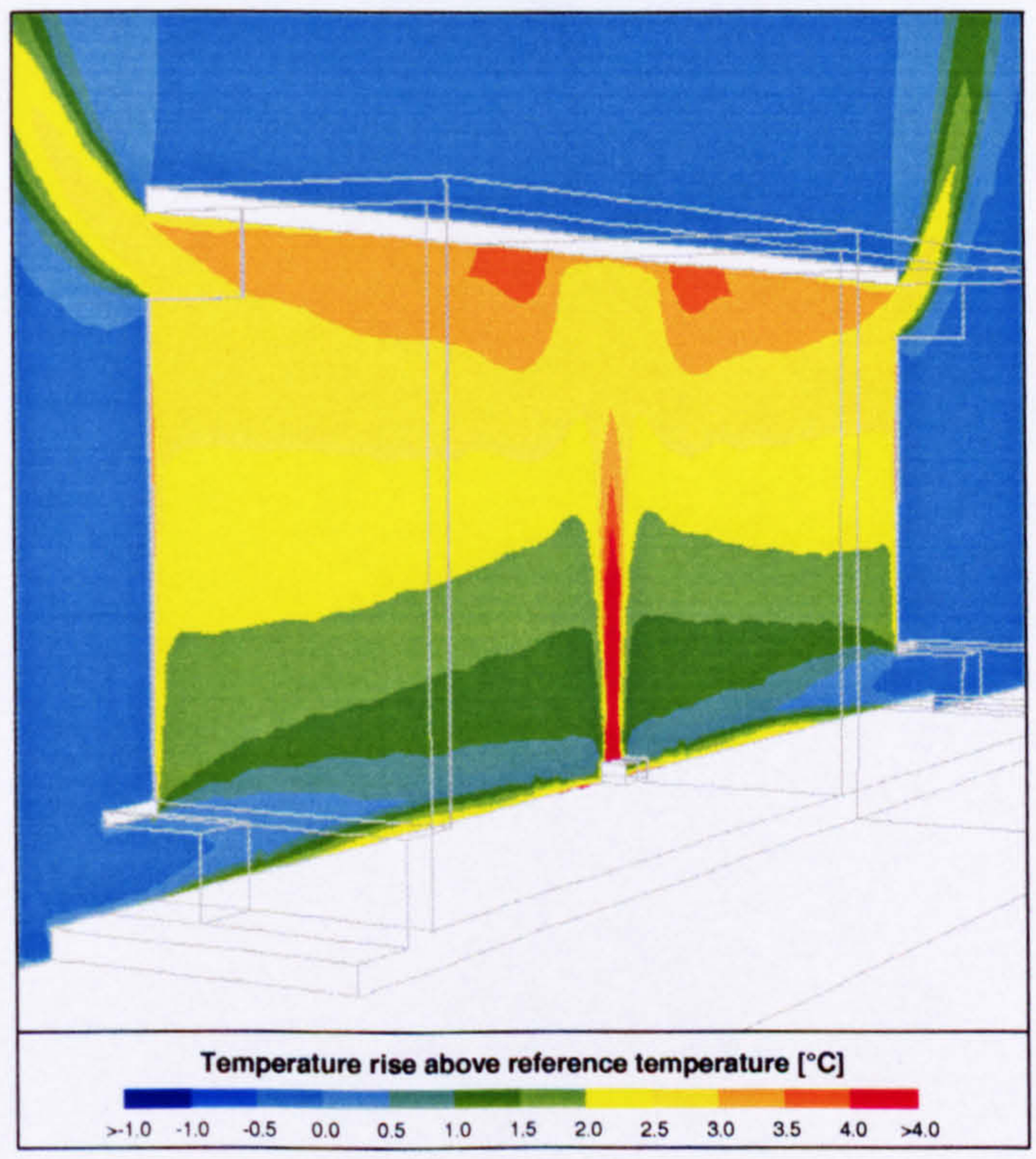

Figure 7.70 - Isopleth map of temperature rise above that at the reference thermometer location on the *x-y* plane of symmetry: 490.5W boiler ring; $A^* = 0.488\text{m}^2$; radiation model enabled, $\kappa = 0.10\text{m}^{-1}$; uniform external temperature enforced at the domain extents; standard-$k\varepsilon$ turbulence model; QUICK differencing employed for convection terms

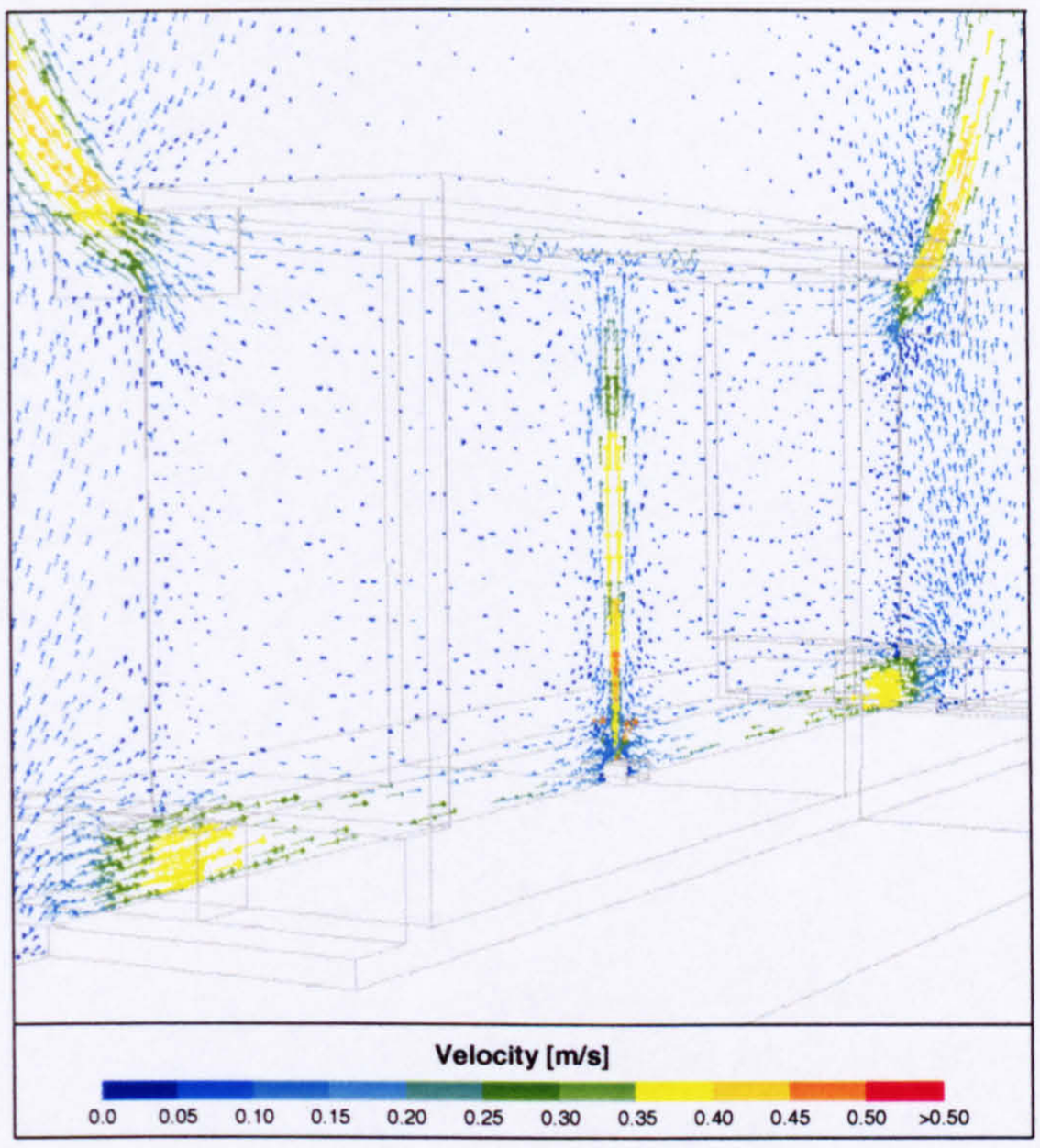

Figure 7.71 - Velocity vector map on the *x-y* plane of symmetry: 490.5W boiler ring; $A^* = 0.488\text{m}^2$; radiation model enabled, $\kappa = 0.10\text{m}^{-1}$; uniform external temperature enforced at the domain extents; standard-$k\varepsilon$ turbulence model; QUICK differencing employed for convection terms

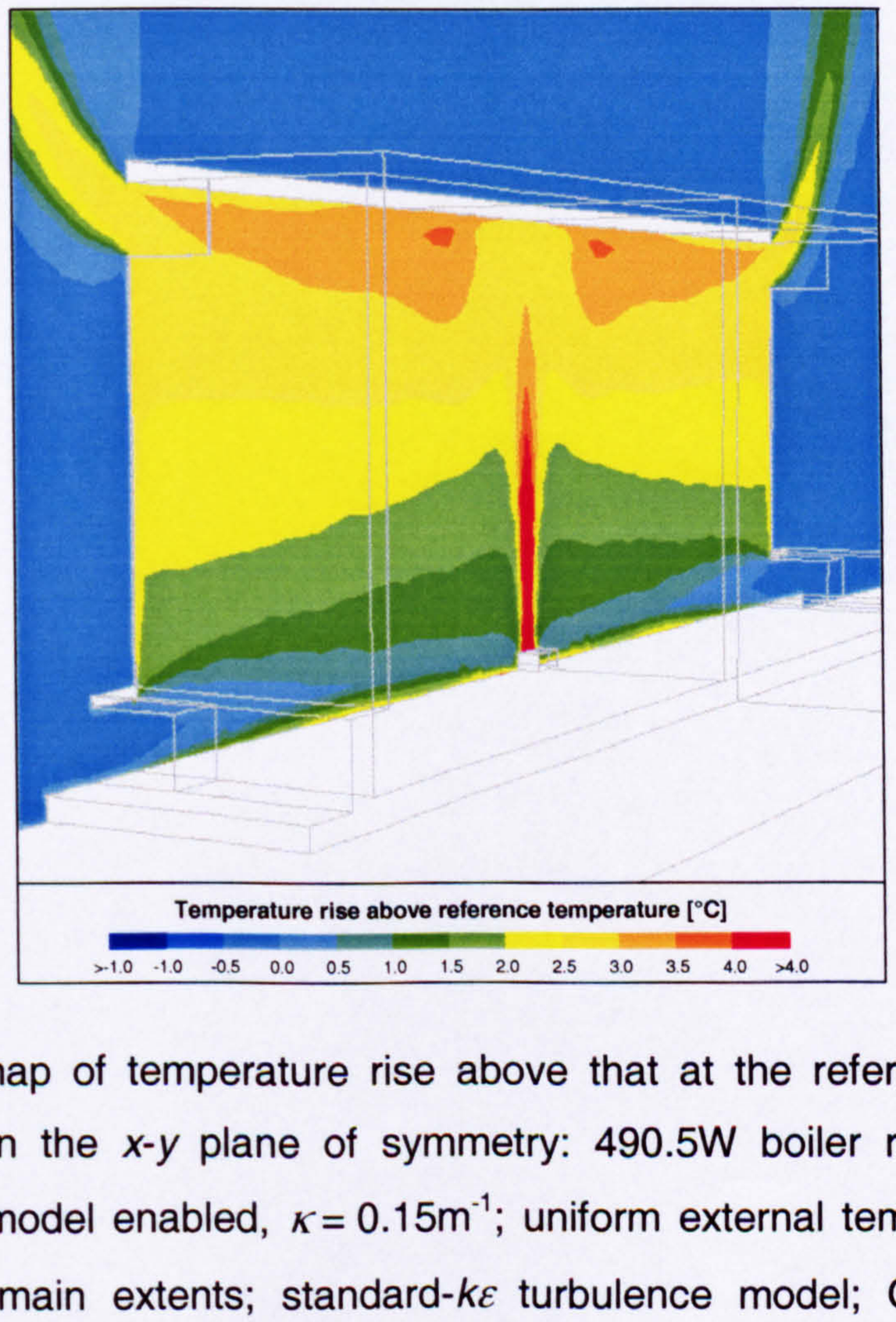

Figure 7.72 - Isopleth map of temperature rise above that at the reference thermometer location on the *x-y* plane of symmetry: 490.5W boiler ring; $A^* = 0.488\text{m}^2$; radiation model enabled, $\kappa = 0.15\text{m}^{-1}$; uniform external temperature enforced at the domain extents; standard-$k\varepsilon$ turbulence model; QUICK differencing employed for convection terms

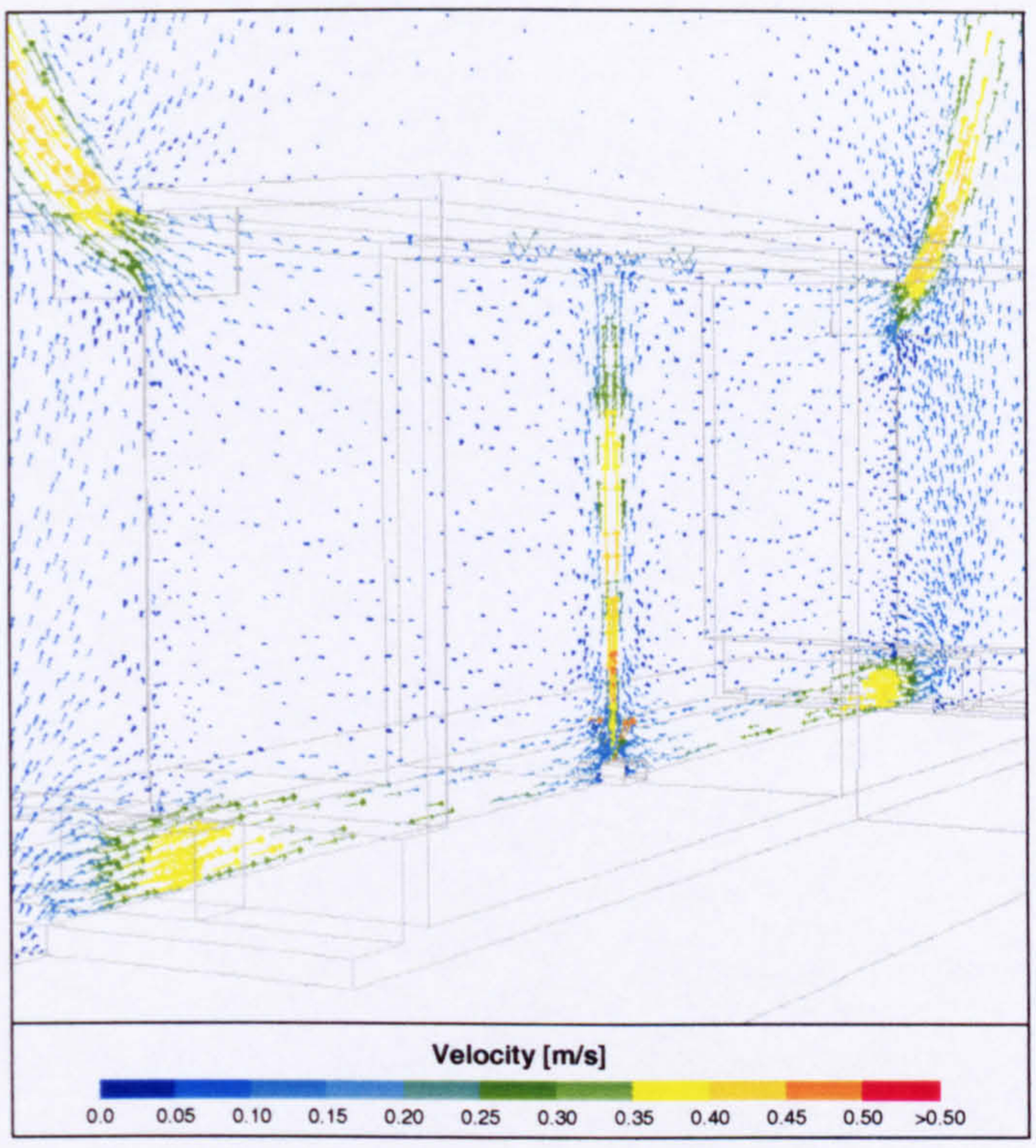

Figure 7.73 - Velocity vector map on the *x-y* plane of symmetry: 490.5W boiler ring; $A^* = 0.488\text{m}^2$; radiation model enabled, $\kappa = 0.15\text{m}^{-1}$; uniform external temperature enforced at the domain extents; standard-$k\varepsilon$ turbulence model; QUICK differencing employed for convection terms

7.3.6 Numerical diffusion and discretization errors

7.3.6.1 Differencing scheme

In accordance with the solution strategy adopted for this CFD investigation, which was described in §7.2.4, the flow was initially solved using first-order upwind differencing as this is the simplest and generally most robust differencing scheme for the convective terms in the discretized governing equations. This was later improved to the third-order QUICK differencing scheme in order to minimize numerical diffusion effects that can be significant on an unstructured tetrahedral computational mesh such as those used for the present analysis.

It was found, however, that the QUICK scheme was often numerically unstable for the cases with the radiation model disabled, regardless of the turbulence model selected. As such, only the predictions employing first-order upwind differencing are presented for those cases. Furthermore, with the boiler ring as the heat source the QUICK scheme was often unstable for the laminar flow predictions with the radiation model enabled but without absorption of radiation throughout the fluid medium, so that for some cases, the QUICK profiles are not available for presentation.

It is thought that for the cases where numerical difficulties were encountered with the QUICK scheme, this may be an indication that there were important physical processes such as thermal radiative transfer excluded from the CFD-model: no such convergence difficulties were encountered with the QUICK scheme when the radiation model was enabled and the absorption of radiation due to the water vapour content of the atmosphere was included within the CFD-model.

7.3.6.2 Spatial discretization

As explained in §3.3.8, there will be a finite error in the CFD-solutions due to the truncation errors inherent in the discretization process of the governing flow equations, which will be manifested as numerical diffusion throughout the flow domain. In order to demonstrate the possible variation due to the spatial discretization of the mesh, a selection of the flow simulations were repeated on a more refined mesh comprising approximately 500,000 computational cells. The edge length for the refined mesh in vicinity of the openings and heat source, within the space generally and outside the space were 0.01m, 0.05m and 0.15m respectively.

The simulations selected for the comparison exercise were those for the boiler ring with a heat output of 490.5W, with the width of the openings equal to 0.8m ($A^* = 0.488m^2$) and the adiabatic assumption in place at the walls of the enclosure. The radiation model was enabled with the absorption coefficient $\kappa = 0.1m^{-1}$, and a uniform external temperature field was applied at the domain extents. The QUICK differencing scheme was used for convective terms in the discretized equations. The comparison comprised four simulations, one for each of the turbulence modelling approaches considered.

The predicted internal temperature profiles using the spatially refined computational mesh are presented in Figure 7.74 below, together with the profiles predicted with the original mesh. It is observed that the profiles are only marginally affected by the refinement of the computational mesh. Perhaps the most apparent difference is an increase in the variation of the surface temperature of the floor. Using the original grid, the range of the variation in the temperature rise at the surface of the floor is of the order of 1.0°C for the standard-$k\varepsilon$ and realizable-$k\varepsilon$ profiles, but this is increased to about 2.0°C with the refined mesh. Likewise, the variation of temperature rise at the floor for the laminar profile is about 2.0°C with the original mesh, and this is increased to 3.0°C with the refined mesh.

For each of the profiles presented for this comparison, however, the vertical temperature gradient and the magnitude of the temperature rise within the space remain practically unchanged. It is therefore reasonable to conclude that the profiles

predicted using the original computational mesh with QUICK differencing are indeed mesh independent in that they do not change significantly as the spatial discretization is refined further.

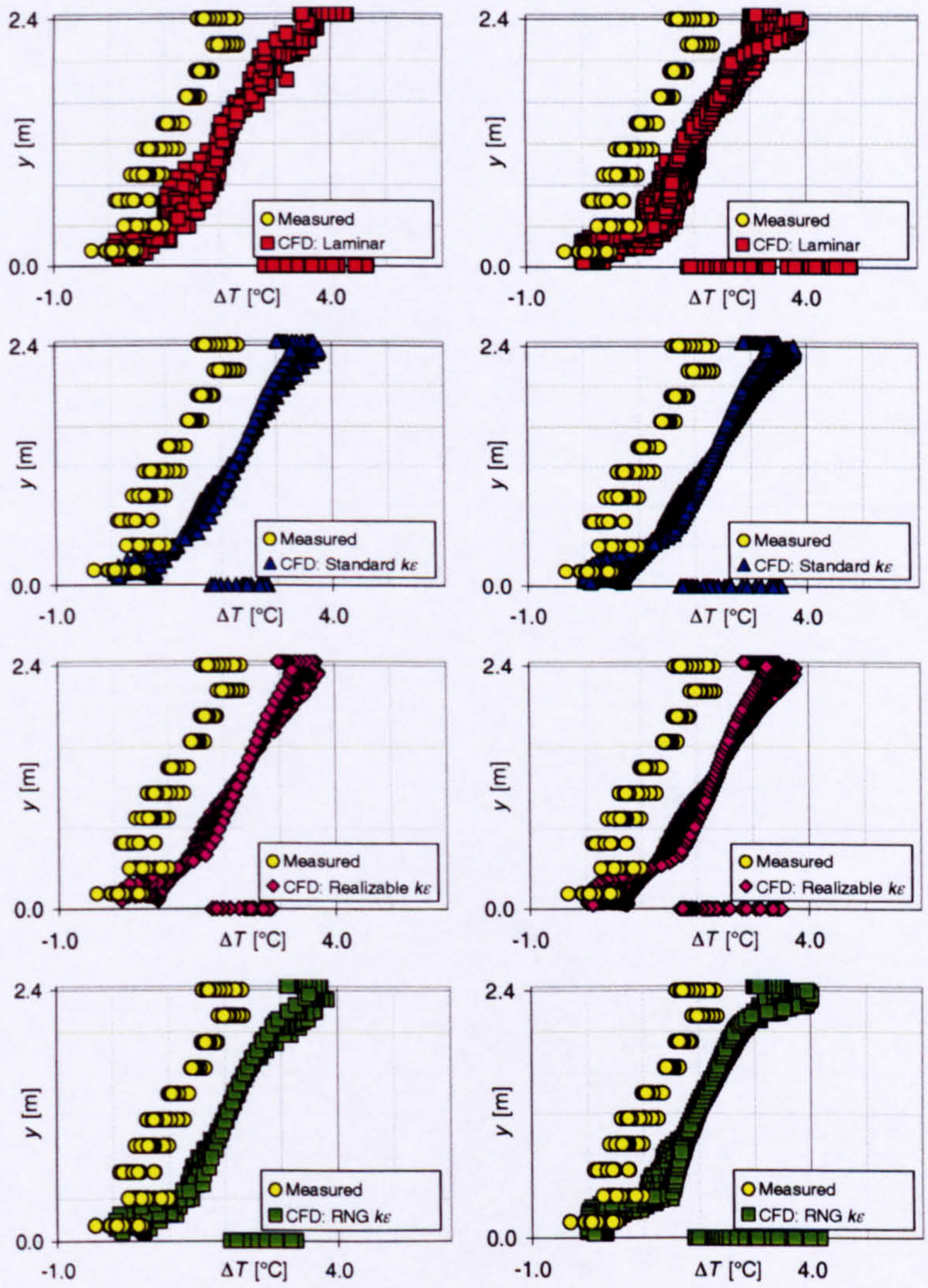

Figure 7.74 - Internal temperature profiles: 490.5W boiler ring; $A^* = 0.488m^2$; radiation model enabled, $\kappa = 0.10m^{-1}$; uniform external temperature at the domain extents; QUICK differencing employed for convection terms; initial grid in left-hand column, refined grid in right-hand column

7.3.6.3 Directional discretization

In addition to the spatial discretization that is required by the CFD approach, when the radiation model is used it is also necessary to discretize direction. As a consequence, further truncation errors are introduced into the resulting algebraic system of radiation equations to be solved.

The sensitivity of the flow field to the directional discretization was investigated for the same four cases that were selected to demonstrate the variation in the solution due to the spatial discretization of the computational mesh. For this comparison, each

octant was divided into 4×4 control directions, so that 128 additional transport equations were solved for the radiative intensity.

The predicted internal temperature profiles using the refined directional discretization are presented in Figure 7.75 below, together with the profiles predicted with the original directional scheme. It is observed that the profiles remain almost unaffected by the refinement of the directional discretization. Indeed, the only detectable difference is a slight increase in the predicted temperature at the surface of the ceiling for the laminar profile and, perhaps, for the RNG-$k\varepsilon$ profile. The vertical temperature gradient and the magnitude of the temperature rise within the space remain unchanged, so that the predicted flow appears to be insensitive to further refinement of the directional discretization.

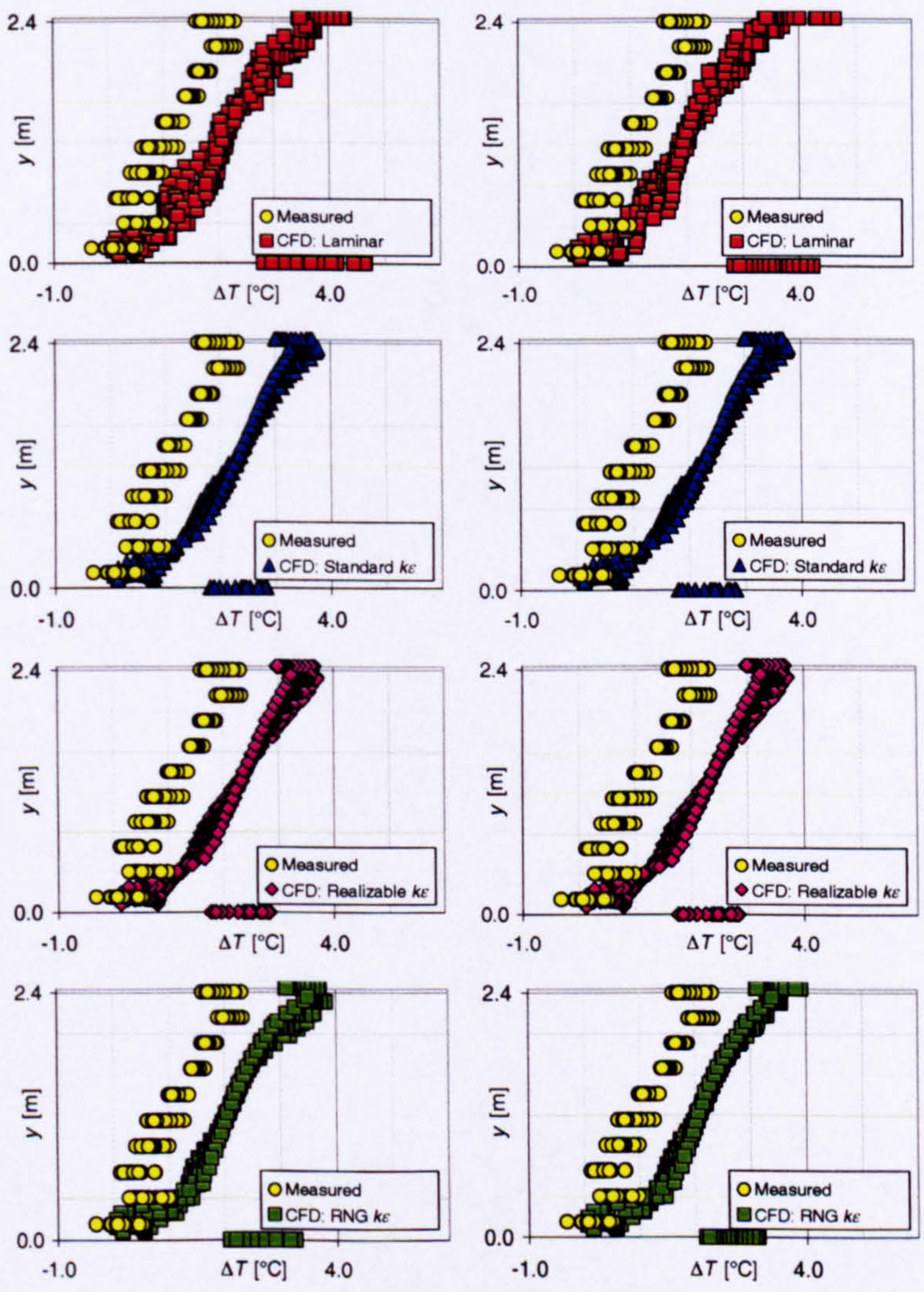

Figure 7.75 - Internal temperature profiles: 490.5W boiler ring; $A^* = 0.732m^2$; radiation model enabled, $\kappa = 0.10m^{-1}$; uniform temperature enforced at the domain extents; QUICK differencing employed for convection terms; initial directional discretization in left-hand column, refined directional discretization in right-hand column

7.4 CFD-predictions for the inward velocity at the low-level openings

The relationship governing the coupling between the internal and external temperature profile and the velocity at the low-level openings was first introduced in §2.7. It was shown that the velocity at the openings is directly related to the magnitude of the temperature rise and upon the shape of the temperature profile within and surrounding the enclosure. In order to accurately and reliably predict the velocity at the openings and, therefore, the volume flow rate through the space, it is first necessary to accurately predict the temperature field throughout the entire fluid domain.

The variation of the predicted inlet velocity at the low-level opening with the effective area of the openings to the enclosure A^* for each of the CFD-modelling approaches considered is presented in Addendum Four. With the adiabatic approximation applied at the enclosure walls, it is generally observed that the temperature rise within the enclosure is over-predicted, particularly for the smaller opening configurations. Correspondingly, the inward component of velocity at the lower opening and the volume flow rate through the enclosure are also over-predicted, in accordance with (2.7.11). With the conduction, radiation or mixed boundary condition employed to predict wall heat transfer, the rise in temperature within the space was under-predicted, with a corresponding fall in the predicted velocity at the low-level openings.

This rather broad observation perhaps demonstrates the limit of any useful analysis of the actual velocity magnitude predicted at the lower opening: other factors contrive to affect the magnitude of the velocity at the opening to such an extent that an accurate and thorough comparison of the measured velocity magnitude and that predicted is not useful. These factors include the errors introduced by the employment of the adiabatic assumption at the walls of the enclosure: if, for example, the CFD-profile correctly predicted the shape of the internal temperature profile but over-predicted the magnitude of the temperature rise by say 0.5°C due to the adiabatic approximation at the enclosure walls, this would have been regarded as a success in terms of predicting the temperature field. The increase in the pressure difference across each of the openings, however, could be of the order of 0.025Pa, which is equivalent to a velocity increase of up to 0.2m/s.

Alternatively, if the shape of the internal temperature profile was poorly predicted but the integral of temperature rise with respect to height happened to have the correct value, then the velocity at the lower-opening would appear to be better predicted.

7.5 Summary

Clearly, when a computational analysis of any fluid flow is performed, the predicted flow field will be dependent upon the combination of physical models used to represent the flow. For the natural displacement ventilation flow through the full-scale enclosure considered as part of this work, five aspects of the physical modelling were identified that required further investigation as part of the CFD study. They are:

- How can the heat transfer at the walls of the enclosure be accurately modelled?
- Should the radiation model be enabled?
- If the radiation model is enabled, should the radiative absorption due to the component of water vapour in the air be included in the model?
- Which turbulence modelling approach should be adopted: should the flow be considered as laminar, or should one of the -$k\varepsilon$ turbulence closures already implemented within the Fluent CFD-solver be used to model the effects of turbulent fluctuations upon the flow field?
- Should the measured external thermal stratification be specified at the extents of the computational domain or is a uniform temperature satisfactory?

7.5.1 Predicting the rates of heat transfer at the walls of the enclosure

It emerged following the experimental phase of this work that the walls of the experimental enclosure were not particularly well insulated, so that significant transfer of thermal energy could occur due to conduction through the fabric of the enclosure walls. In §6.2.3, it was highlighted that for the smaller opening configurations where the volume flow rate and the associated thermal convection loss rate is a minimum, a significant majority of the thermal energy released at the heat source escaped from the space as a thermal conduction loss through the walls of the enclosure. For the larger openings where the volume flow rate through the space is increased, together with the proportion of energy convected out of the space, the rate of heat loss through the enclosure walls by conduction is reduced.

Generally, if the CFD-prediction for the temperature field within the enclosure for this buoyancy-driven flow is to reflect that measured during the experimental phase of this work, then it is necessary that the rate of heat transfer at the walls of the enclosure be predicted reasonably well.

It was discovered during the course of the CFD investigation that if the walls of the enclosure were assumed to be adiabatic, then the rise in temperature within the space was significantly over-predicted, particularly for the smaller openings.

Furthermore, it was found that if the simple methods incorporated into the Fluent CFD-solver were used, then the rates of heat transfer at the enclosure walls were over-predicted, so that the rise in temperature calculated within the space was much less than that measured.

The methods considered as part of this work for predicting the rate of heat transfer at the walls of the enclosure were found to be inadequate, to the extent that it was not possible to achieve realistic CFD-predictions for the temperature field within the space for the smaller opening configurations.

For the larger openings, for which the rates of heat transfer at the enclosure walls were much reduced, the application of the adiabatic assumption at the walls of the enclosure allowed reasonable prediction of the temperature field within the space, and permitted an investigation into the effects upon the flow of the remaining physical modelling aspects identified.

7.5.2 Enabling the thermal radiation model

Prior to the start of the CFD study, it was perhaps not obvious that thermal radiative effects would be significant, since the differences in temperature throughout most of the flow domain would not be significant in comparison to the ambient temperature in absolute terms, the only exception being the heated element of the plate heater or boiler ring.

With the radiation model disabled, each of the CFD-profiles for the rise in temperature within the space predicted the existence of a relatively deep layer of ambient air in the lower part of the space. The presence of such a layer, however, was never observed during the experimental phase of this work.

With the radiation model enabled, significant improvements were observed between the CFD-profiles and the corresponding measured profiles. In particular, the CFD-profiles exhibit a roughly uniform temperature gradient for much of the core of the space, and the gradients predicted are generally representative of those measured within the space.

Following the CFD study, therefore, it would appear that the use of the thermal radiation model is necessary if realistic predictions are to be achieved for the temperature field within the enclosure.

7.5.3 Including radiative absorption effects

It is observed that the agreement between the CFD-profiles for the rise in temperature within the space and the corresponding measured profiles are further improved if a non-zero absorption coefficient is used to account for absorption of radiation due to the water vapour component of the atmosphere. The improvement is particularly apparent in the layer immediately below the ceiling. If radiative absorption is neglected then a significant increase in the vertical temperature gradient in the layer below the ceiling is predicted. With a non-zero absorption coefficient, this increase in the temperature rise is less significant or, indeed, the temperature remains approximately constant, which is generally in better agreement with the experimental observations.

It is therefore recommended that a non-zero absorption coefficient in the range $0.10m^{-1} < \kappa < 0.15m^{-1}$ should be adopted when predicting the natural displacement ventilation flow through a full-scale air enclosure.

7.5.4 Selection of the turbulence modelling approach

It is normally the case that with the radiation model enabled, the predicted temperature field is less affected by the turbulence modelling approach adopted, particularly when a non-zero absorption coefficient is used. It appears, therefore, that the primary modelling concern for predicting this type of natural displacement ventilation flow is that the radiation model should be enabled, and that which turbulence closure is used is really only of secondary importance.

7.5.5 Application of the external thermal stratification

It is observed that a marginal improvement in the agreement between the CFD-predictions and the measured internal temperature profile can be achieved if the measured external temperature stratification is enforced at the domain extents. If the external temperature profile is known a priori, it is recommended that this profile be incorporated into any CFD-simulations.

8.0 Conclusions and suggestions for further work

8.1 Conclusions from this work

This work was concerned with current and emerging methods for predicting buoyancy-driven natural displacement ventilation flows within buildings. There were two main objectives for this research; to conduct a thorough experimental study on the natural ventilation flow through a full-scale enclosure representative of a real building with air as the fluid medium in order to provide benchmark data for model validation and to use this benchmark data to identify the preferred method for predicting detailed airflow patterns and thermal stratification for natural displacement ventilation flows within buildings.

8.1.1 Experimental study with the full-scale air-enclosure

A single benchmark case that has received much attention in the past 15 years was identified for the experimental program: the natural displacement ventilation flow through an enclosure with low-level and high-level openings, driven by a point source of buoyancy at floor level. Despite the widespread interest in this class of ventilation flow, there had not yet been any experimental validation work reported using a full-scale air-based enclosure. To address this, a full-scale air-enclosure was constructed as part of this work and the natural displacement ventilation flow through the space investigated for a number of heat sources for a range of opening configurations. In particular, the temperature stratification established within the enclosure and the displacement flow rates through the space were monitored and are presented. The rate of heat transfer through the walls of the enclosure and the surface temperatures of the walls were not recorded.

This work is the first experimental study to the authors knowledge to consider the natural displacement ventilation flow through a full-scale enclosure with air as the fluid medium. The full-scale experimental enclosure measured 7.32m long × 2.32m wide × 2.44m high so that in terms of geometrical size, it was indeed representative of an occupied space within a real building. Due to budgetary constraints, however, it was constructed from chipboard sheet material rather than more traditional building materials, so that the thermal properties of the walls were not necessarily

representative of a real building. Indeed, it was observed that a significant proportion of the thermal energy introduced into the space by the heat source during the experimental phase escaped from the space by conduction through the fabric of the enclosure walls. This proportion was particularly high for the smaller opening configurations considered. As the openings were increased, this proportion was reduced as the loss by convection through the openings became more significant, so that the adiabatic assumption for the walls of the enclosure became an increasingly realistic approximation. Nonetheless, the experimental data presented does form a valuable set of benchmark data for a naturally-driven ventilation flow with air as the fluid medium that does not suffer from geometrical scaling problems.

8.1.2 Predictive techniques for natural displacement ventilation

It was found that the Cambridge mathematical model introduced in §4.0 and the associated water-based scale-modelling techniques do not compare favourably with the data from the full-scale experimental enclosure. With regard to the temperature distribution within the enclosure, it was observed that no layer of ambient air at low-level within the space was established, nor was there a sharp interface between two layers of fluid at a different temperature. This is in contrast to the stratification observed in the water-based experiments, and that predicted by the Cambridge mathematical model.

This may in part be due to differences in the rate of heat transfer at the enclosure walls: for the Cambridge mathematical model and water-based scale-model experiments the walls are effectively adiabatic, whereas for the full-scale experimental enclosure the rate of heat transfer through the walls was non-zero. For the larger opening configurations with the full-scale enclosure, however, as the amount of energy that was convected through the enclosure was increased, the proportion of thermal energy lost through the walls was reduced, so that the adiabatic approximation at the enclosure walls became increasingly more realistic. Even for the larger openings, however, there was no sharp interface or layer of ambient air at low-level within the space.

Perhaps a more important cause of the observed differences was the presence of additional transport mechanisms within the full-scale room. First of all, the transport of heat by molecular diffusion is not accurately represented by water-based experimental methods. For air, the Prandtl number is equal to

$$Pr_{AIR} = 0.71, \qquad (8.1.1)$$

so that the rate of diffusion of heat in air is comparable to the rate of diffusion of momentum. For the diffusion of salt in water, the Schmidt number is equal to

$$Sc_{NaCl} = 621, \qquad (8.1.2)$$

and for hydrogen bubbles, the Schmidt number is equal to

$$Sc_{H2} = 196. \qquad (8.1.3)$$

The diffusivity of salt in water is, therefore, almost one thousand times less significant than the diffusivity of heat in air, and the diffusivity of hydrogen bubbles is about three-hundred times less significant than the diffusivity of heat in air. Full similarity cannot, therefore, be achieved between the natural displacement flow in the small-scale water-based experiments and that in a full-scale air-enclosure.

In addition, the transport of heat by radiation is absent from the salt-bath and the fine-bubble experiments since they are entirely isothermal. In contrast, the mechanism of thermal radiative transfer was present in the full-scale air enclosure and will be present in a real building.

Finally, the Reynolds number *Re* for the flow within the full-scale enclosure was greater than that for the salt-bath experiments (§4.4.3.2). As the flow within the enclosure away from the plume was likely to be transitional between the laminar and turbulent regimes, the higher Reynolds number for the flow within the full-scale enclosure would indicate that the degree of turbulent diffusion would have been greater than for the similar flows in the salt-bath experiments. This is an additional mechanism that may have contributed to the non-existence of sharp changes in temperature within the full-scale room.

Since the mechanisms of diffusion and thermal radiation are neglected, the application of the Cambridge mathematical model and the water-based experiments to the modelling of natural displacement ventilation flows within full-scale air enclosures was thought to be limited.

Realistic predictions for this type of ventilation flow can be achieved using the CFD technique, which is not affected by scaling restrictions and can be easily extended to model additional physical processes including turbulent transport and thermal radiative transfer. This approach does, however, require further development before it can be used routinely, particularly with respect to the prediction of rates of heat transfer at solid walls. In particular, the standard wall-function method described in §3.7.1 was found to significantly over-predict the rate of heat transfer at the enclosure walls, particularly for the smaller openings considered. For the larger openings, however, the flow rate through the experimental enclosure and the proportion of energy that was convected out of the upper openings was greater, so

that the proportion of energy lost due to conduction through the fabric of the walls of the enclosure was less significant. A useful comparison of the CFD-predictions and the experimental data was, therefore, limited to the flow through the enclosure with larger openings where the adiabatic approximation was adopted at the enclosure walls within the CFD-model.

With the radiation model disabled, the CFD-predictions for the stratification within the computational enclosure exhibited a layer of ambient layer in the lower part of the space. Depending upon which turbulence closure was selected, above this there may have been another layer of buoyant air at a constant temperature, separated from the ambient layer by a relatively sharp interface (standard-$k\varepsilon$ turbulence closure), or the upper layer may have exhibited an approximately constant vertical temperature gradient (laminar model or RNG-$k\varepsilon$ turbulence closure). Interestingly, the CFD-prediction for the standard-$k\varepsilon$ turbulence closure coincides with that of the flow given by the Cambridge mathematical model and which was observed during the water-based experiments, but does not agree with that observed within the full-scale air-enclosure.

The CFD-predictions presented as part of this work that were conducted with the radiation model disabled agree well with those of Cook (1998). A radiation model was not considered as part of that study and it concluded that the CFD-predictions were in good agreement with the Cambridge mathematical model. At that time, however, the only experimental data available was that from the salt-bath technique which also agrees well with the model: there was no experimental data available from a full-scale air-enclosure to suggest that the existing water-based data may not be representative of the flow in a real building. There was, therefore, no reason to consider radiative effects, although one of the suggestions for further work was to conduct an investigation into the effects of radiation for the benchmark case considered.

With the radiation model enabled but with the absorption of radiation within the fluid medium neglected, the CFD-profiles no longer predicted the layer of ambient air in the lower part of the enclosure. Instead, they predicted an approximately constant vertical temperature gradient, which was in better agreement with that observed during the experimental phase of this work. The agreement was further improved if the effects of absorption of radiation due to the water vapour content of the atmosphere were incorporated in to the CFD-model, particularly in the layer of air immediately below the ceiling. It was further observed that with the radiation model and radiative absorption effects enabled, the variation amongst the CFD-profiles for different turbulence modelling approaches became less significant, so that the choice of turbulence closure perhaps may be of secondary importance.

For the natural convection flow considered presently with air as the fluid medium, it would appear that it is necessary to properly account for thermal radiative transfer, including the absorption of radiation throughout the fluid medium, if a realistic representation of the flow within the full-scale air enclosure is to be predicted.

It is concluded that the CFD-technique has the potential to accurately predict the detailed airflow patterns and thermal stratification for buoyancy-driven natural ventilation flows within buildings where simpler analytical models or water-based experimental methods have limitations. A FV-radiation model should be incorporated into the CFD-model, and the absorption coefficient κ should be in the range $0.10m^{-1} < \kappa < 0.15m^{-1}$. If possible, the rate of heat transfer at the walls of an enclosure should be prescribed in advance, as further work is required before this information can be realistically determined as part of a CFD-simulation.

8.2 Suggestions for future work

8.2.1 Future experimental investigation within the laboratory

This work was completed with a relatively small research budget, which placed limitations upon what was feasibly possible. As such, there are many improvements to the current experimental facility that would provide more extensive data for the natural displacement flow considered here. Some improvements are listed below.

1. More thermometers – an array of platinum-resistance thermometers could be constructed within the enclosure in order to allow the instantaneous temperature field throughout the space to be recorded, without the need to traverse the thermometer mast and associated frame. This would also provide detailed information for the transient performance of the enclosure. In addition, a further array of resistance thermometers could be erected in the void surrounding the enclosure so that detailed recordings of the external temperature stratification could be made.
2. Wall temperatures – a knowledge of the temperature distribution on the internal surfaces of the enclosure would be useful, since thermal radiative transfer is thought to greatly affect the flow. This could be achieved by installing an array of thermometers into the fabric of the enclosure walls of interest to monitor the temperature at the surface. Alternatively, heat sensitive paint could be applied to the internal surfaces, or a thermal imaging camera could be used to record the surface temperature of the walls during the course of an experiment.

3. Humidity measurement – the humidity of the air within the larger chamber could be recorded, as the magnitude of the absorption coefficient of the fluid is dependent upon its water vapour content.
4. Velocity measurements in openings – the velocities at the openings could be recorded using particle image velocimetry or PIV. A plane across the openings could be illuminated to allow the instantaneous velocity field at that plane to be recorded for the duration of an experiment. This would also provide information of the transient performance of the enclosure.
5. Velocity measurements within the space – even with current technology, it may be possible to place a light source along the centreline of the floor aimed upwards, with another directly above along the centreline on the ceiling pointing downwards, so that a light-sheet could extend for the entire height within the enclosure. This would allow the instantaneous velocity field on the *xy*-plane of symmetry to be recorded for the duration of an experiment, again providing information of the transient performance of the enclosure.
6. Pressure measurements – rather than deduce the pressure distribution from the measured internal and external temperature profiles, it would be beneficial to measure the actual pressure difference across the vertical walls of the enclosure at a number of selected heights above the floor and in the vicinity of the openings. The pressure differences across the walls will be small, but could be measured using a device such as a Chattock gauge (Duncan, 1928).

If a new experimental enclosure was to be built, then some considerations for the revised design are listed below.

1. Well-insulated walls – a new enclosure could be constructed with well-insulated walls in order to provide reliable experimental benchmark data for the flow through the enclosure with smaller openings.
2. Walls of variable heat capacity – since most natural ventilation flows occur in buildings that are constructed from thermally massive materials, the flow within a real building will always be transient in nature due to the thermal lag of the fabric of the construction. This effect could be investigated with a new facility constructed from heavy materials, the thermal mass of which is known. Alternatively, a network of water tanks could be incorporated into the walls of the facility, so that the heat capacity of the walls could easily be changed to investigate the effect of a varying thermal mass of the enclosure walls.
3. Controllable external environment – the new facility could be constructed within a larger chamber which is better insulated than that available for the present study. This could remove the non-symmetrical effects observed during the current study, and would allow the external stratification to be controlled rather than

merely monitored. Furthermore, if it was possible to accurately control the temperature environment within the larger chamber, in the space surrounding the enclosure, then the effect of different shapes of the external profile of temperature could be investigated.

8.2.2 CFD-simulations

Following the CFD study that forms part of this work, there remain certain issues that require further consideration. Some of them are listed here.

1. Prediction of heat transfer at solid wall boundaries – clearly this was one of the inadequacies of the present CFD study, especially for the flows considered through the enclosure with smaller openings. Another more realistic method for predicting the wall heat flux should be sought. Possible alternatives include the convection wall functions developed by Yuan et. al. (1995), or the use of a low-Re $k\varepsilon$ model of turbulence, maybe one of those included in the review by Patel et. al. (1985).
2. Modelling a non-grey gas – another restriction of the present CFD study is that the radiative absorption coefficient was assumed to be constant across the entire radiative spectrum. This, of course, is a simplification since the absorption bands for water vapour occur only for narrow bands within the spectrum. The grey-gas assumption may, therefore, introduce errors into a CFD-prediction of a flow, especially for longer path lengths. The option of modelling the fluid medium as non-grey, by solving a transport equation for the spectral radiative intensity at the wavelengths corresponding to each absorption band for water vapour, should be investigated.
3. Transient performance – if transient experimental data for the natural displacement ventilation flow within a full-scale air enclosure was available, then this should be used as benchmark data for a transient CFD-study, since most flows in real buildings are transient in nature.
4. Large eddy simulation – although the turbulence modelling approach was identified as a secondary concern in comparison to the radiative modelling approach, the use of LES for modelling the effects of turbulence may provide a useful advance.

9.0 References

Abu-Romia MM, Tien CL: "Appropriate mean absorption coefficients for infrared radiation in gases", J. Heat Trans. 89: 4, pp321-327, 1967.

Anderson RS, Fisher EM and Bohn MS: "Thermal stratification in direct gain passive heating systems with variable heating of the floor and one vertical wall", Proc. 10th Nat. Passive Solar Energy Conf., 1985.

Batchelor GK: An introduction to fluid dynamics, Cambridge University Press, Cambridge, England, 1967.

Boussinesq J: "Théorie de l'écoulement tourbillant", Mem. Présentés par Divers Savants Acad. Sci. Inst. Fr. 23, pp46-50.

Beausoleil-Morrison I, Clarke J: "The implications of using the standard k-ε turbulence model to simulate room air flows which are not fully turbulent", Proc. Roomvent '98, 1998.

Caulfield CP: "Stratification and buoyancy in geophysical flows", Ph. D. Thesis, University of Cambridge, England, 1991.

Choudhury D: "Introduction to the Renormalization Group method and turbulence modelling", TM-107, Fluent Inc, NH, USA, 1993.

Chen MH, Cardoso SSS: "The mixing of liquids by a plume of low-Reynolds number bubbles", Chem. Eng. Sci. 55:14, pp2585-2594, 2000.

Chen Q: "A comparison of different k-ε models for indoor air flow computations", Num. Heat Trans. B28, pp353-369, 1995.

Chen Q, Jiang Z: "Significant questions in predicting room air motion", ASHRAE. Trans. 98:1, pp929-939, 1992.

Chen Q, Moser A, Huber A: "Prediction of buoyant, turbulent flows by a low-Reynolds number $k\varepsilon$ model", ASHRAE. Trans. 96:1, pp564-573, 1990.

Chen ZD, Li Y: "Buoyancy-driven displacement natural ventilation in a single-zone building with three-level openings", Build. Env. 37, pp295-303, 2002.

Chen ZD, Li Y, Mahoney J: "Experimental modelling of buoyancy-driven flows in buildings using a fine-bubble technique", Build. Env. 36, pp447-455, 2001.

CIBSE.: "Energy efficiency in buildings", CIBSE. Guide, Chartered Institution of Building Services Engineers, London, 1998.

Cook M: "An evaluation of computational fluid dynamics for modelling buoyancy-driven displacement ventilation", Ph. D. Thesis, De Montfort University, Leicester, England, 1998.

Cooper P, Linden PF: "Natural ventilation of an enclosure containing two buoyancy sources", J. Fluid Mech. 311, pp153-176, 1996.

Cussler EL: Diffusion mass transfer in fluid systems, 2nd Edn., Cambridge University Press, Cambridge, England, 1997.

Duncan WJ: "The Chattock gauge", J. Sci. Instrum 5, p26, 1928.

Eftekhari M, Marjanovic LD, Hanby VI, D'Ovidio A: "Predicting air flow distribution in a naturally ventilated room", Proc. Roomvent 2000, 2000.

Ferm H: "Measurements and analysis of natural convection in building enclosures", S. M. Thesis, Massachusetts Institute of Technology, Cambridge, MA, USA, 1984.

Ferziger JH: "Large eddy simulation", in Simulation and modeling of turbulent flows (Edited by Gatski TB, Hussaini MY, Lumley JL), Oxford University Press, Oxford, England, 1996.

FLUENT Users Manual, Version 5.4, Fluent Europe Ltd., Sheffield, England, 2000.

GAMBIT Users Manual, Version 2.0, Fluent Europe Ltd., Sheffield, England, 2000.

Glicksman LR, Chen Q: "Interaction of radiation absorbed by moisture in air with other forms of heat transfer in an enclosure", Proc. Roomvent '98, pp111-118, 1998.

Henkes RAWM, van der Vlugt FF, Hoogendoorn CJ: "Natural-convection flow in a square cavity calculated with low-Reynolds-number turbulence models", Int. J. Heat Mass Trans. 34.2, pp377-388, 1991.

Henkes RAWM, Hoogendoorn CJ: "Turbulent natural convection in enclosures; a computational and experimental benchmark study", Proc. Eurotherm Sem. 22, EETI, Paris, France, 1993.

Holford JM, Hunt GR: "Fundamental atrium design for natural ventilation", Build. Env. 38, pp409-426, 2003.

Hottel HC: "Radiant-heat transmission", in Heat transmission (Edited by McAdams WH), 3rd Edn., McGraw-Hill, New York, USA, 1954.

Howell SA: "Natural displacement ventilation for buildings", M. Eng. Final Year Project, University of Newcastle-upon-Tyne, Newcastle-upon-Tyne, England, 1998.

Howell SA, Potts I: "A comparison of predictive techniques for natural displacement of buildings", Proc. CIBSE Nat. Conf., pp156-164, 1998.

Howell SA, Potts I: "On the natural displacement flow through a full-scale enclosure, and the importance of the radiative participation of the water vapour content of the ambient air", Build. Env. 37, pp817-823, 2002.

Hutchinson BR, Raithby GD: "A multigrid method based on the additive correction strategy", Num. Heat Trans. 9, pp511-537, 1986.

Jones WP, Launder BE: "The prediction of laminarization with a two-equation model of turbulence", Int. J. Heat Mass Trans. 15, pp301-314, 1972.

Jones PJ, Whittle GE: "Computational fluid dynamics for building air flow prediction - current status and capabilities", Build. Env. 27, pp321-338, 1992.

Kim SW, Chen CP: "A multi-time-scale turbulence model based on variable partitioning of the turbulent kinetic energy spectrum", Num. Heat Trans. B16, pp193-211, 1989.

Kolmogorov AN: "Equations of turbulent motion of an incompressible fluid", Izvestia Acadamy of Sciences, USSR; Physics 6, pp56-58, 1942.

Kondo Y, Ogasawara T, Fujimura J: "Interactive simulation of room air temperature and absorption/emission of radiative heat with room moisture", Proc. Roomvent 2000, 2000.

Lam CKG, Bremhorst KA: "Modified form of k-ε model for predicting wall turbulence", ASME. J. Fluids Eng. 103, pp456-460, 1981.

Lane-Serff GF: "Heat flow and air movement in buildings", Ph. D. Thesis, University of Cambridge, England, 1989.

Launder BE, Spalding DB: "The numerical computation of turbulent flows", Comp. Meth. App. Mech. Eng. 3, pp269-289, 1974.

Leonard BP: "A stable and accurate convective modelling procedure based on quadratic upstream interpolation", Comp. Meth. App. Mech. Eng. 19, pp59-98, 1979.

Li Y; "Buoyancy-driven natural ventilation in a thermally stratified one-zone building", Build. Env 35, pp207-214, 2000.

Li Y, Delsante A, Chen Z, Sandberg M, Anderson A, Bjerre M, Heiselberg P: "Some examples of multiplicity in natural ventilation", Build. Env. 36, pp851-858, 2001.

Linden PF, Lane-Serff GF, Smeed DA: "Emptying filling boxes: the fluid mechanics of natural ventilation", J. Fluid Mech. 212, pp309-335, 1990.

Linden PF, Cooper P: "Multiple sources of buoyancy in a naturally ventilated enclosure", J. Fluid Mech. 311, pp177-192, 1996.

Linden PF: "The fluid mechanics of natural ventilation", Ann. Rev. Fluid Mech. 31, pp201-238, 1999.

Loomans MGLC: "The measurement and simulation of indoor air flow", Ph. D. Thesis, Technical University of Eindhoven, The Netherlands, 1998.

Mathur SR, Murthy JY: "A pressure-based method for unstructured meshes", Num. Heat Trans. B31, pp195-215, 1997.

Maybrey JFM: "Mean velocity calibration comparison of a laser Doppler anemometer", Dantec Info. 13, pp10-13, 1994.

Mie G: "Optics of turbid media", Ann. Phys. 25.3, pp377-445, 1908.

Modest MF: Radiative heat transfer, McGraw-Hill, New York, USA, 1993.

Morton BR, Taylor GI, Turner JS: "Turbulent gravitational convection from maintained and instantaneous sources", Proc. R. Soc. Lond. A234, pp1-23, 1956.

Murthy JY, Mathur SR: "Finite volume method for radiative heat transfer using unstructured meshes", J. Thermophys. Heat Trans. 12, pp313-321, 1998.

Nansteel MW, Greif R: "Natural convection in undivided and partially divided rectangular enclosures", ASME J. Heat Trans. 103, pp623-629.

Nielsen PV: "The selection of turbulence models for predicting room airflow", ASHRAE. Trans. 104:1B, pp1119-1127, 1998.

Olson DA: "Scale model studies of natural convection in enclosures at high Rayleigh number", Ph. D. Thesis, Massachusetts Institute of Technology, Cambridge, MA, USA, 1986.

Olson DA, Glicksman LR, Ferm H: "Steady-state natural convention in empty and partitioned enclosures at high Rayleigh numbers", ASME. J. Heat Trans. 112, pp640-647, 1990.

Patankar SV, Spalding DB: "A calculation procedure for heat, mass and momentum transfer in three-dimensional parabolic flows", Int. J. Heat Mass Trans. 15, pp1787-1806, 1972

Patankar SV: Numerical Heat Transfer and Fluid Flow, Hemisphere Publishing corporation, Taylor and Francis Group, New York, 1980.

Patel VC, Rodi W, Scheuerer G: "Turbulence models for near-wall and low Reynolds number flows: a review", AIAA J. 23.9, pp1308-1319, 1985.

Pope SB: "An explanation of the turbulent round-jet/plane-jet anomaly", AIAA J. 16.3, pp279-281, 1978.

Prandtl L: "Über ein neues formalsystem für die ausgebildete turbulenz", Nacr. Akad. Wiss. Göttingen, Math-Phys. Kl., pp6-19, 1945.

Rayleigh, Lord: Phil. Mag. 12, 1881.

Reynolds O: "On the dynamical theory of incompressible viscous fluids and the determination of the criterion", Phil. Trans. R. Soc. Lond. A186, p123, 1895.

Rhie CM, Chow WL; "Numerical study of the turbulent flow past an airfoil with trailing edge separation", AIAA J. 21:11, pp1525-1532, 1983.

Rodi W, Spalding DB: "A two-parameter model of turbulence and its application to free jets", Wärme und Stoffübertragung, 1970.

Rodi W: "Experience with two-layer turbulence models combining the $k\varepsilon$ model with a one-equation model near the wall", AIAA-91-0216, 1991.

Rodi W: Turbulence models and their application in hydraulics - a state of the art review, 3rd Edn., IAHR Monograph, Rotterdam, The Netherlands, 1993.

Rothman LS, Rinsland CP, Goldman A, Massie ST, Edwards DP, Flaud JM, Perrin A, Camy-Peyret C, Dana V, Mandin JY, Schroeder J, McCann A, Gamache RR, Wattson RB, Yoshino K, Chance KV, Jucks KW, Brown LR, Nemtchinov V, Varanasi P: "The HITRAN molecular spectroscopic database and HAWKS (HITRAN atmospheric workstation): 1996 edition", J. Quant. Spectrosc. Radiat. Transfer 60.5, pp665-710, 1998.

Rotta JC: "Statistische theorie nichthomogener turbulenz", Zeitschrift fur Physik 129, pp547-572, 1951.

Rouse H, Yih CS, Humphreys HW: "Gravitational convection from a boundary source", Tellus 4, pp201-210, 1952.

Saffman PG: "A model for inhomogeneous turbulent flow", Proc. R. Soc. Lond. A317, pp417-433, 1970.

Scarborough JB: Numerical Mathematical Analysis, 4th Edn., Johns-Hopkins University Press, Baltimore, USA, 1958.

Schenker GN, Keller B: "Line-by-line calculations of the absorption of infrared radiation by water vapour in a box-shaped enclosure filled with humid air", Int. J. Heat Mass Trans. 38, pp3127-3134, 1995

Shih TH, Liou WW, Shabbir A, Zhu J: "A new k-ε eddy-viscosity model for high Reynolds number turbulent flows - model development and validiation", Comput. Fluids 24, pp227-238, 1995.

Siegel R, Howell JR: Thermal Radiation Heat Transfer, 4th Edn., Taylor & Francis, New York, USA, 2002.

Sparrow EM, Cess RD: Radiation Heat Transfer, McGraw-Hill, New York, USA, 1978.

Speziale CG, Abid R, Anderson EC: "A critical evaluation of two-equation models for near-wall turbulence", AIAA-90-1481, 1990.

Tennekes H, Lumley JL: A First Course in Turbulence, MIT Press, Cambridge, MA, USA, 1972.

Wilcox DC: "Reassessment of the scale determining equation for advanced turbulence models", AIAA J. 26.11, pp1299-1310, 1988.

Wilcox DC: Turbulence Modeling for CFD, 2nd Edn., DCW Industries, La Cañada, CA, USA, 1998.

Xu W: "New turbulence models for indoor airflow simulation", Ph. D. Thesis, Massachusetts Institute of Technology, Cambridge, MA, USA, 1998.

Xu W, Chen Q: "Numerical simulation of airflow in a room with differentially heated vertical walls", ASHRAE. Trans. 104:1, 1998.

Yakhot V, Orszag SA: "Renormalisation group analysis of turbulence: 1. Basic theory", J. Sci. Comp. 1, pp3-51, 1986.

Yakhot V, Orszag SA, Thangam S, Gatski TB, Speziale CG: "Development of turbulence models for shear flows by a double expansion technique", Phys. Fluids A4, pp1510-1520, 1992.

Yuan X: "Wall functions for numerical simulation of natural convection along vertical surfaces", Dr. Sc. Techn. Thesis, Laboratorium für Energiesysteme, ETH, Zürich, Switzerland, 1995.

A1 Temperature measurements from the full-scale enclosure

Table of contents

Figure	Heat source	Strength of heat source	Width of opening	Effective area of openings A*
1	Plate heater	225.0W	0.1m	0.061m^2
2	Plate heater	225.0W	0.2m	0.122m^2
3	Plate heater	225.0W	0.3m	0.183m^2
4	Plate heater	225.0W	0.4m	0.244m^2
5	Plate heater	225.0W	0.6m	0.366m^2
6	Plate heater	225.0W	0.6m	0.366m^2
7	Plate heater	225.0W	1.0m	0.610m^2
8	Plate heater	225.0W	1.2m	0.732m^2
9	Plate heater	225.0W	2.4m	1.464m^2
10	Boiler ring	39.6W	0.4m	0.244m^2
11	Boiler ring	91.1W	0.4m	0.244m^2
12	Boiler ring	155.8W	0.4m	0.244m^2
13	Boiler ring	368.0W	0.1m	0.061m^2
14	Boiler ring	368.0W	0.2m	0.122m^2
15	Boiler ring	368.0W	0.3m	0.183m^2
16	Boiler ring	368.0W	0.4m	0.244m^2
17	Boiler ring	368.0W	0.5m	0.305m^2
18	Boiler ring	368.0W	0.6m	0.366m^2
19	Boiler ring	368.0W	0.8m	0.488m^2
20	Boiler ring	368.0W	1.0m	0.610m^2
21	Boiler ring	368.0W	1.2m	0.732m^2
22	Boiler ring	368.0W	1.5m	0.915m^2
23	Boiler ring	368.0W	1.8m	1.098m^2
24	Boiler ring	368.0W	2.4m	1.464m^2
25	Boiler ring	490.5W	0.1m	0.061m^2
26	Boiler ring	490.5W	0.2m	0.122m^2

Figure	Heat source	Strength of heat source	Width of opening	Effective area of openings A*
27	Boiler ring	490.5W	0.3m	0.183m^2
28	Boiler ring	490.5W	0.4m	0.244m^2
29	Boiler ring	490.5W	0.5m	0.305m^2
30	Boiler ring	490.5W	0.6m	0.366m^2
31	Boiler ring	490.5W	0.8m	0.488m^2
32	Boiler ring	490.5W	1.0m	0.610m^2
33	Boiler ring	490.5W	1.2m	0.732m^2

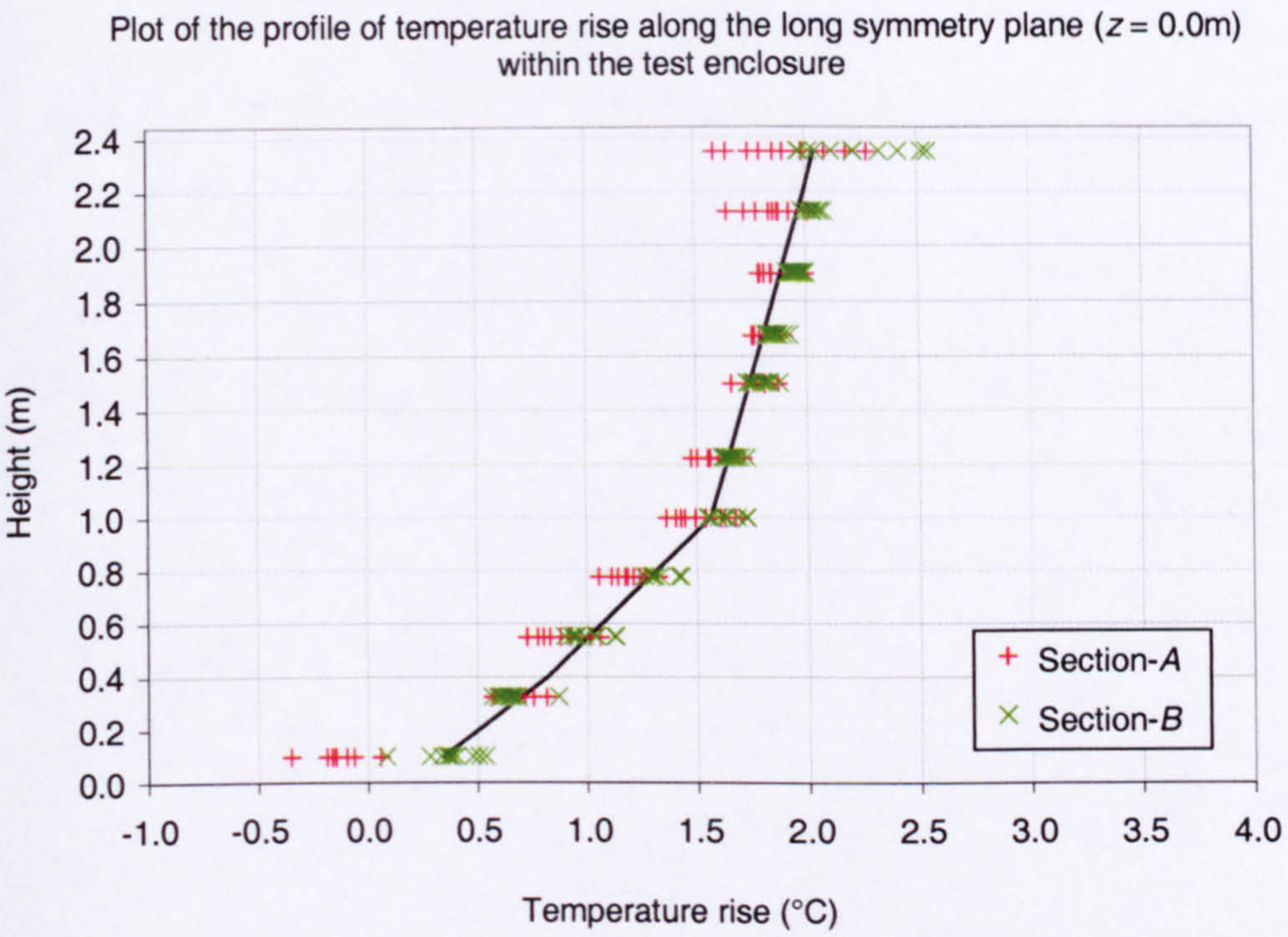

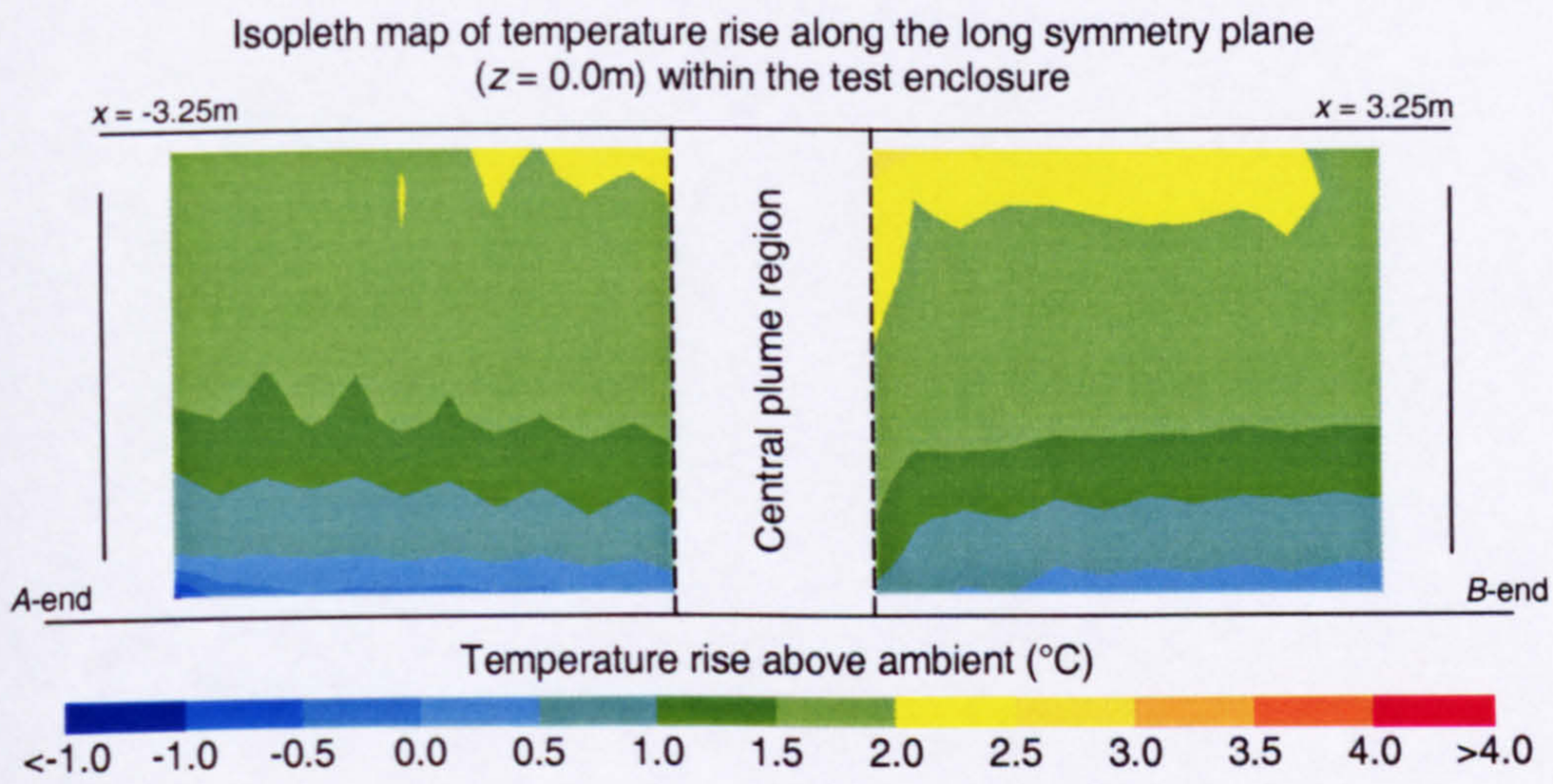

Width of opening:	0.1m
Effective area of opening:	0.061m^2
Heat source:	Plate heater
Strength of heat source:	225.0W

Figure 1

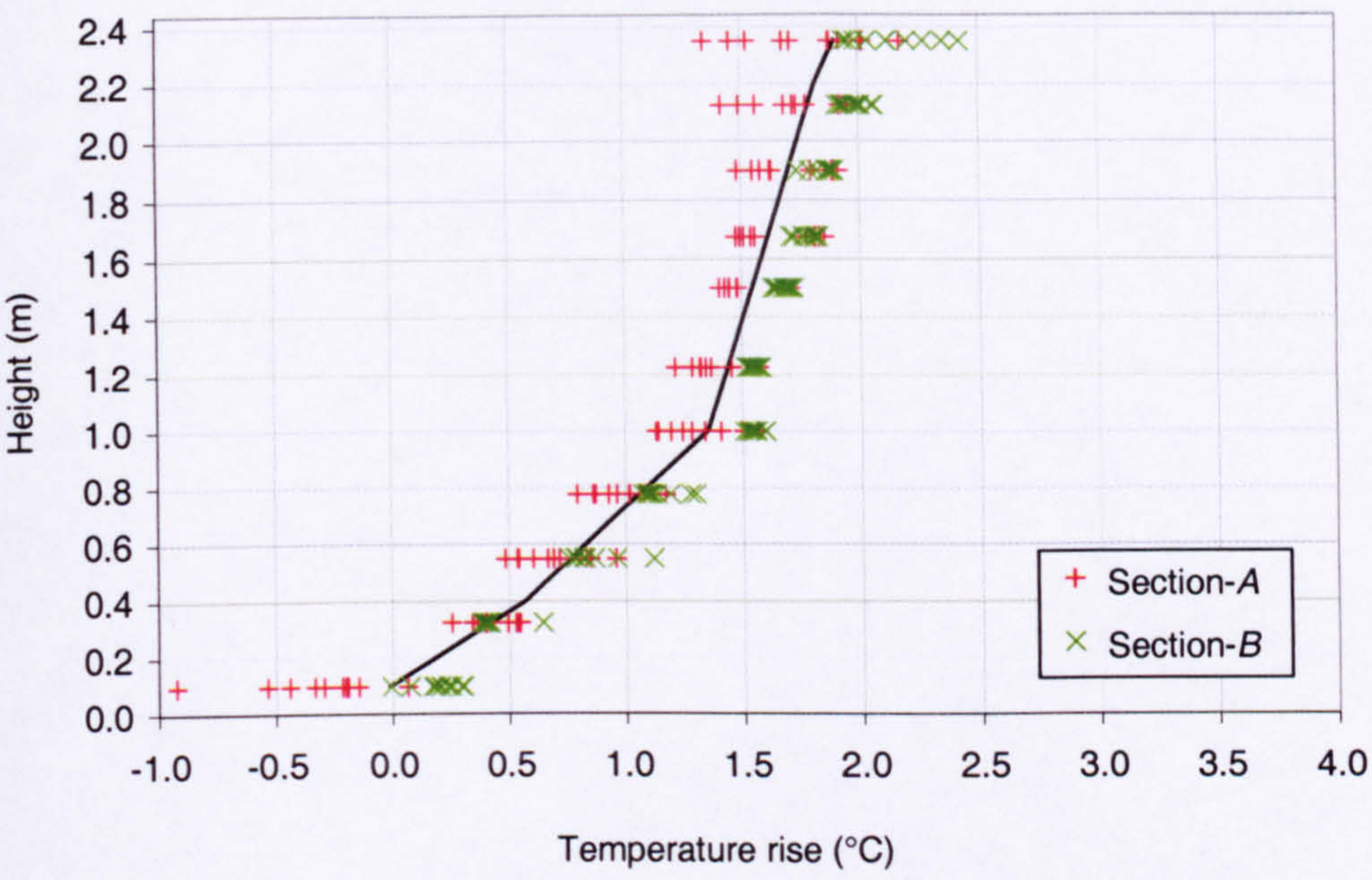

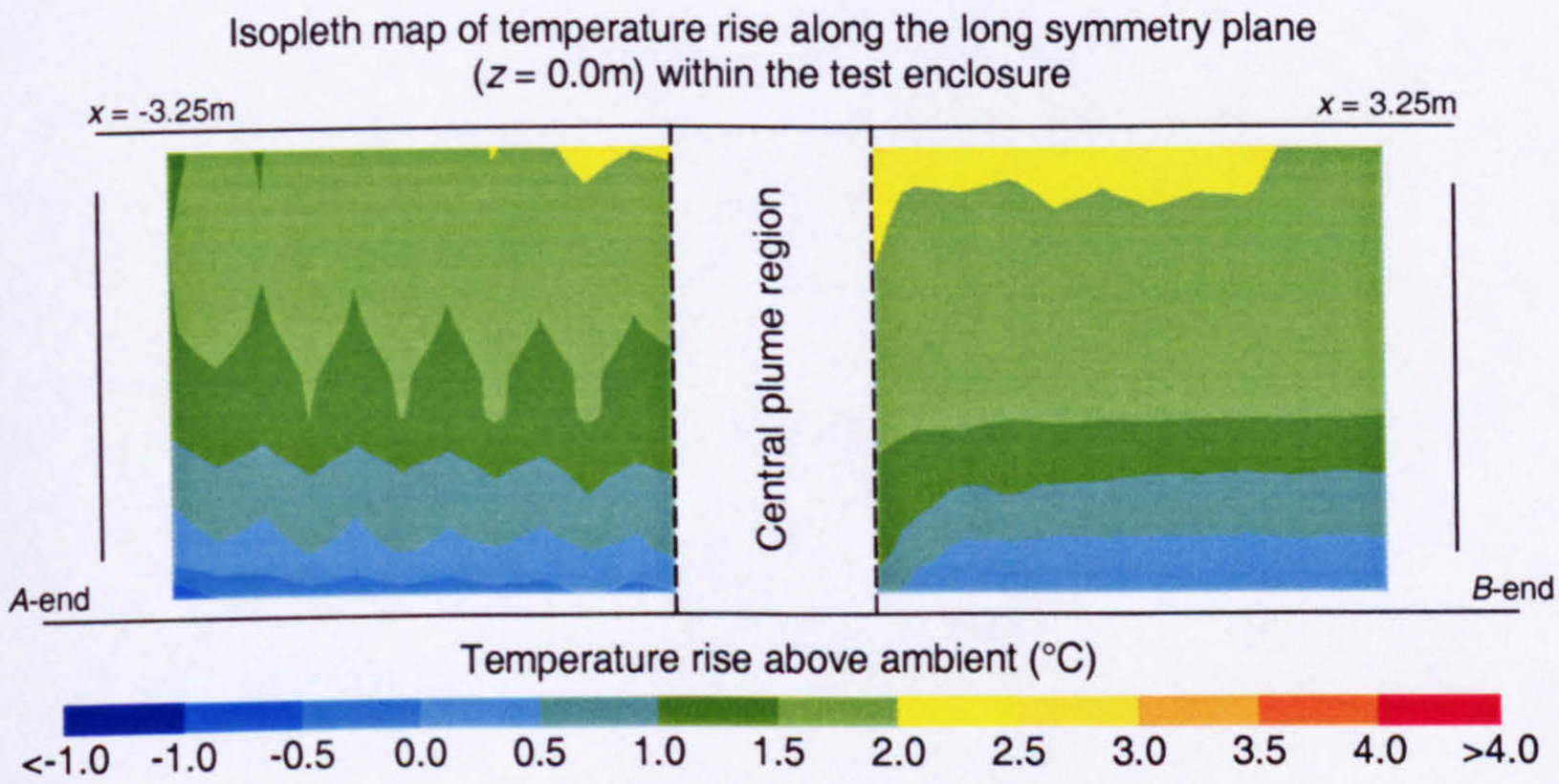

Width of opening:	0.2m
Effective area of opening:	0.122m^2
Heat source:	Plate heater
Strength of heat source:	225.0W

Figure 2

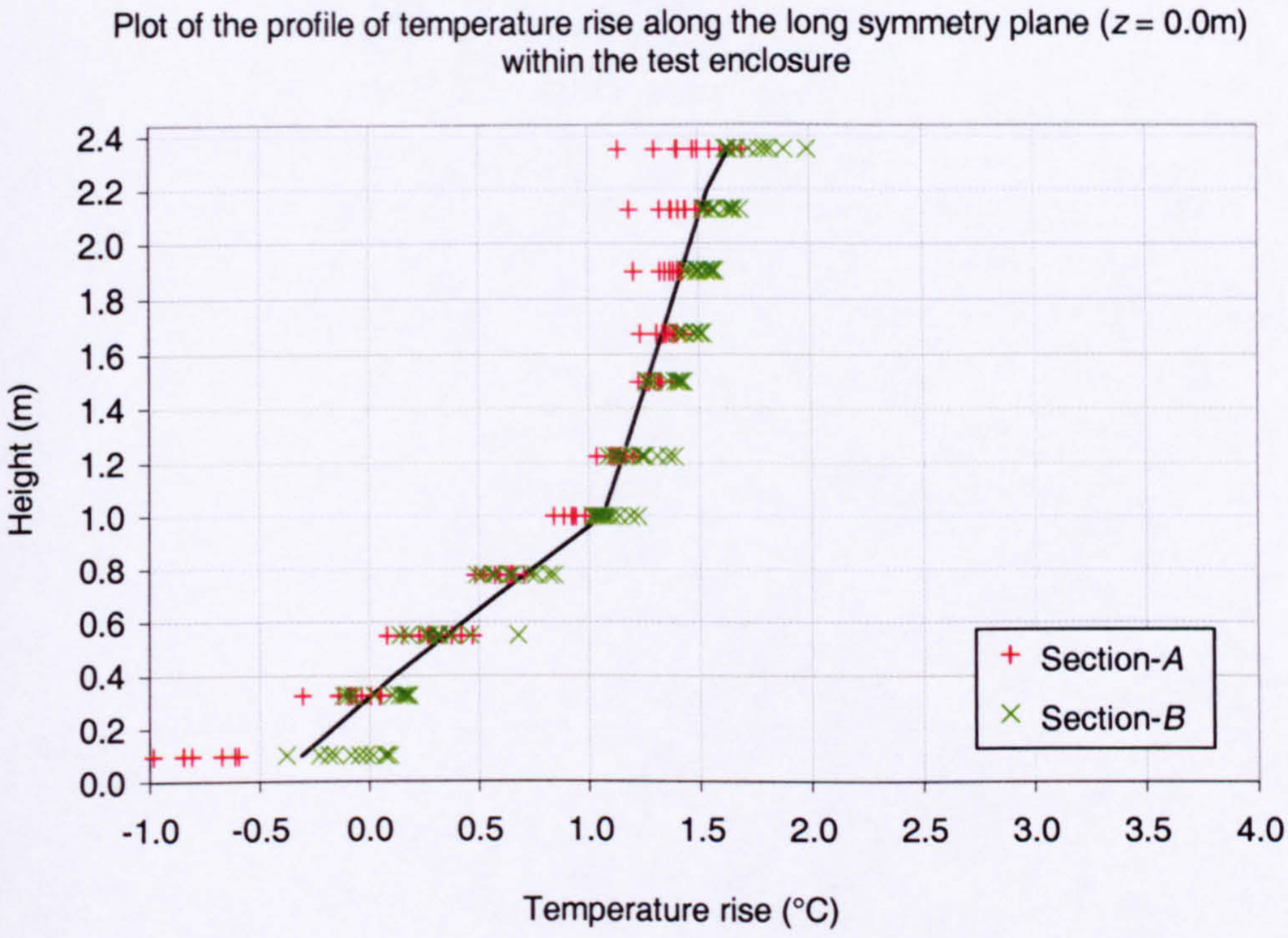

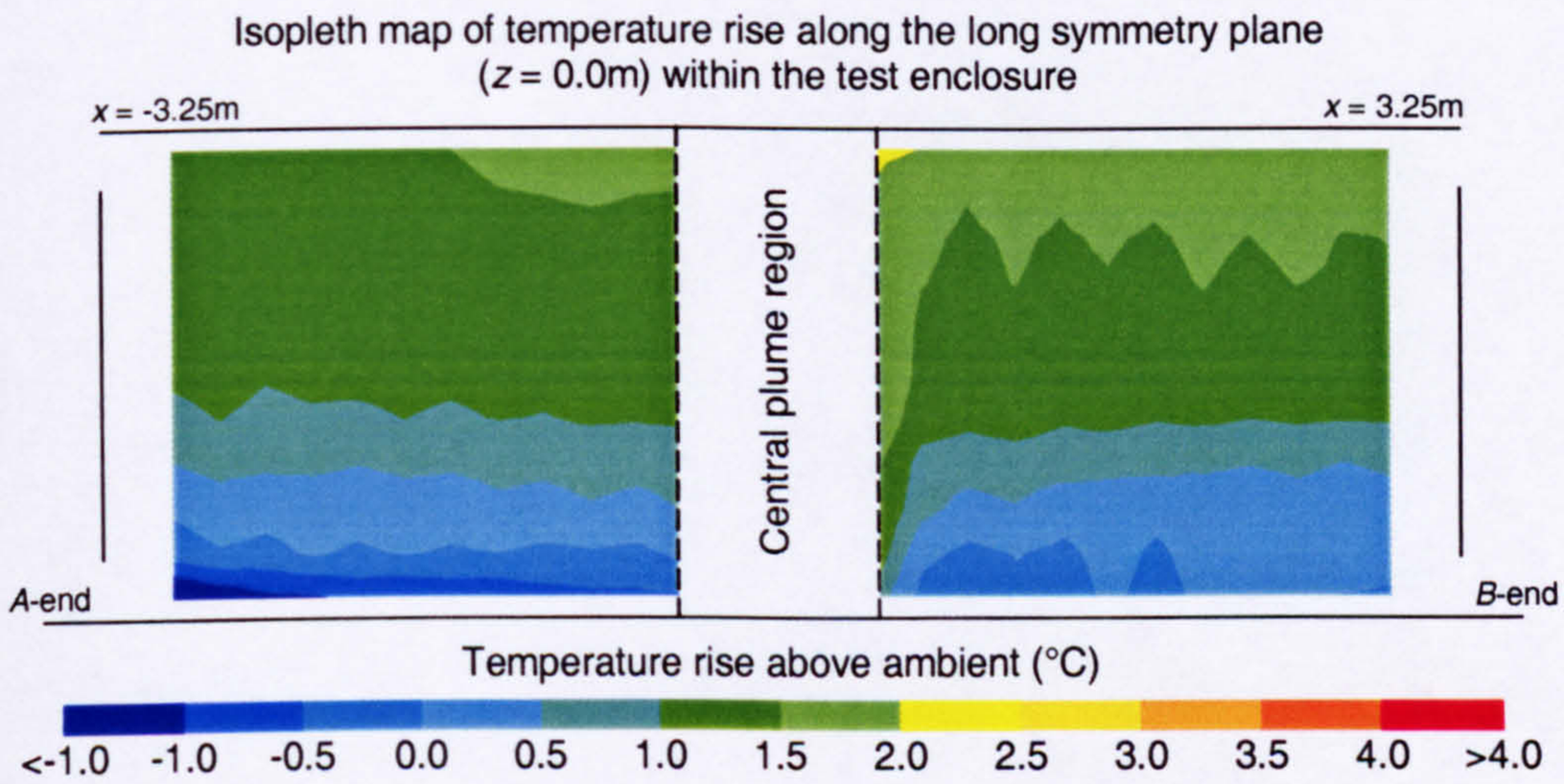

Width of opening:	0.3m
Effective area of opening:	0.183m^2
Heat source:	Plate heater
Strength of heat source:	225.0W

Figure 3

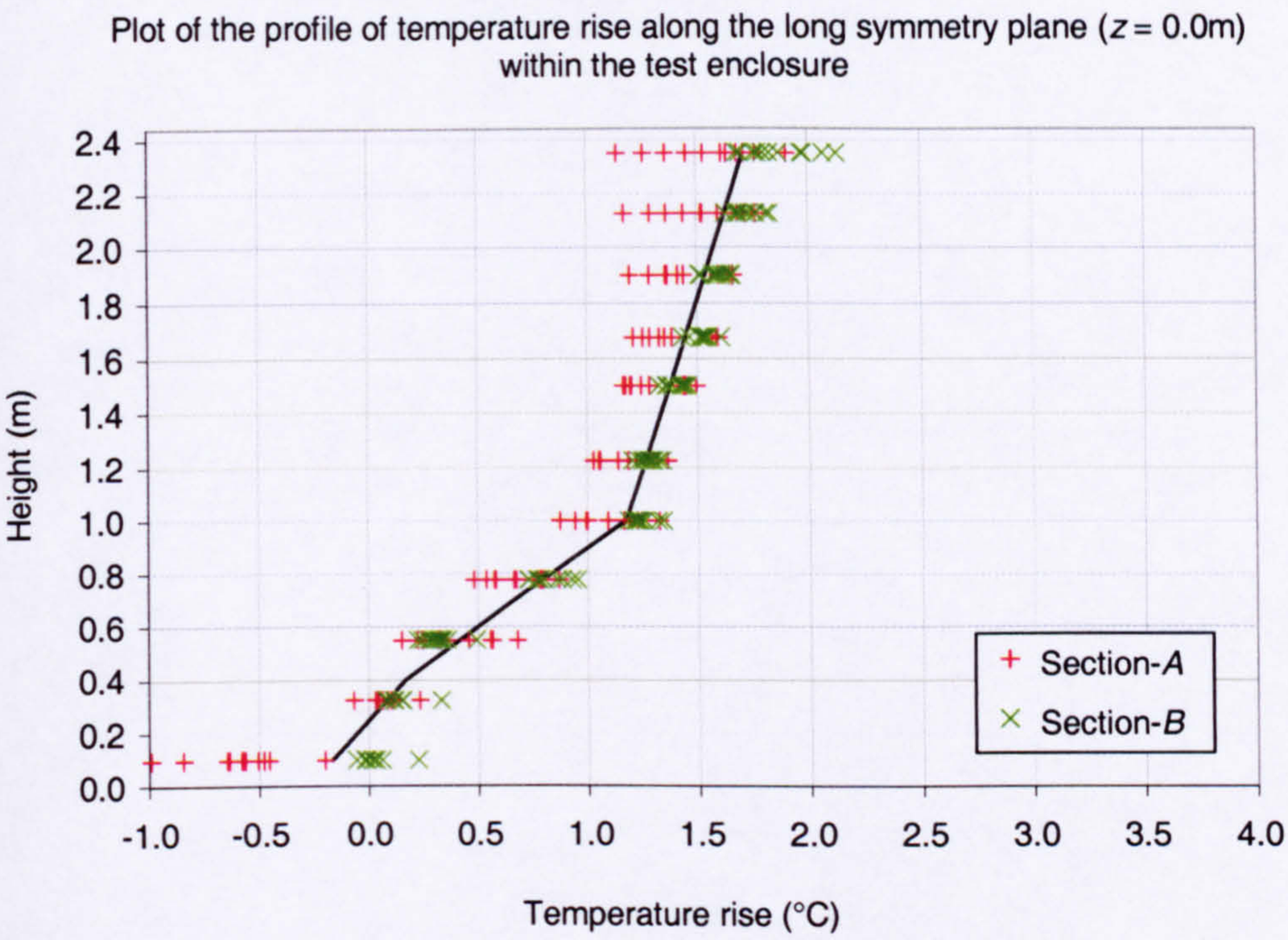

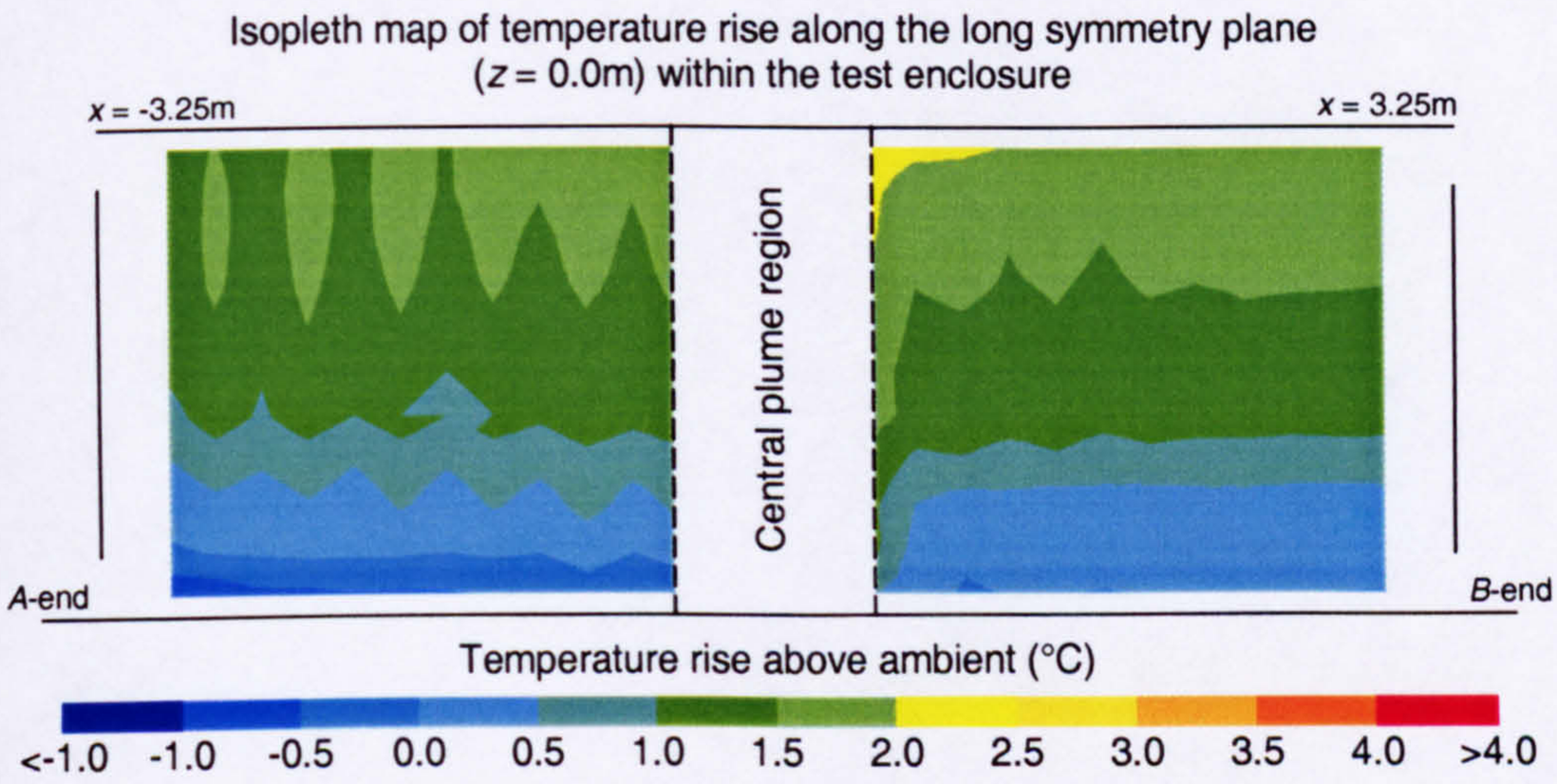

Width of opening:	0.4m
Effective area of opening:	0.244m^2
Heat source:	Plate heater
Strength of heat source:	225.0W

Figure 4

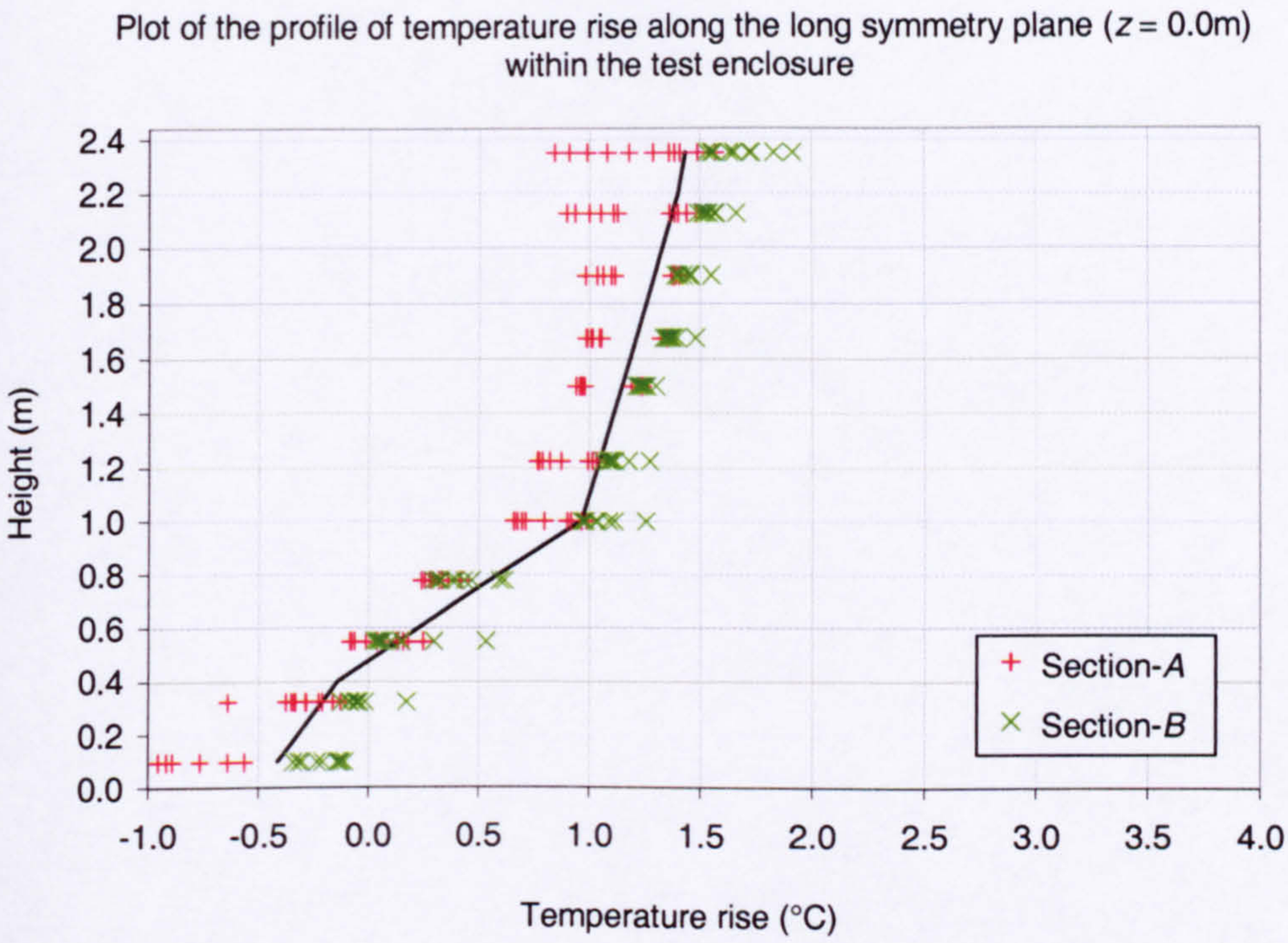

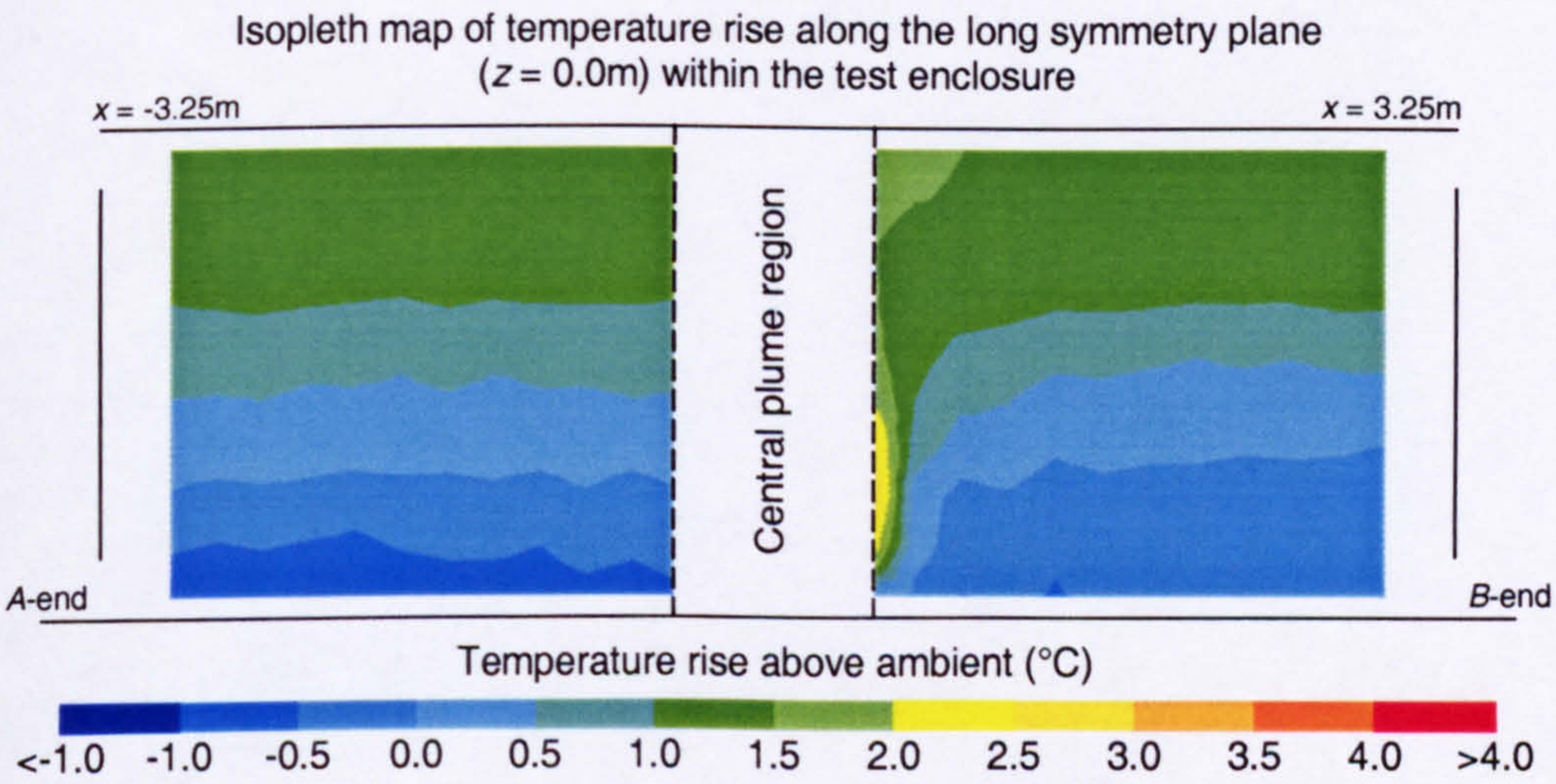

Width of opening:	0.6m
Effective area of opening:	0.366m^2
Heat source:	Plate heater
Strength of heat source:	225.0W

Figure 5

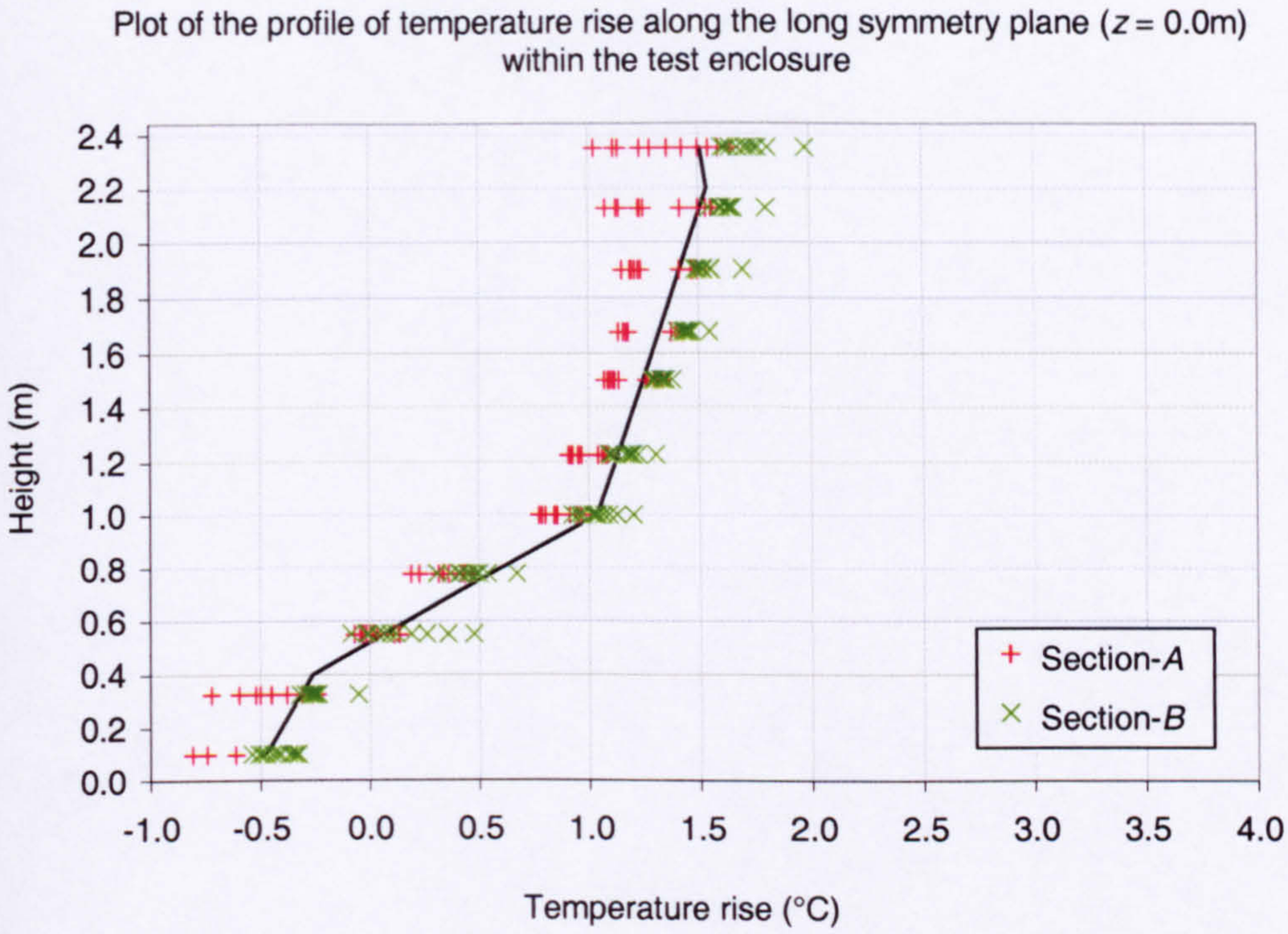

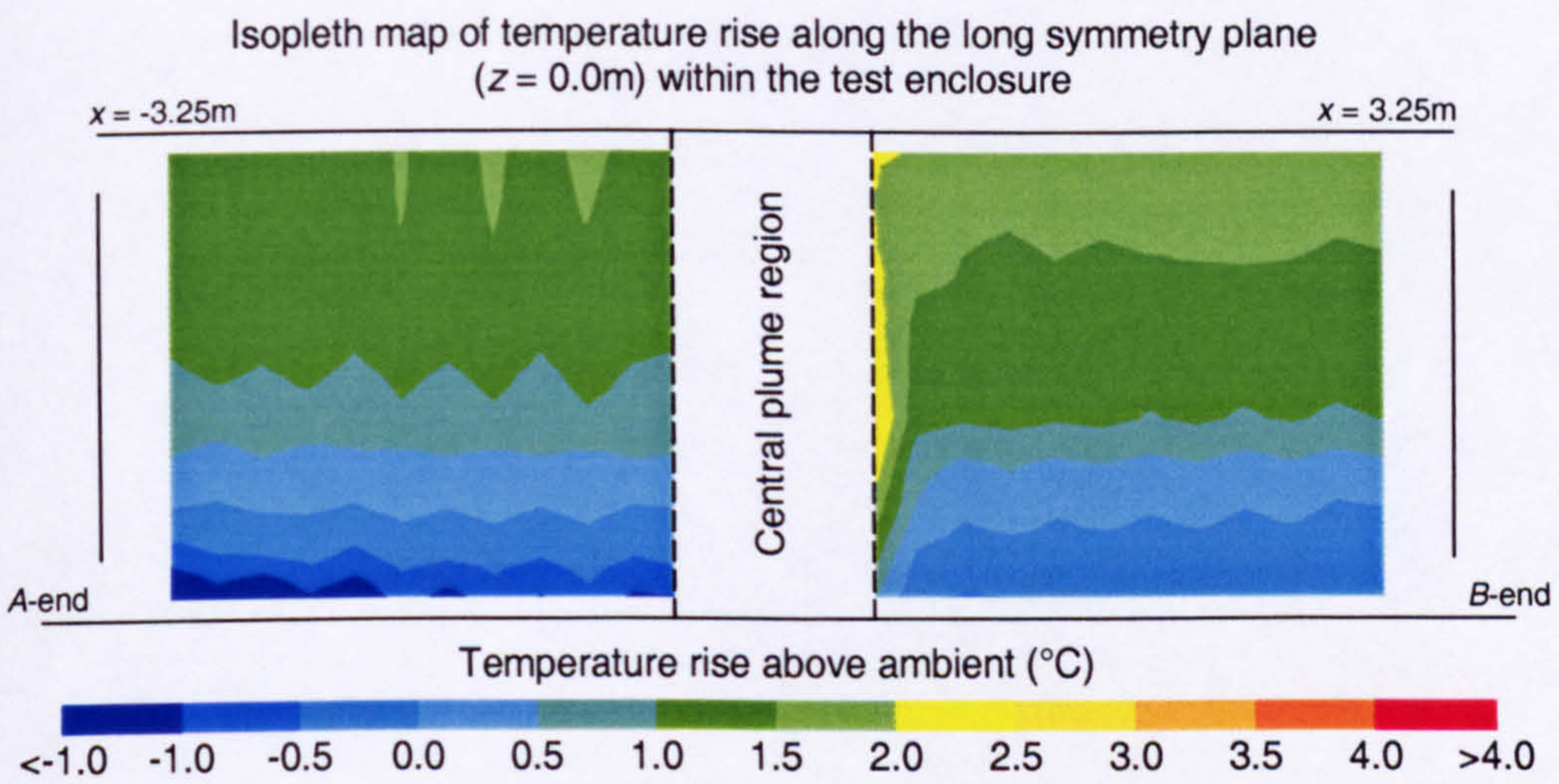

Width of opening:	1.0m
Effective area of opening:	0.610m^2
Heat source:	Plate heater
Strength of heat source:	225.0W

Figure 6

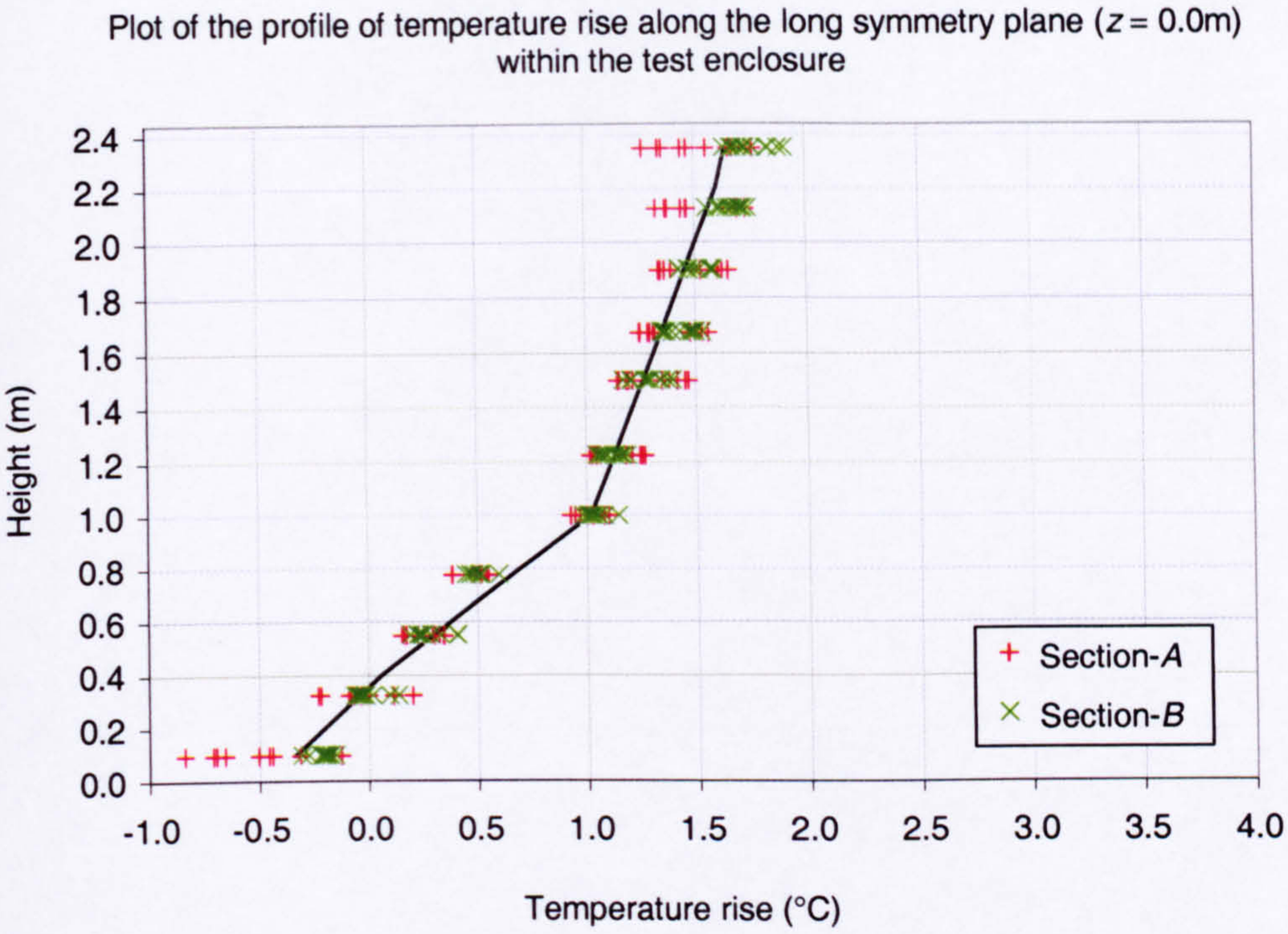

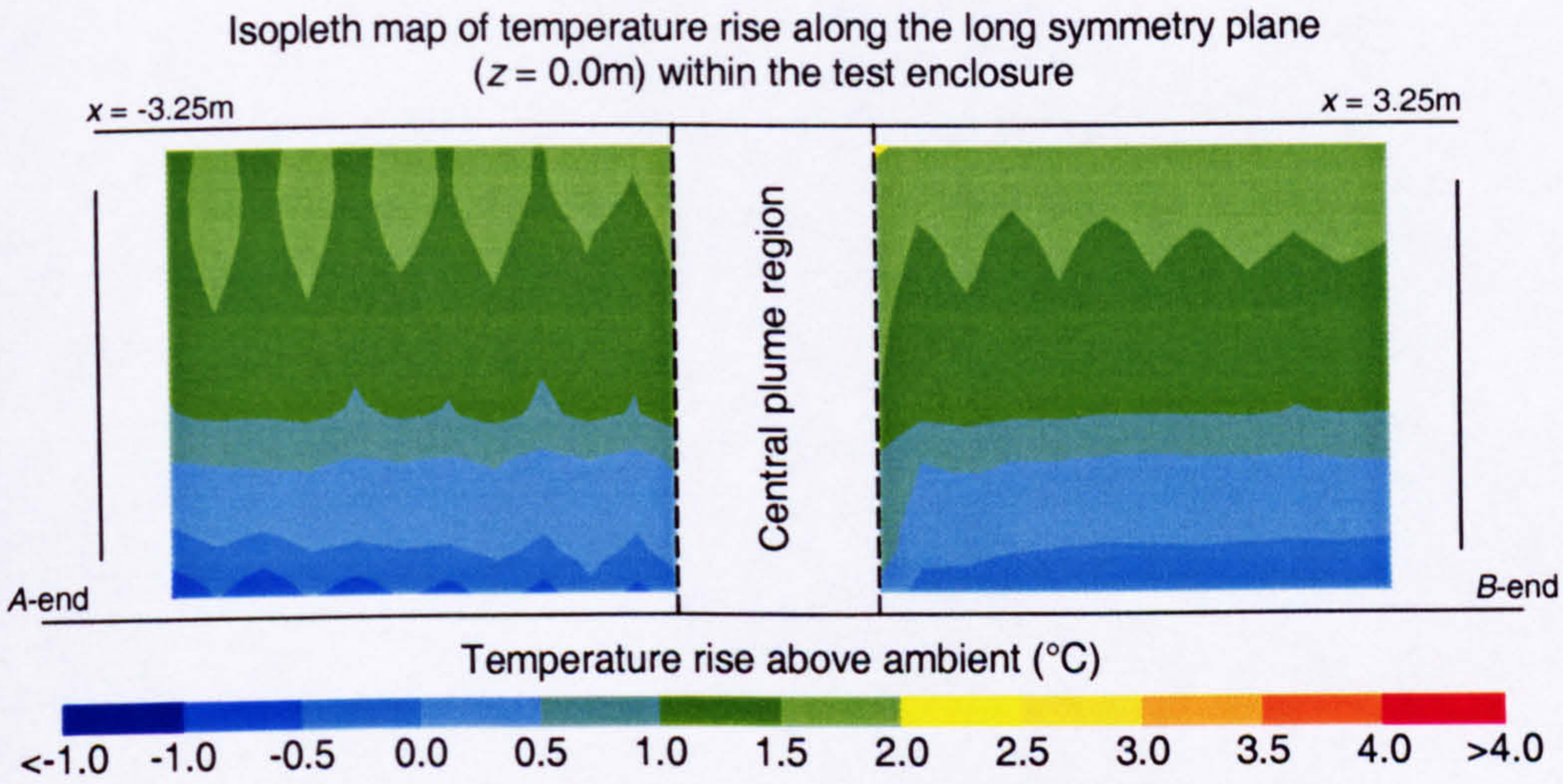

Width of opening:	1.2m
Effective area of opening:	0.732m^2
Heat source:	Plate heater
Strength of heat source:	225.0W

Figure 7

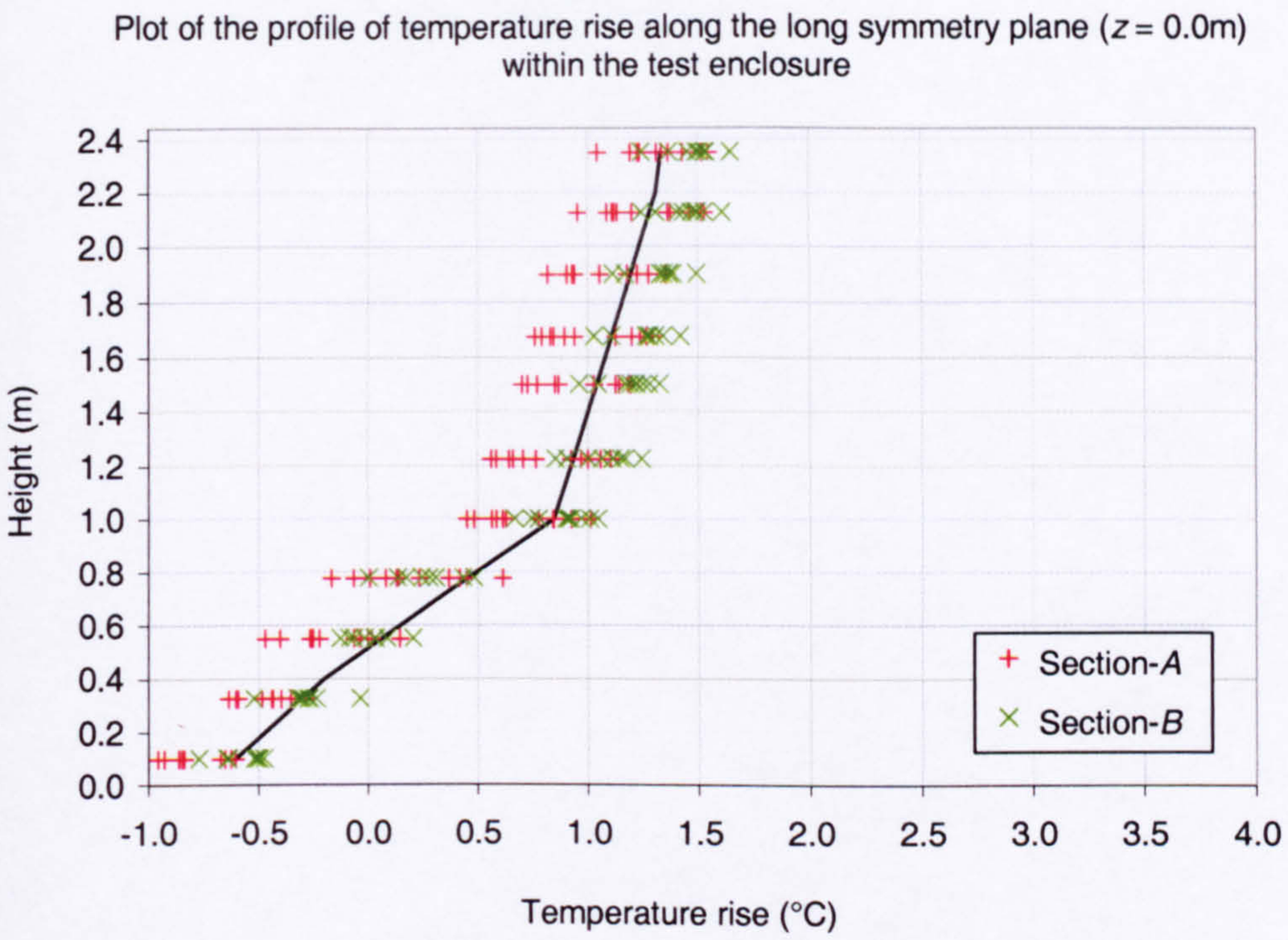

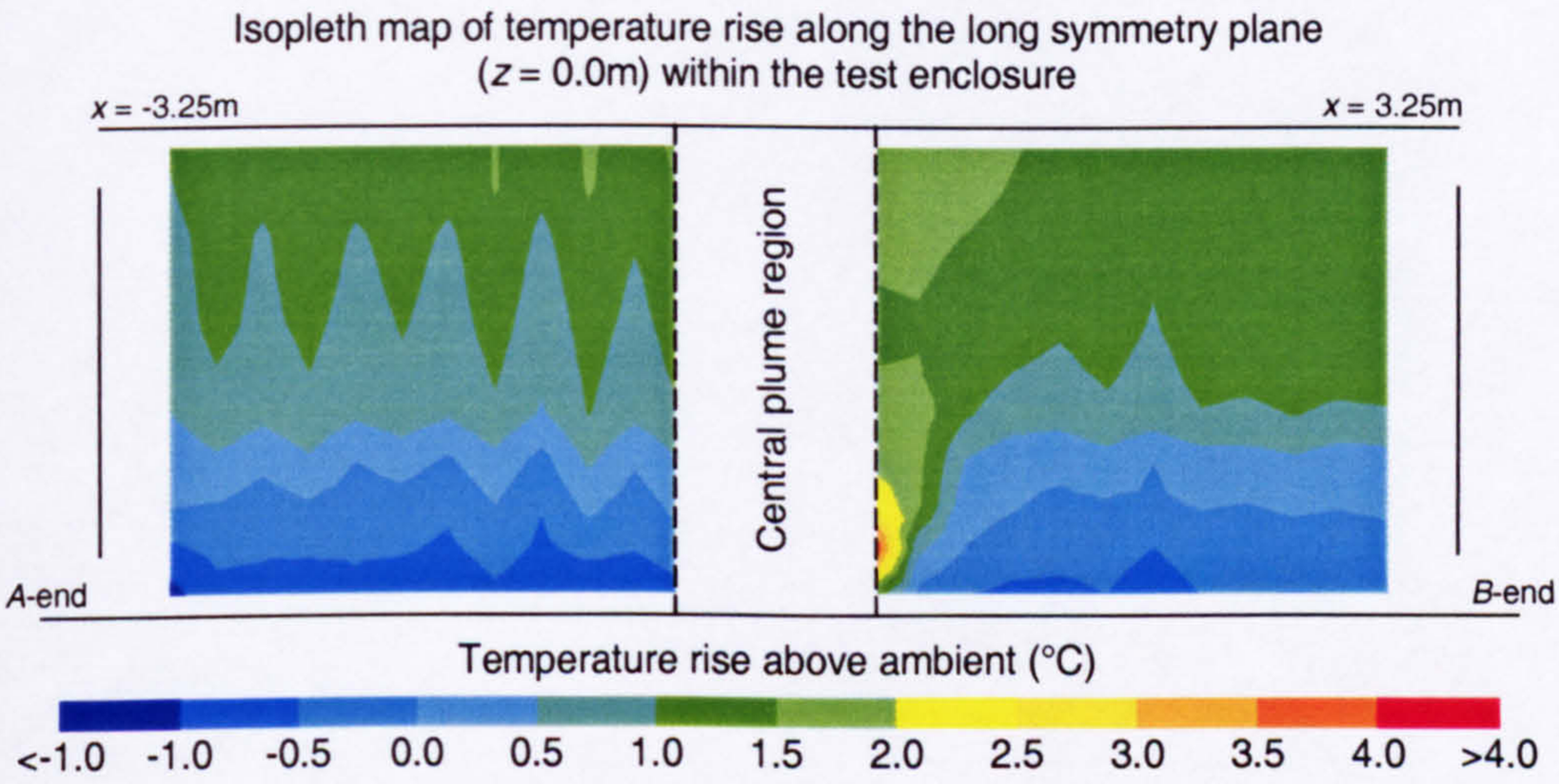

Width of opening:	2.32m
Effective area of opening:	1.415m^2
Heat source:	Plate heater
Strength of heat source:	225.0W

Figure 8

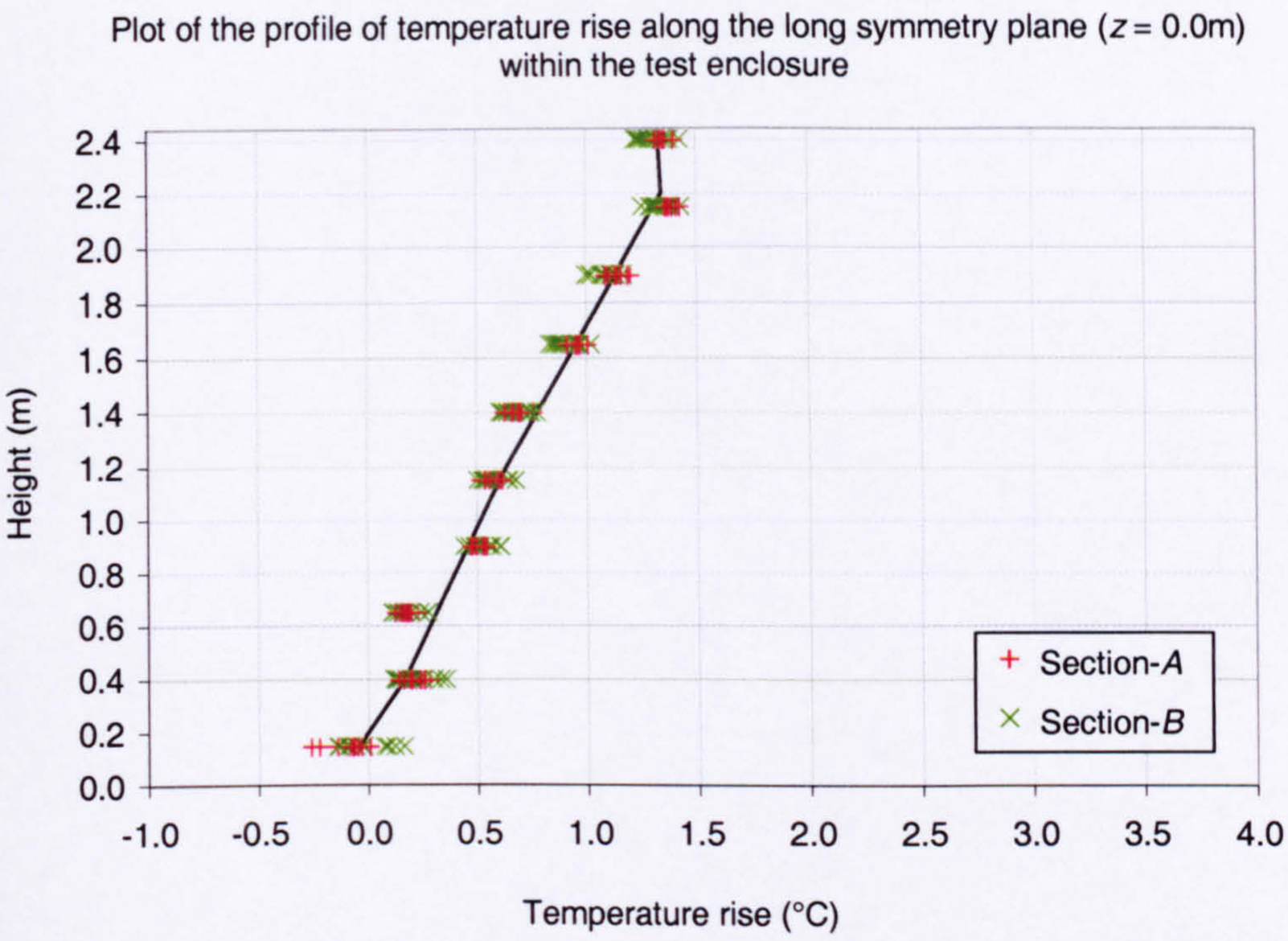

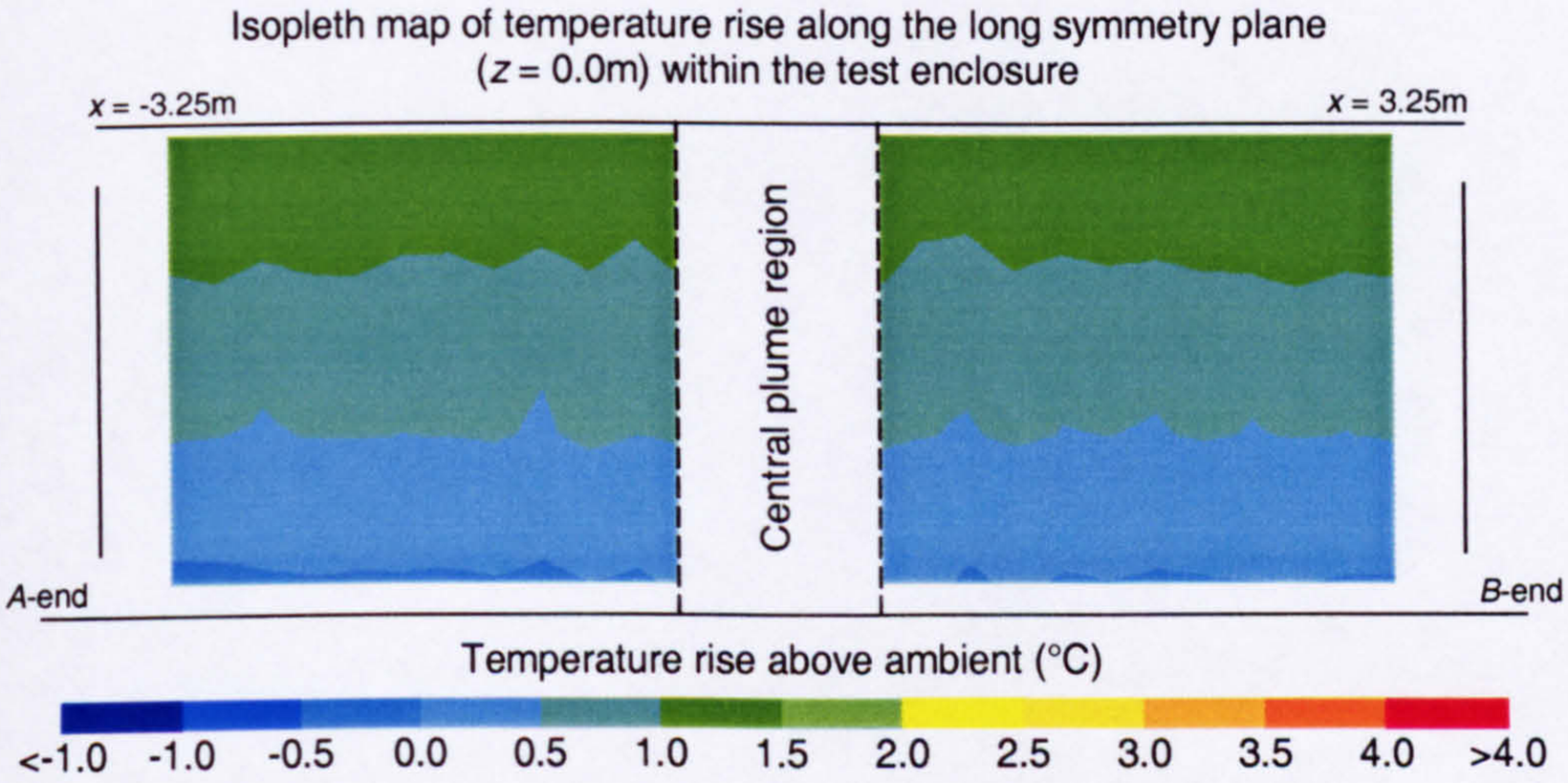

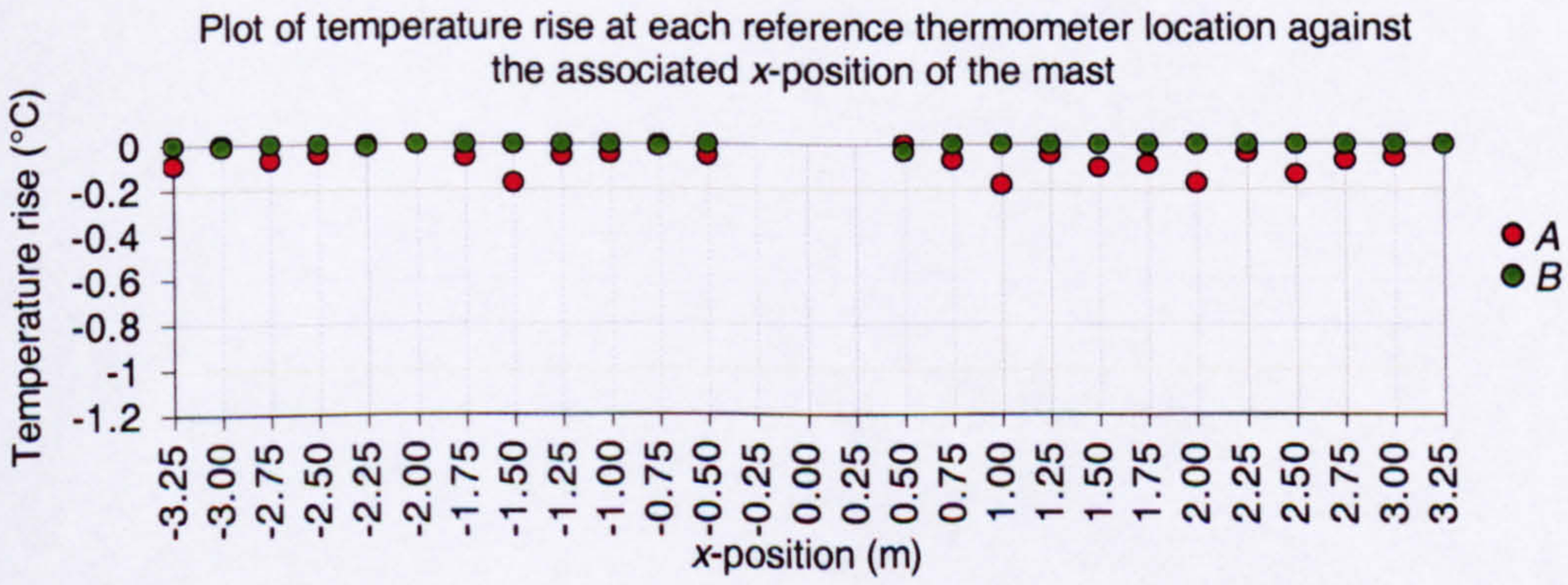

Width of opening:	0.4m
Effective area of opening:	0.244m^2
Heat source:	Boiler ring
Strength of heat source:	39.6W

Figure 9

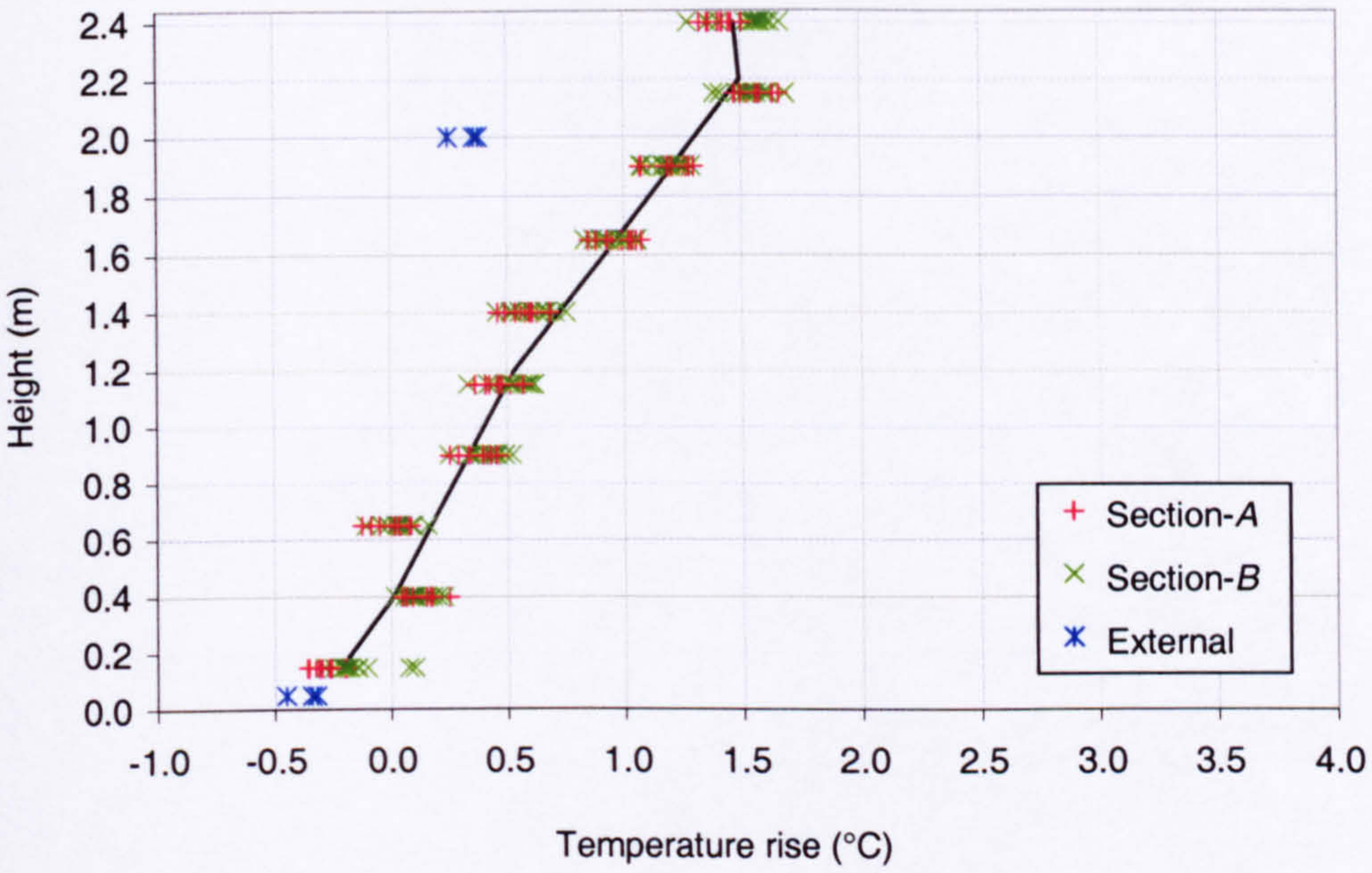

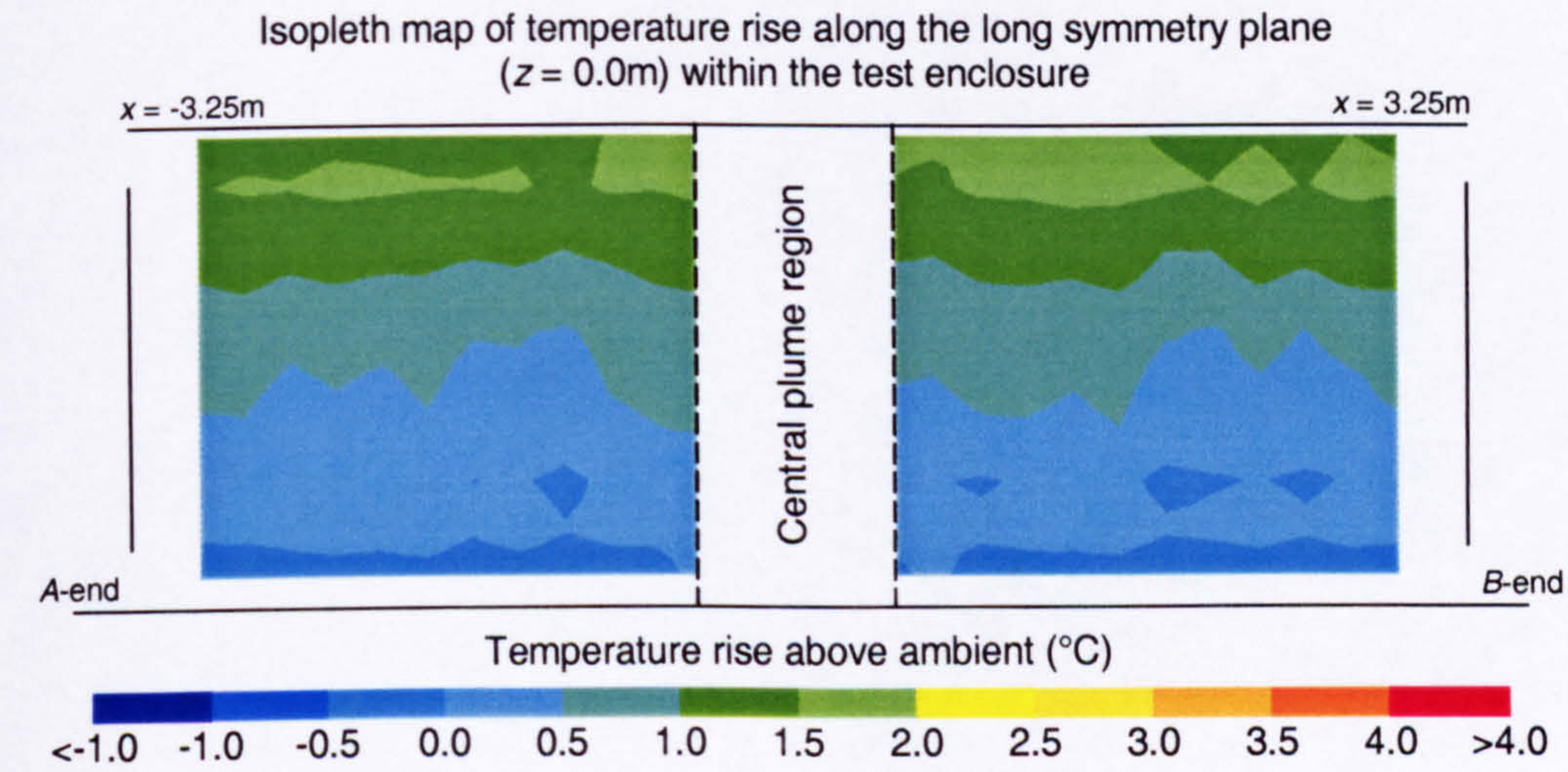

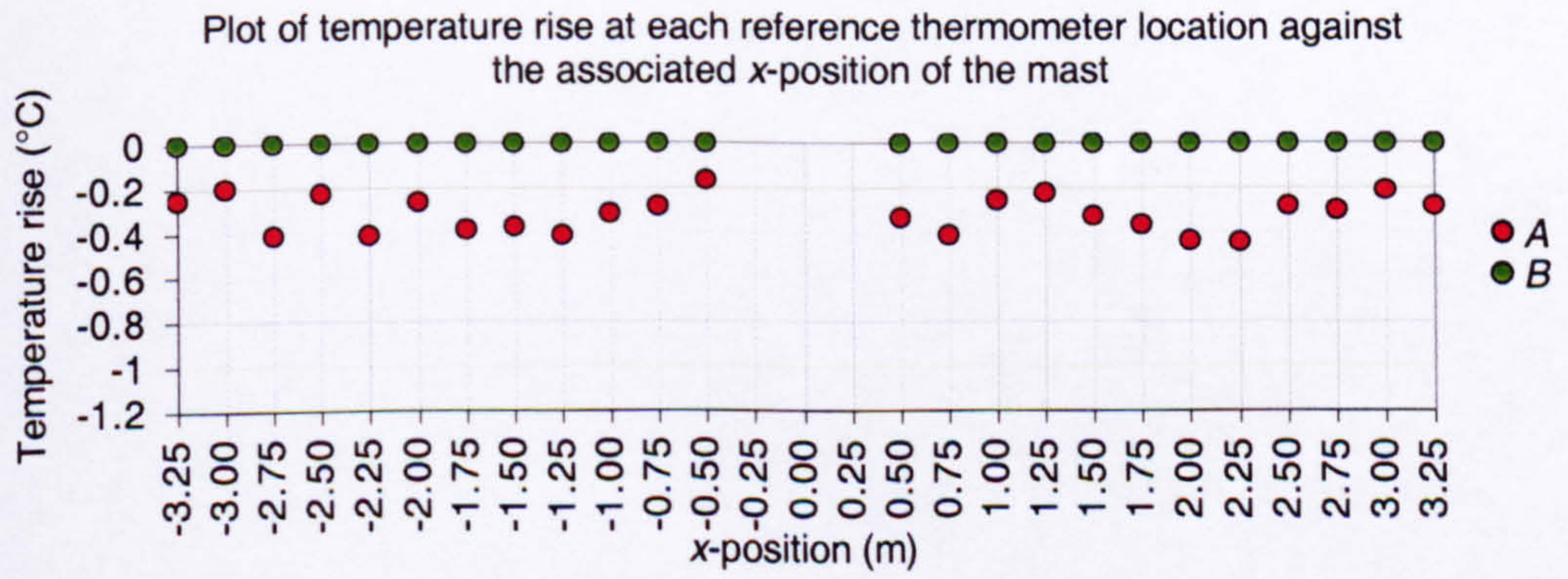

Width of opening:	0.4m
Effective area of opening:	0.244m^2
Heat source:	Boiler ring
Strength of heat source:	91.1W

Figure 10

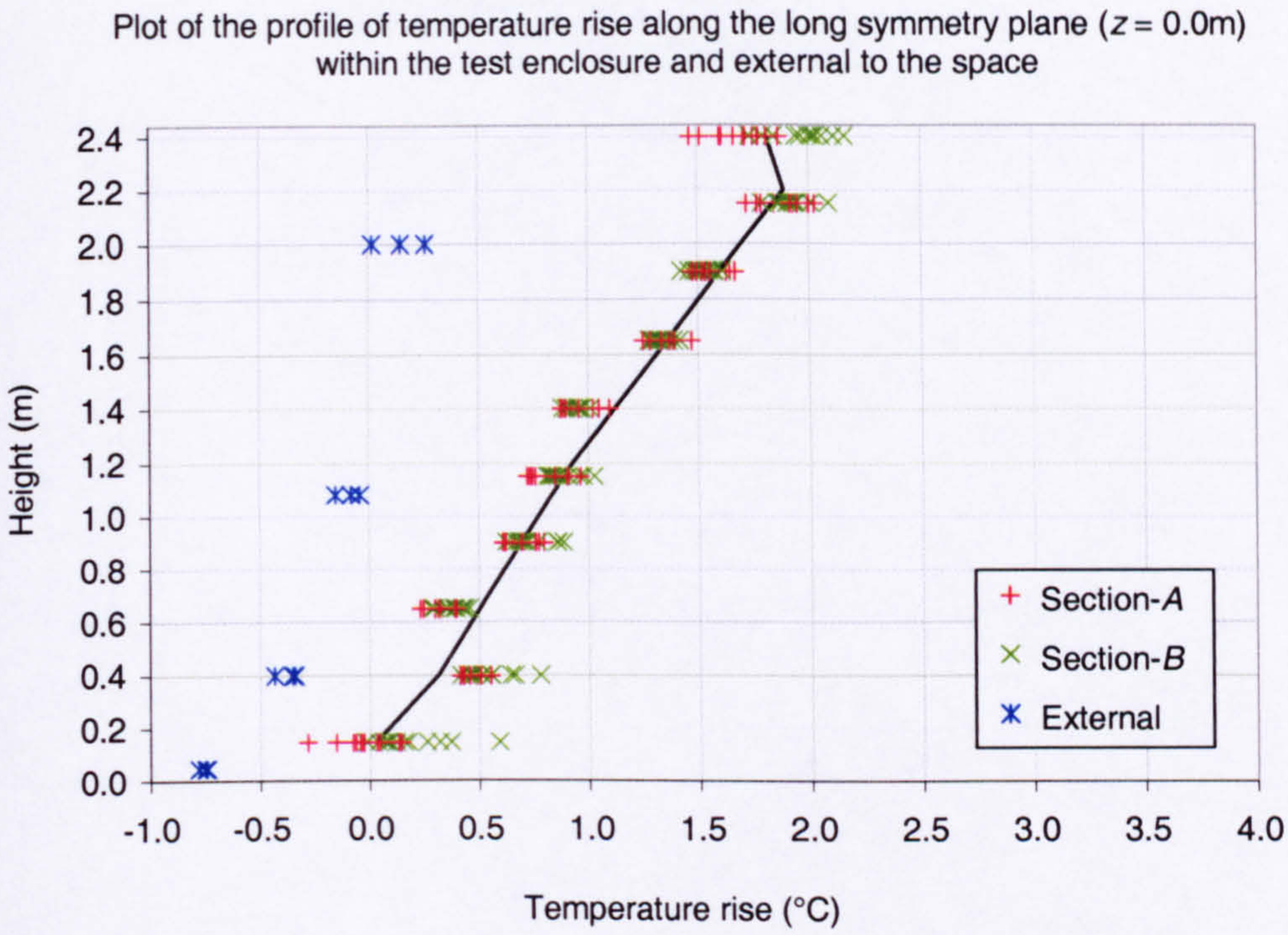

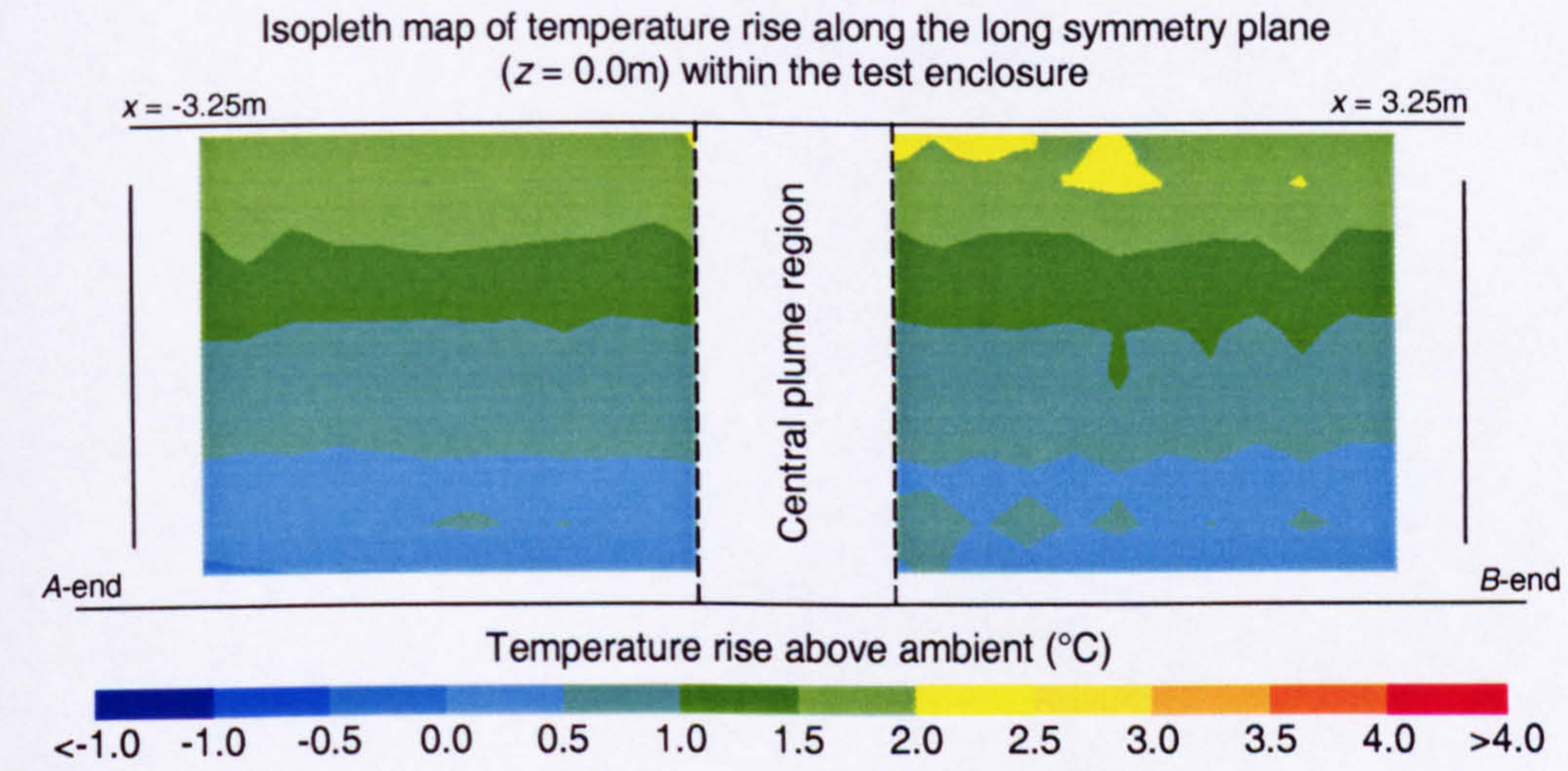

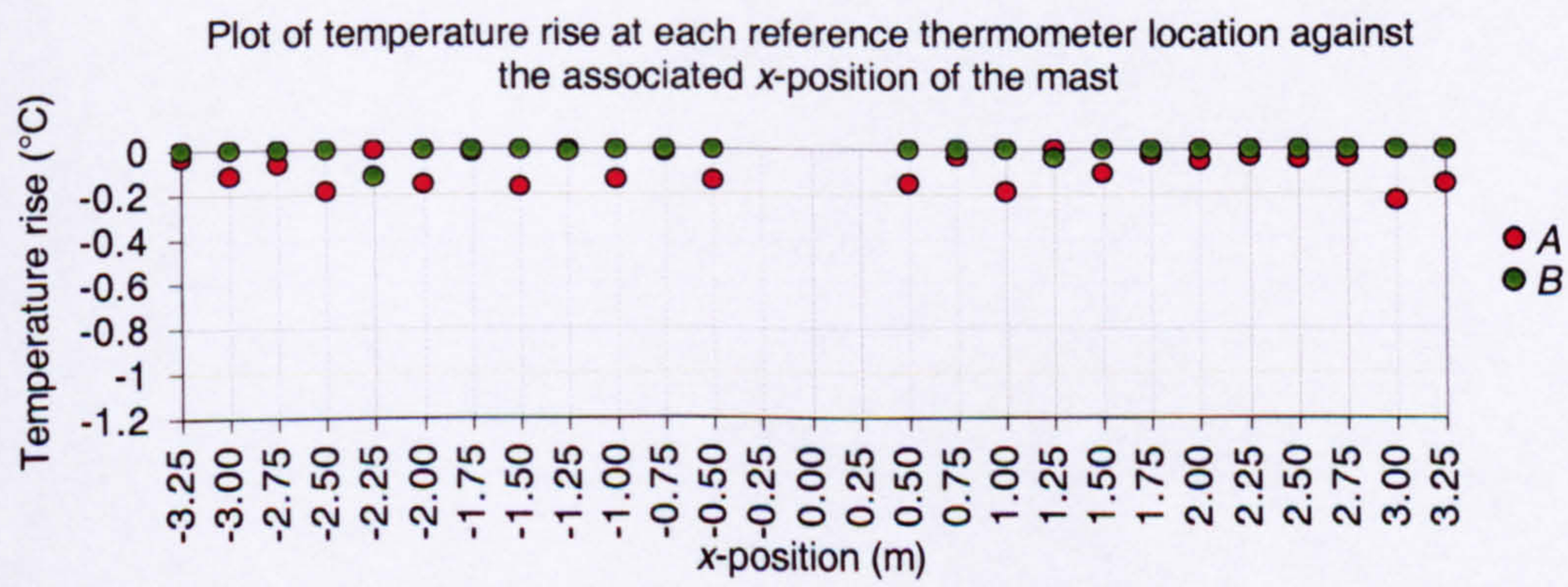

Width of opening:	0.4m
Effective area of opening:	0.244m^2
Heat source:	Boiler ring
Strength of heat source:	155.8W

Figure 11

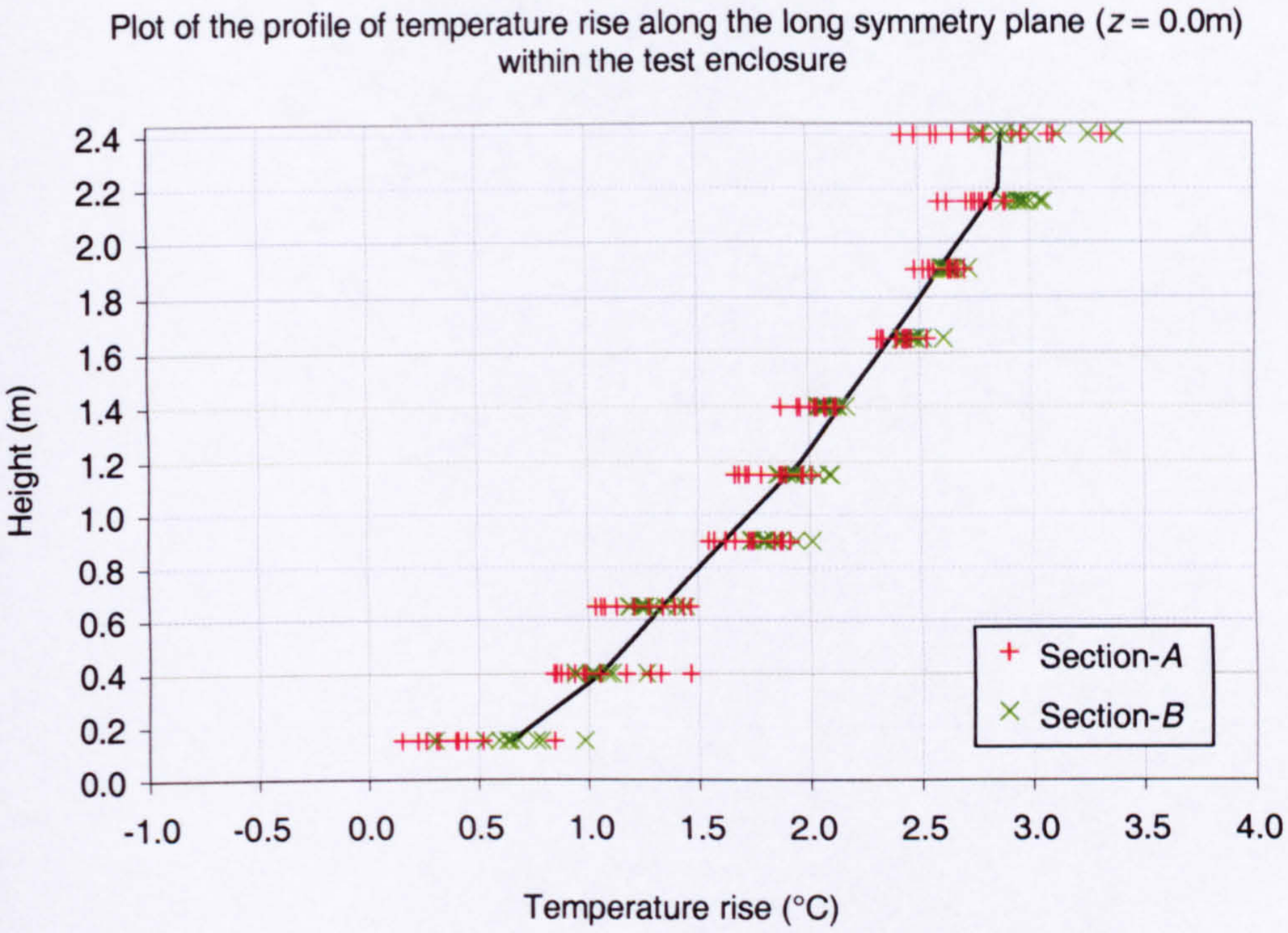

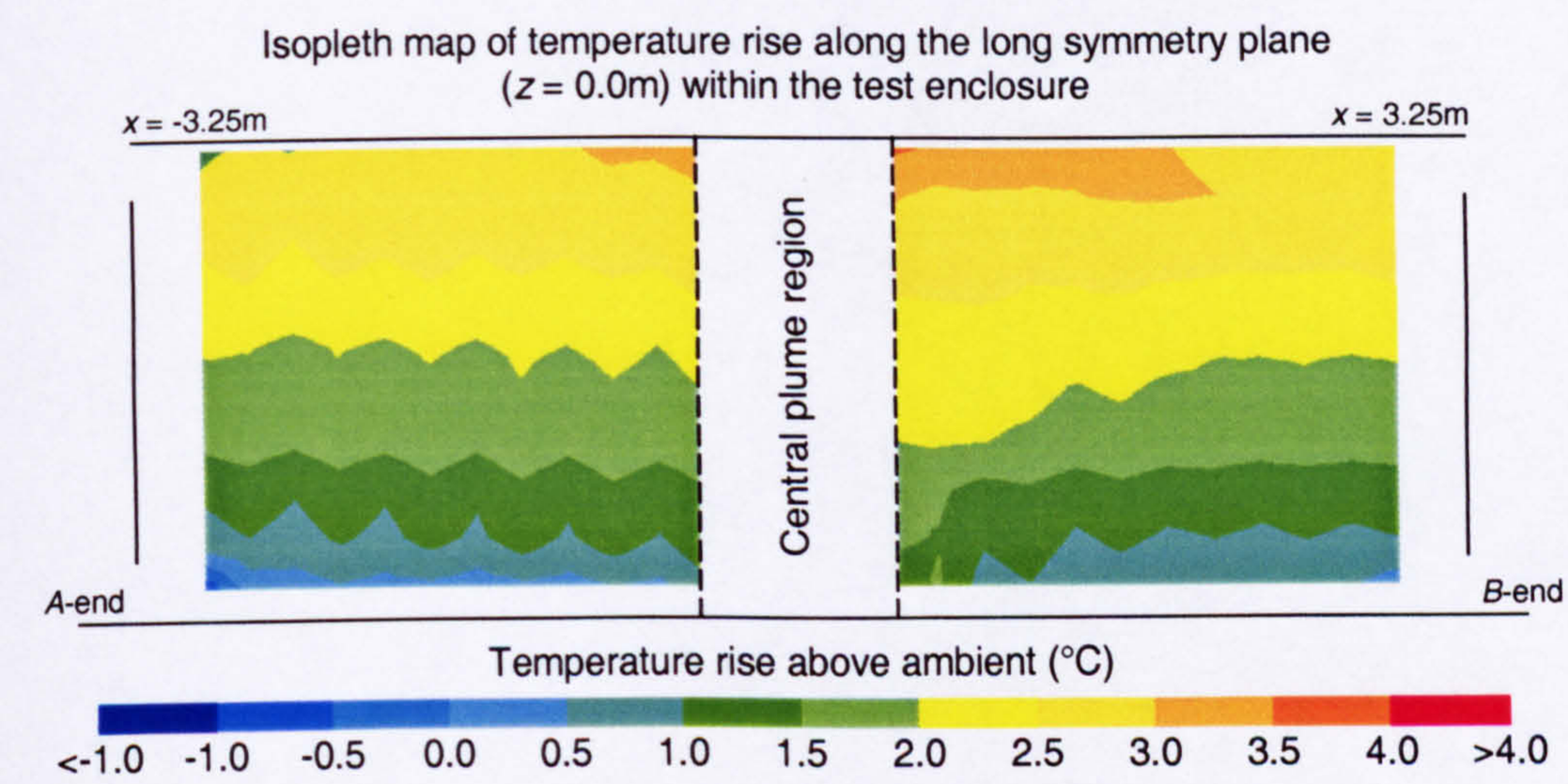

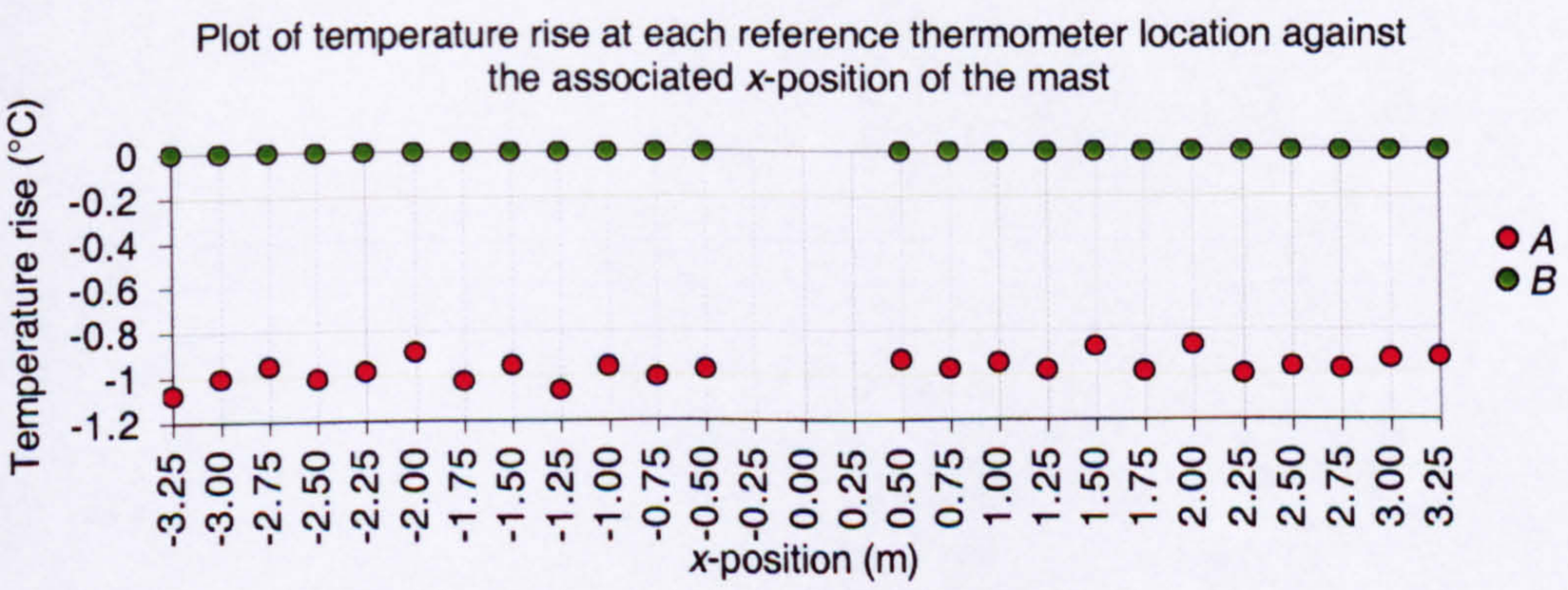

Width of opening:	0.1m
Effective area of opening:	0.061m^2
Heat source:	Boiler ring
Strength of heat source:	368.0W

Figure 12

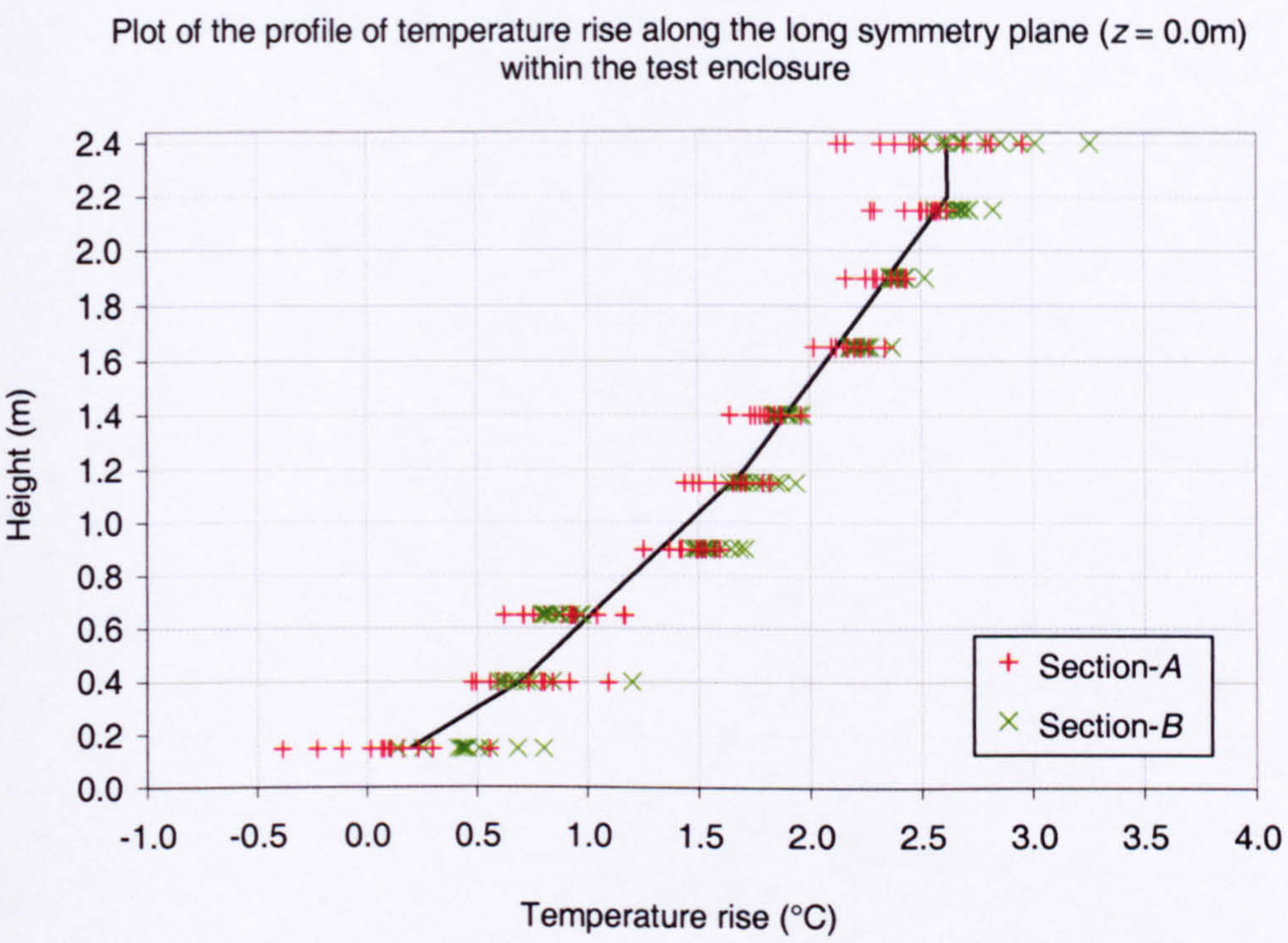

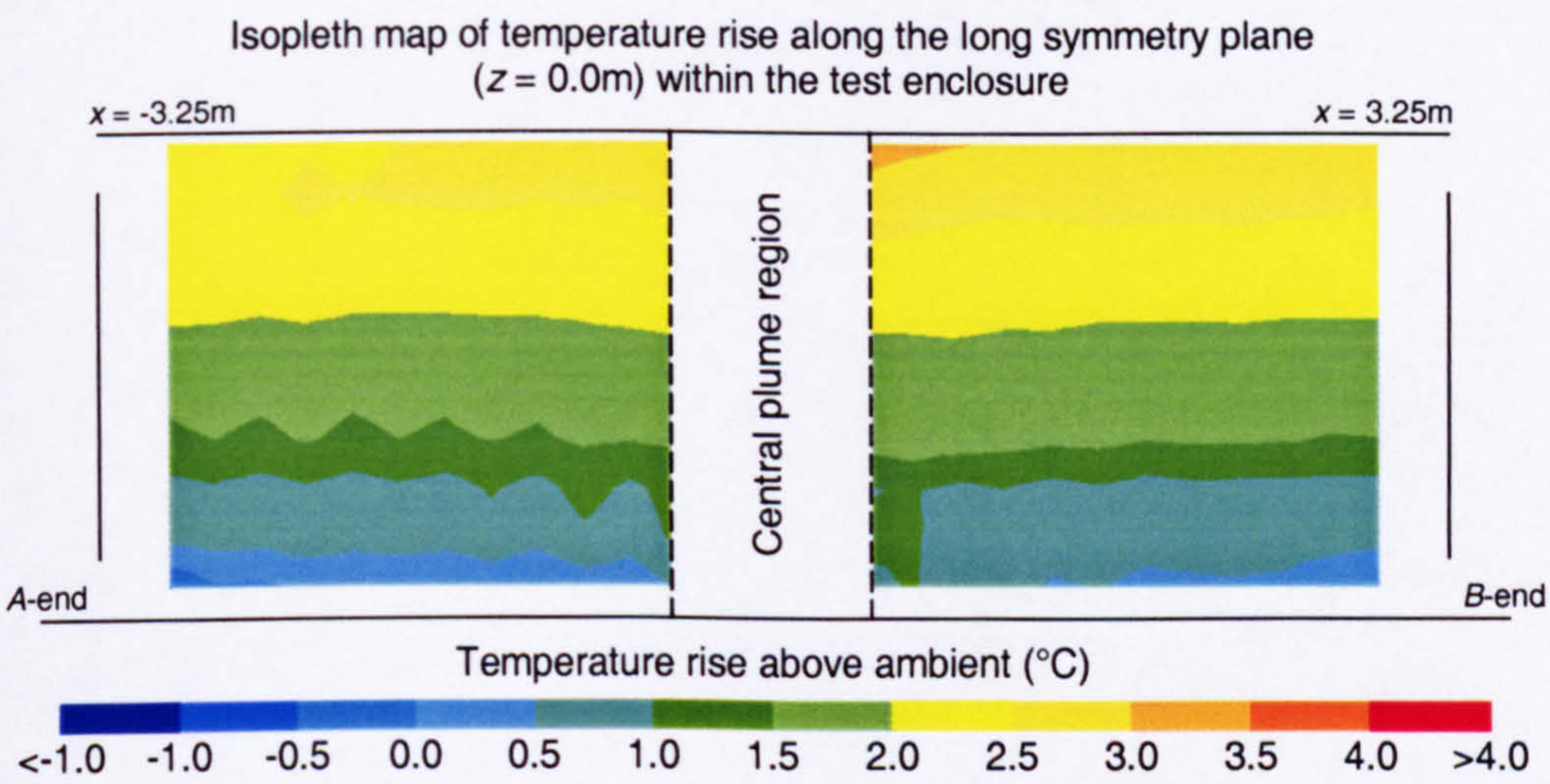

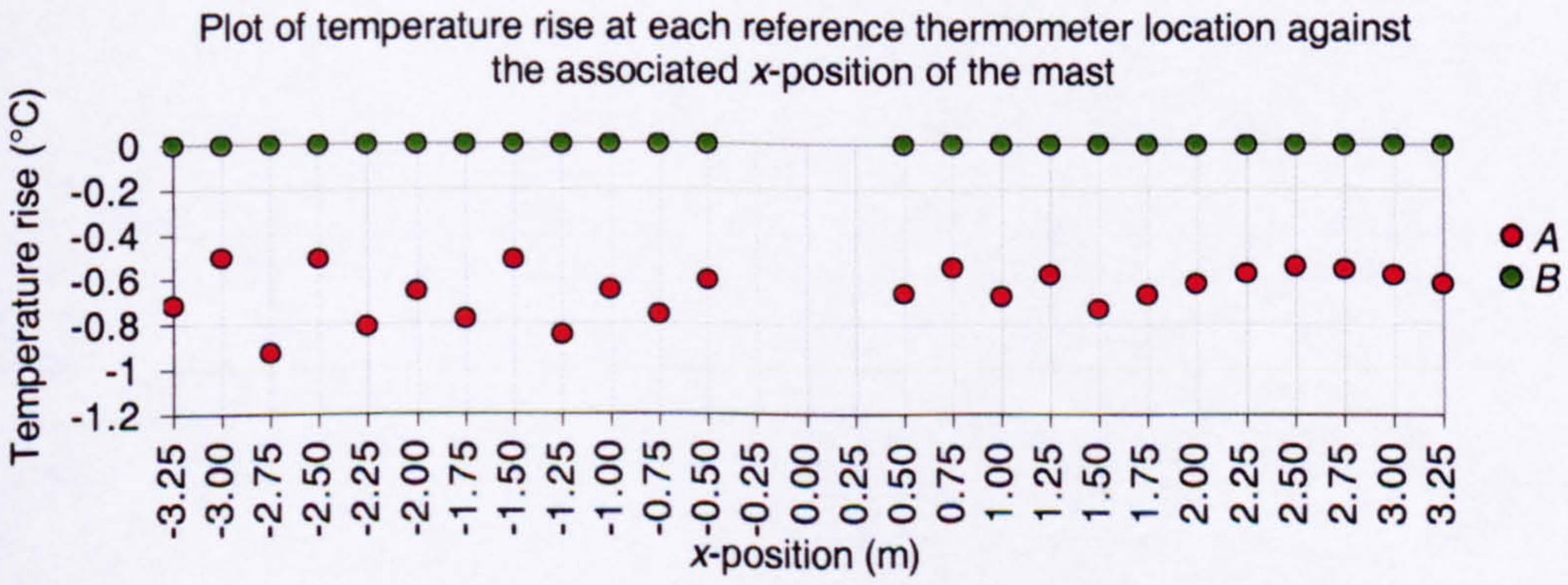

Width of opening:	0.2m
Effective area of opening:	0.122m^2
Heat source:	Boiler ring
Strength of heat source:	368.0W

Figure 13

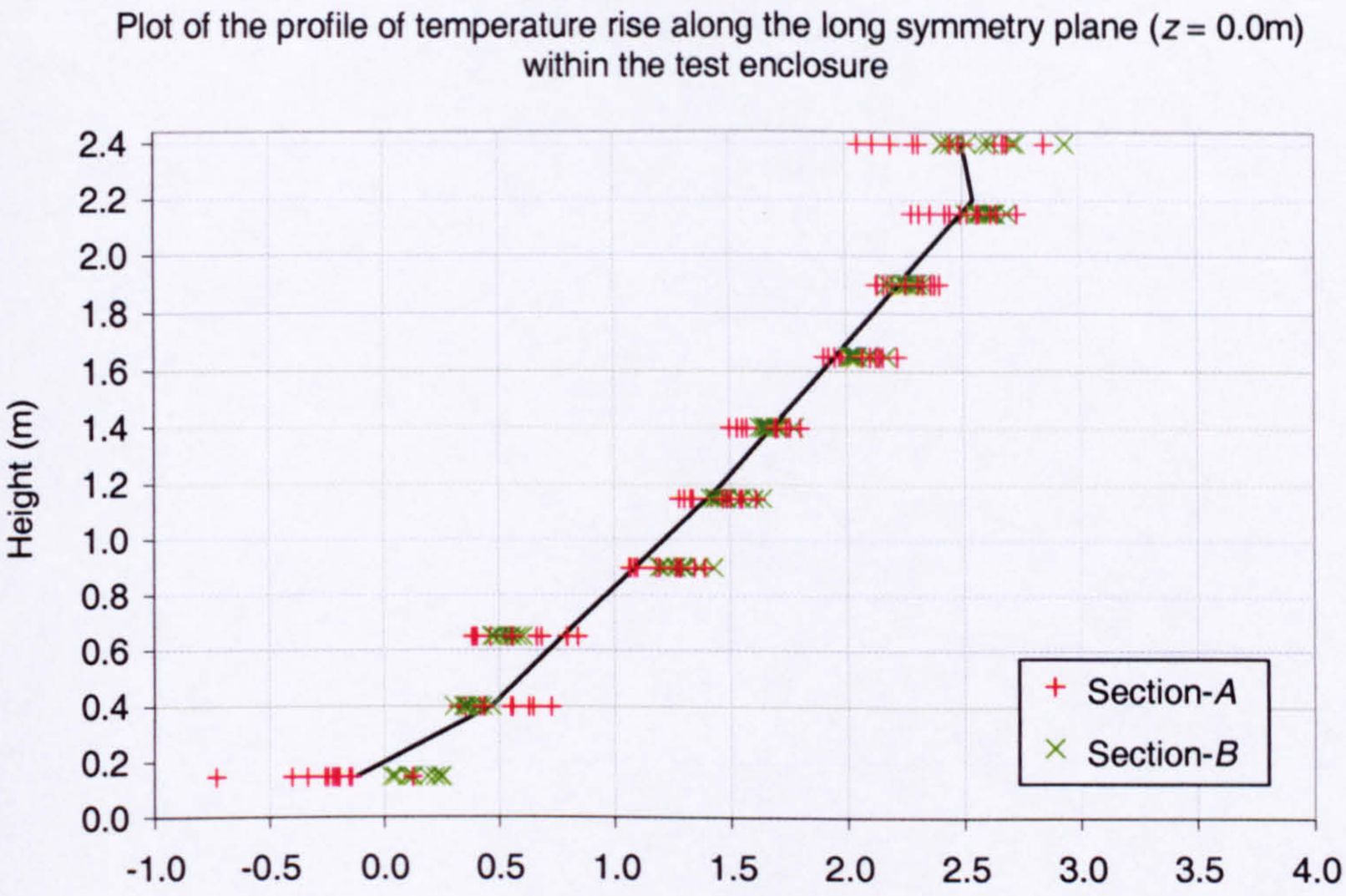

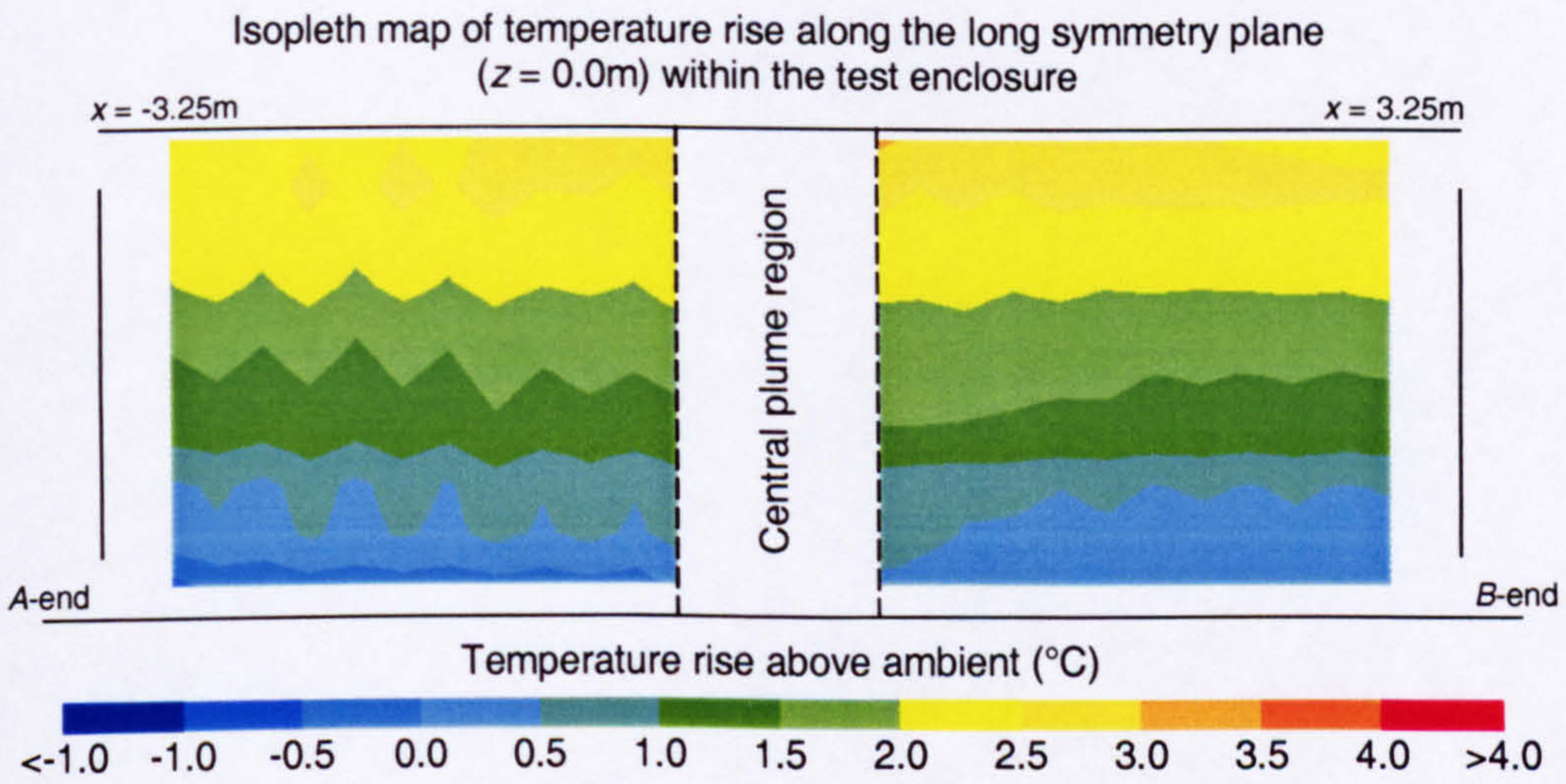

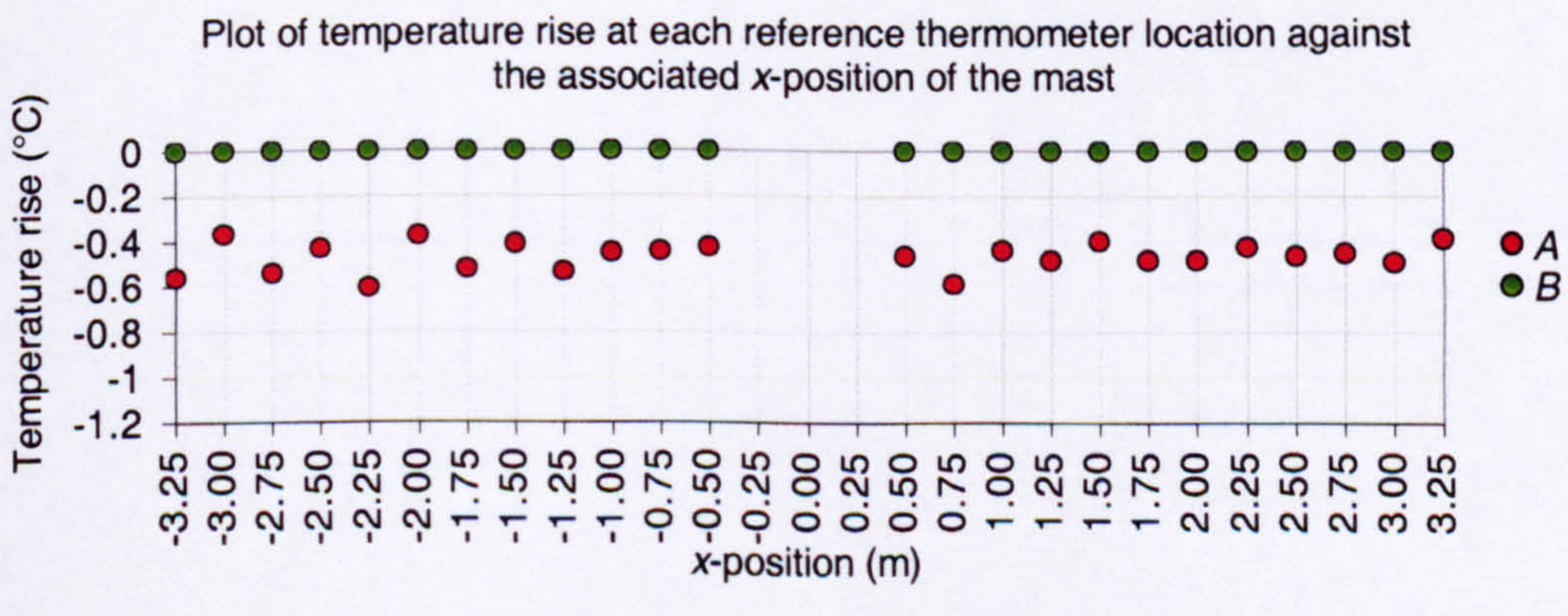

Width of opening:	0.3m
Effective area of opening:	0.183m^2
Heat source:	Boiler ring
Strength of heat source:	368.0W

Figure 14

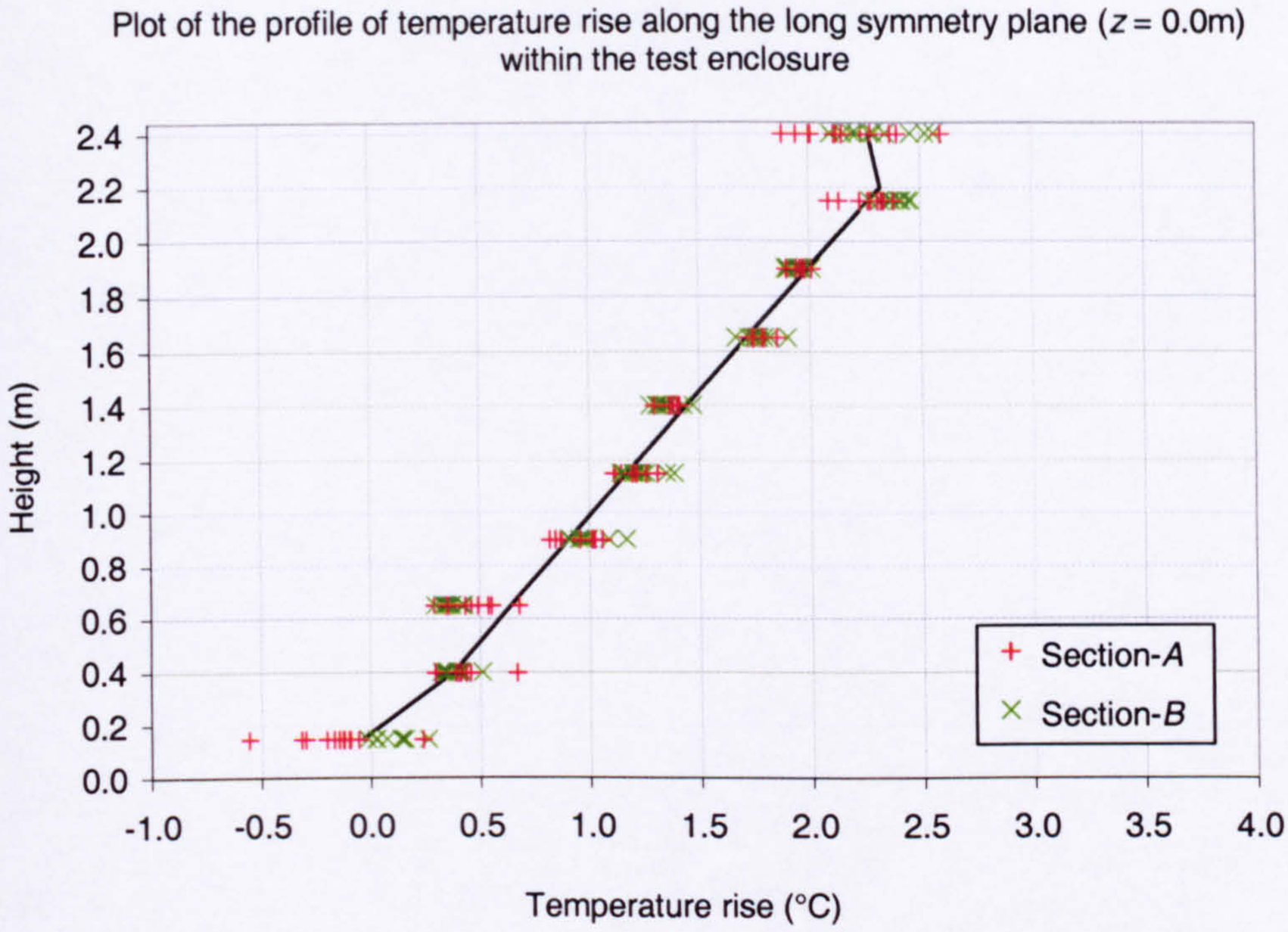

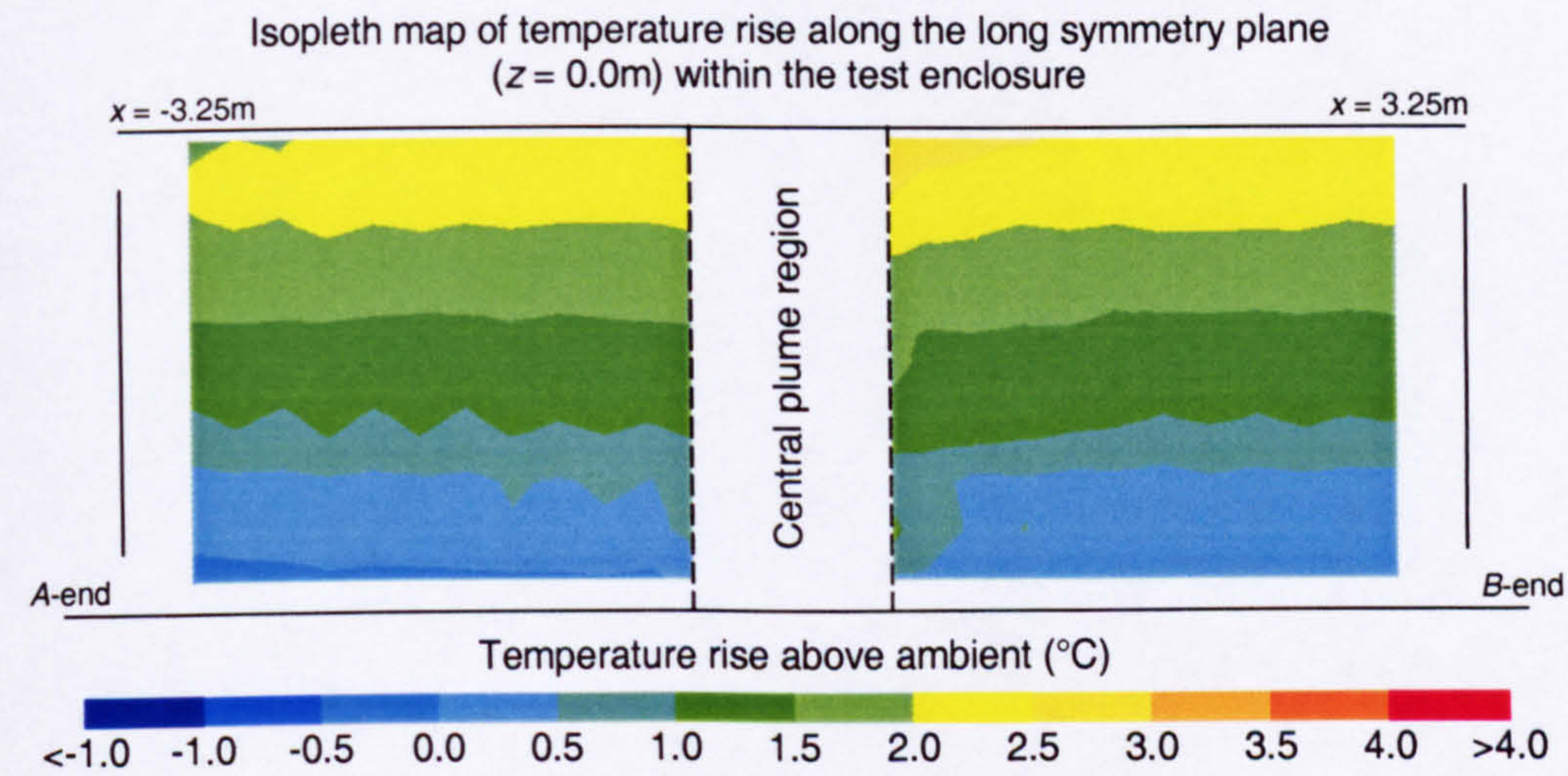

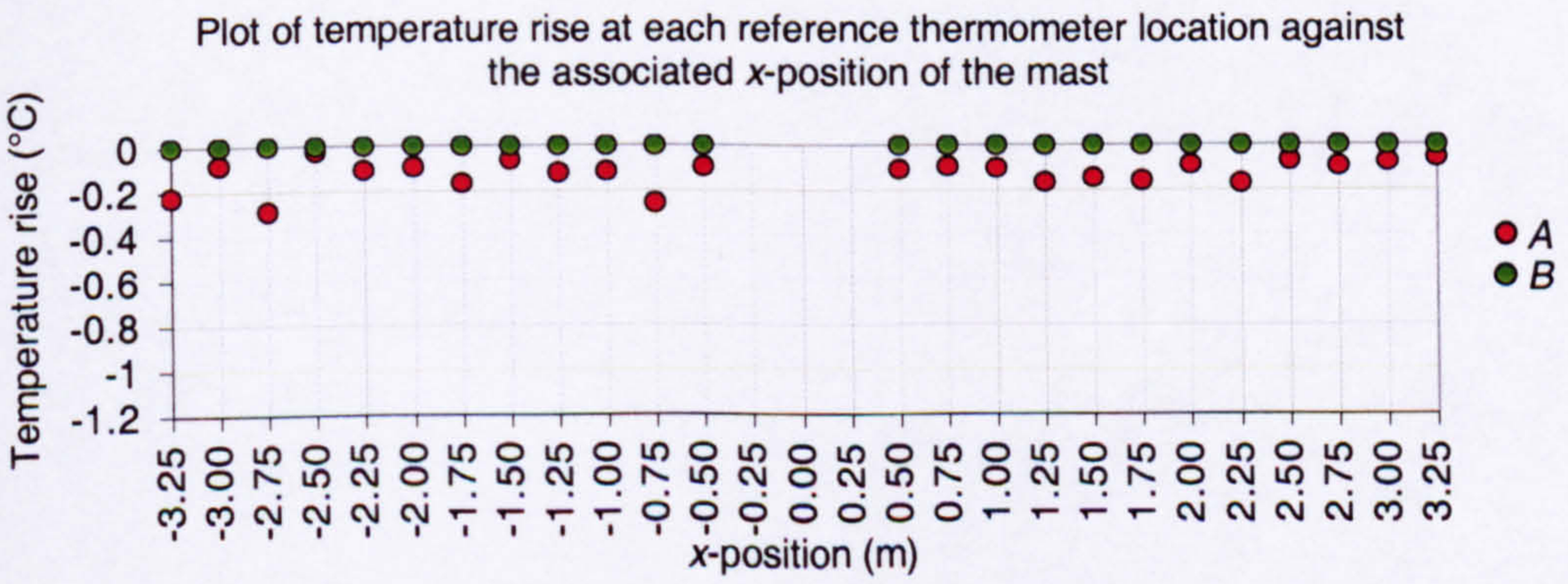

Width of opening:	0.4m
Effective area of opening:	0.244m^2
Heat source:	Boiler ring
Strength of heat source:	368.0W

Figure 15

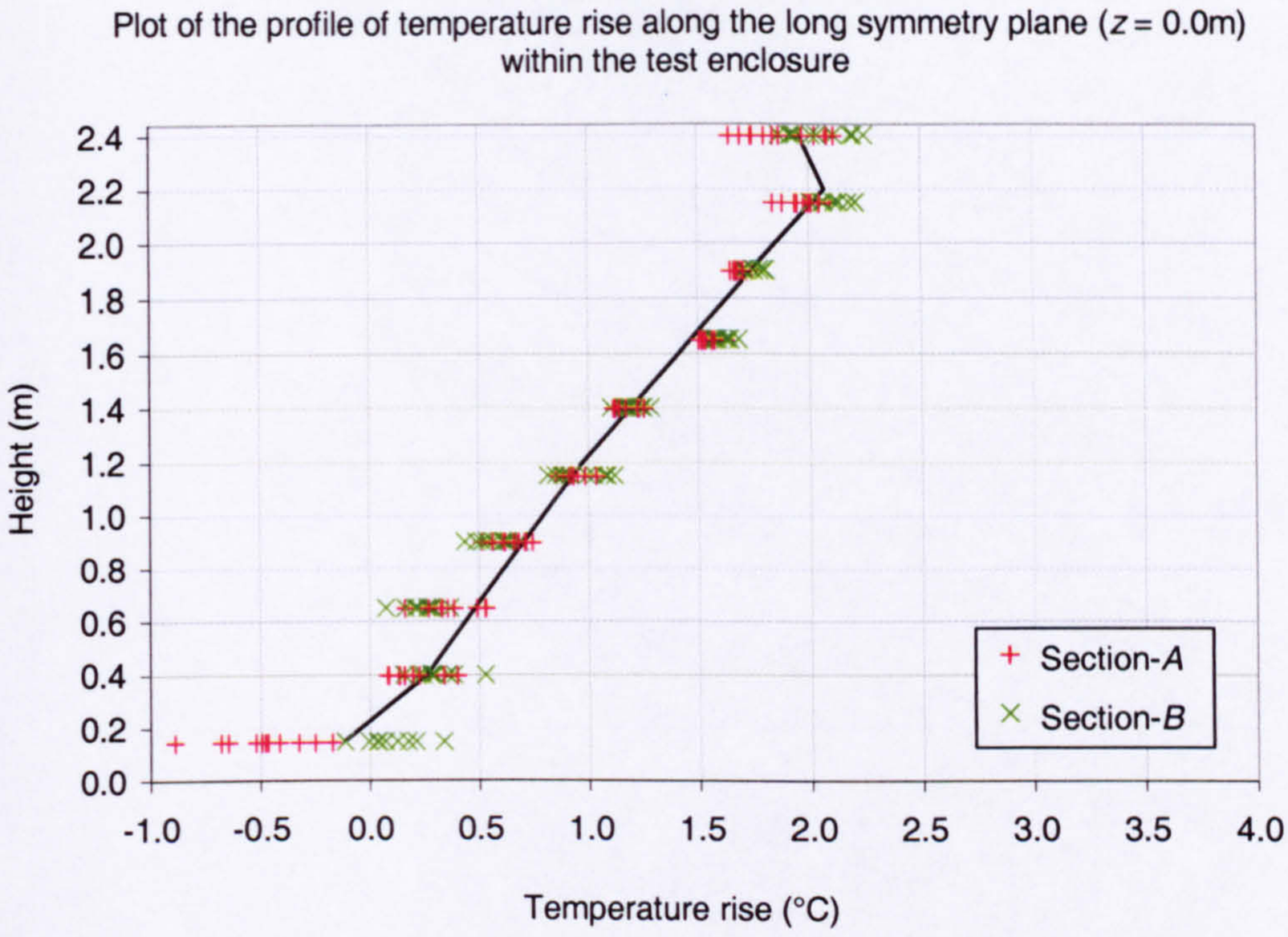

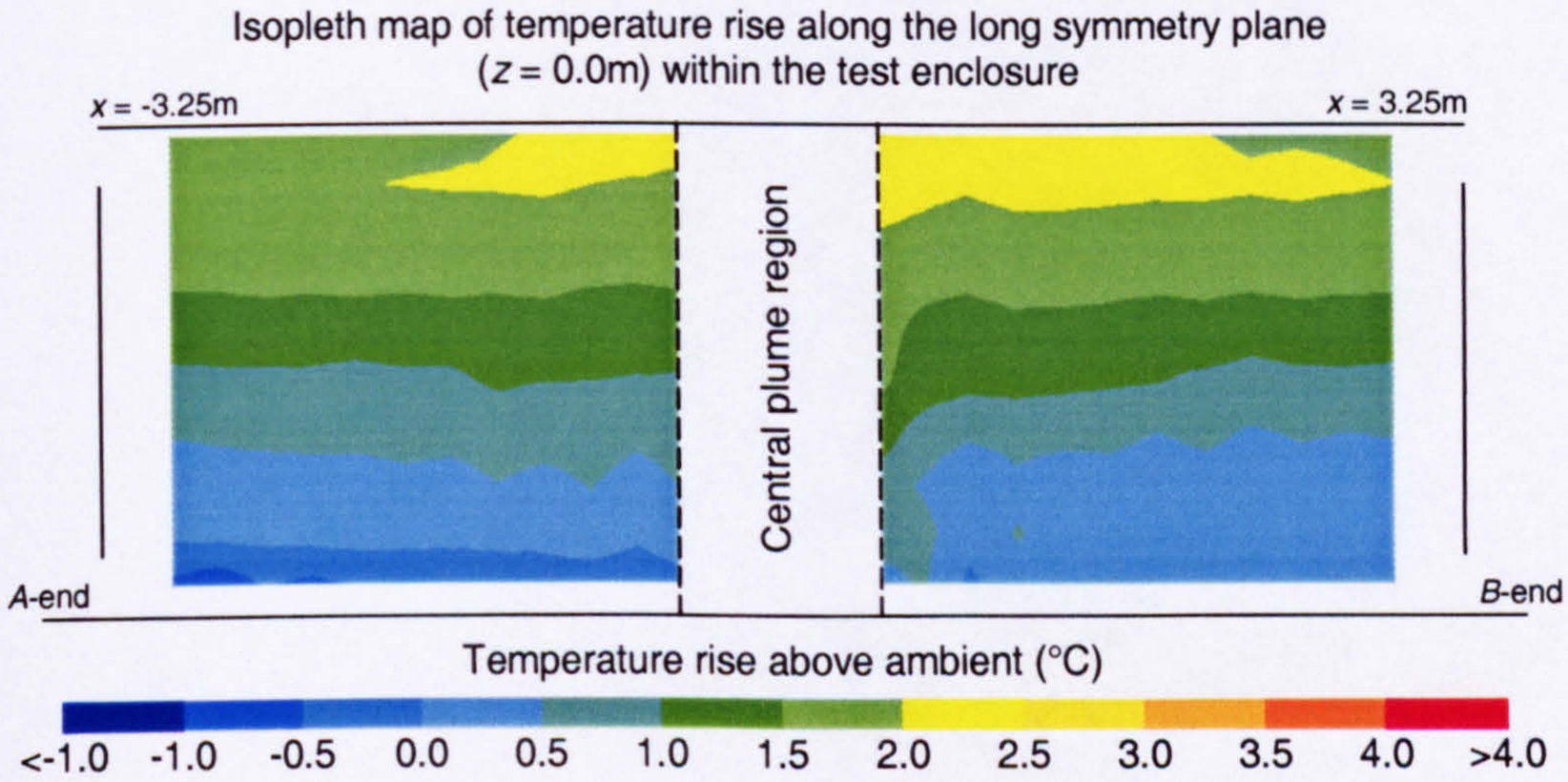

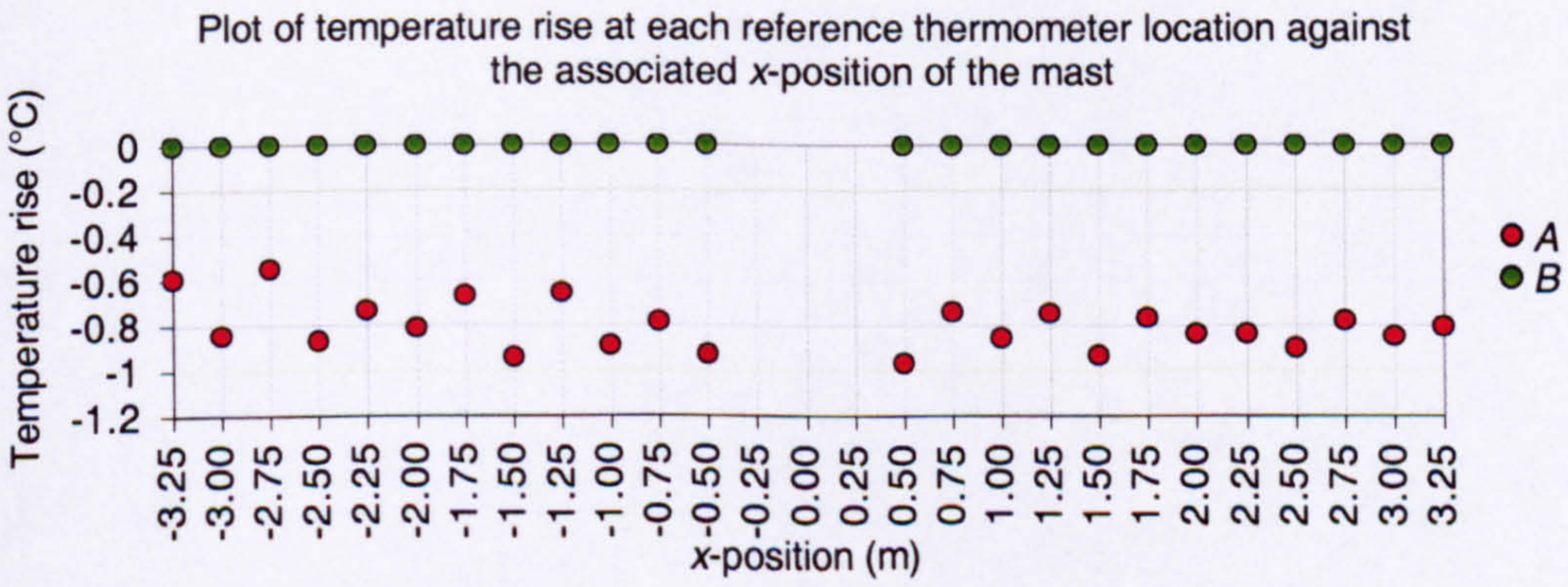

Width of opening:	0.5m
Effective area of opening:	0.305m^2
Heat source:	Boiler ring
Strength of heat source:	368.0W

Figure 16

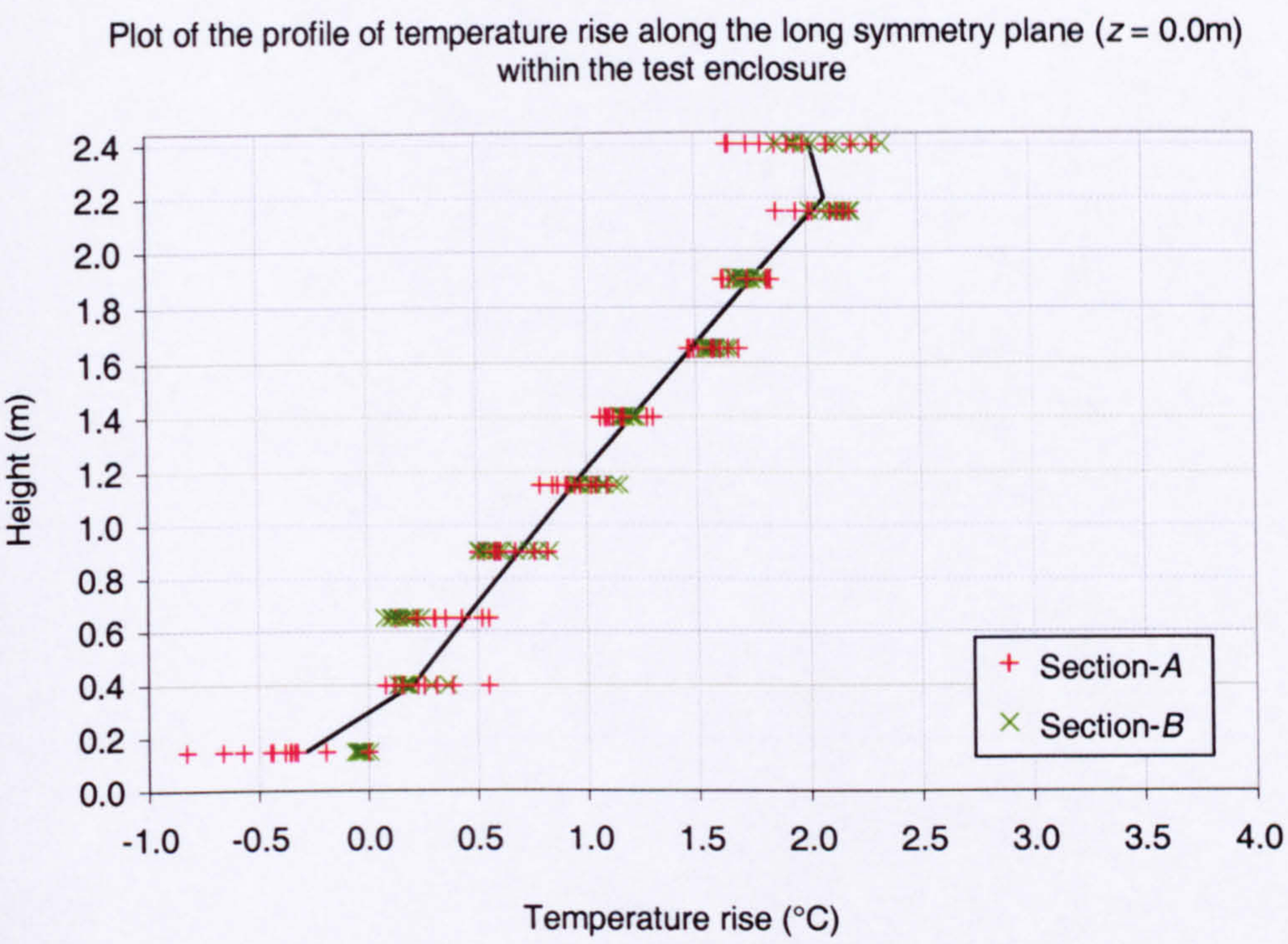

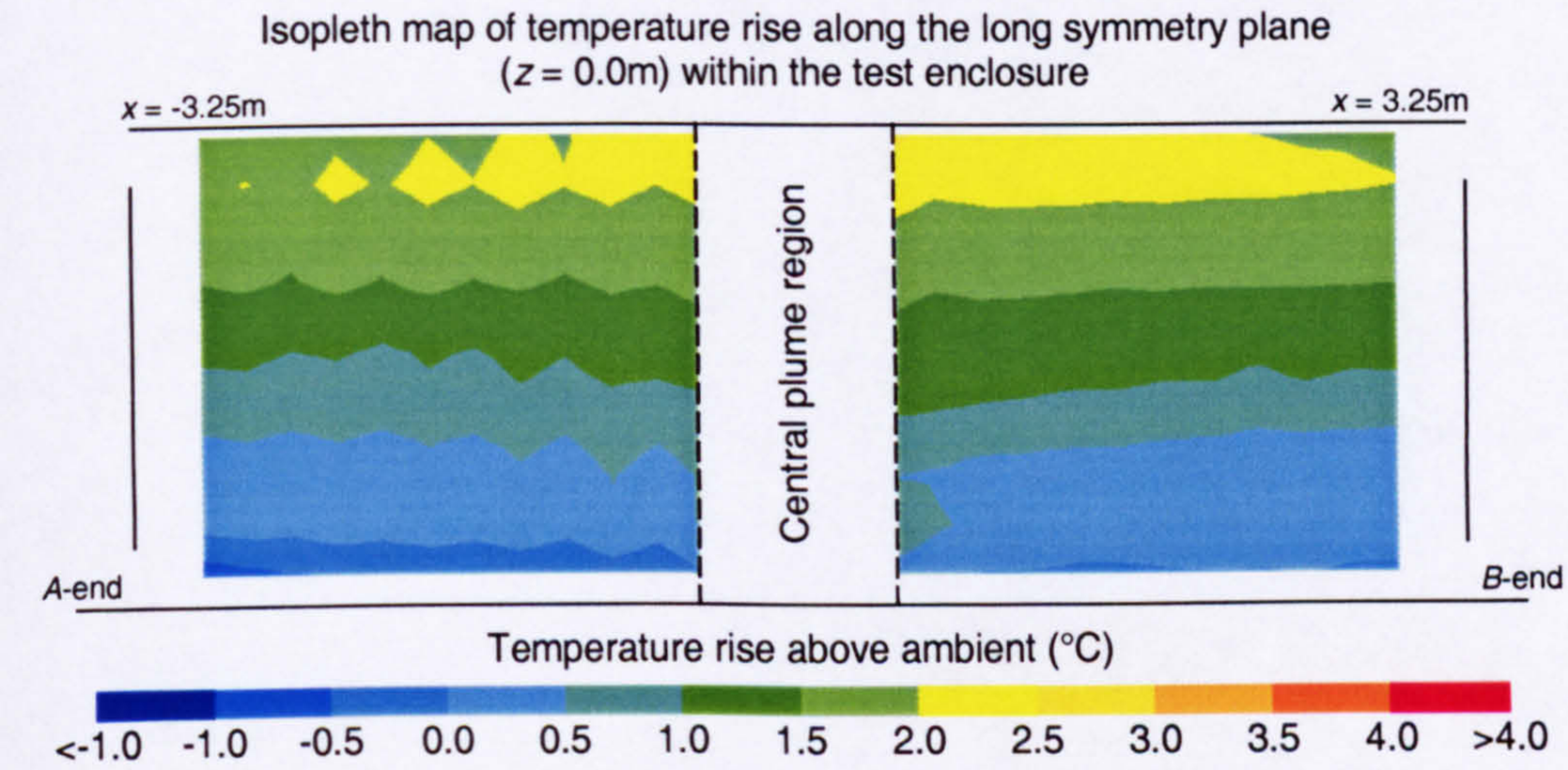

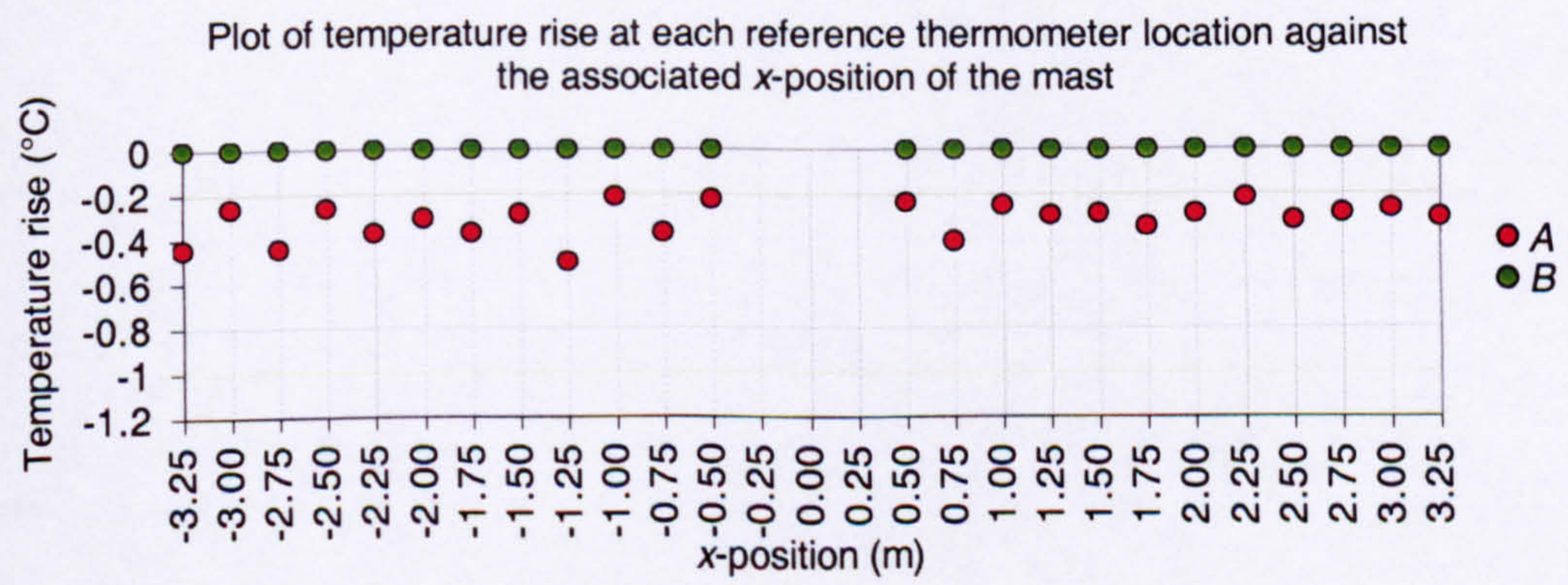

Width of opening:	0.6m
Effective area of opening:	0.366m^2
Heat source:	Boiler ring
Strength of heat source:	368.0W

Figure 17

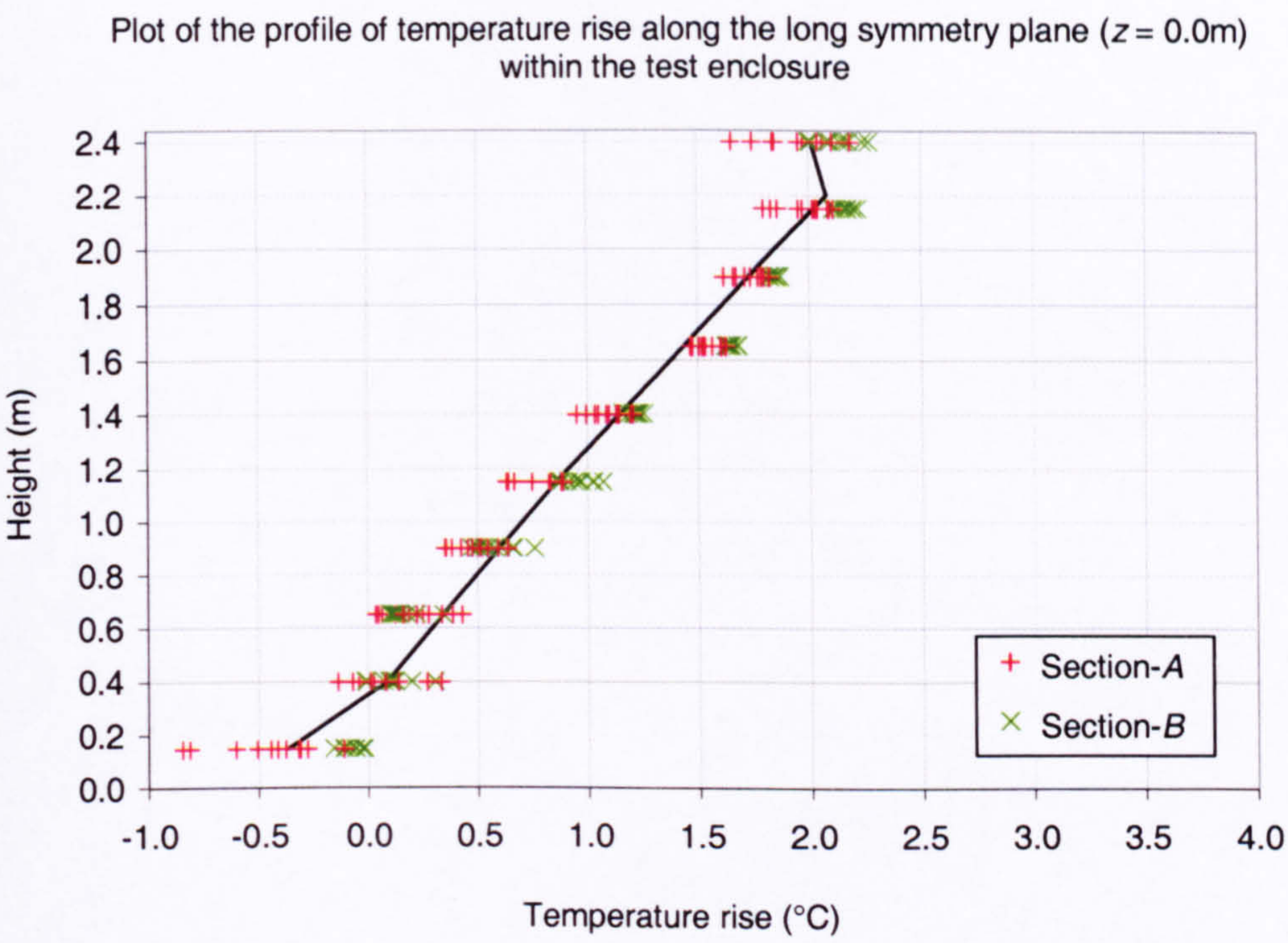

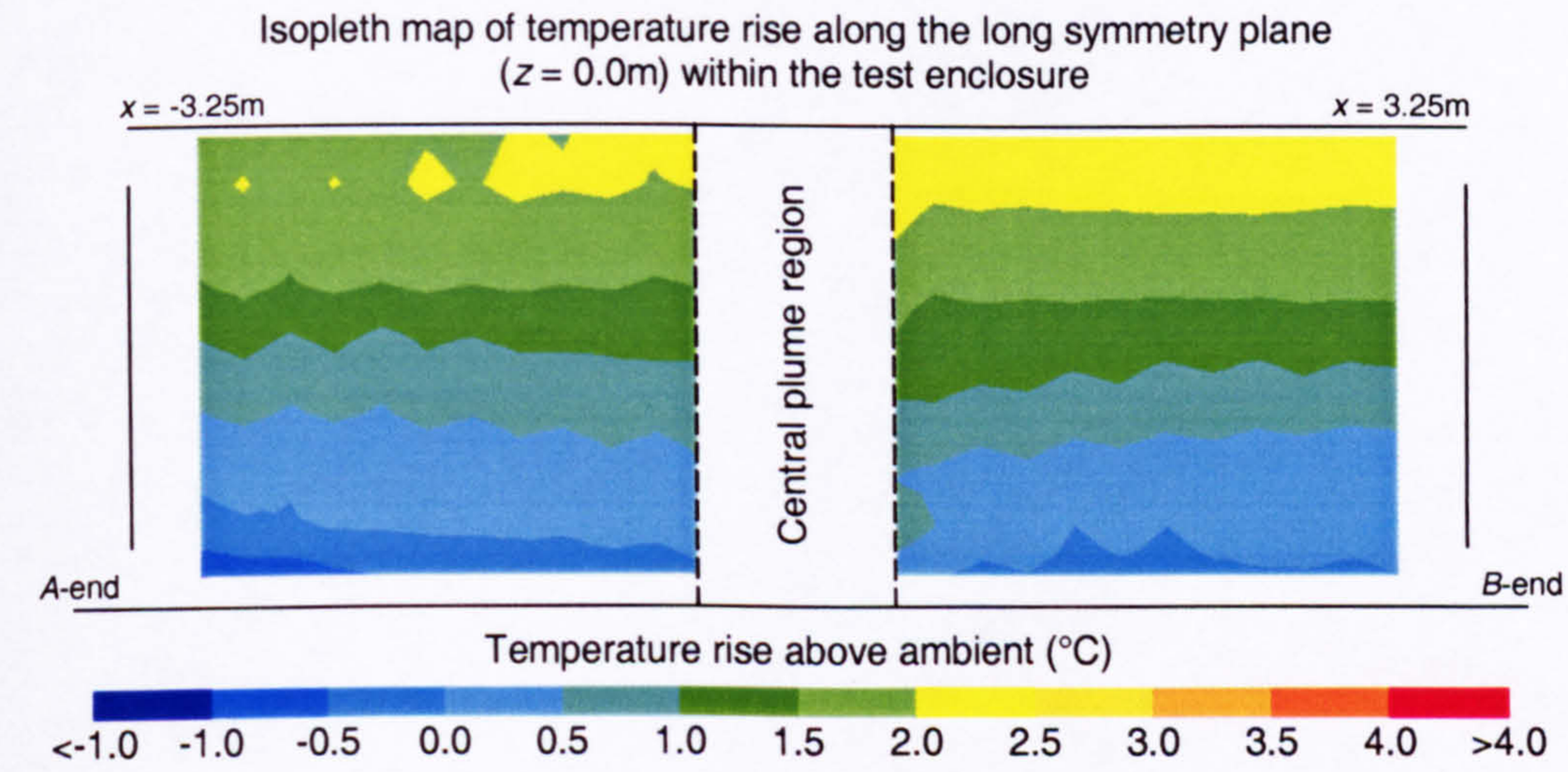

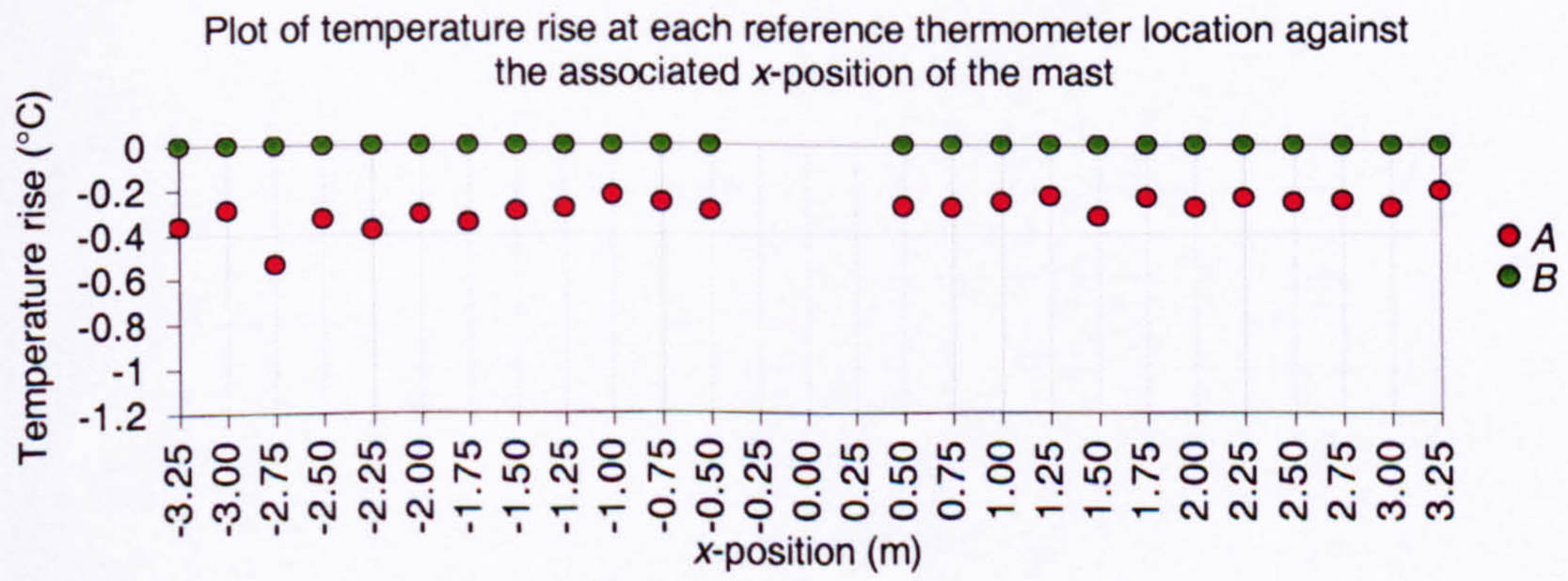

Width of opening:	0.8m
Effective area of opening:	0.488m^2
Heat source:	Boiler ring
Strength of heat source:	368.0W

Figure 18

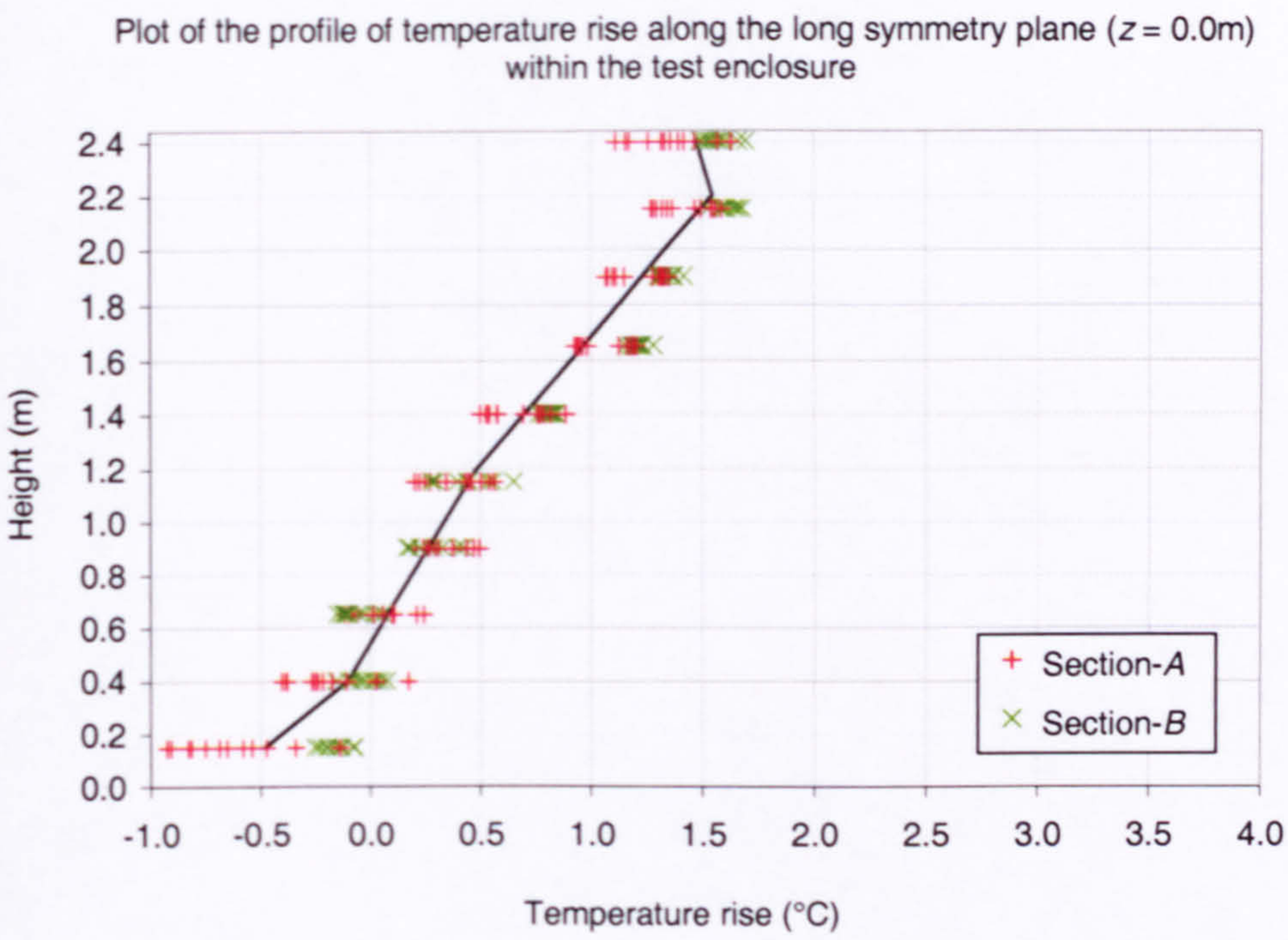

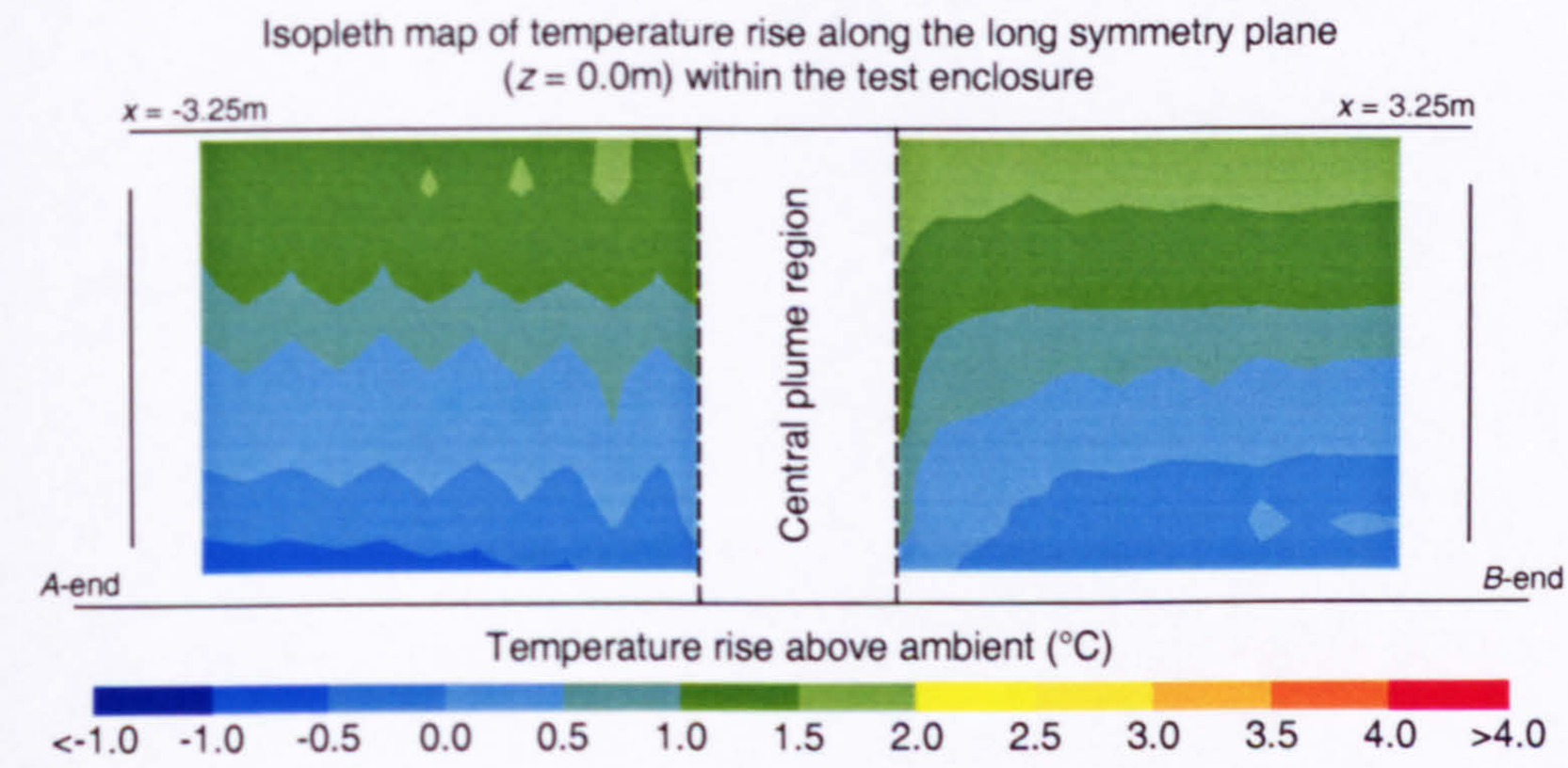

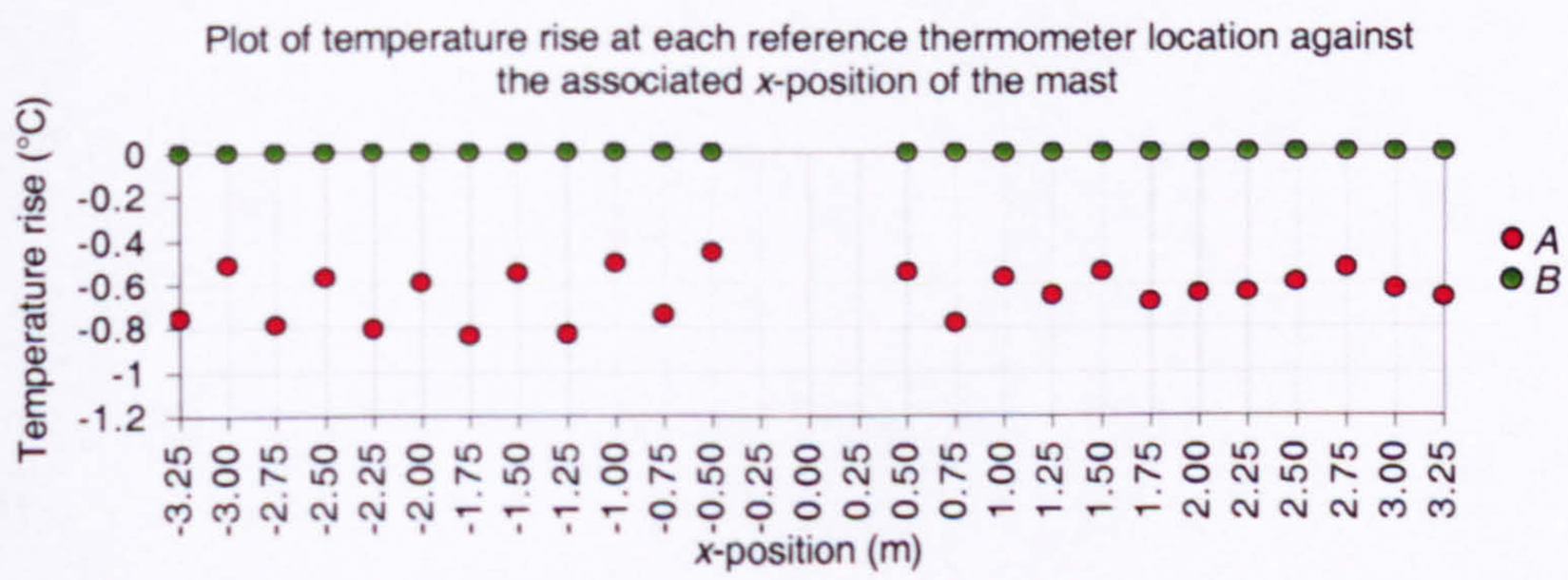

Width of opening:	1.0m
Effective area of opening:	0.610m^2
Heat source:	Boiler ring
Strength of heat source:	368.0W

Figure 19

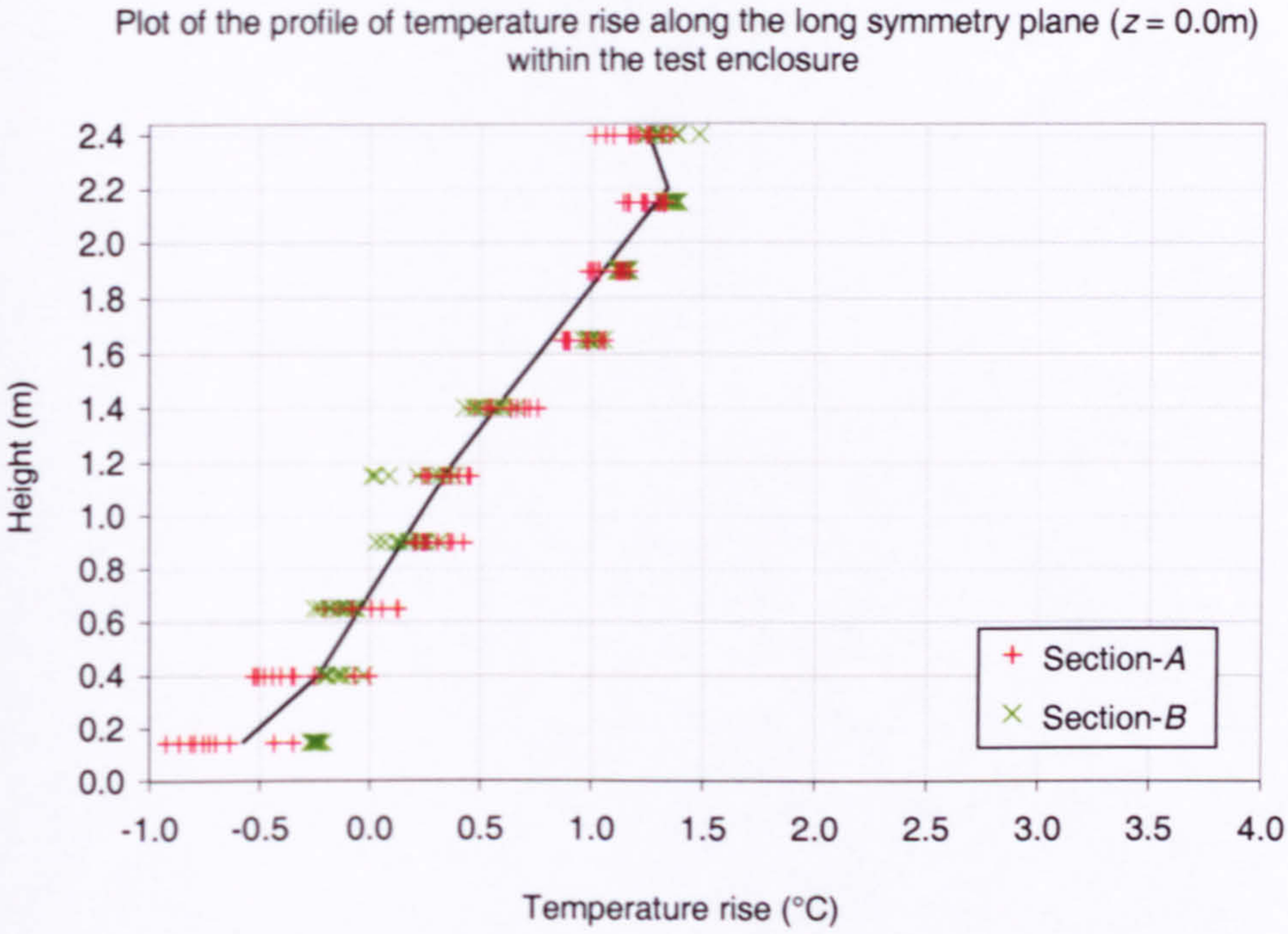

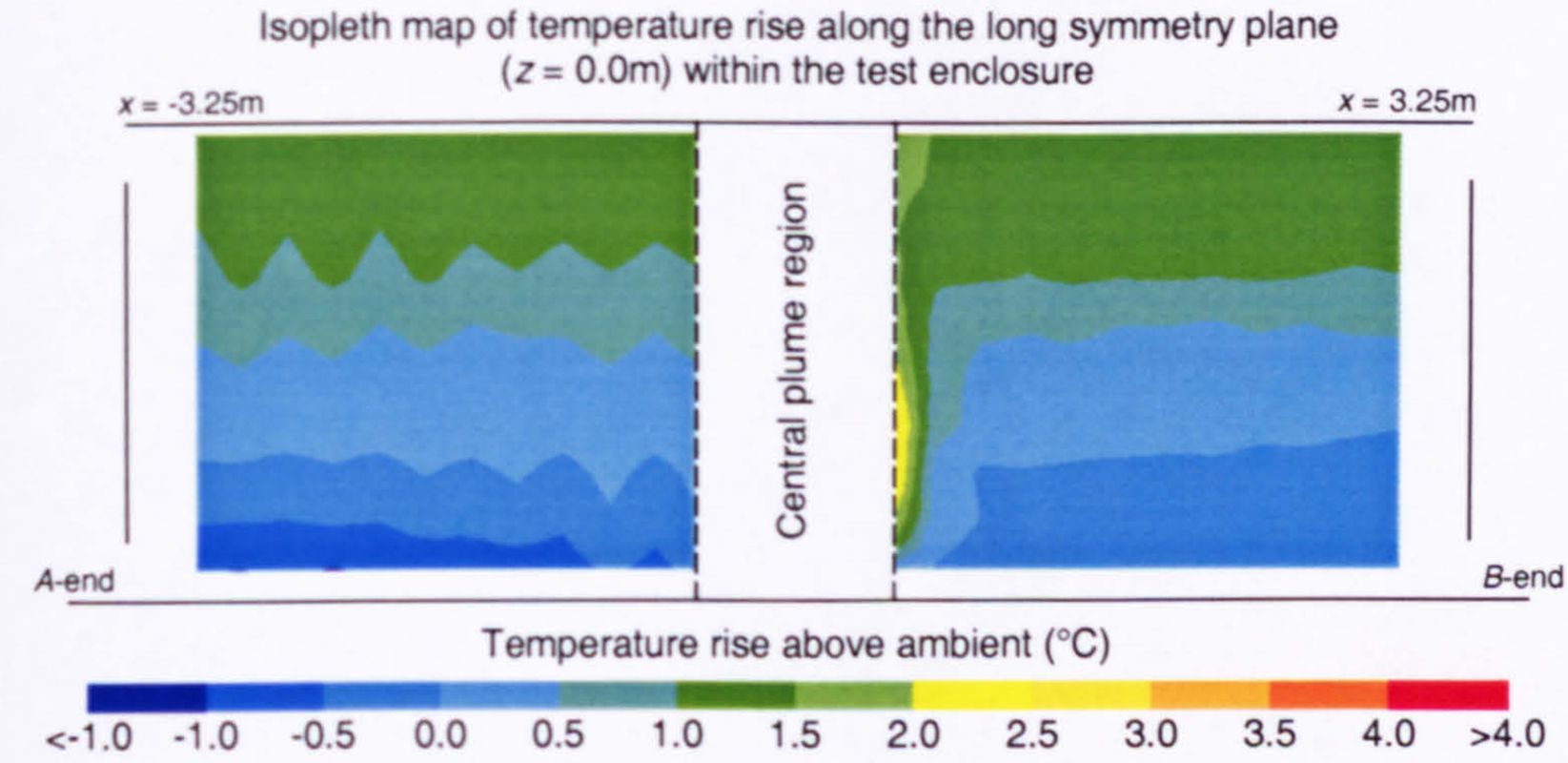

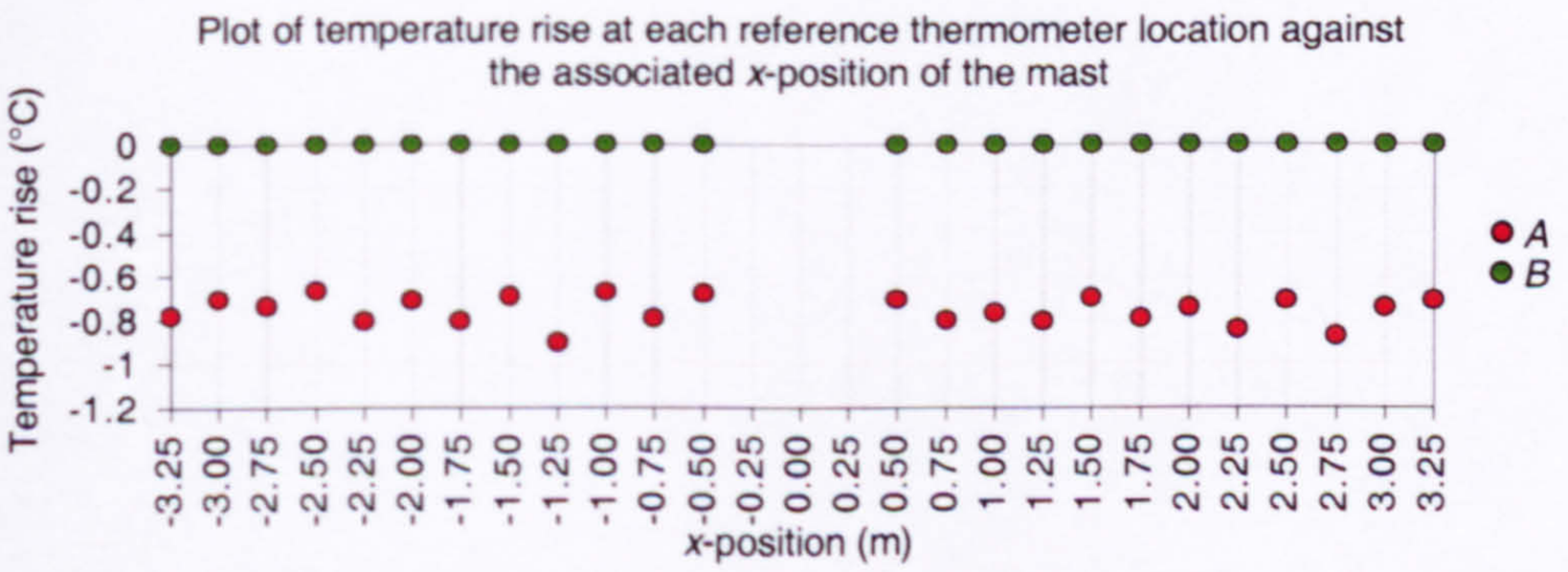

Width of opening:	1.2m
Effective area of opening:	0.732m^2
Heat source:	Boiler ring
Strength of heat source:	368.0W

Figure 20

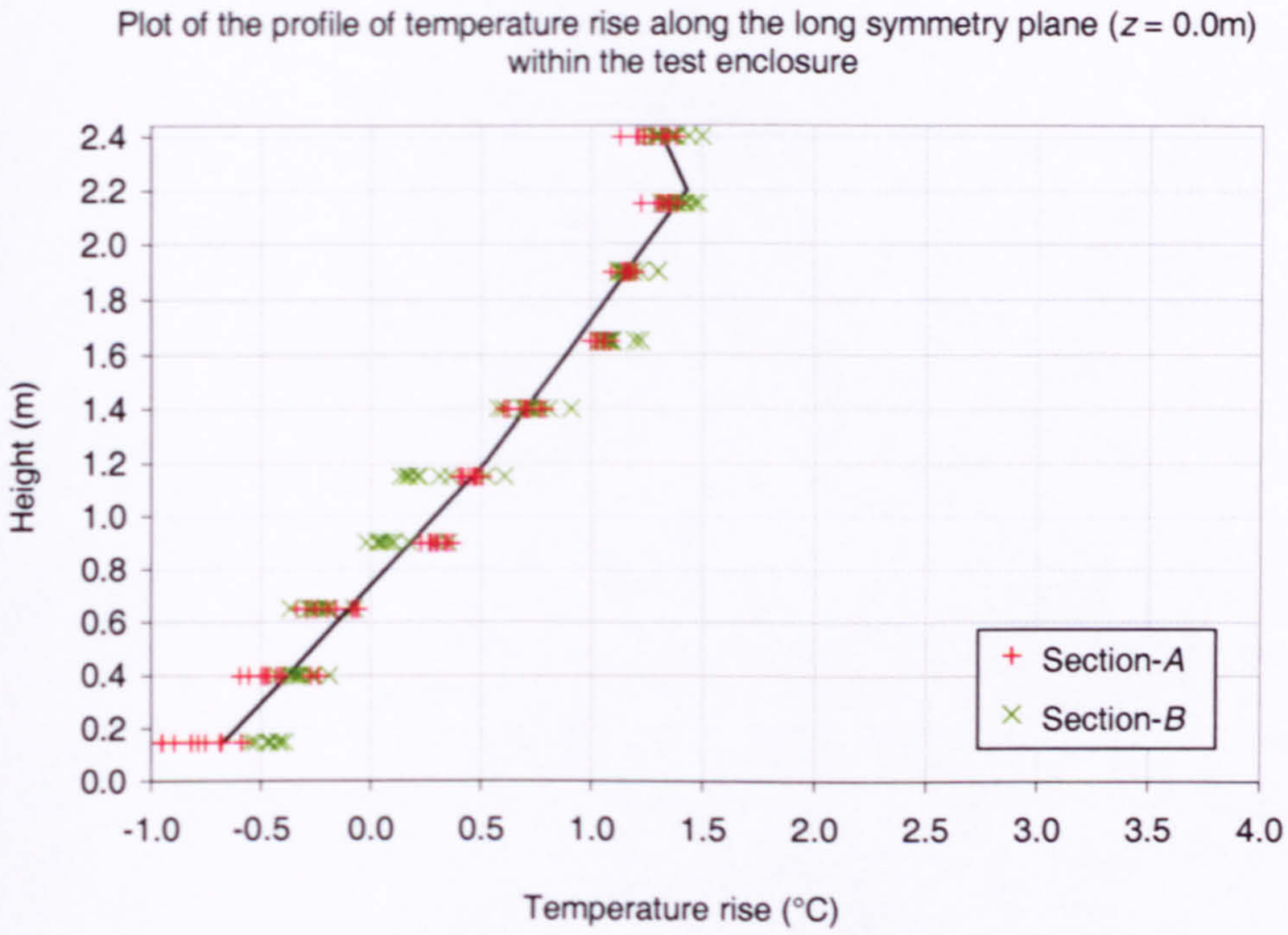

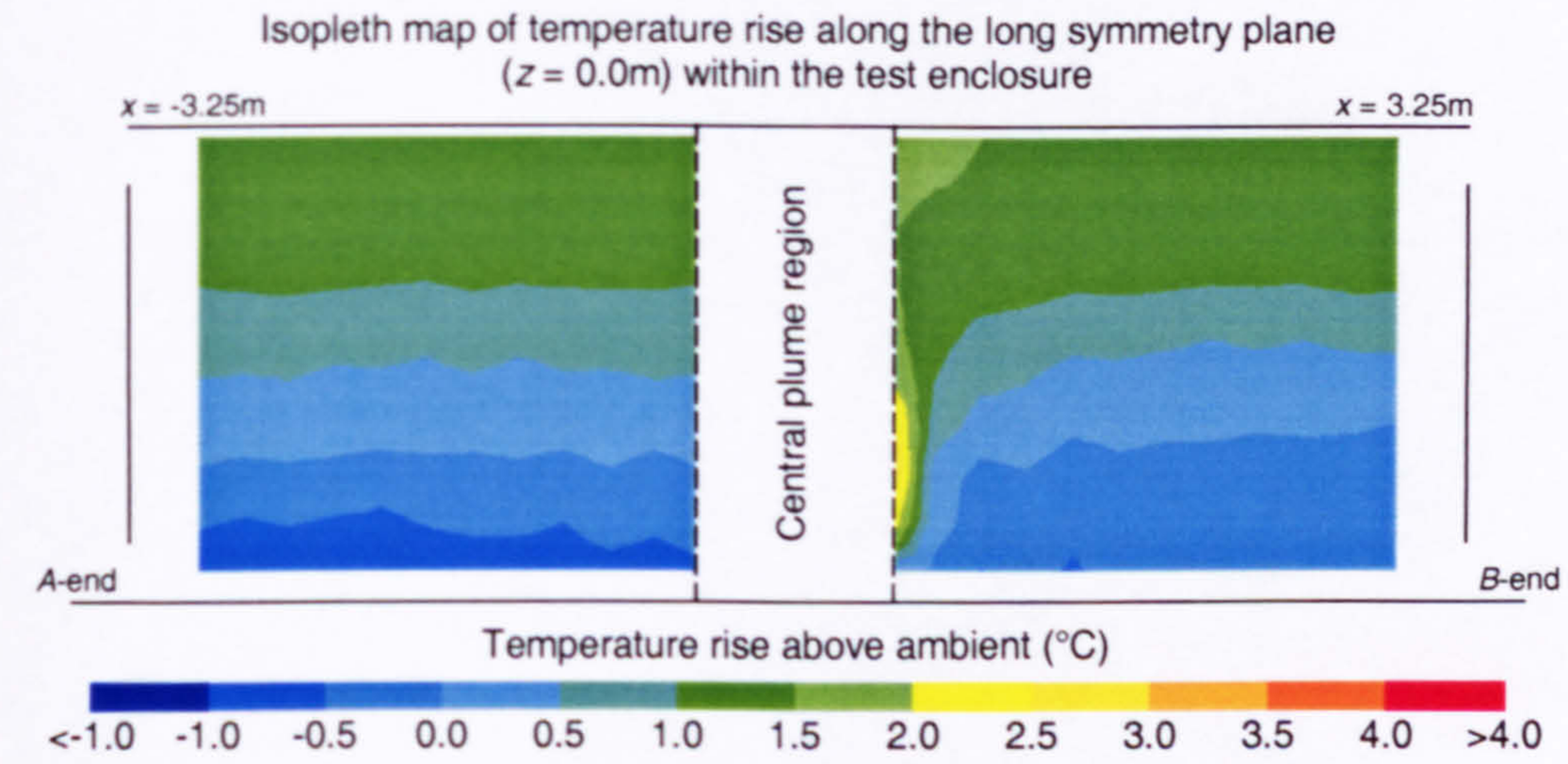

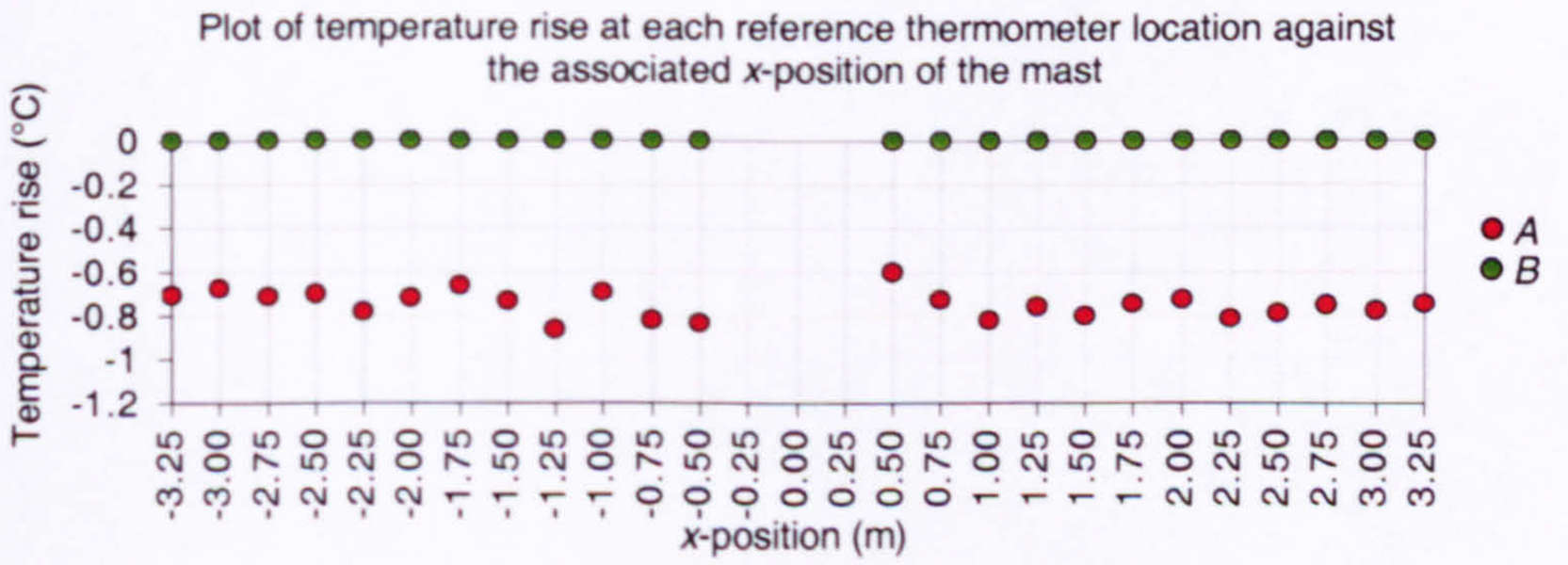

Width of opening:	1.5m
Effective area of opening:	0.915m^2
Heat source:	Boiler ring
Strength of heat source:	368.0W

Figure 21

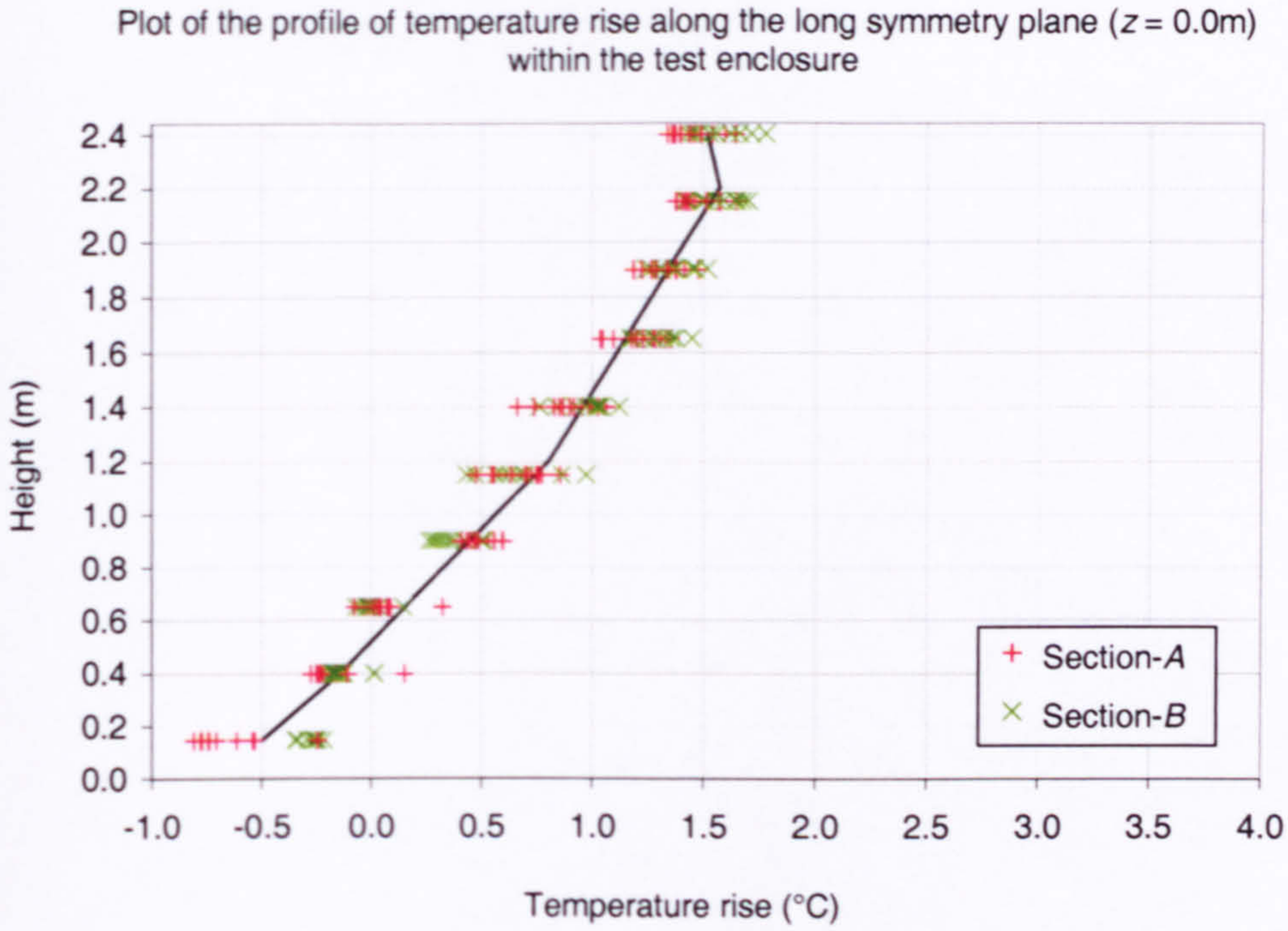

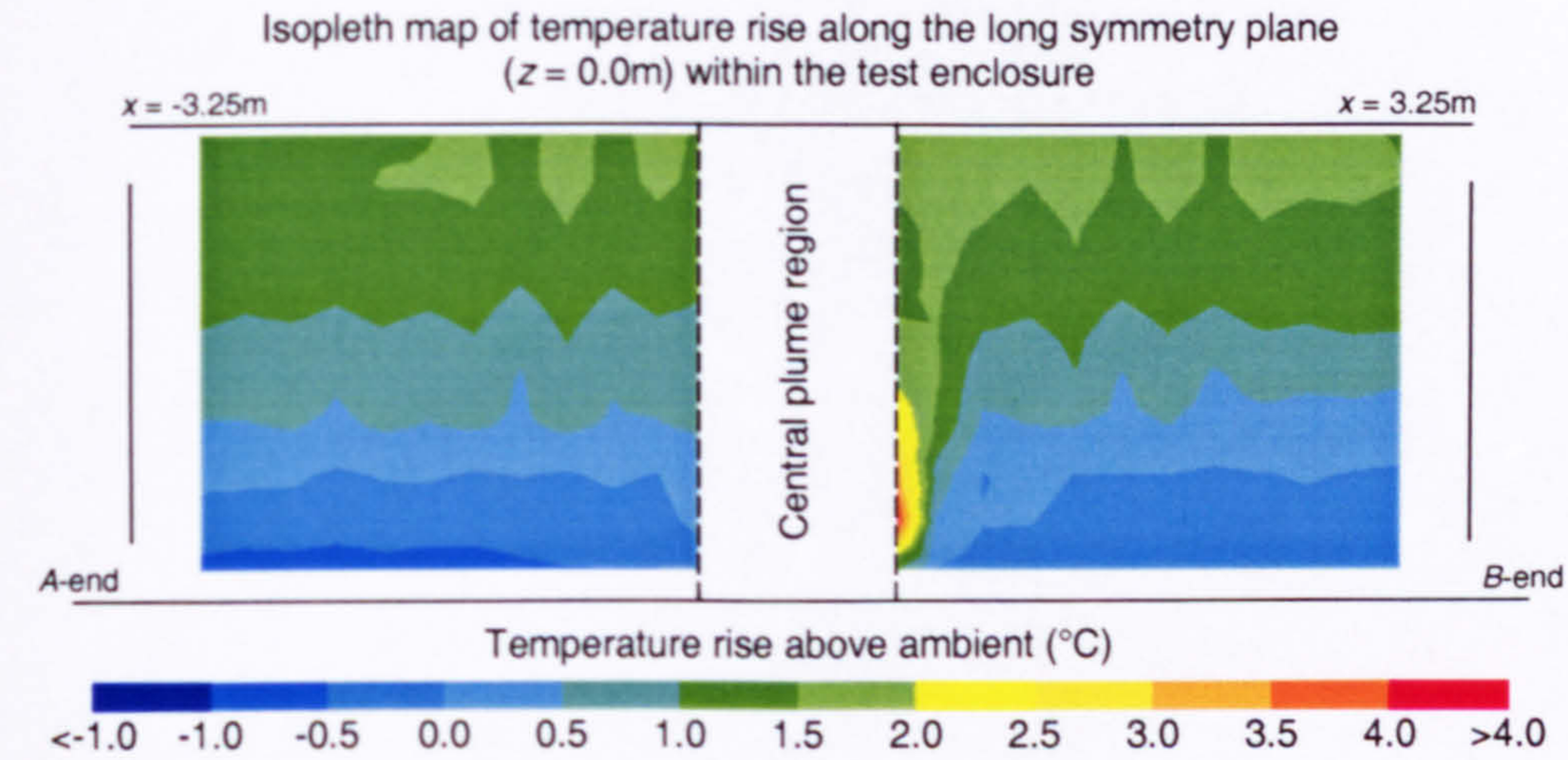

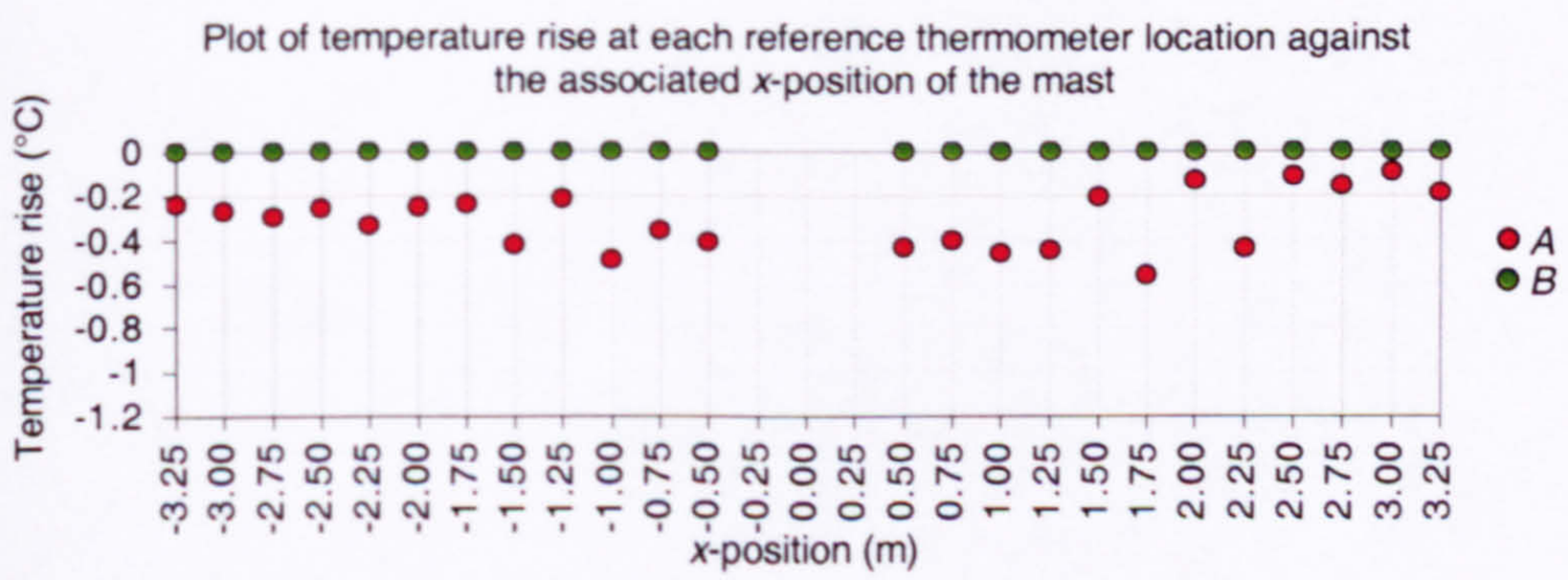

Width of opening:	1.8m
Effective area of opening:	1.098m^2
Heat source:	Boiler ring
Strength of heat source:	368.0W

Figure 22

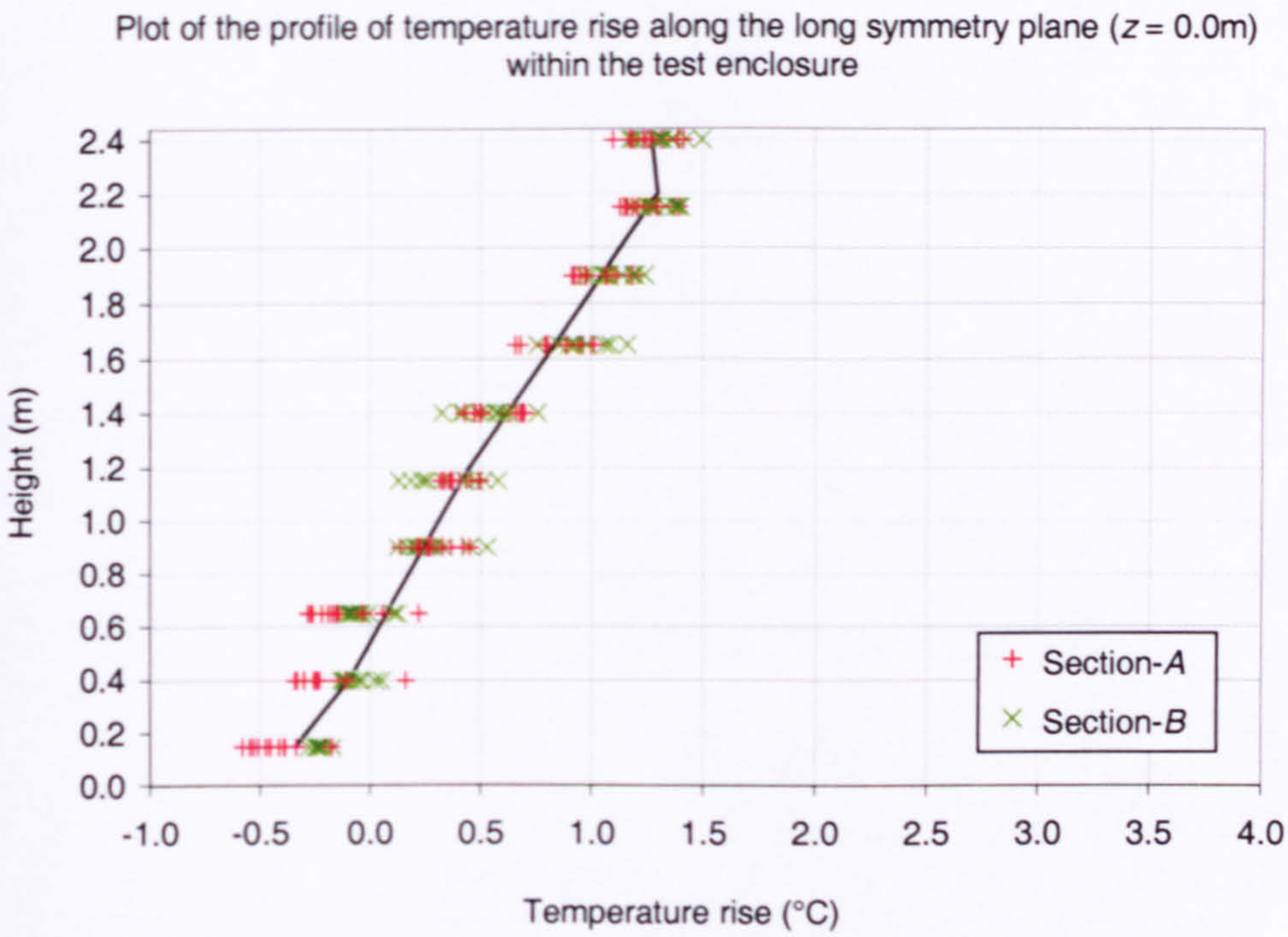

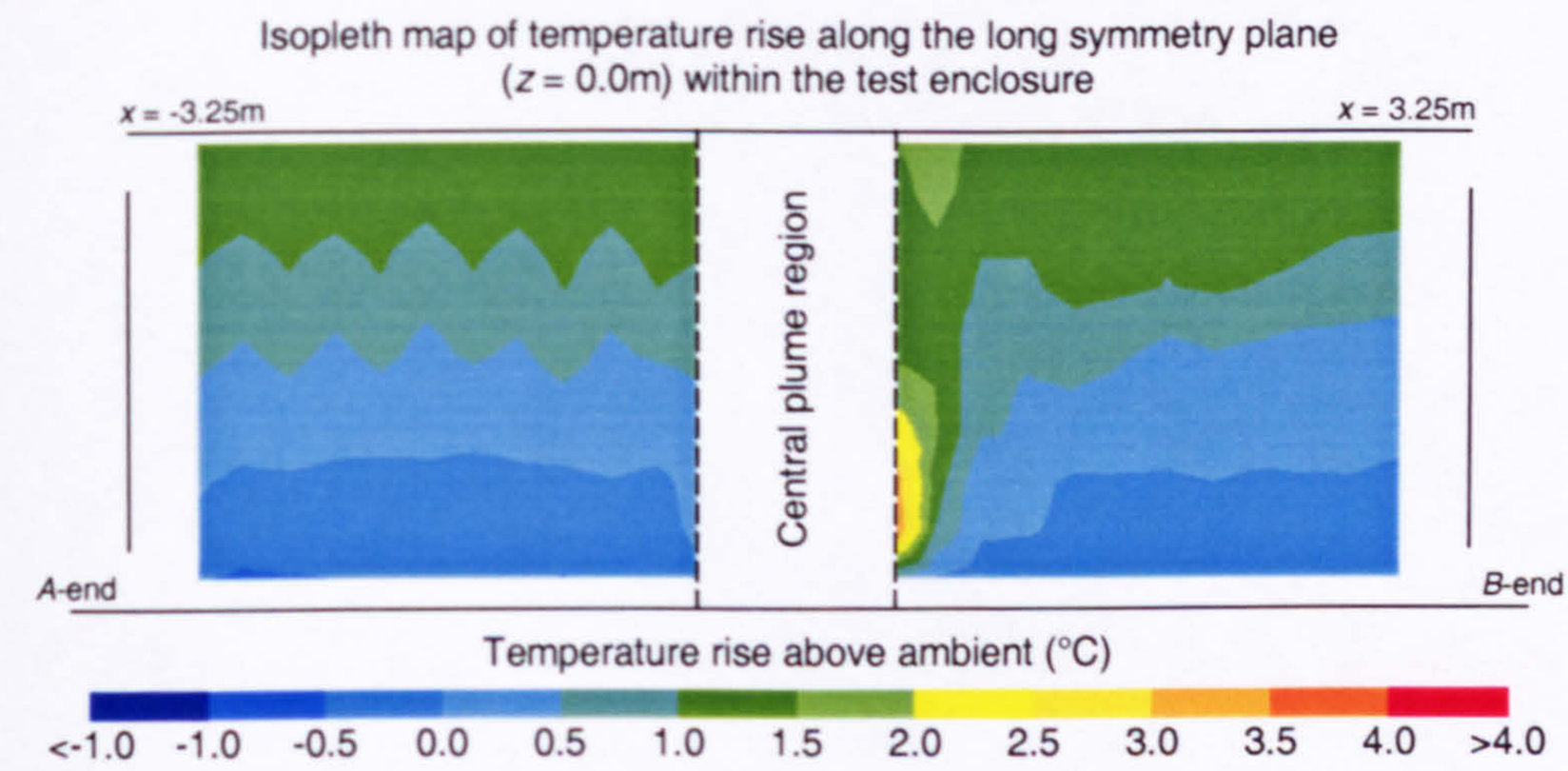

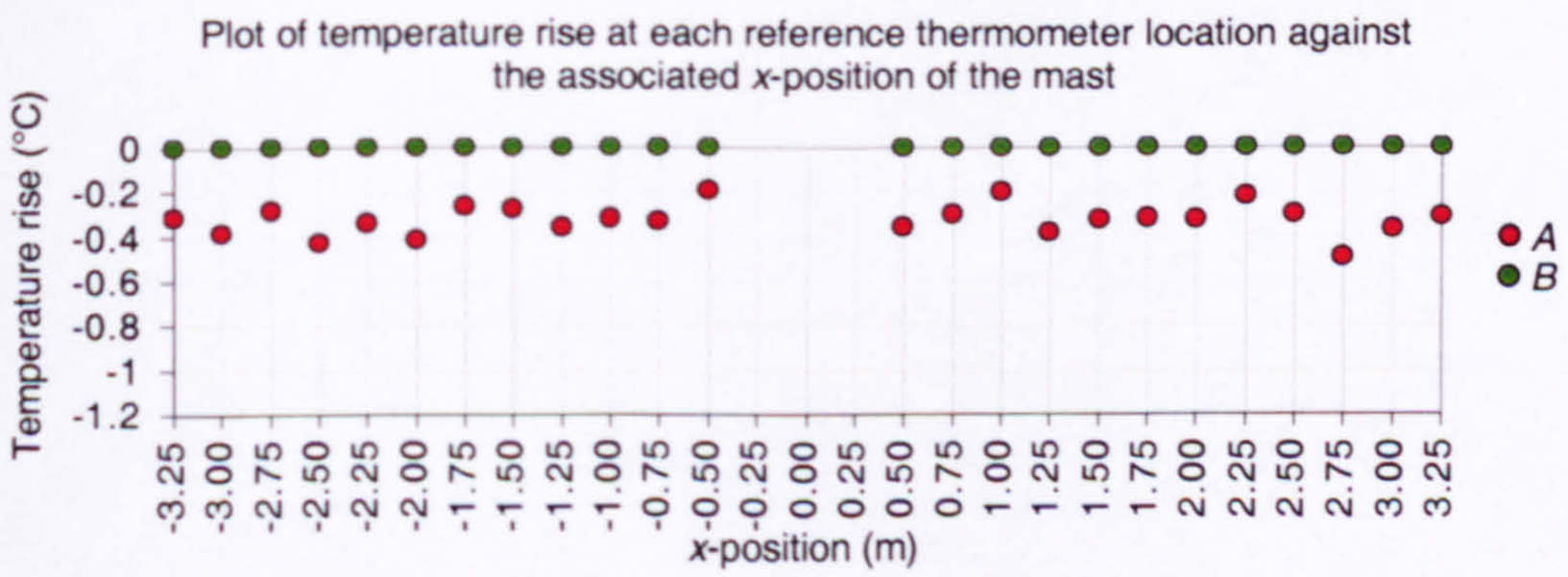

Width of opening:	2.32m
Effective area of opening:	1.415m^2
Heat source:	Boiler ring
Strength of heat source:	368.0W

Figure 23

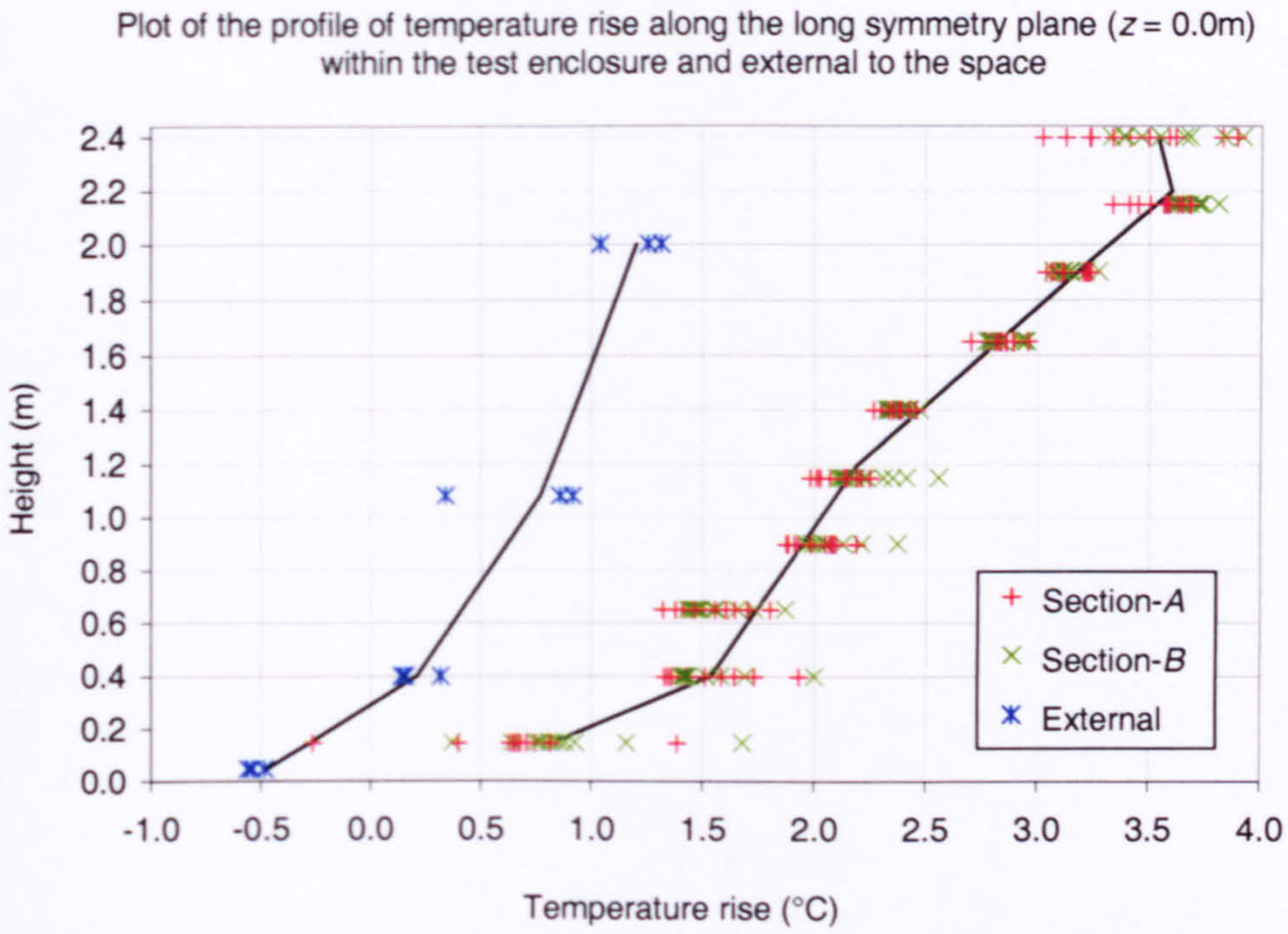

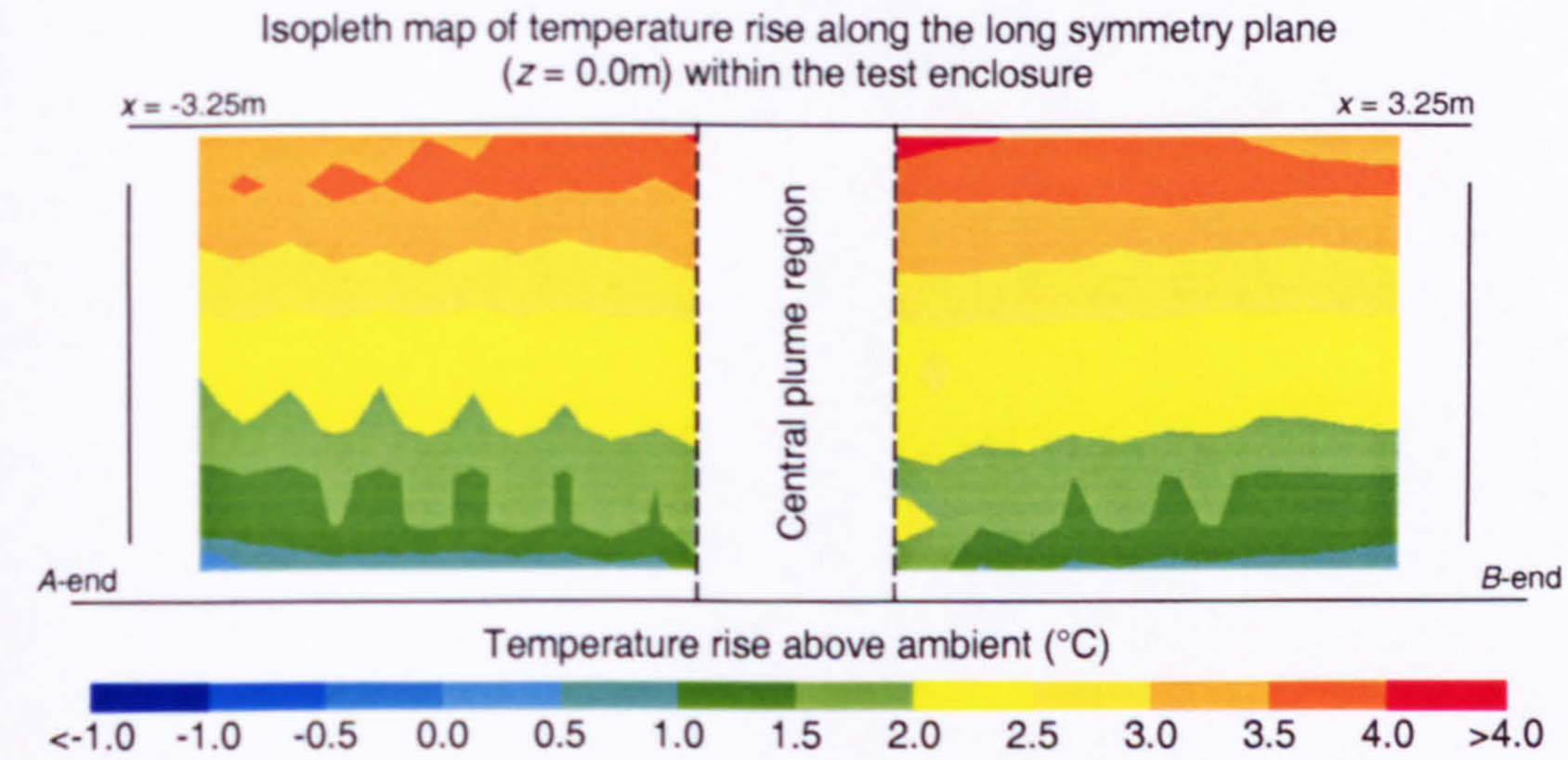

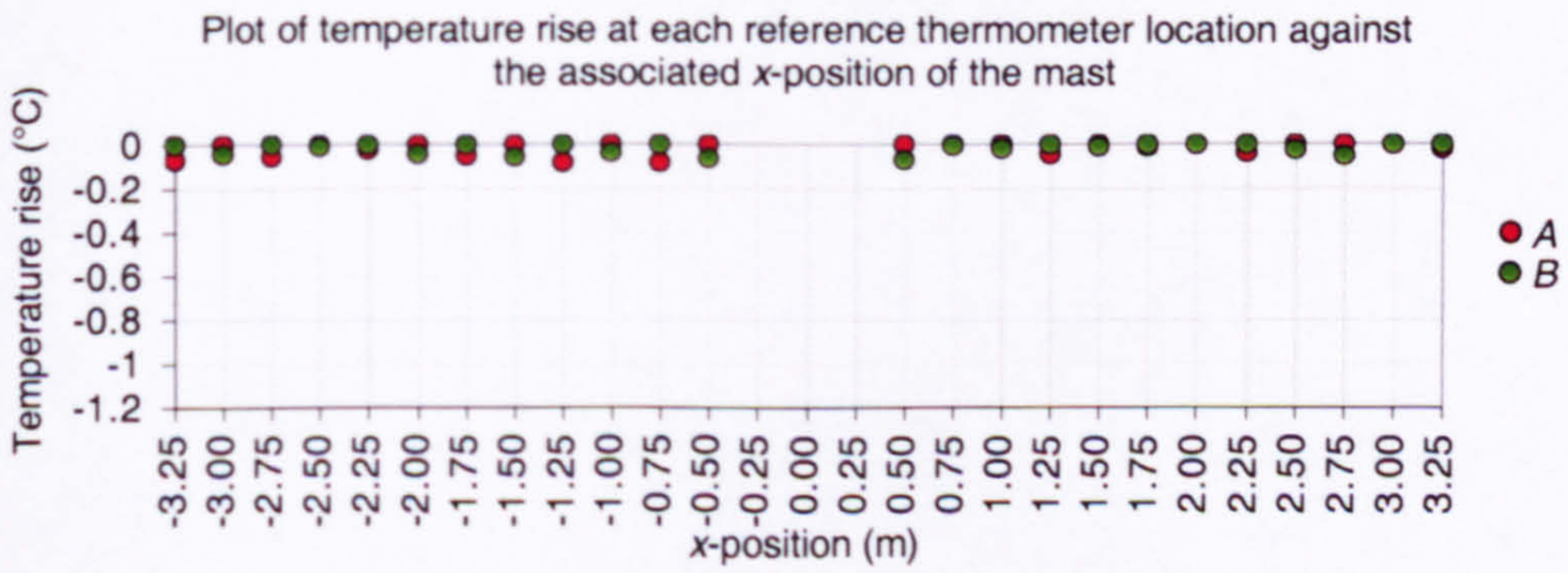

Width of opening:	0.1m
Effective area of opening:	0.061m^2
Heat source:	Boiler ring
Strength of heat source:	490.5W

Figure 24

Plot of the profile of temperature rise along the long symmetry plane (z = 0.0m) within the test enclosure and external to the space

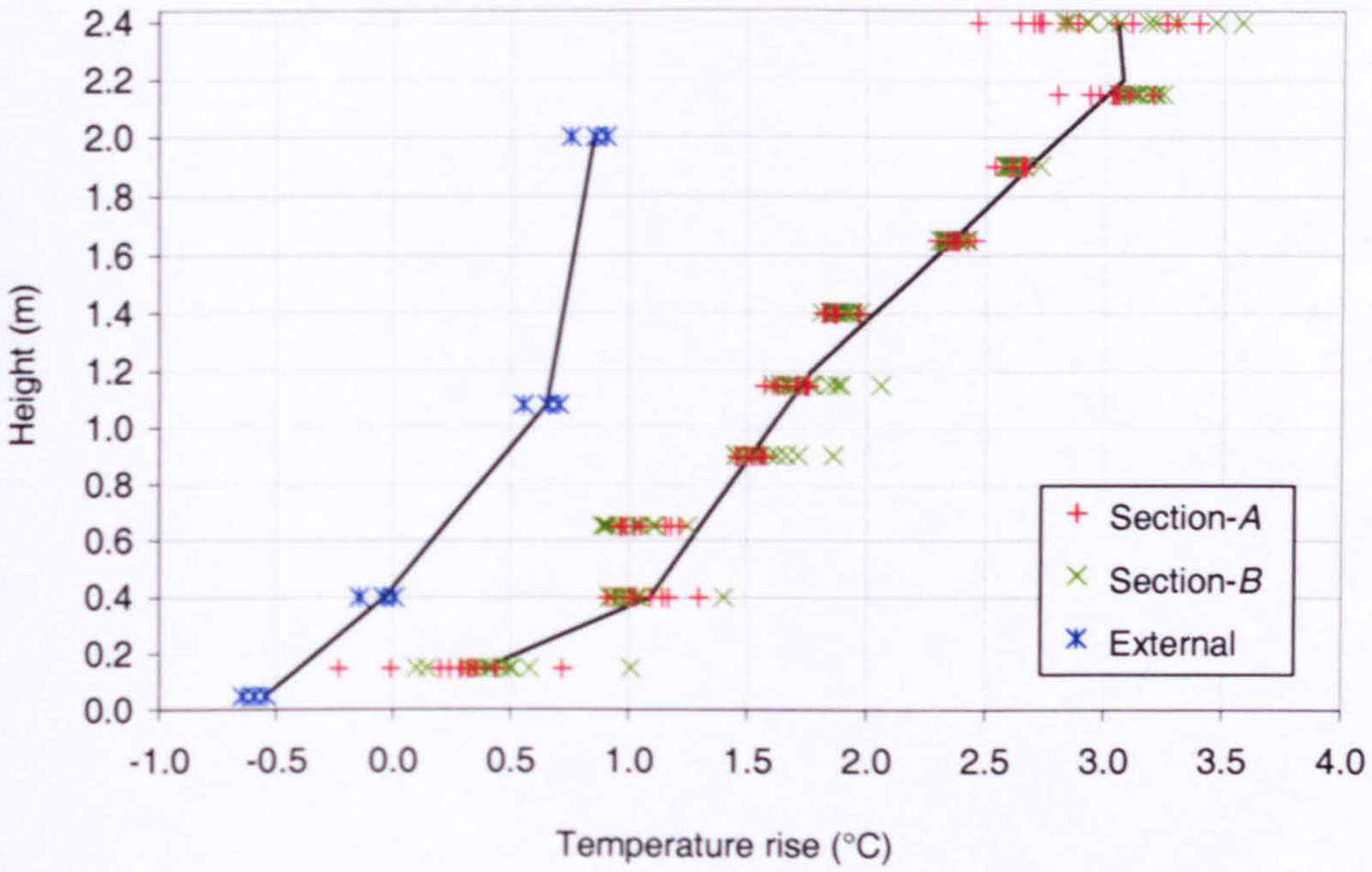

Isopleth map of temperature rise along the long symmetry plane (z = 0.0m) within the test enclosure

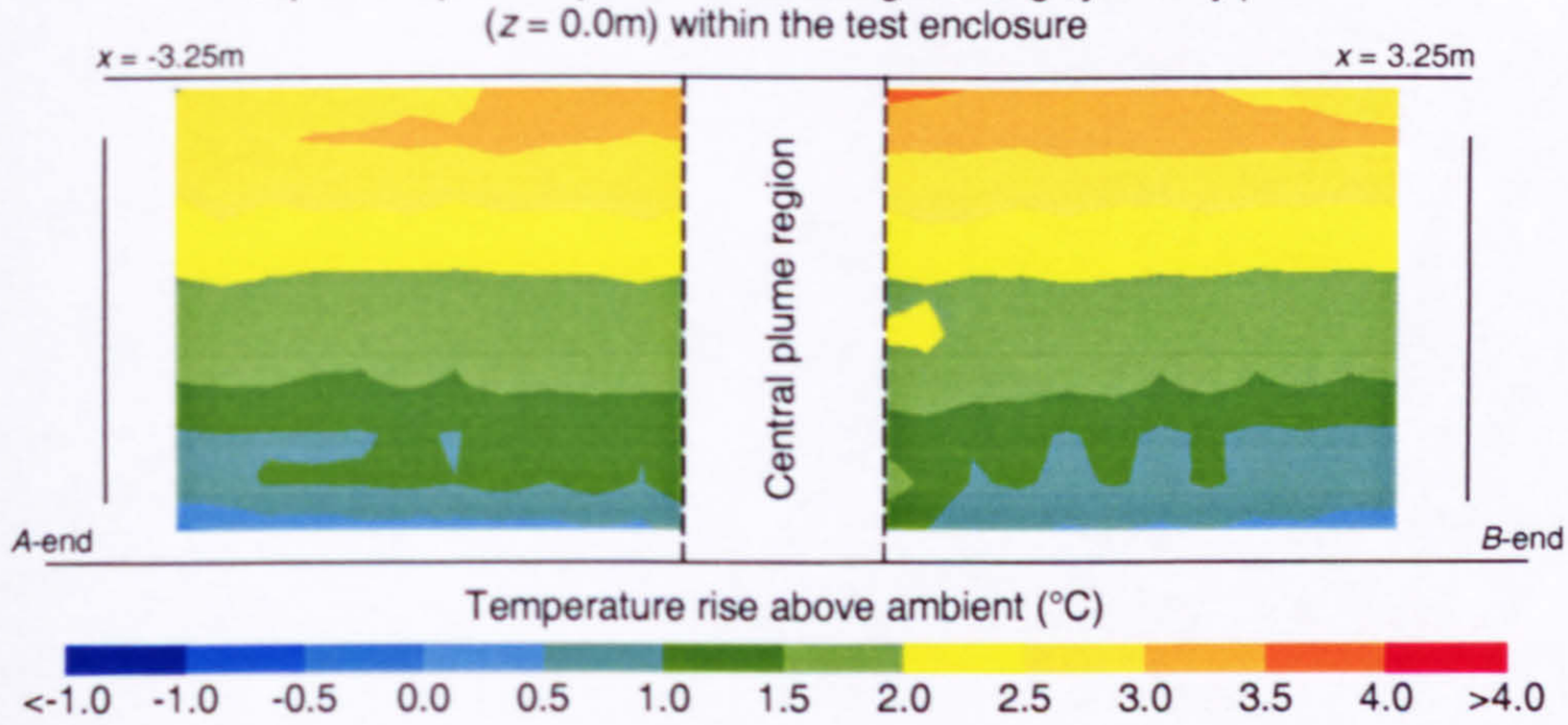

Plot of temperature rise at each reference thermometer location against the associated x-position of the mast

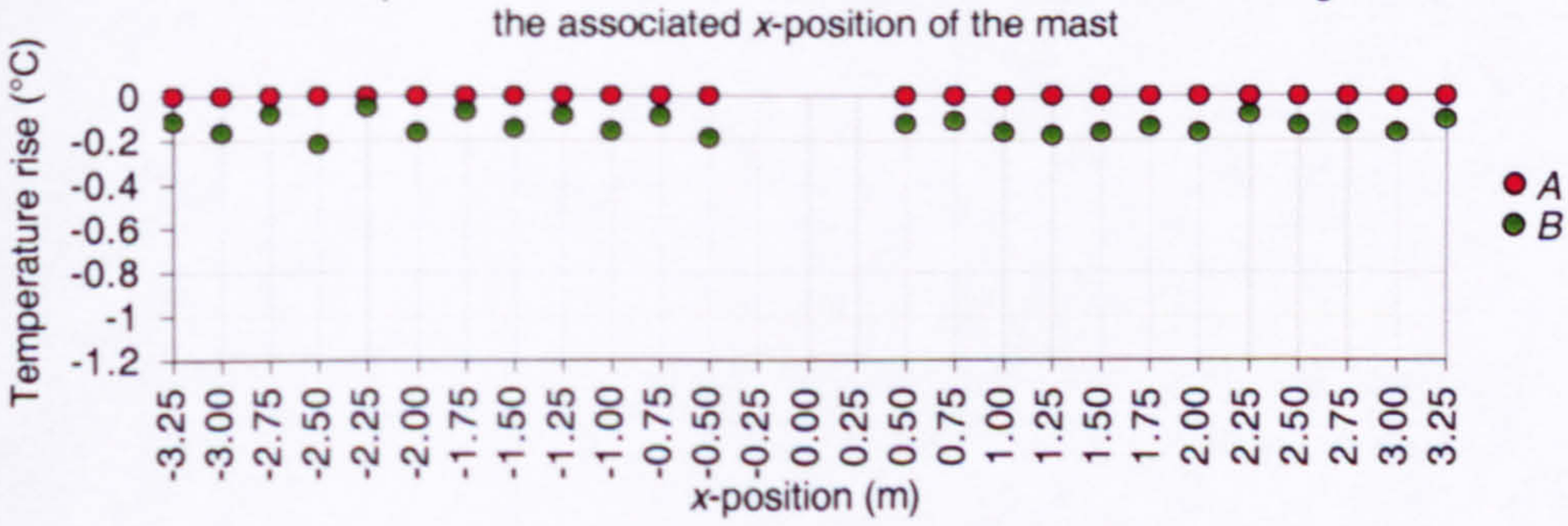

Width of opening:	0.2m
Effective area of opening:	0.122m^2
Heat source:	Boiler ring
Strength of heat source:	490.5W

Figure 25

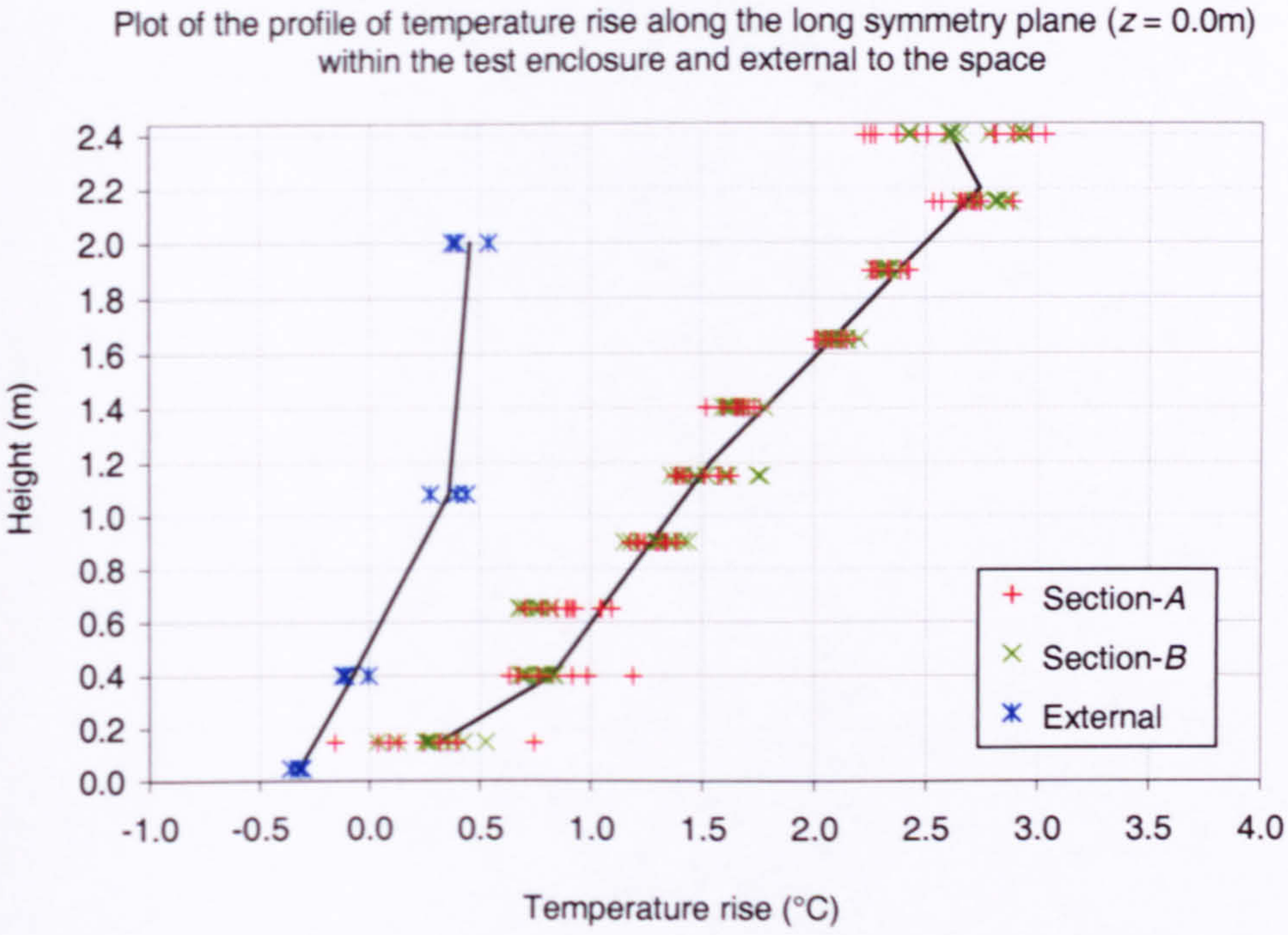

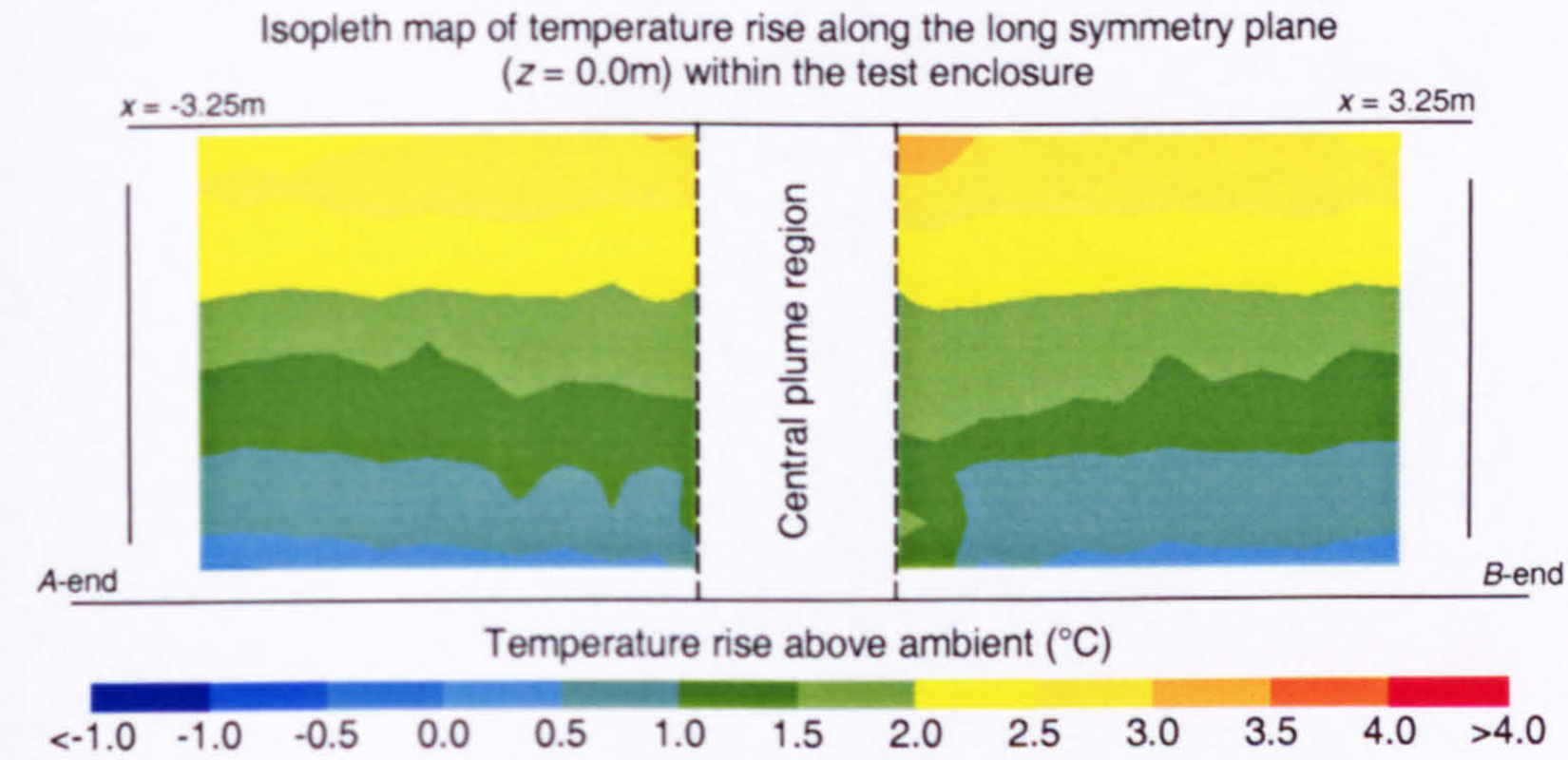

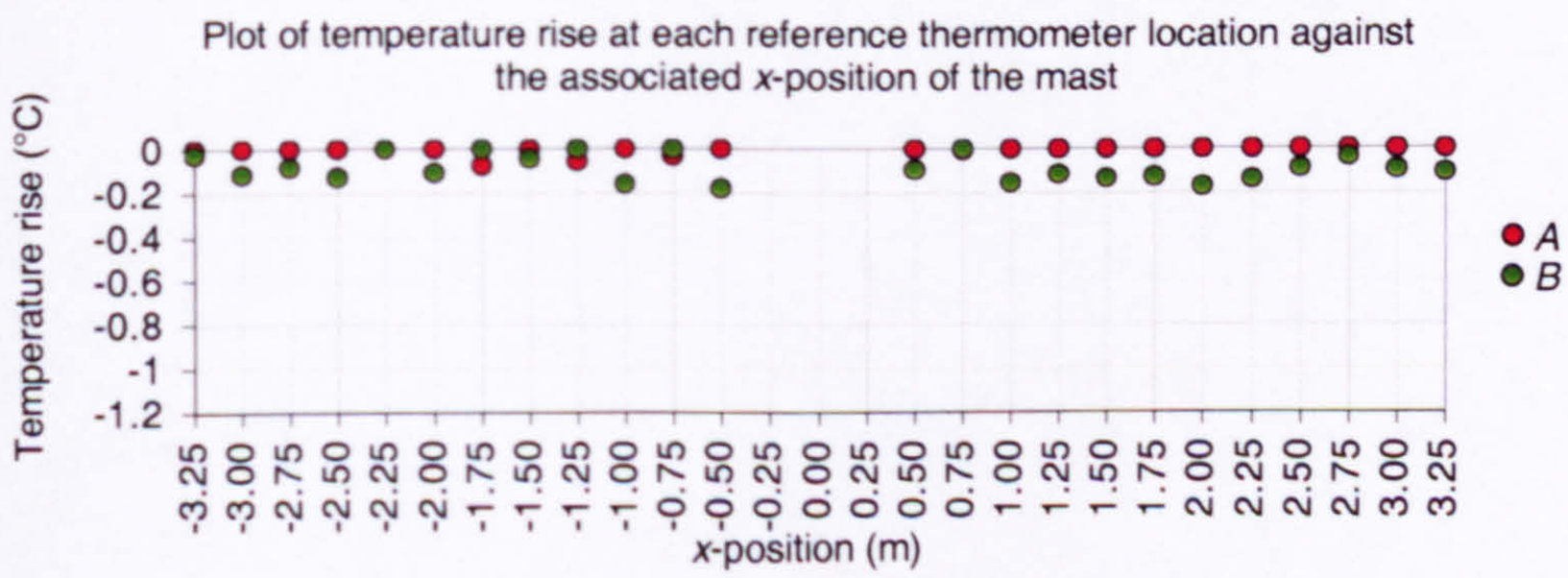

Width of opening:	0.3m
Effective area of opening:	0.183m^2
Heat source:	Boiler ring
Strength of heat source:	490.5W

Figure 26

Plot of the profile of temperature rise along the long symmetry plane (z = 0.0m) within the test enclosure and external to the space

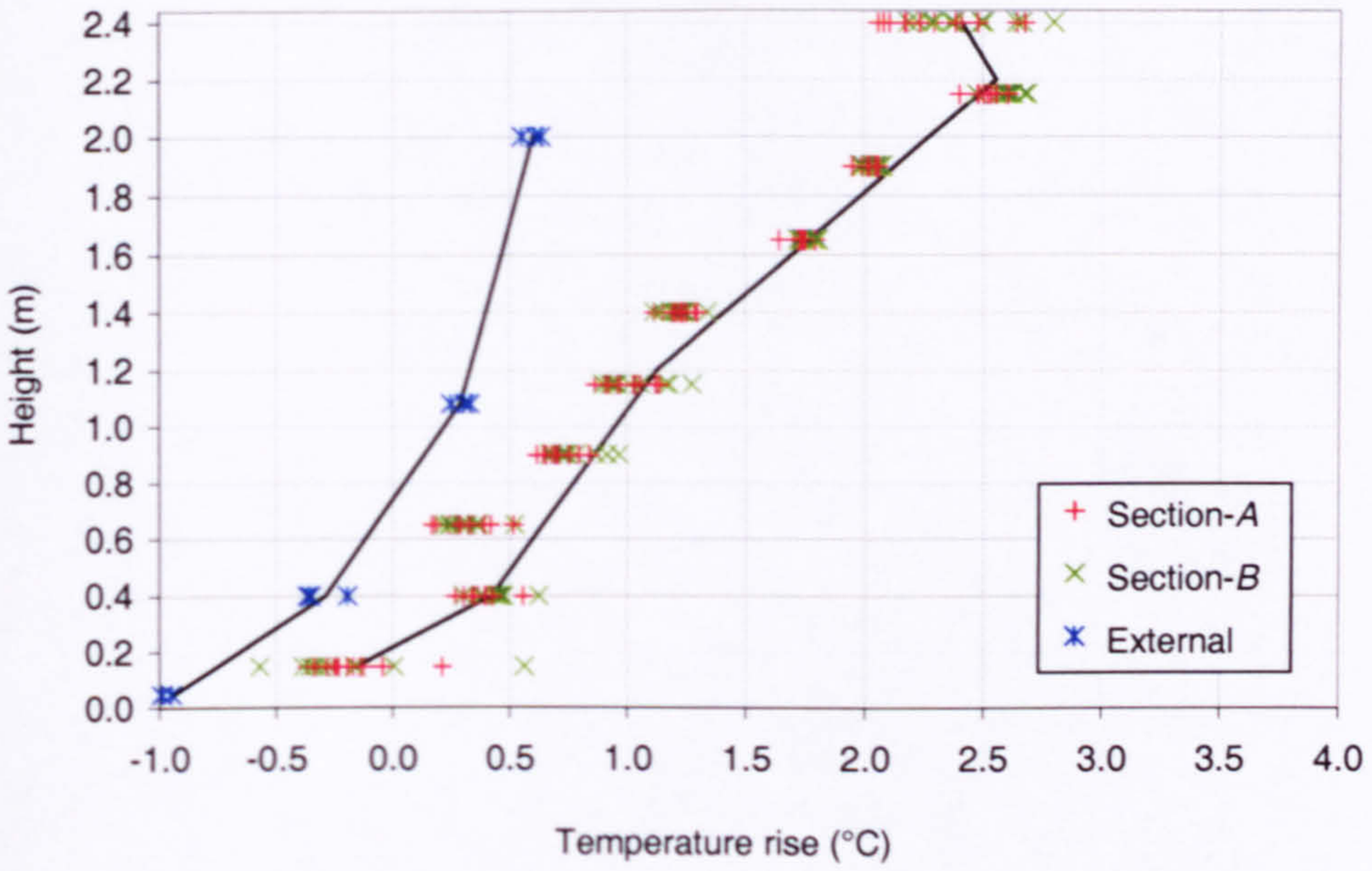

Isopleth map of temperature rise along the long symmetry plane (z = 0.0m) within the test enclosure

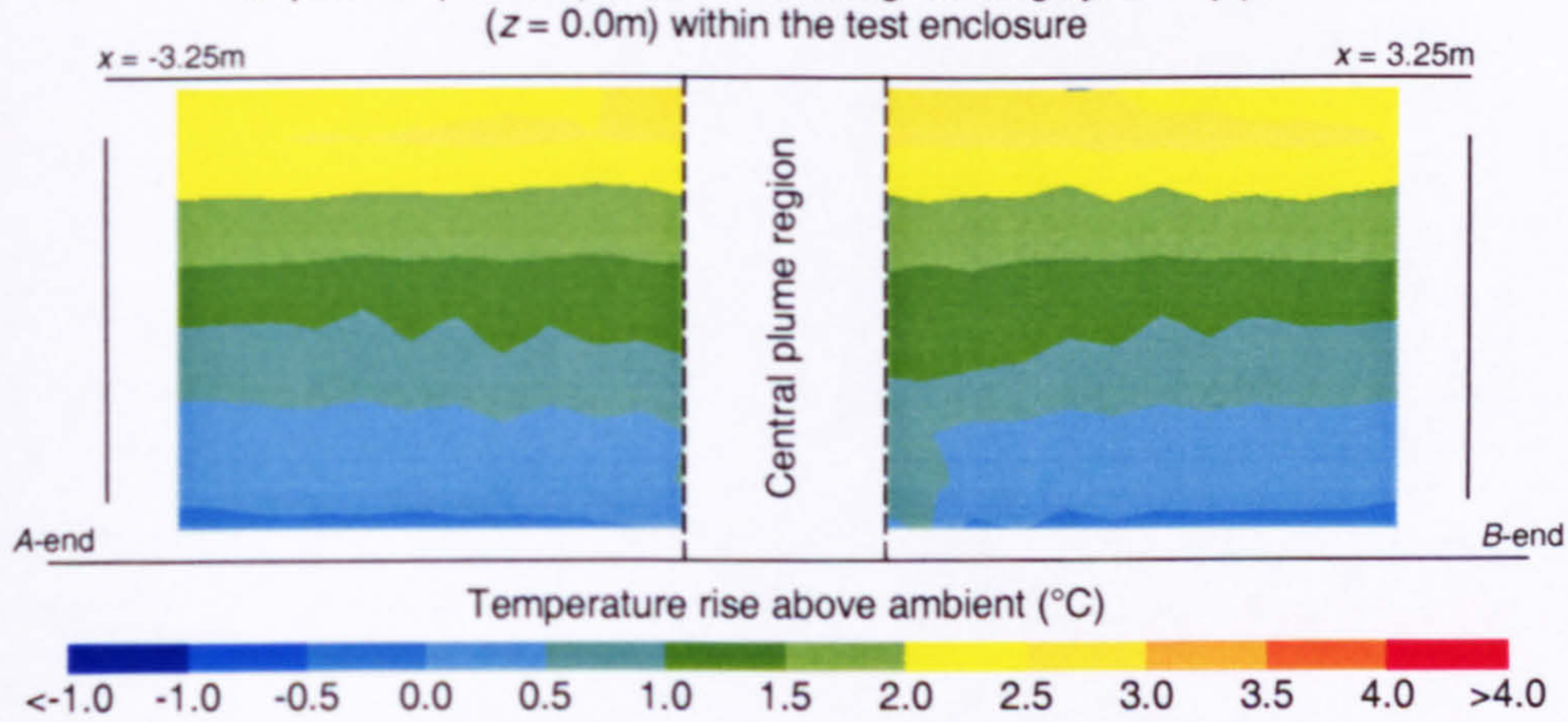

Plot of temperature rise at each reference thermometer location against the associated x-position of the mast

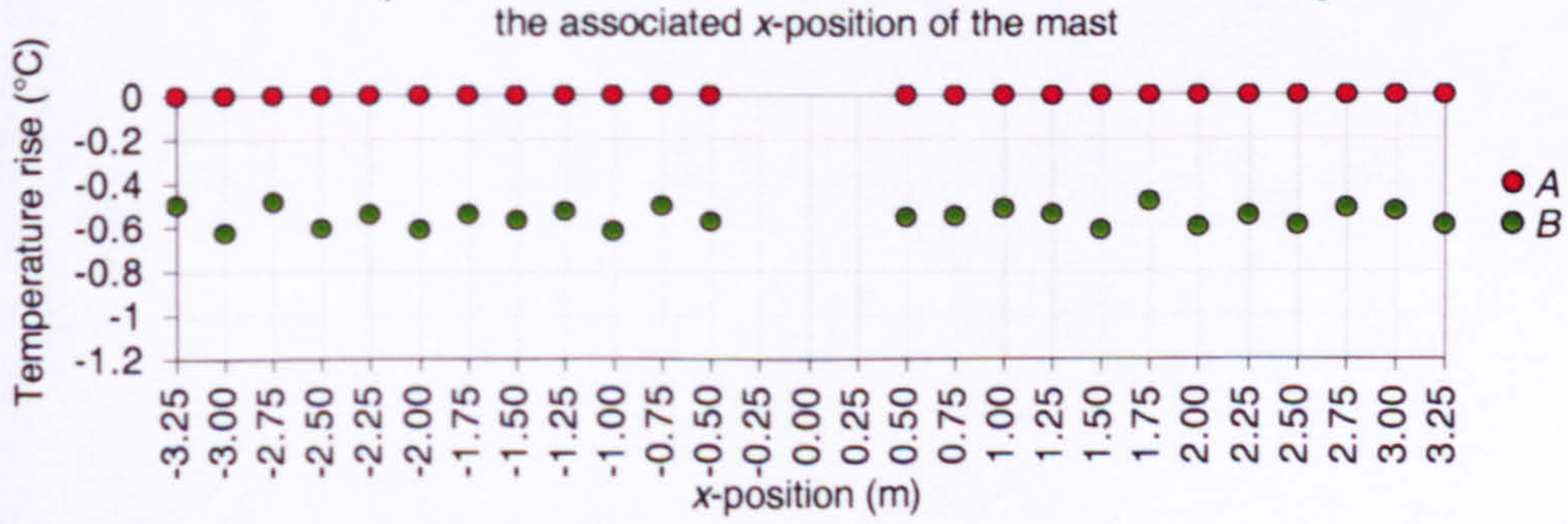

Width of opening:	0.4m
Effective area of opening:	0.244m^2
Heat source:	Boiler ring
Strength of heat source:	490.5W

Figure 27

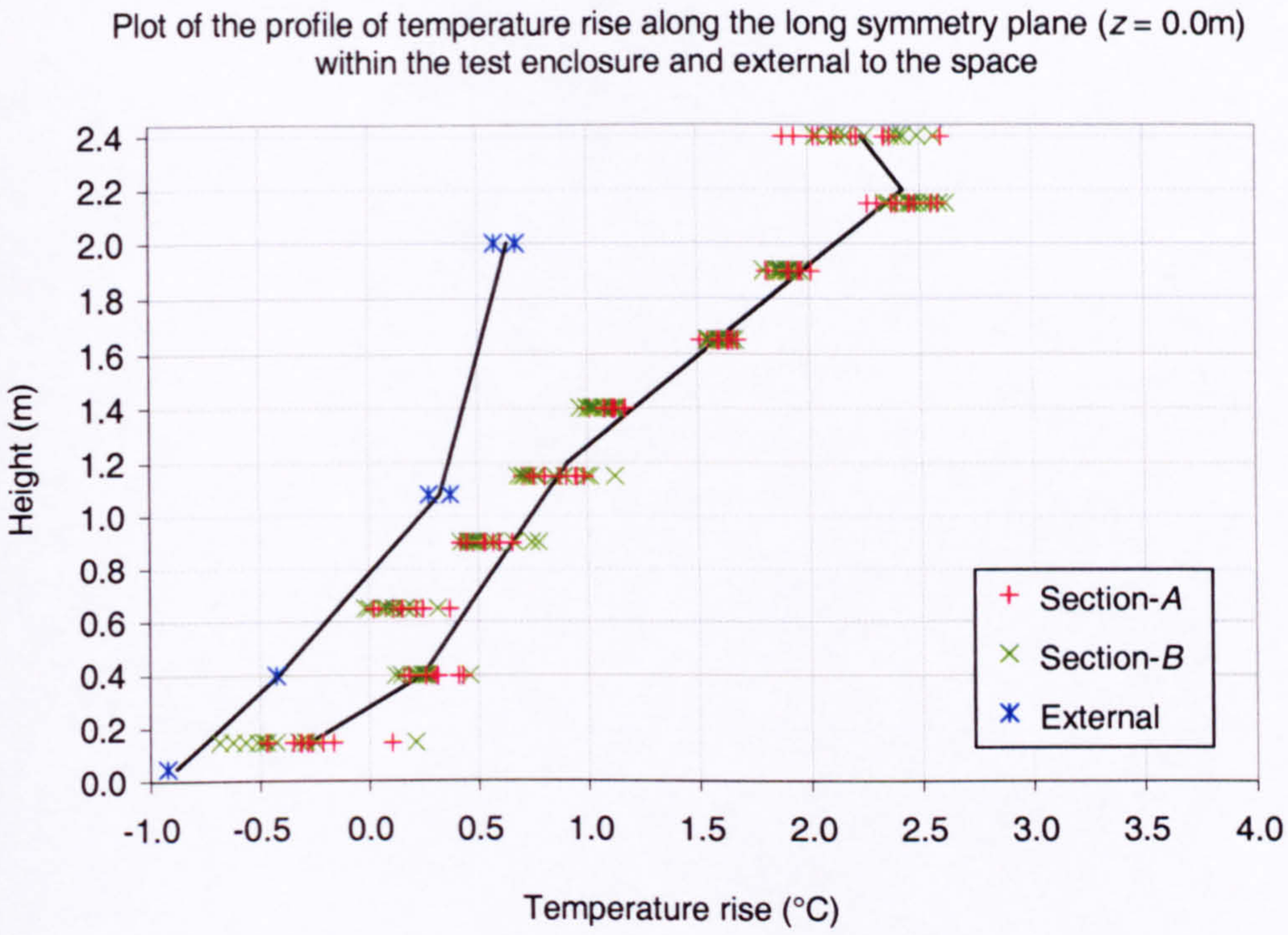

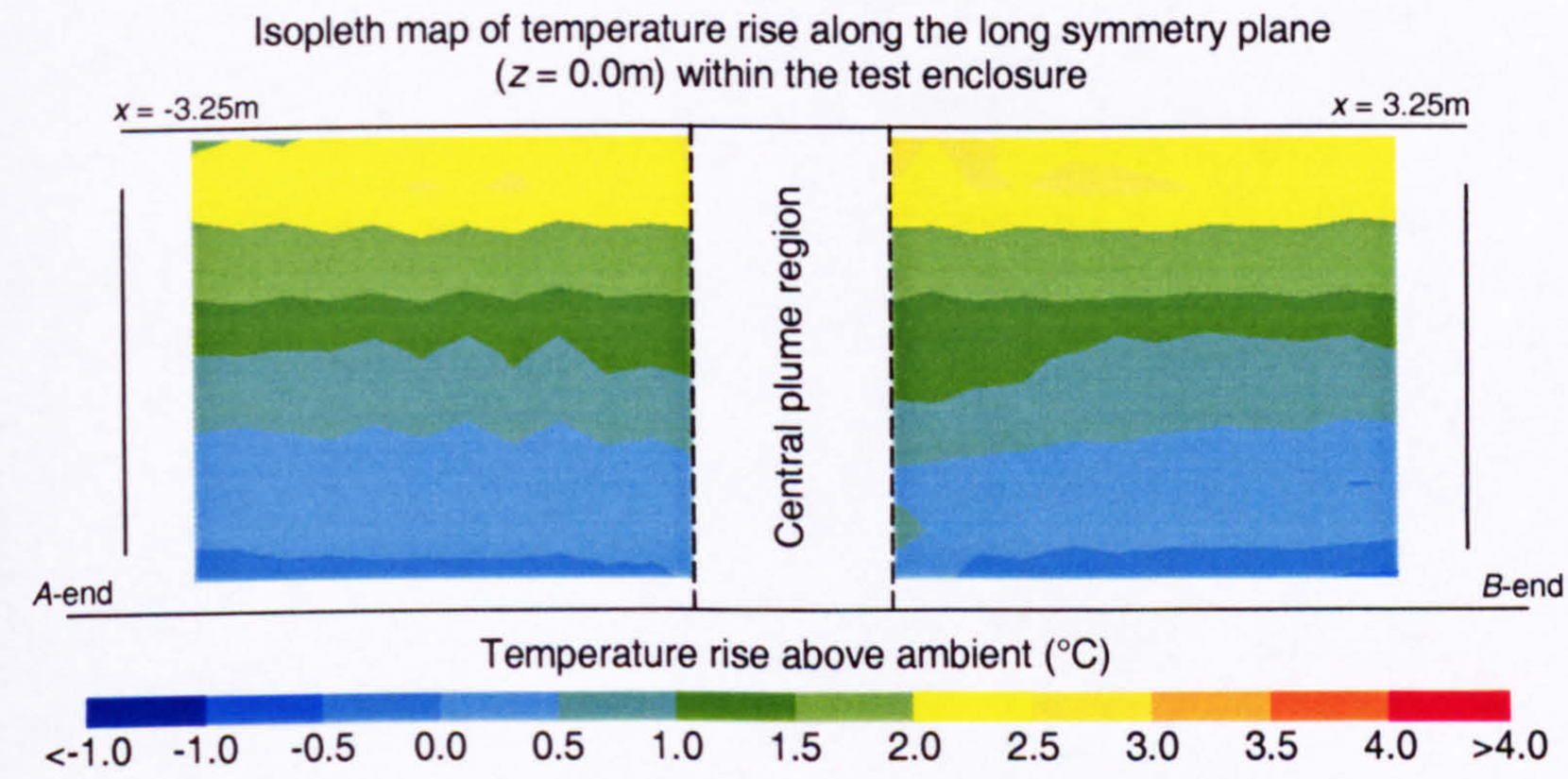

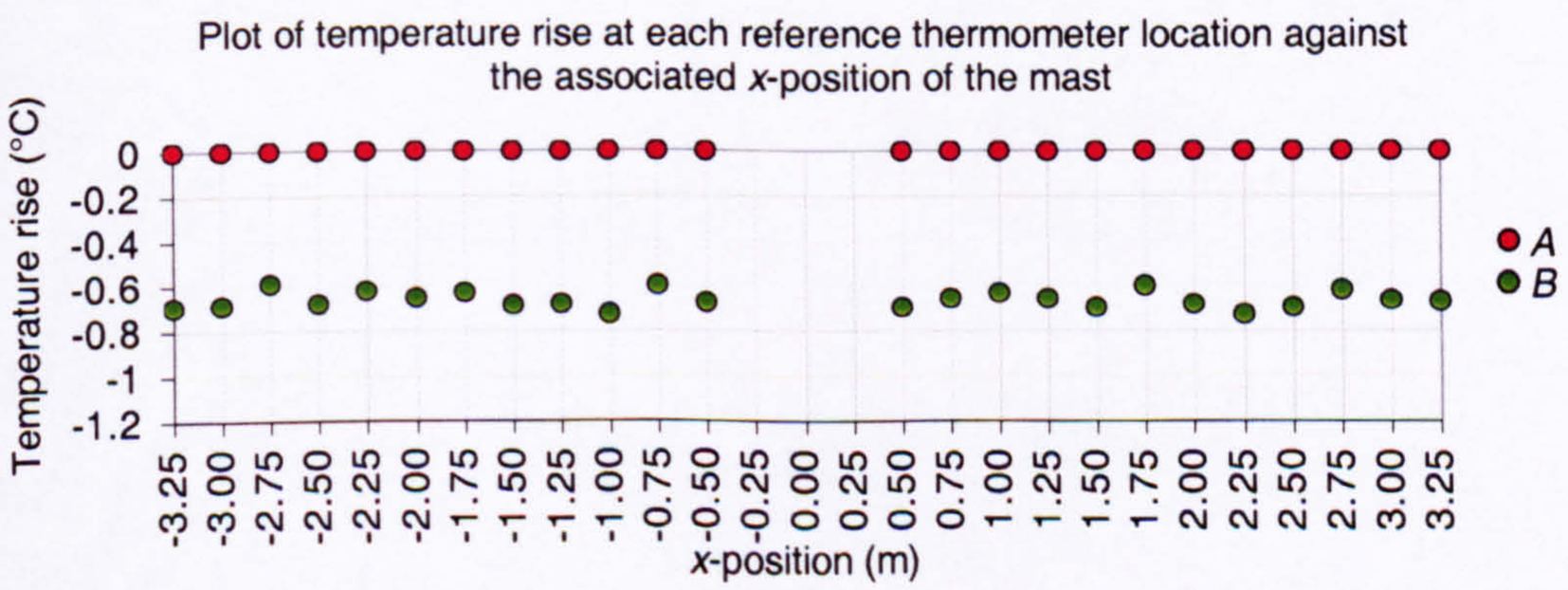

Width of opening:	0.5m
Effective area of opening:	0.305m^2
Heat source:	Boiler ring
Strength of heat source:	490.5W

Figure 28

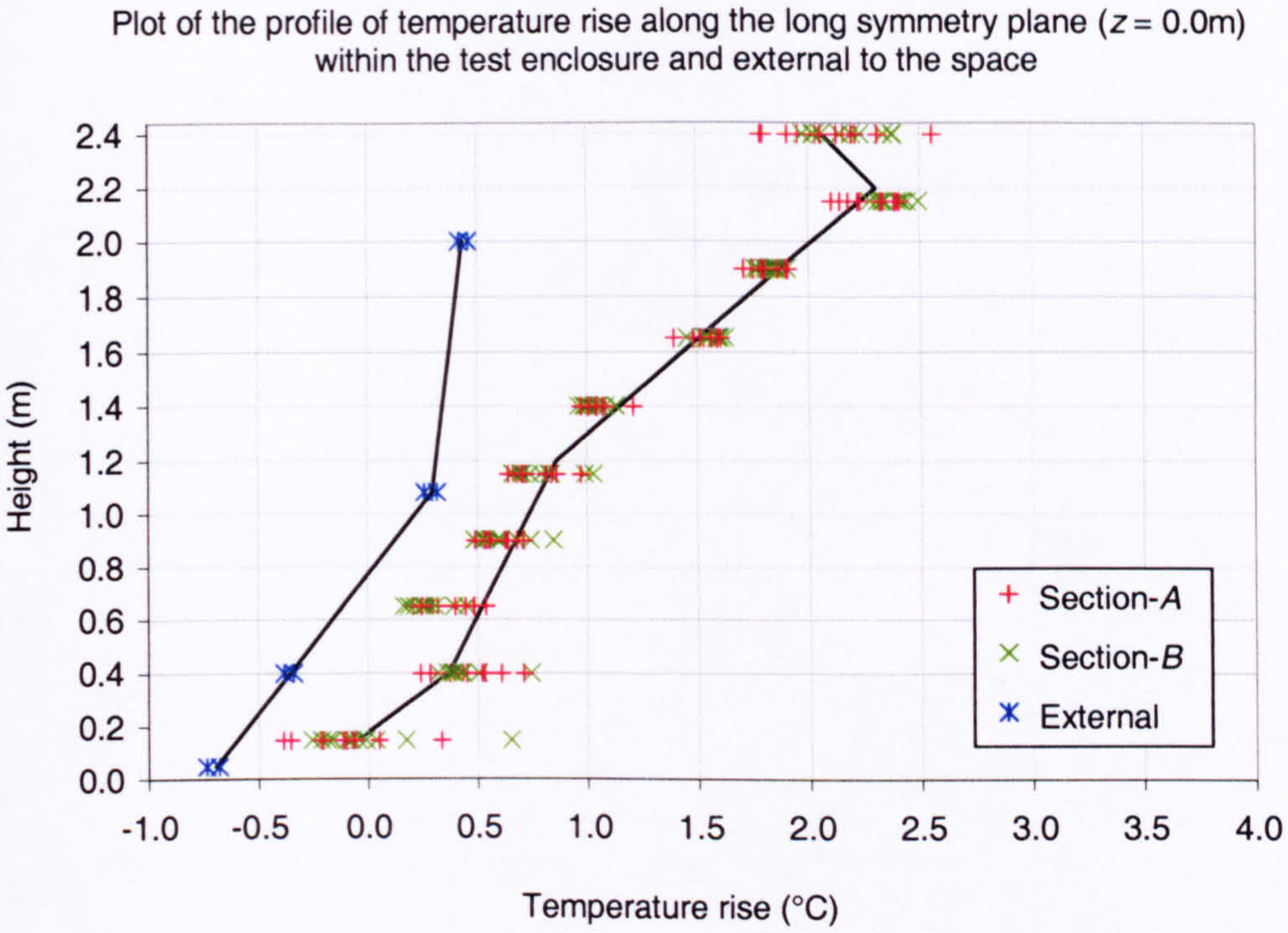

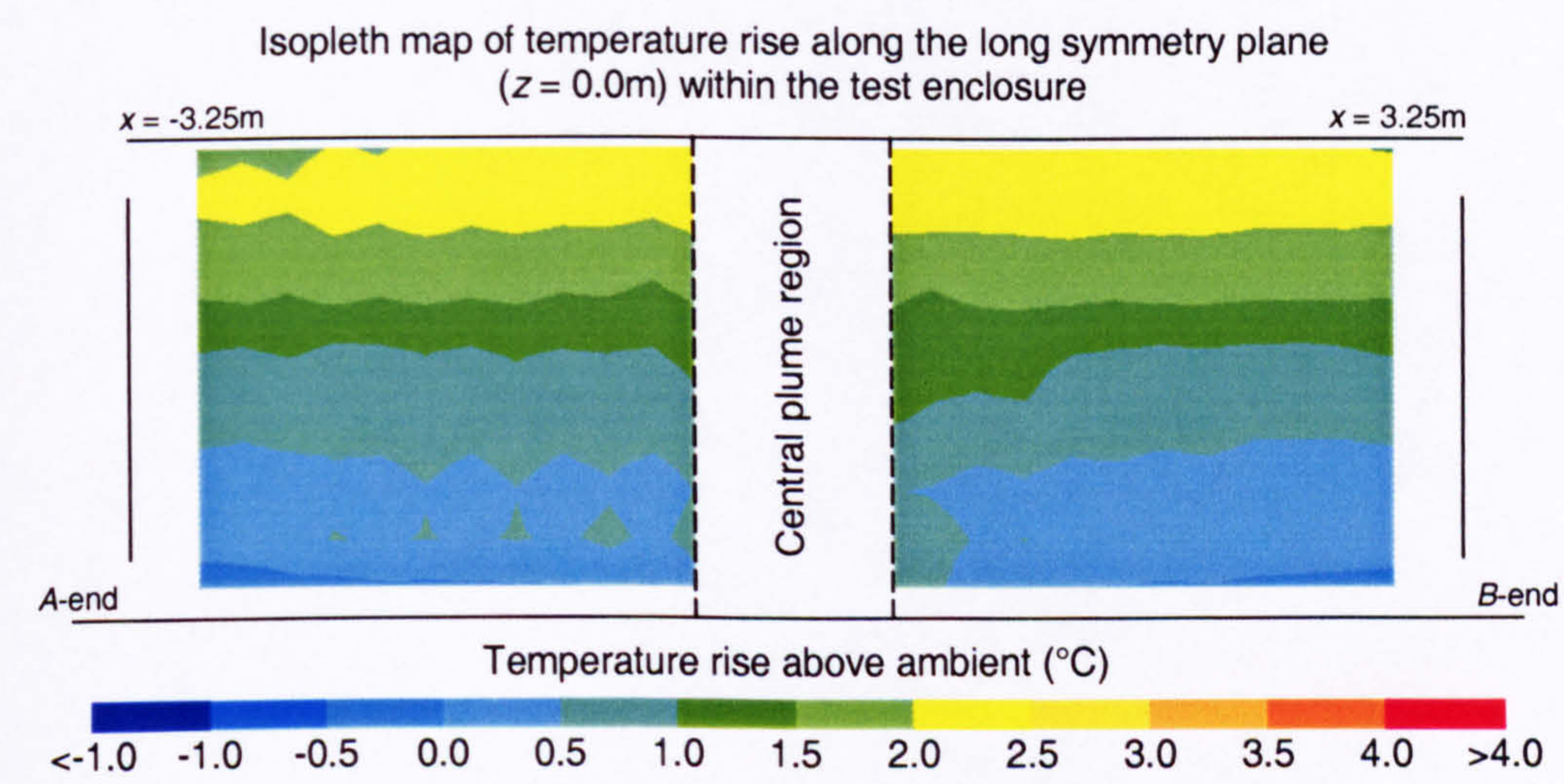

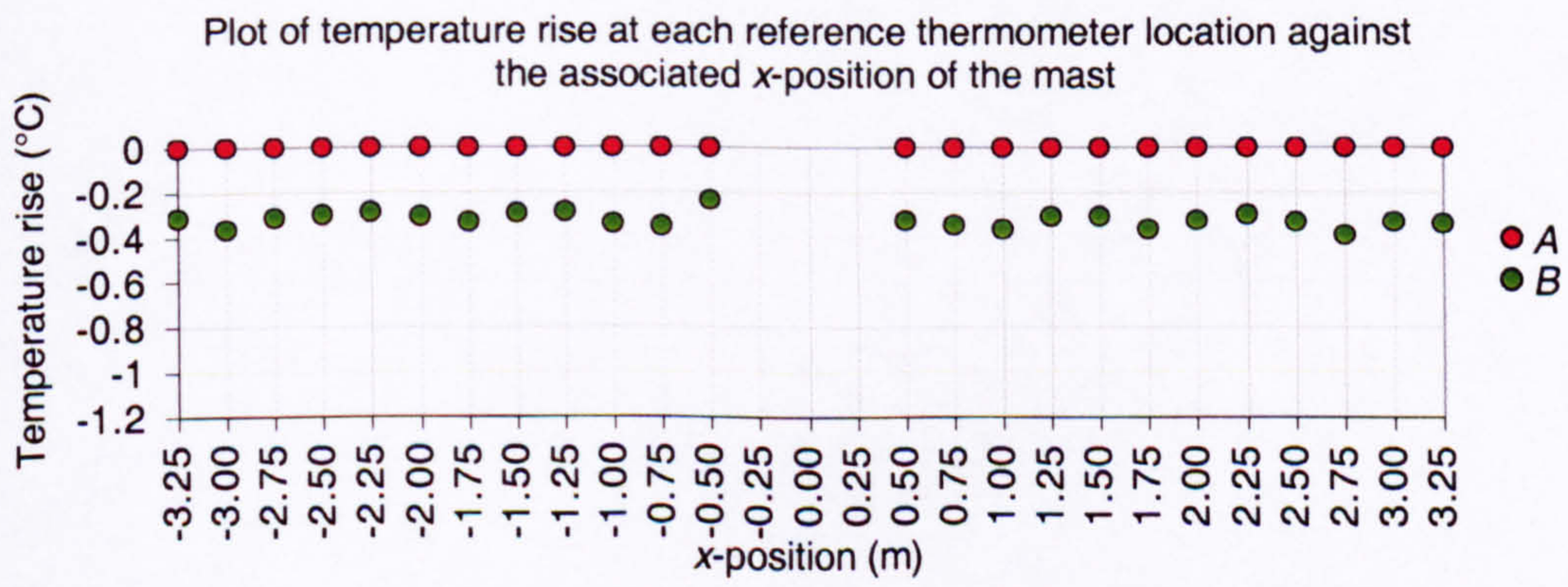

Width of opening:	0.6m
Effective area of opening:	0.366m^2
Heat source:	Boiler ring
Strength of heat source:	490.5W

Figure 29

Plot of the profile of temperature rise along the long symmetry plane (z = 0.0m) within the test enclosure and external to the space

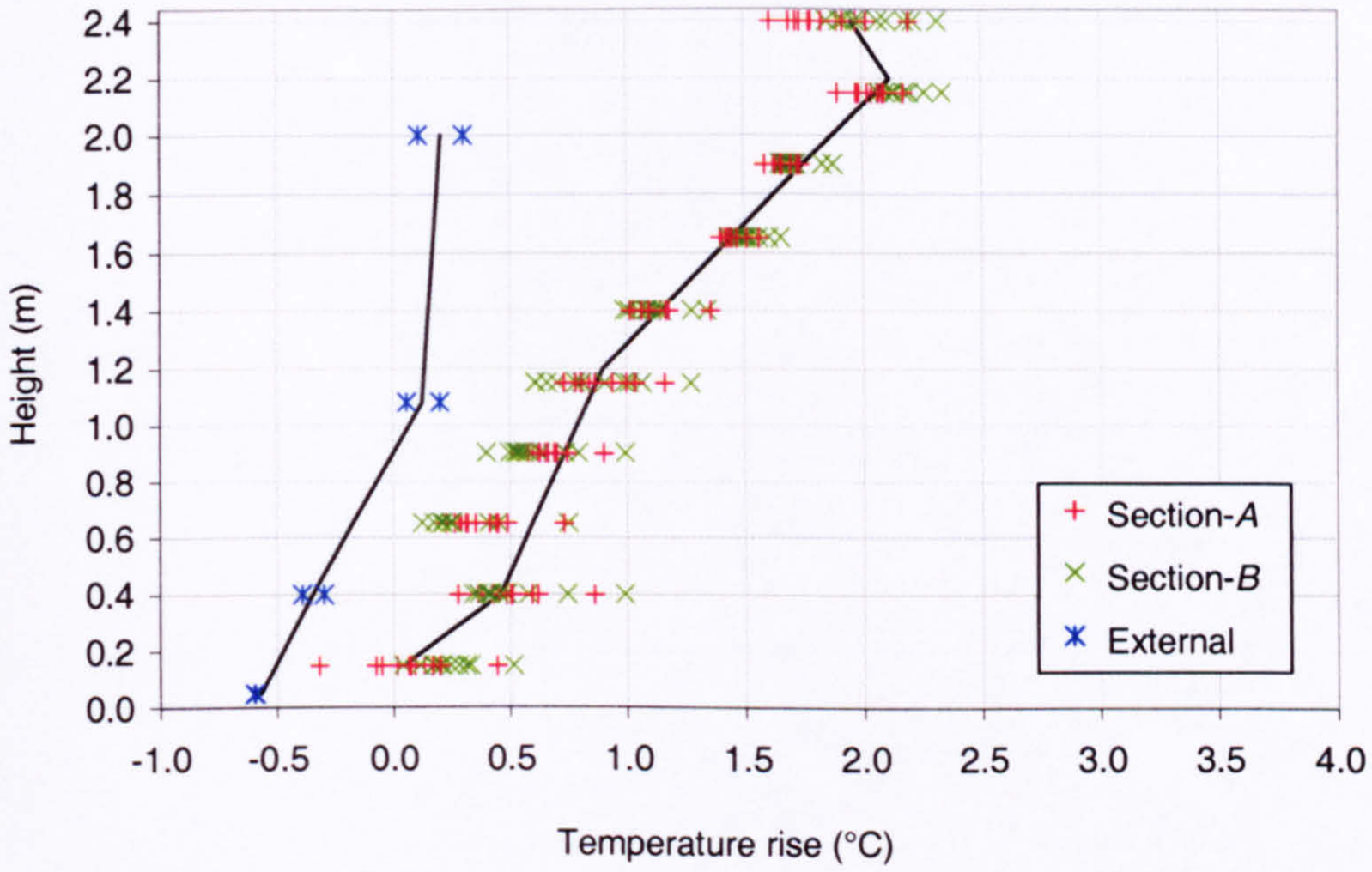

Isopleth map of temperature rise along the long symmetry plane (z = 0.0m) within the test enclosure

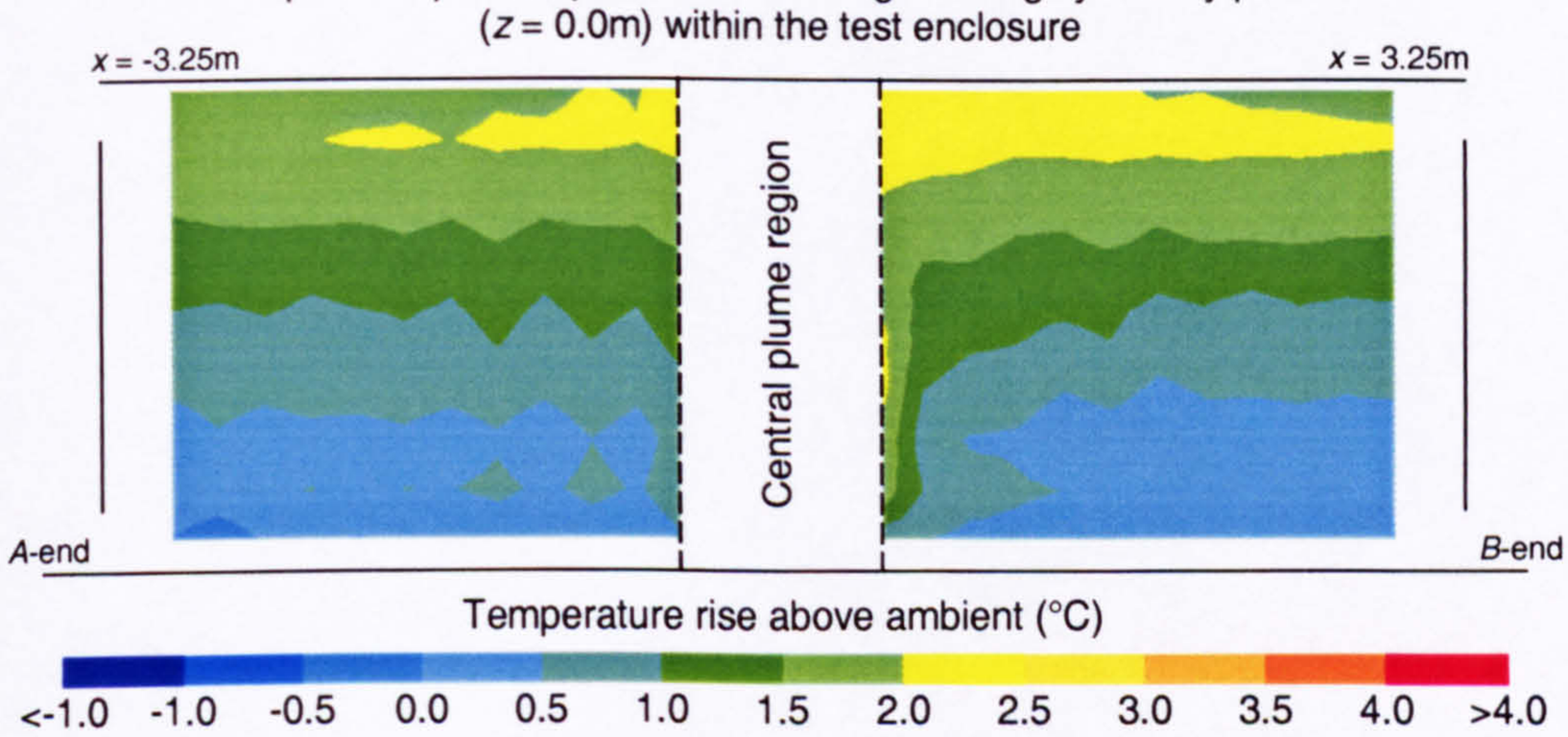

Plot of temperature rise at each reference thermometer location against the associated x-position of the mast

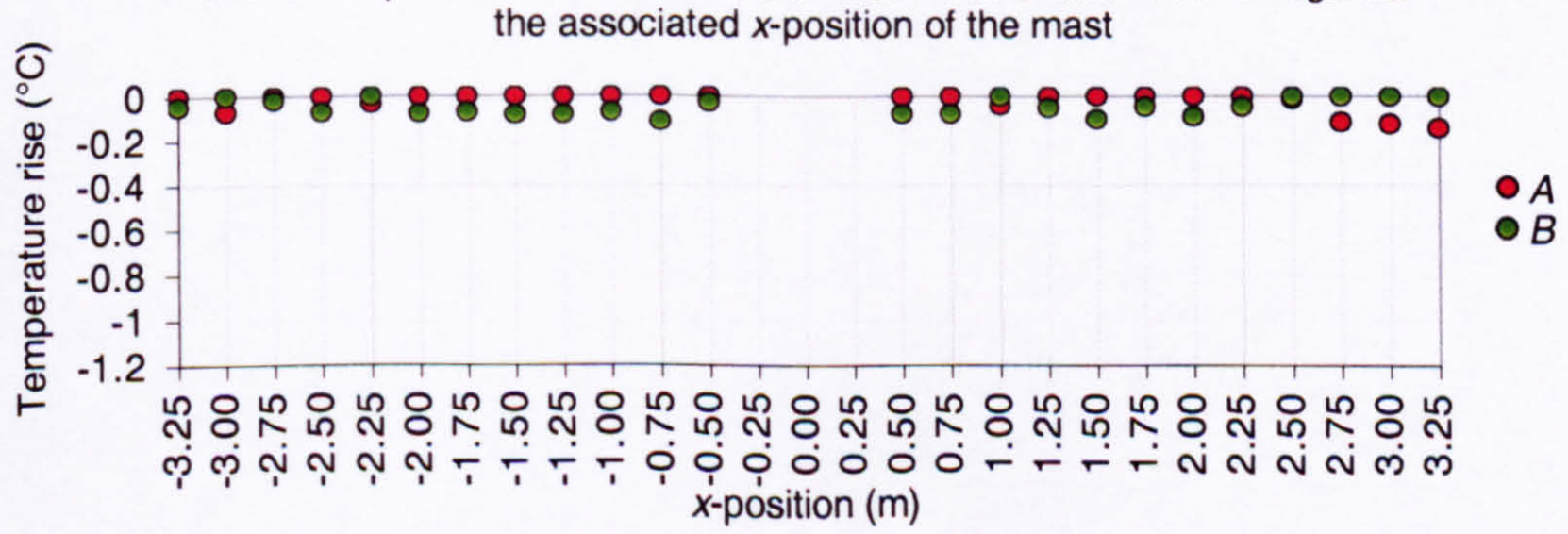

Width of opening:	0.8m
Effective area of opening:	0.488m^2
Heat source:	Boiler ring
Strength of heat source:	490.5W

Figure 30

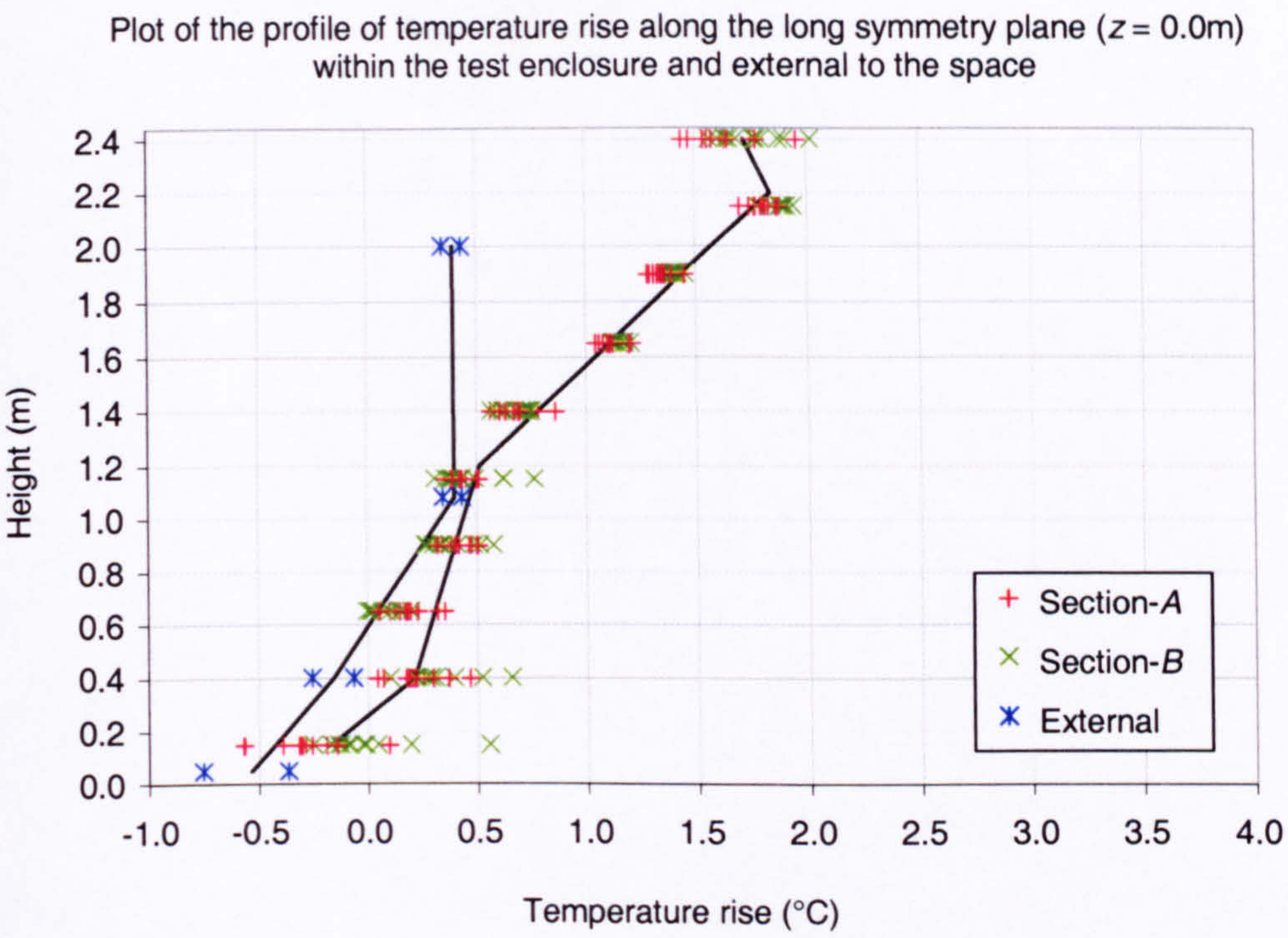

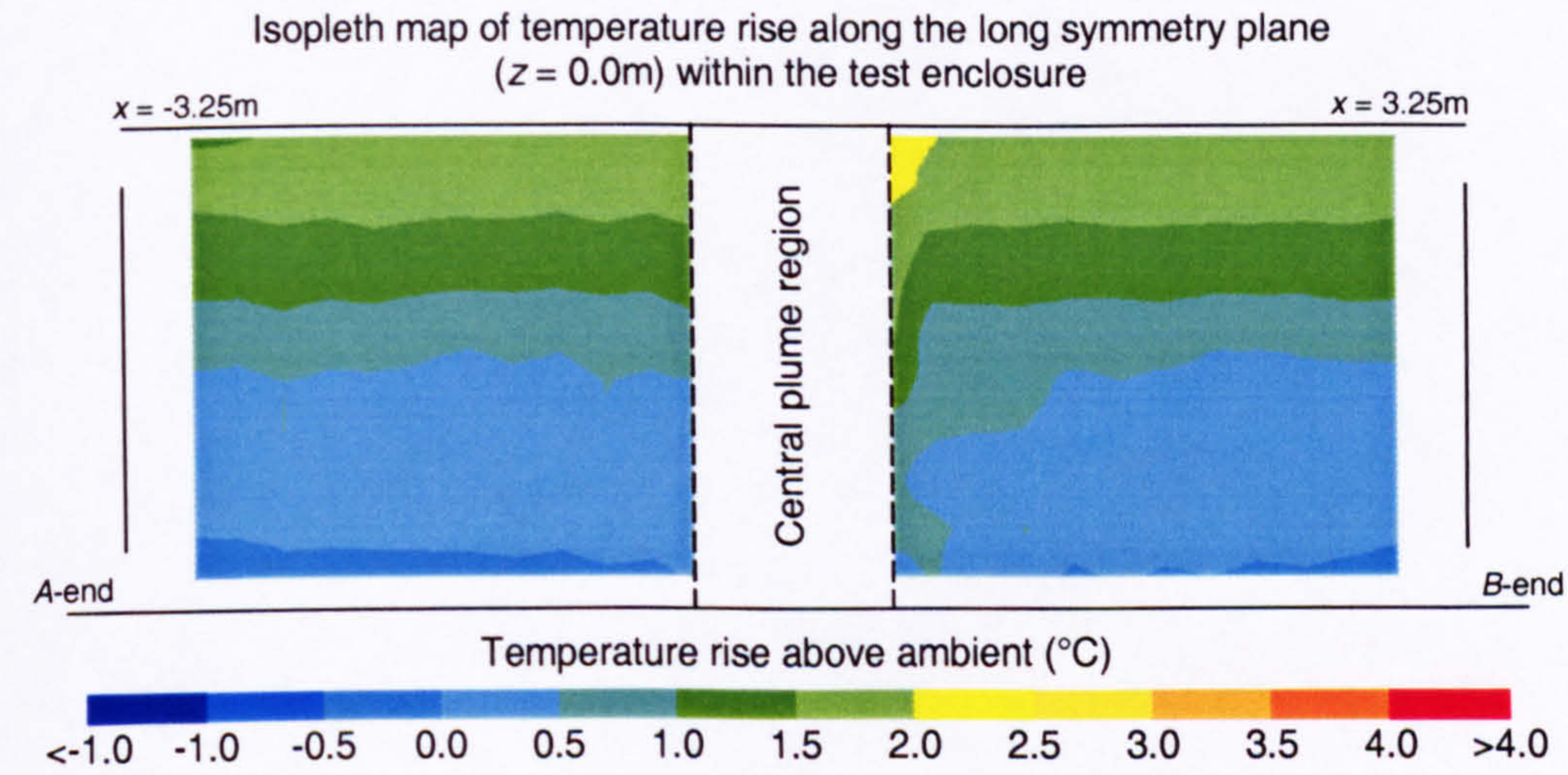

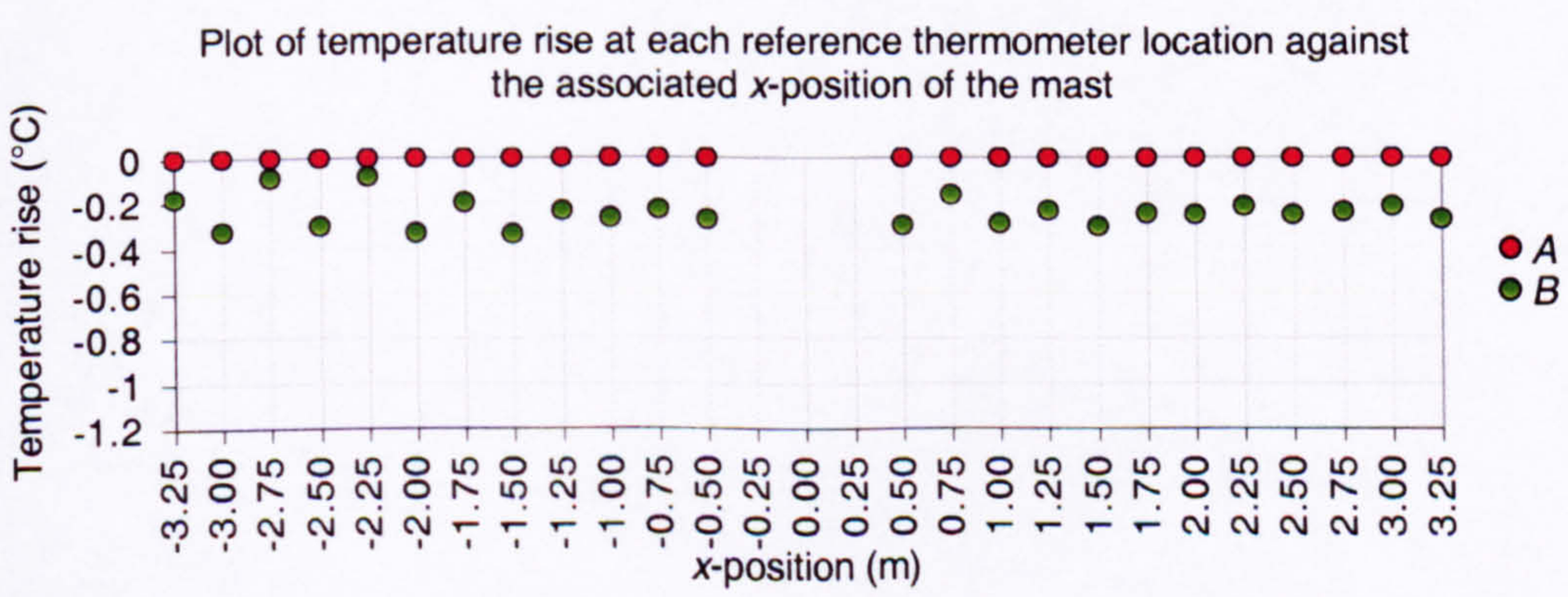

Width of opening:	1.0m
Effective area of opening:	0.610m^2
Heat source:	Boiler ring
Strength of heat source:	490.5W

Figure 31

Plot of the profile of temperature rise along the long symmetry plane (z = 0.0m) within the test enclosure and external to the space

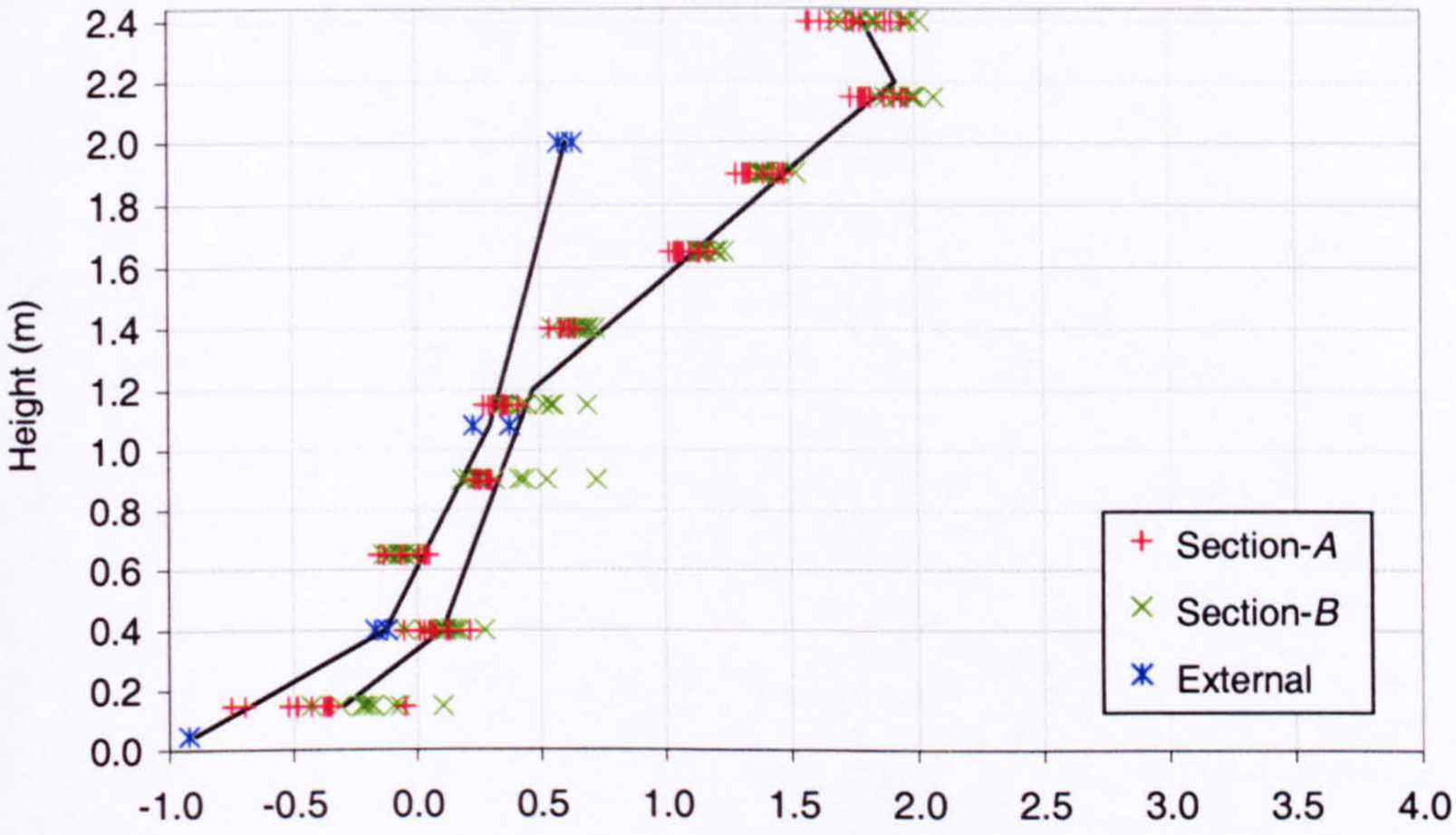

Isopleth map of temperature rise along the long symmetry plane (z = 0.0m) within the test enclosure

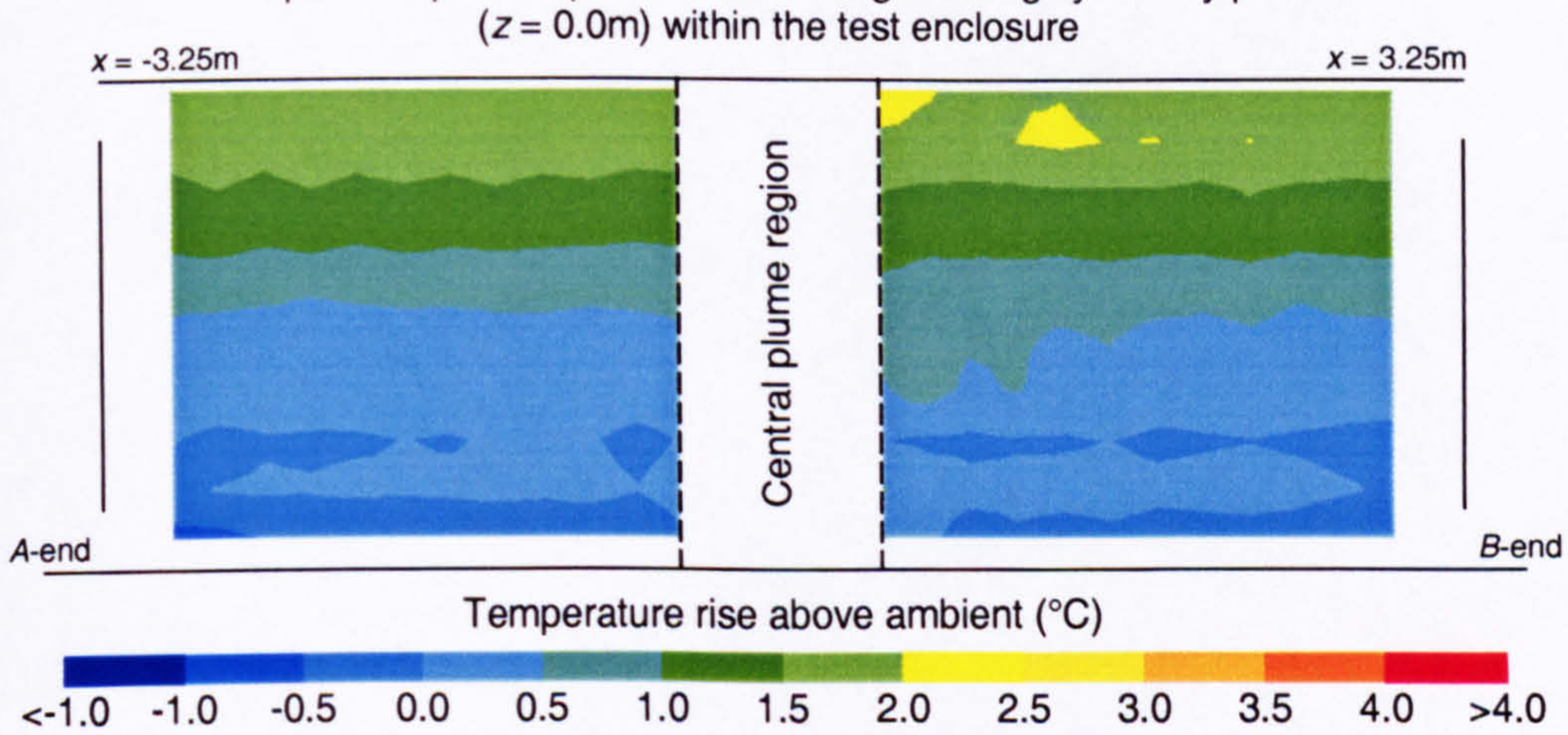

Plot of temperature rise at each reference thermometer location against the associated x-position of the mast

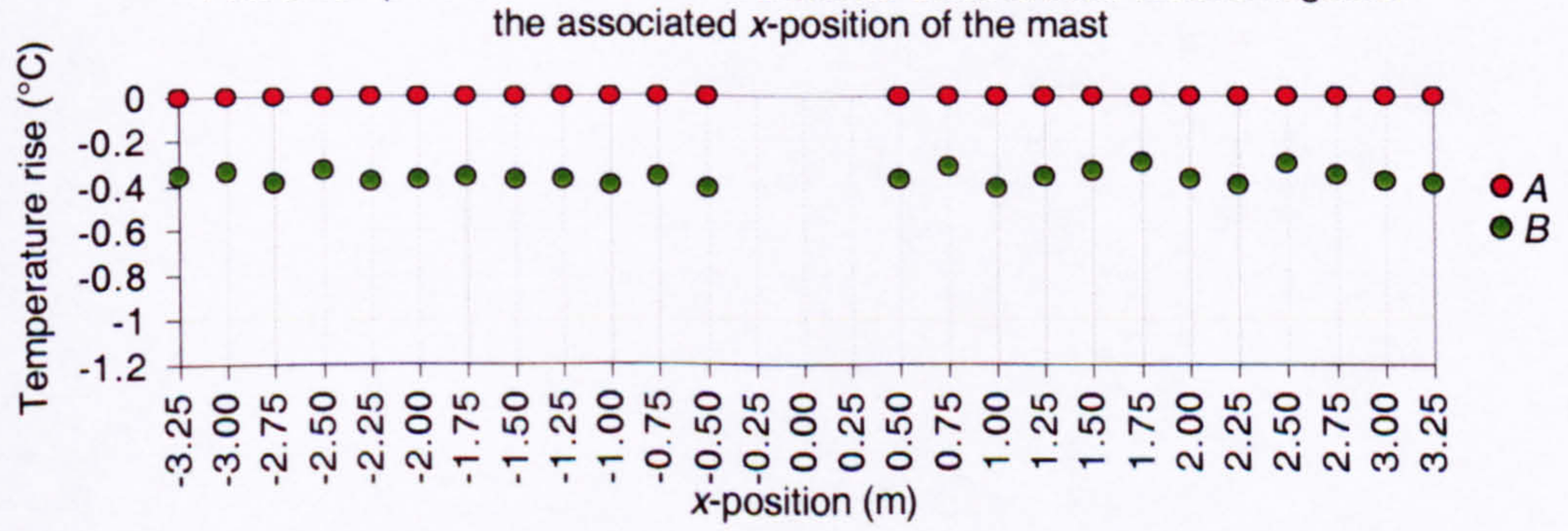

Width of opening:	1.2m
Effective area of opening:	0.732m^2
Heat source:	Boiler ring
Strength of heat source:	490.5W

Figure 32

Heat source	Strength of heat source	Width of opening	Best-fit parameters			
			y_L	y_U	m	c
Plate heater	225.0W	0.1m	0.10	0.40	1.605	0.182
			0.40	1.20	1.233	0.331
			1.20	2.20	0.358	1.206
			2.20	2.35	0.305	1.323
Plate heater	225.0W	0.2m	0.10	0.40	1.940	-0.206
			0.40	1.20	1.303	0.049
			1.20	2.20	0.388	0.964
			2.20	2.35	0.545	0.619
Plate heater	225.0W	0.3m	0.10	0.40	1.408	-0.448
			0.40	1.20	1.587	-0.520
			1.20	2.20	0.398	0.669
			2.20	2.35	0.640	0.137
Plate heater	225.0W	0.4m	0.10	0.40	1.123	-0.279
			0.40	1.20	1.677	-0.501
			1.20	2.20	0.399	0.777
			2.20	2.35	0.390	0.797
Plate heater	225.0W	0.6m	0.10	0.40	0.910	-0.503
			0.40	1.20	1.838	-0.874
			1.20	2.20	0.363	0.601
			2.20	2.35	0.240	0.872
Plate heater	225.0W	0.8m	0.10	0.40	1.608	-1.067
			0.40	1.20	2.657	-1.487
			1.20	2.20	0.383	0.787
			2.20	2.35	-0.090	1.828
Plate heater	225.0W	1.0m	0.10	0.40	0.710	-0.545
			0.40	1.20	2.162	-1.126
			1.20	2.20	0.419	0.617
			2.20	2.35	-0.195	1.968
Plate heater	225.0W	1.2m	0.10	0.40	1.320	-0.467
			0.40	1.20	1.595	-0.577
			1.20	2.20	0.485	0.533
			2.20	2.35	0.275	0.995

Table 1 - Best-fit parameters for internal temperature profiles

Heat source	Strength of heat source	Width of opening	Best-fit parameters			
			y_L	y_U	m	c
Plate heater	225.0W	2.32m	0.10	0.40	1.363	-0.745
			0.40	1.20	1.747	-0.899
			1.20	2.20	0.384	0.464
			2.20	2.35	0.180	0.913
Boiler ring	39.6W	0.4m	0.15	0.40	0.835	-0.164
			0.40	1.20	0.583	-0.063
			1.20	2.20	0.709	-0.215
			2.20	2.40	-0.060	1.477
Boiler ring	91.1W	0.4m	0.15	0.40	0.910	-0.352
			0.40	1.20	0.651	-0.249
			1.20	2.20	0.964	-0.624
			2.20	2.40	-0.120	1.761
Boiler ring	155.8W	0.4m	0.15	0.40	1.135	-0.139
			0.40	1.20	0.765	0.009
			1.20	2.20	0.964	-0.230
			2.20	2.40	-0.395	2.760
Boiler ring	368.0W	0.1m	0.15	0.40	1.610	0.411
			0.40	1.20	1.129	0.604
			1.20	2.20	0.903	0.874
			2.20	2.40	0.060	2.729
Boiler ring	368.0W	0.2m	0.15	0.40	2.008	-0.103
			0.40	1.20	1.261	0.196
			1.20	2.20	0.915	0.611
			2.20	2.40	-0.030	2.690
Boiler ring	368.0W	0.3m	0.15	0.40	2.335	-0.467
			0.40	1.20	1.248	-0.032
			1.20	2.20	1.080	0.169
			2.20	2.40	-0.225	3.040
Boiler ring	368.0W	0.4m	0.15	0.40	1.668	-0.285
			0.40	1.20	1.053	-0.039
			1.20	2.20	1.097	-0.092
			2.20	2.40	-0.270	2.915

Table 1 - Best-fit parameters for internal temperature profiles

Heat source	Strength of heat source	Width of opening	Best-fit parameters			
			y_L	y_U	m	c
Boiler ring	368.0W	0.5m	0.15	0.40	1.515	-0.345
			0.40	1.20	0.894	-0.096
			1.20	2.20	1.091	-0.333
			2.20	2.40	-0.545	3.266
Boiler ring	368.0W	0.6m	0.15	0.40	1.963	-0.578
			0.40	1.20	0.976	-0.184
			1.20	2.20	1.091	-0.321
			2.20	2.40	-0.305	2.750
Boiler ring	368.0W	0.8m	0.15	0.40	1.818	-0.636
			0.40	1.20	1.030	-0.321
			1.20	2.20	1.164	-0.482
			2.20	2.40	-0.335	2.816
Boiler ring	368.0W	1.0m	0.15	0.40	1.515	-0.709
			0.40	1.20	0.734	-0.397
			1.20	2.20	1.068	-0.798
			2.20	2.40	-0.365	2.355
Boiler ring	368.0W	1.2m	0.15	0.40	1.365	-0.776
			0.40	1.20	0.765	-0.536
			1.20	2.20	0.963	-0.774
			2.20	2.40	-0.420	2.269
Boiler ring	368.0W	1.5m	0.15	0.40	1.180	-0.848
			0.40	1.20	1.121	-0.825
			1.20	2.20	0.909	-0.570
			2.20	2.40	-0.545	2.629
Boiler ring	368.0W	1.8m	0.15	0.40	1.425	-0.709
			0.40	1.20	1.181	-0.612
			1.20	2.20	0.770	-0.118
			2.20	2.40	-0.275	2.181
Boiler ring	368.0W	2.32m	0.15	0.40	0.985	-0.485
			0.40	1.20	0.683	-0.364
			1.20	2.20	0.845	-0.559
			2.20	2.40	-0.135	1.597

Table 1 - Best-fit parameters for internal temperature profiles

Heat source	Strength of heat source	Width of opening	Best-fit parameters			
			y_L	y_U	m	c
Boiler ring	490.5W	0.1m	0.15	0.40	2.820	0.411
			0.40	1.20	0.819	1.212
			1.20	2.20	1.406	0.507
			2.20	2.40	-0.310	4.282
Boiler ring	490.5W	0.2m	0.15	0.40	2.790	-0.025
			0.40	1.20	0.849	0.752
			1.20	2.20	1.303	0.206
			2.20	2.40	-0.110	3.315
Boiler ring	490.5W	0.3m	0.15	0.40	2.048	0.011
			0.40	1.20	0.886	0.476
			1.20	2.20	1.206	0.092
			2.20	2.40	-0.650	4.175
Boiler ring	490.5W	0.4m	0.15	0.40	2.310	-0.500
			0.40	1.20	0.879	0.072
			1.20	2.20	1.431	-0.590
			2.20	2.40	-0.735	4.175
Boiler ring	490.5W	0.5m	0.15	0.40	2.065	-0.578
			0.40	1.20	0.826	-0.083
			1.20	2.20	1.516	-0.910
			2.20	2.40	-0.945	4.504
Boiler ring	490.5W	0.6m	0.15	0.40	1.663	-0.295
			0.40	1.20	0.614	0.125
			1.20	2.20	1.441	-0.868
			2.20	2.40	-1.200	4.942
Boiler ring	490.5W	0.8m	0.15	0.40	1.653	-0.200
			0.40	1.20	0.545	0.243
			1.20	2.20	1.216	-0.562
			2.20	2.40	-0.800	3.873
Boiler ring	490.5W	1.0m	0.15	0.40	1.538	-0.400
			0.40	1.20	0.375	0.065
			1.20	2.20	1.321	-1.070
			2.20	2.40	-0.580	3.112

Table 1 - Best-fit parameters for internal temperature profiles

Heat source	Strength of heat source	Width of opening	Best-fit parameters			
			y_L	y_U	m	c
Boiler ring	490.5W	1.2m	0.15	0.40	1.600	-0.535
			0.40	1.20	0.460	-0.079
			1.20	2.20	1.451	-1.268
			2.20	2.40	-0.620	3.288

Table 1 - Best-fit parameters for internal temperature profiles

Heat source	Strength of heat source	Width of opening	Best-fit parameters			
			y_L	y_U	m	c
Boiler ring	490.5W	0.1m	0.05	0.40	1.940	-0.564
			0.40	1.08	0.821	-0.116
			1.08	2.00	0.473	0.259
Boiler ring	490.5W	0.2m	0.05	0.40	1.470	-0.624
			0.40	1.08	1.016	-0.442
			1.08	2.00	0.215	0.423
Boiler ring	490.5W	0.3m	0.05	0.40	0.698	-0.352
			0.40	1.08	0.643	-0.330
			1.08	2.00	0.101	0.255
Boiler ring	490.5W	0.4m	0.05	0.40	1.863	-1.030
			0.40	1.08	0.847	-0.624
			1.08	2.00	0.335	-0.071
Boiler ring	490.5W	0.5m	0.05	0.40	1.333	-0.945
			0.40	1.08	1.087	-0.847
			1.08	2.00	0.336	-0.035
Boiler ring	490.5W	0.6m	0.05	0.40	0.983	-0.745
			0.40	1.08	0.954	-0.734
			1.08	2.00	0.152	0.133
Boiler ring	490.5W	0.8m	0.05	0.40	0.638	-0.600
			0.40	1.08	0.694	-0.623
			1.08	2.00	0.087	0.033
Boiler ring	490.5W	1.0m	0.05	0.40	1.075	-0.588
			0.40	1.08	0.821	-0.486
			1.08	2.00	-0.005	0.405
Boiler ring	490.5W	1.2m	0.05	0.40	2.198	-1.006
			0.40	1.08	0.628	-0.378
			1.08	2.00	0.333	-0.059

Table 2 - Best-fit parameters for external temperature profiles

A2 Velocity measurements from the full-scale enclosure

Table of contents

Figure	Heat source	Strength of heat source	Width of opening	Effective area of openings A*
1	Boiler ring	368.0W	0.1m	0.061m^2
2	Boiler ring	368.0W	0.2m	0.122m^2
3	Boiler ring	368.0W	0.3m	0.183m^2
4	Boiler ring	368.0W	0.4m	0.244m^2
5	Boiler ring	368.0W	0.5m	0.305m^2
6	Boiler ring	368.0W	0.6m	0.366m^2
7	Boiler ring	368.0W	0.8m	0.488m^2
8	Boiler ring	368.0W	1.0m	0.610m^2
9	Boiler ring	368.0W	1.2m	0.732m^2
10	Boiler ring	490.5W	0.1m	0.061m^2
11	Boiler ring	490.5W	0.2m	0.122m^2
12	Boiler ring	490.5W	0.3m	0.183m^2
13	Boiler ring	490.5W	0.4m	0.244m^2
14	Boiler ring	490.5W	0.5m	0.305m^2
15	Boiler ring	490.5W	0.6m	0.366m^2
16	Boiler ring	490.5W	0.8m	0.488m^2
17	Boiler ring	490.5W	1.0m	0.610m^2
18	Boiler ring	490.5W	1.2m	0.732m^2

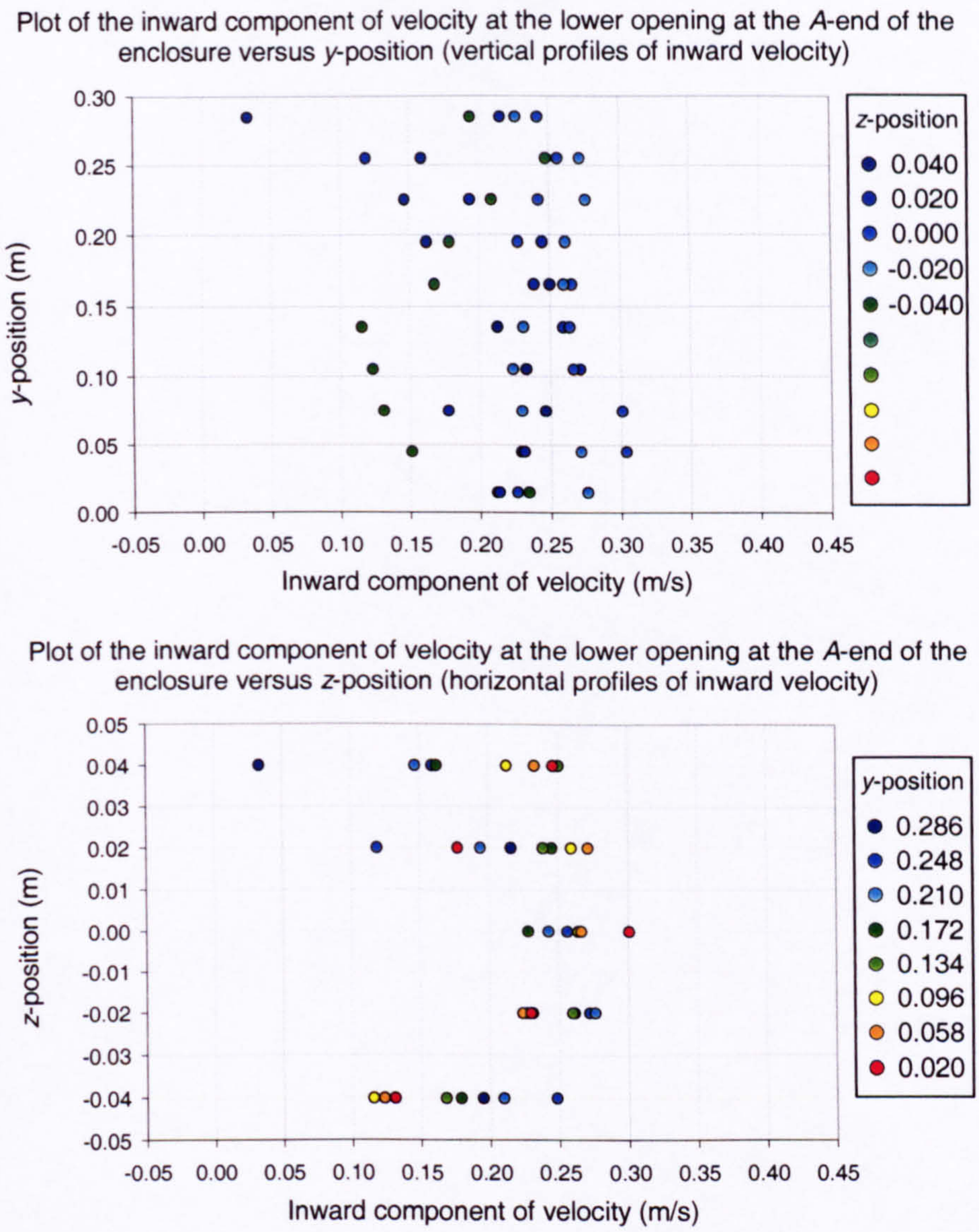

Width of opening:	0.1m
Effective area of opening:	0.061m^2
Heat source:	Boiler ring
Strength of heat source:	368.0W

Figure 1

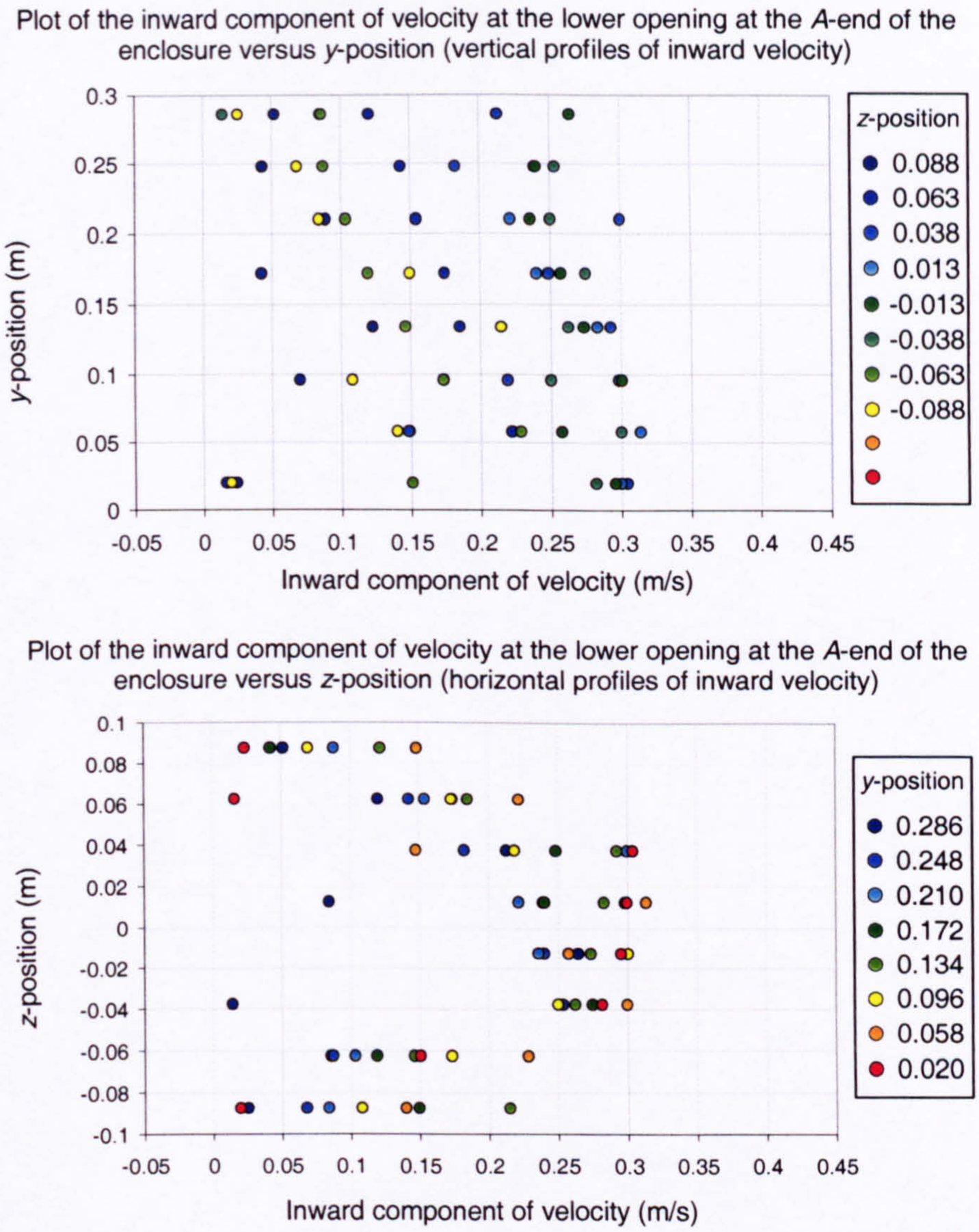

Width of opening:	0.2m
Effective area of opening:	0.122m^2
Heat source:	Boiler ring
Strength of heat source:	368.0W

Figure 2

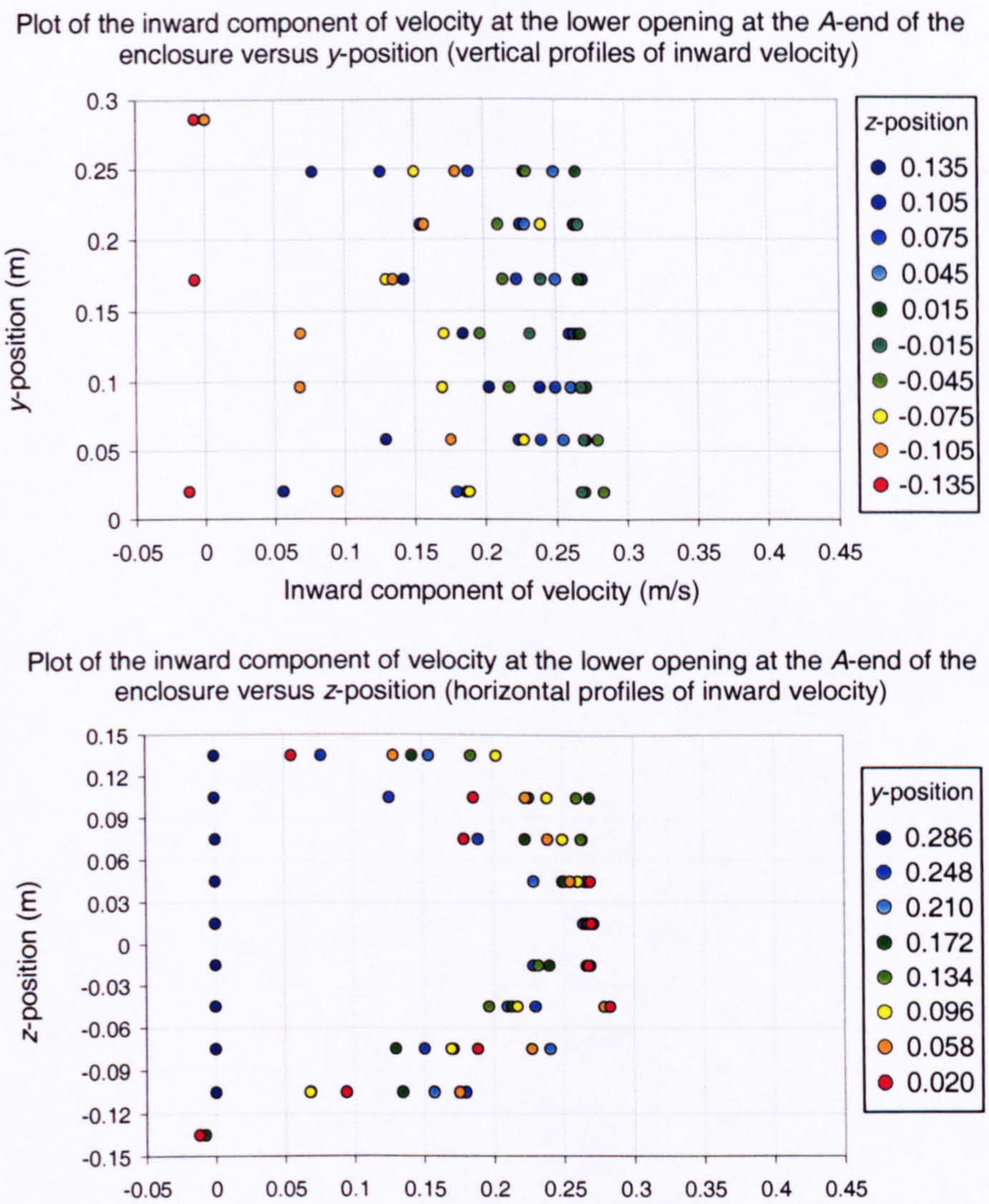

Width of opening:	0.3m
Effective area of opening:	0.183m^2
Heat source:	Boiler ring
Strength of heat source:	368.0W

Figure 3

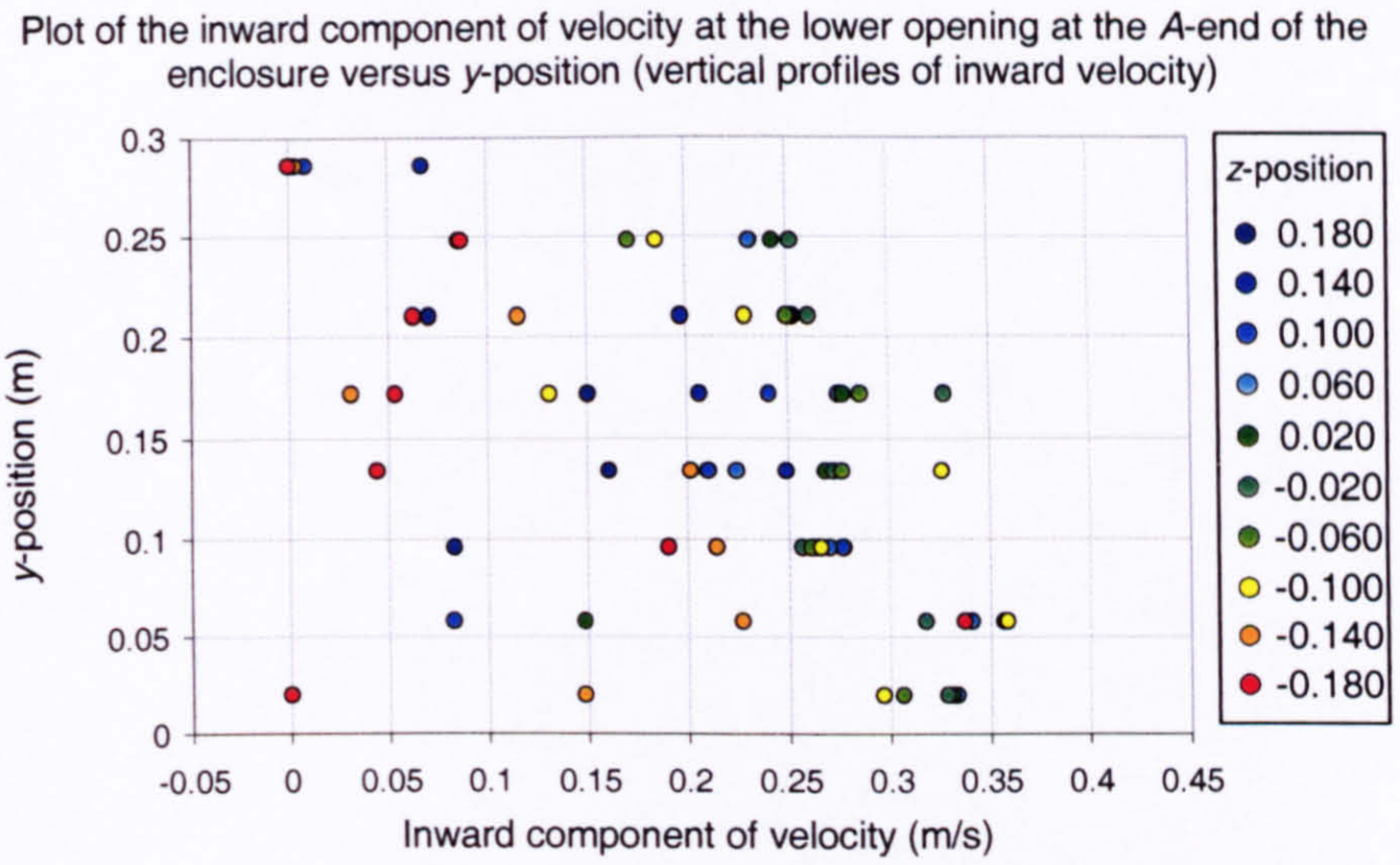

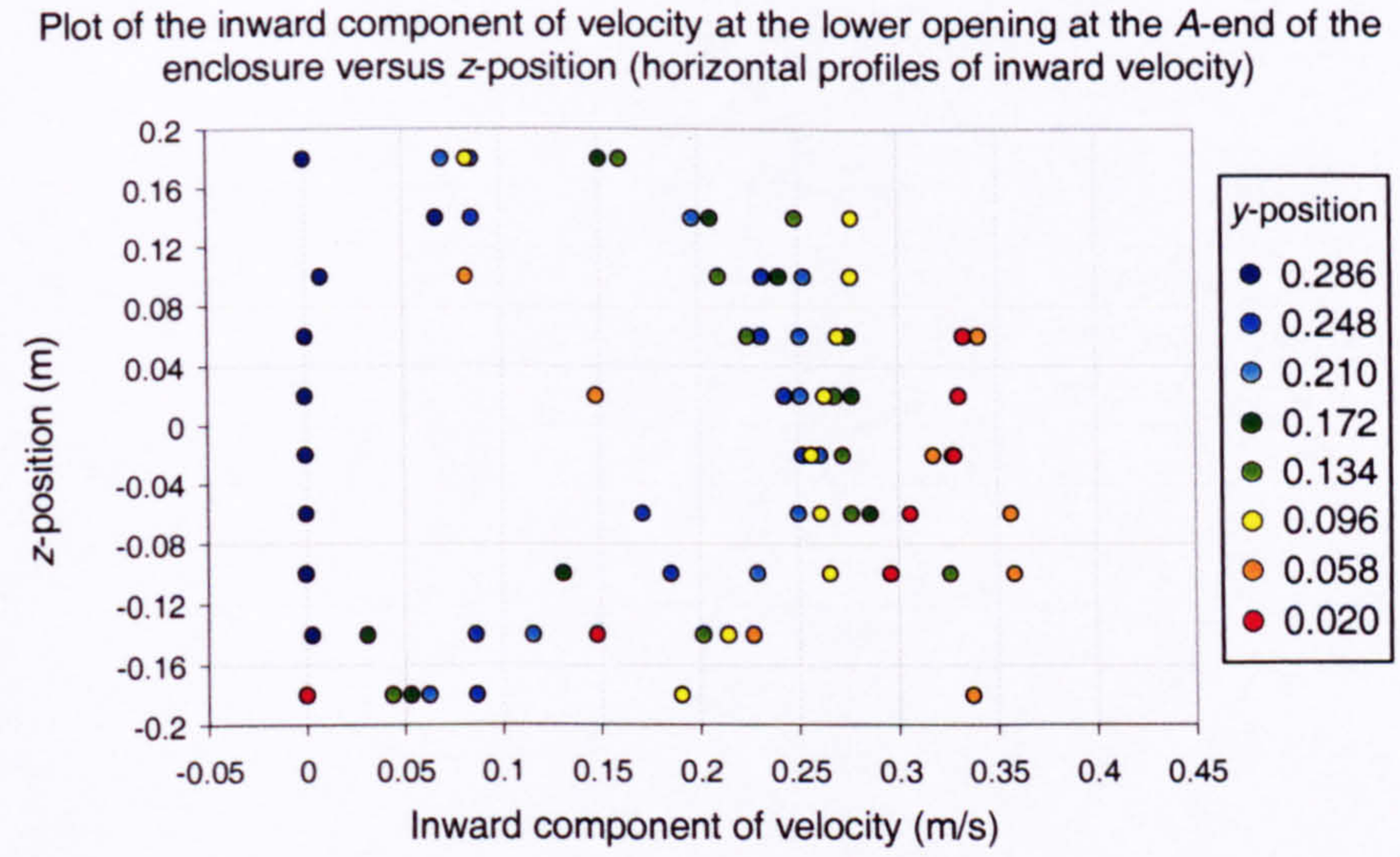

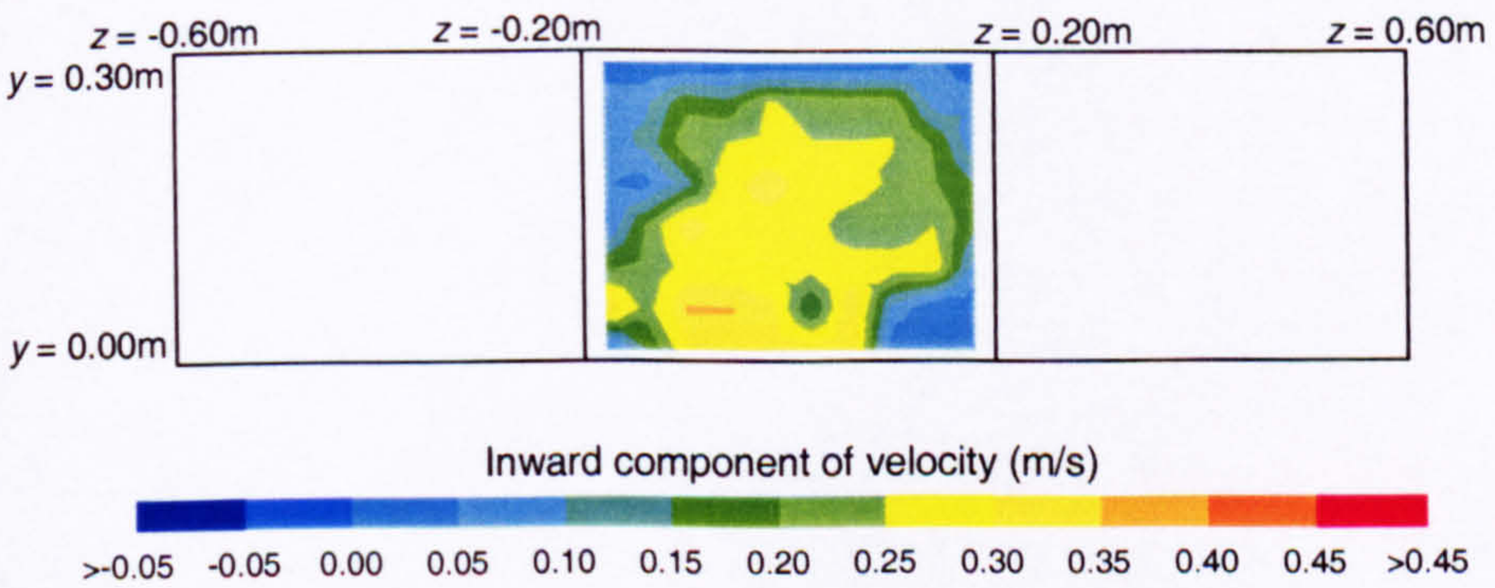

Width of opening:	0.4m
Effective area of opening:	0.244m^2
Heat source:	Boiler ring
Strength of heat source:	368.0W

Figure 4

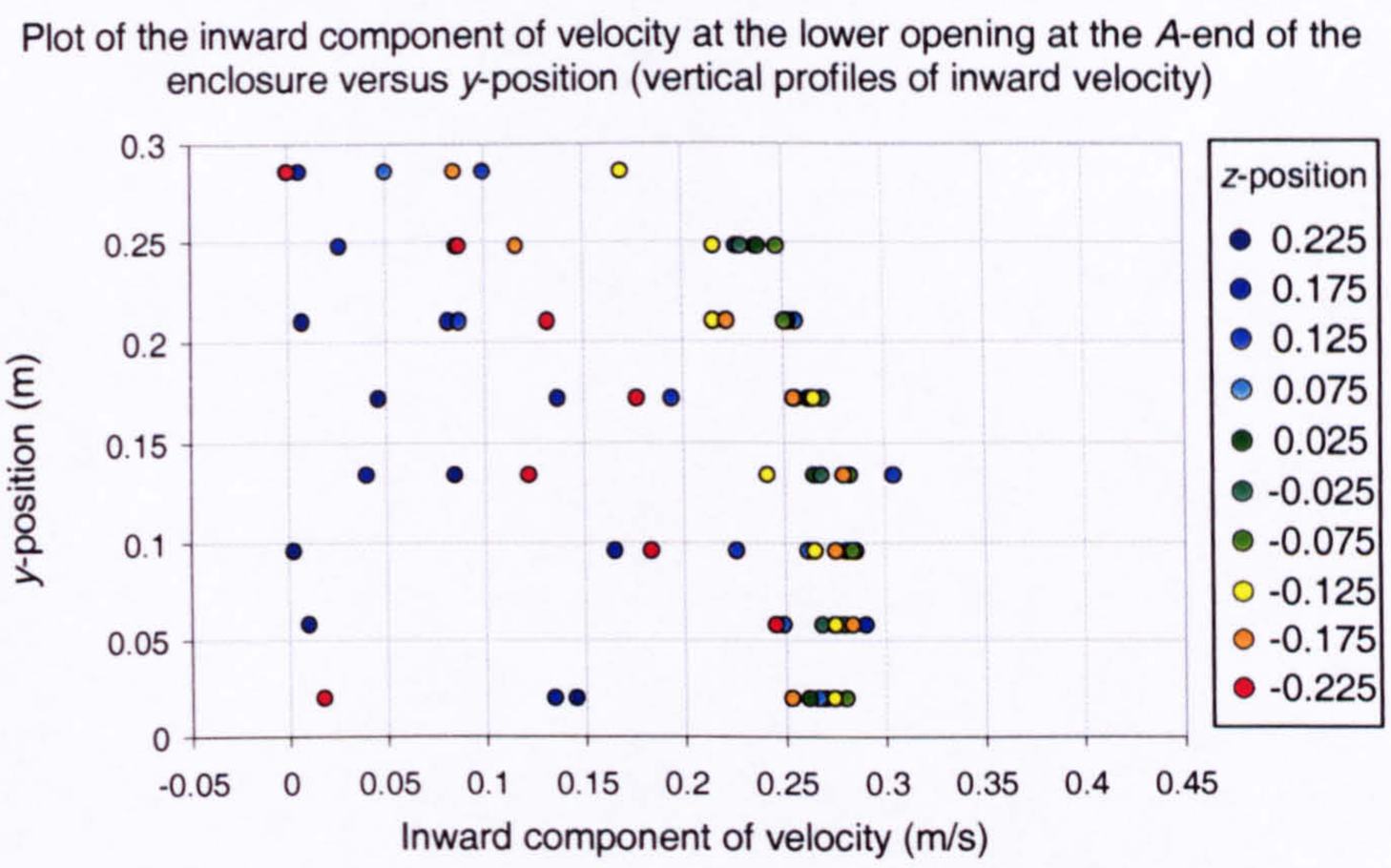

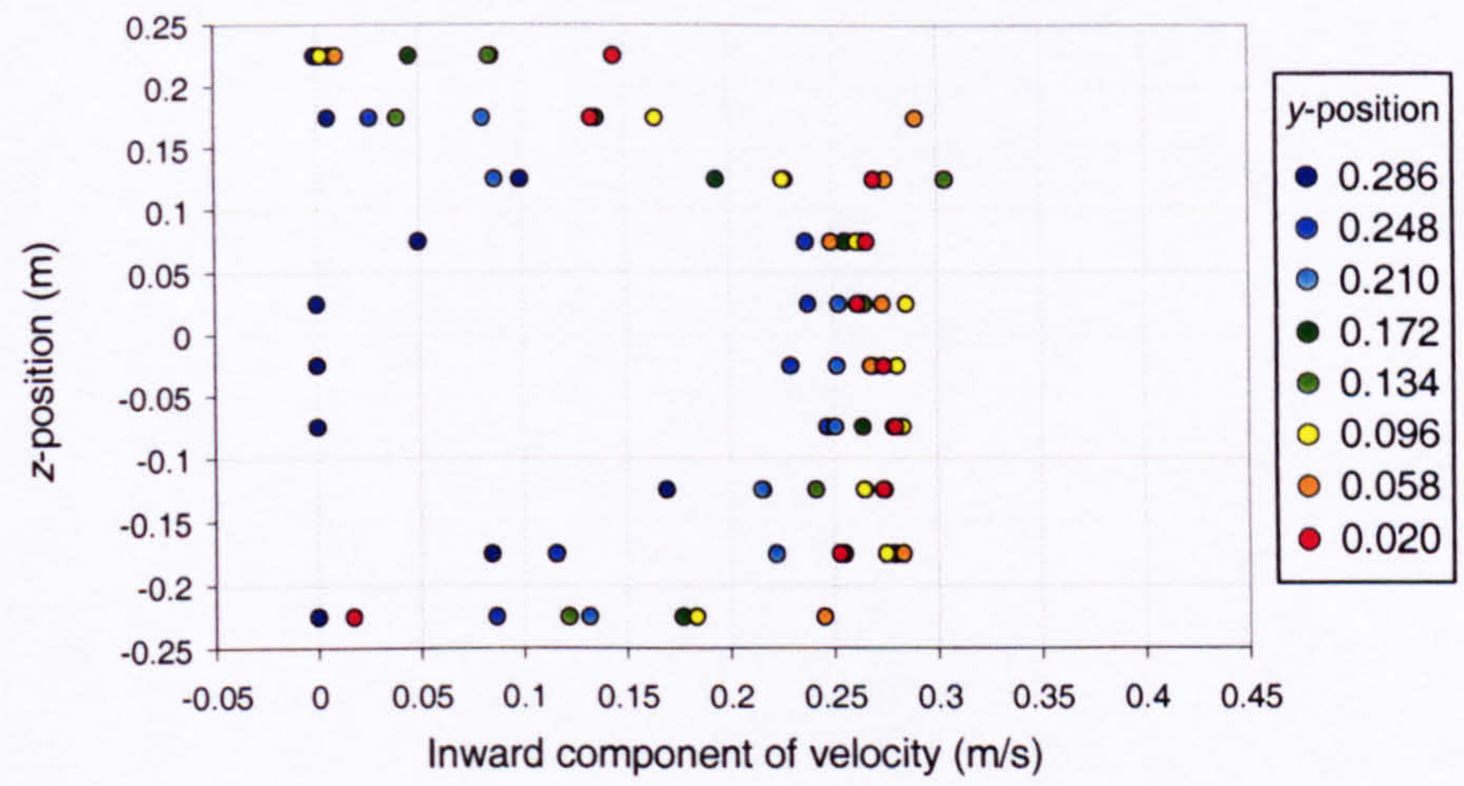

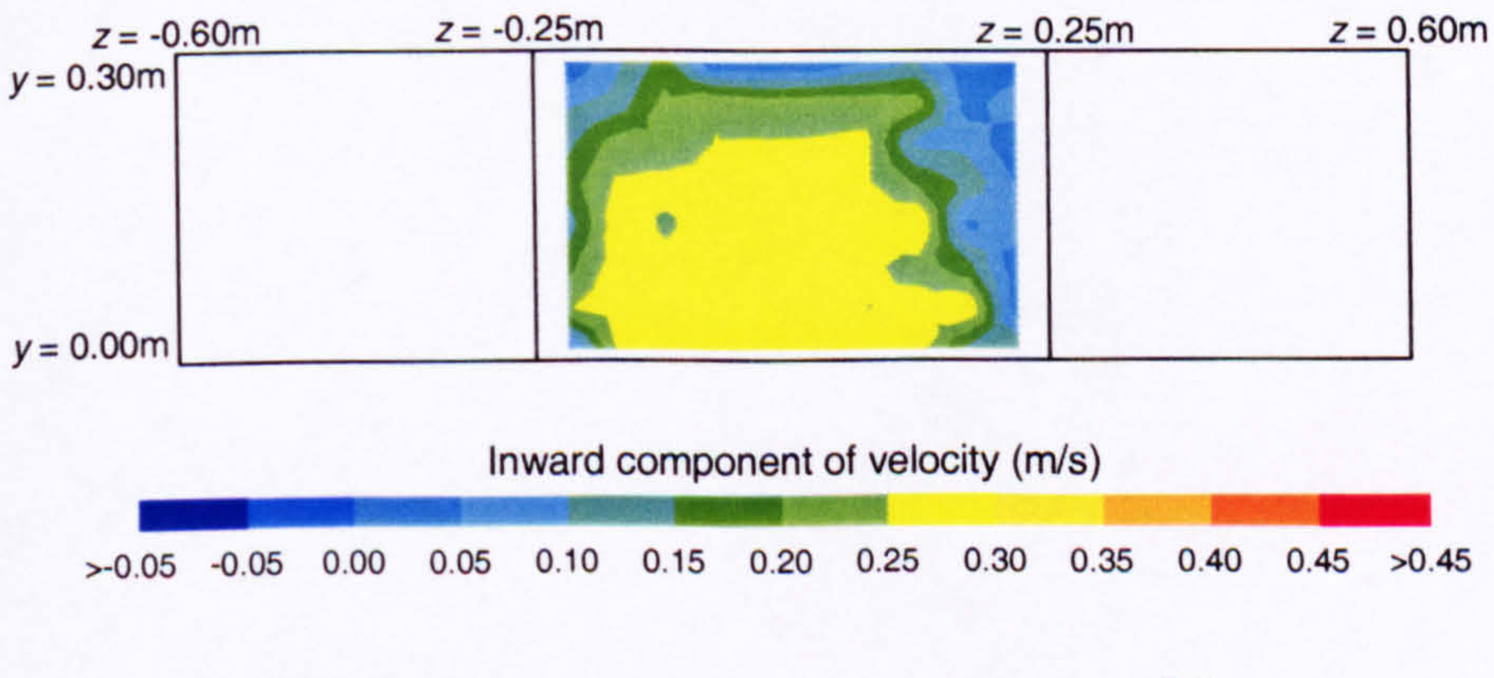

Width of opening:	0.5m
Effective area of opening:	0.305m^2
Heat source:	Boiler ring
Strength of heat source:	368.0W

Figure 5

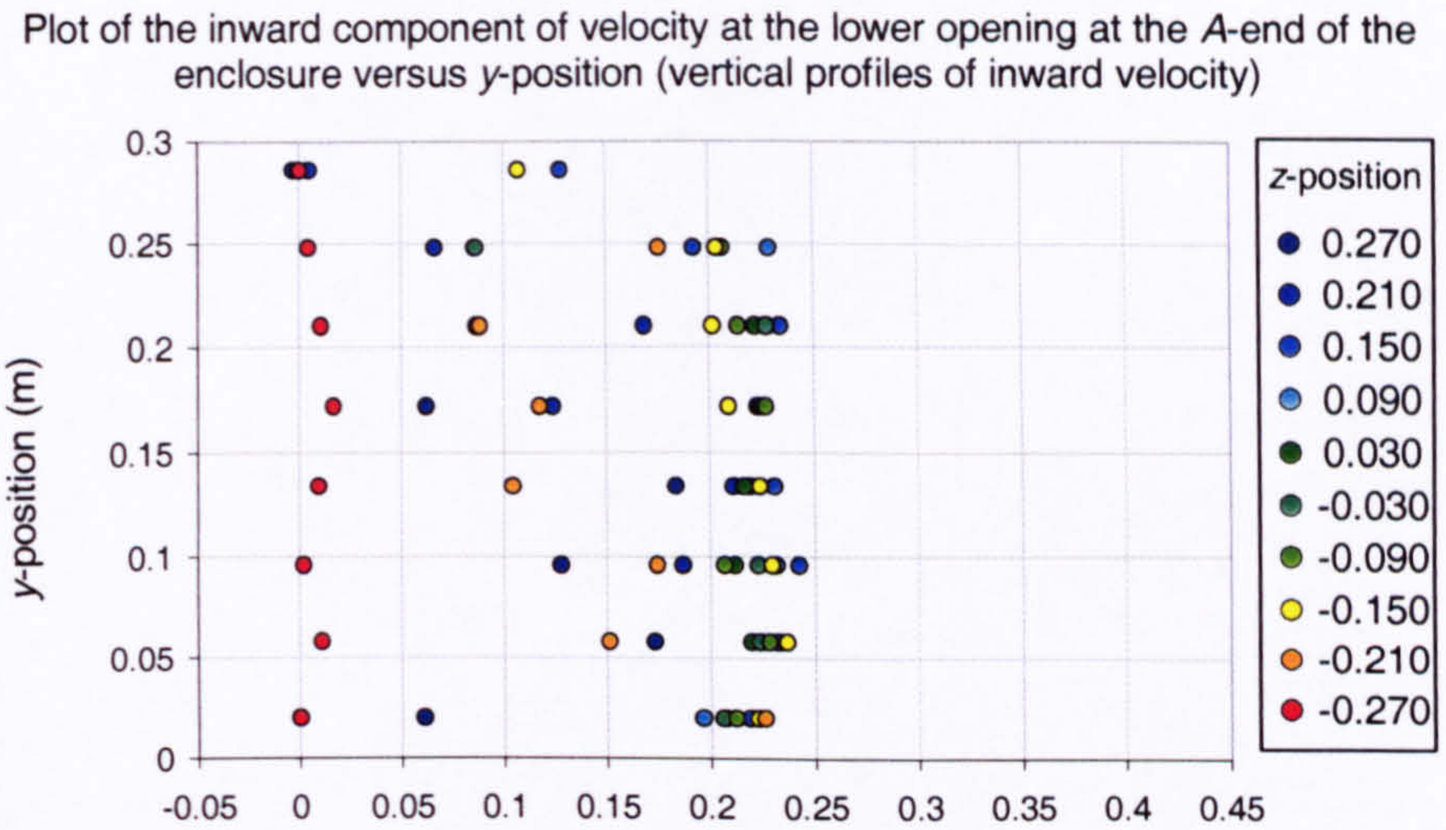

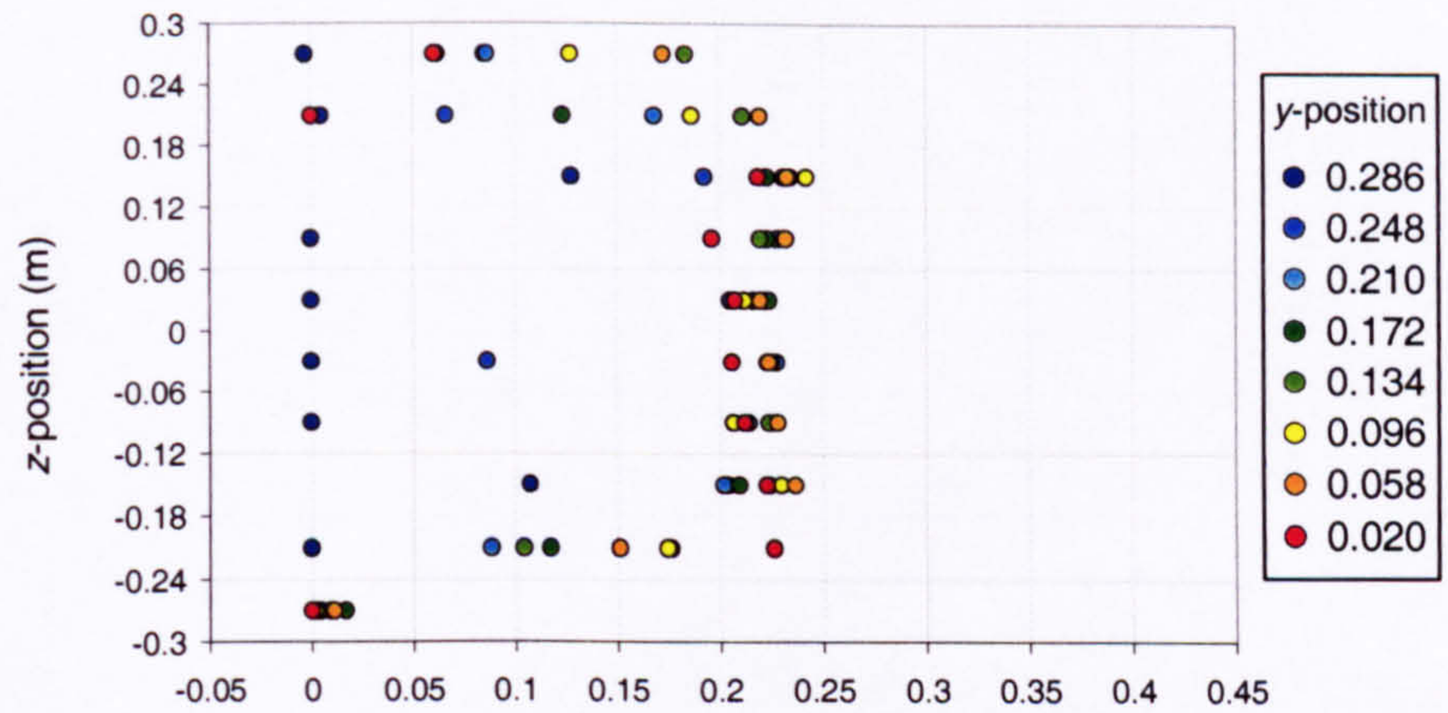

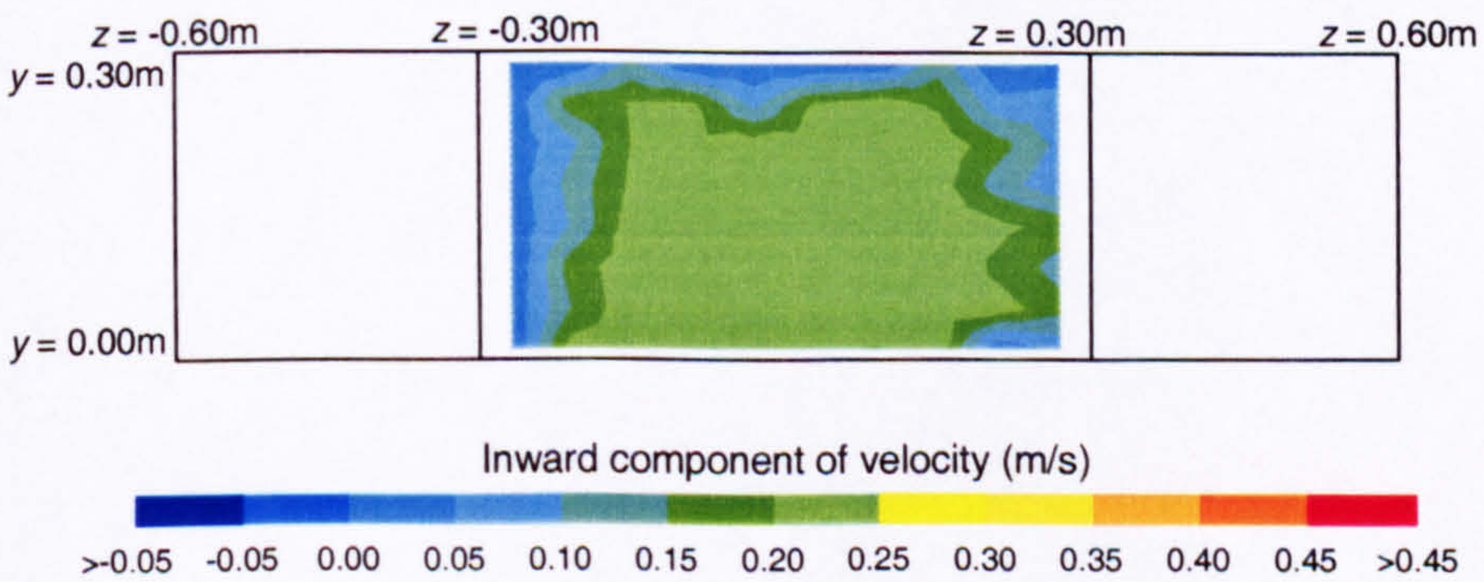

Width of opening:	0.6m
Effective area of opening:	0.366m^2
Heat source:	Boiler ring
Strength of heat source:	368.0W

Figure 6

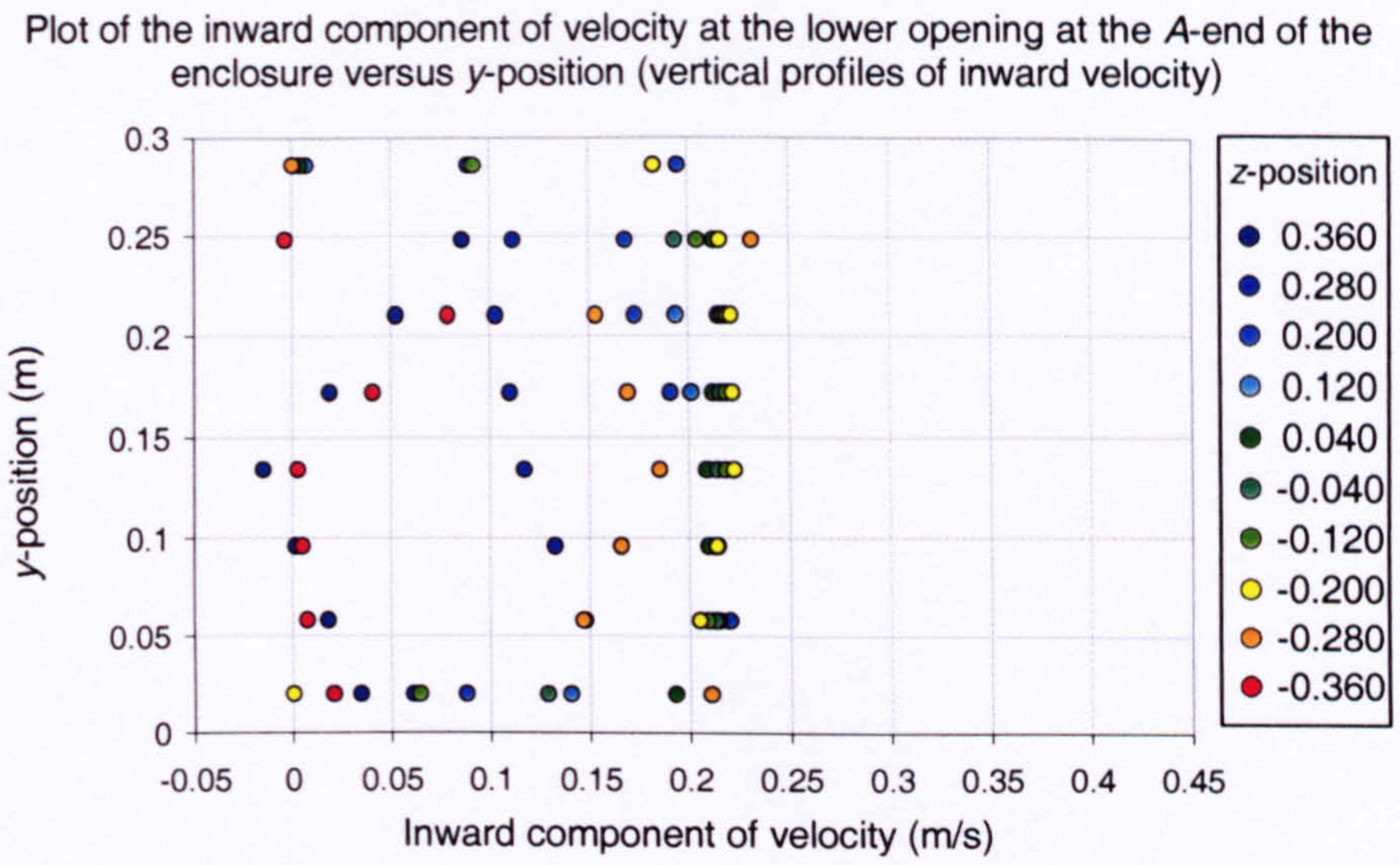

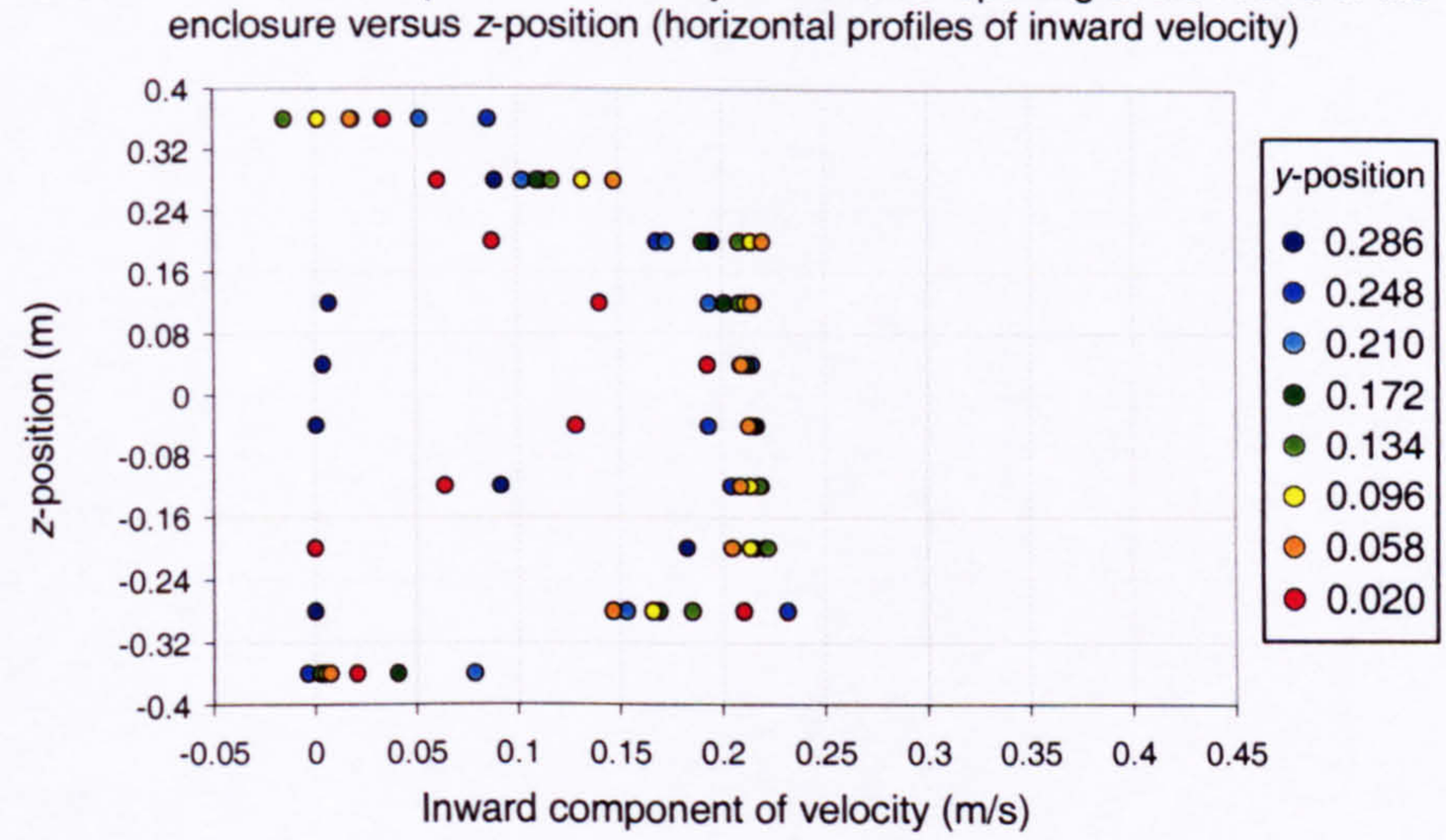

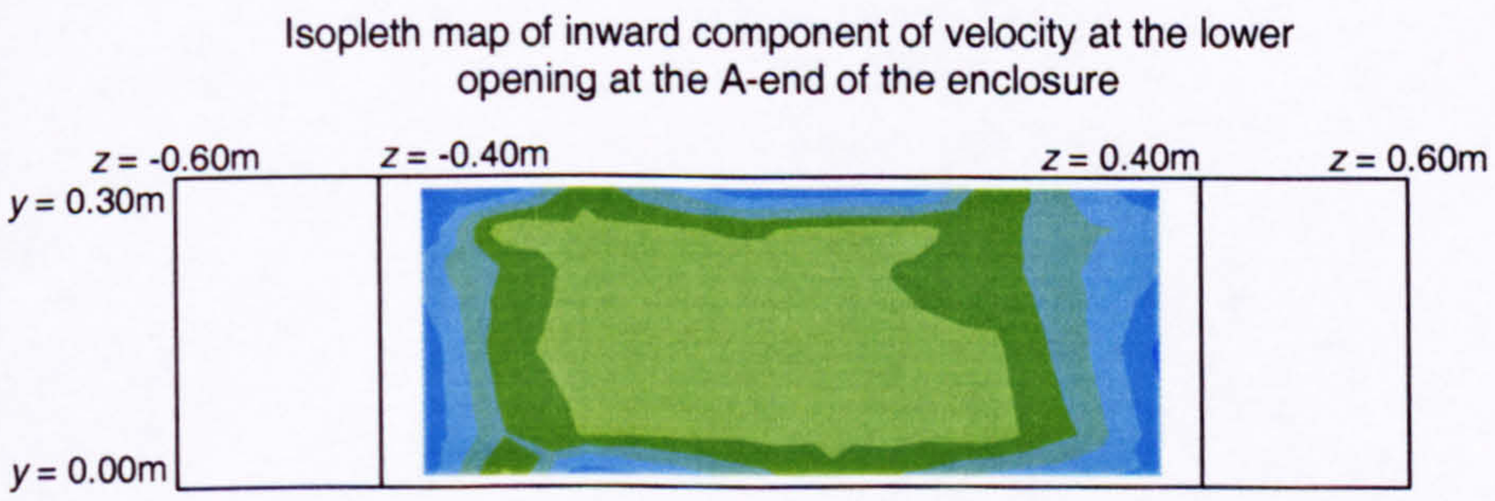

Width of opening:	0.8m
Effective area of opening:	0.488m^2
Heat source:	Boiler ring
Strength of heat source:	368.0W

Figure 7

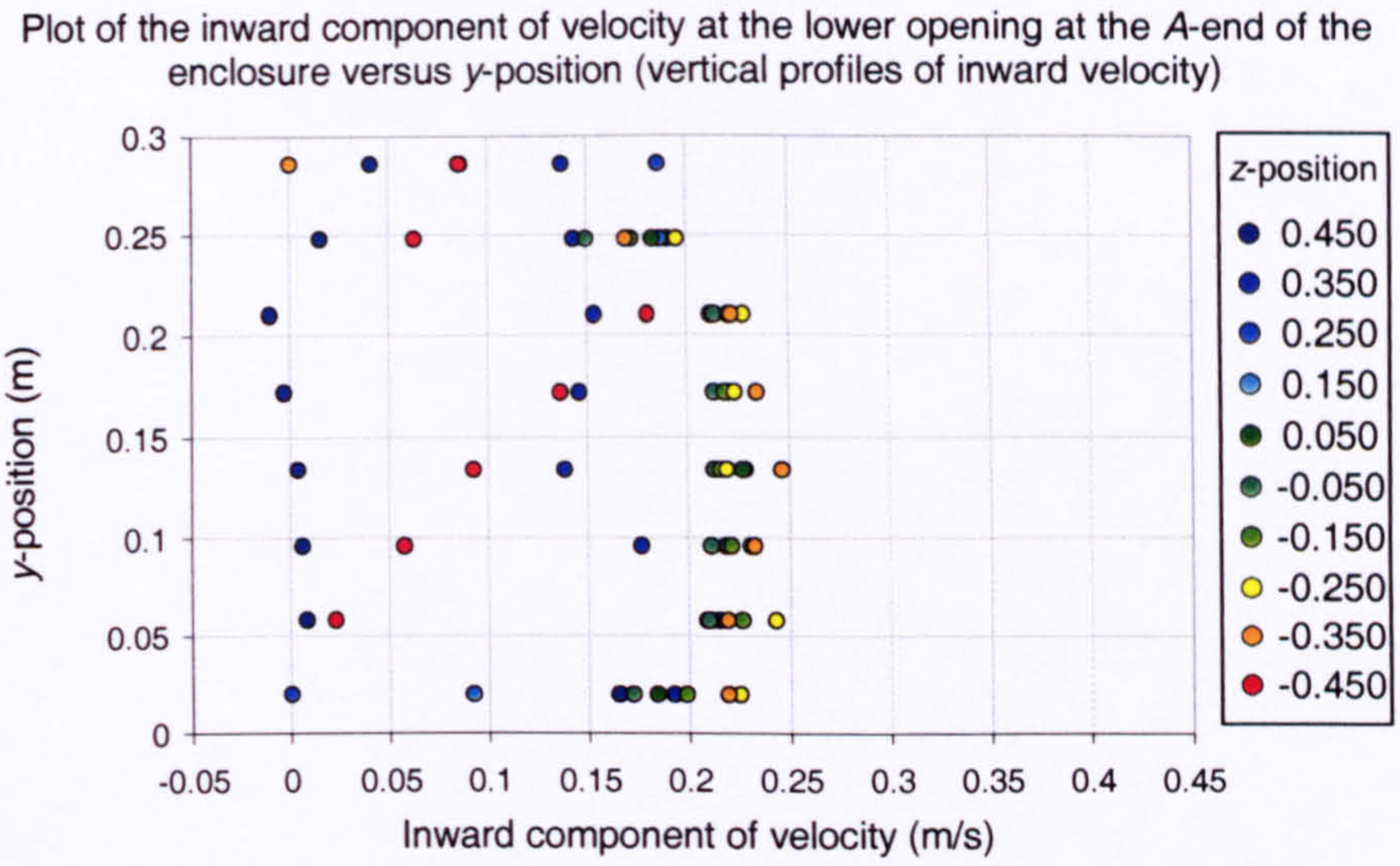

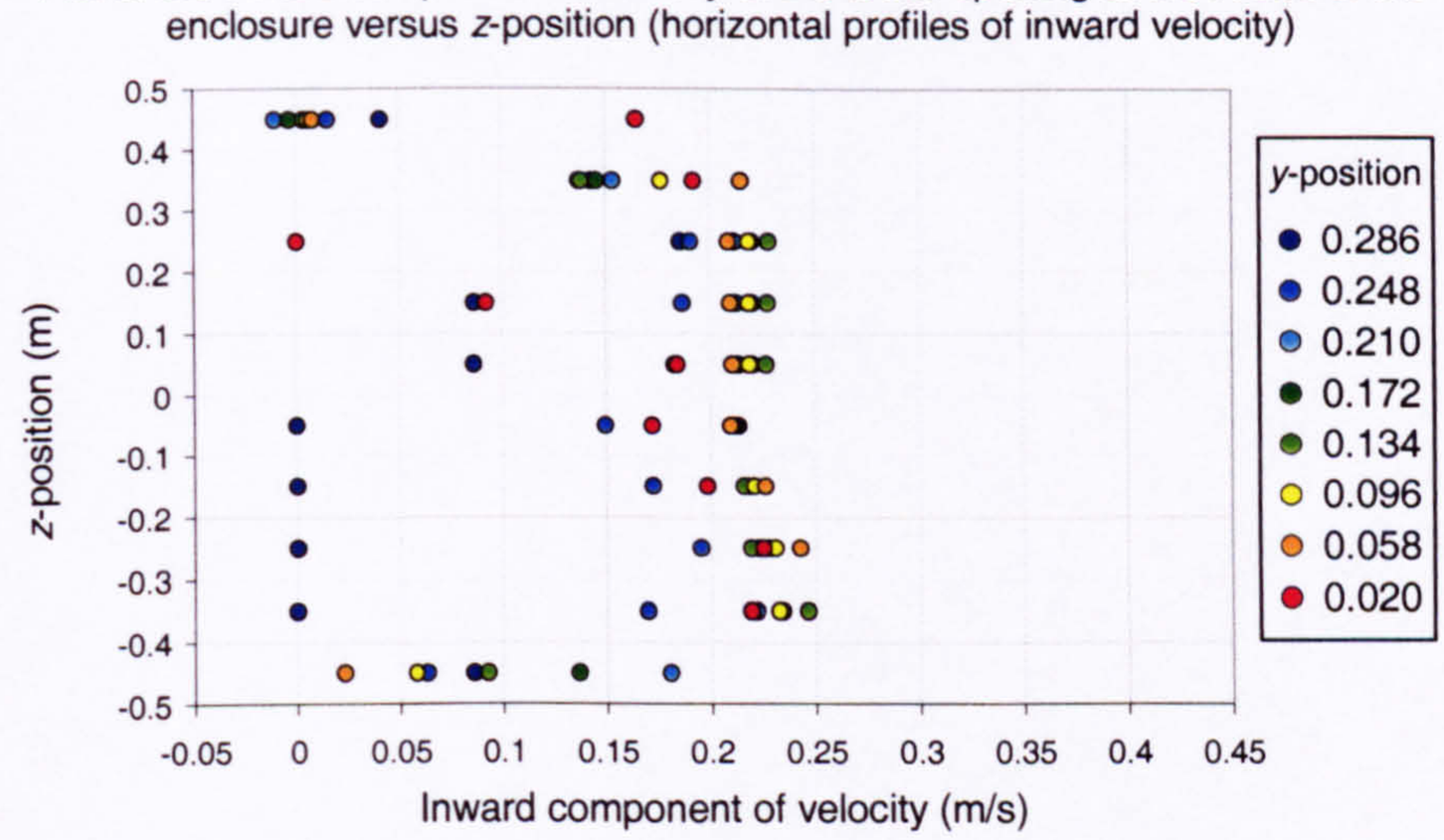

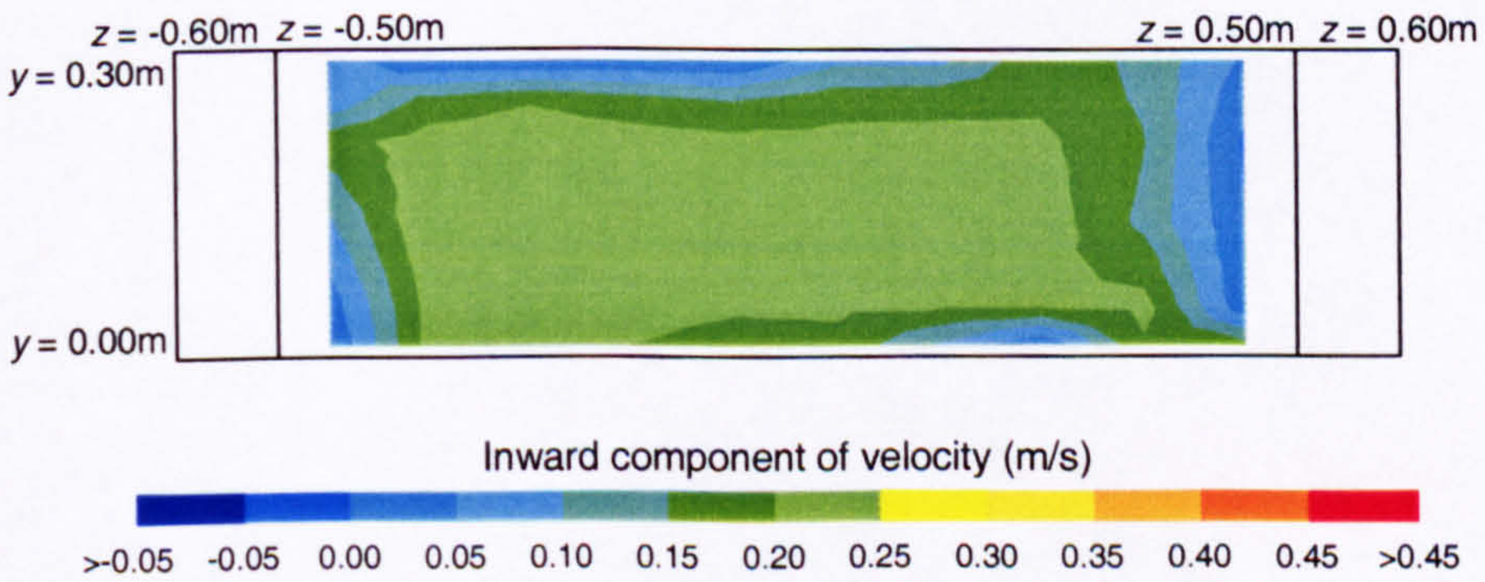

Width of opening:	1.0m
Effective area of opening:	0.610m^2
Heat source:	Boiler ring
Strength of heat source:	368.0W

Figure 8

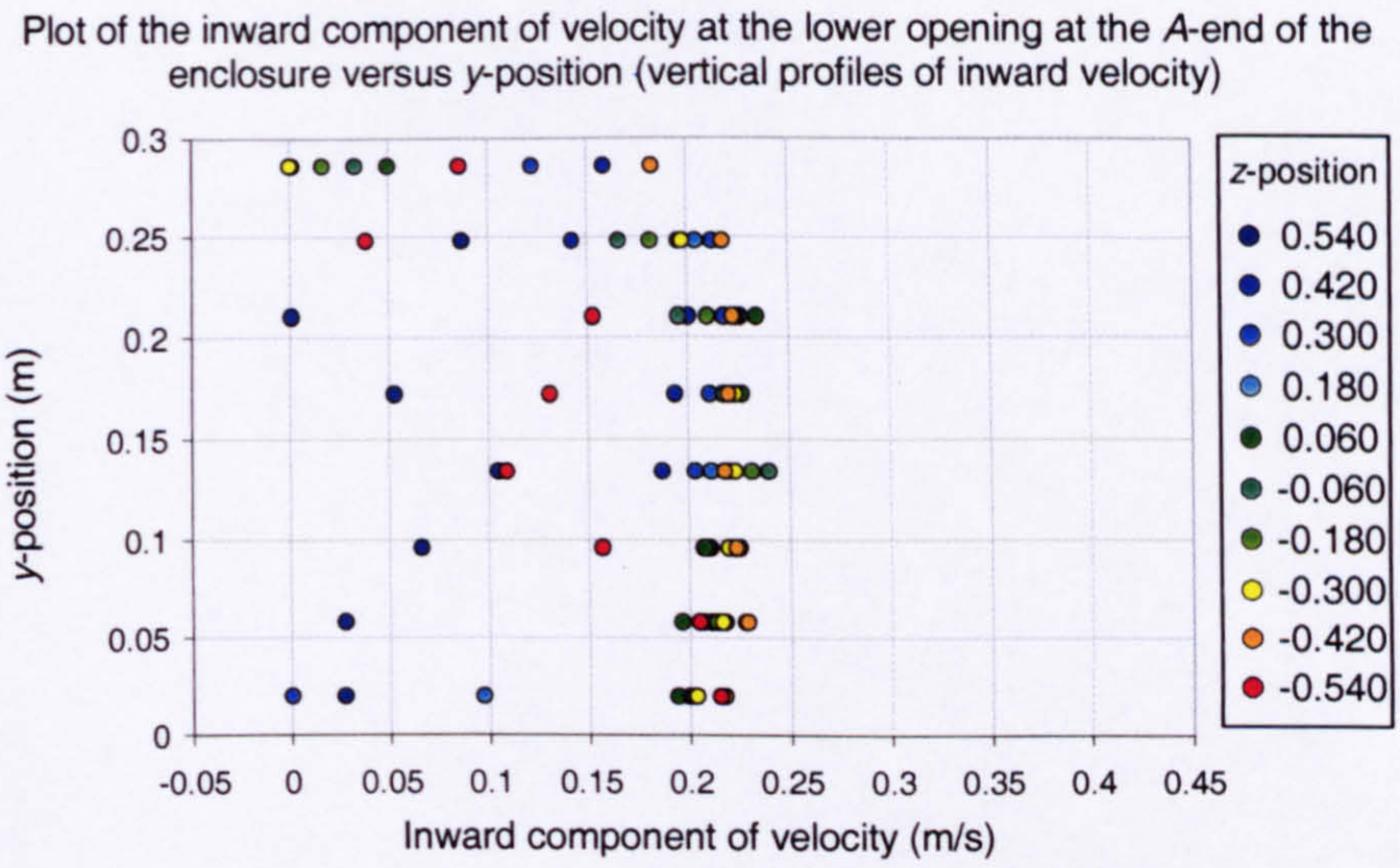

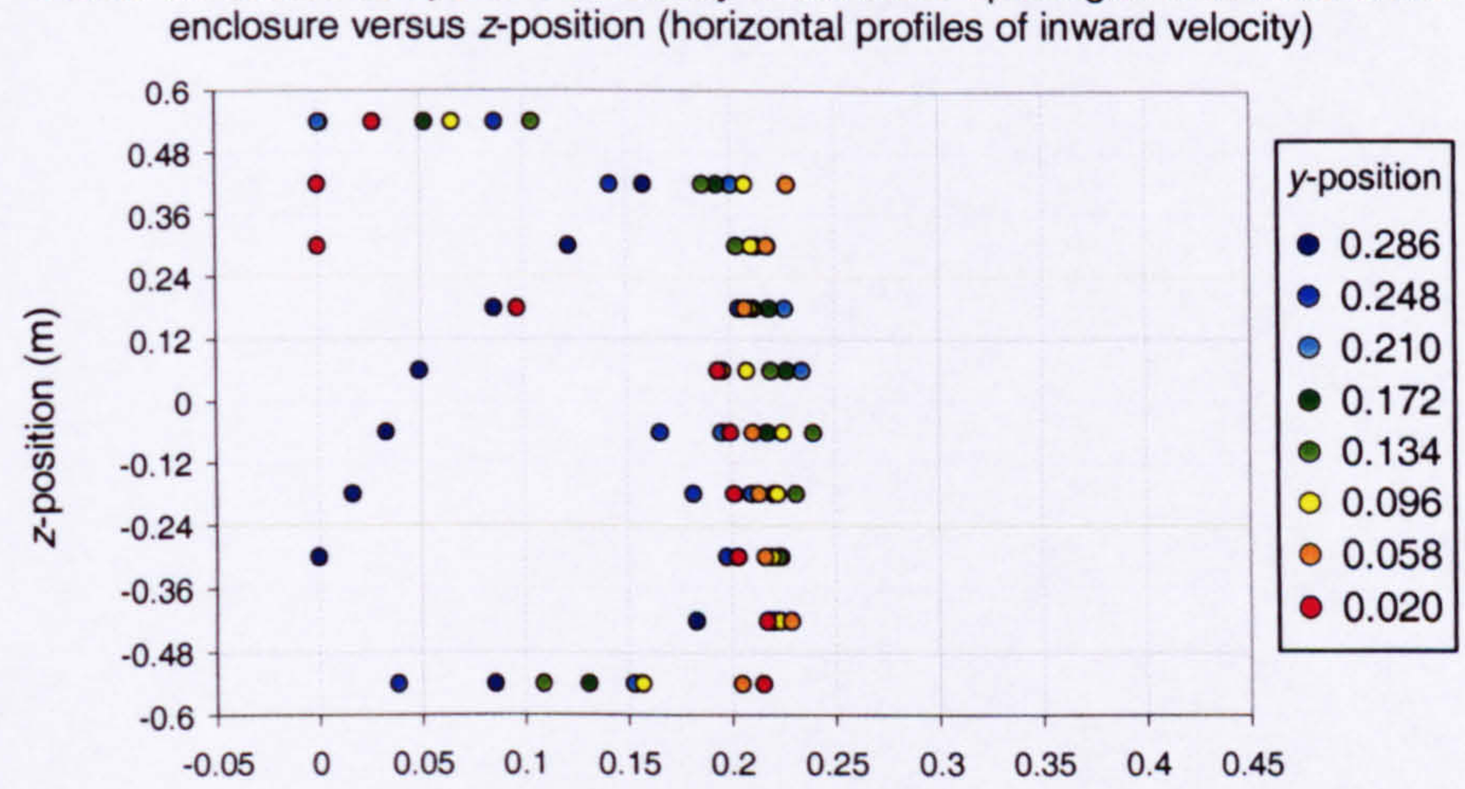

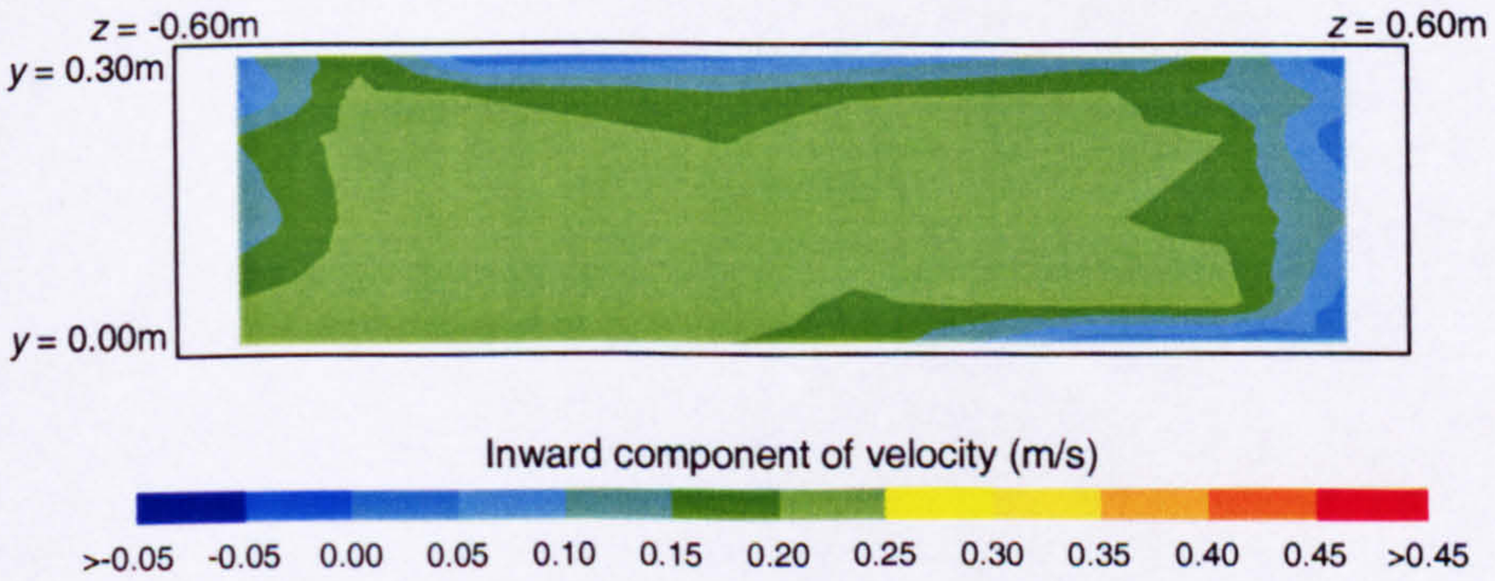

Width of opening:	1.2m
Effective area of opening:	0.732m^2
Heat source:	Boiler ring
Strength of heat source:	368.0W

Figure 9

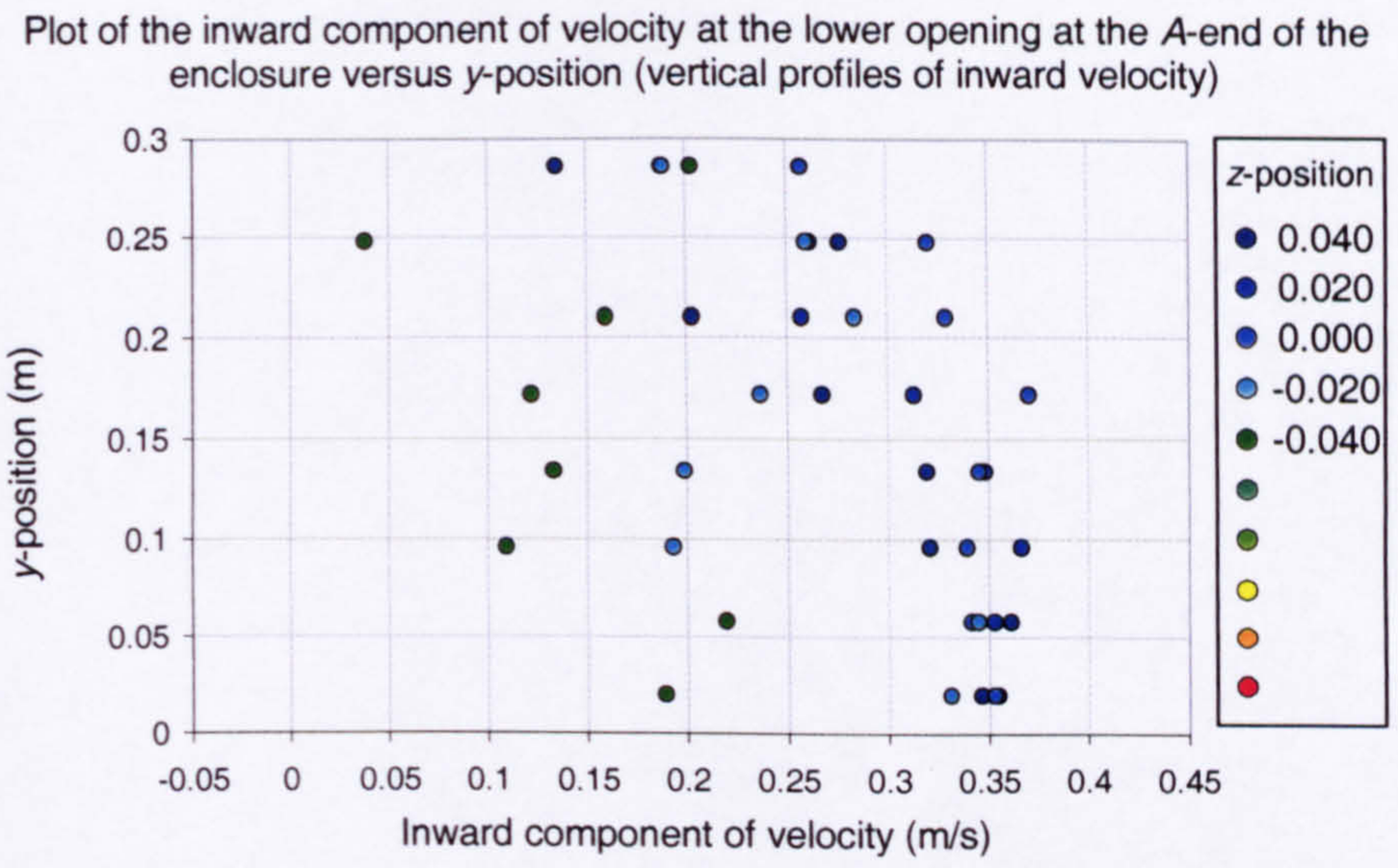

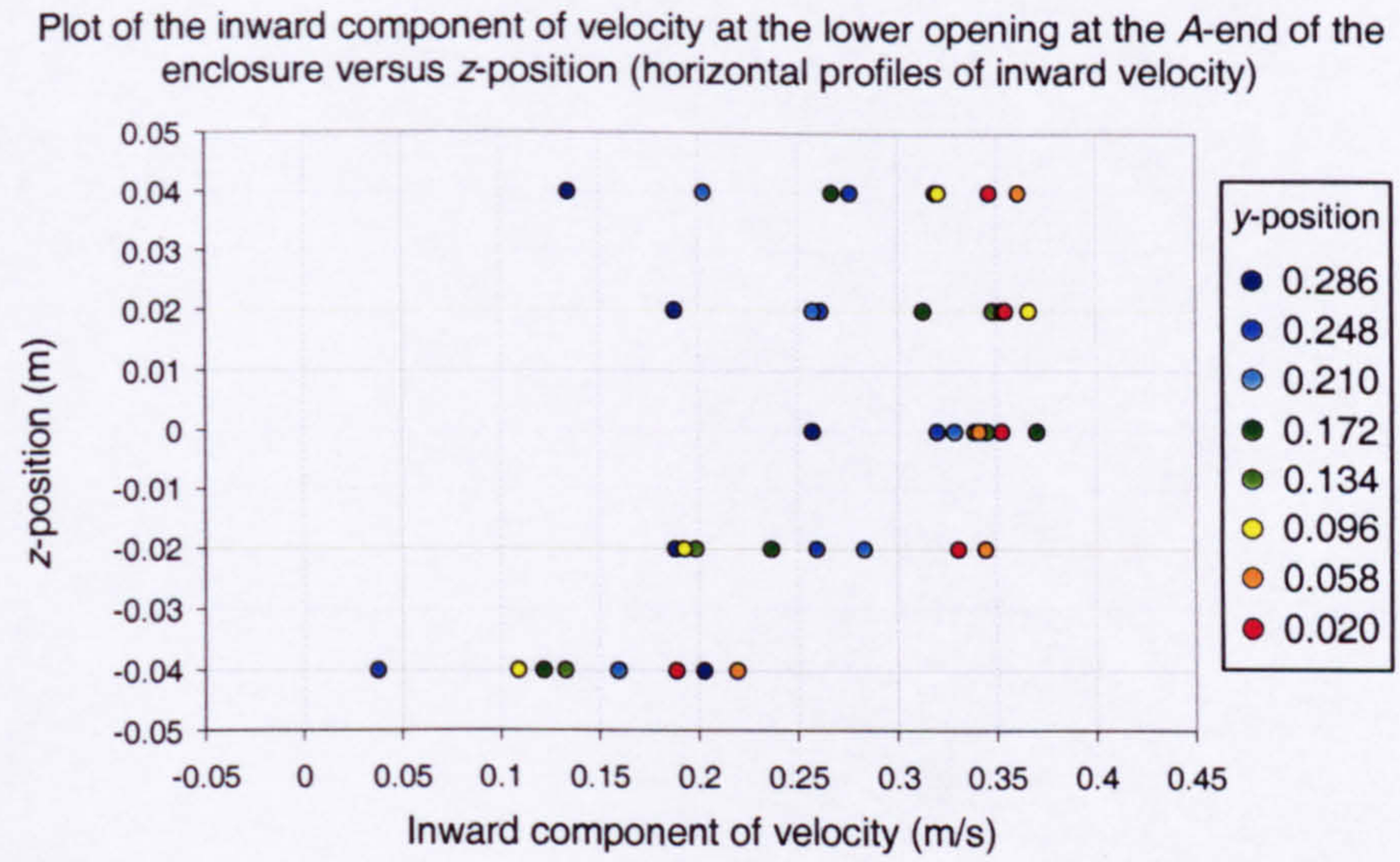

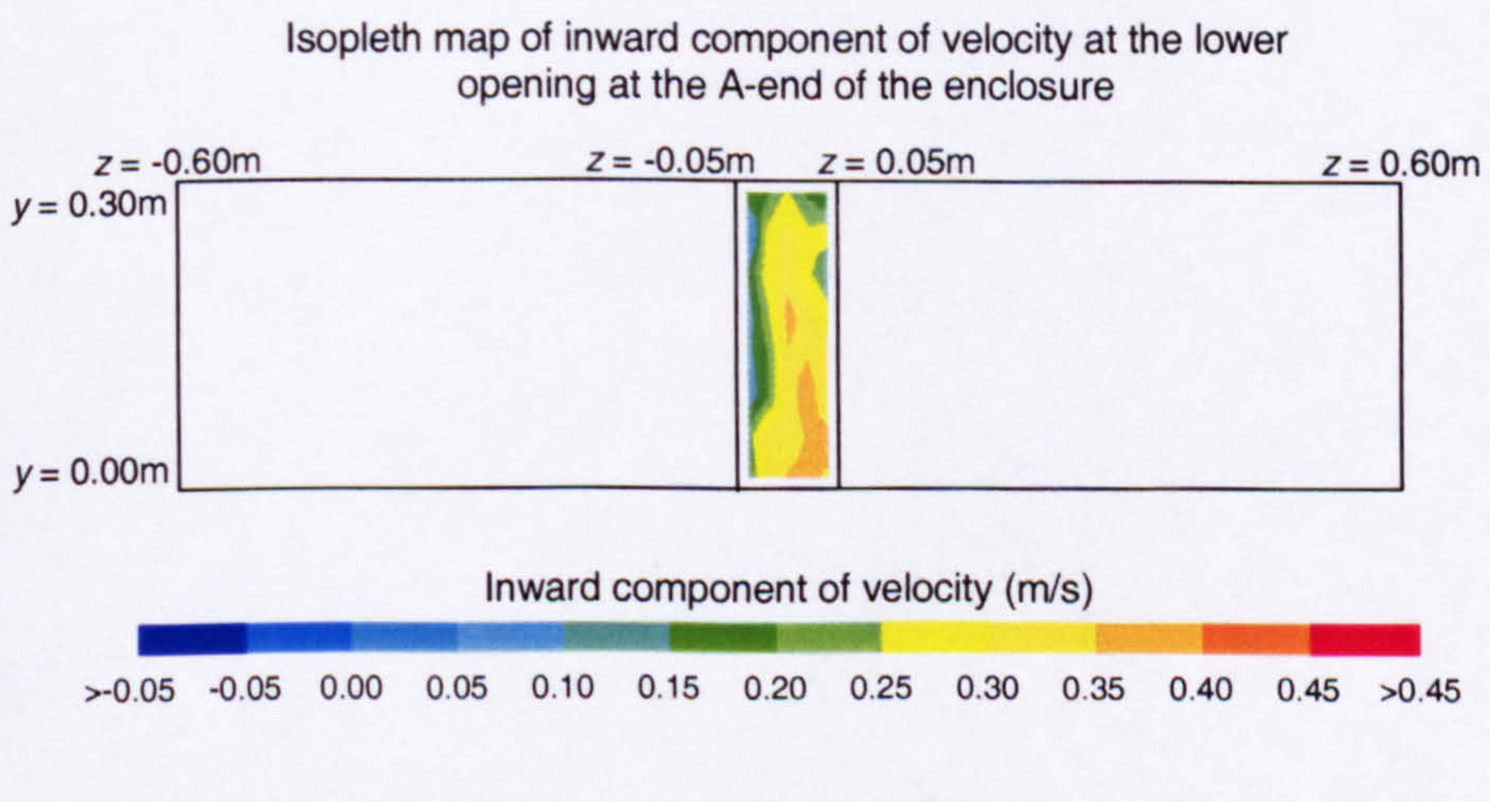

Width of opening:	0.1m
Effective area of opening:	0.061m^2
Heat source:	Boiler ring
Strength of heat source:	490.5W

Figure 10

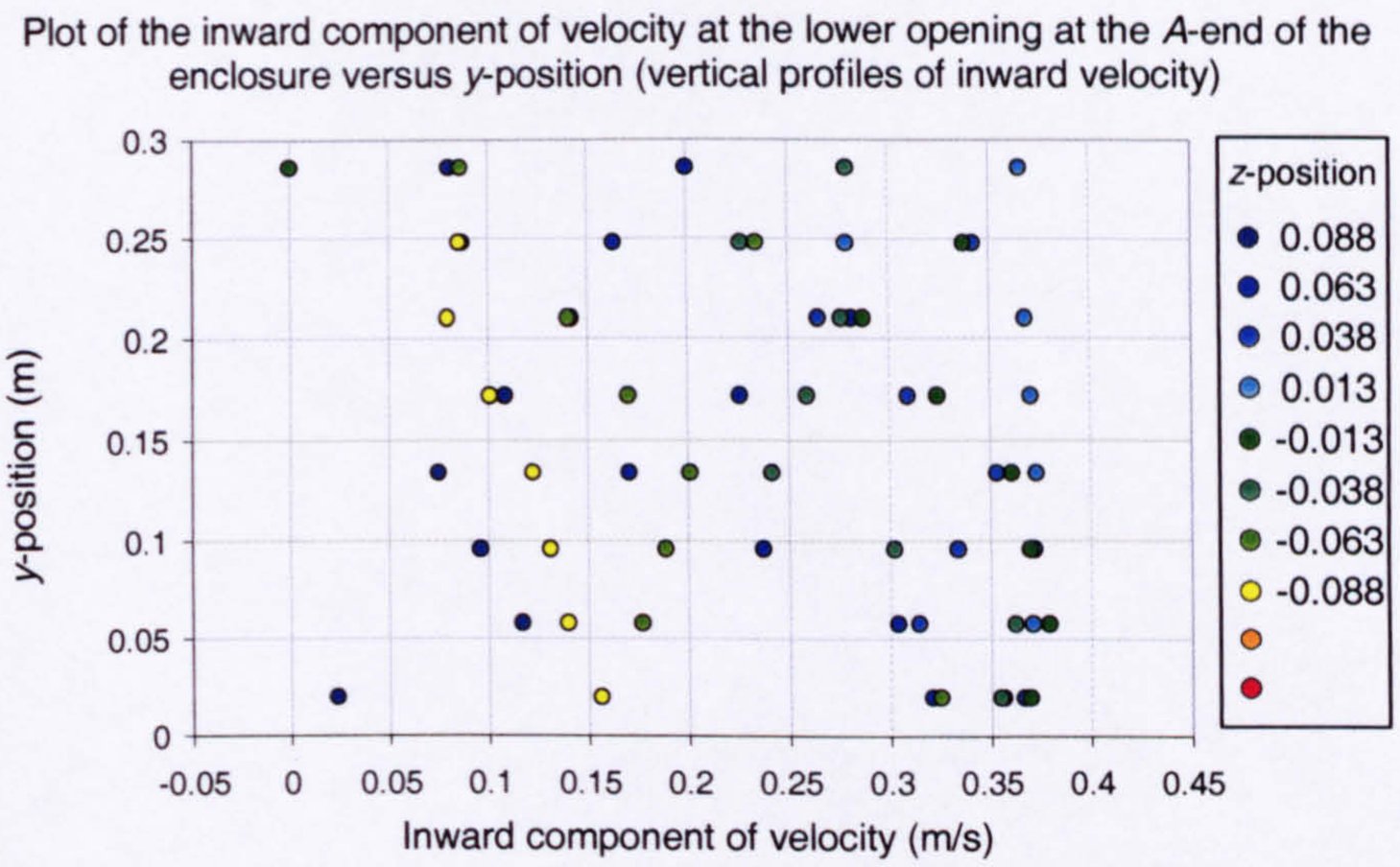

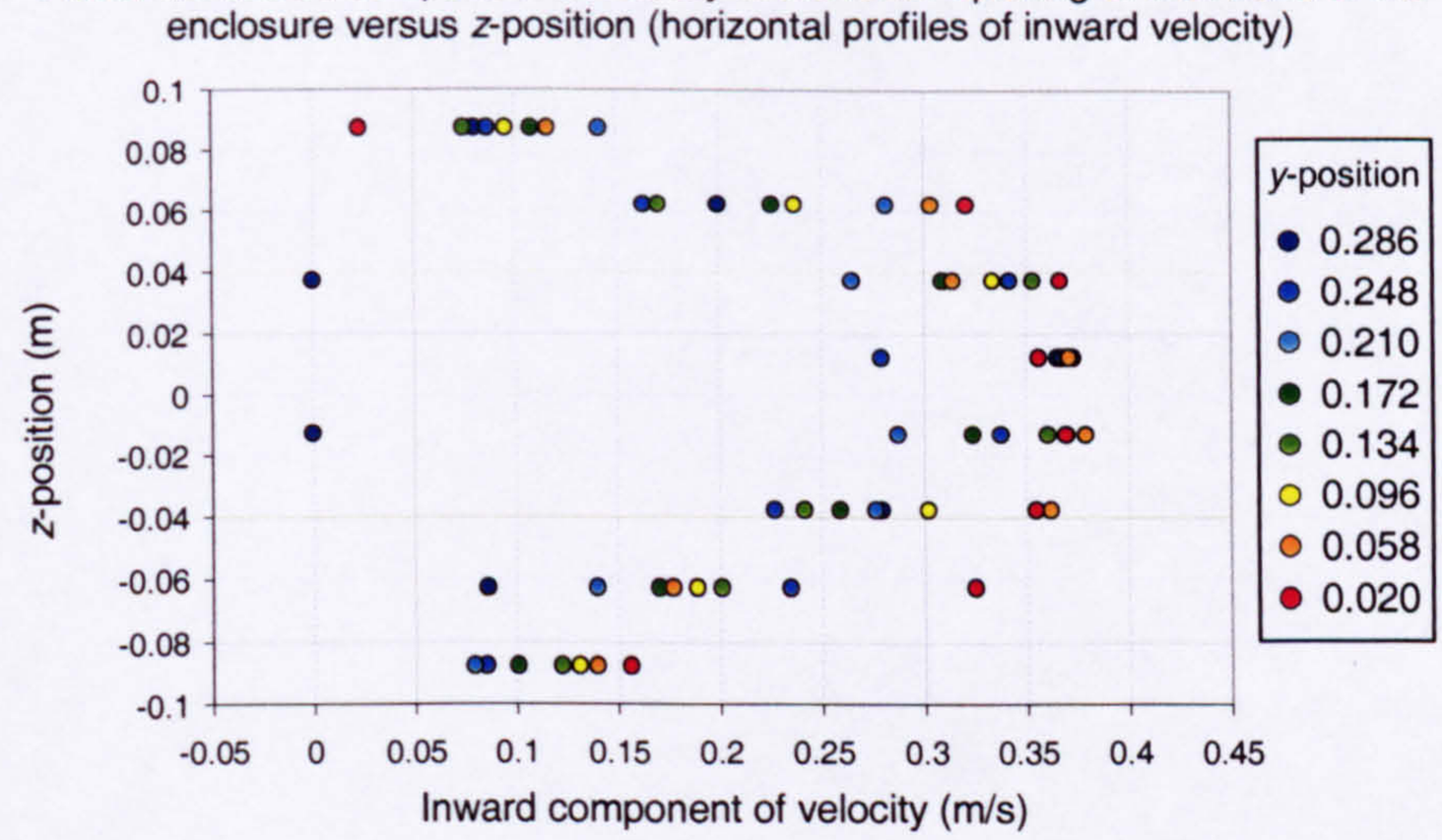

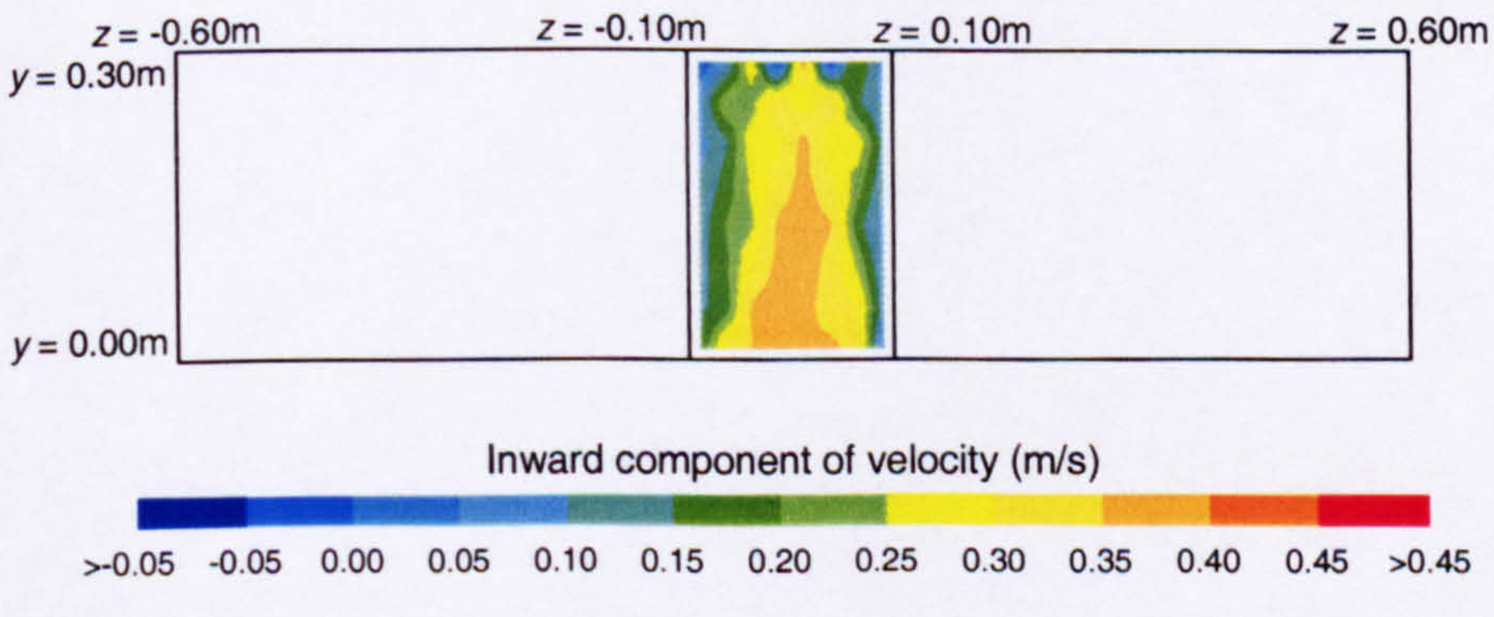

Width of opening:	0.2m
Effective area of opening:	0.122m^2
Heat source:	Boiler ring
Strength of heat source:	490.5W

Figure 11

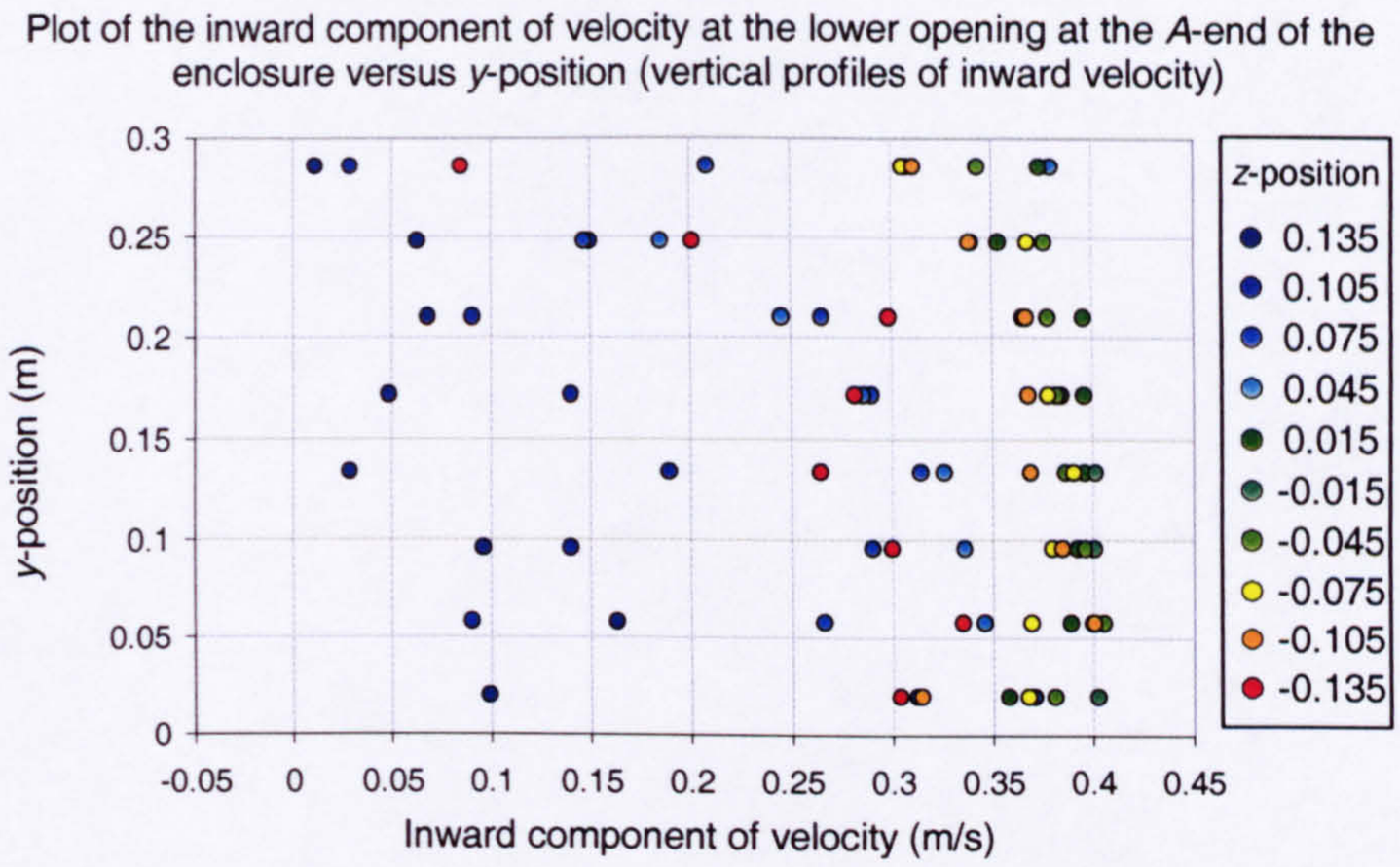

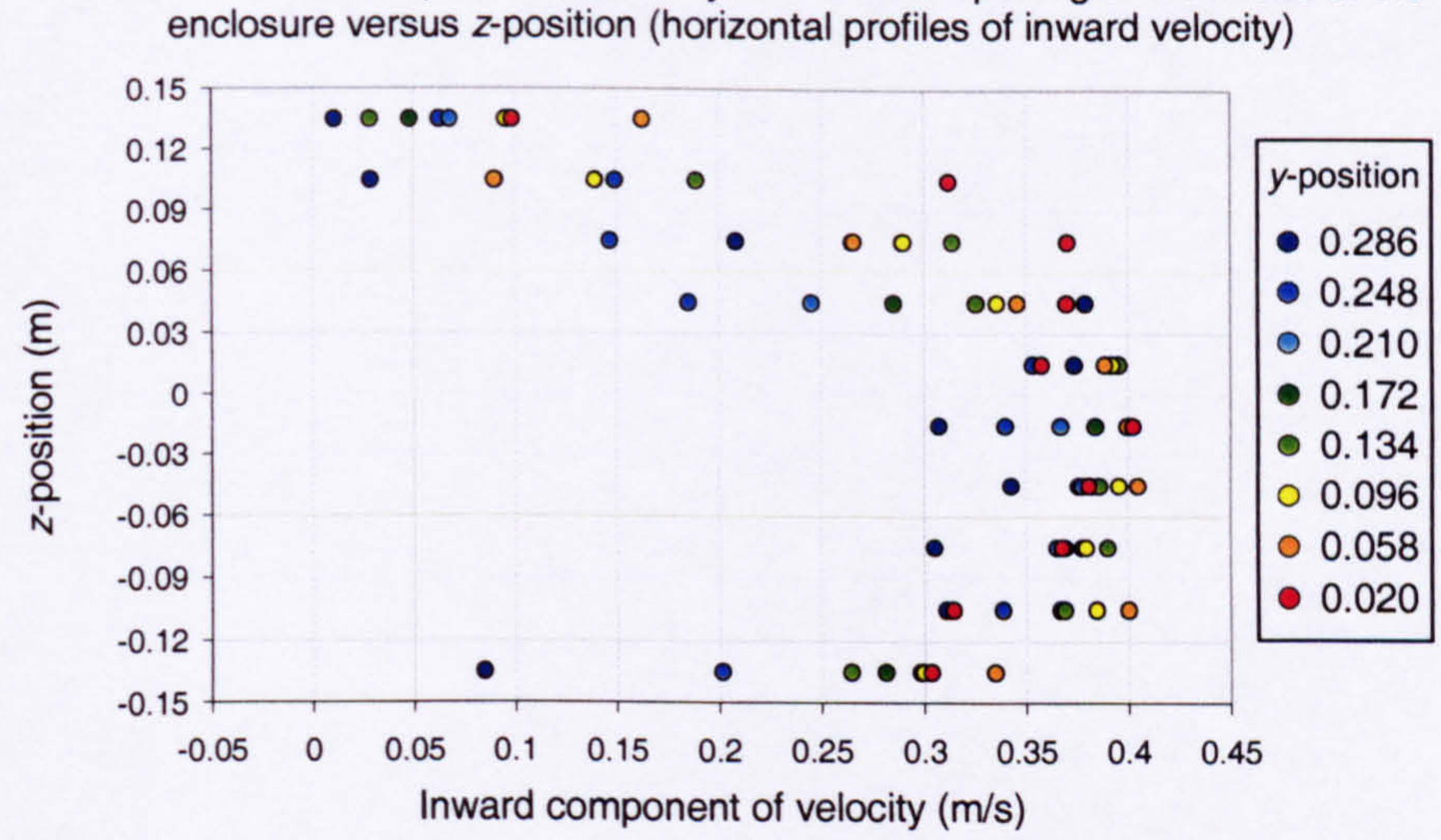

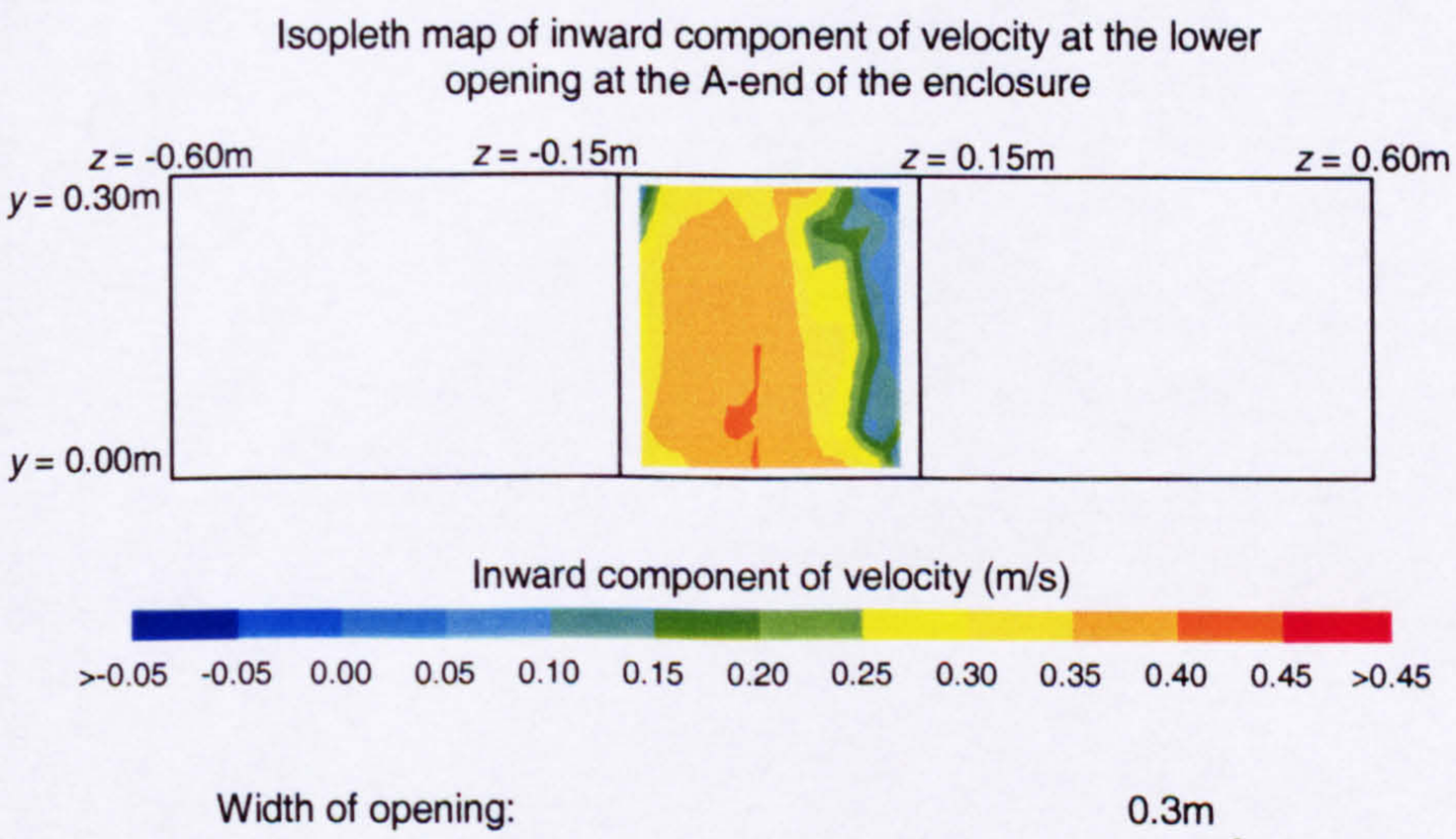

Width of opening:	0.3m
Effective area of opening:	0.183m^2
Heat source:	Boiler ring
Strength of heat source:	490.5W

Figure 12

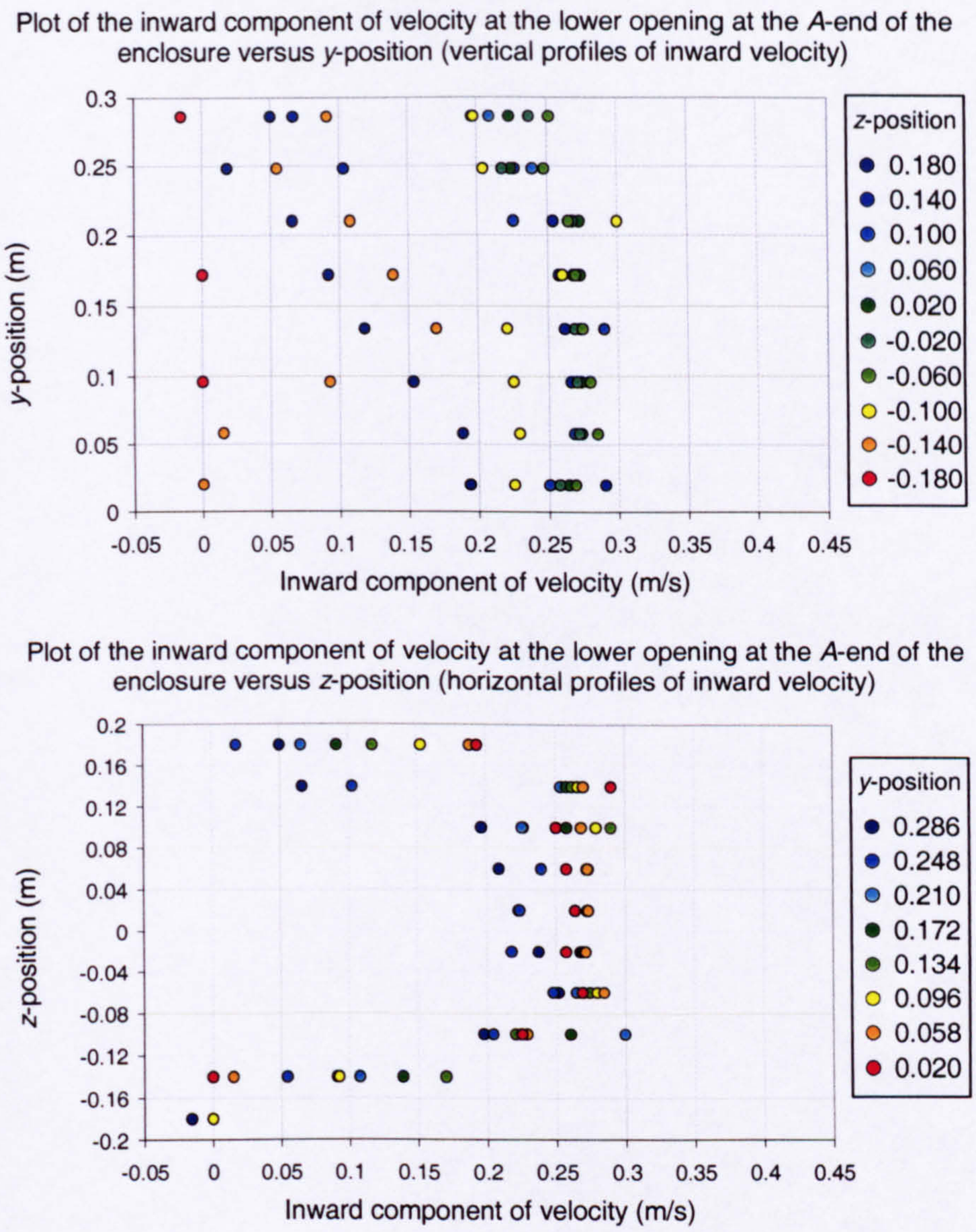

Width of opening:	0.4m
Effective area of opening:	0.244m^2
Heat source:	Boiler ring
Strength of heat source:	490.5W

Figure 13

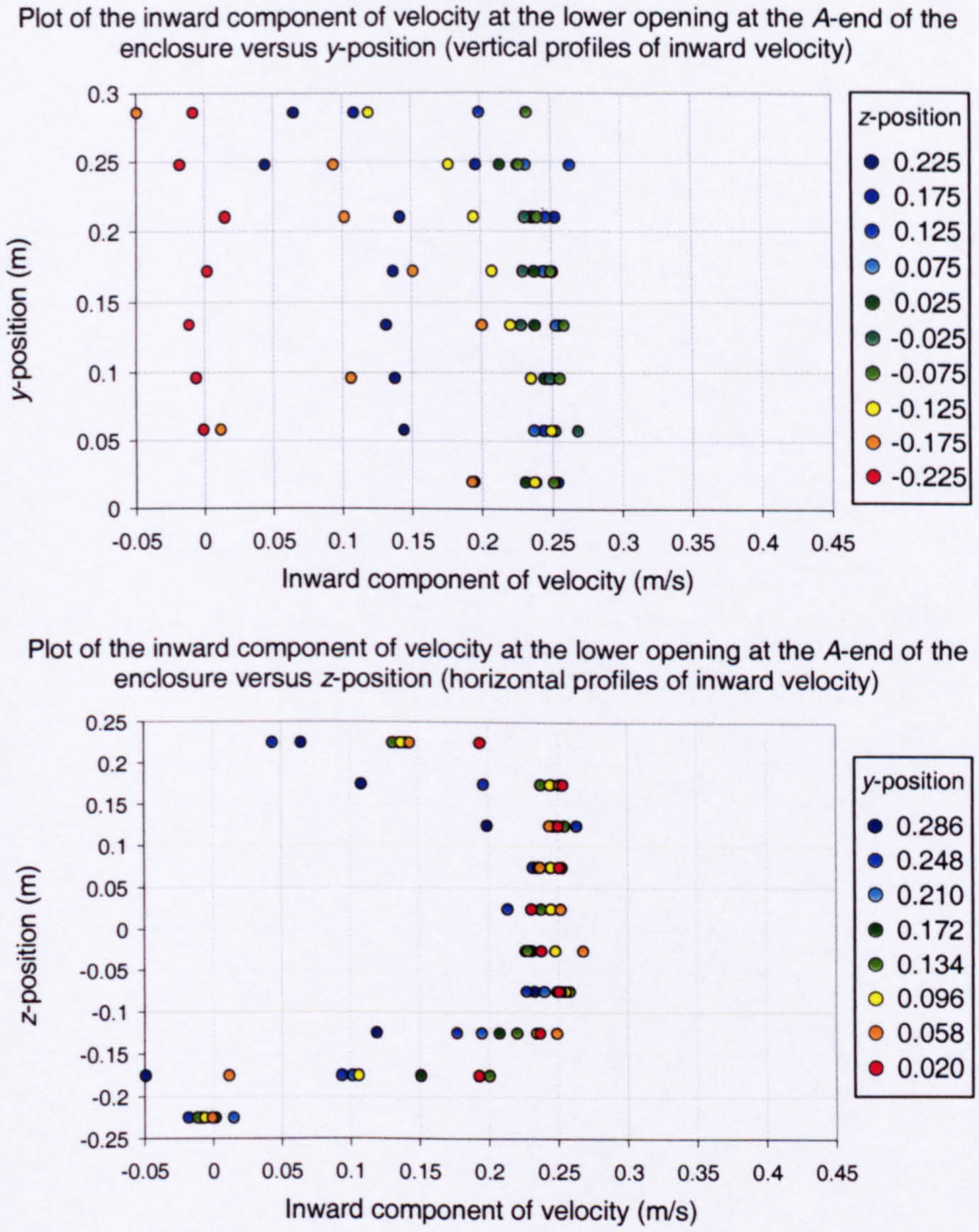

Width of opening:	0.5m
Effective area of opening:	0.305m^2
Heat source:	Boiler ring
Strength of heat source:	490.5W

Figure 14

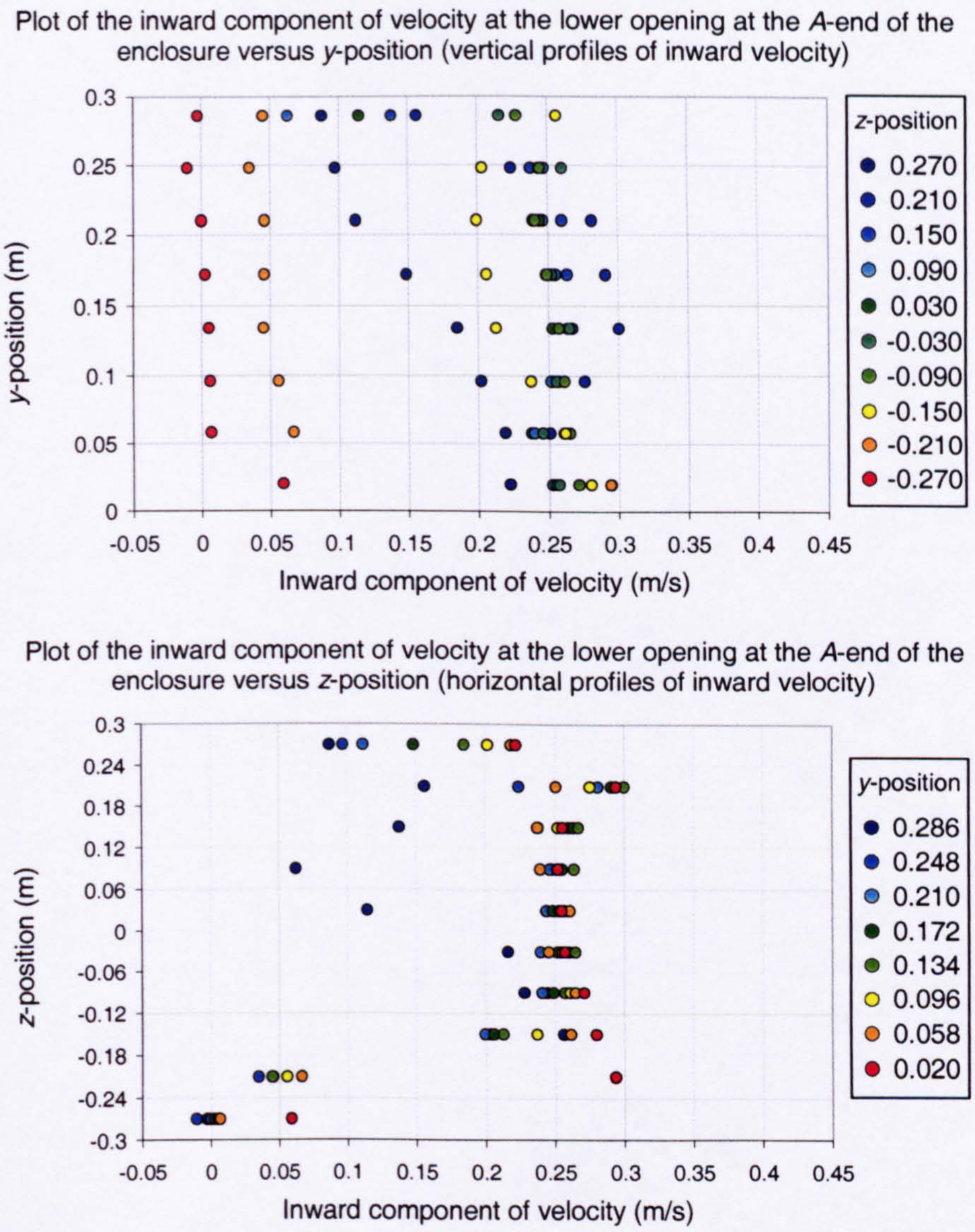

Width of opening:	0.6m
Effective area of opening:	0.366m^2
Heat source:	Boiler ring
Strength of heat source:	490.5W

Figure 15

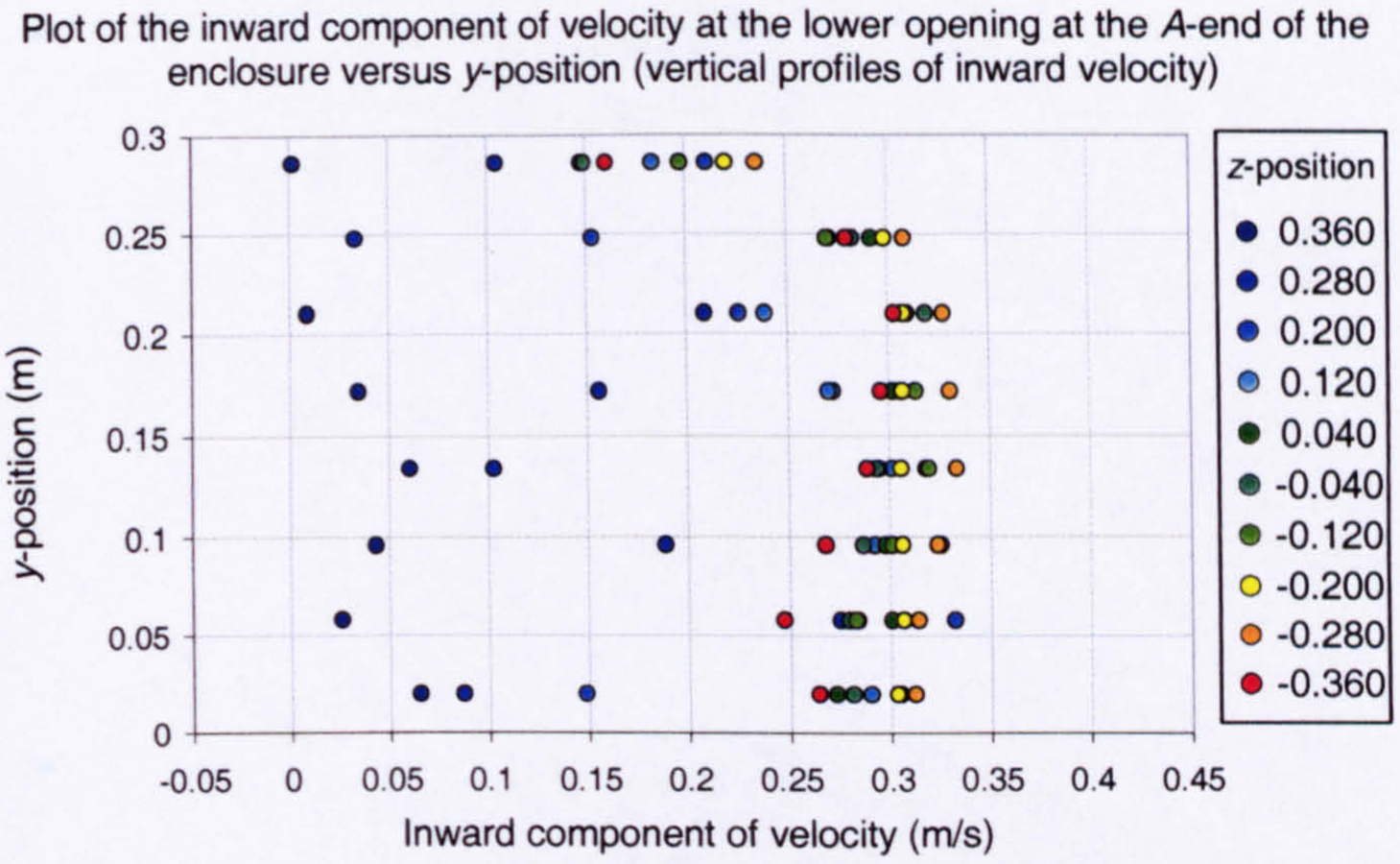

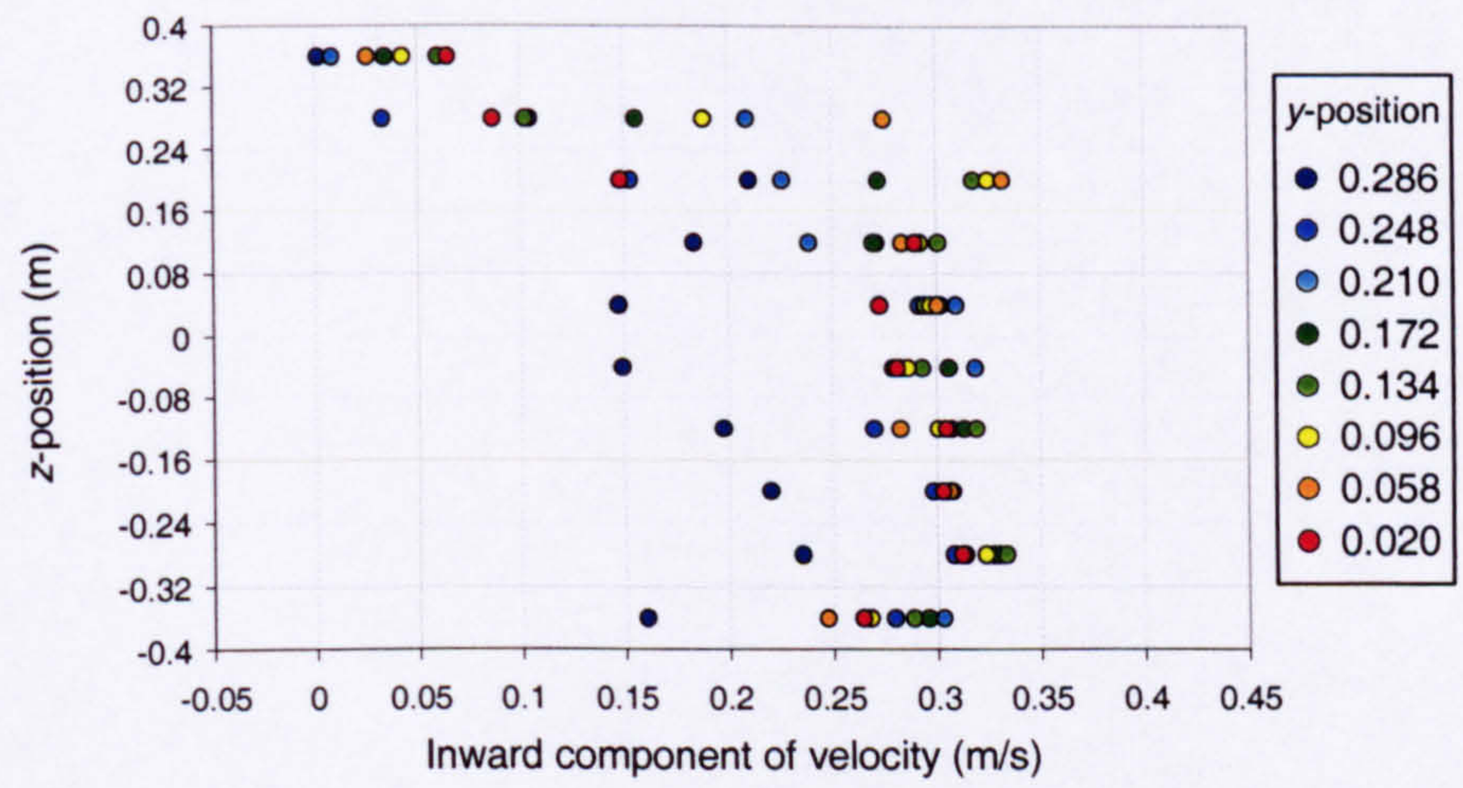

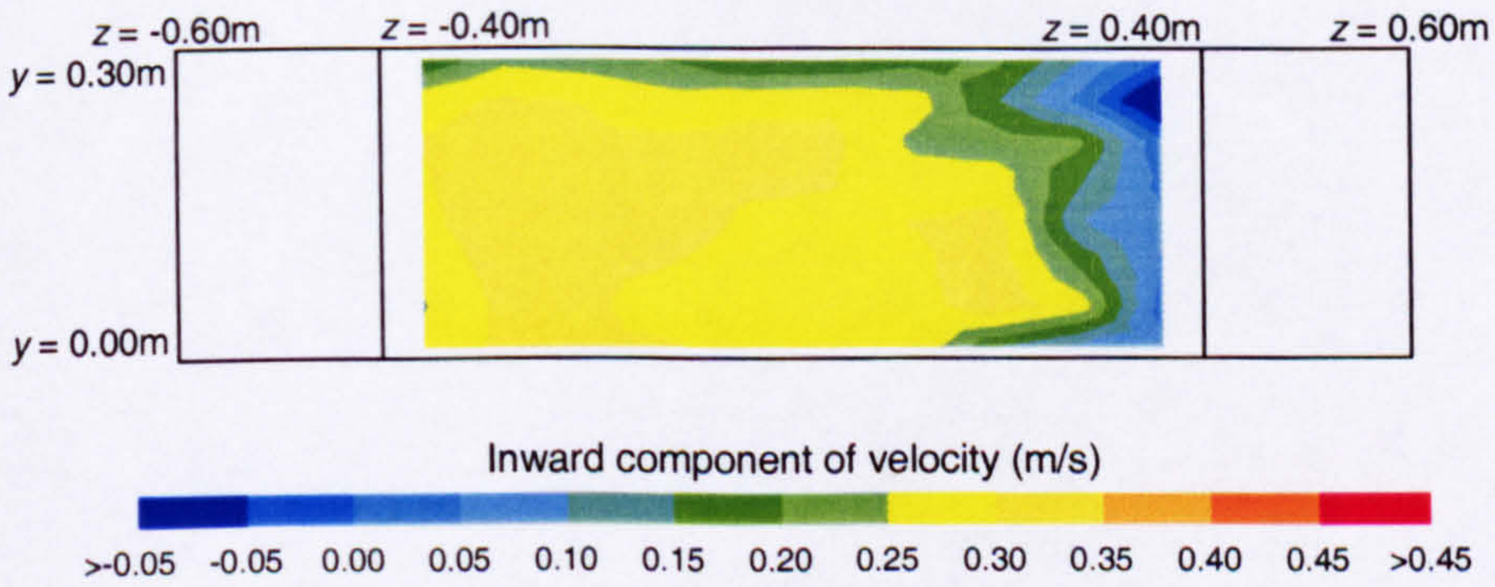

Width of opening:	0.8m
Effective area of opening:	0.488m^2
Heat source:	Boiler ring
Strength of heat source:	490.5W

Figure 16

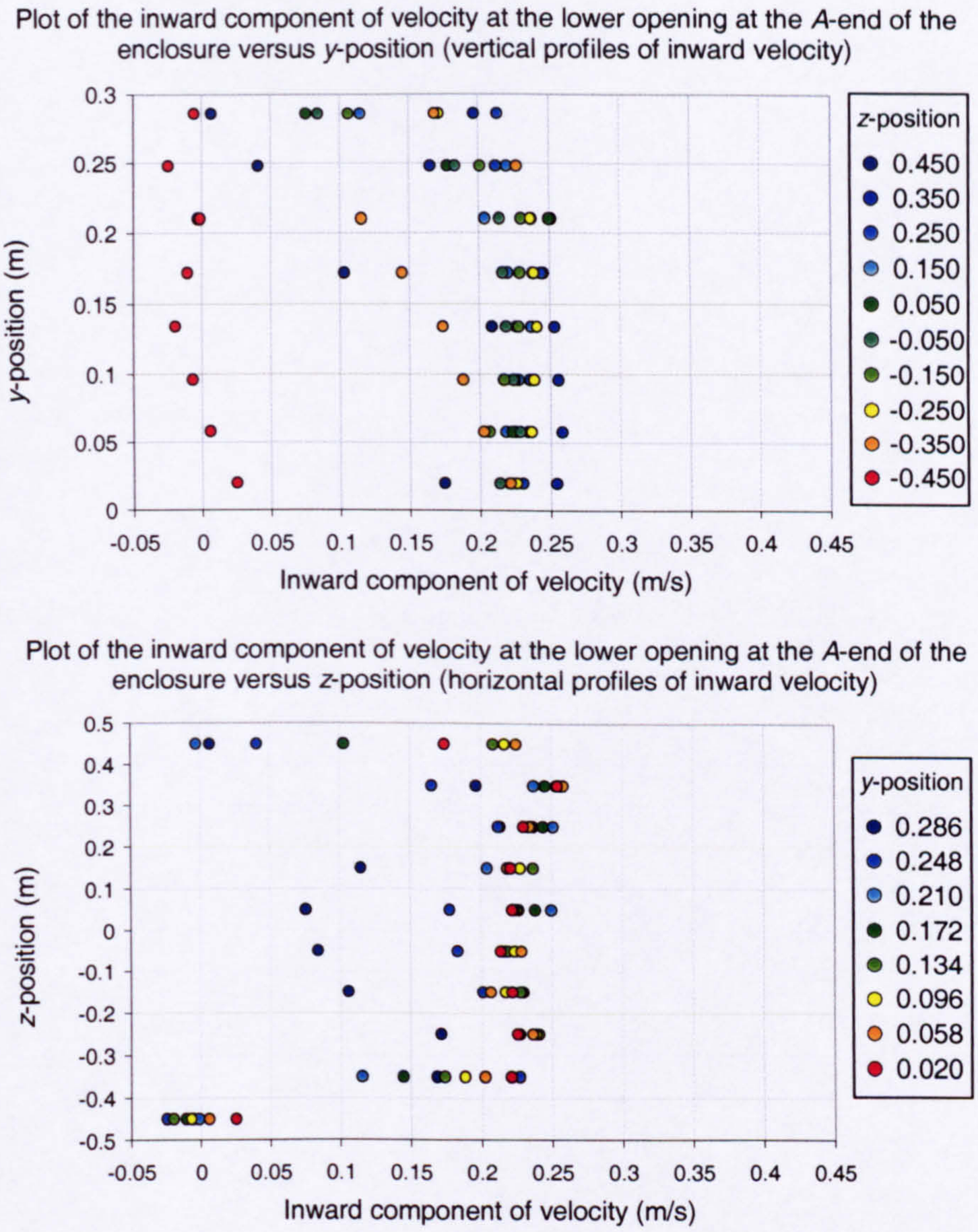

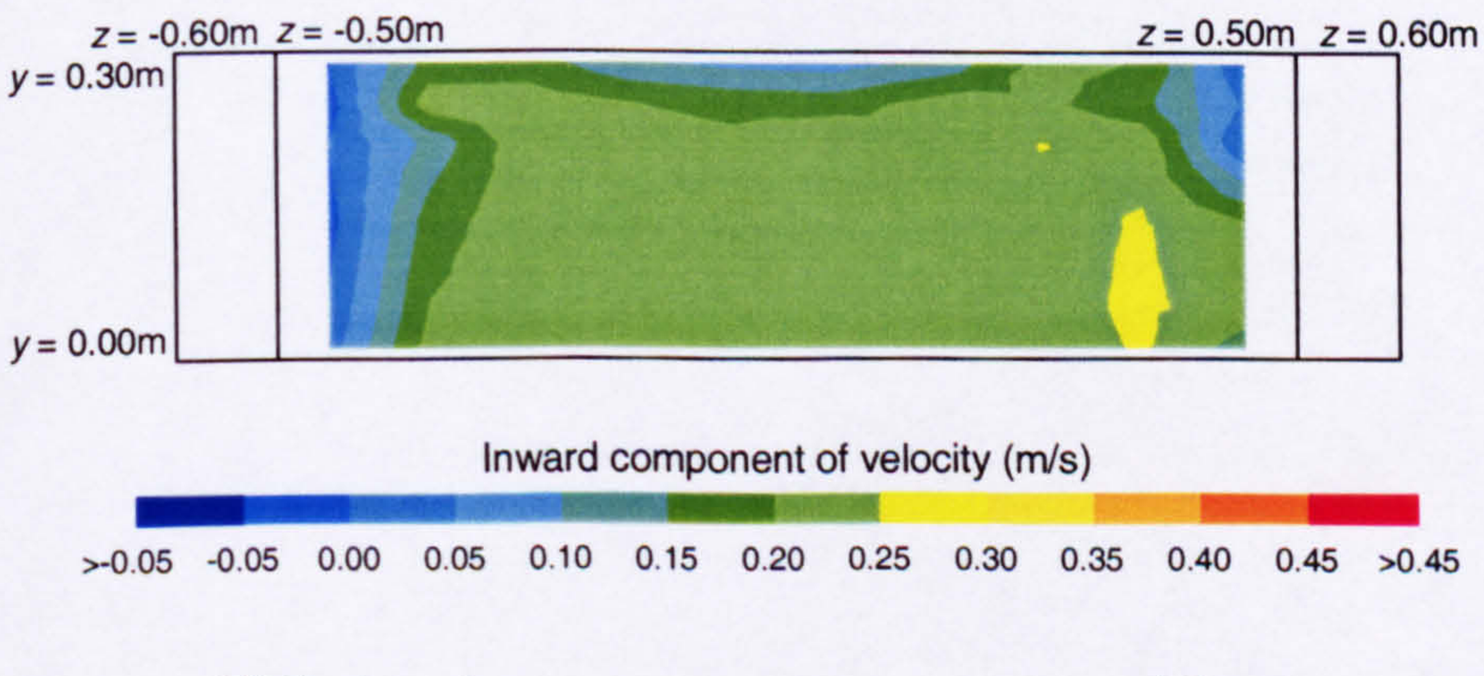

Width of opening:	1.0m
Effective area of opening:	0.610m^2
Heat source:	Boiler ring
Strength of heat source:	490.5W

Figure 17

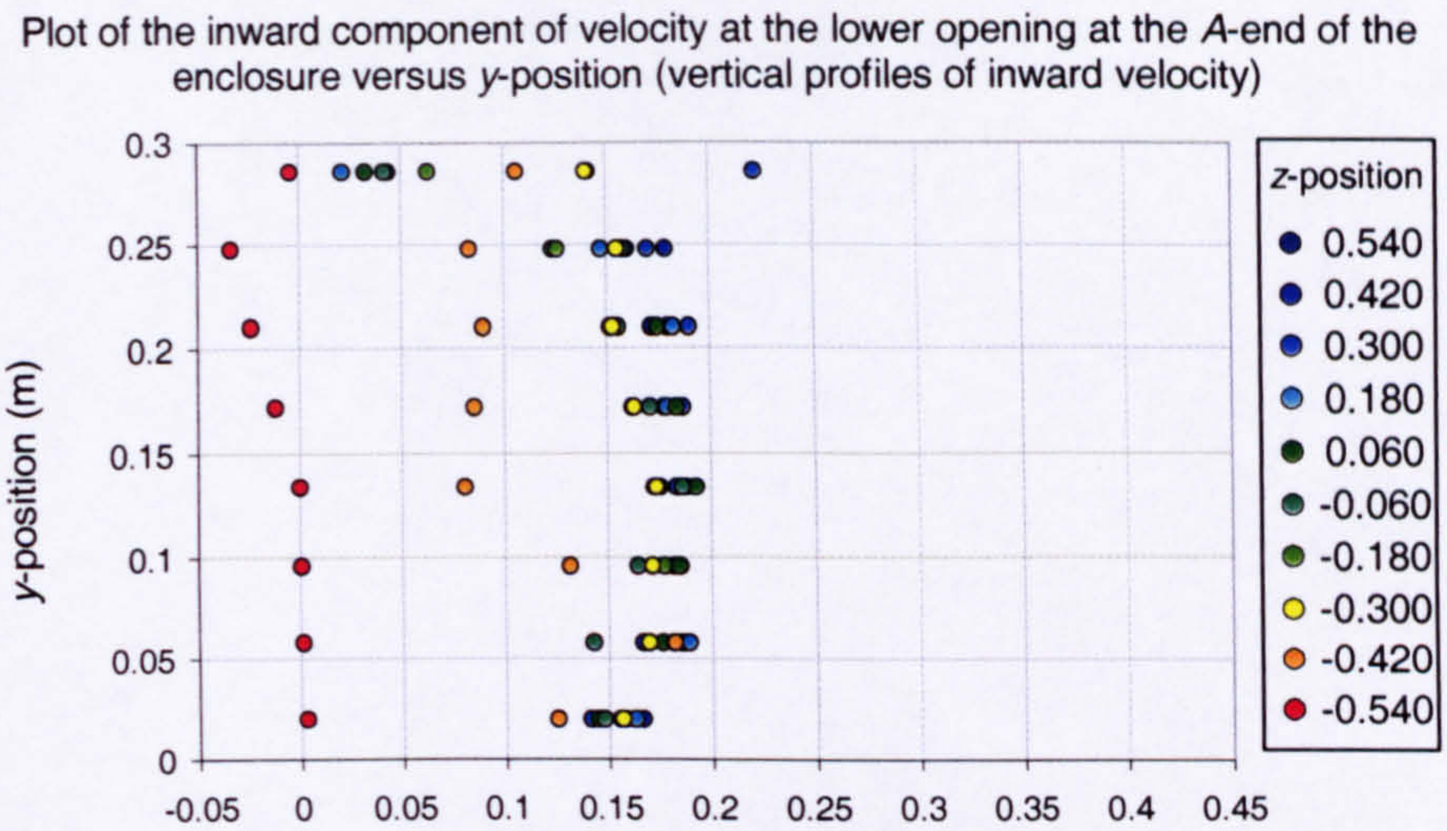

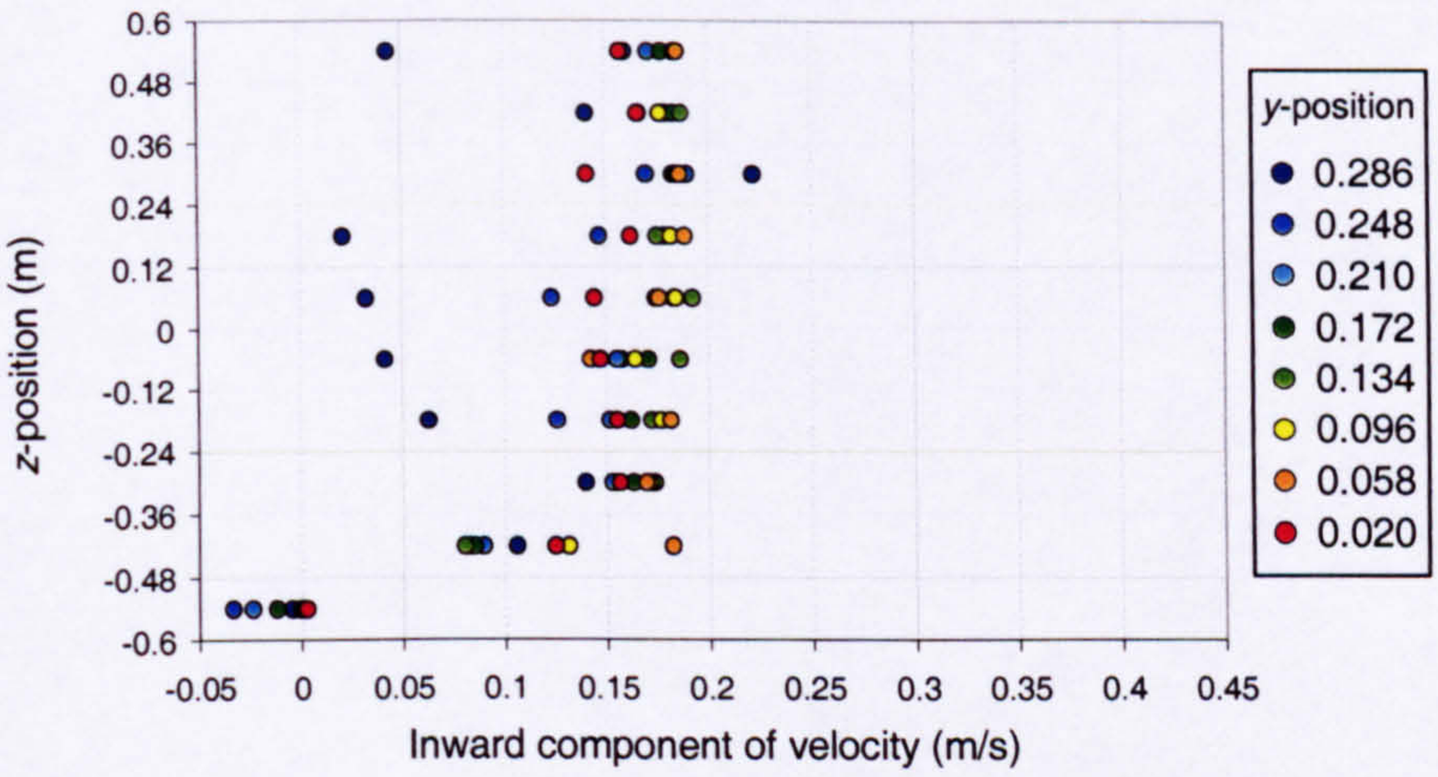

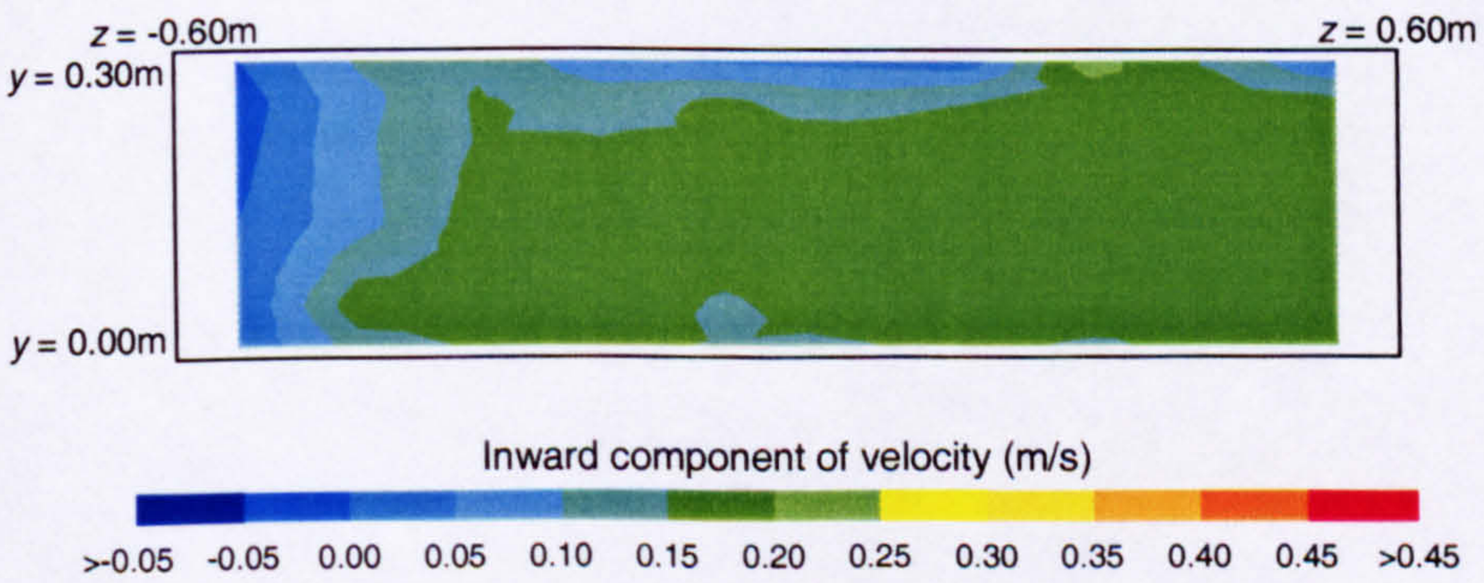

Width of opening:	1.2m
Effective area of opening:	0.732m^2
Heat source:	Boiler ring
Strength of heat source:	490.5W

Figure 18

A3 CFD-predictions for the vertical temperature profile on the *xy*-symmetry-plane within the full-scale enclosure

Table of contents

Figure	Heat source	Strength of heat source	Width of opening	Effective area of openings A*
1	Plate heater	225.0W	0.1m	0.061m^2
2	Plate heater	225.0W	0.2m	0.122m^2
3	Plate heater	225.0W	0.3m	0.183m^2
4	Plate heater	225.0W	0.4m	0.244m^2
5	Plate heater	225.0W	0.5m	0.305m^2
6	Plate heater	225.0W	0.6m	0.366m^2
7	Plate heater	225.0W	0.8m	0.488m^2
8	Plate heater	225.0W	1.0m	0.610m^2
9	Plate heater	225.0W	1.2m	0.732m^2
10	Boiler ring	368.0W	0.1m	0.061m^2
11	Boiler ring	368.0W	0.2m	0.122m^2
12	Boiler ring	368.0W	0.3m	0.183m^2
13	Boiler ring	368.0W	0.4m	0.244m^2
14	Boiler ring	368.0W	0.5m	0.305m^2
15	Boiler ring	368.0W	0.6m	0.366m^2
16	Boiler ring	368.0W	0.8m	0.488m^2
17	Boiler ring	368.0W	1.0m	0.610m^2
18	Boiler ring	368.0W	1.2m	0.732m^2
19	Boiler ring	490.5W	0.1m	0.061m^2
20	Boiler ring	490.5W	0.2m	0.122m^2
21	Boiler ring	490.5W	0.3m	0.183m^2
22	Boiler ring	490.5W	0.4m	0.244m^2
23	Boiler ring	490.5W	0.5m	0.305m^2
24	Boiler ring	490.5W	0.6m	0.366m^2
25	Boiler ring	490.5W	0.8m	0.488m^2

Figure	Heat source	Strength of heat source	Width of opening	Effective area of openings A*
26	Boiler ring	490.5W	1.0m	0.610m^2
27	Boiler ring	490.5W	1.2m	0.732m^2

	Laminar	Standard-$k\varepsilon$	Realizable-$k\varepsilon$	RNG-$k\varepsilon$
Radiation model disabled. Upwind differencing. Adiabatic walls. Uniform external temperature.	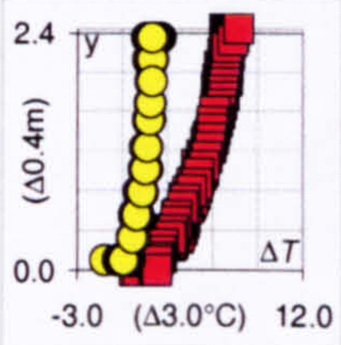	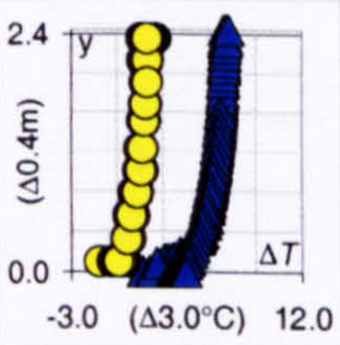	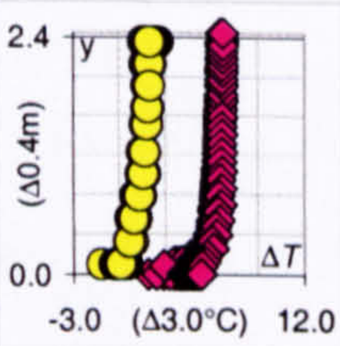	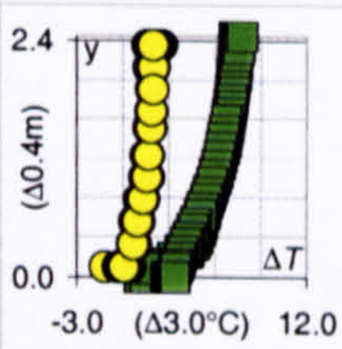
Radiation model disabled. QUICK differencing. Adiabatic walls. Uniform external temperature.	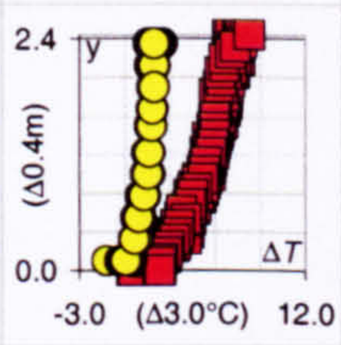	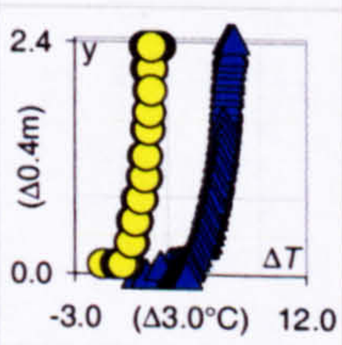	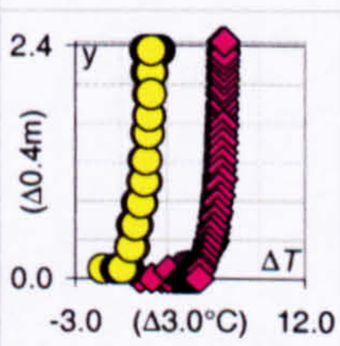	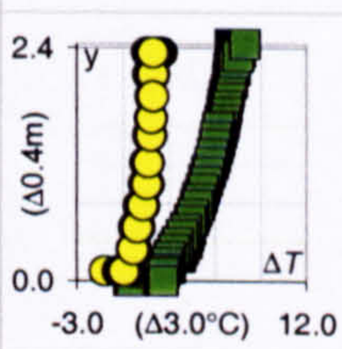
Radiation model enabled, $\alpha = 0.00m^{-1}$ QUICK differencing. Adiabatic walls. Uniform external temperature.	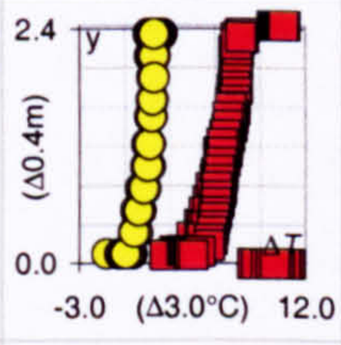	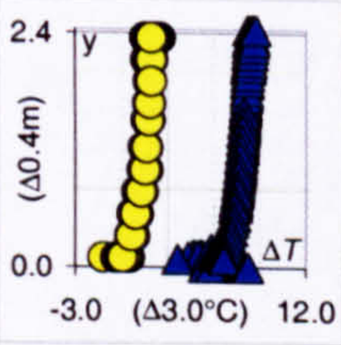	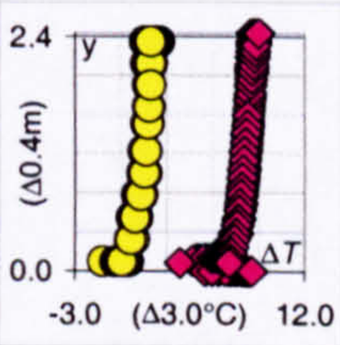	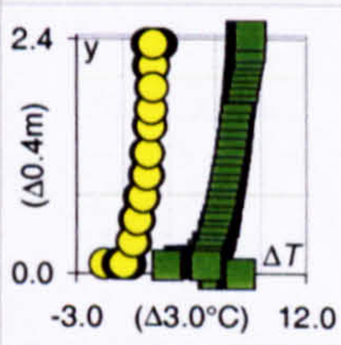
Radiation model enabled, $\alpha = 0.05m^{-1}$ QUICK differencing. Adiabatic walls. Uniform external temperature.	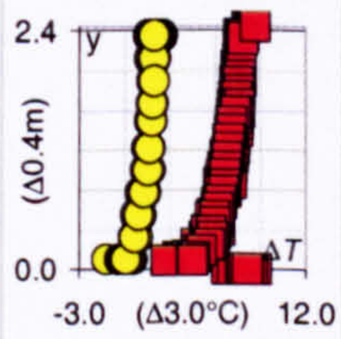	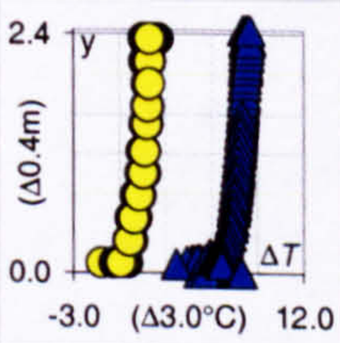	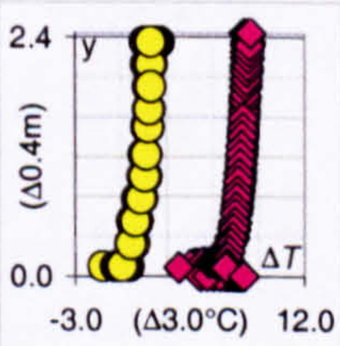	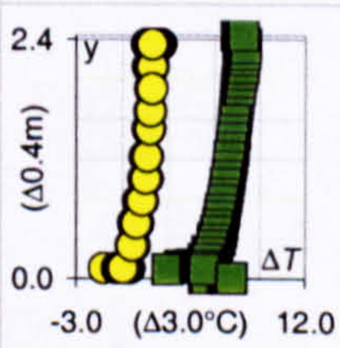
Radiation model enabled, $\alpha = 0.10m^{-1}$ QUICK differencing. Adiabatic walls. Uniform external temperature.	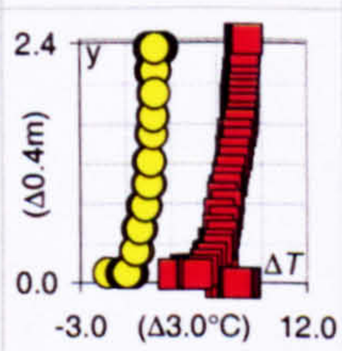	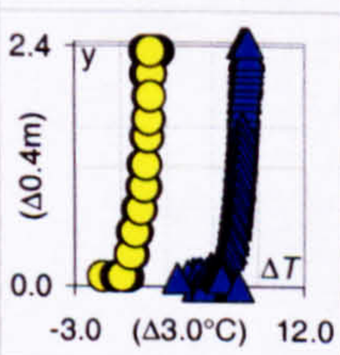	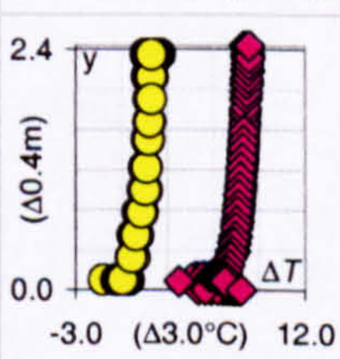	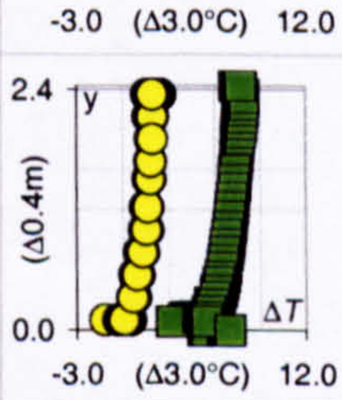
Radiation model enabled, $\alpha = 0.15m^{-1}$ QUICK differencing. Adiabatic walls. Uniform external temperature.	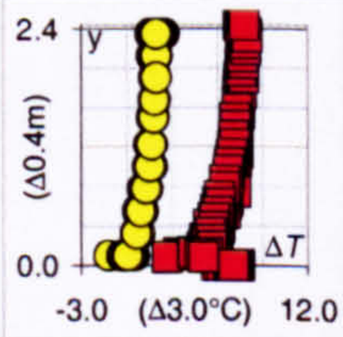	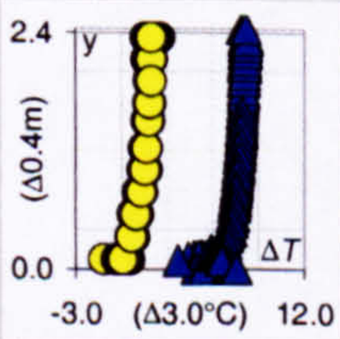	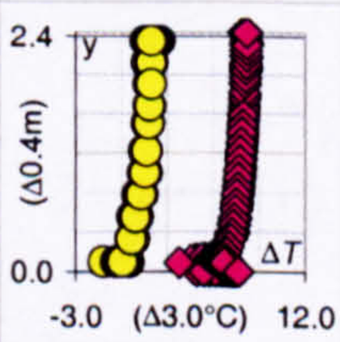	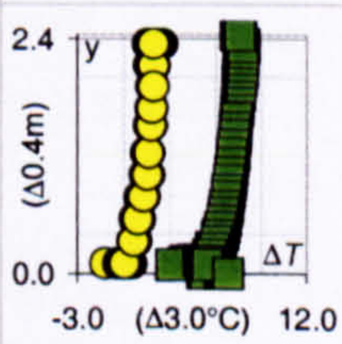

Width of opening: 0.1m
Effective area of opening: 0.061m^2
Heat source: Plate heater
Strength of heat source: 225.0W

Figure 1.a

	Laminar	Standard-$k\varepsilon$	Realizable-$k\varepsilon$	RNG-$k\varepsilon$
Radiation model enabled, $\alpha = 0.00m^{-1}$ QUICK differencing. Convection walls. Uniform external temperature.	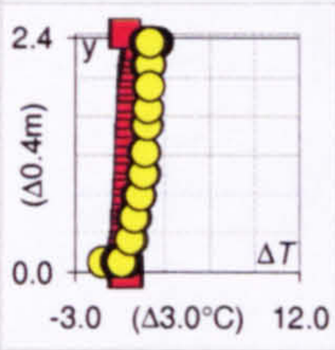	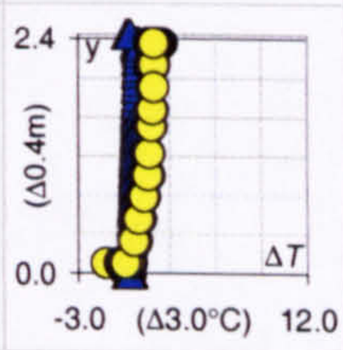	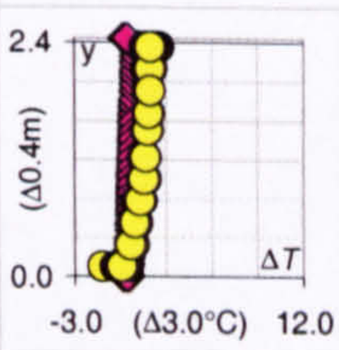	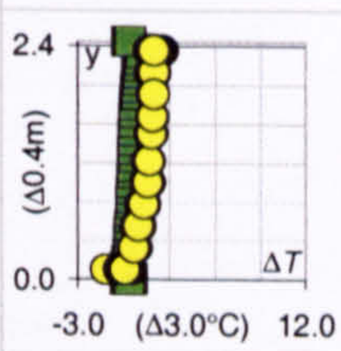
Radiation model enabled, $\alpha = 0.00m^{-1}$ QUICK differencing. Radiation walls. Uniform external temperature.	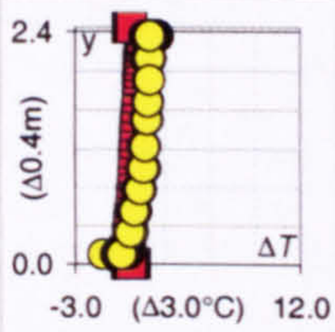	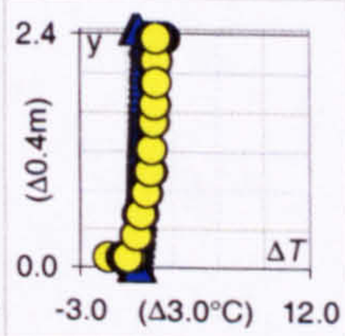	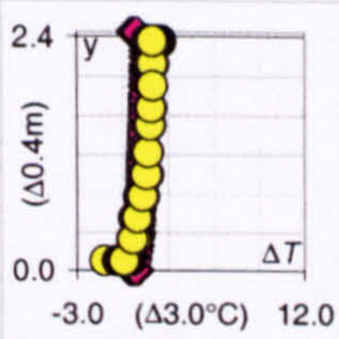	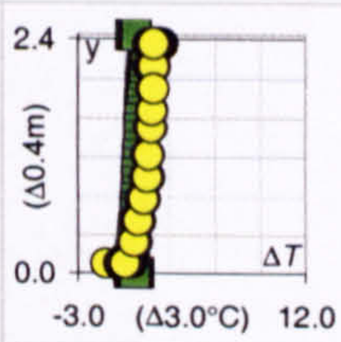
Radiation model enabled, $\alpha = 0.00m^{-1}$ QUICK differencing. Mixed walls. Uniform external temperature.	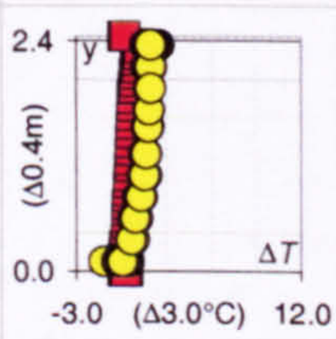	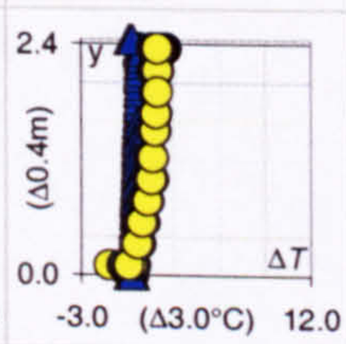	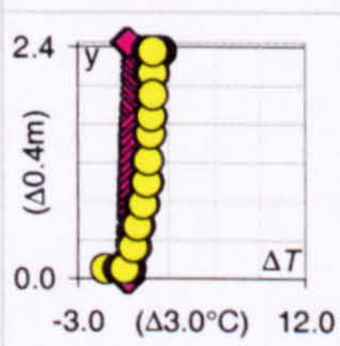	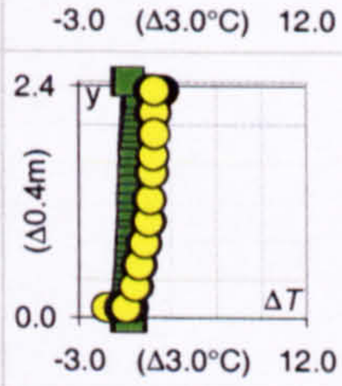
Radiation model enabled, $\alpha = 0.05m^{-1}$ QUICK differencing. Convection walls. Uniform external temperature.	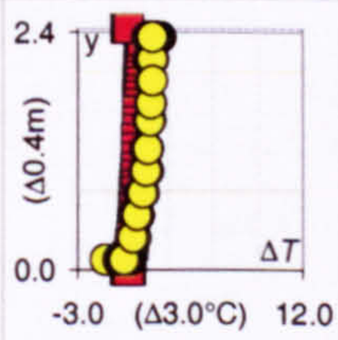	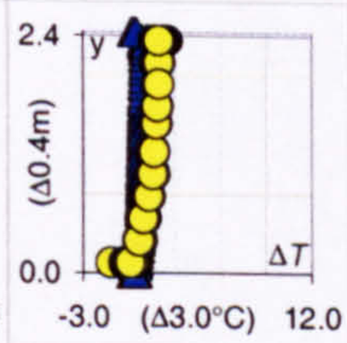	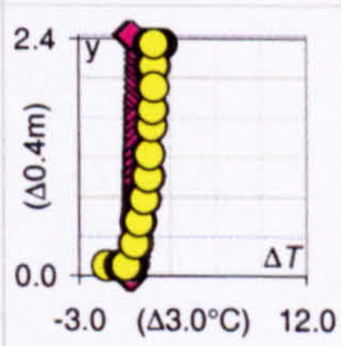	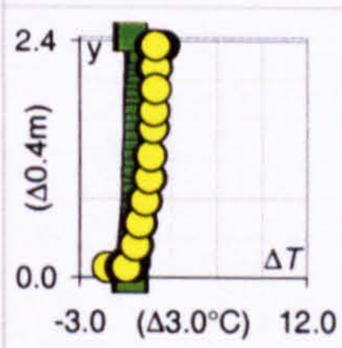
Radiation model enabled, $\alpha = 0.05m^{-1}$ QUICK differencing. Radiation walls. Uniform external temperature.	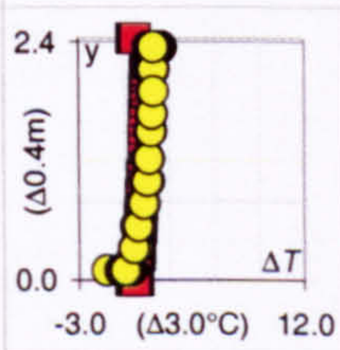	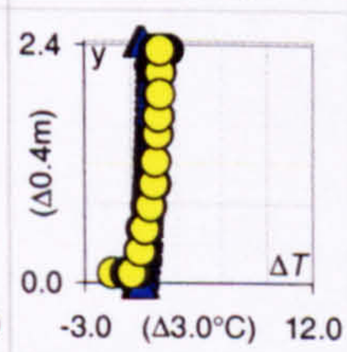	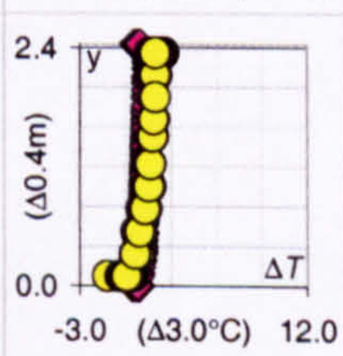	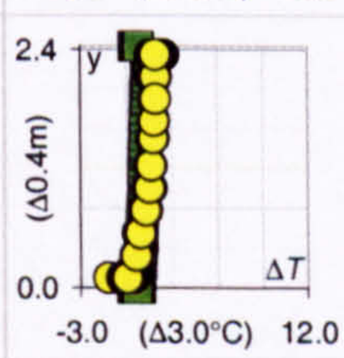
Radiation model enabled, $\alpha = 0.05m^{-1}$ QUICK differencing. Mixed walls. Uniform external temperature.	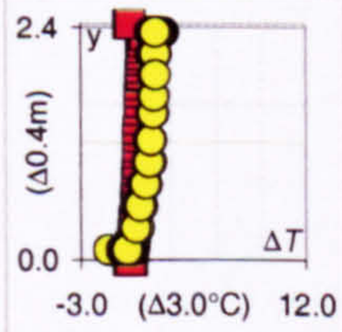	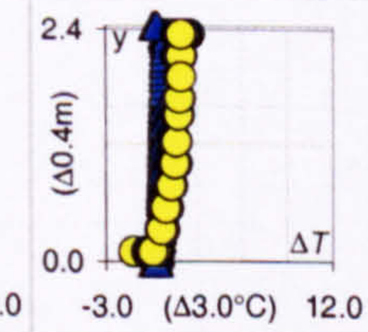	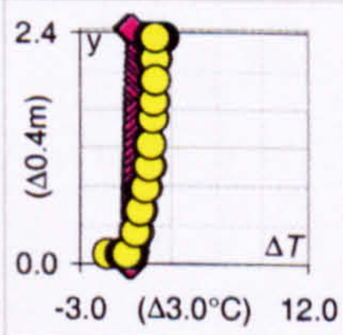	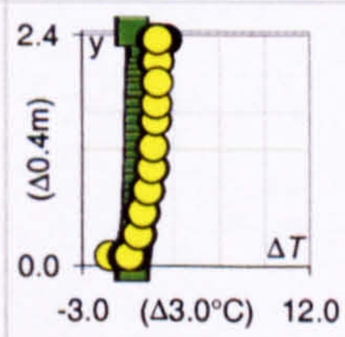

Width of opening: 0.1m
Effective area of opening: $0.061m^2$
Heat source: Plate heater
Strength of heat source: 225.0W

Figure 1.b

	Laminar	Standard-$k\varepsilon$	Realizable-$k\varepsilon$	RNG-$k\varepsilon$
Radiation model disabled. Upwind differencing. Adiabatic walls. Uniform external temperature.	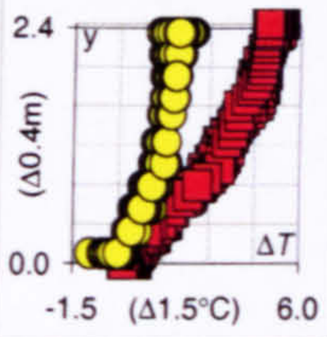	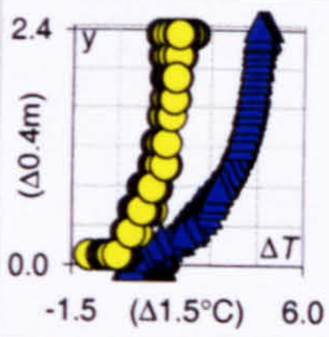	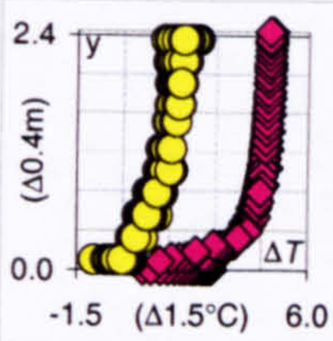	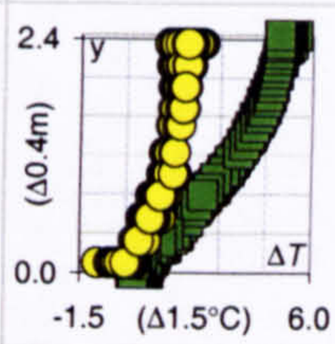
Radiation model disabled. QUICK differencing. Adiabatic walls. Uniform external temperature.	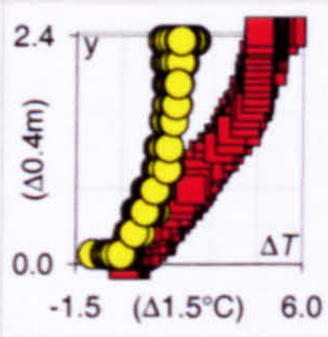	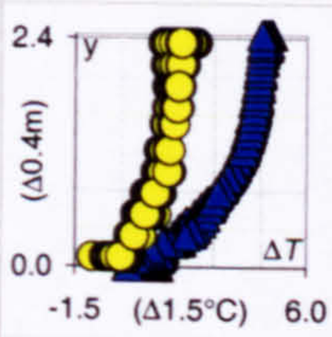	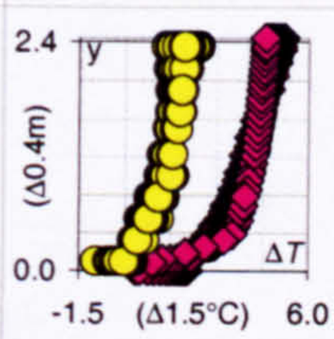	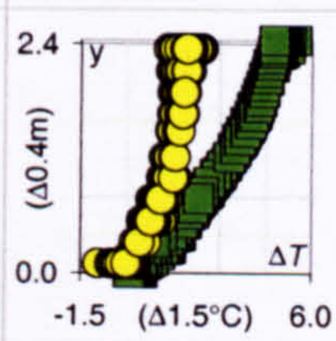
Radiation model enabled, $\alpha = 0.00m^{-1}$ QUICK differencing. Adiabatic walls. Uniform external temperature.	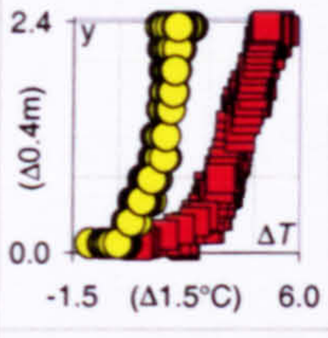	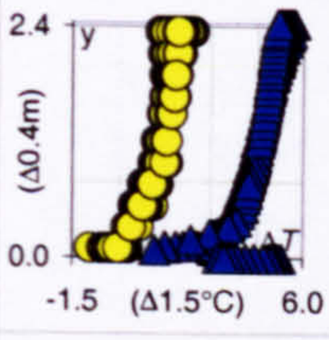	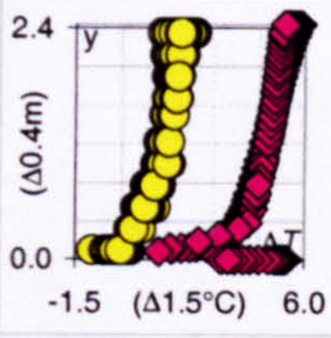	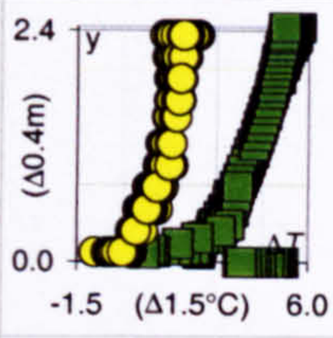
Radiation model enabled, $\alpha = 0.05m^{-1}$ QUICK differencing. Adiabatic walls. Uniform external temperature.	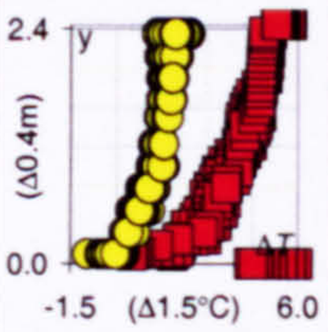	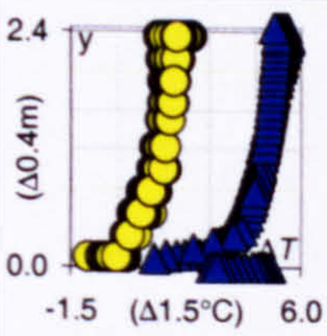	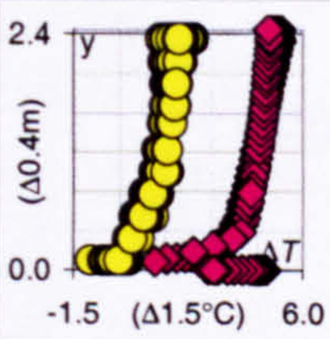	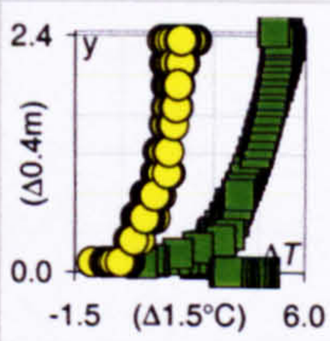
Radiation model enabled, $\alpha = 0.10m^{-1}$ QUICK differencing. Adiabatic walls. Uniform external temperature.	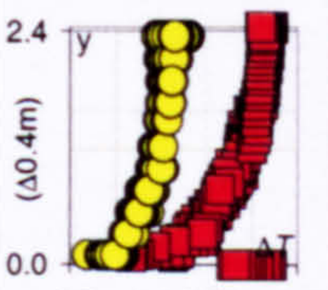	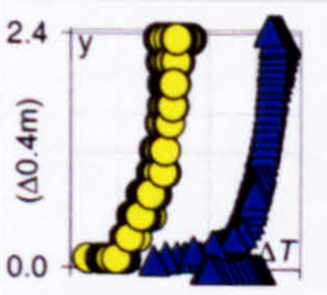	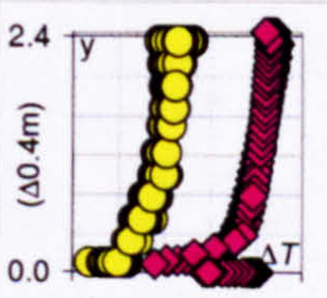	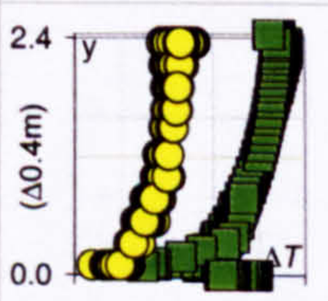
Radiation model enabled, $\alpha = 0.15m^{-1}$ QUICK differencing. Adiabatic walls. Uniform external temperature.	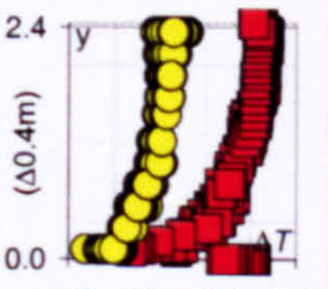	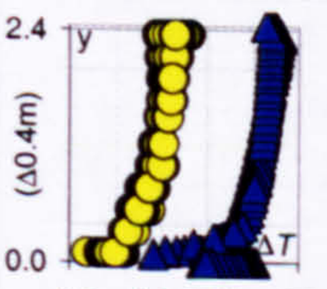	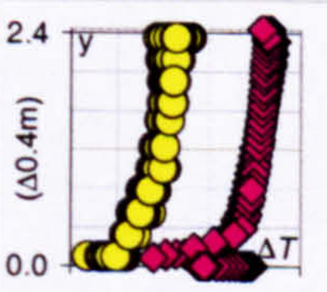	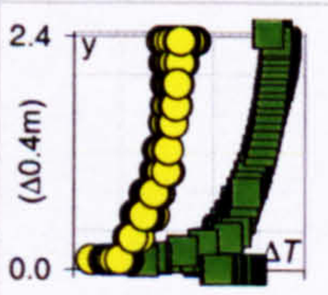

Width of opening: 0.2m
Effective area of opening: $0.122m^2$
Heat source: Plate heater
Strength of heat source: 225.0W

Figure 2.a

	Laminar	Standard-$k\varepsilon$	Realizable-$k\varepsilon$	RNG-$k\varepsilon$
Radiation model enabled, $\alpha = 0.00m^{-1}$ QUICK differencing. Convection walls. Uniform external temperature.	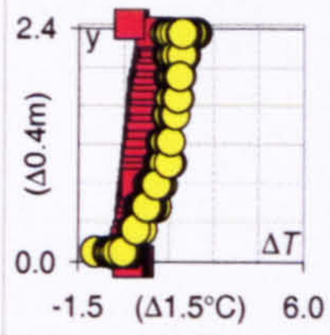	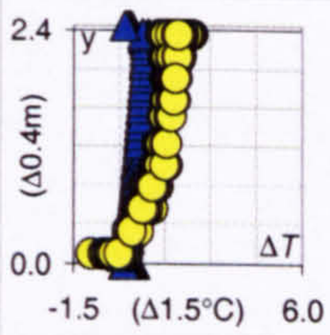	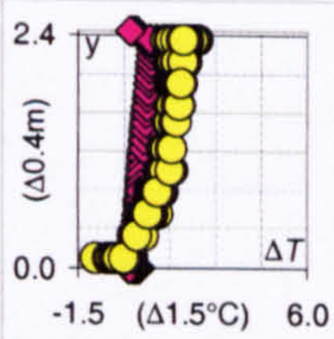	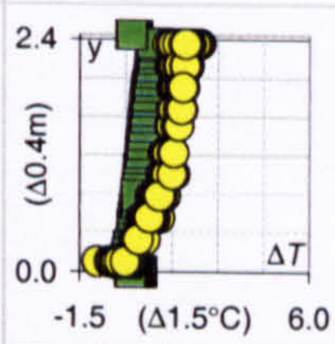
Radiation model enabled, $\alpha = 0.00m^{-1}$ QUICK differencing. Radiation walls. Uniform external temperature.	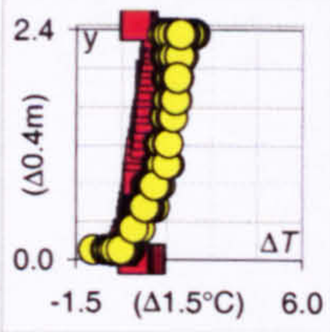	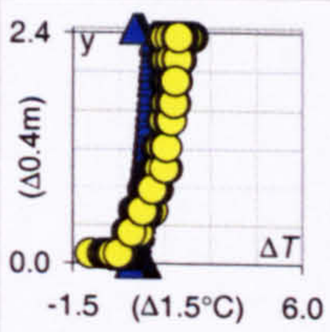	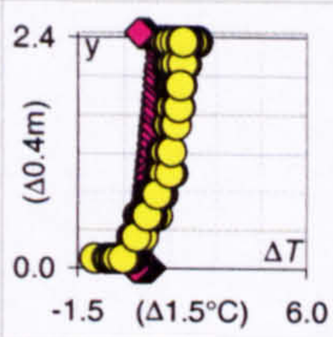	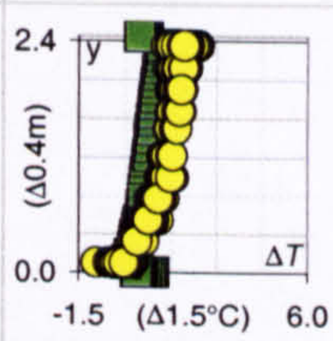
Radiation model enabled, $\alpha = 0.00m^{-1}$ QUICK differencing. Mixed walls. Uniform external temperature.	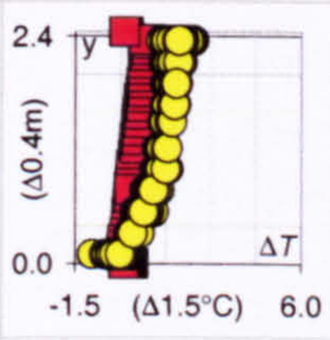	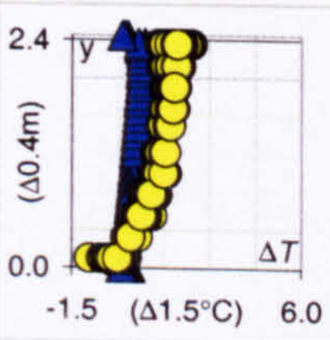	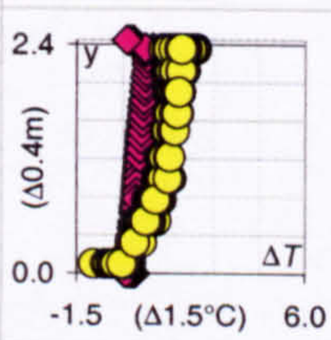	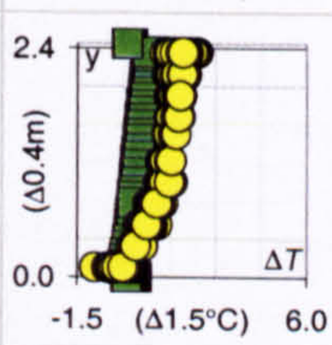
Radiation model enabled, $\alpha = 0.05m^{-1}$ QUICK differencing. Convection walls. Uniform external temperature.	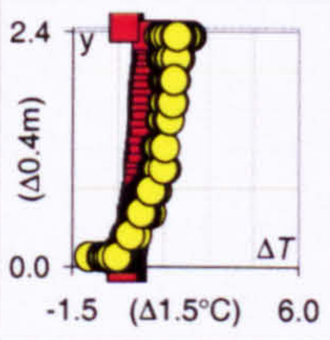	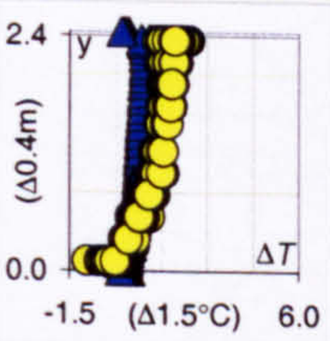	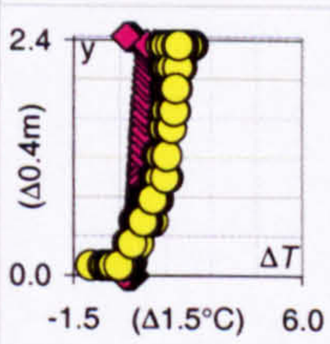	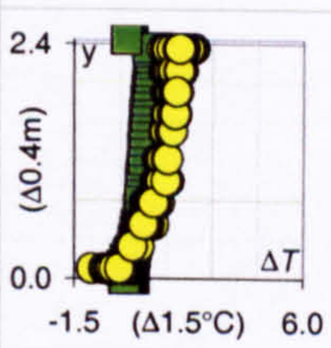
Radiation model enabled, $\alpha = 0.05m^{-1}$ QUICK differencing. Radiation walls. Uniform external temperature.	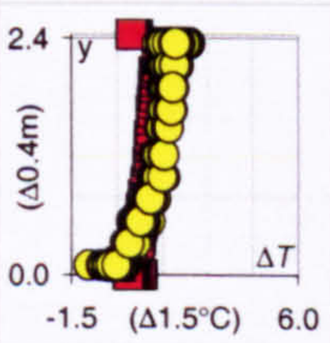	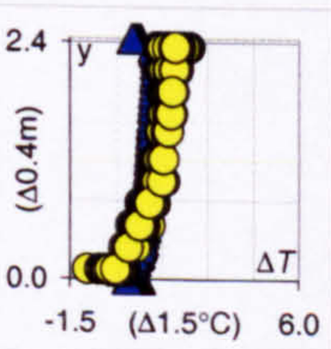	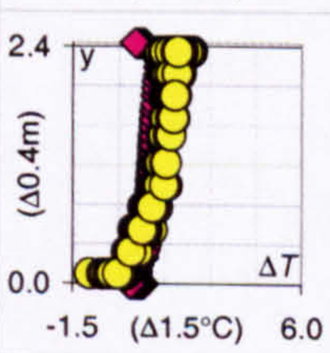	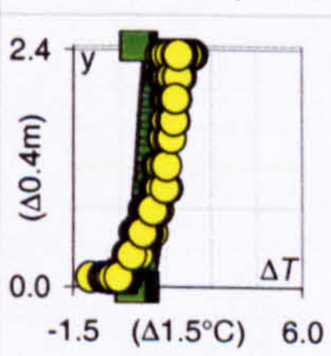
Radiation model enabled, $\alpha = 0.05m^{-1}$ QUICK differencing. Mixed walls. Uniform external temperature.	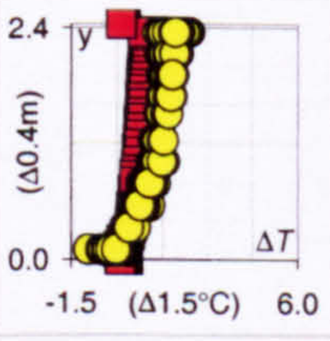	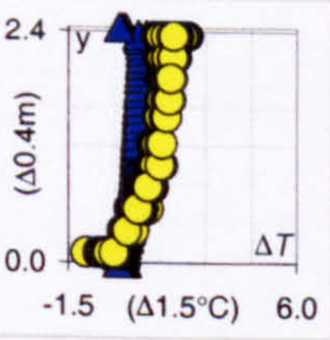	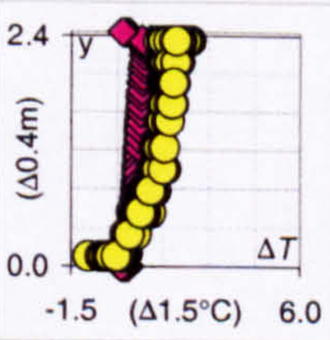	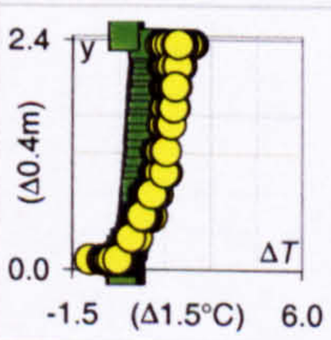

Width of opening:	0.2m
Effective area of opening:	$0.122m^2$
Heat source:	Plate heater
Strength of heat source:	225.0W

Figure 2.b

	Laminar	Standard-$k\varepsilon$	Realizable-$k\varepsilon$	RNG-$k\varepsilon$
Radiation model disabled. Upwind differencing. Adiabatic walls. Uniform external temperature.	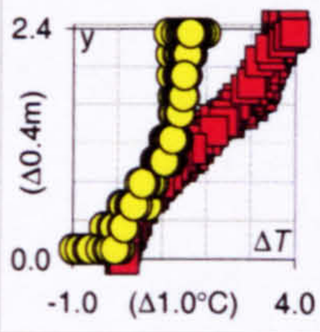	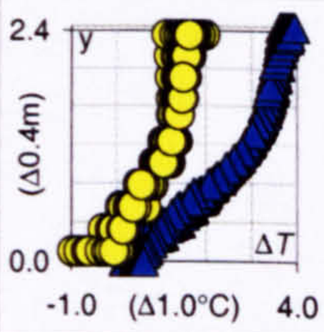	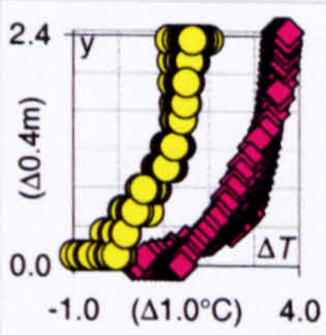	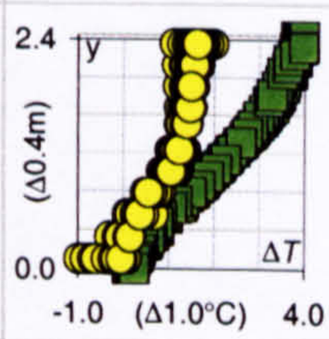
Radiation model disabled. QUICK differencing. Adiabatic walls. Uniform external temperature.	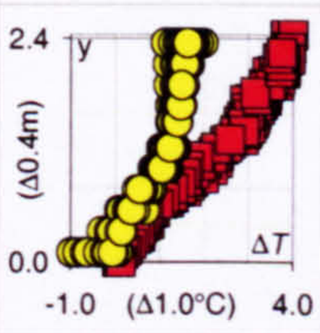	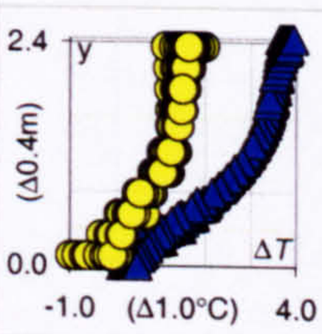	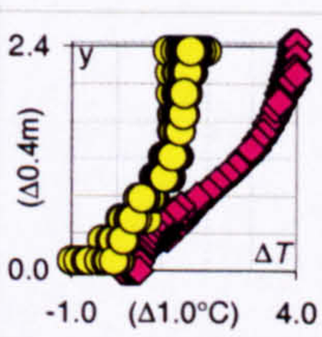	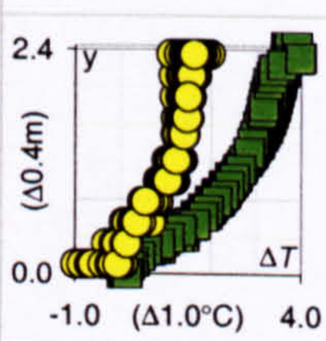
Radiation model enabled, $\alpha = 0.00m^{-1}$ QUICK differencing. Adiabatic walls. Uniform external temperature.	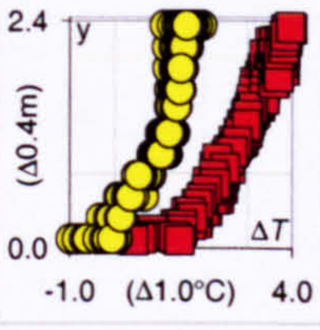	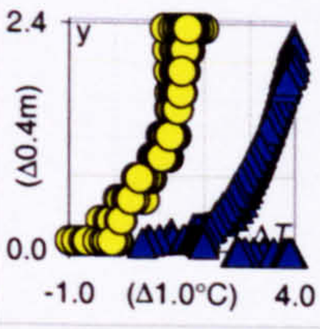	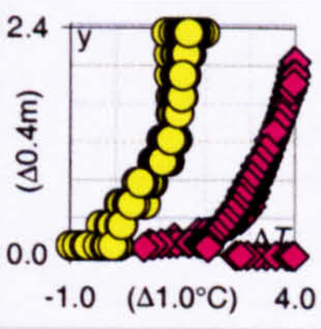	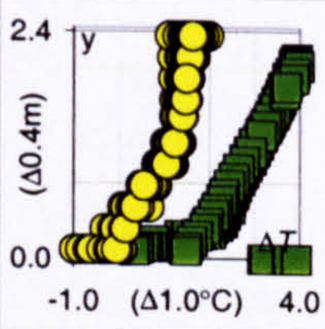
Radiation model enabled, $\alpha = 0.05m^{-1}$ QUICK differencing. Adiabatic walls. Uniform external temperature.	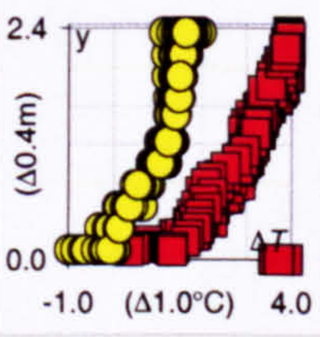	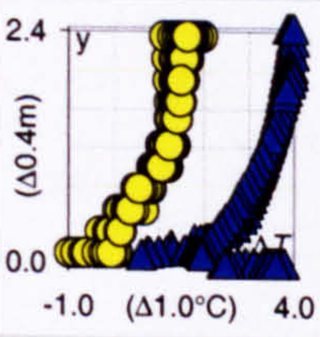	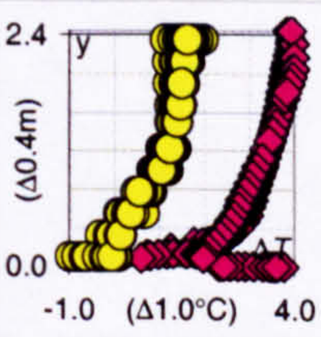	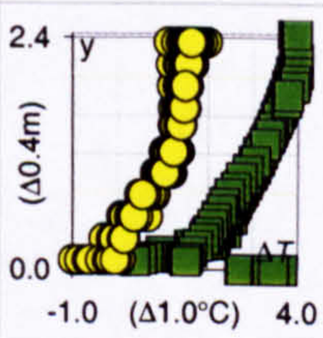
Radiation model enabled, $\alpha = 0.10m^{-1}$ QUICK differencing. Adiabatic walls. Uniform external temperature.	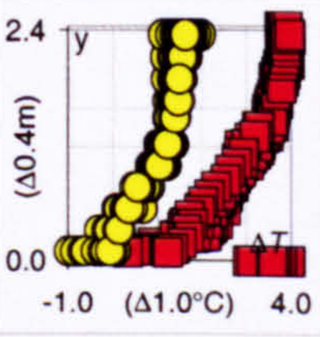	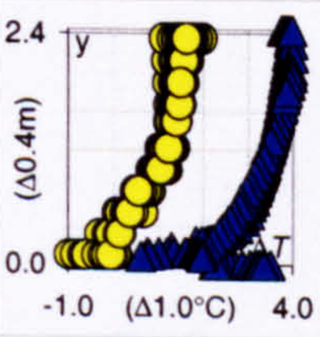	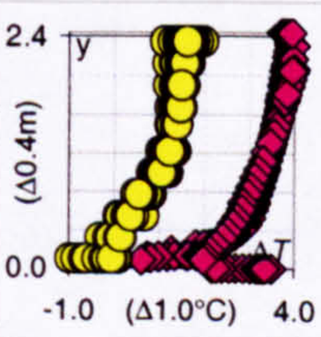	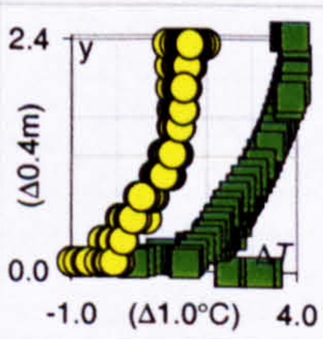
Radiation model enabled, $\alpha = 0.15m^{-1}$ QUICK differencing. Adiabatic walls. Uniform external temperature.	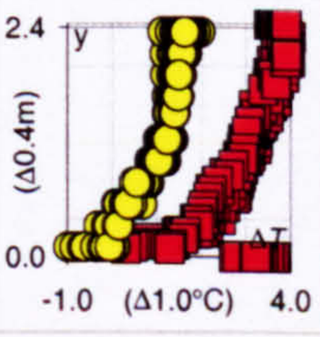	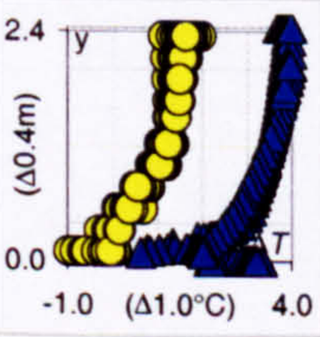	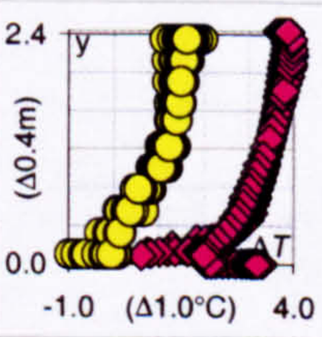	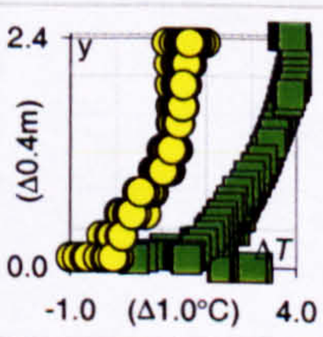

Width of opening:	0.3m
Effective area of opening:	$0.183m^2$
Heat source:	Plate heater
Strength of heat source:	225.0W

Figure 3.a

	Laminar	Standard-$k\varepsilon$	Realizable-$k\varepsilon$	RNG-$k\varepsilon$
Radiation model enabled, $\alpha = 0.00m^{-1}$ QUICK differencing. Convection walls. Uniform external temperature.	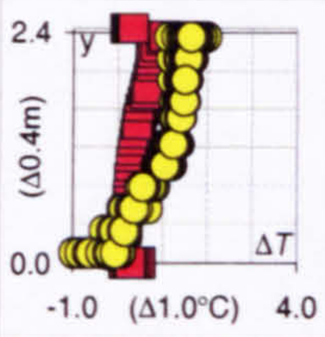	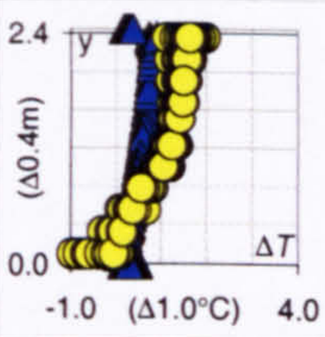	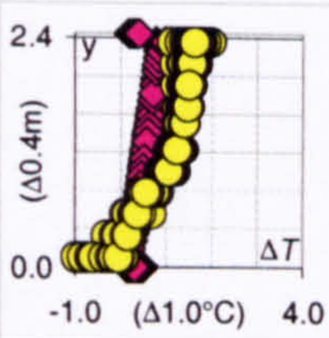	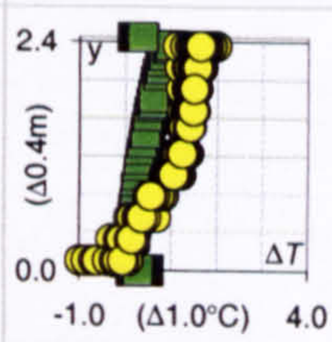
Radiation model enabled, $\alpha = 0.00m^{-1}$ QUICK differencing. Radiation walls. Uniform external temperature.	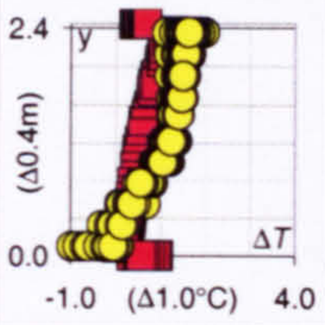	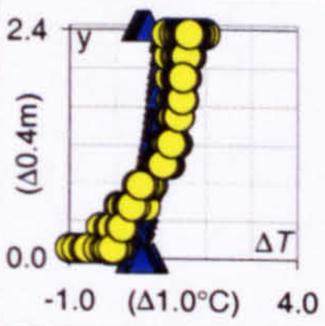	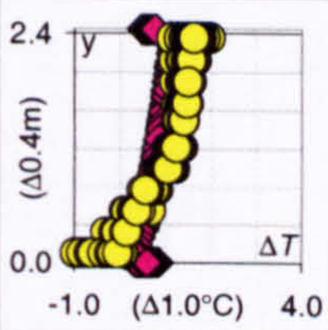	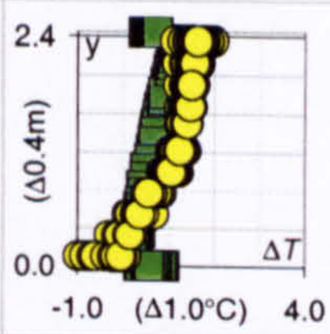
Radiation model enabled, $\alpha = 0.00m^{-1}$ QUICK differencing. Mixed walls. Uniform external temperature.	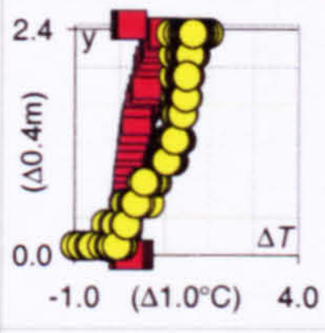	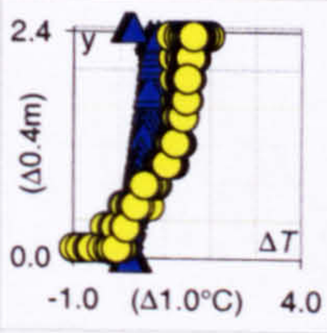	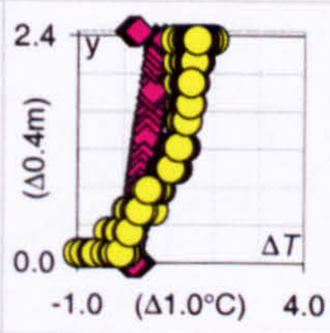	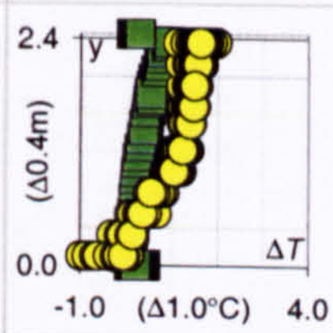
Radiation model enabled, $\alpha = 0.05m^{-1}$ QUICK differencing. Convection walls. Uniform external temperature.	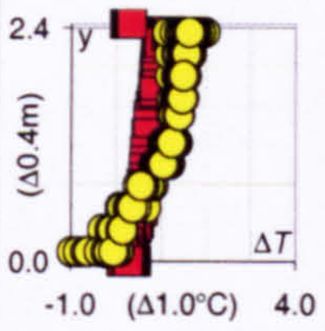	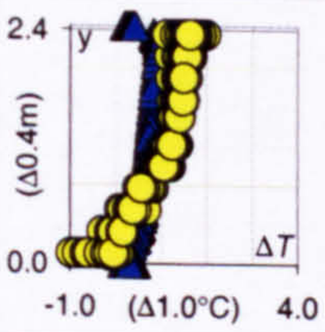	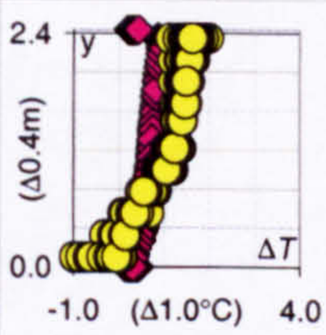	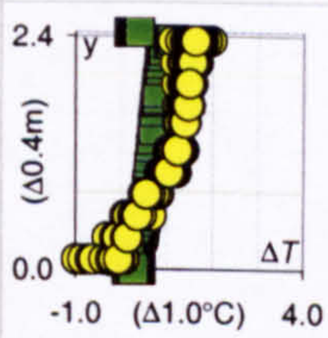
Radiation model enabled, $\alpha = 0.05m^{-1}$ QUICK differencing. Radiation walls. Uniform external temperature.	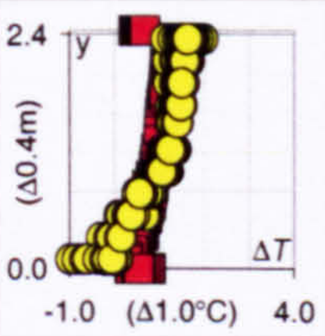	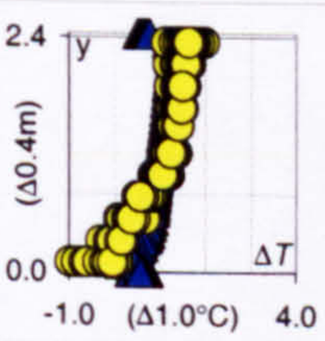	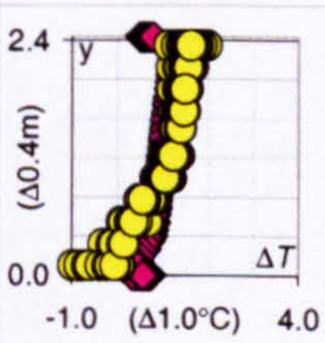	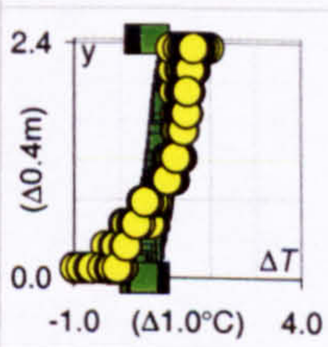
Radiation model enabled, $\alpha = 0.05m^{-1}$ QUICK differencing. Mixed walls. Uniform external temperature.	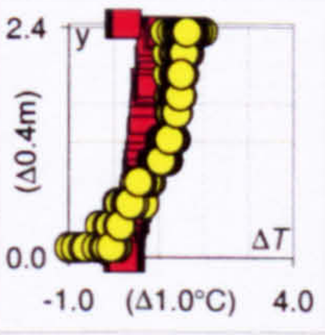	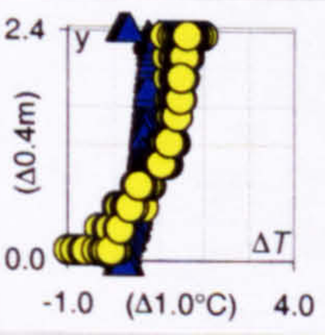	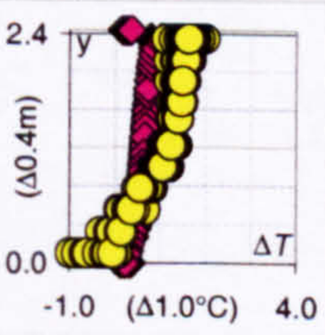	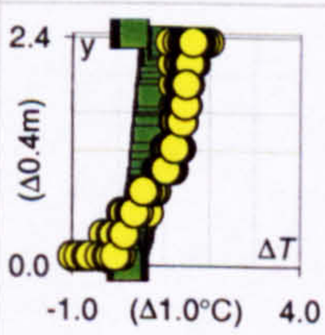

Width of opening:	0.3m
Effective area of opening:	$0.183m^2$
Heat source:	Plate heater
Strength of heat source:	225.0W

Figure 3.b

	Laminar	Standard-$k\varepsilon$	Realizable-$k\varepsilon$	RNG-$k\varepsilon$
Radiation model disabled. Upwind differencing. Adiabatic walls. Uniform external temperature.	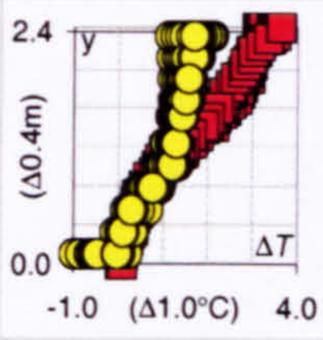	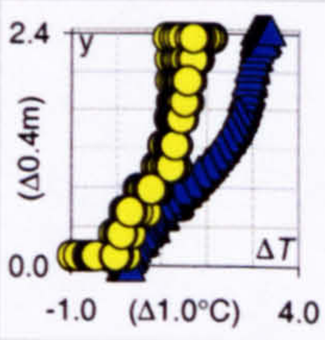	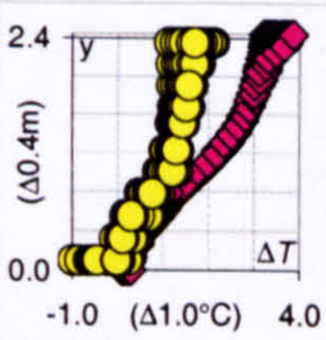	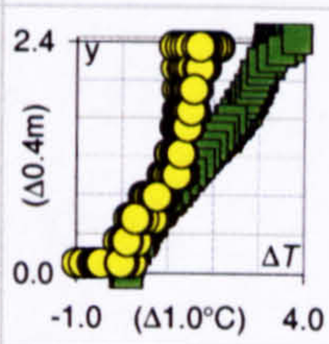
Radiation model disabled. QUICK differencing. Adiabatic walls. Uniform external temperature.	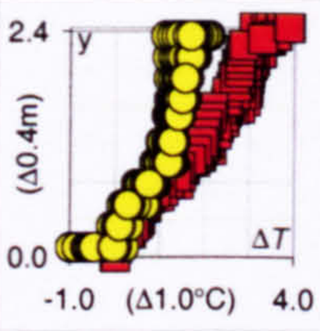	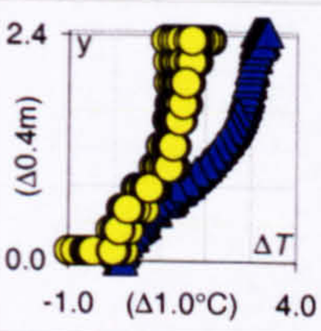	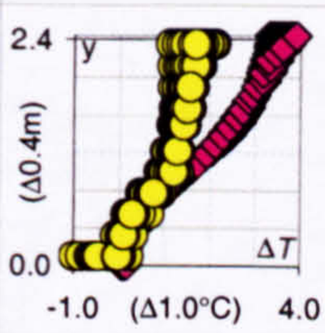	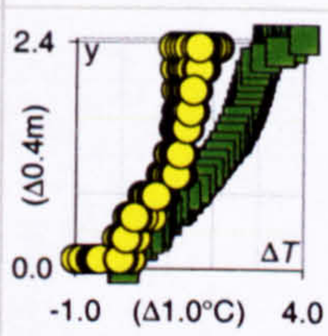
Radiation model enabled, $\alpha = 0.00m^{-1}$ QUICK differencing. Adiabatic walls. Uniform external temperature.	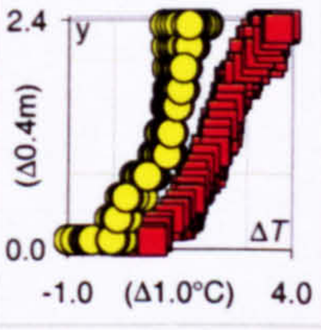	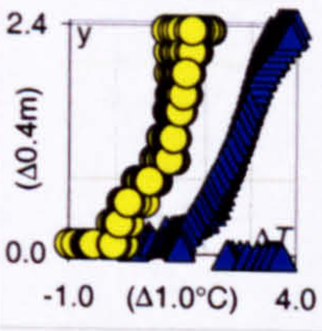	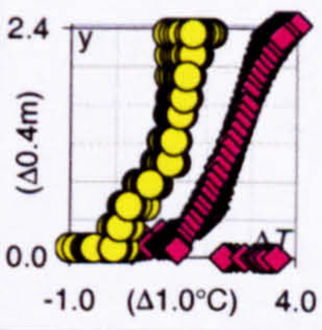	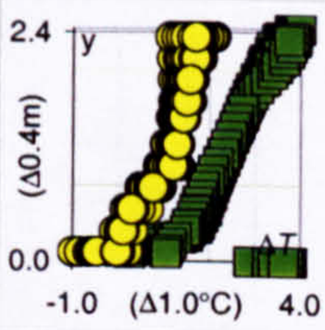
Radiation model enabled, $\alpha = 0.05m^{-1}$ QUICK differencing. Adiabatic walls. Uniform external temperature.	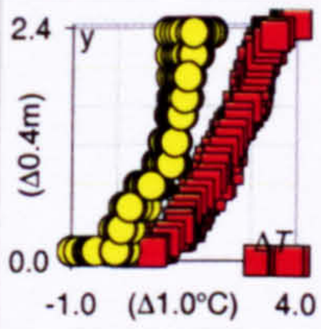	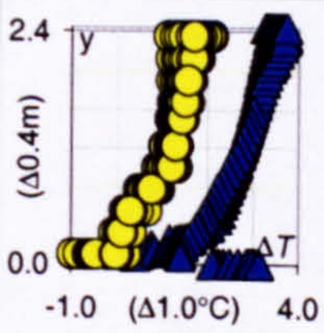	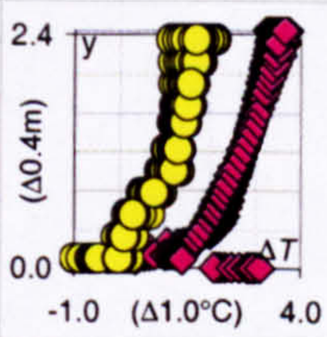	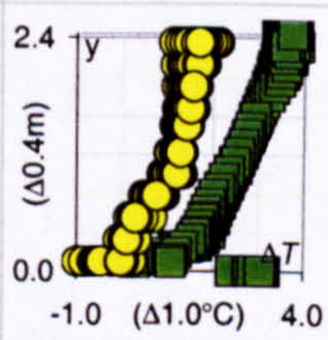
Radiation model enabled, $\alpha = 0.10m^{-1}$ QUICK differencing. Adiabatic walls. Uniform external temperature.	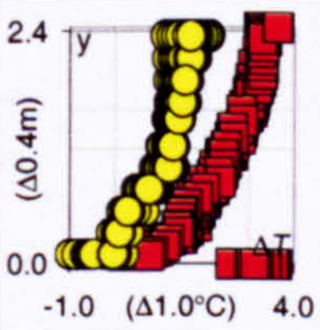	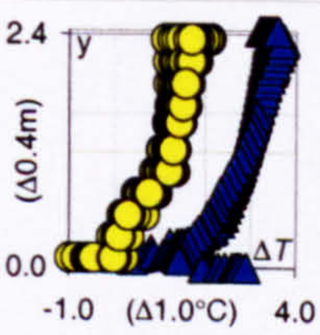	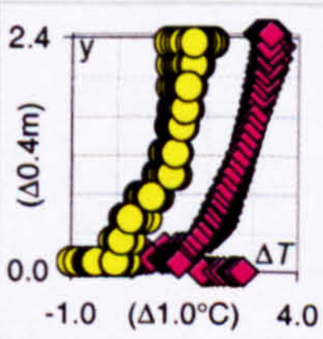	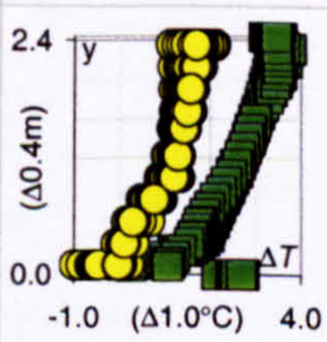
Radiation model enabled, $\alpha = 0.15m^{-1}$ QUICK differencing. Adiabatic walls. Uniform external temperature.	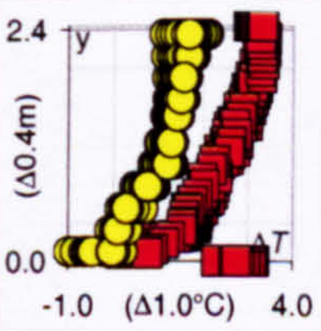	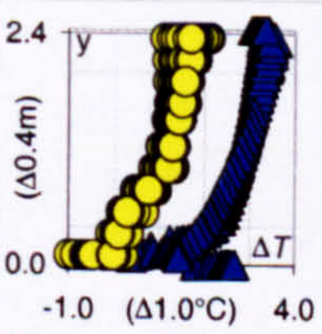	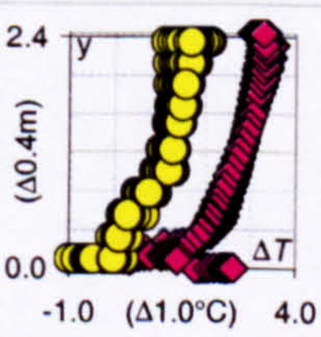	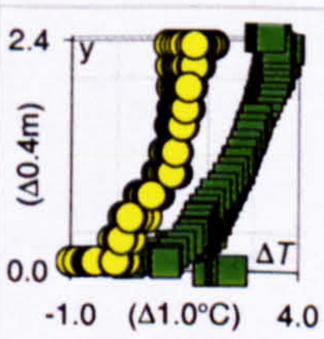

Width of opening:	0.4m
Effective area of opening:	$0.244m^2$
Heat source:	Plate heater
Strength of heat source:	225.0W

Figure 4.a

	Laminar	Standard-$k\varepsilon$	Realizable-$k\varepsilon$	RNG-$k\varepsilon$
Radiation model enabled, $\alpha = 0.00m^{-1}$ QUICK differencing. Convection walls. Uniform external temperature.	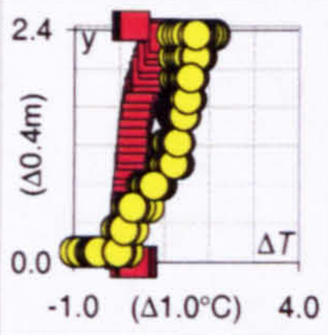	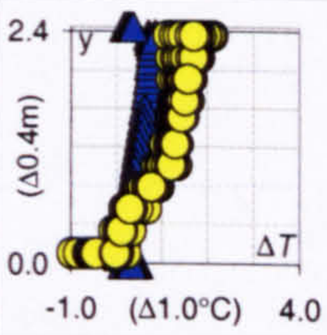	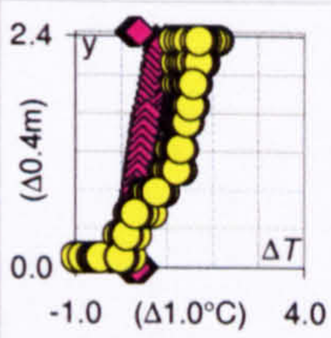	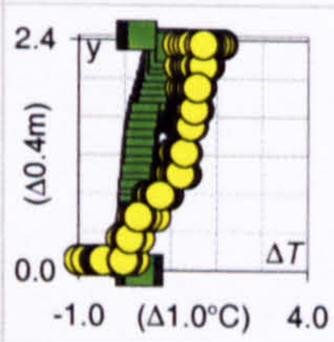
Radiation model enabled, $\alpha = 0.00m^{-1}$ QUICK differencing. Radiation walls. Uniform external temperature.	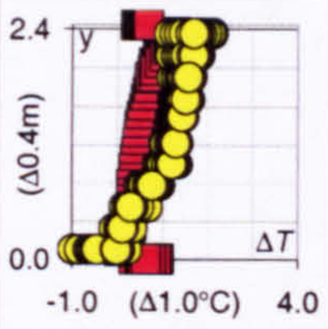	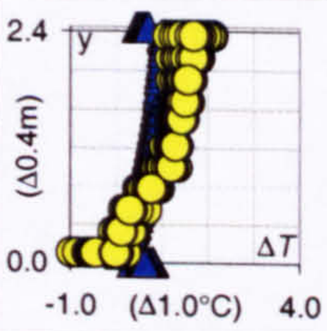	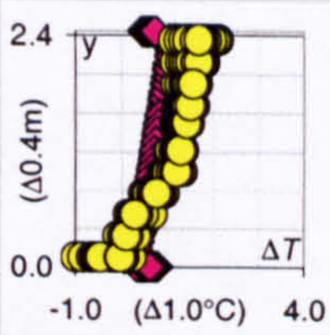	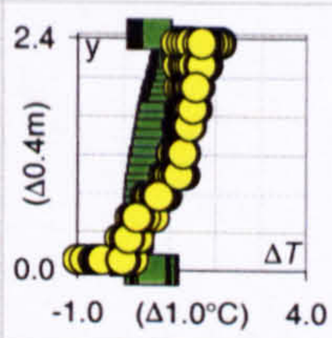
Radiation model enabled, $\alpha = 0.00m^{-1}$ QUICK differencing. Mixed walls. Uniform external temperature.	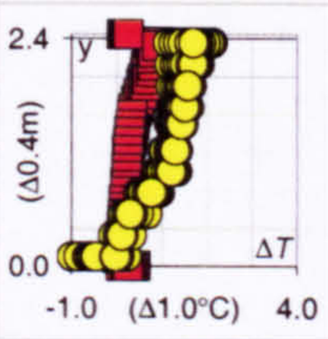	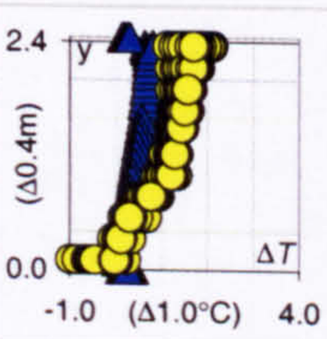	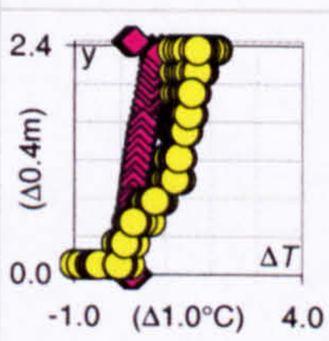	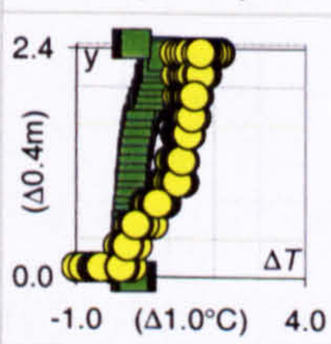
Radiation model enabled, $\alpha = 0.05m^{-1}$ QUICK differencing. Convection walls. Uniform external temperature.	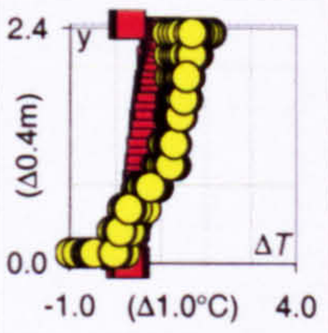	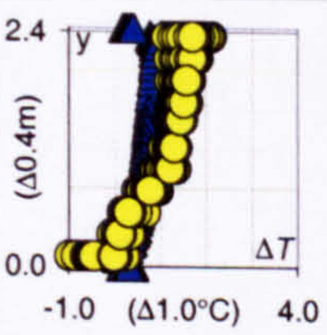	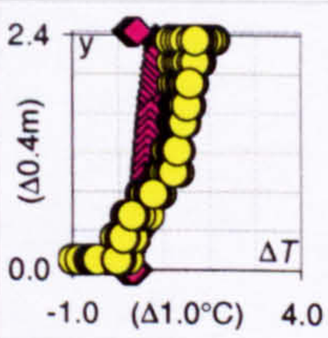	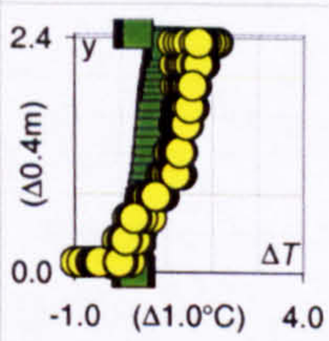
Radiation model enabled, $\alpha = 0.05m^{-1}$ QUICK differencing. Radiation walls. Uniform external temperature.	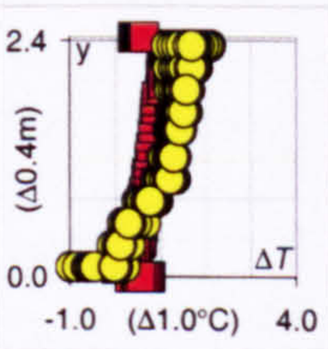	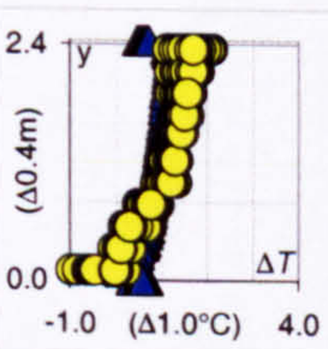	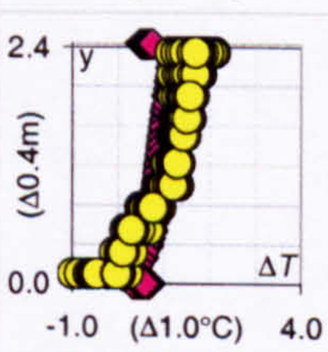	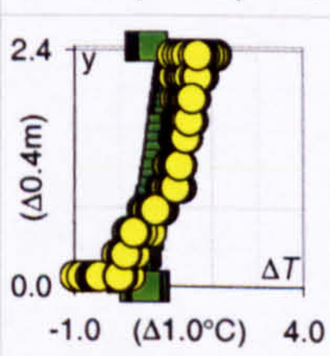
Radiation model enabled, $\alpha = 0.05m^{-1}$ QUICK differencing. Mixed walls. Uniform external temperature.	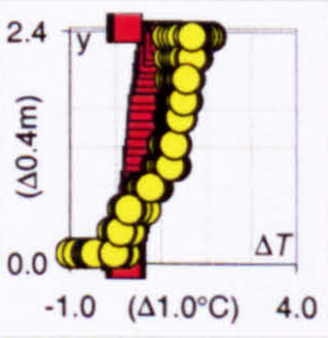	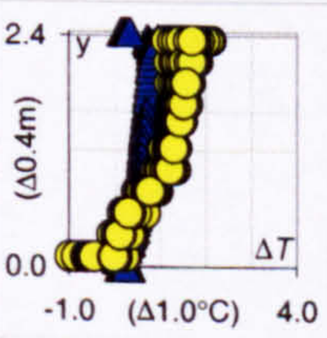	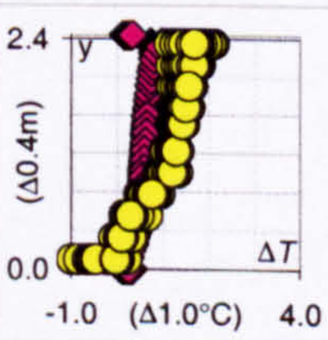	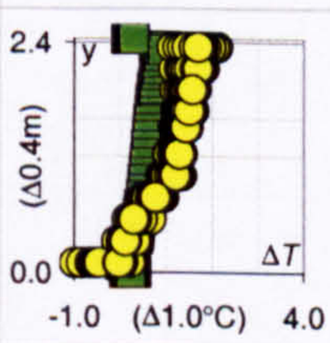

Width of opening:	0.4m
Effective area of opening:	$0.244m^2$
Heat source:	Plate heater
Strength of heat source:	225.0W

Figure 4.b

	Laminar	Standard-$k\varepsilon$	Realizable-$k\varepsilon$	RNG-$k\varepsilon$
Radiation model disabled. Upwind differencing. Adiabatic walls. Uniform external temperature.	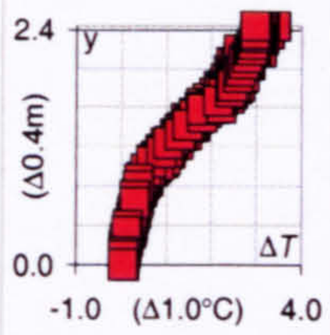	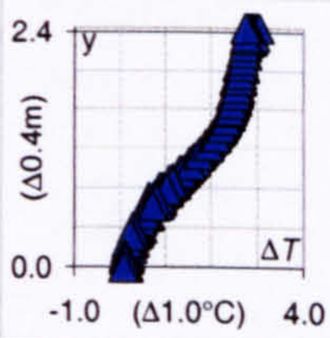	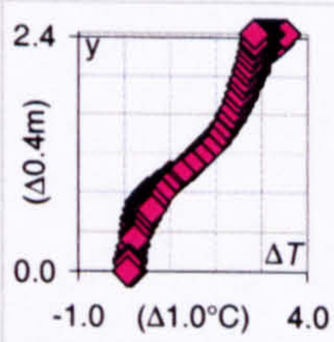	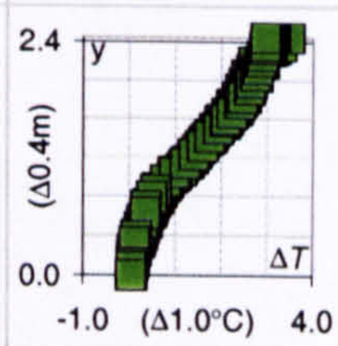
Radiation model disabled. QUICK differencing. Adiabatic walls. Uniform external temperature.	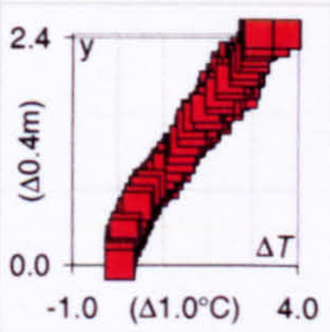	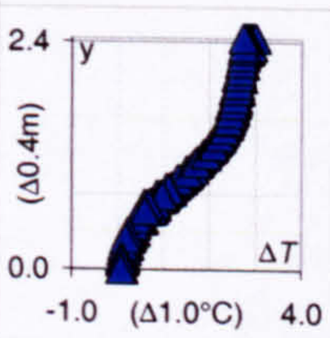	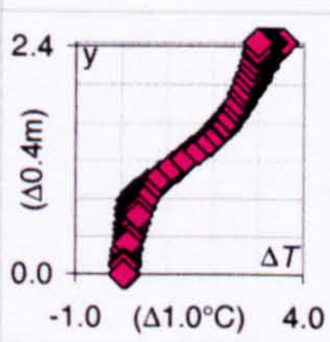	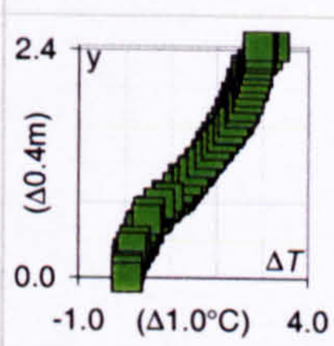
Radiation model enabled, $\alpha = 0.00m^{-1}$ QUICK differencing. Adiabatic walls. Uniform external temperature.	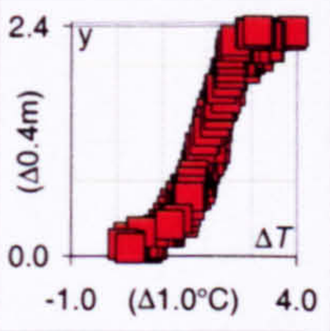	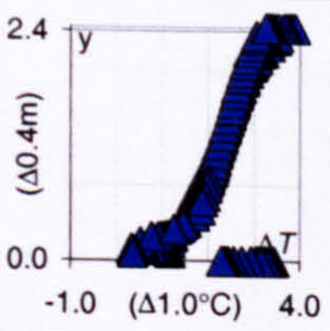	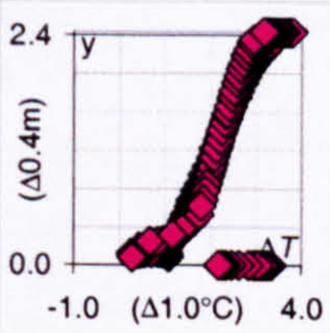	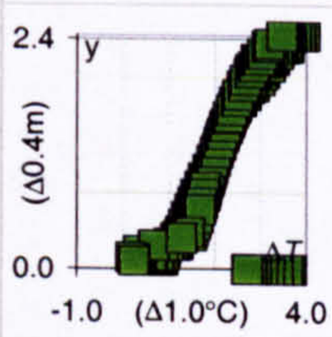
Radiation model enabled, $\alpha = 0.05m^{-1}$ QUICK differencing. Adiabatic walls. Uniform external temperature.	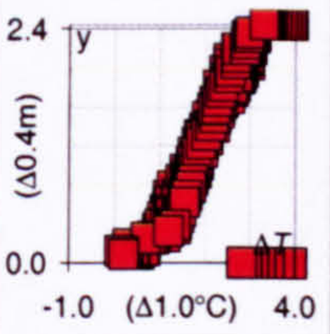	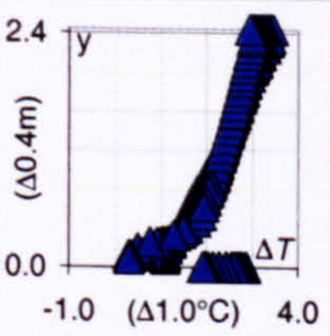	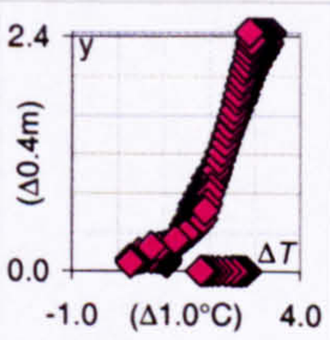	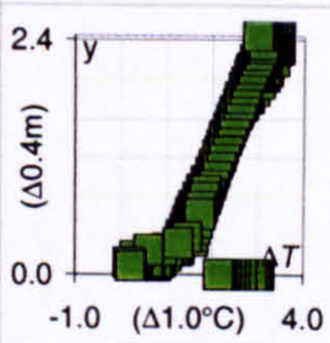
Radiation model enabled, $\alpha = 0.10m^{-1}$ QUICK differencing. Adiabatic walls. Uniform external temperature.	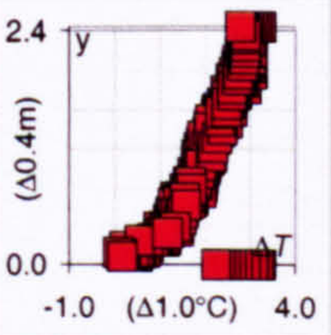	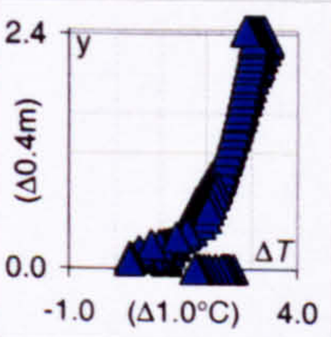	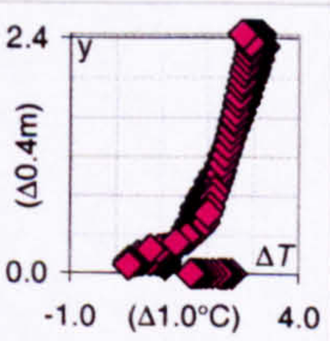	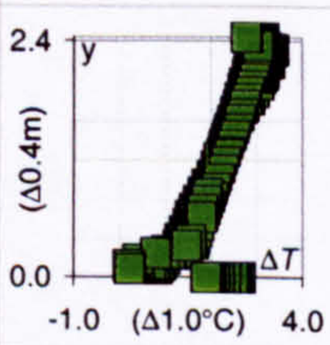
Radiation model enabled, $\alpha = 0.15m^{-1}$ QUICK differencing. Adiabatic walls. Uniform external temperature.	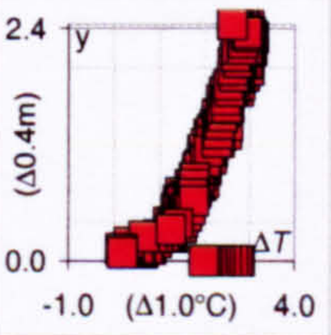	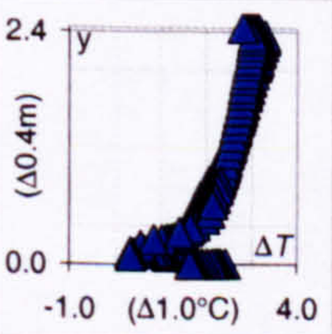	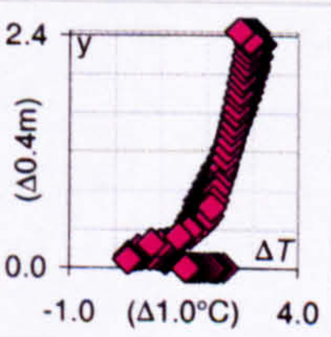	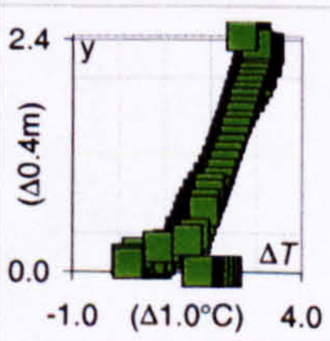

Width of opening:	0.5m
Effective area of opening:	$0.305m^2$
Heat source:	Plate heater
Strength of heat source:	225.0W

Figure 5.a

	Laminar	Standard-$k\varepsilon$	Realizable-$k\varepsilon$	RNG-$k\varepsilon$
Radiation model enabled, $\alpha = 0.00m^{-1}$ QUICK differencing. Convection walls. Uniform external temperature.	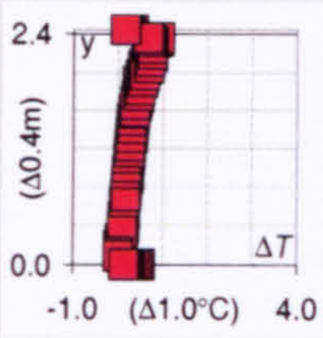	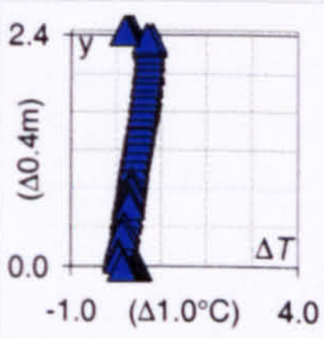	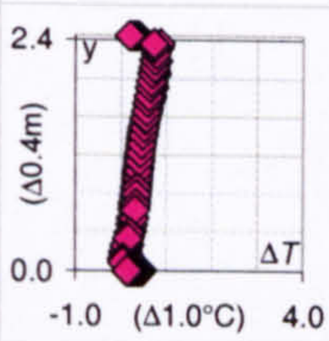	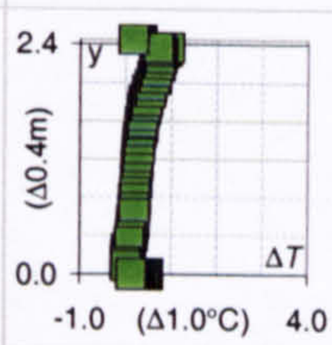
Radiation model enabled, $\alpha = 0.00m^{-1}$ QUICK differencing. Radiation walls. Uniform external temperature.	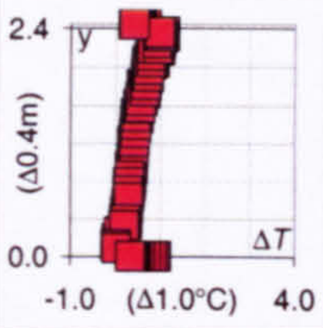	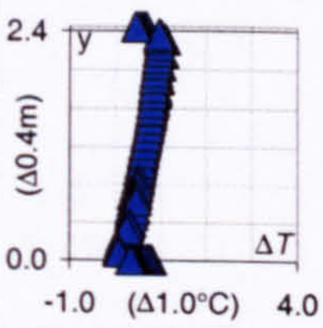	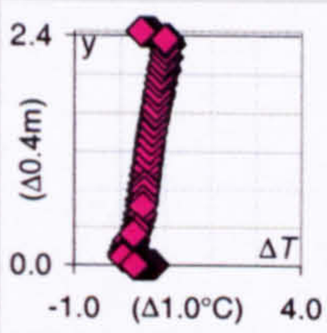	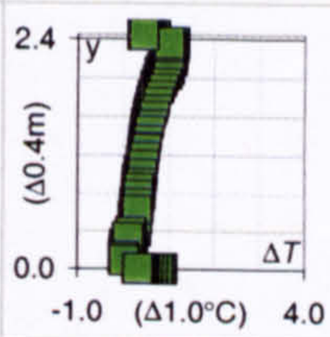
Radiation model enabled, $\alpha = 0.00m^{-1}$ QUICK differencing. Mixed walls. Uniform external temperature.	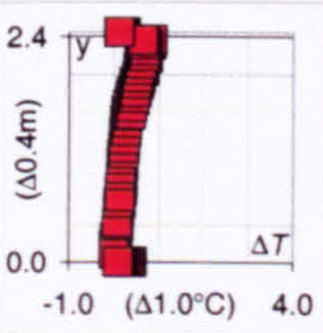	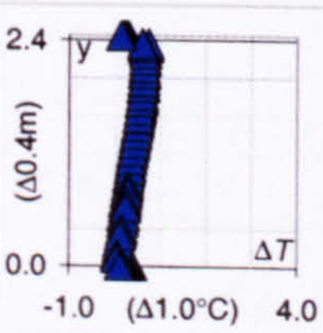	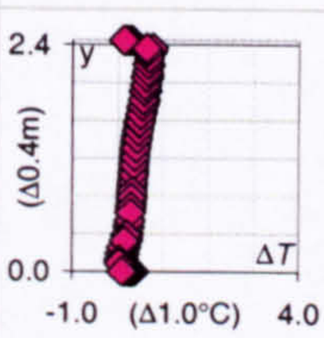	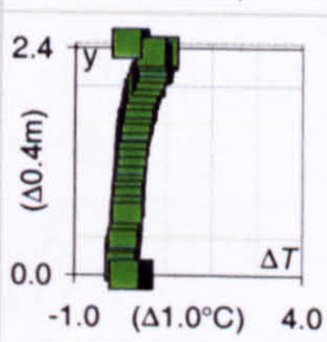
Radiation model enabled, $\alpha = 0.05m^{-1}$ QUICK differencing. Convection walls. Uniform external temperature.	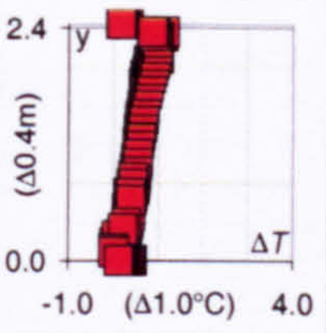	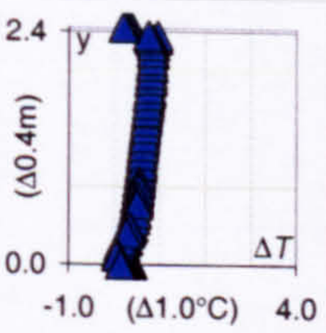	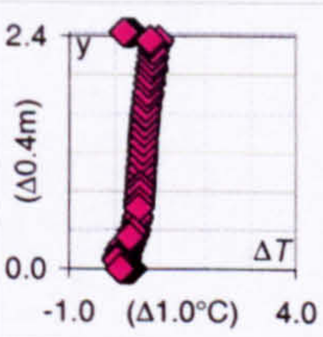	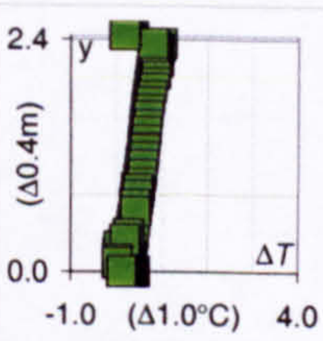
Radiation model enabled, $\alpha = 0.05m^{-1}$ QUICK differencing. Radiation walls. Uniform external temperature.	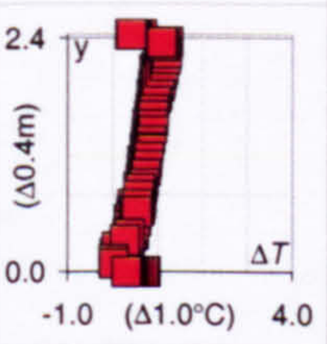	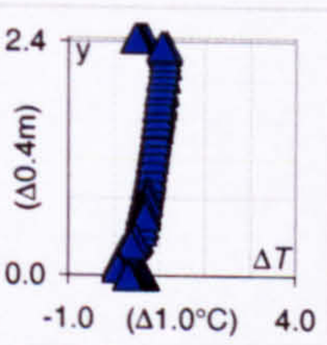	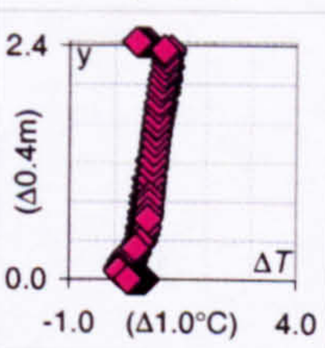	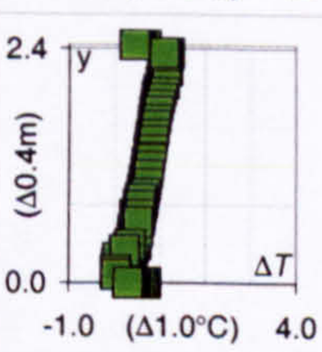
Radiation model enabled, $\alpha = 0.05m^{-1}$ QUICK differencing. Mixed walls. Uniform external temperature.	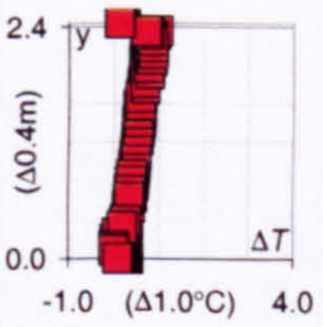	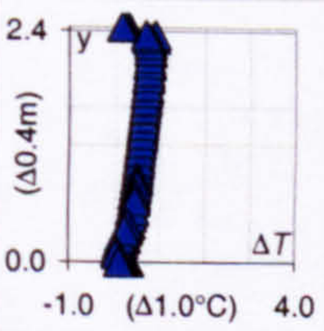	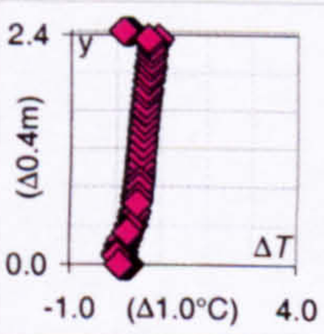	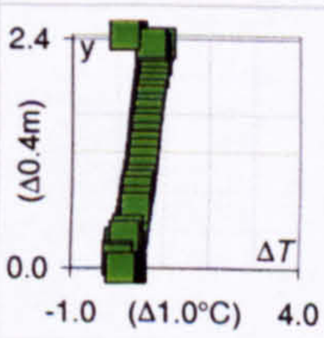

Width of opening: 0.5m
Effective area of opening: 0.305m^2
Heat source: Plate heater
Strength of heat source: 225.0W

Figure 5.b

	Laminar	Standard-$k\varepsilon$	Realizable-$k\varepsilon$	RNG-$k\varepsilon$
Radiation model disabled. Upwind differencing. Adiabatic walls. Uniform external temperature.	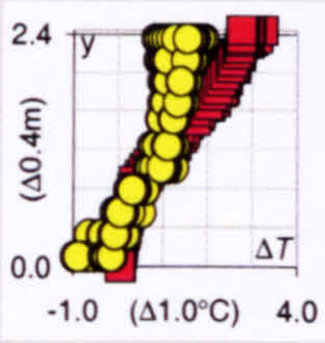	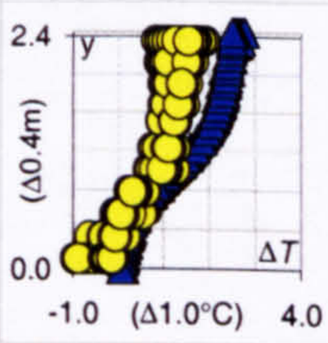	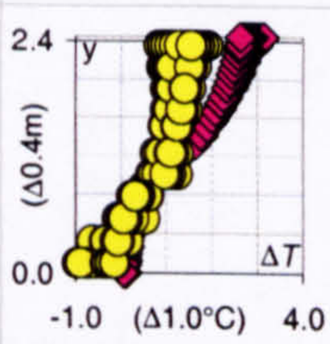	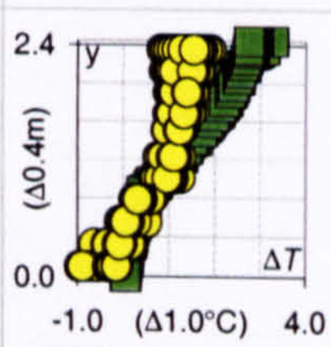
Radiation model disabled. QUICK differencing. Adiabatic walls. Uniform external temperature.	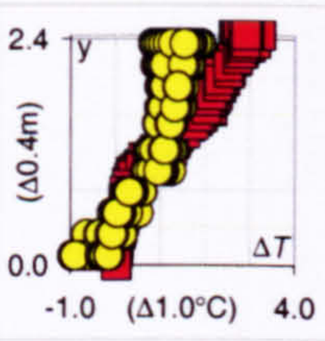	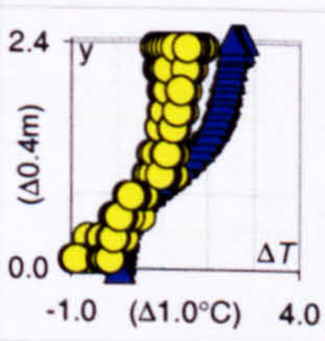	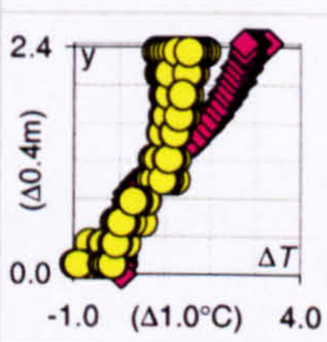	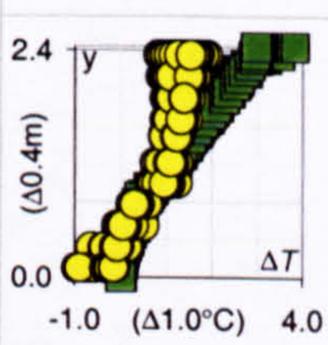
Radiation model enabled, $\alpha = 0.00m^{-1}$ QUICK differencing. Adiabatic walls. Uniform external temperature.	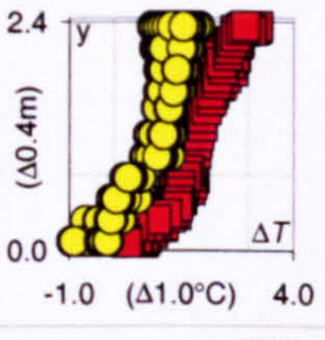	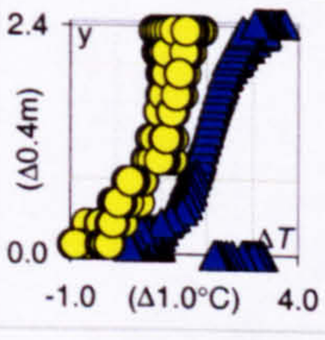	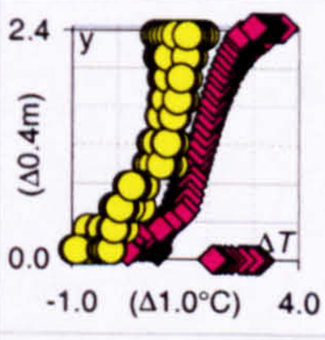	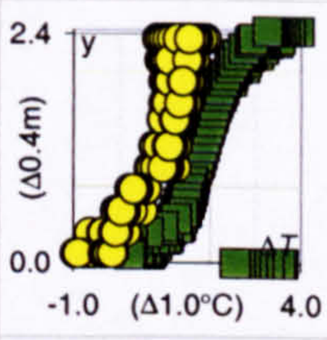
Radiation model enabled, $\alpha = 0.05m^{-1}$ QUICK differencing. Adiabatic walls. Uniform external temperature.	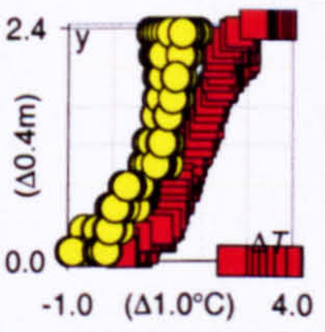	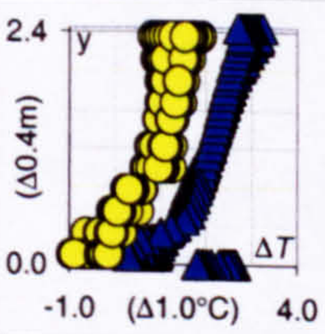	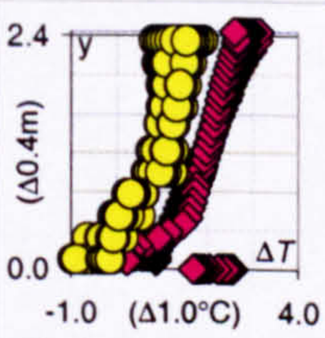	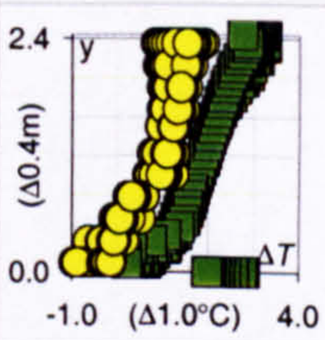
Radiation model enabled, $\alpha = 0.10m^{-1}$ QUICK differencing. Adiabatic walls. Uniform external temperature.	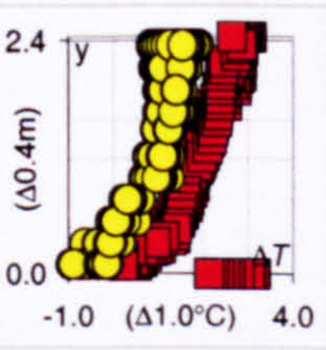	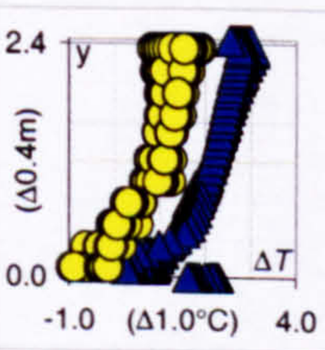	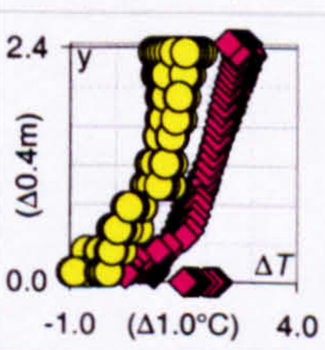	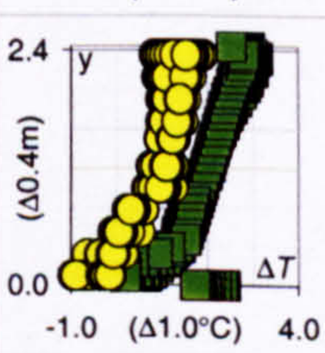
Radiation model enabled, $\alpha = 0.15m^{-1}$ QUICK differencing. Adiabatic walls. Uniform external temperature.	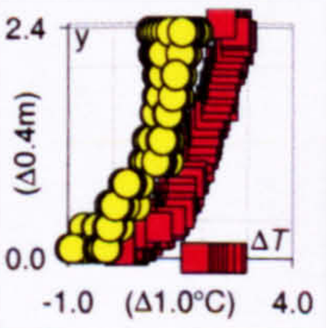	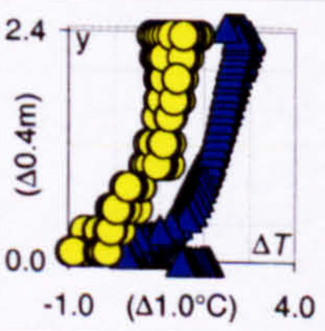	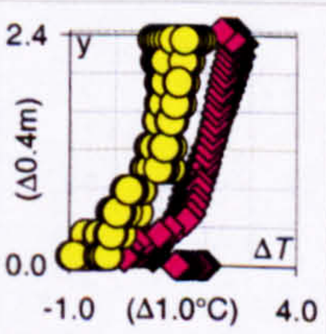	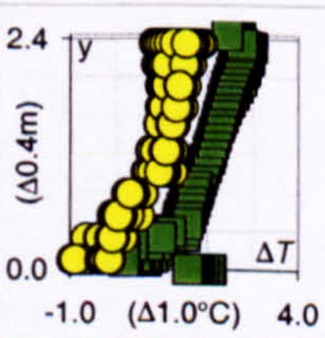

Width of opening:	0.6m
Effective area of opening:	$0.366m^2$
Heat source:	Plate heater
Strength of heat source:	225.0W

Figure 6.a

	Laminar	Standard-$k\varepsilon$	Realizable-$k\varepsilon$	RNG-$k\varepsilon$
Radiation model enabled, $\alpha = 0.00m^{-1}$ QUICK differencing. Convection walls. Uniform external temperature.	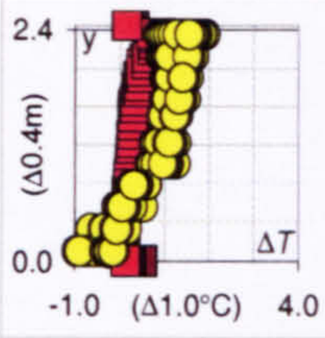	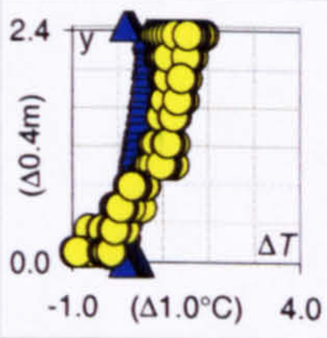	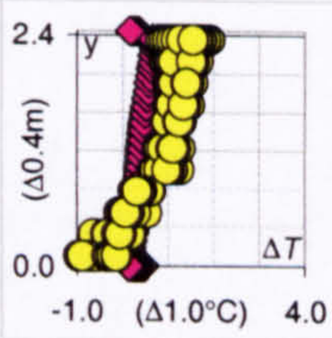	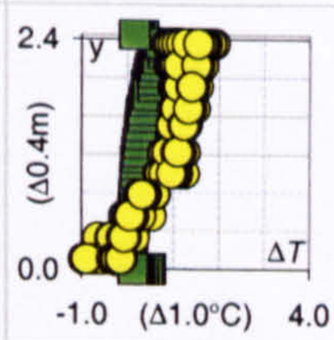
Radiation model enabled, $\alpha = 0.00m^{-1}$ QUICK differencing. Radiation walls. Uniform external temperature.	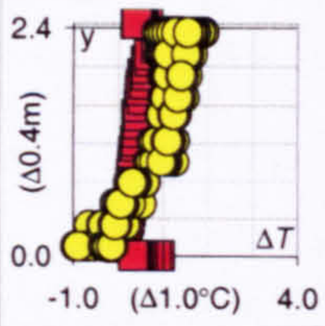	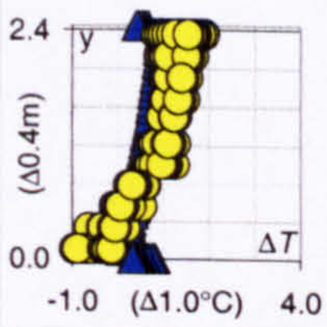	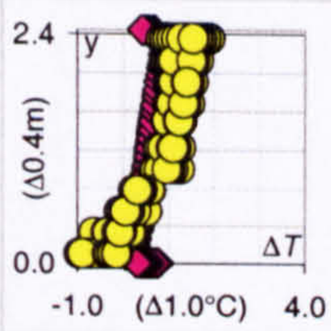	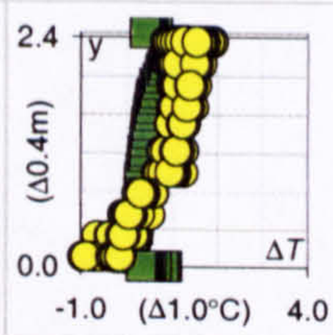
Radiation model enabled, $\alpha = 0.00m^{-1}$ QUICK differencing. Mixed walls. Uniform external temperature.	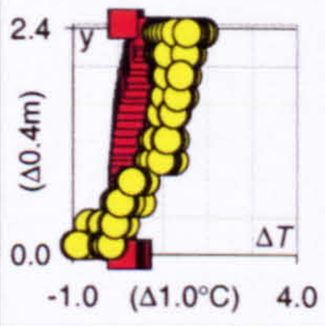	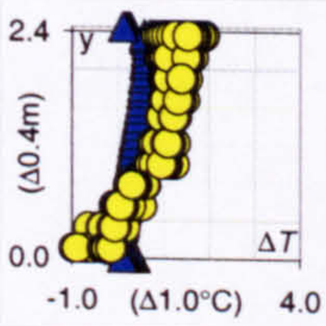	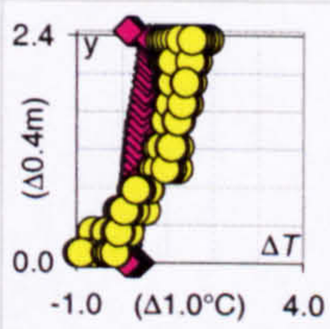	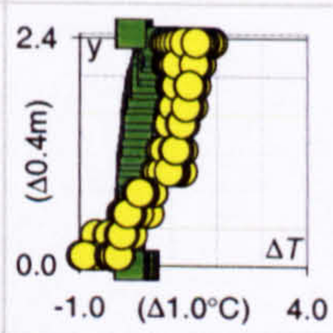
Radiation model enabled, $\alpha = 0.05m^{-1}$ QUICK differencing. Convection walls. Uniform external temperature.	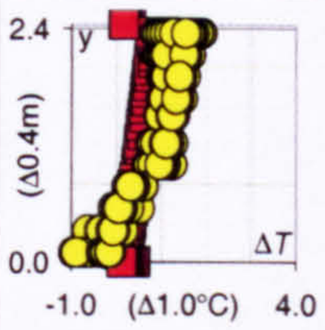	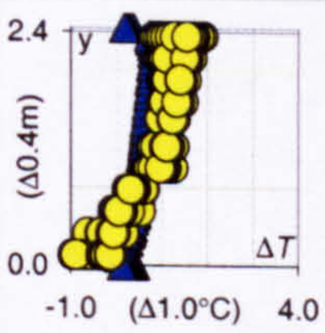	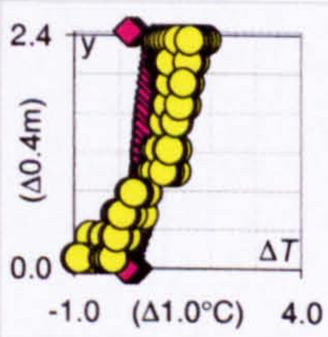	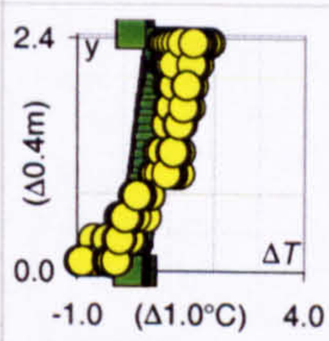
Radiation model enabled, $\alpha = 0.05m^{-1}$ QUICK differencing. Radiation walls. Uniform external temperature.	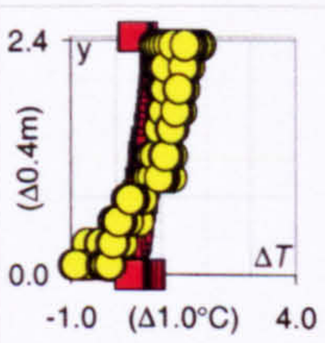	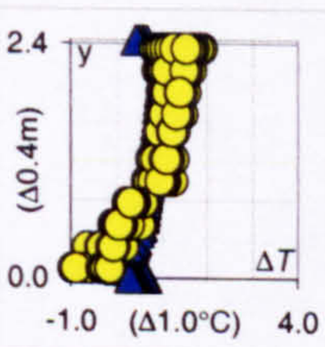	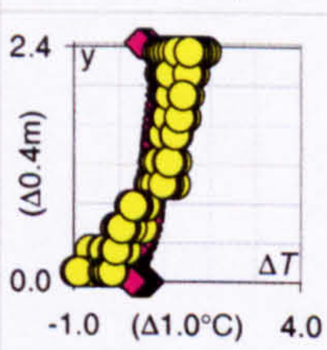	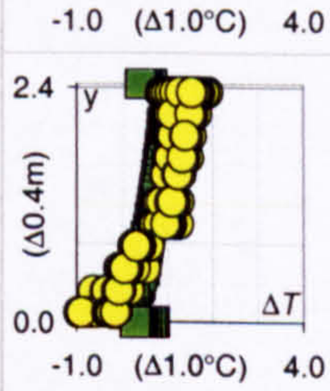
Radiation model enabled, $\alpha = 0.05m^{-1}$ QUICK differencing. Mixed walls. Uniform external temperature.	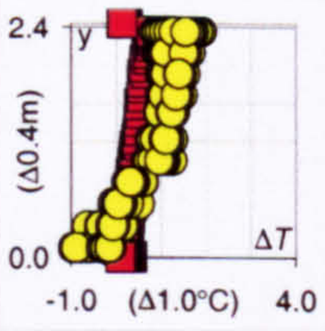	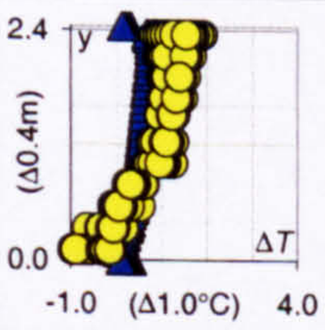	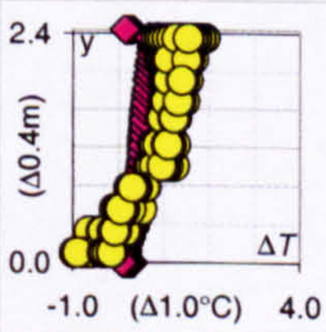	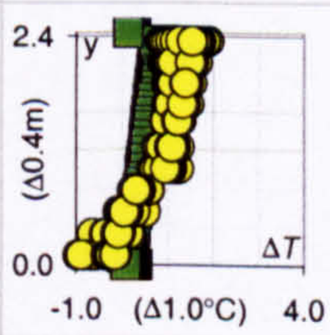

Width of opening:	0.6m
Effective area of opening:	$0.366m^2$
Heat source:	Plate heater
Strength of heat source:	225.0W

Figure 6.b

	Laminar	Standard-$k\varepsilon$	Realizable-$k\varepsilon$	RNG-$k\varepsilon$
Radiation model disabled. Upwind differencing. Adiabatic walls. Uniform external temperature.	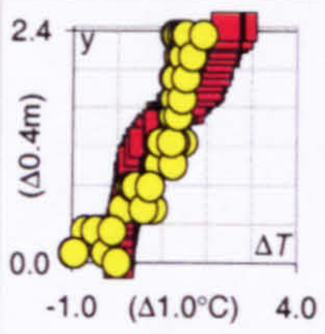	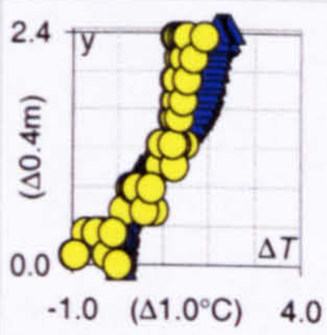	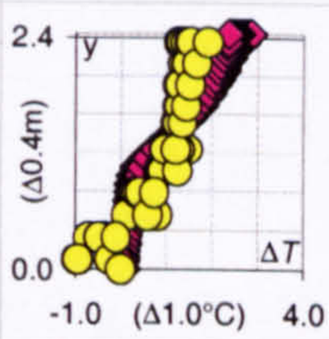	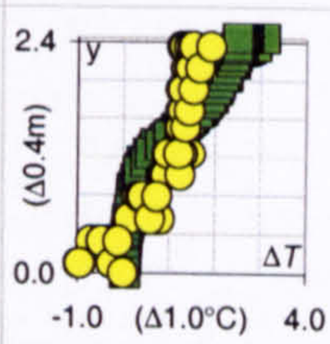
Radiation model disabled. QUICK differencing. Adiabatic walls. Uniform external temperature.	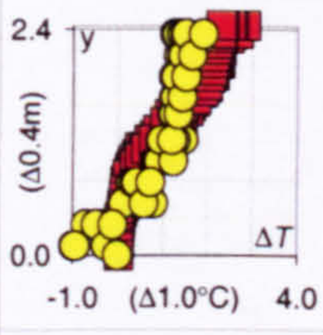	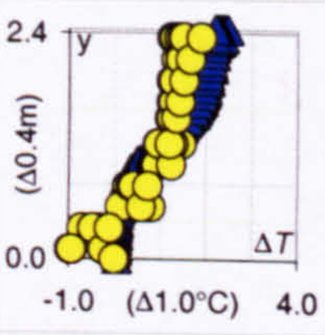	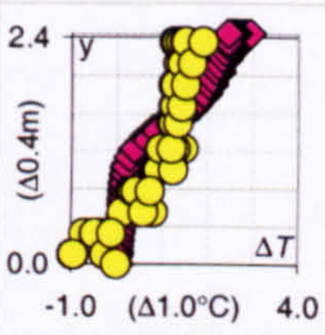	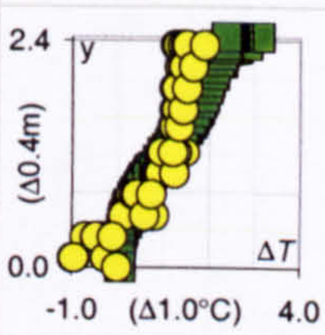
Radiation model enabled, $\alpha = 0.00m^{-1}$ QUICK differencing. Adiabatic walls. Uniform external temperature.	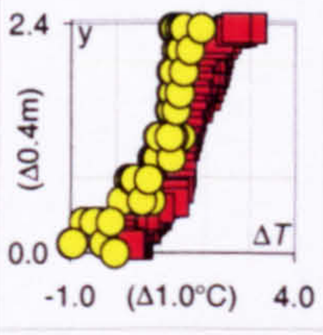	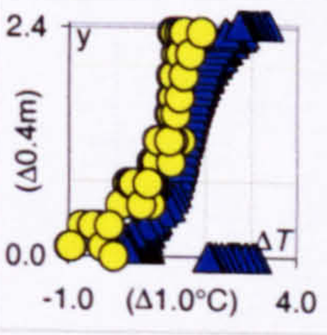	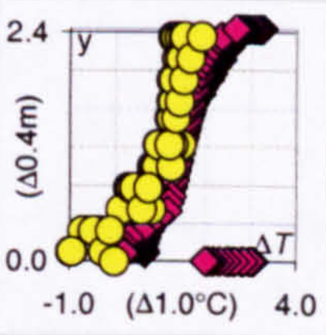	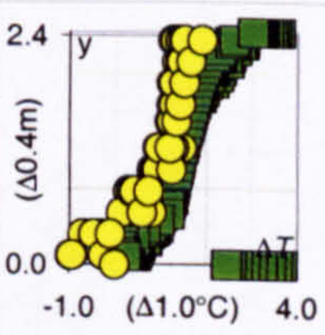
Radiation model enabled, $\alpha = 0.05m^{-1}$ QUICK differencing. Adiabatic walls. Uniform external temperature.	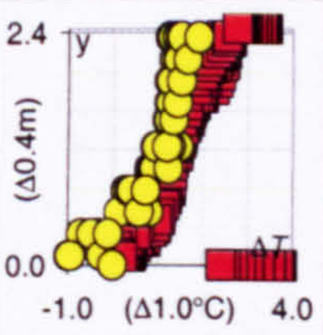	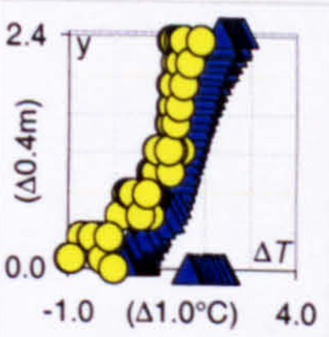	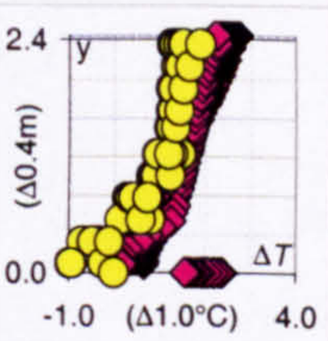	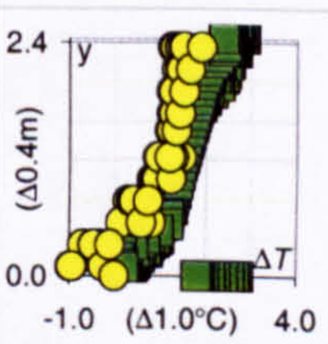
Radiation model enabled, $\alpha = 0.10m^{-1}$ QUICK differencing. Adiabatic walls. Uniform external temperature.	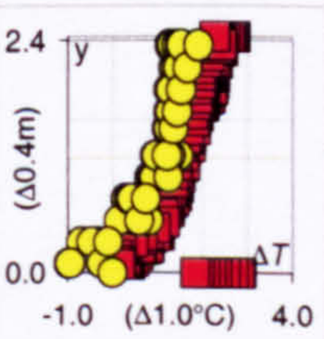	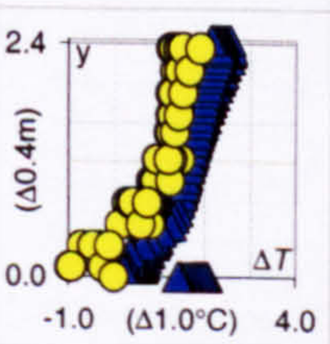	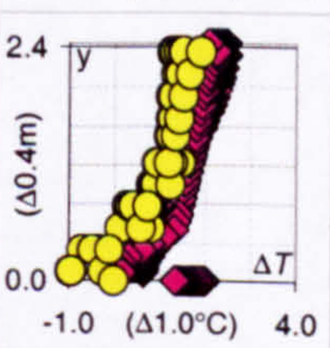	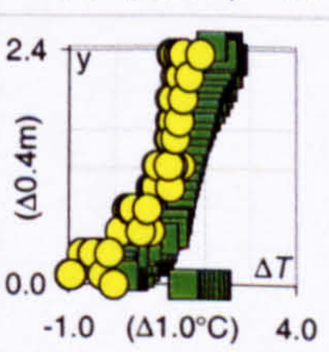
Radiation model enabled, $\alpha = 0.15m^{-1}$ QUICK differencing. Adiabatic walls. Uniform external temperature.	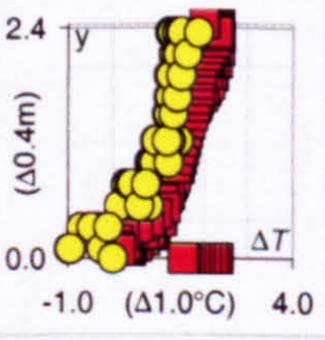	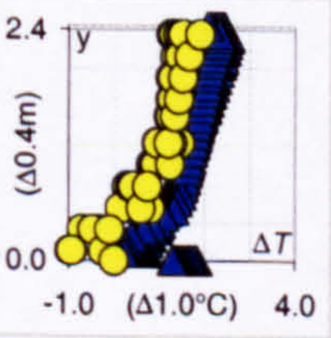	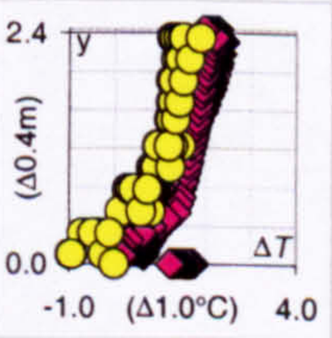	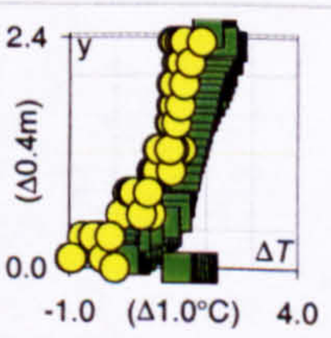

Width of opening:	0.8m
Effective area of opening:	0.488m^2
Heat source:	Plate heater
Strength of heat source:	225.0W

Figure 7.a

	Laminar	Standard-$k\varepsilon$	Realizable-$k\varepsilon$	RNG-$k\varepsilon$
Radiation model enabled, $\alpha = 0.00m^{-1}$ QUICK differencing. Convection walls. Uniform external temperature.	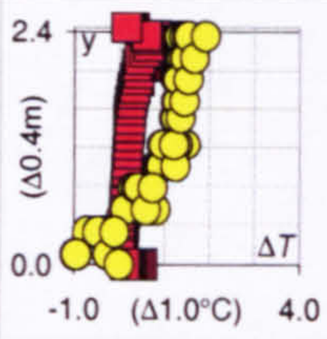	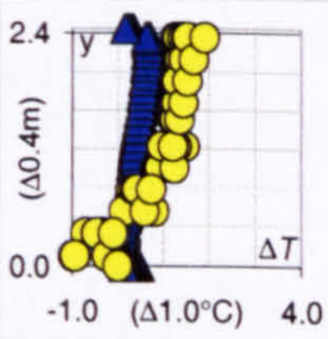	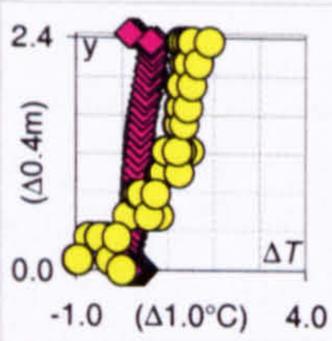	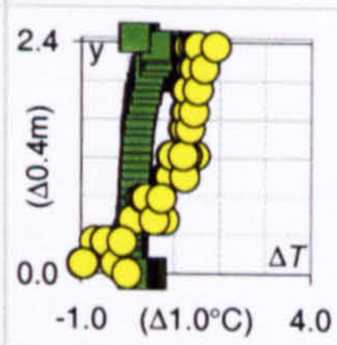
Radiation model enabled, $\alpha = 0.00m^{-1}$ QUICK differencing. Radiation walls. Uniform external temperature.	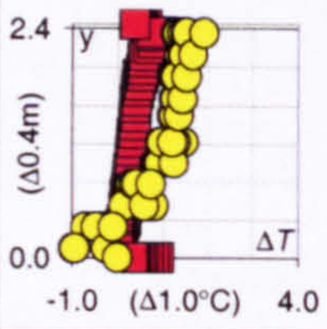	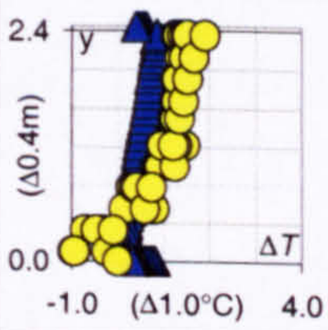	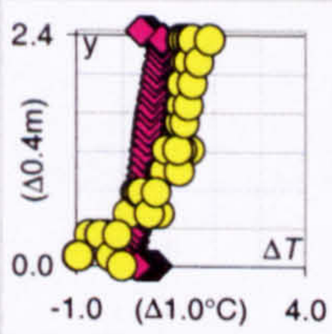	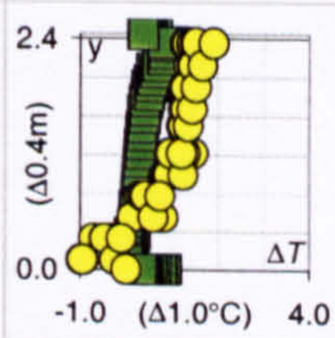
Radiation model enabled, $\alpha = 0.00m^{-1}$ QUICK differencing. Mixed walls. Uniform external temperature.	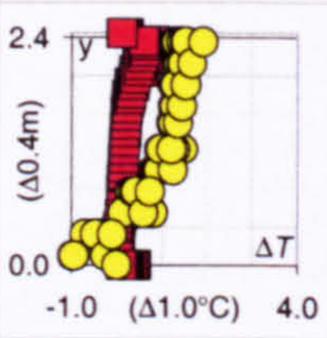	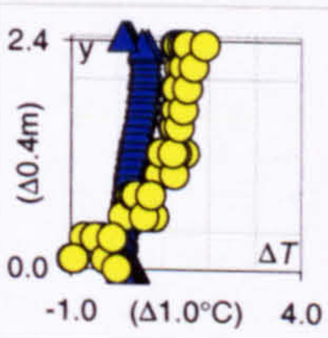	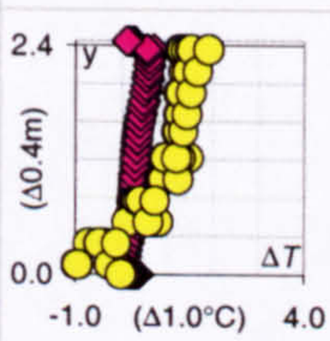	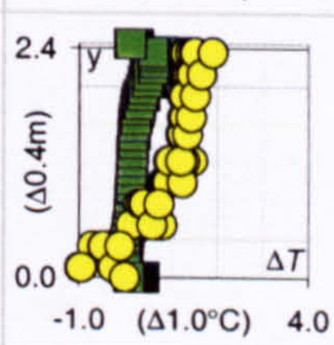
Radiation model enabled, $\alpha = 0.05m^{-1}$ QUICK differencing. Convection walls. Uniform external temperature.	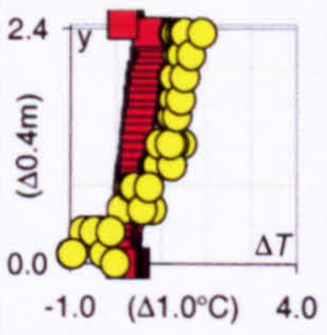	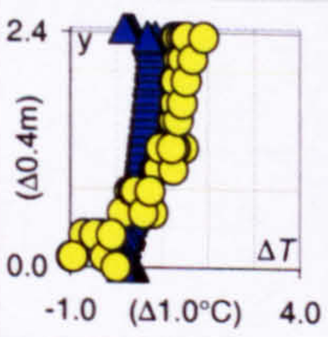	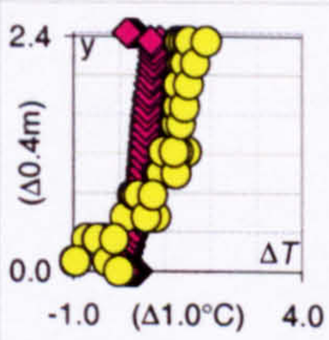	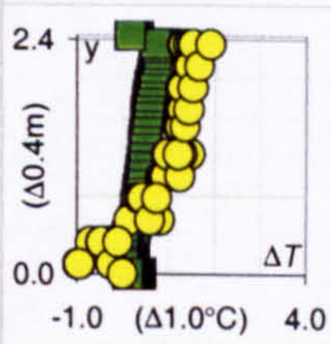
Radiation model enabled, $\alpha = 0.05m^{-1}$ QUICK differencing. Radiation walls. Uniform external temperature.	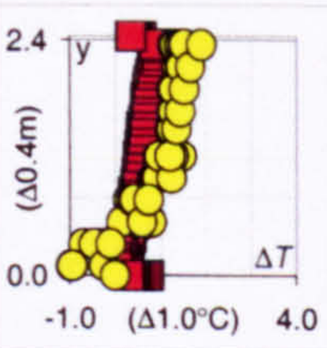	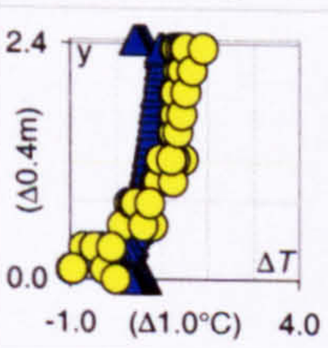	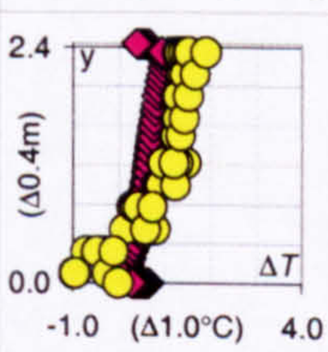	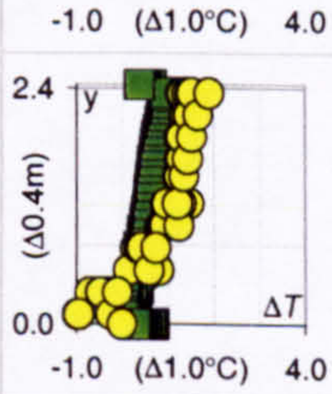
Radiation model enabled, $\alpha = 0.05m^{-1}$ QUICK differencing. Mixed walls. Uniform external temperature.	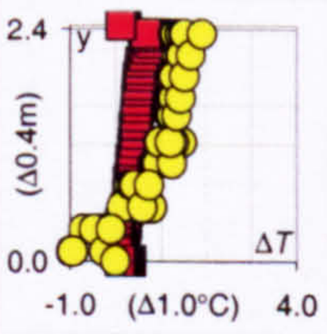	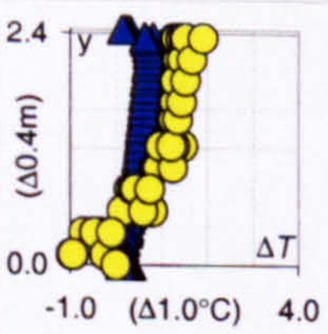	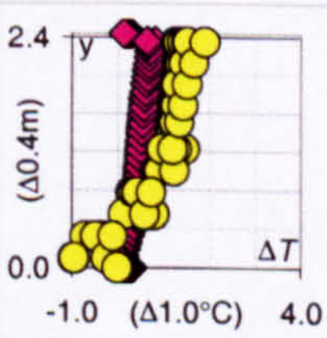	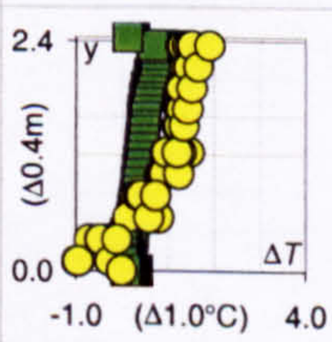

Width of opening:	0.8m
Effective area of opening:	$0.488m^2$
Heat source:	Plate heater
Strength of heat source:	225.0W

Figure 7.b

	Laminar	Standard-$k\varepsilon$	Realizable-$k\varepsilon$	RNG-$k\varepsilon$
Radiation model disabled. Upwind differencing. Adiabatic walls. Uniform external temperature.	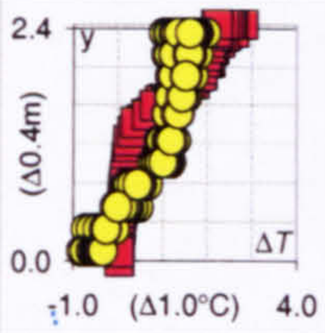	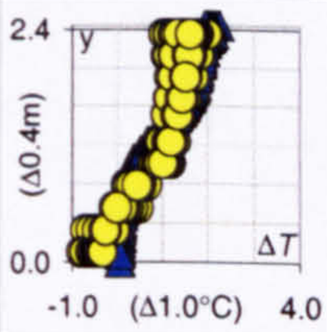	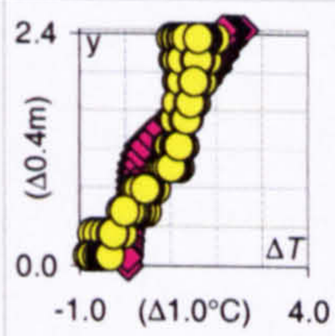	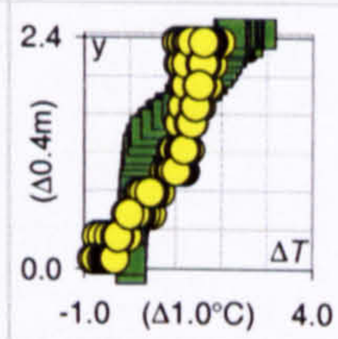
Radiation model disabled. QUICK differencing. Adiabatic walls. Uniform external temperature.	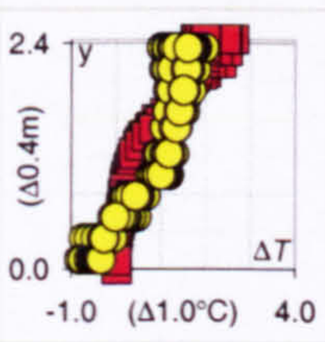	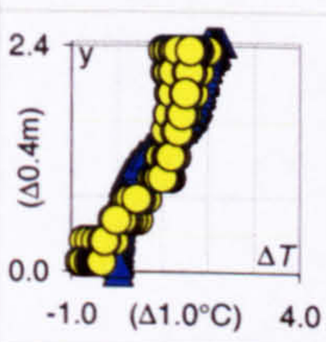	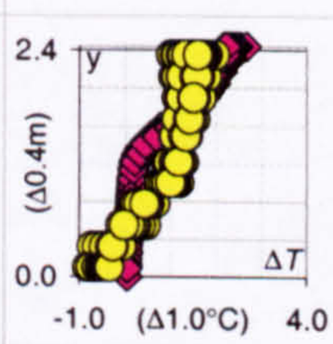	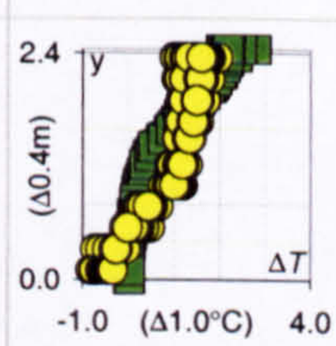
Radiation model enabled, $\alpha = 0.00m^{-1}$ QUICK differencing. Adiabatic walls. Uniform external temperature.	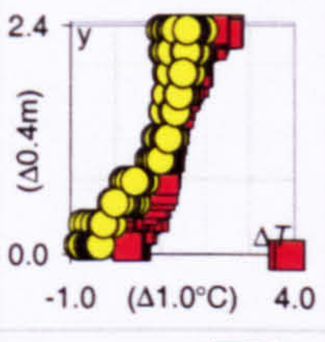	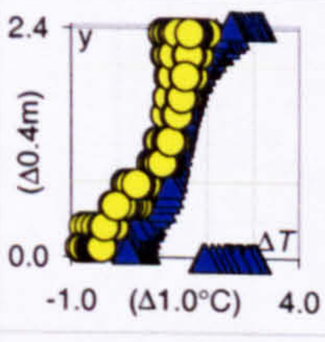	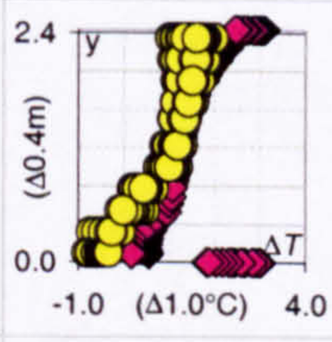	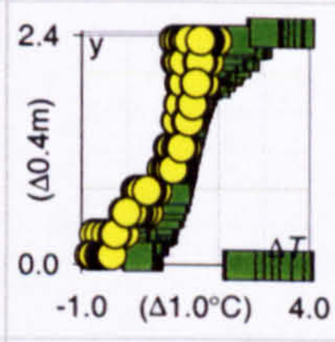
Radiation model enabled, $\alpha = 0.05m^{-1}$ QUICK differencing. Adiabatic walls. Uniform external temperature.	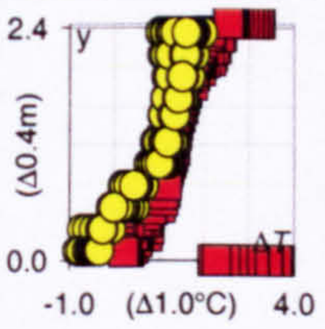	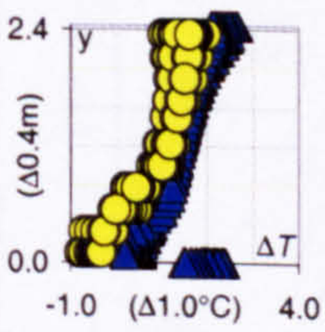	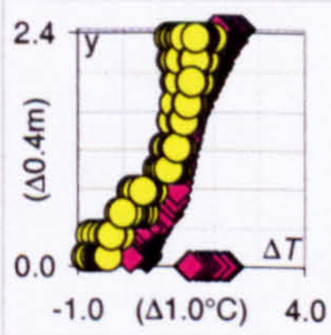	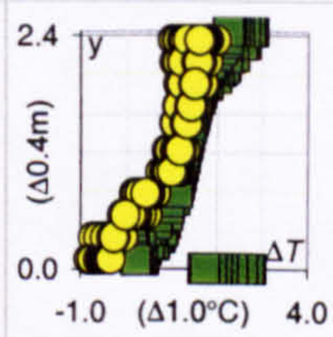
Radiation model enabled, $\alpha = 0.10m^{-1}$ QUICK differencing. Adiabatic walls. Uniform external temperature.	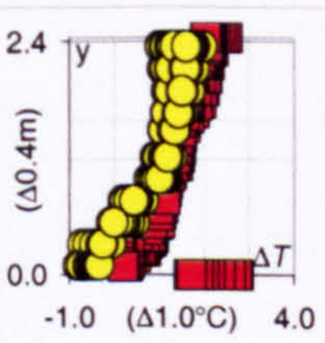	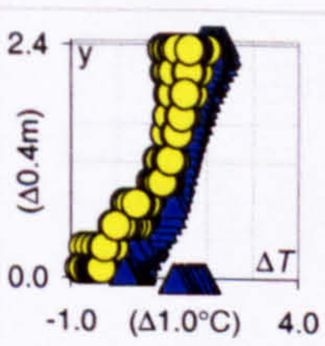	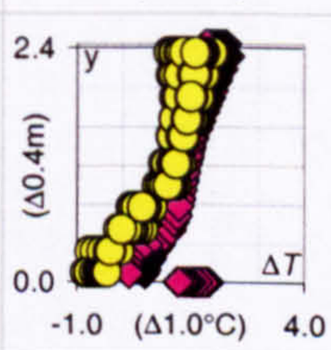	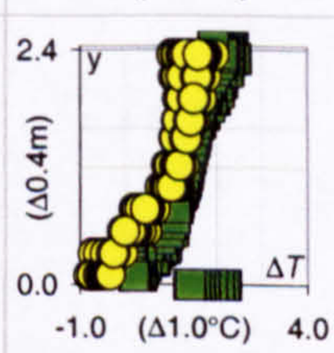
Radiation model enabled, $\alpha = 0.15m^{-1}$ QUICK differencing. Adiabatic walls. Uniform external temperature.	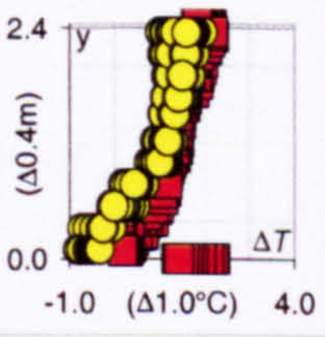	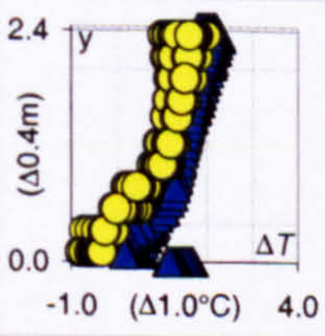	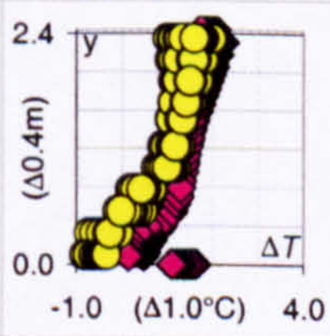	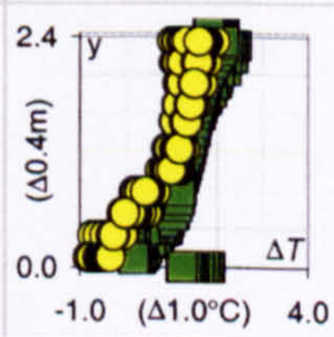

Width of opening:	1.0m
Effective area of opening:	$0.610m^2$
Heat source:	Plate heater
Strength of heat source:	225.0W

Figure 8.a

	Laminar	Standard-$k\varepsilon$	Realizable-$k\varepsilon$	RNG-$k\varepsilon$
Radiation model enabled, $\alpha = 0.00m^{-1}$ QUICK differencing. Convection walls. Uniform external temperature.	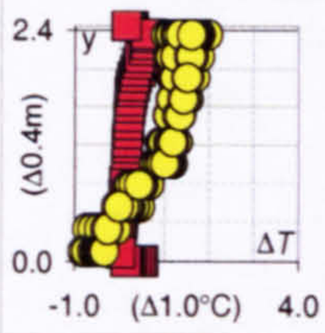	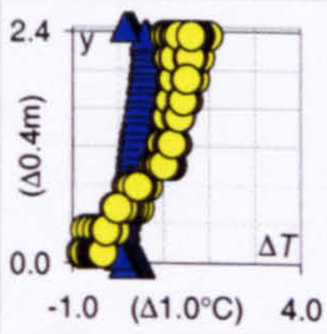	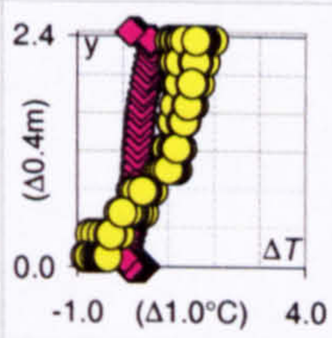	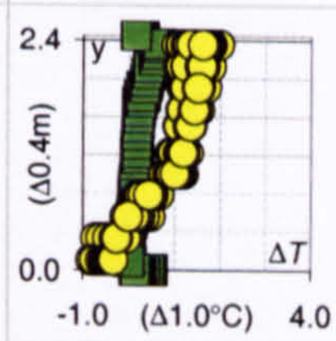
Radiation model enabled, $\alpha = 0.00m^{-1}$ QUICK differencing. Radiation walls. Uniform external temperature.	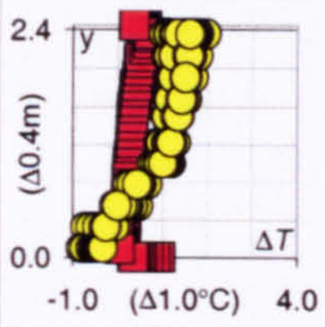	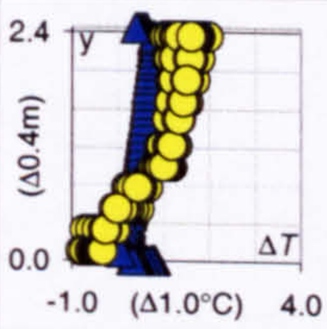	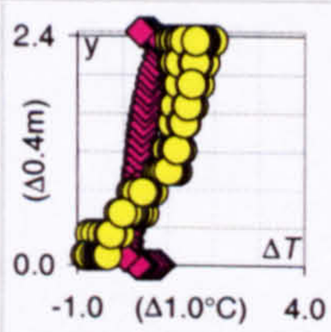	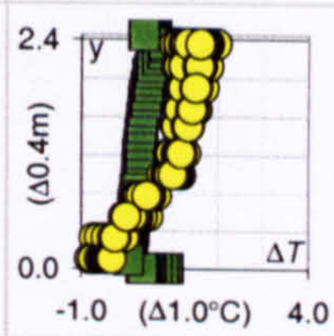
Radiation model enabled, $\alpha = 0.00m^{-1}$ QUICK differencing. Mixed walls. Uniform external temperature.	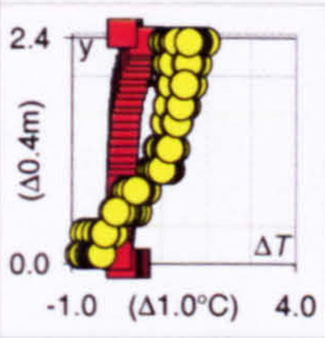	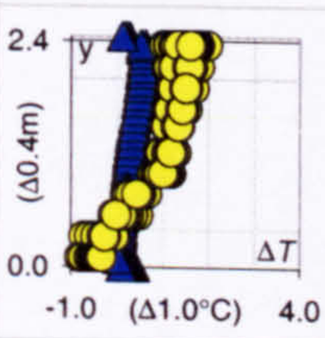	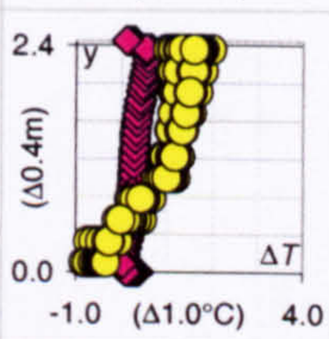	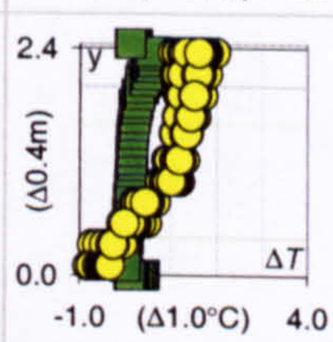
Radiation model enabled, $\alpha = 0.05m^{-1}$ QUICK differencing. Convection walls. Uniform external temperature.	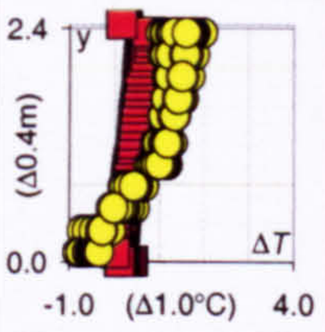	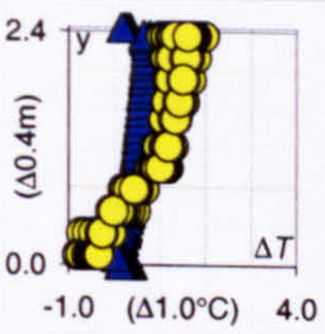	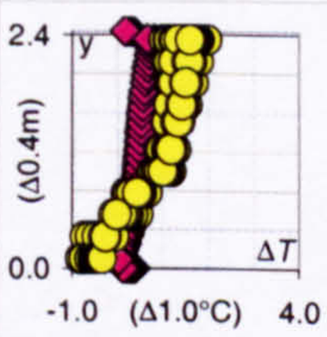	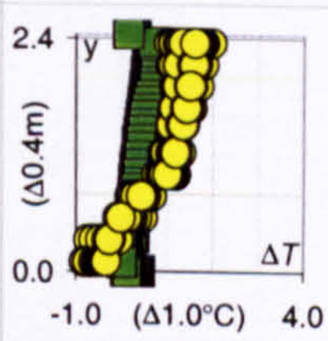
Radiation model enabled, $\alpha = 0.05m^{-1}$ QUICK differencing. Radiation walls. Uniform external temperature.	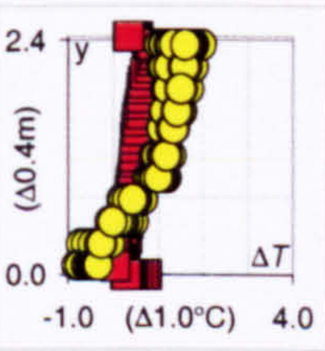	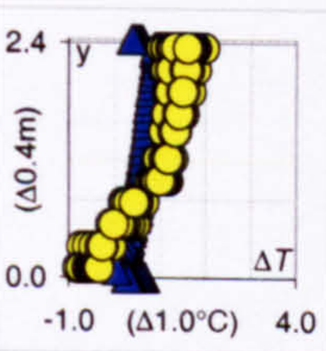	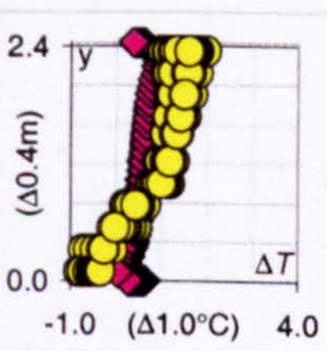	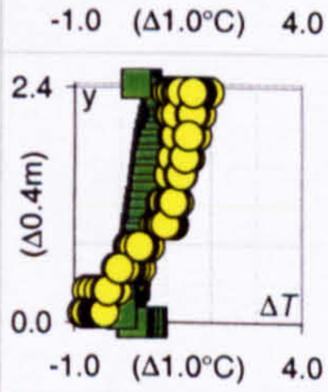
Radiation model enabled, $\alpha = 0.05m^{-1}$ QUICK differencing. Mixed walls. Uniform external temperature.	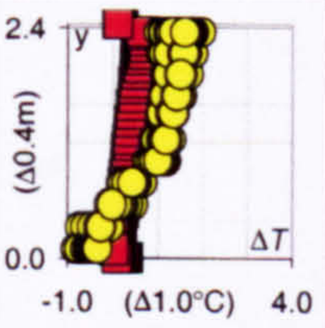	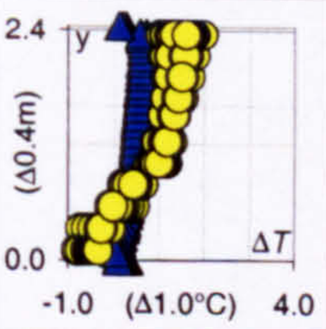	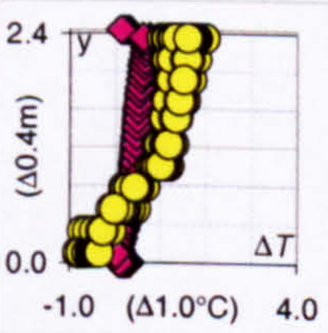	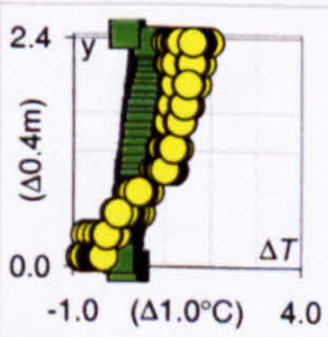

Width of opening:	1.0m
Effective area of opening:	$0.610m^2$
Heat source:	Plate heater
Strength of heat source:	225.0W

Figure 8.b

	Laminar	Standard-$k\varepsilon$	Realizable-$k\varepsilon$	RNG-$k\varepsilon$
Radiation model disabled. Upwind differencing. Adiabatic walls. Uniform external temperature.	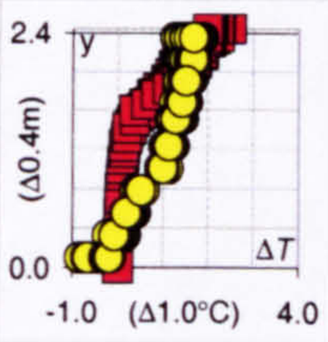	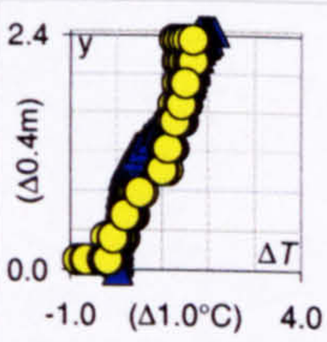	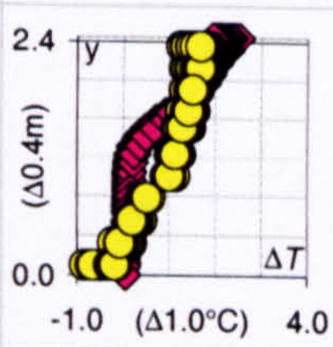	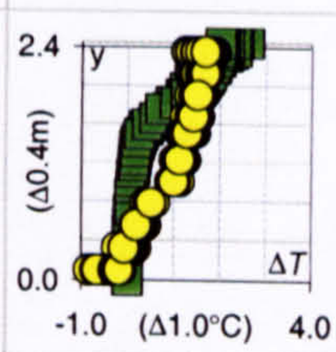
Radiation model disabled. QUICK differencing. Adiabatic walls. Uniform external temperature.	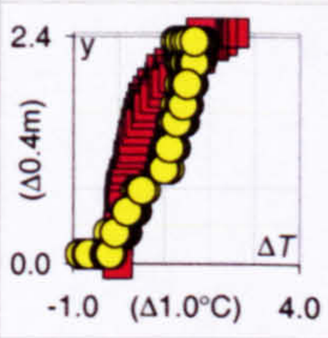	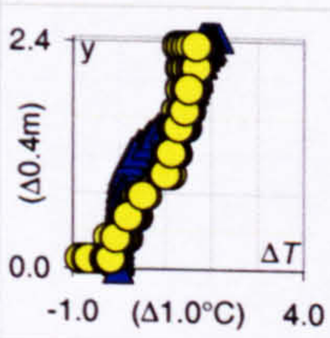	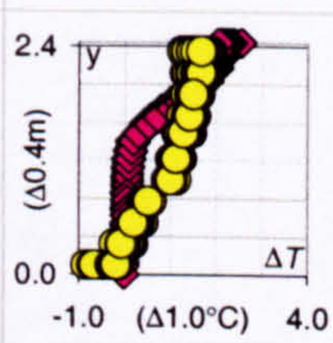	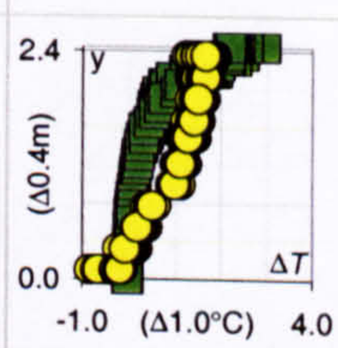
Radiation model enabled, $\alpha = 0.00m^{-1}$ QUICK differencing. Adiabatic walls. Uniform external temperature.	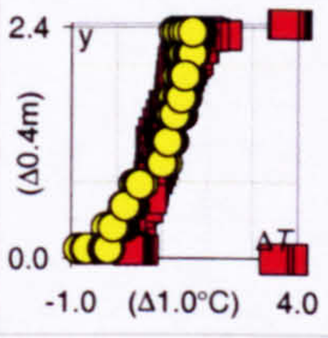	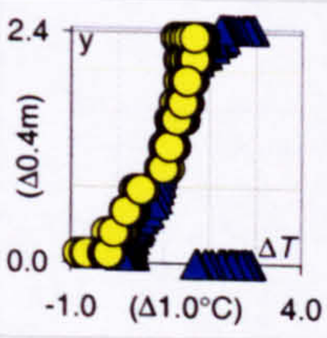	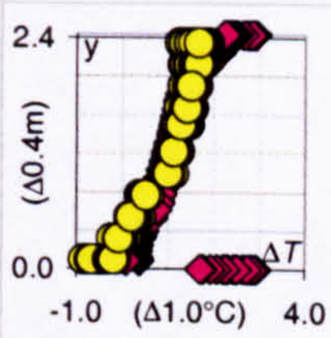	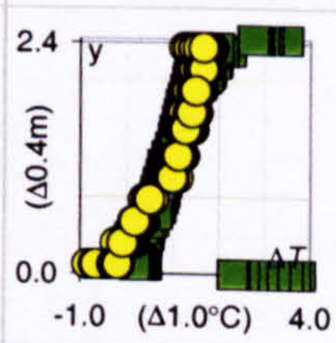
Radiation model enabled, $\alpha = 0.05m^{-1}$ QUICK differencing. Adiabatic walls. Uniform external temperature.	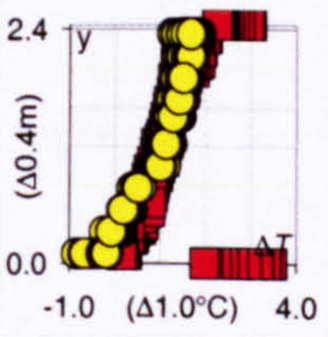	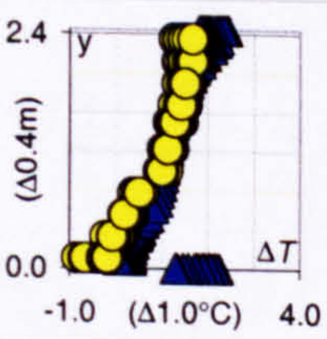	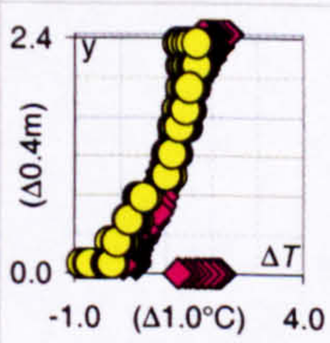	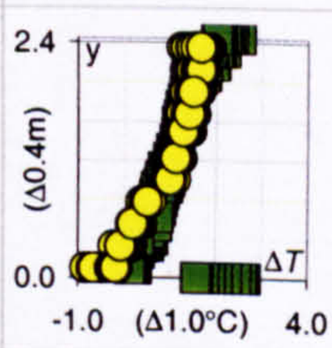
Radiation model enabled, $\alpha = 0.10m^{-1}$ QUICK differencing. Adiabatic walls. Uniform external temperature.	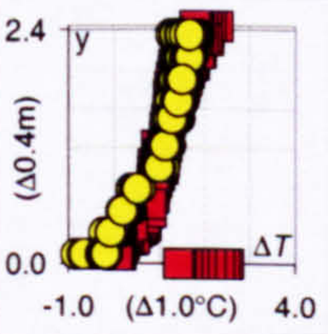	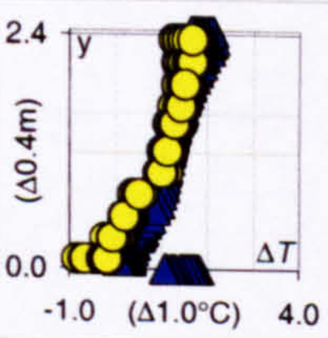	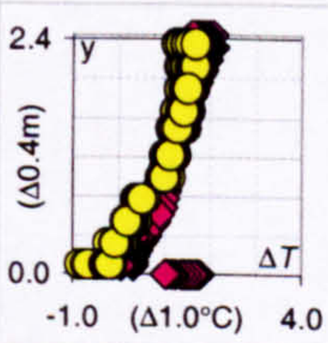	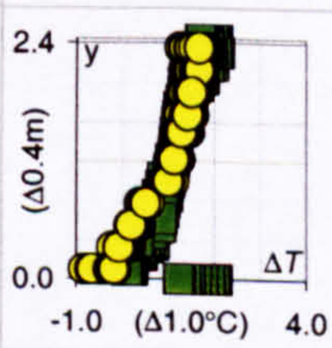
Radiation model enabled, $\alpha = 0.15m^{-1}$ QUICK differencing. Adiabatic walls. Uniform external temperature.	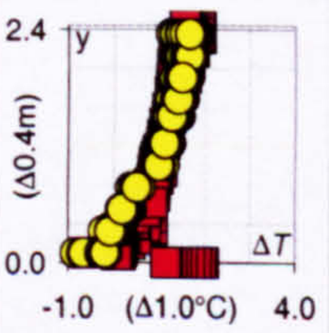	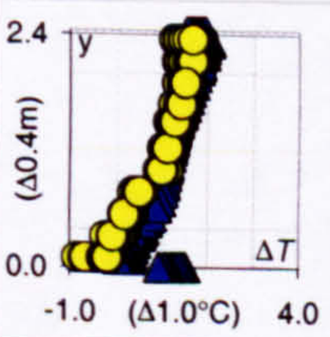	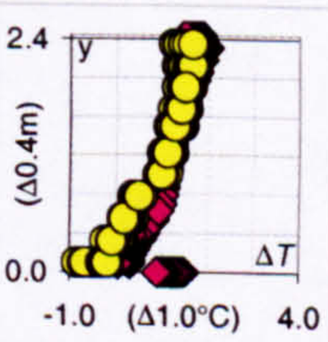	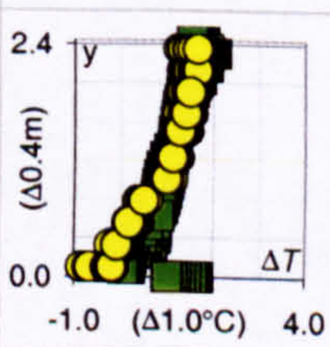

Width of opening:	1.2m
Effective area of opening:	$0.732m^2$
Heat source:	Plate heater
Strength of heat source:	225.0W

Figure 9.a

	Laminar	Standard-$k\varepsilon$	Realizable-$k\varepsilon$	RNG-$k\varepsilon$
Radiation model enabled, $\alpha = 0.00m^{-1}$ QUICK differencing. Convection walls. Uniform external temperature.	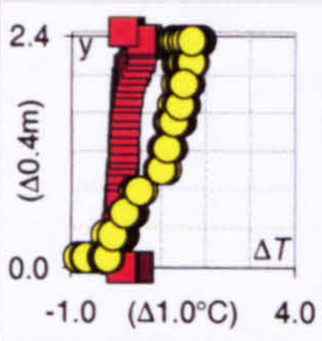	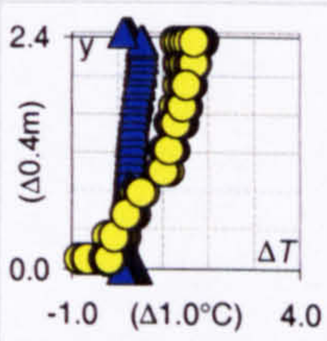	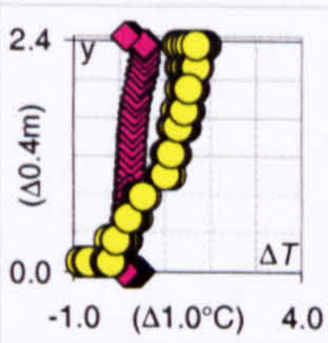	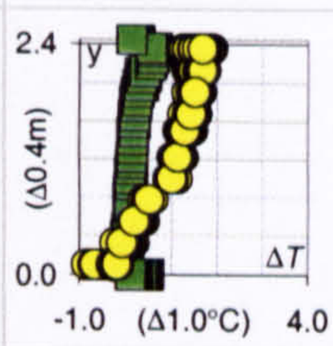
Radiation model enabled, $\alpha = 0.00m^{-1}$ QUICK differencing. Radiation walls. Uniform external temperature.	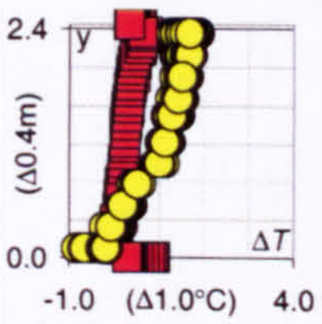	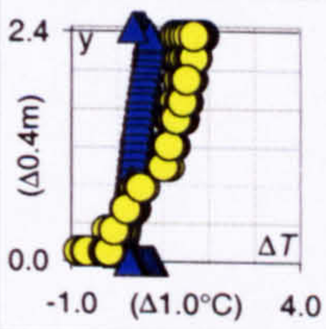	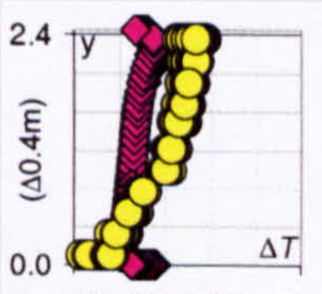	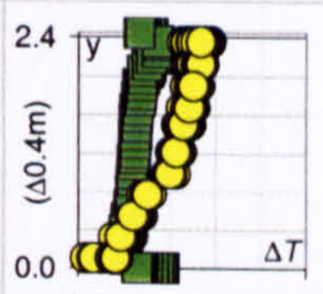
Radiation model enabled, $\alpha = 0.00m^{-1}$ QUICK differencing. Mixed walls. Uniform external temperature.	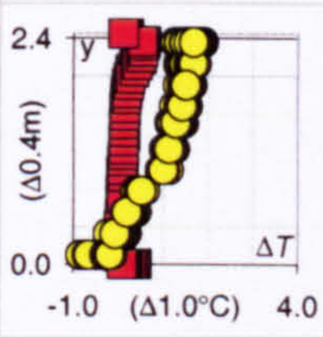	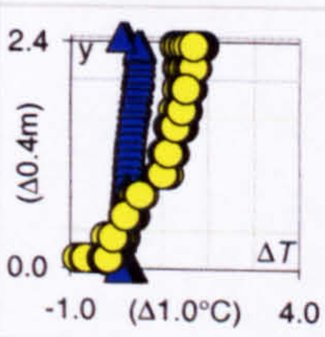	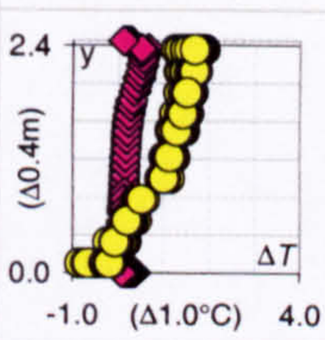	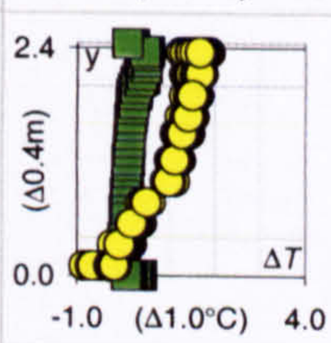
Radiation model enabled, $\alpha = 0.05m^{-1}$ QUICK differencing. Convection walls. Uniform external temperature.	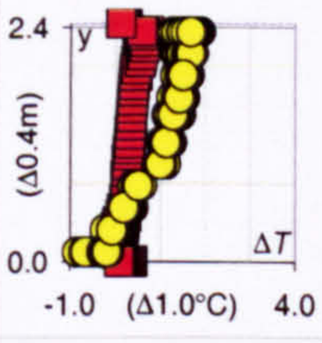	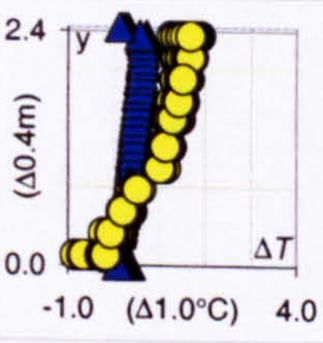	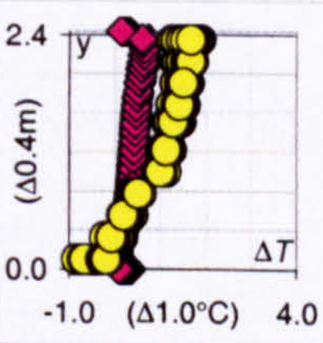	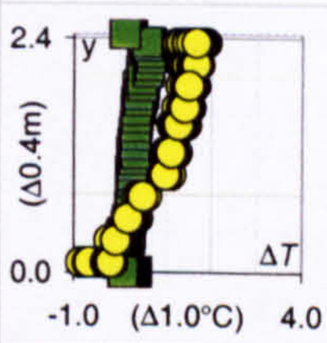
Radiation model enabled, $\alpha = 0.05m^{-1}$ QUICK differencing. Radiation walls. Uniform external temperature.	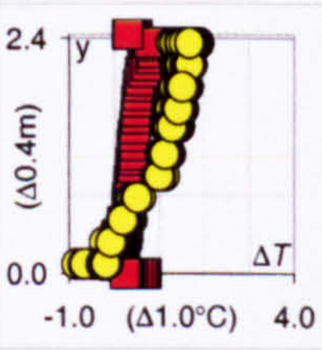	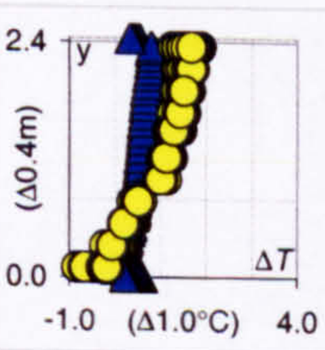	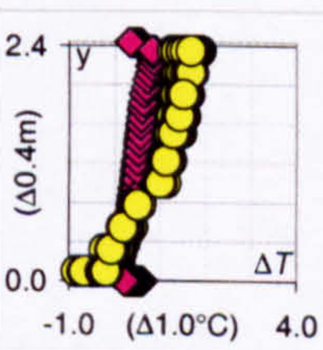	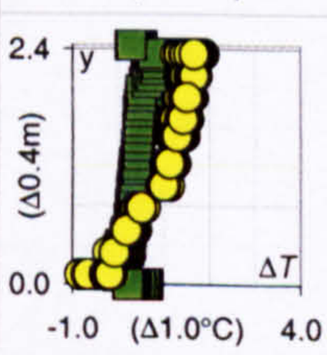
Radiation model enabled, $\alpha = 0.05m^{-1}$ QUICK differencing. Mixed walls. Uniform external temperature.	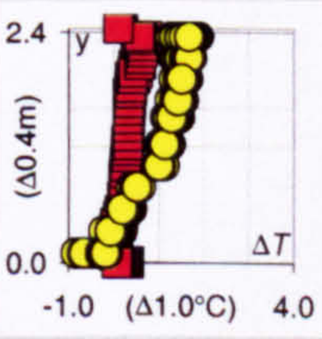	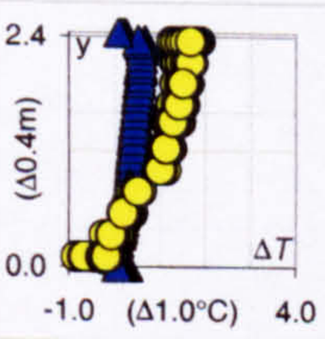	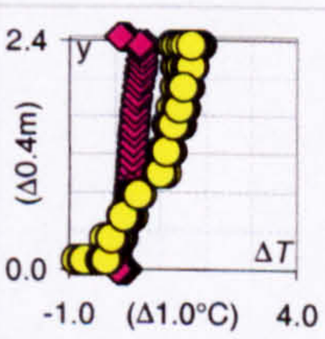	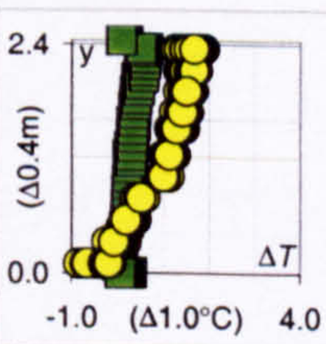

Width of opening:	1.2m
Effective area of opening:	$0.732m^2$
Heat source:	Plate heater
Strength of heat source:	225.0W

Figure 9.b

	Laminar	Standard-$k\varepsilon$	Realizable-$k\varepsilon$	RNG-$k\varepsilon$
Radiation model disabled. Upwind differencing. Adiabatic walls. Uniform external temperature.	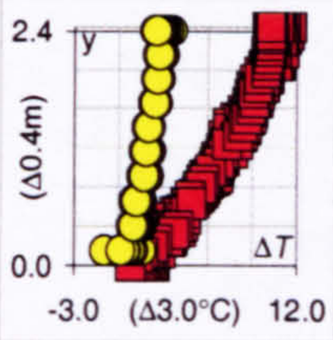	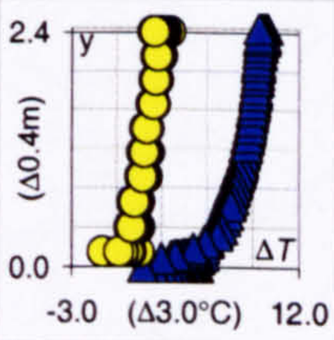	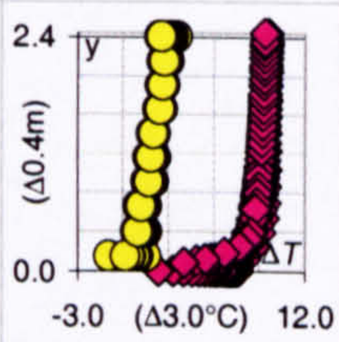	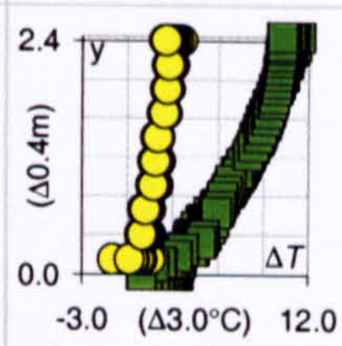
Radiation model disabled. QUICK differencing. Adiabatic walls. Uniform external temperature.	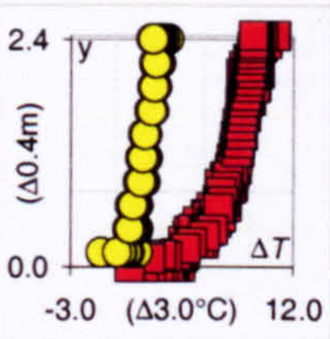	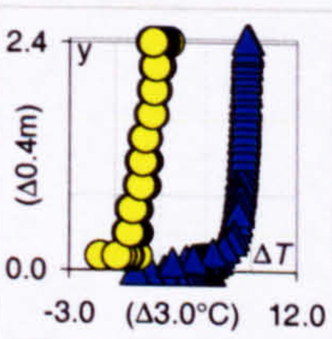	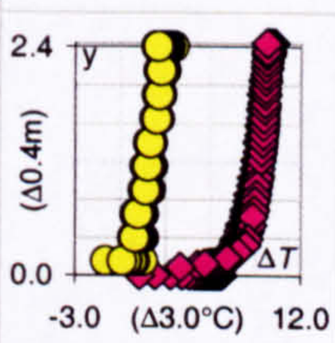	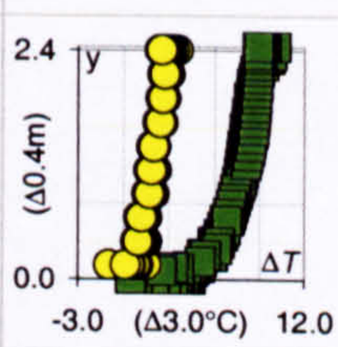
Radiation model enabled, $\alpha = 0.00m^{-1}$ QUICK differencing. Adiabatic walls. Uniform external temperature.	No available solution.	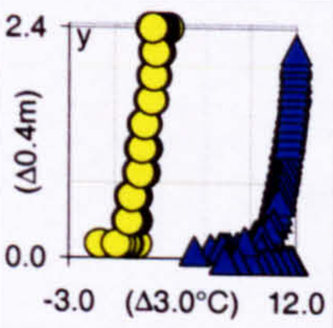	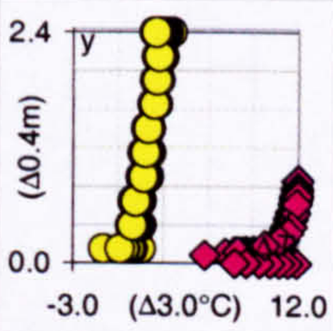	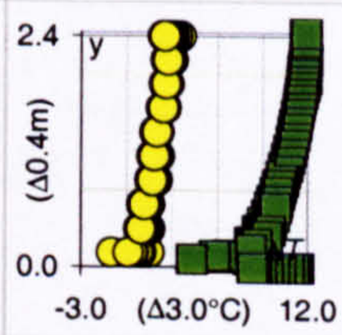
Radiation model enabled, $\alpha = 0.05m^{-1}$ QUICK differencing. Adiabatic walls. Uniform external temperature.	No available solution.	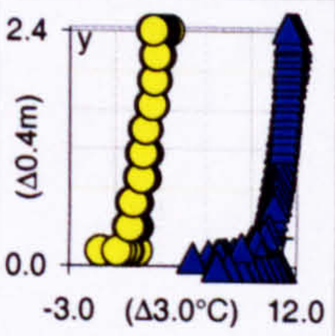	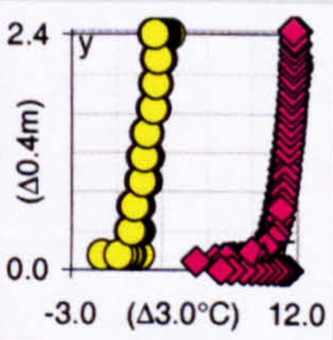	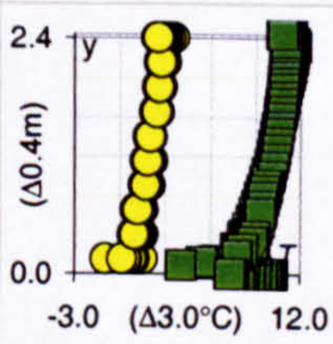
Radiation model enabled, $\alpha = 0.10m^{-1}$ QUICK differencing. Adiabatic walls. Uniform external temperature.	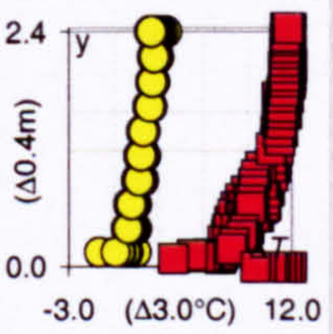	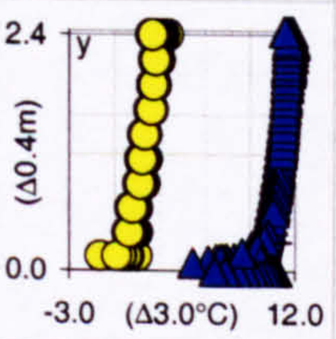	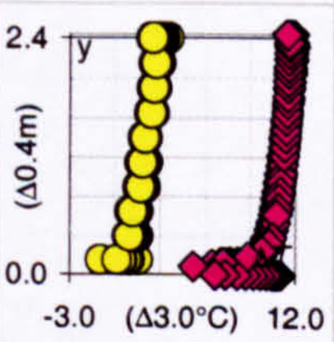	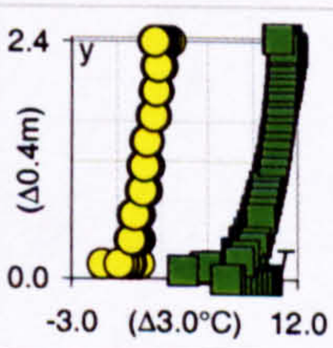
Radiation model enabled, $\alpha = 0.15m^{-1}$ QUICK differencing. Adiabatic walls. Uniform external temperature.	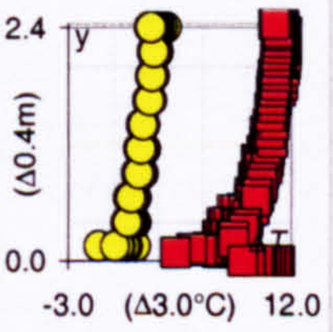	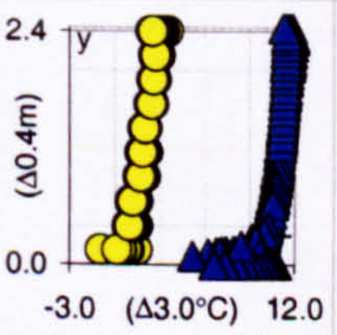	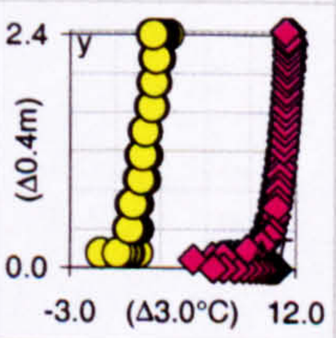	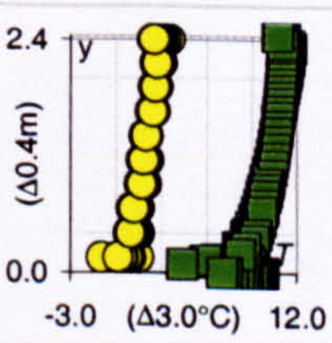

Width of opening:	0.1m
Effective area of opening:	$0.061m^2$
Heat source:	Boiler ring
Strength of heat source:	368.0W

Figure 10.a

	Laminar	Standard-$k\varepsilon$	Realizable-$k\varepsilon$	RNG-$k\varepsilon$
Radiation model enabled, $\alpha = 0.00m^{-1}$ QUICK differencing. Convection walls. Uniform external temperature.	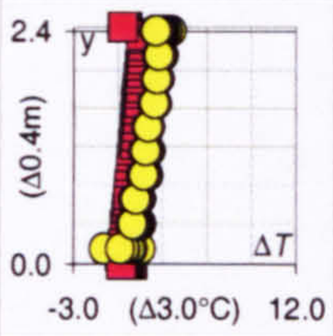	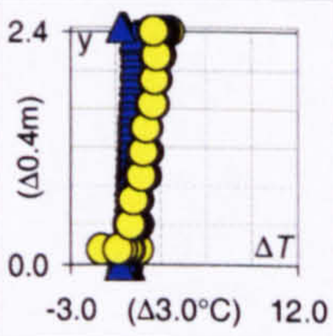	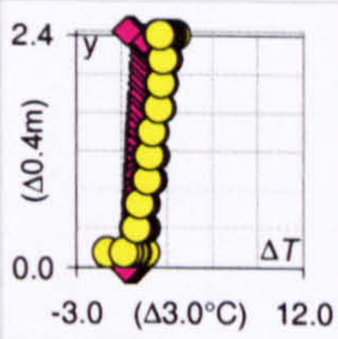	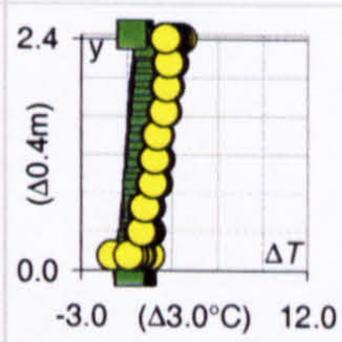
Radiation model enabled, $\alpha = 0.00m^{-1}$ QUICK differencing. Radiation walls. Uniform external temperature.	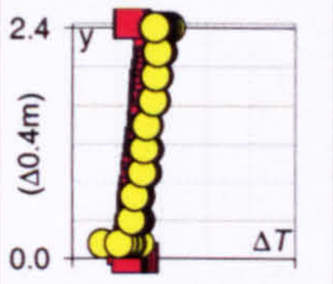	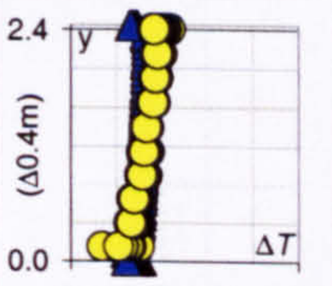	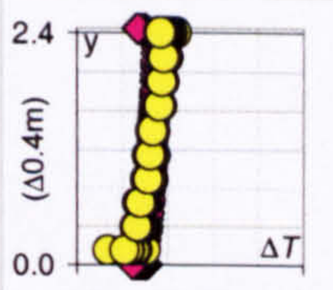	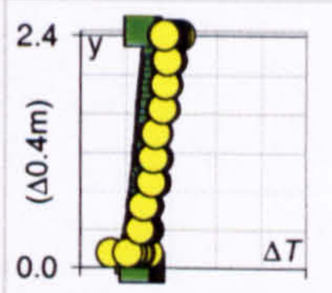
Radiation model enabled, $\alpha = 0.00m^{-1}$ QUICK differencing. Mixed walls. Uniform external temperature.	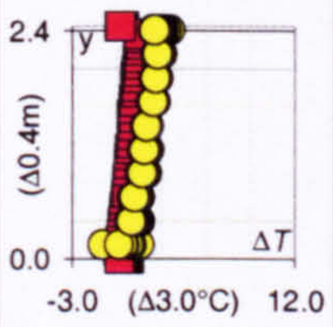	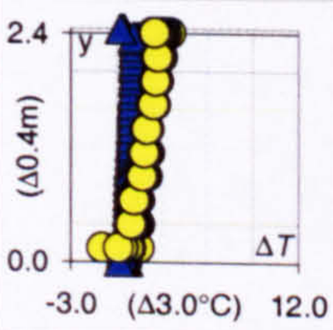	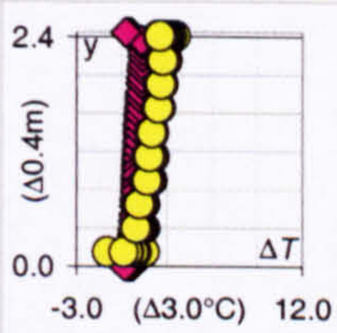	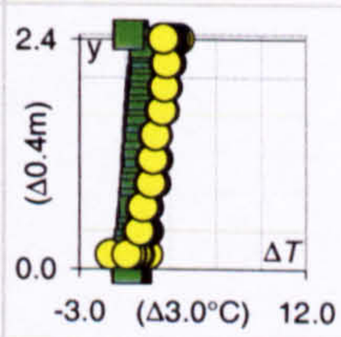
Radiation model enabled, $\alpha = 0.05m^{-1}$ QUICK differencing. Convection walls. Uniform external temperature.	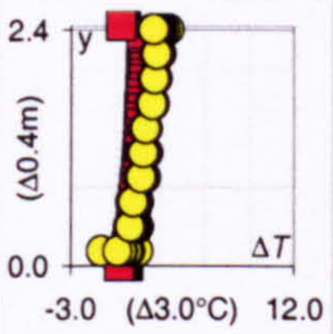	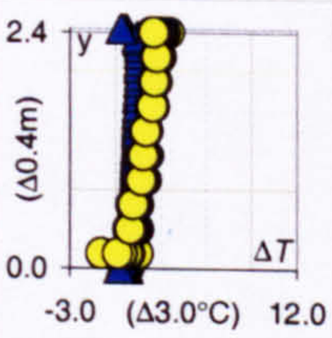	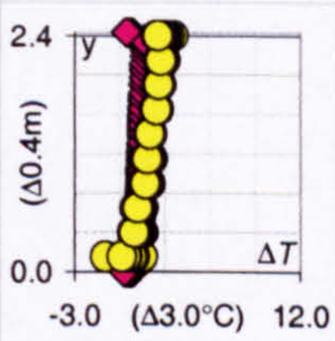	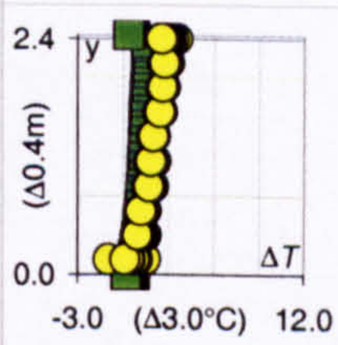
Radiation model enabled, $\alpha = 0.05m^{-1}$ QUICK differencing. Radiation walls. Uniform external temperature.	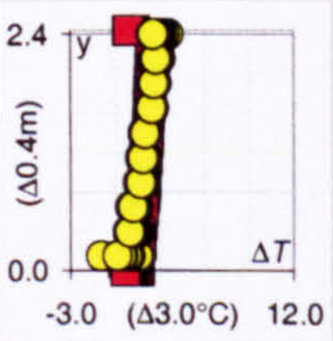	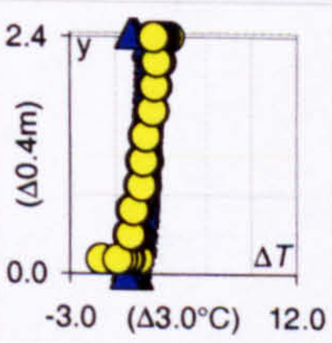	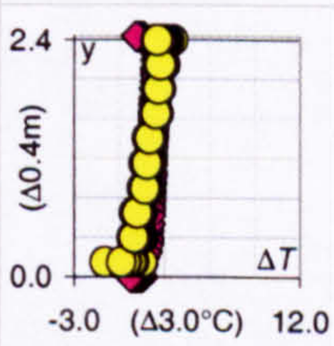	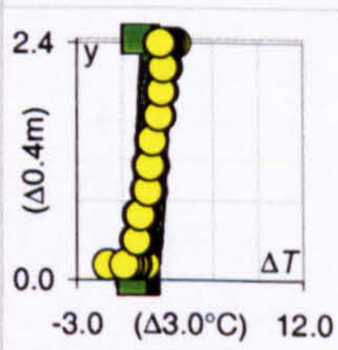
Radiation model enabled, $\alpha = 0.05m^{-1}$ QUICK differencing. Mixed walls. Uniform external temperature.	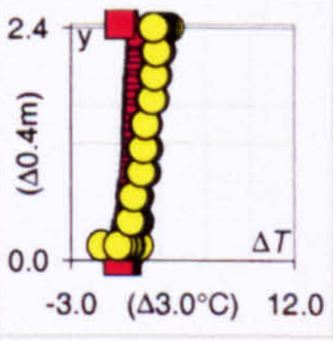	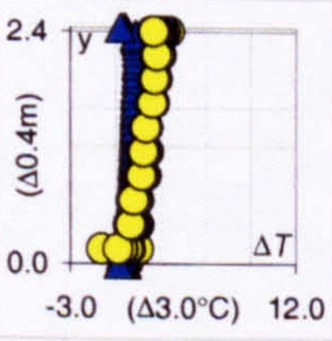	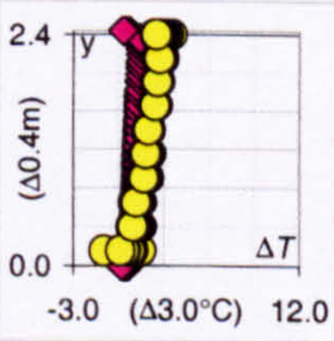	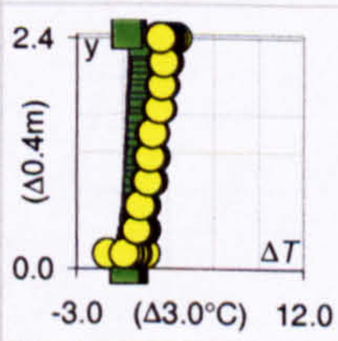

Width of opening:	0.1m
Effective area of opening:	$0.061m^2$
Heat source:	Boiler ring
Strength of heat source:	368.0W

Figure 10.b

	Laminar	Standard-$k\varepsilon$	Realizable-$k\varepsilon$	RNG-$k\varepsilon$
Radiation model disabled. Upwind differencing. Adiabatic walls. Uniform external temperature.	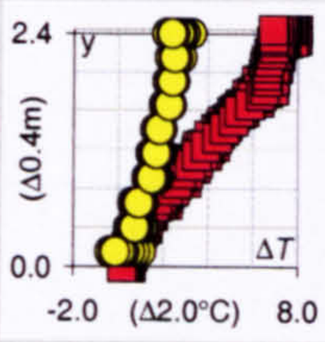	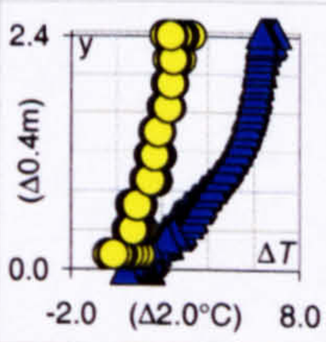	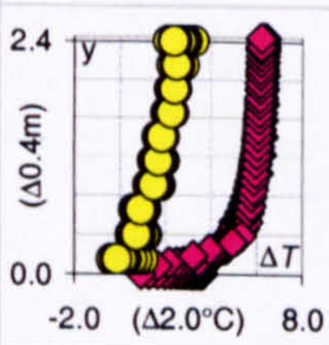	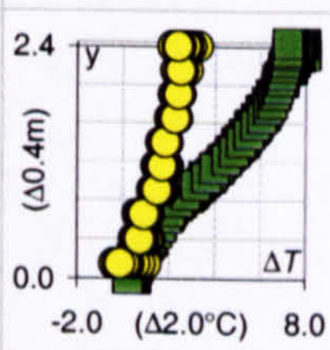
Radiation model disabled. QUICK differencing. Adiabatic walls. Uniform external temperature.	No available solution.	No available solution.	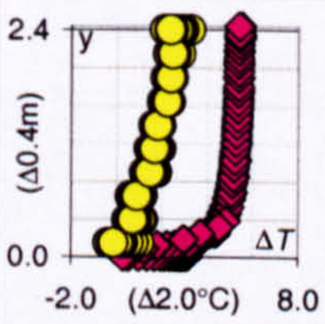	No available solution.
Radiation model enabled, $\alpha = 0.00m^{-1}$ QUICK differencing. Adiabatic walls. Uniform external temperature.	No available solution.	No available solution.	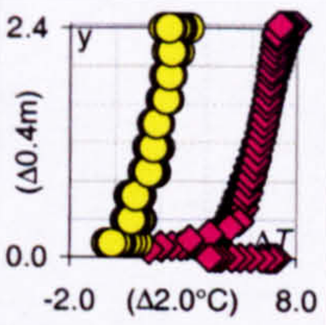	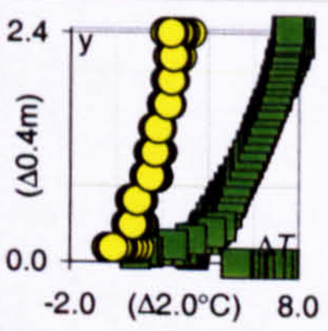
Radiation model enabled, $\alpha = 0.05m^{-1}$ QUICK differencing. Adiabatic walls. Uniform external temperature.	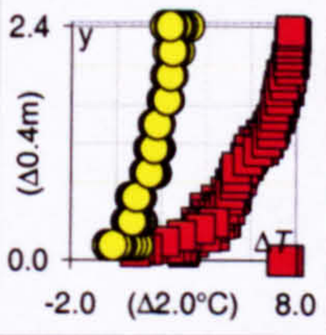	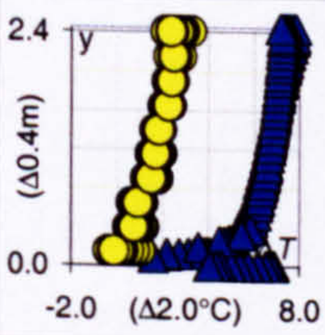	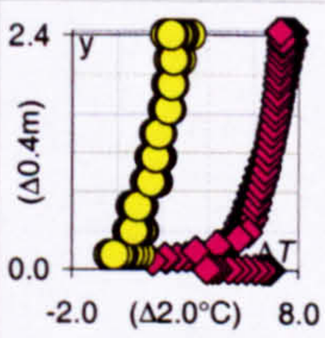	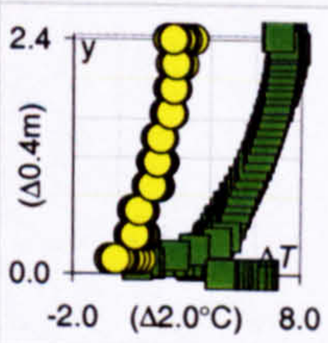
Radiation model enabled, $\alpha = 0.10m^{-1}$ QUICK differencing. Adiabatic walls. Uniform external temperature.	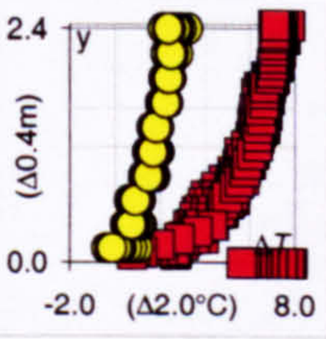	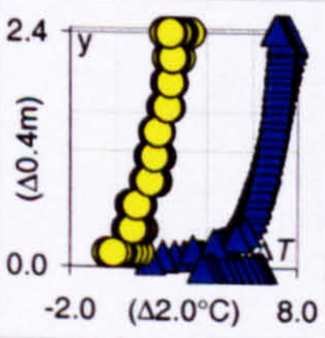	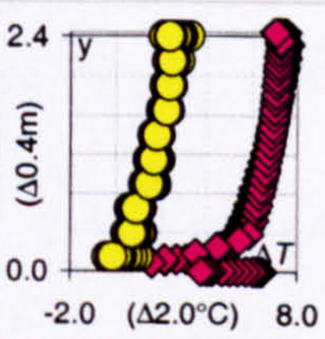	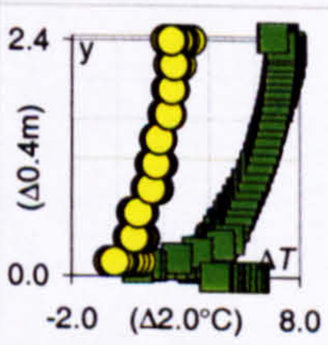
Radiation model enabled, $\alpha = 0.15m^{-1}$ QUICK differencing. Adiabatic walls. Uniform external temperature.	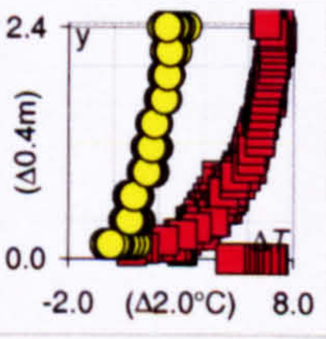	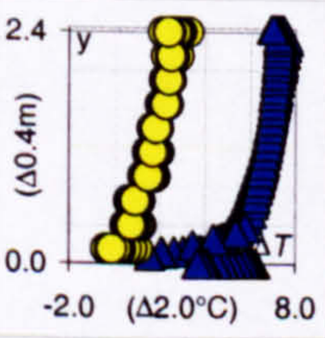	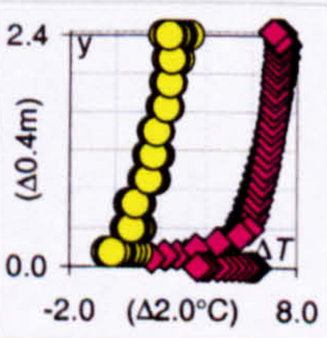	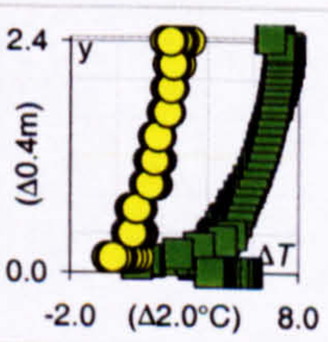

Width of opening: 0.2m
Effective area of opening: 0.122m^2
Heat source: Boiler ring
Strength of heat source: 368.0W

Figure 11.a

	Laminar	Standard-$k\varepsilon$	Realizable-$k\varepsilon$	RNG-$k\varepsilon$
Radiation model enabled, $\alpha = 0.00m^{-1}$ QUICK differencing. Convection walls. Uniform external temperature.	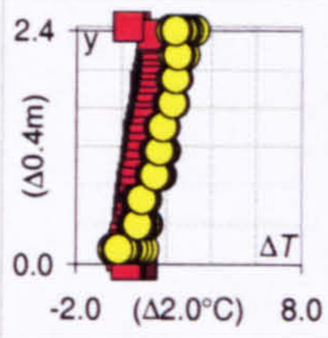	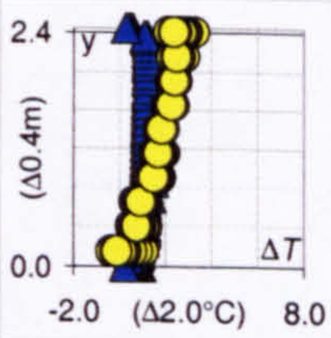	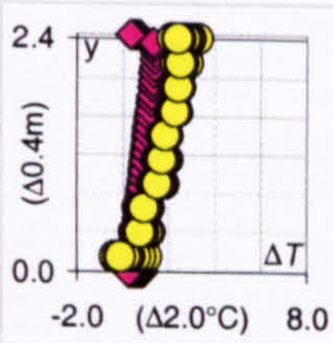	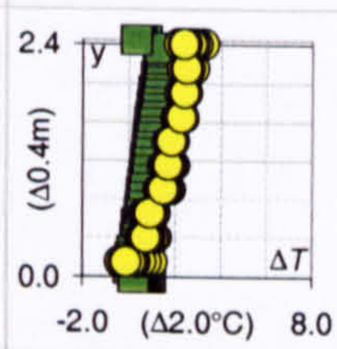
Radiation model enabled, $\alpha = 0.00m^{-1}$ QUICK differencing. Radiation walls. Uniform external temperature.	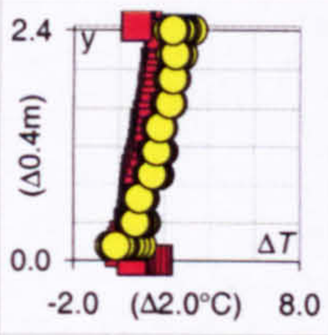	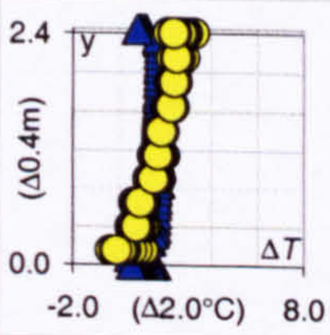	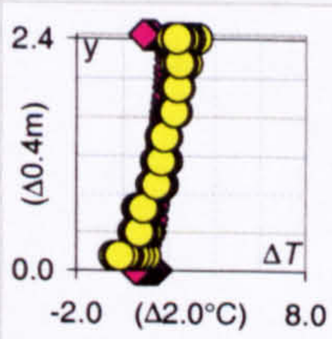	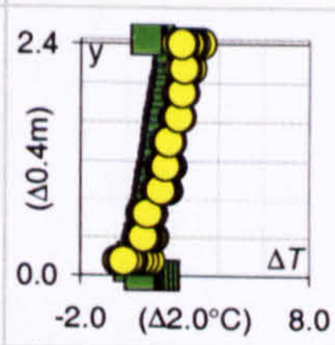
Radiation model enabled, $\alpha = 0.00m^{-1}$ QUICK differencing. Mixed walls. Uniform external temperature.	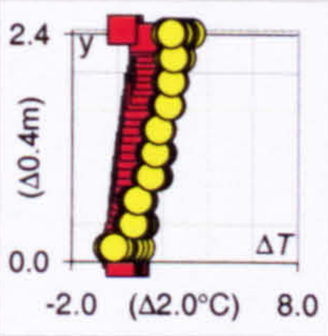	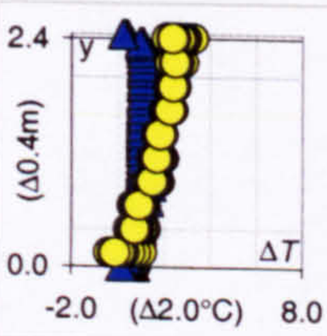	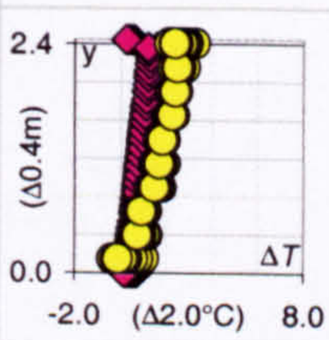	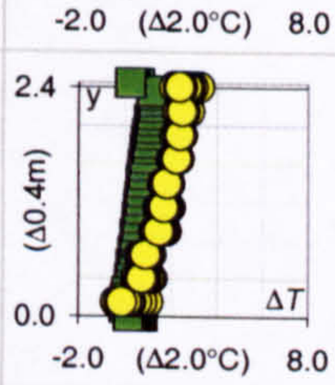
Radiation model enabled, $\alpha = 0.05m^{-1}$ QUICK differencing. Convection walls. Uniform external temperature.	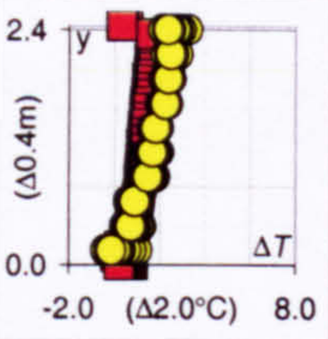	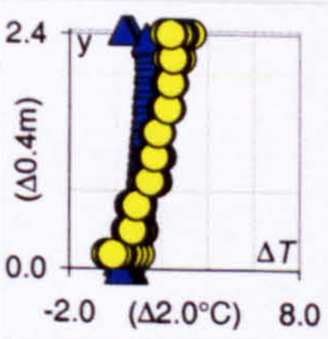	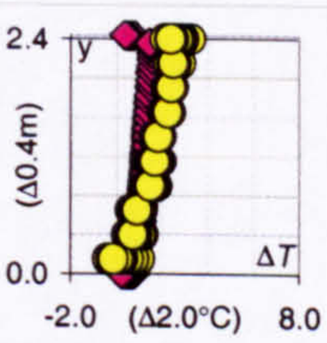	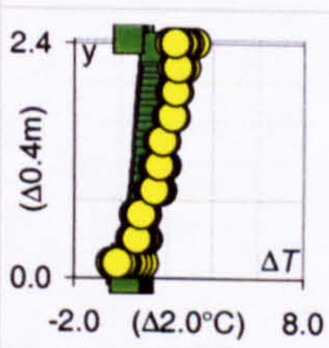
Radiation model enabled, $\alpha = 0.05m^{-1}$ QUICK differencing. Radiation walls. Uniform external temperature.	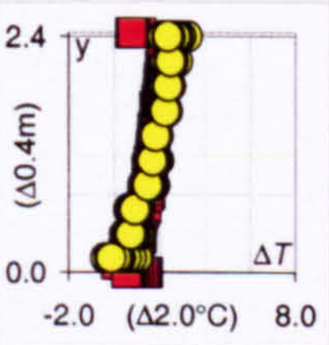	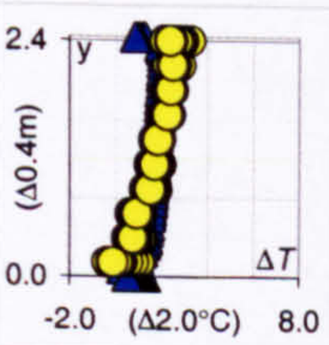	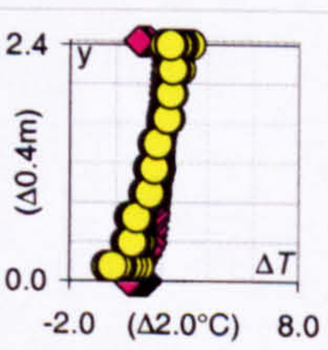	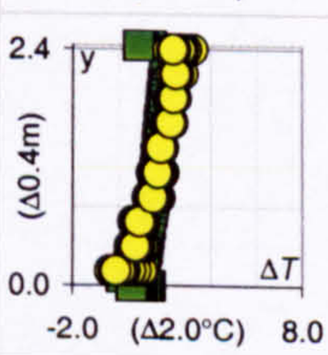
Radiation model enabled, $\alpha = 0.05m^{-1}$ QUICK differencing. Mixed walls. Uniform external temperature.	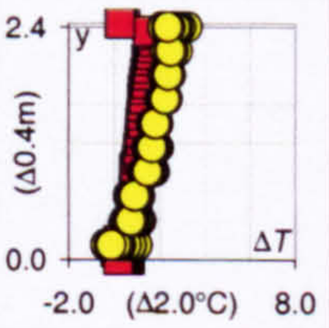	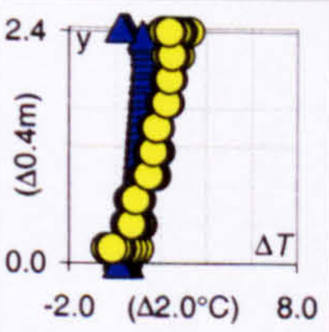	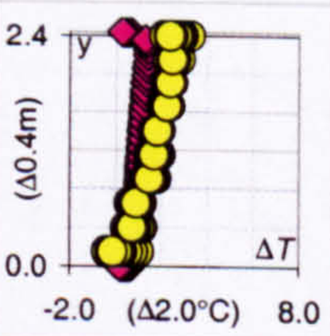	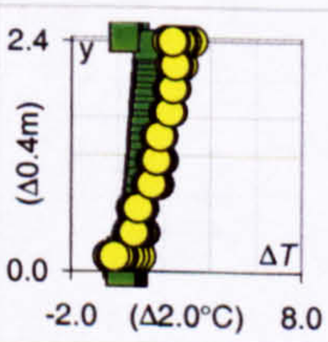

Width of opening:	0.2m
Effective area of opening:	$0.122m^2$
Heat source:	Boiler ring
Strength of heat source:	368.0W

Figure 11.b

	Laminar	Standard-$k\varepsilon$	Realizable-$k\varepsilon$	RNG-$k\varepsilon$
Radiation model disabled. Upwind differencing. Adiabatic walls. Uniform external temperature.	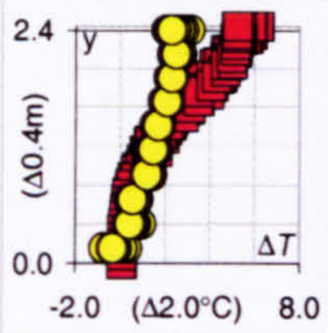	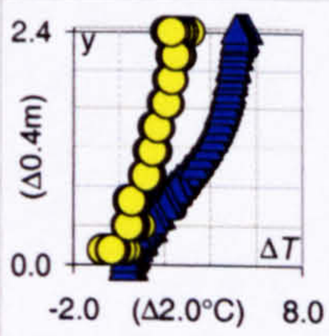	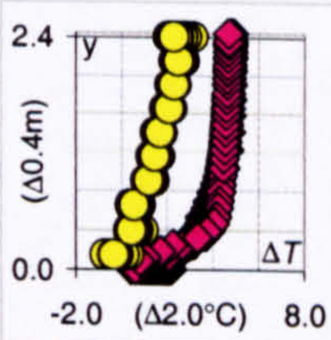	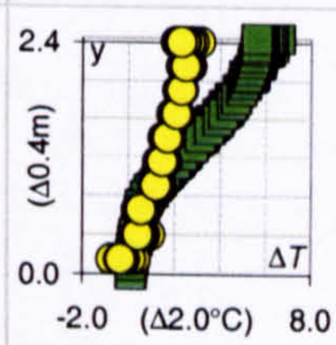
Radiation model disabled. QUICK differencing. Adiabatic walls. Uniform external temperature.	No available solution.	No available solution.	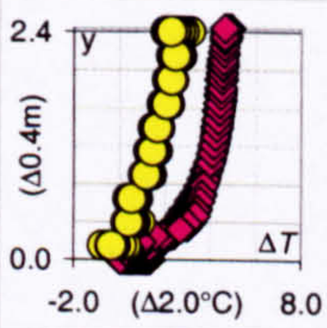	No available solution.
Radiation model enabled, $\alpha = 0.00m^{-1}$ QUICK differencing. Adiabatic walls. Uniform external temperature.	No available solution.	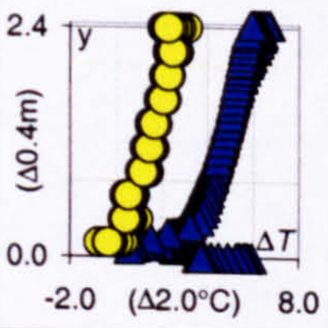	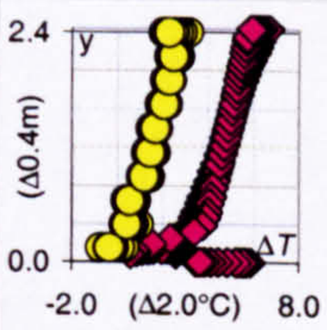	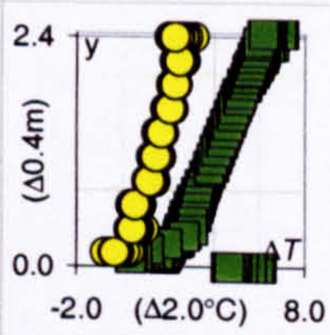
Radiation model enabled, $\alpha = 0.05m^{-1}$ QUICK differencing. Adiabatic walls. Uniform external temperature.	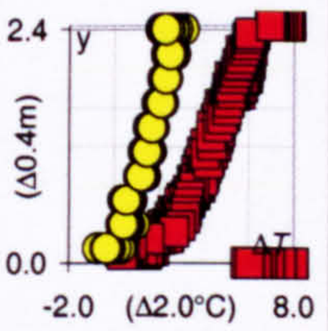	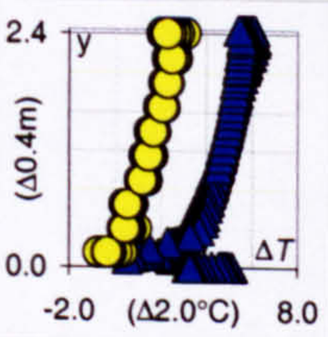	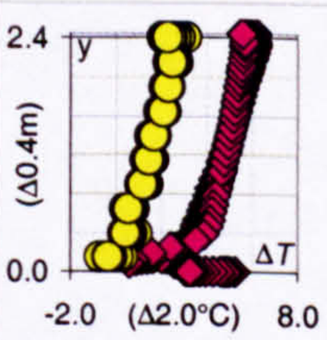	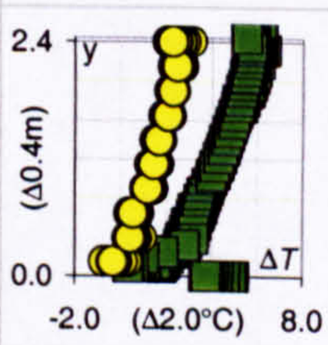
Radiation model enabled, $\alpha = 0.10m^{-1}$ QUICK differencing. Adiabatic walls. Uniform external temperature.	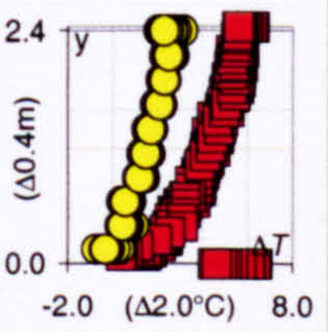	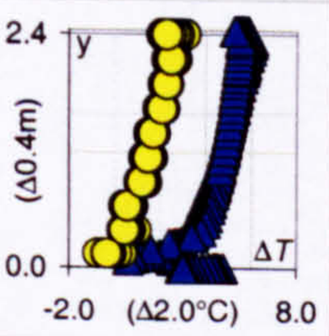	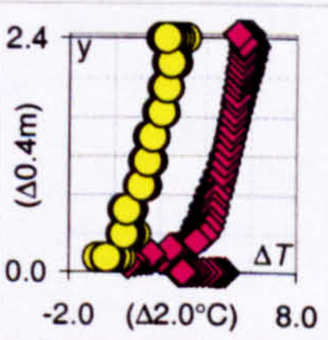	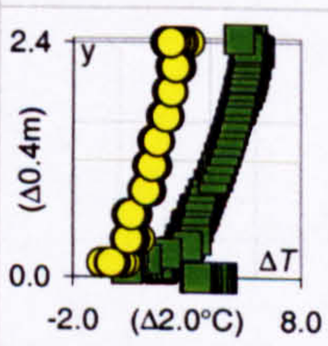
Radiation model enabled, $\alpha = 0.15m^{-1}$ QUICK differencing. Adiabatic walls. Uniform external temperature.	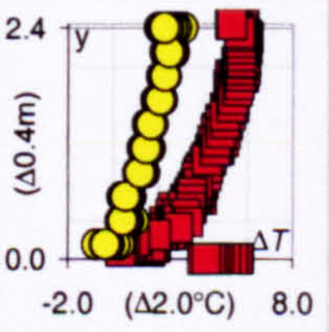	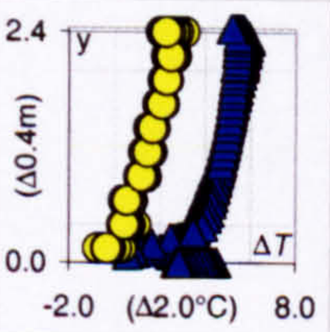	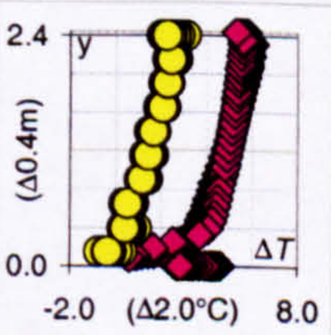	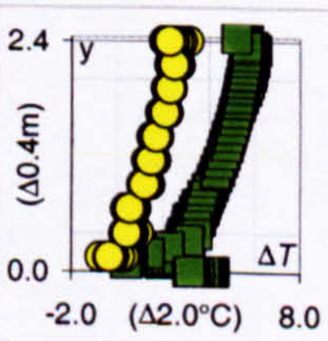

Width of opening:	0.3m
Effective area of opening:	$0.183m^2$
Heat source:	Boiler ring
Strength of heat source:	368.0W

Figure 12.a

	Laminar	Standard-$k\varepsilon$	Realizable-$k\varepsilon$	RNG-$k\varepsilon$
Radiation model enabled, $\alpha = 0.00m^{-1}$ QUICK differencing. Convection walls. Uniform external temperature.	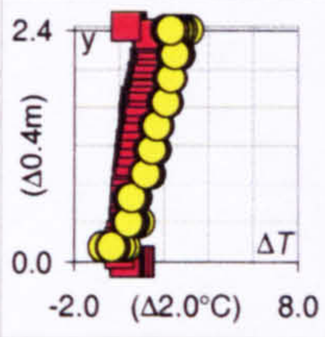	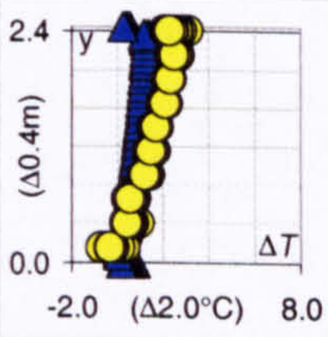	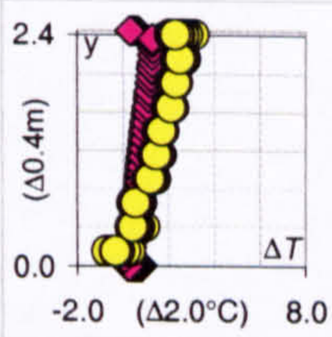	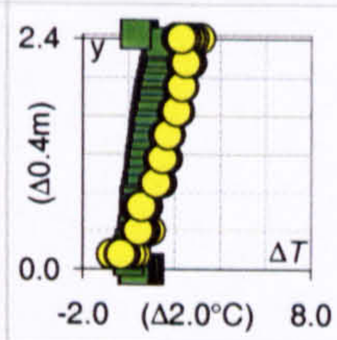
Radiation model enabled, $\alpha = 0.00m^{-1}$ QUICK differencing. Radiation walls. Uniform external temperature.	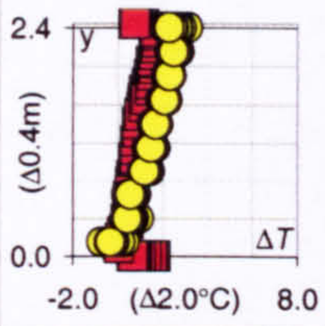	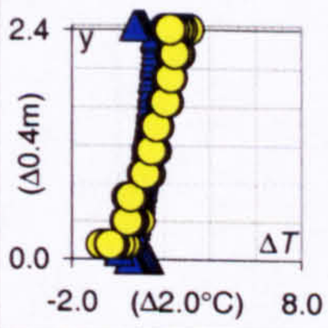	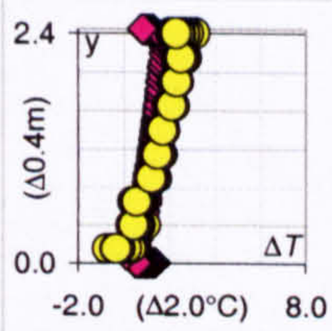	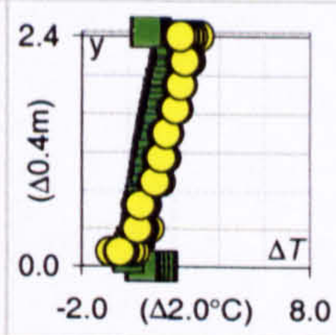
Radiation model enabled, $\alpha = 0.00m^{-1}$ QUICK differencing. Mixed walls. Uniform external temperature.	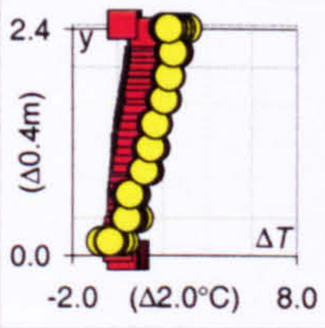	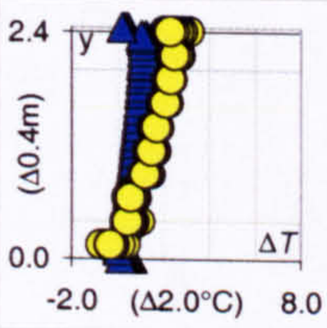	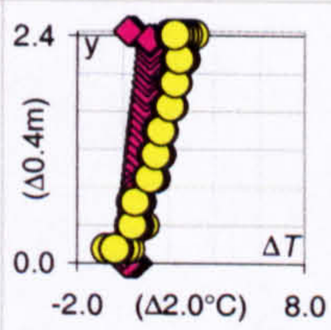	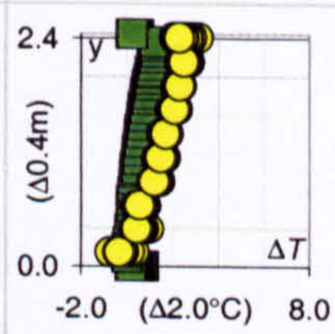
Radiation model enabled, $\alpha = 0.05m^{-1}$ QUICK differencing. Convection walls. Uniform external temperature.	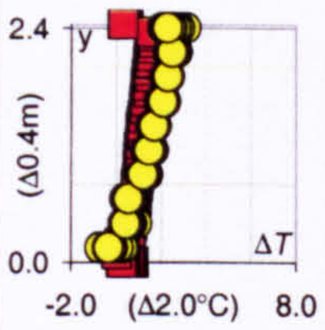	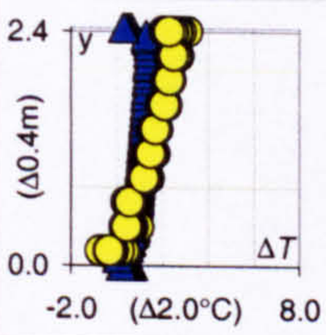	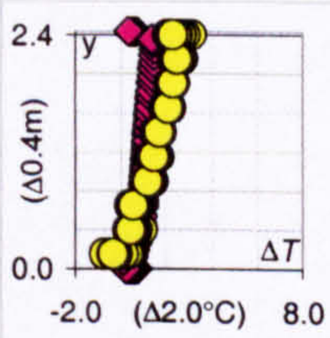	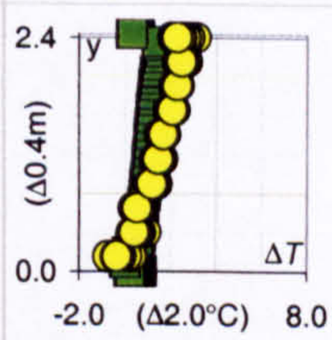
Radiation model enabled, $\alpha = 0.05m^{-1}$ QUICK differencing. Radiation walls. Uniform external temperature.	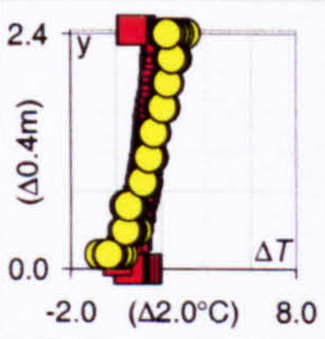	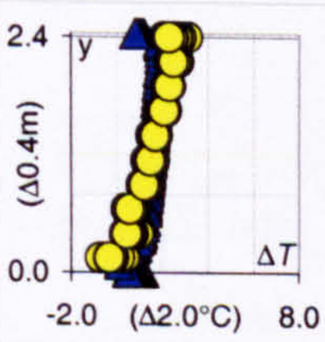	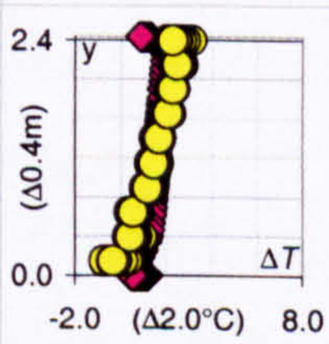	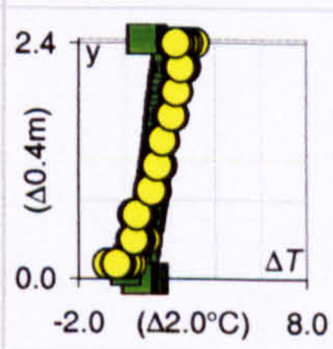
Radiation model enabled, $\alpha = 0.05m^{-1}$ QUICK differencing. Mixed walls. Uniform external temperature.	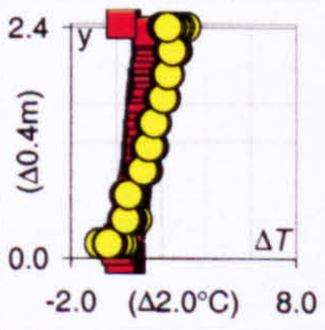	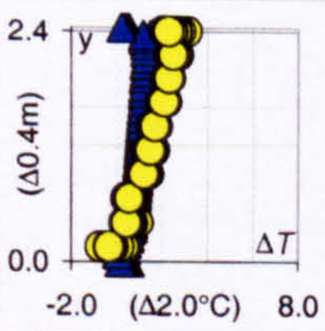	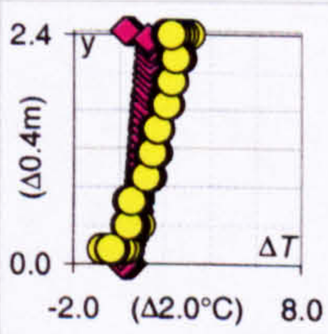	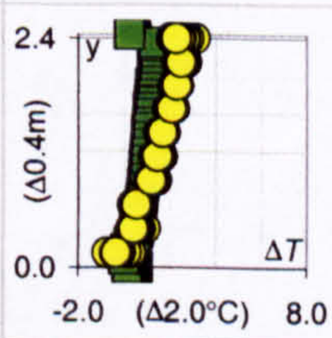

Width of opening:	0.3m
Effective area of opening:	$0.183m^2$
Heat source:	Boiler ring
Strength of heat source:	368.0W

Figure 12.b

	Laminar	Standard-$k\varepsilon$	Realizable-$k\varepsilon$	RNG-$k\varepsilon$
Radiation model disabled. Upwind differencing. Adiabatic walls. Uniform external temperature.	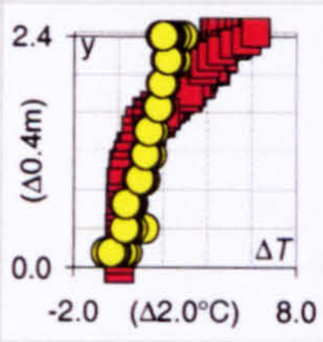	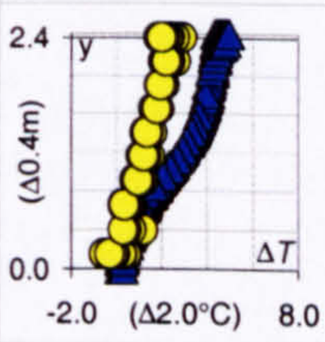	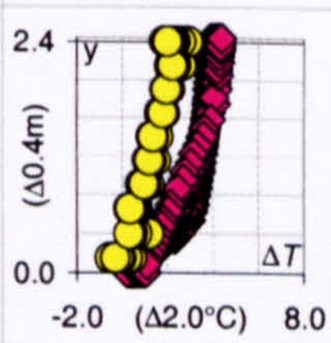	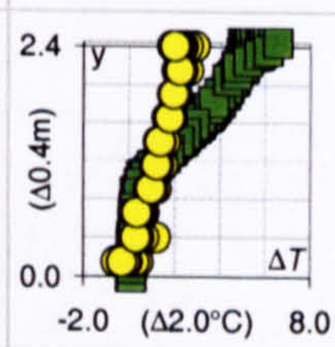
Radiation model disabled. QUICK differencing. Adiabatic walls. Uniform external temperature.	No available solution.	No available solution.	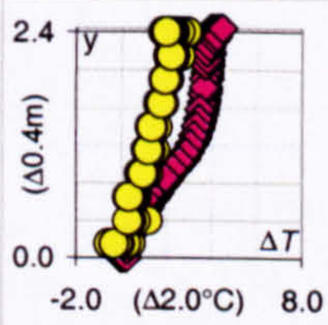	No available solution.
Radiation model enabled, $\alpha = 0.00m^{-1}$ QUICK differencing. Adiabatic walls. Uniform external temperature.	No available solution.	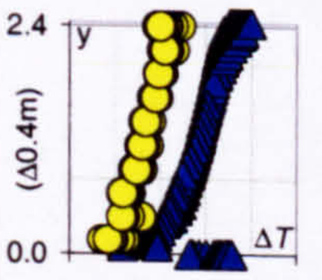	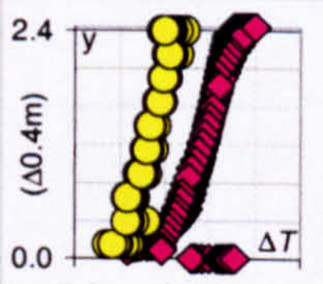	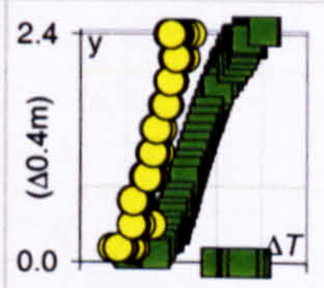
Radiation model enabled, $\alpha = 0.05m^{-1}$ QUICK differencing. Adiabatic walls. Uniform external temperature.	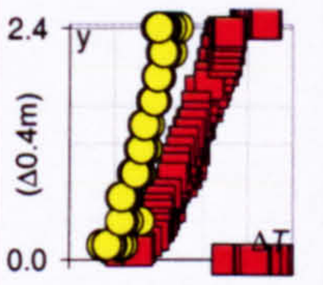	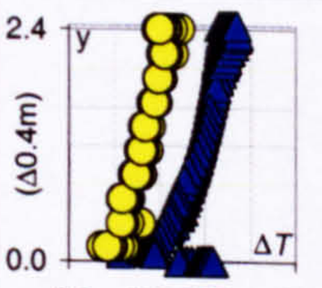	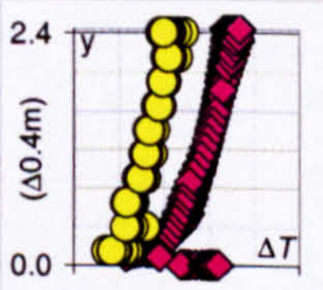	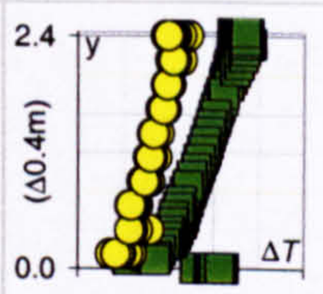
Radiation model enabled, $\alpha = 0.10m^{-1}$ QUICK differencing. Adiabatic walls. Uniform external temperature.	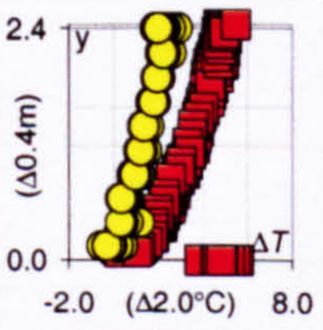	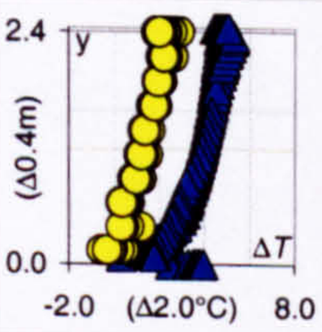	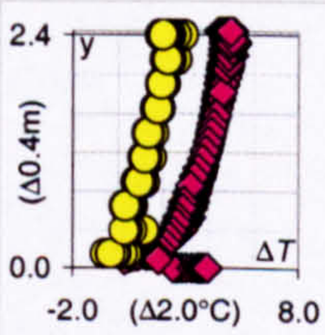	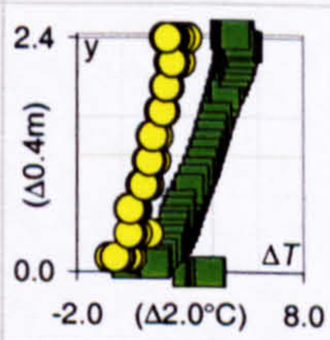
Radiation model enabled, $\alpha = 0.15m^{-1}$ QUICK differencing. Adiabatic walls. Uniform external temperature.	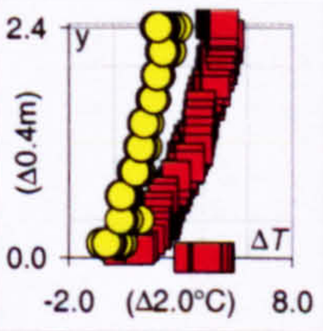	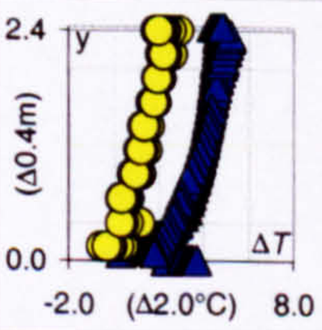	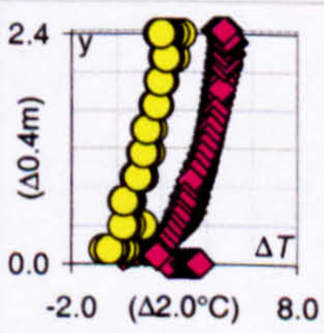	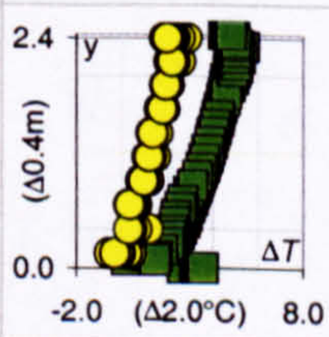

Width of opening:	0.4m
Effective area of opening:	$0.244m^2$
Heat source:	Boiler ring
Strength of heat source:	368.0W

Figure 13.a

	Laminar	Standard-$k\varepsilon$	Realizable-$k\varepsilon$	RNG-$k\varepsilon$
Radiation model enabled, $\alpha = 0.00m^{-1}$ QUICK differencing. Convection walls. Uniform external temperature.	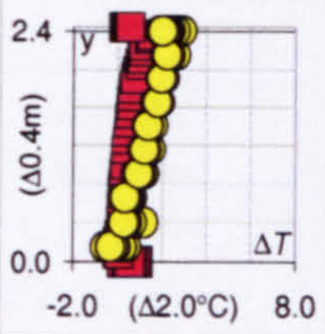	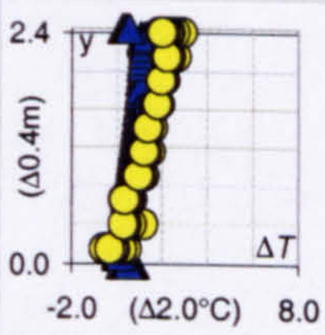	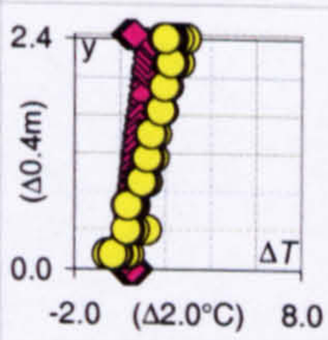	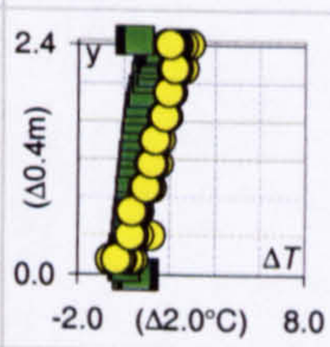
Radiation model enabled, $\alpha = 0.00m^{-1}$ QUICK differencing. Radiation walls. Uniform external temperature.	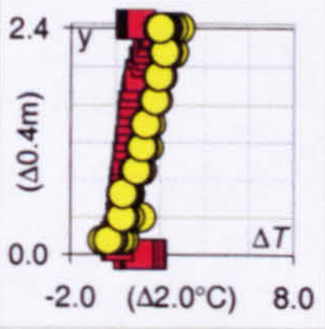	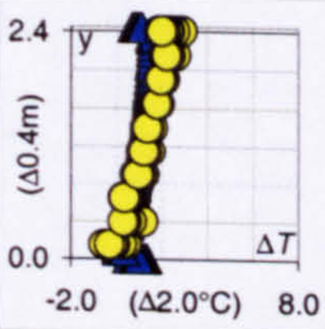	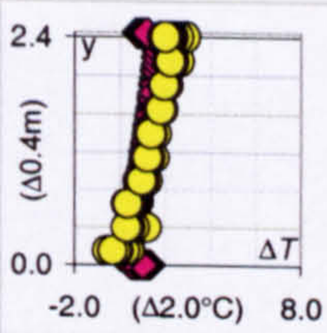	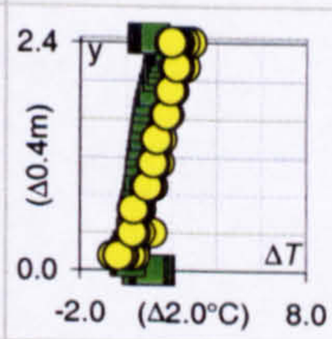
Radiation model enabled, $\alpha = 0.00m^{-1}$ QUICK differencing. Mixed walls. Uniform external temperature.	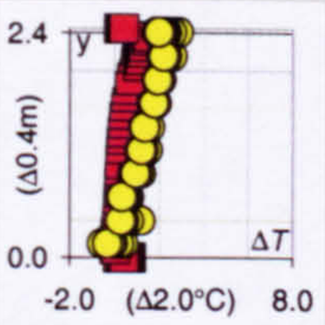	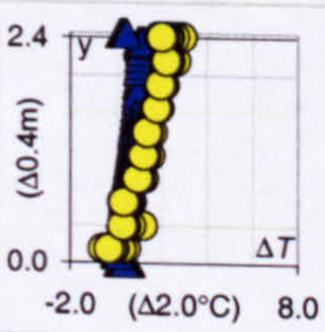	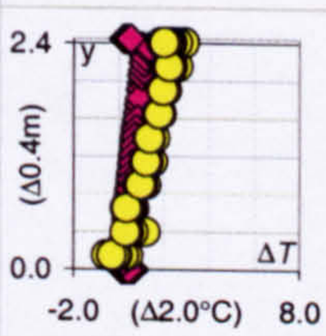	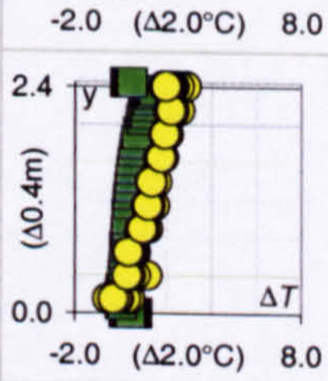
Radiation model enabled, $\alpha = 0.05m^{-1}$ QUICK differencing. Convection walls. Uniform external temperature.	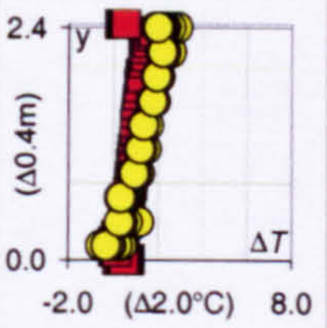	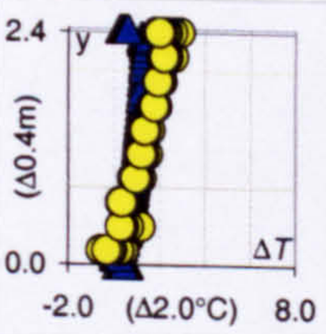	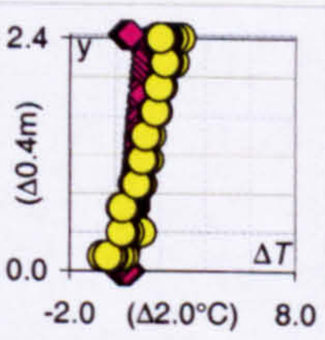	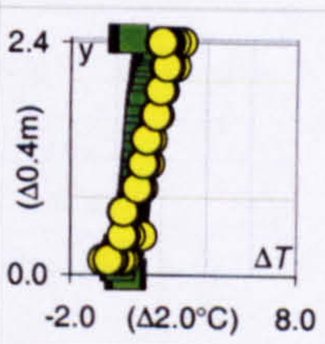
Radiation model enabled, $\alpha = 0.05m^{-1}$ QUICK differencing. Radiation walls. Uniform external temperature.	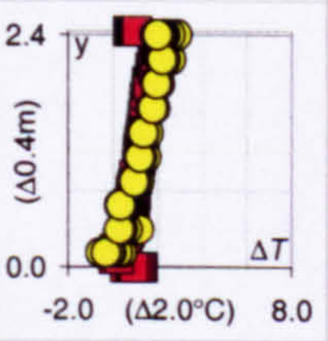	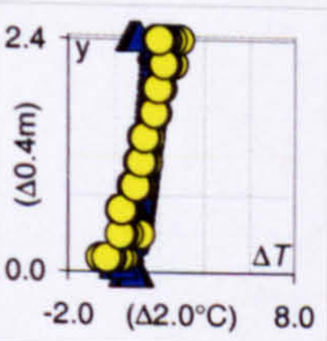	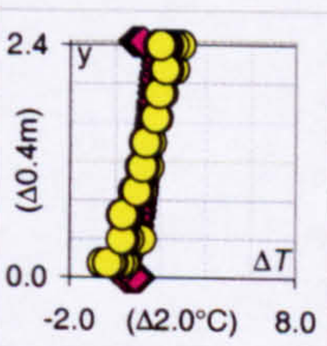	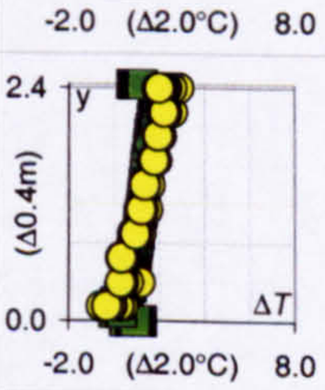
Radiation model enabled, $\alpha = 0.05m^{-1}$ QUICK differencing. Mixed walls. Uniform external temperature.	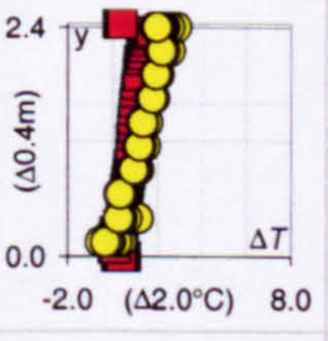	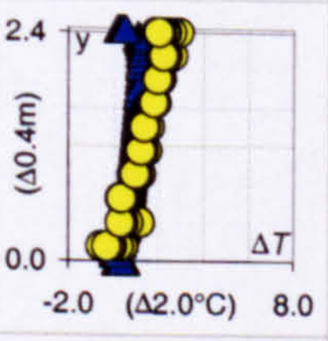	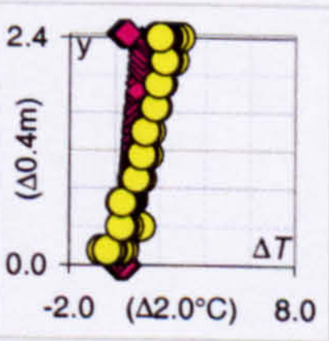	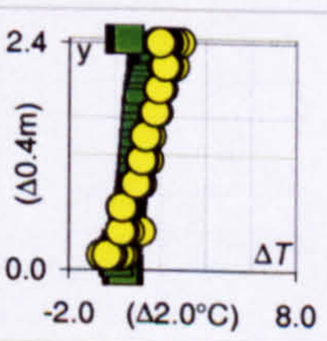

Width of opening:	0.4m
Effective area of opening:	$0.244m^2$
Heat source:	Boiler ring
Strength of heat source:	368.0W

Figure 13.b

	Laminar	Standard-$k\varepsilon$	Realizable-$k\varepsilon$	RNG-$k\varepsilon$
Radiation model disabled. Upwind differencing. Adiabatic walls. Uniform external temperature.	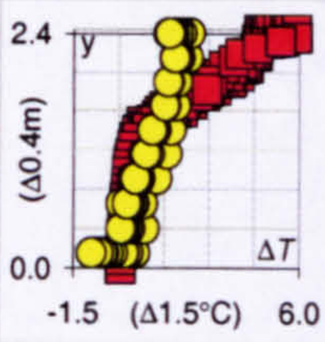	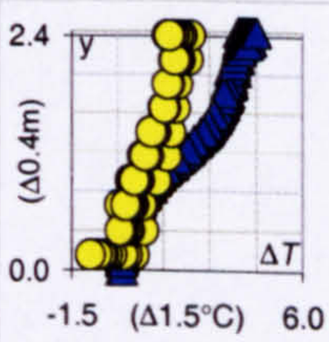	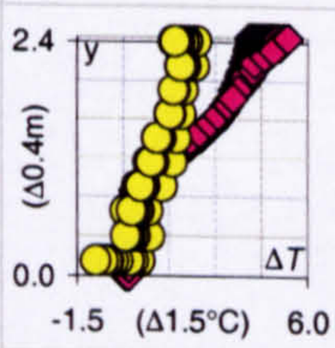	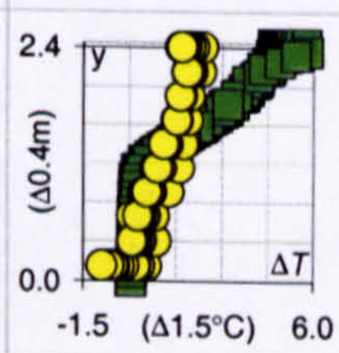
Radiation model disabled. QUICK differencing. Adiabatic walls. Uniform external temperature.	No available solution.	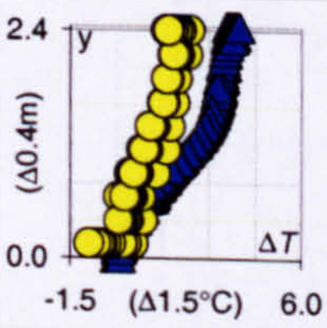	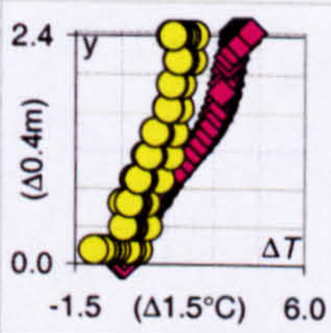	No available solution.
Radiation model enabled, $\alpha = 0.00m^{-1}$ QUICK differencing. Adiabatic walls. Uniform external temperature.	No available solution.	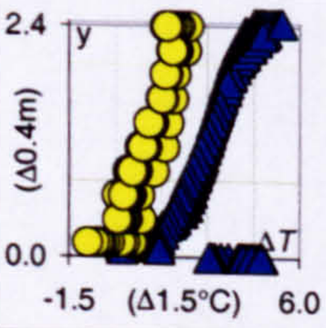	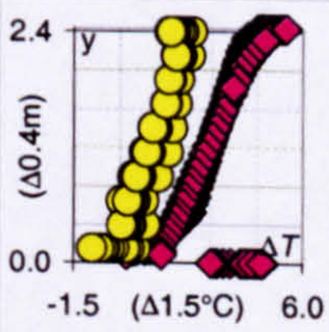	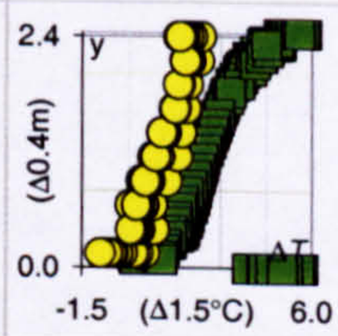
Radiation model enabled, $\alpha = 0.05m^{-1}$ QUICK differencing. Adiabatic walls. Uniform external temperature.	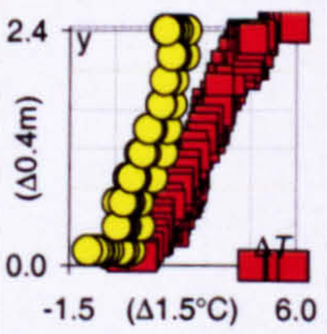	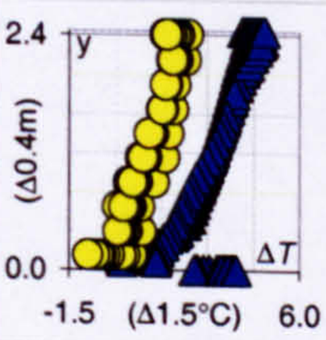	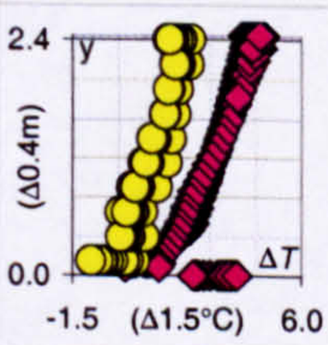	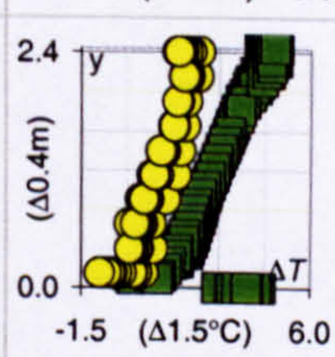
Radiation model enabled, $\alpha = 0.10m^{-1}$ QUICK differencing. Adiabatic walls. Uniform external temperature.	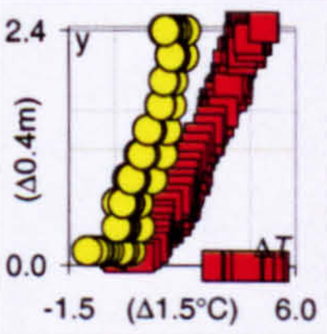	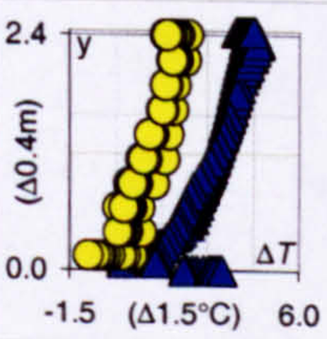	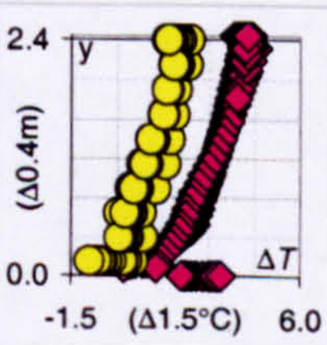	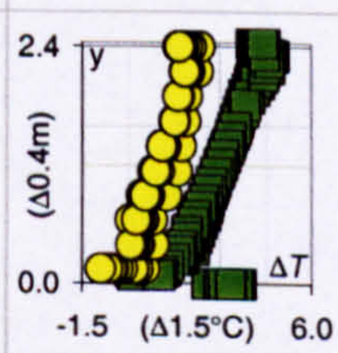
Radiation model enabled, $\alpha = 0.15m^{-1}$ QUICK differencing. Adiabatic walls. Uniform external temperature.	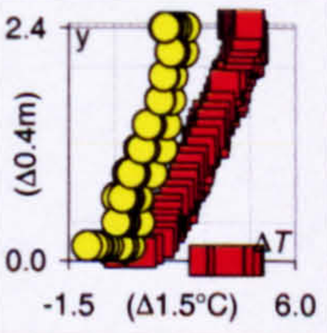	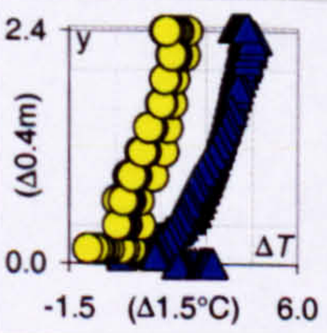	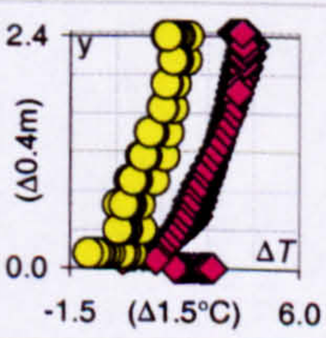	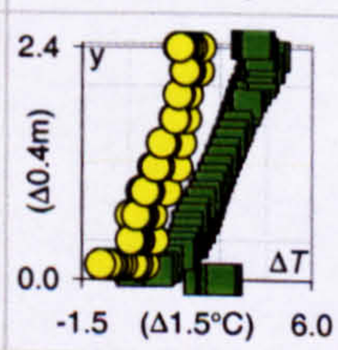

Width of opening:	0.5m
Effective area of opening:	$0.305m^2$
Heat source:	Boiler ring
Strength of heat source:	368.0W

Figure 14.a

	Laminar	Standard-$k\varepsilon$	Realizable-$k\varepsilon$	RNG-$k\varepsilon$
Radiation model enabled, $\alpha = 0.00m^{-1}$ QUICK differencing. Convection walls. Uniform external temperature.	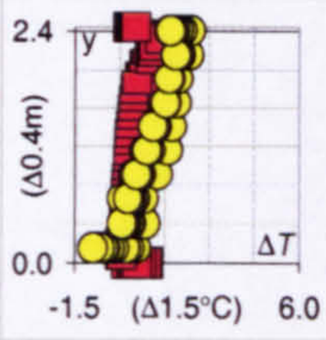	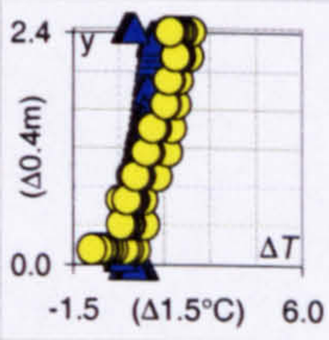	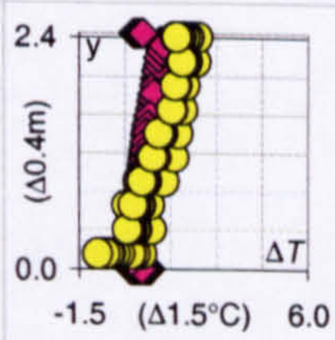	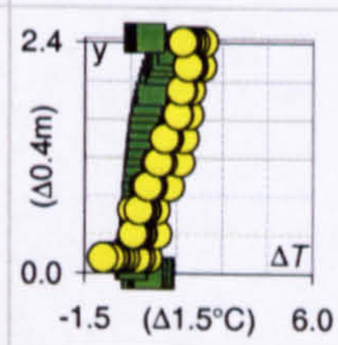
Radiation model enabled, $\alpha = 0.00m^{-1}$ QUICK differencing. Radiation walls. Uniform external temperature.	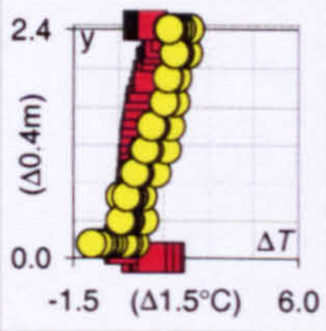	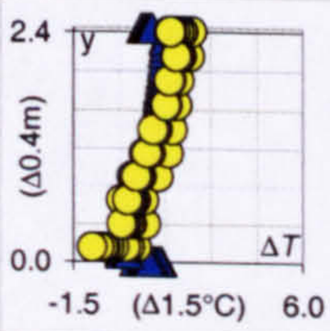	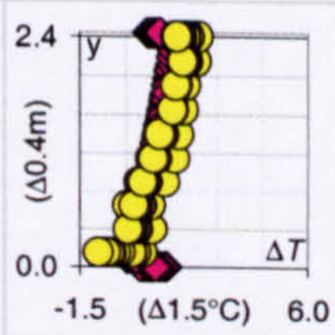	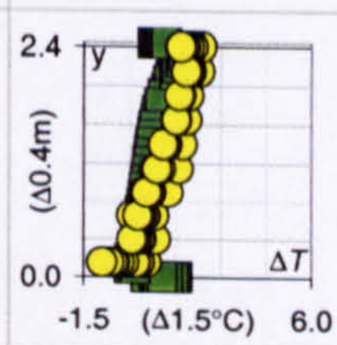
Radiation model enabled, $\alpha = 0.00m^{-1}$ QUICK differencing. Mixed walls. Uniform external temperature.	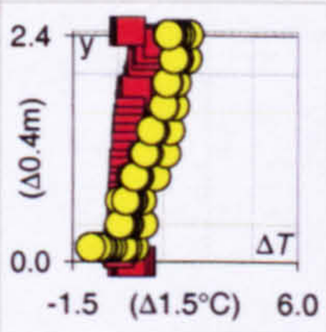	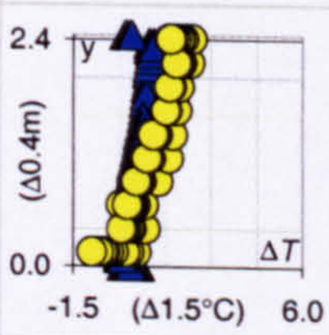	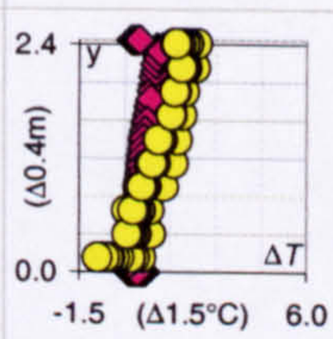	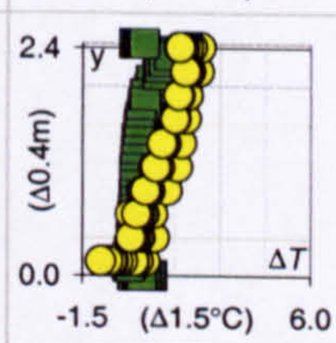
Radiation model enabled, $\alpha = 0.05m^{-1}$ QUICK differencing. Convection walls. Uniform external temperature.	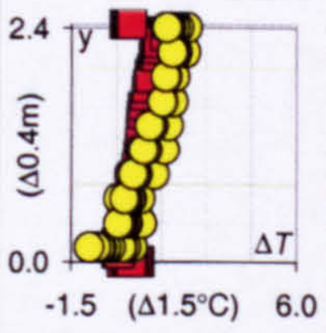	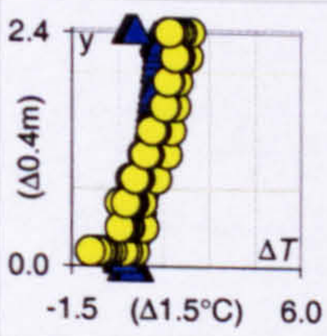	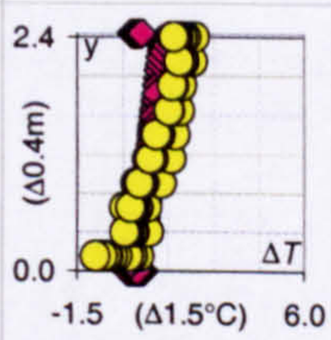	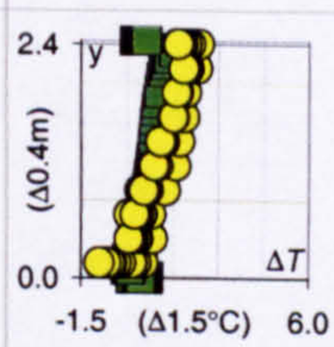
Radiation model enabled, $\alpha = 0.05m^{-1}$ QUICK differencing. Radiation walls. Uniform external temperature.	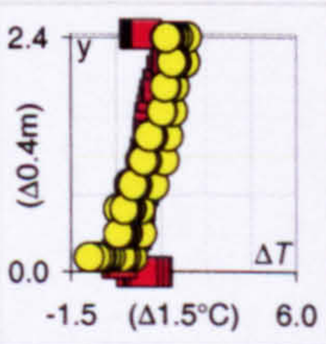	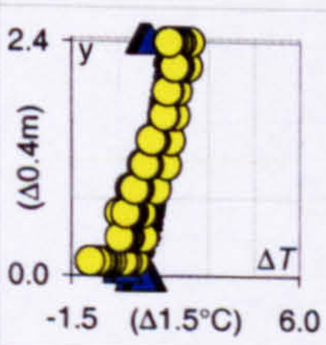	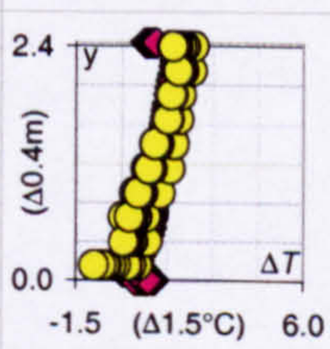	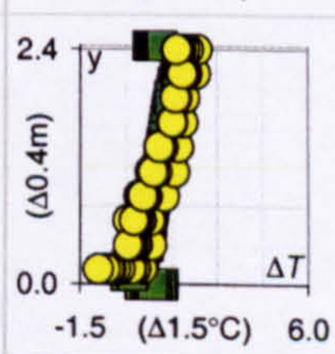
Radiation model enabled, $\alpha = 0.05m^{-1}$ QUICK differencing. Mixed walls. Uniform external temperature.	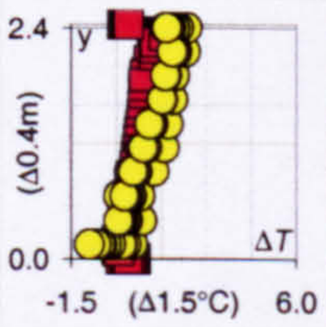	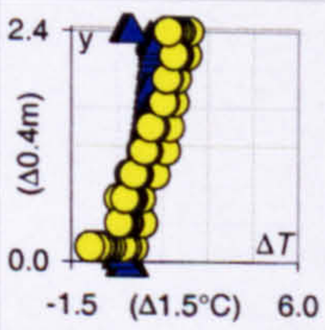	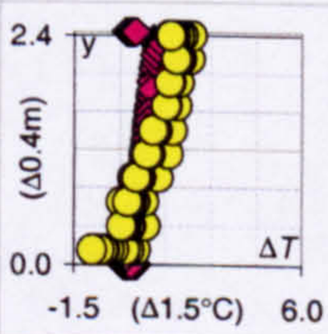	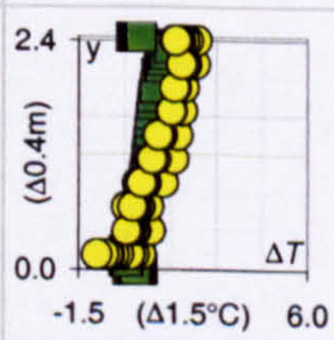

Width of opening:	0.5m
Effective area of opening:	0.305m^2
Heat source:	Boiler ring
Strength of heat source:	368.0W

Figure 14.b

	Laminar	Standard-$k\varepsilon$	Realizable-$k\varepsilon$	RNG-$k\varepsilon$
Radiation model disabled. Upwind differencing. Adiabatic walls. Uniform external temperature.	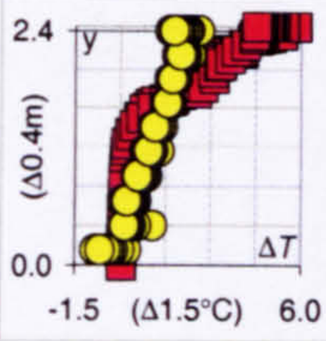	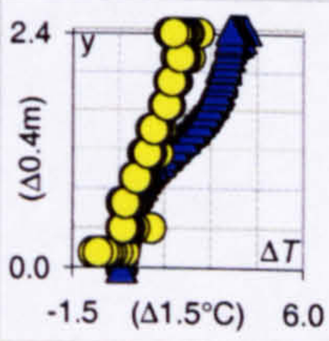	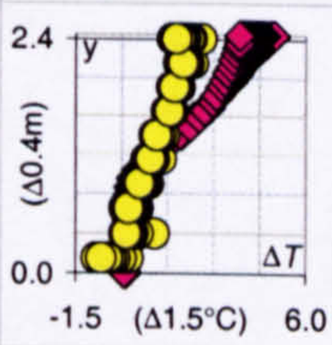	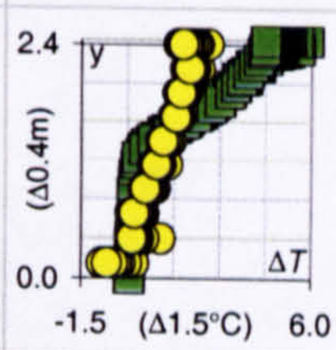
Radiation model disabled. QUICK differencing. Adiabatic walls. Uniform external temperature.	No available solution.	No available solution.	No available solution.	No available solution.
Radiation model enabled, $\alpha = 0.00m^{-1}$ QUICK differencing. Adiabatic walls. Uniform external temperature.	No available solution.	No available solution.	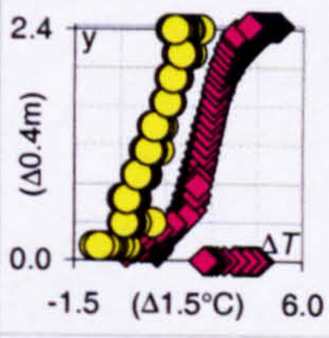	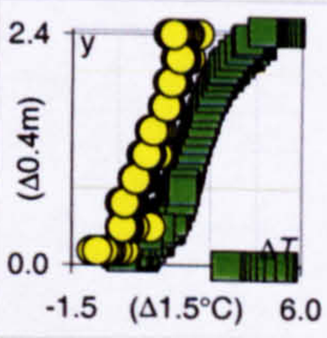
Radiation model enabled, $\alpha = 0.05m^{-1}$ QUICK differencing. Adiabatic walls. Uniform external temperature.	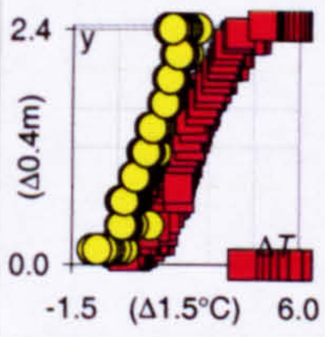	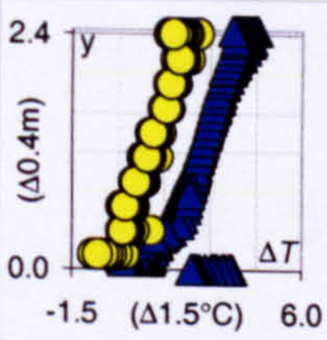	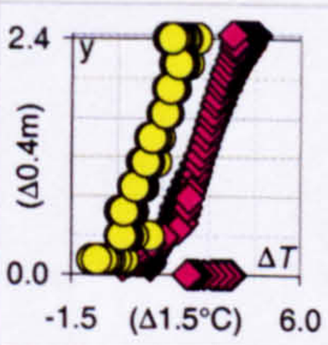	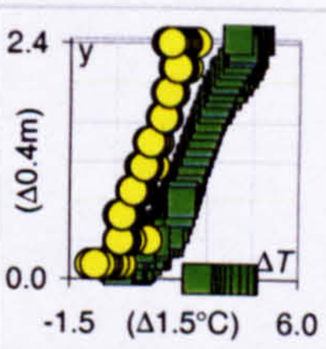
Radiation model enabled, $\alpha = 0.10m^{-1}$ QUICK differencing. Adiabatic walls. Uniform external temperature.	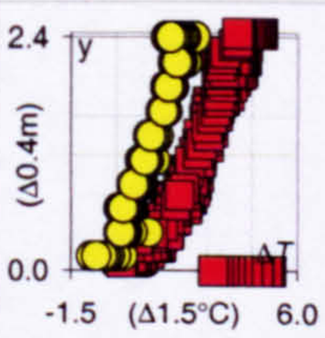	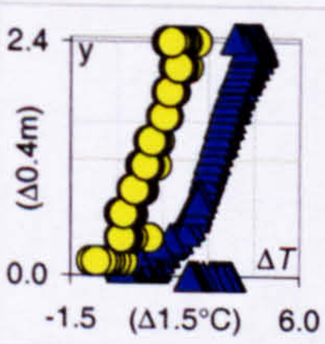	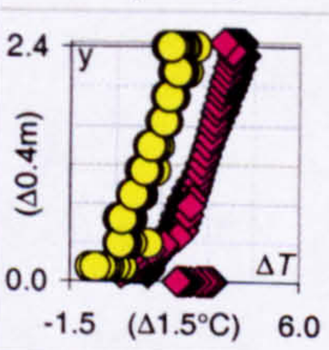	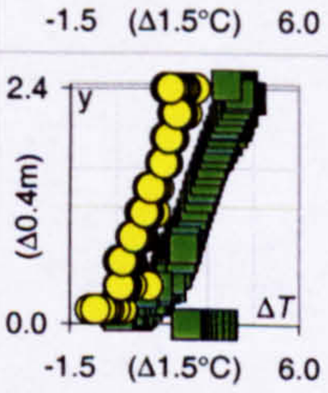
Radiation model enabled, $\alpha = 0.15m^{-1}$ QUICK differencing. Adiabatic walls. Uniform external temperature.	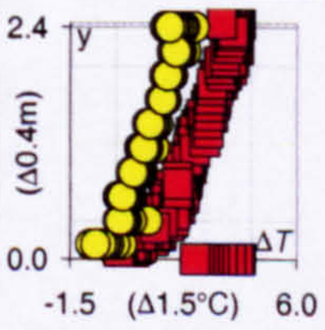	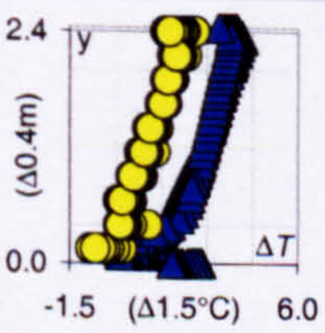	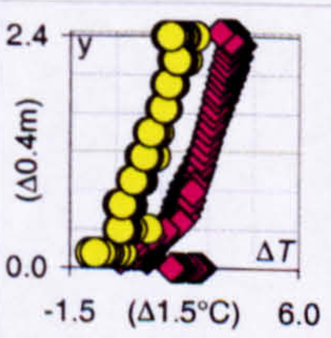	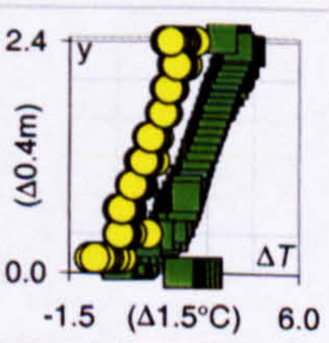

Width of opening:	0.6m
Effective area of opening:	0.366m^2
Heat source:	Boiler ring
Strength of heat source:	368.0W

Figure 15.a

	Laminar	Standard-$k\varepsilon$	Realizable-$k\varepsilon$	RNG-$k\varepsilon$
Radiation model enabled, $\alpha = 0.00m^{-1}$ QUICK differencing. Convection walls. Uniform external temperature.	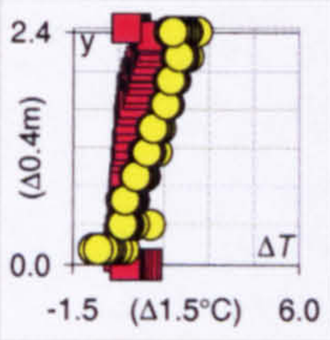	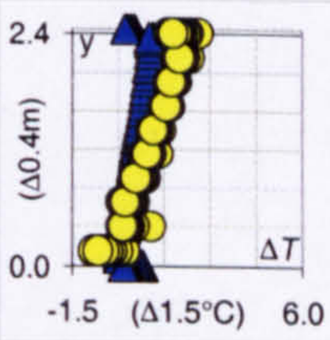	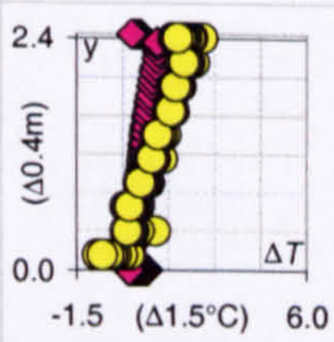	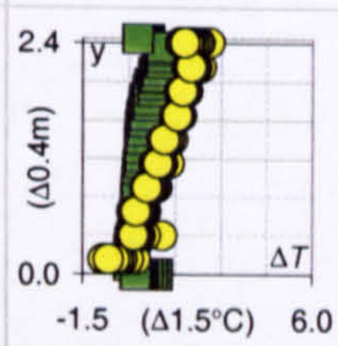
Radiation model enabled, $\alpha = 0.00m^{-1}$ QUICK differencing. Radiation walls. Uniform external temperature.	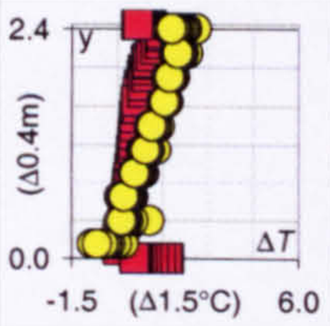	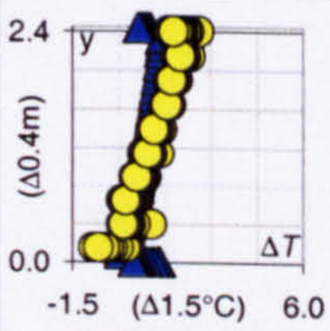	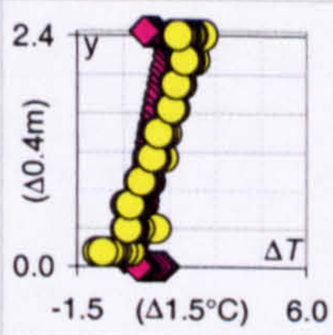	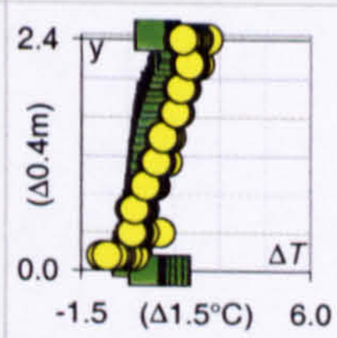
Radiation model enabled, $\alpha = 0.00m^{-1}$ QUICK differencing. Mixed walls. Uniform external temperature.	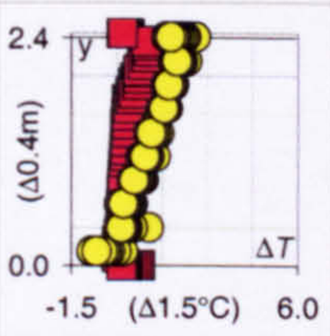	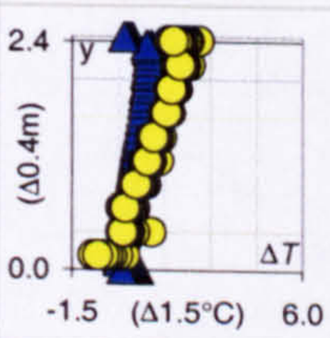	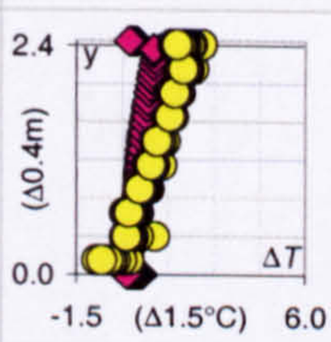	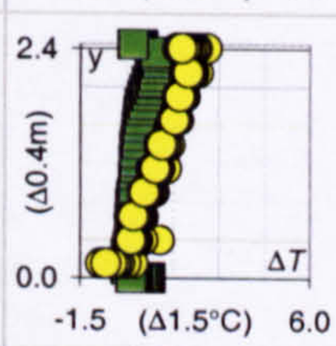
Radiation model enabled, $\alpha = 0.05m^{-1}$ QUICK differencing. Convection walls. Uniform external temperature.	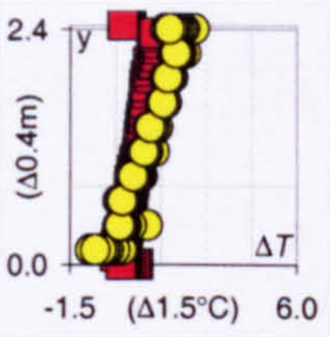	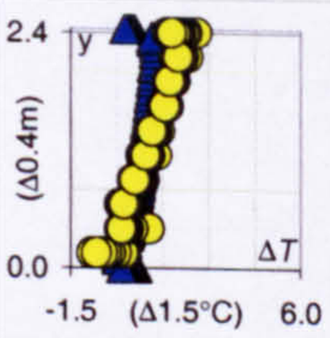	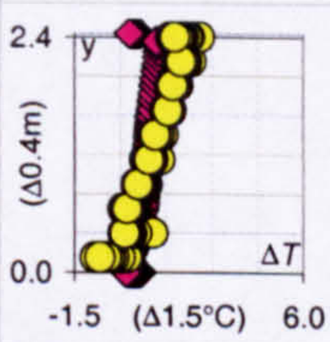	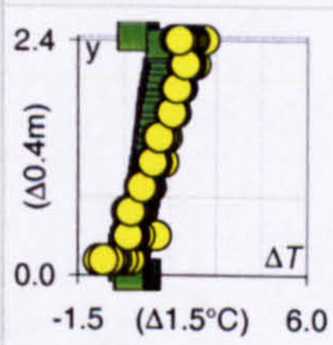
Radiation model enabled, $\alpha = 0.05m^{-1}$ QUICK differencing. Radiation walls. Uniform external temperature.	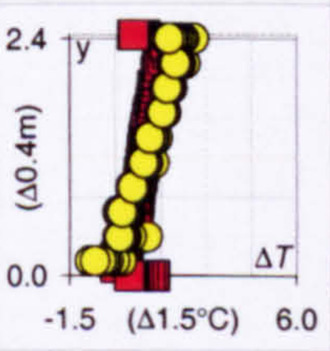	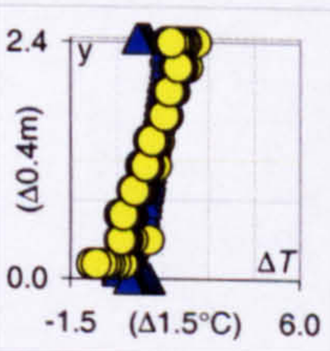	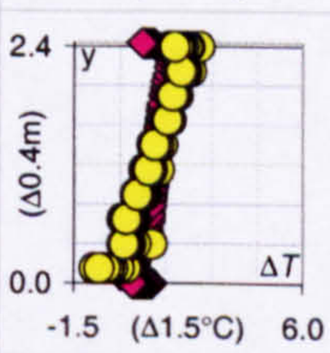	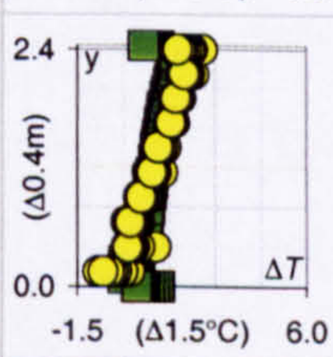
Radiation model enabled, $\alpha = 0.05m^{-1}$ QUICK differencing. Mixed walls. Uniform external temperature.	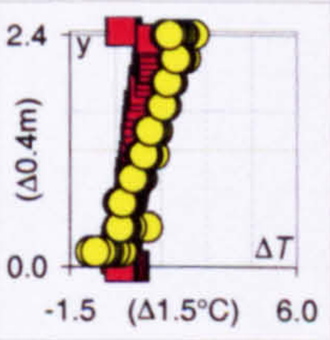	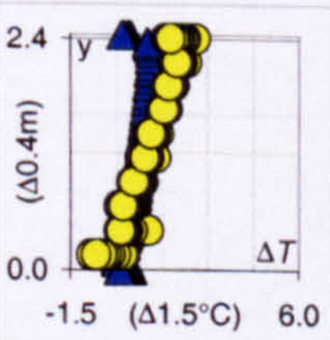	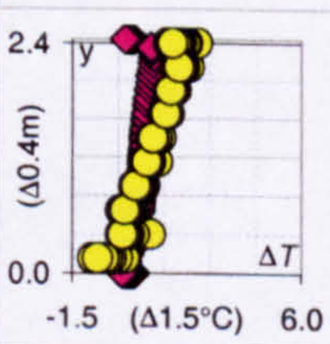	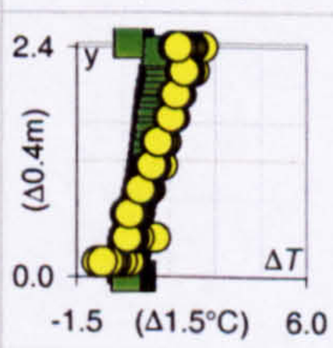

Width of opening:	0.6m
Effective area of opening:	$0.366m^2$
Heat source:	Boiler ring
Strength of heat source:	368.0W

Figure 15.b

	Laminar	Standard-$k\varepsilon$	Realizable-$k\varepsilon$	RNG-$k\varepsilon$
Radiation model disabled. Upwind differencing. Adiabatic walls. Uniform external temperature.	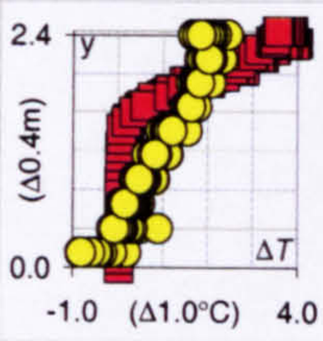	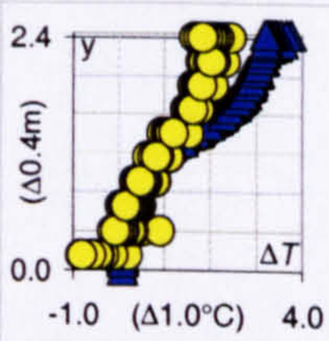	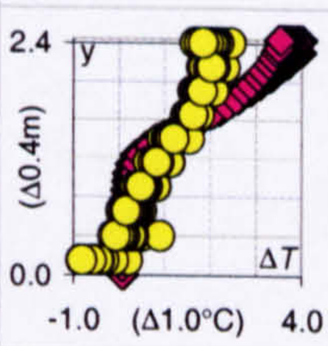	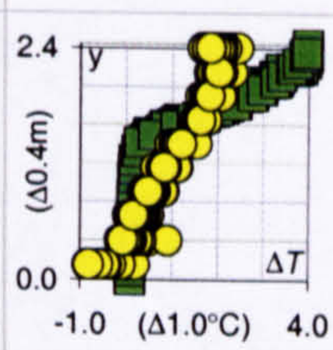
Radiation model disabled. QUICK differencing. Adiabatic walls. Uniform external temperature.	No available solution.	No available solution.	No available solution.	No available solution.
Radiation model enabled, $\alpha = 0.00m^{-1}$ QUICK differencing. Adiabatic walls. Uniform external temperature.	No available solution.	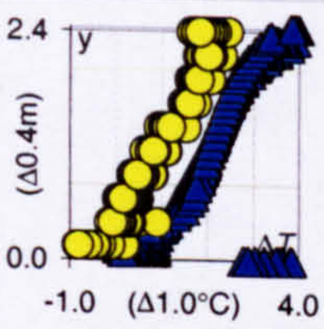	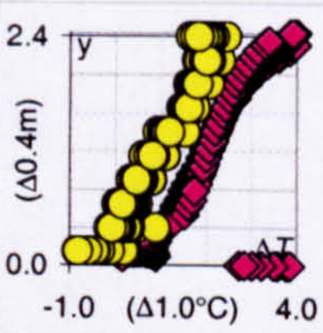	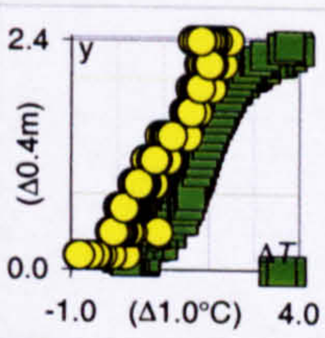
Radiation model enabled, $\alpha = 0.05m^{-1}$ QUICK differencing. Adiabatic walls. Uniform external temperature.	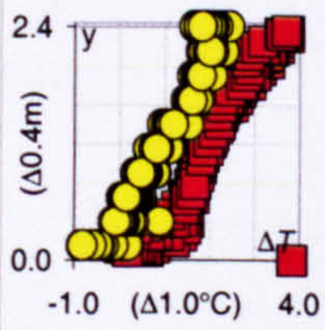	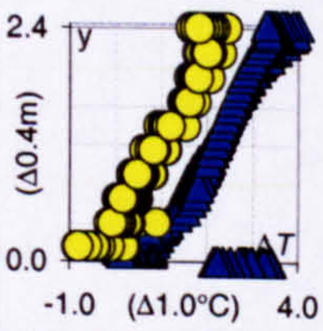	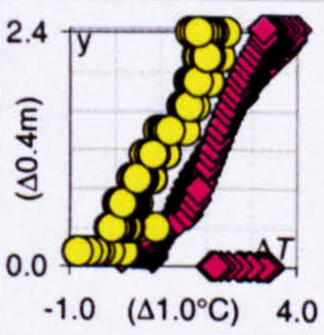	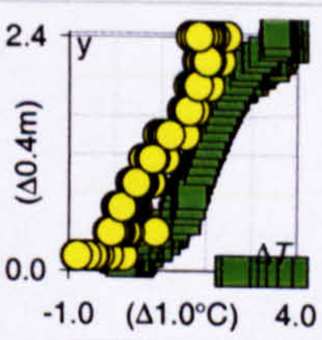
Radiation model enabled, $\alpha = 0.10m^{-1}$ QUICK differencing. Adiabatic walls. Uniform external temperature.	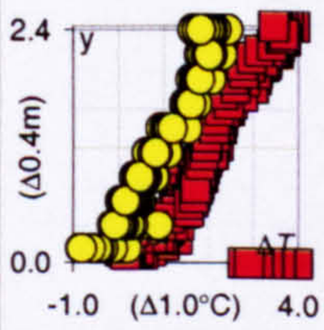	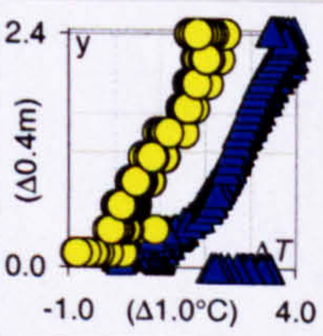	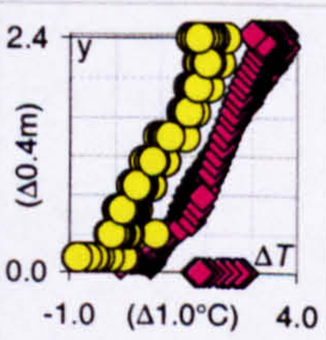	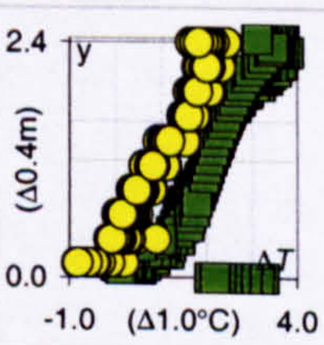
Radiation model enabled, $\alpha = 0.15m^{-1}$ QUICK differencing. Adiabatic walls. Uniform external temperature.	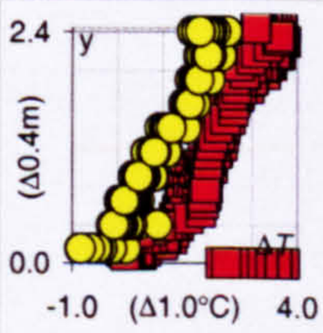	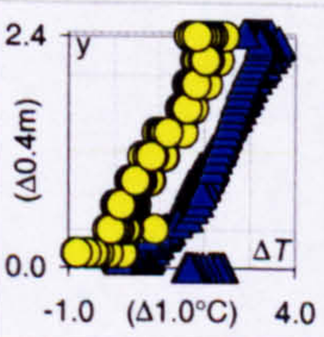	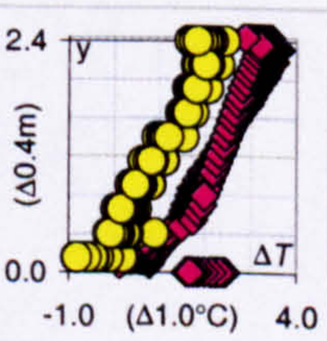	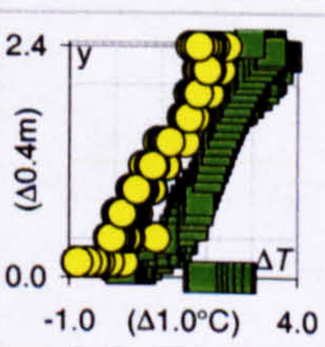

Width of opening:	0.8m
Effective area of opening:	$0.488m^2$
Heat source:	Boiler ring
Strength of heat source:	368.0W

Figure 16.a

	Laminar	Standard-$k\varepsilon$	Realizable-$k\varepsilon$	RNG-$k\varepsilon$
Radiation model enabled, $\alpha = 0.00m^{-1}$ QUICK differencing. Convection walls. Uniform external temperature.	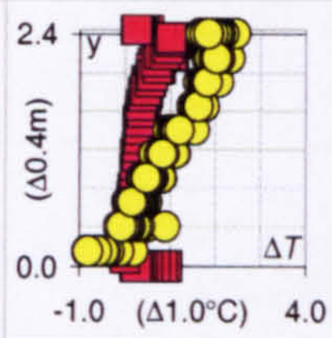	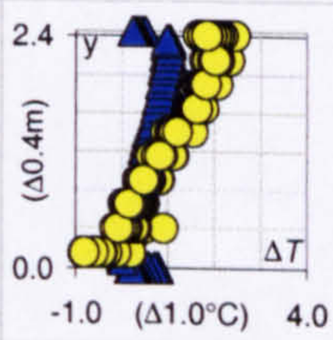	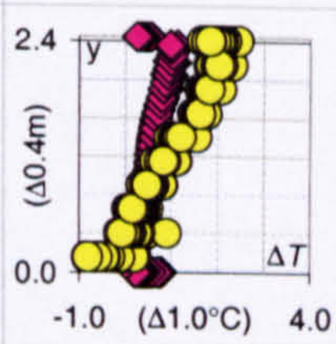	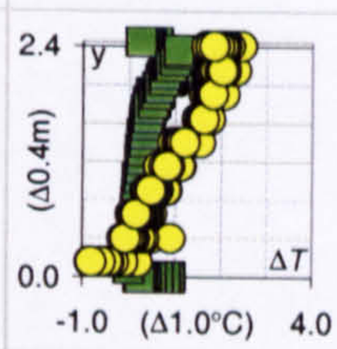
Radiation model enabled, $\alpha = 0.00m^{-1}$ QUICK differencing. Radiation walls. Uniform external temperature.	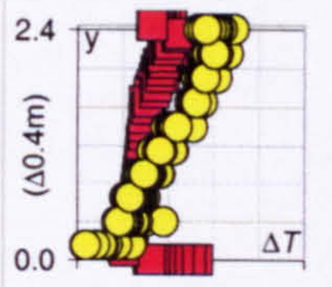	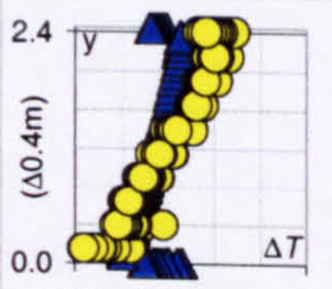	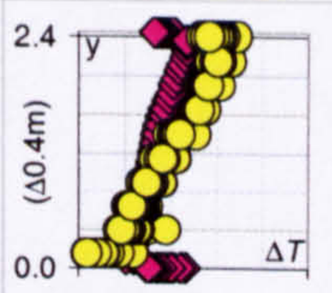	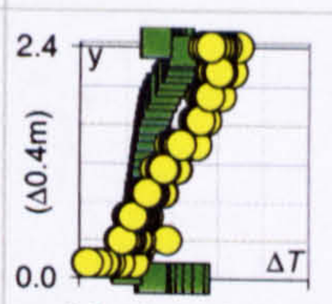
Radiation model enabled, $\alpha = 0.00m^{-1}$ QUICK differencing. Mixed walls. Uniform external temperature.	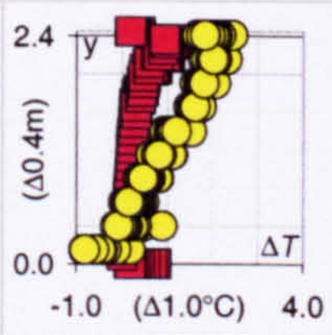	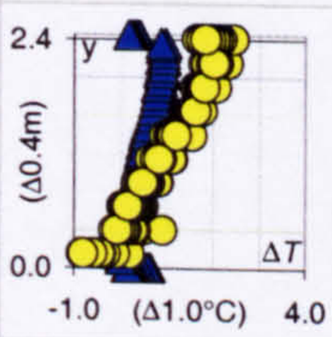	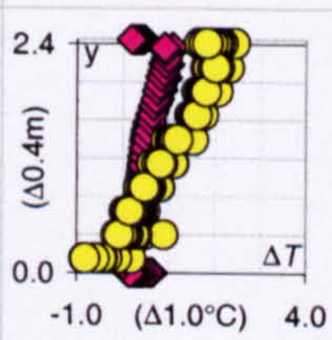	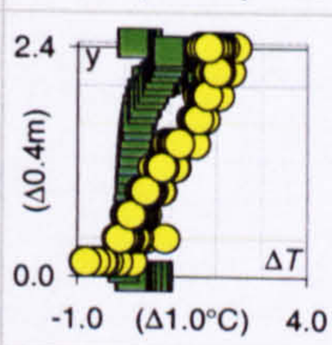
Radiation model enabled, $\alpha = 0.05m^{-1}$ QUICK differencing. Convection walls. Uniform external temperature.	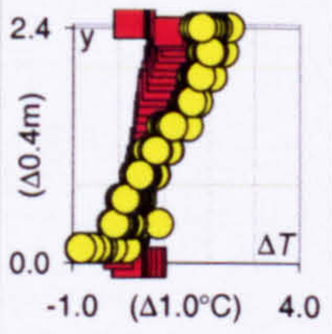	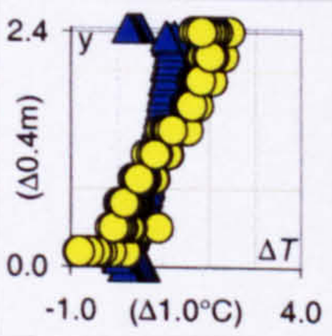	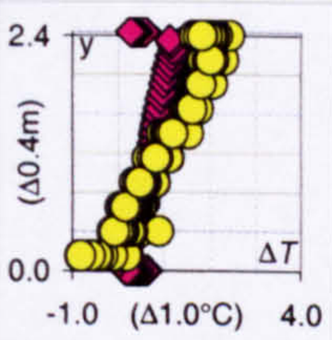	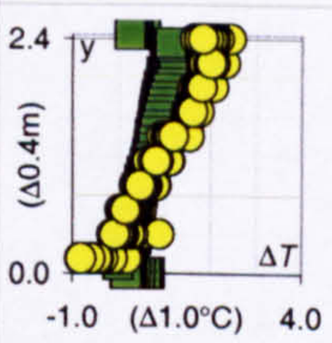
Radiation model enabled, $\alpha = 0.05m^{-1}$ QUICK differencing. Radiation walls. Uniform external temperature.	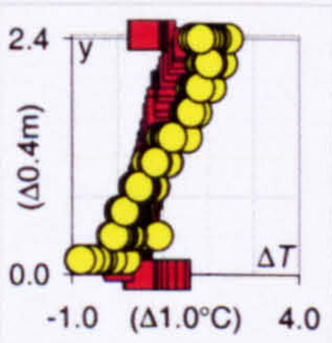	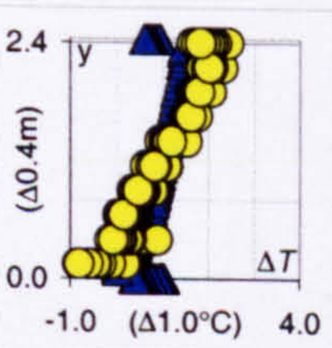	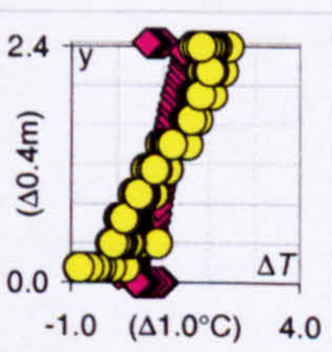	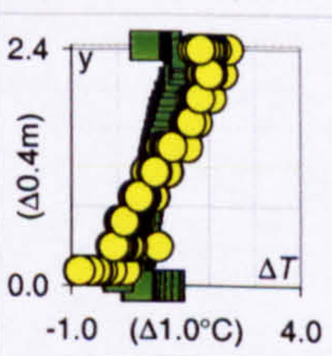
Radiation model enabled, $\alpha = 0.05m^{-1}$ QUICK differencing. Mixed walls. Uniform external temperature.	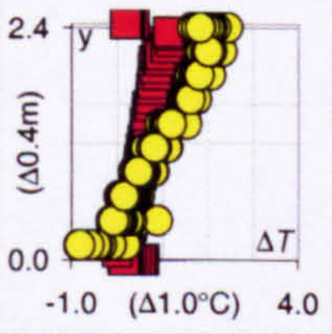	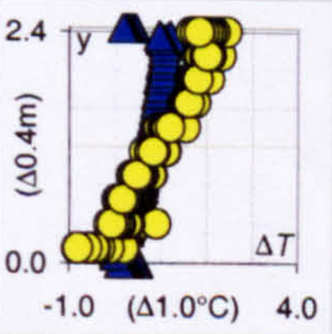	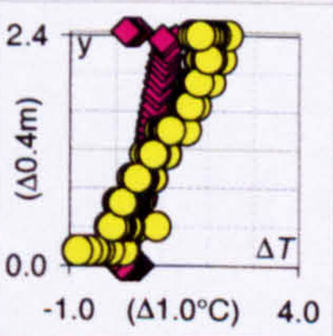	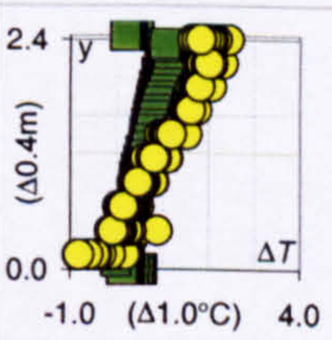

Width of opening:	0.8m
Effective area of opening:	$0.488m^2$
Heat source:	Boiler ring
Strength of heat source:	368.0W

Figure 16.b

	Laminar	Standard-$k\varepsilon$	Realizable-$k\varepsilon$	RNG-$k\varepsilon$
Radiation model disabled. QUICK differencing. Adiabatic walls. Uniform external temperature.	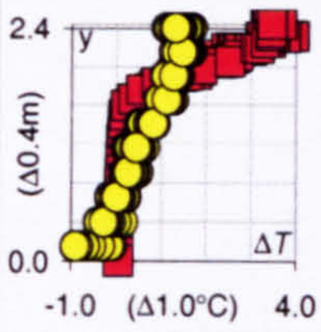	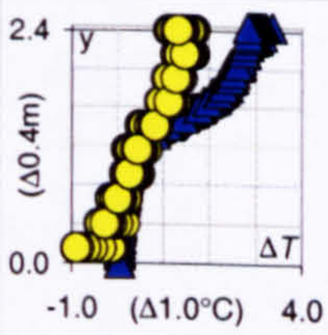	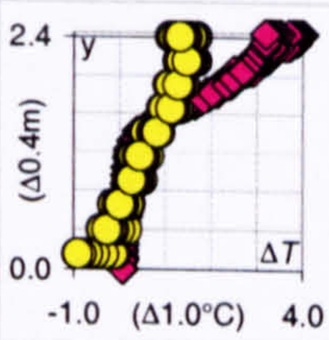	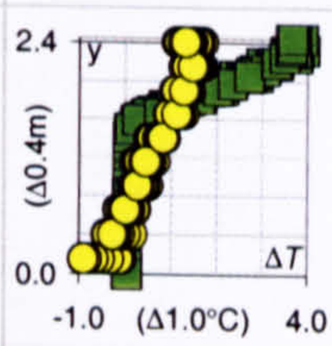
Radiation model disabled. QUICK differencing. Adiabatic walls. Uniform external temperature.	No available solution.	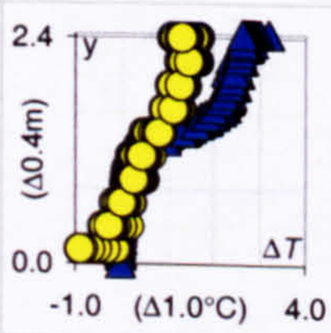	No available solution.	No available solution.
Radiation model enabled, $\alpha = 0.00m^{-1}$ QUICK differencing. Adiabatic walls. Uniform external temperature.	No available solution.	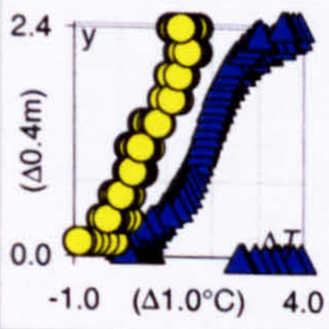	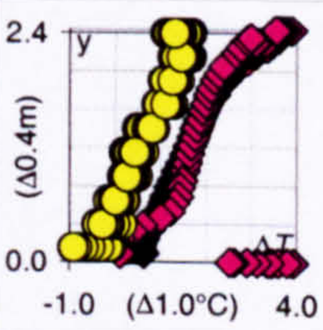	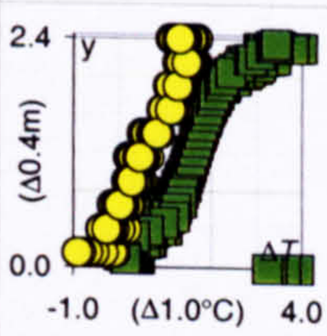
Radiation model enabled, $\alpha = 0.05m^{-1}$ QUICK differencing. Adiabatic walls. Uniform external temperature.	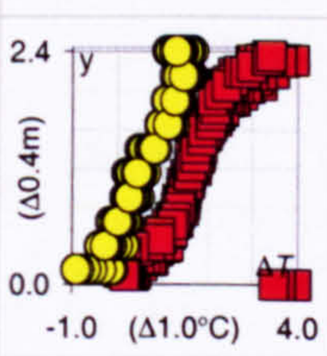	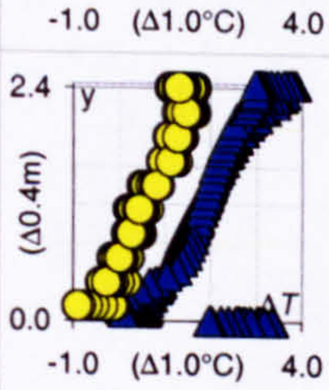	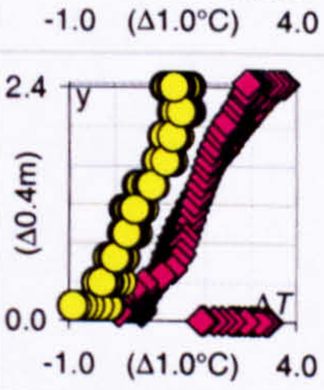	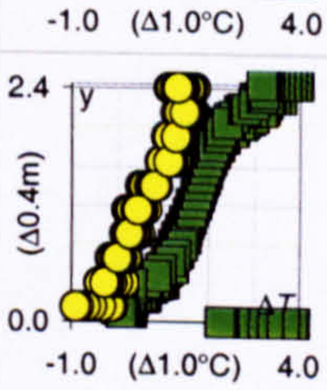
Radiation model enabled, $\alpha = 0.10m^{-1}$ QUICK differencing. Adiabatic walls. Uniform external temperature.	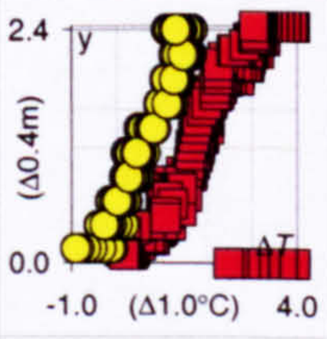	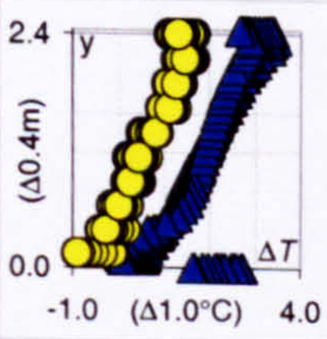	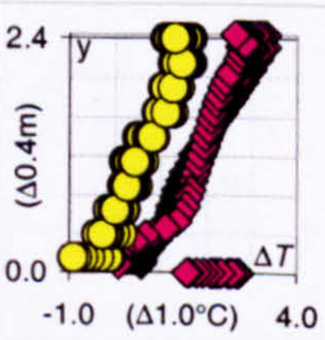	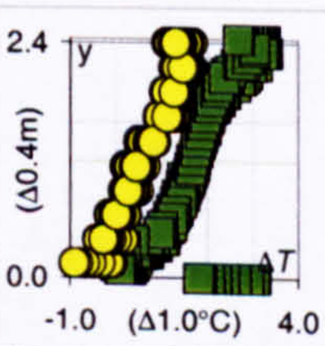
Radiation model enabled, $\alpha = 0.15m^{-1}$ QUICK differencing. Adiabatic walls. Uniform external temperature.	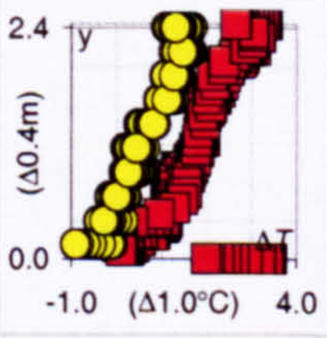	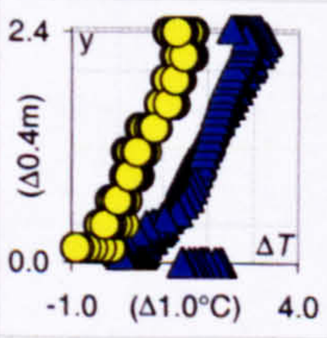	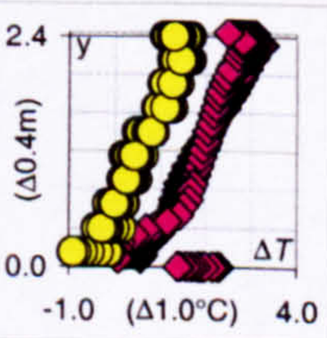	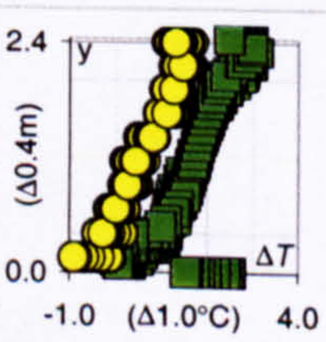

Width of opening:	1.0m
Effective area of opening:	$0.610m^2$
Heat source:	Boiler ring
Strength of heat source:	368.0W

Figure 17.a

	Laminar	Standard-$k\varepsilon$	Realizable-$k\varepsilon$	RNG-$k\varepsilon$
Radiation model enabled, $\alpha = 0.00m^{-1}$ QUICK differencing. Convection walls. Uniform external temperature.	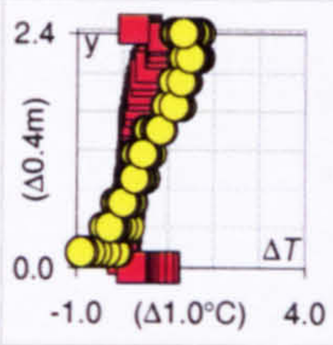	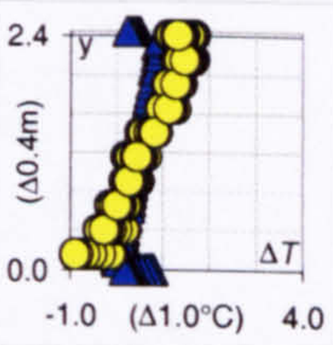	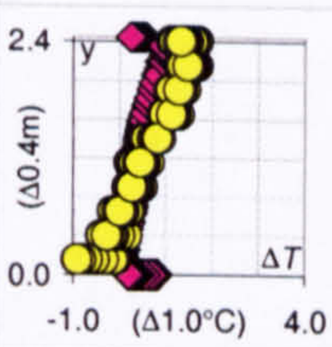	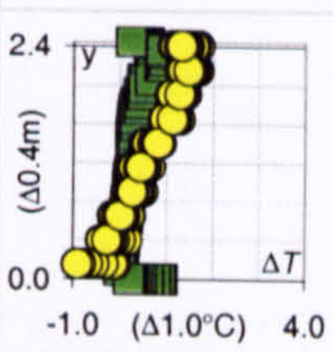
Radiation model enabled, $\alpha = 0.00m^{-1}$ QUICK differencing. Radiation walls. Uniform external temperature.	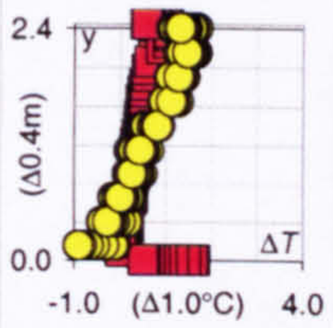	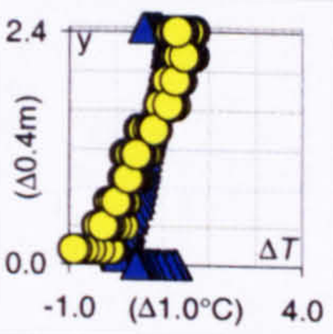	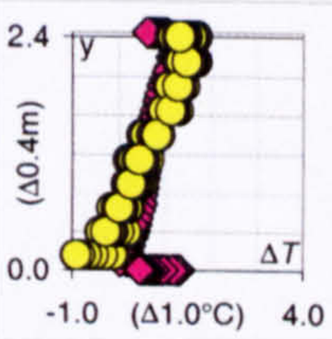	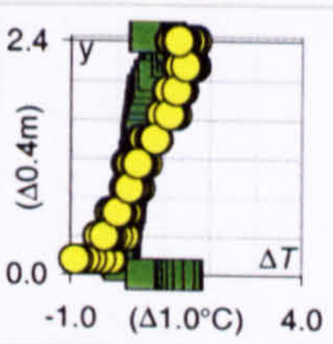
Radiation model enabled, $\alpha = 0.00m^{-1}$ QUICK differencing. Mixed walls. Uniform external temperature.	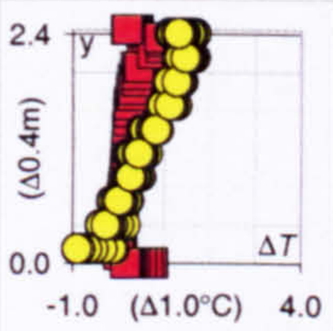	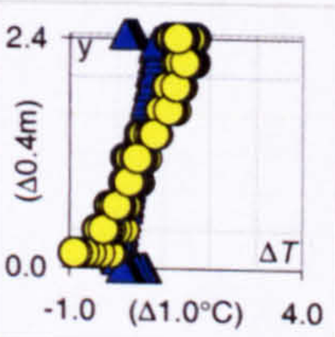	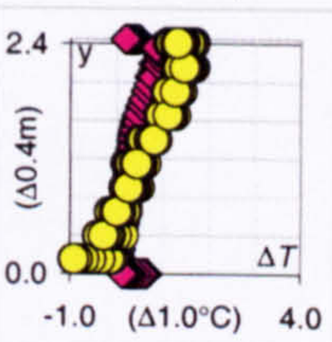	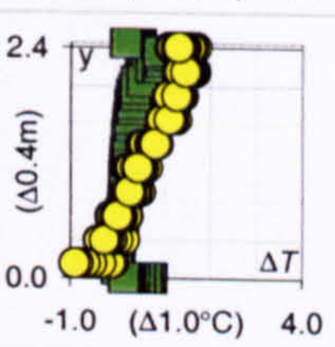
Radiation model enabled, $\alpha = 0.05m^{-1}$ QUICK differencing. Convection walls. Uniform external temperature.	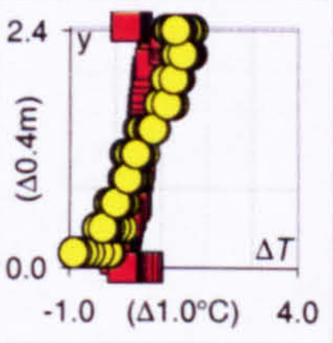	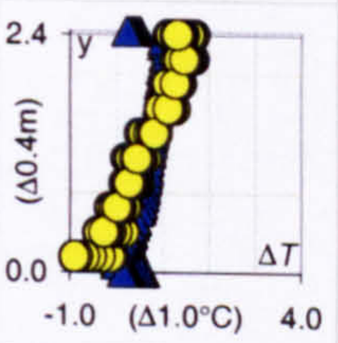	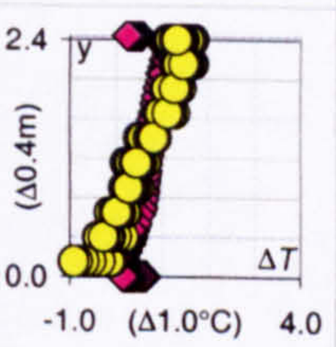	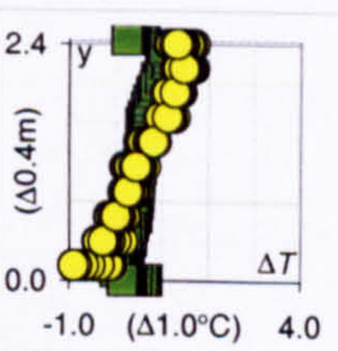
Radiation model enabled, $\alpha = 0.05m^{-1}$ QUICK differencing. Radiation walls. Uniform external temperature.	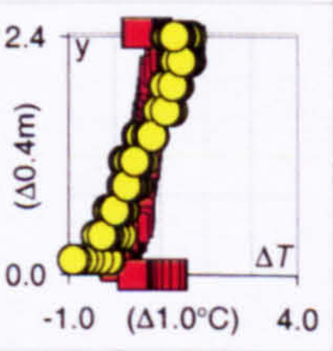	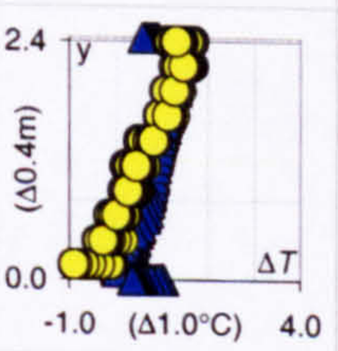	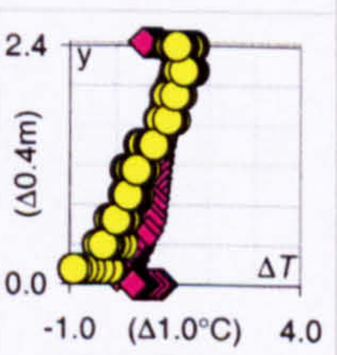	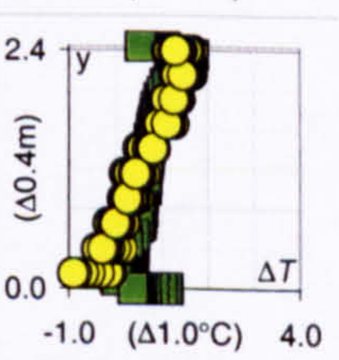
Radiation model enabled, $\alpha = 0.05m^{-1}$ QUICK differencing. Mixed walls. Uniform external temperature.	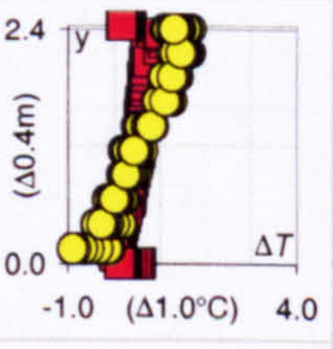	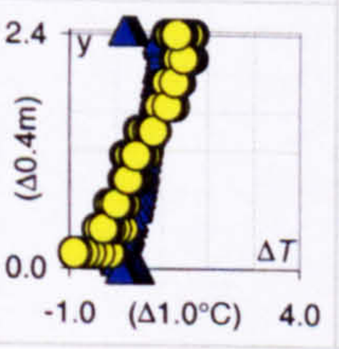	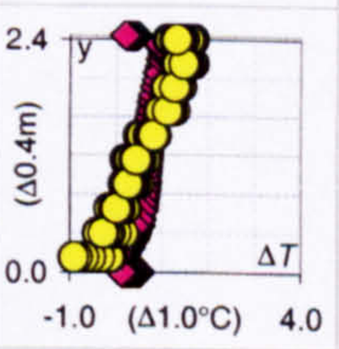	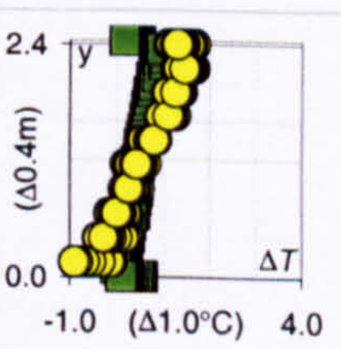

Width of opening:	1.0m
Effective area of opening:	$0.610m^2$
Heat source:	Boiler ring
Strength of heat source:	368.0W

Figure 17.b

	Laminar	Standard-$k\varepsilon$	Realizable-$k\varepsilon$	RNG-$k\varepsilon$
Radiation model disabled. Upwind differencing. Adiabatic walls. Uniform external temperature.	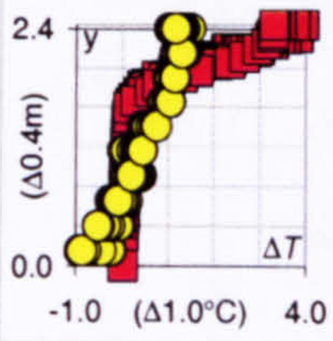	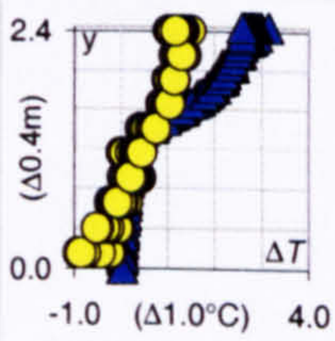	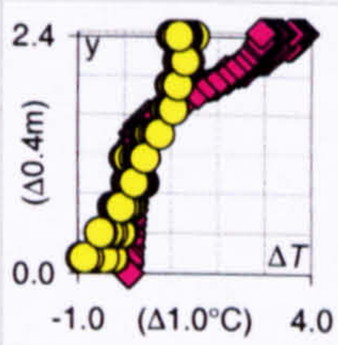	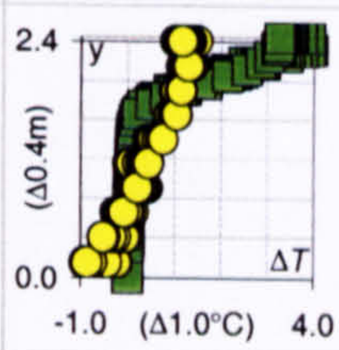
Radiation model disabled. QUICK differencing. Adiabatic walls. Uniform external temperature.	No available solution.	No available solution.	No available solution.	No available solution.
Radiation model enabled, $\alpha = 0.00m^{-1}$ QUICK differencing. Adiabatic walls. Uniform external temperature.	No available solution.	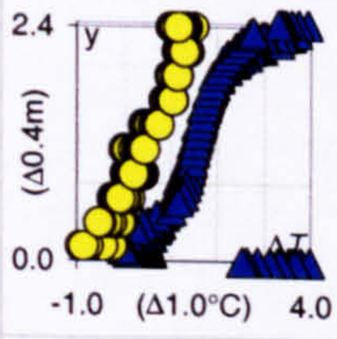	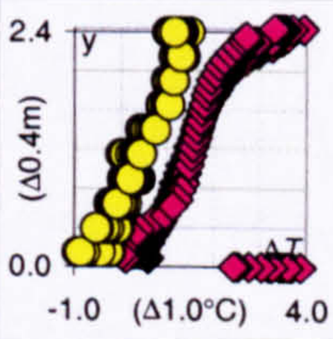	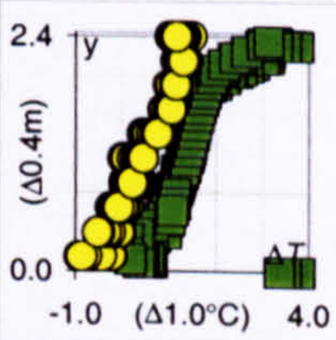
Radiation model enabled, $\alpha = 0.05m^{-1}$ QUICK differencing. Adiabatic walls. Uniform external temperature.	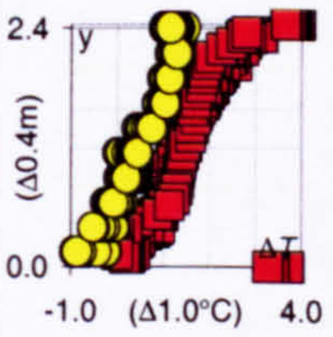	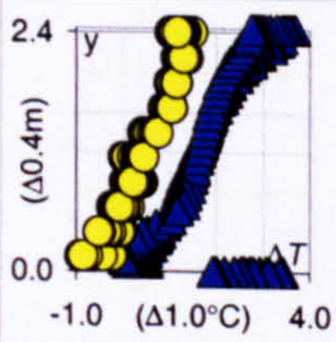	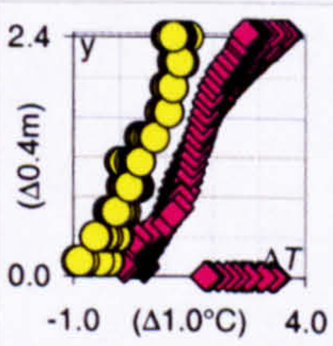	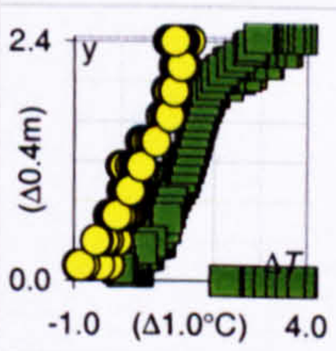
Radiation model enabled, $\alpha = 0.10m^{-1}$ QUICK differencing. Adiabatic walls. Uniform external temperature.	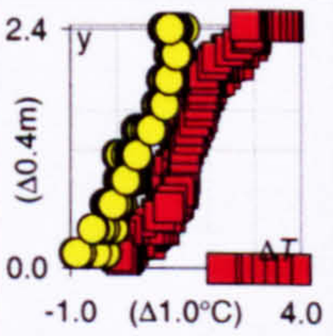	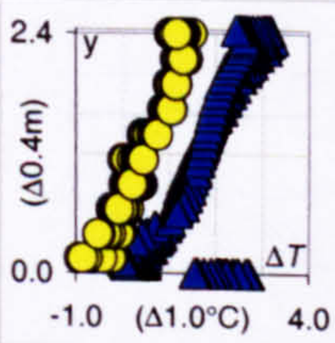	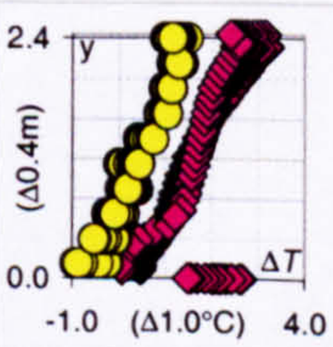	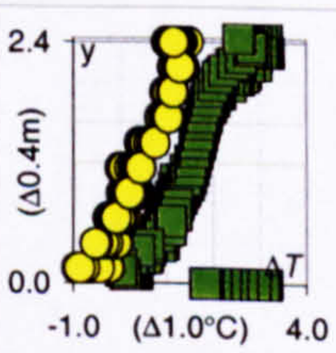
Radiation model enabled, $\alpha = 0.15m^{-1}$ QUICK differencing. Adiabatic walls. Uniform external temperature.	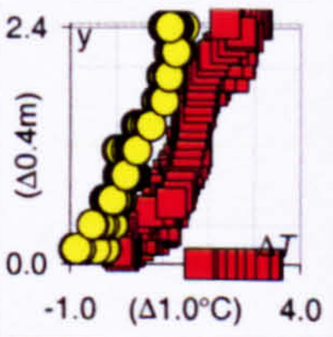	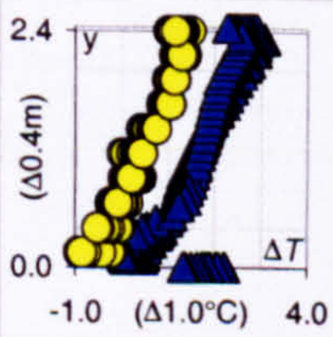	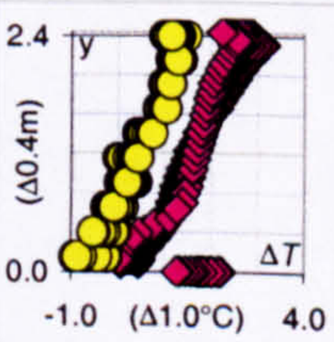	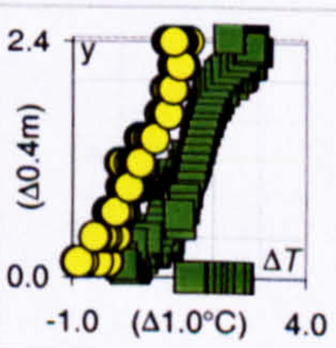

Width of opening:	1.2m
Effective area of opening:	$0.732m^2$
Heat source:	Boiler ring
Strength of heat source:	368.0W

Figure 18.a

	Laminar	Standard-$k\varepsilon$	Realizable-$k\varepsilon$	RNG-$k\varepsilon$
Radiation model enabled, $\alpha = 0.00m^{-1}$ QUICK differencing. Convection walls. Uniform external temperature.	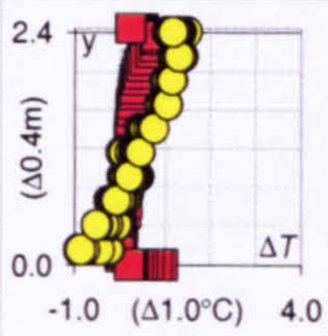	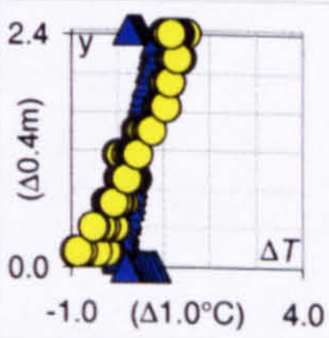	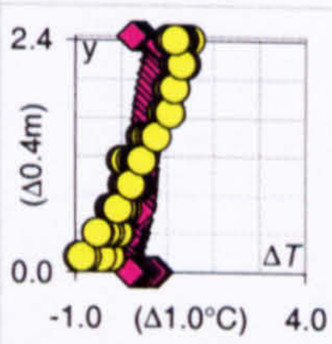	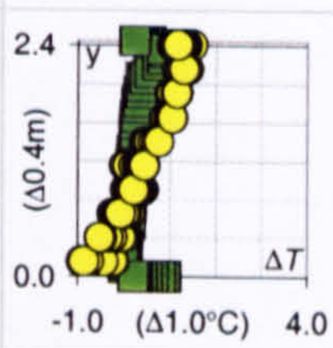
Radiation model enabled, $\alpha = 0.00m^{-1}$ QUICK differencing. Radiation walls. Uniform external temperature.	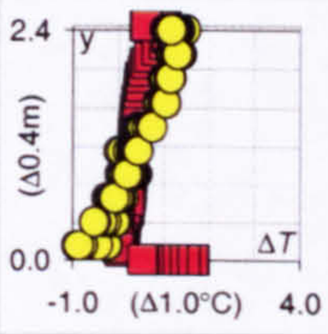	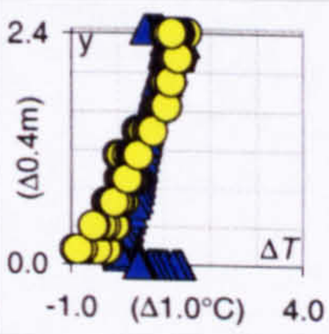	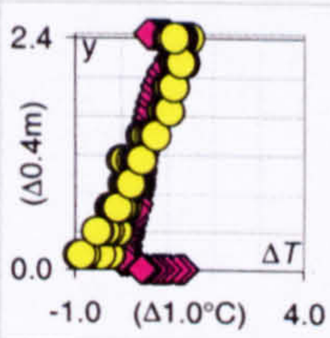	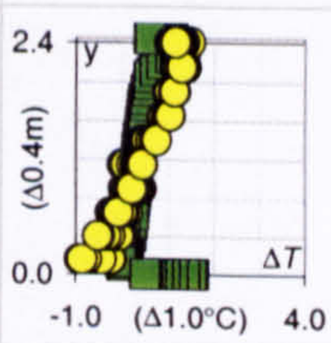
Radiation model enabled, $\alpha = 0.00m^{-1}$ QUICK differencing. Mixed walls. Uniform external temperature.	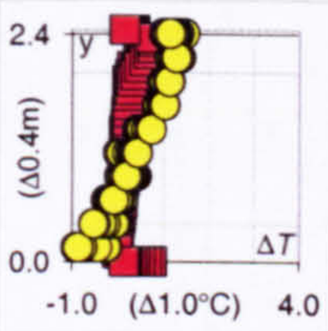	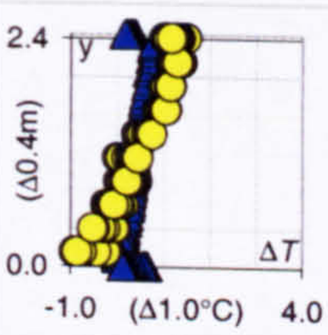	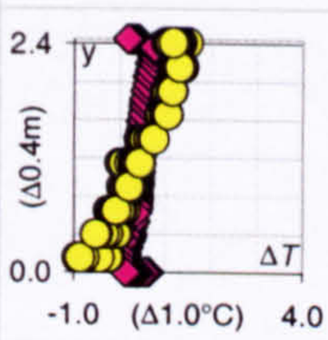	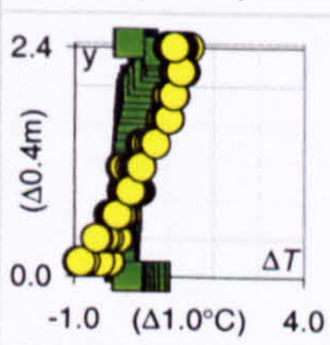
Radiation model enabled, $\alpha = 0.05m^{-1}$ QUICK differencing. Convection walls. Uniform external temperature.	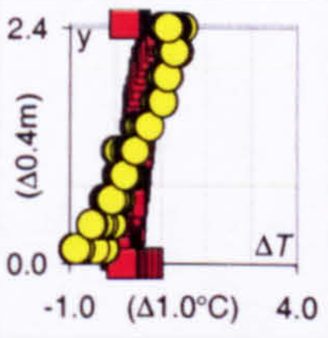	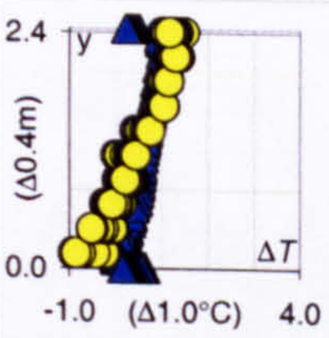	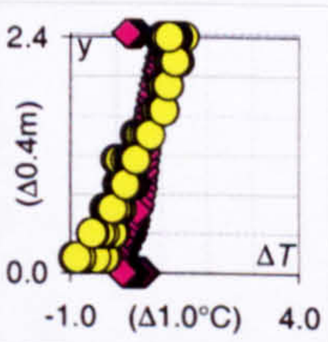	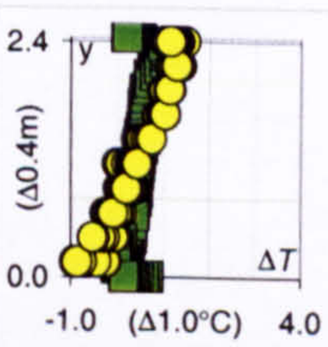
Radiation model enabled, $\alpha = 0.05m^{-1}$ QUICK differencing. Radiation walls. Uniform external temperature.	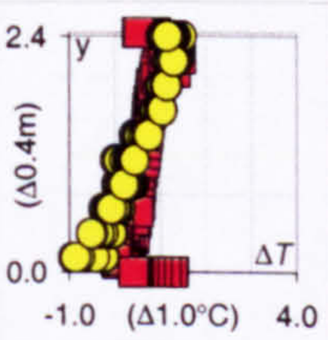	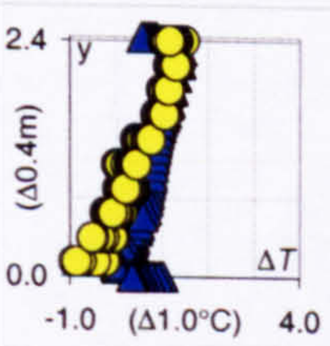	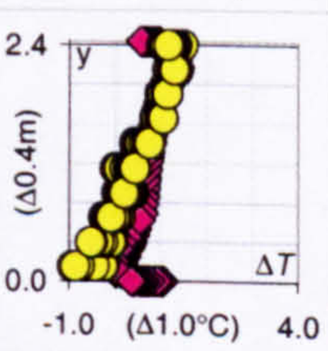	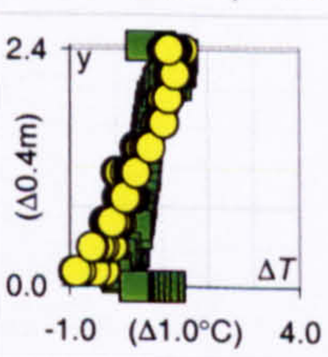
Radiation model enabled, $\alpha = 0.05m^{-1}$ QUICK differencing. Mixed walls. Uniform external temperature.	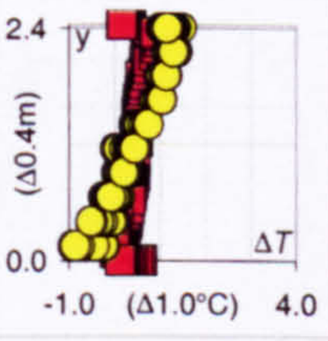	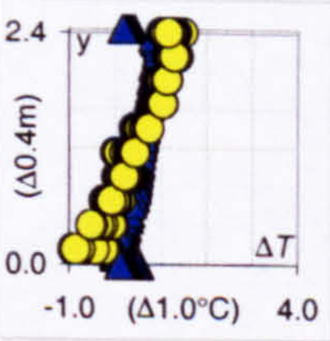	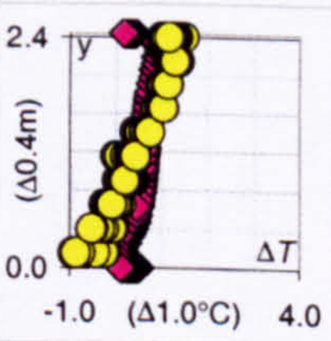	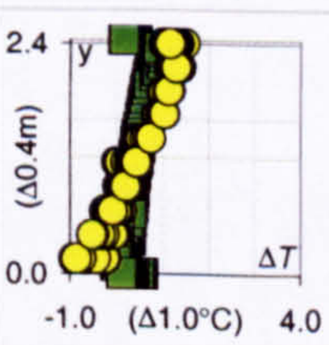

Width of opening: 1.2m
Effective area of opening: $0.732m^2$
Heat source: Boiler ring
Strength of heat source: 368.0W

Figure 18.b

	Laminar	Standard-$k\varepsilon$	Realizable-$k\varepsilon$	RNG-$k\varepsilon$
Radiation model disabled. Upwind differencing. Adiabatic walls. Uniform external temperature.	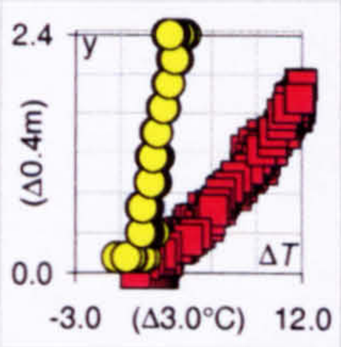	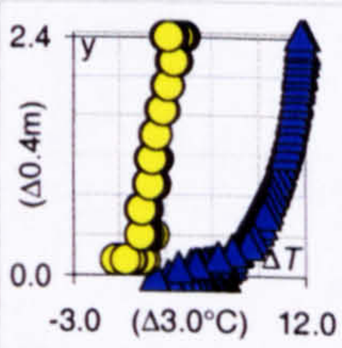	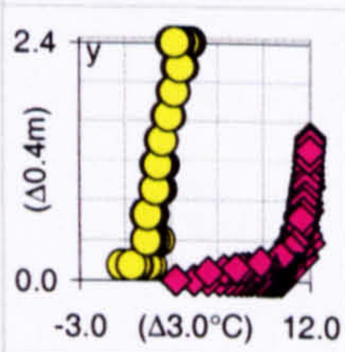	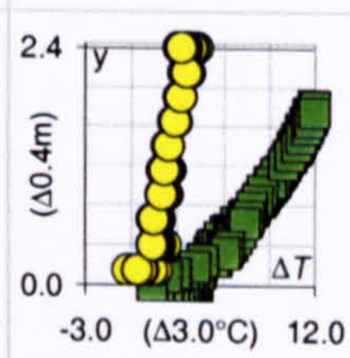
Radiation model disabled. QUICK differencing. Adiabatic walls. Uniform external temperature.	No available solution.	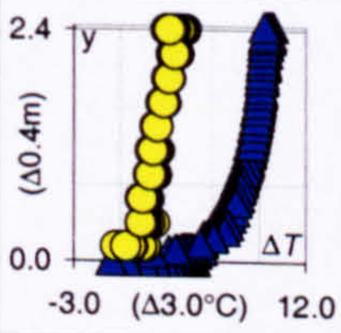	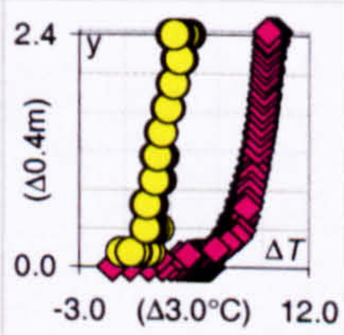	No available solution.
Radiation model enabled, $\alpha = 0.00m^{-1}$ QUICK differencing. Adiabatic walls. Uniform external temperature.	No available solution.	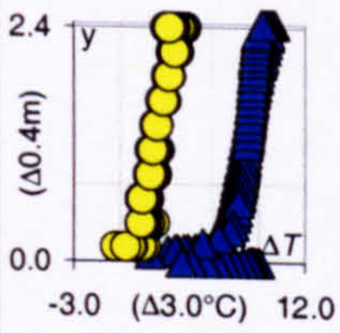	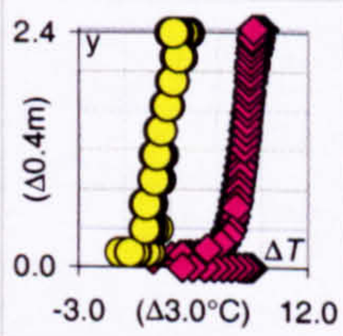	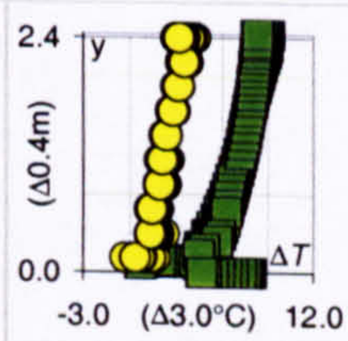
Radiation model enabled, $\alpha = 0.05m^{-1}$ QUICK differencing. Adiabatic walls. Uniform external temperature.	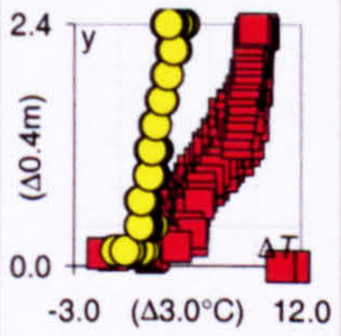	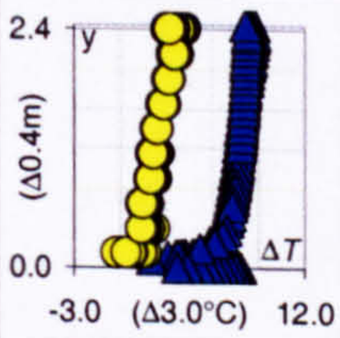	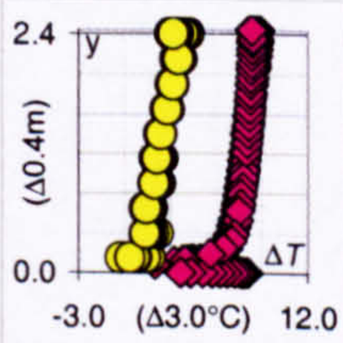	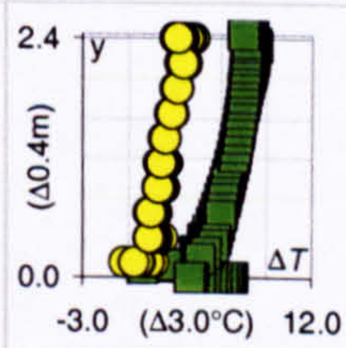
Radiation model enabled, $\alpha = 0.10m^{-1}$ QUICK differencing. Adiabatic walls. Uniform external temperature.	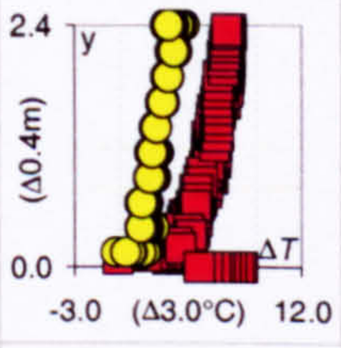	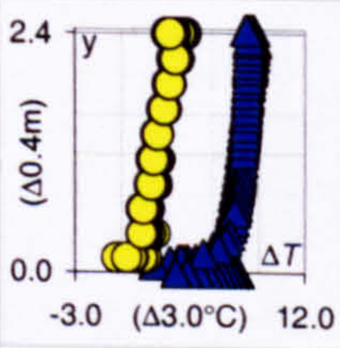	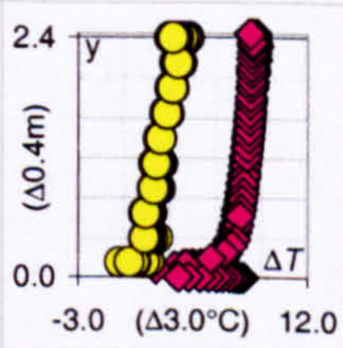	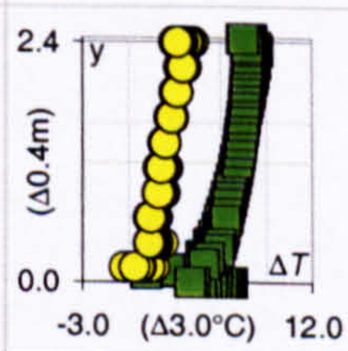
Radiation model enabled, $\alpha = 0.15m^{-1}$ QUICK differencing. Adiabatic walls. Uniform external temperature.	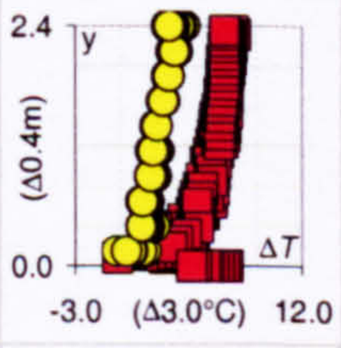	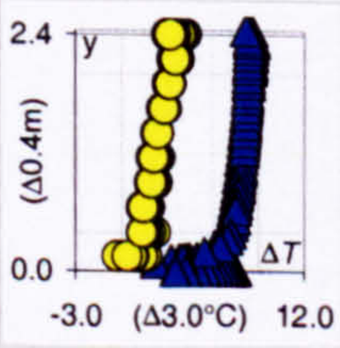	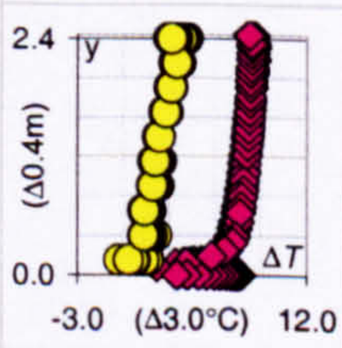	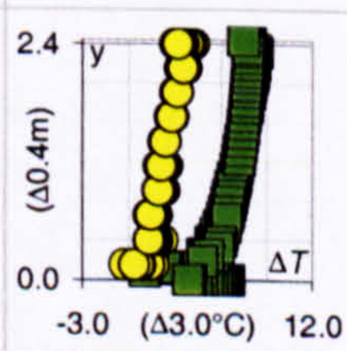

Width of opening:	0.1m
Effective area of opening:	$0.061m^2$
Heat source:	Boiler ring
Strength of heat source:	490.5W

Figure 19.a

	Laminar	Standard-$k\varepsilon$	Realizable-$k\varepsilon$	RNG-$k\varepsilon$
Radiation model enabled, $\alpha = 0.00m^{-1}$ QUICK differencing. Convection walls. Uniform external temperature.	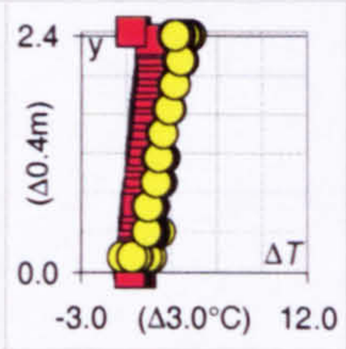	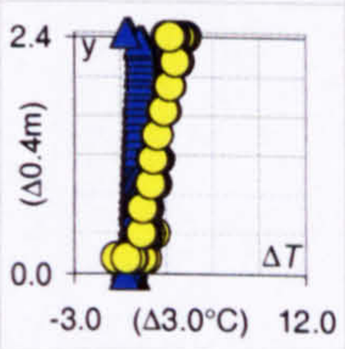	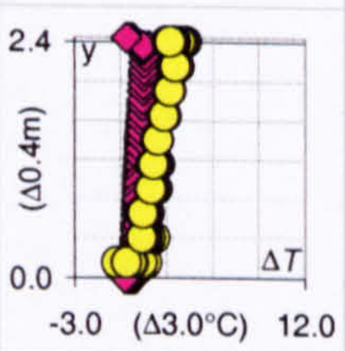	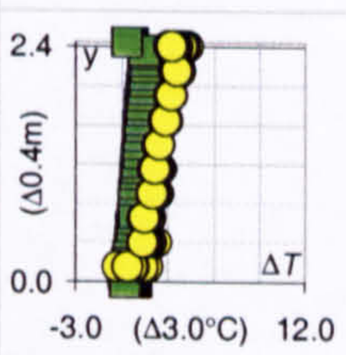
Radiation model enabled, $\alpha = 0.00m^{-1}$ QUICK differencing. Radiation walls. Uniform external temperature.	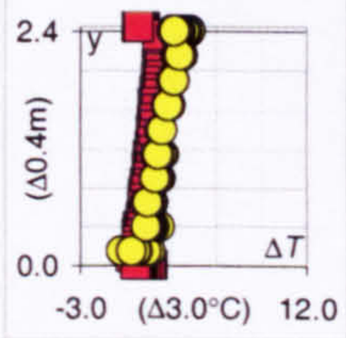	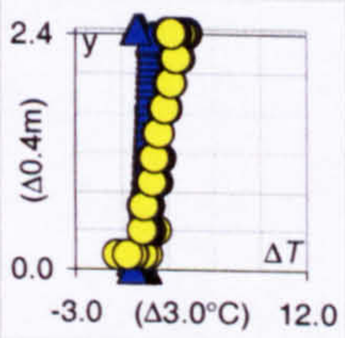	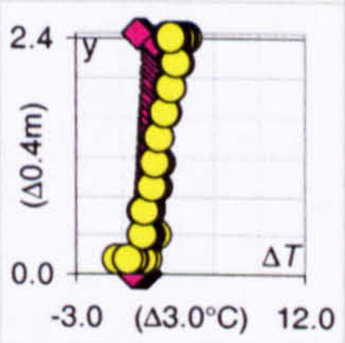	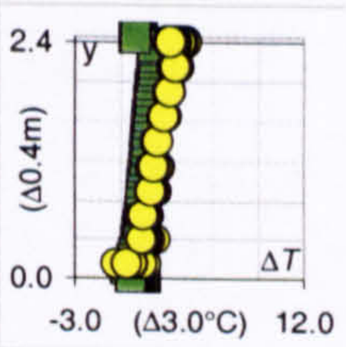
Radiation model enabled, $\alpha = 0.00m^{-1}$ QUICK differencing. Mixed walls. Uniform external temperature.	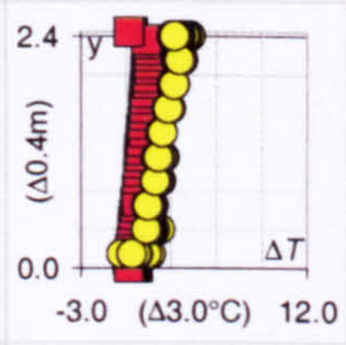	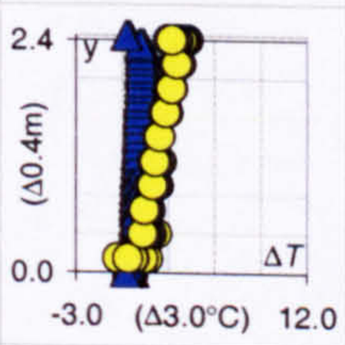	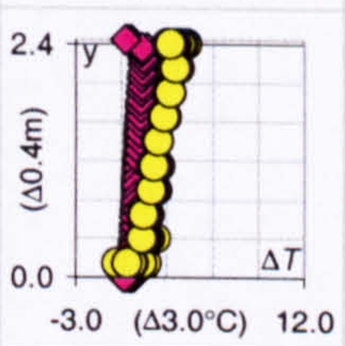	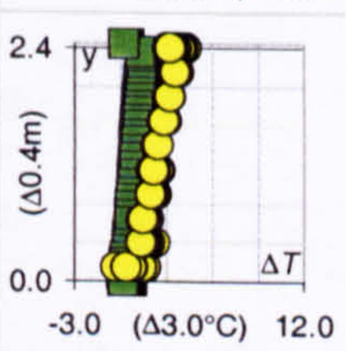
Radiation model enabled, $\alpha = 0.05m^{-1}$ QUICK differencing. Convection walls. Uniform external temperature.	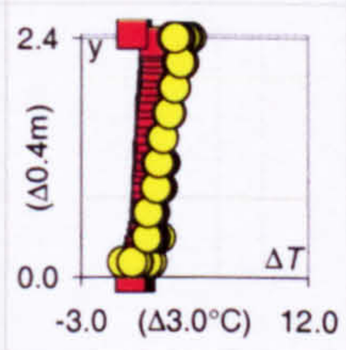	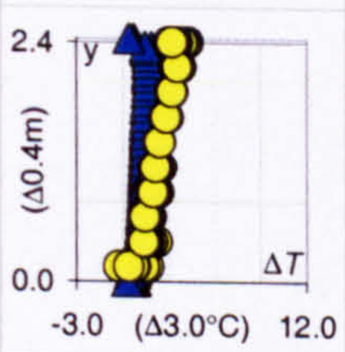	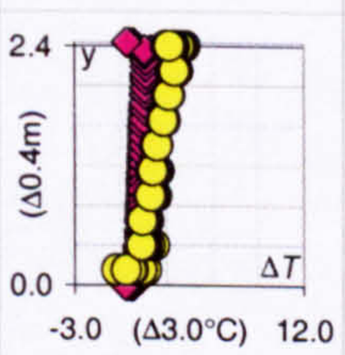	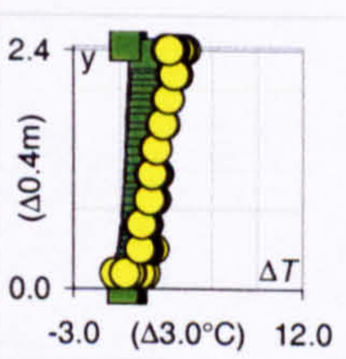
Radiation model enabled, $\alpha = 0.05m^{-1}$ QUICK differencing. Radiation walls. Uniform external temperature.	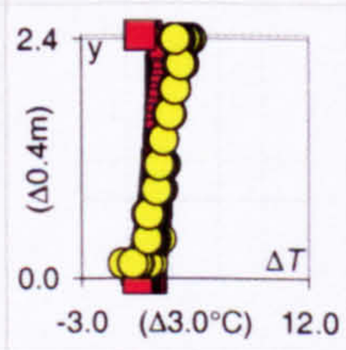	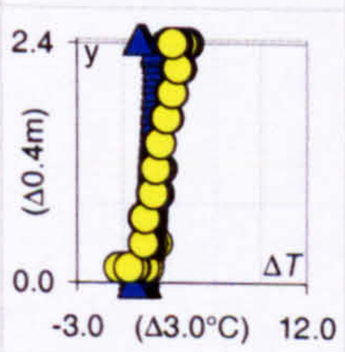	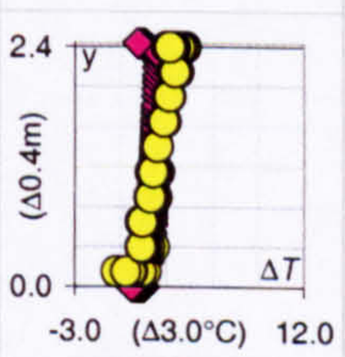	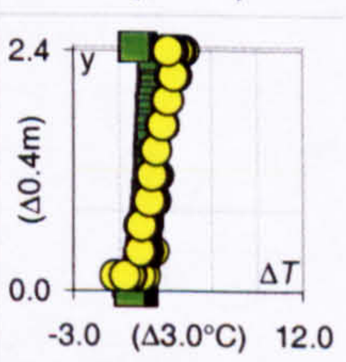
Radiation model enabled, $\alpha = 0.05m^{-1}$ QUICK differencing. Mixed walls. Uniform external temperature.	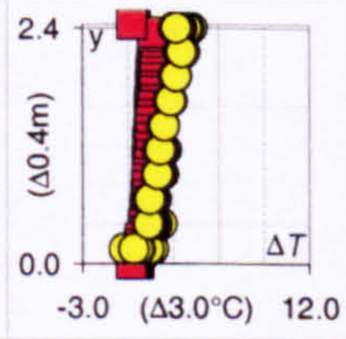	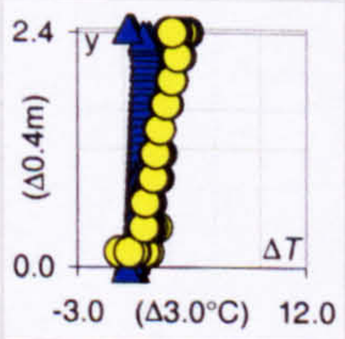	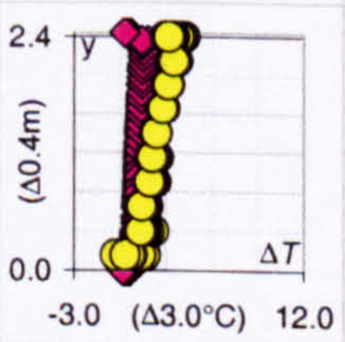	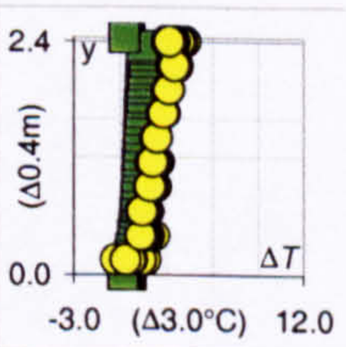

Width of opening:	0.1m
Effective area of opening:	$0.061m^2$
Heat source:	Boiler ring
Strength of heat source:	490.5W

Figure 19.b

	Laminar	Standard-$k\varepsilon$	Realizable-$k\varepsilon$	RNG-$k\varepsilon$
Radiation model disabled. Upwind differencing. Adiabatic walls. Uniform external temperature.	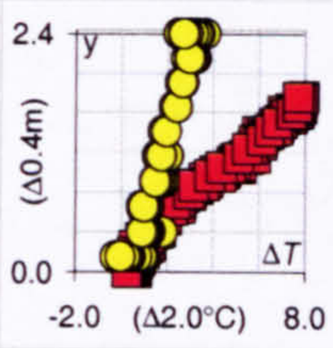	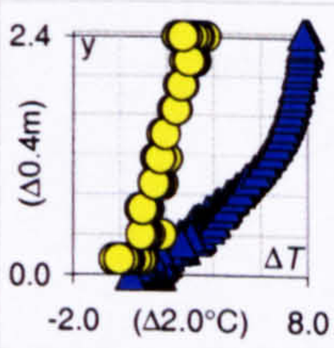	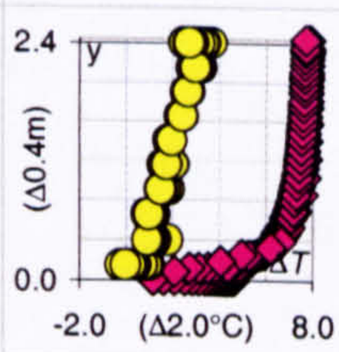	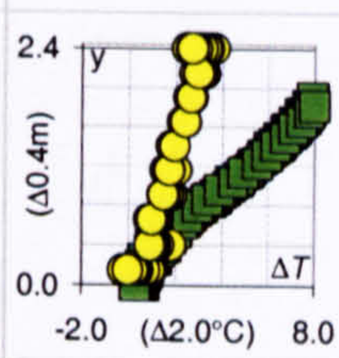
Radiation model disabled. QUICK differencing. Adiabatic walls. Uniform external temperature.	No available solution.	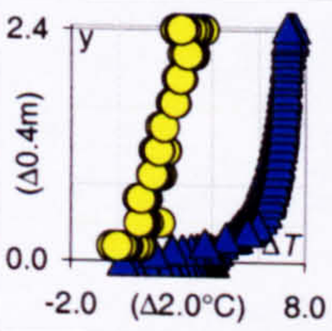	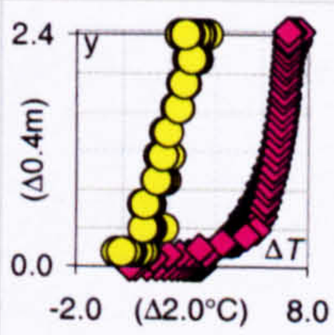	No available solution.
Radiation model enabled, $\alpha = 0.00m^{-1}$ QUICK differencing. Adiabatic walls. Uniform external temperature.	No available solution.	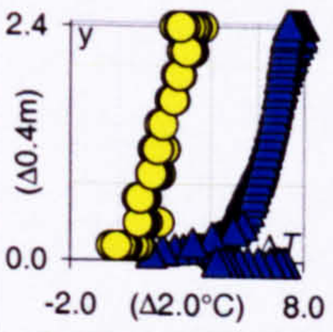	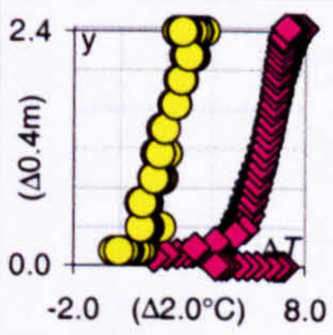	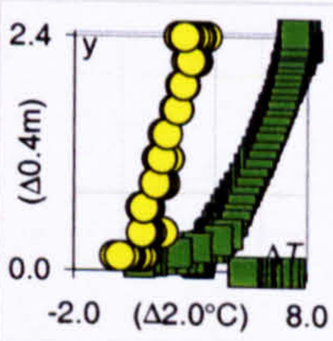
Radiation model enabled, $\alpha = 0.05m^{-1}$ QUICK differencing. Adiabatic walls. Uniform external temperature.	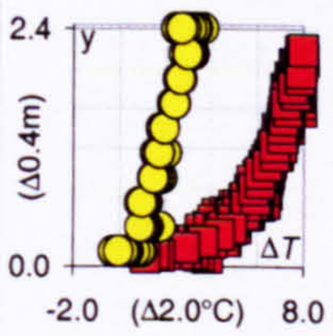	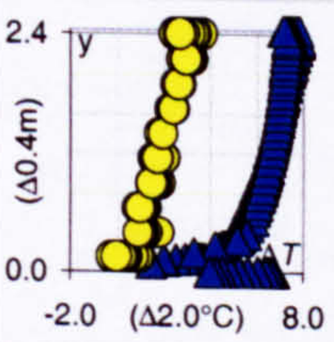	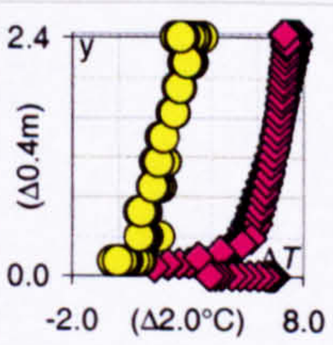	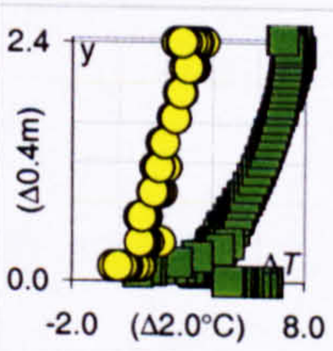
Radiation model enabled, $\alpha = 0.10m^{-1}$ QUICK differencing. Adiabatic walls. Uniform external temperature.	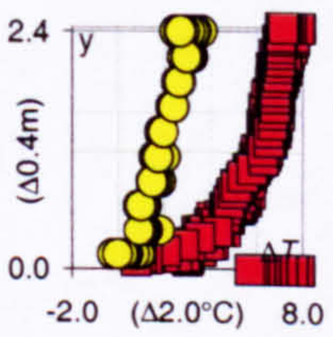	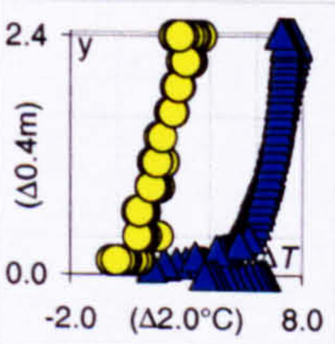	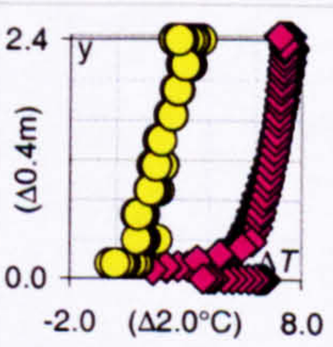	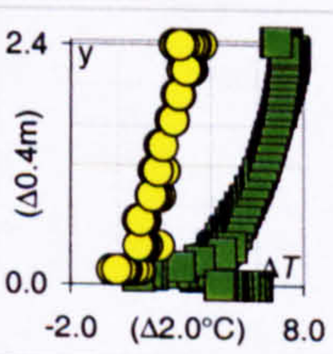
Radiation model enabled, $\alpha = 0.15m^{-1}$ QUICK differencing. Adiabatic walls. Uniform external temperature.	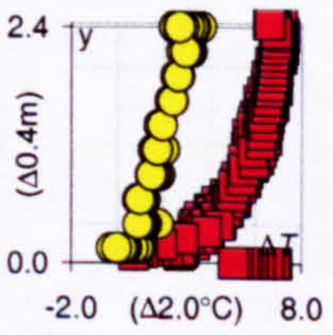	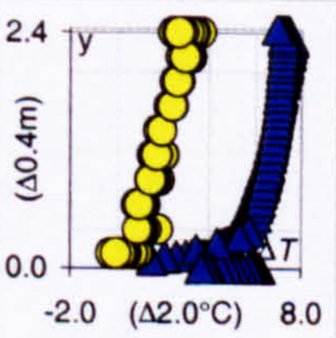	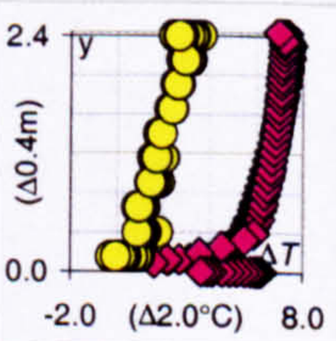	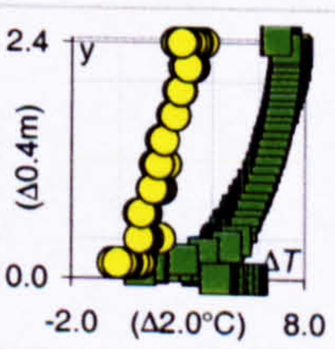

Width of opening:	0.2m
Effective area of opening:	$0.122m^2$
Heat source:	Boiler ring
Strength of heat source:	490.5W

Figure 20.a

	Laminar	Standard-$k\varepsilon$	Realizable-$k\varepsilon$	RNG-$k\varepsilon$
Radiation model enabled, $\alpha = 0.00m^{-1}$ QUICK differencing. Convection walls. Uniform external temperature.	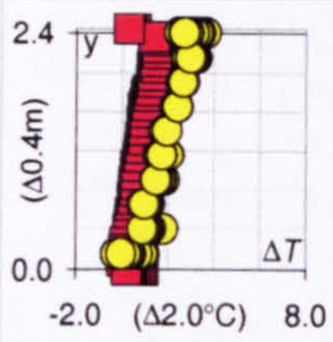	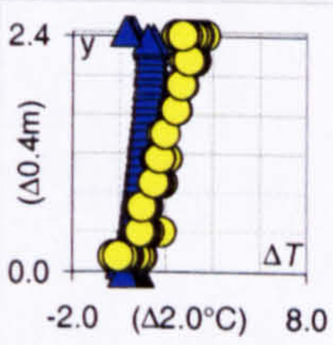	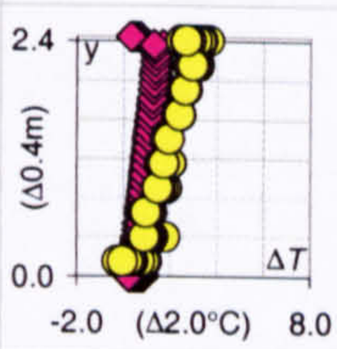	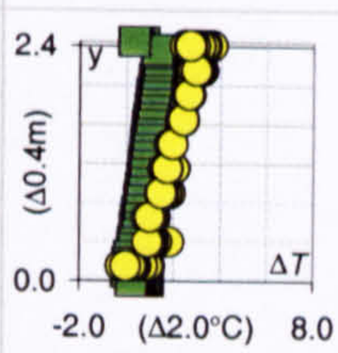
Radiation model enabled, $\alpha = 0.00m^{-1}$ QUICK differencing. Radiation walls. Uniform external temperature.	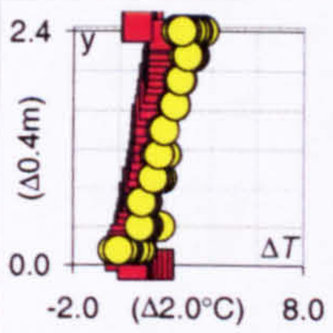	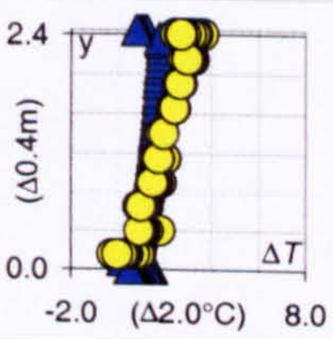	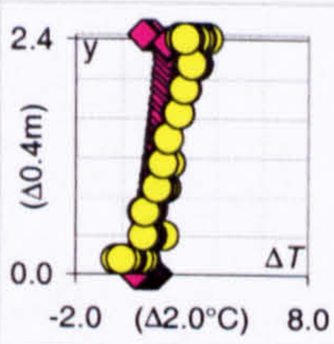	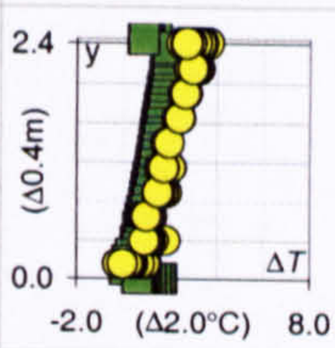
Radiation model enabled, $\alpha = 0.00m^{-1}$ QUICK differencing. Mixed walls. Uniform external temperature.	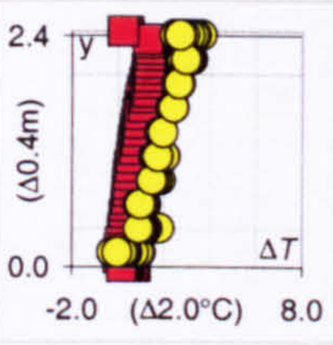	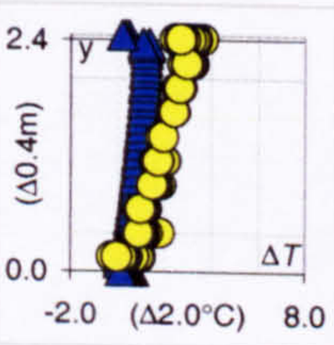	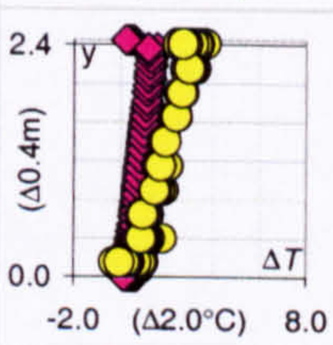	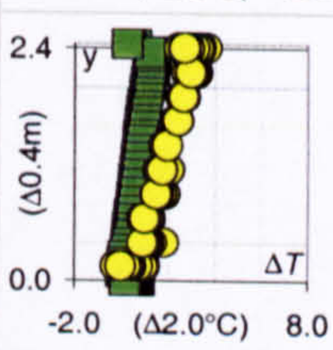
Radiation model enabled, $\alpha = 0.05m^{-1}$ QUICK differencing. Convection walls. Uniform external temperature.	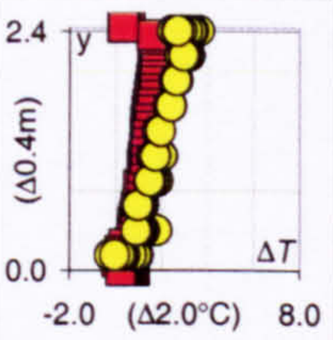	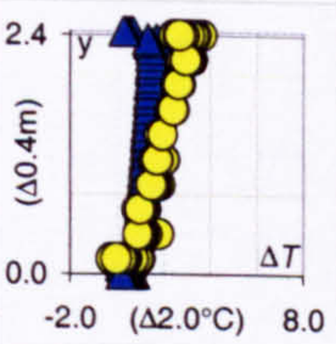	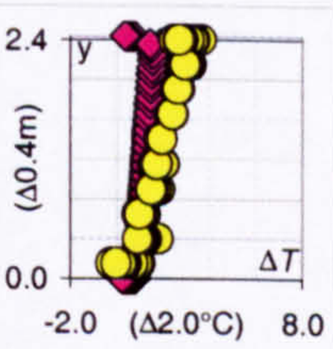	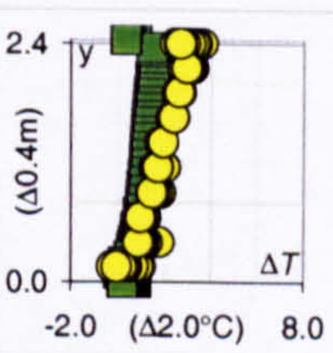
Radiation model enabled, $\alpha = 0.05m^{-1}$ QUICK differencing. Radiation walls. Uniform external temperature.	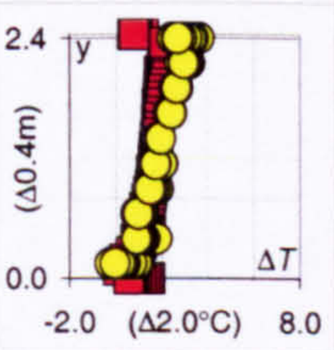	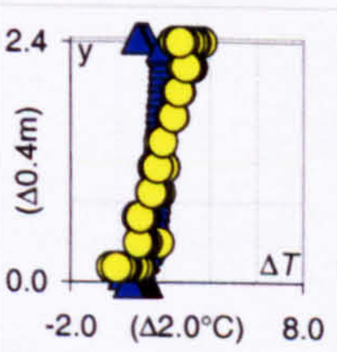	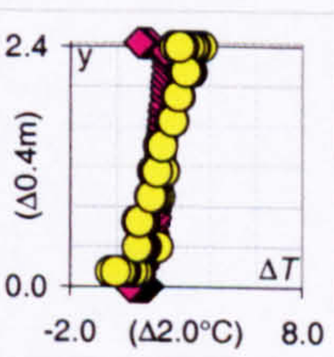	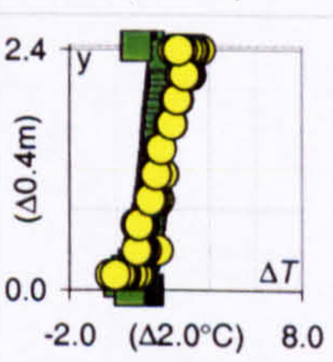
Radiation model enabled, $\alpha = 0.05m^{-1}$ QUICK differencing. Mixed walls. Uniform external temperature.	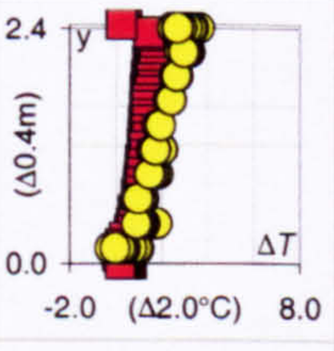	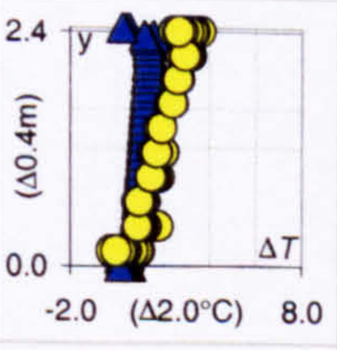	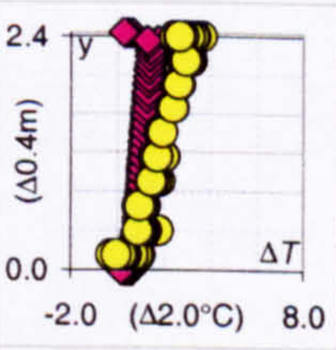	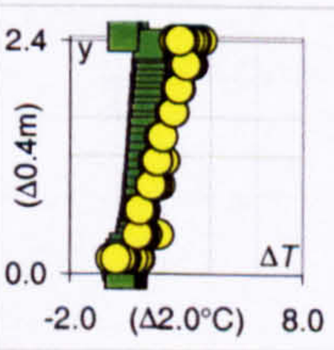

Width of opening:	0.2m
Effective area of opening:	0.122m^2
Heat source:	Boiler ring
Strength of heat source:	490.5W

Figure 20.b

	Laminar	Standard-$k\varepsilon$	Realizable-$k\varepsilon$	RNG-$k\varepsilon$
Radiation model disabled. Upwind differencing. Adiabatic walls. Uniform external temperature.	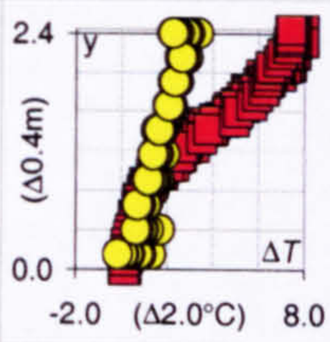	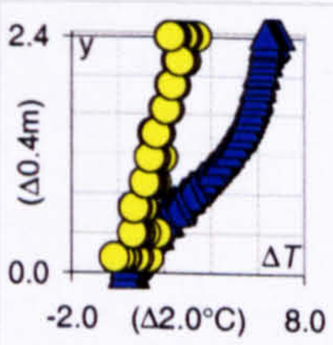	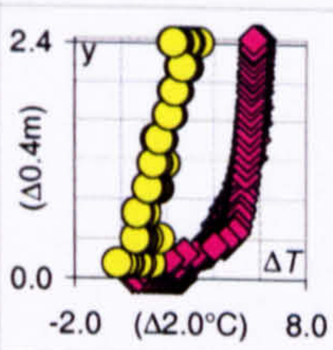	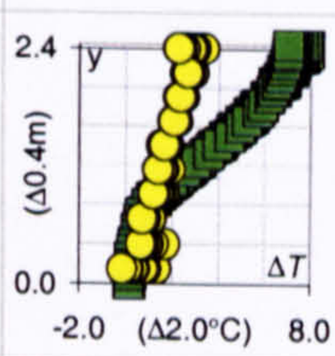
Radiation model disabled. QUICK differencing. Adiabatic walls. Uniform external temperature.	No available solution.	No available solution.	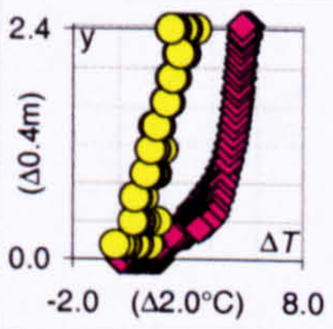	No available solution.
Radiation model enabled, $\alpha = 0.00m^{-1}$ QUICK differencing. Adiabatic walls. Uniform external temperature.	No available solution.	No available solution.	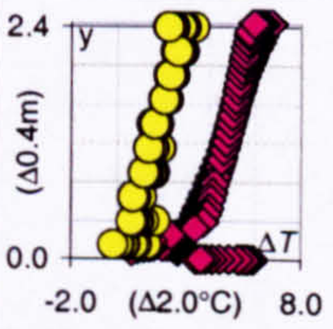	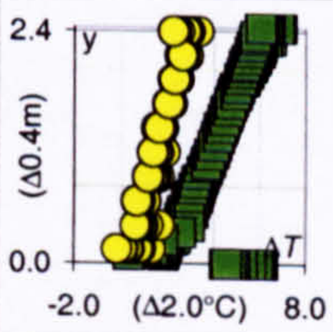
Radiation model enabled, $\alpha = 0.05m^{-1}$ QUICK differencing. Adiabatic walls. Uniform external temperature.	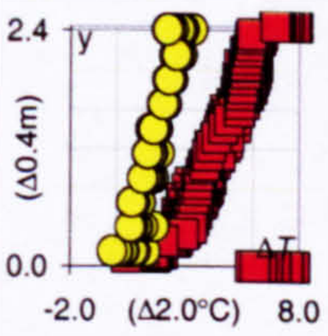	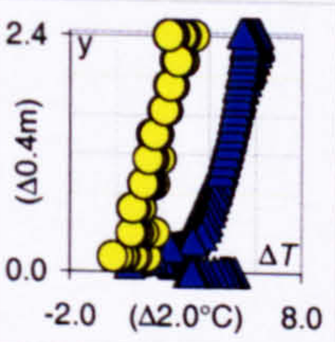	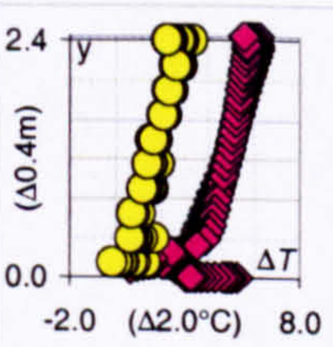	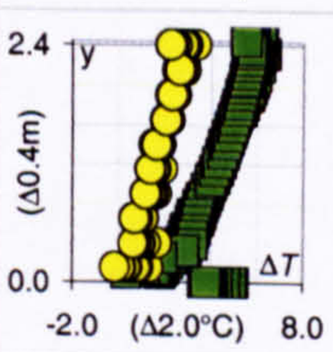
Radiation model enabled, $\alpha = 0.10m^{-1}$ QUICK differencing. Adiabatic walls. Uniform external temperature.	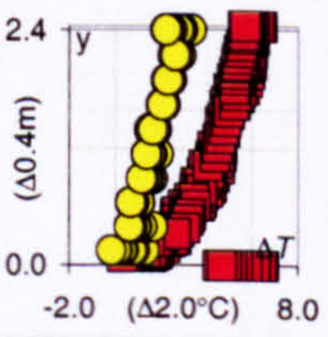	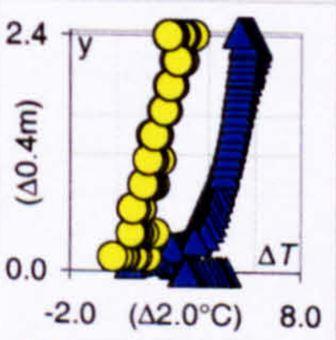	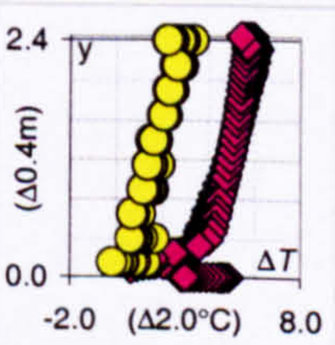	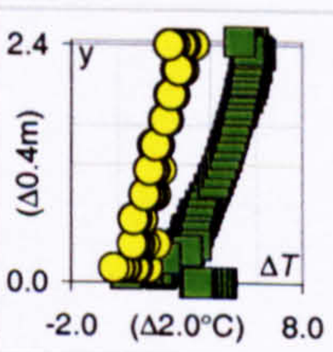
Radiation model enabled, $\alpha = 0.15m^{-1}$ QUICK differencing. Adiabatic walls. Uniform external temperature.	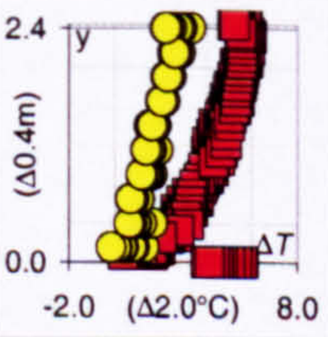	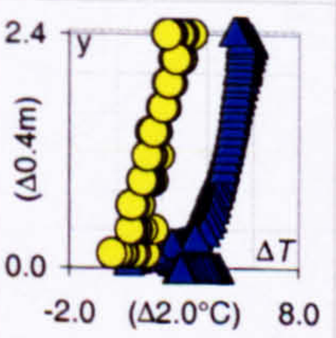	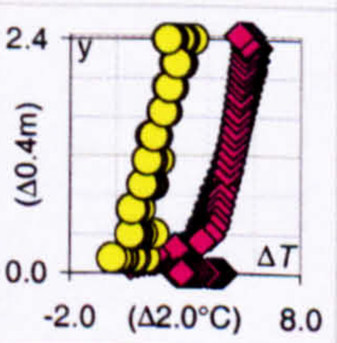	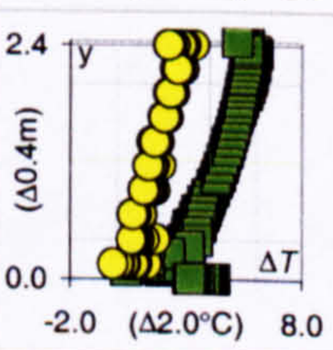

Width of opening:	0.3m
Effective area of opening:	$0.183m^2$
Heat source:	Boiler ring
Strength of heat source:	490.5W

Figure 21.a

	Laminar	Standard-$k\varepsilon$	Realizable-$k\varepsilon$	RNG-$k\varepsilon$
Radiation model enabled, $\alpha = 0.00m^{-1}$ QUICK differencing. Convection walls. Uniform external temperature.	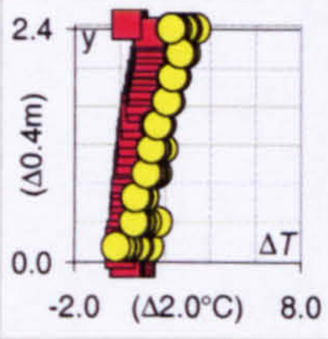	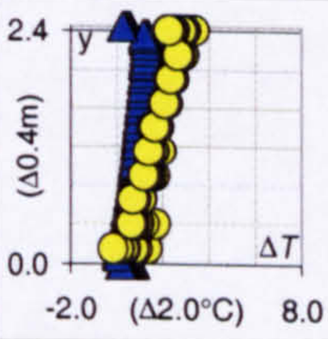	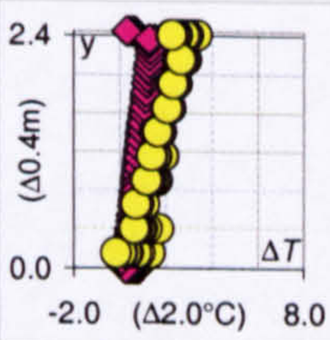	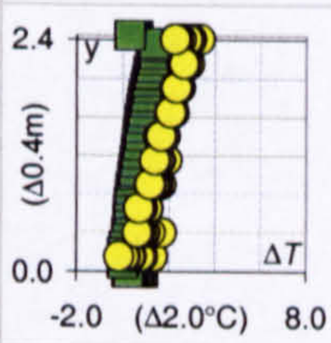
Radiation model enabled, $\alpha = 0.00m^{-1}$ QUICK differencing. Radiation walls. Uniform external temperature.	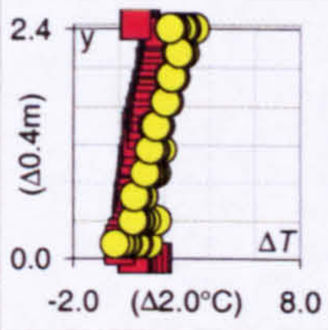	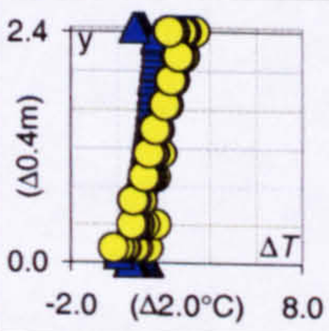	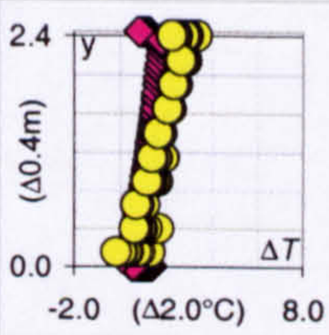	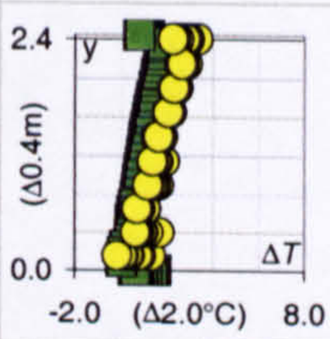
Radiation model enabled, $\alpha = 0.00m^{-1}$ QUICK differencing. Mixed walls. Uniform external temperature.	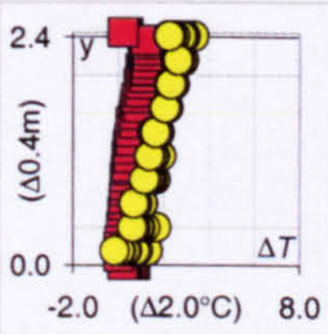	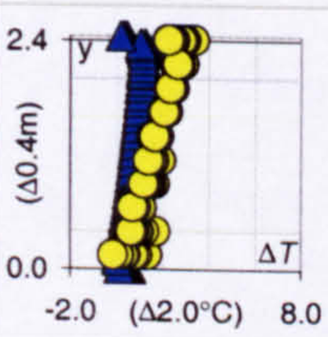	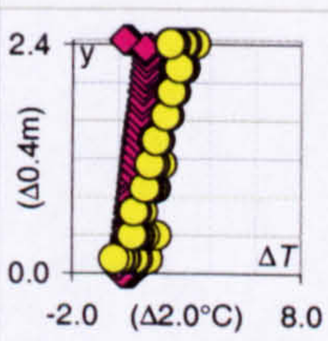	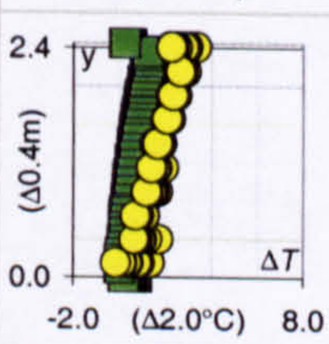
Radiation model enabled, $\alpha = 0.05m^{-1}$ QUICK differencing. Convection walls. Uniform external temperature.	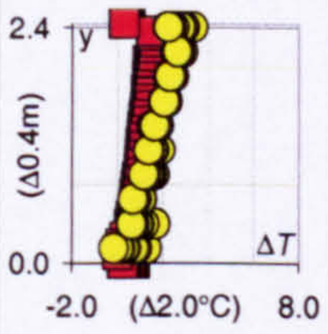	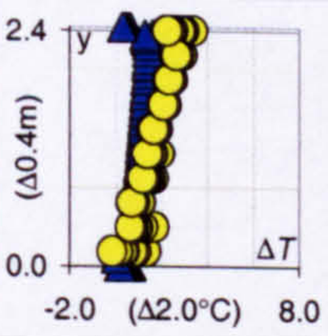	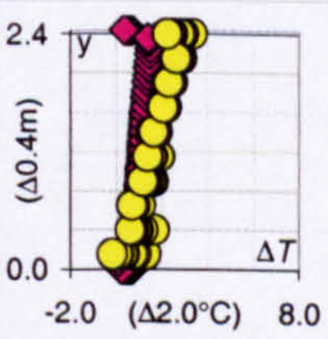	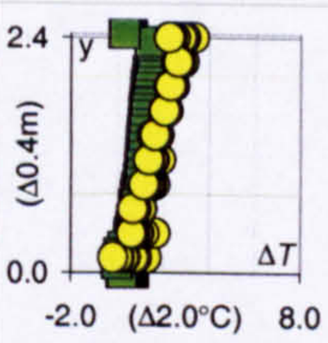
Radiation model enabled, $\alpha = 0.05m^{-1}$ QUICK differencing. Radiation walls. Uniform external temperature.	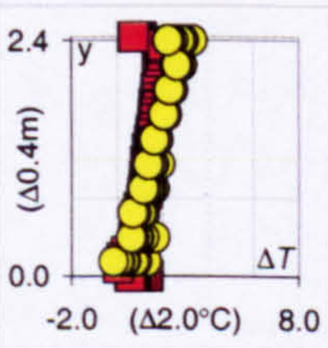	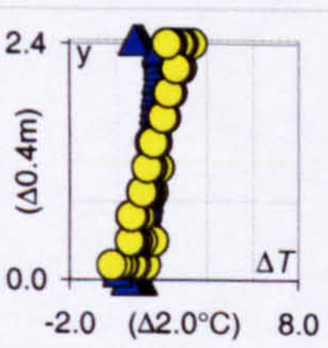	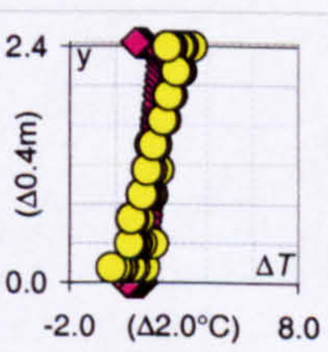	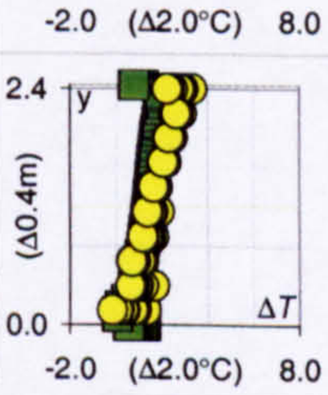
Radiation model enabled, $\alpha = 0.05m^{-1}$ QUICK differencing. Mixed walls. Uniform external temperature.	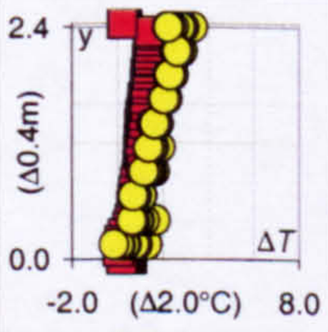	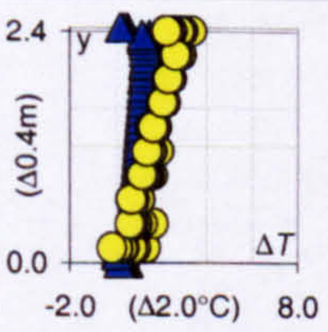	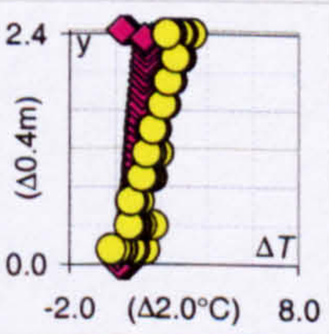	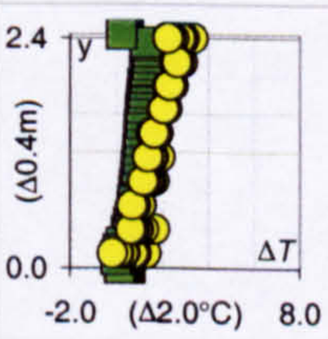

Width of opening:	0.3m
Effective area of opening:	$0.183m^2$
Heat source:	Boiler ring
Strength of heat source:	490.5W

Figure 21.b

	Laminar	Standard-$k\varepsilon$	Realizable-$k\varepsilon$	RNG-$k\varepsilon$
Radiation model disabled. Upwind differencing. Adiabatic walls. Uniform external temperature.	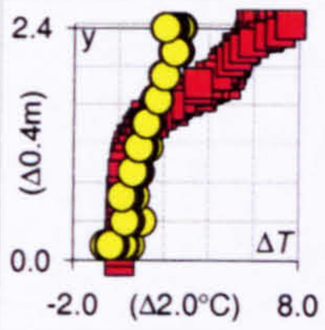	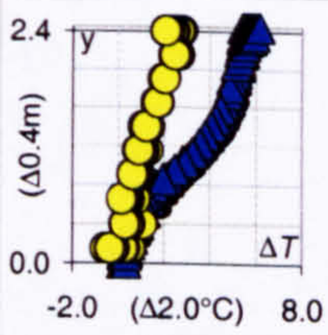	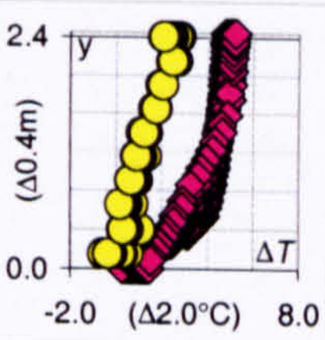	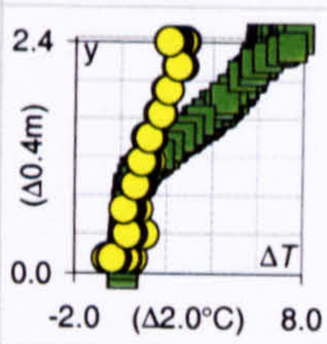
Radiation model disabled. QUICK differencing. Adiabatic walls. Uniform external temperature.	No available solution.	No available solution.	No available solution.	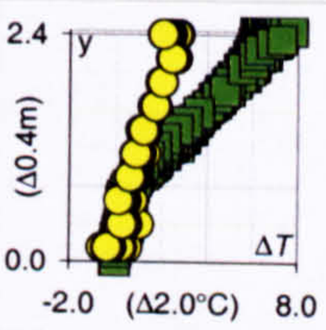
Radiation model enabled, $\alpha = 0.00m^{-1}$ QUICK differencing. Adiabatic walls. Uniform external temperature.	No available solution.	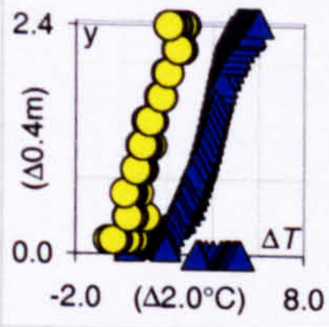	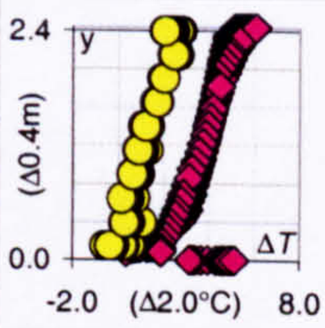	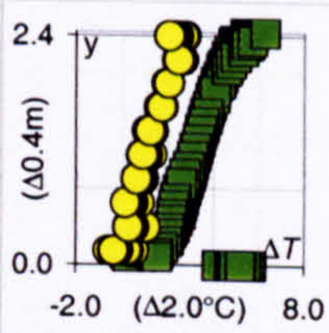
Radiation model enabled, $\alpha = 0.05m^{-1}$ QUICK differencing. Adiabatic walls. Uniform external temperature.	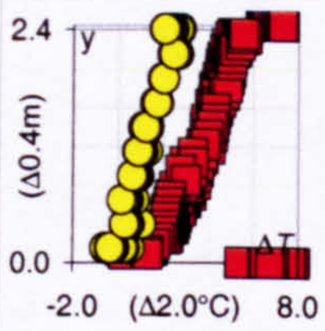	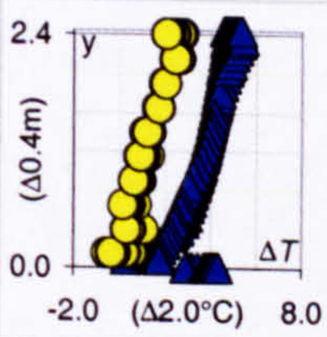	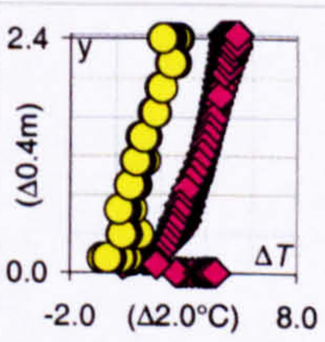	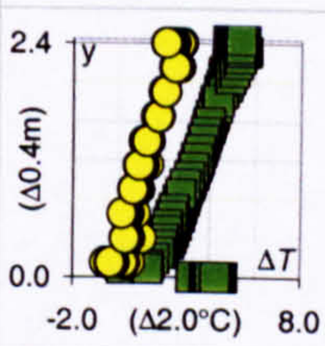
Radiation model enabled, $\alpha = 0.10m^{-1}$ QUICK differencing. Adiabatic walls. Uniform external temperature.	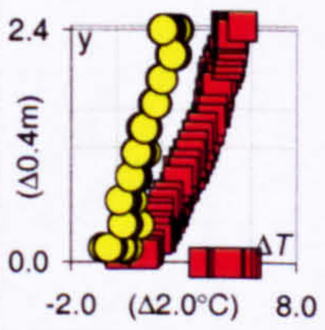	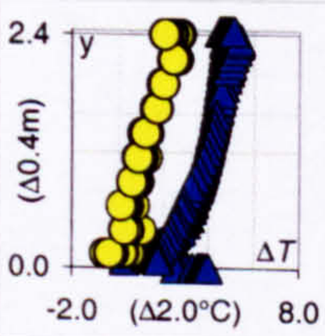	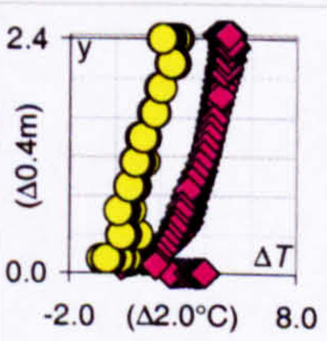	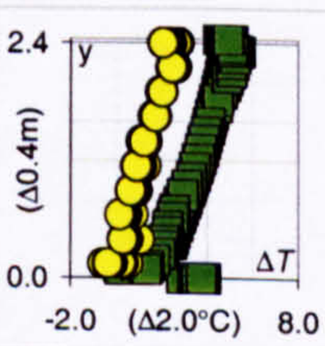
Radiation model enabled, $\alpha = 0.15m^{-1}$ QUICK differencing. Adiabatic walls. Uniform external temperature.	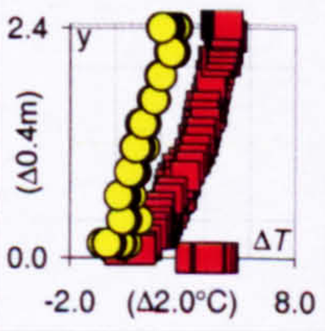	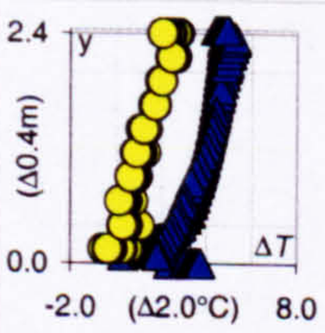	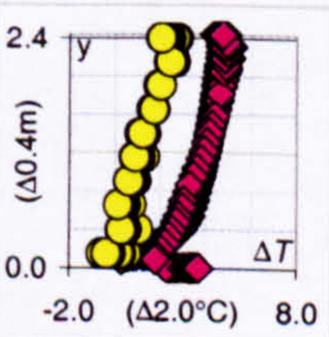	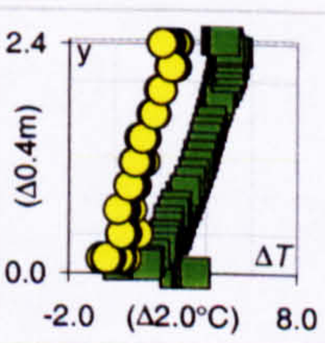

Width of opening:	0.4m
Effective area of opening:	0.244m^2
Heat source:	Boiler ring
Strength of heat source:	490.5W

Figure 22.a

	Laminar	Standard-$k\varepsilon$	Realizable-$k\varepsilon$	RNG-$k\varepsilon$
Radiation model enabled, $\alpha = 0.00m^{-1}$ QUICK differencing. Convection walls. Uniform external temperature.	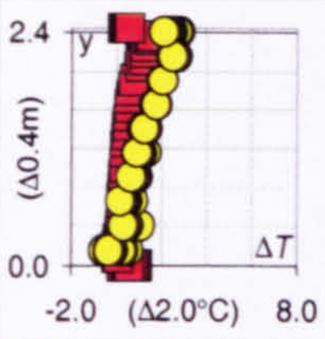	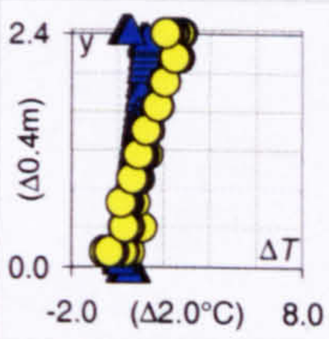	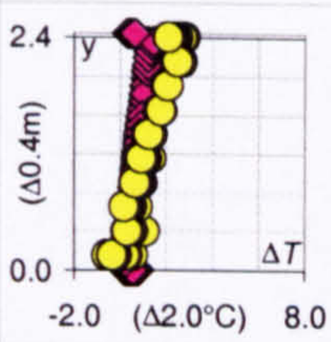	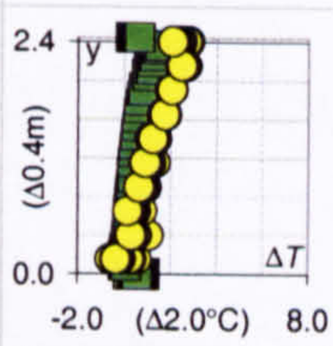
Radiation model enabled, $\alpha = 0.00m^{-1}$ QUICK differencing. Radiation walls. Uniform external temperature.	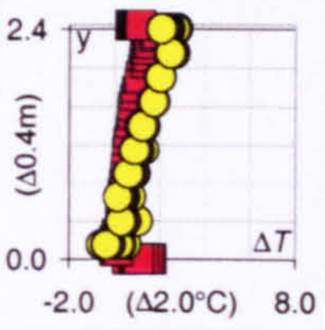	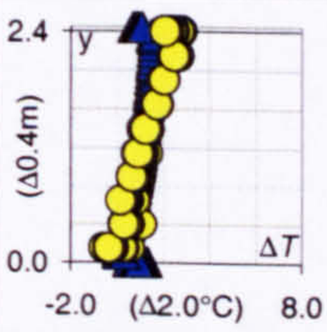	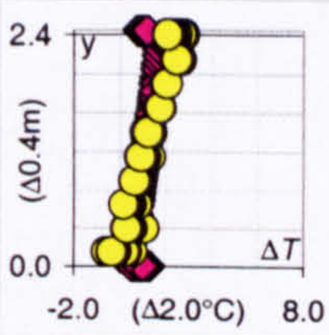	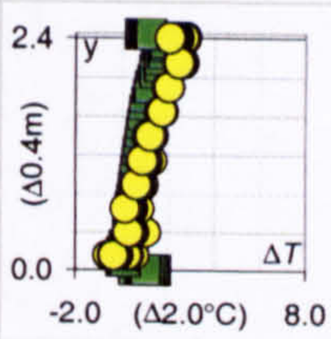
Radiation model enabled, $\alpha = 0.00m^{-1}$ QUICK differencing. Mixed walls. Uniform external temperature.	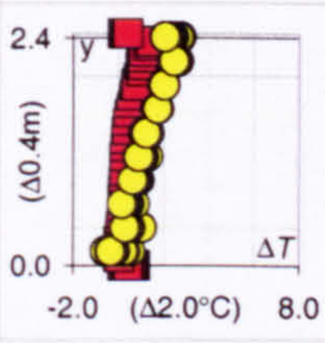	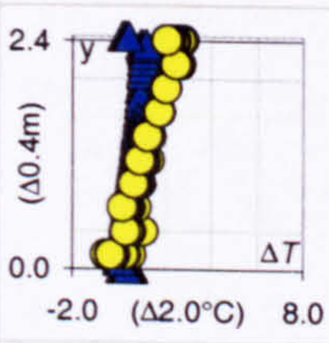	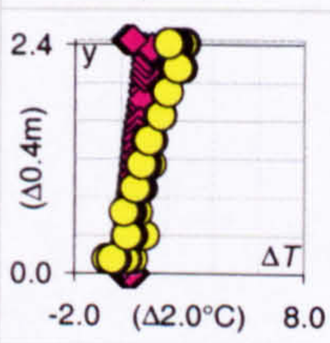	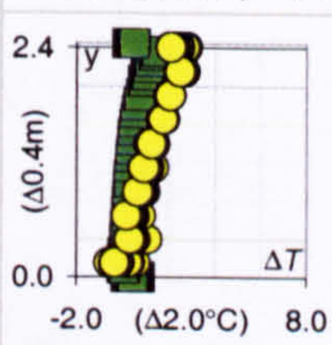
Radiation model enabled, $\alpha = 0.05m^{-1}$ QUICK differencing. Convection walls. Uniform external temperature.	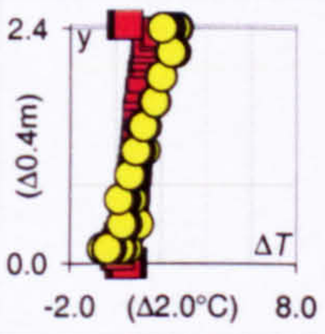	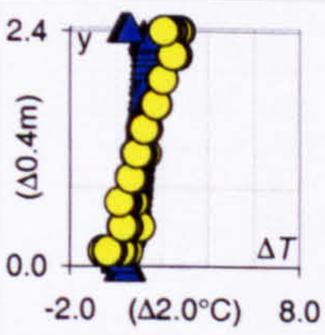	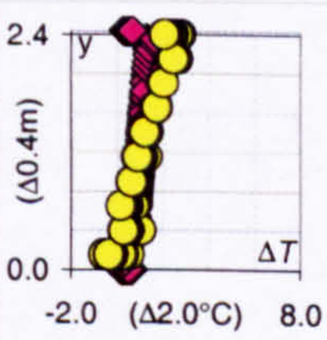	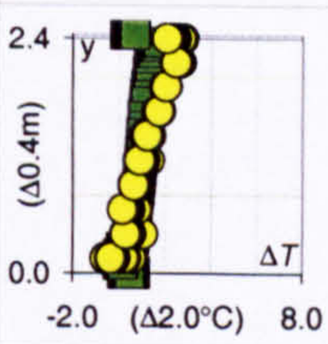
Radiation model enabled, $\alpha = 0.05m^{-1}$ QUICK differencing. Radiation walls. Uniform external temperature.	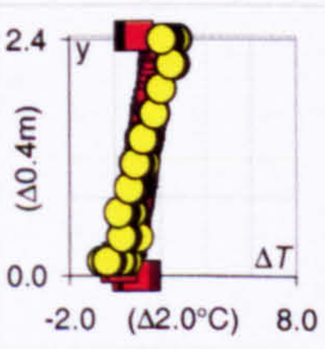	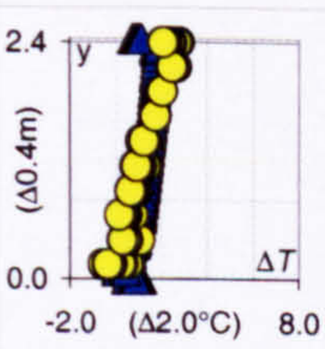	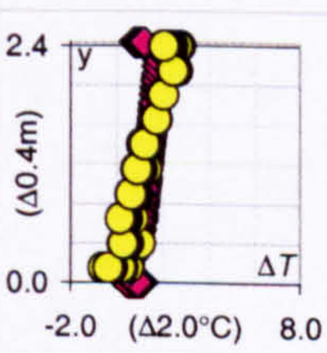	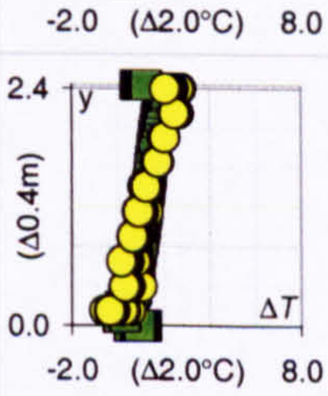
Radiation model enabled, $\alpha = 0.05m^{-1}$ QUICK differencing. Mixed walls. Uniform external temperature.	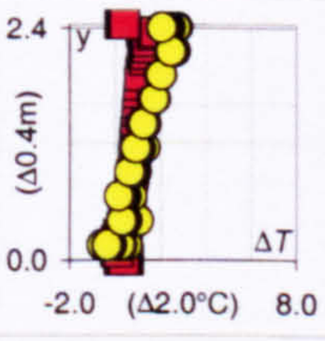	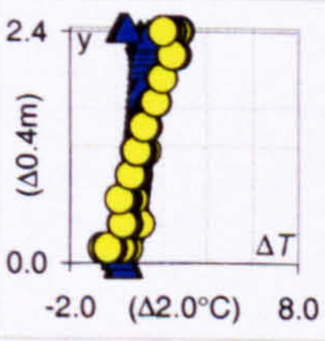	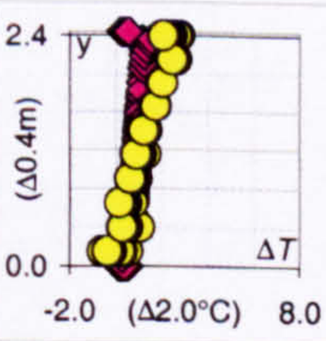	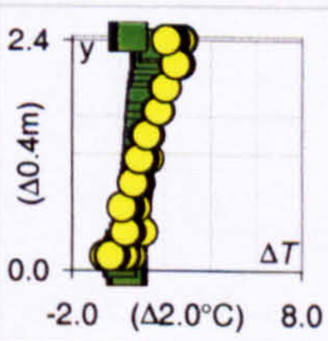

Width of opening:	0.4m
Effective area of opening:	$0.244m^2$
Heat source:	Boiler ring
Strength of heat source:	490.5W

Figure 22.b

	Laminar	Standard-$k\varepsilon$	Realizable-$k\varepsilon$	RNG-$k\varepsilon$
Radiation model disabled. Upwind differencing. Adiabatic walls. Uniform external temperature.	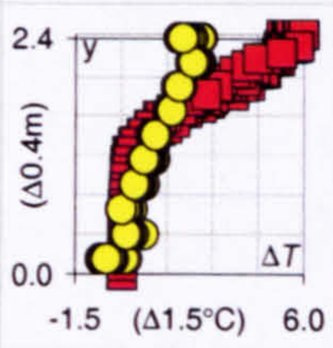	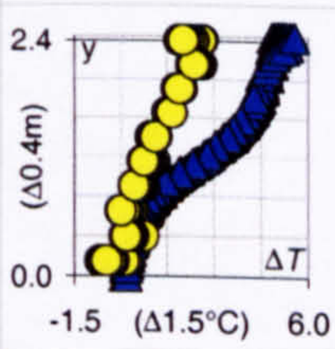	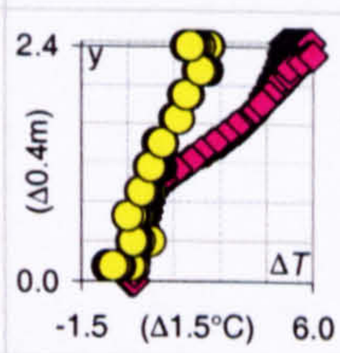	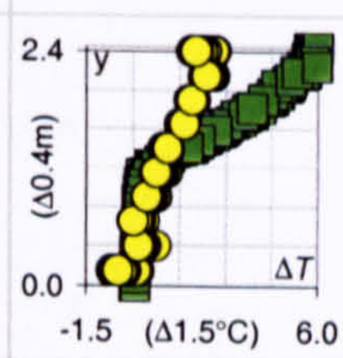
Radiation model disabled. QUICK differencing. Adiabatic walls. Uniform external temperature.	No available solution.	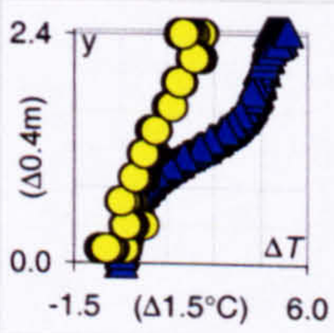	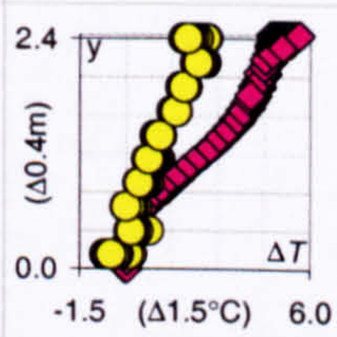	No available solution.
Radiation model enabled, $\alpha = 0.00m^{-1}$ QUICK differencing. Adiabatic walls. Uniform external temperature.	No available solution.	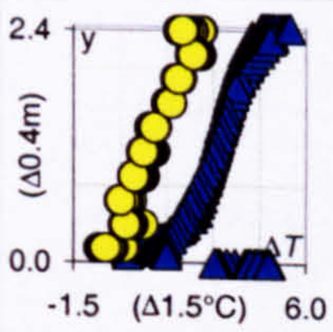	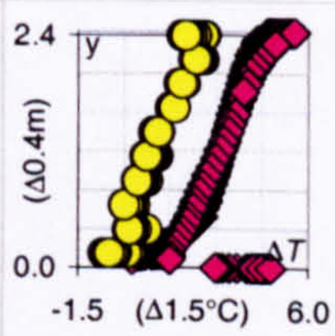	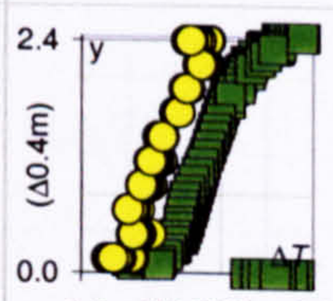
Radiation model enabled, $\alpha = 0.05m^{-1}$ QUICK differencing. Adiabatic walls. Uniform external temperature.	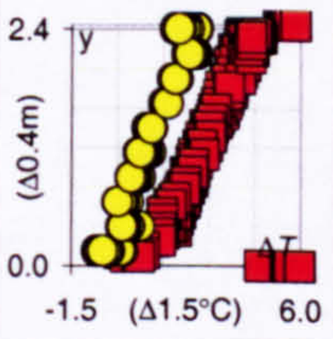	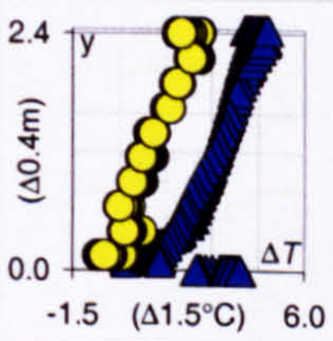	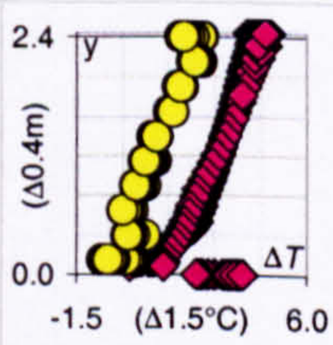	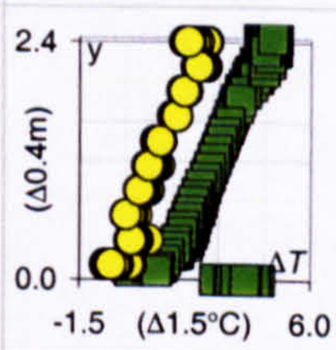
Radiation model enabled, $\alpha = 0.10m^{-1}$ QUICK differencing. Adiabatic walls. Uniform external temperature.	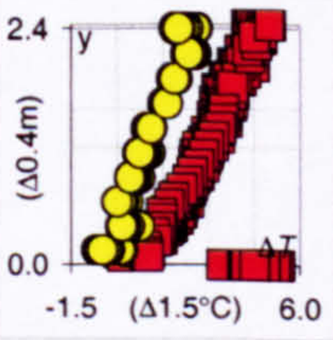	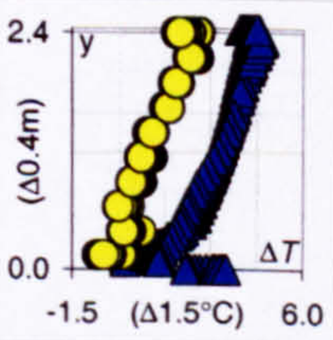	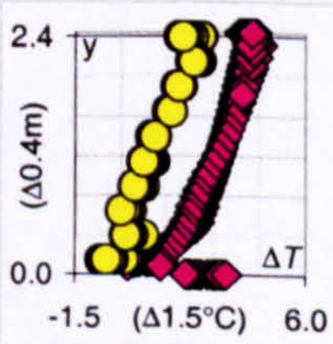	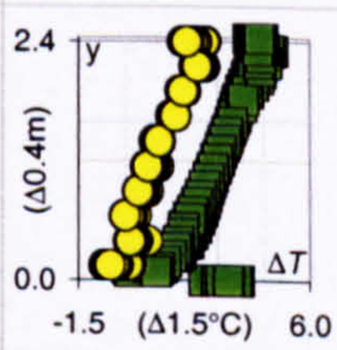
Radiation model enabled, $\alpha = 0.15m^{-1}$ QUICK differencing. Adiabatic walls. Uniform external temperature.	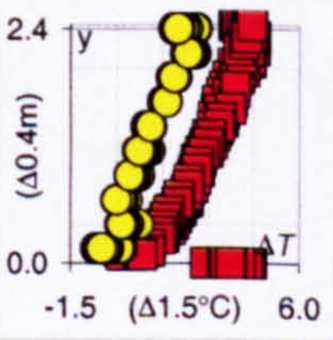	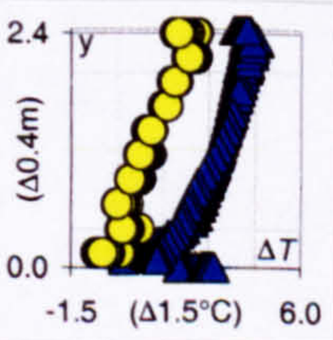	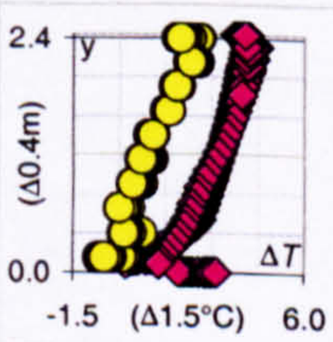	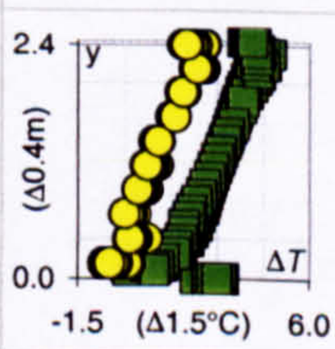

Width of opening:	0.5m
Effective area of opening:	$0.305m^2$
Heat source:	Boiler ring
Strength of heat source:	490.5W

Figure 23.a

	Laminar	Standard-$k\varepsilon$	Realizable-$k\varepsilon$	RNG-$k\varepsilon$
Radiation model enabled, $\alpha = 0.00m^{-1}$ QUICK differencing. Convection walls. Uniform external temperature.	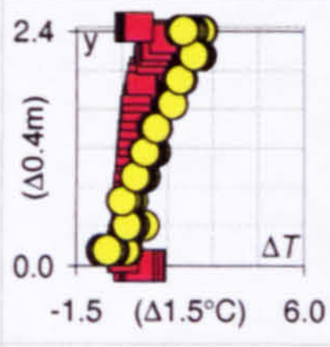	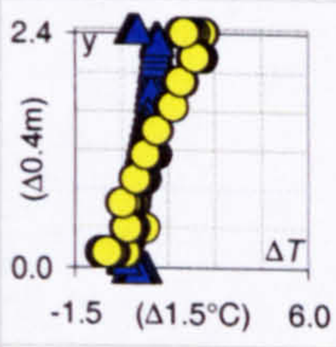	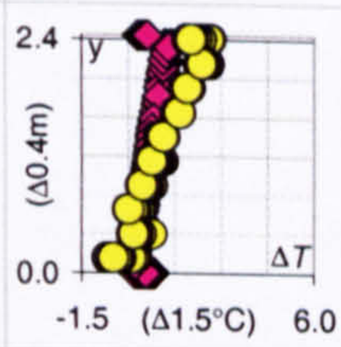	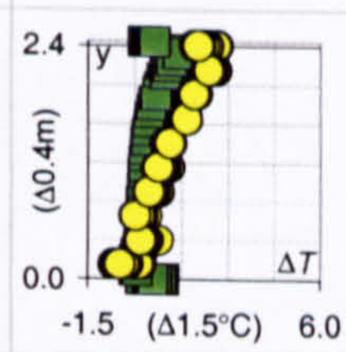
Radiation model enabled, $\alpha = 0.00m^{-1}$ QUICK differencing. Radiation walls. Uniform external temperature.	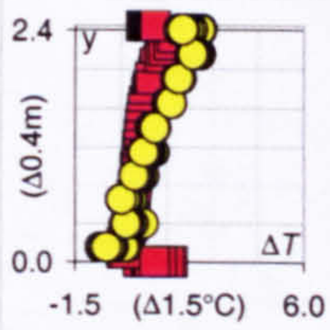	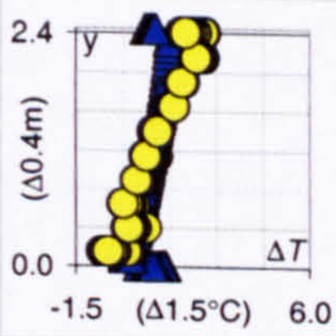	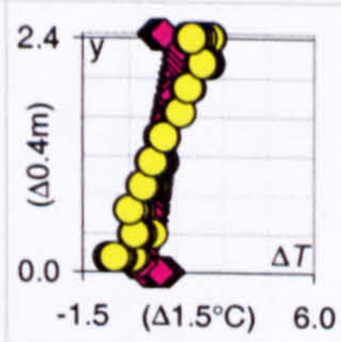	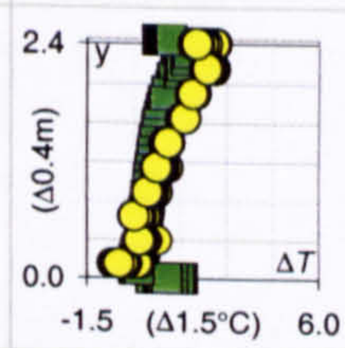
Radiation model enabled, $\alpha = 0.00m^{-1}$ QUICK differencing. Mixed walls. Uniform external temperature.	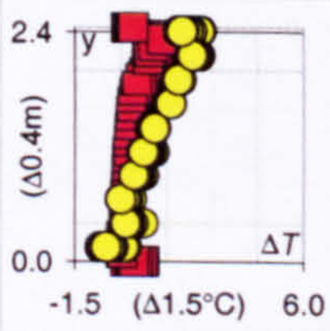	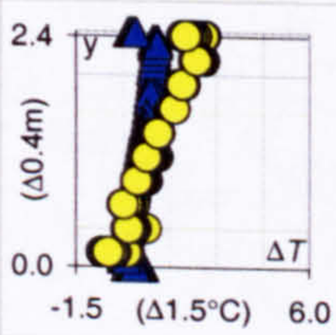	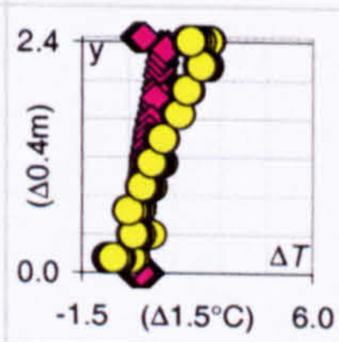	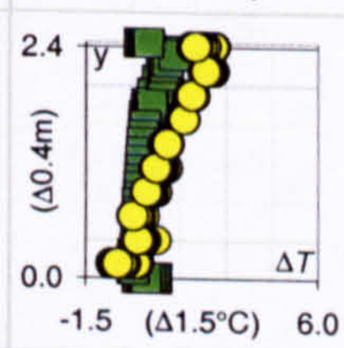
Radiation model enabled, $\alpha = 0.05m^{-1}$ QUICK differencing. Convection walls. Uniform external temperature.	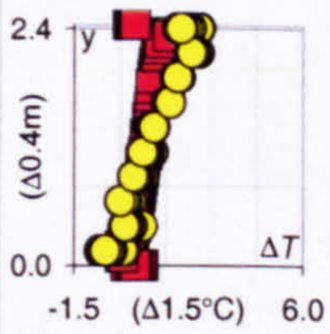	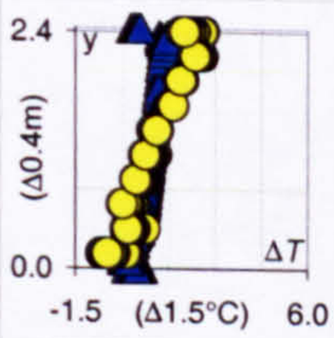	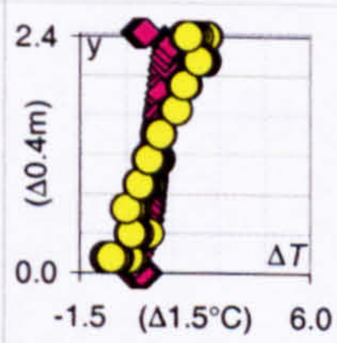	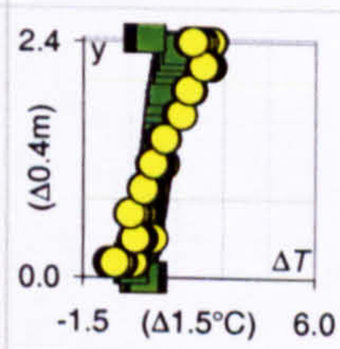
Radiation model enabled, $\alpha = 0.05m^{-1}$ QUICK differencing. Radiation walls. Uniform external temperature.	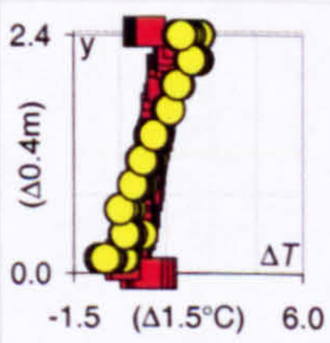	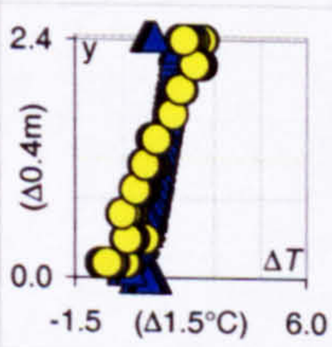	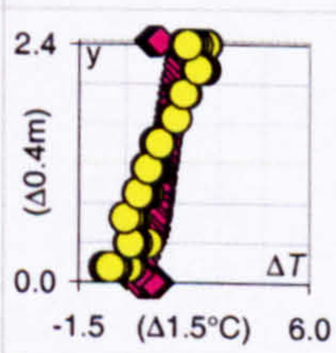	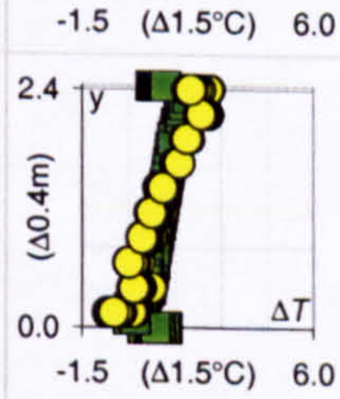
Radiation model enabled, $\alpha = 0.05m^{-1}$ QUICK differencing. Mixed walls. Uniform external temperature.	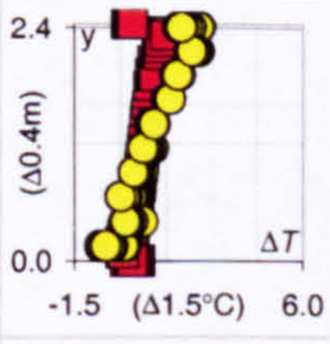	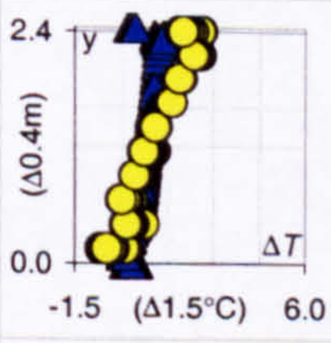	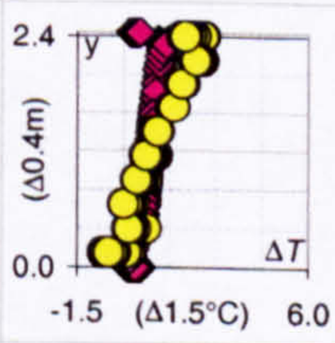	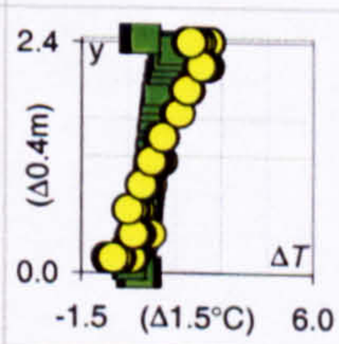

Width of opening:	0.5m
Effective area of opening:	$0.305m^2$
Heat source:	Boiler ring
Strength of heat source:	490.5W

Figure 23.b

	Laminar	Standard-$k\varepsilon$	Realizable-$k\varepsilon$	RNG-$k\varepsilon$
Radiation model disabled. Upwind differencing. Adiabatic walls. Uniform external temperature.	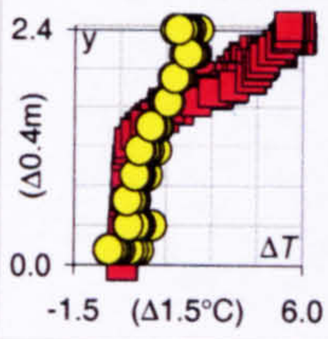	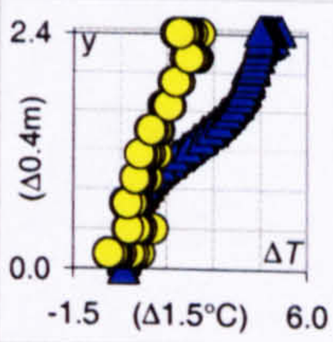	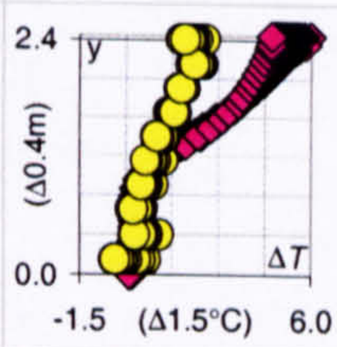	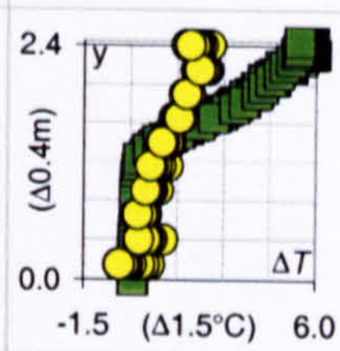
Radiation model disabled. QUICK differencing. Adiabatic walls. Uniform external temperature.	No available solution.	No available solution.	No available solution.	No available solution.
Radiation model enabled, $\alpha = 0.00m^{-1}$ QUICK differencing. Adiabatic walls. Uniform external temperature.	No available solution.	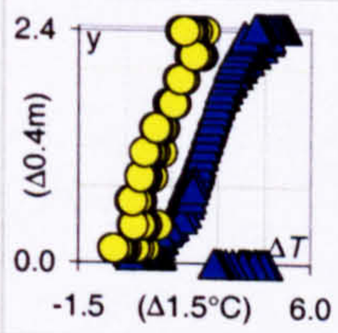	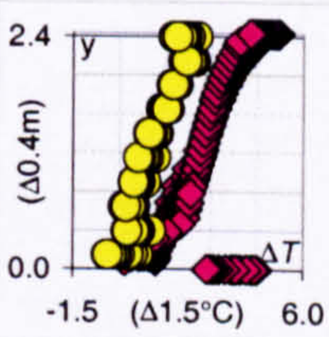	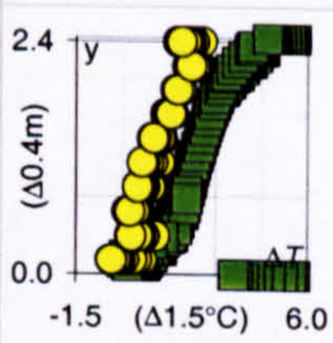
Radiation model enabled, $\alpha = 0.05m^{-1}$ QUICK differencing. Adiabatic walls. Uniform external temperature.	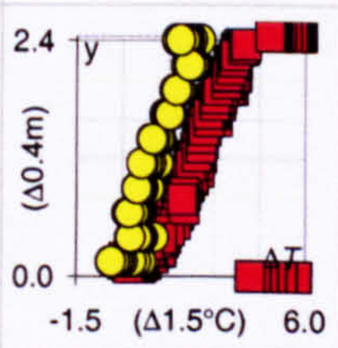	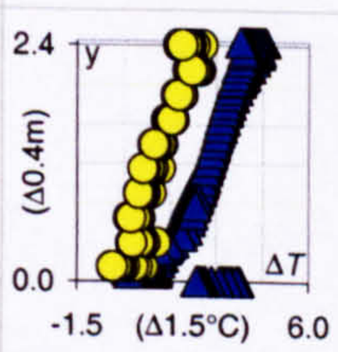	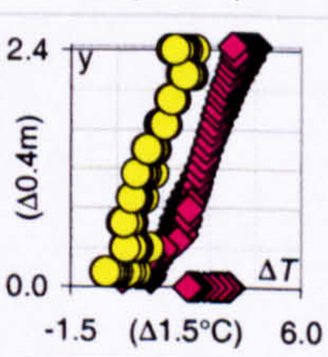	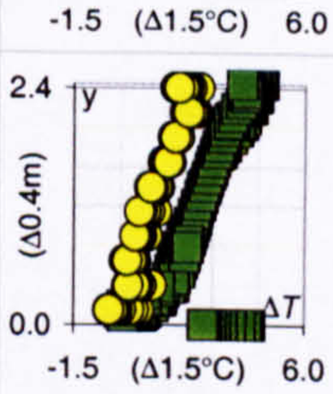
Radiation model enabled, $\alpha = 0.10m^{-1}$ QUICK differencing. Adiabatic walls. Uniform external temperature.	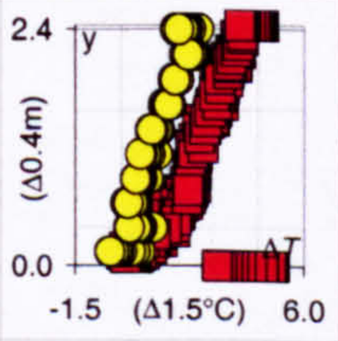	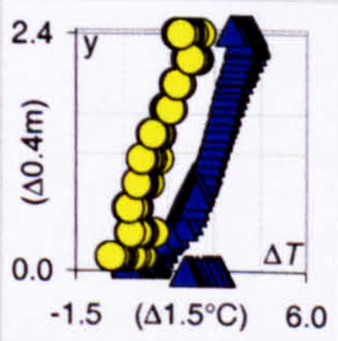	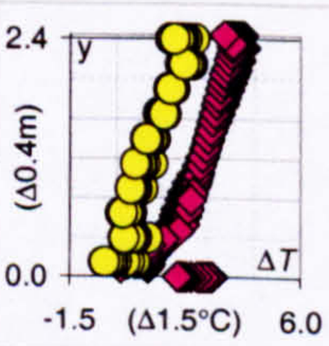	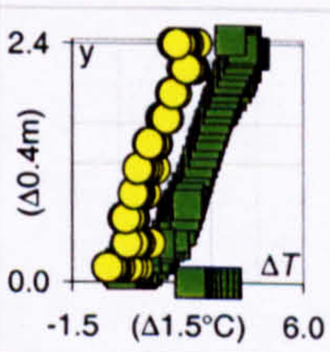
Radiation model enabled, $\alpha = 0.15m^{-1}$ QUICK differencing. Adiabatic walls. Uniform external temperature.	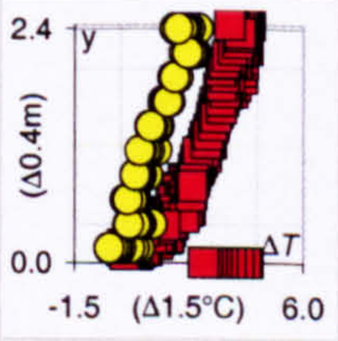	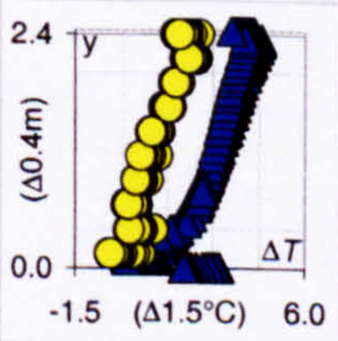	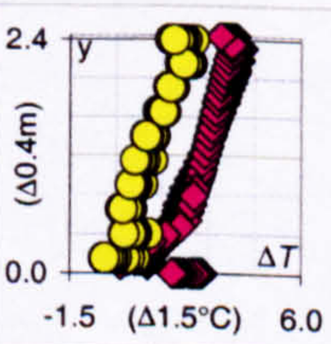	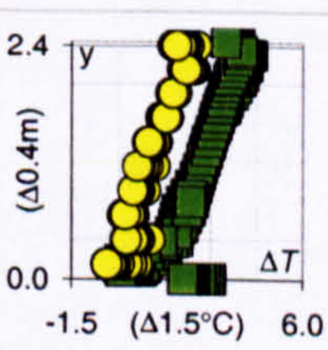

Width of opening:	0.6m
Effective area of opening:	0.366m^2
Heat source:	Boiler ring
Strength of heat source:	490.5W

Figure 24.a

	Laminar	Standard-$k\varepsilon$	Realizable-$k\varepsilon$	RNG-$k\varepsilon$
Radiation model enabled, $\alpha = 0.00m^{-1}$ QUICK differencing. Convection walls. Uniform external temperature.	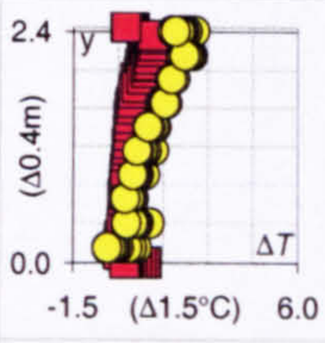	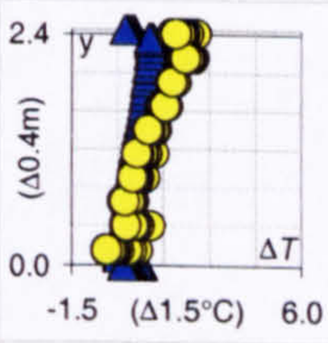	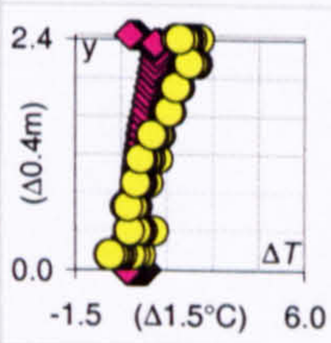	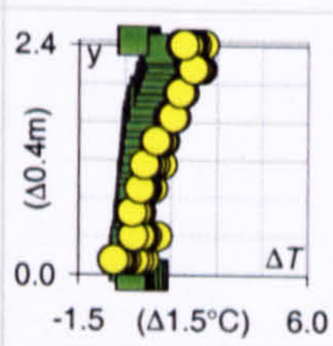
Radiation model enabled, $\alpha = 0.00m^{-1}$ QUICK differencing. Radiation walls. Uniform external temperature.	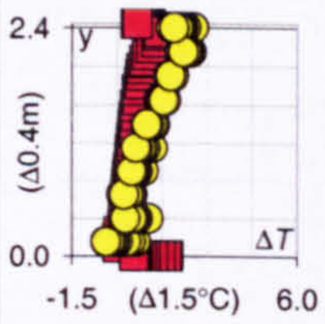	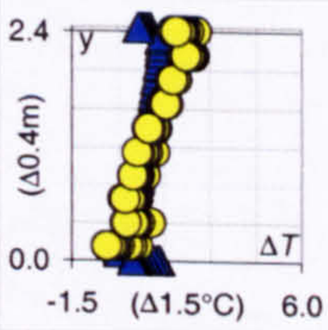	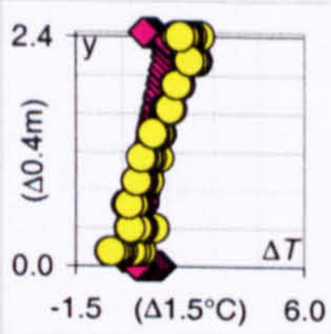	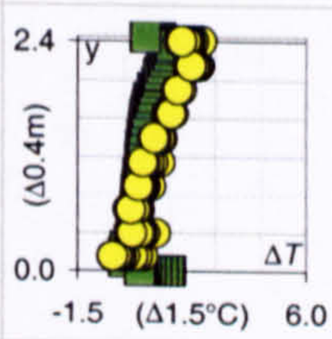
Radiation model enabled, $\alpha = 0.00m^{-1}$ QUICK differencing. Mixed walls. Uniform external temperature.	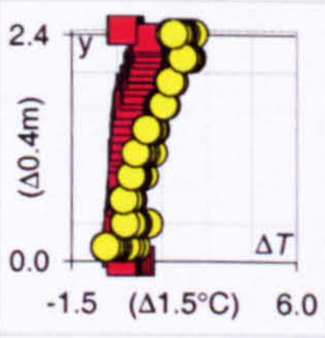	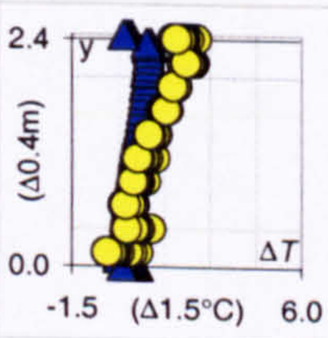	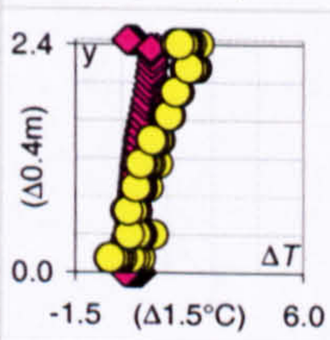	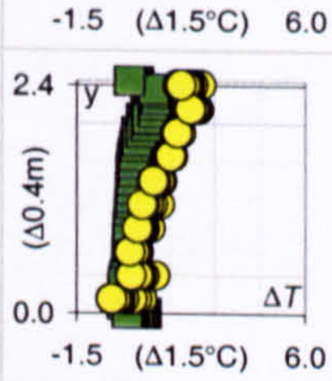
Radiation model enabled, $\alpha = 0.05m^{-1}$ QUICK differencing. Convection walls. Uniform external temperature.	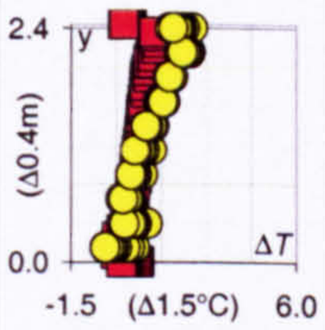	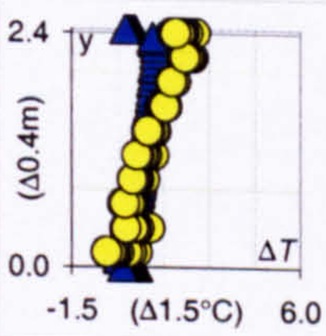	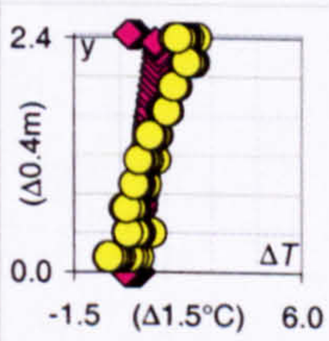	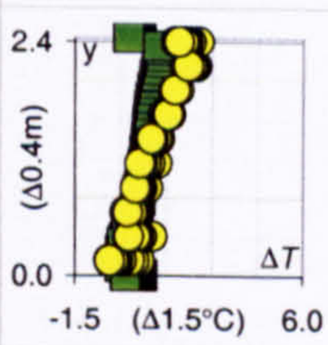
Radiation model enabled, $\alpha = 0.05m^{-1}$ QUICK differencing. Radiation walls. Uniform external temperature.	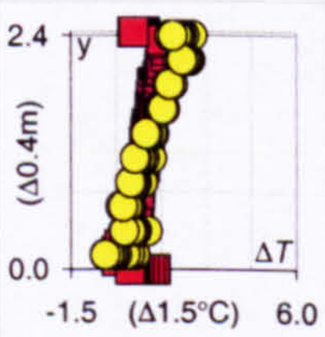	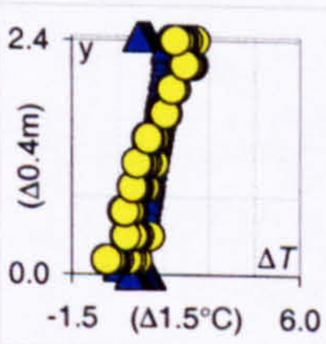	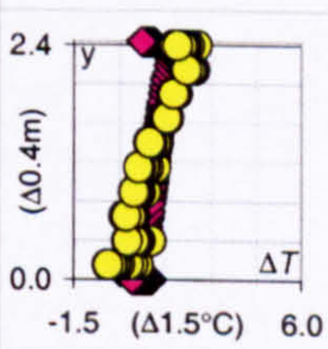	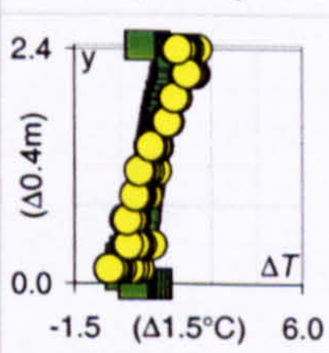
Radiation model enabled, $\alpha = 0.05m^{-1}$ QUICK differencing. Mixed walls. Uniform external temperature.	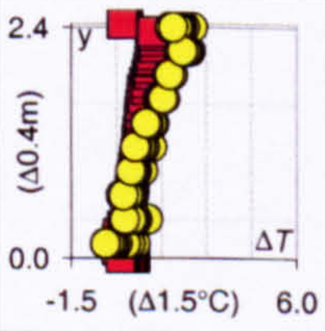	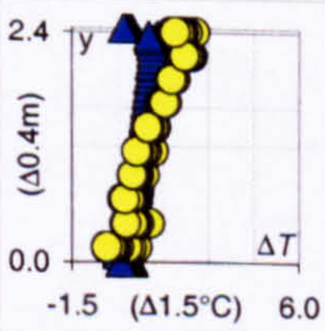	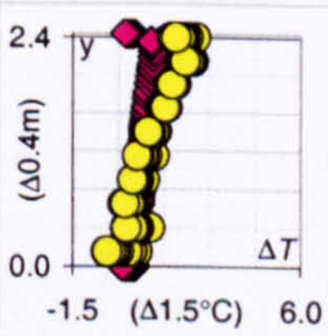	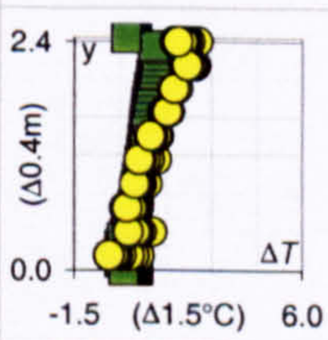

Width of opening:	0.6m
Effective area of opening:	$0.366m^2$
Heat source:	Boiler ring
Strength of heat source:	490.5W

Figure 24.b

	Laminar	Standard-$k\varepsilon$	Realizable-$k\varepsilon$	RNG-$k\varepsilon$
Radiation model disabled. Upwind differencing. Adiabatic walls. Uniform external temperature.	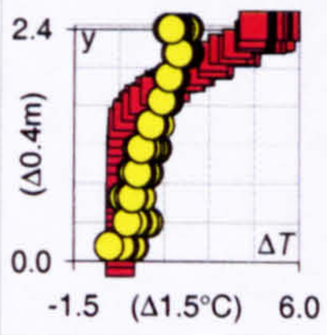	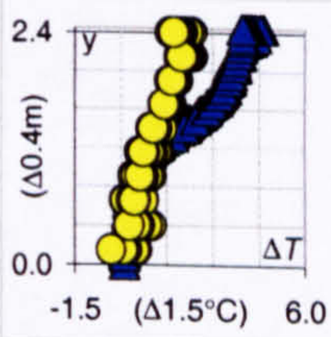	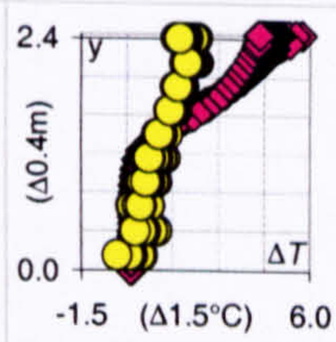	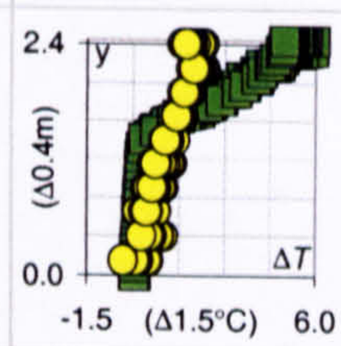
Radiation model disabled. QUICK differencing. Adiabatic walls. Uniform external temperature.	No available solution.	No available solution.	No available solution.	No available solution.
Radiation model enabled, $\alpha = 0.00m^{-1}$ QUICK differencing. Adiabatic walls. Uniform external temperature.	No available solution.	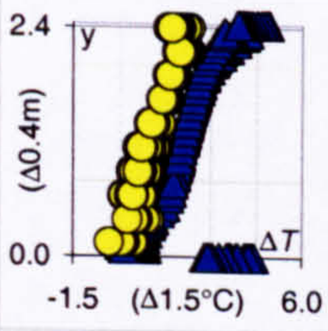	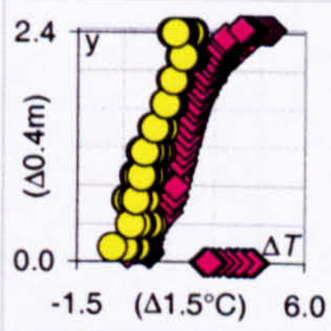	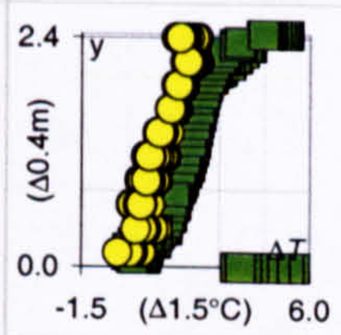
Radiation model enabled, $\alpha = 0.05m^{-1}$ QUICK differencing. Adiabatic walls. Uniform external temperature.	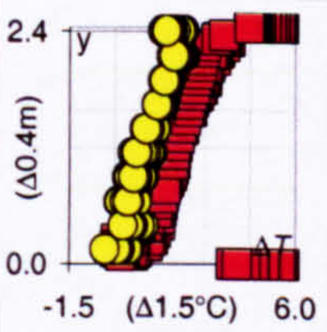	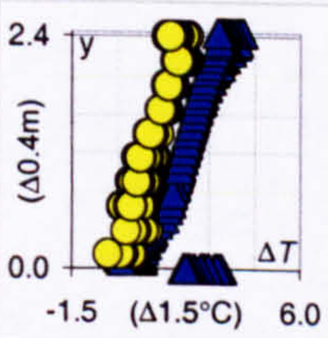	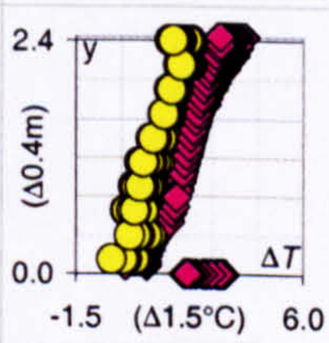	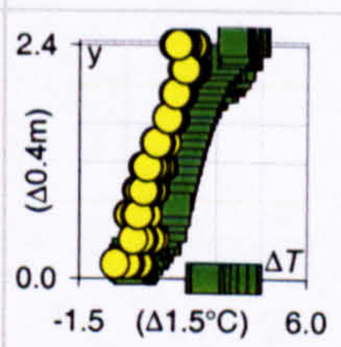
Radiation model enabled, $\alpha = 0.10m^{-1}$ QUICK differencing. Adiabatic walls. Uniform external temperature.	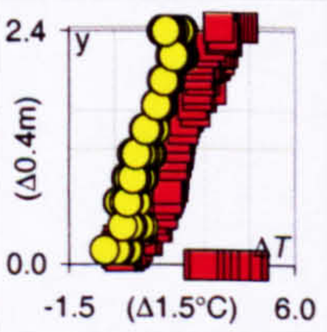	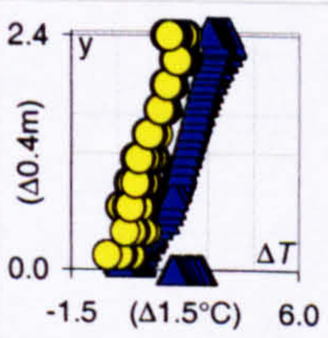	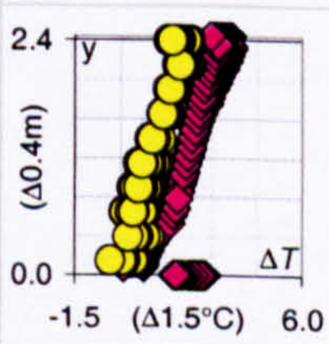	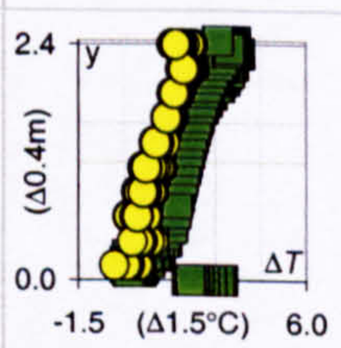
Radiation model enabled, $\alpha = 0.15m^{-1}$ QUICK differencing. Adiabatic walls. Uniform external temperature.	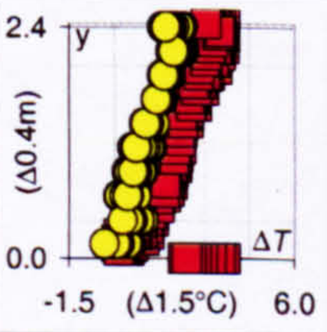	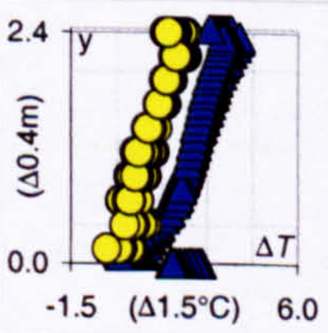	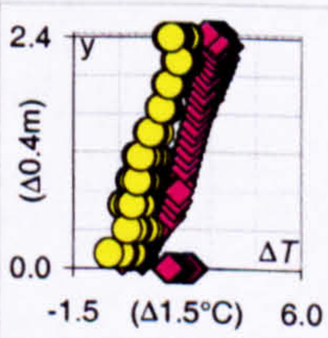	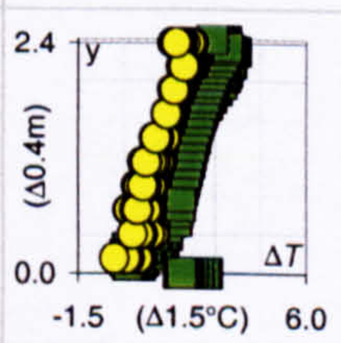

Width of opening:	0.8m
Effective area of opening:	$0.488m^2$
Heat source:	Boiler ring
Strength of heat source:	490.5W

Figure 25.a

	Laminar	Standard-$k\varepsilon$	Realizable-$k\varepsilon$	RNG-$k\varepsilon$
Radiation model enabled, $\alpha = 0.00m^{-1}$ QUICK differencing. Convection walls. Uniform external temperature.	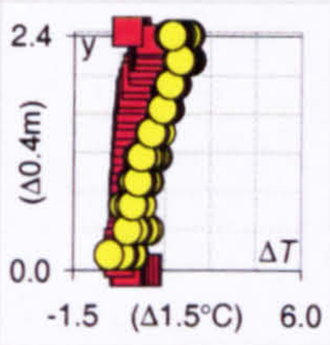	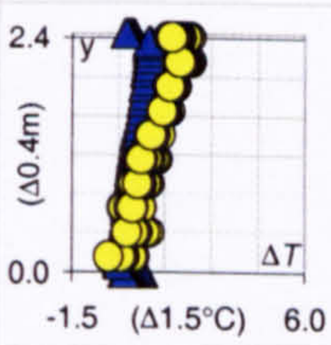	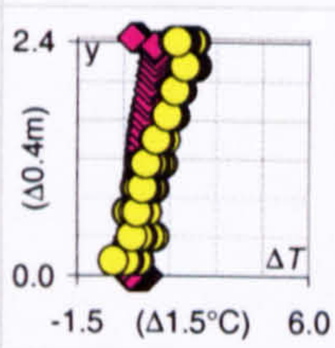	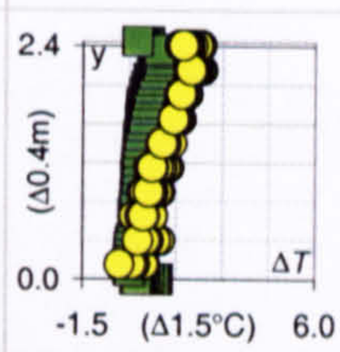
Radiation model enabled, $\alpha = 0.00m^{-1}$ QUICK differencing. Radiation walls. Uniform external temperature.	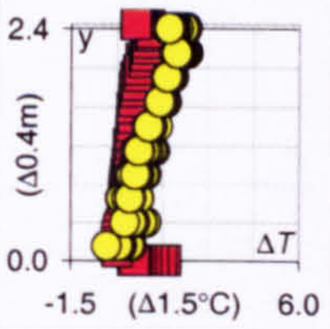	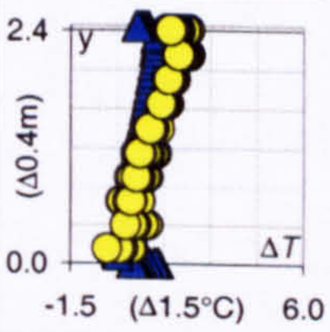	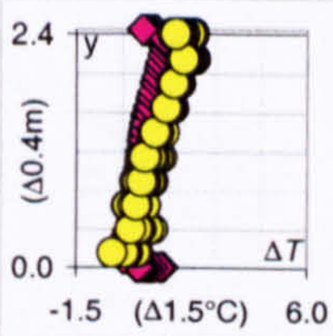	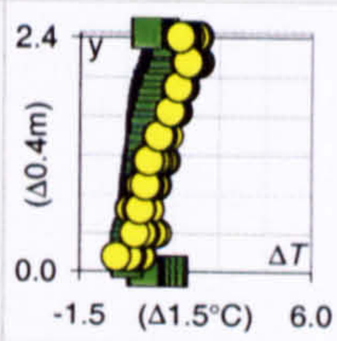
Radiation model enabled, $\alpha = 0.00m^{-1}$ QUICK differencing. Mixed walls. Uniform external temperature.	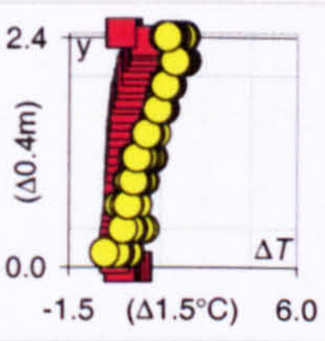	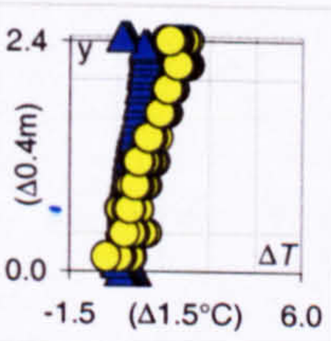	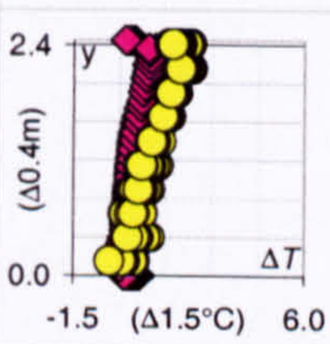	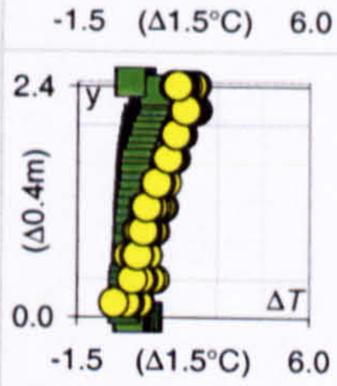
Radiation model enabled, $\alpha = 0.05m^{-1}$ QUICK differencing. Convection walls. Uniform external temperature.	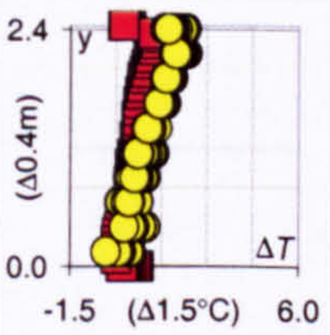	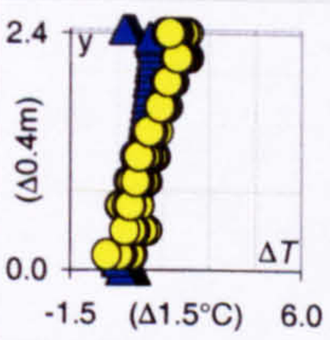	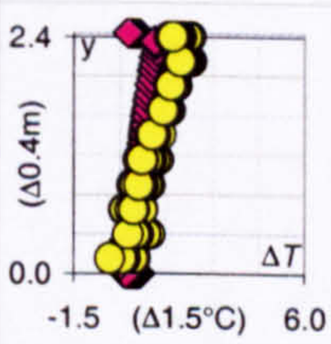	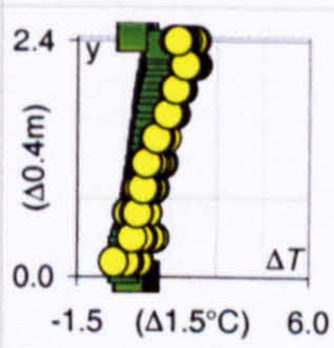
Radiation model enabled, $\alpha = 0.05m^{-1}$ QUICK differencing. Radiation walls. Uniform external temperature.	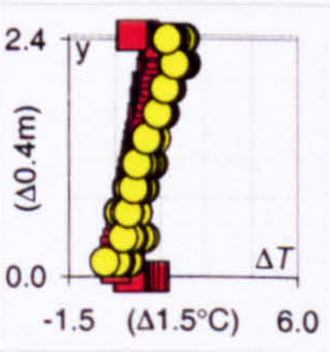	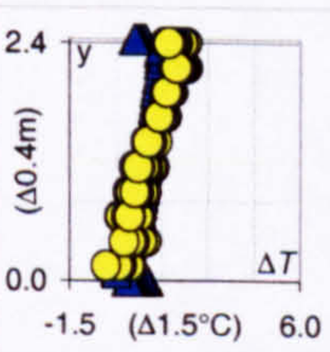	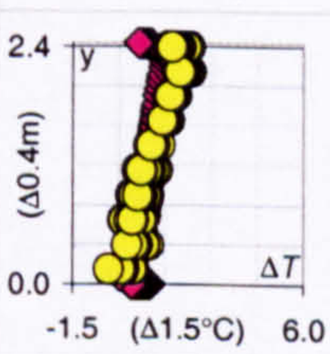	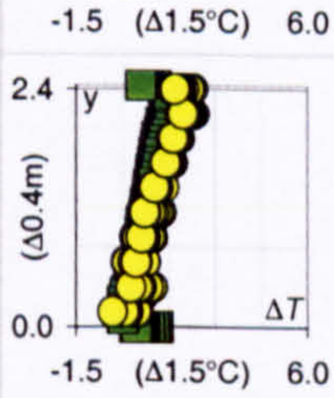
Radiation model enabled, $\alpha = 0.05m^{-1}$ QUICK differencing. Mixed walls. Uniform external temperature.	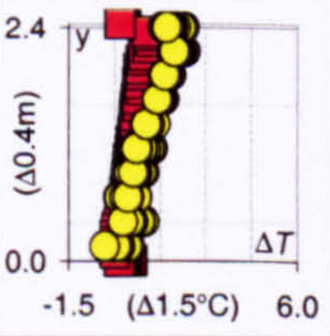	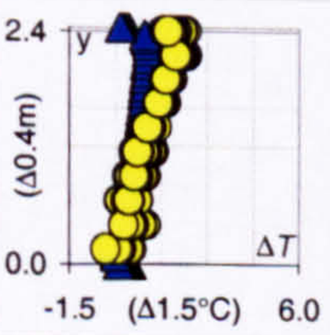	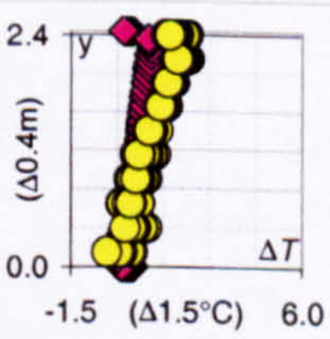	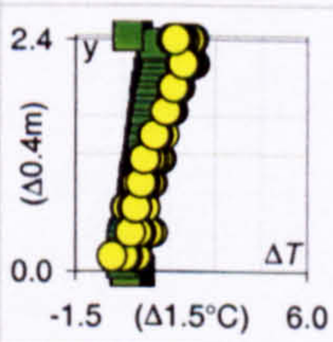

Width of opening:	0.8m
Effective area of opening:	0.488m^2
Heat source:	Boiler ring
Strength of heat source:	490.5W

Figure 25.b

	Laminar	Standard-$k\varepsilon$	Realizable-$k\varepsilon$	RNG-$k\varepsilon$
Radiation model disabled. Upwind differencing. Adiabatic walls. Uniform external temperature.	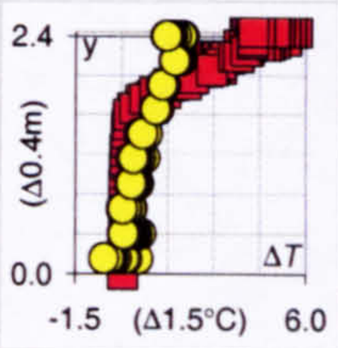	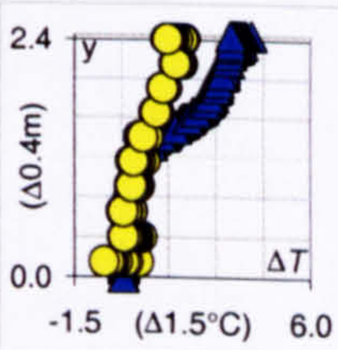	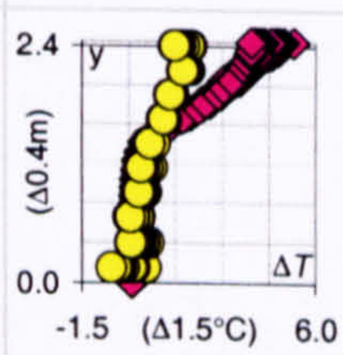	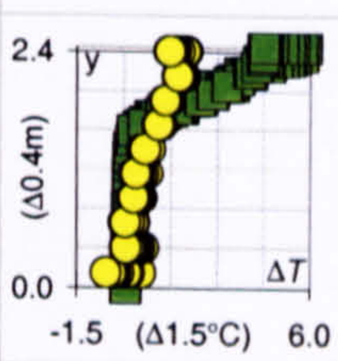
Radiation model disabled. QUICK differencing. Adiabatic walls. Uniform external temperature.	No available solution.	No available solution.	No available solution.	No available solution.
Radiation model enabled, $\alpha = 0.00m^{-1}$ QUICK differencing. Adiabatic walls. Uniform external temperature.	No available solution.	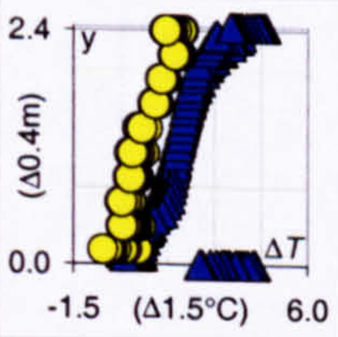	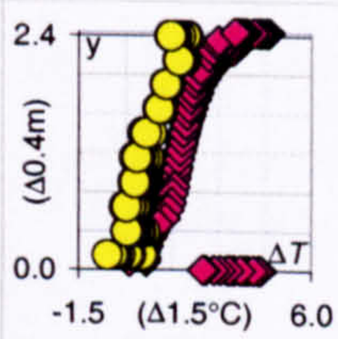	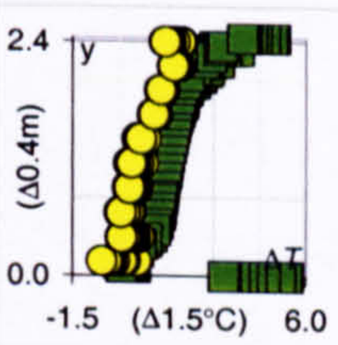
Radiation model enabled, $\alpha = 0.05m^{-1}$ QUICK differencing. Adiabatic walls. Uniform external temperature.	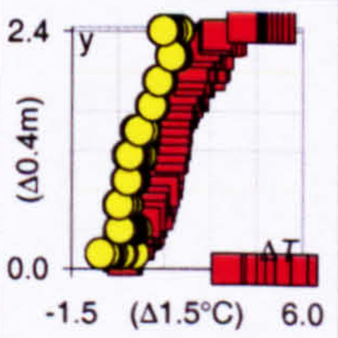	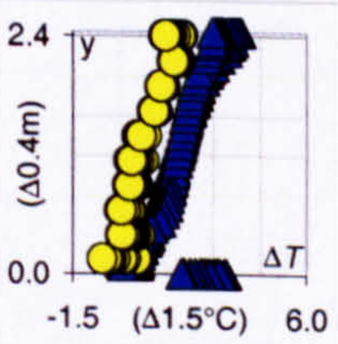	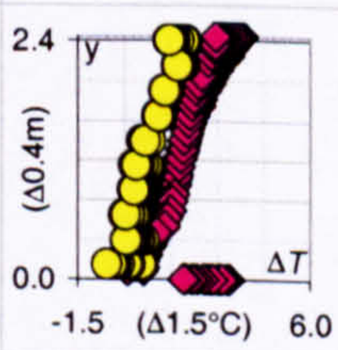	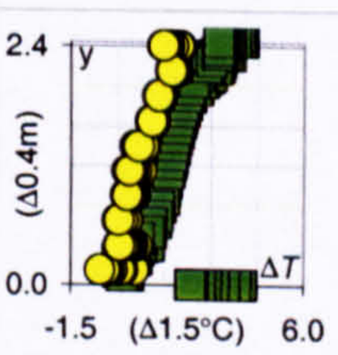
Radiation model enabled, $\alpha = 0.10m^{-1}$ QUICK differencing. Adiabatic walls. Uniform external temperature.	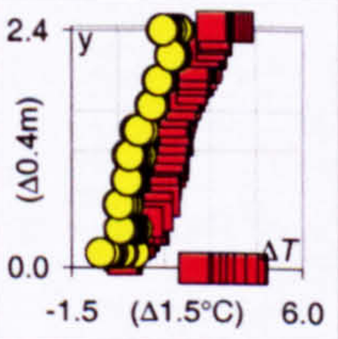	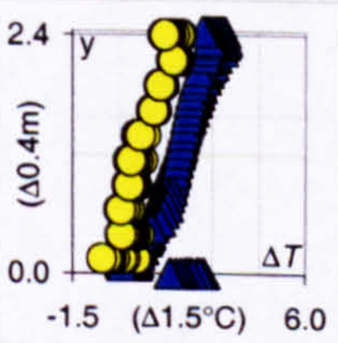	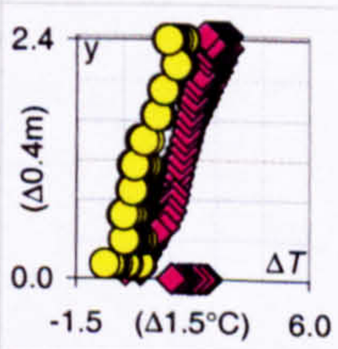	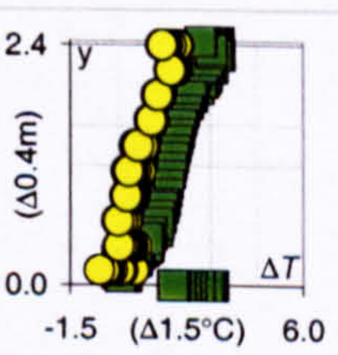
Radiation model enabled, $\alpha = 0.15m^{-1}$ QUICK differencing. Adiabatic walls. Uniform external temperature.	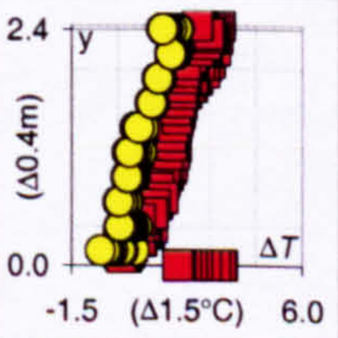	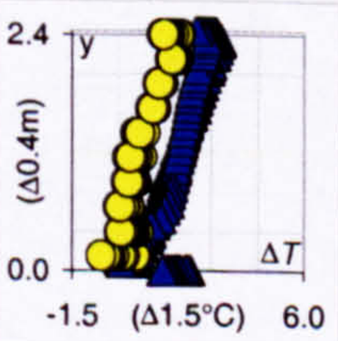	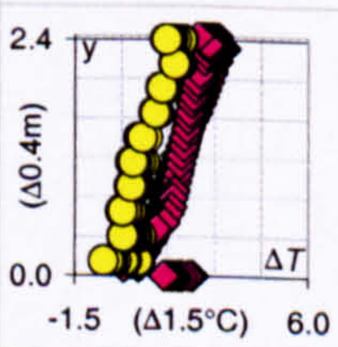	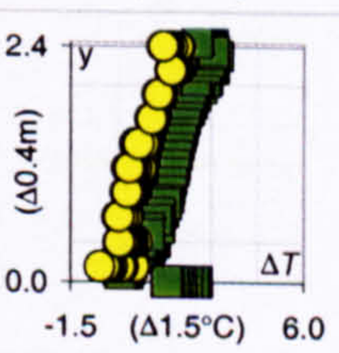

Width of opening:	1.0m
Effective area of opening:	$0.610m^2$
Heat source:	Boiler ring
Strength of heat source:	490.5W

Figure 26.a

	Laminar	Standard-$k\varepsilon$	Realizable-$k\varepsilon$	RNG-$k\varepsilon$
Radiation model enabled, $\alpha = 0.00m^{-1}$ QUICK differencing. Convection walls. Uniform external temperature.	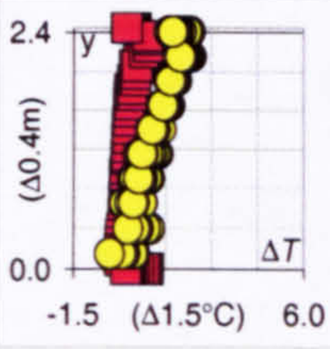	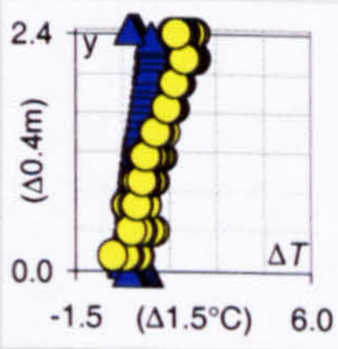	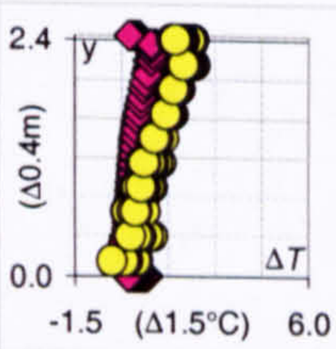	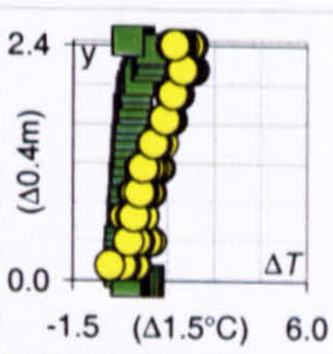
Radiation model enabled, $\alpha = 0.00m^{-1}$ QUICK differencing. Radiation walls. Uniform external temperature.	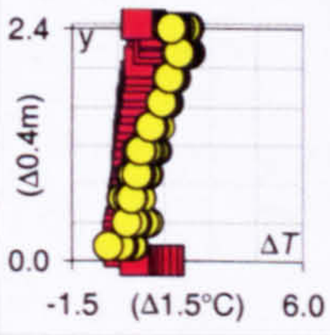	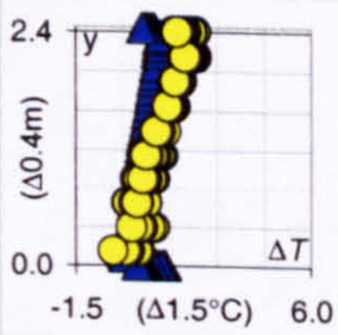	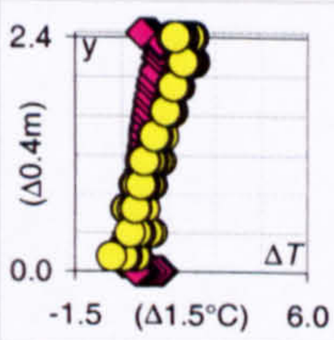	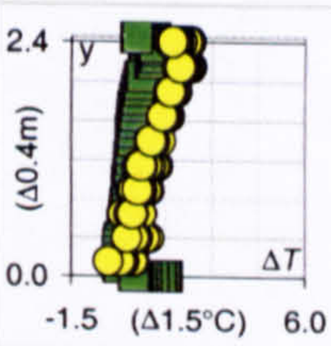
Radiation model enabled, $\alpha = 0.00m^{-1}$ QUICK differencing. Mixed walls. Uniform external temperature.	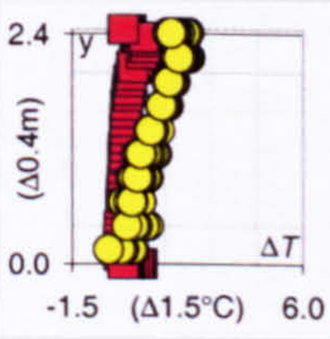	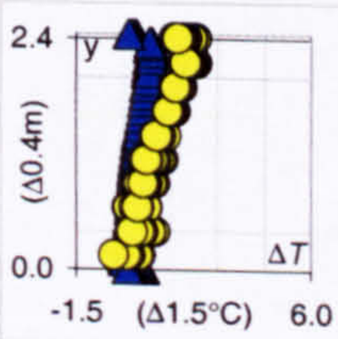	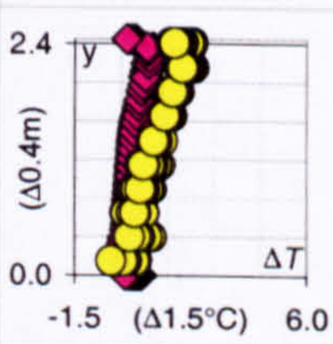	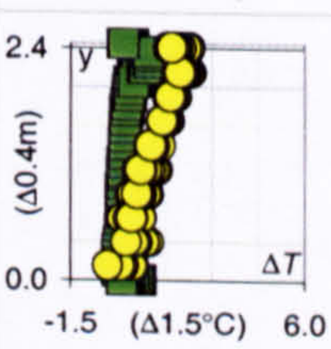
Radiation model enabled, $\alpha = 0.05m^{-1}$ QUICK differencing. Convection walls. Uniform external temperature.	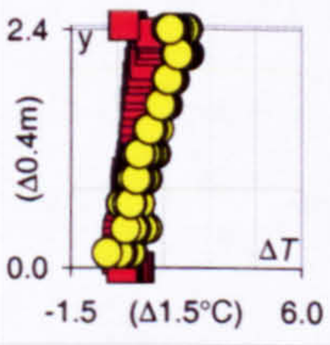	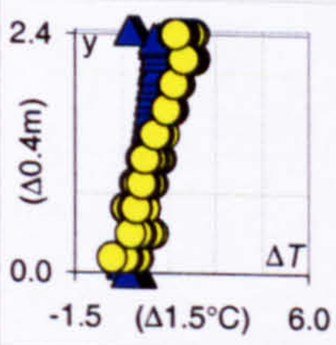	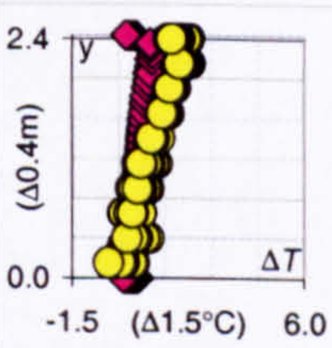	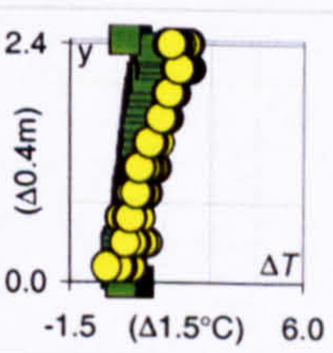
Radiation model enabled, $\alpha = 0.05m^{-1}$ QUICK differencing. Radiation walls. Uniform external temperature.	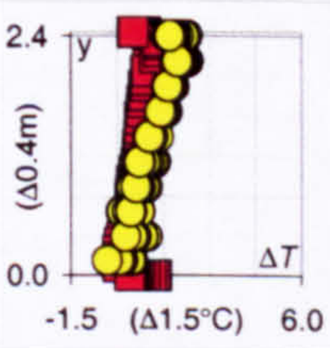	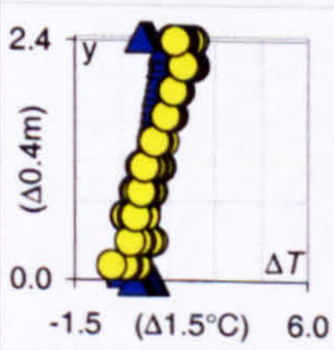	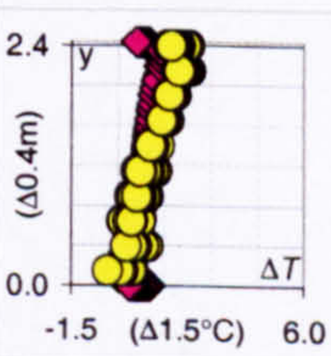	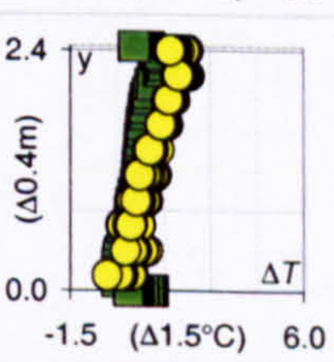
Radiation model enabled, $\alpha = 0.05m^{-1}$ QUICK differencing. Mixed walls. Uniform external temperature.	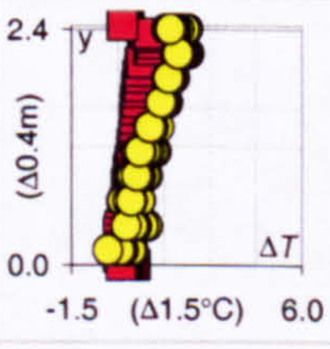	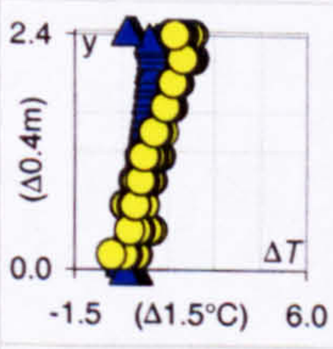	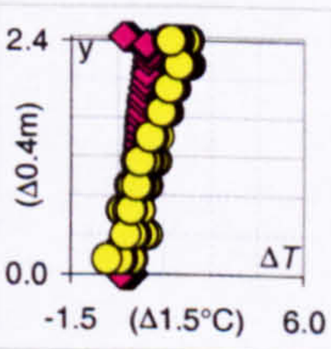	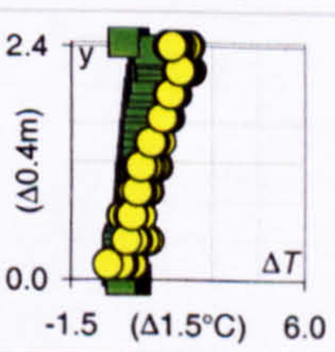

Width of opening:	1.0m
Effective area of opening:	$0.610m^2$
Heat source:	Boiler ring
Strength of heat source:	490.5W

Figure 26.b

	Laminar	Standard-$k\varepsilon$	Realizable-$k\varepsilon$	RNG-$k\varepsilon$
Radiation model disabled. Upwind differencing. Adiabatic walls. Uniform external temperature.	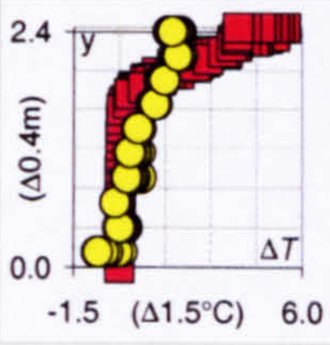	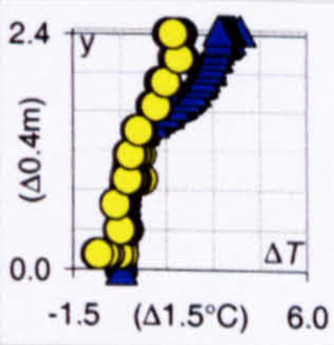	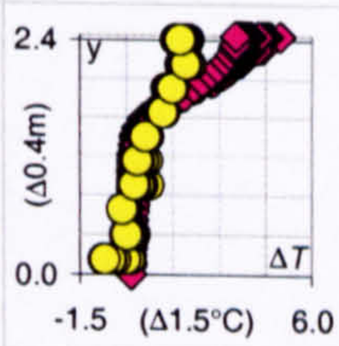	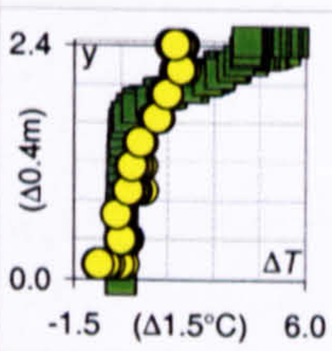
Radiation model disabled. QUICK differencing. Adiabatic walls. Uniform external temperature.	No available solution.	No available solution.	No available solution.	No available solution.
Radiation model enabled, $\alpha = 0.00m^{-1}$ QUICK differencing. Adiabatic walls. Uniform external temperature.	No available solution.	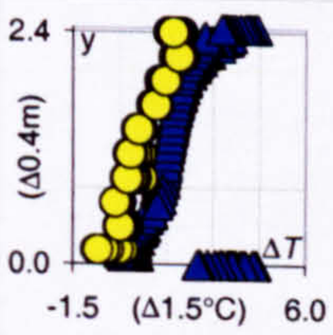	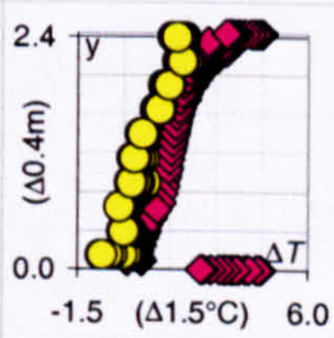	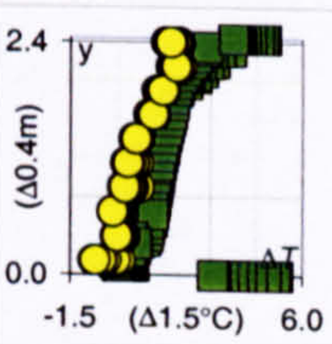
Radiation model enabled, $\alpha = 0.05m^{-1}$ QUICK differencing. Adiabatic walls. Uniform external temperature.	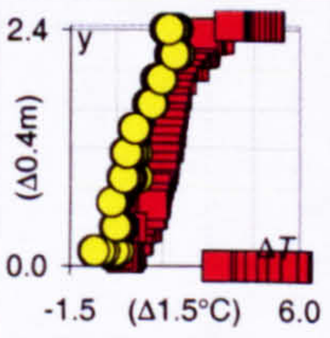	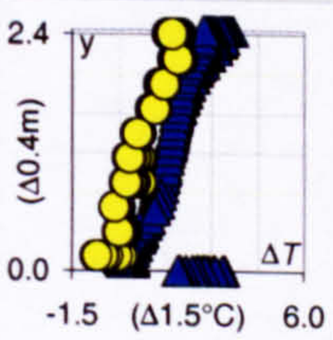	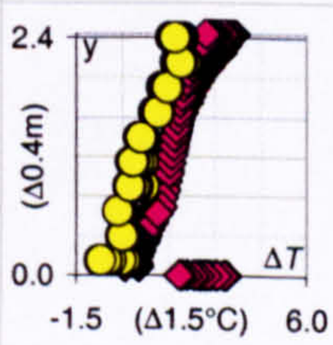	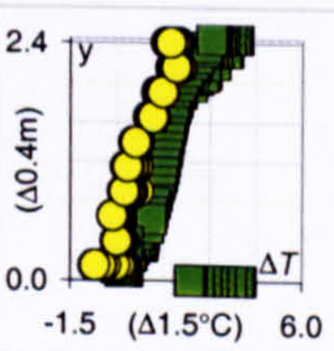
Radiation model enabled, $\alpha = 0.10m^{-1}$ QUICK differencing. Adiabatic walls. Uniform external temperature.	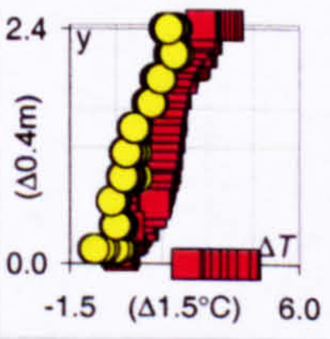	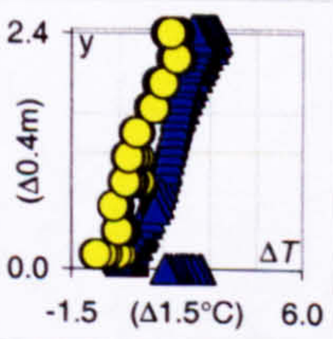	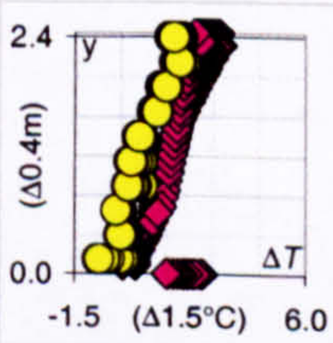	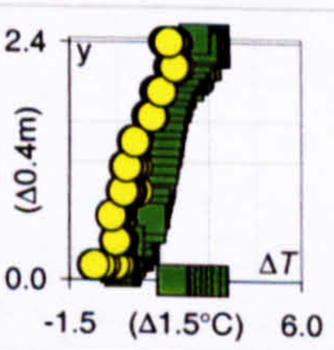
Radiation model enabled, $\alpha = 0.15m^{-1}$ QUICK differencing. Adiabatic walls. Uniform external temperature.	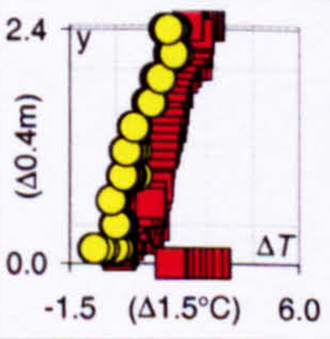	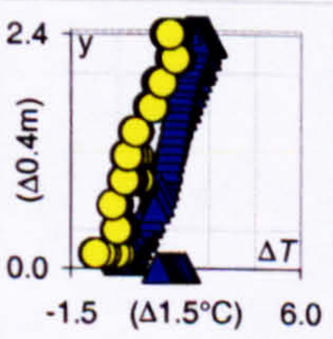	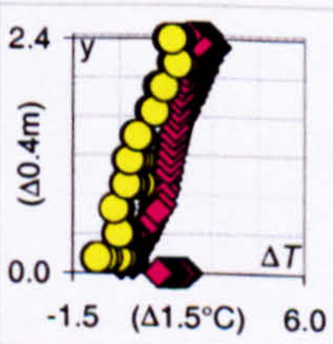	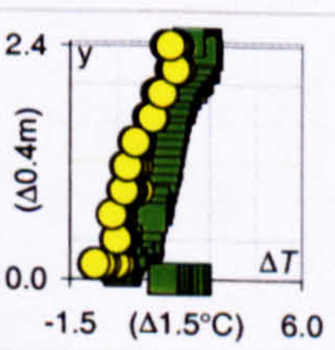

Width of opening:	1.2m
Effective area of opening:	0.732m^2
Heat source:	Boiler ring
Strength of heat source:	490.5W

Figure 27.a

	Laminar	Standard-$k\varepsilon$	Realizable-$k\varepsilon$	RNG-$k\varepsilon$
Radiation model enabled, $\alpha = 0.00m^{-1}$ QUICK differencing. Convection walls. Uniform external temperature.	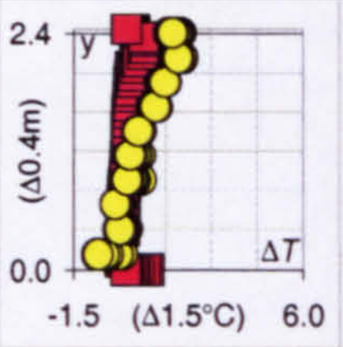	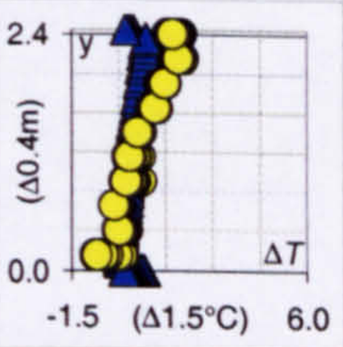	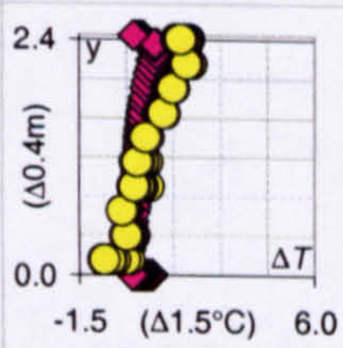	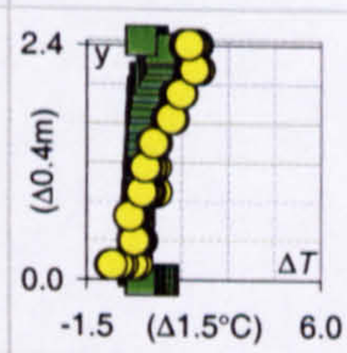
Radiation model enabled, $\alpha = 0.00m^{-1}$ QUICK differencing. Radiation walls. Uniform external temperature.	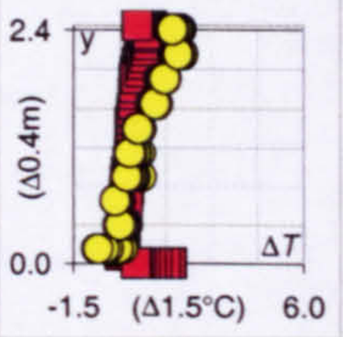	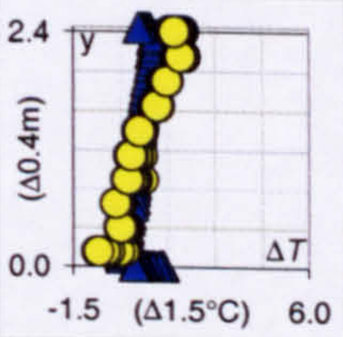	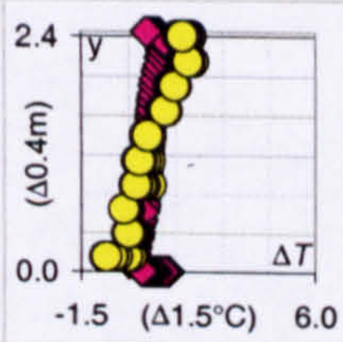	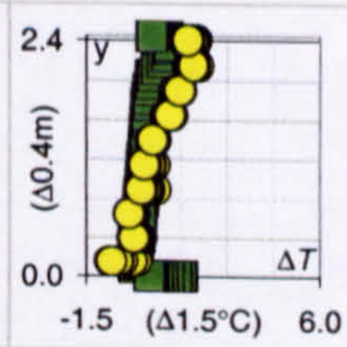
Radiation model enabled, $\alpha = 0.00m^{-1}$ QUICK differencing. Mixed walls. Uniform external temperature.	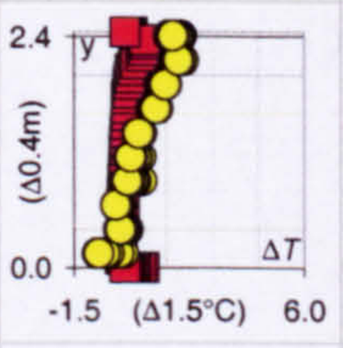	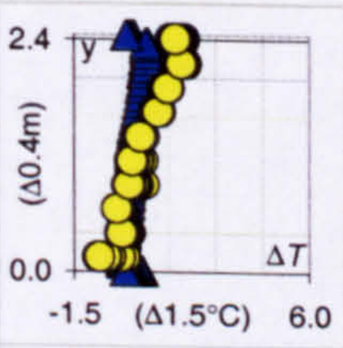	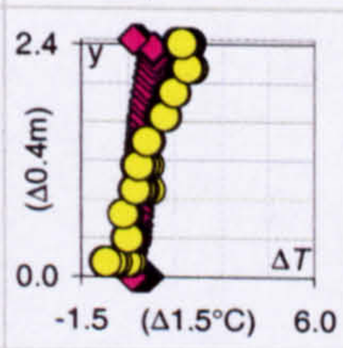	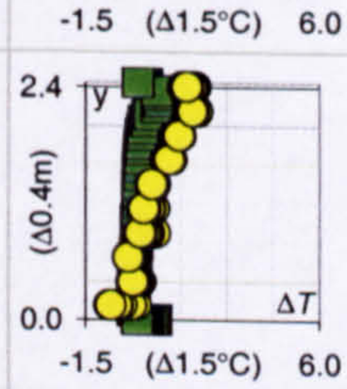
Radiation model enabled, $\alpha = 0.05m^{-1}$ QUICK differencing. Convection walls. Uniform external temperature.	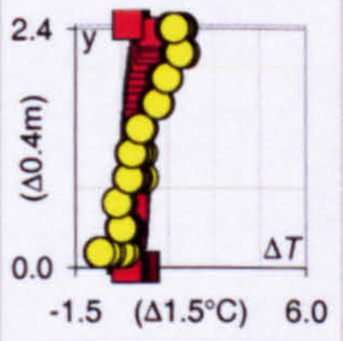	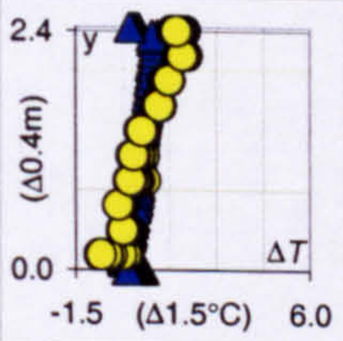	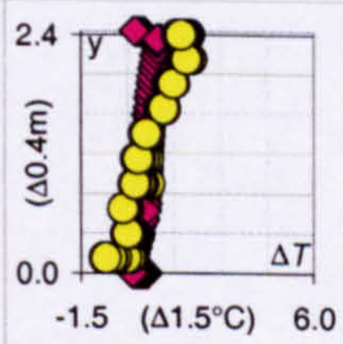	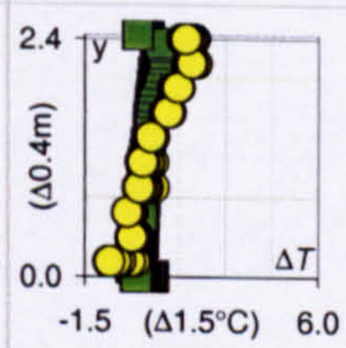
Radiation model enabled, $\alpha = 0.05m^{-1}$ QUICK differencing. Radiation walls. Uniform external temperature.	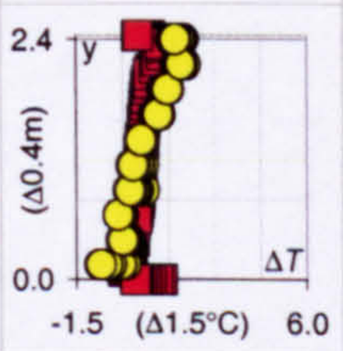	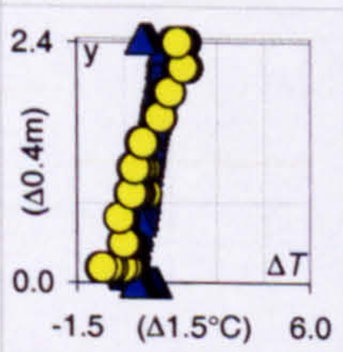	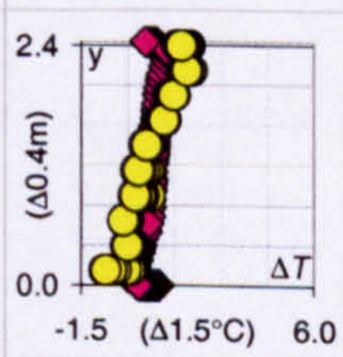	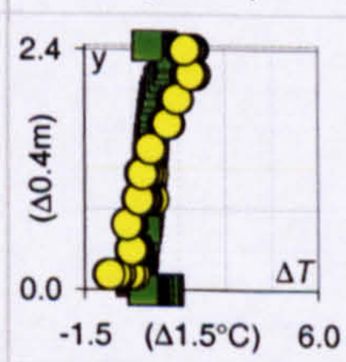
Radiation model enabled, $\alpha = 0.05m^{-1}$ QUICK differencing. Mixed walls. Uniform external temperature.	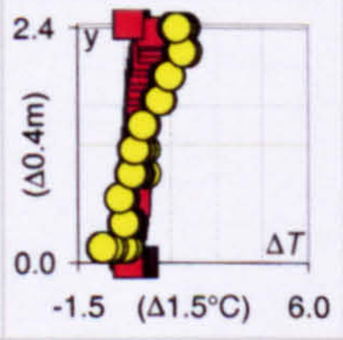	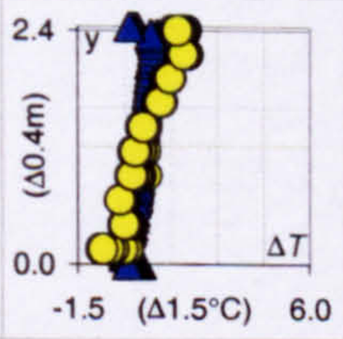	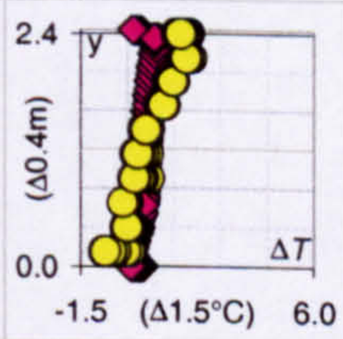	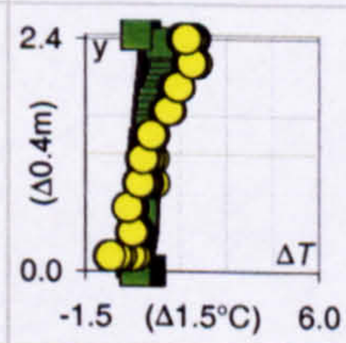

Width of opening:	1.2m
Effective area of opening:	0.732m^2
Heat source:	Boiler ring
Strength of heat source:	490.5W

Figure 27.b

A4 CFD-predictions for the inward component of velocity at the lower opening to the enclosure

Table of contents

Figure	Heat source	Strength of heat source	Width of opening	Effective area of openings A*
1	Plate heater	225.0W	0.1m	0.061m^2
2	Plate heater	225.0W	0.2m	0.122m^2
3	Plate heater	225.0W	0.3m	0.183m^2
4	Plate heater	225.0W	0.4m	0.244m^2
5	Plate heater	225.0W	0.5m	0.305m^2
6	Plate heater	225.0W	0.6m	0.366m^2
7	Plate heater	225.0W	0.8m	0.488m^2
8	Plate heater	225.0W	1.0m	0.610m^2
9	Plate heater	225.0W	1.2m	0.732m^2
10	Boiler ring	368.0W	0.1m	0.061m^2
11	Boiler ring	368.0W	0.2m	0.122m^2
12	Boiler ring	368.0W	0.3m	0.183m^2
13	Boiler ring	368.0W	0.4m	0.244m^2
14	Boiler ring	368.0W	0.5m	0.305m^2
15	Boiler ring	368.0W	0.6m	0.366m^2
16	Boiler ring	368.0W	0.8m	0.488m^2
17	Boiler ring	368.0W	1.0m	0.610m^2
18	Boiler ring	368.0W	1.2m	0.732m^2
19	Boiler ring	490.5W	0.1m	0.061m^2
20	Boiler ring	490.5W	0.2m	0.122m^2
21	Boiler ring	490.5W	0.3m	0.183m^2
22	Boiler ring	490.5W	0.4m	0.244m^2
23	Boiler ring	490.5W	0.5m	0.305m^2
24	Boiler ring	490.5W	0.6m	0.366m^2
25	Boiler ring	490.5W	0.8m	0.488m^2
26	Boiler ring	490.5W	1.0m	0.610m^2
27	Boiler ring	490.5W	1.2m	0.732m^2

	Area	Laminar	Standard-$k\varepsilon$	Realizable-$k\varepsilon$	RNG-$k\varepsilon$
Radiation model disabled. Upwind differencing. Adiabatic walls. Uniform external temperature.	all	0.427 m/s	0.462 m/s	0.438 m/s	0.453 m/s
	centre	0.532 m/s	0.503 m/s	0.448 m/s	0.560 m/s
Radiation model disabled. QUICK differencing. Adiabatic walls. Uniform external temperature.	all	0.443 m/s	0.456 m/s	0.455 m/s	0.427 m/s
	centre	0.565 m/s	0.488 m/s	0.471 m/s	0.534 m/s
Radiation model enabled, $\alpha = 0.00m^{-1}$ QUICK differencing. Adiabatic walls. Uniform external temperature.	all	0.479 m/s	0.507 m/s	0.531 m/s	0.494 m/s
	centre	0.612 m/s	0.540 m/s	0.562 m/s	0.632 m/s
Radiation model enabled, $\alpha = 0.05m^{-1}$ QUICK differencing. Adiabatic walls. Uniform external temperature.	all	0.481 m/s	0.506 m/s	0.518 m/s	0.487 m/s
	centre	0.602 m/s	0.538 m/s	0.547 m/s	0.622 m/s
Radiation model enabled, $\alpha = 0.10m^{-1}$ QUICK differencing. Adiabatic walls. Uniform external temperature.	all	0.480 m/s	0.504 m/s	0.516 m/s	0.484 m/s
	centre	0.596 m/s	0.537 m/s	0.545 m/s	0.601 m/s
Radiation model enabled, $\alpha = 0.15m^{-1}$ QUICK differencing. Adiabatic walls. Uniform external temperature.	all	0.500 m/s	0.503 m/s	0.515 m/s	0.491 m/s
	centre	0.641 m/s	0.536 m/s	0.543 m/s	0.615 m/s

Width of opening:	0.1m
Effective area of opening:	$0.061m^2$
Heat source:	Plate heater
Strength of heat source:	225.0W

Figure 1.a

	Area	Laminar	Standard-$k\varepsilon$	Realizable-$k\varepsilon$	RNG-$k\varepsilon$
Radiation model enabled, $\alpha = 0.00m^{-1}$ QUICK differencing. Convection walls. Uniform external temperature.	all	0.156 m/s	0.159 m/s	0.179 m/s	0.150 m/s
	centre	0.200 m/s	0.170 m/s	0.195 m/s	0.192 m/s
Radiation model enabled, $\alpha = 0.00m^{-1}$ QUICK differencing. Radiation walls. Uniform external temperature.	all	0.187 m/s	0.194 m/s	0.217 m/s	0.184 m/s
	centre	0.239 m/s	0.207 m/s	0.234 m/s	0.237 m/s
Radiation model enabled, $\alpha = 0.00m^{-1}$ QUICK differencing. Mixed walls. Uniform external temperature.	all	0.150 m/s	0.151 m/s	0.168 m/s	0.140 m/s
	centre	0.191 m/s	0.161 m/s	0.183 m/s	0.179 m/s
Radiation model enabled, $\alpha = 0.05m^{-1}$ QUICK differencing. Convection walls. Uniform external temperature.	all	0.189 m/s	0.176 m/s	0.188 m/s	0.172 m/s
	centre	0.244 m/s	0.188 m/s	0.204 m/s	0.220 m/s
Radiation model enabled, $\alpha = 0.05m^{-1}$ QUICK differencing. Radiation walls. Uniform external temperature.	all	0.219 m/s	0.208 m/s	0.213 m/s	0.206 m/s
	centre	0.283 m/s	0.222 m/s	0.227 m/s	0.263 m/s
Radiation model enabled, $\alpha = 0.05m^{-1}$ QUICK differencing. Mixed walls. Uniform external temperature.	all	0.181 m/s	0.168 m/s	0.177 m/s	0.166 m/s
	centre	0.234 m/s	0.179 m/s	0.193 m/s	0.211 m/s

Width of opening:	0.1m
Effective area of opening:	$0.061m^2$
Heat source:	Plate heater
Strength of heat source:	225.0W

Figure 1.b

	Area	Laminar	Standard-$k\varepsilon$	Realizable-$k\varepsilon$	RNG-$k\varepsilon$
Radiation model disabled. Upwind differencing. Adiabatic walls. Uniform external temperature.	all	0.327 m/s	0.349 m/s	0.371 m/s	0.333 m/s
	centre	0.413 m/s	0.413 m/s	0.406 m/s	0.417 m/s
Radiation model disabled. QUICK differencing. Adiabatic walls. Uniform external temperature.	all	0.323 m/s	0.345 m/s	0.370 m/s	0.322 m/s
	centre	0.447 m/s	0.407 m/s	0.413 m/s	0.427 m/s
Radiation model enabled, $\alpha = 0.00m^{-1}$ QUICK differencing. Adiabatic walls. Uniform external temperature.	all	0.364 m/s	0.386 m/s	0.402 m/s	0.380 m/s
	centre	0.492 m/s	0.451 m/s	0.460 m/s	0.494 m/s
Radiation model enabled, $\alpha = 0.05m^{-1}$ QUICK differencing. Adiabatic walls. Uniform external temperature.	all	0.373 m/s	0.394 m/s	0.391 m/s	0.385 m/s
	centre	0.505 m/s	0.461 m/s	0.446 m/s	0.499 m/s
Radiation model enabled, $\alpha = 0.10m^{-1}$ QUICK differencing. Adiabatic walls. Uniform external temperature.	all	0.378 m/s	0.394 m/s	0.393 m/s	0.388 m/s
	centre	0.513 m/s	0.461 m/s	0.449 m/s	0.503 m/s
Radiation model enabled, $\alpha = 0.15m^{-1}$ QUICK differencing. Adiabatic walls. Uniform external temperature.	all	0.377 m/s	0.394 m/s	0.394 m/s	0.391 m/s
	centre	0.510 m/s	0.461 m/s	0.451 m/s	0.506 m/s

Width of opening:	0.2m
Effective area of opening:	$0.122m^2$
Heat source:	Plate heater
Strength of heat source:	225.0W

Figure 2.a

	Area	Laminar	Standard-$k\varepsilon$	Realizable-$k\varepsilon$	RNG-$k\varepsilon$
Radiation model enabled, $\alpha = 0.00m^{-1}$ QUICK differencing. Convection walls. Uniform external temperature.	all	0.142 m/s	0.149 m/s	0.147 m/s	0.140 m/s
	centre	0.186 m/s	0.171 m/s	0.165 m/s	0.190 m/s
Radiation model enabled, $\alpha = 0.00m^{-1}$ QUICK differencing. Radiation walls. Uniform external temperature.	all	0.167 m/s	0.179 m/s	0.179 m/s	0.167 m/s
	centre	0.227 m/s	0.207 m/s	0.200 m/s	0.223 m/s
Radiation model enabled, $\alpha = 0.00m^{-1}$ QUICK differencing. Mixed walls. Uniform external temperature.	all	0.133 m/s	0.141 m/s	0.137 m/s	0.132 m/s
	centre	0.176 m/s	0.161 m/s	0.153 m/s	0.178 m/s
Radiation model enabled, $\alpha = 0.05m^{-1}$ QUICK differencing. Convection walls. Uniform external temperature.	all	0.174 m/s	0.168 m/s	0.166 m/s	0.165 m/s
	centre	0.230 m/s	0.193 m/s	0.186 m/s	0.219 m/s
Radiation model enabled, $\alpha = 0.05m^{-1}$ QUICK differencing. Radiation walls. Uniform external temperature.	all	0.198 m/s	0.196 m/s	0.196 m/s	0.190 m/s
	centre	0.262 m/s	0.226 m/s	0.221 m/s	0.255 m/s
Radiation model enabled, $\alpha = 0.05m^{-1}$ QUICK differencing. Mixed walls. Uniform external temperature.	all	0.165 m/s	0.160 m/s	0.157 m/s	0.158 m/s
	centre	0.220 m/s	0.184 m/s	0.176 m/s	0.216 m/s

Width of opening:	0.2m
Effective area of opening:	$0.122m^2$
Heat source:	Plate heater
Strength of heat source:	225.0W

Figure 2.b

	Area	Laminar	Standard-$k\varepsilon$	Realizable-$k\varepsilon$	RNG-$k\varepsilon$
Radiation model disabled. Upwind differencing. Adiabatic walls. Uniform external temperature.	all	0.273 m/s	0.289 m/s	0.312 m/s	0.273 m/s
	centre	0.355 m/s	0.358 m/s	0.371 m/s	0.354 m/s
Radiation model disabled. QUICK differencing. Adiabatic walls. Uniform external temperature.	all	0.269 m/s	0.286 m/s	0.295 m/s	0.283 m/s
	centre	0.390 m/s	0.352 m/s	0.357 m/s	0.396 m/s
Radiation model enabled, $\alpha = 0.00m^{-1}$ QUICK differencing. Adiabatic walls. Uniform external temperature.	all	0.310 m/s	0.321 m/s	0.337 m/s	0.319 m/s
	centre	0.453 m/s	0.396 m/s	0.411 m/s	0.440 m/s
Radiation model enabled, $\alpha = 0.05m^{-1}$ QUICK differencing. Adiabatic walls. Uniform external temperature.	all	0.312 m/s	0.324 m/s	0.331 m/s	0.321 m/s
	centre	0.454 m/s	0.400 m/s	0.404 m/s	0.453 m/s
Radiation model enabled, $\alpha = 0.10m^{-1}$ QUICK differencing. Adiabatic walls. Uniform external temperature.	all	0.318 m/s	0.326 m/s	0.333 m/s	0.326 m/s
	centre	0.472 m/s	0.403 m/s	0.405 m/s	0.455 m/s
Radiation model enabled, $\alpha = 0.15m^{-1}$ QUICK differencing. Adiabatic walls. Uniform external temperature.	all	0.324 m/s	0.327 m/s	0.333 m/s	0.329 m/s
	centre	0.483 m/s	0.405 m/s	0.405 m/s	0.458 m/s

Width of opening:	0.3m
Effective area of opening:	$0.183m^2$
Heat source:	Plate heater
Strength of heat source:	225.0W

Figure 3.a

	Area	Laminar	Standard-$k\varepsilon$	Realizable-$k\varepsilon$	RNG-$k\varepsilon$
Radiation model enabled, $\alpha = 0.00m^{-1}$ QUICK differencing. Convection walls. Uniform external temperature.	all	0.126 m/s	0.137 m/s	0.135 m/s	0.123 m/s
	centre	0.182 m/s	0.169 m/s	0.162 m/s	0.175 m/s
Radiation model enabled, $\alpha = 0.00m^{-1}$ QUICK differencing. Radiation walls. Uniform external temperature.	all	0.148 m/s	0.163 m/s	0.166 m/s	0.148 m/s
	centre	0.218 m/s	0.202 m/s	0.200 m/s	0.221 m/s
Radiation model enabled, $\alpha = 0.00m^{-1}$ QUICK differencing. Mixed walls. Uniform external temperature.	all	0.118 m/s	0.130 m/s	0.127 m/s	0.116 m/s
	centre	0.174 m/s	0.160 m/s	0.153 m/s	0.167 m/s
Radiation model enabled, $\alpha = 0.05m^{-1}$ QUICK differencing. Convection walls. Uniform external temperature.	all	0.160 m/s	0.157 m/s	0.156 m/s	0.154 m/s
	centre	0.226 m/s	0.193 m/s	0.188 m/s	0.222 m/s
Radiation model enabled, $\alpha = 0.05m^{-1}$ QUICK differencing. Radiation walls. Uniform external temperature.	all	0.179 m/s	0.181 m/s	0.182 m/s	0.176 m/s
	centre	0.258 m/s	0.224 m/s	0.218 m/s	0.253 m/s
Radiation model enabled, $\alpha = 0.05m^{-1}$ QUICK differencing. Mixed walls. Uniform external temperature.	all	0.154 m/s	0.150 m/s	0.149 m/s	0.147 m/s
	centre	0.217 m/s	0.185 m/s	0.179 m/s	0.213 m/s

Width of opening:	0.3m
Effective area of opening:	$0.183m^2$
Heat source:	Plate heater
Strength of heat source:	225.0W

Figure 3.b

	Area	Laminar	Standard-$k\varepsilon$	Realizable-$k\varepsilon$	RNG-$k\varepsilon$
Radiation model disabled. Upwind differencing. Adiabatic walls. Uniform external temperature.	all	0.240 m/s	0.253 m/s	0.258 m/s	0.240 m/s
	centre	0.327 m/s	0.319 m/s	0.325 m/s	0.325 m/s
Radiation model disabled. QUICK differencing. Adiabatic walls. Uniform external temperature.	all	0.237 m/s	0.248 m/s	0.249 m/s	0.239 m/s
	centre	0.358 m/s	0.313 m/s	0.319 m/s	0.366 m/s
Radiation model enabled, $\alpha = 0.00m^{-1}$ QUICK differencing. Adiabatic walls. Uniform external temperature.	all	0.271 m/s	0.285 m/s	0.290 m/s	0.270 m/s
	centre	0.412 m/s	0.358 m/s	0.380 m/s	0.411 m/s
Radiation model enabled, $\alpha = 0.05m^{-1}$ QUICK differencing. Adiabatic walls. Uniform external temperature.	all	0.277 m/s	0.287 m/s	0.295 m/s	0.276 m/s
	centre	0.427 m/s	0.361 m/s	0.385 m/s	0.424 m/s
Radiation model enabled, $\alpha = 0.10m^{-1}$ QUICK differencing. Adiabatic walls. Uniform external temperature.	all	0.278 m/s	0.294 m/s	0.296 m/s	0.280 m/s
	centre	0.428 m/s	0.370 m/s	0.386 m/s	0.422 m/s
Radiation model enabled, $\alpha = 0.15m^{-1}$ QUICK differencing. Adiabatic walls. Uniform external temperature.	all	0.285 m/s	0.292 m/s	0.298 m/s	0.284 m/s
	centre	0.429 m/s	0.368 m/s	0.387 m/s	0.424 m/s

Width of opening:	0.4m
Effective area of opening:	$0.244m^2$
Heat source:	Plate heater
Strength of heat source:	225.0W

Figure 4.a

	Area	Laminar	Standard-$k\varepsilon$	Realizable-$k\varepsilon$	RNG-$k\varepsilon$
Radiation model enabled, $\alpha = 0.00m^{-1}$ QUICK differencing. Convection walls. Uniform external temperature.	all	0.111 m/s	0.128 m/s	0.126 m/s	0.110 m/s
	centre	0.167 m/s	0.162 m/s	0.159 m/s	0.169 m/s
Radiation model enabled, $\alpha = 0.00m^{-1}$ QUICK differencing. Radiation walls. Uniform external temperature.	all	0.132 m/s	0.152 m/s	0.155 m/s	0.132 m/s
	centre	0.197 m/s	0.192 m/s	0.209 m/s	0.208 m/s
Radiation model enabled, $\alpha = 0.00m^{-1}$ QUICK differencing. Mixed walls. Uniform external temperature.	all	0.106 m/s	0.121 m/s	0.119 m/s	0.105 m/s
	centre	0.154 m/s	0.153 m/s	0.151 m/s	0.151 m/s
Radiation model enabled, $\alpha = 0.05m^{-1}$ QUICK differencing. Convection walls. Uniform external temperature.	all	0.140 m/s	0.150 m/s	0.149 m/s	0.141 m/s
	centre	0.219 m/s	0.189 m/s	0.188 m/s	0.215 m/s
Radiation model enabled, $\alpha = 0.05m^{-1}$ QUICK differencing. Radiation walls. Uniform external temperature.	all	0.163 m/s	0.171 m/s	0.171 m/s	0.160 m/s
	centre	0.245 m/s	0.216 m/s	0.222 m/s	0.243 m/s
Radiation model enabled, $\alpha = 0.05m^{-1}$ QUICK differencing. Mixed walls. Uniform external temperature.	all	0.139 m/s	0.144 m/s	0.141 m/s	0.134 m/s
	centre	0.210 m/s	0.182 m/s	0.187 m/s	0.208 m/s

Width of opening:	0.4m
Effective area of opening:	$0.244m^2$
Heat source:	Plate heater
Strength of heat source:	225.0W

Figure 4.b

	Area	Laminar	Standard-$k\varepsilon$	Realizable-$k\varepsilon$	RNG-$k\varepsilon$
Radiation model disabled. Upwind differencing. Adiabatic walls. Uniform external temperature.	all	0.211 m/s	0.226 m/s	0.231 m/s	0.212 m/s
	centre	0.300 m/s	0.285 m/s	0.302 m/s	0.298 m/s
Radiation model disabled. QUICK differencing. Adiabatic walls. Uniform external temperature.	all	0.203 m/s	0.222 m/s	0.219 m/s	0.213 m/s
	centre	0.317 m/s	0.283 m/s	0.288 m/s	0.319 m/s
Radiation model enabled, $\alpha = 0.00m^{-1}$ QUICK differencing. Adiabatic walls. Uniform external temperature.	all	0.248 m/s	0.258 m/s	0.263 m/s	0.246 m/s
	centre	0.371 m/s	0.329 m/s	0.348 m/s	0.374 m/s
Radiation model enabled, $\alpha = 0.05m^{-1}$ QUICK differencing. Adiabatic walls. Uniform external temperature.	all	0.258 m/s	0.266 m/s	0.270 m/s	0.252 m/s
	centre	0.361 m/s	0.338 m/s	0.356 m/s	0.381 m/s
Radiation model enabled, $\alpha = 0.10m^{-1}$ QUICK differencing. Adiabatic walls. Uniform external temperature.	all	0.256 m/s	0.270 m/s	0.274 m/s	0.252 m/s
	centre	0.362 m/s	0.342 m/s	0.360 m/s	0.384 m/s
Radiation model enabled, $\alpha = 0.15m^{-1}$ QUICK differencing. Adiabatic walls. Uniform external temperature.	all	0.254 m/s	0.272 m/s	0.277 m/s	0.255 m/s
	centre	0.383 m/s	0.345 m/s	0.362 m/s	0.388 m/s

Width of opening:	0.5m
Effective area of opening:	$0.305m^2$
Heat source:	Plate heater
Strength of heat source:	225.0W

Figure 5.a

	Area	Laminar	Standard-$k\varepsilon$	Realizable-$k\varepsilon$	RNG-$k\varepsilon$
Radiation model enabled, $\alpha = 0.00m^{-1}$ QUICK differencing. Convection walls. Uniform external temperature.	all	0.103 m/s	0.120 m/s	0.119 m/s	0.100 m/s
	centre	0.155 m/s	0.153 m/s	0.158 m/s	0.155 m/s
Radiation model enabled, $\alpha = 0.00m^{-1}$ QUICK differencing. Radiation walls. Uniform external temperature.	all	0.123 m/s	0.143 m/s	0.143 m/s	0.122 m/s
	centre	0.181 m/s	0.181 m/s	0.202 m/s	0.183 m/s
Radiation model enabled, $\alpha = 0.00m^{-1}$ QUICK differencing. Mixed walls. Uniform external temperature.	all	0.096 m/s	0.114 m/s	0.111 m/s	0.095 m/s
	centre	0.144 m/s	0.145 m/s	0.157 m/s	0.142 m/s
Radiation model enabled, $\alpha = 0.05m^{-1}$ QUICK differencing. Convection walls. Uniform external temperature.	all	0.133 m/s	0.142 m/s	0.138 m/s	0.132 m/s
	centre	0.206 m/s	0.181 m/s	0.191 m/s	0.197 m/s
Radiation model enabled, $\alpha = 0.05m^{-1}$ QUICK differencing. Radiation walls. Uniform external temperature.	all	0.148 m/s	0.162 m/s	0.165 m/s	0.152 m/s
	centre	0.234 m/s	0.205 m/s	0.245 m/s	0.226 m/s
Radiation model enabled, $\alpha = 0.05m^{-1}$ QUICK differencing. Mixed walls. Uniform external temperature.	all	0.130 m/s	0.137 m/s	0.136 m/s	0.125 m/s
	centre	0.197 m/s	0.174 m/s	0.178 m/s	0.194 m/s

Width of opening:	0.5m
Effective area of opening:	$0.305m^2$
Heat source:	Plate heater
Strength of heat source:	225.0W

Figure 5.b

	Area	Laminar	Standard-$k\varepsilon$	Realizable-$k\varepsilon$	RNG-$k\varepsilon$
Radiation model disabled. Upwind differencing. Adiabatic walls. Uniform external temperature.	all	0.191 m/s	0.208 m/s	0.204 m/s	0.193 m/s
	centre	0.275 m/s	0.265 m/s	0.270 m/s	0.276 m/s
Radiation model disabled. QUICK differencing. Adiabatic walls. Uniform external temperature.	all	0.183 m/s	0.203 m/s	0.200 m/s	0.181 m/s
	centre	0.294 m/s	0.267 m/s	0.264 m/s	0.288 m/s
Radiation model enabled, $\alpha = 0.00m^{-1}$ QUICK differencing. Adiabatic walls. Uniform external temperature.	all	0.225 m/s	0.243 m/s	0.247 m/s	0.231 m/s
	centre	0.347 m/s	0.317 m/s	0.329 m/s	0.354 m/s
Radiation model enabled, $\alpha = 0.05m^{-1}$ QUICK differencing. Adiabatic walls. Uniform external temperature.	all	0.233 m/s	0.246 m/s	0.250 m/s	0.233 m/s
	centre	0.353 m/s	0.323 m/s	0.332 m/s	0.353 m/s
Radiation model enabled, $\alpha = 0.10m^{-1}$ QUICK differencing. Adiabatic walls. Uniform external temperature.	all	0.231 m/s	0.250 m/s	0.254 m/s	0.233 m/s
	centre	0.356 m/s	0.324 m/s	0.333 m/s	0.358 m/s
Radiation model enabled, $\alpha = 0.15m^{-1}$ QUICK differencing. Adiabatic walls. Uniform external temperature.	all	0.240 m/s	0.252 m/s	0.253 m/s	0.237 m/s
	centre	0.369 m/s	0.324 m/s	0.330 m/s	0.359 m/s

Width of opening:	0.6m
Effective area of opening:	$0.366m^2$
Heat source:	Plate heater
Strength of heat source:	225.0W

Figure 6.a

	Area	Laminar	Standard-$k\varepsilon$	Realizable-$k\varepsilon$	RNG-$k\varepsilon$
Radiation model enabled, $\alpha = 0.00m^{-1}$ QUICK differencing. Convection walls. Uniform external temperature.	all	0.095 m/s	0.113 m/s	0.113 m/s	0.096 m/s
	centre	0.150 m/s	0.149 m/s	0.164 m/s	0.150 m/s
Radiation model enabled, $\alpha = 0.00m^{-1}$ QUICK differencing. Radiation walls. Uniform external temperature.	all	0.114 m/s	0.134 m/s	0.136 m/s	0.114 m/s
	centre	0.176 m/s	0.176 m/s	0.195 m/s	0.175 m/s
Radiation model enabled, $\alpha = 0.00m^{-1}$ QUICK differencing. Mixed walls. Uniform external temperature.	all	0.091 m/s	0.107 m/s	0.107 m/s	0.091 m/s
	centre	0.139 m/s	0.141 m/s	0.152 m/s	0.139 m/s
Radiation model enabled, $\alpha = 0.05m^{-1}$ QUICK differencing. Convection walls. Uniform external temperature.	all	0.125 m/s	0.135 m/s	0.134 m/s	0.123 m/s
	centre	0.194 m/s	0.176 m/s	0.184 m/s	0.193 m/s
Radiation model enabled, $\alpha = 0.05m^{-1}$ QUICK differencing. Radiation walls. Uniform external temperature.	all	0.138 m/s	0.153 m/s	0.153 m/s	0.140 m/s
	centre	0.217 m/s	0.198 m/s	0.216 m/s	0.211 m/s
Radiation model enabled, $\alpha = 0.05m^{-1}$ QUICK differencing. Mixed walls. Uniform external temperature.	all	0.121 m/s	0.130 m/s	0.128 m/s	0.121 m/s
	centre	0.186 m/s	0.169 m/s	0.177 m/s	0.183 m/s

Width of opening:	0.6m
Effective area of opening:	$0.366m^2$
Heat source:	Plate heater
Strength of heat source:	225.0W

Figure 6.b

	Area	Laminar	Standard-$k\varepsilon$	Realizable-$k\varepsilon$	RNG-$k\varepsilon$
Radiation model disabled. Upwind differencing. Adiabatic walls. Uniform external temperature.	all	0.166 m/s	0.180 m/s	0.172 m/s	0.164 m/s
	centre	0.240 m/s	0.236 m/s	0.233 m/s	0.226 m/s
Radiation model disabled. QUICK differencing. Adiabatic walls. Uniform external temperature.	all	0.166 m/s	0.175 m/s	0.167 m/s	0.171 m/s
	centre	0.250 m/s	0.239 m/s	0.223 m/s	0.254 m/s
Radiation model enabled, $\alpha = 0.00m^{-1}$ QUICK differencing. Adiabatic walls. Uniform external temperature.	all	0.203 m/s	0.210 m/s	0.215 m/s	0.204 m/s
	centre	0.305 m/s	0.284 m/s	0.294 m/s	0.295 m/s
Radiation model enabled, $\alpha = 0.05m^{-1}$ QUICK differencing. Adiabatic walls. Uniform external temperature.	all	0.210 m/s	0.216 m/s	0.216 m/s	0.211 m/s
	centre	0.289 m/s	0.285 m/s	0.305 m/s	0.305 m/s
Radiation model enabled, $\alpha = 0.10m^{-1}$ QUICK differencing. Adiabatic walls. Uniform external temperature.	all	0.213 m/s	0.221 m/s	0.220 m/s	0.211 m/s
	centre	0.316 m/s	0.289 m/s	0.309 m/s	0.306 m/s
Radiation model enabled, $\alpha = 0.15m^{-1}$ QUICK differencing. Adiabatic walls. Uniform external temperature.	all	0.215 m/s	0.224 m/s	0.221 m/s	0.214 m/s
	centre	0.319 m/s	0.293 m/s	0.311 m/s	0.308 m/s

Width of opening:	0.8m
Effective area of opening:	$0.488m^2$
Heat source:	Plate heater
Strength of heat source:	225.0W

Figure 7.a

	Area	Laminar	Standard-$k\varepsilon$	Realizable-$k\varepsilon$	RNG-$k\varepsilon$
Radiation model enabled, $\alpha = 0.00m^{-1}$ QUICK differencing. Convection walls. Uniform external temperature.	all	0.085 m/s	0.104 m/s	0.102 m/s	0.086 m/s
	centre	0.122 m/s	0.141 m/s	0.154 m/s	0.125 m/s
Radiation model enabled, $\alpha = 0.00m^{-1}$ QUICK differencing. Radiation walls. Uniform external temperature.	all	0.106 m/s	0.122 m/s	0.121 m/s	0.105 m/s
	centre	0.153 m/s	0.159 m/s	0.186 m/s	0.147 m/s
Radiation model enabled, $\alpha = 0.00m^{-1}$ QUICK differencing. Mixed walls. Uniform external temperature.	all	0.080 m/s	0.099 m/s	0.096 m/s	0.081 m/s
	centre	0.120 m/s	0.133 m/s	0.145 m/s	0.114 m/s
Radiation model enabled, $\alpha = 0.05m^{-1}$ QUICK differencing. Convection walls. Uniform external temperature.	all	0.118 m/s	0.123 m/s	0.124 m/s	0.118 m/s
	centre	0.173 m/s	0.167 m/s	0.179 m/s	0.175 m/s
Radiation model enabled, $\alpha = 0.05m^{-1}$ QUICK differencing. Radiation walls. Uniform external temperature.	all	0.134 m/s	0.140 m/s	0.142 m/s	0.133 m/s
	centre	0.193 m/s	0.186 m/s	0.197 m/s	0.195 m/s
Radiation model enabled, $\alpha = 0.05m^{-1}$ QUICK differencing. Mixed walls. Uniform external temperature.	all	0.116 m/s	0.119 m/s	0.120 m/s	0.112 m/s
	centre	0.165 m/s	0.161 m/s	0.172 m/s	0.167 m/s

Width of opening:	0.8m
Effective area of opening:	$0.488m^2$
Heat source:	Plate heater
Strength of heat source:	225.0W

Figure 7.b

	Area	Laminar	Standard-$k\varepsilon$	Realizable-$k\varepsilon$	RNG-$k\varepsilon$
Radiation model disabled. Upwind differencing. Adiabatic walls. Uniform external temperature.	all	0.142 m/s	0.159 m/s	0.153 m/s	0.142 m/s
	centre	0.190 m/s	0.214 m/s	0.200 m/s	0.190 m/s
Radiation model disabled. QUICK differencing. Adiabatic walls. Uniform external temperature.	all	0.150 m/s	0.153 m/s	0.146 m/s	0.143 m/s
	centre	0.212 m/s	0.214 m/s	0.187 m/s	0.191 m/s
Radiation model enabled, $\alpha = 0.00m^{-1}$ QUICK differencing. Adiabatic walls. Uniform external temperature.	all	0.188 m/s	0.191 m/s	0.196 m/s	0.180 m/s
	centre	0.261 m/s	0.260 m/s	0.258 m/s	0.238 m/s
Radiation model enabled, $\alpha = 0.05m^{-1}$ QUICK differencing. Adiabatic walls. Uniform external temperature.	all	0.189 m/s	0.196 m/s	0.197 m/s	0.188 m/s
	centre	0.262 m/s	0.263 m/s	0.272 m/s	0.260 m/s
Radiation model enabled, $\alpha = 0.10m^{-1}$ QUICK differencing. Adiabatic walls. Uniform external temperature.	all	0.195 m/s	0.201 m/s	0.199 m/s	0.189 m/s
	centre	0.267 m/s	0.262 m/s	0.277 m/s	0.253 m/s
Radiation model enabled, $\alpha = 0.15m^{-1}$ QUICK differencing. Adiabatic walls. Uniform external temperature.	all	0.197 m/s	0.203 m/s	0.201 m/s	0.191 m/s
	centre	0.270 m/s	0.265 m/s	0.279 m/s	0.262 m/s

Width of opening:	1.0m
Effective area of opening:	$0.610m^2$
Heat source:	Plate heater
Strength of heat source:	225.0W

Figure 8.a

	Area	Laminar	Standard-$k\varepsilon$	Realizable-$k\varepsilon$	RNG-$k\varepsilon$
Radiation model enabled, $\alpha = 0.00m^{-1}$ QUICK differencing. Convection walls. Uniform external temperature.	all	0.078 m/s	0.097 m/s	0.095 m/s	0.079 m/s
	centre	0.120 m/s	0.134 m/s	0.139 m/s	0.111 m/s
Radiation model enabled, $\alpha = 0.00m^{-1}$ QUICK differencing. Radiation walls. Uniform external temperature.	all	0.094 m/s	0.112 m/s	0.110 m/s	0.095 m/s
	centre	0.141 m/s	0.156 m/s	0.148 m/s	0.123 m/s
Radiation model enabled, $\alpha = 0.00m^{-1}$ QUICK differencing. Mixed walls. Uniform external temperature.	all	0.076 m/s	0.091 m/s	0.089 m/s	0.076 m/s
	centre	0.102 m/s	0.127 m/s	0.132 m/s	0.112 m/s
Radiation model enabled, $\alpha = 0.05m^{-1}$ QUICK differencing. Convection walls. Uniform external temperature.	all	0.109 m/s	0.116 m/s	0.115 m/s	0.108 m/s
	centre	0.146 m/s	0.157 m/s	0.163 m/s	0.156 m/s
Radiation model enabled, $\alpha = 0.05m^{-1}$ QUICK differencing. Radiation walls. Uniform external temperature.	all	0.123 m/s	0.130 m/s	0.129 m/s	0.120 m/s
	centre	0.165 m/s	0.175 m/s	0.188 m/s	0.162 m/s
Radiation model enabled, $\alpha = 0.05m^{-1}$ QUICK differencing. Mixed walls. Uniform external temperature.	all	0.106 m/s	0.111 m/s	0.111 m/s	0.105 m/s
	centre	0.148 m/s	0.151 m/s	0.158 m/s	0.146 m/s

Width of opening:	1.0m
Effective area of opening:	$0.610m^2$
Heat source:	Plate heater
Strength of heat source:	225.0W

Figure 8.b

	Area	Laminar	Standard-$k\varepsilon$	Realizable-$k\varepsilon$	RNG-$k\varepsilon$
Radiation model disabled. Upwind differencing. Adiabatic walls. Uniform external temperature.	all	0.132 m/s	0.144 m/s	0.143 m/s	0.128 m/s
	centre	0.175 m/s	0.190 m/s	0.193 m/s	0.172 m/s
Radiation model disabled. QUICK differencing. Adiabatic walls. Uniform external temperature.	all	0.136 m/s	0.138 m/s	0.129 m/s	0.123 m/s
	centre	0.186 m/s	0.188 m/s	0.176 m/s	0.169 m/s
Radiation model enabled, $\alpha = 0.00m^{-1}$ QUICK differencing. Adiabatic walls. Uniform external temperature.	all	0.174 m/s	0.179 m/s	0.177 m/s	0.170 m/s
	centre	0.244 m/s	0.234 m/s	0.236 m/s	0.226 m/s
Radiation model enabled, $\alpha = 0.05m^{-1}$ QUICK differencing. Adiabatic walls. Uniform external temperature.	all	0.179 m/s	0.182 m/s	0.183 m/s	0.175 m/s
	centre	0.248 m/s	0.241 m/s	0.243 m/s	0.236 m/s
Radiation model enabled, $\alpha = 0.10m^{-1}$ QUICK differencing. Adiabatic walls. Uniform external temperature.	all	0.180 m/s	0.185 m/s	0.185 m/s	0.178 m/s
	centre	0.247 m/s	0.241 m/s	0.248 m/s	0.240 m/s
Radiation model enabled, $\alpha = 0.15m^{-1}$ QUICK differencing. Adiabatic walls. Uniform external temperature.	all	0.182 m/s	0.188 m/s	0.187 m/s	0.181 m/s
	centre	0.242 m/s	0.242 m/s	0.251 m/s	0.248 m/s

Width of opening:	1.2m
Effective area of opening:	$0.732m^2$
Heat source:	Plate heater
Strength of heat source:	225.0W

Figure 9.a

	Area	Laminar	Standard-$k\varepsilon$	Realizable-$k\varepsilon$	RNG-$k\varepsilon$
Radiation model enabled, $\alpha = 0.00m^{-1}$ QUICK differencing. Convection walls. Uniform external temperature.	all	0.077 m/s	0.092 m/s	0.090 m/s	0.075 m/s
	centre	0.109 m/s	0.127 m/s	0.126 m/s	0.106 m/s
Radiation model enabled, $\alpha = 0.00m^{-1}$ QUICK differencing. Radiation walls. Uniform external temperature.	all	0.093 m/s	0.106 m/s	0.103 m/s	0.094 m/s
	centre	0.131 m/s	0.143 m/s	0.133 m/s	0.130 m/s
Radiation model enabled, $\alpha = 0.00m^{-1}$ QUICK differencing. Mixed walls. Uniform external temperature.	all	0.072 m/s	0.087 m/s	0.080 m/s	0.070 m/s
	centre	0.103 m/s	0.122 m/s	0.108 m/s	0.101 m/s
Radiation model enabled, $\alpha = 0.05m^{-1}$ QUICK differencing. Convection walls. Uniform external temperature.	all	0.107 m/s	0.110 m/s	0.111 m/s	0.104 m/s
	centre	0.141 m/s	0.146 m/s	0.151 m/s	0.141 m/s
Radiation model enabled, $\alpha = 0.05m^{-1}$ QUICK differencing. Radiation walls. Uniform external temperature.	all	0.117 m/s	0.122 m/s	0.123 m/s	0.117 m/s
	centre	0.165 m/s	0.163 m/s	0.166 m/s	0.163 m/s
Radiation model enabled, $\alpha = 0.05m^{-1}$ QUICK differencing. Mixed walls. Uniform external temperature.	all	0.101 m/s	0.106 m/s	0.107 m/s	0.104 m/s
	centre	0.148 m/s	0.141 m/s	0.146 m/s	0.141 m/s

Width of opening:	1.2m
Effective area of opening:	$0.732m^2$
Heat source:	Plate heater
Strength of heat source:	225.0W

Figure 9.b

	Area	Laminar	Standard-$k\varepsilon$	Realizable-$k\varepsilon$	RNG-$k\varepsilon$
Radiation model disabled. Upwind differencing. Adiabatic walls. Uniform external temperature.	all				
	centre				
Radiation model disabled. QUICK differencing. Adiabatic walls. Uniform external temperature.	all	0.520 m/s	0.554 m/s	0.576 m/s	0.520 m/s
	centre	0.635 m/s	0.598 m/s	0.616 m/s	0.652 m/s
Radiation model enabled, $\alpha = 0.00m^{-1}$ QUICK differencing. Adiabatic walls. Uniform external temperature.	all	No available solution	0.621 m/s	0.647 m/s	0.601 m/s
	centre	No available solution	0.659 m/s	0.685 m/s	0.762 m/s
Radiation model enabled, $\alpha = 0.05m^{-1}$ QUICK differencing. Adiabatic walls. Uniform external temperature.	all	No available solution	0.604 m/s	0.622 m/s	0.586 m/s
	centre	No available solution	0.640 m/s	0.658 m/s	0.744 m/s
Radiation model enabled, $\alpha = 0.10m^{-1}$ QUICK differencing. Adiabatic walls. Uniform external temperature.	all	0.595 m/s	0.603 m/s	0.617 m/s	0.582 m/s
	centre	0.764 m/s	0.640 m/s	0.653 m/s	0.717 m/s
Radiation model enabled, $\alpha = 0.15m^{-1}$ QUICK differencing. Adiabatic walls. Uniform external temperature.	all	0.579 m/s	0.603 m/s	0.615 m/s	0.587 m/s
	centre	0.723 m/s	0.640 m/s	0.651 m/s	0.723 m/s

Width of opening:	0.1m
Effective area of opening:	$0.061m^2$
Heat source:	Boiler ring
Strength of heat source:	368.0W

Figure 10.a

	Area	Laminar	Standard-$k\varepsilon$	Realizable-$k\varepsilon$	RNG-$k\varepsilon$
Radiation model enabled, $\alpha = 0.00m^{-1}$ QUICK differencing. Convection walls. Uniform external temperature.	all	0.205 m/s	0.273 m/s	0.217 m/s	0.194 m/s
	centre	0.261 m/s	0.313 m/s	0.233 m/s	0.249 m/s
Radiation model enabled, $\alpha = 0.00m^{-1}$ QUICK differencing. Radiation walls. Uniform external temperature.	all	0.237 m/s	0.297 m/s	0.268 m/s	0.241 m/s
	centre	0.300 m/s	0.328 m/s	0.287 m/s	0.312 m/s
Radiation model enabled, $\alpha = 0.00m^{-1}$ QUICK differencing. Mixed walls. Uniform external temperature.	all	0.185 m/s	0.263 m/s	0.205 m/s	0.183 m/s
	centre	0.234 m/s	0.303 m/s	0.221 m/s	0.234 m/s
Radiation model enabled, $\alpha = 0.05m^{-1}$ QUICK differencing. Convection walls. Uniform external temperature.	all	0.235 m/s	0.226 m/s	0.236 m/s	0.222 m/s
	centre	0.295 m/s	0.239 m/s	0.256 m/s	0.283 m/s
Radiation model enabled, $\alpha = 0.05m^{-1}$ QUICK differencing. Radiation walls. Uniform external temperature.	all	0.273 m/s	0.268 m/s	0.285 m/s	0.263 m/s
	centre	0.350 m/s	0.284 m/s	0.306 m/s	0.335 m/s
Radiation model enabled, $\alpha = 0.05m^{-1}$ QUICK differencing. Mixed walls. Uniform external temperature.	all	0.224 m/s	0.215 m/s	0.224 m/s	0.212 m/s
	centre	0.286 m/s	0.229 m/s	0.243 m/s	0.271 m/s

Width of opening:	0.1m
Effective area of opening:	$0.061m^2$
Heat source:	Boiler ring
Strength of heat source:	368.0W

Figure 10.b

	Area	Laminar	Standard-$k\varepsilon$	Realizable-$k\varepsilon$	RNG-$k\varepsilon$
Radiation model disabled. Upwind differencing. Adiabatic walls. Uniform external temperature.	all	0.368 m/s	0.396 m/s	0.429 m/s	0.370 m/s
	centre	0.460 m/s	0.469 m/s	0.477 m/s	0.463 m/s
Radiation model disabled. QUICK differencing. Adiabatic walls. Uniform external temperature.	all	No available solution	No available solution	0.421 m/s	No available solution
	centre	No available solution	No available solution	0.477 m/s	No available solution
Radiation model enabled, $\alpha = 0.00m^{-1}$ QUICK differencing. Adiabatic walls. Uniform external temperature.	all	No available solution	No available solution	0.469 m/s	0.462 m/s
	centre	No available solution	No available solution	0.536 m/s	0.597 m/s
Radiation model enabled, $\alpha = 0.05m^{-1}$ QUICK differencing. Adiabatic walls. Uniform external temperature.	all	0.457 m/s	0.472 m/s	0.478 m/s	0.459 m/s
	centre	0.627 m/s	0.552 m/s	0.545 m/s	0.594 m/s
Radiation model enabled, $\alpha = 0.10m^{-1}$ QUICK differencing. Adiabatic walls. Uniform external temperature.	all	0.455 m/s	0.473 m/s	0.480 m/s	0.462 m/s
	centre	0.620 m/s	0.553 m/s	0.548 m/s	0.599 m/s
Radiation model enabled, $\alpha = 0.15m^{-1}$ QUICK differencing. Adiabatic walls. Uniform external temperature.	all	0.454 m/s	0.473 m/s	0.481 m/s	0.465 m/s
	centre	0.606 m/s	0.554 m/s	0.549 m/s	0.602 m/s

Width of opening:	0.2m
Effective area of opening:	$0.122m^2$
Heat source:	Boiler ring
Strength of heat source:	368.0W

Figure 11.a

	Area	Laminar	Standard-$k\varepsilon$	Realizable-$k\varepsilon$	RNG-$k\varepsilon$
Radiation model enabled, $\alpha = 0.00m^{-1}$ QUICK differencing. Convection walls. Uniform external temperature.	all	0.177 m/s	0.196 m/s	0.188 m/s	0.170 m/s
	centre	0.237 m/s	0.222 m/s	0.210 m/s	0.227 m/s
Radiation model enabled, $\alpha = 0.00m^{-1}$ QUICK differencing. Radiation walls. Uniform external temperature.	all	0.210 m/s	0.239 m/s	0.245 m/s	0.212 m/s
	centre	0.277 m/s	0.274 m/s	0.279 m/s	0.287 m/s
Radiation model enabled, $\alpha = 0.00m^{-1}$ QUICK differencing. Mixed walls. Uniform external temperature.	all	0.167 m/s	0.183 m/s	0.177 m/s	0.157 m/s
	centre	0.229 m/s	0.206 m/s	0.199 m/s	0.209 m/s
Radiation model enabled, $\alpha = 0.05m^{-1}$ QUICK differencing. Convection walls. Uniform external temperature.	all	0.222 m/s	0.212 m/s	0.215 m/s	0.208 m/s
	centre	0.304 m/s	0.244 m/s	0.242 m/s	0.280 m/s
Radiation model enabled, $\alpha = 0.05m^{-1}$ QUICK differencing. Radiation walls. Uniform external temperature.	all	0.251 m/s	0.248 m/s	0.263 m/s	0.242 m/s
	centre	0.329 m/s	0.287 m/s	0.300 m/s	0.325 m/s
Radiation model enabled, $\alpha = 0.05m^{-1}$ QUICK differencing. Mixed walls. Uniform external temperature.	all	0.213 m/s	0.203 m/s	0.203 m/s	0.198 m/s
	centre	0.292 m/s	0.233 m/s	0.229 m/s	0.267 m/s

Width of opening:	0.2m
Effective area of opening:	$0.122m^2$
Heat source:	Boiler ring
Strength of heat source:	368.0W

Figure 11.b

	Area	Laminar	Standard-$k\varepsilon$	Realizable-$k\varepsilon$	RNG-$k\varepsilon$
Radiation model disabled. Upwind differencing. Adiabatic walls. Uniform external temperature.	all	0.300 m/s	0.326 m/s	0.365 m/s	0.295 m/s
	centre	0.395 m/s	0.405 m/s	0.431 m/s	0.383 m/s
Radiation model disabled. QUICK differencing. Adiabatic walls. Uniform external temperature.	all	No available solution	No available solution	0.371 m/s	No available solution
	centre	No available solution	No available solution	0.456 m/s	No available solution
Radiation model enabled, $\alpha = 0.00m^{-1}$ QUICK differencing. Adiabatic walls. Uniform external temperature.	all	No available solution	0.388 m/s	0.400 m/s	0.385 m/s
	centre	No available solution	0.478 m/s	0.492 m/s	0.501 m/s
Radiation model enabled, $\alpha = 0.05m^{-1}$ QUICK differencing. Adiabatic walls. Uniform external temperature.	all	0.389 m/s	0.389 m/s	0.403 m/s	0.383 m/s
	centre	0.580 m/s	0.482 m/s	0.493 m/s	0.539 m/s
Radiation model enabled, $\alpha = 0.10m^{-1}$ QUICK differencing. Adiabatic walls. Uniform external temperature.	all	0.384 m/s	0.392 m/s	0.406 m/s	0.388 m/s
	centre	0.574 m/s	0.484 m/s	0.497 m/s	0.532 m/s
Radiation model enabled, $\alpha = 0.15m^{-1}$ QUICK differencing. Adiabatic walls. Uniform external temperature.	all	0.386 m/s	0.394 m/s	0.407 m/s	0.391 m/s
	centre	0.556 m/s	0.487 m/s	0.498 m/s	0.535 m/s

Width of opening:	0.3m
Effective area of opening:	$0.183m^2$
Heat source:	Boiler ring
Strength of heat source:	368.0W

Figure 12.a

	Area	Laminar	Standard-$k\varepsilon$	Realizable-$k\varepsilon$	RNG-$k\varepsilon$
Radiation model enabled, $\alpha = 0.00m^{-1}$ QUICK differencing. Convection walls. Uniform external temperature.	all	0.152 m/s	0.174 m/s	0.174 m/s	0.153 m/s
	centre	0.210 m/s	0.212 m/s	0.213 m/s	0.220 m/s
Radiation model enabled, $\alpha = 0.00m^{-1}$ QUICK differencing. Radiation walls. Uniform external temperature.	all	0.182 m/s	0.208 m/s	0.208 m/s	0.187 m/s
	centre	0.255 m/s	0.255 m/s	0.249 m/s	0.269 m/s
Radiation model enabled, $\alpha = 0.00m^{-1}$ QUICK differencing. Mixed walls. Uniform external temperature.	all	0.146 m/s	0.164 m/s	0.163 m/s	0.143 m/s
	centre	0.201 m/s	0.200 m/s	0.201 m/s	0.205 m/s
Radiation model enabled, $\alpha = 0.05m^{-1}$ QUICK differencing. Convection walls. Uniform external temperature.	all	0.198 m/s	0.198 m/s	0.197 m/s	0.192 m/s
	centre	0.276 m/s	0.244 m/s	0.238 m/s	0.275 m/s
Radiation model enabled, $\alpha = 0.05m^{-1}$ QUICK differencing. Radiation walls. Uniform external temperature.	all	0.224 m/s	0.228 m/s	0.234 m/s	0.222 m/s
	centre	0.317 m/s	0.283 m/s	0.288 m/s	0.311 m/s
Radiation model enabled, $\alpha = 0.05m^{-1}$ QUICK differencing. Mixed walls. Uniform external temperature.	all	0.193 m/s	0.189 m/s	0.188 m/s	0.185 m/s
	centre	0.272 m/s	0.234 m/s	0.228 m/s	0.262 m/s

Width of opening:	0.3m
Effective area of opening:	$0.183m^2$
Heat source:	Boiler ring
Strength of heat source:	368.0W

Figure 12.b

	Area	Laminar	Standard-$k\varepsilon$	Realizable-$k\varepsilon$	RNG-$k\varepsilon$
Radiation model disabled. Upwind differencing. Adiabatic walls. Uniform external temperature.	all	0.259 m/s	0.284 m/s	0.324 m/s	0.253 m/s
	centre	0.351 m/s	0.356 m/s	0.400 m/s	0.343 m/s
Radiation model disabled. QUICK differencing. Adiabatic walls. Uniform external temperature.	all	No available solution	No available solution	0.312 m/s	No available solution
	centre	No available solution	No available solution	0.402 m/s	No available solution
Radiation model enabled, $\alpha = 0.00m^{-1}$ QUICK differencing. Adiabatic walls. Uniform external temperature.	all	No available solution	0.343 m/s	0.351 m/s	0.329 m/s
	centre	No available solution	0.438 m/s	0.451 m/s	0.487 m/s
Radiation model enabled, $\alpha = 0.05m^{-1}$ QUICK differencing. Adiabatic walls. Uniform external temperature.	all	0.344 m/s	0.350 m/s	0.358 m/s	0.327 m/s
	centre	0.466 m/s	0.443 m/s	0.455 m/s	0.499 m/s
Radiation model enabled, $\alpha = 0.10m^{-1}$ QUICK differencing. Adiabatic walls. Uniform external temperature.	all	0.343 m/s	0.349 m/s	0.361 m/s	0.335 m/s
	centre	0.469 m/s	0.439 m/s	0.458 m/s	0.504 m/s
Radiation model enabled, $\alpha = 0.15m^{-1}$ QUICK differencing. Adiabatic walls. Uniform external temperature.	all	0.344 m/s	0.352 m/s	0.364 m/s	0.339 m/s
	centre	0.470 m/s	0.443 m/s	0.461 m/s	0.505 m/s

Width of opening:	0.4m
Effective area of opening:	$0.244m^2$
Heat source:	Boiler ring
Strength of heat source:	368.0W

Figure 13.a

	Area	Laminar	Standard-$k\varepsilon$	Realizable-$k\varepsilon$	RNG-$k\varepsilon$
Radiation model enabled, $\alpha = 0.00m^{-1}$ QUICK differencing. Convection walls. Uniform external temperature.	all	0.137 m/s	0.161 m/s	0.160 m/s	0.135 m/s
	centre	0.202 m/s	0.204 m/s	0.207 m/s	0.206 m/s
Radiation model enabled, $\alpha = 0.00m^{-1}$ QUICK differencing. Radiation walls. Uniform external temperature.	all	0.167 m/s	0.192 m/s	0.194 m/s	0.164 m/s
	centre	0.231 m/s	0.243 m/s	0.246 m/s	0.253 m/s
Radiation model enabled, $\alpha = 0.00m^{-1}$ QUICK differencing. Mixed walls. Uniform external temperature.	all	0.131 m/s	0.153 m/s	0.151 m/s	0.127 m/s
	centre	0.192 m/s	0.193 m/s	0.197 m/s	0.189 m/s
Radiation model enabled, $\alpha = 0.05m^{-1}$ QUICK differencing. Convection walls. Uniform external temperature.	all	0.182 m/s	0.188 m/s	0.187 m/s	0.175 m/s
	centre	0.256 m/s	0.238 m/s	0.240 m/s	0.266 m/s
Radiation model enabled, $\alpha = 0.05m^{-1}$ QUICK differencing. Radiation walls. Uniform external temperature.	all	0.207 m/s	0.214 m/s	0.215 m/s	0.198 m/s
	centre	0.283 m/s	0.271 m/s	0.273 m/s	0.304 m/s
Radiation model enabled, $\alpha = 0.05m^{-1}$ QUICK differencing. Mixed walls. Uniform external temperature.	all	0.178 m/s	0.180 m/s	0.179 m/s	0.169 m/s
	centre	0.248 m/s	0.228 m/s	0.229 m/s	0.254 m/s

Width of opening:	0.4m
Effective area of opening:	$0.244m^2$
Heat source:	Boiler ring
Strength of heat source:	368.0W

Figure 13.b

	Area	Laminar	Standard-$k\varepsilon$	Realizable-$k\varepsilon$	RNG-$k\varepsilon$
Radiation model disabled. Upwind differencing. Adiabatic walls. Uniform external temperature.	all	0.222 m/s	0.253 m/s	0.251 m/s	0.219 m/s
	centre	0.315 m/s	0.319 m/s	0.330 m/s	0.316 m/s
Radiation model disabled. QUICK differencing. Adiabatic walls. Uniform external temperature.	all	No available solution	0.265 m/s	0.273 m/s	No available solution
	centre	No available solution	0.346 m/s	0.362 m/s	No available solution
Radiation model enabled, $\alpha = 0.00m^{-1}$ QUICK differencing. Adiabatic walls. Uniform external temperature.	all	No available solution	0.310 m/s	0.319 m/s	0.317 m/s
	centre	No available solution	0.400 m/s	0.426 m/s	0.415 m/s
Radiation model enabled, $\alpha = 0.05m^{-1}$ QUICK differencing. Adiabatic walls. Uniform external temperature.	all	0.311 m/s	0.318 m/s	0.321 m/s	0.300 m/s
	centre	0.426 m/s	0.410 m/s	0.428 m/s	0.464 m/s
Radiation model enabled, $\alpha = 0.10m^{-1}$ QUICK differencing. Adiabatic walls. Uniform external temperature.	all	0.309 m/s	0.322 m/s	0.323 m/s	0.306 m/s
	centre	0.433 m/s	0.408 m/s	0.425 m/s	0.453 m/s
Radiation model enabled, $\alpha = 0.15m^{-1}$ QUICK differencing. Adiabatic walls. Uniform external temperature.	all	0.306 m/s	0.324 m/s	0.328 m/s	0.310 m/s
	centre	0.464 m/s	0.411 m/s	0.428 m/s	0.453 m/s

Width of opening:	0.5m
Effective area of opening:	$0.305m^2$
Heat source:	Boiler ring
Strength of heat source:	368.0W

Figure 14.a

	Area	Laminar	Standard-$k\varepsilon$	Realizable-$k\varepsilon$	RNG-$k\varepsilon$
Radiation model enabled, $\alpha = 0.00m^{-1}$ QUICK differencing. Convection walls. Uniform external temperature.	all	0.130 m/s	0.152 m/s	0.150 m/s	0.126 m/s
	centre	0.180 m/s	0.193 m/s	0.213 m/s	0.183 m/s
Radiation model enabled, $\alpha = 0.00m^{-1}$ QUICK differencing. Radiation walls. Uniform external temperature.	all	0.148 m/s	0.180 m/s	0.180 m/s	0.153 m/s
	centre	0.228 m/s	0.230 m/s	0.245 m/s	0.231 m/s
Radiation model enabled, $\alpha = 0.00m^{-1}$ QUICK differencing. Mixed walls. Uniform external temperature.	all	0.121 m/s	0.144 m/s	0.140 m/s	0.121 m/s
	centre	0.166 m/s	0.182 m/s	0.203 m/s	0.168 m/s
Radiation model enabled, $\alpha = 0.05m^{-1}$ QUICK differencing. Convection walls. Uniform external temperature.	all	0.170 m/s	0.178 m/s	0.177 m/s	0.164 m/s
	centre	0.247 m/s	0.227 m/s	0.239 m/s	0.252 m/s
Radiation model enabled, $\alpha = 0.05m^{-1}$ QUICK differencing. Radiation walls. Uniform external temperature.	all	0.190 m/s	0.202 m/s	0.205 m/s	0.185 m/s
	centre	0.276 m/s	0.256 m/s	0.294 m/s	0.283 m/s
Radiation model enabled, $\alpha = 0.05m^{-1}$ QUICK differencing. Mixed walls. Uniform external temperature.	all	0.163 m/s	0.171 m/s	0.170 m/s	0.157 m/s
	centre	0.237 m/s	0.218 m/s	0.229 m/s	0.240 m/s

Width of opening:	0.5m
Effective area of opening:	$0.305m^2$
Heat source:	Boiler ring
Strength of heat source:	368.0W

Figure 14.b

	Area	Laminar	Standard-$k\varepsilon$	Realizable-$k\varepsilon$	RNG-$k\varepsilon$
Radiation model disabled. Upwind differencing. Adiabatic walls. Uniform external temperature.	all	0.199 m/s	0.231 m/s	0.226 m/s	0.195 m/s
	centre	0.284 m/s	0.297 m/s	0.306 m/s	0.282 m/s
Radiation model disabled. QUICK differencing. Adiabatic walls. Uniform external temperature.	all	No available solution	No available solution	No available solution	No available solution
	centre	No available solution	No available solution	No available solution	No available solution
Radiation model enabled, $\alpha = 0.00m^{-1}$ QUICK differencing. Adiabatic walls. Uniform external temperature.	all	No available solution	No available solution	0.301 m/s	0.273 m/s
	centre	No available solution	No available solution	0.396 m/s	0.426 m/s
Radiation model enabled, $\alpha = 0.05m^{-1}$ QUICK differencing. Adiabatic walls. Uniform external temperature.	all	0.287 m/s	0.295 m/s	0.302 m/s	0.277 m/s
	centre	0.387 m/s	0.382 m/s	0.399 m/s	0.429 m/s
Radiation model enabled, $\alpha = 0.10m^{-1}$ QUICK differencing. Adiabatic walls. Uniform external temperature.	all	0.277 m/s	0.295 m/s	0.303 m/s	0.278 m/s
	centre	0.413 m/s	0.382 m/s	0.407 m/s	0.427 m/s
Radiation model enabled, $\alpha = 0.15m^{-1}$ QUICK differencing. Adiabatic walls. Uniform external temperature.	all	0.277 m/s	0.301 m/s	0.306 m/s	0.283 m/s
	centre	0.452 m/s	0.386 m/s	0.410 m/s	0.435 m/s

Width of opening:	0.6m
Effective area of opening:	$0.366m^2$
Heat source:	Boiler ring
Strength of heat source:	368.0W

Figure 15.a

	Area	Laminar	Standard-$k\varepsilon$	Realizable-$k\varepsilon$	RNG-$k\varepsilon$
Radiation model enabled, $\alpha = 0.00m^{-1}$ QUICK differencing. Convection walls. Uniform external temperature.	all	0.121 m/s	0.144 m/s	0.153 m/s	0.117 m/s
	centre	0.162 m/s	0.186 m/s	0.212 m/s	0.174 m/s
Radiation model enabled, $\alpha = 0.00m^{-1}$ QUICK differencing. Radiation walls. Uniform external temperature.	all	0.144 m/s	0.171 m/s	0.175 m/s	0.143 m/s
	centre	0.206 m/s	0.222 m/s	0.239 m/s	0.222 m/s
Radiation model enabled, $\alpha = 0.00m^{-1}$ QUICK differencing. Mixed walls. Uniform external temperature.	all	0.108 m/s	0.139 m/s	0.145 m/s	0.109 m/s
	centre	0.162 m/s	0.180 m/s	0.202 m/s	0.168 m/s
Radiation model enabled, $\alpha = 0.05m^{-1}$ QUICK differencing. Convection walls. Uniform external temperature.	all	0.154 m/s	0.170 m/s	0.168 m/s	0.155 m/s
	centre	0.238 m/s	0.219 m/s	0.233 m/s	0.227 m/s
Radiation model enabled, $\alpha = 0.05m^{-1}$ QUICK differencing. Radiation walls. Uniform external temperature.	all	0.172 m/s	0.191 m/s	0.194 m/s	0.175 m/s
	centre	0.270 m/s	0.248 m/s	0.285 m/s	0.257 m/s
Radiation model enabled, $\alpha = 0.05m^{-1}$ QUICK differencing. Mixed walls. Uniform external temperature.	all	0.150 m/s	0.162 m/s	0.160 m/s	0.148 m/s
	centre	0.233 m/s	0.212 m/s	0.225 m/s	0.222 m/s

Width of opening:	0.6m
Effective area of opening:	$0.366m^2$
Heat source:	Boiler ring
Strength of heat source:	368.0W

Figure 15.b

	Area	Laminar	Standard-$k\varepsilon$	Realizable-$k\varepsilon$	RNG-$k\varepsilon$
Radiation model disabled. Upwind differencing. Adiabatic walls. Uniform external temperature.	all	0.170 m/s	0.198 m/s	0.190 m/s	0.165 m/s
	centre	0.232 m/s	0.261 m/s	0.258 m/s	0.225 m/s
Radiation model disabled. QUICK differencing. Adiabatic walls. Uniform external temperature.	all	No available solution	No available solution	No available solution	No available solution
	centre	No available solution	No available solution	No available solution	No available solution
Radiation model enabled, $\alpha = 0.00m^{-1}$ QUICK differencing. Adiabatic walls. Uniform external temperature.	all	No available solution	0.255 m/s	0.257 m/s	0.243 m/s
	centre	No available solution	0.340 m/s	0.352 m/s	0.365 m/s
Radiation model enabled, $\alpha = 0.05m^{-1}$ QUICK differencing. Adiabatic walls. Uniform external temperature.	all	0.247 m/s	0.260 m/s	0.260 m/s	0.249 m/s
	centre	0.377 m/s	0.341 m/s	0.358 m/s	0.361 m/s
Radiation model enabled, $\alpha = 0.10m^{-1}$ QUICK differencing. Adiabatic walls. Uniform external temperature.	all	0.247 m/s	0.259 m/s	0.266 m/s	0.256 m/s
	centre	0.369 m/s	0.341 m/s	0.366 m/s	0.367 m/s
Radiation model enabled, $\alpha = 0.15m^{-1}$ QUICK differencing. Adiabatic walls. Uniform external temperature.	all	0.253 m/s	0.266 m/s	0.269 m/s	0.259 m/s
	centre	0.358 m/s	0.347 m/s	0.369 m/s	0.373 m/s

Width of opening:	0.8m
Effective area of opening:	$0.488m^2$
Heat source:	Boiler ring
Strength of heat source:	368.0W

Figure 16.a

	Area	Laminar	Standard-$k\varepsilon$	Realizable-$k\varepsilon$	RNG-$k\varepsilon$
Radiation model enabled, $\alpha = 0.00m^{-1}$ QUICK differencing. Convection walls. Uniform external temperature.	all	0.102 m/s	0.132 m/s	0.129 m/s	0.105 m/s
	centre	0.159 m/s	0.177 m/s	0.191 m/s	0.152 m/s
Radiation model enabled, $\alpha = 0.00m^{-1}$ QUICK differencing. Radiation walls. Uniform external temperature.	all	0.129 m/s	0.154 m/s	0.151 m/s	0.126 m/s
	centre	0.184 m/s	0.205 m/s	0.202 m/s	0.186 m/s
Radiation model enabled, $\alpha = 0.00m^{-1}$ QUICK differencing. Mixed walls. Uniform external temperature.	all	0.097 m/s	0.125 m/s	0.123 m/s	0.099 m/s
	centre	0.148 m/s	0.168 m/s	0.180 m/s	0.136 m/s
Radiation model enabled, $\alpha = 0.05m^{-1}$ QUICK differencing. Convection walls. Uniform external temperature.	all	0.144 m/s	0.154 m/s	0.155 m/s	0.142 m/s
	centre	0.217 m/s	0.208 m/s	0.214 m/s	0.209 m/s
Radiation model enabled, $\alpha = 0.05m^{-1}$ QUICK differencing. Radiation walls. Uniform external temperature.	all	0.159 m/s	0.174 m/s	0.175 m/s	0.160 m/s
	centre	0.229 m/s	0.232 m/s	0.271 m/s	0.230 m/s
Radiation model enabled, $\alpha = 0.05m^{-1}$ QUICK differencing. Mixed walls. Uniform external temperature.	all	0.136 m/s	0.149 m/s	0.150 m/s	0.137 m/s
	centre	0.202 m/s	0.201 m/s	0.214 m/s	0.204 m/s

Width of opening:	0.8m
Effective area of opening:	$0.488m^2$
Heat source:	Boiler ring
Strength of heat source:	368.0W

Figure 16.b

	Area	Laminar	Standard-$k\varepsilon$	Realizable-$k\varepsilon$	RNG-$k\varepsilon$
Radiation model disabled. Upwind differencing. Adiabatic walls. Uniform external temperature.	all	0.152 m/s	0.178 m/s	0.166 m/s	0.145 m/s
	centre	0.198 m/s	0.226 m/s	0.221 m/s	0.187 m/s
Radiation model disabled. QUICK differencing. Adiabatic walls. Uniform external temperature.	all	No available solution	0.192 m/s	No available solution	No available solution
	centre	No available solution	0.284 m/s	No available solution	No available solution
Radiation model enabled, $\alpha = 0.00m^{-1}$ QUICK differencing. Adiabatic walls. Uniform external temperature.	all	No available solution	0.235 m/s	0.234 m/s	0.220 m/s
	centre	No available solution	0.315 m/s	0.305 m/s	0.313 m/s
Radiation model enabled, $\alpha = 0.05m^{-1}$ QUICK differencing. Adiabatic walls. Uniform external temperature.	all	0.228 m/s	0.235 m/s	0.241 m/s	0.225 m/s
	centre	0.310 m/s	0.312 m/s	0.320 m/s	0.304 m/s
Radiation model enabled, $\alpha = 0.10m^{-1}$ QUICK differencing. Adiabatic walls. Uniform external temperature.	all	0.235 m/s	0.240 m/s	0.242 m/s	0.234 m/s
	centre	0.321 m/s	0.311 m/s	0.329 m/s	0.311 m/s
Radiation model enabled, $\alpha = 0.15m^{-1}$ QUICK differencing. Adiabatic walls. Uniform external temperature.	all	0.233 m/s	0.243 m/s	0.245 m/s	0.235 m/s
	centre	0.317 m/s	0.315 m/s	0.331 m/s	0.319 m/s

Width of opening:	1.0m
Effective area of opening:	$0.610m^2$
Heat source:	Boiler ring
Strength of heat source:	368.0W

Figure 17.a

	Area	Laminar	Standard-$k\varepsilon$	Realizable-$k\varepsilon$	RNG-$k\varepsilon$
Radiation model enabled, $\alpha = 0.00m^{-1}$ QUICK differencing. Convection walls. Uniform external temperature.	all	0.099 m/s	0.121 m/s	0.117 m/s	0.099 m/s
	centre	0.145 m/s	0.166 m/s	0.163 m/s	0.145 m/s
Radiation model enabled, $\alpha = 0.00m^{-1}$ QUICK differencing. Radiation walls. Uniform external temperature.	all	0.119 m/s	0.142 m/s	0.142 m/s	0.120 m/s
	centre	0.169 m/s	0.193 m/s	0.198 m/s	0.151 m/s
Radiation model enabled, $\alpha = 0.00m^{-1}$ QUICK differencing. Mixed walls. Uniform external temperature.	all	0.094 m/s	0.115 m/s	0.110 m/s	0.092 m/s
	centre	0.133 m/s	0.160 m/s	0.153 m/s	0.128 m/s
Radiation model enabled, $\alpha = 0.05m^{-1}$ QUICK differencing. Convection walls. Uniform external temperature.	all	0.139 m/s	0.145 m/s	0.145 m/s	0.134 m/s
	centre	0.185 m/s	0.195 m/s	0.201 m/s	0.180 m/s
Radiation model enabled, $\alpha = 0.05m^{-1}$ QUICK differencing. Radiation walls. Uniform external temperature.	all	0.151 m/s	0.162 m/s	0.161 m/s	0.149 m/s
	centre	0.203 m/s	0.216 m/s	0.240 m/s	0.208 m/s
Radiation model enabled, $\alpha = 0.05m^{-1}$ QUICK differencing. Mixed walls. Uniform external temperature.	all	0.130 m/s	0.140 m/s	0.137 m/s	0.131 m/s
	centre	0.185 m/s	0.188 m/s	0.197 m/s	0.169 m/s

Width of opening:	1.0m
Effective area of opening:	$0.610m^2$
Heat source:	Boiler ring
Strength of heat source:	368.0W

Figure 17.b

	Area	Laminar	Standard-$k\varepsilon$	Realizable-$k\varepsilon$	RNG-$k\varepsilon$
Radiation model disabled. Upwind differencing. Adiabatic walls. Uniform external temperature.	all	0.134 m/s	0.162 m/s	0.155 m/s	0.132 m/s
	centre	0.179 m/s	0.200 m/s	0.202 m/s	0.152 m/s
Radiation model disabled. QUICK differencing. Adiabatic walls. Uniform external temperature.	all	No available solution	No available solution	No available solution	No available solution
	centre	No available solution	No available solution	No available solution	No available solution
Radiation model enabled, $\alpha = 0.00m^{-1}$ QUICK differencing. Adiabatic walls. Uniform external temperature.	all	No available solution	0.212 m/s	0.218 m/s	0.209 m/s
	centre	No available solution	0.280 m/s	0.288 m/s	0.280 m/s
Radiation model enabled, $\alpha = 0.05m^{-1}$ QUICK differencing. Adiabatic walls. Uniform external temperature.	all	0.214 m/s	0.218 m/s	0.219 m/s	0.216 m/s
	centre	0.293 m/s	0.284 m/s	0.292 m/s	0.276 m/s
Radiation model enabled, $\alpha = 0.10m^{-1}$ QUICK differencing. Adiabatic walls. Uniform external temperature.	all	0.218 m/s	0.222 m/s	0.223 m/s	0.216 m/s
	centre	0.276 m/s	0.287 m/s	0.297 m/s	0.282 m/s
Radiation model enabled, $\alpha = 0.15m^{-1}$ QUICK differencing. Adiabatic walls. Uniform external temperature.	all	0.222 m/s	0.224 m/s	0.226 m/s	0.218 m/s
	centre	0.299 m/s	0.290 m/s	0.298 m/s	0.285 m/s

Width of opening:	1.2m
Effective area of opening:	$0.732m^2$
Heat source:	Boiler ring
Strength of heat source:	368.0W

Figure 18.a

	Area	Laminar	Standard-$k\varepsilon$	Realizable-$k\varepsilon$	RNG-$k\varepsilon$
Radiation model enabled, $\alpha = 0.00m^{-1}$ QUICK differencing. Convection walls. Uniform external temperature.	all	0.092 m/s	0.113 m/s	0.113 m/s	0.092 m/s
	centre	0.133 m/s	0.152 m/s	0.172 m/s	0.135 m/s
Radiation model enabled, $\alpha = 0.00m^{-1}$ QUICK differencing. Radiation walls. Uniform external temperature.	all	0.108 m/s	0.133 m/s	0.129 m/s	0.111 m/s
	centre	0.144 m/s	0.176 m/s	0.171 m/s	0.162 m/s
Radiation model enabled, $\alpha = 0.00m^{-1}$ QUICK differencing. Mixed walls. Uniform external temperature.	all	0.086 m/s	0.110 m/s	0.107 m/s	0.086 m/s
	centre	0.119 m/s	0.149 m/s	0.165 m/s	0.119 m/s
Radiation model enabled, $\alpha = 0.05m^{-1}$ QUICK differencing. Convection walls. Uniform external temperature.	all	0.129 m/s	0.136 m/s	0.137 m/s	0.129 m/s
	centre	0.177 m/s	0.181 m/s	0.189 m/s	0.173 m/s
Radiation model enabled, $\alpha = 0.05m^{-1}$ QUICK differencing. Radiation walls. Uniform external temperature.	all	0.139 m/s	0.152 m/s	0.151 m/s	0.146 m/s
	centre	0.191 m/s	0.202 m/s	0.203 m/s	0.191 m/s
Radiation model enabled, $\alpha = 0.05m^{-1}$ QUICK differencing. Mixed walls. Uniform external temperature.	all	0.125 m/s	0.131 m/s	0.131 m/s	0.123 m/s
	centre	0.178 m/s	0.175 m/s	0.182 m/s	0.178 m/s

Width of opening:	1.2m
Effective area of opening:	$0.732m^2$
Heat source:	Boiler ring
Strength of heat source:	368.0W

Figure 18.b

	Area	Laminar	Standard-$k\varepsilon$	Realizable-$k\varepsilon$	RNG-$k\varepsilon$
Radiation model disabled. Upwind differencing. Adiabatic walls. Uniform external temperature.	all	0.528 m/s	0.580 m/s	0.584 m/s	0.561 m/s
	centre	0.651 m/s	0.631 m/s	0.593 m/s	0.691 m/s
Radiation model disabled. QUICK differencing. Adiabatic walls. Uniform external temperature.	all	No available solution	0.595 m/s	0.622 m/s	No available solution
	centre	No available solution	0.639 m/s	0.664 m/s	No available solution
Radiation model enabled, $\alpha = 0.00m^{-1}$ QUICK differencing. Adiabatic walls. Uniform external temperature.	all	No available solution	0.691 m/s	0.619 m/s	0.612 m/s
	centre	No available solution	0.749 m/s	0.654 m/s	0.759 m/s
Radiation model enabled, $\alpha = 0.05m^{-1}$ QUICK differencing. Adiabatic walls. Uniform external temperature.	all	0.794 m/s	0.598 m/s	0.616 m/s	0.578 m/s
	centre	1.086 m/s	0.630 m/s	0.651 m/s	0.740 m/s
Radiation model enabled, $\alpha = 0.10m^{-1}$ QUICK differencing. Adiabatic walls. Uniform external temperature.	all	0.607 m/s	0.600 m/s	0.616 m/s	0.573 m/s
	centre	0.783 m/s	0.635 m/s	0.650 m/s	0.708 m/s
Radiation model enabled, $\alpha = 0.15m^{-1}$ QUICK differencing. Adiabatic walls. Uniform external temperature.	all	0.587 m/s	0.599 m/s	0.615 m/s	0.588 m/s
	centre	0.773 m/s	0.636 m/s	0.649 m/s	0.753 m/s

Width of opening:	0.1m
Effective area of opening:	$0.061m^2$
Heat source:	Boiler ring
Strength of heat source:	490.5W

Figure 19.a

	Area	Laminar	Standard-$k\varepsilon$	Realizable-$k\varepsilon$	RNG-$k\varepsilon$
Radiation model enabled, $\alpha = 0.00m^{-1}$ QUICK differencing. Convection walls. Uniform external temperature.	all	0.199 m/s	0.292 m/s	0.219 m/s	0.192 m/s
	centre	0.252 m/s	0.333 m/s	0.234 m/s	0.248 m/s
Radiation model enabled, $\alpha = 0.00m^{-1}$ QUICK differencing. Radiation walls. Uniform external temperature.	all	0.240 m/s	0.319 m/s	0.269 m/s	0.242 m/s
	centre	0.304 m/s	0.354 m/s	0.287 m/s	0.311 m/s
Radiation model enabled, $\alpha = 0.00m^{-1}$ QUICK differencing. Mixed walls. Uniform external temperature.	all	0.189 m/s	0.277 m/s	0.206 m/s	0.181 m/s
	centre	0.240 m/s	0.314 m/s	0.220 m/s	0.234 m/s
Radiation model enabled, $\alpha = 0.05m^{-1}$ QUICK differencing. Convection walls. Uniform external temperature.	all	0.231 m/s	0.227 m/s	0.235 m/s	0.220 m/s
	centre	0.291 m/s	0.240 m/s	0.252 m/s	0.282 m/s
Radiation model enabled, $\alpha = 0.05m^{-1}$ QUICK differencing. Radiation walls. Uniform external temperature.	all	0.273 m/s	0.268 m/s	0.286 m/s	0.261 m/s
	centre	0.342 m/s	0.284 m/s	0.305 m/s	0.334 m/s
Radiation model enabled, $\alpha = 0.05m^{-1}$ QUICK differencing. Mixed walls. Uniform external temperature.	all	0.226 m/s	0.216 m/s	0.224 m/s	0.210 m/s
	centre	0.291 m/s	0.229 m/s	0.240 m/s	0.269 m/s

Width of opening:	0.1m
Effective area of opening:	$0.061m^2$
Heat source:	Boiler ring
Strength of heat source:	490.5W

Figure 19.b

	Area	Laminar	Standard-$k\varepsilon$	Realizable-$k\varepsilon$	RNG-$k\varepsilon$
Radiation model disabled. Upwind differencing. Adiabatic walls. Uniform external temperature.	all	0.388 m/s	0.436 m/s	0.471 m/s	0.409 m/s
	centre	0.490 m/s	0.517 m/s	0.519 m/s	0.511 m/s
Radiation model disabled. QUICK differencing. Adiabatic walls. Uniform external temperature.	all	No available solution	0.464 m/s	0.482 m/s	No available solution
	centre	No available solution	0.539 m/s	0.555 m/s	No available solution
Radiation model enabled, $\alpha = 0.00m^{-1}$ QUICK differencing. Adiabatic walls. Uniform external temperature.	all	No available solution	0.466 m/s	0.466 m/s	0.451 m/s
	centre	No available solution	0.545 m/s	0.532 m/s	0.584 m/s
Radiation model enabled, $\alpha = 0.05m^{-1}$ QUICK differencing. Adiabatic walls. Uniform external temperature.	all	0.482 m/s	0.471 m/s	0.478 m/s	0.456 m/s
	centre	0.653 m/s	0.550 m/s	0.545 m/s	0.591 m/s
Radiation model enabled, $\alpha = 0.10m^{-1}$ QUICK differencing. Adiabatic walls. Uniform external temperature.	all	0.449 m/s	0.473 m/s	0.480 m/s	0.462 m/s
	centre	0.582 m/s	0.553 m/s	0.548 m/s	0.598 m/s
Radiation model enabled, $\alpha = 0.15m^{-1}$ QUICK differencing. Adiabatic walls. Uniform external temperature.	all	0.460 m/s	0.473 m/s	0.481 m/s	0.464 m/s
	centre	0.647 m/s	0.554 m/s	0.549 m/s	0.600 m/s

Width of opening:	0.2m
Effective area of opening:	$0.122m^2$
Heat source:	Boiler ring
Strength of heat source:	490.5W

Figure 20.a

	Area	Laminar	Standard-$k\varepsilon$	Realizable-$k\varepsilon$	RNG-$k\varepsilon$
Radiation model enabled, $\alpha = 0.00m^{-1}$ QUICK differencing. Convection walls. Uniform external temperature.	all	0.175 m/s	0.190 m/s	0.188 m/s	0.173 m/s
	centre	0.235 m/s	0.218 m/s	0.210 m/s	0.230 m/s
Radiation model enabled, $\alpha = 0.00m^{-1}$ QUICK differencing. Radiation walls. Uniform external temperature.	all	0.205 m/s	0.229 m/s	0.234 m/s	0.209 m/s
	centre	0.282 m/s	0.265 m/s	0.263 m/s	0.281 m/s
Radiation model enabled, $\alpha = 0.00m^{-1}$ QUICK differencing. Mixed walls. Uniform external temperature.	all	0.168 m/s	0.179 m/s	0.177 m/s	0.162 m/s
	centre	0.222 m/s	0.205 m/s	0.199 m/s	0.215 m/s
Radiation model enabled, $\alpha = 0.05m^{-1}$ QUICK differencing. Convection walls. Uniform external temperature.	all	0.216 m/s	0.212 m/s	0.215 m/s	0.207 m/s
	centre	0.286 m/s	0.245 m/s	0.243 m/s	0.276 m/s
Radiation model enabled, $\alpha = 0.05m^{-1}$ QUICK differencing. Radiation walls. Uniform external temperature.	all	0.252 m/s	0.248 m/s	0.259 m/s	0.240 m/s
	centre	0.332 m/s	0.288 m/s	0.294 m/s	0.323 m/s
Radiation model enabled, $\alpha = 0.05m^{-1}$ QUICK differencing. Mixed walls. Uniform external temperature.	all	0.212 m/s	0.203 m/s	0.204 m/s	0.200 m/s
	centre	0.284 m/s	0.234 m/s	0.231 m/s	0.276 m/s

Width of opening:	0.2m
Effective area of opening:	$0.122m^2$
Heat source:	Boiler ring
Strength of heat source:	490.5W

Figure 20.b

	Area	Laminar	Standard-$k\varepsilon$	Realizable-$k\varepsilon$	RNG-$k\varepsilon$
Radiation model disabled. Upwind differencing. Adiabatic walls. Uniform external temperature.	all	0.337 m/s	0.360 m/s	0.401 m/s	0.326 m/s
	centre	0.438 m/s	0.446 m/s	0.474 m/s	0.424 m/s
Radiation model disabled. QUICK differencing. Adiabatic walls. Uniform external temperature.	all	No available solution	No available solution	0.398 m/s	No available solution
	centre	No available solution	No available solution	0.481 m/s	No available solution
Radiation model enabled, $\alpha = 0.00m^{-1}$ QUICK differencing. Adiabatic walls. Uniform external temperature.	all	No available solution	No available solution	0.402 m/s	0.382 m/s
	centre	No available solution	No available solution	0.481 m/s	0.500 m/s
Radiation model enabled, $\alpha = 0.05m^{-1}$ QUICK differencing. Adiabatic walls. Uniform external temperature.	all	0.387 m/s	0.389 m/s	0.403 m/s	0.385 m/s
	centre	0.569 m/s	0.482 m/s	0.484 m/s	0.533 m/s
Radiation model enabled, $\alpha = 0.10m^{-1}$ QUICK differencing. Adiabatic walls. Uniform external temperature.	all	0.377 m/s	0.392 m/s	0.406 m/s	0.387 m/s
	centre	0.569 m/s	0.484 m/s	0.488 m/s	0.534 m/s
Radiation model enabled, $\alpha = 0.15m^{-1}$ QUICK differencing. Adiabatic walls. Uniform external temperature.	all	0.388 m/s	0.394 m/s	0.407 m/s	0.391 m/s
	centre	0.554 m/s	0.487 m/s	0.490 m/s	0.536 m/s

Width of opening:	0.3m
Effective area of opening:	$0.183m^2$
Heat source:	Boiler ring
Strength of heat source:	490.5W

Figure 21.a

	Area	Laminar	Standard-$k\varepsilon$	Realizable-$k\varepsilon$	RNG-$k\varepsilon$
Radiation model enabled, $\alpha = 0.00m^{-1}$ QUICK differencing. Convection walls. Uniform external temperature.	all	0.153 m/s	0.175 m/s	0.172 m/s	0.153 m/s
	centre	0.223 m/s	0.216 m/s	0.206 m/s	0.219 m/s
Radiation model enabled, $\alpha = 0.00m^{-1}$ QUICK differencing. Radiation walls. Uniform external temperature.	all	0.185 m/s	0.208 m/s	0.208 m/s	0.186 m/s
	centre	0.255 m/s	0.257 m/s	0.249 m/s	0.270 m/s
Radiation model enabled, $\alpha = 0.00m^{-1}$ QUICK differencing. Mixed walls. Uniform external temperature.	all	0.146 m/s	0.166 m/s	0.162 m/s	0.143 m/s
	centre	0.210 m/s	0.204 m/s	0.194 m/s	0.206 m/s
Radiation model enabled, $\alpha = 0.05m^{-1}$ QUICK differencing. Convection walls. Uniform external temperature.	all	0.199 m/s	0.198 m/s	0.200 m/s	0.192 m/s
	centre	0.283 m/s	0.245 m/s	0.243 m/s	0.275 m/s
Radiation model enabled, $\alpha = 0.05m^{-1}$ QUICK differencing. Radiation walls. Uniform external temperature.	all	0.225 m/s	0.228 m/s	0.235 m/s	0.222 m/s
	centre	0.320 m/s	0.283 m/s	0.286 m/s	0.311 m/s
Radiation model enabled, $\alpha = 0.05m^{-1}$ QUICK differencing. Mixed walls. Uniform external temperature.	all	0.190 m/s	0.189 m/s	0.189 m/s	0.185 m/s
	centre	0.276 m/s	0.234 m/s	0.228 m/s	0.263 m/s

Width of opening:	0.3m
Effective area of opening:	$0.183m^2$
Heat source:	Boiler ring
Strength of heat source:	490.5W

Figure 21.b

	Area	Laminar	Standard-$k\varepsilon$	Realizable-$k\varepsilon$	RNG-$k\varepsilon$
Radiation model disabled. Upwind differencing. Adiabatic walls. Uniform external temperature.	all	0.271 m/s	0.313 m/s	0.359 m/s	0.279 m/s
	centre	0.379 m/s	0.393 m/s	0.441 m/s	0.380 m/s
Radiation model disabled. QUICK differencing. Adiabatic walls. Uniform external temperature.	all	No available solution	No available solution	No available solution	0.301 m/s
	centre	No available solution	No available solution	No available solution	0.453 m/s
Radiation model enabled, $\alpha = 0.00m^{-1}$ QUICK differencing. Adiabatic walls. Uniform external temperature.	all	No available solution	0.341 m/s	0.355 m/s	0.350 m/s
	centre	No available solution	0.433 m/s	0.455 m/s	0.399 m/s
Radiation model enabled, $\alpha = 0.05m^{-1}$ QUICK differencing. Adiabatic walls. Uniform external temperature.	all	0.349 m/s	0.350 m/s	0.357 m/s	0.333 m/s
	centre	0.542 m/s	0.443 m/s	0.456 m/s	0.494 m/s
Radiation model enabled, $\alpha = 0.10m^{-1}$ QUICK differencing. Adiabatic walls. Uniform external temperature.	all	0.335 m/s	0.353 m/s	0.361 m/s	0.337 m/s
	centre	0.514 m/s	0.448 m/s	0.461 m/s	0.500 m/s
Radiation model enabled, $\alpha = 0.15m^{-1}$ QUICK differencing. Adiabatic walls. Uniform external temperature.	all	0.343 m/s	0.354 m/s	0.363 m/s	0.338 m/s
	centre	0.519 m/s	0.448 m/s	0.464 m/s	0.504 m/s

Width of opening:	0.4m
Effective area of opening:	$0.244m^2$
Heat source:	Boiler ring
Strength of heat source:	490.5W

Figure 22.a

	Area	Laminar	Standard-$k\varepsilon$	Realizable-$k\varepsilon$	RNG-$k\varepsilon$
Radiation model enabled, $\alpha = 0.00m^{-1}$ QUICK differencing. Convection walls. Uniform external temperature.	all	0.140 m/s	0.162 m/s	0.160 m/s	0.138 m/s
	centre	0.201 m/s	0.203 m/s	0.207 m/s	0.199 m/s
Radiation model enabled, $\alpha = 0.00m^{-1}$ QUICK differencing. Radiation walls. Uniform external temperature.	all	0.163 m/s	0.193 m/s	0.195 m/s	0.166 m/s
	centre	0.237 m/s	0.243 m/s	0.255 m/s	0.241 m/s
Radiation model enabled, $\alpha = 0.00m^{-1}$ QUICK differencing. Mixed walls. Uniform external temperature.	all	0.131 m/s	0.153 m/s	0.150 m/s	0.128 m/s
	centre	0.191 m/s	0.192 m/s	0.196 m/s	0.186 m/s
Radiation model enabled, $\alpha = 0.05m^{-1}$ QUICK differencing. Convection walls. Uniform external temperature.	all	0.179 m/s	0.187 m/s	0.186 m/s	0.177 m/s
	centre	0.275 m/s	0.237 m/s	0.241 m/s	0.266 m/s
Radiation model enabled, $\alpha = 0.05m^{-1}$ QUICK differencing. Radiation walls. Uniform external temperature.	all	0.203 m/s	0.214 m/s	0.215 m/s	0.198 m/s
	centre	0.304 m/s	0.271 m/s	0.273 m/s	0.305 m/s
Radiation model enabled, $\alpha = 0.05m^{-1}$ QUICK differencing. Mixed walls. Uniform external temperature.	all	0.175 m/s	0.180 m/s	0.178 m/s	0.169 m/s
	centre	0.254 m/s	0.228 m/s	0.231 m/s	0.256 m/s

Width of opening:	0.4m
Effective area of opening:	$0.244m^2$
Heat source:	Boiler ring
Strength of heat source:	490.5W

Figure 22.b

	Area	Laminar	Standard-$k\varepsilon$	Realizable-$k\varepsilon$	RNG-$k\varepsilon$
Radiation model disabled. Upwind differencing. Adiabatic walls. Uniform external temperature.	all	0.243 m/s	0.279 m/s	0.275 m/s	0.242 m/s
	centre	0.349 m/s	0.352 m/s	0.362 m/s	0.350 m/s
Radiation model disabled. QUICK differencing. Adiabatic walls. Uniform external temperature.	all	No available solution	0.282 m/s	0.284 m/s	No available solution
	centre	No available solution	0.368 m/s	0.362 m/s	No available solution
Radiation model enabled, $\alpha = 0.00m^{-1}$ QUICK differencing. Adiabatic walls. Uniform external temperature.	all	No available solution	0.311 m/s	0.326 m/s	0.317 m/s
	centre	No available solution	0.399 m/s	0.422 m/s	0.382 m/s
Radiation model enabled, $\alpha = 0.05m^{-1}$ QUICK differencing. Adiabatic walls. Uniform external temperature.	all	0.322 m/s	0.315 m/s	0.320 m/s	0.297 m/s
	centre	0.426 m/s	0.398 m/s	0.418 m/s	0.457 m/s
Radiation model enabled, $\alpha = 0.10m^{-1}$ QUICK differencing. Adiabatic walls. Uniform external temperature.	all	0.303 m/s	0.320 m/s	0.323 m/s	0.304 m/s
	centre	0.449 m/s	0.407 m/s	0.420 m/s	0.459 m/s
Radiation model enabled, $\alpha = 0.15m^{-1}$ QUICK differencing. Adiabatic walls. Uniform external temperature.	all	0.306 m/s	0.321 m/s	0.327 m/s	0.310 m/s
	centre	0.446 m/s	0.408 m/s	0.423 m/s	0.454 m/s

Width of opening:	0.5m
Effective area of opening:	$0.305m^2$
Heat source:	Boiler ring
Strength of heat source:	490.5W

Figure 23.a

	Area	Laminar	Standard-$k\varepsilon$	Realizable-$k\varepsilon$	RNG-$k\varepsilon$
Radiation model enabled, $\alpha = 0.00m^{-1}$ QUICK differencing. Convection walls. Uniform external temperature.	all	0.127 m/s	0.152 m/s	0.149 m/s	0.125 m/s
	centre	0.176 m/s	0.192 m/s	0.203 m/s	0.184 m/s
Radiation model enabled, $\alpha = 0.00m^{-1}$ QUICK differencing. Radiation walls. Uniform external temperature.	all	0.147 m/s	0.181 m/s	0.187 m/s	0.156 m/s
	centre	0.224 m/s	0.230 m/s	0.270 m/s	0.216 m/s
Radiation model enabled, $\alpha = 0.00m^{-1}$ QUICK differencing. Mixed walls. Uniform external temperature.	all	0.116 m/s	0.144 m/s	0.141 m/s	0.120 m/s
	centre	0.181 m/s	0.182 m/s	0.190 m/s	0.165 m/s
Radiation model enabled, $\alpha = 0.05m^{-1}$ QUICK differencing. Convection walls. Uniform external temperature.	all	0.167 m/s	0.178 m/s	0.177 m/s	0.165 m/s
	centre	0.251 m/s	0.227 m/s	0.234 m/s	0.248 m/s
Radiation model enabled, $\alpha = 0.05m^{-1}$ QUICK differencing. Radiation walls. Uniform external temperature.	all	0.187 m/s	0.202 m/s	0.202 m/s	0.187 m/s
	centre	0.277 m/s	0.257 m/s	0.276 m/s	0.281 m/s
Radiation model enabled, $\alpha = 0.05m^{-1}$ QUICK differencing. Mixed walls. Uniform external temperature.	all	0.161 m/s	0.171 m/s	0.169 m/s	0.159 m/s
	centre	0.243 m/s	0.218 m/s	0.225 m/s	0.237 m/s

Width of opening:	0.5m
Effective area of opening:	$0.305m^2$
Heat source:	Boiler ring
Strength of heat source:	490.5W

Figure 23.b

	Area	Laminar	Standard-$k\varepsilon$	Realizable-$k\varepsilon$	RNG-$k\varepsilon$
Radiation model disabled. Upwind differencing. Adiabatic walls. Uniform external temperature.	all	0.219 m/s	0.255 m/s	0.250 m/s	0.218 m/s
	centre	0.311 m/s	0.327 m/s	0.341 m/s	0.318 m/s
Radiation model disabled. QUICK differencing. Adiabatic walls. Uniform external temperature.	all	No available solution	No available solution	No available solution	No available solution
	centre	No available solution	No available solution	No available solution	No available solution
Radiation model enabled, $\alpha = 0.00m^{-1}$ QUICK differencing. Adiabatic walls. Uniform external temperature.	all	No available solution	0.286 m/s	0.294 m/s	0.276 m/s
	centre	No available solution	0.370 m/s	0.408 m/s	0.425 m/s
Radiation model enabled, $\alpha = 0.05m^{-1}$ QUICK differencing. Adiabatic walls. Uniform external temperature.	all	0.289 m/s	0.294 m/s	0.300 m/s	0.278 m/s
	centre	0.390 m/s	0.378 m/s	0.411 m/s	0.426 m/s
Radiation model enabled, $\alpha = 0.10m^{-1}$ QUICK differencing. Adiabatic walls. Uniform external temperature.	all	0.279 m/s	0.298 m/s	0.303 m/s	0.280 m/s
	centre	0.438 m/s	0.383 m/s	0.413 m/s	0.425 m/s
Radiation model enabled, $\alpha = 0.15m^{-1}$ QUICK differencing. Adiabatic walls. Uniform external temperature.	all	0.277 m/s	0.298 m/s	0.306 m/s	0.283 m/s
	centre	0.433 m/s	0.383 m/s	0.415 m/s	0.431 m/s

Width of opening:	0.6m
Effective area of opening:	$0.366m^2$
Heat source:	Boiler ring
Strength of heat source:	490.5W

Figure 24.a

	Area	Laminar	Standard-$k\varepsilon$	Realizable-$k\varepsilon$	RNG-$k\varepsilon$
Radiation model enabled, $\alpha = 0.00m^{-1}$ QUICK differencing. Convection walls. Uniform external temperature.	all	0.116 m/s	0.143 m/s	0.143 m/s	0.118 m/s
	centre	0.181 m/s	0.187 m/s	0.209 m/s	0.173 m/s
Radiation model enabled, $\alpha = 0.00m^{-1}$ QUICK differencing. Radiation walls. Uniform external temperature.	all	0.146 m/s	0.169 m/s	0.172 m/s	0.139 m/s
	centre	0.198 m/s	0.220 m/s	0.253 m/s	0.215 m/s
Radiation model enabled, $\alpha = 0.00m^{-1}$ QUICK differencing. Mixed walls. Uniform external temperature.	all	0.109 m/s	0.136 m/s	0.135 m/s	0.110 m/s
	centre	0.169 m/s	0.179 m/s	0.193 m/s	0.167 m/s
Radiation model enabled, $\alpha = 0.05m^{-1}$ QUICK differencing. Convection walls. Uniform external temperature.	all	0.156 m/s	0.169 m/s	0.169 m/s	0.154 m/s
	centre	0.246 m/s	0.221 m/s	0.237 m/s	0.235 m/s
Radiation model enabled, $\alpha = 0.05m^{-1}$ QUICK differencing. Radiation walls. Uniform external temperature.	all	0.172 m/s	0.191 m/s	0.194 m/s	0.174 m/s
	centre	0.280 m/s	0.248 m/s	0.293 m/s	0.261 m/s
Radiation model enabled, $\alpha = 0.05m^{-1}$ QUICK differencing. Mixed walls. Uniform external temperature.	all	0.148 m/s	0.162 m/s	0.161 m/s	0.147 m/s
	centre	0.242 m/s	0.212 m/s	0.229 m/s	0.226 m/s

Width of opening:	0.6m
Effective area of opening:	$0.366m^2$
Heat source:	Boiler ring
Strength of heat source:	490.5W

Figure 24.b

	Area	Laminar	Standard-$k\varepsilon$	Realizable-$k\varepsilon$	RNG-$k\varepsilon$
Radiation model disabled. Upwind differencing. Adiabatic walls. Uniform external temperature.	all	0.191 m/s	0.219 m/s	0.211 m/s	0.186 m/s
	centre	0.257 m/s	0.283 m/s	0.286 m/s	0.251 m/s
Radiation model disabled. QUICK differencing. Adiabatic walls. Uniform external temperature.	all	No available solution	No available solution	No available solution	No available solution
	centre	No available solution	No available solution	No available solution	No available solution
Radiation model enabled, $\alpha = 0.00m^{-1}$ QUICK differencing. Adiabatic walls. Uniform external temperature.	all	No available solution	0.254 m/s	0.257 m/s	0.243 m/s
	centre	No available solution	0.340 m/s	0.349 m/s	0.341 m/s
Radiation model enabled, $\alpha = 0.05m^{-1}$ QUICK differencing. Adiabatic walls. Uniform external temperature.	all	0.250 m/s	0.261 m/s	0.260 m/s	0.249 m/s
	centre	0.361 m/s	0.338 m/s	0.353 m/s	0.359 m/s
Radiation model enabled, $\alpha = 0.10m^{-1}$ QUICK differencing. Adiabatic walls. Uniform external temperature.	all	0.250 m/s	0.264 m/s	0.266 m/s	0.254 m/s
	centre	0.378 m/s	0.344 m/s	0.363 m/s	0.367 m/s
Radiation model enabled, $\alpha = 0.15m^{-1}$ QUICK differencing. Adiabatic walls. Uniform external temperature.	all	0.258 m/s	0.264 m/s	0.269 m/s	0.255 m/s
	centre	0.375 m/s	0.344 m/s	0.366 m/s	0.373 m/s

Width of opening:	0.8m
Effective area of opening:	$0.488m^2$
Heat source:	Boiler ring
Strength of heat source:	490.5W

Figure 25.a

	Area	Laminar	Standard-$k\varepsilon$	Realizable-$k\varepsilon$	RNG-$k\varepsilon$
Radiation model enabled, $\alpha = 0.00m^{-1}$ QUICK differencing. Convection walls. Uniform external temperature.	all	0.103 m/s	0.131 m/s	0.129 m/s	0.101 m/s
	centre	0.152 m/s	0.176 m/s	0.191 m/s	0.161 m/s
Radiation model enabled, $\alpha = 0.00m^{-1}$ QUICK differencing. Radiation walls. Uniform external temperature.	all	0.122 m/s	0.153 m/s	0.151 m/s	0.128 m/s
	centre	0.187 m/s	0.201 m/s	0.197 m/s	0.183 m/s
Radiation model enabled, $\alpha = 0.00m^{-1}$ QUICK differencing. Mixed walls. Uniform external temperature.	all	0.095 m/s	0.125 m/s	0.121 m/s	0.096 m/s
	centre	0.147 m/s	0.167 m/s	0.170 m/s	0.137 m/s
Radiation model enabled, $\alpha = 0.05m^{-1}$ QUICK differencing. Convection walls. Uniform external temperature.	all	0.145 m/s	0.154 m/s	0.156 m/s	0.142 m/s
	centre	0.205 m/s	0.209 m/s	0.208 m/s	0.214 m/s
Radiation model enabled, $\alpha = 0.05m^{-1}$ QUICK differencing. Radiation walls. Uniform external temperature.	all	0.160 m/s	0.173 m/s	0.172 m/s	0.160 m/s
	centre	0.223 m/s	0.235 m/s	0.252 m/s	0.234 m/s
Radiation model enabled, $\alpha = 0.05m^{-1}$ QUICK differencing. Mixed walls. Uniform external temperature.	all	0.138 m/s	0.148 m/s	0.149 m/s	0.137 m/s
	centre	0.202 m/s	0.202 m/s	0.207 m/s	0.203 m/s

Width of opening:	0.8m
Effective area of opening:	$0.488m^2$
Heat source:	Boiler ring
Strength of heat source:	490.5W

Figure 25.b

	Area	Laminar	Standard-$k\varepsilon$	Realizable-$k\varepsilon$	RNG-$k\varepsilon$
Radiation model disabled. Upwind differencing. Adiabatic walls. Uniform external temperature.	all	0.168 m/s	0.196 m/s	0.185 m/s	0.165 m/s
	centre	0.216 m/s	0.247 m/s	0.243 m/s	0.219 m/s
Radiation model disabled. QUICK differencing. Adiabatic walls. Uniform external temperature.	all	No available solution	No available solution	No available solution	No available solution
	centre	No available solution	No available solution	No available solution	No available solution
Radiation model enabled, $\alpha = 0.00m^{-1}$ QUICK differencing. Adiabatic walls. Uniform external temperature.	all	No available solution	0.235 m/s	0.234 m/s	0.229 m/s
	centre	No available solution	0.313 m/s	0.313 m/s	0.334 m/s
Radiation model enabled, $\alpha = 0.05m^{-1}$ QUICK differencing. Adiabatic walls. Uniform external temperature.	all	0.229 m/s	0.238 m/s	0.240 m/s	0.228 m/s
	centre	0.308 m/s	0.313 m/s	0.320 m/s	0.291 m/s
Radiation model enabled, $\alpha = 0.10m^{-1}$ QUICK differencing. Adiabatic walls. Uniform external temperature.	all	0.233 m/s	0.240 m/s	0.243 m/s	0.231 m/s
	centre	0.327 m/s	0.316 m/s	0.322 m/s	0.321 m/s
Radiation model enabled, $\alpha = 0.15m^{-1}$ QUICK differencing. Adiabatic walls. Uniform external temperature.	all	0.234 m/s	0.242 m/s	0.246 m/s	0.228 m/s
	centre	0.325 m/s	0.318 m/s	0.325 m/s	0.303 m/s

Width of opening:	1.0m
Effective area of opening:	$0.610m^2$
Heat source:	Boiler ring
Strength of heat source:	490.5W

Figure 26.a

	Area	Laminar	Standard-$k\varepsilon$	Realizable-$k\varepsilon$	RNG-$k\varepsilon$
Radiation model enabled, $\alpha = 0.00m^{-1}$ QUICK differencing. Convection walls. Uniform external temperature.	all	0.095 m/s	0.121 m/s	0.118 m/s	0.102 m/s
	centre	0.140 m/s	0.169 m/s	0.165 m/s	0.149 m/s
Radiation model enabled, $\alpha = 0.00m^{-1}$ QUICK differencing. Radiation walls. Uniform external temperature.	all	0.118 m/s	0.140 m/s	0.142 m/s	0.118 m/s
	centre	0.173 m/s	0.187 m/s	0.201 m/s	0.164 m/s
Radiation model enabled, $\alpha = 0.00m^{-1}$ QUICK differencing. Mixed walls. Uniform external temperature.	all	0.093 m/s	0.115 m/s	0.111 m/s	0.092 m/s
	centre	0.120 m/s	0.161 m/s	0.156 m/s	0.131 m/s
Radiation model enabled, $\alpha = 0.05m^{-1}$ QUICK differencing. Convection walls. Uniform external temperature.	all	0.133 m/s	0.144 m/s	0.146 m/s	0.134 m/s
	centre	0.191 m/s	0.196 m/s	0.202 m/s	0.181 m/s
Radiation model enabled, $\alpha = 0.05m^{-1}$ QUICK differencing. Radiation walls. Uniform external temperature.	all	0.152 m/s	0.161 m/s	0.163 m/s	0.152 m/s
	centre	0.226 m/s	0.213 m/s	0.224 m/s	0.204 m/s
Radiation model enabled, $\alpha = 0.05m^{-1}$ QUICK differencing. Mixed walls. Uniform external temperature.	all	0.129 m/s	0.138 m/s	0.139 m/s	0.129 m/s
	centre	0.178 m/s	0.188 m/s	0.196 m/s	0.176 m/s

Width of opening:	1.0m
Effective area of opening:	$0.610m^2$
Heat source:	Boiler ring
Strength of heat source:	490.5W

Figure 26.b

	Area	Laminar	Standard-$k\varepsilon$	Realizable-$k\varepsilon$	RNG-$k\varepsilon$
Radiation model disabled. Upwind differencing. Adiabatic walls. Uniform external temperature.	all	0.149 m/s	0.179 m/s	0.180 m/s	0.148 m/s
	centre	0.193 m/s	0.218 m/s	0.228 m/s	0.162 m/s
Radiation model disabled. QUICK differencing. Adiabatic walls. Uniform external temperature.	all	No available solution	No available solution	No available solution	No available solution
	centre	No available solution	No available solution	No available solution	No available solution
Radiation model enabled, $\alpha = 0.00m^{-1}$ QUICK differencing. Adiabatic walls. Uniform external temperature.	all	No available solution	0.213 m/s	0.215 m/s	0.206 m/s
	centre	No available solution	0.279 m/s	0.285 m/s	0.300 m/s
Radiation model enabled, $\alpha = 0.05m^{-1}$ QUICK differencing. Adiabatic walls. Uniform external temperature.	all	0.216 m/s	0.219 m/s	0.222 m/s	0.212 m/s
	centre	0.279 m/s	0.285 m/s	0.293 m/s	0.284 m/s
Radiation model enabled, $\alpha = 0.10m^{-1}$ QUICK differencing. Adiabatic walls. Uniform external temperature.	all	0.217 m/s	0.222 m/s	0.225 m/s	0.214 m/s
	centre	0.308 m/s	0.288 m/s	0.296 m/s	0.289 m/s
Radiation model enabled, $\alpha = 0.15m^{-1}$ QUICK differencing. Adiabatic walls. Uniform external temperature.	all	0.217 m/s	0.224 m/s	0.228 m/s	0.217 m/s
	centre	0.284 m/s	0.290 m/s	0.299 m/s	0.292 m/s

Width of opening:	1.2m
Effective area of opening:	$0.732m^2$
Heat source:	Boiler ring
Strength of heat source:	490.5W

Figure 27.a

	Area	Laminar	Standard-$k\varepsilon$	Realizable-$k\varepsilon$	RNG-$k\varepsilon$
Radiation model enabled, $\alpha = 0.00m^{-1}$ QUICK differencing. Convection walls. Uniform external temperature.	all	0.096 m/s	0.114 m/s	0.113 m/s	0.091 m/s
	centre	0.130 m/s	0.154 m/s	0.156 m/s	0.136 m/s
Radiation model enabled, $\alpha = 0.00m^{-1}$ QUICK differencing. Radiation walls. Uniform external temperature.	all	0.113 m/s	0.133 m/s	0.133 m/s	0.114 m/s
	centre	0.151 m/s	0.177 m/s	0.195 m/s	0.151 m/s
Radiation model enabled, $\alpha = 0.00m^{-1}$ QUICK differencing. Mixed walls. Uniform external temperature.	all	0.086 m/s	0.107 m/s	0.108 m/s	0.088 m/s
	centre	0.124 m/s	0.147 m/s	0.151 m/s	0.121 m/s
Radiation model enabled, $\alpha = 0.05m^{-1}$ QUICK differencing. Convection walls. Uniform external temperature.	all	0.128 m/s	0.136 m/s	0.134 m/s	0.130 m/s
	centre	0.180 m/s	0.181 m/s	0.207 m/s	0.164 m/s
Radiation model enabled, $\alpha = 0.05m^{-1}$ QUICK differencing. Radiation walls. Uniform external temperature.	all	0.142 m/s	0.151 m/s	0.154 m/s	0.145 m/s
	centre	0.200 m/s	0.200 m/s	0.231 m/s	0.192 m/s
Radiation model enabled, $\alpha = 0.05m^{-1}$ QUICK differencing. Mixed walls. Uniform external temperature.	all	0.124 m/s	0.131 m/s	0.128 m/s	0.124 m/s
	centre	0.173 m/s	0.174 m/s	0.194 m/s	0.155 m/s

Width of opening:	1.2m
Effective area of opening:	$0.732m^2$
Heat source:	Boiler ring
Strength of heat source:	490.5W

Figure 27.b